Volume 65
Number 5, 1997

International Journal of

QUANTUM CHEMISTRY

Editor-in-Chief
PER-OLOV LÖWDIN

Editors
ERKKI BRÄNDAS
YNGVE ÖHRN

Associate Editors
OSVALDO GOSCINSKI
STEN LUNELL
JOHN R. SABIN
MICHAEL C. ZERNER

DISTRIBUTION STATEMENT A
Approved for public release;
Distribution Unlimited

Proceedings of the
International Symposium on

Atomic, Molecular, and Condensed Matter Theory and Computational Methods

Held at the Ponce de Leon Resort,
St. Augustine, Florida, March 1–7, 1997

Editor-in-Chief: Per-Olov Löwdin
Special Editors: Yngve Öhrn
John R. Sabin
Michael C. Zerner

19980210 101

DTIC QUALITY INSPECTED 8

A Wiley-Interscience Publication
John Wiley & Sons, Inc.

ISSN 0020-7608

International Journal of

Quantum Chemistry

Editor-in-Chief

Per-Olov Löwdin
University of Florida at Gainesville, USA
Uppsala University, Sweden

Editors

Erkki Brändas
Uppsala University, Sweden
Yngve Öhrn
University of Florida at Gainesville, USA

Associate Editors

Osvaldo Goscinski
Uppsala University, Sweden
Sten Lunell
Uppsala University, Sweden
John R. Sabin
University of Florida at Gainesville, USA
Michael C. Zerner
University of Florida at Gainesville, USA

Honorary Editors

Gerhard Herzberg
National Research Council, Ottawa, Ontario, Canada
Kenichi Fukui
Institute for Fundamental Chemistry at Kyoto, Japan
Jerome Karle
Naval Research Laboratory at Washington, DC, USA
Rudy Marcus
California Institute of Technology at Pasadena, USA

Editorial Board

Jiri Čížek
University of Waterloo, Ontario, Canada
Enrico Clementi
Université Louis Pasteur, Strasbourg, France
Raymond Daudel
Académie Européene de Arts, des Sciences et des Lettres, Paris, France
Ernest Davidson
Indiana University at Bloomington, USA
George G. Hall
University of Nottingham, UK
Laurens Jansen
Kusnacht, Switzerland
Norman H. March
University of Oxford, UK
Roy McWeeny
Università di Pisa, Italy
Saburo Nagakura
Graduate University for Advanced Studies, Yokohama, Japan
Kimio Ohno
Hokkaido Information University, Japan
Josef Paldus
University of Waterloo, Ontario, Canada
Robert G. Parr
University of North Carolina at Chapel Hill, USA
Ruben Pauncz
Technion, Haifa, Israel
John A. Pople
Northwestern University at Evanston, Illinois, USA
Alberte Pullman
Institut de Biologie Physico-Chimique, Paris, France
Paul von Ragué Schleyer
Universität Erlangen-Nürnberg, Erlangen, Germany
Harrison Shull
Naval Postgraduate School, Monterey, California, USA
Tang Au-Chin
Jilin University, Changchun, China
Rudolf Zahradník
Czech Academy of Sciences, Prague, Czech Republic

Advisory Editorial Board

Teijo Åberg
Helsinki University of Technology, Espoo, Finland
Michail V. Basilevsky
Karpov Institute of Physical Chemistry, Moscow, Russia
Axel D. Becke
Queen's University, Kingston, Ontario, Canada
Gian Luigi Bendazzoli
Università di Bologna, Italy
Geza Biczo
Hungarian Academy of Sciences, Budapest, Hungary
Jerzy Cioslowski
The Florida State University at Tallahassee, USA
Timothy Clark
Universität Erlangen-Nürnberg, Germany
Giorgina Corongiu
Centro di Richerche, Sviluppo e Studi Superiori in Sardegna, Cagliari, Italy
Mireille Defranceschi
DPEL/SERGD/LMVT, Fontenay Aux Roses, France
Karl F. Freed
The University of Chicago, Illinois, USA
Peter Fulde
Max-Planck-Institut für Physik Komplexer Systeme, Dresden, Germany
Odd Gropen
University of Tromsø, Norway
Trygve Helgaker
University of Oslo, Norway
Ming-Bao Huang
Academia Sinica, Beijing, People's Republic of China
James T. Hynes
University of Colorado at Boulder, USA
Mu Shik Jhon
Korea Advanced Institute of Science and Technology, Seoul, Korea
Hiroshi Kashiwagi
Kyushu Institute of Technology, Fukuoka, Japan
Peter A. Kollman
University of California at San Francisco, USA
Eugene S. Kryachko
Academy of Sciences of Ukraine, Kiev, Uki
Sven Larsson
Chalmers University of Technology, Gothenburg, Sweden
Lucas Lathouwers
Universitair Centrum (RUCA), Antwerp, Be
Shyi-Long Lee
National Chung Chang University, Taiwan, Republic of China
Claude Leforestier
Université Paris-Sud, Orsay, France
Josef Michl
University of Colorado at Boulder, USA
Nimrod Moiseyev
Israel Institute of Technology, Israel
John D. Morgan III
University of Delaware at Newark, USA
Cleanthes A. Nicolaides
National Hellenic Research Foundation, Gr
J. Vincent Ortiz
Kansas State University at Manhattan, US
Lars Pettersson
University of Stockholm, Sweden
Leon Phillips
University of Canterbury, Christchurch, New Zealand
Martin Quack
ETH Zürich, Switzerland
Leo Radom
Australian National University, Australia
William Reinhardt
University of Washington at Seattle, USA
Sten Rettrup
H. C. Ørsted Institut, Copenhagen, Denmar
C. Magnus L. Rittby
Texas Christian University at Fort Worth, US
Michael Robb
King's College, London, UK
Mary Beth Ruskai
University of Massachusetts at Lowell, US
Harold Scheraga
Cornell University at Ithaca, New York, US
Vipin Srivastava
University of Hyderabad, India
Nicolai F. Stepanov
Moscow State University, Russia
Jiazong Sun
Jilin University, Changchun, People's Republic of China
Colin Thomson
University of St. Andrews, Scotland, UK
Donald G. Truhlar
University of Minnesota at Minneapolis, US
Frank Weinhold
University of Wisconsin at Madison, USA
Harel Weinstein
Mount Sinai School of Medicine, New York, USA
Peter Wolynes
University of Illinois at Urbana, USA
Robert E. Wyatt
The University of Texas at Austin, USA

Editorial Production, John Wiley & Sons: Sheila Kaminsky

UNIVERSITY OF
FLORIDA

Sanibel Symposium

PO Box 118435
Gainesville, FL 32611-8435
(352) 392-1597
Fax: (352) 392-8722

February 6, 1998

Scientific Officer Code: 331
Parbury P. Schmidt
Office of Naval Research
800 North Quincy Street
Arlington, VA 22217–5660

Dear Dr. Schmidt:

I enclose three copies of the 1997 Sanibel Symposium Proceedings on Atomic, Molecular, and Condensed Matter Theory and Computational Methods, which will serve as the Final Report for the Office of Naval Research Grant Number N00014–97–1–0320. The University of Florida number is 4910 5741 430–16, with Yngve Öhrn as P.I.

We thank you for your support of the 1997 Sanibel Symposium and look forward to seeing you again.

If I can be of any further assistance, please do not hesitate to call.

Sincerely,

Judy Parker
Office Manager

/jp

Enclosure: 3 Proceedings
cc: Grant Administrator and 1 copy Proceedings
Defense Technical Information Center and 1 copy Proceedings
Division of Sponsored Research
Contracts & Grants

R.J. Bartlett • H.-P. Cheng • E. Deumens • J.L. Krause • P.-O. Löwdin • D.A. Micha
H.J. Monkhorst • N.Y. Öhrn • J.R. Sabin • S.B. Trickey • M.C. Zerner
Equal Opportunity/Affirmative Action Institution

International Journal of QUANTUM CHEMISTRY

Quantum Chemistry Symposium No. 31

Proceedings of the International Symposium on

Atomic, Molecular, and Condensed Matter Theory and Computational Methods

Held at Ponce de Leon Resort, St. Augustine, Florida, March 1–March 7, 1997

Editor-in-Chief: Per-Olov Löwdin
Special Editors: Yngve Öhrn, John R. Sabin, and Michael C. Zerner

DTIC QUALITY INSPECTED 5

an Interscience® Publication
published by JOHN WILEY & SONS

The *International Journal of Quantum Chemistry* (ISSN 0020-7608) is published semimonthly with one extra issue in January, March, May, July, August, and November by John Wiley & Sons, Inc., 605 Third Avenue, New York, New York 10158.

Copyright © 1997 John Wiley & Sons, Inc. All rights reserved. No part of this publication may be reproduced in any form or by any means, except as permitted under section 107 or 108 of the 1976 United States Copyright Act, without either the prior written permission of the publisher, or authorization through the Copyright Clearance Center, 222 Rosewood Drive, Danvers, MA 01923, (508) 750-8400, fax (508) 750-4470. Periodicals postage paid at New York, NY, and at additional mailing offices.

The code and the copyright notice appearing at the bottom of the first page of an article in this journal indicate the copyright owner's consent that copies of the article may be made for personal or internal use, or for the personal or internal use of specific clients, on the condition that the copier pay for copying beyond that permitted by Sections 107 or 108 of the US Copyright Law.

This consent does not extend to the other kinds of copying, such as copying for general distribution, for advertising or promotional purposes, for creating new collective work, or for resale. Such permission requests and other permission inquiries should be addressed to the Permissions Dept.

Subscription price (Volumes 61–65, 1997): $3,860.00 in the US, $4,160.00 in Canada and Mexico, $4,355.00 outside North America. All subscriptions outside US will be sent by air. Personal rate (available only if there is an institutional subscription): $190.00 in North America, $370.00 outside North America. Subscriptions at the personal rate are available only to individuals. Payment must be made in US dollars drawn on a US bank. Claims for undelivered copies will be accepted only after the following issue has been received. Please enclose a copy of the mailing label. Missing copies will be supplied when losses have been sustained in transit and where reserve stock permits.

Please allow four weeks for processing a change of address. For subscription inquiries, please call (212) 850-6645; e-mail: SUBINFO@Wiley.com.

Postmaster: Send address changes to *International Journal of Quantum Chemistry,* Susan Swanson, Director, Subscription Fulfillment and Distribution, Subscription Department, John Wiley & Sons, Inc., 605 Third Avenue, New York, NY 10158.

Advertising Sales: Inquiries concerning advertising should be forwarded to Susan Levey, Advertising Sales, John Wiley & Sons, Inc., 605 Third Avenue. New York, NY 10158; (212) 850-8832. Advertising Sales, European Contact: Michael Levermore, Advertising Manager, John Wiley & Sons, Ltd., Baffins Lane, Chichester, Sussex PO 19 1UD, England.

Reprints: Reprint sales and Inquiries should be directed to the customer service department, John Wiley & Sons, Inc. 605 Third Ave., New York, NY 10158. Tel: 212-850-8776.

Manuscripts should be submitted in triplicate and accompanied by an executed Copyright Transfer Form to the Editorial Office, *International Journal of Quantum Chemistry,* Quantum Chemistry Group, Uppsala University, Box 518, S-75120, Uppsala, Sweden. Authors may also submit manuscripts to the Editorial Office, *International Journal of Quantum Chemistry,* Quantum Theory Project, Williamson Hall, University of Florida, Gainesville, Florida 32611. **Information for Contributors** appears in the first and last issue of each volume. **All other correspondence** should be addressed to the *International Journal of Quantum Chemistry,* Publisher, Interscience Division, Professional, Reference, and Trade Group, John Wiley & Sons, Inc., 605 Third Avenue, New York, NewYork 10158, U.S.A. The contents of this journal are indexed or abstracted in *Chemical Abstracts, Chemical Titles, Chemical Database, Current Contents/Physical, Chemical, and Earth Sciences, Research Alert (ISI), Science Citation Index (ISI),* and *SCISEARCH Database (ISI).*

This paper meets the requirements of ANSI/NISO Z39. 48–1992 (Permanence of Paper). ♾

International Journal of
Quantum Chemistry
Volume 65
Number 5, December 5, 1997

Contents

Introduction
N. Y. Öhrn, J. R. Sabin, and M. C. Zerner **377**

Foundations of Quantum Mechanics: Building on von Neumann's Heritage
G. G. Emch **379**

Does Quantum Probability Predict Frequency?
W. G. Faris **389**

Nonrigid Systems in Chemistry: A Unified View
M. E. Kellman **399**

Kinetic Energy Functional Derivative for the Thomas–Fermi Atom in *D* Dimensions
N. H. March and S. Kais **411**

On Computing the Molecular Detour Matrix
N. Trinajstić, S. Nikolić, and Z. Mihalić **415**

Many-Body Valence-Bond Theory
D. J. Klein, H. Zhu, R. Valenti, and M. A. Garcia-Bach **421**

Fully Variational Optimization of Modern VB Wave Functions Using the CASVB Strategy
D. L. Cooper, T. Thorsteinsson, and J. Gerratt **439**

Density-Functional Method for Very Large Systems with LCAO Basis Sets
D. Sánchez-Portal, P. Ordejón, E. Artacho, and J. M. Soler **453**

Comparison of Electron Propagator Methods for Calculating Electron Detachment Energies of Anions
O. Dolgounitcheva, V. G. Zakrzewski, and J. V. Ortiz **463**

(continued)

Finite Temperature Ab Initio Calculation by Path Integral Monte Carlo Method
H. Kawabe, K. Kodama, H. Nagao, and K. Nishikawa **471**

Real-Space Multigrid Solution of Electrostatics Problems and the Kohn–Sham Equations
T. L. Beck **477**

Floquet Quasi-Energies and Eigenfunctions of the Parabolic Barrier
R. Lefebvre and A. Palma **487**

Maximum Principles in DFT from Reciprocal Variational Problem
K. Tkacz-Śmiech and W. S. Ptak **499**

Exact Numerical Calculations of Dissociative-Ionization of Molecular Ions in Intense Laser Fields: Non-Born–Oppenheimer Dynamics
S. Chelkowski, C. Foisy, and A. D. Bandrauk **503**

A Quadrature Formula for Correlation Integrals
S.-T. Dai and P. Winkler **513**

Shape Transitions in Polymer Mushrooms Compressed by a Finite-Size Obstacle
G. A. Arteca **519**

Real-Space Multigrid Methods for Large-Scale Electronic Structure Problems
J. Bernholc, E. L. Briggs, D. J. Sullivan, C. J. Brabec, M. B. Nardelli, K. Rapcewicz, C. Roland, and M. Wensell **531**

Relativistic Many-Body Perturbation Calculations for Zn and Cd and Their Singly Ionized Ions
Y. Ishikawa and K. Koc **545**

Hyperfine Structure Constants of $(d + s)^3$ States in La I and the Zr II and Hf II Isoelectronic Sequences
D. R. Beck **555**

Scalar-Relativistic LCGTO DFT Calculations for Atoms Using the Douglas–Kroll Transformation
J. C. Boettger **565**

Correlated Relativistic Calculation of the Giant Resonance in the Gd^{3+} Absorption Spectrum
S. Kotochigova, H. Levine, and I. Tupitsyn **575**

(continued)

Effective Potential for *e*-Atom Scattering by DCS Minimization at Intermediate Energies
J. M. Paikeday **585**

Low-Energy Electron Scattering from a Model H_2 Potential Using Finite Elements in Two Dimensions
C. A. Weatherford, M. Dong, and B. C. Saha **591**

Scattering by a Potential Separable in Ellipsoidal Coordinates
T. Levitina and E. J. Brändas **601**

Transannular Interactions in S_8^{2+} and Se_8^{2+}: Reality or Artifact?
J. Cioslowski and X. Gao **609**

Laser-Induced Alignment Dynamics in Multiphoton Dissociation of H_2^+
O. Atabek **617**

An Ab Initio Study of Oxygen Vacancies and Doping Process of Nb and Cr Atoms on TiO_2 (110) Surface Models
J. R. Sambrano, J. Andrés, A. Beltrán, F. R. Sensato, E. R. Leite, F. M. L. G. Stamato, and E. Longo **625**

Ab Initio Calculations of the Magnetic Exchange Coupling in Sulfur-Bridged Binuclear Ni(II) Complexes
K. Fink, C. Wang, and V. Staemmler **633**

Reaction Path for the Insertion Reaction of $SnCl_2$ into the Pt—Cl Bond: An Ab Initio Study
W. R. Rocha and W. B. De Almeida **643**

Study of Ground and Excited States of Doped Polyacetylene
G. P. Das and D. S. Dudis **651**

Free and Hindered Rotations in Endohedral C_{60} Fullerene Complexes
J. Hernández-Rojas, A. Ruiz, J. Bretón, and J. M. Gomez Llorente **655**

Calculation of Frequency-Dependent Polarizabilities for Open-Shell Systems at the Second-Order Møller–Plesset Perturbation Theory Level Based on the Quasi-Energy Derivative Method
T. Kobayashi, K. Sasagane, and K. Yamaguchi **665**

Electron Correlation Effects upon the Static (Hyper)polarizabilities of Push-Pull Conjugated Polyenes and Polyynes
D. Jacquemin, B. Champagne, and J.-M. André **679**

(continued)

Vibrational Versus Electronic First Hyperpolarizabilities of Mono- and Disubstituted Benzenes: An Ab Initio Coupled Hartree–Fock Investigation
B. Champagne **689**

Theoretical Studies of Second Hyperpolarizability by Path Integral Method: Effects of External Magnetic Field
H. Nagao, K. Ohta, M. Nakano, and K. Yamaguchi **697**

C—H ··· O and N—H ··· O Hydrogen Bonds in Liquid Amides Investigated by Monte Carlo Simulation
J. M. M. Cordeiro **709**

Understanding the Mechanism of the Addition of Organomagnesium Reagents to 2-Hydroxypropanal: An Ab Initio Molecular Orbital Analysis
M. Oliva, V. S. Safont, J. Andrés, R. Castillo, and V. Moliner **719**

A Semiempirical Study on the Ring-Opening Process for the Cyclopropanone, 2, 2-Dimethylcyclopropanone, *trans*-2,3-Di-*tert*-Butylcyclopropanone, and Spiro(bicyclo[2.2.1]heptane-2.1'-cyclopropan)-2'-one Systems in Solution
R. Castillo, J. Andrés, V. Moliner, V. S. Safont, and M. Oliva **729**

Ab Initio Studies on the Ziegler–Natta Polymerization Mechanisms of Ethylene and Propylene. Role of Cocatalysis and Stereoregulation
S. Sakai **739**

Systematic Study of the Lowest Energy States of Au_n ($n = 1$–4) Using DFT
J. M. Seminario and J. M. Tour **749**

Ab Initio Prediction of the Geometry and IR Frequencies of the Mono- and Dihydrated Complexes of the Oxo-amino-Tautomers of Guanine
L. Gorb and J. Leszczynski **759**

A Molecular Orbital Study of the Dimerization Process of Vinyl Monomers
M. A. Mora **767**

CASSCF, MP2, and CASMP2 Studies on Addition Reaction of Singlet Molecular Oxygen to Ethylene Molecule
Y. Yoshioka, T. Tsunesada, K. Yamaguchi, and I. Saito **787**

Quantum Chemical Study of the Molecular Dynamics of Hydrated Li^+ and Be^{2+} Cations
G. Bischof, A. Silbernagl, K. Hermansson, and M. Probst **803**

(continued)

Vibrational Analysis of $TeCl_4$. II. A Hartree–Fock, MP2, and Density Functional Study
A. Kovács and G. I. Csonka **817**

Computation of Vibrational Frequencies for Adsorbates on Surfaces
J. D. Head **827**

Theoretical Studies on the Catalytic Activity of Ag Surface for the Oxidation of Olefins
H. Nakatsuji, Z.-M. Hu, and H. Nakai **839**

Simulations of Laser-Assisted Field Emission Within the Local Density Approximation of Kohn–Sham Density-Functional Theory
M. J. Hagmann **857**

Theoretical Calculation of Carbon Clusters
E. A. Valdes, P. De La Mora, M. Castro, and J. Keller **867**

Spin-Averaged Hartree–Fock Procedure for Spectroscopic Calculations: The Absorption Spectrum of Mn^{2+} in ZnS Crystals
K. K. Stavrev and M. C. Zerner **877**

Calculation of the Absorption Spectrum of Benzene in Condensed Phase. A Study of the Solvent Effects
K. Coutinho, S. Canuto, and M. C. Zerner **885**

Structure of the Correlation–Kinetic Component of the Kohn–Sham Exchange Potential in Atoms and at Metal Surfaces
A. Solomatin and V. Sahni **893**

Forces Between Atoms and Atomic Planes in Condensed Metallic Phases and in Semiconducting Silicon
N. H. March **907**

A Theoretical Study of the Electronic Structure of Transition-Element Carbides M_nC (M = Fe, Ni, Cu, $n = 1, 5$; and M = Ti, $n = 1, 7$) and Their Interactions with an O Atom by DFT Methods
R. M. Sosa, P. Gardiol, and G. Beltrame **919**

Density Matrix Methods for Semiconductor Coulomb Dynamics
J. W. Dufty, C. S. Kim, M. Bonitz, and R. Binder **929**

Electronic and Structural Properties of Defects in c-BN
R. Mota, P. Piquini, T. M. Schmidt, and A. Fazzio **941**

(continued)

Possibilities of Charge- and/or Spin-Mediated Superconductors and Photo-Induced Superconductors in the Intermediate Region of Metal–Insulator Transitions
H. Nagao, M. Mitani, M. Nishino, Y. Yoshioka, and K. Yamaguchi **947**

Two Novel Applications of Shepard-Type Interpolation for Polyatomic Systems: Reduced Dimensionality HOCO and Full Dimensionality Ar-HCO
F. N. Dzegilenko, J. Qi, and J. M. Bowman **965**

Density Functional Cluster Description of Ionic Materials: Improved Boundary Conditions for MgO Clusters with the Help of Cation Model Potentials
I. V. Yudanov, V. A. Nasluzov, K. M. Neyman, and N. Rösch **975**

Late Transition-Metal Multiple Bonding: Platinum Phosphinidenes and Ruthenium Alkylidenes
M. T. Benson and T. R. Cundari **987**

Bethe–Bloch Stopping Power Parameters for Polystyrene, Kapton, and Mylar
L. E. Porter **997**

List of Participants **1005**

Introduction

The 37th Annual Sanibel Symposium, organized by the faculty, students, and staff of the Quantum Theory Project of the University of Florida, was held on March 1–7, 1997. The meeting was again held at the Ponce de Leon Conference Center in St. Augustine, Florida. More than 300 participants gathered for seven days of lectures and informal discussions.

The symposium followed the established format with plenary and poster sessions. This year, the schedule was shortened somewhat with a compact seven-day integrated program of quantum biology, quantum chemistry, and condensed matter physics. The topics of the sessions covered by these proceedings include Density Functional Theory (DFT) and Applications, DFT for Intermolecular Forces, Clusters and Nanostructures, Theory of Floppy Molecules, Exotic Anions, Theoretical Inorganic Chemistry, Foundations of Quantum Mechanics, Non-Linear Optics, Quantum-Classical Molecular Dynamics, and Industrial Application.

The articles have been subjected to the ordinary refereeing procedures of the *International Journal of Quantum Chemistry*. The articles presented in the sessions on quantum biology and associated poster sessions are published in a separate issue of the *International Journal of Quantum Chemistry*.

The organizers acknowledge the following sponsors for their support of the 1997 Sanibel Symposium:

- Army Research Office and U. S. Army Edgewood RD & E Center through Grant #DAAG55-97-1-0020:

  "The views, opinions, and/or findings contained in this report are those of the author(s) and should not be construed as an official Department of the Army position, policy, or decision, unless so designated by other documentation."
- The Office of Naval Research through Grant #N00014-97-1-0320:

  "This work relates to Department of the Navy Grant #N00014-97-1-0320 issued by the Office of Naval Research. The United States Government has the royalty-free license throughout the world in all copyrightable material contained herein."
- IBM Corporation.
- HyperCube, Inc.
- Silicon Graphics.
- The University of Florida.

Very special thanks go to the staff of the Quantum Theory Project of the University of Florida for handling the numerous administrative, clerical, and practical details. The organizers are proud to recognize the contributions of Mrs. Judy Parker, Ms. Sharon Stellato, Ms. Sandra Weakland, and Mr. Greg Pearl. All the graduate students of the Quantum Theory Project, who served as "gofers," are gratefully recognized for their contributions to the 1997 Sanibel Symposium.

N. Y. Öhrn
J. R. Sabin
M. C. Zerner

International Journal of Quantum Chemistry, Vol. 65, 377 (1997)
© 1997 John Wiley & Sons, Inc.
CCC 0020-7608 / 97 / 050377-01

Foundations of Quantum Mechanics: Building on von Neumann's Heritage

GÉRARD G. EMCH
Department of Mathematics, University of Florida, Gainesville, Florida 32611-8105

Received 28 March 1997; accepted 10 April 1997

ABSTRACT: From 1927 to 1943, the mathematical and conceptual foundations of quantum mechanics, and their prolongations into the formulation of statistical mechanics, were either the direct subject of or one of the primary motivations for several publications by von Neumann. We contrast the reception received by the work done during the first 5 years (1927–1932) and that received by the monumental mathematical constructs wrought in the second period (1934–1943); we describe how the latter were to lead to the elaboration of a formalism generalizing the fundamental structures of quantum mechanics so that they can encompass and deal consistently with situations typical of the quantum many-body problems of statistical mechanics. © 1997 John Wiley & Sons, Inc. Int J Quant Chem **65:** 379–387, 1997

Introduction

Von Neumann died almost exactly 40 years ago (February 8, 1957). A mathematician had passed away, who—like Poincaré and Gauss before him—had contributed to such a vast array of mathematical endeavors that it is a trite question to ask whether he was of a pure or applied persuasion. Every participant in this symposium is aware of the impact von Neumann has left upon the methods that we rely on in our everyday scientific activities; to wit: his 1932 book is still recognized today as one of the landmarks one can turn to for a concise formulation of the foundations of quantum mechanics; and the computer, which he created, is an evermore powerful investigative tool that is pervasive in the present company. It seems therefore proper to pay him homage here, not only for his having enabled us to cultivate our field so intensively, but chiefly for having opened the fences of the quantum pastures toward the greater outdoors, as yet not fully surveyed.

1. The Familiar Landscape (1927–1932)

The first article [1] witnessing the interest von Neumann was to show in the foundations of quantum mechanics originated in a course given by Hilbert in Göttingen during the winter semester 1926/27; the notes were prepared by Nordheim, and we are told that von Neumann contributed "important parts" of the mathematical developments. One of the overt aims was to digest, mathematically and conceptually, the ideas of Jordan

International Journal of Quantum Chemistry, Vol. 65, 379–387 (1997)
© 1997 John Wiley & Sons, Inc.
CCC 0020-7608 / 97 / 050379-09

and of Dirac. The stimulating and very direct influence of the pioneering work of Heisenberg, Born, and Jordan is explicitly acknowledged from the very beginning of the article, while the last section is devoted to the Schrödinger equation. The synthesis is clearly on the making, *fusing into the theory of operators* acting on a Hilbert space the two forms of quantum mechanics which we now routinely recognize to be equivalent—as Schrödinger himself had pointed out only shortly before: the *algebraic formulation*, then called the "matrix-mechanics," of quantum theory (Heisenberg), and the *analytic formulation*, via partial-differential equations, the so-called "wave-mechanics" (Schrödinger).

The same year, von Neumann published three other articles on the foundations of quantum mechanics, its probabilistic background, and the thermodynamics of quantum mechanical ensembles [2–4]. His interest was also directed toward more specific problems, such as the quantum spectral properties of the electron [5–7]; a discussion of the extension of ergodic theory and the H-theorem to the "new mechanics" [8]; and several other articles as well, with ostensibly mathematical titles (e.g., [9]), witnessing to the fact that von Neumann was profoundly involved in trying to attack the mathematical (or conceptual) foundations of the theory from as many angles as possible.

1931 is the year of the theorem most universally attached to von Neumann's name in the physics community; it is the statement and the proof of the uniqueness of the Schrödinger representation [10]. Specifically, this theorem establishes the remarkable fact that if W^{2n+1} denotes the group generated by exponentiating the position and momentum to obtain the Weyl form of the CCR (canonical commutation relations) then W^{2n+1} has *exactly one* irreducible representation, the one found by Schrödinger. In the spirit of the early 1930s, this result is worth comparing with the richness of the inequivalent irreducible representations that were known to exist for most of the other groups used in physics; in particular, spectroscopists knew how to exploit the fact that the rotation group in three dimensions has as many irreducible representations as there are complex, finite-dimensional vector spaces. By contrast, von Neumann's uniqueness theorem is why we can teach quantum mechanics and start by telling our students that the momentum and position operators are *canonically* realized as differentiation $(P_k\Psi)(x) = -i(\partial_{x_k}\Psi)(x)$, and as multiplication $(Q_k\Psi)(x) = x_k\Psi(x)$, with $k = 1, 2, \ldots, n$, where Ψ are elements of the Hilbert space $\mathscr{L}^2(\mathbf{R}^n, \mathbf{C})$, i.e., are complex-valued functions, defined on the configuration space $\mathbf{R}^n$, and assumed to be square-integrable with respect to the Lebesgue measure.

Finally, the culminating achievement arrived with the epoch-marking *Mathematische Grundlagen der Quantenmechanik* [11]. I often wondered why this jewel saw its first English translation only in 1955; was this simply due to the towering preeminence of Dirac's book, or could it be a reflection from the forced emigration to the United States of so many of the scientists who were conversant with the subject matter in the original language? In the meantime, translation or not, von Neumann's book certainly became for a large part of the physics community *the* standard reference on the conceptual, as well as the mathematical, foundations of quantum mechanics (QM). In particular, its introduction of the *density matrix*, rather than the wave function, as the fundamental concept for a quantum mechanical state is quite remarkable; the discussion of the "measuring process" inscribed there is both compelling and so profoundly unsatisfactory that it created a semantic controversy that has not yet really abated; the task of elucidating the problems involved in the elusive interpretation of the quantum measuring process has benefited, in particular, from the sustained attention of Wigner, who was in a position to add to his own penetrating reflections [12], the authority of his lifelong friendship with von Neumann.

As far as the treatment of the mechanics of quantum systems with *finitely many degrees of freedom* is concerned, the formulation of scattering theory seems to be the only postwar conceptual and mathematical development not anticipated in von Neumann's book. This lacuna has now been tended to in [13] (see also its predecessor [14]), and it can be fairly said that this did not require any drastic reconsiderations of the conceptual mold in which von Neumann's book had cast QM.

Indeed, after the publication of von Neumann's book, most physicists had apparently every reason to "know" that the *observables* of QM are the self-adjoint operators acting in a fixed Hilbert space; that the *states* are the density matrices associated to this Hilbert space; and that this representation is uniquely determined by the configuration space of the system to be considered.

Well, almost every reason, as we shall now see.

2. Two Brief Excursions (1934–1936)

It is commonly acknowledged that somewhere around the turn of the 1930s, something went tangy in quantum physics. A perception might have appeared according to which the success of quantum spectroscopy in atomic and molecular physics was not going to carry smoothly over to quantum electrodynamics. The rather difficult upbringing of the still impetuous quantum field theory might indeed have suggested that the principles and/or the formalism were not quite right. For instance, in an article that we shall briefly review later in this section [15], we read of an alternate "suitable starting point for a generalization of the present quantum mechanical theory. The need of such a generalization arises from the (probably) fundamental difficulties resulting when one attempts to apply quantum mechanics to questions in relativistic and nuclear phenomena."

While the above were powerful physical motivations indeed, it seems that it was also for reasons of a different order that von Neumann became dissatisfied with the foundations of QM. In one of his other modes of operation, he had mingled mightily into the foundations of pure mathematics; even to us, it is clear that the foundations of quantum physics were not on a footing acceptable to the likes of Hilbert, nor were they on par with Kolmogorov's axiomatization of probability theory. Note incidentally that von Neumann had himself contributed also to the allied field of mathematics called measure theory. Therefore, von Neumann's reasons to probe further into the foundations of quantum physics participated significantly from longings ambient in the mathematical community.

Yet, one does not need to indulge in much guessing or tentative reconstructions of his deepest motivations: the published record shows that von Neumann decided to concentrate his quest, at first, on analyzing the necessity of Hilbert spaces in the formulation of quantum theory.

The first excursion in this direction is [15], from which the above quote was taken. It is the predecessor of the modern algebraic approach. The purpose was to focus on the set of observables and thus to try to abstract the structure of the set $\mathscr{B}_{sa}$ of all (bounded) self-adjoint operators, dispensing with the reference to an underlying Hilbert space. Since such operators do not necessarily commute, their products are not necessarily self-adjoint; and therefore do not necessarily belong to $\mathscr{B}_{sa}$; the substitute advanced in this article is to consider instead of the ordinary product, AB the symmetric product

$$A \circ B = \tfrac{1}{2}(AB + BA) = \tfrac{1}{2}[(A + B)^2 - A^2 - B^2].$$

While this product is clearly commutative, it is not associative; thus, $\mathscr{B}_{sa}$ points to the necessity of studying a new algebraic structure, which is now referred to as a *Jordan algebra.* The article pursued this new theory far enough to be able to classify all the "simple" *finite-dimensional* objects in this category. All of them, except one, are, in fact, the self-adjoint part of some matrix algebra, over the reals, the complex numbers, or the quaternions. These are called "special" Jordan algebras, to distinguish them from the "exceptional" one they had obtained, involving Caley numbers; the latter, however, has not yet found useful physical applications. Its interest is mostly to point to the existence of Jordan algebras that are not special. For many years, to determine whether a Jordan algebra is "special" (i.e., is the self-adjoint part of an associative algebra) was an open problem for infinite—dimensional Jordan algebras, even when these algebras are equipped with a norm; the answer [16] somewhat surprisingly was reduced to the question of whether a consistent orientability condition in the state space of these algebras is satisfied (for an elementary description of what is involved, see, for instance, pp. 378–381 in [17]).

Von Neumann's second excursion [18] in the direction of probing further the role of the Hilbert space formulation that he had described in [11] was to abstract the structure of the family L of all projectors on a Hilbert space or, equivalently, the structure of the set of its closed subspaces. Under the usual inclusion, one can define the intersection of two projectors as the largest projector contained in both of them and the union of two such projectors as the smallest projector containing them both. There is a smallest element, the zero projector, and a largest element, the identity map. Finally, a complementation is defined, attributing to every projector P the projector $I - P$, its orthogonal complement. The result of this description is that L is a complemented lattice, in much the same way as the collection of all measurable subsets (or their indicator functions) of a probability space is a

complemented lattice. There is, however, a major difference: the latter is Boolean, i.e., the intersection and union enjoy the familiar distributive relations. This property is not true for L, and this reflects an essential feature of QM, the noncommutativity of the operators acting on the Hilbert space. The question asked in [18] was how to characterize L intrinsically or, phrasing this in more physical terms, how to define abstractly the quantum equivalent of a classical probability space. Birkhoff and von Neumann only found a partial answer: an abstract property—called modularity—seemed to be a good substitute to replace the classical notion of distributivity; however, Birkhoff and von Neumann pointed out that this property is not sufficient to capture the structure of the set of *all* the projectors, since it is satisfied only when the Hilbert space if *finite-dimensional*, clearly not an acceptable restriction for the purpose of QM. A weakened version of modularity was found a quarter of century later [19]. In physical terms (i.e., here in purely lattice-theoretical terms), the weak modularity condition requires that if P implies Q (i.e., $P \subseteq Q$, or, equivalently, in the language of projections operators acting on a Hilbert space, $PQ = P$), then P and Q are compatible (i.e., the sublattice of L generated by P, Q, $P^{\perp}$, $Q^{\perp}$ is Boolean or, equivalently, in the operator language, $PQ = QP$). To obtain that this weak modularity characterizes the lattice of *all* projectors in a Hilbert space, one must add an atomicity condition exploiting the presence of minimal projections (also called "atoms" or "points"), a condition the omission of which led later to interesting structures von Neumann was to explore; see next section.

The lattice theoretical approach to QM captures enough of the fundamental structure of the theory that it is sufficient to define symmetries as automorphisms of L preserving its structure, in order to obtain—at long last—an elementary proof for the theorem by Wigner [20] according to which, in a Hilbert space formalism where *all* bounded self-adjoint operators correspond to physical observables, symmetries are implemented either by unitary or by antiunitary operators; for the proof, see [21], and for a critical assessment, [22] and references therein.

By 1936 therefore, one could hope that some useful information would be retrieved from the study of the algebra of observables or from the lattice of projections that generate this algebra; the main problem was to find the topological conditions allowing one to relax the conditions enough to encompass infinite-dimensional situations. This is a story for the next section.

3. The Great Outdoors (1936–Onwards)

Many problems that the traditional QM does not seem able to cope with in a consistent manner are related to the appearance of infinitely many (real or virtual) degrees of freedom. In the latter case, and in contrast with von Neumann's uniqueness theorem (see Section 2), we know [23], that the Fock space representation is only one among uncountably many inequivalent representations of the canonical commutation (or anticommutation) relations. We further know that the Fock representation is attached to the vacuum state and that it cannot accommodate the finite density of particles needed for many applications to statistical mechanics. A manifestation of this phenomenon was pointed out in connection with the gauge-symmetry breaking occurring in the BCS model for superconductivity [24].

The natural frame to collect these phenomena was prepared by Murray and von Neumann in a series of articles [25]. The mathematical strategy of these articles can be explained physically as a way to see QM as a generalization of classical mechanics in the following manner.

First, let us agree to view (a large class of) the observables in classical mechanics as (essentially) bounded functions on the classical phase space, mathematically a measure space (Ω, μ); for instance, μ could be the Lebesgue measure on the space $\mathbf{R}^{2n}$. These functions are the real elements of an algebra $\mathscr{A} = L^{\infty}_{C}(\Omega)$ that comes naturally equipped with an involution (here, the complex conjugation) and a norm satisfying $\|A^*A\| = \|A\|^2$. In modern terms, this is to say that $\mathscr{A}$ is a *C*-algebra*. Moreover, $\mathscr{A}$ is the dual of a Banach space, namely, the space $L^1(\Omega, \mu)$ of integrable functions on (Ω, μ). The latter property makes $\mathscr{A}$ what is called a *W*-algebra*. Note that the states on these classical systems are given by the positive elements ρ of $L^1(\Omega, \mu)$ that are normalized by requiring that their total weight is 1, so that $\rho\, d\mu$ is a probability measure. Hence, the expectation value of the observable A in the state ρ is given by $\langle \rho; A \rangle = \int A(\omega)\rho(\omega)\, d\mu$.

We can now take advantage of this perspective on *classical* mechanics to provide a natural link to

the formalism of *quantum* mechanics. Let us indeed represent the algebra $\mathscr{A}$ as the algebra of operators on $L^2(\Omega, \mu)$ operating by multiplication, i.e., for every vector $\Psi \in L^2(\Omega, \mu)$, the vector $A\Psi$ is defined by $(A\Psi)(\omega) = A(\omega)\Psi(\omega)$. It is easy to see that, in this representation,

$$\mathscr{A} = \mathscr{A}'$$
$$\text{where } \mathscr{A}' \equiv \{B \in \mathscr{B} \mid AB = BA \ \forall A \in \mathscr{A}\}. \quad (3.1)$$

This relation implies that

$$\mathscr{A} = \mathscr{A}'', \qquad \text{where } \mathscr{A}'' \equiv \{\mathscr{A}'\}'. \quad (3.2)$$

(In general, $\mathscr{A}'$ is called the *commutant* of $\mathscr{A}$, and $\mathscr{A}''$, the *bicommutant* of $\mathscr{A}$.) Hence, $\mathscr{A}$ is a *von Neuman algebra*, i.e., an algebra of operators such that it is self-adjoint (i.e., $A \in \mathscr{A}$ implies that its adjoint A^* also belongs to $\mathscr{A}$) and satisfies (3.2) (i.e., it coincides with its bicommutant).

Von Neumann algebras are the mathematical objects proposed for study in [25] under the now obsolete name of "rings of operators"; the current name seems to have come into general practice after the publication of [26].

It is of utmost importance in our argument that we include (3.2) but not (3.1) in the definition of a von Neumann algebra; indeed, (3.1) requires *in addition* that the algebra be Abelian [$\mathscr{A} \subseteq \mathscr{A}'$], which we do *not* want in general, since we want to include in this structure algebras that are *not* Abelian, such as the algebra of all bounded operators on a Hilbert space. It is significant for our purpose that classical mechanics and ordinary QM appear in this language as two extreme cases: to classical systems are associated algebras which coincide with their commutant [$\mathscr{A} = \mathscr{A}'$], whereas the algebras that are associated with ordinary quantum systems are irreducible, i.e., their commutant is trivial [$\mathscr{A}' = \mathbf{C}I$]. Von Neumann and Murray concentrated on an intermediary case obtained when the center of $\mathscr{A}$ is trivial [$\mathscr{A} \cap \mathscr{A}' = \mathbf{C}I$]; these von Neumann algebras are called *factors*. Mathematically, they turn out to be the building blocks from which one can construct all von Neumann algebras. Physically, they occur under very specific circumstances, e.g., in connection with the description of pure thermodynamical phases as extremal KMS states (see below).

Before we arrive there, we should return briefly to the question of the justification for the role Hilbert spaces in quantum theory; or, stated differently, whether one can avoid putting Hilbert spaces explicitly in the very axioms of the theory; or putting it still differently, whether one can build in the theory enough flexibility so that different physical situations may be described by different Hilbert space representations.

The answer to this question is predicated on the prior construction of a C^*-algebra (see the beginning of this section), the self-adjoint elements of which are the observables of the system considered. For instance, in the study of a Heisenberg magnet, i.e., of spins distributed on a lattice Λ, one can associate to every part $\Lambda_N \subset \Lambda$ containing N sites (with N finite) the C^*-algebra $\mathscr{A}_N$ of all $2^N \times 2^N$ matrices. The set-theoretical inclusion in the family of all finite subsets of Λ induces a natural inclusion relation in the family of all corresponding C^*-algebras. It is then possible to construct (by a method called the C^*-inductive limit) a C^*-algebra $\mathscr{A}$ and mutually consistent injective maps from each $\mathscr{A}_N$ to $\mathscr{A}$, in such a manner that the set theoretical union of their images in $\mathscr{A}$ is dense in $\mathscr{A}$. $\mathscr{A}$ is then identified as the C^*-algebra of the infinite lattice of spins. Note that no mention of a Hilbert space has been made in connection with the global algebra $\mathscr{A}$.

The general GNS construction associates then to every *state* on any C^*-algebra $\mathscr{A}$ a specific Hilbert space representation. As this construction seems to capture much of the physics, let us sketch it. First, a state is viewed here as a linear map:

$$\phi: A \in \mathscr{A} \mapsto \langle \phi; A \rangle \in \mathbf{C} \qquad \text{with}$$
$$\langle \phi; A^* \rangle = \langle \phi; A \rangle^*; \quad \langle \phi; A^*A \rangle \geq 0 \qquad \forall A \in \mathscr{A}$$
$$\text{and} \quad \sup_{A \in \mathscr{A}, \|A\| \leq 1} |\langle \phi; A \rangle| = 1. \quad (3.3)$$

Note that, while the above properties are not mathematically independent, they all have significance for the physical interpretation of the theory; moreover, in the usual situation where $\mathscr{A}$ has a unit I, the last of the above conditions reads simply $\langle \phi; I \rangle = 1$.

The state ϕ on $\mathscr{A}$ being given, a sesquilinear form on $\mathscr{A}$ is naturally defined by

$$(A, B) = \langle \phi; A^*B \rangle. \quad (3.4)$$

A Hilbert space

$$\mathscr{H}_\phi = \overline{\mathscr{A}/\mathrm{Ker}_\phi} \quad (3.5)$$

is then obtained as the completion of the pre-Hilbert space $(\mathscr{A}/\mathrm{Ker}_\phi)$, where the kernel $\mathrm{Ker}_\phi = \{A \in \mathscr{A} \mid \langle \phi; A^*A \rangle = 0\}$ is a closed left-ideal of $\mathscr{A}$. We identify the vector $\Phi_A \in \mathscr{H}_\phi$ as the equivalence

class of $A \in \mathscr{A}$ modulo Ker_ϕ. As these vectors form a dense subspace of $\mathscr{H}_\phi$, we can define for every $A \in \mathscr{A}$ a bounded operator $\pi_\phi(A)$ by

$$\pi_\phi(A)\Phi_B = \Phi_{AB} \qquad \forall\, B \in \mathscr{A}. \tag{3.6}$$

Note that the map

$$\pi_\phi\colon A \in \mathscr{A} \mapsto \pi_\phi(A) \in \mathscr{B}(\mathscr{H}_\phi) \tag{3.7}$$

is a Hilbert space representation of $\mathscr{A}$:

$$\begin{aligned} \pi_\phi(c_1 A_1 + c_2 A_2) &= c_1\pi_\phi(A_1) + c_2\pi_\phi(A_2) \\ \pi_\phi(A_1 A_2) &= \pi_\phi(A_1)\pi_\phi(A_2) \\ \pi_\phi(A^*) &= \pi_\phi(A)^*, \end{aligned} \tag{3.8}$$

for all $c_1, c_2 \in \mathbf{C}$ and all $A_1, A_2 \in \mathscr{A}$. Note also that

$$\mathscr{H}_\phi = \overline{\{\pi_\phi(A)\Phi_I \mid A \in \mathscr{A}\}} \tag{3.9}$$

and

$$\left(\Phi_I, \pi_\phi(A)\Phi_I\right) = \langle \phi; A\rangle \qquad \forall\, A \in \mathscr{A}, \tag{3.10}$$

i.e., in this representation, the vector Φ_I is cyclic and represents the state ϕ. These two properties determine the representation up to a unitary equivalence.

For two familiar examples, let ϕ be the vacuum state on the algebra of the CCR; if the system considered has finitely many degrees of freedom, the representation π_ϕ is the Schrödinger representation; and when the system considered has infinitely many degrees of freedom, the representation π_ϕ is the Fock space representation. The familiar fact that these representations are irreducible is a reflection on the fact that the vacuum state is a pure state (i.e., cannot be decomposed into a convex mixture of other states). Since W^*-algebras are C^*-algebras, the GNS applies to them as well.

As indicated above, for the special case of the Heisenberg ferromagnet, it is possible to construct abstractly the C^*-algebra corresponding to an infinite system. Similar procedures can be followed in much more general circumstances; for instance, an axiomatization of quantum field theory was presented along such line in an article that injected a new vigor in the *algebraic approach* to quantum theory [27]. The general idea is as follows. Suppose that a C^*-algebra $\mathscr{A}$ has been obtained that describes the infinite system to be considered. Suppose further that a state ϕ as been selected, e.g., the thermodynamical limit of the canonical equilibrium states of the corresponding local systems; we shall discuss below a characterization of the states obtained in this manner. One then performs the GNS construction associated to this state to obtain the representation π_ϕ that is thus specifically based on the state ϕ. It is now a matter of convenience to consider the von Neumann algebra $\pi_\phi(\mathscr{A})''$ acting on the Hilbert space $\mathscr{H}_\phi$.

The main advantage of considering the von Neumann algebra $\pi_\phi(\mathscr{A})''$ rather than the C^*-algebra $\pi_\phi(\mathscr{A})$ is that the topology of von Neumann algebras is better adapted to apply some of the methods of functional analysis. For instance, a von Neumann algebra $\mathscr{N}$ is always generated by its projectors (whereas a $\mathbf{C}^*$-algebra might have no non-zero projector among its elements). A spectral theory can be formulated then, entirely at the level of the von Neumann algebra. In fact, the lattice $L(\mathscr{N})$ of the projectors of a von Neumann algebra $\mathscr{N}$ essentially contains all the intrinsic information provided by $\mathscr{N}$ itself. In particular, when $\mathscr{N}$ is a factor, a dimension function d can be defined on $L(\mathscr{N})$. Up to a multiplicative constant, the range R of d can be of either of the following five types:

$$\begin{aligned} &\text{type } I_n\text{:} && R = \{1, 2, \ldots, n\} \\ &\text{type } I_\infty\text{:} && R = \{1, 2, \ldots, \infty\} \\ &\text{type } II_1\text{:} && R = [0, 1] \\ &\text{type } II_\infty\text{:} && R = [0, \infty] \\ &\text{type } III\text{:} && R = \{0, \infty\}. \end{aligned} \tag{3.11}$$

From a mathematical point of view, we emphasize that the range of the dimension function for the factors of type I is discrete: the lattice of their projectors is atomic. By contrast, for the factors of type II_1, the dimension function takes all values in the finite closed interval $[0, 1]$; these factors are the candidates for the "geometries without points." The search for such geometries seems to have been one of the motivations von Neumann had, not only for the series of articles under discussion, but also for the article with Birkhoff discussed in the previous section, where they had isolated the modularity condition.

For the purposes of physics, factors of type II and III nowadays occur routinely and typically in the study of systems with infinitely many degrees of freedom, be they obtained in relativisitic quantum field theory or in the statistical mechanics of the thermodynamical limit. We will concentrate

our attention on the latter in the sequel. To prepare for this, the case of canonical equilibrium states for finite systems is still worth considering in some detail. Specifically, we want to illustrate that, as the GNS representation depends on the state ϕ, one should expect that it expresses also some of the special circumstances of the physical situation described by the state ϕ.

The following explicit particular case is typical in the structures that it brings to light. Consider, indeed, the representation obtained by the GNS construction for the canonical equilibrium state of a 1-dimensional harmonic oscillator; it acts on the Hilbert space known as the Liouville space of the system $\mathscr{H}_\phi \equiv \mathscr{H}_o \otimes \mathscr{H}_0$, where $\mathscr{H}_o$ denotes the Hilbert space of the Schrödinger representation. This is the space of all Hilbert–Schmidt operators on $\mathscr{H}_o$, i.e., the Hilbert space spanned by the density matrices on $\mathscr{H}_o$. With $\{\psi_k \mid k = 0, 1, 2, \ldots\}$ denoting an orthonormal basis of eigenvectors of the Hamiltonian H of our oscillator, $\{\Psi_{kl} = \psi_k \otimes \psi_l \mid k, l = 0, 1, 2, \ldots\}$ gives an orthonormal basis in $\mathscr{H}_\phi$. We have then

$$\pi_\phi(A) = A \otimes I,$$
$$\text{i.e., } \pi_\phi(A)(\psi_k \otimes \psi_l) = (A\psi_k) \otimes \psi_l \quad (3.12)$$

and

$$\Phi_I = \sqrt{\rho} \qquad \text{with } \rho = e^{-\beta H}/Tre^{-\beta H},$$
$$\text{i.e., } \Phi = \sum_k \sqrt{\rho_k}\,\Psi_{kk}. \quad (3.13)$$

This representation is evidently not irreducible, a reflection of the fact that the canonical equilibrium state ρ is a mixture. Moreover, it is instructive to notice that

$$\pi_\phi(\mathscr{A})' = \{I \otimes A \mid A \in \mathscr{A}\} \quad \text{and, thus,}$$
$$\pi_\phi(\mathscr{A}) \cap \pi_\phi(\mathscr{A})' = \mathbf{C}, \quad (3.14)$$

i.e., $\pi_\phi(\mathscr{A})$ is a factor which is antiunitarily equivalent to its commutant, through the antiunitary operator J defined by

$$J\left(\sum_{kl} c_{kl}\Psi_{kl}\right) = \sum_{kl} c_{kl}^*\Psi_{lk}. \quad (3.15)$$

Notice, furthermore, that the operators $U_\phi(t)$ defined on $\mathscr{H}_\phi$ by

$$U_\phi(t)\Phi_A = \Phi_{V(t)AV(-t)}$$
$$\text{where } V(t) = e^{-iHt} \text{ and } A \in \mathscr{A} \quad (3.16)$$

satisfy the relations

$$U_\phi(t)\Phi = \Phi \quad \text{and}$$
$$U_\phi(t)\pi(A)U_\phi(-t) = \pi(V(t)AV(-t))$$
$$\forall A \in \mathscr{A}. \quad (3.17)$$

These operators are realized explicitly by

$$U_\phi(t) = V(t) \otimes V(-t) \quad (3.18)$$

so that

$$JU_\phi(t)J = U_\phi(-t) \quad \text{and} \quad H_\phi = H \otimes I - I \otimes H, \quad (3.19)$$

where H_ϕ, the generator of U_ϕ, has therefore a spectrum that is symmetric around zero and, in particular is not bounded below. As $\mathscr{H}_\phi$ is called the Liouville space of the system, H_ϕ is referred to as the Liouville operator.

So far, we are still in somewhat familiar territory. Yet, the remarkable feature about the representation that we just discussed is that much of the structure to which it has pointed persists in the thermodynamical limit where the usual formalism of QM loses its power since the Fock space does not accommodate states with a finite particle density and factors do appear that are *not* of type *I*. This was first noticed for the Bose gas [28].

This structure is now known indeed to be a general consequence [29] (for a textbook account, see [17]) of a characterization of the canonical equilibrium state that carries over to the thermodynamical limit. This is the abstract formulation [30] (the so-called KMS condition [31]) of an analyticity property of thermal Green functions.

Given a time-evolution α (i.e., a continuous, one-parameter group of automorphisms of the algebra of observables for the system considered) and given also a temperature $\beta = 1/kT$, the KMS condition on the state ϕ expresses that the correlation functions satisfy (in essence, although some caution on domains should be exercised)

$$\langle \phi; \alpha(t)[A]B\rangle = \langle \phi; B\alpha(t + i\beta)[A]\rangle$$
$$\forall A, B \in \mathscr{A}. \quad (3.20)$$

The states that satisfy this condition are called KMS states.

For finite systems, it is immediate to see that there is only one such state and that it is given by the usual canonical equilibrium density matrix.

For infinite systems, however, this uniqueness disappears, but the set $\mathcal{S}_\beta^\alpha$ of the states that satisfy the KMS condition (for the evolution α and the temperature β) form a convex set that is a simplex, i.e., a convex set the elements of which can be decomposed in a *unique* manner as a convex combination of their extreme points (as every chemist who has dealt with mixtures of three reactants knows, an equilateral triangle is a simplex; a circle is not). This additional freedom is exactly what was looked for when one wished the thermodynamical limit would allow one to describe phase transitions. The extremal KMS states are to be interpreted as pure thermodynamical phases, and it seems important for the interpretation that canonical equilibrium states be *uniquely* decomposable in their extremal components, the pure thermodynamical phases. This very special property of quantum canonical equilibrium states is a classical feature of quantum statistical mechanics that is made manifest only in the thermodynamical limit. The GNS representation for a KMS state ϕ, which does *not* describe a pure thermodynamical phase, is *not* a factor; the spectrum of its nontrivial center then labels the pure thermodynamical phases of which ϕ is a mixture.

The canonical decomposition of KMS states in extremal states satisfying the KMS condition has been a useful tool to discuss the phenomena of spontaneous symmetry breaking, see, e.g., [32]. For nonequilibrium situations as well, the flexibility of the algebraic approach has allowed some progress on a variety of fronts, such as

1. The construction of a model in which one can implement the four requirements Bohr wanted to impose on a quantum measuring process, namely: (i) the collapse of the wave packet, e.g., the collapse of the state of the system from a coherent superposition of eigenstates (relative the observable measured) to an incoherent mixture of these eigenstates; (ii) the transfer of information from the system to the apparatus; (iii a) the measuring apparatus is macroscopic (a rather vague notion that can be sharpened in a formalism where the passage to the thermodynamical limit is allowed); (iii b) the measuring process is stable under small (i.e., local) perturbations of the initial state of the measuring apparatus; (iv) the process is governed by the laws of Quantum Mechanics (which as applied to infinite systems, means that the dynamics is obtained as the thermodynamical limit of a Hamiltonian evolution describing completely the coupling between the system and the apparatus) [33].
2. The extension to the quantum realm of the concept of Kolmogorov flows, inherited from classical probabilistic ergodic theory (e.g., Brownian motion) [34]; this involves discussions of the physical manifestations of such ergodic behavior, including various notions of mixing (i.e., various forms for the decay of correlation functions), as well as finer notions such as the Lebesgue spectrum, the nonvanishing of dynamical entropy, and quantum diffusion-type equations.
3. The exploration of quantum equivalents to the classical notions of Anosov systems, chaos, and/or Liapunov exponents; the latter project is still involved in some controversy in which the algebraic approach helped the formulation, and sorting out, of various options [35].

Quantum field theory, elementary particle theory, braid groups, and knots, and noncommutative differential geometry are other fields of physics and of mathematics where the algebraic and analytic methods pioneered by von Neumann have opened new conceptual vistas; these, however, are not within the scope of the present lecture.

References

1. D. Hilbert, J. von Neumann, and L. Nordheim, Math. Ann. **98**, 1 (1927).
2. J. von Neumann, Gött. Nach. **1**, 1 (1927).
3. J. von Neumann, Gött. Nach. **1**, 245 (1927).
4. J. von Neumann, Gött. Nach. **1**, 273 (1927).
5. J. von Neumann and E. P. Wigner, Zschr. Phys. **47**, 203 (1928); *Ibid.* **49**, 73 (1928); **51**, 844 (1928).
6. J. von Neumann, Zschr. Phys. **48**, 868 (1928).
7. J. von Neumann and E. P. Wigner, Phys. Zschr. **30**, 465 (1929); *Ibid.*, Phys. Zschr. **30**, 467 (1929).
8. J. von Neumann, Zschr. Phys. **57**, 30 (1929).
9. J. von Neumann, Math. Ann. **102**, 49 (1929); *Ibid.*, J. Math. **161**, 208 (1929); *Ibid.*, Ann. Math. **32**, 191 (1931).
10. J. von Neumann, Math. Ann. **104**, 570 (1931).
11. J. von Neumann, *Mathematische Grundlagen der Quantenmechanik* (Springer, Berlin, 1932), *Ibid.*, *Mathematical Foundations of Quantum Mechanics*, B. T. Beyer, translator (Princeton University Press, Princeton, 1955).
12. E. P. Wigner, *The Collected Works* (Springer, Berlin, 1997), Vol. III, Part II, *Ibid.* (1995), Vol. VI.

13. W. O. Amrein, J. M. Jauch, and K. B. Sinha, *Scattering Theory in Quantum Mechanics* (W. A. Benjamin, Reading, MA, 1977).
14. R. G. Newton, *Scattering Theory of Waves and Particles* (McGraw-Hill, New York, 1966).
15. P. Jordan, J. von Neumann, and E. P. Wigner, Ann. Math. **38**, 29 (1934).
16. E. M. Alfsen, H. Hanche-Olsen, and F. Schultz, Acta Math. **144**, 267 (1980).
17. G. G. Emch, *Mathematical and Conceptual Foundations of 20th-Century Physics* (North-Holland, Amsterdam, 1984).
18. G. Birkhoff and J. von Neumann, Ann. Math. **36**, 823 (1936).
19. C. Prion, PhD. Thesis (Université de Lausanne, Switzerland, 1964); *Ibid.*, Helv. Phys. Acta **37**, 439 (1964); G. G. Emch and J. M. Jauch, Dialectica **19**, 259 (1965); J. M. Jauch, *Foundations of Quantum Mechanics* (Addition-Wesley, Reading, MA, 1968), C. Piron, *Foundations of Quantum Physics* (Benjamin, New York, 1976).
20. E. P. Wigner, *Gruppentheorie und Ihre Anwendungen auf die Quatenmechanik der Atmospektren* (Vieweg, Brauschweig, 1931).
21. G. G. Emch and C. Piron, J. Math. Phys. **4**, 469 (1963); announced in Helv. Phys. Acta **35**, 542 (1962).
22. V. Bargmann, J. Math. Phys. **5**, 862 (1964).
23. L. Garding and A. S. Wightman, Proc. Natl. Acad. Sci. U.S.A. **40**, 617 (1954); *Ibid.* **40**, 622 (1954).
24. R. Haag, Nuovo Cim. **25**, 287 (1962); G. G. Emch and M. Guenin, J. Math. Phys. **7**, 915 (1966); W. Thirring and A. Wehrl, Commun. Math. Phys. **4**, 303 (1967); W. Thirring, Commun. Math. Phys. **7**, 181 (1968).
25. F. J. Murray and J. von Neumann, Ann. Math. **37**, 116 (1936); *Ibid.*, Trans. Am. Math. Soc. **41**, 208 (1937); *Ibid.*, Ann. Math. **41**, 94 (1940); *Ibid.* **44**, 716 (1943).
26. J. Dixmier, *Les Algèbres d'Opérateurs dans l'Espace Hilbertien (Algèbres de von Neumann)* (Gauthier-Villars, Paris, 1957, 2nd ed. (1969); *Ibid., Les C*-Albèbres et leurs Représentations* (Gauthier-Villars, Paris, 1964).
27. R. Haag and A. Kastler, J. Math. Phys. **5**, 848 (1964).
28. H. Araki and E. J. Woods, J. Math. Phys. **4**, 637 (1963).
29. M. Takesaki, *Tomita's Theory of Modular Hilbert Algebras and its Applications, Lecture Notes in Mathematics*, Vol. 128 (Springer, New York 1970); *Ibid.*, Commun. Math. Phys. **17**, 33 (1970); *Ibid.*, in *Statistical Mechanics and Mathematical Problems*, Lecture Notes in Physics, Vol. 20 (Springer, New York, 1973).
30. R. Haag, N. Hugenholtz and M. Winninck, Commun. Math. Phys. **5**, 215 (1967).
31. R. Kubo, J. Phys. Soc. Jpn. **12**, 570 (1957); P. C. Martin and J. Schwinger, Phys. Rev. **115**, 1342 (1959).
32. G. G. Emch, H. J. F. Knops and E. J. Verboven, J. Math. Phys. **11**, 1655 (1970); G. G. Emch, in *Groups, Systems, and Many-Body Physics*, P. Kramer and M. Dal Cin, Eds. (Vieweg, Braunschweig, 1980).
33. B. Whitten-Wolfe and G. G. Emch, Helv. Phys. Acta **49**, 45 (1976).
34. G. G. Emch, Commun. Math. Phys. **49**, 191 (1976).
35. G. G. Emch, H. Narnhofer, W. Thirring, and G. L. Sewell, J. Math. Phys. **35**, 5582 (1994); G. G. Emch, in *Quantizations, Deformations and Coherent States* (Polish Scientific, Warsaw, to appear); G. G. Emch, *Beyond Irreducibility and Back, Proceedings of the 1996 Bialowieza Workshop*, to appear.

Does Quantum Probability Predict Frequency?

WILLIAM G. FARIS*

Division of Mathematical Sciences, National Science Foundation, 4201 Wilson Blvd., Arlington, Virginia 22230

Received 4 March 1997; accepted 7 March 1997

ABSTRACT: In probability theory an event is characterized by a set of outcomes. The probability of an event is a prediction of the relative frequency of the outcomes that lie in the set, when the experiment is repeated independently. In quantum mechanics an event is identified with a closed subspace of Hilbert space. Do the probabilities of quantum events predict relative frequencies in the same way? The famous analysis of Bell shows that this cannot happen in general, for all quantum events. Nevertheless the probabilities must predict something, and if not relative frequencies then what? There are several answers to the question of how to interpret quantum probabilities as relative frequencies, but they all involve restrictions on the events that are considered. This article surveys three such interpretations, which correspond to three possible choices: measured events, macroscopic events, and position events. © 1997 John Wiley & Sons, Inc. Int J Quant Chem 65: 389–398, 1997

Introduction

Does quantrum probability predict frequency? If so, frequency of what? We put these questions in a mathematical framework and present possible answers. The purpose is to clarify the physical content of quantum mechanics. This article is expository; the goal is to explain the issues in as elementary a way as possible.

In ordinary probability theory there is a fixed set of outcomes. An event is characterized by a set of outcomes. The probability of an event is a number between zero and one. The ordinary interpretation of probability in physical science is the frequency interpretation. Suppose there are many independent repetitions of the same situation. Each time there is an actual physical outcome. The relative frequency of the repetitions for which the outcome makes the event happen should be close to the probability prediction. If this frequency interpretation of probability is to be viable, then the probability assignment must satisfy basic principles of probability theory, such as addivity.

In quantum mechanics an event is identified with a closed subspace of Hilbert space. When the quantum state is specified, each quantum event has a probability. This again is a number between

* Permanent address: Department of Mathematics, University of Arizona, Tucson AZ 85721.

© 1997 John Wiley & Sons, Inc.
CCC 0020-7608 / 97 / 050389-10

zero and one. However, conjunctions of quantum events are defined only in special cases, when the events are compatible. Can the probabilities, for all quantum events simultaneously, be regarded as predictions of relative frequency? Can the quantum events be reinterpreted as determining sets of outcomes? The answer is no. The probabilities of quantum events violate additivity.

The famous analysis of Bell gave a deeper perspective on this fact. If the probability assignment depends on which set of compatible quantum events is considered, then the ordinary probability laws can be satisfied. The physical apparatus that defines the particular quantum events influences the probabilities. However, Bell found a new constraint. Assume that the system satisfies two conditions: active locality and passive locality. Then again the quantum probability assignment conflicts with probability laws. Thus if quantum mechanical probabilities are to predict frequencies in the usual way, then either active locality or passive locality must fail.

In any case, if quantum probabilities are to predict the frequencies of certain events, then these events must be defined in terms of sets of outcomes. There are several answers to the question of how to pick the set of outcomes and the corresponding events, corresponding to different interpretations of quantum mechanics. We survey three such interpretations.

According to the Copenhagen interpretation, the set of possible outcomes depends on an external choice of what to measure. Once this choice has been made, then there is only a small collection of compatible events for which the probabilities give frequency predictions.

Another interpretation attempts to describe a single set of outcomes consisting of macroscopic histories. The laws of probability apply to macroscopic events for which a decoherence condition is satisfied.

Yet another class of interpretations describes the world on the atomic level, and the set of possible outcomes consists of particle trajectories. The only quantum events that persist in this picture are position events.

So the answer is that quantum probability predicts frequencies, but only of certain events. In each interpretation it predicts the frequencies of events characterized by sets of outcomes. The problem is that there is no agreement over what the outcomes should be.

The entire discussion here is in the context of the elementary quantum mechanics of particles. Of course, current physical theory regards quantum fields as the fundamental dynamical entities. In particular, quarks and leptons are described by Fermi fields and interactions between them by gauge fields. The direct physical significance of these fields is subtle, and so the implication for the interpretation of quantum mechanics is yet obscure.

Probability

Our first task is to review standard probability theory in order to contrast it with quantum mechanics. In probability there is a set Ω of all *outcomes* of an experiment. An *event* A is a condition that determines a subset of Ω to which a probability may be assigned. The logical operations and, or, not on events correspond to set theory operations intersection, union, complement on subsets. The *probability* $P[A]$ of an event A is a number between 0 and 1. The probability assignment must satisfy the usual laws of probability. For instance, a typical condition is additivity in the form

$$P[A] = P[A \text{ and } B] + P[A \text{ and not } B].$$

The *frequency interpretation* of probability is as a prediction of relative frequency. Suppose the situation is repeated many times under independent conditions. Then the relative frequency of the repetitions for which a given event happens should be close to the probability of the event.

Here is an example of a probability assignment. Consider the set Ω consisting of the six triples 110, 101, 100, 011, 010, and 001. Let A be the event that the first element is a 1, let B be the event that the second element is 1, and let C be the event that the third element is 1. Thus B, for example, corresponds to the three-element subset 110, 011, 010. Assign the probability uniformly over the six points. Then the events A, B, and C and their negations each have probability $\frac{1}{2}$. However, note that events such as the compound event (A and not B) have probability $\frac{1}{3}$. (The corresponding subset is 101, 100, and these are two out of six.) Thus there is a conspiracy that makes A and B tend not to happen together. However, there is a limit to the possible magnitude of such a conspiracy. This limit is given by the following elementary probability theorem.

ELEMENTARY PROBABILITY THEOREM

Consider an arbitrary probability assignment. Then

$$P[\,A \text{ and not } B] + P[\,B \text{ and not } C] + P[C \text{ and not } A] \leq 1.$$

This theorem is completely trivial as a theorem of probability theory, but we shall see that there is an analogous result that is false in quantum mechanics.

Quantum Mechanics

We briefly review this theory. The mathematical framework of quantum mechanics is Hilbert space. Each *quantum event* is identified with a closed subspace A of the Hilbert space. (Often the subspace is identified with the orthogonal projection operator onto the subspace.) The *quantum state* is a fixed one-dimensional subspace of the Hilbert space. For each quantum event A, the probability of A is given by

$$P[\,A] = \cos^2(\theta),$$

where $\cos^2(\theta)$ is the square of the cosine of the angle between the one-dimensional subspace determining the state and the subspace corresponding to the A. [Of course, the Hilbert space is complex, but $\cos^2(\theta)$ may be defined as the effect on the state of projecting onto A and then back.]

In this framework, the *negation* not A of the event A is defined by the orthogonal complement $A^{\perp}$ of the subspace corresponding to A, so that

$$P[\text{not } A] = \sin^2(\theta).$$

In particular,

$$P[\,A] + P[\text{not } A] = 1.$$

If A and B are closed subspaces, the intersection $A \cap B$ is a closed subspace. We say that A and B are *compatible* if the four subspaces $A \cap B$, $A \cap B^{\perp}$, $A^{\perp} \cap B$, $A^{\perp} \cap B^{\perp}$ have direct sum the entire Hilbert space. (This geometrical condition is equivalent to having the corresponding projections commute.) When A and B are compatible, we define their *conjunction* A and B to be the intersection $A \cap B$. Thus, when A and B are compatible, we have all the usual probability laws, for example, additivity in the form

$$P[\,A] = P[\,A \text{ and } B] + P[\,A \text{ and not } B].$$

It would be unwise to define conjunction as intersection of subspaces when the subspaces are not compatible. To see this in a dramatic way, take A and B to be one-dimensional subspaces that are not parallel or perpendicular, and take the state along A. The additivity equation then reads $1 = 0$, as bad a failure as one could imagine.

The relation of compatibility is not transitive. Say that A is compatible with B and also B is compatible with C. It does not necessarily follow that A is compatible with C.

What is to be made of the existence of incompatible quantities A and B? In the Copenhagen interpretation of quantum mechanics it is sometimes said that one must choose to measure either A or B, and the measurement of one makes impossible the measurement of the other. Furthermore, a quantum event has no particular truth value until it is measured. So from this perspective it is reasonable there is no meaningful quantum event that combines A with B.

Bell's Theorems

Bell discovered a remarkably simple way of characterizing some of the puzzling aspects of quantum mechanics. His essays on this subject have been collected [1]. In this account we draw on the appendix to Wick's book [2] for a particularly elementary account.

Suppose that we have a fixed quantum state and two compatible events A and A'. We say that A is *equivalent* to A' with respect to the state if

$$P[\,A] = P[\,A \text{ and } A'] = P[\,A'].$$

These events will happen or not happen together, with probability 1.

Bell made a remarkable discovery about the quantum system consisting of two spin $\frac{1}{2}$ particles in the singlet state. There are events A, B, and C associated with the spin of the first particle and events A', B', and C' associated with the spin of the second particle. They have the following properties:

1. Each of the events A, B, C is compatible with each of the events A', B', C'.

2. The event A is equivalent to A', the event B is equivalent to B', and the event C is equivalent to C'. These events all have probability $\frac{1}{2}$.
3. The probabilities of the events (A and not B'), (B and not C'), (C and not A') are each $\frac{3}{8}$. There is a very strong conspiracy for A and B' not to happen together.

This gives what we shall refer to as Bell's first theorem:

BELL'S FIRST THEOREM

There can be no single probability model that reproduces the results of quantum mechanics for this system.

Proof. If there were, we could replace the events A', B', and C' by the equivalent events A, B, C and get

$$P[A \text{ and not } B] + P[B \text{ and not } C] + P[C \text{ and not } A] = \tfrac{9}{8}.$$

This contradicts the elementary probability theorem.

This theorem is remarkable, but its implication for quantum mechanics is not quite as strong as it seems. If one admits that quantum events only become true or false when they are measured, then one must be prepared to admit that a measurement can have an effect on the system. Thus the probability assignment might be affected by what is measured.

In the example of the two particles, there is a magnetic field in the vicinity of the first particle that is oriented in a particular direction. It can deflect the particle in one of two different ways. The event A corresponds to one of the two possible deflections (and the event not A to the other one). If the magnetic field is oriented in another way, we get the event B and its negation. A third orientation defines C and its negation. Only one of these orientations is physically possible in a given situation. There are similar possible magnetic field arrangements for the second particle, with corresponding events A', B', C' and their negations.

Thus we could write P_{ab} for the probability when we have decided to introduce magnetic fields to decide between A and not A for the first particle and between B' and not B' for the second particle. In this notation the three probabilities would be $P_{ab}[A \text{ and not } B']$, $P_{bc}[B \text{ and not } C']$, and $P_{ca}[C \text{ and not } A']$. Even though these probabilities are each $\frac{3}{8}$, there is no way of combining the events in a situation where a single probability assignment is relevant. It would seem that the argument would no longer apply to this situation. Bell, however, showed that under additional hypotheses it still works.

Let $\mathcal{F}$ be events associated with the first particle, and let $\mathcal{F}'$ be events associated with the second particle. Let $\mathcal{F}_0$ be another collection of events; we think of these as occurring in the past. Let P_{ij} be the probability assignment with apparatus setting i for the first particle and j for the second particle.

It seems reasonable that there should be no possibility of intervention over long distances. This would say that the P_{ij} probabilities of events in $\mathcal{F}$ associated with the first particle do not depend on the apparatus setting j for the second particle. Correspondingly, the P_{ij} probabilities of events in $\mathcal{F}'$ associated with the second particle do not depend on the apparatus setting i for the first particle.

The following two locality conditions refer to a chosen collection of past events. Active locality rules out intervention and also rules out influence on the past events. Passive locality is relative to the same collection of past events.

AL: Active locality: The P_{ij} probabilities of events defined by events in $\mathcal{F}$ and $\mathcal{F}_0$ do not depend on j. The P_{ij} probabilities of events defined by events in $\mathcal{F}'$ and $\mathcal{F}_0$ do not depend on i. (An intervention on one particle cannot affect the relation of the other particle to its past.)
Note: It follows that probabilities of past events in $\mathcal{F}_0$ are computed with a probability assignment P that depends on neither apparatus setting.

PL: Passive locality: If an event A in $\mathcal{F}$ is equivalent to an event A' in $\mathcal{F}'$ with respect to P_{ij}, then they are both equivalent to an event A_0 in $\mathcal{F}_0$. (A perfect coincidence must have an explanation in a common past.)

BELL'S SECOND THEOREM

Under the hypotheses of active and passive locality, there can be no family of probability models that reproduces the results of quantum mechanics.

The proof is not difficult, and here is a sketch. Let A in $\mathcal{F}$ be associated with one particle, and let A' in $\mathcal{F}'$ be associated with the other. Take them equivalent. By passive locality, A is equivalent to a past event A_0 in $\mathcal{F}_0$ with respect to the probabilities P_{aa}. By active locality, for these events we get the same results if we compute with the probabilities P_{ab}. Thus, A is equivalent to A_0 with respect to the probabilities P_{ab}.

By similar reasoning, B' is equivalent to B_0 with respect to the probabilities P_{ab}.

It then follows from simple probability arguments that (A and not B') is equivalent to (A_0 and not B_0) with respect to the probabilities P_{ab}. However, the probability of the past event (A_0 and not B_0) is computed with a probability assignment P not depending on the apparatus.

It follows that

$$P_{ab}[\, A \text{ and not } B'\,] = P[\, A_0 \text{ and not } B_0\,].$$

This can be repeated with all three terms. The probabilities no longer depend on the decision on the apparatus. Thus we can now prove Bell's second theorem with exactly the argument used for Bell's first theorem.

The conclusion of this theorem is that if quantum mechanics is a correct way to make probability predictions, then we must give up the combination of active and passive locality. We shall see how this happens in the various interpretations.

Notice that in order to apply the theorem in a specific case one must define the collection of past events $\mathcal{F}_0$. There may be some choice in this definition. Let us look at two extreme examples.

Example 1. Assume there is no relevant past. This means that the only past events are trivial: the sure event with probability one and the impossible event with probability zero. In this case active locality is merely the condition that there is no possibility of intervention. If this is so, then it is only passive locality that fails.

Example 2. Assume that for each pair of apparatus settings i, j the theory is deterministic except for random initial conditions at the past time. The probability assignment P_{ij} makes every event equivalent to a corresponding event in $\mathcal{F}_0$. Passive locality obviously holds, so active locality must fail. How does this happen? Suppose an event A in $\mathcal{F}$ is equivalent to A_0 in $\mathcal{F}_0$ with respect to the probability measure P_{aa}. Then A may be equivalent to some other event $\tilde{A}_0$ with respect to the probability measure P_{ab}. The change of the apparatus setting for the second particle has changed the relation between past and future for the first particle.

Quantum mechanics has been well tested, and there is now considerable experimental support for the strong correlations over long distances predicted by the theory. Quantities accessible to experiment seem to be local in the sense that the correlations cannot be used to make interventions. However, according to Bell's result, there is no collection of past events that simultaneously satisfy active and passive locality. The correlations seem unexplainable by a common past.

Measured Events

The traditional textbook interpretation of quantum mechanics is the Copenhagen interpretation. In this interpretation each consistent set of quantum events defines probabilities having a frequency interpretation. But which consistent set of events is chosen comes from outside the theory, by a choice of external measuring device.

The problem that some people see with the Copenhagen interpretation is that it gives no account of a reality that is not subject to measurement. According to Heisenberg, "the idea of an objective real world whose smallest parts exist objectively in the same sense as stones and trees exist, independently of whether we observe them... is impossible." (The quote is from W. Heisenberg, *Physics and Philosophy*, Harper and Row, New York, 1958, p. 129). There must always be a measuring apparatus external to the quantum system. One can perhaps draw the line between quantum system and measuring apparatus at various levels, but there is never a theory of what happens in a system that is not undergoing measurement.

Furthermore, it is not evident what counts as a suitable external measurement. Clearly a person with a Ph.D. in physics and a research grant is allowed to perform a measurement. Maybe the measurement can be conducted automatically with the experimental apparatus purchased on the grant. But how about the world before grants. Can a dinosaur perform a measurement? And how about the world on a grander scale? Does the universe have a quantum description?

The Copenhagen interpretation does not evade the locality issues. It is trivially true that different

probability measures correspond to different choices of measurement. The event (A and not B') is not compatible with the event (B and not C'). Thus $P_{ab}[\,A$ and not $B']$ is computed with a different probability measure from that used for $P_{bc}[\,B$ and not $C']$. However, the coincidences are still present, and according to Bell's second theorem they have no explanation in a common past.

Macroscopic Events

Perhaps there should be an interpretation that does not depend on the notion of measurement. There are a number of more recent proposals, due to various authors, that I will put in one category. The Gell-Mann and Hartle version is perhaps representative [3]. They key concepts are consistent history, macroscopic event, and decoherence.

In Bell's theorem the original conjunctions of quantum events are between compatible events. So any peculiar features of quantum mechanics are already present in this case. Nevertheless, some authors have proposed that problems of interpretation may be clarified by defining the probabilities of conjunctions of certain incompatible events. Griffiths was one of the pioneers in the direction [4]. Here is a brief description of how this works.

We now describe an operation known as *reduction* or *collapse* of the state. Consider a fixed state, given by a one-dimensional subspace of the Hilbert space. Let B be an event with nonzero probability $P[\,B]$. The collapsed state is the projection of the one-dimensional subspace onto the subspace corresponding to B. It is a new quantum state. Let us denote the probability of some other event A computed with respect to the collapsed state by $P[\,A|B]$. We might want to call this the conditional probability of A given B. Sometimes we may think of B as being defined before A, so that this is a probability computed in the course of a history.

Given the conditional probability, we might try to define the probability of the history by the usual formula

$$P[\,A \text{ and } B] = P[\,A|B]P[\,B].$$

It is important to realize that the probability of the conjunction is thought of as being computed with respect to the original state. The collapse is merely a stage in the mathematics.

When the events are not compatible, this definition can lead to paradoxes. Consider A and B to be one-dimensional subspaces at an angle of $\pi/4$. Take the state to be perpendicular to A but at an angle $\pi/4$ from B. Then $P[\,B] = \frac{1}{2}$, $P[\,A|B] = \frac{1}{2}$ so $P[\,A$ and $B] = \frac{1}{4}$. Yet $P[\,A] = 0$.

All that remains of the additivity condition is the equation

$$P[A] = P[\,A \text{ and } B] + P[A \text{ and not } B] + I(A, B).$$

The *interference term* satisfies $-\frac{1}{2} \le I(A, B) \le \frac{1}{2}$ and measures the failure of additivity.

Let A and B be arbitrary quantum events. We say that B followed by A form a *consistent history* with respect to the given quantum state if

$$P[\,A] = P[\,A \text{ and } B] + P[\,A \text{ and not } B].$$

This says that for this particular state the interference term is zero.

The idea now is that this should apply to a certain class of macroscopic events. For this class, the *decoherence* effect should make the interference terms vanishingly small. Decoherence is a property of large systems that says that it is impossible to distinguish quantum mechanics from ordinary probability without examining in detail every particle in the system. One of the early formulations of decoherence is by Hepp and Lieb [5]; see [6] for extensions. There is survey of the subject and its history in the article by Zurek [7]. The book of Omnès [8] has an extensive discussion. The decoherence effect is not automatic; it is supposed to be a consequence of the dynamics of the particular system.

To see how this might work, consider a system with two rather separate parts. One part is associated with *collective events*, typically macroscopic events defined by the values of collective coordinates (center of mass and so on). The other part is an environment, presumably part of the atomic world. This part is associated with *environmental events*. It is assumed that the collective events are compatible with the environment events.

We consider a situation where the two parts have interacted in such a way that the environmental part has become correlated with the collective part. We say that the state makes a collective event B *decoherent* if B is equivalent to some environmental event E with respect to the state. The environment thus contains a record of the event B, in that when B happens or does not happen, the corresponding E happens or does not happen.

DECOHERENCE THEOREM

Let A and B be collective events. Suppose the state makes B decoherent. Then the history B followed by A is consistent with respect to the state.

Proof. Let E be the environmental event that makes B decoherent in the given state. Since A and E are compatible, we have

$$P[A] = P[A \text{ and } E] + P[A \text{ and not } E].$$

Since B and E are equivalent in the state, the collapsed state with respect to B is the same as the collapsed state with respect to E. Not only $P[B] = P[E]$, but also $P[A|B] = P[A|E]$. Hence we can replace E by B (and similarly not E by not B) and obtain

$$P[A] = P[A \text{ and } B] + P[A \text{ and not } B].$$

The prediction of such a theory consists of probabilities of sets of histories of macroscopic objects. The histories are part of the world independent of anyone's choice of what to measure. The outcome in a particular situation is the history that actually occurs.

The construction of such a theory in full detail is a formidable task. The purpose of the theory is to make frequency predictions about sets of consistent histories, independent of any notion of measurement. Therefore it must specify which particular collection of consistent histories is relevant. Gell-Mann and Hartle [3] have given criteria that such a collection must satisfy. However, questions of the existence and of the uniqueness of such a collection are difficult.

The puzzling aspect of such an interpretation is that it gives little role to the subatomic world except as a way of making predictions about the world on a large scale. If there were a universe of only a few particles, in which decoherence effects did not play a role, then such an interpretation would be vacuous.

Note also that any such interpretation must confront the implications of Bell's theorems. By Bell's first theorem, there will not be a macroscopic event in the set of consistent histories corresponding to each quantum event. There may be macroscopic events corresponding to certain atomic level quantum events, those for which a suitable coupling to the macroscopic world exists. An example of this might be the pointer reading corresponding to the deflection of a particle by a magnetic field. Perhaps there is no possibility of intervention over long distances. However, according to Bell's second theorem, the interpretation must admit the violation of the combination of active and passive locality.

Position Events

Another class of interpretation describes the world on the atomic scale, but only to events defined in terms of the position of particles. One can look at the positions over time, so one can assign probabilities to sets of particle trajectories. The outcome in a given situation is a particular particle trajectory.

Two variants are Bohm's theory (Bohmian mechanics) and Nelson's theory (stochastic mechanics). The literature on Bohm's theory can be traced back from a recent collection [9], and work is ongoing [10, 11]. Nelson's theory is explained in his books [12, 13]. The fact that there are two competing theories, giving different predictions for the particle trajectories, is a weakness. Perhaps there is some comfort in the fact that the fixed time position probabilities are the same in both theories and agree with those of quantum mechanics. And this may be all that is possible to measure in practice.

These theories discard the usual elaborate superstructure of quantum mechanics, in which there are events of all sort. Probability is only assigned to position events (at various times). It is surprising how little this seems to matter. It is wise to consider these theories before making general declarations on the interpretation of quantum mechanics, since often they provide a counterexample.

The Bell theorems again apply to these theories. Spin is determined by introducing certain magnetic fields, which deflect the particles, eventually resulting in a change in position. The introduction of the magnetic fields does change the probabilities, as envisaged in Bell's second theorem [14]. The main defect of these theories is that with the natural definition of past events they violate active locality, at least on the level of the trajectories. However, if one looks only at the final positions of the particles, the predictions agree with quantum mechanics. So again there is no practical possibility of active intervention for such events, and the situation is as for the Copenhagen interpretation.

I find stochastic mechanics attractive, so I will give a brief account. I will begin with the description of the time-reversible stationary diffusion process associated with the quantum mechanical ground state. Then I will give some indication of the diffusion process associated with a quantum state that evolves in time. In both cases the outcome of the probability experiment is a particular particle trajectory.

In ordinary quantum mechanics the position events at fixed time are compatible, but position events at different time are usually not compatible. With the diffusion process we can define the conjunction of position events at different times. Of course, this is a deviation from the usual interpretation of quantum mechanics.

Consider the Hilbert space of square integrable wave functions and the Schrödinger operator

$$H = -\frac{1}{2}\frac{\hbar^2}{m}\nabla_x^2 + V(x).$$

Assume that H has a lowest energy eigenfunction $\psi > 0$ with

$$H\psi = E\psi.$$

A position event at fixed time is defined by a subset of position space. If A is such a subset, then there is a corresponding indicator function. This function is 1 on the set A and 0 on its complement. We also denote the indicator function by A. Multiplication by the indicator function is the projection onto the corresponding closed subspace of Hilbert space.

We let $A(s)$ be the event that the trajectory of a particle is in the set A at time s. Let A_s be the operator $\exp[-s(H-E)/\hbar)A\exp(s(H-E)/\hbar)]$.

Now consider two such position events, A and B and corresponding times $s \le t$. Then the probability of the particle being A at time s and in B at time t is given by

$$P[A(s) \text{ and } B(t)] = \langle \psi, A_s B_t \psi \rangle$$
$$= \langle \psi, Ae^{-(t-s)(H-E)/\hbar}B\psi \rangle.$$

Note that this is a well-defined probability for the position of the particle at two different times. For $t = s$ the particles have not moved, so this is just the probability that the particle is in the intersection of the two sets. However, as $t - s$ becomes infinite, the probability approaches $\langle \psi, A\psi \rangle \langle \psi, B\psi \rangle$. This says that the two particle positions become independent.

The probability calculation may be reproduced in the language of diffusion theory. Define the *backward diffusion operator* L and *forward diffusion operator* L^* by

$$L = -\frac{1}{\psi}(H-E)/\hbar\psi$$

and

$$L^* = -\psi(H-E)/\hbar\frac{1}{\psi}.$$

Note that $L1 = 0$ and $L^*\rho = 0$, where $\rho = \psi^2$.

The explicit form of these operators is as follows. Define the diffusion coefficient $\sigma^2 = \hbar/m$. Define the drift vector field u to be

$$u = \sigma^2\frac{\nabla_x\psi}{\psi}.$$

Then the backward diffusion operator is

$$L = \tfrac{1}{2}\sigma^2\nabla_x^2 + u\cdot\nabla_x.$$

The backward diffusion operator gives the expected values at future times as a function of the initial point. Thus $e^{tL}f(x)$ is the expected value of f of the particle position at time t, when the particle is started at point x. The forward diffusion operator is

$$L^* = \tfrac{1}{2}\sigma^2\nabla_x^2 - \nabla_x\cdot(u\quad).$$

The forward diffusion operator describes how probability evolves. Thus, if g is the probability density at time zero, then $e^{tL^*}g$ is the probability density at time t.

The quantum mechanical operator $-(H-E)/\hbar$ and the diffusion operators L and L^* all have the same spectrum, since they are similar. So this is a perfect correspondence between quantum mechanics and diffusion theory.

We can now rewrite the probability that a diffusing particle is in A at time s and in B at time t. This is

$$P[A(s) \text{ and } B(t)] = \langle \rho, Ae^{(t-s)L}B\rangle$$
$$= \langle e^{(t-s)L^*}(A\rho), B\rangle.$$

The backward operator maps events from future to present, while the forward operator maps probabilities from present to future.

We may write the forward diffusion equation explicitly as a partial differential equation

$$\frac{\partial p}{\partial t} = L^* p = \frac{1}{2}\sigma^2 \nabla_x^2 p - \nabla_x \cdot (up).$$

This describes how probability evolves when a particle is diffusing randomly with diffusion constant σ^2 and drift u. The drift vector field u is space-dependent. If we start the particle at a fixed point x_0, then the solution is a function $p(x_0, x, t)$ that describes the probability density after time t.

If we start the particle at a random position with density ρ, then the probability density at a later time is $\int \rho(x_0) p(x_0, x, t)\, dx_0$. The condition for a stationary density is

$$\int \rho(x_0) p(x_0, x, t)\, dx_0 = \rho(x).$$

This is equivalent to

$$0 = L^* \rho = \tfrac{1}{2}\sigma^2 \nabla_x^2 \rho - \nabla_x \cdot (u\rho).$$

As we have seen, the solution is $\rho = \psi^2$. The equilibrium for the diffusion is the quantum mechanical density. In fact, the equilibrium is maintained by the mechanism of *detailed balance*, which says that the equilibrium is due to a local balance between the density gradient and the drift. This is expressed mathematically as

$$0 = \tfrac{1}{2}\sigma^2 \nabla_x \rho - u\rho.$$

This leads to the following physical picture for a particle in a quantum mechanical eigenstate. The particle diffuses randomly, but the drift is such that it compensates for the diffusion and leads to an equilibrium. This probability for the position of the particle in this equilibrium agrees at every time with the prediction of quantum mechanics. However, the diffusion model provides a picture of the random trajectory of the diffusing particle. Such a picture is forbidden in the ordinary interpretation of quantum mechanics.

In the general case one gets a diffusion process, but it is no longer homogeneous in time. Consider a solution ψ of the time-dependent Schrödinger equation. Such a solution is in general complex. Define two vector fields, a drift u and a velocity, v, by

$$\sigma^2 \frac{\nabla_x \psi}{\psi} = u + iv.$$

These are both drift terms in the diffusion equation. Sometimes u is called an osmotic velocity and v a current velocity. In any case, the corresponding diffusion process is given by the forward equation

$$\frac{\partial p}{\partial t} = \frac{1}{2}\sigma^2 \nabla_x^2 p - \nabla_x \cdot ((u + v)p)$$

with diffusion coefficient σ^2 and drift $u + v$. The coefficients are now both space and time dependent. Consider the solution where the particle is started at point x_0 at time t_0. The solution $p(x_0, x, t_0, t)$ describes the probability density for diffusion to x at time t.

If we start the solution at time t_0 with probability density $\rho(x_0, t_0)$ then the probability at a later time is

$$\rho(x, t) = \int \rho(x_0, t_0) p(x_0, x, t_0, t)\, dx_0.$$

We can find such density explicitly by taking $\rho = |\psi|^2$, the quantum mechanical prediction. Then it turns out that there are separate equations involving u and v. The equation involving u is just the detailed balance equilibrium we had before, but with time-dependent coefficient:

$$0 = \tfrac{1}{2}\sigma^2 \nabla_x \rho - u\rho.$$

The equation involving v is the transport equation:

$$\frac{\partial \rho}{\partial t} = -\nabla_x \cdot (v\rho).$$

Together these equations imply that ρ satisfies the forward diffusion equation with diffusion coefficient σ^2 and total drift $u + v$.

The fact that the diffusion equation involves two vector fields u and v at first seems difficult to motivate. However, u does not change under time reversal, while v changes sign under time reversal. Thus the role of the drift u is to attempt to establish equilibrium, while the role of the velocity v is to effect overall movement.

Bohm's theory differs from stochastic mechanics in that the motion is deterministic, except for the random initial conditions. In Bohm's theory the motion is given by the velocity field v alone. Clearly there is a sense in which Bohm's theory is much simpler. However, stochastic mechanics has the attractive feature that it gives a natural role to the diffusion constant $\sigma^2 = \hbar/m$ that is derived

from Planck's constant and the mass. It is amusing to note that when m is the mass of an electron, the diffusion constant σ^2 has a rather memorable and reasonable value, about one square centimeter per second.

Conclusion

According to the mathematical apparatus of quantum mechanics, each quantum event has a probability. The question is whether these events correspond to sets of outcomes, so that the probability has a frequency interpretation. Here is the situation in the three interpretations. (i) In the Copenhagen interpretation each compatible collection of quantum events has a corresponding set of outcomes. However, the possible outcomes are not intrinsic to the system but depend on a choice of external measurement. (ii) In interpretations where events consist of sets of consistent histories subject to a decoherence condition, the outcomes are macroscopic histories. However, there need be no frequency interpretation for the probabilities of quantum events on the atomic scale. (iii) In the interpretations in which the outcomes are particle trajectories, the only relevant probabilities are those corresponding to position events at various times. So the probabilities of other quantum events either have no frequency interpretation or their interpretation is ultimately expressed by position events.

The subspaces of Hilbert space describes a huge collection of events. Any interpretation of quantum mechanics must provide an additional criterion to select a relatively small collection of events for which the probabilities have a frequency interpretation. In the Copenhagen interpretation this is given by choice of a measurement and a corresponding set of outcomes. Unfortunately, this choice is external to the theory. On the other hand, the macroscopic event and position event interpretations have a single set of outcomes and assign probabilities to at least some quantum events. They point the way to a possible understanding of quantum mechanics as a description of an isolated system. Perhaps that is enough.

References

1. J. S. Bell, *Speakable and Unspeakable in Quantum Mechanics* (Cambridge University Press, Cambridge, 1987).
2. D. Wick, *The Infamous Boundary: Seven Decades of Controversy in Quantum Physics*, (Springer-Verlag, New York, 1996).
3. M. Gell-Mann and J. Hartle, Phys. Rev. D **47**, 3345 (1993).
4. R. B. Griffiths, J. Stat. Phys. **36**, 219 (1984).
5. K. Hepp and E. H. Lieb, Helv. Phys. Acta **46**, 573 (1973).
6. B. Whitten-Wolfe and G. Emch, Helv. Phys. Acta **49**, 45 (1976).
7. W. H. Zurek, Physics Today, **44**, 36 (1991).
8. R. Omnès, *The Interpretation of Quantum Mechanics* (Princeton University Press, Princeton, 1994).
9. J. T. Cushing, A. Fine, and S. Goldstein, Eds., *Bohmian Mechanics and Quantum Theory: An Appraisal* (Kluwer, Dordrecht, 1996).
10. D. Dürr, S. Goldstein, and N. Zanghì, J. Stat. Phys. **67**, 843 (1992).
11. K. Berndl, D. Dürr, S. Goldstein, and N. Zanghì, Phys. Rev. A **53**, 2062 (1996).
12. E. Nelson, *Dynamical Theories of Brownian Motion* (Princeton University Press, Princeton, 1967).
13. E. Nelson, *Quantum Fluctuations* (Princeton University Press, Princeton, 1985).
14. W. Faris, Found. Phys. **12**, 1 (1982).

Nonrigid Systems in Chemistry: A Unified View

MICHAEL E. KELLMAN

Department of Chemistry, University of Oregon, Eugene, Oregon 97403

ABSTRACT: Recent discoveries show that phenomena in highly excited states of atoms and molecules are qualitatively different from the standard "planetary" model of the atom and the near-rigid model of molecules, characteristic of these systems in their low-energy states. Highly excited states of two-electron atoms show "molecular" behavior of a nonrigid linear structure undergoing collective rotation and vibration. Highly excited states of molecules display strong effects of normal mode anharmonicity and coupling that induce bifurcations on the route to molecular chaos and isomerization. Hints of a unified view for both systems are emerging in terms of approximate dynamical symmetry principles and methods of nonlinear classical mechanics such as bifurcation theory.
© 1997 John Wiley & Sons, Inc. Int J Quant Chem **65:** 399–409, 1997

Introduction

A surge of new knowledge, experimental and theoretical, of highly excited quantum states of few-body systems is leading to a new view of the motion of electrons in atoms and of atoms in molecules. We are accustomed to thinking of atoms in their ground states in terms of the "planetary" model of independent particles, described by an electronic configuration, e.g., the $1s^2$ configuration of the ground state of helium. In contrast to this nearly uncorrelated, nonrigid structure of an atom in its ground state, the ground- and low-energy rotation–vibration states of molecules are described in terms of the normal mode picture of small amplitude, nearly harmonic motion about a rigid equilibrium structure. However, efforts of many workers in recent years show that in highly excited states each system at high energy shows some resemblance to the behavior that describes the other at low energy. In highly excited states, the motion of electrons in atoms takes on characteristics similar to molecular rotation–vibration modes, while the motion of atoms in highly excited vibrational states, especially in systems undergoing isomerization, shows drastic departures from the low-energy normal mode picture. Moreover, the tools used to describe high-energy behavior, such as effective Hamiltonians, are beginning to give signs of a unified *formal* description of the two systems.

My purpose here was to highlight some of the most important of these developments. I give reference to some of the key original sources, in

Based on a plenary lecture at the Sanibel Symposium, March 1–7, 1997, St. Augustine, Florida.

Contract grant sponsor: Department of Energy.

Contract grant number: DE-FG06-92ER14236.

© 1997 John Wiley & Sons, Inc.
CCC 0020-7608 / 97 / 050399-11

which can be found many other important references that must be left out here. Elsewhere [1, 2], I have presented distinct points of view regarding some aspects of the work discussed here.

The "Molecular Atom:" Rotations, Vibrations, and Supermultiplets

The electrons in atoms and molecules do not have fixed positions relative to the atomic nuclei, and it is not evident that they have a "structure" in any geometrical sense. In the classical model of the hydrogen atom, the electron orbits the nucleus in an ellipse. In a multielectron atom, the Coulomb repulsion between electrons substantially perturbs the elliptical orbits. This is the problem of electron correlation. Two-electron atoms continue to elicit intense interest as the simplest prototype of the correlation problem. Conventionally, one describes an excited state of the atom in terms of a configuration. For example, a state with both electrons in a $2p$ orbital has a configuration $2p^2$. This independent particle configuration description is the quantum mechanical analog of the planetary model. By the late 1970s, accumulating evidence was showing that the configuration description is severely inadequate for highly excited states. Nonetheless, it came as something of a shock [3–6] to discover that the excited atom had many properties in common with the motion of a triatomic molecule. There is now compelling evidence that in states with both electrons excited from the ground level the atom behaves according to a "molecular" model of collective rotations and vibrations, similar to a highly nonrigid linear XYX molecule, with the electrons correlated on opposite sides of the nucleus.

I will outline how this picture has developed, emphasizing the physical ideas, but giving highlights of the formal development. The interested reader should consult the references for the many technical details.

APPROXIMATE DYNAMICAL SYMMETRY OF THE TWO-ELECTRON ATOM

Classically, the electron in a one-electron atom with Coulomb potential follows an elliptical (Kepler or planetary) orbit, in which the angular momentum $\vec{\mathbf{L}}$ is an exact constant of motion. The three components of the angular momentum vector $\vec{\mathbf{L}}$ generate the group of rotations in three-dimensional space, denoted O(3).

The elliptical Kepler orbit has far more symmetry than demanded merely by rotational invariance, however, a planetary orbit that conserves angular momentum $\vec{\mathbf{L}}$ could still have a precessing perihelion. The Kepler orbit has a constant of the motion [7] in addition to the angular momentum, the Runge–Lenz vector $\vec{\mathbf{A}}$. This vector points along the semimajor axis of the ellipse. It is defined in terms of the instantaneous position and momentum at each point in the orbit, but as a constant of motion, it is invariant in size and direction. The vector $\vec{\mathbf{A}}$ together with the angular momentum $\vec{\mathbf{L}}$ generates the group O(4) of rotations in an abstract four-dimensional space, which contains the ordinary angular momentum group O(3) as a subgroup.

In the two-electron atom, because the system is invariant under rotations in space, the total angular momentum

$$\vec{\mathbf{L}} = \vec{\mathbf{L}}_1 + \vec{\mathbf{L}}_2 \tag{1}$$

is an exact constant of motion that generates a group $O(3)_{12}$. By analogy with the one-electron atom, one might think to combine $\vec{\mathbf{L}}$ with the total Runge–Lenz vector

$$\vec{\mathbf{A}} = \vec{\mathbf{A}}_1 + \vec{\mathbf{A}}_2 \tag{2}$$

to form a two-electron $O(4)_{12}$ group. If the two-electron system behaved like a "planetary" atom, each electron would move in an independent elliptical orbit, with $\vec{\mathbf{A}} = \vec{\mathbf{A}}_1 + \vec{\mathbf{A}}_2$ a conserved quantity. However, this is not the case, because $\vec{\mathbf{A}}$ is badly broken as a constant of motion by the strong Coulomb repulsion between electrons.

Even though this $O(4)_{12}$ group is not an exact symmetry, it is reasonable to try to use it as an *approximate* symmetry. One might hope this would be of use in ordering the spectrum, but in a less complete way than if $O(4)_{12}$ were exact. This would be very much in the spirit of the use of approximate symmetries earlier in nuclear and elementary particle physics, where these kinds of ideas led to developments such as the quark model. Unfortunately, when this was tried for the two-electron atom, it was found [8] that $O(4)_{12}$ was not of much use even in this limited sense of an approximate symmetry.

A key advance came when Wulfman [9] and, independently, Herrick and Sinanoglu [10, 11]

tried, instead $\vec{A}$ of (2), the operator

$$\vec{B} = \vec{A}_1 - \vec{A}_2, \qquad (3)$$

where the crucial difference is the minus sign. A heuristic physical picture of the electron correlation is shown in Figure 1. The idea is that overall maximizing the *difference* between the Runge–Lenz vectors $\vec{A}_1$ and $\vec{A}_2$ minimizes the Coulomb repulsion between the electrons. It was found that $\vec{B}$ is an approximate constant of motion, unlike the experience with $\vec{A}$. Furthermore, it is easily shown from the commutation relations [7] that $\vec{L}$ and $\vec{B}$ together generate a distinct O(4) group. I will call this approximate symmetry group $O(4)'_{12}$ to distinguish it from the unsuccessful $O(4)_{12}$ of Eqs. (1) and (2).

ROTATIONS AND VIBRATIONS OF THE "MOLECULAR" ATOM

Of course, the heuristic picture in Figure 1 of electrons moving in stable ellipses is far from a literal image of either the classical or quantum mechanics of the atom. A more realistic depiction of a quantum state of the atom with both electrons in the same shell is given in Figure 2. The atomic structure is like that of an elongated cloud or blob of charge, with the density of the two electrons concentrated at the ends. This can be rationalized by saying that the repulsion of the electrons tends to correlate them on opposite sides of the nucleus. At the same time, a residual effect of the quantum mechanical configuration (with both electrons in the same shell in Fig. 2) is to concentrate the electrons very loosely at a most favored distance from the nucleus. This structure of the electron cloud surrounding the nucleus is that of a highly nonrigid system. Nonetheless, the correlation gives

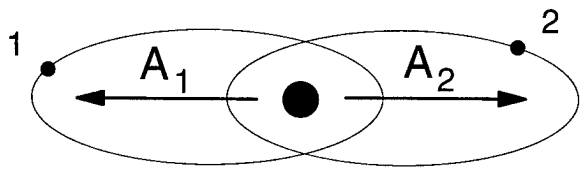


FIGURE 1. Heuristic picture of electron correlation in two-electron atom with both electrons in the same shell. Because of the electronic repulsion, the most favorable configuration maximizes the *difference* $\vec{B} = \vec{A}_1 - \vec{A}_2$ of Runge–Lenz vectors.

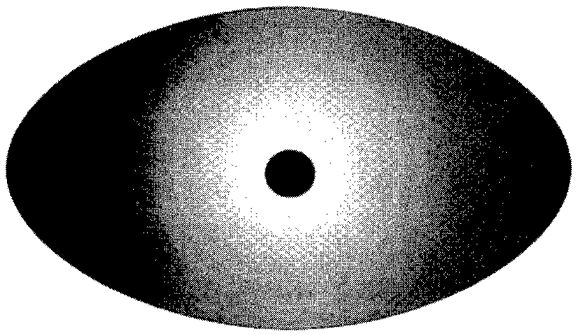


FIGURE 2. A depiction of the two-electron atom with both electrons in the same shell (which may be an excited shell). The atom has the structure of a "blob" of charge. The electrons are concentrated on opposite sides of the nucleus, because of the electronic repulsion, and are concentrated at some most probable distance, because of the shell structure. The overall structure has the symmetry of a linear, symmetric XYX molecule, with X's the electrons and Y the nucleus.

the atom a distinct shape—in fact, a shape with the symmetry of the molecular point group $D_{\infty h}$.

If the atom has a structure with a symmetrical shape, it is natural to wonder if this structure can exhibit collective modes, e.g., rotations and vibrations. The beginning of the "molecular" model of the atom came when Kellman and Herrick [3] used the $O(4)'_{12}$ group structure to classify the atomic levels into "rotor series," i.e., $O(4)'_{12}$ multiplets or sets of states that behaved like a nonrigid rotor. Next [4–6], the $O(4)'_{12}$ multiplets were combined into "supermultiplets." The collection of the $O(4)'_{12}$ rotor series into the more comprehensive supermultiplet classification describes bending vibrations of the "molecular" atom. (The role of radial excitations in this picture, which came to be better understood later, is discussed below.) Figure 3 depicts the rotations and bending vibrations of the electron cloud in the "molecular" atom. The supermultiplets give the classification of "intrashell" states of the atom with both electrons in the $n = 2$, 3, 4, and 5 shells and also "intershell" states with the electrons in different shells. The supermultiplets for both electrons in $n = 3$ are shown in Figure 4, indicating the role in the classification of rotational excitations, bending vibrations with vibrational angular momentum along the "molecular" symmetry axis, and bending vibrations with no angular momentum. Clearly, this classification reveals a great deal of order in a spectrum which does not at first show much order at all. Not only is the spectral pattern of Figure 4 similar to that of

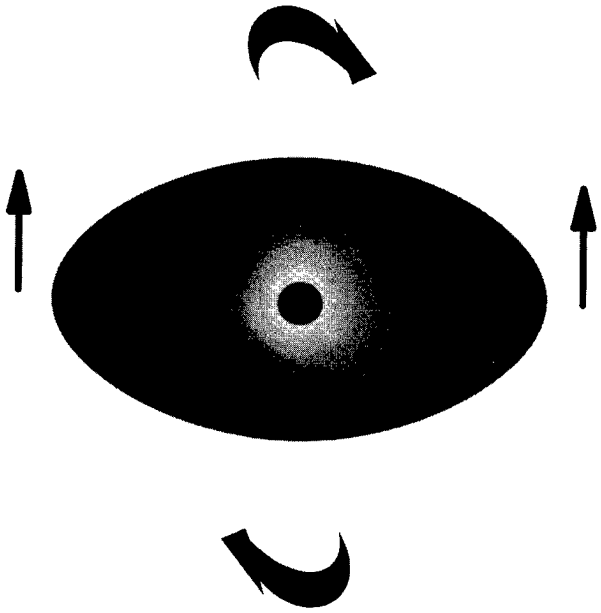


FIGURE 3. Collective rotation–vibration modes of the "molecular" atom. The structure has degenerate bending vibrations and overall rotations, like a linear triatomic molecule.

a linear, nonrigid triatomic molecule, but the pattern of terms $^{2S+1}L^{\pi}$ matches that of a symmetric triatomic molecule with rotor–vibrator states obeying the constraints imposed by Fermi statistics of the outer particles, i.e., the spin-orbital-parity classifications of the terms derived from atomic shells and the symmetry restrictions of the XYX molecule dovetail perfectly [6].

There have been significant developments since the work of Herrick and Kellman. Some highlights: I showed [12] that the molecular picture could be applied to atoms with two electrons outside a closed shell, i.e., alkaline earth atoms. Berry and co-workers [13, 14] analyzed the atomic wave functions in terms of a basis with bending vibration and stretching modes. In the original model of Kellman and Herrick, the molecule was taken to have rotations and bending vibrations, but not stretching excitations, inasmuch as the radial degrees of freedom seemed quite reasonably to be encompassed in the $n = 2, 3, \ldots$ shell structure. Ezra et al. [15] developed a semiclassical treatment of the radial motion of a collinear atom and found evidence for radial motions that can be described as an antisymmetric stretch. Rost et al. [16, 17] gave a unified "molecular orbital" treatment of the radial, bending, and rotational motion. They found an intricate interweaving of bend and stretch excitations. These investigations strongly support the idea of the atom as being like a highly nonrigid triatomic molecule, but now understood to have a systematic involvement of radial motion in the classification. Richter et al. [18] discovered the

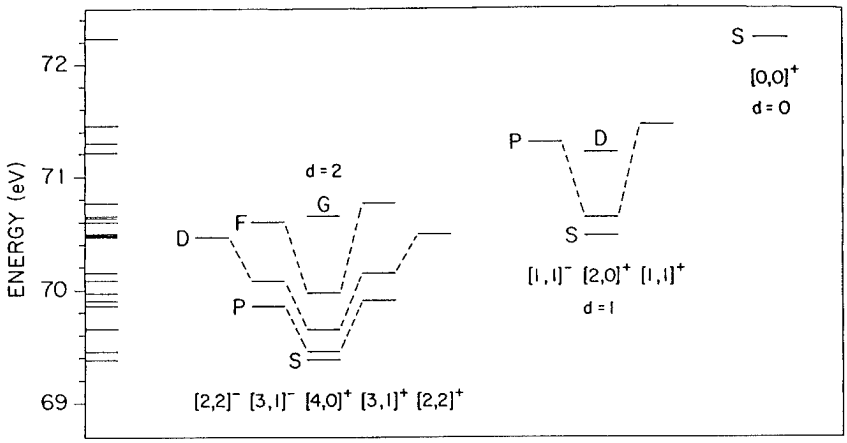


FIGURE 4. Supermultiplet rotor–vibrator "molecular" classification of doubly excited states of He with both electrons excited to the $n = 3$ shell, from [4]. In the largest, $d = 2$ supermultiplet, the column labeled $[4, 0]^+$ is a multiplet of O $(4)'_{12}$. This multiplet is a "rotor series" of pure rotational excitations with $L = 0, 1, 2, 3, 4$, built on the lowest energy state, which is $^1S^e$. Adjacent columns of the $d = 2$ supermultiplet are rotor series built on excitations of the bending vibration, which have $l = 1$ unit of angular momentum along the symmetry axis of the "molecular" atom. The $d = 1$ supermultiplet is built on an $^1S^e$ state with two bending quanta and $l = 0$ units of angular momentum along the symmetry axis. It has its own rotor series and $l = 1$ excitations. The $d = 0$ supermultiplet is a lone $^1S^e$ state with four bending quanta and $l = 0$. See [4, 6] for more details.

existence of "frozen planet" states, in which the two electrons are locked in a stable configuration on the *same* side of the nucleus. Ostrovsky and Prudov [19] found frozen planet states in which radial and bending modes of the "molecule" are in an approximate 2:1 frequency ratio, suggestive of molecular Fermi resonance! Finally, as described later, I have been investigating some connections of the atomic supermultiplet classification with recent models of molecular vibrations that use Lie group symmetries.

Order in Chaos in Highly Excited Molecules?

We have seen that the spectrum of a highly excited two-electron atom resembles that of a linear molecular structure undergoing rotation and vibration. This can be turned around to ask, What happens to a real molecule when it is excited high above the ground state? How does one describe the changes that must occur from the low-energy picture of small-amplitude oscillations about a near-rigid structure?

The spectrum of vibrational excitations is traditionally described in terms of normal modes [20]. However, at high energies, the modes can become strongly coupled to each other. As the atoms perform progressively large excursions from the equilibrium rigid structure, the motion can become chaotic, in the sense of nonlinear dynamical systems. Eventually, the atoms may rearrange into a different molecular structure or the molecule can fragment. The normal modes' description, adequate for a rational account of the spectrum at low energies, is no longer physically valid. But it is precisely here that the spectrum may become fearsomely complex. Spectra may be our window on the molecular world, through which to obtain information such as the forces between atoms which govern molecular dynamics and reactivity, but as with all visualization, a great deal of sophisticated processing is necessary to extract the information encoded in the raw data of experience. The search for new ways to model spectra and organize them into meaningful patterns, if any such exist, has been a concerted effort of fundamental chemical science of the past two decades.

Even though the standard approach starts with the notion of a set of normal modes [20], at all but the lowest energies, it is necessary to take into account anharmonicity of the modes. In addition, there are important couplings: In general, the vibrations are not truly separable into independent modes. (For simplicity, I will neglect rotation. Most of the statements carry over when rotation is included.) At low energy, the combination of anharmonicity and coupling for the most part can be "swept under the rug." But this becomes untenable at higher energy, where anharmonicity and coupling become inexorably more important.

Here, I will discuss two aspects of this problem of complex spectra of polyatomics: (1) When the most important couplings are taken into account, are there any remaining approximate constants of motions? If so, these intact dimensions of the molecular phase space act as "bottlenecks" to energy flow within the molecule. This will be important, e.g., in efforts to control molecular dynamics with intense laser pulses. (2) What happens to the dimensions of phase space that are not left intact? This is the problem of the branching of the normal modes in bifurcations on the route to molecular chaos. I will outline some promising approaches to these problems, developed through intense efforts of many workers.

THE SPECTROSCOPIC FITTING HAMILTONIAN WITH NORMAL MODE COUPLINGS

I begin by describing the standard effective Hamiltonian used to fit experimental spectra. The spectroscopic Hamiltonian (SH) is intended as an "effective Hamiltonian" to bridge the gap between experimental spectral data and the fundamental description of the true molecular quantum mechanics. A natural question is how the SH is related to the true Hamiltonian. Fried and Ezra [21] and independently Sibert [22] showed how to obtain the SH by beginning with a potential surface and transforming approximately to SH form by means of perturbation theory.

The SH is a quantum mechanical model of vibrational normal modes and their couplings. The SH contains a number of variable parameters. These are optimized to give the best fit to experimental data. The SH is in no sense a fundamental description of the molecule. That involves treating it as a collection of nuclei and electrons and essentially solving for the exact quantum mechanics. When feasible, as for a few small molecules, that leads to a molecular potential energy surface, with

vibrations emerging as quantum mechanical motion of the atoms on this potential. This is very difficult to carry out in practice.

The starting point of the SH is a set of elementary normal modes described by a Hamiltonian function $\mathbf{H}_0$, which depends on the number of quanta n_i in each of the modes i. The simplest model is just a set of N harmonic normal modes. However, anharmonicity is evident from the spectra even at low energy. It is therefore standard to use an $\mathbf{H}_0$ with harmonic terms proportional to the number of quanta n_i and frequency ω_i in each mode, but also anharmonic terms proportional to higher powers of the quantum numbers, including cross-terms:

$$\mathbf{H}_0 = \sum_{i=1}^{N} \omega_i(n_i) + \sum_i \chi_{ii}(n_i)^2 + \sum_{i<j}^{N} \chi_{ij}(n_i)(n_j) + \cdots . \quad (4)$$

One can try to fit an experimental spectrum by optimizing the parameters ω_i, etc., in $\mathbf{H}_0$. For many systems, especially at low energy, this may suffice to give a good match with experiment. However, a Hamiltonian of the form $\mathbf{H}_0$ often is not adequate. In such cases, coupling between the normal modes must be introduced beyond the cross-anharmonic terms $\chi_{ij}(n_i)(n_j)$. For example, Darling and Dennison [23] found that an interaction must be added to $\mathbf{H}_0$ which couples the stretch normal modes in a molecule such as H_2O. This is called "Darling–Dennison resonance" because of the near-resonant frequencies of the symmetric and antisymmetric stretches s and a. Addition of the Darling–Dennison coupling $\mathbf{V}_{sa}^{DD}$ gives a Hamiltonian $\mathbf{H} = \mathbf{H}_0 + \mathbf{V}_{sa}^{DD}$ which is no longer separable into modes s and a.

The Darling–Dennison coupling $\mathbf{V}_{DD}$ is for two modes s and a which have approximately the same frequency. This is sometimes called a 1:1 resonance coupling. Other couplings can arise between modes with frequency ratio $n{:}m$. These are referred to as Fermi resonances [24]. For example, there is a prominent 2:1 Fermi resonance in H_2O between the symmetric stretch and bend. A global fit of the spectrum, including states with prominent excitation of all three modes, requires a *multiresonance* Hamiltonian:

$$\mathbf{H} = \mathbf{H}_0 + \mathbf{V}_{sa}^{DD} + \mathbf{V}_{sbb}^{Fermi}. \quad (5)$$

The multiresonance character of the spectra has an important connection with identifying approximate constants of motion of the molecule. These act to channel energy flow within the molecular phase space, simplifying the spectra and the corresponding intramolecular dynamics. However, within the energy flow channels or pathways defined by the constants, the resonances can produce bifurcations of the normal modes and classical chaos, with considerable complications. I will consider these in turn.

POLYAD SYMMETRY, APPROXIMATE CONSTANTS, AND CHANNELS FOR MOLECULAR ENERGY FLOW

Approximate constants of motion are quantum numbers that are left intact when the resonance couplings needed to fit the spectrum are taken into account. If these exist, they are very important because they are related to patterns that can be uncovered in the experimental spectrum. In dynamical terms, on the time scale corresponding to the level of energy resolution in the spectral fit, they channel energy flow in the molecular phase space when energy is deposited at some specific location in the molecule. This could be crucial for efforts to control molecules with intense beams of coherent light pulses. The theory [21, 25] for finding approximate constants and energy channels uses a simple "resonance vector" analysis of the SH. The quantum numbers that are preserved are "polyad" numbers which are special combinations of the zero-order quantum numbers.

The resonance vector method was first applied for experimental data [25] to absorption spectra of acetylene (C_2H_2) of Smith and Winn [26] that probe the flow of energy initially deposited in the C—H stretch motions. There are a multiplicity of resonance couplings at high energy. Nonetheless, two good quantum numbers are found [25] to remain from the resonance vector analysis. The polyad analysis was applied by Jonas et al. [27] to spectra which probe the bends of acetylene, with a bearing on observation of hierarchies of time scales for the energy flow. Temsamani and Herman [28, 29] analyzed the polyads in constructing an effective SH Hamiltonian. Solina et al. [30, 31] directly "unzipped" the C_2H_2 spectrum into polyads. When viewed as individual polyads, the spectra reveal a great deal of order that is not otherwise evident. Most recently, direct absorption and fluorescence data were jointly analyzed [32] from the

point of view of polyad constants, with the goal of constructing the SH from as global a view of the molecular phase space as possible. An open question is whether the polyads can be further "unzipped" into subpolyads, revealing still more hidden order in the spectrum.

BRANCHING OF THE NORMAL MODES AND THE STRUCTURE OF MOLECULAR CHAOS

As shown by the need to use multiresonance Hamiltonians, it is evident that the couplings preclude using the normal modes by themselves in all but the coarsest description of the spectra. Some approximate constants of motion may be left intact as polyad numbers. As seen above, these are extremely important, yet easy to abstract from the SH fit to the experimental spectrum. However, knowledge of the intact polyad numbers leaves crucial questions unanswered. What happens when the individual normal modes are destroyed or modified by couplings? What are the signatures of this in the spectrum? What are the dynamical consequences, e.g., the changes in the natural motions of the molecule? These questions are important for using spectra to infer information about molecular potentials and may be crucial for efforts at coherent control of polyatomic molecules. From the viewpoint of classical mechanics, the destruction of the normal modes occurs when they undergo *bifurcations*. When a normal mode bifurcates, new types of anharmonic or nonlinear motions are formed in place of, or in addition to, the original modes. The goal of recent work [1, 33–37] has been to characterize the bifurcations associated with the SH applied to data of specific molecules, in order to identify the new nonlinear modes and related spectral patterns that result at high energy.

A difficult aspect of using bifurcation theory in spectral analysis is the high number of degrees of freedom in a polyatomic molecule. One confronts the not-well-understood problem of bifurcations in a high-dimensional classical phase space. In addition, the classical dynamics, in general, shows a mixture of chaotic and regular motion, so one also faces the notorious problem of the connection between chaotic classical dynamics and quantum states in this "mixed" regime.

Completely solving for the bifurcations of a chaotic Hamiltonian is presently impossible and probably not very useful. Instead, using as an exemplar the three-mode spectroscopic Hamiltonian of (5) for H_2O, work has focused [36–40] on obtaining and exploiting the *large-scale bifurcation structure*. By this is meant the principal branchings of the original normal modes as the system becomes chaotic. This gives the principal structure around which the chaotic phase space is organized. This information has been used in several methods for assignment of spectra and analysis of energy-level patterns [37–40]. Although successfully carried out for H_2O, the assignment with spectral pattern recognition is largely unchartered territory for larger molecules, with investigations currently in progress.

More Alike at Higher Energy?

We have seen that at high energy the two-electron atom has spectral patterns similar to the rotation–vibration modes of a molecule, while in actual molecules at high energy the vibrational modes are transformed in bifurcations because of resonant couplings. To a certain extent, the "planetary" atom has become like a "molecular" atom and the rigid molecule less regular. Still, the two systems could become even more similar. A real molecule can have excursions of the atoms completely out of its equilibrium configuration, with the possibility of multiple minima in the potential energy surface, as in isomerization. Could the motion of these "wandering atoms" come to resemble the correlated but nonrigid motion of the electrons in an atom? On the other hand, could electrons in atoms sometimes become rigidly localized to such an extent as to speak of Fermi resonances between modes of well-defined frequency? Also, could atoms show multiple quasi-rigid configurations, analogous to an isomerizing molecule? There is evidence that two-electron atoms have "frozen planet" states [18] in which the electrons really are locked into a second "molecular" configuration, with the electrons on the *same* side of the nucleus. Furthermore, there are indications [19] that the frequencies of the normal modes of these states are well defined and may sometimes be in Fermi resonance, i.e., have close to integral ratios. On the other hand, evidence about isomerizing molecules is now starting to accumulate [41–47], and distinct experimental and theoretical hallmarks are appearing. So, there is the prospect of soon understanding just what are the similarities and correspondences between truly nonrigid molecules and highly correlated atoms.

ISOMERIZING MOLECULES

If spectra are one of our clearest windows on the microscopic world of molecules, one of the most elusive behaviors to "catch in the act" is molecular rearrangement or isomerization. However, rapid progress [41–47] is being made on two prototype systems: the isomerization of HCP to HPC and that of HCN to HNC. In particular, a bifurcation of the type known as "tangent" or "saddle node" has been predicted from numerical studies [46] in connection with the approach of HCP to the isomerization barrier. Most interestingly, distinct changes in the spectrum, quite possibly associated with this bifurcation, have recently been observed [46]. Calculated vibrational wave functions [47] on a potential surface also show interesting behavior. An exciting challenge will be the development of spectroscopic Hamiltonians for isomerizing systems, including the description of the new bifurcation phenomena.

OF "FROZEN" PLANETS AND FERMI RESONANCES IN ATOMS

There have been important developments in the study of collective behavior of the electrons in atoms since the rotor–vibrator supermultiplet model. Some highlights include investigation of molecular-type electronic wave functions, with distinct approaches pursued by Berry and co-workers [13, 14] and Rost and co-workers [16, 17]. Another development is the investigation of radial motion [15] and how radial motion fits [16, 17] into the supermultiplet scheme. Finally, a most interesting development [18] is the prediction of "frozen planet" states. In these states, both electrons are on the same side of the nucleus! As illustrated in Figure 5, the outer, "frozen" electron hardly moves at all and the inner electron oscillates along the axis connecting the outer electron to the nucleus. Ostrovsky and Prudov [19] investigated the relative frequencies of radial and bending modes of the "molecular" atom in the frozen planet configuration. They predicted circumstances in which the modes are in an approximate 2:1 frequency ratio, suggestive of molecular Fermi resonance. This suggests an analogy with bifurcation phenomena in molecular vibrations. Interestingly, recent classical calculations of Ostrovsky and Prudov [48] on the frozen planet states show phase space behavior similar to that observed by Li et al. [33, 34] in resonant molecular vibrations. Further interesting parallels may be expected between the frozen planet states and the isomerization of linear molecules, including the novel bifurcation phenomena in the latter.

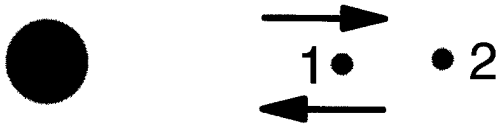


FIGURE 5. "Frozen planet" states of a two-electron atom. Electron 2 is nearly frozen in place, while electron 1 oscillates along the axis between electron 2 and the nucleus. See [18, 19, 48] for more discussion of frozen planet states.

A Unified Model?

We have seen that highly excited vibrations and rotations of molecules involve significant departures from the orderly, rigid structures of the ground state, while highly excited states of electrons in atoms behave in some ways like highly nonrigid molecular structures. The relationships discussed so far consist of analogies between physical descriptions that are rooted in very different formal descriptions: in the case of atoms, the O(4) hydrogenic shell structure, and in the case of molecules, the motion of atoms on a potential energy surface, abstracted in the spectroscopic Hamiltonian (SH). But if both types of systems display more and more features in common, such as collective modes, resonances with bifurcations, and multiple stable configurations, it is reasonable to ask, Can there be a unified *formal* description encompassing both types of system? These questions are in the early stages of exploration, and I do not believe definitive answers or conclusions about the choice of formalism are anywhere near at hand. Nonetheless, I would like to discuss one possible approach to at least a partially unified description. This approach uses Lie algebras to describe the spectra of both atoms and molecules. For atoms, this is not surprising, given the prominence of the O(4) algebra in the work on atoms already described. Perhaps more surprising, formally related approaches have been developed for molecular rotation–vibration spectra. One of these has come to be known as the vibron model [49–51]; another uses so-called quantum groups [52, 53]. I have used a vibron-type model for an investiga-

tion of the atomic supermultiplets [54] that is described below. The reason that such models are candidates for a unified picture is that they start with a group theoretical shell structure, similar to the O(4) description of the atom, yet they encompass an effective rotation–vibration Hamiltonian, much like the standard spectroscopic Hamiltonian (SH).

THE VIBRON MODEL

The "vibron" model [49–51] is related to early work on rigid and nonrigid molecular systems in terms of correlation diagrams [55, 56]. The basic idea is to represent the rotation–vibration spectrum of each bonded pair of atoms in a molecule in terms of representation of a continuous group. The group is the unitary group $U(4)$, which is related to the O(4) rotation group described above for atoms. The unitary group can be thought of as the generalization of rotations to spaces of complex numbers. In the vibron model, a set of n bonded pairs is described by first coupling a separate $U(4)$ for each bond: $U(4)_1 \times U(4)_2 \times \cdots \times U(4)_n$.

Then, subgroup chains are used to describe operators which resemble terms in the standard zero-order Hamiltonian (4). Couplings analogous but not identical to the Darling–Dennison or Fermi resonance couplings can also be defined in terms of the group operators. Although this procedure might appear far different from the SH, there is a term-by-term correspondence of a vibron Hamiltonian to a similar Hamiltonian built in the standard way. It is therefore not surprising that sufficiently elaborate versions of the vibron model (with enough independent terms in the Hamiltonian) can give spectral fits of comparable accuracy to the SH.

A RELATION TO THE SUPERMULTIPLETS?

The vibron model also turns out to have a possible relation to the supermultiplet description of two-electron atoms. Despite the spectral patterns revealed by the supermultiplets and the compelling physical motivation, one fundamental aspect of the supermultiplets was mysterious from the beginning. This was the formal group theoretical basis of the supermultiplet classification. The supermultiplets were constructed by collecting together the approximate two-electron $O(4)'_{12}$ multiplets into larger entities—the supermultiplets. The mystery was that despite the beauty of their structure and "molecular" interpretation the supermultiplets did not appear to correspond to any larger *mathematical* group structure encompassing the two-electron $O(4)'_{12}$. In a recent article [54], I was able to shed some light on this by embedding the O(4) group structure in a larger group, $U(4)$. The $U(4)$ lends its structure to a larger organization scheme, the supermultiplets, than can be obtained from O(4) alone. This embedding of the atomic problem in a $U(4)$ structure is similar to the way the vibron model embeds the molecular states. In both cases, the suitability of the embedding seems related to the observation that the pattern of correlation from nonrigid to rigid states in linear molecules [56] results in groupings analogous to the atomic supermultiplets.

FUTURE PROSPECTS

One aspect of the $U(4)$ embedding of the supermultiplets is still puzzling, but possibly connected to important future insight into the atomic problem and maybe even isomerizing molecules. This is that the $U(4)$ embedding leads to "extra" states beyond those obtained from the $O(4)_1 \times O(4)_2$ structure assumed in starting from the single-particle "planetary" model of the atom. In the $U(4)_1 \times U(4)_2$ scheme [54], I took pains to try to rationalize away these extra states. However, it would not be necessary to do this if the "extra" states really were *new physical states* not accounted for by assuming an $O(4)_1 \times O(4)_2$ planetary structure as a starting point. Is there any evidence for such states? Some but not all of the "frozen planet" states really appear to be new states. This is not surprising, because it is hard to see why frozen planet states would originate from an $O(4)_1 \times O(4)_2$ independent particle picture. Suggestively, the *first* frozen planet state in a shell corresponds to the highest ordinary supermultiplet state in the shell, i.e., the $^1S^e$ supermultiplet state with the most bending excitation. It is as if the frozen planet sequences are taking off from where the shell-based supermultiplets leave off—hinting that both are part of some larger classification. Of course, this does not prove that the frozen planet states are the "extra" states of the $U(4)_1 \times U(4)_2$ scheme. Indeed, that scheme predicts many more new states than the frozen planet states already known. It is unknown how many dynamically stable states will eventually be discovered or what the systematics of their classification will look like. However, it is

an exciting possibility to try to use group theoretical schemes, such as the $U(4)_1 \times U(4)_2$ model, to make predictions for computational and experimental searches for novel states.

Another challenge is the development of spectroscopic Hamiltonians for isomerizing systems, including the description of the novel bifurcation phenomena now being uncovered in experiments and numerical studies. This opens up many exciting possibilities for the development not only of spectroscopic Hamiltonians of the standard molecular form, but also effective Hamiltonians using Lie algebraic methods. It will be fascinating in coming years to watch the interplay of these new developments in highly excited electron correlation in atoms and highly excited, nonrigid molecules. These undertakings are likely to lead to a new understanding of fundamental problems of correlation, of general interest not only for atoms and molecules but throughout the many areas of physical science where correlation problems are important.

ACKNOWLEDGMENT

Support of the Department of Energy under Basic Energy Sciences Grant DE-FG06-92ER14236 is gratefully acknowledged.

References

1. M. E. Kellman, Annu. Rev. Phys. Chem. **46**, 395 (1995).
2. M. E. Kellman, Proc. Natl. Acad. Sci. U.S.A. **93**, 14287 (1996).
3. M. E. Kellman and D. R. Herrick, J. Phys. B **24**, L755 (1978).
4. D. R. Herrick and M. E. Kellman, Phys. Rev. A **21**, 418 (1980).
5. D. R. Herrick, M. E. Kellman, and R. D. Poliak, Phys. Rev. A **22**, 1517 (1980).
6. M. E. Kellman and D. R. Herrick, Phys. Rev. A **22**, 1536 (1980).
7. B. G. Wybourne, *Classical Groups for Physicists* (Wiley, New York, 1974).
8. E. Chacon, M. Moshinsky, O. Novaro, and C. E. Wulfman, Phys. Rev. A **3**, 166 (1971).
9. C. E. Wulfman, Chem. Phys. Lett. **23**, 370 (1973).
10. O. Sinanoglu and D. R. Herrick, J. Chem. Phys. **62**, 886 (1975).
11. D. R. Herrick and O. Sinanoglu, Phys. Rev. A **11**, 97 (1975).
12. M. E. Kellman, Phys. Rev. Lett. **55**, 1738 (1985).
13. J. L. Krause and R. S. Berry, J. Chem. Phys. **83**, 5153 (1985).
14. J. E. Hunter III and R. S. Berry, Phys. Rev. A **36**, 3042 (1987).
15. G. S. Ezra, K. Richter, G. Tanner, and D. Wintgen, J. Phys. B **24**, L413 (1991).
16. J. M. Rost, R. Gersbacher, K. Richter, J. S. Briggs, and D. Wintgen, J. Phys. B **24**, 2455 (1991).
17. J. M. Rost and J. S. Briggs, J. Phys. B **24**, 4293 (1991).
18. K. Richter, J. S. Briggs, D. Wintgen, and E. A. Solov'ev, J. Phys. B **25**, 3929 (1992).
19. V. N. Ostrovsky and N. V. Prudov, Phys. Rev. A **51**, 1936 (1995).
20. G. Herzberg, *Infrared and Raman Spectra* (Van Nostrand, New York, 1950).
21. L. E. Fried and G. S. Ezra, J. Chem. Phys. **86**, 6270 (1987).
22. E. L. Sibert III, J. Chem. Phys. **90**, 2672 (1989).
23. B. T. Darling and D. M. Dennison, Phys. Rev. **57**, 128 (1940).
24. E. Fermi, Z. Phyz. **71**, 250 (1931).
25. M. E. Kellman, J. Chem. Phys. **93**, 6330 (1990); M. E. Kellman and G. Chen, J. Chem. Phys. **95**, 8671 (1991).
26. B. C. Smith and J. S. Winn, J. Chem. Phys. **94**, 4120 (1991).
27. D. M. Jonas, S. A. B. Solina, B. Rajaram, R. J. Silbey, R. W. Field, K. Yamanouchi, and S. Tsuchiya, J. Chem. Phys. **99**, 7350 (1993).
28. M. A. Temsamani and M. Herman, J. Chem. Phys. **102**, 6371 (1995).
29. M. A. Temsamani and M. Herman, J. Chem. Phys. **105**, 1355 (1996).
30. S. A. B. Solina, J. P. O'Brien, R. W. Field, and W. F. Polik, Ber. Bunsenges. Phys. Chem. **99**, 555 (1995).
31. S. A. B. Solina, J. P. O'Brien, R. W. Field, and W. F. Polik, J. Phys. Chem. **100**, 7797 (1996).
32. M. A. Temsamani, M. Herman, S. A. B. Solina, J. P. O'Brien, and R. W. Field, J. Chem. Phys. **105**, 11357 (1996).
33. Z. Li, L. Xiao, and M. E. Kellman, J. Chem. Phys. **92**, 2251 (1990).
34. L. Xiao and M. E. Kellman, J. Chem. Phys. **93**, 5805 (1990).
35. J. Svitak, Z. Li, J. Rose, and M. E. Kellman, J. Chem. Phys. **102**, 4340 (1995).
36. Z.-M. Lu and M. E. Kellman, Chem. Phys. Lett. **247**, 195 (1995).
37. Z.-M. Lu and M. E. Kellman, J. Chem. Phys. **107**, 1 (1997).
38. J. P. Rose and M. E. Kellman, J. Chem. Phys. **105**, 7348 (1996).
39. S. Keshavamurthy and G. S. Ezra, Chem. Phys. Lett. **259**, 81 (1996).
40. S. Keshavamurthy and G. S. Ezra, J. Chem. Phys. **107**, 156 (1997).
41. K. K. Lehmann, S. C. Ross, and L. L. Lohr, J. Chem. Phys. **82**, 4460 (1985).
42. Y.-T. Chen, D. M. Watt, R. W. Field, and K. K. Lehmann, J. Chem. Phys. **93**, 2149 (1990).
43. X. Yang, C. A. Rogaski, and A. M. Wodtke, J. Chem. Phys. **92**, 2111 (1990).

44. X. Yang, C. A. Rogaski, and X. Yang, J. Opt. Soc. Am. B **7**, 1835 (1990).
45. H. Ishikawa, C. Nagao, N. Mikami, and R. W. Field, J. Chem. Phys. **106**, 2980 (1997).
46. S. C. Farantos, H.-M. Keller, R. Schinke, K. Yamanuchi, and K. Morokuma, J. Chem. Phys. **104**, 10055 (1996).
47. J. M. Bowman and B. Gazdy, Chem. Phys. Lett. **237**, 27 (1995).
48. V. N. Ostrovsky and N. V. Prudov, J. Phys. B **30**, 151 (1997).
49. R. D. Levine and C. Wulfman, Chem. Phys. Lett. **60**, 372 (1979).
50. F. Iachello and R. D. Levine, *Algebraic Theory of Molecules* (Oxford University Press, New York, 1994).
51. S. Oss, Adv. Chem. Phys. **93**, 455 (1996).
52. D. Bonatsos and C. Daskaloyannis, Phys. Rev. A **48**, 3611 (1993).
53. D. Bonatsos, C. Daskaloyannis, and P. Kolokotronis, J. Chem. Phys. **106**, 605 (1997).
54. M. E. Kellman, Phys. Rev. Lett. **73**, 2543 (1994).
55. M. E. Kellman, F. Amar, and R. S. Berry, J. Chem. Phys. **73**, 2387 (1980).
56. M. E. Kellman, Chem. Phys. **48**, 89 (1980).

Kinetic Energy Functional Derivative for the Thomas–Fermi Atom in *D* Dimensions

NORMAN H. MARCH,[1,*] SABRE KAIS[2]

[1]*Oxford University, Oxford, England*

[2]*Department of Chemistry, Purdue University, West Lafayette, Indiana 47907*

Received 26 March 1997; accepted 29 April 1997

ABSTRACT: The self-consistent Thomas–Fermi atom satisfying Poisson's equation in D dimensions has a functional derivative of the kinetic energy T with respect to the ground-state density $n(r)$ proportional to $n^{2/D}$. But the Poisson equation relates $n^{1-2/D}$ to "reduced" density derivatives $n^{-1}(d^2n/dr^2)$. Thus $\delta T/\delta n$ can be written also, quite compactly, solely in terms of these derivatives. An analytic solution to the Thomas–Fermi equation in D dimensions can be presented as an expansion about the known analytic solution at $D = 2$. © 1997 John Wiley & Sons, Inc. Int J Quant Chem 65: 411–413, 1997

Introduction

There is a good deal of interest currently in the role played by electron density gradients in density functional theory [1]. The purpose of the present study is to explicitly demonstrate that the self-consistent Thomas–Fermi (TF) atom discussed in D dimensions by Kventsel and Katriel [2, 3] has the following property. The kinetic energy T, of the form [4]

$$T^{(D)} = c_k^{(D)} \int n^{1+2/D} d\tau,$$

$$c_k^{(D)} = \frac{\hbar^2 D}{2m(D+2)} \left(\frac{D}{2K_D} \right)^{2/D} \tag{1}$$

where the constant K_D satisfies the recurrence relation

$$K_{D+2} = \frac{K_D}{2\pi D}, \qquad K_1 = \frac{1}{\pi}, \qquad K_2 = \frac{1}{2\pi} \tag{2}$$

has a functional derivative $\delta T/\delta n$ that can be written either in the conventional "local" form

$$\frac{\delta T^{(D)}}{\delta n} = \left(1 + \frac{2}{D} \right) c_K^{(D)} n^{2/D} \tag{3}$$

or in a quite equivalent form in terms solely of $n^{-1}(dn/dr)$ and $n^{-1}(d^2n/dr^2)$.

*Corresponding address: 6 Northcroft Road, Egham, Surrey TW 20 ODU, England.

Contract grant sponsor: Leverhulme Trust, UK.

Contract grant sponsor: Office of Naval Research.

© 1997 John Wiley & Sons, Inc.

CCC 0020-7608 / 97 / 050411-03

Differential Equation for Ground-State Density

The first step in the proof of the above statement is to establish the differential equation satisfied by the ground-state density $n(r)$ in D dimensions. The starting point to do this is the D-dimensional Poisson equation [1, 2], which from phase space considerations takes the form

$$\frac{\partial^2\Psi}{\partial r^2} + \frac{D-1}{r}\frac{\partial\Psi}{\partial r} = \beta_D\Psi^{D/2}. \tag{4}$$

Here the chemical potential μ, constant throughout the entire electronic charge cloud of the atom, and the self-consistent potential energy $V(r)$, are related to Ψ in Eq. (4) by

$$\mu - V = e\Psi \tag{5}$$

while the constant β_D is given by

$$\beta_D = 8\pi e\left(\frac{2\pi me}{h^2}\right)^{D/2}\Gamma\left(1+\frac{D}{2}\right). \tag{6}$$

Explicitly, for a point charge of magnitude Ze, $\Psi(r)$ behaves as $r \to 0$ as

$$\Psi(r) \to \left[\frac{4\pi Ze}{(D-2)\Omega_D}\right]r^{2-D}, \qquad D \geq 3 \tag{7}$$

with

$$\Omega_D = \frac{D\pi^{D/2}}{\Gamma\left(1+\frac{D}{2}\right)} \tag{8}$$

The integral of $n(r)$ through all space diverges for $D \geq 4$, but as one of us has pointed out previously [3], this trouble can be "cured" by introducing a finite nucleus.

Evidently, from Eq. (4), the electron density $n(r)$ is related to $\Psi(r)$ by [4]

$$n(r) = \frac{\beta_D}{4\pi e}\Psi^{D/2}. \tag{9}$$

Writing Eq. (9) as $\Psi(r) \propto n(r)^{2/D}$, one can substitute for $\Psi(r)$ in Eq. (4) to obtain the differential equation satisfied by the electron density $n(r)$ in D dimensions. After a short calculation, this can be obtained in the form

$$\left[\frac{1}{n}\frac{\partial^2 n}{\partial r^2} + \frac{D-1}{r}\left(\frac{1}{n}\frac{\partial n}{\partial r}\right) + \left(\frac{2}{D}-1\right)\left(\frac{1}{n}\frac{\partial n}{\partial r}\right)^2\right] = \frac{D}{2}(4\pi e)^{1-2/D}\beta_D^{2/D}n^{1-2/D}. \tag{10}$$

This generalizes the known result [5] for the original TF atom with $D = 3$, namely

$$\left[\frac{\nabla^2 n}{n} - \frac{1}{3}\left(\frac{\nabla n}{n}\right)^2\right] = \frac{n^{1/3}}{l}, \qquad l = \frac{1}{4}\left(\frac{3}{\pi}\right)^{-1/3}a_0 \tag{11}$$

since from Eq. (6), $\beta_3 = (32\pi^2 e/3h^3)(2me)^{3/2}$, to D dimensions.

Analytic Solution to the TF Equation in *D* Dimensions

Using the spatial dimension D as a free parameter has been widely employed to obtain an approximate results for $D = 3$ for a variety of physical problems [6]. The TF equation in $D = 3$ is a nonlinear equation. But the case $D = 2$ from Eq. (9) yields a linear equation which has been solved previously in terms of Bessel functions [2].

Recently, Bender et al. [7] have proposed a new approach to the analytic solution of a variety of nonlinear problems. Laurenzi [8] has shown that one can use this approach to obtain an analytic solution for the TF equation.

In this section we would like to show that one can use the D-perturbation expansion method to obtain an analytic solution for the D dimensional TF equation. We do this by replacing Eq. (4) with

$$\frac{d^2\Psi}{dx^2} + \frac{2\epsilon+1}{x}\frac{d\Psi}{dx} = \Psi\Psi^{\epsilon} \tag{12}$$

where $x = \beta_D^{1/2}r$ and $\epsilon = (D-2)/2$ is a measure of the nonlinearity of the TF equation. The potential Ψ is then expanded in a power series in ϵ:

$$\Psi = \Psi_0 + \epsilon\Psi_1 + \epsilon^2\Psi_2 + \cdots. \tag{13}$$

This, in turn, produces a set of inhomogeneous equations for the perturbation functions Ψ_n:

$$\frac{d^2\Psi_n}{dx^2} + \frac{1}{x}\frac{\Psi n}{dx} - \Psi_n = \chi_n(x) \tag{14}$$

where the first few inhomogeneous terms are given by:

$$\chi_0 = 0, \tag{15}$$

$$\chi_1 = \Psi_0 \ln \Psi_0 - \frac{2}{x}\frac{d\Psi_0}{dx}, \tag{16}$$

$$\chi_2 = \Psi_1 \ln \Psi_0 - \frac{2}{x}\frac{d\Psi_1}{dx} + \Psi_1 + \frac{1}{2}\Psi_0 \ln \Psi_0^2. \tag{17}$$

The zero-order equation, which is the TF equation at $D = 2$, has been solved previously in terms of modified Bessel functions $I_0(x)$ and $K_0(x)$

$$\Psi_0 = \alpha_1 I_0(x) + \alpha_2 K_0(x), \tag{18}$$

where the constants α_1 and α_2 can be fixed by the boundary conditions at zero and infinity [2]. By eliminating the first derivative $d\Psi_n/dx$ in the set of linear equations, Eq. (14), one can use the Green's function approach to construct a general solution for Ψ_n [8]. This generalizes to D dimensions the previous work of Laurenzi [8] for the three-dimensional solutions of the TF equation.

Functional Derivative of Kinetic Energy T in D Dimensions

Returning to Eq. (3), one can raise Eq. (9) to the power $2/(D-2)$ to obtain a different, though, of course, equivalent, form of the functional derivative $\delta T^{(D)}/\delta n(r)$. The result is

$$\frac{\delta T^{(D)}}{\delta n(r)} = \gamma^{(D)}\left[\frac{1}{n}\frac{\partial^2 n}{\partial r^2} + \left(\frac{D-1}{r}\right)\frac{1}{n}\frac{\partial n}{\partial r} + \left(\frac{2}{D} - 1\right)\left(\frac{1}{n}\frac{\partial n}{\partial r}\right)^2\right]^{2/D-2}, \tag{19}$$

where

$$\gamma^{(D)} = \left(1 + \frac{2}{D}\right)c_k^{(D)}\left(\frac{2}{D}\right)^{2/(D-2)} \times (4\pi e)^{-2/D}\beta_D^{4/D(2-D)}. \tag{20}$$

This is the main result of the present work and generalizes to D dimensions the previous work of one us for the three-dimensional TF neutral atom, namely

$$\frac{\delta T^{(3)}}{\delta n(r)} = \frac{5}{3}c_k^{(3)}l^2\left[\frac{\nabla^2 n}{n} - \frac{1}{3}\left(\frac{\nabla n}{n}\right)^2\right]^2. \tag{21}$$

Conclusion

The conclusion is that for the self-consistent TF atom in D dimensions, the functional derivative of the kinetic energy T can be expressed in terms of "reduced" density gradient terms $(1/n)(\partial n/\partial r)$ and $(1/n)(\partial^2 n/\partial r^2)$. The local form (3) and the density gradient (nonlocal) form (21) are, of course, entirely equivalent. This is because of the differential Eq. (10) satisfied by the self-consistent ground-state electron density in the TF atom in D dimensions.

ACKNOWLEDGMENTS

One of us (N.H.M.) would like to thank Dr. A. Holas (PAS, Warsaw) for many valuable discussions on the kinetic energy in functional theory and the Leverhulme Trust, UK, for partial financial support for his work on density functional theory. S.K. is grateful for support received from the Office of Naval Research.

References

1. See, for instance, M. Pearson, E. Smargiassi, and P. A. Madden, J. Phys. C **5**, 3321 (1993).
2. G. F. Kventsel and J. Katriel, Phys. Rev. A **24**, 2299 (1981).
3. N. H. March, J. Math. Phys. **26**, 554 (1985).
4. A. Holas and N. H. March, Phil. Mag. **69**, 787 (1994).
5. N. H. March, Phys. Rev. A, to appear.
6. For reviews, see D. R. Herschbach, J. Avery, and O. Goscinski, *Dimensional Scaling in Chemical Physics* (Kluwer, Dordercht, 1993).
7. C. M. Bender, K. A. Milton, S. S. Pinsky, and L. M. Simmons, J. Math. Phys. **30**, 1447 (1989).
8. B. J. Laurenzi, J. Math. Phys. **31**, 2535 (1990).

On Computing the Molecular Detour Matrix

N. TRINAJSTIĆ,[1] S. NIKOLIĆ,[1] Z. MIHALIĆ[2]

[1]*The Rugjer Bošković Institute, HR-10001 Zagreb*

[2]*The Faculty of Science, The University of Zagreb, HR-10001 Zagreb, The Republic of Croatia*

Received 1 March 1997; revised 16 April 1997; accepted 16 April 1997

ABSTRACT: A method for computing the (molecular) detour matrix is proposed.

© 1997 John Wiley & Sons, Inc. Int J Quant Chem **65**: 415–419, 1997

The detour matrix was introduced into the mathematical literature in 1969 [1] and 25 years later into the chemical literature under the name of the maximum path matrix of a molecular graph by Ivanciuc and Balaban [2].

The detour matrix can be used to compute the so-called detour index [3, 4] in the same way as the distance matrix [5] can be employed to generate the Wiener index [6]. The detour index, which is a Wiener-like index, was also introduced by Ivanciuc and Balaban [2] as the half-sum of the maximum path sums and independently by John [7] and us [3]. Lukovits, who introduced the term "the detour index," studied the properties of this index [4, 8]. He was also first to use this index in structure–property modeling [4]. The present report was stimulated by Lukovit's remark [8a]: "*The usefulness of the detour index is deflated by the fact that to date no method (but inspection) is available to compute this index.*" Or, in other words, there is no method available to compute the detour matrix but by hand. In attempting to remedy the above, we propose here a computer method for constructing the detour matrix for graphs of moderate sizes and a limited number of cycles.

Correspondence to: N. Trinajstić.

Contract grant sponsor: Ministry of Science and Technology of the Republic of Croatia.

Contract grant number: 00980606.

The detour matrix $\mathbf{\Delta} = \mathbf{\Delta}(G)$ of a labeled connected (molecular) graph G is a real symmetric $N \times N$ matrix whose (i, j)-entry is the length of the *longest* path [9a] from vertex i to vertex j:

$$(\mathbf{\Delta})_{ij} = \begin{cases} \sigma_{ij} & \text{if } i \neq j \\ 0 & \text{if } i = j \end{cases}, \qquad (1)$$

where σ_{ij} is the number of steps in a longest path (i.e., the *maximum* number of edges) in G between vertices i and j.

This definition is exactly the "opposite" of the definition of the traditional graph-theoretical distance matrix, whose off-diagonal entries are the lengths of the *shortest* paths between the vertices

© 1997 John Wiley & Sons, Inc.

CCC 0020-7608 / 97 / 050415-05

in G [5, 9b]:

$$(\mathbf{D})_{ij} = \begin{cases} d_{ij} & \text{if } i \neq j \\ 0 & \text{if } i = j \end{cases} \quad (2)$$

where d_{ij} is the number of steps in a shortest path (i.e., the *minimum* number of edges) in G between vertices i and j. As examples, the distance and detour matrices for a simple bicyclic labeled graph G are given in Figure 1.

The detour index Ω is defined in the same as is the Wiener index W [10], i.e., the detour index is equal to the half-sum of the elements of the detour matrix $\mathbf{\Delta}$ [2–4]:

$$\Omega = (1/2)\sum_i \sum_j (\mathbf{\Delta})_{ij} \quad (3)$$

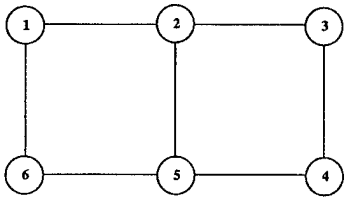
$$W = (1/2)\sum_i \sum_j (\mathbf{D})_{ij}. \quad (4)$$

The Wiener index and the detour index for a bicyclic graph G are also given in Figure I.

It is obvious from (3) and (4) that the Wiener index and the detour index are identical for acyclic structures. For polycyclic structures, they are not particularly intercorrelated indices. For example, the linear correlation between W and Ω for a set of 37 diverse polycyclic structures has a modest correlation coefficient ($r = 0.79$) [3a].

The computation of the detour matrix is a nontrivial problem of long standing [11]. We propose a procedure for computing the (molecular) detour matrix from the (molecular) distance matrix since there are several algorithms available in the literature for computing the distance matrix [9b]. We will also use the adjacency matrix to generate the distance matrix. The procedure is based on the computation of distance matrices for sets of selected subgraphs of a considered graph G. These subgraphs are created from G by removing successively edges whose vertices are at least divalent until the set of spanning trees is reached. For each subgraph, the distance matrix is computed and is compared to the starting distance matrix corresponding to G. If any of the distances d_{ij} in the newly created distance matrix is larger than the corresponding element $(d_{ij})_0$ in the initial distance matrix, then $(d_{ij})_0$ should be replaced with d_{ij}. The final distance matrix, obtained after the considered set of subgraphs is inspected, is the detour matrix. After the detour matrix is obtained, the computation of the detour index is straightforward.

The block diagram of our computational procedure is given in Figure 2. As an illustrative example, we computed the detour matrix for the same bicyclic graph G that was considered before in Figure 1. This computation is shown in Figure 3.



G

$$\mathbf{D} = \begin{bmatrix} 0 & 1 & 2 & 3 & 2 & 1 \\ 1 & 0 & 1 & 2 & 1 & 2 \\ 2 & 1 & 0 & 1 & 2 & 3 \\ 3 & 2 & 1 & 0 & 1 & 2 \\ 2 & 1 & 2 & 1 & 0 & 1 \\ 1 & 2 & 3 & 2 & 1 & 0 \end{bmatrix} \qquad \Delta = \begin{bmatrix} 0 & 5 & 4 & 5 & 4 & 5 \\ 5 & 0 & 5 & 4 & 3 & 4 \\ 4 & 5 & 0 & 5 & 4 & 5 \\ 5 & 4 & 5 & 0 & 5 & 4 \\ 4 & 3 & 4 & 5 & 0 & 5 \\ 5 & 4 & 5 & 4 & 5 & 0 \end{bmatrix}$$

W = 25 $\qquad$ Ω = 67

FIGURE 1. The distance matrix (**D**) and the detour matrix ($\mathbf{\Delta}$) of a labeled bicyclic graph G.

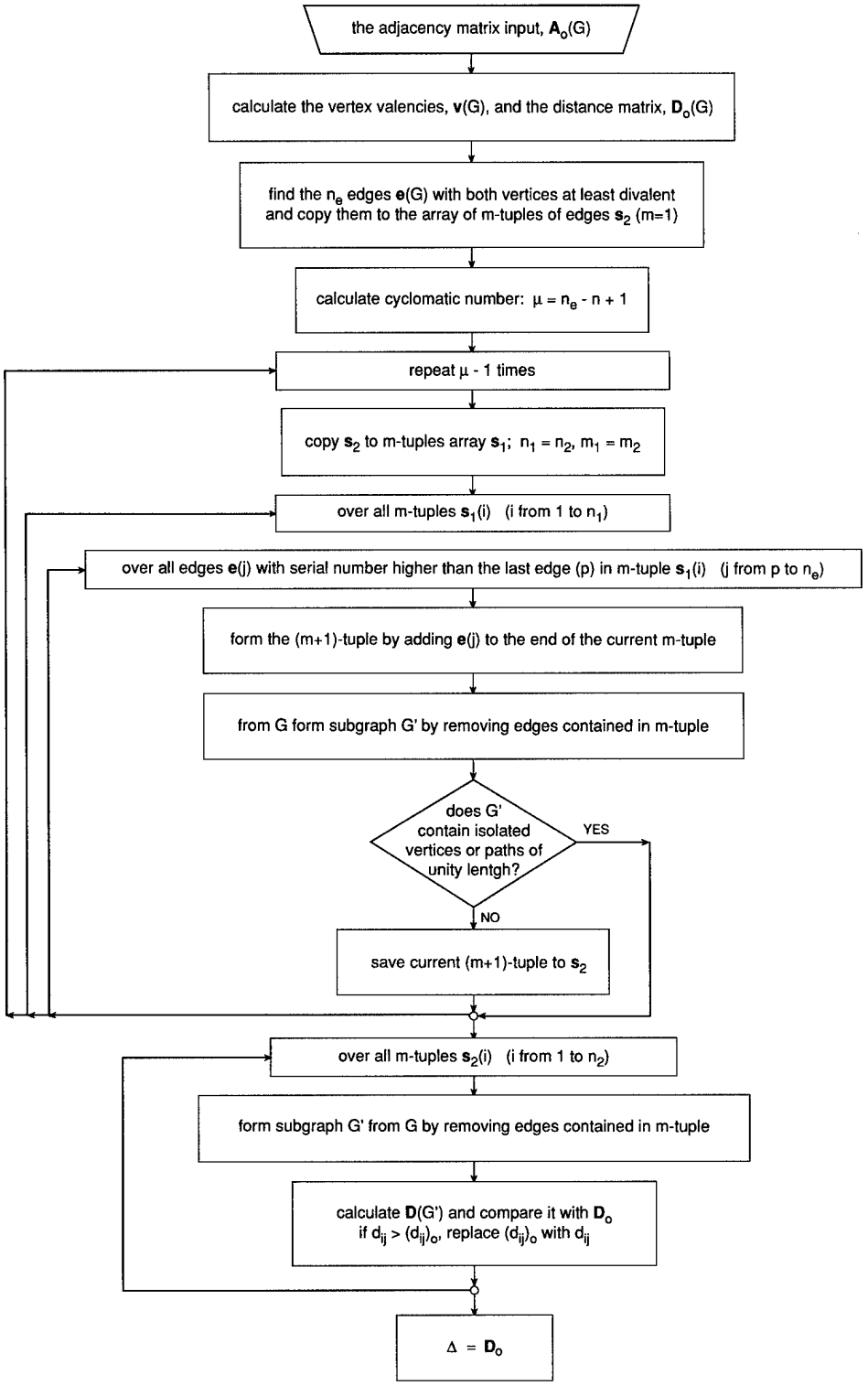
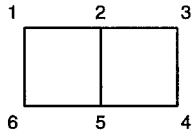


FIGURE 2. A block-diagram of the computer program.



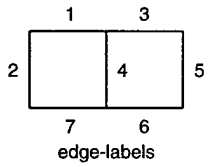
G

1) Generate the adjacency matrix $\mathbf{A}_0$ and calculate distance matrix $\mathbf{D}_0$ of graph G.

$$\mathbf{A}_0 = \begin{bmatrix} 0 & 1 & 0 & 0 & 0 & 1 \\ 1 & 0 & 1 & 0 & 1 & 0 \\ 0 & 1 & 0 & 1 & 0 & 0 \\ 0 & 0 & 1 & 0 & 1 & 0 \\ 0 & 1 & 0 & 1 & 0 & 1 \\ 1 & 0 & 0 & 0 & 1 & 0 \end{bmatrix} \qquad \mathbf{D}_0 = \begin{bmatrix} 0 & 1 & 2 & 3 & 2 & 1 \\ 1 & 0 & 1 & 2 & 1 & 2 \\ 2 & 1 & 0 & 1 & 2 & 3 \\ 3 & 2 & 1 & 0 & 1 & 2 \\ 2 & 1 & 2 & 1 & 0 & 1 \\ 1 & 2 & 3 & 2 & 1 & 0 \end{bmatrix}$$

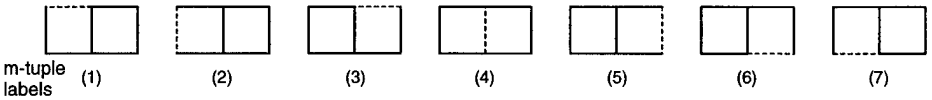
2) Find edges **e**(G) with both vertices at least divalent and copy them to array of m-tuples of edges (m = 1).

edge	vertices	valencies
1	1-2	2-3
2	1-6	2-2
3	2-3	3-2
4	2-5	3-3
5	3-4	2-2
6	4-5	2-3
7	5-6	3-2



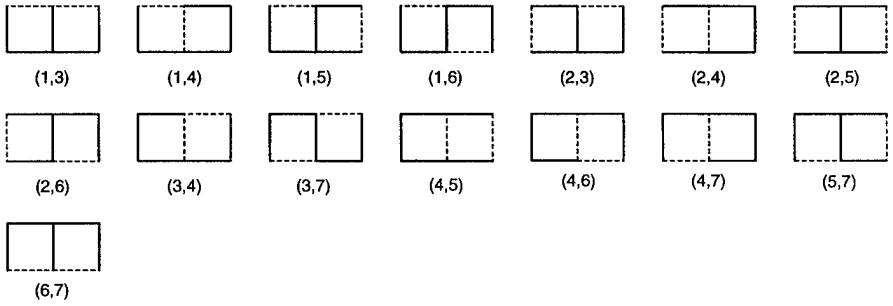
edge-labels

3) For every m-tuple, disconnect edge(s) in the m-tuple, disregarding graphs that contain disconnected vertices and paths of length one.



$m_1 = 1$ n_1 (number of m-tuples) = 7

4) From m-tuples, form the (m+1)-tuples by adding the edges (found in step 2) with the edge serial numbers higher than the serial number of the last m-tuple edge.



m_2 (number of m+1-tuples) = 2 n_2 (number of m+1-tuples) = 15

(a)

FIGURE 3. Computation of the detour matrix for the bicyclic graph *G* using the proposed method.

5) Copy (m+1)-tuples to array of m-tuples, and go to the step 3. Continue repeating steps 3 and 4 until spanning trees disconnecting level is achieved (i.e., m+1 = cyclomatic number).

In the present example, there is no need to go back to the step 3.

6) Calculate the distance matrix **D** for every subgraph obtained by m+1 disconnections. If any of the distances d_{ij} is larger than the corresponding element in $\mathbf{D}_o$, replace $(d_{ij})_o$ with d_{ij}.

7) The detour matrix Δ is equal to the final distance matrix.

$$\Delta = \begin{bmatrix} 0 & 5 & 4 & 5 & 4 & 5 \\ 5 & 0 & 5 & 4 & 3 & 4 \\ 4 & 5 & 0 & 5 & 4 & 5 \\ 5 & 4 & 5 & 0 & 5 & 4 \\ 4 & 3 & 4 & 5 & 0 & 5 \\ 5 & 4 & 5 & 4 & 5 & 0 \end{bmatrix}$$

8) Calculate the detour index.

$\Omega = 67$

(b)

FIGURE 3. (Continued).

The CPU time need to construct the detour matrix for G in Figure 3 was 1 s on the workstation HP-735.

ACKNOWLEDGMENT

This work was supported by the Ministry of Science and Technology of the Republic of Croatia through Grant No. 00980606. We thank the referees for constructive comments.

References

1. F. Harary, *Graph Theory* (Addison-Wesley, Reading, MA, 1969), p. 203.
2. O. Ivanciuc and A. T. Balaban, Math. Chem. (MATCH) **30**, 141 (1994).
3. (a) D. Amić and N. Trinajstić, Croat. Chem. Acta **68**, 53 (1995). (b) S. Nikolić, N. Trinajstić, A. Jurić, and Z. Mihalić, Croat. Chem. Acta **69**, 1577 (1996). (c) N. Trinajstić, S. Nikolić, B. Lučić, D. Amić, and Z. Mihalić, J. Chem. Inf. Comput. Sci. (in press).
4. I. Lukovits, Croat. Chem. Acta **69**, 873 (1996).
5. (a) Z. Mihalić, D. Veljan, D. Amić, S. Nikolić, D. Plavšić, and N. Trinajstić, J. Math. Chem. **11**, 223 (1992). (b) Z. Mihalić, S. Nikolić, and N. Trinajstić, J. Chem. Inf. Comput. Sci. **32**, 28 (1992).
6. (a) H. Hosoya, Bull. Chem. Soc. Jpn. **44**, 2332 (1971). (b) S. Nikolić, N. Trinajstić, and Z. Mihalić, Croat. Chem. Acta **68**, 105 (1995).
7. P. E. John, Math. Chem. (MATCH) **32**, 207 (1995).
8. (a) I. Lukovits, J. Chem. Inf. Comput. Sci. **36**, 65 (1996). (b) H.-Y. Zhu, D. J. Klein, and I. Lukovits, J. Chem. Inf. Comput. Sci. **36**, 420 (1996). (c) I. Lukovits and M. Razinger, J. Chem. Inf. Comput. Sci. **37**, 283 (1997).
9. N. Trinajstić, *Chemical Graph Theory*, 2nd ed. (CRC Press, Boca Raton, FL, 1992). (a) pp. 9–11; (b) pp. 52–57.
10. H. Wiener, J. Am. Chem. Soc. **69**, 17 (1948).
11. F. Buckley and F. Harary, *Distance in Graphs* (Addison-Wesley, Reading, MA, 1990), pp. 213–214.

Many-Body Valence-Bond Theory

D. J. KLEIN,[1] H. ZHU,[2] R. VALENTI,[3] M. A. GARCIA-BACH[4]

[1]*Texas A & M University-Galveston, Galveston, Texas 77553-1675*
[2]*Sealy Center for Biomolecular Structure, University of Texas Medical Branch, Galveston, Texas*
[3]*Institut für Physik, Universitat Dortmund, 44221 Dortmund, Germany*
[4]*Fisica Fonomental, Universitat de Barcelona, Diagonal 647, 08028-Barcelona, Spain*

Received 29 March 1997; accepted 1 June 1997

ABSTRACT: The classical theory of chemical valence, first, is naturally formalized in mathematics in the area of graph theory and, second, finds an extension in quantum mechanics in terms of the Heitler–London–Pauling "valence-bond" (VB) theory. Thus, VB theory stands in a fairly unique position, although in quantum chemistry, there often has been a preference for the alternative (perhaps even "complementary") molecular orbital (MO) theory, presumably in large part because of computational efficacy for general molecular structures. Indeed, as formulated by Pauling and others, VB theory was described as a configuration interaction (CI) problem when there were multiple relevant classical valence structures for the same molecular structure. Also, as now recognized, a direct assault on CI is computationally intensive, prone to size-inconsistency problems, and effectively limited to smaller systems—whereas indirect approaches, e.g., via wave-function cluster expansions or renormalization-group theory, often neatly avoid these problems. Thus, what is (and perhaps always has been) needed is "many-body" schemes for VB computations (as well as for higher-order MO-based approaches, too). Here, then, certain such many-body VB-amenable computational schemes are to be discussed, in the context of semiempirical (explicitly correlated) graphical models. The collection of models are described and interrelated in a fairly comprehensive systematic manner. A selection of many-body cluster expansion methods are then discussed with special reference to resonating VB wave functions and the fundamental graph-theoretic nature of the consequent problems (such as also are noted to arise in lattice-discretized statistical-mechanical problems, too). Some examples are described incorporating resonance among exponentially great numbers of VB structures as applied: for large icosahedral-symmetry fullerenic structures, for the (polyacetylenic) linear chain, and for ladderlike conjugated polymers. It is contended that practicable many-body VB-theoretic methods are now available, retaining clear links to classical chemical valence theory. Hopefully, too, these methods may soon find use beyond the semi-empirical framework.
© 1997 John Wiley & Sons, Inc. Int J Quant Chem **65:** 421–438, 1997

Correspondence to: D. J. Klein.
Contract grant sponsor: Welch Foundation of Houston, Texas.
Contract grant sponsor: DGICYT.
Contract grant number: PB92-0868.

© 1997 John Wiley & Sons, Inc.
CCC 0020-7608 / 97 / 050421-18

1. Introductory Survey

The idea of *valence structures* goes back to classical chemistry. Also, indeed, then it was at the heart of chemistry, although the theory was primitive in a quantitative mode. There are both brief surveys [1] encompassing this history, as well as whole books on the subject [2].

Soon after the advent of quantum mechanics, several valence-bond developments were made:

- First, with the ab initio H_2 computations of Heitler and London [3] who presented a fundamental quantum mechanical description of the covalent bond;
- Second, with Rumer's [4] realization of a basis of such *covalent* electronic configurations in suggestive correspondence with classical chemical-bonding structures;
- Third, with Pauling's identification [5] of oriented *hybrid* orbitals as precursors for bond orbitals such as could be used in conjunction with Rumer basis functions; and
- Fourth, with Pauling and others' development [6] of such Rumer-type *valence-bond* bases as a foundation for a classically connected theory of molecular electronic structure with extension to incorporate *resonance* to describe delocalized bonding.

Thus, a quantum mechanically founded valence-bond (VB) theory had auspicious beginnings, although as reviewed just a bit more completely elsewhere [7, 8], a slow period of development followed. The alternative molecular orbital (MO) theory began development roughly at the same time by Hund, Hückel, and Mulliken, but continued with further theoretical developments by Coulson and co-workers while a significant computational advance was made by Roothaan and Hall in the form of a discrete-orbital-basis self-consistent-field theory. Several supposed difficulties with VB, both computationally and conceptually (e.g., involving nonorthogonality and size-consistency), were brought to attention. Presumably, largely due to the greater computational efficacy of MO theory, it came to dominance—then further various semiempirically formulated MO-based theorems were developed, e.g., by Longuet-Higgins and Dewar, and, finally, the MO-based Woodward–Hoffmann rules only further enhanced this dominance of MO theory. The fact that VB theory related so nicely in a conceptual (but seemingly noncomputational) way back to classical chemical-bonding ideas may have actually disinclined some researchers to this approach—it being viewed that the numerically correct answers should come out of "pure" quantum mechanics (i.e., solely out of physics) without folding in any classical chemical concepts, at least if one expends sufficient computational effort.

Moreover, in physics, many-body methods were developed largely in terms of the MO (or band-orbital-theoretic or momentum-space) picture. Some conceptual problems concerning size-consistency were resolved in this context and related to powerful computational procedures: many-body perturbation theory, Green's-function decoupling techniques, and cluster-expanded wave functions. Also, ultimately, these computational techniques were all adapted (in the 1970s and 1980s) for extensive ab initio molecular computations. Also, MO-related density functional theory was developed in a powerful computational format.

Through the 1950s, 1960s, and 1970s, there were still a few researchers in the area of VB theory (including Coulson, Daudel, Gallup, Goddard, Löwdin, Matsen, McConnell, McWeeny, Oosterhoff, and Simonetta, although most of these researchers had much diversified interests). But especially starting in the 1980s (primarily with a new group of researchers), it became clear that VB theory is far from dead. On the ab initio side, there are the especially notable accurate small-molecule computations of Gerratt and co-workers [9, 10]. On a more theoretical side, Anderson [11] suggested that a VB picture may be crucial to understanding high-temperature superconductivity, so that now there are a variety of formal many-body resonating VB developments made by physicists, e.g., as reviewed in [12]. Also, on the semiempirical chemical side, there have been (and are reviewed [13]) many developments, amusingly often linking up with the ideas now developed in conjunction with high-temperature superconductivity.

Now, it seems that there are many-body techniques which are fairly widely recognized to encompass either MO- or VB-based approaches. One such is the renormalization-group-theoretic ideas, although an efficacious general computational scheme for general molecular structures has yet to

have reached any general recognition. Another powerful computational approach is via the *Monte Carlo* statistical techniques, which, again, have yet to reach any general utility, although in the hands of experts, there are some high-accuracy results on selected systems. Also, more and more, it seems that techniques earlier thought to be MO-based can be formulated as well in a VB-format.

Here, wave-function cluster expansions developed in the context of semiempirical VB-theoretic models are to be considered. Notably, it is believed that the semiempirical context is not necessary. But before describing the different types of cluster expansions based on local structures, some further general theoretical characterization of VB-theoretic ideas in the next section is appropriate. Beyond the description of different types of locally represented cluster-expanded wave functions, Section 3 goes on to indicate the form of the overlap and Hamiltonian matrix elements, as generating functions for the counting of certain types of subgraphs of the parent molecular graph. Section 4 notes certain qualitative features of the different types of wave functions, with attention to the structural circumstances for best applicability and to types of long-range order which can arise. Finally, Section 5 reports and compares numerical results on three different types of structures: icosahedral-symmetry fullerenes, the infinite linear (polyacetylenic) chain, and the infinite ladder.

2. VB Theory: Bases, Models, and Resonance

As the first step, some of the nomenclature and framework should be clarified. A *VB* basis consists of configurations of spin-paired localized orbitals, at least for the overall spin singlet case, while for higher spins, there is augmentation by unpaired spins. Typical *VB* spin-pairing diagrams in correspondence with the basis elements for the case of six electrons in six orbitals (as for the six occupied atomic π-orbitals of benzene) appear as in Figure 1 and display an evident close analogy to the primary classical *valence structures* for benzene, especially if augmented with the rest of the spin-pairing diagram for the σ-orbitals. Rumer [4] focused on the singlet case with orbitals singly occupied, it being recognized that the extension to states with doubly occupied orbitals is straightforward. Also, Pauling [6] pointed out early the ready extension to the overall spin doublet case, and the approach taken hinted at further extension, e.g., as done in Simonetta's group [14]. But it is to be emphasized that there are other possibilities—anticipated to be most significant when the VB structures as formalized by Rumer, Weyl, and Teller [15] do not correspond so closely to classical VB structures. I.e., this *Rumer* basis is built in terms of pairings around a cycle, and in many cases, a chemical structure may have little to do with a simple cycle. More important from a chemical viewpoint should be spin-pairing patterns involving pairing between nearest pairs of localized orbitals, independently of a relation to the formal basis of Rumer et al. [15].



FIGURE 1. Five independent covalent VB structures for six orbitals. These VB structures are also the Rumer structures.

Granted a VB basis, a semiempirical model represented on such a basis often is described as a "VB" model. Of course, such models can be represented on any basis spanning the same space, although the semiempirical integral approximations are (usually) motivated from considerations in terms of the localized (atomic) orbitals as they appear in VB basis states. Here, a *VB* model is taken to be a model where the atomic orbitals which appear are viewed to be non-orthogonal. One such circumstance is the VB model of Pauling and Wheland [16] expressed by the covalent space of configurations built from singly occupied orbitals. Indeed, the model so developed turns out to be essentially the Heisenberg spin Hamiltonian, more often expressed by the basis of what is essentially Slater determinants of atomic orbitals, and each determinant is distinguished solely via the spin assignment. Now, most commonly, the model is re-represented equivalently to act just on spin space; hence, the Hamiltonian takes the general form

$$H = \sum_P J_P P^{spin} \tag{2.1}$$

where P^{spin} are spin space permutations and J_P are parameters. The simplest (and usual) approximation retains just the terms involving a transposition $P = (ij)$ exchanging the *ith* and *jth* indices; hence, the exchange parameter can [17] be approx-

imated to be of the form

$$J_{(ij)} = \{ES_{ij} - \langle\Phi|(ij)H|\Phi\rangle\}/\{1 - S_{ij}^2\}, \quad (2.2)$$

with $E \equiv \langle\Phi|H|\Phi\rangle$, $S_{ij} \equiv \langle\Phi|(ij)|\Phi\rangle$, and Φ most simply being taken as a product of nonorthogonal atomiclike orbitals, one assigned to each center. Further, the interaction may be represented in terms of ordinary spin operators:

$$(ij)^{spin} = 2\mathbf{s}_i \cdot \mathbf{s}_j + 1/2$$
$$= 2s_i^z s_j^z + s_i^+ s_j^- + s_i^- s_j^+ + 1/2. \quad (2.3)$$

Then, the Hamiltonian (with a further shift of the 0 of energy) is written as

$$H = \sum_{i\sim j} J_{ij} 2\mathbf{s}_i \cdot \mathbf{s}_j, \quad (2.4)$$

which is the more commonly presented form; hence, it is known as the Heisenberg spin Hamiltonian, often with i and j restricted to nearest neighbors. Evidently, reference to Rumer or VB bases is now quite hidden, and many other bases are used. Bases involving "spin-waves" are not uncommon in physics, but working with representations on such alternative bases can lead to nonlocally interpreted wave functions, and results can end up being rather far divorced from apparent classical chemical connection and interpretation.

A variety of VB models arise, with possibly the most natural hierarchy indicated in Figure 2. There, also, a systematic derivational scheme is indicated, based on successive steps which are either restrictions to ever smaller spaces or orthogonalizations of natural (initially nonorthogonal) many-particle bases for these spaces. It should be noted that older criticisms concerning non-orthogonality or size-consistency "catastrophes" connected with several of the intermediate models are largely irrelevant or misleading, as addressed elsewhere [18].

Resonating VB theory should make explicit use of VB states, especially the more *chemical* corresponding to the more local spin-pairing patterns. This really is the focus of this review, especially for the *many-body* case. The use of the phrase *VB theory* (without the adjective *resonating*) should be more general, but it might best be taken to describe a treatment with connection back to the classical chemical-bonding ideas, using a VB basis adapted to the molecular structure under consideration, although, often, researchers refer to anything using the Rumer basis as "VB theory," i.e., when a system has a structure little related to a single cycle, then the standard Rumer basis often does not include many locally spin-paired structures. The *Pauling–Wheland resonance-theoretic model*

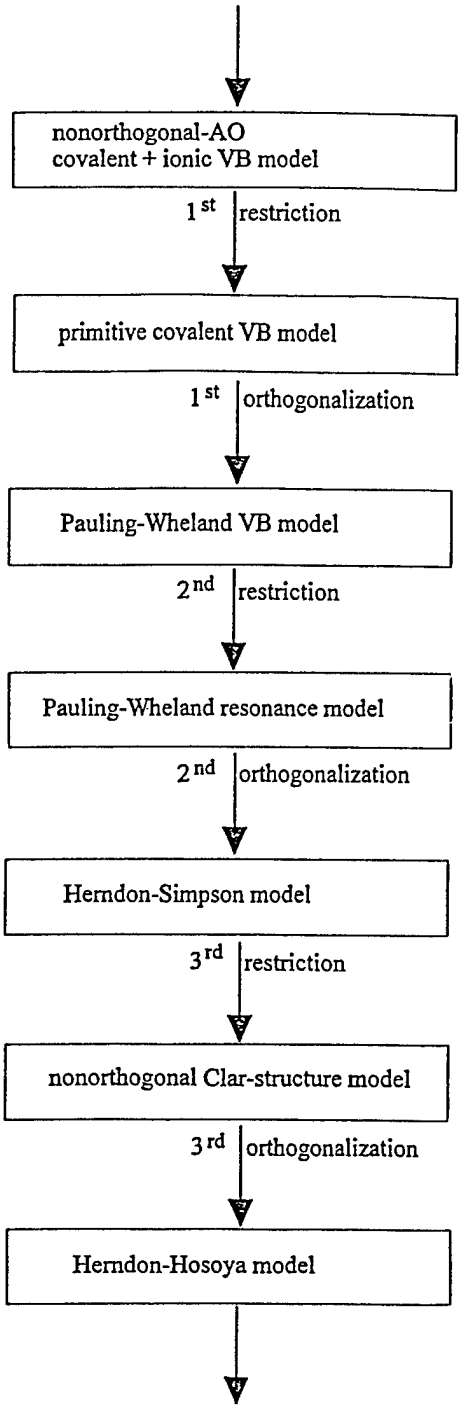


FIGURE 2. A hierarchy of VB-theoretic models.

(of Fig. 2) is obtained as the restriction of the covalent-space (Heisenberg) VB model just to the subspace of *Kekule structures* which are those VB structures with spin-pairings solely between near-neighboring pairs of sites. The molecular structure is conveniently mathematically encoded in terms of a molecular *graph* G which is specified by the sites (which here are the various π-orbitals) and by the set of pairs of neighbor sites. The Kekule structures are nonorthogonal, but they may be subjected to Löwdin symmetric orthogonalization in a systematic fashion [19] to yield what is known as the Herndon–Simpson model [20], which most simply takes the form

$$H_{\mathrm{HS}} = R_1 \sum_{\alpha} \Lambda_{\alpha} + R_2 \sum_{\beta} \Lambda_{\beta}, \qquad (2.5)$$

where R_1 and R_2 are parameters, the α- and β-sums are over the 6- and 10-cycles of G, and Λ_{α} and Λ_{β} are operators which give a nonzero result only if they act on a Kekule structure with a pattern of alternating π bonds around the cycle (α or β), in which case they reverse the pattern of alternation around that cycle. Then, utilizing a ground-state wave-function *Ansatz* as an equally weighted sum of all Kekule structures, there results [21] a resonance energy expressed in an elegant graph-theoretic form, which, in fact, can also be motivated [22] from purely classical chemical-bonding ideas.

Additional models are also indicated in Figure 2. Any of these models can be expressed in a graph-theoretic form, and all involve explicit electron correlation. Also, although a number of many-body solution techniques are possible as briefly discussed elsewhere [23], focus here is to be on a class of wave-function cluster expansions where local structures are manifest. Indeed, three types of such wave-function cluster expansions are here described in some detail.

3. Wave-function Cluster Expansions

One general type of approach to the solution of such models is via the localized cluster expansion of system wave functions. Now, wave-function cluster expansions seem (at least in an ab initio framework) most commonly to be carried out in the coupled-cluster format [24] based on a single-determinantal MO reference, although it is understood [25] that the technique can be applied in a local format based on a reference built from localized orbitals. Also, such localized-orbital coupled-cluster techniques have quite successfully been utilized on the Heisenberg model (as well as the Hubbard model). But, especially for the lower models in the hierarchy of Figure 2, this has not been done, and, indeed, it is often not so clear what role such orbitals would play. Here, then, we consider a general type of local substructure cluster expansion for wave functions. Considerations here are limited to developments for the Heisenberg spin Hamiltonian and the Herndon–Simpson Hamiltonian, although much the same sort of ideas should be rather much more generally applicable. Even within the stated limitations, there are different types of local cluster expansions, and they are here discussed separately, but the three discussed are formulated in graph-theoretic language.

One presumes a molecular *graph* G, which may be thought of as the classical molecular connectivity pattern. The graph G is presumed to be *connected* in the sense that there exists a sequence of edges leading from any site to any other. Further, often, it is here assumed that G is *bipartite* in the sense that the set of sites may be partitioned into two subsets termed *starred* and *unstarred* subsets such that sites of one subset have neighbors solely in the other subset. For instance, all the classical benzenoids form bipartite networks, although several lattices arising in solid-state problems are also. It is to be emphasized that the presumption of a graph does not in itself engender any limitations—but, rather, it guides the form of the expansions, which when truncated in low order engenders an approximation. Different types of subgraphs composed from subsets of sites and subsets of edges of G are of relevance, and often these can be disconnected. In particular, each Kekule structure K is represented by a subgraph where the subset of sites for K is the full set of G and the subset of edges of K is to be such that every site has exactly one edge incident thereon in K.

3.1. NEEL-STATE-BASED CLUSTER EXPANSION

The first type of wave-function cluster expansion to be considered is the most nearly conventional and has at least in its simple two-site form been proposed several times [26] independently

and now used [27–30] quite successfully. For a bipartite graph G for the Heisenberg model, this systematic cluster expansion is based on the so-called *Neel* state which is a product of spins with α spins on the starred subset of sites and β spins on the unstarred subset of sites:

$$|\Phi\rangle \equiv \prod_i^{\star} \alpha(i) \prod_j^{\circ} \beta(j). \tag{3.1.1}$$

Even by itself, this may be viewed to be a zero-order estimate for the ground state of the antiferromagnetically signed Heisenberg model. But building from this, a cluster-expanded wave function may be considered of the form

$$|\Psi\rangle \equiv \exp_U(T^+)|\Phi\rangle, \tag{3.1.2}$$

where the subscript U indicates a slightly modified exponential function to be explained a little later and T is an excitation operator which may be written as a sequence of terms involving subgraphs of one-, two-, three-, four-sites and beyond:

$$\begin{aligned} T^+ \equiv & \sum_i x_i s_i^\sigma + \sum_{i\sim j} x_{ij} s_i^\sigma s_j^\sigma \\ & + \sum_{i\sim j\sim k} (x_{ijk} s_i^\sigma s_j^\sigma s_k^\sigma + x_{i(j)k} s_i^\sigma s_k^\sigma) \\ & + \sum_{i\sim j\sim k\sim l} (x_{ijkl} s_i^\sigma s_j^\sigma s_k^\sigma s_l^\sigma + x_{ij(k)l} s_i^\sigma s_j^\sigma s_l^\sigma \\ & + x_{i(j)kl} s_i^\sigma s_j^\sigma s_k^\sigma + x_{i(jk)l} s_i^\sigma s_l^\sigma) + \ldots, \end{aligned} \tag{3.1.3}$$

where the various $x_{\star}$ are variational parameters and the s_m^σ are spin-lowering or spin-raising operators s_m^- or s_m^+ for site m, i.e., the s_m^σ change the spin occurring in the Neel state Φ at site m. Also, note that within the three- and four-site terms there are what would usually be called pair excitations but involve pairs of sites as far apart as those which appear in the "proper" three- and four-site terms appearing within these same terms. This may be recast in a general form thusly:

$$T^+ \equiv \sum_{\gamma}^{\subseteq G} \sum_{\mathscr{S}}^{\gamma} x_{\gamma,\mathscr{S}} \prod_i^{\epsilon\mathscr{S}} s_i^\sigma, \tag{3.1.4}$$

where the first sum is over (connected) subgraphs γ of G, the second sum is over subsets $\mathscr{S}$ of sites of γ such that the set $\mathscr{S}$ occurs in no smaller subgraph, and the product is over the sites in $\mathscr{S}$. Then, the wave function may be expanded in terms of subgraphs $\boldsymbol{\gamma}$ which have many components disconnected from one another, it now being understood that the subscript U on the exponential in Eq. (3.1.2) indicates the deletion of any terms in the Taylor series expansion of the exponential involving products of subgraph terms with any sites in common. Then, the resultant "disentangled" form for the wave function is

$$|\Psi\rangle = \sum_{\boldsymbol{\gamma}}^{G} \sum_{\mathscr{S}}^{\boldsymbol{\gamma}} X(\boldsymbol{\gamma},\mathscr{S}) \prod_i^{\mathscr{S}} s_i^\sigma |\Phi\rangle, \tag{3.1.5}$$

where $\mathscr{S}$ is a subset of the sites of $\boldsymbol{\gamma}$ and the coefficient $X(\boldsymbol{\gamma},\mathscr{S})$ breaks up into a product of $x_{\gamma,\mathscr{S}}$ labeled by the different components γ of $\boldsymbol{\gamma}$ and by the sets $\mathscr{S}$ of sites of $\mathscr{S}$ which occur in γ:

$$X(\boldsymbol{\gamma},\mathscr{S}) = \prod_{\gamma}^{\boldsymbol{\gamma}} \prod_{\mathscr{S}}^{\mathscr{S}\&\gamma} x_{\gamma,\mathscr{S}}. \tag{3.1.6}$$

Really, Eqs. (3.1.5) and (3.1.6) specify the present *Ansatz* quite completely, the form of Eqs. (3.1.1)–(3.1.4) simply being more like the usual manner of presentation in the conventional coupled-cluster literature. But, a further important point (which much simplifies matters) is that if the net number of spins is to be conserved (as for the isotropic Heisenberg model) then the excitations not so conserving this number may be omitted, i.e., all the terms involving an odd number of excitations may be omitted, and, in addition, realizing that the graph G is presumed to be bipartite, terms without a balance of starred and unstarred sites [such as that associated with $x_{i(j)k}$] may be omitted. Thus, Eq. (3.1.4) reduces to

$$\begin{aligned} T^+ \equiv & \sum_{i\sim j} x_{ij} s_i^\sigma s_j^\sigma + \sum_{i\sim j\sim k\sim l} (x_{ijkl} s_i^\sigma s_j^\sigma s_k^\sigma s_l^\sigma \\ & + x_{i(jk)l} s_i^\sigma s_l^\sigma) + \ldots, \end{aligned} \tag{3.1.7}$$

although, again, all the simplification may be envisaged in the form of Eq. (3.1.5). Finally, with symmetry, many of the x-parameters may be identified as equal. With all sites translationally equivalent, all the x_{ij} can be taken as the same.

3.2. HULTHEN–KASTELEYN *ANSATZ*

This approach originally considered by Hulthen [31] and Kasteleyn [32] and evidently independently by Huse and Elser [23] may be viewed to be also based on Neel-state-related ideas. Again,

special note of neighbor pairs of α and β spins is made as they occur in a general N-site product,

$$|\sigma(N)\rangle \equiv |\sigma_1(1)\sigma_2(2)\sigma_3(3)\ldots\sigma_N(N)\rangle, \quad (3.2.1)$$

of such sites spins $\sigma_i = \alpha, \beta$; i.e., with $s(\sigma(N), G)$ the number of β spins assigned to unstarred sites in $\sigma(N)$, the Hulthen–Kasteleyn cluster-expansion *Ansatz* is

$$|\Psi_{\mathrm{HK}}\rangle \equiv \sum_{\sigma(N)} (-1)^{s(\sigma(N),G)} \prod_{i\sim j}^{G} x_{ij}(\sigma_i\sigma_j)|\sigma(N)\rangle, \quad (3.2.2)$$

where the variational x-parameters take the value 1 if $\sigma_i \neq \sigma_j$. The phase factor here is convenient since it is known [34] that upon inclusion of this in the product basis vectors the ground-state wave function (for the nearest-neighbor Heisenberg on a bipartite G) appears *nodeless*, in the sense that the correct expansion coefficients for the $(-1)^{s(\sigma(N),G)}|\sigma(N)\rangle$ can all be chosen non-negative. If all the neighbor pairs are translationally equivalent (while also there is spin-symmetry under the interchange of α and β), then all the $x_{ij}(\alpha\alpha) = x_{ij}(\beta\beta) \equiv x$ for $i - j$. Now, if $\#(\alpha\beta; \sigma(N), G)$ is defined as the number of α, β pairs in $\sigma(N)$ which are neighbors in G, then the ground-state *Ansatz* becomes

$$|\Psi_{\mathrm{HK}}\rangle \equiv \sum_{\sigma(N)} x^{\#(\alpha\beta;\sigma(N),G)}(-1)^{s(\sigma(N);G)}|\sigma(N)\rangle. \quad (3.2.3)$$

Moreover, one can imagine a way to generalize this *Ansatz* to higher orders, with variational parameters $x_\gamma(\sigma(\gamma))$ dependent on the spin configuration $\sigma(\gamma)$ on a (connected) subgraph of type γ, i.e., we let $\#(\sigma(\gamma), \gamma; \sigma(N), G)$ denote the number of subgraphs of type γ in G such that the spin configuration $\sigma(\gamma)$ appears in $|\sigma(N)\rangle$, and then we take the general ground state to be expressed as

$$|\Psi\rangle \equiv \sum_{\sigma(N)} \prod_{\gamma}^{G} \{x_\gamma(\sigma(\gamma))\}^{\#(\sigma(\gamma),\gamma;\sigma(N),G)} \cdot(-1)^{s(\sigma(N),G)}|\sigma(N)\rangle. \quad (3.2.4)$$

If subgraphs up to the size of G are kept, then this includes the exact wave-function. In fact, in the form given, there is an overabundance of parameters—one need not use subgraphs γ which are included in any other retained subgraphs. (Or if such smaller subgraphs are kept, the associated variational parameters can be chosen, say, to take the values as determined when there were no larger subgraphs included in the earlier truncated cluster expansion.)

3.3. RESONATING VB CLUSTER EXPANSION

Neither of the more nearly conventional cluster-expansion *Ansätze* of the preceding two sections really incorporate VB-theoretic ideas for wave functions, but this now is to be done. Strangely, though the most closely related to classical chemical ideas, it seems to be the most recently considered [29, 35–37]. This VB-theoretic *Ansatz* is definable in terms of standard singlet spin-pairing functions

$$\Theta[i, j] \equiv \alpha(i)\beta(j) - \beta(i)\alpha(j). \quad (3.3.1)$$

Then, presuming that G has at least a nonzero number of fully paired Kekule structures K, the lowest-order resonating VB wave function is taken to be

$$|\Psi_{\mathrm{RVB}}\rangle \equiv \sum_{K}^{G} \left(\prod_{i}^{\star} x_{ii(K)} \right) \prod_{j}^{\star} \Theta[j, j(K)], \quad (3.3.2)$$

where the sum is over Kekule structures of G, the two products are over the starred sites of G, and $i(K)$ denotes the site to which i is paired in K. For a higher-order *Ansatz*, one considers the Rumer structures R with spin-pairing between more distant sites but always such that starred and unstarred sites are paired. The wave function makes use of the idea of *convex* subgraphs γ of G, which is such that for every pair of vertices i and j of γ every shortest path of G between i and j is also in γ. Then, the general resonating VB wave-function takes the form

$$|\Psi_{\mathrm{RVB}}\rangle \equiv \sum_{R}^{G} \left(\prod_{\gamma}^{\mathrm{R}\wedge\mathrm{G}} x_\gamma \right) \prod_{j}^{\star} \Theta[j, j(R)], \quad (3.3.3)$$

where the γ-product here is over the components of the smallest (convex) subgraph of G such that R entails the pairing of no sites in different compo-

nents. Of course, the variational parameters x_γ are expected to become ever smaller as the (connected) subgraph component γ becomes ever larger, and usually one will truncate the *Ansatz* to keep just smaller size γ.

3.4. OTHER POSSIBLE CLUSTER-EXPANSION ANSÄTZE

There are slightly different ways to set up each of the types of cluster expansions noted in the preceding sections. First, for the Neel-state-based *Ansatz*, one need not utilize the "unlinked" subscript U on the exponential, although, then, the "disentangling" in matrix elements as in the next subsection would not be quite so complete (and the results would be numerically different at a given order of truncation), at least as far as the higher-order *Ansätze* are concerned. Second, for the lattice-gas *Ansatz*, one could seek to utilize the extra freedom in the $x_\gamma(\sigma(\gamma))$ imposing extra conditions, say by "factoring" the variational coefficients to pair factors $x_{ij}(\sigma_i\sigma_j)$ independently of whether i and j are neighbors or not; hence, the overlap reduces to the partitions function for an lattice-gas model solely with pair interactions. Third, for the reasoning VB model, the freedom connected with the overcompleteness of the full set of Rumer structures might be sought to be utilized, say again by a similar sort of factorization to pair terms. Although neither of these pair factorization assumptions is known to include the exact ground state, there is some empirical evidence [29, 33] of very high accuracy.

But there are at least a couple of other somewhat different sorts of possibilities for cluster-expansion *Ansätze*, although seemingly less well developed. One "sequentially" spin-adapted cluster expansion is related to the Young–Yamanouchi basis in somewhat the same sense that the resonating VB *Ansatz* is related to the set of locally paired VB structures. In this approach, the product basis $|\sigma(N)\rangle$ again is considered, and the z-component of spin at site i is denoted by m_i ($= +1/2$ for $\sigma_i = \alpha$ and $= -1/2$ for $\sigma_i = \beta$). Also, it is convenient to define

$$M_i \equiv \sum_{j=1}^{i} m_j \tag{3.4.1}$$

and we let S_i denote a total spin (quantum number) for indices $1 \to i$. Then, in a lower-order approximation,

$$|\Psi_{\text{seq}}\rangle \equiv \sum_{\sigma(N)} \sum_{S(N)} \left\{ \prod_{i=1}^{N-1} x_i(S_i, S_{i+1}) \times (S_i M_i \times \sigma_{i+1} | S_{i+1} M_{i+1}) \right\} |\sigma(N)\rangle, \tag{3.4.2}$$

where $S(N) \equiv (S_1, S_2, \ldots, S_N)$, the $x(S_i, S_{i+1})$ are variational parameters, and the $(S_i M_i \times \sigma_{i+1} | S_{i+1} M_{i+1})$ are Clebsch–Gordon (or spin-coupling) coefficients. More generally, in place of the two-site approximation with just $x_i(S_i, S_{i+1})$, one would (at the $k+1$-site approximation) instead have $x_i(S_i, S_{i+1}, S_{i+2}, \ldots, S_{i+k})$. But, further, in invoking an approximation, one limits the values which the S_i may take—e.g., variational x-parameters with S_j arguments exceeding some selected value are taken as 0. Presumably, though, because of the manner of the spin-coupling, this *Ansatz* (in its lower-order forms) is really only well adapted to quasi-1-dimensional systems (i.e., the chemical graph-theoretic circumstance is rather special).

Also, finally, a cluster-expansion on a "basis" of cluster-expanded wave functions might be mentioned as a possibility. Granted a localized cluster-expansion as any in the preceding sections, the local x-parameters can be viewed as separate variables which in the ground state for translationally symmetric systems fall into a relatively few equivalence classes, so that changing one at a time away from the ground-state value to give a result orthogonal to the ground state yields what may be viewed as candidate excited states or, alternatively, as new basis states. But in the local picture, this gives $\sim N$ such "single" excitations with changes to just one local x-parameter, and one can inquire what happens when two or more such changes are made. Of course, when such changes are made for well-separated regions, additional "multiple" excitations arise so that something approximating a new cluster-expanded basis seems to be arising. With such a new basis, a new representation for the Hamiltonian can be made, such new representation still being essentially local, and any standard many-body solution technique might be attempted on this new basis. In particular, a new cluster expansion might be made. Sometimes, the basis functions may not fully span the original space, as is the case with the Neel-state-based *Ansatz* if the excitations are built from a low-order primary cluster expansion, although, even so, the

secondary cluster expansion can provide some degree of improvement. The same limitation occurs with a low-order resonating VB *Ansatz*, but notably for the lattice-gas *Ansatz* for a linear chain, the new basis is essentially complete, as discussed elsewhere [38].

3.5. OVERLAP MATRIX-ELEMENT COMBINATORICS

Of course, the manner in which one computes with the cluster-expanded wave functions of the preceding sections is of crucial importance. The most standard approach at least for the more conventional MO-based cluster expansions is via Cizek's coupled-cluster method [24]. Also, indeed, this can conceivably be done for the localized-site cluster expansions as suggested previously [39] and as implemented [25, 30] in practice for (what is a slightly modified version of) the Neel-state-based *Ansatz* of Section 3.1. But, in fact, at least for quasi-1-dimensional (or finite) systems, all the *Ansätze* of the preceding subsections can be treated in a purely variational manner, which emphasizes interesting statistical mechanical analogies. Hence, one sees clearly possibilities for different types of long-range orders (as discussed in a following section)—and there are possibilities for novel types of phase transitions.

Here, the variational combinatorial form might be briefly considered for the Neel-state-based *Ansatz* of 3.1. Most simply, restriction might be made to just the two-site *Ansatz*, for which the overlap matrix element takes the form

$$\begin{aligned}\langle\Psi|\Psi\rangle &= \sum_{\gamma}\sum_{\mathscr{S}}\sum_{\gamma'}\sum_{\mathscr{S}'} X(\gamma,\mathscr{S})^* \\ &\quad\times\langle\Phi|\Big(\prod_i s_i^{\sigma}\Big)^{\dagger}\prod_j s_j^{\sigma}|\Phi\rangle X(\gamma',\mathscr{S}') \\ &= \sum_{\gamma}\sum_{\mathscr{S}}\sum_{\gamma'} X(\gamma,\mathscr{S})^* X(\gamma',\mathscr{S}). \quad (3.5.1)\end{aligned}$$

This may be refined further in a general form in terms of "superposition" graphs (composed from pairs γ and γ'). But as an introduction, the graph-theoretic elegance might be illustrated with consideration of the case with just nearest-neighbor symmetry-equivalent pair excitations. For this circumstance, then, the overlap may be represented as a sum over terms associated to different subgraphs of G, each subgraph corresponding to suitable products of the x_{ij} corresponding to the edges of the subgraph. Each site-excitation in the ket needs to be matched by one in the bra, so that two types of connected components can arise in these subgraphs: even cycles with pair excitations from ket and bra alternating around the cycle and isolated edges where a pair excitation in the ket and one in the bra exactly match. Hence, the overlap is a weighted sum over such *sesquivalent* subgraphs S, and the weights are a product over weights for each component: $2x^M$ for an even M-cycle of S, with the 2 arising because there are two ways to have alternation of the pair excitations around the cycle between ket and bra, and x^2 for an isolated edge of S. Then,

$$\langle\Psi|\Psi\rangle = \sum_{S}^{G} 2^{c(S)} x^{e(S)+i(S)}, \quad (3.5.2)$$

where the sum is over sesquivalent subgraphs of G, $c(S)$ is the number of cycles in S, $e(S)$ is the total number of edges in S, and $i(S)$ is the number of isolated edges in S. This may be expressed [40] in terms of the permanent of a weighted molecular graph G:

$$\langle\Psi|\Psi\rangle = per\{\mathbf{I} + x\mathbf{A}\}, \quad (3.5.3)$$

where $\mathbf{A}$ is the adjacency matrix of G. Graph theoretically, this is a type of *subgraph-generating function* associated to the parent graph G—the parameter x appears as the dummy variable in this generating function. In a statistical mechanical context, the mathematical form of $\langle\Psi|\Psi\rangle$ is the same as that of a partition function for allowed subgraph conformations, with x corresponding to a statistical mechanical *activity*.

In fact, the graph-theoretic and statistical forms of $\langle\Psi|\Psi\rangle$ appearing like that of a generating function or a partition function persists to higher-order or alternative cluster-expansion wave-function *Ansätze*. The simple resonating VB *Ansatz* which involves just Kekule structures leads [36, 37] to an overlap given as a different sum over spanning sesquivalent graphs. The simple *Ansatz* for the conjugated-circuit case yields an overlap which is just a count of the Kekule structures. For the nearest-neighbor Hulthen–Kastelyen *Ansatz*, the overlap becomes [35] essentially the Ising model, and higher-order such *Ansätze* are just elaborated "lattice-gas" models.

3.6. HAMILTONIAN MATRIX-ELEMENT COMBINATORICS

To obtain the energy, one considers the Hamiltonian matrix element. For the Heisenberg spin Hamiltonian, it is a sum over matrix elements of pair interactions $(ij)^{spin}$ for neighbor sites $i \sim j$. The Hamiltonian matrix element may then be developed in a diagrammatic form with a special type of edge (perhaps represented by a wiggly line segment) for each pair interaction. For the nearest-neighbor Heisenberg model utilizing the simplest Neel-state based *Ansatz*, this, then, involves just replacing one of the x-parameters by an exchange parameter from the Hamiltonian; hence, one ultimately finds [40]

$$\langle \Psi | H | \Psi \rangle = J \partial_x \langle \Psi | \Psi \rangle. \qquad (3.6.1)$$

But now if we hark back to the permenental formula for $\langle \Psi | \Psi \rangle$, one can obtain a formula in terms of a sum of ratios of permanental minors to the full permanent. In statistical mechanical contexts, just such ratios appear as logarithmic derivatives (with respect to activities). In a graph theoretic context, these ratios appear in average (weighted) subgraph counts. Amusingly, also, such a ratio is much reminiscent of those that appear in bosonic SCF problems.

But such graph-theoretic and statistical mechanical analogies apply for both higher-order *Ansätze* and for the other cluster-expansion *Ansätze* earlier discussed. Of course, the higher-order *Ansätze* become much more elaborate with many additional "activities." For the nearest-neighbor Hulthen–Kastelyen *Ansatz*, the Hamiltonian matrix appears as a type of a derivative of the partition function (or overlap) of the Ising model, and higher-order such *Ansätze* similarly involve just elaborated "lattice-gas" models. For the nearest-neighbor resonating VB *Ansatz* "derivatives" of the overlap subgraph, generating polynomial arise [36]. In general [39], the analogies arising in these problems for the overlap matrix elements and for the Hamiltonian expectation values may be summarized as in Figure 3. Rather, generally, both overlaps and partition functions represent sums over relative probabilities which tend to correlate only nearer sites, and the Hamiltonian expectations should involve much the same probability structure modified in some manner to give a size-extensive result, as is done by a logarithmic derivative.

The analogies of Figure 3, of course, mean that methods used to solve one problem can be utilized in solving another. Thus, e.g., the statistical mechanical *transfer-matrix* method [41, 42] to deal with partition functions and associated expectation values can be utilized for the wave-function problems, too—quite generally in a computationally amenable fashion for quasi-1-dimensional problems [43]. Or the Metropolis Monte Carlo method [44] can be neatly translated [29, 33] to the variational wave-function-based sort of problem indicated here. But, besides computational methods, there are conceptual many-body features, such as long-range order and phase transitions.

4. Qualitative Results

Results for the various cluster expansion *Ansätze* of the preceding sections might be compared to one another and several other approximation schemes in some global way. But, too, the Neel-based and resonating VB-theoretic approaches may be understood to apply for different structural

$$\langle \Psi | \Psi \rangle \equiv \{\text{overlaps}\} \longleftrightarrow \left\{ \begin{array}{c} \text{subgraph-generating} \\ \text{polynomial} \end{array} \right\} \longleftrightarrow \{\text{partition functions}\} \equiv Z$$

$$\frac{\langle \Psi | H | \Psi \rangle}{\langle \Psi | \Psi \rangle} \equiv \left\{ \begin{array}{c} \text{wave-} \\ \text{function} \\ \text{expectations} \end{array} \right\} \longleftrightarrow \left\{ \begin{array}{c} \text{subgraph} \\ \text{counting} \\ \text{averages} \end{array} \right\} \longleftrightarrow \left\{ \begin{array}{c} \text{statistical} \\ \text{mechanical} \\ \text{expectations} \end{array} \right\} = \frac{\partial_x Z}{Z}$$

FIGURE 3. A correspondence among quantities: first, for cluster-expanded wave functions; second, for graph-theoretic generating functions; and, third, for statistical mechanics.

circumstances. This was perhaps first suggested in the context of a particular case (namely, the triangular lattice) by Anderson and Fazekas [45], but the argument can be made [46] much more generally, i.e., one may compare the (0-order) energies for a simple Neel-state and a single Kekule structure. The energy per site for a Neel state on a bipartite graph is readily obtained as

$$\varepsilon^{(0)}(\text{Neel}) = -Jz/4, \tag{4.1}$$

where z is the mean number of neighbor sites (i.e., the mean coordination number). The energy per site for a single Kekule structure (on a graph which admits at least one Kekule structure) is readily obtained as

$$\varepsilon^{(0)}(\text{Kekule}) = -J3/4. \tag{4.2}$$

Hence, one can summarize the situation in the plot of Figure 4, where also is shown the results of further refinement of the resonance-theoretic approach. For the Kekule-structure-based approach, a resonating VB result based on an equally weighted combination of all Kekule structures as applied [36] to a special sequence of benzenoid polymer strips (of varying mean coordination number) is included in the plot. As a result, one sees that

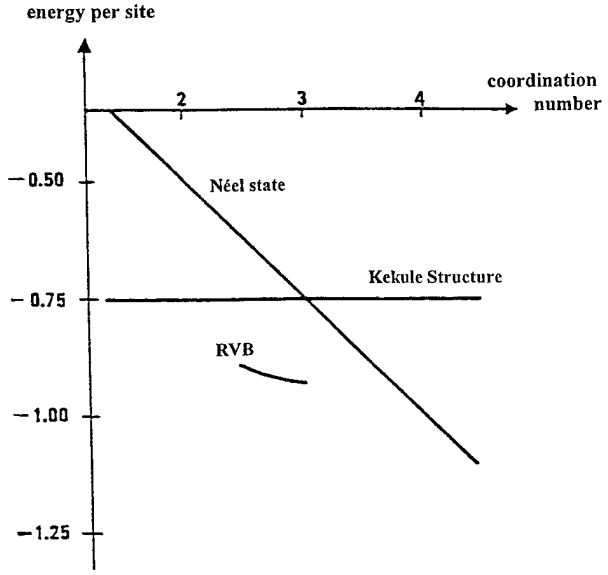


FIGURE 4. Plots of Neel-state energy per site and Kekule-structure energy per site for the nearest-neighbor Heisenberg (or VB) model as a function of the mean coordination number z. The Neel-state result is for bipartite graphs, while that for a Kekule structure presumes that the graph admits at least one Kekule structure.

- Resonance-theoretic descriptions are most appropriate for (benzenoid or aromatic) systems with low mean coordination number ($z \leq 3$) and with many Kekule structures per site.
- Neel-state-based descriptions are most appropriate for (3-dimensional) structures with high mean coordination numbers and low extents of frustration (i.e., with few small odd cycles of antiferromagnetically-signed interactions).

Indeed, these conclusions are quite naturally supported by the experimental successes of resonance-theoretic ideas in organic chemistry in application to the types of systems of the first proposition, and of Neel-state-based ideas in solid-state magnetic materials science in application to the types of systems of the second proposition.

Another distinction between resonance-theoretic and Neel-state-based approaches is that each seem to exhibit a qualitative difference as regards long-range ordering. Indeed, the Neel-state-based *Ansatz* involves the "classical" type of Neel antiferromagnetic ordering with order parameter

$$m(i,j) \equiv (\pm)\left\langle \{s_i^z - \langle s_i^z \rangle\}\{s_j^z - \langle s_j^z \rangle\}\right\rangle \to m_\infty, \quad \text{as } d(i,j) \to \infty, \tag{4.3}$$

where the $\pm$ sign applies as the sites are or are not of the same type (starred or unstarred), $d(i,j)$ is the distance between sites i and j, and the expectations $\langle s_i^z \rangle$ and $\langle s_j^z \rangle$ can be anticipated to be 0 (in the absence of a magnetic field). Many of the conventional many-body techniques (Green's functions, spin waves, Neel-state-based many-body perturbation theory, etc.) lead to this type of long-range ordering, although each different scheme can lead to different nonzero values. But the resonating VB-theoretic approaches turn out to lead [29, 34, 47] to another type of long-range spin-pairing order involving a spin-pairing correlation function for pairs of bonds, say e and f,

$$\Phi(e,f) \equiv \left\langle \{\mathbf{s}_{a(e)} \cdot \mathbf{s}_{b(e)} - p(e)\}\{\mathbf{s}_{a(f)} \cdot \mathbf{s}_{b(f)} - p(f)\}\right\rangle, \tag{4.4}$$

where $a(e)$ and $b(e)$ are the sites at the two ends of a bond e, and $p(e)$ is the pairing expectation $\langle \mathbf{s}_{a(e)} \cdot \mathbf{s}_{b(e)} \rangle$. Then, this correlation function can approach different limits for distant bonds, depending on the equivalence classes of the two bonds e and f. Indeed, this type of long-range order can be readily appreciated from consideration of classical neighbor VB-bonding diagrams or *Kekule* structures. For example, consider the two Kekule structures shown in Figure 5 for a polyanthracenoid polymer. In either case, there are many other related Kekule structures that can be drawn by rearranging a few double bonds independently within each anthracene unit, while the bond interconnecting anthracene units must remain always single or always double, i.e., if for one Kekule structure the bond order for one of these interconnecting bonds is known, then it is known for all such interconnecting bonds (even those in the long-range limit). Also, of course, the Kekule structures in different bond-order classes are different in every monomer unit so that in the long-polymer limit they are noninteracting (via any finite-particle interaction); hence, each class gives rise to its own ground state. Finally, this long-range order persists with the inclusion of VB structures beyond Kekule structures so long as the range of the spin-pairings is limited (or even if it is not limited but the contributions of longer spin-paired structures falls off sufficiently fast, as one might expect if the resonance-theoretic description is to be reasonable). For polymers with multiple interconnections between monomer units, the bond localization often is not so severe but still occurs to some degree differently for different classes of Kekule structures. For example, consider the two Kekule structures of the polynaphthalenoid polymer of Figure 6, where the Kekule structures are representatives from two classes with either 0 or 1 of the inter-connecting bonds between naphthalene units always being double. (A third class with two such bonds always double contains but a single Kekule structure.) Further, these different classes with associated ground states lead to a consideration of the possibility of solitonic excitations, as discussed elsewhere [48].

Finally, it may be mentioned that there are a number of rigorously proved [49] theorems concerning ground-state symmetries for the nearest-neighbor Heisenberg for a bipartite graph. Also, for this case, there are theorems [50] concerning long-range antiferromagnetic ordering at finite (nonzero) temperatures.

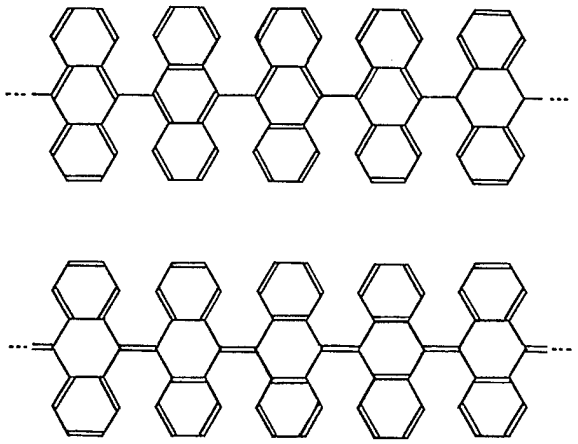


FIGURE 5. Two Kekule structures for a polymeric string of adjoined anthracene units. Note that with the first bond between adjoining anthracenes being single all the remaining interunit bonds are single, whereas with the first bond between adjoining anthracenes being double, all the remaining adjoining bonds are double.

5. Example Quantitative Results

Results for the various cluster expansion *Ansätze* of earlier sections might be illustrated for a few representative cases. When possible, comparison of different approximation schemes might be made. The first example cases here though will be for the conjugated-circuits model which is believed to be quite accurately solved by the uniformly weighted RVB cluster *Ansatz*. The second and third example cases return to the consideration of the nearest-neighbor Heisenberg model.

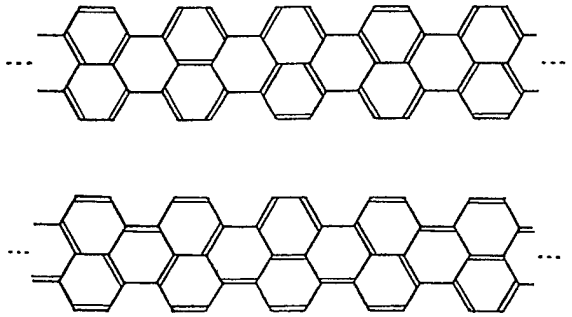


FIGURE 6. Two Kekule structures for a doubly adjoined ladderlike chain of naphthalene units. Note the requisite long-range ordering manifested in the number of double bonds that occur between successive naphthalene units.

5.1. ICOSAHEDRAL-SYMMETRY FULLERENES VIA CONJUGATED-CIRCUIT THEORY

A general class of interesting molecules is that of the fullerenes of icosahedral symmetry, the C_{60} member being the "uniquely elegant" truncated icosahedron structure [51], for whose discovery the 1996 Nobel prize in chemistry was awarded. This high-symmetry class of fullerenes has now been studied for almost a decade [52, 53], and a great deal of effort has been directed [54] to solutions of the Hückel model, although more complete quantum chemical models have also been utilized [55]. The study via resonance-theoretic models is rather meager, in part, because the phases of the Kekule structures are not so readily specified as for the bipartite case (with starred and unstarred sites). But the conjugated-circuits model can be applied in a rather empirical mode (where such phase problems are simply presumed not to be explicitly manifested), and the six structures with up through 240 sites have been treated [52] by the conjugated-circuits model. But, in fact, the powerful computational procedure of [56] is quite readily applicable to much larger systems (so long as one remains within the conjugated-circuit framework, with orthogonal Kekule structures). Hence, in Table I, we here report the results for all the 20 icosahedral-symmetry fullerene structures of up to 980 sites (so long as they have isolated pentagons, which seems to be a reasonable criterion for stability of fullerenes [57]). Such icosahedral-symmetry fullerene cages are uniquely identified [52–54, 58] by a pair of numbers h and k, which characterize an equilateral-triangular-network fragment, 20 copies of which when appropriately joined together may be viewed to compose the whole cage. Such a triangular fragment may be obtained by cutting from the graphite honeycomb network an equiliateral triangle with apices in the centers of three hexagons—the numbers h and k represent the coordinates of one apex relative to another in a skew coordinate system as indicated in Figure 7, where also the unit of distance is the (shortest) distance across a hexagon. Once one has 20 copies of one of these equilateral triangular fragments, "gluing" each to one of the same-sized faces of a regular icosahedron yields the fullerene cage, with one 5-membered ring appearing at each of the apices of the underlying icosahedron. The cages are characterized by $0 \leq k \leq h > 0$; they have $N = 20(h^2 + hk + k^2)$ sites, and, evidently, the symmetry of the resulting graph is $\mathcal{I}$ if $h = k$ or $k = 0$, while, otherwise, it is of symmetry $\mathcal{I}_h$. One may observe that the results of the Table I reveal that the total Kekule-structure counts increase rather dramatically with cage size, but a suitable graph-theoretical computational method [57] is still able to handle the results for the simple wavefunction cluster-expansion. Although the total Kekule-structure count evidently diverges exponentially fast with cage size, the Kekule structure counts per site (defined as $K^{1/N}$, where K is the total count) rather rapidly approach a finite limit, which must be that for graphite. A similar slightly more slowly converging behavior is seen in Table I to apply for the conjugated-circuit resonance energy per site. Notably, though, the cages with $h-k$ not divisible by 3 exhibit [53, 54, 59] a HOMO–LUMO gap of 0, so that they should be reactive (perhaps near the 12 apices of the underlying icosahedron, where the structures are least like graphite). Notably, this partitioning of the cages in accordance with the divisibility of $h-k$ by 3 is manifested in terms of the per-site conjugated-circuit resonance energies and even (to a lesser extent though) in terms of the per-site Kekule-structure counts, i.e., if $h-k$ is divisible by 3, then the resonance energy (per site) is somewhat less stabilizing than usual otherwise (and a related behavior can be discerned for $K^{1/N}$). Finally, it may be noted that the $N = 240$ result in this table corrects slightly an earlier reported result [52].

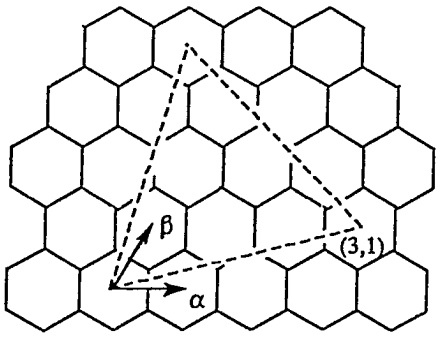


FIGURE 7. An illustration for $(h, k) = (3, 1)$ of the associated equilateral triangle to be cut from the graphite lattice graph, whereafter 20 copies of such triangles may be fused together on the surface of an icosahedron with faces of the same size so as to yield an icosahedral-symmetry fullerene.

TABLE I
Kekulé-structure counts and conjugated-circuit resonance energies for icosahedral fullerenes.

N	(h,k)	K	$K^{1/N}$	E_{res}/NR_1
60	(1,1)	12,500	1.17026	0.14271
80	(2,0)	140,625	1.15971	0.09717
140	(2,1)	2,178,836,352	1.16601	0.15262
180	(3,0)	1,389,029,765,625	1.16804	0.17977
240	(2,2)	21,587,074,966,666,816	1.16966	0.18490
260	(3,1)	249,276,672,312,858,144	1.16656	0.16632
320	(4,0)	4,742,708,922,019,216,416,528	1.16879	0.17816
380	(3,2)	63,052,896,815,923,948,794,000,000	1.16921	0.17976
420	(4,1)	55,853,910,213,101,170,303,889,310,104	1.17070	0.19122
500	(5,0)	$1.05984557486917155901 \times 10^{34}$	1.16964	0.18198
540	(3,3)	$1.31669745812355346381 \times 10^{37}$	1.17149	0.19307
560	(4,2)	$1.65980752921912098393 \times 10^{38}$	1.17017	0.18432
620	(5,1)	$3.05480054527886621321 \times 10^{42}$	1.17091	0.18766
720	(6,0)	$4.24881220361973614246 \times 10^{49}$	1.17200	0.19477
740	(4,3)	$6.53828524614458400211 \times 10^{50}$	1.17130	0.18886
780	(5,2)	$6.64523410371069994773 \times 10^{53}$	1.17220	0.19513
860	(6,1)	$1.30985649576953680262 \times 10^{59}$	1.17150	0.18940
960	(4,4)	$2.49942403779921924432 \times 10^{66}$	1.17264	0.19596
980	(5,3)	$3.29588295422837584208 \times 10^{67}$	1.17191	0.19093
980	(7,0)	$3.84734704509710763917 \times 10^{67}$	1.17210	0.19188
∞	(∞,k)	—	1.17531	0.19962

5.2. THE HEISENBERG MODEL FOR AN INFINITE CHAIN

One natural (and oft initially considered) system on which to make a comparison of various strong correlation approximation methods is the simple case of the 1-dimensional chain of sites. Also, such a comparison for the infinite-length chain is made in Table II, where energies per site are reported for the three types of cluster-expanded wave functions discussed in Sections 4–6 along with results reported via other many-body methods and the exact result [31], known for cyclic chain systems, via a (Bethe-*Ansatz*) method which does not seem to be very readily extendable to other structures. It may be noted that the so-called Jordan–Wigner-transformed RHF and UHF results are restricted [60] and unrestricted [61] Hartree–Fock solutions for the Hamiltonian after a transformation of the Pauli operators in $\mathbf{s}_i \cdot \mathbf{s}_{i+1}$ to a Fermionic form, and, again, this approach seems not too readily extendable to other structures. The spin-wave result involves [62] a Hartree–Fock solution after transformation to Bosonic operators, and is applicable to all kinds of structures, but the bosonic operators are defined on an enlarged space of which the physically realizable space is only a small part, while, however, the approximate Hartree–Fock solution admixes in this nonphysical space, so that it is not evident that one obtains a variational bound to the physical ground state. This Bosonic method seems not to be ordinarily applied to other than Heisenberg models, although there is some possibility [63]. These various approximation schemes which seem to us not so amenable to other structures or to other models are indicated in Table II by placing their energy values in parentheses. Now, in light of the discussion in connection with Figure 4, this system is not expected to be exceptionally well described via either the Neel-state-based or resonance-VB-theoretic approaches. But, nevertheless, rather reasonable results are obtained at least when any of these types of cluster-expanded wave functions are taken beyond the lowest order. Indeed, the results are quite good in comparison with a variety of standard many-body methods, e.g., as compared to the unrestricted Hartree–Fock limit (at -0.5000) which is one of the poorer results in the table, i.e., sizable portions of the so-called "correlation energy," are obtained. The Monte Carlo methods of which there

TABLE II
Energies per site for various methods as applied to the nearest-neighbor Heisenberg Model for an infinite ladder.

Method	{Energy} / *JN*	Ref.
Neel-state energy	−0.5000	
Ordinary UHF limit of the Hubbard model	−0.5000	
Single Kekule structure	−0.7500	
3 → 1 first-order real-space renormalization	−0.7826	[64]
Hulthen–Kasteleyn *Ansatz*	−0.8156	[31, 32]
Jordan–Wigner-transformed RHF	(−0.8383)	[60]
9 → 1 first-order real-space renormalization	−0.8423	[65]
Cluster-expansion of cluster expansion	−0.8469	To appear
Two-site Neel-state-based cluster expansion *Ansatz*	−0.8558	[26]
(Non-variational) antiferro-magnetic spin-wave	(−0.8634)	[62]
Jordan–Wigner-transformed UHF	(−0.8646)	[61]
19 → 1 first-order real-space renormalization	−0.8650	[66]
Two-bond-range resonating VB *Ansatz*	−0.8716	[35]
First sequential cluster expansion of Eq. (3.4.2)	−0.8737	To appear
Four-site Neel-state-based cluster-expansion *Ansatz*	−0.8758	[27]
Three-bond-range resonating VB *Ansatz*	−0.8790	Present
Exact	(−0.886294)	[31]
Monte Carlo $N = 48$ ring	−0.887	[67]
3 → 1 additive-cluster renormalization	−0.8969	[68]
Neel-state-based second-order perturbation theory	−1.0000	[69]
Limit to Hubbard Green's function approximant	−1.2188	[70]

are different sorts exhibit what seems the highest accuracy for a variety of systems and models.

5.3. THE HEISENBERG MODEL FOR THE INFINITE LADDER

Another example system is that of a ladder, the structure of which pictured in Figure 8 can be viewed as a strip cut from the square-planar lattice. Here, various results are reported in Table III. This system satisfies conditions enunciated in connection with Figure 4 so as to make a resonating VB picture more favorable: This system is of a fairly low mean coordination number $z = 3$, and it has many Kekule structures. Indeed, for a chain of n-fused squares, the number of Kekule structures is known to be given by the $(n + 1)th$ Fibonacci number F_{n+1}, which, in turn, can be expressed in very many ways, e.g.,

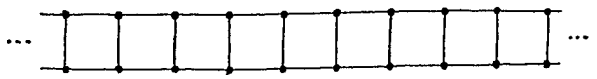


FIGURE 8. A square-planar lattice strip.

$$F_m = \{(2 + \phi_+)\phi_+^m + (2 + \phi_-)\phi_-^m\}/5, \quad (5.3.1)$$

where $\phi_+ \equiv (1 + \sqrt{5})/2 \approx 1.61803399$ is the "golden mean" and $\phi_- = 1 - \phi_+$ is some sort of complement. In concert with the expectations, the resonating VB-theoretic results seem to be quite good.

But perhaps a few words should be said as to just what systems these results might apply. Basically, in application to conjugated π-networks with 4-membered rings, the Heisenberg model should have important higher-order terms, which, if not included, predict too large a resonance stabilization, e.g., for cyclobutadiene. Thus, the quoted results for the current nearest-neighbor model do not apply to such conjugated π-networks.

But the current nearest-neighbor model is believed to be well applicable to ladderlike structures of Cu^{2+}-containing perovskites (of the general structural class of high-temperature supercon-

TABLE III
Energies per site for various methods as applied to the nearest-neighbor Heisenberg Model for an infinite ladder.

Method	(Energy) / *JN*	Ref.
Neel-state energy	−0.7500	
Single Kekule structure	−0.7500	
Two-site Neel-state-based *Ansatz*	−1.1014	Present
One-bond-range RVB *Ansatz*	−1.1138	[68]
Neel-state 2*nd*-order perturbation theory	−1.1250	[69]
Two-bond-range RVB *Ansatz*	−1.1462	Present
Numerical extrapolation (from exact diagonalizations)	−1.156	[68]

ductors), and, indeed, these ladder structures have been much studied [71–73] in this context in the last few years. Interestingly, there is an important difference in relative applicability of Neel-state-based and resonating-VB-theoretic wave functions for the current case of ladders with two legs in comparison with a ladder with three legs. This difference can be readily understood in terms of the relative abundances of Kekule structures as mediated by the long-range spin-pairing orders discussed in Section 4 here, although these earlier understood [68] consequences were termed [71] "surprising" when first studied in connection with the experimentally realized perovskites. Basically, if the long-range spin-pairing order deviates much from the optimal resonance-theoretic circumstance for which spin-pairing from one site to every neighbor occurs with equal probability, then resonance makes a lesser contribution and the alternative Neel-state description is relatively more preferred.

6. Prospects

Many-body VB theory is seen to be implementable in several different manners, even upon focus on the circumstance of variationally treated cluster-expanded wave functions. Much has been done with the simplest *Ansätze*, but a number of computations with higher-order *Ansätze* indicate even further promise. Such results at least in some cases seem to be of quite high accuracy. Within a variational format, it is a challenge to apply the methods to extended systems of 2- or 3-dimensional systems, although for the Heisenberg model on the square-planar lattice, there has been a certain degree of work (in connection with high-temperature superconductivity, and some further indication of this work is given in the reviews of [12]).

There appear some qualitative differences between many-body MO-based and VB-based wave functions. Also, it may be emphasized that, in practice, these differences can persist to somewhat high orders, most especially for extended many-body systems. Such a point has occasionally been made previously [74]. But, here, with the recognition of the correspondence to statistical-mechanical quantities, as in Figure 3, two different types of wave functions might be imagined to fall into what in statistical mechanics are termed different "universality classes," e.g., exhibiting different types of long-range order and exhibiting different critical point behavior (independent of perturbative corrections to a zero-picture). Thus, many-body VB-theoretic cluster-expanded wave functions can be imagined to be much more than just another way to do a computation equivalent to that for an MO-based many-body wave function—the two descriptions need not in any achievable high order be equivalent. The question then devolves to just which systems each of the two types of descriptions apply.

Thus, there appears a certain need for VB-theoretic descriptions. Although the computations described here have focused on Heisenberg and conjugated-circuit models, there is also some (lesser amount of) work on Hubbard or PPP semiempirical models. It is hoped that the methods will be applied in an ab initio framework.

ACKNOWLEDGMENTS

The support of the Welch Foundation of Houston, Texas, is acknowledged. One of us (M. A. G. B.) acknowledges the DGICYT (Project PB95-0884).

References

1. H. M. Leicester, J. Chem. Ed. **36,** 328 (1959). D. F. Larder, J. Chem. Ed. **44,** 661 (1967). L. Pauling, J. Chem. Ed. **61,** 201 (1984).
2. C. A. Russell, *The History of Valency* (University Press, Leicester, 1971). A. N. Stranges, *Electrons and Valence* (Texas A & M University Press, College Station, 1982).
3. W. Heitler and F. London, Z. Phys. **44,** 455 (1927).
4. G. Rumer, Göttinger Nach. Ges. Wiss. 337 (1932).
5. L. Pauling, J. Am. Chem. Soc. **53,** 1376 (1931).
6. L. Pauling, J. Chem. Phys. **1,** 280 (1933).
7. S. R. La Paglia, *Introductory Quantum Chemistry* (Harper & Row, New York, 1971), Chap. 1. D. J. Klein and N. Trinajstić, J. Chem. Ed. **67,** 633 (1990).
8. D. J. Klein and N. Trinajstić, Eds., *Valence-Bond Theory & Chemical Structure* (Elsevier, Amsterdam, 1990).
9. D. L. Cooper, J. Gerratt, and M. Raimondi, Nature **323,** 699 (1986).
10. J. Gerratt, D. L. Cooper, and M. Raimondi, in *Valence-Bond Theory & Chemical Structure,* D. J. Klein and N. Trinajstić, Eds. (Elsevier, Amsterdam, 1990), pp. 287–350.
11. P. W. Anderson, Science **235,** 1196 (1987).
12. E. Manousakis, Rev. Mod. Phys. **63,** 1 (1991). T. Barnes, Intl. J. Mod. Phys. C **2,** 659 (1991). G. Senatore and N. H. March, Rev. Mod. Phys. **66,** 445 (1994). E. Dagotto, Rev. Mod. Phys. **66,** 763 (1994).
13. D. J. Klein, Top. Curr. Chem. **153,** 59 (1990).

14. M. Simonetta, E. Gianinetti, and I. Vandoni, J. Chem. Phys. **48,** 1579 (1968).
15. G. Rumer, E. Teller, and H. Weyl, Gött. Nach. Ges. Wiss. 499 (1932).
16. L. Pauling and G. W. Wheland, J. Chem. Phys. **1,** 362 (1933).
17. W. T. Simpson, J. Chem. Phys. **25,** 1124 (1956). P.-O. Löwdin, Adv. Phys. **5,** 1 (1956).
18. D. J. Klein, Pure Appl. Chem. **55,** 299 (1982).
19. D. J. Klein and N. Trinajstić, Pure Appl. Chem. **61,** 2107 (1989). D. S. Rokhsar and S. A. Kivelson, Phys. Rev. Lett. **61,** 2376 (1988). S. A. Kivelson, Phys. Rev. B **39,** 259 (1989).
20. W. T. Simpson, J. Am. Chem. Soc. **75,** 597 (1953). W. C. Herndon, J. Am. Chem. Soc. **95,** 2404 (1973).
21. W. C. Herndon, Thermochim. Acta **8,** 225 (1974). L. J. Schaad and B. A. Hess, Jr., Pure Appl. Chem. **54,** 1097 (1982).
22. M. Randić, Tetrahedron **33,** 1905 (1977). M. Randić, J. Am. Chem. Soc. **99,** 444 (1977). D. J. Klein, J. Chem. Ed. **69,** 691 (1992).
23. D. J. Klein, *Pauling Appreciation,* Z. Maksic, ed. (Elsevier, to appear, 1997).
24. J. Cizek, J. Chem. Phys. **45,** 4256 (1966).
25. M. Roger and J. H. Hetherington, Europhys. Lett. **11,** 255 (1990). R. F. Bishop, Theor. Chim. Acta **80,** 95 (1991). C. F. Lo, E. Manousakis, and Y. L. Wang, Phys. Lett. A **156,** 42 (1991). L. Petit and M. Roger, Phys. Rev. B **49,** 3453 (1994).
26. C. Vroelant and R. Daudel, Bull. Soc. Chim. **16,** 36 (1949). I. Nebanzahl, Phys. Rev. **177,** 1001 (1969). R. R. Bartowski, Phys. Rev. B **55,** 4536 (1972). D. J. Klein, J. Chem. Phys. **64,** 4868 (1976). M. A. Suzuki, J. Stat. Phys. **43,** 883 (1986).
27. M. A. Garcia-Bach and D. J. Klein, Int. J. Quantum Chem. **12,** 273 (1977). G. Baskaran, Z. Zou, and P. W. Anderson, Solid State Commun. **69,** 973 (1987). I. Affleck and J. B. Marston, Phys. Rev. B **37,** 316 (1988). C. Zeng and J. B. Parkinson, Phys. Rev. B **51,** 11609 (1995).
28. S. Liang, N. Doucet, and P. W. Anderson, Phys. Rev. Lett. **61,** 365 (1988).
29. M. A. Garcia-Bach, A. Penaranda, and D. J. Klein, Phys. Rev. B **45,** 10891 (1992).
30. R. F. Bishop, J. B. Parkinson, and Y. Xian, Phys. Rev. B **44,** 9425 (1991). F. E. Harris, Phys. Rev. B **47,** 7903 (1993). R. F. Bishop, R. G. Hale, and Y. Xian, Phys. Rev. Lett. **73,** 3157 (1994).
31. L. Hulthen, Arkiv Mat. Astron. Fys. A **26**(11), 1 (1938).
32. P. W. Kasteleyn, Physica **28,** 104 (1952).
33. D. A. Huse and V. Elser, Phys. Rev. Lett. **60,** 2531 (1988).
34. W. Marshall, Proc. R. Soc. (Lond.) A **232,** 48 (1955).
35. D. J. Klein and M. A. Garcia-Bach, Phys. Rev. B **19,** 877 (1979).
36. D. J. Klein, T. G. Schmalz, G. E. Hite, A. Metropoulos, and W. A. Seitz, Chem. Phys. Lett. **120,** 367 (1985). G. E. Hite, A. Metropoulos, D. J. Klein, T. G. Schmalz, and W. A. Seitz, Theor. Chim. Acta **69,** 393 (1986).
37. T. Oguchi, H. Nishimori, and Y. Taguchi, J. Phys. Soc. Jpn. **55,** 323 (1986). S. Kivelson, D. Rokhsar, and J. Sethna, Phys. Rev. B **35,** 8865 (1987). B. Sutherland, Phys. Rev. B **37,** 3786 (1988). B. Sutherland, Phys. Rev. B **38,** 7192 (1988). D. S. Rokhsar and S. Kivelson, Phys. Rev. Lett. **61,** 2376 (1988). S. Sachdev, Phys. Rev. B **40,** 5204 (1989). N. Read and S. Sachdev, Nucl. Phys. B **316,** 609 (1989). T. Blum and Y. Shair, J. Stat. Phys. **59,** 333 (1990).
38. M. A. Garcia-Bach and D. J. Klein, J. Phys. A **29,** 103 (1996).
39. D. J. Klein, Intl. J. Quantum Chem. Symp. **20,** 153 (1986).
40. D. J. Klein, Mol. Phys. **31,** 811 (1976).
41. E. W. Montroll, J. Chem. Phys. **9,** 706 (1941).
42. C. J. Thompson, *Mathematical Statistical Mechanics* (Macmillan, New York, 1972). N. L. Biggs, *Interaction Models* (Cambridge University Press, Cambridge, 1977).
43. D. J. Klein, T. G. Schamalz, and G. E. Hite, J. Comp. Chem. **7,** 443 (1986).
44. N. Metropolis, A. W. Rosenbluth, M. N. Rosenbluth, A. H. Teller, and E. Teller, J. Chem. Phys. **21,** 1087 (1953).
45. P. W. Anderson, Mat. Res. Bull. **8,** 153 (1973). P. W. Anderson and P. Fazekas, Philos. Mag. **30,** 423 (1974).
46. D. J. Klein, S. A. Alexander, W. A. Seitz, T. G. Schmalz, and G. E. Hite, Theor. Chim. Acta **69,** 393 (1986).
47. D. J. Klein, T. P. Zivković, and R. Valenti, Phys. Rev. B **43,** 723 (1991).
48. D. J. Klein, T. G. Schmalz, W. A. Seitz, and G. E. Hite, Int. J. Quantum Chem. Symp. **19,** 707 (1986).
49. E. H. Lieb and D. C. Mattis, J. Math. Phys. **3,** 749 (1962). D. J. Klein, J. Chem. Phys. **77,** 3098 (1982).
50. N. D. Mermin and H. Wagner, Phys. Rev. Lett. **17,** 1133 (1966). D. J. Klein, C. J. Nelin, S. A. Alexander, and F. A. Matsen, J. Chem. Phys. **77,** 3101 (1982).
51. H. W. Kroto, J. R. Heath, S. C. O'Brien, R. F. Curl, and R. E. Smalley, Nature **318,** 162 (1985). W. R. Krätschmer, L. D. Lamb, K. Fostiropoulos, and D. R. Huffman, Nature **347,** 354 (1990).
52. D. J. Klein, W. A. Seitz, and T. G. Schmalz, Nature **323,** 703 (1986).
53. P. W. Fowler and J. M. Woolrich, Chem. Phys. Lett. **127,** 78 (1986).
54. A. C. Tang, F. Q. Huang, Q. S. Li, and R. Z. Liu, Chem. Phys. Lett. **227,** 579 (1994). C. G. Liu, Y. H. Shao, and Y. S. Jiang, Chem. Phys. Lett. **228,** 131 (1994). C. G. Liu, M. M. Wang, Y. H. Shao, and Y. S. Jiang, Phys. Lett. A **196,** 120 (1994). A. C. Tang and F. Q. Huang, Phys. Rev. B **51,** 13830 (1995). A. C. Tang and F. Q. Huang, Chem. Phys. Lett. **245,** 561 (1995). A. C. Tang and F. Q. Huang, Chem. Phys. Lett. **247,** 494 (1995). A. C. Tang, F. Q. Huang, and R. Z. Liu, Phys. Rev. B **53,** 7442 (1996).
55. D. Bakoweis and W. Thiel, J. Am. Chem. Soc. **113,** 3704 (1991). B. I. Dunlap, D. W. Brenner, J. W. Mintmire, R. C. Mowrey, and C. T. White, J. Phys. Chem. **95,** 8737 (1991). D. York, J. P. Lu, and W. Yang, Phys. Rev. B **49,** 8526 (1994). G. E. Scuseria, Chem. Phys. Lett. **243,** 193 (1995). D. Bakowies, M. Bühl, and W. Thiel, Chem. Phys. Lett. **247,** 491 (1995). D. Bakowies, M. Bühl, and W. Thiel, J. Am. Chem. Soc. **117,** 10113 (1995). C. H. Xu and G. E. Scuseria, Chem. Phys. Lett. **262,** 219 (1996).
56. P. W. Kasteleyn, in *Graph Theory & Theoretical Physics,* F. Harary, Ed. (Academic Press, New York, 1967), Chap. 2. D. J. Klein and X. Liu, J. Comp. Chem. **12,** 1260 (1991).
57. T. G. Schmalz, W. A. Seitz, D. J. Klein, and G. E. Hite, J. Am. Chem. Soc. **110,** 1113 (1988).
58. M. Goldberg, Tohoka Math. J. **43,** 104 (1937).
59. P. W. Fowler, J. E. Cremmona, and J. I. Steer, Theor. Chim. Acta **73,** 1 (1988).

60. S. Rodriquez, Phys. Rev. **116,** 1474 (1959).
61. T. W. Ruijgrok and S. Rodriguez, Phys. Rev. **119,** 596 (1960). T. Oguchi, Phys. Rev. Lett. **11,** 266 (1963). Z. G. Soos, J. Chem. Phys. **43,** 1121 (1965).
62. P. W. Anderson, Phys. Rev. **86,** 694 (1952). R. Kubo, Phys. Rev. **87,** 568 (1952).
63. M. D. Girardeau, J. Math. Phys. **4,** 1096 (1961); *Ibid.*, **12,** 1799 (1971). *Ibid.*, **16,** 1901 (1975). J. D. Gilbert, J. Math. Phys. **18,** 791 (1977). M. D. Girardeau, Int. J. Quantum Chem. **27,** 25 (1980). H. Barentzen, J. Phys. A **20,** 121 (1987).
64. H. P. van de Braak, W. J. Caspers, and M. W. M. Willemse, Phys. Lett. A **67,** 147 (1978).
65. J. N. Fields, Phys. Rev. B **19,** 2637 (1979). J. N. Fields, H. W. J. Blöte, and J. C. Bonner, J. Appl. Phys. **50,** 1807 (1979).
66. T. G. Schmalz and D. J. Klein, Croat. Chem. Acta **66,** 185 (1993).
67. T. Barnes and G. J. Daniell, Phys. Rev. B **37,** 3637 (1988).
68. T. P. Zivković, B. L. Sandleback, T. G. Schmalz, and D. J. Klein, Phys. Rev. B **41,** 2249 (1990).
69. H. Hartmann, Z. Naturforsch. A **2,** 259 (1947). D. Maynau, Ph. Durand, J. P. Dauday, and J.-P. Malreiu, Phys. Rev. A **28,** 3193 (1983).
70. J. Linderberg and Y. Öhrn, J. Chem. Phys. **49,** 716 (1968).
71. E. Dagotto and T. M. Rice, Science **271,** 618 (1996).
72. T. Barnes, E. Dagotto, J. Riera, and E. S. Swanson, Phys. Rev. B **47,** 3196 (1993). S. R. White, R. M. Noack, and D. J. Scalapino, Phys. Rev. Lett. **73,** 886 (1994). Y. Nishiyama, N. Hatano, and M. Suzuki, J. Phys. Soc. Jpn. **64,** 1967 (1995). Y. Xian, Phys. Rev. B **52,** 12485 (1995). H. Watanbe, Phys. Rev. B **52,** 12508 (1995). A. W. Sandvik, E. Dagotto, and D. J. Scalapino, Phys. Rev. B **53,** R2934 (1996). M. Santos and W. Figueiredo, J. Phys. A **29,** 2435 (1996). G. Sierra, J. Phys. A **29,** 3299 (1996). C. A. Hayward, D. Polblanc, and D. J. Scalapino, Phys. Rev. B **53,** R8863 (1996). A. G. Rojo, Phys. Rev. B **53,** 9172 (1996).
73. T. M. Tranquada, B. J. Sternlieb, J. D. Axe, Y. Nakamura, and S. Uchida, Nature **375,** 561 (1995). Z. Hirol and M. Takano, Nature **377,** 41 (1995).
74. J. H. Choi and W. Thorson, J. Chem. Phys. **57,** 252 (1972). W. R. Thorson, J. H. Choi, and R. G. Hake, Int. J. Quantum Chem. Symp. **1,** 487 (1967).

Fully Variational Optimization of Modern VB Wave Functions Using the CASVB Strategy

DAVID L. COOPER[1], THORSTEIN THORSTEINSSON[2], JOSEPH GERRATT[3]

[1] *Department of Chemistry, University of Liverpool, P.O. Box 147, Liverpool L69 72Z, United Kingdom*

[2] *Chemistry Laboratory IV, Copenhagen University, Universitetsparken 5, DK-2100 Copenhagen Ø, Denmark*

[3] *School of Chemistry, University of Bristol, Cantocks Close, Bristol BS8 ITS, United Kingdom*

Received 1 March 1997; revised 4 March 1997

ABSTRACT: We outline the CASVB strategy, which may be used either to generate very compact modern valence bond representations of CASSCF wave functions or to optimize general types of modern VB wave function. A simple algorithm is presented for the elimination of redundant or constrained parameters from the appropriate second-order optimization problems. Selected results for three systems—benzene, the allyl radical, and LiH—are used to illustrate various ways in which CASVB procedures can be used to perform fully variational optimizations of nonorthogonal orbitals and structure coefficients in modern VB wave functions. © 1997 John Wiley & Sons, Inc. Int J Quant Chem 65: 439–451, 1997

Key words: CASVB; modern VB; nonorthogonal orbital optimization; multiconfiguration spin-coupled; CASSCF

Introduction

The initial aim of developing our CASVB procedures [1–4] was to exploit the invariance of wave functions of "full configuration interaction (CI)" form to general nonunitary linear transformation of the active orbitals, so as to generate alternative representations of CASSCF wave functions in which a dominant component adopts modern VB form. By a wave function of "modern VB" form, we mean here one or more spatial configurations constructed from general, nonorthogonal orbitals, and combined with all allowed ways of coupling together the electron spins so as to obtain the required resultant. The prototype sin-

Correspondence to: D. L. Cooper.

International Journal of Quantum Chemistry, Vol. 65, 439–451 (1997)
© 1997 John Wiley & Sons, Inc.
CCC 0020-7608 / 97 / 050439-13

gle-configuration wave function of this type is the spin-coupled wave function [5]:

$$\Psi_{SC} = \mathscr{A}\left(\varphi_1^2\varphi_2^2 \ldots \varphi_n^2\Theta_{pp}^{2n}\phi_1\phi_2 \ldots \phi_N\Theta_{SM}^N\right) \quad (1)$$

in which the singly occupied nonorthogonal orbitals ϕ_μ accommodate the active electrons, and the doubly occupied orthogonal orbitals φ_i accommodate the inactive ones. The spin eigenfunction Θ_{SM}^N is fully optimized in the full spin space for N electrons with total spin S and projection M, and Θ_{pp}^{2n} represents perfect pairing of the spins of the $2n$ inactive electrons.

It was anticipated from the outset that it would be desirable to incorporate our CASVB procedures into molecular orbital (MO) CI packages that feature powerful CASSCF codes. This could make it possible to use such "standard" packages to carry out the fully variational optimization of quite general types of modern VB wave function, by alternating optimization of the active and external parameter sets in an iterative two-step procedure. The CASVB procedures have already been made available as part of the MOLPRO package [6], in which they are interfaced to a very efficient CASSCF program [7], and we hope to see them incorporated into many others in due course.

Since almost all of the technical details underpinning our approach are available elsewhere [1–4], we present in the next section only a brief overview of the methodology. An important aspect of actual calculations is our scheme for eliminating redundant or constrained parameters from the second-order optimization procedures; this is described here for the first time. We then use selected results for three systems—benzene, the allyl radical, and LiH—to illustrate some of the ways in which the CASVB procedures can be utilized to perform fully variational optimizations of nonorthogonal orbitals and structure coefficients in modern VB wave functions.

CASVB Method

Consider a normalized CASSCF wave function Ψ_{CAS} consisting of N_{CI} structures Φ_I built from m active orbitals, ϕ_i. A general, nonunitary, nonsingular $m \times m$ linear transformation of the orbitals

$$\{\phi'\} = \{\phi\}\mathbf{O} \quad (2)$$

induces a corresponding $N_{CI} \times N_{CI}$ transformation of the structure space

$$\{\Phi'\} = \{\Phi\}\mathbf{T}(\mathbf{O}). \quad (3)$$

Without explicitly constructing $\mathbf{T}(\mathbf{O})$, its effect on the complete structure space can be realized in a very efficient manner by writing $\mathbf{O}$ as a product of m^2 simple updates and utilizing the general property of full CI spaces that

$$\mathbf{O} = \mathbf{O}_1\mathbf{O}_2 \Leftrightarrow \mathbf{T}(\mathbf{O}) = \mathbf{T}(\mathbf{O}_1)\mathbf{T}(\mathbf{O}_2). \quad (4)$$

The simple updates take the form

$$\mathbf{O}_{\mu\nu}(\lambda)\colon \phi_\nu \rightarrow \phi_\nu + \lambda\phi_\mu, \quad (5)$$

for which the corresponding transformation of the structure space can be achieved by application of the operator

$$\hat{I} + \lambda\hat{E}_{\mu\nu}^{(1)} + \lambda^2\hat{E}_{\mu\nu}^{(2)}, \quad (6)$$

in which $\hat{E}_{\mu\nu}^{(1)}$ and $\hat{E}_{\mu\nu}^{(2)}$ generate spin-averaged single and double excitations. This highly efficient strategy [1–4, 8] for realizing exactly the effects of the structure transformation in Eq. (3) is central to the viability of the CASVB approach. We have also presented expressions for the first and second derivatives of $\mathbf{T}(\mathbf{O})$ with respect to the λ parameters [2].

Consider now a modern VB wave function Ψ_{VB} consisting of a linear combination of a subset of the N_{CI} structures in the CASSCF expansion, but constructed instead from m *nonorthogonal* orbitals. An appealing criterion for choosing the orbital transformation $\mathbf{O}$ in Eq. (2) is to maximize the overlap S_{VB} between Ψ_{VB} and Ψ_{CAS},

$$S_{VB} = \frac{\langle\Psi_{CAS}|\Psi_{VB}\rangle}{\langle\Psi_{VB}|\Psi_{VB}\rangle^{1/2}}. \quad (7)$$

An efficient second-order Newton–Raphson strategy for maximizing S_{VB} was presented in Ref. [2]. This approach provides a relatively inexpensive scheme for representing CASSCF wave functions in modern VB form. Very high values of S_{VB}, on the order of 0.99, may typically be achieved with a single spin-coupled-like configuration [Eq. (1)].

An alternative to maximization of S_{VB} is to choose $\mathbf{O}$ by minimizing the expectation of the energy, E_{VB}, defined according to

$$E_{VB} = \frac{\langle\Psi_{VB}|\hat{H}|\Psi_{VB}\rangle}{\langle\Psi_{VB}|\Psi_{VB}\rangle}. \quad (8)$$

The nonorthogonality problem implicit in evaluating the matrix elements in this expression may be circumvented by transforming back to the original basis of orthogonal molecular orbitals, using the identities

$$\mathbf{H}' = \mathbf{T}^{\dagger}(\mathbf{O})\mathbf{H}\mathbf{T}(\mathbf{O}), \tag{9}$$

$$\mathbf{S}' = \mathbf{T}^{\dagger}(\mathbf{O})\mathbf{S}\mathbf{T}(\mathbf{O}), \tag{10}$$

and

$$\mathbf{c}' = \mathbf{T}^{-1}(\mathbf{O})\mathbf{c} = \mathbf{T}(\mathbf{O}^{-1})\mathbf{c}, \tag{11}$$

in which **H**, **S**, and **c** are the Hamiltonian matrix, overlap matrix, and CI vectors appropriate to $\{\Phi\}$, whereas the primed quantities relate to $\{\Phi'\}$. An efficient second-order Newton–Raphson strategy for minimizing E_{VB} was presented in Ref. [2]. The resulting Ψ_{VB} is optimal for the given choice of active space and corresponds to a representation of the full CASSCF wave function in which a small number of modern VB structures dominate the total energy. It is our experience that analogous overlap- and energy-optimized wave functions are always in very good qualitative agreement. The viability of the energy optimization method depends on the availability of highly efficient algorithms for realizing the action of the Hamiltonian operator on a full-CI vector [9, 10].

Furthermore, optimization of the energy expectation value E_{VB} with respect to core-active, core-virtual, and active-virtual orbital rotations can be achieved using standard CASSCF procedures. As a consequence, fully variational modern VB calculations can be performed by alternating optimization of the active and external parameter sets in an iterative two-step procedure. This has been implemented as part of the MOLPRO package [6]. We have also presented practical approaches [3] for the proper utilization of molecular point group symmetry in modern VB approaches that involve the optimization of nonorthogonal orbitals.

Elimination of Redundant or Constrained Parameters

We consider in this section the optimization of a general multiconfiguration modern VB wave function of the form

$$\psi^{\mathrm{act}} = \sum_{I=1}^{N_{\mathrm{struc}}} c_I \psi_I \tag{12}$$

in which the structures ψ_I are defined in terms of a set of m orbitals, $\{\phi_\mu\}$, with varying occupations and spin functions. We have used the notation ψ^{act} to remind ourselves that the total wave function can, without loss of generality, also include orbitals that are doubly occupied in all structures. The active orbitals are allowed to be nonorthogonal, and are expanded in a set of basis functions $\{\chi_i\}$ according to

$$\phi_\mu = \sum_{i=1}^{m_{\mathrm{bas}}} o_{i\mu}\chi_i. \tag{13}$$

It is convenient to collect the "primitive" variational parameters from Eqs. (12) and (13) into a vector **x**, such that $\mathbf{x}(1{:}m_{\mathrm{bas}})$ contains the expansion coefficients for orbital ϕ_1, $\mathbf{x}(m_{\mathrm{bas}}+1{:}2m_{\mathrm{bas}})$ contains the expansion coefficients for orbital ϕ_2, etc., and $\mathbf{x}(m\times m_{\mathrm{bas}}+1{:}m\times m_{\mathrm{bas}}+N_{\mathrm{struc}})$ holds the structure coefficients. Our procedure seeks to minimize the energy $E_{\mathrm{VB}}(\mathbf{x})$ based on a second-order model of the form

$$E_{\mathrm{VB}}(\mathbf{x}+\delta\mathbf{x}) \approx E_{\mathrm{VB}}(\mathbf{x}) + \mathbf{g}^{\mathrm{T}}\,\delta\mathbf{x} + 1/2\,\delta\mathbf{x}^{\mathrm{T}}\mathbf{G}\,\delta\mathbf{x}, \tag{14}$$

in which **g** is the (column) vector of first derivatives of E with respect to the variational parameters, and **G** is the corresponding matrix of second derivatives (Hessian). There are many variants of such procedures, such as, for example, stabilized Newton–Raphson schemes or augmented Hessian approaches [11–13].

Methods for eliminating redundant or constrained parameters from such second-order optimization problems are well known in the literature (see, e.g., Ref. [11]). A common way of taking constraints into account is to include Lagrange multipliers in the objective function. It is well known, however, that such approaches can adversely affect the convergence characteristics. An attractive alternative is the use of *nonlinear* elimination in a constrained minimization scheme that involves first and second derivatives of the constraints with respect to the variational parameters [13]. The second-order nonlinear elimination constrained minimization algorithm described in Ref. [13] has proved invaluable in the direct calculation of core-optimized spin-coupled wave functions.

We have strived here for a computationally somewhat simpler approach, bearing in mind that the number of variational parameters can be quite considerable in practical applications. Some of the

methodology described here has now also been implemented in our determinant-based spin-coupled code [14]. Direct comparisons with the nonlinear elimination approach show no appreciable degradation in convergence characteristics, but a significant reduction in the computational overhead. Analogous considerations to those described here apply also to CASVB calculations that involve maximization of $S_{VB}(\mathbf{x})$ rather than minimization of $E_{VB}(\mathbf{x})$.

One can of course always define nonsingular linear transformations of the parameters

$$\mathbf{y} = \mathbf{L}\mathbf{x}, \tag{15}$$

and rewrite the second-order model in the form

$$E_{VB}(\mathbf{y} + \boldsymbol{\delta}\mathbf{y}) \approx E_{VB}(\mathbf{y}) + (\mathbf{g}^y)^T \boldsymbol{\delta}\mathbf{y} + 1/2\, \boldsymbol{\delta}\mathbf{y}^T \mathbf{G}^y \boldsymbol{\delta}\mathbf{y}, \tag{16}$$

with

$$\mathbf{g}^y = (\mathbf{L}^{-1})^T \mathbf{g} \tag{17}$$

and

$$\mathbf{G}^y = (\mathbf{L}^{-1})^T \mathbf{G} \mathbf{L}^{-1}. \tag{18}$$

It is useful to point out here the practical advantage of choosing $\mathbf{L}$ to be an orthogonal transformation, so that $\mathbf{L}^{-1} = \mathbf{L}^T$.

At the start of each iteration, $\mathbf{x}$ is modified (if necessary) so that Ψ_{VB} obeys all of the constraints. Our primary concern in the optimization procedure is then to define a rectangular transformation matrix $\mathbf{L}$ such that our constraints are necessarily satisfied in the updated vector, $\mathbf{x} + \boldsymbol{\delta}\mathbf{x}$. In the CASVB strategy, we can distinguish three classes of constraint:

1. Simple constraints of the form $\mathbf{c}^T\mathbf{x} = 0$
2. Normalization conditions for orbital and structure coefficients
3. Orthogonality constraints

These are in order of increasing complexity but, in practice, the elimination of parameters associated with normalizations must always be carried out last.

SIMPLE CONSTRAINTS

Constraints that may be expressed in the form

$$\sum_i \mathbf{c}(i)\mathbf{x}(i) = 0 \tag{19}$$

include various simple cases such as, for example, forcing a single expansion coefficient to be zero (in which case $\mathbf{c}$ has only one nonzero coefficient) or setting pairs of coefficients equal or opposite. However, much more complicated conditions, such as symmetry requirements for orbitals, are also covered here. The symmetry condition on a single orbital

$$\hat{O}^S \phi_\mu = \lambda \phi_\mu, \tag{20}$$

can be satisfied by diagonalizing the matrix representation of the symmetry operation $\hat{O}^S$ in the basis of $\{\chi_i\}$, and then expanding ϕ_μ in the (right hand) eigenvectors corresponding to the eigenvalue λ [3]. If n_λ such eigenvectors exist, then the symmetry condition embodied in Eq. (20) generates $m_{bas} - n_\lambda$ simple constraints, where the constraints vectors will span the orthogonal complement to the eigenspace associated with λ. When two orbitals are related by symmetry, as in

$$\hat{O}^S \phi_\mu = \phi_\nu, \tag{21}$$

then the set of allowed parameter vectors can be found by the matrix multiply

$$\mathbf{c}(i + (\nu - 1)m_{bas}) = \sum_j (\mathbf{O}^S)_{ij} \mathbf{c}(j + (\mu - 1)m_{bas}), \quad i = 1, \ldots, m_{bas}, \tag{22}$$

for each of the m_{bas} linearly independent vectors describing updates to ϕ_μ. As before, the constraints may be defined as the m_{bas} parameter vectors spanning the orthogonal complement. Calculations employing symmetry conditions on the orbitals are described later for the allyl radical and for LiH.

NORMALIZATION CONDITIONS

In order for an orbital normalization to be stationary, i.e.,

$$\langle \phi_\mu + \delta\phi_\mu | \phi_\mu + \delta\phi_\mu \rangle - \langle \phi_\mu | \phi_\mu \rangle = 0, \tag{23}$$

we require (to first order) that $\langle \phi_\mu | \delta\phi_\mu \rangle = 0$. This condition can be expressed as

$$(\mathbf{O}^{(\mu)})^T \mathbf{S}\, \delta\mathbf{O}^{(\mu)} = 0 \tag{24}$$

in which $\mathbf{O}^{(\mu)}$ is the μth column of the orbital transformation matrix, and $\mathbf{S}$ is the matrix of overlaps between basis functions. In terms of the constraints vector $\mathbf{c}$, this then becomes

$$\mathbf{c}(i + (\mu - 1)m_{\text{bas}}) = \left((\mathbf{O}^{(\mu)})^{\mathrm{T}}\mathbf{S}\right)_i, \quad i = 1, \ldots, m_{\text{bas}}. \quad (25)$$

The elimination of the normalization parameters may thus be carried out in a very similar fashion to the elimination of the simple constraints described above. The slight difference in this case is that the condition is now on the *update* vector only, i.e., of the form $\mathbf{c}^{\mathrm{T}}\,\delta\mathbf{x} = 0$. The normalization condition associated with the structure coefficients can be eliminated in an exactly analogous manner.

ORTHOGONALITY CONSTRAINTS

Although the CASVB procedures are primarily intended for the determination of intrinsically nonorthogonal orbitals, there are various situations in modern VB calculations in which it may be advantageous to enforce orthogonality between some of the orbitals. Such an example is given later for LiH.

For the elimination of the constraint associated with $\langle\phi_\mu|\phi_\nu\rangle = 0$ we write the update of orbital ϕ_μ in the form $\delta\phi_\mu = \delta(a\phi_\nu + b\phi_\nu^\perp)$, where $\langle\phi_\nu|\phi_\nu^\perp\rangle = 0$. Similarly, $\delta\phi_\nu = \delta(c\phi_\mu + d\phi_\mu^\perp)$. The condition

$$\langle\phi_\mu + \delta\phi_\mu|\phi_\nu + \delta\phi_\nu\rangle = 0 \quad (26)$$

requires, to first order in the orbital changes, that $a = -c$. In practical terms, this leads to a constraints vector that is very similar to the normalization case:

$$\mathbf{c}(i + (\mu - 1)m_{\text{bas}}) = \left((\mathbf{O}^{(\nu)})^{\mathrm{T}}\mathbf{S}\right)_i,$$
$$\mathbf{c}(i + (\nu - 1)m_{\text{bas}}) = \left((\mathbf{O}^{(\mu)})^{\mathrm{T}}\mathbf{S}\right)_i, \quad i = 1, \ldots, m_{\text{bas}}. \quad (27)$$

While this is not exact, because $\phi_\mu^\perp$ and $\phi_\nu^\perp$ will not in general be orthogonal, it does become a very good approximation close to convergence. The main effects of the approximation are likely to be on the global convergence characteristics, but in our applications so far this has not been a problem.

Since the elimination of orthogonality constraints is only approximate, the orthogonality must be reimposed after each update in an iteration. This must be achieved without affecting the simple orbital constraints outlined above and so we have adopted what might best be termed a pairwise symmetric orthogonalization. For each orthogonalization pair in turn, we solve

$$\langle\phi_\mu + \Delta\phi_\mu|\phi_\nu + \Delta\phi_\nu\rangle = 0 \quad (28)$$

for the two update vectors $\Delta\phi_\mu$ and $\Delta\phi_\nu$. We have used the notation $\Delta\phi_\mu$ to avoid confusion with the update $\delta\phi_\mu$ predicted by the second-order model. The updates must be "allowed." For example, $\Delta\phi_\mu$ must be orthogonal to constraints vectors involving ϕ_μ as well as to any orbitals ϕ_σ for which $\langle\phi_\mu|\phi_\sigma\rangle = 0$ has previously been enforced. Furthermore, it is useful to require that $\Delta\phi_\mu$ is orthogonal to ϕ_μ. The natural choice for this update vector is clearly the projection of ϕ_ν onto the allowed space, because this will require a minimal change to both orbitals (ϕ_μ and ϕ_ν) to achieve orthogonality. If both orbitals have nonzero projections on the opposite allowed space, we can solve for the value of c in

$$\left\langle \phi_\mu + c\frac{\Delta\phi_\mu}{|\Delta\phi_\mu|} \middle| \phi_\nu + c\frac{\Delta\phi_\nu}{|\Delta\phi_\nu|} \right\rangle = 0 \quad (29)$$

($\Delta\phi_\mu$ and $\Delta\phi_\nu$ are here the projections of the other orbital). The special cases where the projection of either of ϕ_μ or ϕ_ν is null are treated separately in a similar manner.

IMPLEMENTATION

We can see that all three types of constraint can be expressed as conditions on the update, taking the form

$$\mathbf{c}_i^{\mathrm{T}}\,\delta\mathbf{x} = 0, \qquad i = 1, \ldots, N_{\text{con}}. \quad (30)$$

The set of free variables of the problem can therefore be found as the orthogonal complement of this set of N_{con} vectors. We find it by a series of standard Gram–Schmidt orthogonalizations, as follows:

1. The N_{con} constraints vectors $\mathbf{c}_i^{\mathrm{T}}$ are first orthogonalized, discarding any with a norm below an appropriate threshold.
2. The full set of unit vectors is orthogonalized to the surviving constraints.
3. The resulting vectors are finally orthogonalized, discarding any with a norm below the threshold.

The first step not only facilitates the evaluation of the orthogonal complement, but it also has the effect of eliminating any linear dependencies among the constraints vectors. The final orthogonalization not only establishes the minimum linearly independent set of free parameters, but it also ensures that the transformation matrix **L** becomes orthogonal.

The orthogonal complement could of course be found in various other ways, but we have found that the above procedure, starting from a full set of unit vectors, tends to give a transformation matrix **L** of maximum sparseness. This can significantly influence the efficiency of the transformation of the Hessian embodied in Eq. (18).

Results

We have chosen three sets of examples to indicate some of the various ways in which the CASVB code can be used to carry out fully variational optimizations of nonorthogonal orbitals in modern VB wave functions: benzene, the allyl radical, and LiH. All of the calculations described here were carried out using the appropriate modules now available in the MOLPRO [6] suite of programs.

BENZENE

For benzene (D_{6h}) we adopted bond lengths $r_{CC} = 139.64$ pm and $r_{CH} = 108.31$ pm. The s/p basis functions for carbon and the s basis functions for hydrogen were taken from correlation consistent pVTZ basis sets [15]. These were augmented with polarization functions with exponents $d_C = 0.8$ and $p_H = 1.0$, so that the basis sets for C/H consist of $(10s5p1d/5s1p)$ Cartesian GTOs contracted to $[4s3p1d/3s1p]$. A 6-in-6 CASSCF calculation was performed for the π electrons, keeping the 36 σ electrons in an optimized closed-shell core. The nondynamical correlation energy incorporated in this wave function is ~ 73 millihartrees (see Table I). By definition, the RHF wave function $[\text{core}](a_{2u})^2(e_{1g})^4$ accounts for none of this correlation energy. The weight of the configuration $[\text{core}](a_{2u})^2(e_{1g})^4$ in the full CASSCF wave function is 88.4%.

Spin-coupled calculations, with an active space corresponding to the six π electrons, were carried out (using the CASVB code) with a frozen core, taken directly from the CASSCF calculation. This

TABLE I
Calculated energies for benzene.

Calculation	E, hartrees	$E - E_{CAS}$, millihartrees	Proportion of $E_{CAS} - E_{RHF}$
CASSCF	−230.8368216	0	100%
SC	−230.8293315	7.49	89.7%
SC (f.c.)	−230.8293314	7.49	89.7%
RHF	−230.7640556	72.77	0%

calculation, labeled SC (f.c.) in Table I, recovers nearly 90% of the nondynamical energy and the overlap with the CASSCF wave function exceeds 0.995. The further energy lowering and change in S_{VB} on optimizing the σ "core" is negligible (calculation SC in Table I).

Although no such constraints were imposed, and the calculations were actually performed in C_{2v} symmetry, we find six symmetry-equivalent spin-coupled π orbitals that may be transformed into one another by successive $\hat{C}_6$ rotations. Numbering the orbitals sequentially around the ring, the symmetry-unique overlap integrals are $\langle\phi_1|\phi_2\rangle = 0.524$, $\langle\phi_1|\phi_3\rangle = 0.029$, and $\langle\phi_1|\phi_4\rangle = -0.157$. Each orbital consists of a deformed $C(2p_\pi)$ function associated with a given carbon atom, but it exhibits some deformation toward the neighboring atoms in the ring (see Fig. 1). This outcome is, of course, entirely consistent with all of the previous spin-coupled studies of this molecule [3, 16–22]. The deformations of the orbitals play a crucial role; without them, it would be essential to incorporate also the plethora of ionic structures with double occupancy of one or more orbitals.

Expressed in the Rumer basis [23], often employed in classical VB calculations, the total spin function corresponds to weights of 40.6% each for the two Kekulé structures and of 6.3% each for the three para-bonded ("Dewar") structures. Using the same set of orbitals, the energy change on restricting the spin space to just one of the Kekulé structures corresponds to a resonance energy of 83.5 kJ mol^{-1}.

Hirao et al. [24] have adopted the same name, i.e., CASVB, for calculations in which they transformed the CASSCF wave function to a representation based on orthogonal localized molecular orbitals. In the case of benzene, they report weights of 7.8% each for the Kekulé structures and of 2.6% each for the para-bonded structures. In their model, 76.6% of the benzene ground-state wave function is ionic. Analogous conclusions, but by no means

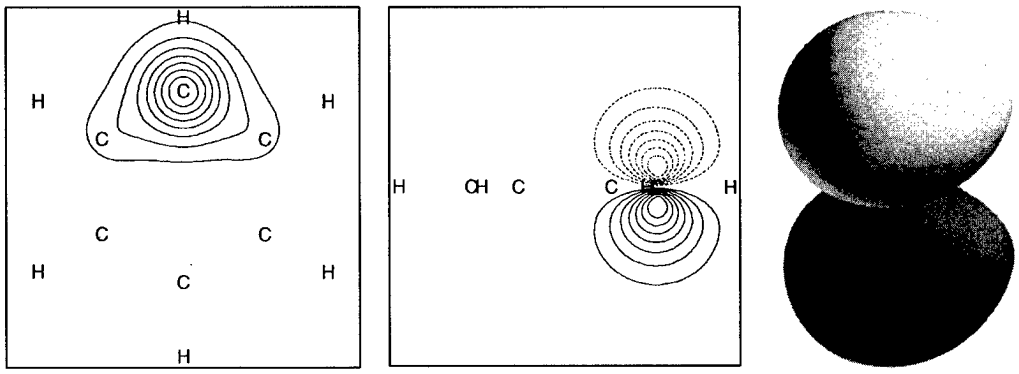


FIGURE 1. Various representations of a symmetry-unique spin-coupled π orbital for benzene. (Left) Contours in the horizontal plane 1 bohr above the molecular plane. (Center) Contours in a vertical mirror plane. (Right) A representative three-dimensional contour (isosurface).

quite so extreme, arise in classical VB descriptions based on strictly localized orbitals [25]. It should be clear why the present authors prefer modern VB calculations with fully-optimized nonorthogonal orbitals.

The Chirgwin–Coulson weight [26] of Ψ_{VB} in Ψ_{CAS} is 99.1%, so that spin-coupled ionic configurations amount to just 0.9% of the total wave function. Nonetheless, this very small component, with $1 - S_{VB} < 0.005$, accounts for some 10% of the nondynamical correlation energy, and so it is natural to analyze it further. We find that doubly ionic configurations are the more important contributors, with an accumulated Chirgwin–Coulson weight of 0.55%. This is in line with the expected diminished importance of singly ionic configurations in wave functions based on fully optimized nonorthogonal orbitals. Furthermore, from the dominance in the total wave function of the two Kekulé-like configurations, we can expect singly ionic configurations with charges in ortho positions to be the least important. This is borne out by the total weights of the various singly ionic configurations, which decrease in the order meta > para > ortho. We find that charges in meta positions give a total weight of 0.32%, whereas para and ortho contributions are orders of magnitude smaller.

ALLYL RADICAL

As a test of the convergence characteristics of the CASVB code, we have reinvestigated the $^2A_2$ ground state of the allyl radical, C_3H_5, treating as active the three π electrons. The spin-coupled VB approach (see also the discussion of LiH) has recently been employed by Oliva et al. [27] to study the doublet valence states and the $n = 3$ Rydberg excited states of the allyl radical below the first ionization potential (8.13 eV). In general, the excitation energies compare favorably with those obtained in analogous three-electron full CI calculations.

The calculations in the present work were performed in C_{2v} symmetry, using the same geometry as Oliva et al. [27] and the basis set they denoted basis II, except that the most diffuse d function (exponent 0.015) was placed on all three carbon atoms, rather than just on the central one. The total number of contracted Cartesian GTOs is 120 ($52A_1, 39B_1, 17B_2, 12A_2$). A 3-in-3 CASSCF calculation was performed for the π electrons, with the 20 σ electrons accommodated in an optimized closed-shell core. Our various total energies are collected in Table II.

As was also found in previous work [28], a fully variational spin-coupled calculation with the same choice of active and inactive spaces generates a total wave function that is identical to that from the CASSCF, albeit in much more compact form. One of the spin-coupled orbitals, ϕ_3, takes the

TABLE II
Calculated energies for the allyl radical ($^2A_2$).

Calculation	E, hartrees	$E - E_{CAS}$ millihartrees
3-in-3 CASSCF	−116.522760	0
SC: antipair orbitals	−116.522760	0.00
SC: localized orbitals	−116.521438	1.32
RHF	−116.483356	39.40

form of a deformed C($2p_\pi$) function associated with the central C atom, but with deformations toward the terminal C atoms. The remaining spin-coupled orbitals, ϕ_1 and ϕ_2, adopt *antipair* form, as is shown in the top row of Figure 2: they resemble in- and out-of-phase combinations of deformed C($2p_\pi$) functions associated with the terminal C atoms. The corresponding electron spins are predominantly, but not exclusively, triplet coupled. Expressed in the Kotani or Serber bases [23], the mode with triplet coupling of these two spins accounts for 99.1% of the total spin function. The only nonzero overlap is $\langle\phi_1|\phi_3\rangle = 0.744$.

It proved possible in a previous study [28] to locate also a rival spin-coupled solution in which ϕ_1 and ϕ_2 adopt more localized forms, in which they are equivalent with respect to reflection in the σ_v mirror plane perpendicular to the molecular plane. In a somewhat smaller basis set, and without full optimization of the σ core, the energy of a solution based on localized orbitals was found to be inferior to that of the antipair solution by 1.5 millihartrees [28].

In the present work, we used the CASVB code to optimize a constrained spin-coupled wave function in which ϕ_1 and ϕ_2 are permuted by reflection in the σ_v mirror plane, but ϕ_3 is invariant to this operation. The doubly occupied core orbitals were fully optimized simultaneously with the spin-coupled π orbitals. The convergence characteristics of the constrained optimization procedure were found to be excellent. The resulting spin-coupled π orbitals are shown in the bottom row of Figure 2. No constraints were applied to the spin space, but it turns out that in order to achieve the correct overall $^2A_2$ symmetry the spins associated with orbitals ϕ_1 and ϕ_2 are required to be strictly triplet coupled. The nonzero overlaps are $\langle\phi_1|\phi_3\rangle = \langle\phi_2|\phi_3\rangle = 0.501$ and $\langle\phi_1|\phi_2\rangle = -0.184$. The difference in energy from the antipair solution (1.32 millihartrees, see Table II) is similar to the value found previously [28] and arises from the removal of all the spin degrees of variational freedom. Convergence to this localized orbital solution is only possible with the appropriate symmetry constraints; without them, this solution corresponds only to a saddle point in the full spin-coupled variational space.

LiH

It is useful to describe first the key features of a previous spin-coupled VB study of the $X^1\Sigma^+$ ground state of LiH [29]. The spin-coupled wave

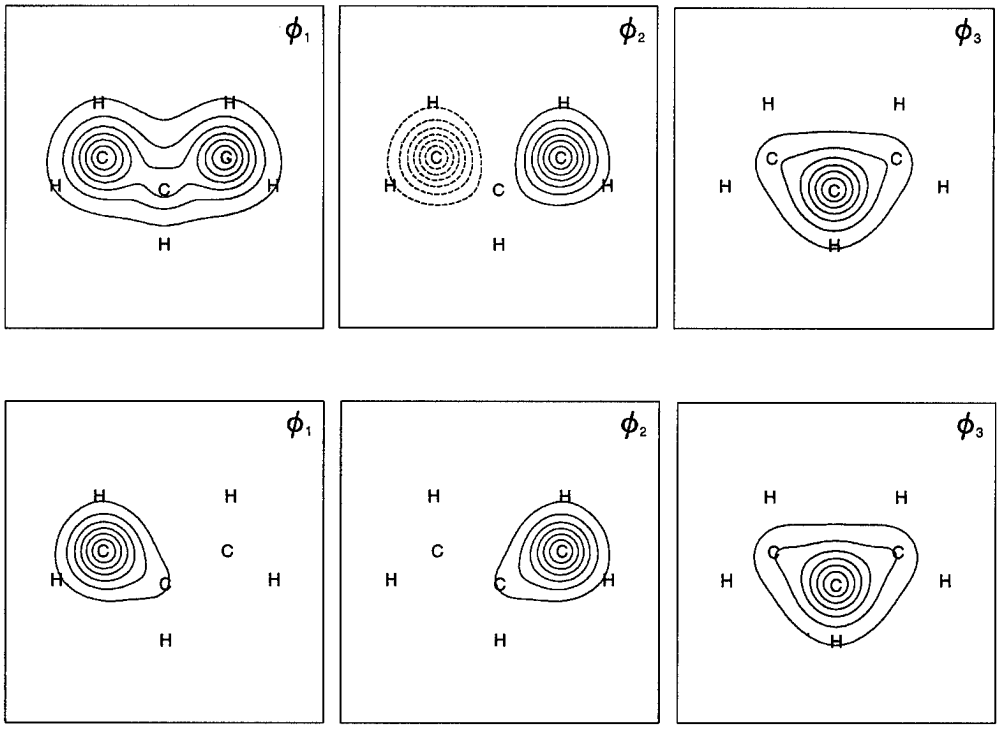


FIGURE 2. Spin-coupled π orbitals for the $^2A_2$ ground state of the allyl radical, shown as contours in the horizontal plane 1 bohr above the molecular plane.

function may be written in the form

$$\Psi_{SC} = \mathscr{A}\left(\phi_1\phi_2\phi_3\phi_4 \sum_{k=1}^{2} c_{0k}\Theta^4_{00;k} \right) \equiv \{\phi_1\phi_2\phi_3\phi_4\} \tag{31}$$

with four singly occupied nonorthogonal orbitals. For four electrons with a net spin of zero, the full spin space [23] consists of just two linearly independent modes of spin coupling. The two spin-coupling coefficients (c_{0k}) were optimized simultaneously with the orbitals, without any constraints that would alter the total wave function.

The converged spin-coupled orbitals all possess σ symmetry. At large nuclear separations, they correspond to Li($1s1s'2s$) and H($1s$). We found that the two "core" orbitals, and the overlap between them (~ 0.93), remain essentially unchanged as the atoms approach. The H($1s$) function also changes relatively little. On the other hand, dramatic changes occur in the orbital initially associated with Li($2s$). As the atoms approach, electron density is transferred from lithium to the hydrogen atom, in the form of a rather diffuse deformed H($1s$) function. For nuclear separations around R_e, the form of the two valence orbitals implies considerable Li^+H^- character [29]. Perfect pairing remains the dominant mode of spin coupling for all values of R.

At convergence, each occupied orbital gives rise to a "stack" of orthonormal virtual orbitals, determined in an effective field which excludes the occupied orbital. Virtual orbitals in different stacks are not in general orthogonal to one another. Further spatial configurations were generated by means of excitations from valence spin-coupled orbitals (σ_3 and σ_4) into corresponding virtual orbitals, and the corresponding wave functions, total energies and dipole moments were obtained in very compact nonorthogonal CI calculations. A suitably constructed series of such spin-coupled VB expansions [29] exhibited very rapid convergence onto a dipole moment function previously calculated by means of accurate MO CI calculations.

The calculations in the present work were performed in C_{2v} symmetry using the density-matrix averaged atomic natural orbital basis sets of Widmark et al. [30]. For Li/H, these sets consist of ($14s9p4d3f/8s4p3d$) spherical GTOs contracted to [$6s5p3d2f/4s3p2d$], generating a total of 73 GTOs ($32A_1, 17B_1, 17B_2, 7A_2$). A full-valence CASSCF calculation for this molecule involves just two active electrons, with the orbitals partitioned:

- Optimized core (double occupancy): $1a_1$ (i.e., 1σ)
- Active (variable occupancy): $2a_1$–$4a_1$, $1b_1$, and $1b_2$ (i.e., 2σ–4σ and 1π)
- Virtual (unoccupied): $5a_1$–$32a_1$, $2b_1$–$17b_1$, $2b_2$–$17b_2$, $1a_2$–$7a_2$

A two-electron full-CI calculation, with the doubly occupied $1a_1$ orbital taken from the full-valence CASSCF wave function, requires fairly trivial computing resources, and gives a clear indication of the best that we can expect to achieve in frozen-core calculations with this basis set.

Computed equilibrium geometries, together with the corresponding total energies and dipole moments, are collected in Table III. Starting from the RHF wave function, the single largest energy improvement corresponds to the radial correlation introduced by opening up the $3a_1$ orbital (i.e., 3σ). Almost as large is the angular correlation introduced by opening up the degenerate $1b_1$ and $1b_2$

TABLE III
RHF, CASSCF, and full-CI equilibrium geometries for LiH.

Active orbitals	Inactive space	R_e, Å	E, hartrees	μ, Debyes
(RHF)	—	1.606	−7.987257	6.02
$2a_1, 3a_1$	$(1a_1)^2$	1.634	−8.003784	5.74
$2a_1, 3a_1, 4a_1$	$(1a_1)^2$	1.633	−8.009548	5.88
$2a_1, 1b_1, 1b_2$	$(1a_1)^2$	1.589	−8.001320	5.98
$2a_1, 3a_1, 1b_1, 1b_2$	$(1a_1)^2$	1.611	−8.015914	5.78
$2a_1, 3a_1, 4a_1, 1b_1, 1b_2$	$(1a_1)^2$	1.611	−8.021112	5.89
(full CI)[a]	$(1a_1)^2$	1.608	−8.023861	—

[a] Doubly occupied $1a_1$ core orbital taken from the corresponding full-valence CASSCF.

orbitals (i.e., 1π). The full-valence CASSCF calculation gives a value of R_e that is very close to that from the two-electron full CI, and the minimum energies are within 3 millihartrees of one another. This full-CI calculation gives an equilibrium bond length of 1.6076 Å, and all subsequent calculations were carried out at this geometry. The experimentally determined value of R_e is 1.595 Å [31].

Energies from various four-electron CASSCF calculations are collected in Table IV, for a nuclear separation of 1.6076 Å. Comparing with the corresponding two-electron CASSCF calculations at the same geometry, it is clear that opening up the $1a_1$ core orbital results in a fairly dramatic energy lowering. There are of course further energy lowerings on opening up also the $5a_1$, $6a_1$, $2b_1$, and $2b_2$ orbitals, and it is clear that the all-electron full-valence CASSCF wave function is still far from the corresponding full CI. Note that three of the CASSCF calculations have been labeled A, B, or C in Table IV in order to facilitate the subsequent discussion.

As we have indicated, computationally the most inexpensive use of the CASVB code is to generate modern VB representations of CASSCF wave functions by means of the overlap criterion [Eq. (7)]. Applying this criterion to CASSCF calculation A leads to a representation in which the total wave function is overwhelmingly dominated by a spin-coupled-like component $\{\phi_1\phi_2\phi_3\phi_4\}$. The overlap between this dominant component and the full wave function (S_{VB}, see Table V) is very close to unity. The energy E_{VB} corresponding to the spin-coupled-like component accounts for all but ~ 7.3 microhartrees of the total CASSCF energy. This small difference could of course be reduced if the orbital transformation were chosen instead using the energy criterion [Eq. (8)]. A fully variational calculation for the spin-coupled configuration $\{\phi_1\phi_2\phi_3\phi_4\}$ provides an energy within 7.3 microhartrees of that provided by the CASSCF calculation. All four spin-coupled orbitals were found to be of pure σ symmetry (i.e., a_1).

For calculation B, we considered the three-configuration modern VB wave function

$$\Psi_B = C_1\mathscr{A}\left(\phi_1\phi_2\phi_3\phi_4\sum_{k=1}^{2}c_{0k}\Theta^4_{00;k}\right) + C_2\mathscr{A}\left(\phi_1\phi_2\phi_5\phi_5\Theta^4_{pp}\right) + C_2\mathscr{A}\left(\phi_1\phi_2\phi_6\phi_6\Theta^4_{pp}\right) \quad (32)$$

in which Θ^4_{pp} is the four-electron perfect-pairing spin function. There can, of course, only be one mode of spin coupling for the configurations with a doubly occupied orbital (ϕ_5 or ϕ_6), on account of the Pauli principle. Orbitals ϕ_1–ϕ_4 were constrained to be of σ symmetry (i.e., a_1), and orbitals

TABLE IV

RHF CASSCF, and full-CI results for LiH at 1.6076 Å.

Active orbitals	Inactive space	E, hartrees	μ, Debyes
(RHF)	—	−7.987257	6.03
Two active electrons:			
$2a_1, 3a_1$	$(1a_1)^2$	−8.003710	5.70
$2a_1, 3a_1, 4a_1$	$(1a_1)^2$	−8.009480	5.84
$2a_1, 1b_1, 1b_2$	$(1a_1)^2$	−8.001275	6.02
$2a_1, 3a_1, 1b_1, 1b_2$	$(1a_1)^2$	−8.015913	5.77
$2a_1, 3a_1 4a_1 1b_1, 1b_2$	$(1a_1)^2$	−8.021111	5.88
(full CI)[a]	$(1a_1)^2$	−8.023861	—
Four active electrons:			
A $(1-4)a_1$	—	−8.016846	5.71
B $(1-4)a_1, 1b_1, 1b_2$	—	−8.029067	5.78
$(1-4)a_1, 1b_1, 2b_1, 1b_2, 2b_2$	—	−8.035753	5.76
$(1-5)a_1, 1b_1, 1b_2$	—	−8.034309	5.88
$(1-5)a_1, 1b_1, 2b_1, 1b_2, 2b_2$	—	−8.035003	5.88
C $(1-6)a_1, 1b_1, 1b_2$	—	−8.038302	5.88
$(1-6)a_1, 1b_1, 2b_1, 1b_2, 2b_2$	—	−8.044885	5.87

[a] Doubly occupied $1a_1$ core orbital taken from the corresponding full-valence CASSCF.

TABLE V
Various CASSCF and CASVB results for LiH, as described in the text.[a]

	CASSCF	Overlap criterion			Variational MCSC	
	E_{CAS}, hartrees	$1 - S_{VB}$	E_{VB}, hartrees	ΔE, μhartrees	E_{MCSC}, hartrees	μ_{MCSC}, Debyes
A	−8.016846	5.3×10^{-7}	−8.016839	7.3	−8.016839	5.71
B	−8.029067	2.3×10^{-6}	−8.029048	19.2	−8.029048	5.78
C	−8.038302				−8.033347	5.86

[a] The labels in the first column correspond to those in Table IV.

ϕ_5 and ϕ_6 to be a π pair (i.e., b_1 and b_2). Using the overlap criterion [Eq. (7)], we may generate an alternative representation of the CASSCF wave function in which a component of the form of Eq. (32) is overwhelmingly dominant. The optimal value of S_{VB} (see Table V) is remarkably close to unity, and the corresponding expectation value of the energy is only 19.2 microhartrees inferior to that from the full CASSCF calculation. A fully variational optimization of the multiconfiguration spin-coupled (MCSC) wave function Ψ_B leads to an energy that is 19.0 microhartrees inferior to CASSCF B.

In the case of CASSCF calculation C, we proceeded directly to the fully variational optimization of a four-configuration MCSC wave function of the form

$$\begin{aligned}\Psi_C = {} & C_1 \mathscr{A}\left(\phi_1\phi_2\phi_3\phi_4 \sum_{k=1}^{2} c_{0k}\Theta^4_{00;k} \right) \\ & + C_2 \mathscr{A}\left(\phi_1\phi_2\phi_5\phi_6 \sum_{k=1}^{2} c'_{0k}\Theta^4_{00;k} \right) \\ & + C_3 \mathscr{A}\left(\phi_1\phi_2\phi_7\phi_7\Theta^4_{pp} \right) \\ & + C_3 \mathscr{A}\left(\phi_1\phi_2\phi_8\phi_8\Theta^4_{pp} \right). \end{aligned} \tag{33}$$

Orbitals ϕ_1–ϕ_6 were constrained to be of a_1 symmetry, and orbitals ϕ_7 and ϕ_8 to be the b_1 and b_2 pair. In order to maintain some distinction between $\{\phi_1\phi_2\phi_3\phi_4\}$ and $\{\phi_1\phi_2\phi_5\phi_6\}$, we constrained ϕ_5 and ϕ_6, to be orthogonal to both of ϕ_1 and ϕ_2. Such a calculation, which utilizes numerous features of our constrained optimization procedure, converges rapidly to a total energy within about 5 millihartrees (see Table V) of that from the full CASSCF wave function.

We find that the converged orbitals ϕ_1–ϕ_4, and the overlaps between them (see Table VI), are very similar to those obtained from the single-configuration spin-coupled calculation [Eq. (31)] and the three-configuration MCSC calculation [Eq. (32)]. The overlaps of ϕ_3 and ϕ_4 with ϕ_5 and ϕ_6, turn out to be rather small (see Table VI), and this suggests that it could be a reasonable approximation in future work to restrict orbitals ϕ_5 and ϕ_6 to lie in the orthogonal complement of orbitals ϕ_1–ϕ_4. As might be anticipated, the dominant component of all three modern VB wave functions, Ψ_{SC}, Ψ_B, and Ψ_C, is the combination of the perfect-pairing spin function with the orbital string $\phi_1\phi_2\phi_3\phi_4$.

Multiconfiguration spin-coupled calculations for LiH were first performed by Pyper and Gerratt [32]. The Pyper–Gerratt (PG) wave function for

TABLE VI
Overlaps between the nonorthogonal orbitals in the MCSC wave function ψ_C [Eq. (33)].

	ϕ_1	ϕ_2	ϕ_3	ϕ_4	ϕ_5	ϕ_6	ϕ_7	ϕ_8
ϕ_1	1	0.926	0.123	0.064	0	0	0	0
ϕ_2	0.926	1	0.197	0.096	0	0	0	0
ϕ_3	0.123	0.197	1	0.774	0.047	−0.028	0	0
ϕ_4	0.064	0.096	0.774	1	0.066	0.006	0	0
ϕ_5	0	0	0.047	0.066	1	0.585	0	0
ϕ_6	0	0	−0.028	0.006	0.585	1	0	0
ϕ_7	0	0	0	0	0	0	1	0
ϕ_8	0	0	0	0	0	0	0	1

this molecule takes the form

$$\Psi_{PG} = C_1\{\sigma_1\sigma_2\sigma_3\sigma_4\} + C_2 \sum_{\alpha=x,\,y} \{\sigma_1\sigma_2\pi_\alpha\pi'_\alpha\}. \quad (34)$$

The orbitals were fully optimized according to their designated symmetry properties simultaneously with the C_i coefficients, but the mode of spin coupling was restricted to perfect pairing. It should be clear that the appropriate all-electron CASSCF wave function with which to compare is the one with an active space consisting of $(1-4)a_1$, $(1-2)b_1$, and $(1-2)b_2$. According to the energies listed in Table IV, the energy improvement of the PG wave function relative to the spin-coupled configuration should be considerable. Penotti [33] has recently developed a full generalization of the PG method in which the orbitals, spin-coupling coefficients, and structure coefficients are fully optimized simultaneously. The computational demands turn out to be very much larger than those of the approach we have presented here. Penotti has also considered simultaneous optimization of the basis set [33].

An attractive alternative to the exact optimization of MCSC wave functions has recently been explored by Clarke et al. [34], who examined a four-configuration description of the form

$$\Psi_{SCVB^*} = C_1\{\sigma_1\sigma_2\sigma_3\sigma_4\} + C_2\{\sigma_1\sigma_2\sigma_5\sigma_6\} + C_3 \sum_{\alpha=x,\,y} \{\sigma_1\sigma_2\pi_\alpha\pi'_\alpha\}. \quad (35)$$

In the spirit of a spin-coupled VB expansion [29], orbitals σ_1–σ_4 were taken from a standard spin-coupled calculation, without further optimization. In order to overcome convergence problems, spin-coupled orbitals σ_1–σ_4 were projected out of the m_{bas} basis functions, and Gram–Schmidt orthogonalization was used to extract a set of $m_{bas} - 4$ linearly independent functions. Orbital σ_5 was then expressed as a linear combination of σ_1, σ_2, σ_4, and the linearly independent projected functions. Similarly, orbital σ_6 was expressed as a linear combination of σ_1, σ_2, σ_3, and the linearly independent projected functions. In this form, orbitals σ_5 and σ_6 were optimized simultaneously with π_α and π'_α ($\alpha = x, y$) and the C_i coefficients, but the spin-coupling coefficients in each configuration were fixed to be the same as those in the spin-coupled wave function $\{\sigma_1\sigma_2\sigma_3\sigma_4\}$. The main simplifications, which should make the approach viable also for systems with more active electrons, are the use of a second-order perturbation theory expression for the energy and an approximation to the required elements of the Hessian. Of course, once the orbitals have been (approximately) optimized in this way, they may be used to construct a variational spin-coupled VB wave function, relaxing also the constraints on the spin-coupling coefficients, but without further orbital optimization. The various CASSCF and fully variational MCSC calculations described in the present work should prove to be useful benchmarks for assessing the accuracy and computational demands of this type of approach, and further results will be published in due course. The most appropriate all-electron CASSCF wave function with which to compare Ψ_{SCVB^*} is, of course, the one with an active space consisting of $(1-6)a_1$, $(1-2)b_1$, and $(1-2)b_2$.

Summary and Conclusions

We have outlined the CASVB approach for the fully variational optimization of general types of modern valence bond wave function, and we have presented a simple algorithm for the elimination of redundant or constrained parameters from the appropriate second-order optimization problems. The CASVB code may also be used to generate very compact modern VB representations of CASSCF wave functions, with the overlap criterion [Eq. (7)] being relatively inexpensive.

Various ways in which the CASVB procedures may be used were illustrated by means of selected results for benzene, the allyl radical, and LiH, including the incorporation of symmetry conditions and the generation of fully variational multiconfiguration spin-coupled (MCSC) wave functions. We have also established useful benchmarks for assessing the accuracy and computational demands of various other MCSC approaches that are currently being pursued [33, 34].

Since the modern VB wave function in the CASVB approach can be viewed as a constrained form of CASSCF wave function, a multitude of techniques immediately become available for modern VB methods, including the incorporation of dynamical correlation and the direct, on-the-fly evaluation of integrals over basis functions. In the case of the implementation of CASVB in MOLPRO [6], the CASSCF part of the code provides for the efficient evaluation of energy gradients, enabling, for example, geometry optimizations with fully variational, core-optimized MCSC wave functions.

References

1. T. Thorsteinsson, D. L. Cooper, J. Gerratt, P. B. Karadakov, and M. Raimondi, Theor. Chim. Acta **93**, 343 (1996).
2. T. Thorsteinsson and D. L. Cooper, Theor. Chim. Acta **94**, 233 (1996).
3. T. Thorsteinsson, D. L. Cooper, J. Gerratt, and M. Raimondi, Theor. Chim. Acta **95**, 131 (1997).
4. T. Thorsteinsson, D. L. Cooper, J. Gerratt, and M. Raimondi, Molec. Eng., to appear.
5. For a review of applications see, for example, D. L. Cooper, J. Gerratt, and M. Raimondi, Chem. Rev. **91**, 929 (1991).
6. MOLPRO is a package of ab initio programs written by H.-J. Werner and P. J. Knowles, with contributions from J. Almlöf, R. D. Amos, A. Berning, M. J. O. Deegan, F. Eckert, S. T. Elbert, C. Hampel, R. Lindh, W. Meyer, A. Nicklaβ, K. Peterson, R. Pitzer, A. J. Stone, P. R. Taylor, M. E. Mura, P. Pulay, M. Schütz, H. Stoll, T. Thorsteinsson, and D. L. Cooper.
7. H.-J. Werner and P. J. Knowles, J. Chem. Phys. **82**, 5053 (1985); P. J. Knowles and H.-J. Werner, Chem. Phys. Lett. **115**, 259 (1985).
8. P.-Å. Malmqvist, Int. J. Quant. Chem. **30**, 479 (1986).
9. P. E. M. Siegbahn, Chem. Phys. Lett. **109**, 417 (1984).
10. J. Olsen, B. O. Roos, P. Jørgensen, and H. J. Aa. Jensen, J. Chem. Phys. **89**, 2185 (1988); S. Zarrabian, C. R. Sarma, and J. Paldus, Chem. Phys. Lett. **155**, 183 (1989); R. J. Harrison and S. Zarrabian, Chem. Phys. Lett. **158**, 393 (1989).
11. R. Fletcher, *Practical Methods of Optimization*, 2nd. ed. (Wiley, New York, 1987).
12. J. Olsen, D. L. Yeager, and P. Jørgensen, Adv. Chem. Phys. **54**, 1 (1983).
13. P. B. Karadakov, J. Gerratt, M. Raimondi, and D. L. Cooper, J. Chem. Phys. **97**, 7637 (1992).
14. D. L. Cooper, J. Gerratt, M. Raimondi, M. Sironi, and T. Thorsteinsson, Theor. Chim. Acta. **85**, 261 (1993).
15. T. H. Dunning, J. Chem. Phys. **90**, 1007 (1989); the pVTZ basis was taken directly from the MOLPRO library.
16. D. L. Cooper, J. Gerratt, and M. Raimondi, Nature **323**, 699 (1986).
17. J. Gerratt, Chem. Brit. **23**, 327 (1987).
18. D. L. Cooper, S. C. Wright, J. Gerratt, and M. Raimondi, J. Chem. Soc. Perkin Trans. 2, 255 (1989).
19. D. L. Cooper, S. C. Wright, J. Gerratt, P. A. Hyams, and M. Raimondi, J. Chem. Soc. Perkin Trans. 2, 719 (1989).
20. E. C. da Silva, J. Gerratt, D. L. Cooper, and M. Raimondi, J. Chem. Phys. **101**, 3866 (1994).
21. G. Raos, J. Gerratt, D. L. Cooper, and M. Raimondi, Chem. Phys. **186**, 233 (1994).
22. G. Raos, J. Gerratt, P. B. Karadakov, D. L. Cooper, and M. Raimondi, J. Chem. Soc. Faraday Trans. **91**, 4011 (1995); G. Raos, L. Astorri, M. Raimondi, D. L. Cooper, J. Gerratt, and P. B. Karadakov, J. Phys. Chem. A **101**, 2886 (1997).
23. R. Pauncz, *Spin Eigenfunctions: Construction and Use* (Plenum, New York, 1979).
24. K. Hirao, H. Nakano, K. Nakayama, and M. Dupuis, J. Chem. Phys. **105**, 9227 (1996).
25. J. M. Norbeck and G. A. Gallup, J. Am. Chem. Soc. **95**, 4460 (1973); J. M. Norbeck and G. A. Gallup, J. Am. Chem. Soc. **96**, 3386 (1974); G. A. Gallup and J. M. Norbeck, J. Am. Chem. Soc. **97**, 970 (1975); G. F. Tantardini, M. Raimondi, and M. Simonetta, J. Am. Chem. Soc. **99**, 2913 (1977).
26. B. A. Chirgwin and C. A. Coulson, Proc. Roy. Soc. Lond. A **201**, 196 (1950).
27. J. M. Oliva, J. Gerratt, D. L. Cooper, P. B. Karadakov, and M. Raimondi, J. Chem. Phys. **106**, 3663 (1997).
28. P. B. Karadakov, J. Gerratt, G. Raos, D. L. Cooper, and M. Raimondi, J. Am. Chem. Soc. **116**, 2075 (1994).
29. D. L. Cooper, J. Gerratt, and M. Raimondi, Chem. Phys. Lett. **118**, 580 (1985).
30. P.-O. Widmark, P.-Å. Malmqvist, and B. O. Roos, Theor. Chim. Acta **77**, 291 (1990).
31. C. R. Vidal and W. C. Stwalley, J. Chem. Phys. **77**, 883 (1982).
32. N. C. Pyper and J. Gerratt, Proc. R. Soc. Lond. A **355**, 406 (1977).
33. F. E. Penotti, Int. J. Quant. Chem. **59**, 349 (1996).
34. N. J. Clarke, M. Raimondi, M. Sironi, J. Gerratt, and D. L. Cooper, to appear.

Density-Functional Method for Very Large Systems with LCAO Basis Sets

DANIEL SÁNCHEZ-PORTAL,[1] PABLO ORDEJÓN,[2]
EMILIO ARTACHO,[1] JOSÉ M. SOLER[1]

[1] *Departamento de Física de la Materia Condensada, C-III, and Instituto Nicolás Cabrera, Universidad Autónoma de Madrid, E-28049 Madrid, Spain*
[2] *Departamento de Física, Universidad de Oviedo, 33007 Oviedo, Spain*

Received 2 March 1997; revised 22 April 1997; accepted 22 April 1997

ABSTRACT: We have implemented a linear scaling, fully self-consistent density-functional method for performing first-principles calculations on systems with a large number of atoms, using standard norm-conserving pseudopotentials and flexible linear combinations of atomic orbitals (LCAO) basis sets. Exchange and correlation are treated within the local-spin-density or gradient-corrected approximations. The basis functions and the electron density are projected on a real-space grid in order to calculate the Hartree and exchange–correlation potentials and matrix elements. We substitute the customary diagonalization procedure by the minimization of a modified energy functional, which gives orthogonal wave functions and the same energy and density as the Kohn–Sham energy functional, without the need of an explicit orthogonalization. The additional restriction to a finite range for the electron wave functions allows the computational effort (time and memory) to increase only linearly with the size of the system. Forces and stresses are also calculated efficiently and accurately, allowing structural relaxation and molecular dynamics simulations. We present test calculations beginning with small molecules and ending with a piece of DNA. Using double-z, polarized bases, geometries within 1% of experiments are obtained. © 1997 John Wiley & Sons, Inc. Int J Quant Chem **65**: 453–461, 1997

Introduction

The ability to perform reliable simulations of molecules and solid systems with thousands of atoms has enormous payoffs in many fields, especially for the materials and pharmaceutical industries. With the rapid increase of computational power, the emphasis is changing from semiempirical potentials and force fields to ab initio quantum mechanical methods [1]. However, a major problem of these methods is that, in general, their computational cost scales as N^3, with the number of atoms N. In the last few years, much effort has been devoted to overcome this problem, and a number of methods have been

Correspondence to: J. M. Soler.

© 1997 John Wiley & Sons, Inc.
CCC 0020-7608 / 97 / 050453-09

developed with "order-N" [O(N)] scaling, i.e., whose computational cost scales only linearly with the number of atoms [2–7]. Most of these efforts and methods are based on simplified, non-self-consistent, tight-binding or Harris-functional models, although the first steps toward self-consistent methods have also been made, using Gaussian orbitals [8] or a real-space grid to define the electron wave functions [9]. These last methods are very demanding in computer time and memory, requiring large computers and becoming competitive only for extremely large systems.

We have developed a fully self-consistent density-functional method, based on flexible linear combination of atomic orbitals (LCAO) basis sets, with actual and efficient O(N) scaling. It allows from extremely fast simulations, on the one hand, using minimal basis sets, to very accurate calculations, on the other hand, using expanded bases (multiple-z, polarization, off-site orbitals), the choice depending on the size of the system, required accuracy, and available computational power. In previous studies [10, 11] we have described preliminary versions of this method, where the essentials of the linear scaling were already put forward (see Fig. 2 in Ref. [10]). The main improvements that we describe in this work are: (i) the flexibilization of the basis sets to include essentially any desired functions and (ii) the implementation of new features, like spin polarization, generalized gradient corrections (GGA) exchange–correlation, or the calculation of the stress tensor.

Basic Approximations

Apart from that of Born and Oppenheimer, the most basic approximations used here concern the treatment of exchange and correlation, and the elimination of core electrons, which are replaced by pseudopotentials. Exchange–correlation is treated within the framework of the Kohn–Sham [12] version of density-functional theory. We allow for both the local (spin) density approximation (LDA/ LSD) [13], with several possible parametrizations, or the generalized-gradient-corrections (GGA) approximation, in the fully ab initio (non-empirical) version of Perdew, Burke, and Ernzerhof [14].

Since we calculate on a real-space grid (see below), we use standard norm-conserving pseudopotentials [15] to avoid the computations for core electrons and to smooth the valence charge density. These pseudopotentials are transformed to their Kleinman–Bylander form [16] for improved simplicity and efficiency. This implies that only two-center integrals are required to calculate the nonlocal part of the pseudopotential matrix elements. The nonlinear partial-core correction, for the treatment of exchange and correlation in the core region [17], is also allowed to treat special cases, like alkaline atoms.

Basis Sets

In order to have a finite range for the matrix elements, one can either neglect them beyond a given distance or use confined basis orbitals, i.e., orbitals that are strictly zero beyond a certain radius [18]. We have adopted this last approach because it keeps the energy strictly variational, thus facilitating the test of the convergence with respect to the radius confinement.

The algorithms used in our method (explained in the following) perform all the required calculations numerically. No analytical expression of any kind is needed. We are, therefore, not bound to Gaussians, and adjusting the radial wave function to the core region (pseudopotential) or to other features is easy and inexpensive. Multiple-z bases can be introduced, and also polarization and off-site orbitals (orbitals centered anywhere). Some procedures are implemented for the generation of the basis starting from the solution of the separate atomic problems with the corresponding pseudopotentials, but the user can introduce his/her favorite basis, too.

In the case of a minimal basis set, we have found convenient and efficient the method of Sankey and Niklewski [18]. Their basis functions are the (angular-momentum-dependent) numerical eigenfunctions of the atomic pseudopotential, for an energy chosen so that the first node occurs at the desired cutoff radius r_c (which may depend on the atomic species and angular momentum). Beyond that radius, the basis functions are zero. The effect of the confinement is shown below.

One obvious possibility for multiple-z bases is obtained by using the set of pseudopotential eigenfunctions with an increasing number of nodes. This set has the virtue of being asymptotically complete. The efficiency, however, of this kind of

bases depends on the radii of confinement of the different orbitals, since the excited states of the pseudopotential problem are usually unbound. In the following some examples are shown of the results on molecular geometries when using this kind of bases, changing the confinement radii variationally.

Split valence bases are also easily generated by incorporating suited Gaussian orbitals [19] as extra basis functions, on top of the minimal basis defined above. In general, we find that double-z plus single-z-polarization bases reproduce the molecular geometries obtained with a planewave basis set within 1% in the cases that we have studied. Nevertheless, it is well known that the election of good basis sets is a delicate task, and lots of efforts have been devoted to it. It must be considered, however, that the use of pseudopotentials and numerical (but confined) functions makes previous experience on basis sets not directly applicable.

Matrix Elements

Within the nonlocal-pseudopotential approximation, the standard Kohn–Sham Hamiltonian may be written as

$$H = T + \sum_I \left[V_I^{\text{local}}(\mathbf{r}) + V_I^{\text{nl}} \right] + V^H(\mathbf{r}) + V^{\text{xc}}(\mathbf{r}), \tag{1}$$

where I is an atom index, lm are angular momentum quantum numbers, $T = p^2/2m$ is the kinetic energy operator, $V^H(\mathbf{r})$ and $V^{\text{xc}}(\mathbf{r})$ are the Hartree and exchange–correlation potentials, and

$$V_I^{\text{nl}} = \sum_{lm} |\phi_{Ilm}^{\text{KB}}\rangle \epsilon_{Il}^{\text{KB}} \langle \phi_{Ilm}^{\text{KB}}| \tag{2}$$

is the nonlocal (nl) part of the pseudopotential, in its Kleinman–Bylander (KB) form. ϕ_{Ilm}^{KB} are the so-called Kleinman–Bylander projectors, which obey

$$\phi_{Ilm}^{\text{KB}}(r) = \left[V_{Il}(r) - V_I^{\text{local}}(r) \right] \psi_{Ilm}(r), \tag{3}$$

$$\epsilon_{Il}^{\text{KB}} = \langle \psi_{Ilm} | V_{Il} - V_I^{\text{local}} | \psi_{Ilm} \rangle^{-1}, \tag{4}$$

where $\psi_{Ilm}(r)$ are the atomic pseudoorbitals, i.e., the solutions to the radial Schrödinger equation with potentials $V_{il}(r)$ (without any cutoff radius). Since $V_{Il} - V_I^{\text{local}}$ is nonzero only inside a small pseudopotential core radius r_I^{core}, the functions ϕ_{Ilm}^{KB} are also zero outside this radius.

In order to eliminate the long range of V^{local}, we screen it with a sum $\rho^{\text{atom}}(\mathbf{r})$ of atomic electron densities $\rho_I^{\text{atom}}(|\mathbf{r} - \mathbf{r}_I|)$, constructed by populating the basis functions with appropriate valence atomic charges. Notice that, since the atomic basis orbitals are zero beyond r_c, the screened "neutral-atom" potentials V_I^{na} are also zero beyond this radius [18]. Let now $\delta\rho(\mathbf{r})$ be the difference between the self-consistent electron density $\rho(\mathbf{r})$ and the sum of atomic densities $\rho^{\text{atom}}(\mathbf{r})$, and let $\delta V^H(\mathbf{r})$ be the Hartree potential generated by $\delta\rho(\mathbf{r})$. Then the total Hamiltonian may be rewritten as

$$H = T + \sum_I V_I^{\text{nl}} + \sum_I V_I^{\text{na}}(\mathbf{r}) + \delta V^H(\mathbf{r}) + V^{\text{xc}}(\mathbf{r}). \tag{5}$$

The matrix elements of the first two terms involve only two-center integrals which are easily calculated in reciprocal space and tabulated as a function of interatomic distance [18]. This is done at the beginning of the calculation with great accuracy, representing a very small computational effort.

The remaining terms involve potentials which are calculated in a real-space grid. The third term is a sum of short-range screened pseudopotentials which are tabulated as a function of the distance to the atoms and easily interpolated at any desired grid point. The last two terms require the calculation of the electron density at the grid. To do this, we first find the atomic basis orbitals at the grid points, also by interpolation from numerical tables. Then the electron density is given by

$$\rho(\mathbf{r}) = \sum_{\mu\nu} \rho_{\mu\nu} \phi_\mu(\mathbf{r}) \phi_\nu(\mathbf{r}), \tag{6}$$

where μ, ν run over all the atomic basis orbitals ϕ_μ, and $\rho_{\mu\nu}$ is the one-electron density matrix in this basis, obtained as explained below. Since the method is aimed at molecules and large solid supercells, Brillouin zone integrals for repeated structures are approximated by the Γ point ($k = 0$), so that all the wave functions can be made real. Notice that only overlapping orbital pairs contribute to the sum at their intersection, so that the calculation of the density can be performed in $O(N)$ operations using sparse-matrix multiplication techniques. Once the density is available in

the grid, we solve Poisson's equation with a fast Fourier transform to obtain $\delta V^H(\mathbf{r})$, adding it to $V^{na}(\mathbf{r})$ and $V^{xc}(\mathbf{r})$. The matrix elements of these three terms are then computed by integration in the same real space grid, also in $O(N)$ operations.

Total Energy and Forces

Let us forget for the moment that we want an order-N method. Then, once the Kohn–Sham Hamiltonian has been obtained, we can solve the eigenvalue problem to find the electron eigenfunctions in the LCAO basis

$$|\psi_i\rangle = \sum_\mu c_{i\mu}|\phi_\mu\rangle \tag{7}$$

and the density matrix

$$\rho_{\mu\nu} = \sum_i w_i c_{i\mu} c_{i\nu}, \tag{8}$$

where w_i are occupation weights which, at $T = 0$, will be either zero or two (spin polarization is not considered in this discussion for simplicity). The electron density can be obtained from Eq. (6) and the Kohn–Sham total energy can then be written as

$$E^{tot} = \sum_{\mu\nu} \rho_{\mu\nu} H_{\mu\nu} - \frac{1}{2}\int V^H(\mathbf{r})\rho(\mathbf{r})\, d^3\mathbf{r} + \int (\epsilon^{xc}(\mathbf{r}) - V^{xc}(\mathbf{r}))\rho(\mathbf{r})\, d^3\mathbf{r} + \frac{1}{2}\sum_{IJ} \frac{e^2 Z_I Z_J}{|\mathbf{r}_I - \mathbf{r}_J|}, \tag{9}$$

where Z_I are the valence pseudoatom charges and $\epsilon^{xc}(\mathbf{r})\rho(\mathbf{r})$ is the exchange–correlation energy density. In order to avoid the long-term interactions of the last term, it is convenient to define the "local-pseudopotential charge density" ρ_I^{local} as that which produces an electrostatic potential equal to V_I^{local}:

$$\rho_I^{local}(\mathbf{r}) = -\frac{1}{4\pi e}\nabla^2 V_I^{local}(\mathbf{r}). \tag{10}$$

This positive charge density is confined within r_I^{core} and produces a potential eZ_I/r outside. Therefore, assuming that the core radian do not overlap [20], the last term in (9) may be written as

$$\frac{1}{2}\sum_{IJ}\frac{e^2 Z_I Z_J}{|\mathbf{r}_I - \mathbf{r}_J|} = \frac{1}{2}\sum_{IJ}\int V_I^{local}(\mathbf{r})\rho_J^{local}(\mathbf{r})\, d^3\mathbf{r} - \sum_I U_I^{local}, \tag{11}$$

where

$$U_I^{local} = \int V_I^{local}(r)\rho_I^{local}(r) 4\pi r^2\, dr. \tag{12}$$

Taking into account that $\rho^{na} = \rho^{local} + \rho^{atom}$, Eq. (9) can be transformed, after some manipulations, into

$$E^{tot} = \sum_{\mu\nu}\rho_{\mu\nu}\left(T_{\mu\nu} + V_{\mu\nu}^{nl}\right) + \frac{1}{2}\sum_{IJ}\int V_I^{na}(\mathbf{r})\rho_J^{na}(\mathbf{r})\, d^3\mathbf{r} - \sum_I U_I^{local} \tag{13}$$

$$+ \int V^{na}(\mathbf{r})\,\delta\rho(\mathbf{r})\, d^3\mathbf{r} + \frac{1}{2}\int \delta V^H(\mathbf{r})\,\delta\rho(\mathbf{r})\, d^3\mathbf{r} + \int \epsilon^{xc}(\mathbf{r})\rho(\mathbf{r})\, d^3\mathbf{r}. \tag{14}$$

The first two terms involve two-center integrals which are interpolated from initially calculated tables, as described previously, and the third term is found trivially from (12). The last three terms are calculated using the real space grid.

Apart from getting rid of all long-range potentials [except that implicit in $\delta V^H(\mathbf{r})$], the advantage of (13) is that, except for the relatively slowly varying exchange–correlation energy density, the grid integrals involve $\delta\rho(\mathbf{r})$, which is generally much smaller than $\rho(\mathbf{r})$. Thus, the errors associated with the finite grid spacing are drastically reduced. Also critical is that the kinetic energy matrix elements can be calculated almost exactly, without any grid integrations. Figure 1 presents the convergence of the total energy for a diamond supercell of 64 atoms as a function of the planewave cutoff associated to the grid [$E_{cut}(\text{Ry}) = (\pi/a)^2$, with a being the separation between grid points in atomic units], used to represent the electron *density* [21]. This convergence is considerably faster than that typical of planewave calculations, which require a larger cutoff to represent accurately the kinetic energy.

Atomic forces and stresses are obtained by direct derivation of (13) with respect to atomic posi-

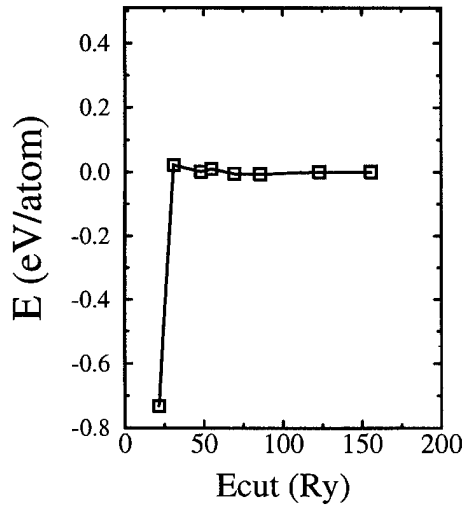


FIGURE 1. Convergence of the total energy versus grid cutoff for a supercell of diamond with 64 C atoms.

tions and obtained simultaneously with E^{tot}. Complete formulas will be given elsewhere and here we provide only a brief sketch. Thus, $\partial T_{\mu\nu}/\partial \mathbf{r}_I$ can be obtained by straightforward derivation of the interpolating functions which represent $T_{\mu\nu}$, and

$$\frac{\partial}{\partial \mathbf{r}_I}\int \epsilon^{\text{xc}}(\mathbf{r})\rho(\mathbf{r})\,d^3\mathbf{r} = \int V^{\text{xc}}(\mathbf{r})\frac{\partial \rho(\mathbf{r})}{\partial \mathbf{r}_I}\,d^3\mathbf{r} = -2\sum_{\mu_I \nu} \rho_{\mu_I \nu}\langle \nabla\phi_{\mu_I}|V^{\text{xc}}|\phi_\nu\rangle, \tag{15}$$

where index μ_I runs only through the basis orbitals of atom I. Similar expressions are obtained for the derivatives of the other integrals in (13). Except for the gradient in front of ϕ_{μ_I}, the matrix elements involved in the contribution to the forces of the last three terms of (13) are the same as those of the Hamiltonian, and are calculated by the same techniques. The calculation of the forces as derivatives of the energy assures that Pulay corrections are automatically included. The stress tensor can also be calculated simultaneously with the forces, since it involves the product of each force contribution times a distance. For example,

$$\frac{\partial T_{\mu_I \nu_J}}{\partial \epsilon_{xy}} = x_{IJ}\frac{\partial T_{\mu_I \nu_J}}{\partial y_{IJ}}, \tag{16}$$

where ϵ_{xy} is the xy component of the strain tensor and x_{IJ} and y_{IJ} are the x and y components of the vector between atoms I and J.

Order-N Functional

Once the Kohn–Sham Hamiltonian matrix in the LCAO basis has been computed for a given charge density, we seek to solve it in order-N operations. For that purpose, we must avoid the N^3 scaling of the eigenvalue problem, which appears if either direct diagonalization or standard iterative solution are performed (in the latter case because of the explicit orthogonalization step necessary during the energy minimization). To avoid this problem, several methods have been proposed in the last years. Here we use the approach proposed by Mauri et al. [3] and by Ordejón et al. [4, 5], although any other linear scaling procedure could in principle be used. The method of Mauri and Ordejón contains two basic ingredients. The first is the calculation of the wave functions ψ_i describing the ground state of the system by the minimization of a modified energy functional, which does not require an explicit orthogonalization step, but for which the wave functions become automatically orthonormal at the minimum. More generally, we use a modification of the Mauri–Ordejón functional, which was proposed by Kim it et al. [6]. This functional takes the form:

$$\tilde{E} = 2\sum_{i,j}^{M}(Hij - \eta S_{ij})(2\delta_{ij} - S_{ij}) + \eta N, \tag{17}$$

where the two in front of the sum is for spins, N is the number of electrons, and $H_{ij} = \langle\psi_i|H|\psi_j\rangle$, $S_{ij} = \langle\psi_i|\psi_j\rangle$ are the Hamiltonian and overlap elements between the wave functions. The sum is done over a set of functions equal or larger than the number of occupied states ($N/2$), and the total charge is controlled by the Fermi level parameter η. The minimization of this functional with respect to variations of the wave functions ψ_i (in terms of their expansion in the LCAO basis) provides the exact ground state of the given H (in the space spanned by the basis set) and orthonormal wave functions [6].

The second ingredient of the order-N solution is the restriction of the minimization of the functional in Eq. (17) to wave functions which are localized in space. These are Wannier-like wave functions centered on different positions of the system, which are truncated beyond a given cutoff

radius R_c (different from the cutoff of the LCAO basis orbitals r_c). This R_c is a variational parameter which controls the accuracy of the calculation, and it is the only approximation involved in the $O(N)$ solution of the Hamiltonian. A detailed description of the accuracy of that truncation can be found in Ref. [5].

Once the wave functions solution of H have been obtained with the order-N functional, a new Kohn–Sham Hamiltonian is built from the new charge density, and the procedure is iterated until self-consistency is achieved. At this point, the energy and atomic forces are evaluated by means of the expressions given in the previous section.

Accuracy and Efficiency Tests

SMALL MOLECULES

Several tests on the performance of the approximations used in our method are presented here, especially for the bases and their confinement. Table I shows the results for the interatomic distance in diatomic molecules as compared with experiment and with other LDA calculations performed with converged augmented plane waves. They are all calculated within LDA. Several bases are compared. The single-z basis is as explained above, using a sufficiently long radius of confinement. Its performance is improved by scaling the radial dependence with appropriate scale factors, which are obtained variationally. Double-z bases are used in the split-valence scheme, and the effect of confinement on them is also shown.

Table II displays results of polarized bases. The accuracy obtained is within 1% of the experimental numbers (except for hydrogen, since its small size makes the percentual error larger). This shows the high quality attainable with short-range basis functions. The transferability of the previous bases is tried on CO and NO (within Table I) and also for HCN (Table III), which also performs very well with double-z bases (both split-valence and short-range).

More delicate is the description of subtle bondings like the hydrogen bonds. A couple of water molecules is studied, and the results for the geometry are compared with experiments and with other calculations. Table IV displays the results using LDA exchange–correlation. Table V does the same for the results of GGA calculations. It can be concluded that: (i) with a double-z, polarized basis the results obtained for the geometry are perfectly comparable in accuracy with converged plane waves results, (ii) a good comparison with experiment requires the use of GGA, and (iii) the binding energies are in general difficult to describe with our methods, requiring both long r_c and ample bases.

DNA

We present here first ab initio results for the structure of deoxyribonucleic acid (DNA). It is performed on a turn of the double helix with ten guanine-cytosine base pairs, which is repeated periodically making an infinite structure with a unit cell containing 650 atoms. It is relaxed starting

TABLE I

Bond lengths (in Å) calculated for some diatomic molecules using different bases.[a]

	Experiment [22]	APW [22]	SZ	SZ(scaled)	SZ(SR)	DZ(SV)	DZ(SR)
H_2	0.741	0.767	0.928	0.772	0.789	0.773	0.727
C_2	1.244	1.249	1.425	1.348	1.332	1.279	1.262
N_2	1.098	1.098	1.283	1.255	1.194	1.123	1.125
O_2(LDA)	1.207	1.212	1.487	1.445	1.296	1.366	1.259
O_2(LSD)	1.207	—	1.406	1.388	1.284	1.293	1.241
CO	1.127	1.132	1.309	1.276	1.206	1.172	1.156
NO	1.148	1.148	1.409	1.376	1.252	1.233	1.234

[a] SZ: single-z pseudoatomic orbitals with large cutoff radius (r_c = 6.2 a.u.); SZ(SR) same with short r_c (3.3 a.u. for H, 4.1 a.u. for C, 3.6 a.u. for N, and 3.2 a.u. for O); SZ (scaled) scales the SZ bases with scale factors determined variationally: 0.950 for C, 0.975 for N, 0.980 for O, and 0.800 for H. For CO and NO the scaling factors are found to be the same as for the dimer of each element; DZ(SV): split-valence double-z for long r_c orbitals; DZ(SR): short r_c double-z bases.

TABLE II

Calculated bond lengths (in Å) for some diatomic molecules adding polarization orbitals to double-z (DZP) short range (SR) basis sets.[a]

	Exp.	100 Ry DZP(SR)	200 Ry DZP(SR)
H_2	0.741	0.729 (1.49%)	0.726 (2.01%)
C_2	1.244	1.253 (0.74%)	1.250 (0.46%)
N_2	1.098	1.103 (0.45%)	1.092 (0.55%)
O_2(LDA)	1.207	1.215 (0.66%)	1.206 (0.08%)
O_2(LSD)	1.207	1.203 (0.32%)	1.197 (0.83%)
CO	1.127	1.117 (0.89%)	1.118 (0.75%)
NO	1.148	1.144 (0.31%)	1.142 (0.55%)

[a] r_c for the polarization orbitals minimize the total energy. In parenthesis, the relative error with respect to experiment.

from the experimental geometry [29], which was obtained from X-ray diffraction experiments on microcrystalline fibers, refined with a least-squares method using "standard" bond lengths.

TABLE III

Bond lengths (in Å) for HCN using different basis sets.

	Exp.	SZ(SR)	DZ(SR)	DZ(SV)
d(HC)	1.066	1.136	1.070	1.083
d(CN)	1.153	1.211	1.159	1.174

This calculation is, to our knowledge, the first self-consistent ab initio calculation of such a structure [30] and represents quite a challenge because of both the complexity and the importance of the system. In a first step presented here, the simplest scheme has been used, namely, LDA for exchange and correlation, minimal basis set, and quite short confinement radii [30] (3.3 a.u. for H, 4.1 a.u. for C, 3.6 a.u. for N, 3.2 a.u. for O, and 4.7 a.u. for P). The grid cutoff was 113 Ry. The approximations are substantial but constitute a beginning toward finer calculations (higher cutoff, double-z, somewhat longer r_c's, GGA instead of LDA).

TABLE IV

LDA results for the H_2O dimer using different basis sets.[a]

	SZ(SR)	DZ(SR)	DZP(SR)	SZ	DZ	DZP	PLW-VWN [23]	LCAO-VWN [24]	Exp. [23]
r(O–O)	2.628	2.575	2.687	2.723	2.590	2.747	2.70	2.71	2.98 ± 0.01
$r(O_a–H)$	1.012	0.971	0.976	1.049	0.999	0.986	0.961	0.980	—
ϕ_a	105.6	110.1	106.1	108.7	112.2	106.7	106.2	104.7	—
$r(O_d–H_1)$	1.042	0.999	0.988	1.069	1.026	1.002	0.980	0.997	—
$r(O_d–H_2)$	1.007	0.972	0.971	1.041	1.000	0.981	0.961	0.977	—
ϕ_d	103.0	106.9	105.6	107.5	113.3	107.3	106.1	105.4	
θ_d	1.2	0.4	6.3	6.7	7.1	7.5	4.84	9.0	6 ± 20
BE	19.39	20.39	19.37	14.21	15.54	11.01	9.06	9.16	5.44 ± 0.7

[a] For notation see Ref. [23]. Lengths in Å and angles in degrees. PLW: plane-wave calculation. VWN: Vosko, Wilk, and Nusair [25] functional for correlation. BE: Binding energy (kcal / mol).

TABLE V

GGA[14] results for the H_2O dimer using different basis sets.

	SZ(SR)	DZ(SR)	DZP(SR)	SZ	DZ	DZP	PLW-B [23]	LCAO-B [24]	LCAO-PW [24]	MP2 [28]
r(O–O)	2.663	2.641	2.715	2.837	2.752	2.902	2.98	2.886	2.877	2.911
$r(O_a–H)$	1.013	0.967	0.971	1.051	0.996	0.981	—	0.979	0.981	0.957
ϕ_a	105.2	109.2	105.8	107.2	111.2	106.2	—	106.2	104.4	—
$r(O_d–H_1)$	1.039	0.989	0.987	1.066	1.015	0.988	—	0.990	0.990	0.964
$r(O_d–H_2)$	1.008	0.967	0.967	1.045	0.997	0.980	—	0.977	0.979	—
ϕ_d	103.2	106.6	105.3	107.1	110.8	104.7	—	106.2	106.0	—
θ_d	−0.8	0.1	4.9	6.9	2.6	4.7	—	7.0	15.1	4.5
BE	15.17	15.92	15.57	10.16	11.76	7.36	4.90	4.51	5.993	5.44

[a] For notation see Ref. [23]. Lengths in Å and angles in degrees. BE: Binding energy (kcal / mol). B: Becke [26] functional for GGA. PW: Perdew–Wang91 [27] functional for GGA. MP2: Second-order Møller–Plesset with a 6-311++G(2d, 2p) basis [28].

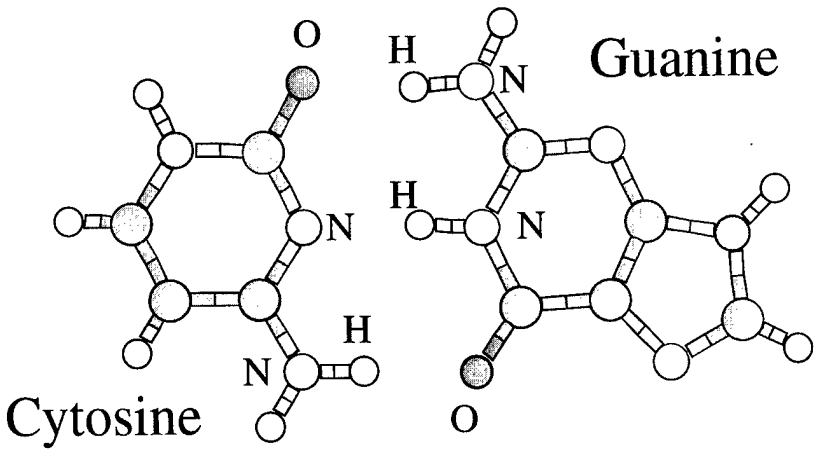


FIGURE 2. Guanine–cytosine pair.

Let us show first results for an isolated guanine–cytosine pair. Figure 2 shows the structure of the pair, with its three hydrogen bonds. Table VI shows the distances obtained for them. The bridge distances (N–N or O–N) are 10–15% shorter than that obtained from other more elaborate calculations [31, 32]. This may be due to the short r_c employed in the calculations. The position of the hydrogen atoms in between tends too much toward the middle of the bridge. It has been argued that this is a pathology of LDA that can be corrected using GGA instead, but it could also be due (or enhanced) by the fact of using nonscaled single-z basis for H, which gives too long O–H and N–H bonds.

The DNA calculation required about 500 Mb of computer memory. For the order-N solution of the electronic problem, a cutoff of 4.0 Å was used for the electronic wave functions, which were reduced to only occupied states (i.e., $M = N/2$). The energy functional [Eq. (17)] therefore reduces to the original Mauri–Ordejón functional [3, 4]. The full relaxation of the structure needed over 200 minimization steps, which amounted to around 5 days of CPU time in a HP C110 workstation. The deviation from the experimental geometry of Ref. [29] is

$$\sigma = \sqrt{\frac{\Sigma(\mathbf{r}_{th} - \mathbf{r}_{exp})^2}{N}} = 0.23 \text{ Å}. \qquad (18)$$

The hydrogen bonds between guanine and cytosine display similar pathologies as the ones showed by the isolated pair of bases, as can be seen in Table VII. It is interesting to note, however, that the skeleton shows much smaller deviations, as,

TABLE VII

Distances (in Å) for the H bonds in a guanine (Gu) – cytosine (Cy) pair within the DNA structure.

Gu–Cy	d(Gu–Cy)$_{th}$	d(Gu-Cy)$_{exp}$
N–N	2.58	2.85
N–O	2.63	2.78
O–N	2.50	2.80

TABLE VI

Distances (in Å) for the H-bonds in the guanine (Gu) – cytosine (Cy) isolated pair.[a]

Gu–Cy	d(Gu–H)	d(H–Cy)	d(Gu–Cy)	d(Gu–Cy)$_{MP2}$	Exp.
N–H–N	1.24	1.37	2.61	3.05	2.95
N–H–O	1.17	1.36	2.53	3.01	2.86
O–H–N	1.23	1.28	2.51	2.93	2.91

[a] MP2 refers to the Møller–Plesset calculation of Ref. [32] using a 6-31G* basis. Experimental result are taken from Saenger [33].

for example, can be seen in a characteristic distance between the C atoms in the sugar molecules supporting a basis pair at opposite sides, R, characteristic of the interhelix distance:

$$R_{exp} = 10.70 \text{ Å}, \qquad R_{th} = 10.61 \text{ Å}. \qquad (19)$$

The structure is not relaxed along the helix axis. However, the calculated stress along that direction is quite small (11 kbars) allowing us to expect a small relaxation in that direction. A more detailed account of the results will be presented elsewhere.

Conclusions

An efficient method for ab initio calculations has been presented. It is based on the density-functional theory (DFT) and utilizes LCAO and standard norm-conserving pseudopotentials. It has also been shown how the computational effort scales linearly with the system size. After a description of its different aspects, calculations have been presented for testing its capabilities, beginning with small molecules and finishing with DNA. The quality of the results has been shown to be mostly related to the quality of the LCAO basis set.

ACKNOWLEDGMENTS

We are grateful to James Lewis for useful discussions and to J. Sponer for making his coordinates of the nitrogen base pairs available to us. This work has been supported by Spain's DGICyT grant PB95-0202.

References

1. R. Car and M. Parrinello, Phys. Rev. Lett. **55**, 2471 (1985).
2. G. Galli and M. Parrinello Phys. Rev. Lett. **69**, 3547 (1992).
3. F. Mauri, G. Galli, and R. Car, Phys. Rev. B **47**, 9973 (1993).
4. P. Ordejón, D. A. Drabold, M. P. Grumbach, and R. M. Martin, Phys. Rev. B **48**, 14646 (1993).
5. P. Ordejón, D. A. Drabold, R. M. Martin, and M. P. Grumbach, Phys. Rev. B **51**, 1456 (1995).
6. J. Kim, F. Mauri, and G. Galli, Phys. Rev. B **52**, 1640 (1995).
7. X.-P. Li, R. W. Nunes, and D. Vanderbilt, Phys. Rev. B **47**, 10891 (1993).
8. W. Hierse and E. B. Stechel, Phys. Rev. B **50**, 17811 (1994).
9. E. Hernandez and M. Gillan, Phys. Rev. B **51**, 10157 (1995).
10. P. Ordejón, E. Artacho, and J. M. Soler, Phys. Rev. B **53**, R10441 (1996).
11. P. Ordejón, E. Artacho, and J. M. Soler, Mat. Res. Soc. Symp. Proc. **408**, 85 (1996).
12. W. Kohn and L. J. Sham, Phys. Rev. **140**, 1133 (1965).
13. J. P. Perdew and A. Zunger, Phys. Rev. B **23**, 5075 (1981).
14. J. P. Perdew, K. Burke, and M. Ernzerhof, Phys. Rev. Lett. **77**, 3865 (1996).
15. N. Troullier and J. L. Martins, Phys. Rev. B **43**, 1993 (1991).
16. L. Kleinman and D. M. Bylander, Phys. Rev. Lett. **48**, 1425 (1982).
17. S. G. Louie, S. Froyen, and M. L. Cohen, Phys. Rev. B **26**, 1738 (1982).
18. O. F. Sankey and D. J. Niklewski, Phys. Rev. B **40**, 3979 (1989). For a study of the performance of these basis sets by projecting plane-waves results see, D. Sánchez-Portal, E. Artacho and, J. M. Soler, J. Phys.: Condens. Matter **8**, 3859 (1996).
19. S. Huzinaga, et al., *Gaussian Basis Sets for Molecular Calculations* (Elsevier Science, Amsterdam, 1984); R. Poirier, R. Kari, and R. Csizmadia, *Handbook of Gaussian Basis Sets* (Elsevier Science, 1985).
20. For the case where they do overlap a simple pairwise interaction correction is simply added to the energy.
21. The energy cutoff in the context of planewave codes is the one used to represent the wave functions. The density requires four times that value, i.e., a planewave calculation converging with a cutoff of 50 Ry, requires 200 Ry for the density. Figure 1 shows that our code converges diamond with 50 Ry directly for the density.
22. P. A. Serena, A. Baratoff, and J. M. Soler, Phys. Rev. B **48**, 2046 (1993).
23. R. N. Barnett and U. Landman, Phys. Rev. B **48**, 2081 (1993).
24. F. Sim, A. St-Amant, I. Papai, and D. R. Salanub, J. Am. Chem. Soc. **114**, 4391 (1992).
25. S. H. Vosko, L. Wilk, and M. Nusair, Can. J. Phys. **58**, 1200 (1980).
26. A. D. Becke, Phys. Rev. A **38**, 3098 (1988); A. D. Becke, J. Chem. Phys. **98**, 1372 (1993).
27. J. P. Perdew, in *Electronic Structure of Solids '91*, P. Ziesche and H. Eschrig, Eds. (Berlin, Akademie Verlag, 1991).
28. M. J. Frisch, J. E. Del Bene, J. S. Binkley, and H. F. Schaeffer III, J. Chem. Phys. **84**, 2279 (1986).
29. R. Chandrasekaran and S. Arnott, in *Landolt-Börnstein New Series, Group VII: Byophysics, Vol. I, Nucleic Acids, Subvolume b: Crystallographic and Structural Data II*, W. Saenger, Ed. (New York, Springer Verlag, 1989).
30. Calculations on a similar isolated DNA segment with 10 cytosine-guanine base pairs using the non-self-consistent Harris functional, with some modifications for the H-bonds, can be found in J. Lewis, P. Ordejón, and O. Sankey, Phys. Rev. B **55**, 6880 (1997) .
31. J. Sponer, J. Leszczynski, and P. Hobza, J. Phys. Chem **100**, 1965 (1996).
32. I. R. Gould and P. A. Kollman, J. Am. Chem. Soc. **116**, 2493 (1994).
33. W. Saenger, *Principles of Nucleic Acid Structure* (New York, Springer Verlag, 1984), pp. 123 and 124 and references therein.

Comparison of Electron Propagator Methods for Calculating Electron Detachment Energies of Anions

O. DOLGOUNITCHEVA, V. G. ZAKRZEWSKI, J. V. ORTIZ
Department of Chemistry, Kansas State University, Manhattan, Kansas 66506-3701

Received 26 March 1997; revised 29 April 1997; accepted 7 May 1997

ABSTRACT: Electron propagator methods for calculating vertical electron detachment energies of closed-shell anions are compared with respect to accuracy and efficiency. Examination of self-energy terms and numerical tests on typical anions show that the partial third-order (P3) quasi-particle approximation is superior to the third-order and outer valence Green's function methods in both respects. © 1997 John Wiley & Sons, Inc. Int J Quant Chem **65**: 463–469, 1997

Introduction

The chemistry and physics of gas-phase anions exhibit several lively trends where theory and experiment interact. Double Rydberg anions demonstrate the importance of diffuse basis functions and electron correlation in describing electron pairs bound to a molecular cation [1]. Thorough calculations continue to identify superhalogens: molecules with electron affinities exceeding those of the halogen atoms [2]. Doubly charged and multiply charged metal fluoride complexes have been studied computationally [3]. Carbon cluster dianions [4] have been examined with several theoretical techniques [5]. Advances in preparative and computational capabilities portend an expansion of interest in larger species such as fullerenes [6] and organic polyanions [7]. A need therefore exists for correlated methods that are accurate and feasible for systems that require hundreds of basis functions.

Among the most important properties of an anion are its electron detachment energies, both vertical and adiabatic. Because of the variety and unprecedented character of bonding patterns found in anions, a theory of electron detachment energies should be free of model potentials, should be systematically improvable with respect to electron correlation, and should include no arbitrary parameters. Some ab initio techniques satisfy these requirements. Accuracy and feasibility criteria, especially the scaling of arithmetic operations and storage requirements, often determine which of

Correspondence to: J. V. Ortiz.
Contract grant sponsor: National Science Foundation.
Contract grant number: CHE-9321434.
Contract grant sponsor: Petroleum Research Fund.
Contract grant number: 29848-AC6.
Contract grant sponsor: Gaussian, Inc.

© 1997 John Wiley & Sons, Inc.
CCC 0020-7608 / 97 / 050463-07

these techniques will be most advantageous for a given system. Electron propagator methods [8–15] excel in calculations of many types of electron binding energies and have proven to be useful tools in the study of anions [16].

A recent propagator approximation is compared here with methods that have been extensively applied. Closed-shell anions with subtle correlation effects and extensive orbital relaxation in the corresponding neutral radicals are considered. Calculations are performed with various basis sets in order to estimate the behavior of the propagator approximations in the limit of a complete basis set.

Theory

The r, s element of the electron propagator [8] is

$$G_{rs}(E) \equiv \langle\langle a_r^\dagger; a_s \rangle\rangle = \lim_{\eta \to 0} \left\{ \sum_n \frac{\langle N|a_r^\dagger|N-1, n\rangle\langle N-1, n|a_s|N\rangle}{E + E_n(N-1) - E_0(N) - i\eta} + \sum_m \frac{\langle N|a_s|N+1, m\rangle\langle N+1, m|a_r^\dagger|N\rangle}{E - E_m(N+1) + E_0(N) + i\eta} \right\}. \quad (1)$$

Through introduction of superoperators and a corresponding metric, the propagator may be represented more compactly [9, 17]. Superoperators act on field operator products, X, where the number of annihilators exceeds the number of creators by one. The identity superoperator, $\hat{I}$, and the Hamiltonian superoperator, $\hat{H}$, are defined by

$$\hat{I}X = X \quad (2)$$

and

$$\hat{H}X = [X, H]_-, \quad (3)$$

respectively. The superoperator metric, defined by

$$(\mu|\nu) = \langle N|[\![\mu^\dagger, \nu]\!]_+|N\rangle, \quad (4)$$

depends on the choice of the N-electron reference state, $|N\rangle$. In this notation,

$$\langle\langle a_r^\dagger; a_s \rangle\rangle \equiv G_{rs}(E) = \left(a_r|(E\hat{I} - \hat{H})^{-1} a_s\right). \quad (5)$$

A matrix generalization of Eq. (5) is

$$\mathbf{G}(E) = \left(\mathbf{a}|(E\hat{I} - \hat{H})^{-1}\mathbf{a}\right). \quad (6)$$

After the inner projection,

$$\mathbf{G}(E) = (\mathbf{a}|\mathbf{u})\left(\mathbf{u}|(E\hat{I} - \hat{H})\mathbf{u}\right)^{-1}(\mathbf{u}|\mathbf{a}), \quad (7)$$

where $\mathbf{u}$ is the vector of all X field operator products. If $\mathbf{u}$ is partitioned into the primary space, $\mathbf{a}$, and an orthogonal space, $\mathbf{f}$, then the partitioned form of the propagator matrix reduces to

$$\mathbf{G}(E) = [\mathbf{1}\ \mathbf{0}]\begin{bmatrix} E\mathbf{1} - (\mathbf{a}|\hat{H}\mathbf{a}) & -(\mathbf{a}|\hat{H}\mathbf{f}) \\ -(\mathbf{f}|\hat{H}\mathbf{a}) & E\mathbf{1} - (\mathbf{f}|\hat{H}\mathbf{f}) \end{bmatrix}^{-1}\begin{bmatrix}\mathbf{1}\\ \mathbf{0}\end{bmatrix}. \quad (8)$$

After a few elementary matrix manipulations, a convenient form of the inverse propagator matrix emerges, where

$$\mathbf{G}^{-1}(E) = E\mathbf{1} - (\mathbf{a}|\hat{H}\mathbf{a}) - (\mathbf{a}|\hat{H}\mathbf{f})[E\mathbf{1} - (\mathbf{f}|\hat{H}\mathbf{f})]^{-1}(\mathbf{f}|\hat{H}\mathbf{a}). \quad (9)$$

Elements of the zeroth-order inverse propagator matrix are

$$\left[\mathbf{G}_0^{-1}(E)\right]_{rs} = (E - \epsilon_r)\delta_{rs}. \quad (10)$$

(The poles equal Koopmans' theorem results.) The inverse propagator matrix and its zeroth-order counterpart therefore are related through

$$\mathbf{G}^{-1}(E) = \mathbf{G}_0^{-1}(E) - \mathbf{\Sigma}(\infty) - \mathbf{\Sigma}'(E), \quad (11)$$

where

$$\mathbf{\Sigma}(\infty)_{rs} = \left(a_r|\hat{H}a_s\right)_{correlation} = \sum_{tu}(rs\|tu)\rho_{tu}^c \quad (12)$$

and

$$\mathbf{\Sigma}'(E) = (\mathbf{a}|\hat{H}\mathbf{f})[E\mathbf{1} - (\mathbf{f}|\hat{H}\mathbf{f})]^{-1}(\mathbf{f}|\hat{H}\mathbf{a}). \quad (13)$$

Corrections to the zeroth-order propagator in Eq. (11) are gathered together in a term known as the self-energy matrix $\mathbf{\Sigma}(E)$. The Dyson equation may be written as

$$\mathbf{G}^{-1}(E) = \mathbf{G}_0^{-1}(E) - \mathbf{\Sigma}(E). \quad (14)$$

In the self-energy matrix, there are energy-independent terms and energy-dependent terms:

$$\mathbf{\Sigma}(E) = \mathbf{\Sigma}(\infty) + \mathbf{\Sigma}'(E). \quad (15)$$

In the limit of $|E| \to \infty$, $\mathbf{\Sigma}(E)$ approaches its energy-independent component, $\mathbf{\Sigma}(\infty)$. At a pole energy,

$$det\{\mathbf{G}(E)\} \to \infty. \quad (16)$$

Poles may be found by requiring that

$$det\{\mathbf{G}^{-1}(E)\} = 0. \tag{17}$$

Previous Approximations

The second-order self-energy matrix,

$$\boldsymbol{\Sigma}^{(2)}(E) = \left(\mathbf{a}|\hat{H}\mathbf{f}_3\right)^{(1)}\left[E\mathbf{1} - \left(\mathbf{f}_3|\hat{H}\mathbf{f}_3\right)^{(0)}\right]^{-1}\left(\mathbf{f}_3|\hat{H}\mathbf{a}\right)^{(1)}, \tag{18}$$

follows from zeroth- and first-order choices for superoperator blocks defined in terms of the $\mathbf{a}$ and $\mathbf{f}_3$ ($2h$–p and $2p$–h) operator manifolds [9]. (Superscripts in parentheses denote the order through which a superoperator matrix element is evaluated.) Upon retention of first-order terms in $(\mathbf{f}_3|\hat{H}\mathbf{f}_3)$, third- and higher-order contributions to the self-energy matrix are generated. Third-order terms also are created by perturbative improvements in the ground-state averages [18]. The third-order self-energy matrix contains contributions of both types and may be expressed as

$$\begin{aligned}\boldsymbol{\Sigma}^{(3)}(E) &= \boldsymbol{\Sigma}^{(2)}(E) + \left(\mathbf{a}|\hat{V}\mathbf{a}\right)^{(3)} \\ &+ \left(\mathbf{a}|\hat{H}\mathbf{f}_3\right)^{(2)}\left[E\mathbf{1} - \left(\mathbf{f}_3|\hat{H}_0\mathbf{f}_3\right)^{(0)}\right]^{-1}\left(\mathbf{f}_3|\hat{H}\mathbf{a}\right)^{(1)} \\ &+ \left(\mathbf{a}|\hat{H}\mathbf{f}_3\right)^{(1)}\left[E\mathbf{1} - \left(\mathbf{f}_3|\hat{H}_0\mathbf{f}_3\right)^{(0)}\right]^{-1}\left(\mathbf{f}_3|\hat{H}\mathbf{a}\right)^{(2)} \\ &+ \left(\mathbf{a}|\hat{H}\mathbf{f}_3\right)^{(1)}\left[E\mathbf{1} - \left(\mathbf{f}_3|\hat{H}_0\mathbf{f}_3\right)^{(0)}\right]^{-1}\left(\mathbf{f}_3|\hat{V}\mathbf{f}_3\right)^{(1)} \\ &\times\left[E\mathbf{1} - \left(\mathbf{f}_3|\hat{H}_0\mathbf{f}_3\right)^{(0)}\right]^{-1}\left(\mathbf{f}_3|\hat{H}\mathbf{a}\right)^{(1)}, \end{aligned} \tag{19}$$

where $\hat{V}$ is the superoperator for the fluctuation potential.

Results on valence ionization energies and electron affinities of closed-shell molecules generally indicate that off-diagonal elements of the self-energy matrix in the canonical basis are small and have a negligible effect on poles. Quasi-particle approximations explicitly neglect these matrix elements. The associated pole search becomes especially easy, for the zeroes of the diagonal elements of the Dyson equation can be found by solving

$$E = \epsilon_p + \Sigma_{pp}(E). \tag{20}$$

Simple measures for estimating fourth- and higher-order terms have been applied widely. Once a third-order pole is found, various terms are rearranged to make these estimates. The A version of the outer valence Green's function (OVGF) methods [14], e.g., corrects canonical orbital energies with

$$\boldsymbol{\Sigma}_{rr}^{(A,OVGF)}(E) = \boldsymbol{\Sigma}_{rr}^{(2)}(E) + (1 + X_r)^{-1}\boldsymbol{\Sigma}_{rr}^{(3)}(E), \tag{21}$$

where E is chosen to be the third-order pole and

$$X_r = -2\frac{\left\{\left(\mathbf{a}|\hat{H}\mathbf{f}_3\right)^{(2)}\left\{E\mathbf{1} - \left(\mathbf{f}_3|\hat{H}\mathbf{f}_3\right)^{(0)}\right\}^{-1}\left(\mathbf{f}_3|\hat{H}\mathbf{a}\right)^{(1)}\right\}_{rr}}{\left\{\left(\mathbf{a}|\hat{H}\mathbf{f}_3\right)^{(1)}\left\{E\mathbf{1} - \left(\mathbf{f}_3|\hat{H}\mathbf{f}_3\right)^{(0)}\right\}^{-1}\left(\mathbf{f}_3|\hat{H}\mathbf{a}\right)^{(1)}\right\}_{rr}}. \tag{22}$$

The B approximation is similar, but separates the energy-dependent $2p$–h and $2h$–p contributions through

$$\boldsymbol{\Sigma}_{rr}^{(B,OVGF)}(E) = \boldsymbol{\Sigma}_{rr}^{(2)}(E) + \left(\mathbf{a}|\hat{V}\mathbf{a}\right)_{rr}^{(3)} + (1 + X_r^{2h-p})^{-1}\boldsymbol{\Sigma}_{rr}^{(3,2h-p)}(E) + (1 + X_r^{2p-h})^{-1}\boldsymbol{\Sigma}_{rr}^{(3,2p-h)}(E), \tag{23}$$

where

$$X_r^{2h-p} = -2\frac{\left\{\left(\mathbf{a}|\hat{H}\mathbf{f}_{2h-p}\right)^{(2)}\left\{E\mathbf{1} - \left(\mathbf{f}_{2h-p}|\hat{H}\mathbf{f}_{2h-p}\right)^{(0)}\right\}^{-1}\left(\mathbf{f}_{2h-p}|\hat{H}\mathbf{a}\right)^{(1)}\right\}_{rr}}{\left\{\left(\mathbf{a}|\hat{H}\mathbf{f}_{2h-p}\right)^{(1)}\left\{E\mathbf{1} - \left(\mathbf{f}_{2h-p}|\hat{H}\mathbf{f}_{2h-p}\right)^{(0)}\right\}^{-1}\left(\mathbf{f}_{2h-p}|\hat{H}\mathbf{a}\right)^{(1)}\right\}_{rr}} \tag{24}$$

and

$$X_r^{2p-h} = -2\frac{\left\{\left(\mathbf{a}|\hat{H}\mathbf{f}_{2p-h}\right)^{(2)}\left\{E\mathbf{1} - \left(\mathbf{f}_{2p-h}|\hat{H}\mathbf{f}_{2p-h}\right)^{(0)}\right\}^{-1}\left(\mathbf{f}_{2p-h}|\hat{H}\mathbf{a}\right)^{(1)}\right\}_{rr}}{\left\{\left(\mathbf{a}|\hat{H}\mathbf{f}_{2p-h}\right)^{(1)}\left\{E\mathbf{1} - \left(\mathbf{f}_{2p-h}|\hat{H}\mathbf{f}_{2p-h}\right)^{(0)}\right\}^{-1}\left(\mathbf{f}_{2p-h}|\hat{H}\mathbf{a}\right)^{(1)}\right\}_{rr}}. \quad (25)$$

Note that the constant terms are not scaled in this approximation. These schemes function best when the third-order numerators in Eqs. (22), (24), and (25) are small compared to the second-order denominators. For other cases, the C recipe often is preferable. The self-energy correction is

$$\mathbf{\Sigma}_{rr}^{(C,OVGF)}(E) = \mathbf{\Sigma}_{rr}^{(2)}(E) + (1 + X_r^C)^{-1}\mathbf{\Sigma}_{rr}^{(3)}(E), \quad (26)$$

where

$$X_r^C = \frac{X_r^{2h-p}\mathbf{\Sigma}_{rr}^{(3,2h-p)}(E) + X_r^{2p-h}\mathbf{\Sigma}_{rr}^{(3,2p-h)}(E)}{\mathbf{\Sigma}_{rr}^{(3,2h-p)}(E) + \mathbf{\Sigma}_{rr}^{(3,2p-h)}(E)}. \quad (27)$$

The utility of quasi-particle approximations was tested recently through a comparison of third-order and OVGF results for 25 ionization energies of 10 closed-shell molecules with H, C, N, O, and F nuclei [19]. Calculations were performed with a correlation-consistent, triple ζ basis [20]. Root mean-square errors with respect to experiment in eV were 1.25 for Koopmans's theorem, 0.67 for third order, 0.27 for OVGF-A, 0.33 for OVGF-B, and 0.32 for OVGF-C. After employment of numerical criteria [19] for choosing a recommended OVGF value (i.e., a selection from one of the three versions), the root mean-square error is 0.25 eV. Once third-order results are available, OVGF estimates are very efficient tools for making assignments and predicting ionization energies.

Partial Third-order Theory

The usual choice of superoperator metric starts from a Hartree–Fock wavefunction plus perturbative corrections:

$$(Y|Z) = \langle HF|(1 + T^\dagger)[Y^\dagger, Z]_+(1 + T)|HF\rangle, \quad (28)$$

where

$$T = T_2^{(1)} + T_1^{(2)} + T_2^{(2)} + T_3^{(2)} + T_4^{(2)} + \cdots. \quad (29)$$

The level of excitation in $T_e^{(f)}$ is indicated by the subscript, e, and the order is defined by the superscript, f. For example, second-order triple excitations are represented by $T_3^{(2)}$. Coupled-cluster parametrizations of this metric suggest an alternative form:

$$(Y|Z) = \langle HF|e^{-T}[Y^\dagger, Z]_+ e^T|HF\rangle. \quad (30)$$

This choice produces asymmetric superoperator matrices. A simplified final form for the self-energy matrix that does not require optimization of cluster amplitudes is sought presently; the approximation

$$e^T \approx 1 + T_2^{(1)} \quad (31)$$

therefore is made.

With this choice, several third-order terms that appeared with the usual metric are eliminated. The new self-energy matrix in third order is asymmetric and is expressed by

$$\begin{aligned}\mathbf{\Sigma}(E) &= \left(\mathbf{a}|\hat{H}\mathbf{f}_3\right)^{(1)}\left\{E\mathbf{1} - \left(\mathbf{f}_3|\hat{H}\mathbf{f}_3\right)^{(0)}\right\}^{-1}\left(\mathbf{f}_3|\hat{H}\mathbf{a}\right)^{(1)} \\ &+ \left(\mathbf{a}|\hat{H}\mathbf{f}_3\right)^{(1)}\left\{E\mathbf{1} - \left(\mathbf{f}_3|\hat{H}\mathbf{f}_3\right)^{(0)}\right\}^{-1}\left(\mathbf{f}_3|\hat{H}\mathbf{a}\right)^{(2)} \\ &+ \left(\mathbf{a}|\hat{H}\mathbf{f}_3\right)^{(1)}\left\{E\mathbf{1} - \left(\mathbf{f}_3|\hat{H}\mathbf{f}_3\right)^{(0)}\right\}^{-1}\left(\mathbf{f}_3|\hat{V}\mathbf{f}_3\right)^{(1)} \\ &\times\left\{E\mathbf{1} - \left(\mathbf{f}_3|\hat{H}\mathbf{f}_3\right)^{(0)}\right\}^{-1}\left(\mathbf{f}_3|\hat{H}\mathbf{a}\right)^{(1)}. \quad (32)\end{aligned}$$

Note that energy-independent terms in the third-order self-energy matrix are not retained.

Two observations suggest additional economies: First, numerical results for ionization energies show that third-order, $2p$–h terms in Eq. (32) are small relative to their $2h$–p counterparts [21].

Terms arising from these operators are important in second order, however. Second, evaluation of one of the third-order $2p-h$ terms requires electron repulsion integrals with four virtual indices, according to

$$T_{picd}(E) = \frac{1}{2}\sum_{ab}^{vir}\frac{\langle pi||ab\rangle\langle ab||cd\rangle}{E+\epsilon_i-\epsilon_a-\epsilon_b}, \qquad (33)$$

where $i, j, k, \ldots$ are occupied indices, $a, b, c, \ldots$ are virtual indices, and $p, q, r, \ldots$ are general indices. Storage of these integrals is often avoided through semidirect algorithms [22]. Contractions involving integrals with four virtual indices remain the arithmetic bottleneck in third-order quasi-particle theory, for the scaling factor for a given final state with index p is OV^4, where O is the number of occupied orbitals and V is the number of virtual orbitals.

Neglect of third-order, $2p-h$ terms produces this self-energy matrix:

$$\Sigma(E)_{pq} = \frac{1}{2}\sum_{iab}\frac{\langle pi||ab\rangle\langle ab||qi\rangle}{E+\epsilon_i-\epsilon_a-\epsilon_b} + \frac{1}{2}\sum_{aij}\frac{\langle pa||ij\rangle W_{qaij}}{E+\epsilon_a-\epsilon_i-\epsilon_j} + \frac{1}{2}\sum_{aij}\frac{U_{paij}(E)\langle ij||qa\rangle}{E+\epsilon_a-\epsilon_i-\epsilon_j}, \qquad (34)$$

where

$$W_{qaij} = \langle qa||ij\rangle + \frac{1}{2}\sum_{bc}\frac{\langle qa||bc\rangle\langle bc||ij\rangle}{\epsilon_i+\epsilon_j-\epsilon_b-\epsilon_c} + (1-P_{ij})\sum_{bk}\frac{\langle qk||bi\rangle\langle ba||jk\rangle}{\epsilon_j+\epsilon_k-\epsilon_a-\epsilon_b} \qquad (35)$$

and

$$U_{paij}(E) = -\frac{1}{2}\sum_{kl}\frac{\langle pa||kl\rangle\langle kl||ij\rangle}{E+\epsilon_a-\epsilon_k-\epsilon_l} - (1-P_{ij})\sum_{bk}\frac{\langle pb||jk\rangle\langle ak||bi\rangle}{E+\epsilon_b-\epsilon_j-\epsilon_k}. \qquad (36)$$

This partial third-order expression is designated by the abbreviation P3.

Comparison of the self-energy matrix elements of Eq. (34) with older, related methods [14, 23] reveals the advantages of the P3 approximation. OVGF results [14] and the third-order quasi-particle calculations on which they are based require the evaluation of the diagonal elements of the self-energy matrices given in Eq. (18) (second-order terms) and Eq. (19) (third-order terms). The second term (the third-order, energy-independent diagrams) and the third term in Eq. (19) are not present in the P3 self-energy. Furthermore, the $2p-h$ operators included in the fourth and fifth terms of Eq. (19) are dropped in P3 theory as well. Another difference between P3 and OVGF is the absence of scaling factors, such as those in Eqs. (21)–(27), in P3.

In the P3 quasi-particle propagator, only diagonal elements of the self-energy matrix are retained. The first contraction in Eq. (35) is the most demanding, for it has an arithmetic scaling factor of O^2V^3 for a given q. This step also requires electron repulsion integrals with one occupied and three virtual indices. The W_{qaij} intermediate is energy-independent and must be evaluated once only for each final state.

A quasi-particle implementation of the P3 method was applied to 19 ionization energies of six closed-shell molecules with a correlation-consistent, triple ζ basis [21]. Comparisons with results of more costly propagator techniques were made by applying the same basis sets. The average absolute errors in eV are 1.34 for Koopmans's theorem, 0.25 for OVGF-B, and 0.19 for P3. The P3 procedure exhibits accuracy at least as good as that of other methods, superior arithmetic scaling, and no need for electron repulsion integrals with four virtual indices.

Results

Electron propagator calculations were performed on F^-, OH^-, NH_2^-, Cl^-, SH^-, and PH_2^- with a modified version of Gaussian 94 [24]. The geometries of the anions were optimized with MBPT(2) [25] and the 6-31 + G(d,p) basis [26]. Propagator calculations employ three basis sets: 6-311 + + G(2df,2pd) [27], aug-cc-pVDZ, and aug-cc-pVTZ [20]. Core orbitals were dropped from all summations pertaining to the propagator self-energies. Several diagonal self-energy approximations were examined: second order, third order, OVGF-A, OVGF-B, OVGF-C, the recommended OVGF (OVGF-R) value arising from a selection procedure [19], and P3.

TABLE I
Electron detachment energies (eV).

Anion	Basis	KT	2	3	A	B	C	R	P3	Expt. [28]
F^-	6-311++G(2*df*,2*pd*)	4.83	1.23	5.69	3.83	4.39	4.17	4.39	3.72	
	aug-cc-pVDZ	4.93	1.03	6.61	4.32	5.05	4.62	5.05	3.79	
	aug-cc-pVTZ	4.92	1.21	6.75	4.24	5.00	4.66	5.00	4.15	3.399 ± 0.003
OH^-	6-311++G(2*df*,2*pd*)	2.88	−0.01	3.59	1.92	2.38	2.28	2.38	2.12	
	aug-cc-pVDZ	2.95	−0.17	4.22	2.26	2.86	2.58	2.86	2.11	
	aug-cc-pVTZ	2.97	−0.02	4.43	2.24	2.86	2.67	2.86	2.48	1.828
NH_2^-	6-311++G(2*df*,2*pd*)	1.30	−0.38	1.36	0.52	0.77	0.81	0.77	0.77	
	aug-cc-pVDZ	1.31	−0.51	1.53	0.64	0.97	0.91	0.97	0.64	
	aug-cc-pVTZ	1.34	−0.30	1.65	0.68	1.01	1.02	1.01	0.96	0.779 ± 0.037
Cl^-	6-311++G(2*df*,2*pd*)	4.08	3.04	3.68	3.39	3.54	3.57	3.54	3.41	
	aug-cc-pVDZ	4.10	2.91	3.85	3.49	3.70	3.68	3.70	3.35	
	aug-cc-pVTZ	4.09	3.08	3.88	3.51	3.73	3.74	3.73	3.50	3.615
SH^-	6-311++G(2*df*,2*pd*)	2.56	1.80	2.27	2.03	2.18	2.20	2.18	2.08	
	aug-cc-pVDZ	2.58	1.70	2.39	2.09	2.29	2.28	2.29	2.01	
	aug-cc-pVTZ	2.58	1.88	2.48	2.16	2.38	2.39	2.38	2.19	2.319 ± 0.010
PH_2^-	6-311++G(2*df*,2*pd*)	1.20	0.89	1.06	0.95	1.06	1.05	1.06	0.98	
	aug-cc-pVDZ	1.21	0.81	1.10	0.94	1.10	1.09	1.09	0.88	
	aug-cc-pVTZ	1.23	0.99	1.22	1.06	1.22	1.21	1.21	1.09	1.271 ± 0.010

F^-, OH^-, and NH_2^- were challenging tests for perturbative quasi-particle methods. Table I summarizes these calculations and shows that third-order results (see the column labeled 3) may be worse than the predictions of Koopmans's theorem (see the KT column). Such behavior is rare for ionization energies of closed-shell molecules. Second-order results are relatively unreliable and may even produce the wrong sign. It is also worth noting that third-order pole strengths often exceed unity for OH^- and NH_2^-. (The analytic behavior of the self-energy matrix elements does not assure the correct sign of the derivatives with respect to E.) OVGF scaling procedures reduce the errors, but discrepancies remain large. The A version of OVGF behaves best for F^-, OH^-, and NH_2^-, but OVGF-R (see the column labeled R) generally favors the B version. As basis sets are improved, electron detachment energy results generally increase. The overestimation of these quantities by third-order and OVGF methods implies that discrepancies will grow in calculations with basis sets of higher quality. It also is possible for fortuitous cancellations of basis-set and correlation errors to produce accurate predictions.

The situation is markedly different for Cl^-, SH^-, and PH_2^-. Here, agreement with experiment is good for third-order and OVGF methods, even though an overestimate of the electron detachment energies occurs for certains of pairs of methods and basis sets. For Cl^- and SH^-, better basis sets will produce poorer results with third-order and the B and C versions of OVGF. A reexamination of the OVGF selection procedure and its parameters may be advisable for anions.

P3 results for F^-, OH^-, and NH_2^- indicate that substantial errors have been overcome with this approximation, but that more terms must be added to obtain close agreement with experiment. Fortuitous agreement with experiment is clearly a danger with the 6-31++G(2*df*,2*pd*) basis, especially for NH_2^-. Basis sets larger than aug-cc-pVTZ are likely to produce greater errors. This method must be used with caution when orbital relaxation is important in the final, neutral state.

P3 behaves better with respect to basis-set saturation for Cl^-, SH^-, and PH_2^-. Use of aug-cc-pVQZ basis sets will probably produce very close agreement with experiment, for the aug-cc-pVTZ results are still below the experimental values. In these three cases, relaxation and correlation corrections to Koopmans theorem results are relatively small and perturbative arguments can be expected to be more successful.

Conclusions

The P3 quasi-particle approximation is more computationally efficient than are the third-order

and OVGF methods. The bottleneck contraction of P3 requires O^2V^3 operations, whereas the most difficult contraction of third order (and therefore OVGF) scales as OV^4. The latter step must be repeated for each energy iteration, but the O^2V^3 step present in P3 must be performed only once per final state. No electron repulsion integrals with four virtual indices are needed in a P3 calculation.

Results on the electron detachment energies of anions suggest that P3 is a more reliable method than are the third-order and OVGF approximations in the limit of a complete basis set. For F^-, OH^-, and NH_2^-, large discrepancies with experiment remain for all of the methods, although the errors are not as large for P3. For Cl^-, SH^-, and PH_2^-, where relaxation and correlation effects are not as large, P3 results produce close agreement with experiment and are likely to be superior to third order and OVGF for saturated basis sets.

ACKNOWLEDGMENTS

This work was supported by the National Science Foundation under grant CHE-9321434, the Petroleum Research Fund under Grant 29848-AC6, and by Gaussian, Incorporated.

References

1. J. V. Ortiz, J. Phys. Chem. **94**, 4762 (1990); M. Gutowsky and J. Simons, Chem. Rev. **91**, 669 (1991).
2. G. L. Gutsev and A. I. Boldyrev, Adv. Chem. Phys. **61**, 169 (1985).
3. G. L. Gutsev and A. I. Boldyrev, J. Phys. Chem. **94**, 2256 (1990); M. Gutowski, A. I. Boldyrev, J. V. Ortiz, and J. Simons, J. Am. Chem. Soc. **101**, 9262 (1994).
4. S. N. Schauer, P. Williams, and R. N. Compton, Phys. Rev. Lett. **65**, 625 (1990).
5. J. Watts and R. J. Bartlett, J. Chem. Phys. **97**, 3445 (1992); T. Sommerfeld, M. K. Scheller, and L. S. Cederbaum, J. Phys. Chem. **98**, 8914 (1994); V. G. Zakrzewski and J. V. Ortiz, J. Chem. Phys. **102**, 294 (1995).
6. R. L. Hettich, R. N. Compton, and R. H. Ritchie, Phys. Rev. Lett. **67**, 1242 (1991).
7. R. C. Dougherty, J. Chem. Phys. **50**, 1896 (1969); W. P. M. Maas and N. M. M. Nibbering, Int. J. Mass Spectrom. Ion Processes **88**, 257 (1989).
8. J. Linderberg and Y. Öhrn, Propagators in Quantum Chemistry (Academic Press, New York, 1973).
9. B. Pickup and O. Goscinski, Mol. Phys. **26**, 1013 (1973).
10. L. S. Cederbaum and W. Domcke, Adv. Chem. Phys. **26**, 206 (1977).
11. J. Simons, Theor. Chem. Adv. Persp. **3**, 1 (1978).
12. Y. Öhrn and G. Born, Adv. Quantum Chem. **13**, 1 (1981).
13. M. F. Herman, K. F. Freed, and D. L. Yeager, Adv. Chem. Phys. **48**, 1 (1981).
14. W. von Niessen, J. Schirmer, and L. S. Cederbaum, Comput. Phys. Rep. **1**, 57 (1984).
15. J. V. Ortiz, in Computational Chemistry, Reviews of Current Trends, J. Leszczynski, Ed., (World Scientific, Singapore, 1997), Vol. 2.
16. J. Simons, Annu. Rev. Phys. Chem. **28**, 15 (1977).
17. O. Goscinski and B. Lukman, Chem. Phys. Lett. **7**, 573 (1970).
18. J. Simons and W. D. Smith, J. Chem. Phys. **58**, 4899 (1973); G. D. Purvis and Y. Öhrn, Chem. Phys. Lett. **33**, 396 (1975).
19. V. G. Zakrzewski, J. V. Ortiz, J. A. Nichols, D. Heryadi, D. L. Yeager, and J. T. Golab, Int. J. Quantum Chem. **60**, 29 (1996).
20. T. H. Dunning, J. Chem. Phys. **90**, 1007 (1989).
21. J. V. Ortiz, J. Chem. Phys. **104**, 7599 (1996).
22. V. G. Zakrzewski and J. V. Ortiz, Int. J. Quantum Chem., Quantum Chem. Symp. **28**, 23 (1994); V. G. Zakrzewski and J. V. Ortiz, Int. J. Quantum Chem. **53**, 583 (1995).
23. J. V. Ortiz, J. Chem. Phys. **99**, 6716 (1993).
24. M. J. Frisch, G. W. Trucks, H. B. Schlegel, P. M. W. Gill, B. G. Johnson, M. A. Robb, J. R. Cheeseman, T. A. Keith, G. A. Peterson, J. A. Montgomery, K. Raghavachari, M. A. Al-Laham, V. G. Zakrzewski, J. V. Ortiz, J. B. Foresman, J. Cioslowski, B. B. Stefanov, A. Nanayakkara, M. Challacombe, C. Y. Peng, P. Y. Ayala, W. Chen, M. W. Wong, J. L. Andres, E. S. Replogle, R. Gomperts, R. L. Martin, D. J. Fox, J. S. Binkley, D. J. Defrees, J. Baker, J. J. P. Stewart, M. Head-Gordon, C. Gonzales and J. A. Pople, *Gaussian 94* (Gaussian, Inc., Pittsburgh PA, 1995).
25. R. J. Bartlett, Annu. Rev. Phys. Chem. **32**, 359 (1981).
26. W. J. Hehre, R. Ditchfield, and J. A. Pople, J. Chem. Phys. **56**, 2257 (1972); T. Clark, J. Chandrasekhar, G. W. Spitznagel, and P. v. R. Schleyer, J. Comp. Chem. **4**, 294 (1983).
27. R. Krishnan, J. S. Binkley, R. Seeger, and J. A. Pople, J. Chem. Phys. **72**, 650 (1980), and references therein; M. J. Frisch, J. A. Pople, and J. S. Binkley, J. Chem. Phys. **80**, 3265 (1984); T. Clark, J. Chandrasekhar, G. W. Spitznagel, and P. v. R. Schleyer, J. Comp. Chem. **4**, 294 (1983).
28. F^- and Cl^-: H. Hotop and W. C. Lineberger, J. Phys. Chem. Ref. Data **4**, 539 (1975). OH^-: F. A. Schultz, R. D. Mead, P. L. Jones, and W. C. Lineberger, J. Chem. Phys. **77**, 1153 (1982). SH^-: B. Steiner, J. Chem. Phys. **49**, 5097 (1969). NH_2^-: R. J. Celotta, R. A. Bennett, and J. L. Hall, J. Chem. Phys. **60**, 1740 (1974). PH_2^-: P. K. Zittel and W. C. Lineberger, J. Chem. Phys. **65**, 1236 (1976).

Finite Temperature Ab Initio Calculation by Path Integral Monte Carlo Method

H. KAWABE,[1] K. KODAMA,[2] H. NAGAO,[3] K. NISHIKAWA[2]

[1] *Secretarial Department, Kinjo College, Matto City 924, Japan*
[2] *Departmental of Computational Science, Faculty of Science, Kanazawa University, Kanazawa 920-11, Japan*
[3] *Department of Optical Materials, Osaka National Research Institute, Ikeda 563, Japan*

Received 2 March 1997; revised 3 July 1997; accepted 19 July 1997

ABSTRACT: We develop the path integral method for quantum chemistry, apply the Monte Carlo method to an evaluation of the path integral, and calculate the ensemble average of the energy. For finite temperature, a simple Monte Carlo evaluation of the path integral brings out the negative-sign problem. In this work, to avoid this problem in the numerical evaluation, we apply the new reweighting method to the Monte Carlo integration, and calculate effectively the ensemble average of the energy for finite temperature. © 1997 John Wiley & Sons, Inc. Int J Quant Chem **65**: 471–476, 1997

Introduction

The path integral introduced by Feynman [1] has been applied to many problems in quantum mechanics. In the path integral, the physical quantity can be handled as a commuting variable like a classical one. Thus the physical processes can be understood more clearly than in ordinary quantum mechanics. When we apply the path integral method directly to the electron field described by the anticommuting field operator, we must deal with the corresponding anticommuting c-numbers, the Grassmann numbers. However, the properties of the Grassmann numbers are, in general, not so well known [2, 3], so that, in the field of quantum chemistry, the path integral method has not been widely applied to the many-electron problems.

Recently the path integral method has been applied to the Hückel model [4] and the many-electron problem [5]. We have also developed the path integral method without using the Grassmann numbers to estimate the electron correlation in molecules [6]. In that work, we derived the new closure relation in terms of the Linear Combination of Atomic Orbital (LCAO) coefficients of the molecular orbital, and have constructed a path integral form of some physical quantities using the LCAO closure relation. In the previous work [7], we presented the new closure relations that could be derived from an arbitrary complete set of state vectors, applied the closure relation to construct the partition function in the path integral form,

Correspondence to: H. Kawabe.

© 1997 John Wiley & Sons, Inc.
CCC 0020-7608 / 97 / 050471-06

and evaluated the ensemble average of the energy. In these treatments, there appear no Grassmann numbers corresponding to the electron field operator but the c-numbers corresponding to LCAO coefficients or state amplitudes.

The essence of the path integral is a sum of histories, and the path integral is usually expressed as a multidimensional integral with a huge number of variables. Therefore, we cannot directly carry out this integration by ordinary ways and will be forced to use statistical methods, such as the Monte Carlo method. Therefore, we have applied the Monte Carlo method to evaluate the path integral [7].

The ordinary quantum Monte Carlo method is a very powerful tool in order to estimate thermal and quantal fluctuations of interacting quantum spin systems and strongly correlated electron systems [8]. This method is based on the generalized Trotter formula, and the quantum fluctuation is expressed in the ordinary path integral form. In simulations of quantum systems, however, some of the local Boltzmann factors become negative, which leads to deteriorated statistics [9]. This difficulty is called the negative-sign problem. The negative-sign problem is particularly serious in low-temperature regions of frustrated quantum spin systems and fermion systems [10, 11].

To reduce the difficulties of the negative-sign problem, the reweighting method has been proposed [12]. In this method, the Monte Carlo sampling is performed under the virtual Boltzmann weight instead of the original one, which is positive definite and describes well the original system, and a value of a physical quantity is reweighted by the correction factor, the ratio of the original and virtual Boltzmann factor.

Conventionally, one has been simulating the system by the absolute value of the Boltzmann factor of the original system as the virtual Boltzmann factor. However, in the quantum Monte Carlo calculation, it has been difficult to get a quick convergence in numerical integrations using the absolute value weight function.

In this work, we apply the new reweighting method to the Monte Carlo integration, and calculate effectively the ensemble average of the energy for finite temperature. In the second section, we briefly summarize the path integral formulation for the ensemble average of the energy. In the third section, the negative-sign problem in the Monte Carlo method is discussed and a new reweighting function, the midpoint procedure, is proposed to avoid this problem in the numerical evaluation. Finally, we apply this method to the hydrogen molecule, evaluate the ensemble average of the energy, and compare a quickness of convergence in numerical integrations between the conventional weight function and ours.

Path Integral Formulation

In this section, we briefly summarize our closure relations and the path integral formulation of the ensemble average of energy [7].

Now, we assume the orthonormal set, $\{|k\rangle\}$, spans the Hilbert space as

$$\mathbf{1} = \sum_{k=1}^{M} |k\rangle\langle k|, \tag{1}$$

$$\langle k|k'\rangle = \delta_{kk'}, \tag{2}$$

where M is a dimension of the vector space $\{|k\rangle\}$. The state $|k\rangle$ could be either the single-particle state or the many-electron configurational one. Then we could construct a generalized state vector by the linear combination of the above state vectors, as

$$|C\rangle = \sum_{k=1}^{M} C_k|k\rangle, \tag{3}$$

here, the coefficient C_k is an arbitrary complex number. If we choose the atomic orbital as $|k\rangle$, then $|C\rangle$ corresponds to the molecular orbital, and if $|k\rangle$ is the many-electron configuration, it becomes the configuration interaction (CI) state.

Here, let us assume that C_k are variables, and change these parameters arbitrarily. Then resulting $|C\rangle$ is transformed into an arbitrary state vector. It is important to notice that the space spanned by the state vector $|C\rangle$, generated by changing C_k arbitrarily, could include every state in the Hilbert space, namely the set $\{|C\rangle\}$ is an overcomplete set. Thus, we could construct the closure relations,

$$\mathbf{1} = \int \prod_{k=1}^{M} \frac{dC_k^* \, dC_k}{2\pi i} \exp\left(- \sum_{k=1}^{M} |C_k|^2 \right) |C\rangle\langle C|, \tag{4}$$

and

$$\mathbf{1} = M! \int \prod_{k=1}^{M} \frac{dC_k^* \, dC_k}{2\pi i} \delta\left(\sum_{k=1}^{M} |C_k|^2 - 1 \right) |C\rangle\langle C|. \quad (5)$$

The delta function ensures the normalization condition of the state vectors. Thus, in this case, each variable varies only on the surface of the unit sphere in the complex space.

Next, we restrict C_k in Eq. (3) to be real. Then, we could get the real number closure relations,

$$\mathbf{1} = 2 \int \prod_{k=1}^{M} \frac{dC_k}{\sqrt{\pi}} \exp\left(- \sum_{k=1}^{M} C_k^2 \right) |C\rangle\langle C|, \quad (6)$$

and

$$\mathbf{1} = 2\Gamma\left(\frac{M}{2}\right) \int \prod_{k=1}^{M} \frac{dC_k}{\sqrt{\pi}} \delta\left(\sum_{k=1}^{M} C_k^2 - 1 \right) |C\rangle\langle C|. \quad (7)$$

Consider a partition function, $Z = \mathrm{Tr}\, e^{-\beta H}$, where Tr implies a trace operation, and $\beta = (k_B T)^{-1}$ with the Boltzmann constant k_B and a temperature T. Let us divide the temperature interval β into L infinitesimal slices, i.e., $\beta = L\tau$, and inserting the closure relation among segments, then Z becomes

$$Z = \lim_{L \to \infty} \frac{1}{\Xi} \int d\mu[C^*, C] Z[C^*, C], \quad (8)$$

where

$$d\mu[C^*, C] = \prod_{l=1}^{L} \prod_{k=1}^{M} \frac{dC_k^*(l) \, dC_k(l)}{2\pi i} \times \prod_{l=1}^{L} W[C^*(l), C(l)], \quad (9)$$

$$Z[C^*, C] = \prod_{l=1}^{L} \langle C(l)| e^{-\beta H/L} |C(l-1)\rangle, \quad (10)$$

and

$$\Xi = \mathcal{N}^L. \quad (11)$$

$W[C^*(l), C(l)]$ is the Gaussian weight function or the delta function corresponding to Eq. (4) or (5), respectively, and $\mathcal{N}$ is the normalization factor appearing in the denominator of the closure relation. The trace operation in the partition function imposes a periodic boundary condition upon $|C(l)\rangle$ as

$$|C(0)\rangle = |C(L)\rangle. \quad (12)$$

The ensemble average of the Hamiltonian can be calculated as

$$\langle H \rangle = \frac{\mathrm{Tr}(e^{-\beta H} H)}{\mathrm{Tr}\, e^{-\beta H}} = \lim_{L \to \infty} \frac{\int d\mu[C^*, C] Z[C^*, C] \frac{1}{L} \times \sum_{l=1}^{L} \frac{\langle C(l)|H|C(l-1)\rangle}{\langle C(l)|C(l-1)\rangle}}{\int d\mu[C^*, C] Z[C^*, C]}. \quad (13)$$

Note that, in the above expression, the normalization factor Ξ has disappeared. It is impossible to evaluate Eq. (13) by direct numerical integration because of its huge amount of integration variables generated by slicing β and the presence of the two-body interactions. Therefore, we should approximate the above integral or should adopt other integration methods such as the Monte Carlo method.

Negative-Sign Problem and Reweighting Method

An estimation of Eq. (13) requires the numerical calculation of two multidimensional integrals over $M \times L$ variables with large enough L, but we cannot directly carry out this integration by ordinary ways. Therefore we apply the Monte Carlo method to do it.

If we carry out the Monte Carlo integration, we would encounter the negative-sign problem. The negative-sign problem has its origin in the fact that some of the off-diagonal elements of the local Boltzmann factors, $\langle C(l)|e^{-\beta H/L}|C(l-1)\rangle$ become negative.

If the factor becomes negative, we cannot carry out the Monte Carlo integration. To tackle the problem, we apply the reweighting method to Monte Carlo integration [12]. In this method, a virtual Boltmann factor, $B(l, l-1)$ is introduced, which is a positive definite weight function.

$$\langle C(l)|e^{-\beta H/L}|C(l-1)\rangle = B(l, l-1) \frac{\langle C(l)|e^{-\beta H/L}|C(l-1)\rangle}{B(l, l-1)}. \quad (14)$$

We regard the correction factor, which is the second factor in the above, as a part of the integrand and perform the importance sampling through the stochastic process defined by the virtual Boltzmann weight.

When the virtual system, which is described by the virtual Boltzmann weight, serves as a good approximation of the original system, we could obtain correct values for a smaller number of the Monte Carlo steps. One condition of a useful virtual system is that the ground-state energy of the virtual system is close to that of the original system. From this point of view, various virtual Boltzmann factors and effective Hamiltonians were proposed as candidates for the better virtual system [12]. In the conventional approach [9], the absolute value of the Boltzmann factor is used as a weight function, i.e.,

$$B(l, l-1) = |\langle C(l)|e^{-\beta H/L}|C(l-1)\rangle|. \quad (15)$$

However, in the quantum Monte Carlo calculation, it is difficult to get a quick convergence in numerical integrations using the absolute value weight function.

For the path integral formulation, the local Boltzmann factor is approximated as

$$\langle C(l)|e^{-\beta H/L}|C(l-1)\rangle \approx \langle C(l)|C(l-1)\rangle \times \exp\left[-\frac{\beta}{L}\frac{\langle C(l)|H|C(l-1)\rangle}{\langle C(l)|C(l-1)\rangle}\right]. \quad (16)$$

Therefore, the origin of the problem is reduced to the overlap $\langle C(l)|C(l-1)\rangle$. In our Monte Carlo algorithm [7], because we randomly generate the state $|C(l)\rangle$ from $|C(l-1)\rangle$, it is possible that the overlap becomes negative. Considering this fact, we propose a new weight function as

$$B(l, l-1) = \langle C(l)|e^{-\beta H/(2L)}|t\rangle \times \langle t|e^{-\beta H/(2L)}|C(l-1)\rangle, \quad (17)$$

where

$$|t\rangle = \frac{|C(l-1)\rangle + |C(l)\rangle}{\sqrt{2 + \langle C(l)|C(l-1)\rangle + \langle C(l-1)|C(l)\rangle}}. \quad (18)$$

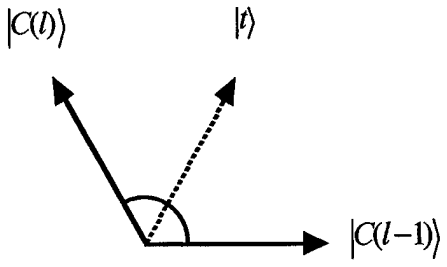


FIGURE 1. Midpoint state. We introduce the midpoint state, $|t\rangle$ between $|C(l-1)\rangle$ and $|C(l)\rangle$.

Here we introduced the midpoint state, $|t\rangle$ between $|C(l-1)\rangle$ and $|C(l)\rangle$. (See Fig. 1.) In this case, $B(l, l-1)$ is approximated as

$$B(l, l-1) \approx \langle C(l)|t\rangle\langle t|C(l-1)\rangle \times \exp\left[-\frac{\beta}{2L}\left(\frac{\langle C(l)|H|t\rangle}{\langle C(l)|t\rangle} + \frac{\langle t|H|C(l-1)\rangle}{\langle t|C(l-1)\rangle}\right)\right]. \quad (19)$$

By using Eq. (18), the preexponential factor becomes

$$\langle C(l)|t\rangle\langle t|C(l-1)\rangle = \frac{(1 + \langle C(l)|C(l-1)\rangle)(1 + \langle C(l-1)|C(l)\rangle)}{2 + \langle C(l)|C(l-1)\rangle + \langle C(l-1)|C(l)\rangle}. \quad (20)$$

Then the weight function $B(l, l-1)$ is always positive and the negative-sign problem is absent.

Our new weight function, the midpoint procedure, is interpreted as follows. Under the original local Boltzmann factor, the system freely evolves from $|C(l-1)\rangle$ to $|C(l)\rangle$, as in Figure 2(a), and we must consider every path between them. On the

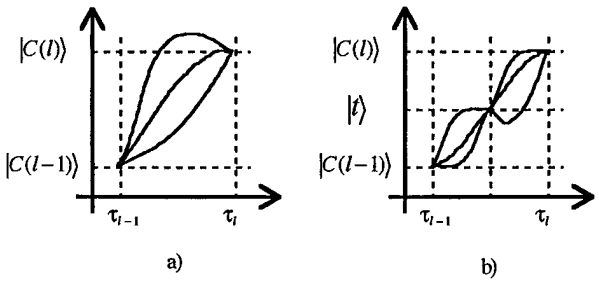


FIGURE 2. Paths between $|C(l-1)\rangle$ and $|C(l)\rangle$. (a) Paths under the original Boltzmann factor. We must consider every path between them. (b) Paths under the midpoint procedure. Every path must passes $|t\rangle$ at the middle of the time interval β/L.

other hand, under the midpoint procedure, the system evolves from $|C(l-1)\rangle$ to $|C(l)\rangle$ but becomes $|t\rangle$ at the middle of the time interval, β/L, as in Figure 2(b). For large enough L or small enough time interval, we could expect that the system behaved as if it were a classical one and reached the midpoint at the middle of the time interval. Thus, our midpoint procedure is a good approximation of the original Boltzmann factor and does not bring the negative-sign problem.

We will show the effectiveness of the midpoint procedure by evaluating the ensemble average of the energy in the next section.

Numerical Examples: Hydrogen Molecule

To demonstrate that our new reweighting function works, we calculate here the average energy $\langle H \rangle$ of the hydrogen molecule.

The calculation is carried out with the minimum STO ($\zeta = 1.0$) and 4-31G basis sets at the internuclear distance of 1.4 a.u. The Monte Carlo integrations were done changing the virtual Boltzmann factor, the absolute value weight, and the midpoint procedure. The number of samplings is 100,000 and the temperature is 10 K. Calculations are executed on the S-4/1000 (FUJITSU Co. Ltd.). The convergence of $\langle H \rangle$ are presented in Figures 3(a) and 3(b) corresponding to the minimum STO basis set and the 4-31G one, respectively. In the figures, the solid curves mean the energies calculated by the midpoint procedure, and the dashed ones that by the absolute value weight. We omitted error bars in the figures, because the width of the error bar depends upon the sampling period in the Monte Carlo integration. Note that the full CI energies are -1.821140 and -1.867025 a.u. for those basis sets, respectively. For both of calculations, the calculated energies monotonously approach to the full CI energies, but the calculation by the midpoint procedure converges faster than that by the absolute value weight.

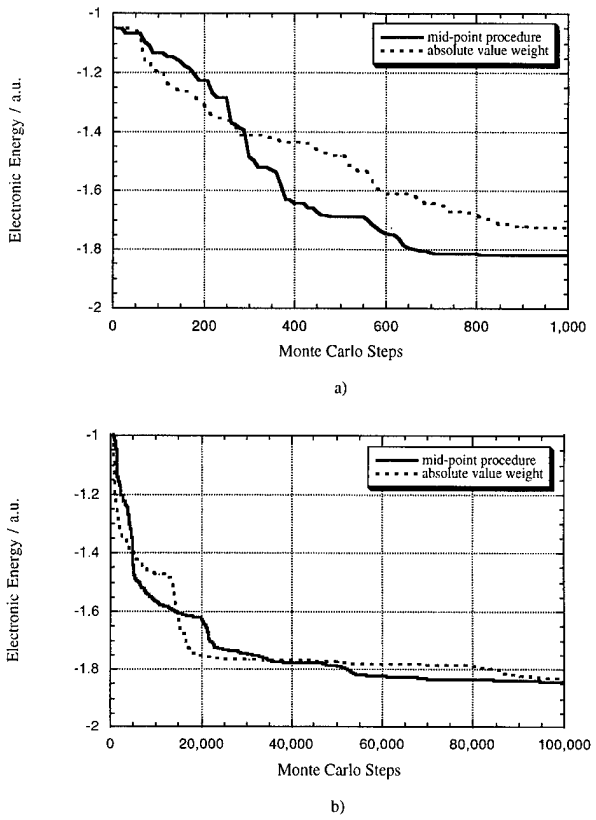


FIGURE 3. Convergence of the ensemble average of energy of the hydrogen molecule. The solid curve means the energy calculated by the midpoint procedure and the dashed one that by the absolute value weight. (a) Calculations with the minimum STO basis set. (b) Calculations with the 4-31G basis set.

Concluding Remarks

We have introduced the midpoint procedure in the reweighting method. We could imagine that in short enough time the system behaved as if it were a classical one and reached the midpoint at the middle of the time interval. Therefore, the physical meaning of the procedure is clear and reasonable. We have calculated the ensemble average of the energy and have shown that calculations with the midpoint procedure converged faster than that with the conventional absolute value weight.

The reweighting method is a useful tool to evaluate integrals by the Monte Carlo method, especially those with the negative-sign problem. The reweighting method has a freedom of the choice of the reweighting function, and it should be chosen by the physical insights. To choose the better reweighting function, it is necessary that the function is hard to be negative and the virtual system specified by the function has close properties to

the original one. If the properties of the virtual system are very different from the original one, we could not expect a quick convergence of calculations. The fast convergence of calculations and clearness of the physical meaning shows that our midpoint procedure is a good approximation to the original system.

In the Monte Carlo method for the Fermi system, the negative-sign problem always occurs whatever closure relations one uses; however, we can expect that the midpoint procedure is effective on the Monte Carlo integration with any closure relation because of the above arguments.

Using the midpoint procedure, we can easily and quickly evaluate physical quantities by the path integral Monte Carlo method not only for the zero temperature but also for the finite temperature. In this work, we have used the δ function closure relation, Eq. (4), and have calculated the energy with the midpoint procedure only for the hydrogen molecule. In the future, we will calculate other quantities as well as the energy at the finite temperature for many species with various closure relations.

References

1. R. P. Feynman and A. R. Hibbs, *Quantum Mechanics and Path Integrals* (McGraw-Hill, New York, 1965).
2. L. H. Ryder, *Quantum Field Theory* (Cambridge University Press, London, 1984).
3. F. A. Berezin, *Method in Second Quantization* (Academic, New York, 1966).
4. H. Nagao, K. Nishikawa, and S. Aono, Chem. Phys. Lett. **190**, 97 (1992); *Ibid.*, **215**, 5 (1993).
5. H. Kawabe, K. Nishikawa, and S. Aono, Int. J. Quant. Chem. **51**, 265 (1994).
6. H. Kawabe, H. Nagao, and K. Nishikawa, Int. J. Quant. Chem. **59**, 457 (1996).
7. H. Kawabe, H. Nagao, and K. Nishikawa, Int. J. Quant. Chem. **30**, 11 (1996).
8. M. Suzuki, Ed., *Quantum Monte Carlo Methods in Condensed Matter Physics* (World Scientific, Singapore, 1993).
9. M. Suzuki, Ed., *Quantum Monte Carlo Methods in Equilibrium and Nonequilibrium Systems* (Springer, Berlin, 1987).
10. E. Y. Loh, J. E. Gubernatis, R. T. Scaletter, S. R. White, D. J. Scalapino, and R. L. Sugar, Phys. Rev. B **41**, 9301 (1990).
11. N. Furukawa and M. Imada, J. Phys. Soc. Jpn. **60**, 810 (1991).
12. T. Nakamura, N. Hatano, and H. Nishimori, J. Phys. Soc. Jpn. **61**, 3494 (1992).

Real-Space Multigrid Solution of Electrostatics Problems and the Kohn–Sham Equations

THOMAS L. BECK

Department of Chemistry, University of Cincinnati, Cincinnati, Ohio 45221-0172

Received 29 March 1997; revised 11 August 1997; accepted 14 August 1997

ABSTRACT: A multigrid method for numerically solving electrostatics and quantum chemical problems in real space is discussed. Multigrid techniques are used to solve both the linear Poisson equation and the nonlinear Kohn–Sham and Poisson–Boltzmann equations. The electrostatic potential, Laplacian, charge densities (electrons and nuclei), Kohn–Sham DFT orbitals, and the self-consistent field potential are all represented discretely on the Cartesian grid. High-order finite differences are utilized to obtain physically reasonable results on modestly sized grids. The method is summarized and numerical results for all-electron atomic and molecular structure are presented. The strengths and weaknesses of the method are discussed with suggested directions for future developments, including a new high-order conservative differencing scheme for accurate composite grid computations which preserves the linear scaling property of the multigrid method. © 1997 John Wiley & Sons, Inc. Int J Quant Chem **65**: 477–486, 1997

Introduction

Numerical grid-based approaches offer an alternative to traditional basis-set methods for electronic structure. Several groups have recently begun to develop real-space grid techniques, including Becke [1], Bernholc et al. [2–4] Chelikowsky et al. [5], Gygi and Galli [6], Kaxiras et al. [7], and Beck et al. [8–11]. In addition to these methods, there have been other developments which point to the possibility of linear scaling electronic structure. The various linear scaling ideas (besides multigrid) are not discussed here but the reader is referred to the growing literature [12–23].

The distinct advantages of the grid methods are (1) the convergence of the "basis set free" method is controlled only by the grid spacing and the order of the difference equations (or accuracy of

Contract grant sponsor: NSF.
Contract grant number: CHE-9632309.

© 1997 John Wiley & Sons, Inc.
CCC 0020-7608 / 97 / 050477-10

the finite element approximation), (2) the methods are flexible in that solution effort and accuracy can be focused in specific regions of space (all iteration steps are local), (3) finite or periodic systems are treated with equal difficulty; there is no need for supercells as with plane waves, and (4) linear scaling is possible with multigrid acceleration or related techniques. The principal disadvantage is that large grids may be required to obtain the desired accuracy so the methods can be memory-intensive. However, recent pseudopotential calculations [3–5] have shown that storage requirements are comparable to the corresponding plane-wave methods. In fact, it is somewhat surprising that results of decent accuracy can be obtained at all when the grids (if Cartesian) do not respect any physical atomic or molecular symmetry. It will be shown below that reasonable accuracy can indeed be obtained in all-electron calculations even on uniform grids where the core states are relatively poorly represented. Grid refinement techniques will allow improvement in those regions without a substantial increase in computational cost while still maintaining the favorable linear scaling property of the multigrid.

In previous work, we first developed a multigrid method for solving the three-dimensional Poisson equation [10]. The charges were represented directly on a Cartesian grid. The technique was tested on several finite and periodic problems. Using high-order finite difference representations, it yielded accurate results for analytic atomic models and for periodic lattice problems which tested the method's ability to handle long-ranged interactions. Systems as large as a 4096 atom ionic crystal lattice were examined, and the known linear scaling of the multigrid method was observed [11]. It is interesting to note that for the infinite lattice problem the (local) iterations in real space are performed within the calculation box with neighboring wraparound interactions only as far as the finite difference Laplacian extends in space. The periodicity is enforced simply by making the potential equal on the opposite boundaries. The resulting solution gives the same physical result as the higher-scaling Ewald method.

The Poisson solver was then used in the multigrid solution of the Kohn–Sham equation [8, 9]. The entire problem was represented discretely on the grid, including the nuclear charge density. In this way, the full electrostatic problem for all electrons and nuclei is solved in a single linear scaling step. The time spent in solving the Coulomb problem composes only a small portion of the overall computational cost. The evolving self-consistent effective potential was generated by a combination of the electrostatic potential and the VWN exchange correlation term [24]. The accuracy of the method was tested in several model atomic and molecular systems. While accurate results were obtained for small Z atoms, the core states of atoms such as Ne are not accurately represented on a uniform grid large enough to handle the $2s$ and $2p$ orbitals.

The purpose of the present article is to present further numerical tests of the real-space multigrid methods. I first give a brief review of our multigrid method and then summarize the equations which are solved numerically, namely, the Poisson, Kohn–Sham, and Possion–Boltzmann equations. Then results are presented for atomic structure and it is shown that the full approximation scheme (FAS) multigrid method of Brandt et al. [25] works well for small Z atoms on uniform grids, but fails for larger Z due to poor representation of the $1s$ core and the $2s$ state. Nonetheless, converged numerical results can be obtained by a simple nested iteration procedure. Results are also presented for the CO molecule which provides a good test since the dipole moment is a difficult quantity to obtain accurately. New methods for solving the nonlinear Poisson–Boltzmann equation in ab initio colloid simulations (colloids treated explicitly, ions as a field) and for carrying out high-order conservative electrostatic computations are also described.

Our work is related to recent work of the groups of Chelikowsky et al. [5], Bernholc et al. [4], and Gygi and Galli [6] However, each of these methods has employed pseudopotentials for the core states, while in our work we have treated the nucleus and core electrons also explicitly on the numerical grid. Part of the advantage of the real-space grids is that varying resolution can be employed in different parts of space without huge computational overheads, and we seek to exploit this feature in the all-electron calculations. Gygi and Galli [6] utilized curvilinear coordinate calculations for variable resolution, but care must be taken to ensure that the correct order of approximation is obtained during the multigrid coarse grid corrections or else the accuracy of the solution can be sacrificed [26]. Our high-order conservative equations method maintains the correct order over the whole domain [27].

Multigrid Description

The multigrid technique was developed in the 1970s to overcome the critical slowing down (CSD) problem which occurs in real-space relaxation methods for solving partial differential equations [28]. In short, multigrid combines iterations on the finest scale with correction cycles which pass to a sequence of coarser scales to smooth modes of the error on a large range of length scales. In this way, the solution is obtained to within the errors caused by placing the problem on the grid in roughly 10–20 fine-scale iterations. The methods were first developed to solve linear elliptic problems like the Poisson equation. Subsequently, more general multigrid algorithms were developed to handle nonlinear problems including eigenvalue problems [25]. Here, I describe our multigrid method; another detailed discussion was given in a recent article [8].

The technique employed here is the FAS nonlinear multigrid method. The method is equivalent to the standard full multigrid method for linear problems, but can treat nonlinear problems such as the Kohn–Sham equations and the Poisson–Boltzmann equation as well. Consider the Poisson equation represented in real-space matrix notation:

$$LU = f, \tag{1}$$

where L is the finite difference Laplacian, U is the potential (u denotes the current approximation); and f is $-4\pi\rho$ (where ρ is the charge density). This matrix equation can be solved by one of the standard iterative relaxation techniques such as the Jacobi method or successive overrelaxation (SOR, used here for the multigrid smoothing steps on each scale). However, for a given grid spacing, the solution stalls after initial rapid reduction of the errors.

This is the point at which the multigrid coarse grid correction cycle is performed to decimate errors at longer wavelengths. The problem is passed to the next coarser grid ($H = 2h$, where H and h are the coarse and fine grid spacings, respectively), and a modified equation is solved (consider a two-level problem here where level one is the coarse scale, and level two, the fine):

$$L^1U^1 = I_2^1 f^2 + \tau^1. \tag{2}$$

The superscript labels indicate the coarser level; I_2^1 is an operator which locally averages (or restricts) the charge density; and τ^1 is the defect correction and is given by

$$\tau^1 = L^1 I_2^1 u^2 - I_2^1 L^2 u^2. \tag{3}$$

This function causes the coarse grid problem to "optimally mimic" the fine grid problem; put another way, if the exact solution were passed from the fine grid, no correction would occur.

Iterations are performed on Eq. (2), and then the fine grid solution is corrected via

$$u^2 \leftarrow u^2 + I_1^2(u^1 - I_2^1 u^2). \tag{4}$$

Here, I_1^2 is the interpolation operator which takes the correction back to the fine scale, level 2. The FAS approach can be used for nonlinear problems since the iterations are performed on the function itself on all scales, and thus no linearity of the equations is assumed. A clear and detailed description of the FAS method is given in the eigenvalue paper of Brandt et al. [25].

We used a high-order finite difference representation for the Laplacian [8, 29]. Along one of the three orthogonal axes, the eighth-order Laplacian is given by

$$\begin{aligned}\nabla^2 u(i) = \frac{1}{5040h^2}[&-9u(i-4) + 128u(i-3)\\ &-1008u(i-2) + 8064u(i-1)\\ &-14350u(i) + 8064(i+1)\\ &-1008u(i+2) + 128u(i+3)\\ &-9u(i+4)] + O(h^8).\end{aligned} \tag{5}$$

The three-dimensional version is just the sum of the three orthogonal components. Hence, there are $3x9 - 2 = 25$ terms in the Laplacian, as opposed to 7 for the second-order case. There is thus a three- to fourfold increase in the time of each iteration; however, a significant gain in accuracy results which allows a much larger grid spacing h, and this benefit far outweighs the increase in time of each iteration. The present calculations on a uniform grid would not be feasible with just the second-order form. The charge density is represented on the grid, with the nuclei occupying a single grid point with a charge density of Z/h^3. For the Poisson–Boltzmann equation, the charge density is replaced by the nonlinear exponential terms (below). The orbitals in the Kohn–Sham equations are represented similarly as a $3d$ array on the grid.

In solving the Kohn–Sham self-consistent eigenvalue equations, we closely followed the FAS prescription given by Brandt et al. [25] with the addition of the self-consistent loop as the effective potential changes during the solution process. The same FAS equations apply, except the Laplacian L is replaced by the Hamiltonian in coordinate space and eigenvalue and orthogonalization steps must be added. In the Brandt method, they proposed that these steps need only be performed on the coarse scales since they are global operations. This dramatically reduces the computational cost since a Gram–Schmidt process scales as q^2N_{grid}, where q is the number of orbitals and N_{grid} is the total number of grid points. Therefore, this step scales as the third power of the number of electrons. By carrying out the orthogonalization on the next coarser scale, the overall time is reduced by a factor of 8. Also, it has recently been shown that accurate results can be obtained with localized orbitals [16], so the orthogolization can, in principle, be reduced effectively to order N.

We compute the eigenvalues on the next coarser scale to the finest scale and perform the orthogonalization there also. The eigenvalues from the coarse scale are then used in the propagation of the orbitals on the fine scale. This method requires that an accurate representation of the orbitals is possible on the coarser scale to the point of yielding eigenvalues which correctly mimic those on the finer scale. This condition is not satisfied for the higher Z atoms, especially for the $2s$ state which has a cusp and an oscillation not too distant from the nucleus. The method works well for multiple orbitals of the hydrogen atom and the ground state of the helium atom on a uniform grid, but not for the C, O, and Ne atoms examined here. However, a simple nested procedure where the solution just passes successively from coarse to fine scales (without coarse grid corrections) converges and we have used this method to obtain the numerical results for those cases. It is clear that the grid refinements will allow a faithful representation in the more strongly varying regions. These difficulties are not encountered in the electrostatics computations. At the end of the self-consistency steps, we perform one final Gram–Schmidt process on the fine scale followed by a Ritz projection which generates the optimal occupied subspace (i.e., all errors are orthogonal to the occupied subspace).

Theory

For the quantum chemical calculations, the Kohn–Sham equations of the density functional theory [30] were solved using the VWN [24] parametrization of the exchange correlation potential. All calculations were carried out at the spin-restricted level. The Kohn–Sham equations are as follows:

$$\left[-\tfrac{1}{2}\nabla^2 + v_{eff}\right]\psi_i(\mathbf{r}) = \epsilon_i\psi_i(\mathbf{r}), \tag{6}$$

with

$$v_{eff}(\mathbf{r}) = v_{ion}(\mathbf{r}) + \int \frac{\rho(\mathbf{r}')}{|\mathbf{r} - \mathbf{r}'|}\, d\mathbf{r}' + v_{xc}(\rho(\mathbf{r})). \tag{7}$$

The electron density is obtained from the orbitals:

$$\rho(\mathbf{r}) = 2\sum_{i=1}^{N/2} \psi_i^2. \tag{8}$$

The evolving electrostatic potential is obtained by multigrid solution of the Poisson equation:

$$\nabla^2\phi(\mathbf{r}) = -4\pi\rho_{tot}(\mathbf{r}). \tag{9}$$

As mentioned above, the nucleus is represented discretely on the grid and the Poisson equation is thus solved simultaneously for the potential due to the nuclei and electrons in a single linear scaling step. This yields the first two terms on the rhs of Eq. (7). Note that a self-energy for the nuclear distribution must be subtracted in computing total energies. This is a one-time calculation on a finite grid for a given order of the Laplacian, since the self-energy scales as Z^2/h.

In related work, we have begun to examine efficient numerical techniques for simulating colloid systems at the ab initio level where the point ions of the solution are represented as a field and the charged colloids are discrete charges on the lattice [31]. These methods stem from the lattice field theory derived by Coalson and Duncan [32, 33]. This is an exact statistical mechanical theory of the ion gas in the field of the colloids, and the Poisson–Boltzmann equation emerges as the saddle point (mean field) in their functional integral representation. Corrections to the Poisson–Boltzmann equation can be made but are very costly computationally. The Poisson–Boltzmann

equation is known to be quite accurate for monovalent ions at low to moderate concentrations in solution. Typically, with colloid particles of charge, say $600e$, something on the order of 10^5 ions would be required, which is far beyond the capabilities of current simulation methods for charged systems. Thus, the Poisson–Boltzmann equation makes a bridge from a continuum description of the ions to a discrete representation of the colloids:

$$\vec{\nabla}\cdot\left(\epsilon(\vec{r})\vec{\nabla}\phi(\vec{r})\right) = -4\pi\Big[\,\rho_s(\vec{r}) + q\bar{n}_+ e^{-\beta q\phi(\vec{r})-v(\vec{r})} - q\bar{n}_- e^{\beta q\phi(\vec{r})-v(\vec{r})}\Big]. \qquad (10)$$

In this nonlinear equation, $\epsilon(\vec{r})$ is the (perhaps) spatially varying dielectric constant, $\rho_s(\vec{r})$ is the colloid source charge, $\bar{n}_+$ is the equilibrium charge density at infinity for the positive ions (similarly for the negative ions), and $v(\vec{r})$ is an excluded volume potential preventing the ions from penetrating into the colloid. In our preliminary calculations, we have held $\epsilon(\vec{r})$ constant in space. The Helmholtz free energy of the ion gas (potential of mean force for the colloids) can be obtained from the potential $\phi(\vec{r})$ [32]. The FAS multigrid technique was used to solve this equation for a pair of colloid particles over a range of separations to generate the interaction potential in aqueous solution. The same FAS method as used for solving the Poisson equation applies as long as the charge density is replaced by the full nonlinear expression on the rhs of Eq. (10).

Numerical Results

The hydrogen atom presents a prototype problem with a fixed potential to examine the performance of the eigenvalue solver by itself. The electrostatic potential was generated numerically on the grid using the Poisson solver with the nuclear charge at the center of the calculation box. An eighth-order finite difference representation was used for the Laplacian, both for the Poisson and Kohn–Sham equations. All the computations discussed here were carried out on a 33^3 grid except the Poisson–Boltzmann calculations (below) which were on a 65^3 grid. The first five eigenfunctions and eigenvalues were computed, corresponding to the $1s$, $2s$, and $2p$ orbitals.

The numerical data are presented in Table I. The eigenvalues are most accurate for the $2p$ states, which do not have a density at the nucleus. The $1s$ and $2s$ eigenvalues are in error by 4 and 2%, respectively, while the $2p$ eigenvalues are only 0.02% in error. The three $2p$ orbitals are degenerate to 5 decimal places, which is some indication of the accuracy of the method. The difference in accuracy between $1s/2s$ and $2p$ states reflects the impact of the distributed nucleus and the grid representation on the orbitals with a cusp. Note that the coarse grid (CG) eigenvalues are very close to the final fine grid results, which shows that a relatively good representation is possible there. The first orbital moments are also given and these also show that the $1s$ and $2s$ states have the largest errors. Cuts through orbitals are shown in Figure 1; the errors in the $1s$ and $2s$ states concentrate near the nucleus. The FAS multigrid data were obtained with 20 fine-scale iterations. While the multigrid cycles converge to results very close to the fully converged grid results, the least converged orbital (as monitored by the residual) is the $2s$ state, which, again, provides some indication of the difficulty this orbital causes during the multigrid corrections.

TABLE I
Multigrid data for hydrogen atom.

	H atom multigrid data		
	Exact	MG	CG
$\lambda(1s)$	−0.50000	−0.51873	−0.51874
$\lambda(2s)$	−0.12500	−0.12727	−0.12889
$\lambda(2p.1)$	−0.12500	−0.12477	−0.12472
$\lambda(2p.2)$	−0.12500	−0.12477	−0.12472
$\lambda(2p.3)$	−0.12500	−0.12477	−0.12473
$\langle r\rangle(1s)$	1.5	1.348	
$\langle r\rangle(2s)$	6.0	5.859	
$\langle r\rangle(2p.1)$	5.0	5.006	
$\langle r\rangle(2p.2)$	5.0	5.006	
$\langle r\rangle(2p.3)$	5.0	5.013	

The fine grid spacing was $h = 1.0$ au. All data are given in au.

The Kohn–Sham DFT self-consistency step was then introduced into the multigrid solver. Here, I present numerical results for the He and Ne atoms, since our previous results contained a minor error in the VWN potential. This only slightly changed the quantitative results for total energies but did alter the individual eigenvalues. The multigrid solver located the ground state of the He atom with 15 fine-scale iterations; the computed energy

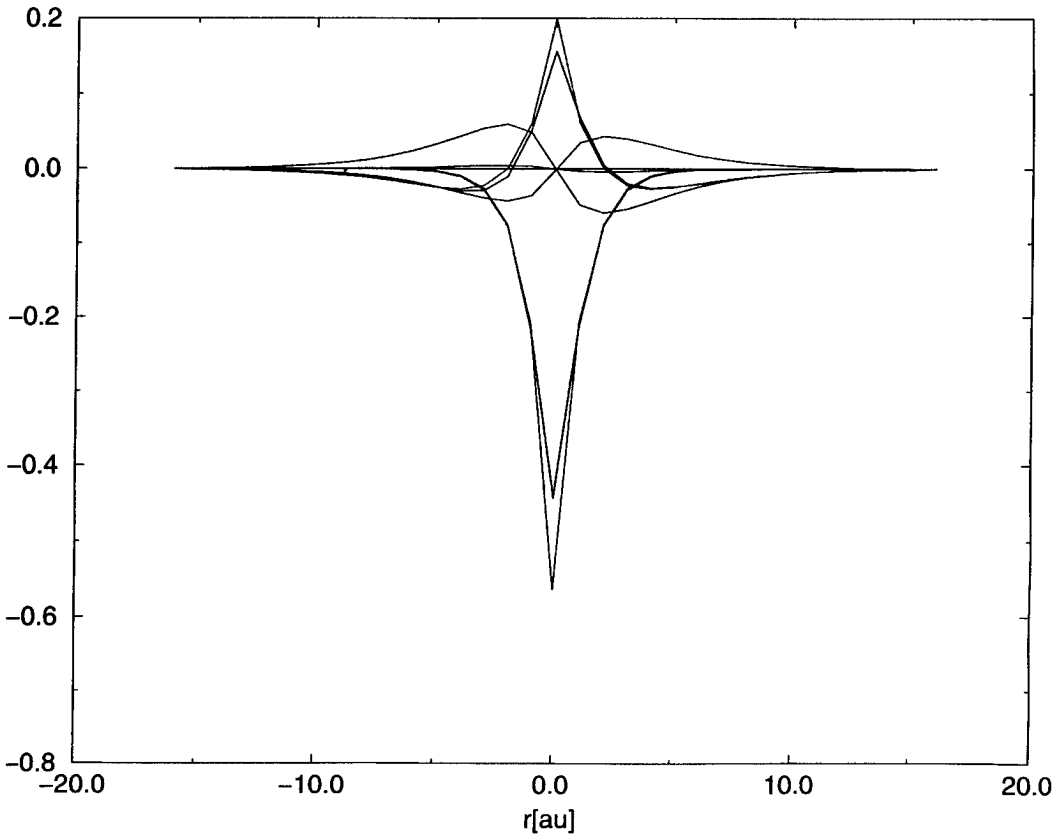


FIGURE 1. One-dimensional cuts through the five hydrogen orbitals. The analytic curves are also presented for the 1*s* and 2*s* states (dotted curves with larger magnitude at the nucleus). One of the *p* orbitals is nearly a node along this direction.

was −2.832 au vs. the exact result of −2.835 au.* The first moment of the ground state orbital ($\langle r \rangle$) was 0.926 au as compared to the exact Hartree–Fock value of 0.927 au [34].

The all-electron Ne atom provides a more severe challenge, and the multigrid solver did not converge on the uniform grid due to the difficulties discussed above. The coarse grid eigenvalues were substantially different from the converged fine grid results (especially the 2*s* orbital), so the coarse grid corrections did not further reduce the errors. In this case, a simple nested procedure was used, passing successively from coarse to fine scales. In previous multigrid work [8], we computed eigenvalues and orthogonalized on all scales, and this technique converged (at more computational expense). The computed total energy of the Ne atom was −128.417 au, which compares with the exact numerical result of −128.233 au. The eigenvalues were 1*s* (−29.253 vs. −30.306 exact), 2*s* (−1.690 vs. −1.323 exact), and 2*p* (−0.438 vs. −0.498 exact). The orbital moments were very close to our previous results. In agreement with the findings for the hydrogen atom, the 2*p* orbitals are better represented on the grid than are the 1*s* and 2*s* states.

An important question for molecular systems is to what extent errors near the nucleus might affect electron densities for valence electrons and, thus, chemical binding. The CO molecule was chosen since both the atoms have an even number of electrons, and the molecule has a relatively simple "closed-shell" electronic structure (as compared say to C_2). The results were obtained by nested iterations as discussed above (Table II). The separated atom energies obtained in the spin-restricted approximation were adjusted according to the recent study of Baerends et al. [35] to obtain the correct spin-polarized separated atom limit. Spin restriction should have only a very minor effect on

* We obtained numerically exact VWN results from Dr. Svetlana Kotochigova in the atomic physics research group directed by Dr. Charles Clark at NIST.

TABLE II
Data for the CO molecule calculation.

	CO molecular data	
	Exact	Grid
λ(1s(O core))	−18.745(Xα)	−16.619
λ(1s(C core))	−9.912(Xα)	−9.376
$\lambda(1\sigma)$	−1.045(Xα)	−1.194
$\lambda(2\sigma)$	−0.489(Xα)	−0.562
$\lambda(1\pi \times 2)$	−0.413(Xα)	−0.403
$\lambda(3\sigma)$	−0.304(Xα)	−0.319
E_B	12.8 eV(LDA)	13.3 eV
E_B	11.2 eV(expt)	
E_B	7.9 eV(HF)	
E_{tot}	−112.79(HF)	−109.54
E_{tot}	−113.377(expt)	
Dipole	0.24 D(Xα)C^-O^+	0.266 D C^-O^+
Dipole	0.112 D(expt) C^-O^+	
Dipole	0.274 D(HF) C^+O^-	

The fine grid spacing was $h = 0.3560$ au, which implies a grid cutoff of $E_{cut} = 39$ Ry. The internuclear separation was 2.136 au. All energies are in au unless otherwise indicated. The individual eigenenergies are first given, followed by molecular binding energies and dipole moments in Debyes. HF refers to the Hartree–Fock limit.

the CO molecule. In the molecular calculations, the boundary potential was obtained by a multipole expansion (to quadrupole order) of the charge density.

The eigenvalues for comparison were obtained from the Xα calculations of te Velde and Baerends [36]. Thus, it is a close but not exact comparison. Generally, except for the core states, the agreement is reasonable. The binding energy is quite close to the exact LDA result [37] and is an improvement over the pseudopotential result (11.1 eV) of Chelikowsky et al. [5] The dipole moment is very close to the numerically exact Xα result [37], which should be quite close to the full LDA number. Pseudopotential calculations [5] gave a result (0.10 D C^-O^+) which differs appreciably from the exact DFT–Xα number. The highest-lying σ orbital is shown in a contour plot in Figure 2. This compares closely to the corresponding Hartree–Fock orbital given by Huo [38].

The accuracy for the binding energy and dipole moment are surprising in view of the crudity of the treatment near the two atomic nuclei. The effective cutoff in the grid representation is only 39 Ry, which is far smaller than would be required to obtain fully converged all-electron plane-wave results. At any rate, the results are encouraging and show that viable numerical results for molecular binding are possible with the grid techniques. The next step is to improve the resolution in the core region via grid refinement techniques (below) to test how this affects the overall accuracy and multigrid efficiency of the method.

Next, results are presented for the computation of interaction free energies between colloid particles where the ion gas is modeled at the mean-field level. Here, a second-order Laplacian was employed, and the Poisson–Boltzmann equation was solved with the FAS multigrid nonlinear technique. Twenty iterations were used on the fine scale, and the free energy was converged to a small fraction of kT by this point. The interaction energy curve is presented in Figure 3. Consistent with previous studies, the pair interaction is purely repulsive in the solution. Recent experiments by Larson and Grier [39] suggested that potential minima may exist when the colloid particles are confined between plates or when in a crystal geometry. We are beginning to examine the many-body colloid interactions to probe whether nonadditive effects occur for trimers and higher n-mers. In preliminary results, we see no indication of nonadditivity for the trimer [40]. While the Poisson–Boltzmann equation is inherently nonlinear and thus many-body, it neglects ion correlations, so the lack of nonadditivity in our calculations may reflect this fact.

Finally, I discuss a new high-order conservative equation scheme which should allow accurate computations on composite grids [27]. As dis-

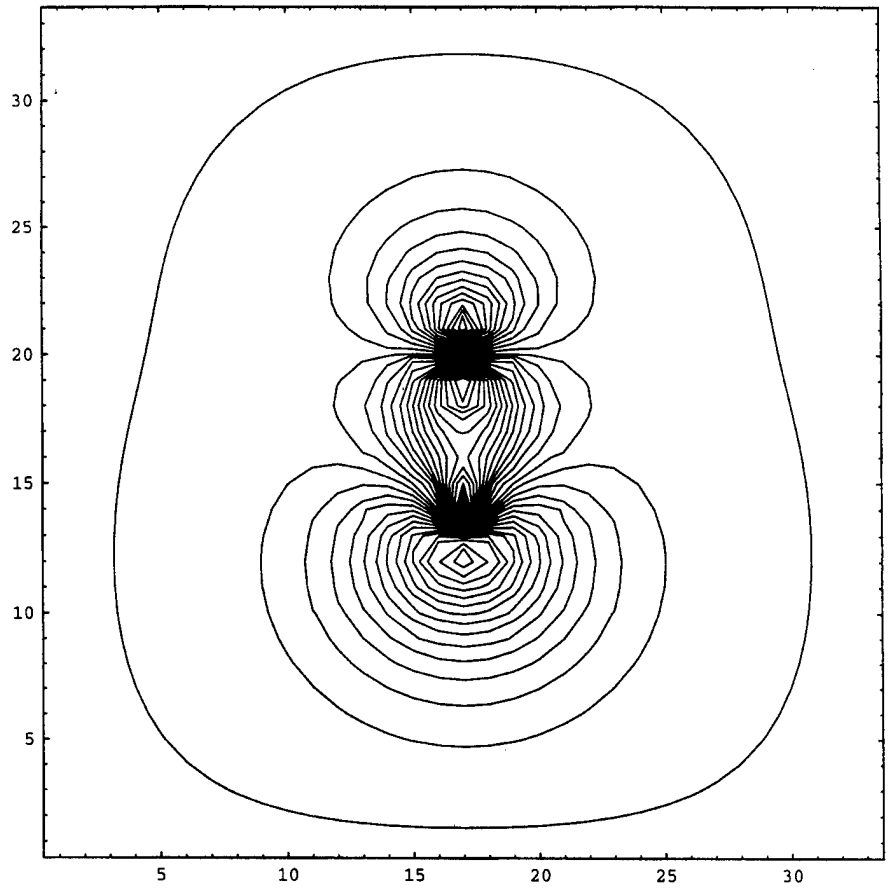


FIGURE 2. Contour plot of the highest-lying σ orbital of the CO molecule. The carbon atom is on the bottom.

cussed above, these refinements will be crucial both for accuracy and multigrid convergence reasons, especially in the region of atomic nuclei in all-electron calculations. To motivate the need for the conservative equations, imagine a simple two-dimensional compositive grid with a patch in the center with grid spacing one-half the rest of the domain. When the multigrid correction cycle is carried out on the coarser scale, the defect correction τ is defined only over the region covered by the refinement patch. It is easy to show that the sum of τ over the patch is not zero. Most of the terms actually do cancel in the interior, but some terms are left near the boundaries. By looking at Eq. (2), we can see this implies that the total source strength has been changed. Nonconservation of source strength can pollute the solution over the whole domain, especially in the case of the long-ranged Coulomb force. Bai and Brandt [26] developed a second-order scheme to balance the fluxes on the boundary and applied it to a two-dimensional problem. We extended their technique to three dimensions (finite and periodic systems) and have now generalized it for higher-order equations. The method also requires high-order interpolation near the patch boundary to ensure correct behavior over the whole domain. The resulting τ boundary terms resemble higher-order flux operators, but do not correspond exactly. The net result is that the sum of τ is zero to machine precision and high-order solutions are possible over the whole composite domain. Details of the method will be presented shortly [27]. Efforts are underway to incorporate the conservative equations into the Poisson and Kohn–Sham solvers to improve the resolution near the nuclei.

Summary

A real-space multigrid method has been developed for solving the linear Poisson and nonlinear Kohn–Sham and Poisson–Boltzmann equations. The advantages of the grid techniques include

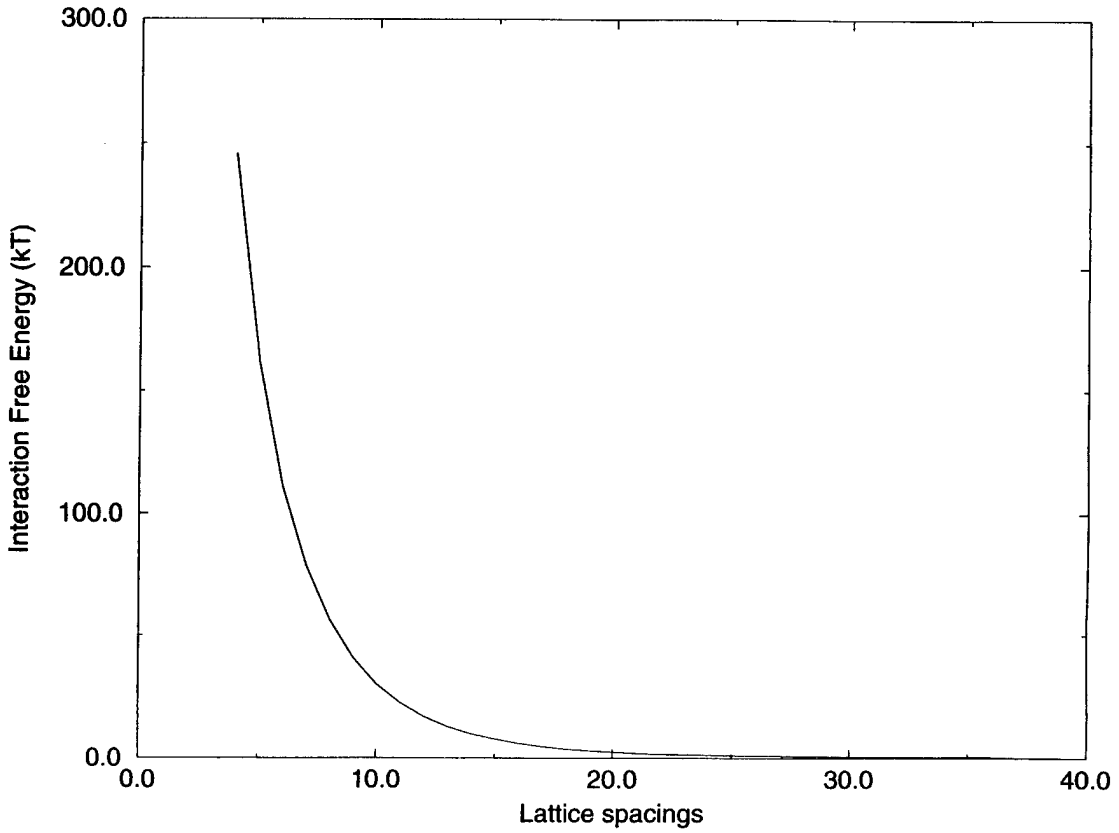


FIGURE 3. Interaction potential of mean force between two colloid particles as a function of lattice spacing. The computation was performed on a 65^3 grid. The lattice spacing was 1600 au and the charge on each colloid was 600*e*. The bulk ion concentration yielded a total number of 48,000 positive ions and 49,200 negative ions in the calculation box. The dielectric constant was taken to be that of bulk water at room temperature. The mean Debye length under these conditions is roughly 8000 au, or five lattice spacings. The colloids occupied one cubical lattice unit. The interaction is given in units of *kT*.

adaptivity and linear scaling capabilities. For the Kohn–Sham case, tests have been carried out on atoms and small molecules. The results show promise that the grid techniques can generate relatively accurate all-electron results, even though the core region is treated crudely if the grid is uniform. With the incorporation of composite grid techniques, greater accuracy can be located near the nuclei with only a small increase in computational cost. Future work will focus on incorporating our new high-order conservative equations scheme [27] into the quantum chemical grid method. Other areas of interest are the finite temperature DFT theory of Alavi et al. [41] and real-space density matrix methods [13, 18, 19]. In related work, the Poisson–Boltzmann solver will be used to study colloid interactions in large systems and carry out Monte Carlo simulations of colloids and polyelectrolyte chains in solution.

ACKNOWLEDGMENTS

I would like to thank my co-workers who have contributed a great deal to this research: Michael Merrick, Karthik Iyer, Rob Coalson, Achi Brandt, and Daan Frenkel. The work was supported by NSF (Grant CHE-9632309). I thank Daan Frenkel and the FOM Institute-AMOLF in Amsterdam for many interesting discussions and support during a recent sabbatical leave there.

References

1. A. D. Becke, J. Chem. Phys. **76**, 6037 (1982).
2. J. Bernholc, J.-Y. Yi, and D. J. Sullivan, Faraday Discuss. **92**, 217 (1991).
3. E. L. Briggs, D. J. Sullivan, and J. Bernholc, Phys. Rev. B **52**, R5471 (1995).

4. E. L. Briggs, D. J. Sullivan, and J. Bernholc, Phys. Rev. B **54**, 14362 (1996).
5. J. R. Chelikowsky, N. Troullier, K. Wu, and Y. Saad, Phys. Rev. B **50**, 11355 (1994).
6. F. Gygi and G. Galli, Phys. Rev. B **52**, R2229 (1995).
7. G. Zumbach, N. A. Modine, and E. Kaxiras, Solid State Commun. **99**, 57 (1996).
8. T. L. Beck, K. A. Iyer, and M. P. Merrick, Intl. J. Quantum Chem. **61**, 341 (1997).
9. K. A. Iyer, M. P. Merrick, and T. L. Beck, J. Chem. Phys. **103**, 227 (1995).
10. M. P. Merrick, K. A. Iyer, and T. L. Beck, J. Phys. Chem. **99**, 12478 (1995).
11. M. P. Merrick, K. A. Iyer, and T. L. Beck, in *Quantum Mechanical Simulation Methods for Studying Biological Systems, Les Houches, France*, D. Bicout and M. Field, Eds. (Centre de physique des Houches, Springer, New York, 1996).
12. W. Yang and T.-S. Lee, J. Chem. Phys. **103**, 5674 (1995).
13. W. Kohn, Phys. Rev. Lett. **76**, 3168 (1996).
14. G. Galli and M. Parrinello, Phys. Rev. Lett. 69, 3547 (1992).
15. E. B. Stechel, A. R. Williams, and P. J. Feibelman, Phys. Rev. B **49**, 10088 (1994).
16. P. Ordejon, E. Artacho, and J. M. Soler, Phys. Rev. B **53**, R10441 (1996).
17. F. Mauri and G. Galli, Phys. Rev. B **50**, 4316 (1994).
18. M. S. Daw, Phys. Rev. B **47**, 10895 (1993).
19. X. P. Li, R. W. Nunes, and D. Vanderbilt, Phys. Rev. B **47**, 10891 (1993).
20. A. E. Carlsson, Phys, Rev. B **51**, 13935 (1995).
21. E. Hernandez and M. J. Gillan, Phys. Rev. B **51**, 10157 (1995).
22. M. C. Strain, G. E. Scuseria, and M. J. Frisch, Science **271**, 51 (1996).
23. C. A. White, B. G. Johnson, P. M. W. Gill, and M. Head-Gordon, Chem. Phys. Lett. **253**, 268 (1996)
24. S. H. Vosko, L. Wilk, and M. Nusair, Can. J. Phys. **58**, 1200 (1980).
25. A. Brandt, A. McCormick, and J. Ruge, SIAM J. Sci. Stat. Comput. **4**, 244 (1983).
26. D. Bai and A. Brandt, SIAM J. Sci. Stat. Comput. **8**, 109 (1987).
27. T. L. Beck, M. P. Merrick, and A. Brandt, in preparation.
28. A. Brandt, Math. Comput. **31**, 333 (1977).
29. R. W. Hamming, *Numerical Methods for Scientists and Engineers* (Dover, New York, 1962).
30. R. G. Parr and W. Yang, *Density-Functional Theory of Atoms and Molecules* (Oxford University Press, Oxford, 1989).
31. R. D. Coalson and T. L. Beck, *Encyclopedia of Computational Chemistry* (Springer-Verlag, New York, 1997).
32. R. D. Coalson and A. Duncan, J. Chem. Phys. **97**, 5653 (1992).
33. A. M. Walsh and R. D. Coalson, J. Chem. Phys. **100**, 1559 (1994).
34. C. F. Fischer, *The Hartree-Fock Method for Atoms—A Numerical Approach* (Wiley, New York, 1977).
35. E. J. Baerends, V. Branchadell, and M. Sodupe, Chem. Phys. Lett. **265**, 481 (1997).
36. G. te Velde and E. J. Baerends, Phys. Rev. B **44**, 7888 (1991).
37. E. J. Baerends, personal communication.
38. W. M. Huo, J. Chem. Phys. **43**, 624 (1965).
39. A. E. Larson and D. G. Grier, Nature **385**, 230 (1997).
40. T. L. Beck and D. Frenkel, in preparation.
41. A. Alavi, J. Kohanoff, M. Parrinello, and D. Frenkel, Phys. Rev. Lett. **73**, 2599 (1994).

Floquet Quasi-Energies and Eigenfunctions of the Parabolic Barrier

R. LEFEBVRE,[1] A. PALMA[2]

[1]*Laboratoire de Photophysique Moléculaire, Campus d'Orsay, 91405 Orsay and UFR de Physique Fondamentale et Appliquée, Université Pierre et Marie Curie, 75230, Paris, France*
[2]*Instituto de Física, Apdo. Postal J-48, Benemérita Universidad Autónoma de Puebla, Puebla, Pue. 72570 and Instituto Nacional de Astrofísica, Optica y Electrónica (INAOE), AP 51 y 216, Puebla, Pue. 72000 México*

Received 1 March 1997; revised 24 March 1997; accepted 26 March 1997

ABSTRACT: A parabolic potential supports resonances. We examine how the resonance energies are transformed into Floquet quasi-energies when the particle is simultaneously subjected to a monochromatic electric field. © 1997 John Wiley & Sons, Inc.
Int J Quant Chem **65:** 487–497, 1997

Key words: Floquet theory; parabolic barrier; coupled-channel methodology; resonances; complex scaling

Introduction

The parabolic (or inverted harmonic) potential has been studied extensively for the same reason, which gives a special importance to the harmonic potential. The lowest energy levels in a well of arbitrary shape can often be calculated accurately from a local quadratic approximation of the potential around the equilibrium position. The diatomic molecule is the best example of this situation [1]. For a polyatomic molecule, the normal mode approximation reduces complicated potential energy surfaces to a sum of harmonic potentials [2]. When a chemical reaction is considered, the potential energy surface in the region of the transition state is usually written as a sum of harmonic potentials plus a parabolic term expressed with the reaction coordinate [3]. In a one-dimensional treatment of the reaction the transmissivity through the parabolic barrier represents the cumulative reaction probability, which is the basic quantity to calculate the microcanonical and canonical reaction rate constants [4]. Bell [5] has made an extensive use of this approximation. An interesting application to heavy-atom tunneling as an explanation for the automerization of cyclobutadiene is given by Carpenter [6]. Use of a parabolic barrier has also been considered as a useful test for the elaboration of the method based on autocorre-

Correspondence to: R. Lefebvre.

© 1997 John Wiley & Sons, Inc.
CCC 0020-7608 / 97 / 050487-11

lation functions of the reactive flux operator to calculate thermal rate constants [7]. This approach avoids the preliminary evaluation of state-to-state reaction probabilities.

Because the scattering of a particle by a parabolic barrier is one of the few exactly soluble problems of nonrelativistic quantum mechanics [8–10], this is the starting point of the mapping method advanced by Miller and Good [11] to derive a semiclassical scattering method valid close to the top of an arbitrary barrier, both below and above the barrier maximum. It has also been possible to define solutions of the wave equation with outgoing boundary conditions, which are the analog of the resonant states (that is corresponding to poles of the scattering matrix) [10, 12]. The idea of associating resonances to barriers has been further extended and applied to the identification of reaction thresholds by Friedman and Truhlar [13, 14]. As an example it has been shown [14] that the lifetimes of the transition states of the reactive collision $H + H_2 \rightarrow H_2 + H$ are well accounted for by the resonances of smallest width of the effective parabolic barriers associated with the potential maxima along the vibrationnally adiabatic potential curves.

New perspectives have been opened recently in a quite different field, which could make the parabolic potential to correspond to a realistic situation. It has been shown by Sundaram et al. [15] that by grading the composition x in superlattices of type $GaAs/Al_xGa_{1-x}$ it is possible to grow a sample presenting a so-called parabolic quantum well (in fact a harmonic well) between two barriers. This is useful to produce a resonant tunneling transistor with equally spaced peaks in the characteristics [16, 17]. This grading technique can, in principle, be used to produce a potential of arbitrary shape, among which the parabolic barrier.

In this study we consider the scattering of a particle by a parabolic barrier in the presence of a monochromatic field. The effect of a field on a particle trapped in a double-well potential has been very actively studied in recent years. The most spectacular result is that under certain conditions tunneling through the barrier separating the wells can be completely suppressed [18–20]. Our problem is somewhat different since the barrier separates two regions where free (rather than bound) motion is possible. We are thus close to the situations met when a rearrangement takes place, for instance electron or atom exchange. We will show that the Floquet quasi-energies and wave functions of this situation can be exactly determined. These resonances should play a role in the reaction in the presence of the field since methods exist to reconstruct the cumulative reaction probability from Siegert eigenvalues and eigenfunctions [4, 21] even when the resonances do not correspond to the intuitive idea of metastable states with long lifetimes.

In the following section we recall that the resonance energies and eigenfunctions for a parabolic barrier can be derived in a very simple way with the help of the complex rotation method with a particular value given to the rotation angle. The third section is devoted to the derivation of the Floquet quasi-energies and eigenfunctions when the particle is interacting with a monochromatic field. The interaction is written in the length gauge. We show in the fourth section that the quasi-energies can also be obtained from a limiting procedure applied to the eigenvalues of a time-independent Hamiltonian [22]. This procedure is valid for an arbitrary oscillator interacting with a one-mode field and yields analytical results in the present case. Finally the fifth section describes a numerical method applicable also to an arbitrary oscillator. This is based on a propagation plus matching technique [23] that yields directly the Fourier components of the Floquet wave function. Some examples of multicomponent Floquet eigenfunctions for the parabolic barrier are presented. Complex rotation (or scaling) of the coordinate is required to implement this method. We study the transition from complete scaling to incomplete (or exterior) scaling. This allows for an investigation of the shape of the components of the wave function as they would result from a treatment without scaling since it is possible to extend arbitrarily far the point of junction between real and complex integration paths.

Resonances of a Parabolic Barrier

For a Hamiltonian written in reduced units:

$$H = -\frac{\partial^2}{\partial x^2} - \omega_0^2 x^2, \tag{1}$$

the elements of the scattering matrix have poles given by the formula

$$E_v = -i\omega_0(2v + 1). \tag{2}$$

This result can also be obtained in a very simple way with a complex rotation of the coordinate [4, 12]. Because this technique will be useful when a time-periodic term is added to the Hamiltonian, we repeat here this derivation. After substitution of $\rho e^{i\theta}$ to x in the wave equation, one looks for solutions vanishing for $\rho \to \pm\infty$ of the equation:

$$\left[-e^{-2i\theta}\frac{\partial^2}{\partial\rho^2} - e^{2i\theta}\omega_0^2\rho^2\right]\chi(\rho) = E\chi(\rho). \quad (3)$$

With the choice $\theta = \pi/4$ the wave equation is transformed into:

$$\left[i\frac{\partial^2}{\partial\rho^2} - i\omega_0^2\rho^2\right]\chi(\rho) = E\chi(\rho). \quad (4)$$

After multiplication by i this becomes:

$$\left[-\frac{\partial^2}{\partial\rho^2} + \omega_0^2\rho^2\right]\chi(\rho) = iE\chi(\rho). \quad (5)$$

This shows that $\chi(\rho)$ is an eigenfunction of the harmonic oscillator $\chi_v(\rho) = \chi_v(xe^{-i(\pi/4)})$ and iE_v the corresponding eigenenergy $\omega_0(2v+1)$. Equation (2) for E_v is recovered. In Ref. [12] it has been shown in detail how to recover the harmonic oscillator wave functions by the substitution $x \to xe^{-i(\pi/4)}$ into the parabolic cylinder functions which are the solutions of the unscaled wave equation of the parabolic barrier.

Floquet Eigenfunctions and Quasi-energies for a Particle Scattered by a Parabolic Barrier and Interacting with an External Field

The Hamiltonian is now:

$$H_l = -\frac{\partial^2}{\partial x^2} - \omega_0^2 x^2 + \lambda x\cos(\omega t). \quad (6)$$

We start from the general solution of the time-dependent Schrödinger equation given by Kerner [24] for a harmonic oscillator interacting with the same field [the Hamiltonian differs just by the sign given to the potential in Eq. (6)]:

$$\Psi_v(x,t) = \chi_v(x - x_c(t))\exp(-i(2v+1)\omega_0 t) \times \exp\left[i\left(\int_0^t L(\tau)d\tau + \frac{\dot{x}_c(t)}{2}(x - x_c(t))\right)\right] \quad (7)$$

where $\chi_v(x)$ is the free oscillator wave function of quantum number v and $x_c(t)$ is a solution of the classical equation of motion:

$$\frac{\ddot{x}_c}{2}(t) + 2\omega_0^2 x_c(t) + \lambda\cos(\omega t) = 0. \quad (8)$$

$L(\tau)$ is the Lagrangian:

$$L(\tau) = \frac{\dot{x}_c^2(\tau)}{4} - \omega_0^2 x_c^2(\tau) - \lambda x_c(\tau)\cos(\omega\tau). \quad (9)$$

In the spirit of the method giving the resonances of the field-free case, we scale $x - x_c(t)$ in the factor, which gives the spatial behavior of the wave function. This variable becomes $u(t) = \eta x - \eta x_c(t)$. We also make the appropriate sign changes in the classical equation of motion and the Lagrangian. The time-dependent wave function is written:

$$\Psi(u,t) = \xi(u(t))\exp(-iEt) \times \exp\left[i\left(\int_0^t L(\tau)d\tau + \frac{\dot{x}_c(t)}{2}\eta^{-1}u(t)\right)\right]. \quad (10)$$

After introduction of this function in the time-dependent Schrödinger equation and some algebra, it is found that most terms compensate and that $\xi(u)$ obeys the equation:

$$E\xi(u) = -\eta^2\frac{\partial^2\xi(u)}{\partial u^2} - \eta^{-2}\omega_0^2 u^2\xi(u). \quad (11)$$

Choosing $\eta = e^{-i(\pi/4)}$ gives the time-independent equation of a harmonic oscillator already met in the field-free case [Eq. (4)]. This shows that $\xi(u)$ is in fact $\chi_v((x - x_c(t))e^{-i(\pi/4)})$ and that E is $-i\omega_0(2v+1)$. However to identify a Floquet quasi-energy, it is necessary to obtain a solution of the time-dependent Schrödinger equation of the form:

$$\Psi^F(x,t) = \exp[-iE_F t]\Phi^F(x,t) \quad (12)$$

with $\Phi^F(x,t)$ a periodic function of time. This defines the Floquet quasi-energy E_F and the Floquet eigenfunction $\Phi^F(x,t)$. In order to achieve this goal we choose a periodic solution of the classical equation of motion for $x_c(t)$ and we separate out the nonperiodic time-dependent factor in the wave function (Breuer and Holthaus [25]). The

periodic solution of the classical equation is:

$$x_c(t) = \frac{2\lambda \cos(\omega t)}{\omega^2 + 4\omega_0^2} \tag{13}$$

and the nonperiodic factor in the wave function is:

$$\exp[-i\omega_0(2v+1)t]\exp\left[-i\frac{\int_0^T L(\tau)d\tau}{T}t\right]. \tag{14}$$

Introduction of $x_c(t)$ as given by Eq. (13) into the Lagrangian allows for the calculation of the integral in Eq. (14). The Floquet quasi-energies are finally:

$$E_v = -i\omega_0(2v+1) + \frac{\lambda^2}{2(\omega^2 + 4\omega_0^2)}. \tag{15}$$

We note the similarity of this result with that of the harmonic oscillator [22, 25]. The shift with respect to the field-free energy (purely imaginary in the present case) is independent of the quantum number and differs by a change in the sign of the contribution of the potential.

Another Route to the Floquet Quasi-Energies of the Parabolic Barrier

We show now that these quasi-energies can be obtained in an extremely simple way already used with success for the harmonic oscillator [22].

A Floquet solution of the time-dependent Schrödinger equation can be written:

$$\Psi^F(x,t) = \exp[-iE_F t]\sum_{n=-\infty}^{n=+\infty} U_n(x)e^{in\omega t}. \tag{16}$$

The $U_n(x)$'s obey the coupled differential equation

$$\left[-\frac{\partial^2}{\partial x^2} + V(x)\right]U_n(x) + \frac{\lambda x}{2}[U_{n-1}(x) + U_{n+1}(x)] = (E_F - n\omega)U_n(x). \tag{17}$$

We consider also the time-independent Hamiltonian:

$$\tilde{H}(x,y) = -\frac{\partial^2}{\partial x^2} - \omega_0^2 x^2 - \frac{\partial^2}{\partial y^2} + \left(\frac{\omega}{2}\right)^2 y^2 + \tilde{\lambda} xy. \tag{18}$$

The eigenfunctions of the y oscillator can be used to perform a diabatic expansion of an eigenfunction of this Hamiltonian:

$$\Theta(x,y) = \sum_n W_n(x)\chi_n(y). \tag{19}$$

The coupled equations for the $W_n(x)$ are found to be:

$$\left[-\frac{\partial^2}{\partial x^2} - \omega_0^2 x^2\right]W_n(x) + \tilde{\lambda} x\left[\sqrt{\frac{n}{\omega}}\,W_{n-1}(x) + \sqrt{\frac{n+1}{\omega}}\,W_{n+1}(x)\right] = (E - n\omega)W_n(x). \tag{20}$$

For very large values of n the couplings for the relevant $W_n(x)$'s for a given $\tilde{\lambda}$ depend weakly on n. As shown by Shirley [26], in this limit the components of the wave function of the time-independent approach merge into the components of the Floquet eigenfunction. For this equivalence to hold use the correspondence rule

$$\frac{\lambda}{2} = \lim_{\tilde{\lambda}\to 0,\, n\to\infty} \frac{\tilde{\lambda}\sqrt{n}}{\sqrt{\omega}}. \tag{21}$$

The eigenfunctions and eigenenergies of $\tilde{H}(x,y)$ can be calculated exactly. The limit given by Eq. (21) is to be taken afterward. With two new variables x' and y' written:

$$\begin{aligned} x' &= x\cos(\theta) - y\sin(\theta), \\ y' &= x\sin(\theta) + y\cos(\theta), \end{aligned} \tag{22}$$

the Hamiltonian becomes separate if θ satisfies:

$$\tan(2\theta) = \frac{\tilde{\lambda}}{\frac{\omega^2}{4} + \omega_0^2}. \tag{23}$$

The new frequencies are given by:

$$-\Omega_1^2 = -\omega_0^2\cos^2(\theta) + \left(\frac{\omega}{2}\right)^2\sin^2(\theta) - \frac{\tilde{\lambda}}{2}\sin(2\theta), \tag{24}$$

$$\left(\frac{\Omega_2}{2}\right)^2 = -\omega_0^2\sin^2(\theta) + \left(\frac{\omega}{2}\right)^2\cos^2(\theta) + \frac{\tilde{\lambda}}{2}\sin(2\theta). \quad (25)$$

The eigenenergies are the sums of the resonance energies of the new parabolic barrier and of the eigenenergies of the decoupled harmonic oscillator:

$$E_{n_1,n_2} = -i(2n_1 + 1)\Omega_1 + (n_2 + \tfrac{1}{2})\Omega_2. \quad (26)$$

The shift induced by the coupling is:

$$\Delta_{n_1,n_2} = -i(2n_1 + 1)(\Omega_1 - \omega_0) + (n_2 + \tfrac{1}{2})(\Omega_2 - \omega). \quad (27)$$

As $\tilde{\lambda} \to 0$, we have $\Omega_1 \to \omega_0$ and $\Omega_2 \to \omega$. However, the correspondence rule requires n_2 to go to infinity. We are left with:

$$\Delta_{n_1,n_2} = n_2(\Omega_2 - \omega). \quad (28)$$

Since, as $\tilde{\lambda} \to 0$, we have $\theta \to 0$, θ can be given the value:

$$\theta = \frac{\tilde{\lambda}}{2\left(\frac{\omega^2}{4} + \omega_0^2\right)}. \quad (29)$$

The frequency Ω_2 can be obtained from:

$$\left(\frac{\Omega_2}{2}\right)^2 = -\omega_0^2\theta^2 + \left(\frac{\omega}{2}\right)^2(1 - \theta^2) + \tilde{\lambda}\theta = \left(\frac{\omega}{2}\right)^2\left[1 + \frac{4\tilde{\lambda}^2}{\omega^2(\omega^2 + 4\omega_0^2)}\right]. \quad (30)$$

A binomial expansion gives

$$\Omega_2 \sim \omega + \frac{2\tilde{\lambda}^2}{\omega(\omega^2 + 4\omega_0^2)}. \quad (31)$$

The shift is:

$$\Delta_{n_1,n_2} = n_2(\Omega_2 - \omega) = 2n_2\frac{\tilde{\lambda}^2}{\omega(\omega^2 + 4\omega_0^2)}. \quad (32)$$

After introduction of the correspondence rule [Eq. (21)], with n_1 identified with v and n_2 dropped the shift is:

$$\Delta_v = \frac{\lambda^2}{2(\omega^2 + 4\omega_0^2)}. \quad (33)$$

in complete agreement with Eq. (15).

Algorithm for Resonance Wave Functions

The Floquet wave function given in Eq. (10) can be written in principle in a standard way [cf. Eq. (16)] showing the spatial function $U_n(x)$ associated to each "photon" state (i.e., is to each exponential $e^{in\omega t}$). However, the wave function is a product of five exponentials of periodic functions of time. The Fourier expansion of the Floquet function is therefore a product of five Fourier series which could at least formally be written compactly with generalized Bessel functions [27]. Rather than trying to analyze this rather complicated expression, we will show that the graphical display of these Fourier components can be easily obtained from a rather general numerical algorithm.

We have developed previously [23] an efficient method to obtain the eigenenergy and the eigenfunction of a resonance in a multichannel situation. This search for a Floquet quasi-energy and its associated wave function belongs to this class of problem. We recall here the main steps in this approach. The Fox–Goodwin propagation method [28] is used. This consists first in the definition on a grid of the inward and outward matrices:

$$\mathbf{P}_m^i = \mathbf{U}_{m+1}^i(\mathbf{U}_m^i)^{-1}, \quad (34)$$

$$\mathbf{P}_m^o = \mathbf{U}_{m-1}^o(\mathbf{U}_m^o)^{-1}. \quad (35)$$

where the $\mathbf{U}_m$'s are matrices of independent vector solutions of the coupled equations at point m of the grid.

The propagation is performed with:

$$\mathbf{P}_{m-1}^i = \left[2\beta(x) - \alpha(x + h)\mathbf{P}_m^i\right]^{-1}\alpha(x - h), \quad (36)$$

and

$$\mathbf{P}_{m+1}^o = \left[2\beta(x) - \alpha(x - h)\mathbf{P}_m^o\right]^{-1}\alpha(x + h), \quad (37)$$

where $\alpha(x)$ and $\beta(x)$ are the Numerov matrices:

$$\alpha(x) = h\left[\mathbf{1} + \frac{h^2}{12}\mathbf{W}(x)\right], \tag{38}$$

$$\beta(x) = h\left[\mathbf{1} - \frac{5h^2}{12}\mathbf{W}(x)\right], \tag{39}$$

with $\mathbf{W}(x) = E\mathbf{1} - \mathbf{V}(x)$, $\mathbf{V}(x)$ being the potential matrix. The matching condition at point n is:

$$\det|\mathbf{P}_n^i - (\mathbf{P}_{n+1}^o)^{-1}| = 0. \tag{40}$$

The initial values for the **U**'s can be taken as zero in classically forbidden regions, since there is spontaneous generation [29] of the appropriate boundary conditions when propagating from such a region toward a matching point in the classically allowed region. This spontaneous generation holds also when complex rotation is used, since this has the same effect on the wave function as propagation into a classically forbidden region.

The entire procedure leads to an estimate of the left-hand side of Eq. (40) and is repeated until this condition is satisfied. The Newton–Raphson procedure can be applied because we look for a zero of an analytic function of the complex energy. The matching relation is also the compatibility condition for a set of homogeneous equations satisfied at the matching point by the components of the vector solution. It is possible to calculate them, except for a normalization factor, and then to propagate them away from the matching point in both directions by using the matrices $\mathbf{P}_m^i$ and $\mathbf{P}_m^o$. The same prescription is used in Johnson's renormalized Numerov method [30]. The storage of all these matrices guarantees [31] that no overflow in closed channels or loss of independence occurs when reaching a classically forbidden region (or equivalently a region with damping of the components when complex rotation is used).

Examination of Some Floquet Eigenfunctions of the Parabolic Barrier

The emphasis in the context of resonances associated to barriers has been so far on the associated complex energies [8–10]. Little has been said about the behavior of the resonance wave functions. In Ref. [12] some scattering wave functions calculated at an energy equal to the top barrier energy have been shown. This energy represents the real part of all resonance energies [cf. Eq. (2)] of the field-free case. The scattering wave functions show clearly a localization in the region of maximum potential energy. In Ref. [21] the resonance energies of the Eckart barrier are derived and a particle-in-a-box technique is used to calculate some resonance functions for both the symmetric and nonsymmetric cases. Localization within the potential region is again demonstrated.

We will display now some resonance complex wave functions of both the field-free case and field-on case for a parabolic barrier.

FIELD-FREE CASE

We consider the following values for the parameters:

$$\omega = 1.2, \quad \omega_0 = 0.8, \quad \lambda = 0.5 \text{ (arbitrary units)} \tag{41}$$

The "zero-point" field-free ($v = 0$) resonance is studied first. Two options are examined

Complete Scaling of the Coordinate

Coordinate x is changed into $xe^{i\theta}$ everywhere. A grid of 2000 points with step 0.01 is used. Although the choice $\theta = \pi/4$ has been shown to transform a resonance wave function of the barrier into a bound-state wave function of the harmonic well (cf. discussion in second section), examination of the factor $e^{(i\omega_0 x^2)/2}$ which is common to all resonance wave functions shows that localization is obtained for a range of angles, with $0 < \theta < \pi/2$. We give in Figure 1 the field-free resonance wave function for the following values of the rotation angle: $\theta = \pi/4$, 0.5, 0.3, and 0.5 rad. For all values of θ except the smallest one, the resonance energy has a seven-figure agreement with the expected result ($-i0.8$). For $\theta = 0.05$ rad the resonance energy is found to be $-0.001658 - i0.7948$. This poor estimate is due to the fact that vanishing of the wave function at the two edges of the grid begins to be a constraint, as shown on the figure (panel with $\theta = 0.05$). A wider grid would restore the accuracy.

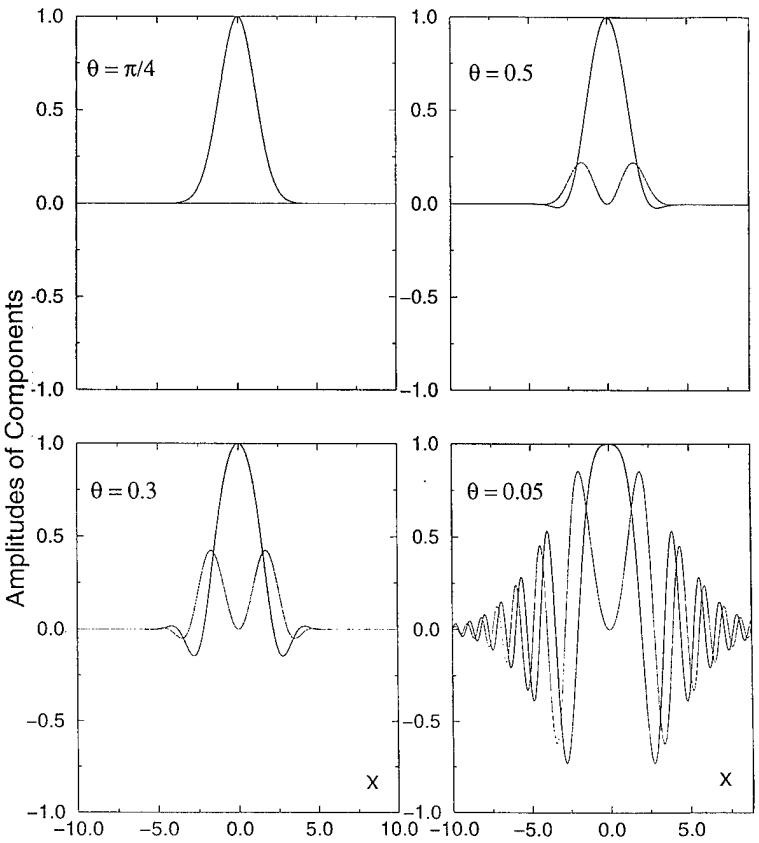


FIGURE 1. Field-free resonance wave functions of a barrier with complete scaling and various rotation angles. Parameters in arbitrary units are: barrier half frequency $\omega_0 = 0.8$, field frequency $\omega = 1.2$, coupling constant $\lambda = 0.5$. The grid extends from -10 to 10 (arbitrary units). The calculation with $\theta = 0.05$ rad does not localize strongly enough the wave function, and a poor estimate of the resonance energy is obtained (see text). For $\theta = \pi/4$, the wave function is real. For all other values of the angle the wave function is complex. The normalization in all cases is chosen so as to give unit value to the amplitude of the real part of the wave function at the matching point ($x = 0$). The panels give the real and the imaginary parts of the wave function, the imaginary parts being given by the thiner curves.

Exterior Scaling [32–34]

Coordinate x is changed into $x_0 + (x - x_0)e^{i\theta}$ for $x > x_0$ and into $-x_0 + (x + x_0)e^{i\theta}$ for $x < -x_0$, x_0 being some positive abcissa. The real part of the integration range extends from $-x_0$ to $+x_0$. This has the advantage of displaying on the real segment the wave function as it would look in a real coordinate treatment (with complex boundary conditions compatible with the asymptotic behavior). With this procedure the asymptotic conditions for starting the left to right and the right to left propagations are again the vanishing of the components of the resonance wave function. We take $x_0 = 5$. The coordinate axis is deformed in the following way: from -10 to -5 the integration axis makes an angle $\pi + 0.5$ rad, with the real axis; between -5 and $+5$ it is along the real axis; from $+5$ to $+10$ the integration axis makes an angle $+0.5$ rad with the real axis.

Figure 2 gives the wave function of the field-free resonance wave function for quantum number $v = 0$. The energy was found to be $-i0.80000017$. The effect of complex rotation for $|x| \geq 5$ is clearly visible.

FIELD-ON RESONANCE WAVE FUNCTION

The parameters are now $\omega_0 = 0.5$, $\omega = 1$, and $\lambda = 1$. We note that for such a choice the shift of the harmonic oscillator has a singularity, since in Eq. (15) ω_0 has to be replaced by $i\omega_0$. The calculation is now a multichannel one done with the

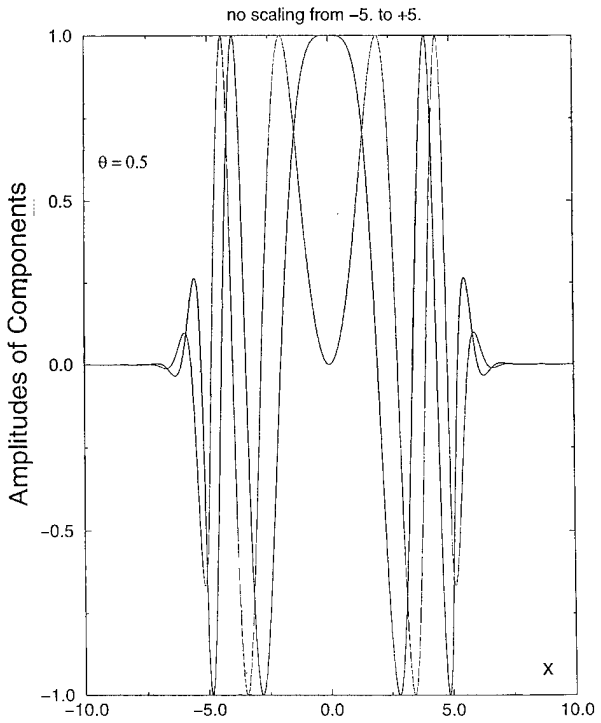


FIGURE 2. A field-free resonance wave function of a barrier with exterior scaling. Parameters are those of Figure 1. The grid extends from -10 to 10 (arbitrary units). The scaling is applied to the two segments from -10 to -5 and from $+5$ to $+10$ with an angle $\theta = 0.5$ rad. The energy provided by the calculation is $E = -0.13(-6) - i0.800017$ (expected value $E = -0.8$). Normalization as in Figure 1, the real part of the wave function being unity at $x = 0$.

procedure described in the third section. The strategy is as follows: the coupled equations [Eq. (17)] are infinite in number, and truncation is obviously necessary. We call the channel with $n = 0$ the *reference channel*. With no field present the resonance energies and eigenfunctions of this channel are considered as describing the system. We note that the uncoupled channel with arbitrary n also represent the field-free system, but with eigenenergies displayed by $n\omega$. This is a distinctive feature of the Floquet theory. When the field is present, the energies close to those of the reference channel are being determined. The additional channels are introduced in a symmetrical way, one above and one below the reference channel at a time. Convergence with respect to the number of channels is then studied, since the critical number for a given accuracy of the quasi-energy can vary widely. Table I shows how the exact energy is approached progressively. A 7-figure accuracy is achieved in this example with 13 channels. Figure 3 gives five of the components of the 13-channel Floquet eigenfunction, including the reference channel (panel $n = 0$), and two channels above ($n = 1, 2$) and two below ($n = -1, -2$). Despite the number of channels needed for an accurate result, the amplitude of the wave function of the reference channel is still dominating the Floquet wave function (the components are not drawn on the same scale).

TABLE I

Convergence toward the correct resonance energy with the number *N* of channels in the multichannel approach to Floquet treatment of a parabolic barrier.[a]

N	Resonance energy
1	$-0.90(-11) - i0.50000000$
3	$0.23492517 - i0.56062542$
5	$0.25010394 - i0.49954770$
7	$0.24982569 - i0.50052883$
9	$0.25003014 - i0.500000811$
11	$0.24999985 - i0.50000035$
13	$0.25000008 - i0.50000002$

[a]Parameters are in arbitrary units: barrier half-frequency $\omega_0 = 0.5$, frequency of the field $\omega = 1$, coupling $\lambda = 1$, rotation angle $\theta = 0.5$ rad. The results with complete scaling or exterior scaling for $|x| > 5$ differ at most by one unit in the last figure. Expected resonance energy: $E = 0.25 - i0.5$. $N = 1$ is the field-free calculation.

Figure 4 shows the Floquet wave functions of the same model, with the same choice of functions, but with now exterior scaling for $|x| > 5$. The wave functions on the interval $-5 < x < +5$ are calculated for real x: this is exactly how they would appear if (complicated) boundary conditions valid for a real coordinate treatment were introduced in the solution of the coupled equations.

Conclusions

We have shown that the methods (both analytical and numerical) which can be used to obtain the Floquet quasi-energies and eigenfunctions of the harmonic oscillator require little change to give the corresponding information for the parabolic bar-

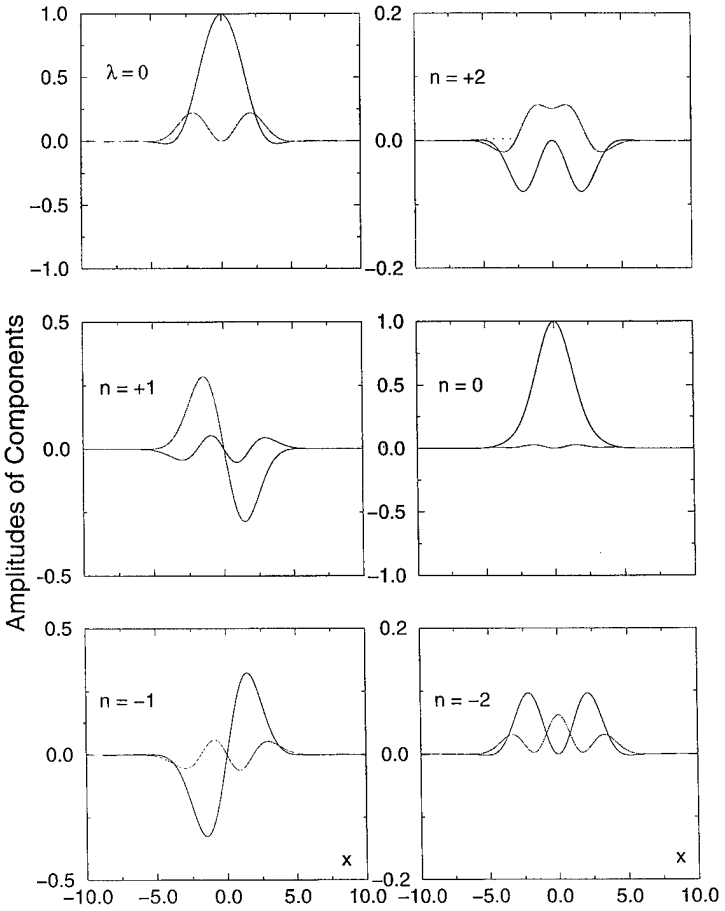


FIGURE 3. Field-free and field-on resonance wave functions for a parabolic barrier, with complete scaling (c. sc.). The parameters are given in Table I. Panel $\lambda = 0$: the complex resonance wave function of the parabolic barrier in the absence of the field. In the other panels: five of the components of the 13-channel Floquet eigenfunction which leads to an accurate determination of the resonance energy (7-figure agreement with the analytical result, see Table I) The reference channel has $n = 0$. Channels $n = +1$ and $n = +2$ are above the reference channel, $n = -1$ and $n = -2$ are below. Every wave function or component wave function is complex. The real parts of the wave function when the field is off ($\lambda = 0$), or of the reference channel wave function ($n = 0$) when the field is on, are unity at $x = 0$. The thiner curves represent the imaginary parts of the functions. Note that the components are not drawn all on the same scale.

rier. This shows that the Floquet problem of the parabolic barrier can be added to the very few soluble cases of Floquet theory. Since the Floquet eigenfunctions make up a complete set for the expansion of an arbitrary solution of the time-dependent Schrödinger equation, they could be used to examine how the transmission across a barrier is affected by the presence of a field. It is legitimate, when the energy approaches that of the potential maximum, to use locally a parabolic approximation for the potential. This is under study.

It is also interesting to note that in the high-frequency regime ($\omega \gg \omega_0$) the shift in Eq. (15) goes to the ponderomotive energy $\lambda^2/2\omega^2$. If a barrier maximum is interpreted as a reaction threshold [13, 14], this means that the threshold is displaced upward by the ponderomotive energy, in a way similar to the shift occurring for the ionization threshold in an intense field [35].

ACKNOWLEDGMENTS

This work has benefited from an agreement between CNRS (France) and CONACYT (Mexico) under project 2110-E9302. Part of it has been done while one of the authors (R. L.) was visiting the Department of Chemistry of the Technion, Haifa (Israel).

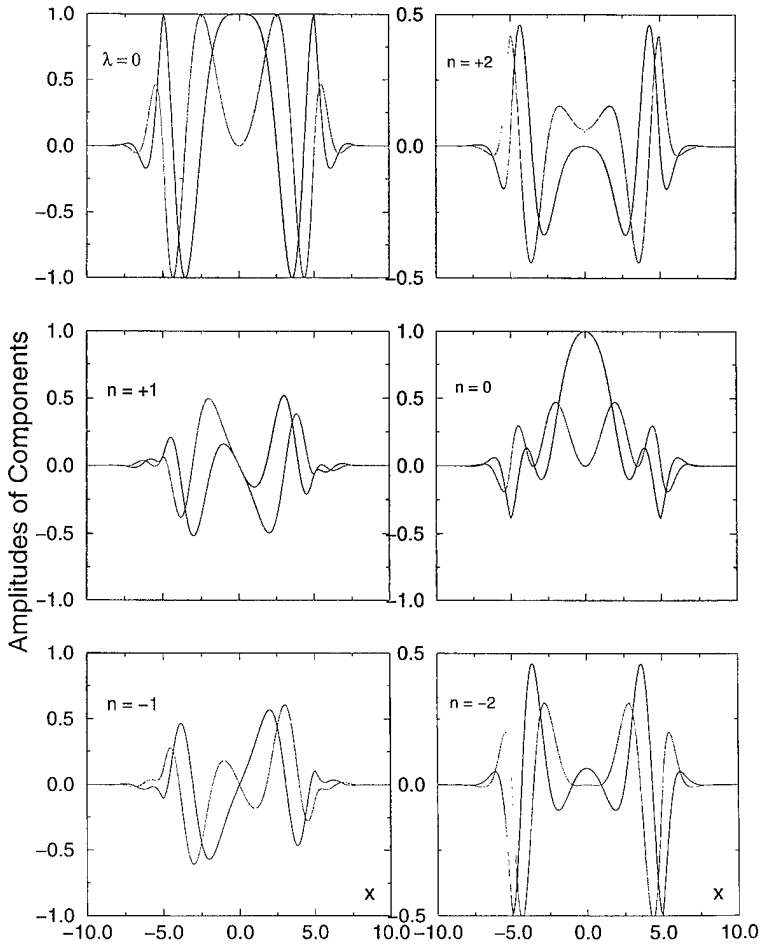


FIGURE 4. The model and selection of wave functions are the same as in Table I and Figure 3, but now exterior scaling (ext. sc.) is applied for $|x| > 5$ on the integration grid. Damping of the functions starts outside the real interval $-5 < x < +5$. Same conventions and remarks for normalization as in Figure 3.

References

1. G. Herzberg, *Molecular Spectra and Molecular Structure. I. Spectra of Diatomic Molecules* (Krieger, Malabar, 1989).
2. E. B. Wilson, J. C. Decius, and P. C. Cross, *Molecular Vibrations* (Dover, New York, 1980).
3. W. H. Miller, Faraday Discussion Chem. Soc. **62**, 40 (1977).
4. T. Seideman and W. H. Miller, J. Chem. Phys. **95**, 1768 (1991).
5. R. P. Bell, *The Proton in Chemistry*, 2nd ed. (Cornell University Press, Ithaca, NY, 1973).
6. B. K. Carpenter, J. Am. Chem. Soc. **105**, 1700 (1983).
7. W. H. Miller, S. D. Schwartz, and J. W. Tromp, J. Chem. Phys. **79**, 4889 (1983).
8. J. N. L. Connor, Mol. Phys. **15**, 37 (1968).
9. Y. Plotnikov, Opt. Spectr. **29**, 453 (1970).
10. N. Rowley, J. Phys. A **12**, L7 (1979).
11. S. C. Miller and R. H. Good, Phys. Rev. **91**, 174 (1953).
12. O. Atabek, R. Lefebvre, M. Garcia-Sucre, J. Gomez-Llorente, and H. Taylor, Int. J. Quant. Chem. **40**, 211 (1991).
13. R. S. Friedman and D. G. Truhlar, Chem. Phys. Lett. **183**, 539 (1991).
14. R. S. Friedman and D. G. Truhlar, in *Multiparticle Quantum Scattering with Applications to Nuclear, Atomic and Molecular Physice*, D. G. Truhlar and B. Simon, Eds. (Springer Verlag, New York, 1997).
15. M. Sundaram, A. C. Gossard, J. H. English, and R. M. Westervelt, Superlatt; Microstruct. **4**, 683 (1988).
16. F. Capasso and R. A. Kiehl, J. Appl. Phys. **58**, 1366 (1985).
17. S. Sen, F. Capasso, A. C. Gossard, R. A. Spah, A. L. Hutchinson, and S. N. G. Ghu, Appl. Phys. Lett. **51**, 1428 (1987).
18. F. Grossman, T. Dittrich, P. Jung, and P. Hänggi, Phys. Rev. Lett. **67**, 516 (1991).
19. F. Grossman, T. Dittrich, P. Jung, and P. Hänggi, Z. Phys. **B84**, 315 (1991).
20. J. M. Gomez Llorente and J. Plata, Phys. Rev. A **45**, R6958 (1992).

21. V. Ryaboy and N. Moiseyev, J. Chem. Phys. **98**, 9618 (1993).
22. R. Lefebvre and A. Palma, J. Mol. Structure (THEOCHEM) **390**, 23 (1997).
23. O. Atabek and R. Lefebvre, Phys. Rev. A **22**, 1817 (1980).
24. E. H. Kerner, Can. J. Phys. **36**, 371 (1958).
25. H. P. Breuer and M. Holthaus, Z. Phys. D **11**, 1 (1989).
26. J. H. Shirley, Phys. Rev. **138**, B979 (1965).
27. R. M. Potvliege and R. Shakeshaft, Phys. Rev. A **40**, 3061 (1989).
28. D. W. Norcross and M. J. Seaton, J. Phys. B: At. Mol. Phys. **6**, 614 (1973).
29. M. Chrysos, R. Lefebvre, and O. Atabek, J. Phys. B: At. Mol. Phys. **27**, 3005 (1994).
30. B. R. Johnson, J. Chem. Phys. **69**, 4678 (1978).
31. R. Lefebvre, Phys. Rev. A **46**, 6071 (1992).
32. C. A. Nicolaides and D. R. Beck, Phys. Lett. A **65**, 11 (1978).
33. B. Simon, Phys. Lett. A **71**, 211 (1979).
34. M. Chrysos, O. Atabek, and R. Lefebvre, Phys. Rev. A **48**, 3845, 3855 (1993).
35. K. Burnett, V. C. Reed, and P. L. Knight, J. Phys. B **26**, 561 (1993).

Maximum Principles in DFT from Reciprocal Variational Problem

KATARZYNA TKACZ-ŚMIECH, W. S. PTAK

Technical University of Mining and Metallurgy, Faculty of Materials Science and Ceramics, Al. Mickiewicza 30, 30059 Kraków, Poland

Received 3 March 1997; revised 30 May 1997

ABSTRACT: Formalism of density-functional theory (DFT) is based on the calculus of variation. In the Hohenberg and Kohn theorem, a variational equation minimizing electronic energy with respect to an electron density is constructed. The calculus of variation allows one to formulate a problem which is reciprocal to an original one. Also, we may consider the problem of finding the electron density determining a given energy $E = E[\rho]$ for a maximum number $N = N[\rho]$ of the electrons forming the system. In this work, the reciprocal variational problem is discussed. Mathematical considerations are followed by a presentation of an application of the reciprocal problem (maximum entropy principle). Other possibilities of the applications are sketched. © 1997 John Wiley & Sons, Inc. Int J Quant Chem **65**: 499–501, 1997

Key words: density-functional theory; variational principle; reciprocal problem; maximum principle

Introduction

There are many similarities among various applications of density-functional methods. One of the main properties of this parallelism is an obligation of a variational principle. The most fundamental application of the variational principle is a minimization of the electronic energy which, according to the Hohenberg–Kohn theorem, is a unique functional $E = E_v[\rho]$ of an electron density for a given external potential $v = v(\mathbf{r})$ [1]. The ground-state density-functional theory (DFT) can be generalized to equilibrium states in ensembles of very many positive and negative ions at temperature θ and chemical potential μ [2–5]. Having a variational principle in hand, one can construct a variational equation dependent on the external potential $v(\mathbf{r})$.

Generally, three minimum principles can be applied in DFT:

(i) For the ground-state energy,
$$E_v = F_{HK} + \int v \cdot \rho \, d\tau;$$
(ii) For the equilibrium Helmholz free energy,
$$H = E_v - \theta S;$$
(iii) For the grand canonical potential,
$$\Omega = E_v - \theta S - \mu N,$$

Correspondence to: K. Tkacz-Śmiech.

© 1997 John Wiley & Sons, Inc.
CCC 0020-7608 / 97 / 050499-03

where H and Ω may be derived as Legandre's transforms of the energy while $S = S[\rho]$ is an entropy and $N = N[\rho]$ determines a number of the particles in the system. In the variational treatment, one minimizes the functionals for $E_v[\rho]$, $H[\rho]$, and $\Omega[\rho]$ via a variation of the electronic density function $\rho(\mathbf{r})$.

Reciprocal Principle in Zero-temperature Limit

Assuming differentiability of the energy functional $E_v[\rho] \equiv E[\rho]$, the variational principle states that the density ρ, which minimizes energy functional, is that one which satisfies the equation

$$\delta\{E[\rho] - \mu N[\rho]\} = 0 \tag{1}$$

or, in the form of the Euler–Lagrange equation,

$$\frac{\delta E[\rho]}{\delta \rho} = \mu. \tag{2}$$

The constancy of μ is a result of variation of the ρ function under an isoperimetric condition $N[\rho] =$ const.

As a functional $E = E[\rho]$ is, in general, a many-to-one relation, the calculus of variation gives no unique inverse of the derivative (2) [6]. But the calculus of variation allows one to consider a reciprocal problem which is formulated through a change of the roles of the optimized functional and the constraint [7]. According to the reciprocal principle, a stationary state of a system of constant energy is that one which is constructed by a maximum number of the electrons.

Let a given energy be equal to

$$E = \text{const} \tag{3}$$

and ρ be a corresponding electron density due to a maximum number of the electrons. We can replace the density ρ by a density ρ' such that $N[\rho'] = N'$, $E' < E$ and then deform ρ' so that it goes into ρ'' while N' and E' are increased. It can be performed so that the energy again becomes equal to E. But, then, there is $N'' > N'$, i.e., $N'' > N$, which contradicts the definition of N. In the general case, we speak about a stationary value of the functional $N[\rho]$ with a constrained $E[\rho] = E_0$. The problem may be reduced to a solution of the Euler's equation corresponding to the functional

$$\tilde{N} = N - \lambda E. \tag{4}$$

It results from the above that

$$\tilde{N} = N - \lambda E = -\lambda\left(E - \frac{1}{\lambda}N\right) = -\lambda(E - \tilde{\mu}N), \tag{5}$$

and from a necessary condition of maximization,

$$\frac{\delta(N - \lambda E)}{\delta \rho} = 0 \tag{6}$$

and

$$1 = \lambda\frac{\delta E}{\delta \rho}. \tag{7}$$

Consequently, after cancellation, the same equation as in the simple problem can be obtained:

$$\frac{-\lambda\delta(E - \tilde{\mu}N)}{\delta \rho} = 0 \tag{8}$$

and, finally [compare with Eq. (2)],

$$\frac{\delta E}{\delta \rho} = \tilde{\mu}. \tag{9}$$

Also, $\tilde{\mu}$ equals the chemical potential: $\tilde{\mu} = \mu =$ const.

It follows from the above that the calculus of variation allows one to treat the problem of the stability of the electronic system through the equivalent reciprocal problem of maximization of the electron number for a given energy of the analyzed system.

Reciprocal Variational Principle at Nonzero-temperature Limit

Let us take a system at $T \neq 0$ and consider the changes which preserve the number of the electrons $N = N[\rho]$. The energy $E[\rho]$ of the electronic system must be minimized subject to the following constraints:

(i) The electron density integrates to the constant number of the electrons, to which the Lagrange's multiplier μ is attached; and
(ii) The entropy equals the observed value, $S = S[\rho] =$ const, with the Lagrange's multiplier θ.

The variational principle states that

$$\delta\{E_v[\rho] - \theta S[\rho] - \mu N[\rho]\} = 0, \quad (10)$$

or in the form of the Euler's variational equation,

$$\frac{\delta E}{\delta \rho} - \theta \frac{\delta S}{\delta \rho} - \mu = 0. \quad (11)$$

According to the reciprocal principle, the equilibrium state can be achieved for a given N, E = const and for the electron density that gives a maximum entropy $S[\rho]$. In this case, the maximum condition reads

$$\delta \tilde{S} = 0 \quad (12)$$

for the functional

$$\tilde{S} = S - \alpha E - \beta N. \quad (13)$$

The respective Euler's equation is

$$\frac{\delta \tilde{S}}{\delta \rho} = \frac{\delta(S - \alpha E - \beta N)}{\delta \rho} = 0 \quad (14)$$

and, after transformation,

$$\frac{\delta E}{\delta \rho} + \frac{\beta}{\alpha} - \frac{1}{\alpha}\frac{\delta S}{\delta \rho} = 0. \quad (15)$$

Comparison of the above expression with Eq. (11) proves that, for the multipliers $1/\alpha = \theta$ and $\beta/\alpha = -\mu$, there is an equivalency of the simple problem of the energy minimization and the reciprocal problem of the maximization of the entropy.

Summary

Calculus of variation allows one to consider the reciprocal problem of the original problem minimizing the energy of the electronic system. This, as we have shown, can be established directly by constructing and solving the corresponding Euler–Lagrange equation. The proposed method can be used in the description of the equilibrium state of a given energy, equal to the experimental value, but of a varying number of the electrons forming the system. Such an attitude seems to be of a special significance from the point of view of possible application for the cases with a charge flow between chosen loges. In [8], a metallic crystal composed of spherical muffin-tins was considered. It seems that further applications, e.g., in making a population analysis for molecules, may be interesting. A reciprocal principle maximizing $N[\rho]$ for the assumed experimental electronic energy gives a theoretical basis for semiempirical methods.

Another maximum principle presented in this work is the maximum entropy principle. It is of interest as to how the maximum hardness principle [9–11] may be established from the reciprocal problem. One must look for an answer using the second equation of the hierarchy of the equation for the energy functionals [8, 12–13].

References

1. P. Hohenberg and W. Kohn, Phys. Rev. B **136**, 864 (1964).
2. N. D. Mermin, Phys. Rev. A **137**, 1441 (1965).
3. R. Evans, Adv. Phys. **28**, 143 (1979).
4. J. S. Rowlinson and B. Widom, *Molecular Theory of Capillarity* (Clarendon Press, Oxford, 1982).
5. R. G. Parr and W. Yang, *Density-Functional Theory of Atoms and Molecules* (Oxford University Press, New York: Clarendon Press, Oxford, 1989), pp. 60–69.
6. R. G. Parr and W. Yang, *Density-Functional Theory of Atoms and Molecules* (Oxford University Press, New York; Clarendon Press, Oxford, 1989), Appendix A.
7. A. D. Myskis, *Advanced Mathematics for Engineers* (translated from Russian) (Mirr, Moscow, 1975), pp. 317–385.
8. K. Tkacz-Smiech, in preparation.
9. G. Pearson, J. Chem. Ed. **64**, 561 (1987).
10. P. K. Chattaraj, G. H. Liu, and R. G. Parr, Chem. Phys. Lett. **237**, 171 (1995).
11. P. K. Chattaraj, A. Cedillo, and R. G. Parr, *J. Chem. Phys.* **103**, 17 (1995).
12. A. Nagy, Phys. Rev. A **47**, 2715 (1993).
13. A. Nagy, in *Recent Advances in Density Functional Methods*, D. P. Chong, Ed. (World Scientific, Singapore, 1995).

Exact Numerical Calculations of Dissociative-Ionization of Molecular Ions in Intense Laser Fields: Non-Born–Oppenheimer Dynamics

S. CHELKOWSKI, C. FOISY, A. D. BANDRAUK

Laboratoire de Chimie Théorique, Faculté des Sciences, Université de Sherbrooke, Sherbrooke, Québec, Canada J1K 2R1

Received 12 March 1997; revised 19 May 1997; accepted 22 May 1997

ABSTRACT: The time-dependent Schrödinger equation for the 1-D H_2^+ molecule (with both nuclear and electronic degrees of freedom included) was solved numerically. A wave–function splitting technique was used, which allows one to circumvent the problem of lost information due to commonly used absorbing boundaries of the electron flux. This technique allows us to calculate the above-threshold ionization (ATI) photoelectron kinetic energy spectra in the presence of moving nuclei, as well as complete spectra of dissociating protons, beyond the Born–Oppenheimer approximation. A considerable enhancement of the ATI spectra, with respect to the spectra generated by a H atom, were found. The peaks seen in calculated Coulomb explosion spectra of protons agree well with the predictions of recent theoretical work related to the phenomenon of charge-resonance-enhanced ionization (CREI). © 1997 John Wiley & Sons, Inc. Int J Quant Chem **65**: 503–512, 1997

Introduction

The interaction of intense laser pulses (intensity $I > 10^{13}$ W/cm^2) with atoms and molecules leads to many new interesting multiphoton, nonperturbative phenomena such as high-order harmonic generation and above-threshold ionization (ATI). This has been an area of active research in the past decade [1–4] and there has been extensive progress in the understanding of these processes in atoms. The situation for molecules is not as advanced because of the complexity arising from the additional nuclear degrees of freedom. Despite the fact that the electronic and nuclear characteristic time scales are very different (attosecond, 10^{-18} s vs. femtosecond, 10^{-15} fs), the intense laser field induces a

Correspondence to: A. D. Bandrauk.

Contract grant sponsor: Natural Sciences and Engineering Research Council of Canada.

© 1997 John Wiley & Sons, Inc.
CCC 0020-7608 / 97 / 050503-10

complex correlation between both motions, which we attempt to study by solving numerically the time-dependent Schrödinger equation (TDSE) using the exact, 1-D, three-body Hamiltonian for a H_2^+ molecular ion in an intense, linearly polarized laser field. We reported earlier results of simulations based on TDSE for H_2^+ with 3-D electron and 1-D protons for 212 and 600 nm wavelength [5,6]. Similar calculations for 1-D electrons and 1-D protons were also reported recently [7]. In all these studies, absorbing boundaries were used to remove the electron flux from the finite electron grid (in [7], a nuclei absorber was used as well). Therefore, so far, ATI kinetic spectra in presence of moving nuclei have not been calculated. Similarly, removing the electron flux causes the loss of information about Coulomb exploding protons, with which the lost electron flux was linked (i.e., the information about the $p + p + e^-$ channel was lost) and, consequently, the high-energy part of the reported proton spectrum was incomplete.

We report, in the present article, the first complete calculations of Coulomb explosion spectra of protons and the ATI electron kinetic energy spectra from the dissociating H_2^+. The difficulty with the lost information through absorbing boundaries is overcome with the help of the wave-function splitting technique [8,9], which allows one to propagate in time the absorbed part of the wave function in the asymptotic region (i.e., for the electron coordinate z far from the molecular center of mass) using a much faster algorithm than that used in the zone close to nuclei. We first describe this technique for the frozen internuclear distance, in detail, in the following section of our article. In the third section, we present details of our exact (and, therefore, non-Born–Oppenheimer, with unfrozen nuclei) calculations and show how the wave-function splitting technique was implemented for the case of moving nuclei. In the fourth section, we present the kinetic energy spectra of the dissociating nuclear fragments, which show clear signatures of the charge-resonance-enhanced-ionization (CREI) phenomenon. CREI was first discussed in [10] and further studied using models with frozen nuclear motion [11–13]. Thus, it remained to be investigated whether the effect of enhanced ionization would be washed out by the nuclear dynamics. Our previous non-Born–Oppenheimer calculations [5,6] did not show very clear CREI peaks in the proton spectra due to the above-mentioned electron flux losses through the absorbing boundaries. By contrast, the wave-function splitting technique yields sharp Coulomb explosion peaks due to CREI and also a weaker peak originating from the center of the initial wave packet. The fifth section contains the ATI electron spectra from H_2^+, showing considerable enhancement of peaks, both in the low-energy part and in high-energy part: A very broad high energy tail in energy spectra of electrons are seen, extending up to $16U_p$, where $U_p = e^2E_M^2/4m\omega^2$ is the electron ponderomotive energy. Typically, the bulk of (about 99%) ionized electrons have strong ATI peaks in the energy range less than $3U_p$ (this limit corresponds to the maximum drift velocity for electrons born in the continuum with zero kinetic energy [14]). Recently, it was pointed out that, contrary to the harmonics generation spectra, the ATI electron spectra do not have a sharp cutoff but extend much further than $3U_p$ due to the rescattering of an electron returning to the nucleus [14–17]. So far, these effects were much discussed for ATI from atoms. Recent measurements of extremely hot (multi-keV) electrons ejected from a xenon cluster [18] suggest that these rescattering effects may be much stronger in molecules and clusters than in atoms since the electrons ionizing toward neighboring dissociating nuclei can scatter on them and absorb additional photons. Obviously, such a possibility does not exist in atoms or atomic ions. Therefore, the hot electrons are less likely in atoms, since they can originate only from the returning electrons scattered on one nucleus, while in the dissociating molecule, an ionizing electron can encounter directly on its path another scatterer on which additional photons can be absorbed. The investigation of this issue is the main focus of the fifth section.

We use, in the present article, a 1-D model for both electronic and nuclear degrees of freedom. It appears that the 1-D dynamics describes reasonably well the movement of the atomic electrons [2] in the linearly polarized, intense laser fields ($I \geq 10^{14}$ W/cm^2) and reproduces correctly such phenomena as high harmonic generation or ATI. Since the molecules in intense fields are aligned, due to the torque from laser-induced polarizabilities [19], one may expect that 1-D molecular dynamics can also reproduce the most saliant features of the dynamics in intense laser fields (($I \geq 10^{14}$ W/cm^2, i.e., above the ionization threshold), in particular, in the long wavelength regime, when the molecule dissociates via the bond softening mechanism and the vibrational trapping does not take place [4] (it was shown recently [20] that for wavelengths much

shorter than 600 nm and for intensities below the ionization threshold the vibrational trapping can cause dissociating fragments to be emitted at right angles to the polarization direction). Such a 1-D molecular dynamics was presented recently [7]. It appear that the potential surfaces resulting from 1-D electron motion are quite close to exact 3-D surfaces, providing, thus, a model for nuclear motions with correct molecular harmonic and anharmonic constants as well as correct dissociation energy [7].

Description of the Wave Function Splitting Algorithm for Solving the Time-dependent Schrödinger Equation

One of the theoretical approaches to calculate the ATI spectra relies on exact numerical solutions of the time-dependent Schrödinger equation (TDSE) on recently available powerful computers. So far, this approach has been successfully applied to one-electron atoms and molecules (or two 1-D electrons [21]). Typically, in such numerical simulations, the initial wave function of the electron is well localized in space and later becomes spread over very large distances. For a short, intense, 40 fs laser pulse, the front edge of the wave packet of the ionizing electron can be as far as 4000 bohr from the nucleus (for $I = 2 \times 10^{14}$ and $\lambda =$ 600 nm) and continues to expand for longer times. Thus, to avoid reflections from the boundaries, prohibitively large boxes (grids with 32,000 points or more), in which the electron wave packet is fully contained, must be used. The most common solution to this difficulty is to use much smaller boxes with absorbing boundary conditions. This approach allows one to calculate the ionization rates and harmonic generation spectra but it does not allow one to calculate the photoelectron (or ATI) spectra, since the external part of the wave function is absorbed and lost. Also, in our recent 3-D numerical studies of competition between ionization and dissociation [5,6], the use of absorber for the electron flux led to a considerable loss of information about the nuclear movement, i.e., we were unable to reproduce completely the spectra of dissociating fragments from the Coulomb explosion channel since these fragments were linked with the absorbed electron flux. In this article, we develop a technique which allows one to reconstruct the absorbed electron wave packet in momentum space and propagate it in time, analytically, to any time after the pulse turn-off. Thus, with the help of this technique, one can calculate efficiently the photoelectron spectra after the turn-off of the pulse. A similar technique was used earlier [22] for calculating the kinetic energy spectra of photodissociation products, with the laser–molecule coupling neglected in the asymptotic region. Recently [23], this technique has been generalized for nondecaying (for large distances) dipole couplings (for dissociating molecules) and for the calculation of the ATI spectra from time-dependent Schrodinger equation [8,9,24]. In the present work, we extend this technique for solving the TDSE for molecules with moving nuclei. Since the wave-function splitting technique is quite complex in practice, we present, first, this technique for the case of frozen nuclei (or for the hydrogen atom) and explain in the next section how the technique was implemented for the case when the nuclei move. Let us consider a time-dependent, 1-D Schrödinger equation written (in au) in the following form:

$$i\frac{\partial\psi(z,t)}{\partial t} = \left(-\frac{1}{2}\frac{\partial^2}{\partial z^2} + V_C(z,R) + zE(t)\right)\psi(z,t), \tag{1}$$

where

$$V_C(z,R) = -\frac{1}{\sqrt{1+(z-R/2)^2}} - \frac{1}{\sqrt{1+(z+R/2)^2}} \tag{2}$$

and $E(t)$ is the laser electric field. This equation is usually discretized and solved numerically for $|z| < z_M$. We tested this method [8] for the case of the $1-D$ H atom in the laser field of intensity $I = 2.2 \times 10^{14}$ W/cm^2, $\lambda = 630$ nm, and $t_p = 20$ cycles (1 cycle = 2.17 fs). We compared our results with those from [17]. The photoelectron spectra from this reference show a plateau extending up to $8U_p = 70$ eV with a slowly decaying tail up to 130 eV (70 photons absorbed), where $U_p = e^2E_M^2/(4m\omega^2)$ is the electron ponderomotive energy. Thus, the fastest electron has a speed $v_M =$ 2.3 au and in $t_p = 43$ fs can be as far as 4050 bohr. Typically, the integration step in space is $\delta z = 0.25$ bohr, which means that the grids with over 32,000 grid points must be used for a 43 fs pulse. For n

times longer pulses, n time greater grids should be used. This constitutes a serious difficulty, even for 1-D problems. Therefore, a fast algorithm for large z's is very desirable. In particular, since the Coulomb forces are smooth and negligible for large z's, larger integration steps in space δz, as well as much larger steps in time, can be used asymptotically.

Let us divide the total grid into three overlapping regions in space, in which different evolution algorithms will be used: the internal and two external (asymptotic, for positive and negative z's) parts defined by

$$\textit{internal}: \quad |z| < z_{in} \quad \textit{and external}: \quad z_{ex} < |z| < z_M, \tag{3}$$

where $z_{in} - z_{ex} = z_0 > 0$ is the size of the overlap of both regions. In this overlapping (or "matching") region, an absorbing potential is introduced, which we have chosen in the following form:

$$V_{abs}(z) = iV_0\left(\frac{z - z_{ex}}{z_0}\right)^2 \quad \textit{for} \quad z_{ex} < |z| < z_{in}. \tag{4}$$

The electron wave function $\psi(z, R, t)$ is split into internal ψ_{int} and external ψ_{ext} parts, by applying this absorbing potential in the overlapping region, at times $t = k\,\delta t$, where δt is much larger than the integration time dt ($dt = 0.03$ au, $\delta t = 150\,dt = 0.05$ cycle, i.e., in our simulations for $\lambda = 600$ nm, δt is much less than is the laser cycle) with the help of the following formulas:

$$\psi(z, R, t) = \psi_{in}(z, R, t) + \psi_{ex}(z, R, t), \tag{5}$$

$$\psi_{in}(z, R, t) = f(z, \delta t)\psi(z, R, t), \tag{6}$$

$$\psi_{ex}(z, R, t) = (1 - f(z, \delta t))\psi(z, R, t), \tag{7}$$

where

$$f(z, \delta t) = \exp(-\delta t\, V_{abs}(z)) \quad \text{for} \quad z_{ex} < |z| < z_{in}, \tag{8}$$

$$f(z, \delta t) = 1 \quad \text{for} \quad |z| < z_{ex}, \tag{9}$$

and

$$f(z, \delta t) = 0 \quad \text{for} \quad |z| > z_{in}. \tag{10}$$

Our calculation scheme relies on the assumption that in the asymptotic zone (defined by $|z| > z_{ex}$) the Coulomb potential can be neglected. This allows us to perform the time evolution exactly and over an arbitrary time interval by calculating first the wave function in the velocity gauge $\psi_v(z, t)$ with the help of the formula

$$\psi_v(z, R, t) = \exp(-i\,\Delta(t, 0)z)\psi_{ex}(z, R, t), \tag{11}$$

where

$$\Delta(t_2, t_1) = -\int_{t_1}^{t_2} E(t)\,dt \tag{12}$$

is the electric field area over the interval t_1, t_2. Next, we calculate the Fourier transform $\varphi_v(p, t)$ of $\psi_v(z, t)$, which evolves in time according to the equation

$$\varphi_v(p, R, t_2) = U(t_2, t_1)\varphi_v(p, R, t_1), \tag{13}$$

where the exact propagator U is given by

$$U(t_2, t_1) = \exp\left(-\frac{i}{2}\int_{t_1}^{t_2}(p^2 + 2\,\Delta(t, 0)p + \Delta^2(t, 0))\,dt\right). \tag{14}$$

In our algorithm, we perform the series of following operations at each time $t_k = k\,\delta t$:

(i) The exact time evolution (including field + Coulomb potential) of ψ_{in} is evaluated in the internal zone ($|z| < z_{in}$) using the split-operator spectral method [25], as originally applied to H_2^+ [25].

(ii) The outgoing wave is eliminated from the internal zone with the help of Eq. (6).

(iii) The splitting operation described by Eq. (7) is performed to provide the outgoing wave ψ_{ex} defined in the "matching zone," $z_{ex} < |z| < z_{in}$.

(iv) The velocity gauge wave function ψ_v (in the external region) and its Fourier transform φ_v are calculated in the overlap region:

$$\varphi_v(p, t_k) = (2\pi)^{-\frac{1}{2}}\int_{z_{ex}}^{z_{in}} \exp(-ipz)\psi_v(z, t_k)\,dz. \tag{15}$$

(v) The momentum wave function $\varphi(p, t_f)$ is propagated to some final time $t_f \geq t_p$ (at which the photoelectron spectra are to be calculated), using the exact formula

$$\varphi_v(p, R, t_f) = U(t_f, t_k)\varphi_v(p, R, t_k). \tag{16}$$

(vi) The momentum wave function $\varphi_v(p, R, t_f)$ is added to $\varphi_v^{(k-1)}(p, R, t_f)$'s accumulated at previous steps, i.e.:

$$\varphi_v^{(k)}(p, R, t_f) = \varphi_v^{(k-1)}(p, R, t_f) + \varphi_v(p, R, t_f).$$

(vii) The loop ends here and calculation starts at step (i) with the integer k replaced by $k + 1$.

The most difficult part of the scheme presented here is the choice of the free parameters: V_{abs}, δt, z_{in}, and z_0. Several obvious necessary (but not sufficient) physical condition should be satisfied. First, the external zone ($|z| > z_{ex}$) in our scheme is the asymptotic region in which we neglect the Coulomb forces; therefore, we must require that at $z = z_{ex}$ the Coulomb force is much less than the electric force eE_M, i.e.:

$$\frac{e^2}{z_{ex}^2} \ll eE_M. \tag{17}$$

Second, our scheme is based on the assumption that the wave entering the "matching" zone (of length z_0) does not return back to the nucleus, as well as the wave exiting this zone does not return to it. This means that we should require that the classical ponderomotive radius α_0 is much smaller than is z_{ex} and also smaller than the size of the matching "zone" z_0:

$$\alpha_0 \ll z_{ex} \quad \text{and} \quad \alpha_0 \ll z_0, \quad \text{where } \alpha_0 = \frac{eE}{m\omega^2}. \tag{18}$$

The above conditions, (17) and (18), ensure also that all possible interferences in continuum (which are expected to take place in the near nuclei zone) are appropriately taken into account by the exact algorithm used in the internal zone. In addition, we must require that the matching should be redone after the time interval δt shorter than the time necessary to move for the fastest electron across the matching "zone." Assuming that the fastest electron has the energy $E_{max} = 8U_p$, we thus get

$$\delta t \ll \frac{z_0}{4\sqrt{mU_p}}. \tag{19}$$

In our calculations, δt is also much less than the laser cycle. Finally, the absorption should occur on the distance z_0 longer that de Broglie wavelength of the slowest electron. Assuming that the slowest electron has the energy $\hbar\omega$, we thus get

$$z_0 \gg \pi\sqrt{\frac{2}{(\hbar\omega)}}. \tag{20}$$

For the maximal laser intensity chosen in this article, $I = 2.0 \times 10^{14}$ W/cm^2, and the wavelength $\lambda = 600$ nm, the values of two relevant parameters are $\alpha_0 = 13.1$ bohr, $U_p = 0.24$ au $= 6.5$ eV, and $\omega = 0.076$ au $= 2.066$ eV. We list in Table I the values of all parameters which we used in our calculation and which satisfy all inequalities Eqs. (17)–(20).

The spectra of ionized electrons, defined for each R, where calculated according to the formula

$$S(E, R) = \left(\left|\varphi_+\left(p(E), R, t_f\right)\right|^2 + \left|\varphi_-\left(p(E), R, t_f\right)\right|^2\right)\frac{m}{p(E)}, \tag{21}$$

where $\varphi_+, (\varphi_-)$ are wave function corresponding to the electron moving in the direction of positive (negative) direction along the z axis, respectively, and $p(E) = \sqrt{2mE}$. We checked the method by comparing our results for a 1-D H-atom with those of [17,24] and with the results from the one-box calculations. Slight disagreement between the heights (not positions) of several first photoelectron peaks was seen if our spectra were calculated right at the end of the pulse. This disagreement disappears when the spectra are calculated at later

TABLE I
Values of parameters (in atomic units) used in the wave-function splitting scheme.

dt	δt	dz	z_{ex}	z_0	n_{in}	n_{ex}	V_{abs}	R_{max}	n_R
0.03	4.5	0.25	512	150	4196	7168	2	70	840

n_{in} is number of grid points in the internal zone ($|z| < z_{in}$) and n_{ex} is the number of grid points in the external zone, in momentum space with the momentum resolution $\Delta p = 2\pi/7168$ a.u.

times, $t_f > t_p$ (with the laser turned-off for $t_f > t_p$), since then all slow electrons have enough time to leave the matching zone. Therefore, in all calculations, we allow the system to evolve without the laser field for several subsequent cycles and then calculate the ATI spectra (see [8] for more details).

The two-box integration technique presented here was first applied for calculating the ATI spectra from a H_2^+ molecule frozen at an internuclear distance R [8] and those results were used later for comparison with the full non-Born–Oppenheimer calculations, presented in next sections.

A Non-Born–Oppenheimer 1-D Model of H_2^+ in Intense Laser Fields

We solved numerically the complete, three-body, time-dependent Schrödinger equation for moving electrons and nuclei (in au):

$$i\frac{\partial\psi(z,t)}{\partial t} = H(z,R,t)\psi(z,R,t)$$

where

$$H(z,R,t) = H_R(R) + V_C(z,R) + H_z(z), \quad (22)$$

$$H_z(z) = -\beta\frac{\partial^2}{\partial z^2} - \kappa z E(t),$$

$$H(R) = -\frac{1}{m_p}\frac{\partial^2}{\partial R^2} + \frac{1}{R}, \quad (23)$$

$$\beta = \frac{(2m_p + m_e)}{4m_p m_e}, \qquad \kappa = 1 + \frac{m_e}{2m_p + m_e}, \quad (24)$$

and m_e and m_p ($m_e = 1$ in au) are, respectively, the electron and proton masses. The Hamiltonian of Eq. (22) is the *exact* three-body Hamiltonian obtained after separation of the center-of-mass motion [5]. The time evolution of the internal wave function ψ_{in} was performed in the same way as described in [5,25] (using the split-operator method), whereas the external part (obtained recovered from the absorber at each δt step) $\varphi^{(k)}(p,R,t)$ was evolved with the help of the propagator [Eq. (14)] for times t_1 and $t_2 = t_1 + \delta t$, where $\delta t = 150\,dt$ (as previously). After each "big" time step δt was accomplished, the new portion $\varphi(p,R,t+\delta t)$ was added to the previously accumulated portion. The operation $\exp(-idt\,H(R))$ was applied to the accumulated part of $\varphi^{(k)}(p,R,t)$ at each "small" time step dt. The potential $V_C(z,R)$ was neglected in the external zone, whereas the Coulomb repulsion $1/R$ was retained in $H(R)$.

We used laser pulses of total duration 20 cycles (40 fs), having the wavelength $\lambda = 600$ nm, with a five-cycle rise and fall. The values of various parameters used in the present calculations are given in Table I. We performed numerically the time evolution of the wave functions $\psi_{in}(z,R,t)$ and the external $\varphi(p,R,t)$ for an additional three cycles (6 fs), i.e., up to the final time $t_f = 23$ cycles, using the Hamiltonian without the electric field, in order to allow some more electron–proton waves to leave the interaction region.

The initial wave function, at $t = 0$, was assumed to be in the following form:

$$\psi(z,R,0) = \chi(R)\psi_0(R,z), \quad (25)$$

where $\psi_0(R,z)$ was the eigenfunction of the electron Hamiltonian in H_2^+ (without the laser field) at fixed R. Two distinct initial condition at $t = 0$ were used:

(i) H_2^+ was initially prepared in its vibrational $v = 6$ $\chi(R) = \chi_6(R)$ state, or

(ii) at $t = 0$, H_2^+ was prepared in a superposition of H_2^+ vibrational states, coinciding with the ground vibrational state of the H_2 molecule, i.e.,

$$\chi(R) = \chi_0^{H_2} = \sum_{v=0} c_v \chi_v(R), \quad (26)$$

where

$$c_v = \int_0^\infty dR\, \chi_v(R)\, \chi_0^{H_2}(R) \quad (27)$$

are the Franck–Condon factors.

The latter initial condition, (ii), is close to the experiments, in which H_2^+ is prepared by a steeply rising edge of a pulse, which rapidly ionizes the H_2 molecule.

To interpret the full calculation results, we first calculated the ionization rates for 170 values of R's, frozen, in the range from 3 to 33 bohr. The ionization rates for the laser wavelength $\lambda = 600$ nm are displayed in Figure 1. One observes strong charge resonance enhanced ionization (CREI) peaks around 7 bohr, which were discussed recently by many authors [10–13]. The CREI effect is incredibly strong for the relatively low intensity $I = 5 \times$

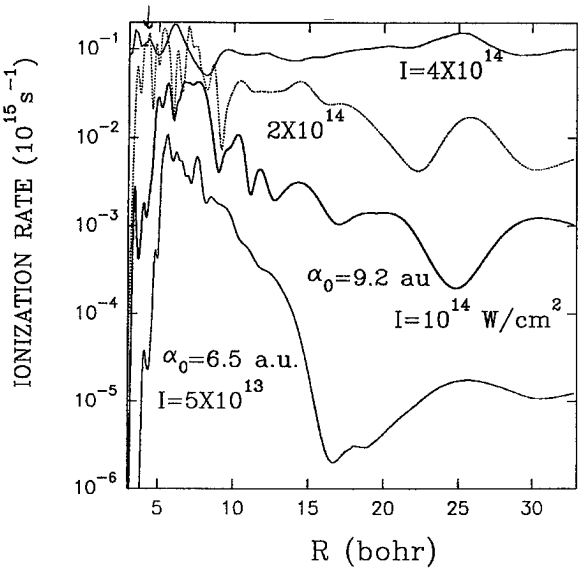


FIGURE 1. Ionization rates as a function of internuclear distance for laser intensities $I = 5 \times 10^{13}$, 10^{14}, 2×10^{14}, and 4×10^{14} W/cm^2 at wavelength 600 nm.

10^{13} W/cm^2 and practically disappears at $I = 4 \times 10^{14}$ W/cm^2, when at a short internuclear distance $R = 4$ au, the H_2^+ ion ionizes with a rate close to the H-atom rate and the ionization rate curve is relatively flat. Note that in addition to those peaks some unexpected features appear for larger R values; in particular, for lower intensities, $I = 5 \times 10^{13}$ W/cm^2, one observes a deep minimum in the ionization rate at $R = 16$ bohr. It originates from the fact that an ionizing electron from one proton comes under the influence of the second proton and does not have enough time to escape from the second proton before the electric-field changes sign. Thus, this electron becomes "trapped" between the two protons. One may expect that the position of this minimum is proportional to the classical radius of the electron in the laser field α_0. This is indeed confirmed by the position of this minimum for a twice higher intensity, which occurs $\sqrt{2}$ times further. We are currently attempting to explain this minimum using classical dynamics of the electron [26,27].

Kinetic Energy Spectra of Dissociating Nuclear Fragments

The wave functions $\psi_{in}(z, R, t_f)$, $\varphi(p, R, t_f)$ allow us to calculate the simultaneous spectra of nuclear fragments $S_{in}(z, p_R, t_f)$ and $S_{ex}(p, p_R, t_f)$, where p, p_R are the momenta of the electron and the protons, by simply calculating the Fourier transform of the asymptotic part (large R) of $\psi_{in}(z, R, t_f)$, $\varphi(p, R, t_f)$ with respect to the R variable and next calculating the square of absolute values of Fourier transforms (see [6] for details). The integrated over electronic degrees of freedom spectra $S(p_R)$ are plotted in Figure 2 (the contributions from internal and external boxes are added up).

Two different initial condition were used in our calculations (see the previous section for a description of these conditions), on which the spectra depend strongly. We show in Figure 2(a) spectra obtained from H_2^+ which initially, at $t = 0$, was prepared in its vibrational $v = 6$ state (two laser intensities were used $I = 10^{14}$ and 2×10^{14}

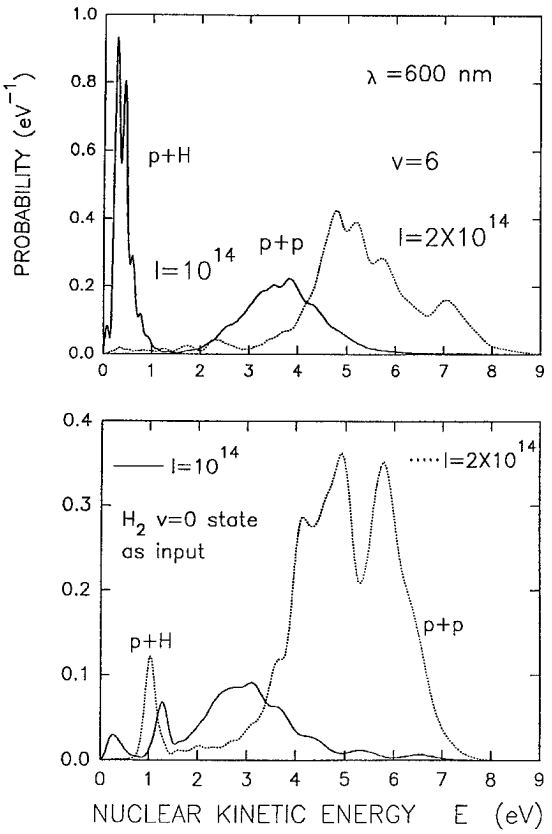


FIGURE 2. Kinetic energy spectra of dissociating nuclear fragments. The numerical simulation was initialized either (a) from the $v = 6$ state of the H_2^+ or (b) from the Franck–Condon superposition of vibrational states of H_2^+, defined by Eqs. (26) and (27). Laser intensities used: (——) $I = 10^{14}$ W/cm^2; (· · · · · ·) $I = 2 \times 10^{14}$ W/cm^2, the wavelength $\lambda = 600$ nm.

W/cm^2), whereas in Figure 2(b), we show the spectra resulting from H_2^+ prepared, at $t = 0$, in a superposition of vibrational states, coinciding with the ground vibrational state of the H_2 molecule, multiplied by the electronic wave function of H_2^+ [see Eqs. (25)–(27)]. Figure 3 shows the same spectra on a logarithmic scale. The low-energy peaks, seen Figure 2, are related to the bond-softening mechanism [4]: In Figure 2(a), there are two very close peaks, at 0.26 and 0.43 eV. Their position is close to the net absorption of one photon (presumably via a multiphoton process) from the $v = 6$ state: The energy released into the dissociation channel from this process, when, initially, the molecule was in its vibrational state v, is given by a simple, conservation energy formula:

$$E = n\hbar\omega - (-I_p - E_v), \qquad (28)$$

where $I_p = 0.67$ au is the ionization potential of the 1-D H atom, the energy vibrational level v of H_2^+ (from which photons are absorbed), and n is the net number of absorbed photons (in general, it is a multiphoton process: an absorption of m photons followed by the reemission of k photons, with the condition that $n = m - k > 0$). For the wavelength $\lambda = 600$ nm used in the present work, $\hbar\omega = 2.066$ eV. Thus, from $v = 6$, for $n = 1$, a peak at 0.542 eV is expected, and from $v = 5$, at 0.343 eV. Two factors may be responsible for the fact that in our simulation two peaks are seen, instead of one expected at 0.542 eV: (i) First, a rapid rise, in five cycles, can populate the neighboring $v = 5$ state (or, in other words, the peak is shifted by the fact that our pulse is spectrally very broad), and (ii) the downward Stark shift of the level $v = 6$ occurs. Similarly, the low-energy peak seen in Figure 2(b) originates from the net two-photon absorption from low vibrational states: Using $n = 2$, $v = 0$, 1 or 2, one gets the peak positions at 1.25, 1.50, or 1.74 eV, respectively, whereas the simulation (which used the H_2 $v = 0$ state, as initial input for the vibrational wave function) yields a broad peak at $E = 1.06$ eV. Again, a considerable spectral width of our pulse and the Stark shifts are the main reason of the observed discrepancy between the position of expected and seen peaks, i.e., the presence of photons having a frequency only 5% less than that of the carrier frequency can shift the peak by 0.2 eV or more and thus explain the observed shifts.

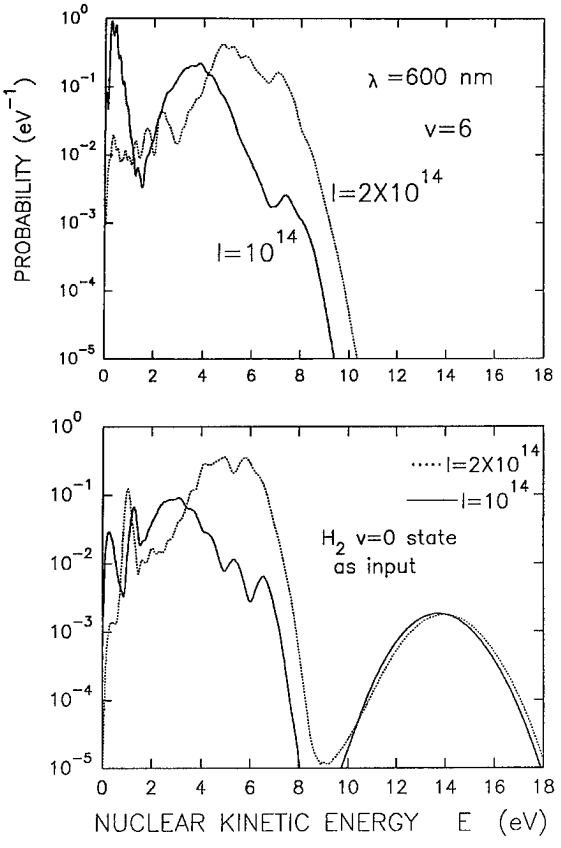


FIGURE 3. Same as in Figure 2 but on a logarithmic scale.

The high-energy broad peaks, $E > 3.8$ eV, represent the $p + p + e^-$ Coulomb explosion channel, since in our calculation, they originate from the external part of the wave function $\varphi(p, R, t_f)$. At laser intensity $I = 10^{14}$ W/cm^2, we see a broad peak at $E = 3.8$ eV. If the Coulomb explosion occurred with initial kinetic energy equal to zero, then we can conclude that the Coulomb explosion should be initiated at $R = R_c = 7.16$ bohr, in order to release the Coulomb energy $E_{Coulomb} = 3.8$ eV (according to the relation $E_{Coulomb} = 27.21$ eV$/R_c$, where R_c is in bohr), which is in agreement with Figure 1, in which three peaks are seen, at 5.6, 6.8 and 7.6 bohr. If, in addition, one takes into account the fact that at $R = R_c$ the dissociating $H + p$ have an initial nonzero kinetic energy [varying between 0.2 to 0.8 eV; see the first peak in Fig. 2(a)], one can easily understand the appearance of a broad peak centered at 3.8 eV: Simply, the explosions from three CREI peaks seen in Figure 1 will merge to one broad structure. At higher intensities, Figure 1 shows a considerable shift of CREI peaks toward the lower values of R, in

agreement with the shift of the Coulomb explosion peak resulting from our calculations [seen in Fig. 2(b)], which is now centered at $E = 4.8$ eV and is broader than at the lower intensity. It extends up to 8 eV, which agrees well with the lower limit of CREI peak in Figure 1, which is sharply cut at 3.05 bohr. Summarizing, the broad peaks in the $p + p$ channel seen in Figure 3 agree well with the expectations for the CREI peaks based on the model with frozen nuclei.

We display in Figure 3 the same spectra as in Figure 2 but on a logarithmic scale, in order to discuss the high-energy tail. One notes that the tail of proton spectra depends dramatically on the initial conditions: Initializing our simulation from the $v = 6$ of H_2^+ yields spectra sharply cut below 10 eV [Fig. 3(a)], whereas the initialization from the $v = 0$ state of H_2 gives a small (100 times lower than the principal peak) but a clear peak at $E = 14$ eV [Fig. 3(b)] which originates from the Coulomb explosion from the equilibrium position of the H_2 molecule $R_e = 2$ au (note that the equilibria positions in our 1-D model are 2.0 and 2.6 au, instead of 1.6 and 2, for H_2 and for H_2^+, respectively).

Kinetic Energy Electron Spectra from a Dissociating Ion

The ATI spectra presented in this section were obtained by integrating over R the formula (21), in which the external box function $\varphi(p, R, t_f)$, obtained from the complete, non-Born–Oppenheimer calculation was used. The normalized (i.e., the area under the spectrum curve is the ionization probability P_I) ATI spectra are shown in Fig. 4 ($I = 10^{14}$ W/cm^2) and in Figure 5 (2×10^{14} W/cm^2). Our exact non-Born–Oppenheimer results (solid lines) are compared with the ATI spectra originating from the 1-D H atom (□ □ □) and from H_2^+ frozen at $R = R_c$ (△ △ △). One notes a considerable enhancement of the spectrum around $3U_p$ and enhancement at very large energies, up to $16U_p$. A frozen nuclei calculation shows such enhancement at particular large distances (33 au or more [9]), which presumably are close to integer multiples of the classical radius α_0: Classical trajectory calculations show that the electron reaches its maximal kinetic energy at distances z_{max} given by [26,27]

$$z_{max} = m\pi(v_0/\omega + \alpha_0), \qquad (29)$$

where v_0 is the electron's initial velocity.

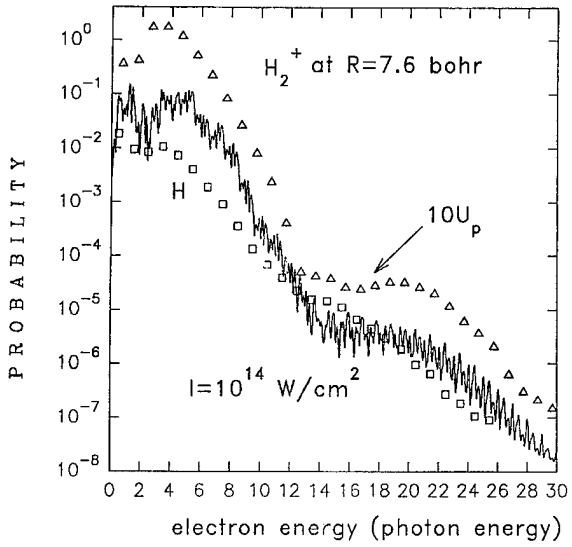


FIGURE 4. (——) ATI photoelectron kinetic energy spectrum from H_2^+ complete non-Born–Oppenheimer calculations compared (△ △ △) with spectra of the nuclei frozen at $R = R_c = 7.6$ au and (□ □ □) with spectra of 1-D H atom. The laser intensity $I = 10^{14}$ W/cm^2, the wavelength $\lambda = 600$ nm, and the simulation was initialized from the v = 6 state of H_2^+. The pulse duration was 20 cycles (1 cycle = 2 fs), with a five-cycle rise and five-cycle turn-off. The ATI spectrum was calculated after 40 cycles. All spectra are normalized: The area under each curve is equal to the ionization probability.

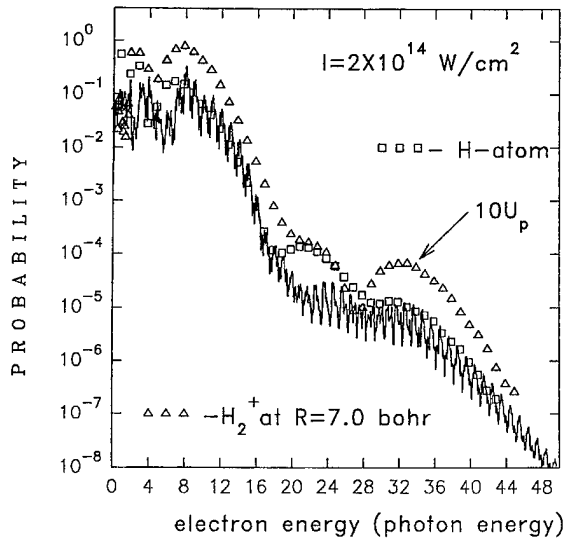


FIGURE 5. Same as in Figure 4 but for the laser intensity $I = 2 \times 10^{14}$ W/cm^2 and $R_c = 7.0$ au.

Concluding Remarks

We have reported that dissociative-ionization of molecular ions exhibits several interesting features seen in nuclear fragment and electron kinetic energy spectra. The expected (theoretical and experimental) low-energy peaks in proton spectra do show up in our spectra calculated from the non-Born–Oppenheimer dynamics. The positions of these peaks agree well with theoretical predictions for Coulomb explosions released from the CREI critical distance R_c. In addition to those peaks, we observe one- and two-photon absorption peaks, as well as weak peaks related to the Coulomb explosion from the H_2 equilibrium internuclear distance. The ATI electron kinetic energy spectra show unexpectedly high tails, extending up to $15U_p$, related, presumably, to the inelastic collisions of electrons moving from one nucleus to another. Finally, we emphasize the usefulness of the wave-function splitting technique for exact calculations of kinetic energy spectra of photofragments emerging from high-intensity laser interaction with molecules. This technique allowed us to recover the electron flux usually lost at absorbing boundaries in previous calculations, with a considerable saving in computer memory and CPU time.

ACKNOWLEDGMENT

The financial support from the Natural Sciences and Engineering Research Council of Canada is gratefully acknowledged.

References

1. G. Mainfray and C. Manus, Rep. Prog. Phys. **54**, 1333 (1991).
2. J. H. Eberly, J. Javanainen, and K. Rzazewski, Phys. Rep. **204**, 331 (1991).
3. A. L'Huillier, K. J., Schafer, and K. C. Kulander, J. Phys. B **24**, 3315 (1991).
4. A. D. Bandrauk, Ed., *Molecules in Laser Fields*, (Marcel Dekker, New York, 1993).
5. S. Chelkowski, T. Zuo, O. Atabek, and A. D. Bandrauk, Phys. Rev. A **52**, 2977 (1995).
6. S. Chelkowski, A. Conjusteau, T. Zuo, and A. D. Bandrauk, Phys. Rev. A **54**, 3235 (1996).
7. K. C. Kulander, F. H. Mies, and K. J. Schafer, Phys. Rev. A **53**, 2562 (1996).
8. S. Chelkowski and A. D. Bandrauk, Int. J. Quantum Chem., Quantum Chem. Symp. **30**, 473 (1996).
9. S. Chelkowski and A. D. Bandrauk, Laser Phys. **7**, 797 (1997).
10. T. Zuo, S. Chelkowski, and A. D. Bandrauk, Phys. Rev. A **48**, 3837 (1993).
11. T. Zuo and A. D. Bandrauk, Phys. Rev. A **52**, R2511 (1995).
12. S. Chelkowski and A. D. Bandrauk, J. Phys. B **28**, L723 (1995).
13. T. Seideman, M. Ivanov, and P. B. Corkum, Phys. Rev. Lett. **75**, 2819 (1995).
14. K. J. Schafer, B. Yang, L. F. DiMauro, and K. C. Kulander, Phys. Rev. Lett. **70**, 1599 (1993).
15. J. Z. Kaminski, A. Jaron, and F. Ehlotzky, Phys. Rev. A **53**, 1756 (1996).
16. G. G. Paulus, W. Becker, and H. Walther, Phys. Rev. A **95**, 2851 (1994).
17. G. G. Paulus, W. Nicklich, Huale Xu, P. Lambropoulus, and H. Walther, Phys. Rev. Lett. **72**, 2851 (1994).
18. Y. L. Shao, T. Ditmire, and H. Hutchinson, Phys. Rev. Lett. **77**, 3343 (1996).
19. B. Friedrich and D. Herschback, Phys. Rev. Lett. **74**, 4623 (1995); P. Dietrich, D. T. Strickland, M. Laberge, and P. Corkum, Phys. Rev. A **47**, 2305 (1993); D. Normand, L. A. Lompré, and C. Cornaggia, J. Phys. B: At. Mol. Opt. Phys. **25** L497 (1992).
20. R. Numico, A. Keller, and O. Atabek, Phys. Rev. A **52**, 1298 (1995).
21. H. Yu, T. Zuo, and A. D. Bandrauk, Phys. Rev. A **54**, 3290 (1996).
22. R. Heather and H. Metiu, J. Chem. Phys. **86**, 5009 (1987).
23. A. Keller, Phys. Rev. A **52**, 1450 (1995).
24. T. Millack, Phys. Rev. A **48**, 786 (1993).
25. S. Chelkowski, T. Zuo, and A. D. Bandrauk, Phys. Rev. A **46**, 5342 (1992); *Ibid.*, J. Phys. B **28**, L349 (1995).
26. P. Moreno, L. Plaja, and L. Roso, J. Opt. Soc. Am. B **13**, 430 (1996).
27. A. D. Bandrauk, S. Chelkowski, H. Yu, and E. Constant, Phys. Rev. A (1997), to appear.

A Quadrature Formula for Correlation Integrals

SONG-TAO DAI, PETER WINKLER

University of Nevada, Department of Physics / 220, Reno, Nevada 89557-0058

Received 3 March 1997; accepted 17 April 1997

ABSTRACT: A convenient Gauss–Laguerre quadrature formula is presented for integrands which depend on the radial coordinates r_1 and r_2 of two bodies as well as on their relative distance r_{12}. This formula generalizes the analytic method by Calais and Löwdin [J. Mol. Spectrosc. **8,** 203 (1962)] to cases when the analytical evaluation is not possible and defaults to an exact method when it is. © 1997 John Wiley & Sons, Inc. Int J Quant Chem **65:** 513–518, 1997

Introduction

Prompted by renewed interest in experimental studies of highly charged ions, small atomic systems have again become the focus of theoretical and experimental investigations. Heliumlike systems, in particular, are once more center stage in a variety of different research projects. Parallel to this development in ion physics runs a similar activity in the study of atomic processes in plasmas. Here, too, multiply ionized two-electron systems are being studied as well as negative ions—predominantly, the negative hydrogen atom, which is an important agent of opacity in astrophysical plasmas.

Dedicated to the memory of Jean-Louis Calais.

Correspondence to: P. Winkler.

Contract grant sponsor: Division of Chemical Sciences, Office of Basic Energy Sciences, Office of Energy Research, U.S. Department of Energy.

The focus of much of modern atomic physics is on electron correlation in various systems and processes. This interest is shared by new developments in the physics of highly ionized systems, including clusters, and by studies of atomic systems in plasma environments. Two-electron systems, in particular, play an important role in this research because of the relative ease with which correlation effects can be identified and calculated. New aspects such as the need to include relativistic effects in highly charged ions, for instance, or the direct inclusion of screening potentials in atomic calculations [1, 2] call for new or at least modified theoretical approaches.

The present research originated from ideas to include realistic, time-dependent screening potentials into atomic calculations *from scratch*, and, by doing so, to calculate line broadening and the lowering of the continuum threshold simultaneously and on the same footing. While the time-dependent aspect is not our focus here, the need for wave functions of larger angular momenta than *S*

© 1997 John Wiley & Sons, Inc.
CCC 0020-7608 / 97 / 050513-06

and P states for heliumlike ions stimulated the present study which builds on the landmark article by Calais and Löwdin [3] in which the authors gave an analytic expression for nested triple integrals of the type "exponential function times integer powers" in all three arguments. Their Eq. (28) reads

$$
\begin{aligned}
[KLM] \equiv & \int_0^\infty dr_1 r_1^K e^{-Ar_1} \int_0^\infty dr_2 r_2^L e^{-Br_2} \\
& \times \int_{|r_1-r_2|}^{r_1+r_2} dr_{12}\, r_{12}^M e^{-Cr_{12}} \\
= & \, 2K!L!M! \sum_{p=0}^{K} \sum_{q=0}^{L} \sum_{r=0}^{M} \frac{(p+q)!}{q!p!} \\
& \times \frac{(K-p+r)!}{r!(K-p)!} \frac{(L-q+M-r)!}{(M-r)!(L-q)!} \\
& \times (A+B)^{-(p+q+1)} (A+C)^{-(K+1-p+r)} \\
& \times (B+C)^{-(L+1-q+M-r)}. \qquad (1)
\end{aligned}
$$

Computationally, this formula—whenever it can be applied—is advantageous over the quadrature formula to be presented in the third section. In many cases of interest, however, the latter provides substantial convenience for programming without compromising accuracy. Furthermore, it can be generalized to the case of more general integrands for which analytic results cannot be obtained. In these cases, the quadrature will no longer be exact but still of a high degree of accuracy.

A Quadraure Formula for Integrals of the Calais–Löwdin Type

The following development makes use of four well-known properties of the Gauss–Laguerre quadrature formula:

- Accuracy: The quadrature replacement

$$\int_0^\infty f(x) e^{-x} dx \simeq \sum_{n=1}^{N} f(x_n) W_n$$

  is exact if $f(x)$ is a polynomial in x of degree $2N+2$ or less and the quantities x_n and W_n are the standard Laguerre points and weights as given, e.g., in Abramowitz and Stegun [4].

- Scaling: An integral of the form

$$
\begin{aligned}
\int_0^\infty f(y) e^{-Ay} dy &= \frac{1}{A} \int_0^\infty f\left(\frac{x}{A}\right) e^{-x} dx \\
&= \frac{1}{A} \sum_{n=1}^{N} f\left(\frac{x_n}{A}\right) W_n
\end{aligned}
$$

  with exactly the same weights W_n.

- Shifting of the lower integral limit:

$$
\begin{aligned}
& \int_0^\infty f(x) e^{-x} dx \\
& \qquad = e^{-y} \int_0^\infty f(\xi + y) e^{-\xi} d\xi.
\end{aligned}
$$

- Interchanging of nested integrals:

$$
\begin{aligned}
& \int_0^\infty dx f(x) e^{-Ax} \int_0^x dy g(y) e^{-By} \\
& \qquad = \int_0^\infty dx g(x) e^{-Bx} \int_x^\infty dy f(y) e^{-Ay}.
\end{aligned}
$$

Repeated application of these simple procedures leads to a convenient quadrature representation of the Calais–Löwdin integral of Eq. (1). We first replace r_1, r_2, and r_{12} by x, y, and z, respectively, and get rid of the absolute value in the lower limit by separating the two possibilities $x < y$ and $x > y$. Furthermore, we want the upper limit to be infinite and—in the end—the lower limit to be zero in order to be able to apply Gauss–Laguerre quadrature techniques:

$$
\begin{aligned}
[KLM] = & \int_0^\infty dx x^K e^{-Ax} \int_x^\infty dy y^L e^{-By} \\
& \times \left[\int_{y-x}^\infty dz z^M e^{-Cz} - \int_{y+x}^\infty dz z^M e^{-Cz} \right] \\
& + \int_0^\infty dy y^L e^{-By} \int_y^\infty dx x^K e^{-Ax} \\
& \times \left[\int_{x-y}^\infty dz z^M e^{-Cz} - \int_{x+y}^\infty dz z^M e^{-Cz} \right]. \qquad (2)
\end{aligned}
$$

With the following replacements, the integrals in the square brackets are changed to the desired form: $\sigma = C[z - (y - x)]$, so that $dz = (1/C)d\sigma$ (we notice that $y - x$ is a *constant* limit for the first of the integrals). Similarly, we substitute in the remaining integrals $\sigma = C[z - (y + x)]$, $\sigma = C[z - (x - y)]$ and $\sigma = C[z - (x + y)]$, respec-

tively. By this, the two square brackets change to

$$\left[\frac{e^{-C(y-x)}}{C}\int_0^\infty d\sigma\left(\frac{\sigma}{C}+y-x\right)^M e^{-\sigma} - \frac{e^{-C(y+x)}}{C}\int_0^\infty d\sigma\left(\frac{\sigma}{C}+y+x\right)^M e^{-\sigma}\right]$$

and

$$\left[\frac{e^{-C(x-y)}}{C}\int_0^\infty d\sigma\left(\frac{\sigma}{C}+x-y\right)^M e^{-\sigma} - \frac{e^{-C(x+y)}}{C}\int_0^\infty d\sigma\left(\frac{\sigma}{C}+x+y\right)^M e^{-\sigma}\right].$$

We combine the square brackets with the integrals on their immediate left after substituting $\tau = (B + C)(y - x)$ and $\tau = (A + C)(x - y)$, respectively:

$$\frac{e^{-Bx}}{C(B+C)}\int_0^\infty d\tau\left(\frac{\tau}{B+C}+x\right)^L e^{-\tau} \times\int_0^\infty d\sigma\left(\frac{\sigma}{C}+\frac{\tau}{B+C}\right)^M e^{-\sigma} - \frac{e^{-Cx}e^{-(B+C)x}}{C(B+C)} \times\int_0^\infty d\tau\left(\frac{\tau}{B+C}+x\right)^L e^{-\tau} \times\int_0^\infty d\sigma\left(\frac{\sigma}{C}+\frac{\tau}{B+C}+2x\right)^M e^{-\sigma}.$$

and

$$\frac{e^{-Ay}}{C(A+C)}\int_0^\infty d\tau\left(\frac{\tau}{A+C}+y\right)^K e^{-\tau} \times\int_0^\infty d\sigma\left(\frac{\sigma}{C}+\frac{\tau}{A+C}\right)^M e^{-\sigma} - \frac{e^{-Cy}e^{-(A+C)y}}{C(A+C)} \times\int_0^\infty d\tau\left(\frac{\tau}{A+C}+y\right)^K e^{-\tau} \times\int_0^\infty d\sigma\left(\frac{\sigma}{C}+\frac{\tau}{A+C}+2y\right)^M e^{-\sigma}.$$

The final integrations require only scaling but no shifting of the quadrature. The overall result is

$$\begin{aligned}[KLM] = {} & \frac{1}{(A+B)C(B+C)}\int_0^\infty d\rho\left(\frac{\rho}{A+B}\right)^K e^{-\rho} \\ & \times\int_0^\infty d\tau\left(\frac{\tau}{B+C}+\frac{\rho}{A+B}\right)^L e^{-\tau} \\ & \times\int_0^\infty d\sigma\left(\frac{\sigma}{C}+\frac{\tau}{B+C}\right)^M e^{-\sigma} \\ & -\frac{1}{(A+B+2C)C(B+C)} \\ & \times\int_0^\infty d\rho\left(\frac{\rho}{A+B+2C}\right)^K e^{-\rho} \\ & \times\int_0^\infty d\tau\left(\frac{\tau}{B+C}+\frac{\rho}{A+B+2C}\right)^L e^{-\tau} \\ & \times\int_0^\infty d\sigma\left(\frac{\sigma}{C}+\frac{\tau}{B+C}+\frac{2\rho}{A+B+2C}\right)^M e^{-\sigma} \\ & +\frac{1}{(A+B)C(A+C)}\int_0^\infty d\rho\left(\frac{\rho}{A+B}\right)^L e^{-\rho} \\ & \times\int_0^\infty d\tau\left(\frac{\tau}{A+C}+\frac{\rho}{A+B}\right)^K e^{-\tau} \\ & \times\int_0^\infty d\sigma\left(\frac{\sigma}{C}+\frac{\tau}{A+C}\right)^M e^{-\sigma} \\ & -\frac{1}{(A+B+2C)C(A+C)} \\ & \times\int_0^\infty d\rho\left(\frac{\rho}{A+B}\right)^L e^{-\rho} \\ & \times\int_0^\infty d\tau\left(\frac{\tau}{A+C}+\frac{\rho}{A+B+2C}\right)^K e^{-\tau} \\ & \times\int_0^\infty d\sigma\left(\frac{\sigma}{C}+\frac{\tau}{A+C}+\frac{2\rho}{A+B+2C}\right)^M e^{-\sigma}. \end{aligned} \quad (3)$$

The corresponding quadrature formula is given as

$$\begin{aligned}[KLM] = {} & \frac{1}{C(B+C)}\left\{\frac{1}{A+B}\sum_{k=1}^{N_k} W_k\left(\frac{\rho_k}{A+B}\right)^K \right. \\ & \times\sum_{l=1}^{N_l} W_l\left(\frac{\tau_l}{B+C}+\frac{\rho_k}{A+B}\right)^L \\ & \times\sum_{m=1}^{N_m} W_m\left(\frac{\sigma_m}{C}+\frac{\tau_l}{B+C}\right)^M \\ & -\frac{1}{(A+B+2C)}\sum_{k=1}^{N_k} W_k\left(\frac{\rho_k}{A+B+2C}\right)^K \\ & \times\sum_{l=1}^{N_l} W_l\left(\frac{\tau_l}{B+C}+\frac{\rho_k}{A+B+2C}\right)^L \\ & \left.\times\sum_{m=1}^{N_m} W_m\left(\frac{\sigma_m}{C}+\frac{\tau_l}{B+C}+\frac{2\rho_k}{A+B+2C}\right)^M\right\} \end{aligned}$$

$$+\frac{1}{C(A+C)}\left\{\frac{1}{A+B}\sum_{k=1}^{N_k}W_k\left(\frac{\rho_k}{A+B}\right)^L \times\sum_{l=1}^{N_l}W_l\left(\frac{\tau_l}{A+C}+\frac{\rho_k}{A+B}\right)^K \times\sum_{m=1}^{N_m}W_m\left(\frac{\sigma_m}{C}+\frac{\tau_l}{A+C}\right)^M -\frac{1}{(A+B+2C)}\sum_{k=1}^{N_k}W_k\left(\frac{\rho_k}{A+B+2C}\right)^L \times\sum_{l=1}^{N_l}W_l\left(\frac{\tau_l}{A+C}+\frac{\rho_k}{A+B+2C}\right)^K \times\sum_{m=1}^{N_m}W_m\left(\frac{\sigma_m}{C}+\frac{\tau_l}{A+C}+\frac{2\rho_k}{A+B+2C}\right)^M\right\}. \tag{4}$$

We notice, in particular, that all integrands have the general form of a polynomial multiplied by an exponential function. The quadrature gives in these cases exact results provided that the number of quadrature points is at least equal to $(D/2) - 1$, where D is the degree of the polynomial in one variable. In the present case, the degree for the variable ρ is equal to $M + K + L$, while for the variables τ and σ, it is $M + K$ (or $M + L$) and M, respectively.

The General Quadrature Formula

The more general integral

$$I \equiv \int_0^\infty dr_1 f(r_1)e^{-Ar_1}\int_0^\infty dr_2 g(r_2)e^{-Br_2} \times\int_{|r_1-r_2|}^{r_1+r_2} dr_{12}\,h(r_{12})e^{-Cr_{12}}$$

can as well be represented by a quadrature formula. Again, if the functions f, g, and h are polynomials in their respective arguments, the representation will be exact provided that the number of quadrature points is sufficiently large. In this case, the sole benefit of a quadrature representation over the direct evaluation by the Calais–Löwdin techniques is a substantial saving in programming work. If, however, the functions are not polynomials, an optimally scaled Gauss–Laguerre quadrature is still an efficient way to evaluate the necessary integrals. The various procedures of scaling, shifting, and interchanging of integrals are exactly as in the preceding section and need not be repeated here. The final quadrature formula is given as

$$I=\frac{1}{C(B+C)}\left\{\frac{1}{A+B}\sum_{k=1}^{N_k}W_k f\left(\frac{\rho_k}{A+B}\right) \times\sum_{l=1}^{N_l}W_l g\left(\frac{\tau_l}{B+C}+\frac{\rho_k}{A+B}\right) \times\sum_{m=1}^{N_m}W_m h\left(\frac{\sigma_m}{C}+\frac{\tau_l}{B+C}\right)\right\} -\frac{1}{(A+B+2C)}\left\{\sum_{k=1}^{N_k}W_k f\left(\frac{\rho_k}{A+B+2C}\right) \times\sum_{l=1}^{N_l}W_l g\left(\frac{\tau_l}{B+C}+\frac{\rho_k}{A+B+2C}\right) \times\sum_{m=1}^{N_m}W_m h\left(\frac{\sigma_m}{C}+\frac{\tau_l}{B+C}+\frac{2\rho_k}{A+B+2C}\right)\right\} +\frac{1}{C(A+C)}\left\{\frac{1}{A+B}\sum_{k=1}^{N_k}W_k f\left(\frac{\rho_k}{A+B}\right) \times\sum_{l=1}^{N_l}W_l g\left(\frac{\tau_l}{A+C}+\frac{\rho_k}{A+B}\right) \times\sum_{m=1}^{N_m}W_m h\left(\frac{\sigma_m}{C}+\frac{\tau_l}{A+C}\right)\right\} -\frac{1}{(A+B+2C)}\left\{\sum_{k=1}^{N_k}W_k f\left(\frac{\rho_k}{A+B+2C}\right) \times\sum_{l=1}^{N_l}W_l g\left(\frac{\tau_l}{A+C}+\frac{\rho_k}{A+B+2C}\right) \times\sum_{m=1}^{N_m}W_m h\left(\frac{\sigma_m}{C}+\frac{\tau_l}{A+C}+\frac{2\rho_k}{A+B+2C}\right)\right\}. \tag{5}$$

This formula requires $4N_k$ evaluations of the function f and $4N_k \times N_l$ evaluations of g, while the function h needs to be calculated $4N_k \times N_l \times N_m$ times.

Representative Results

The results of this section—energies of excited P and D states of the helium atom—were selected

to assess the accuracy of both the method and the computer program. Their physical relevance will be discussed in a forthcoming publication. The evaluation of eigenenergies of the helium atom has a long history. After groundbreaking work by Hylleraas [5, 6] and Pekeris [7, 8], the use of perimetric coordinates has become almost customary for bound- and resonance-state calculations (see, e.g., [9–11]). To our knowledge, only the S-state and the P-state energies have actuallly been calculated so far. Because of the present interest in atomic processes in plasmas, all Coulomb interactions in the Hamiltonian were replaced in the present work by screened interactions of the Debye–Hückel type ($e^{-r/D}/r$). In this scheme, one approximates matrix elements with pure Coulomb interactions to a high degree of accuracy by setting the parameter D equal to a very large number. In the present examples, D has been chosen equal to 2.0×10^6 when comparison with Coulombic results was wanted.

As in the earlier work, the form of the wave functions was chosen as

$$ {}^{\sigma}\Psi_L = \sum_{i,j,k} C_{i,j,k}\{r_1^L P_L(\cos\theta_1)e^{-\alpha_i r_1 - \beta_j r_2} \pm r_2^L P_L(\cos\theta_2)e^{-\beta_j r_1 - \alpha_i r_2}\}e^{-\gamma_k r_{12}}. \quad (6) $$

Here, σ indicates the spin multiplicity. Singlet states are associated with the upper (+) sign, and triplet states, with the negative sign. The letter L indicates the overall orbital angular momentum and P_L is the Legendre polynomial of order L. While the linear parameters C_{ijk} are obtained from the diagonalization of the Hamiltonian matrix, the best choice of the nonlinear parameters α_i, β_j, and γ_k is an open question. Different strategies were used in the previous publications [9, 10]. In the present work, we follow the guidelines of the former with the exception that we scale the α, β, and γ parameters in groups until satisfaction of the quantum virial theorem has been achieved, because we hold the correct distribution of kinetic and potential energy for an important property of stationary states. The results of these calculations are shown in Table I, rows 3–5. The entries of row 3 are very close to the data in row 2. This is to be expected because with a Debye parameter as large as 2×10^6 the Debye potential is almost identical to the Coulomb potential. The calculations were performed with 56 basis functions for the P states and 84 for the D states. The quadrature formula

TABLE I

For various values of the Debye parameter D, the binding energies of the lowest states of overall P and D symmetry of the helium atom in a Debye plasma environment are calculated (rows 3 – 5) and compared to previously available data for the case of only Coulomb interactions (row 2).

D in au	^1P	^3P	^1D	^3D
∞	2.12384[a]	2.13316[a]	2.05579[b]	2.05580[b]
2×10^6	2.12353	2.13308	2.05557	2.05560
200	2.10861	2.11816	2.04072	2.04075
20	1.98121	1.99020	1.91864	1.91875

The results of rows 3–5 were obtained from the nonrelativistic Hamiltonian in which all Coulomb interactions were replaced by Debye potentials $e^{-r/D}/r$.

[a] Nonrelativistic calculations by Thakkar and Smith [10].

[b] Experimental data taken from [12].

for the spatial integration was used with six (P states) or seven (D states) quadrature points and weights for each of the three radial coordinates.

It should be emphasized that the results of Table I can, in principle, all be calculated from the original formula by Calais and Löwdin [Eq. (1)]. Numerical quadrature is not required in the computation of D states of two-electron systems even when all Coulomb interactions are replaced by Debye potentials. To employ the quadrature formula in cases where an analytical formula is not available, the quadrature formula has been used to calculate two-electron matrix elements in which the r_{12}^{-1} term has been replaced by a parameterized polarization potential [13]. These potentials contain products such as

$$ \frac{1 - \exp(-ar_1^3)}{r_1^2} \frac{1 - \exp(-ar_2^3)}{r_2^2}. $$

Analytic evaluation is no longer possible. Although the numerators are rather steep cutoff functions, and, hence, difficult to integrate numerically, the Laguerre quadrature yielded in all cases considered an accuracy of three digits with 20 Laguerre points and five digits or better with 52 points. Product wave functions of very diffuse Slater-type orbitals were included in the studies, but no systematic investigation has been done yet.

ACKNOWLEDGMENT

This work was supported by the Division of Chemical Sciences, Office of Basic Energy Sciences,

Office of Energy Research, U.S. Department of Energy.

References

1. P. Winkler, Phys. Rev. E **53,** 1 (1996).
2. L. Zhang and P. Winkler, Int. J. Quantum Chem. **S30** 431 (1996).
3. J. L. Calais and P.-O. Löwdin, J. Mol. Spectrosc. **8,** 203 (1962).
4. M. Abramowitz and I. A. Stegun, *Handbook of Mathematical Functions* (National Bureau of Standards, Washington, DC, 1968).
5. E. A. Hylleraas, Z. Phys. **65,** 209 (1930).
6. E. A. Hylleraas, Rev. Mod. Phys. **35,** 421 (1963).
7. C. L. Pekeris, Phys. Rev. **126,** 1470 (1962).
8. C. L. Pekeris, Phys. Rev. **127,** 509 (1962).
9. P. Winkler and R. N. Porter, J. Chem. Phys. **61,** 2038 (1974).
10. A. J. Thakkar and V. H. Smith, Phys. Rev. A **15,** 16 (1977).
11. P. Winkler and R. Yaris, J. Phys. B: Atom. Mol. Phys. **11,** 4257 (1978).
12. C. E. Moore, *Atomic Energy Levels,* NBJ Circular No. 467 U.S. Govt. Printing Office, Washington, DC, 1949.
13. C. Laughlin and G. A. Victor, *Atomic Physics,* Vol. 3 (Plenum, New York, 1973), p. 247.

Shape Transitions in Polymer Mushrooms Compressed by a Finite-Size Obstacle

GUSTAVO A. ARTECA

Département de Chimie et Biochimie, Laurentian University-Université Laurentienne, Ramsey Lake Road, Sudbury, Ontario, Canada P3E 2C6

Received 3 March 1997; revised 14 April 1997; accepted 17 April 1997

ABSTRACT: We study the interrelation between molecular-shape changes and configurational transitions in isolated grafted chains ("polymer mushrooms") under geometrical confinement. The confinement effects are due to a finite-size obstacle, representing a simple model for the tip of an *atomic-force microscope*. Using an off-lattice polymer model, we monitor how the molecular shape of a short chain is affected by the geometry of the tip. We show the occurrence of shape transitions as the chain "tries to dodge" the approaching obstacle. These transitions can be correlated with changes in the nature of the dominant chain conformations. Using a descriptor of self-entanglements in the polymer chain, we propose a "phase diagram" indicating the regions characterized by free chains, confined chains, chains that can "escape" the tip, and chains whose escape is "frustrated." The results help in better understanding polymer behavior under compression, and they can be useful for designing interphases with targeted properties.
© 1997 John Wiley & Sons, Inc. Int J Quant Chem **65**: 519–530, 1997

Introduction

The study of macromolecules at solid–liquid interfaces finds applications in the modeling of important phenomena such as film adhesion, lubrication, and oil recovery [1]. In addition, the behavior of polymers confined within interfaces is central for understanding the dynamics in cell membranes and the stability of the vesicles used in drug delivery [2].

The models commonly used to study polymers at interfaces include two basic features: (a) a number of chain molecules grafted onto a flat surface [3–9], and (b) various perturbations acting on the chains, e.g., compression or a liquid flow [10–19]. In the limit of low surface coverage, one can neglect chain–chain interactions and reduce the

Contract grant sponsors: Fonds de Recherche de l'Université Laurentienne (FRUL); Natural Sciences and Engineering Researsch Council (NSERC) of Canada.

© 1997 John Wiley & Sons, Inc.
CCC 0020-7608 / 97 / 050519-12

model to a single grafted chain under various deformations, i.e., a "polymer mushroom" [20]. In this work, we deal with the deformation of a permanently grafted polymer mushroom under confinement.

The configurational properties of geometrically confined polymer mushrooms has received a good deal of attention recently [11, 20–24]. In the case of confining grafted chains to an infinite slab, we have shown that pressure affects differently the various features that characterize the shape of a polymer [24]. For instance, it is found that molecular size, molecular anisometry, and the complexity of the chain's self-entanglements do not behave identically during configurational changes [24]. (The notion of "molecular size" is reserved in this work for the mean three-dimensional space actually spanned by the distribution of atoms in a polymer configuration. It must not be confused with the "contour length" of the polymer chain or the number of monomers.)

Geometrical confinement can also be used to study other phenomena. For instance, a polymer mushroom compressed by a *finite-size* obstacle can be used to simulate the effect on macromolecules of a scanning-tunneling microscope or *atomic-force microscope* tip (AFM-tip) [20, 21]. Recent studies predicted the occurrence of marked changes in molecular size as the chain "tries to dodge" an approaching AFM-tip. These changes can take the form of "escape transitions" or, under special conditions, hysteresis [20, 21]. Previous studies in the literature have analyzed these configurational transitions by looking at the scaling regimes in the molecular size [3, 20, 21]. These analyses, based on mean-field approximations, use the notion that a chain can be broken up into a number of "blobs" whose effective size is predicted from the partial number of monomers (i.e., using scaling arguments) [3]. This approach, however, breaks down in short polymers [3, 10] or in arbitrarily long polymers under strong compression [21]. In addition, previous work has neglected other aspects of polymer shape that do not necessarily behave in the same fashion (cf. [24]). In the present work, we want to explore these molecular-shape transitions in more detail for systems where scaling arguments [3] are not applicable.

In practice, we analyze the deformation of a *short* polymer chain by an approaching AFM-tip. Within this context, we address the following questions:

(a) Are there recognizable configurational transitions when the effect of confinement is purely entropic (i.e., when the AFM-tip changes only the configurational space and *not* the energy of the chains)? This situation corresponds to the simplest polymer model, where monomers present only a purely repulsive (excluded-volume) interaction and there are no energy barriers.

(b) Can molecular features, other than molecular size, detect the occurrence of configurational transitions during compression?

(c) What are the shape features characteristic of the dominant chain configurations found under all possible confinement conditions? Is there a finite-size analog to a "phase diagram," where the configurational "phases" have distinct molecular shape features?

We address these issues by performing computer simulations of an AFM-tip interacting repulsively with the polymer mushroom. The AFM-tip consists of a truncated cone with a flat disklike face exposed to the grafting surface. The polymer chain is modeled as an off-lattice continuum with excluded-volume interaction. Within the specifications of this simple model, we explore the compression of the polymer mushroom under AFM-tips with variable disk radii and distance to the grafting surface.

The work is organized as follows: The next section discusses the models used for the tip and the chain, as well as the sampling of configurational space. A following section discusses the evaluation of the mean values for molecular-shape descriptors. Another section presents the results for shape transitions and configurational changes. Further comments and conclusions are found in the closing section.

Configurations of a Model Polymer Mushroom with Confinement

We deal with a single polymer chain, permanently grafted by a terminal point to a flat, impenetrable surface. The grafted chain has a constant number of monomers n. The polymer is approxi-

mated by a bead-and-string "necklace" model, consisting of n monomers ("beads") and a constant bond length l between consecutive beads [25]. In absence of confinement, the linear chain is allowed to adopt all possible conformations subject to two constraints: (a) the chain does not penetrate the grafting surface, and (b) the monomers satisfy an *excluded volume* condition. The excluded volume is a repulsive interaction between monomers, where nonbonded beads are kept at distances of at least r_{ex} (the radius of excluded volume). Configurations are found as long as $r_{ex} < 2l$. (In the limit $r_{ex} \to 2l$, the chain becomes a rigid rod.)

In this work, we deal only with the effects of confinement on one type of polymer chain. Therefore, r_{ex}, l, and n are taken as constants. To produce chains whose dimensions are comparable to grafted oligopeptides in the presence of a "good solvent," we have chosen $l = 3.8$ Å, $r_{ex} = 3.43$ Å, and $n = 25$. The r_{ex} value is taken from the repulsive part of the Sutherland potential of the molecule of CO_2 [26]. Its value is representative of the effective mean size of an amino acid residue in a polypeptide chain in a good solvent.

The chain is terminally grafted to the plane by the first bead, which is taken as the origin for the coordinate framework. The first bond (between beans "1" and "2") is chosen perpendicular to the plane, and it defines the "z" axis. (This particular grafting condition is only introduced for simplifying the computation of self-entanglements [24]. It has little influence on the accessible mean molecular shapes.)

The 25-bead polymer chains are modeled by an off-lattice continuum. The accessible molecular shapes are known for "free" (unconfined) linear chains [25, 27] and chains confined to a slab defined by two parallel planes [24]. In our present case, a finite-size obstacle introduces new constraints on the accessible configurations.

The confining AFM-tip is modeled as a large truncated cone, pointing toward the grafting surface. The base is a chosen as circular disk parallel to the surface, centered over the grafted terminal end of the chain. The shape of the tip is specified by three parameters, as illustrated in Figure 1. The distance between the base of the tip and the grafting plane is indicated by L and the radius of the base is ρ. The conical shape is defined by the angle α. In this work, only one value of the angle was considered ($\alpha = 45°$).

The parameters L and ρ control the confinement. A number of special cases are noted:

(i) For a fixed L value ($L > l$), confinement within a slab is ensured when $\rho = (n - 2)l$, representing the maximum distance a grafted chain can be stretched parallel to the surface. Therefore, strong confinement corresponds to the case of large ρ and small L values.

(ii) For a fixed ρ value ($\rho > 0$), the effects of confinement will disappear if $L > (n - 1)l$. (In practice, they disappear at smaller L values, *vide infra*). At this point, we find the mean shape of the free grafted chain. We refer to this case as the "free" or "unconfined" chain limit.

(iii) For an arbitrary L value, the unconfined chain limit is also reached if the disk is vanishingly small ($\rho \to 0$). The limits (ii) and (iii) provide a test for the accuracy of the simulations.

The AFM-tip is a repulsive barrier to the polymer mushroom. Therefore, "acceptable" configurations must have *neither bead nor bond* penetrating the tip. This condition is checked bead by bead as the chain is built. We proceed as follows: From the second bead, we start a random walk, with constant step-length l. Let $\mathbf{r}_i = (x_i, y_i, z_i)$ be the position vector of a bead that meets the excluded volume criteria. This tentatively accepted bead lies

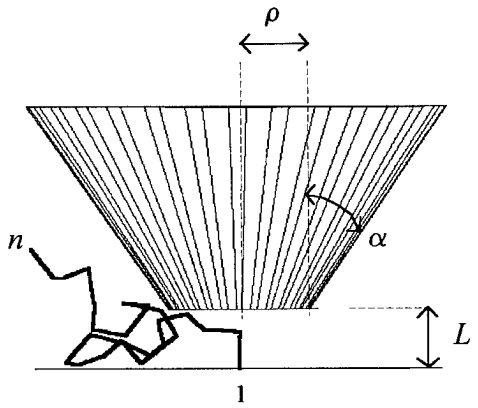


FIGURE 1. Geometrical parameters defining the shape of the AFM-tip model.

outside the tip if

$$x_i^2 + y_i^2 > [\,\rho + (z_i - L)\tan\alpha]^2, \qquad \text{for } z_i > L. \tag{1}$$

Whenever Eq. (1) is not satisfied, the partial chain conformation is rejected and the search restarts. However, two bonded beads could still lie outside the tip, yet their bond intersects it. Our model excludes also this possibility. Whenever two connected beads with positions $\mathbf{r}_i$ and $\mathbf{r}_{i-1}$ satisfy Eq. (1), one must ensure that all points $\mathbf{r}$ along their bond lie *outside* the three-dimensional space occupied by the tip, Ω_{tip}, i.e.,

$$\mathbf{r} = \mathbf{r}_{i-1} + t(\mathbf{r}_i - \mathbf{r}_{i-1}) \notin \Omega_{tip}, \quad \text{for all } t \in [0,1]. \tag{2}$$

This condition is satisfied if the following second-degree equation for t:

$$X_i(t)^2 + Y_i(t)^2 = [\,\rho + (Z_i(t) - L)\tan\alpha]^2, \tag{3}$$

has *no real solutions* within $t \in [0,1]$, where $Q_i(t) = q_{i-1} + t(q_i - q_{i-1})$, with $Q = X, Y, Z$ used when $q = x, y, z$, respectively. Whenever a partially built chain satisfies Eq. (3) with $t \in [0,1]$, it is rejected and the search restarts with a chain grown anew from the grafted terminal.

Our procedure samples the configurational space of the confined grafted chains by generating *uncorrelated conformers*. (Our approach is essentially the simplest Monte Carlo search [28], where zero-energy conformers are accepted and infinite-energy conformers are rejected.) When the grafted polymers are "grown" in the presence of the AFM-tip, all chains that fail the criterion for excluded volume or tip repulsion are abandoned and not continued. We retain only those chains that are built by adding all beads sequentially *without a single rejection*. These off-lattice simulations are computationally demanding, but they produce a convenient set of independent conformers. Simple statistics can then be used to compute mean molecular-shape properties and study the effect of confinement on them. A few thousand "accepted" conformers are enough to reach accurate estimates.

Our approach poses a heavy demand on the random number generators used for sampling conformations. One must ensure that the generator is not exhausted when the configurational space become very small, e.g., for small L and large ρ values. The performance of different generators was tested and compared. Overall, the most reliable generator is the one by L'Ecuyer [29, 30], which combines two random sequences, with additional shuffling to produce a period of length ca. 2×10^{18}. This is the only generator that gives acceptable results in the limit of strong confinement. At lower confinement, an optimized "shuffled" version [29] of the built-in generator in DEC-Fortran (*MTH$Random*, with a period of ca. 10^{12}) produces statistically identical results, with a slightly faster performance. (All computations were carried out on a DEC 255/233 AXP workstation.)

As an illustrative example of representative polymer configurations, Figure 2 shows a series of AFM-tips with the same radius ($\rho = 20$ Å), approaching the grafted polymer. The "accepted" configurations satisfy the criteria above with $r_{ex} = 3.43$ Å and $n = 25$.

Figure 2 illustrates a number of features observed in our simulations: First, as the tip ap-

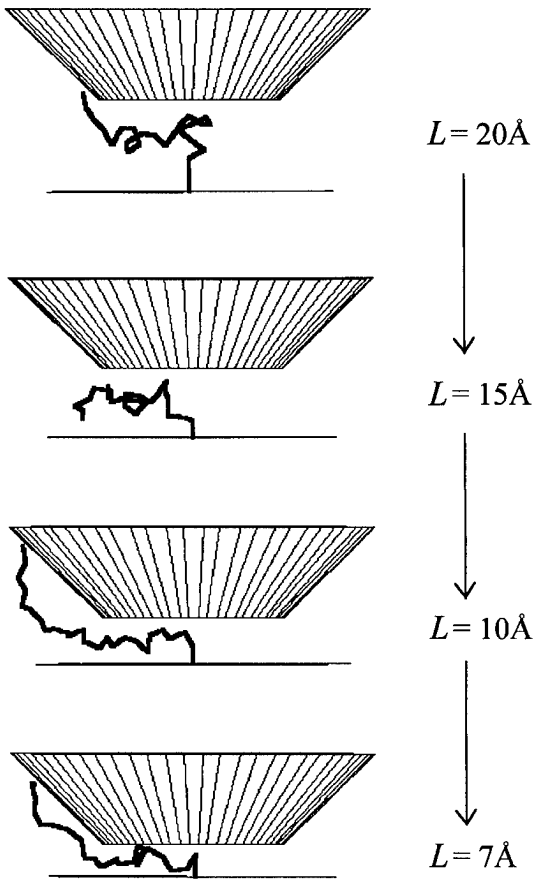


FIGURE 2. Typical deformations of grafted chains caused by an approaching AFM-tip with constant radius, $\rho = 20$ Å.

proaches, deformed chains fold underneath it (i.e., they become effectively "confined"). However, if compression is increased (and the shape of the tip allows it), the polymer chain can "escape" the approaching tip by stretching to the border of the disk and folding outside the confining space. (Actual physical escape, of course, is not possible because the chain is permanently grafted.) In the next sections, we discuss in detail these transformations by calculating the mean molecular-shape features of sampled chains.

Note that we do *not* analyze the dynamics of deformation and "escape" from the tip. Rather, we extract static information by computing a large number of polymer configurations, compatible with the imposed geometrical constraints. Moreover, all phenomena studied in this work are strictly due to the interplay between the spatial configurations and their associated shape. There is *no energy cost* to the chain deformations, since the polymer has only a hard-sphere potential. All effects on molecular shape are *exclusively entropic* and due to a change in configurational space volume during compression. In this sense, the present approach complements other models used in the literature to study confinement on polymer mushrooms [20, 21].

Mean Molecular-Shape Features for Grafted Polymer Configurations

An "accepted" chain configuration, denoted by K_i, can be characterized by a number of molecular-shape features. These properties include some that depend exclusively on nuclear (or "bead") coordinates, such as molecular size and anisometry. Other important features can be conveyed by characterizing the chain's self-entanglements, which depend both on nuclear coordinates and chain connectivity [31]. (Self-entanglements refer to the "twists and turns" in a given linear chain configuration. In principle, entanglements do not depend explicitly on the molecular size.) Recently, we showed that the simultaneous use of molecular size and self-entanglement can provide a thorough characterization of confined polymer conformations [24], as well as configurational transitions during molecular dynamics [32]. These shape features do not necessarily behave the same way during compression [24]. In this work, we follow both molecular size and self-entanglements when the AFM-tip approaches the grafted chains. Our goal is to test whether chain self-entanglements can be used to monitor the occurrence of configurational "escape" transitions.

Molecular size is measured by the radius of gyration. Let $\mathbf{R}_M$ be the position of the center of mass and $\{\mathbf{r}_i, i = 1, 2, \ldots, n\}$ the coordinates for the n beads, both measured with their origin at the grafted terminal. The "instantaneous" square radius of gyration for a given conformer is

$$R_G^2 = \frac{1}{n}\sum_{i=1}^{n} \|\mathbf{r} - \mathbf{R}_M\|^2. \qquad (4)$$

We also follow the *mean height* of the polymer (h), measured from the grafting plane. Using the coordinates in Eq. (1), we have

$$h = \frac{1}{n}\sum_{i=1}^{n} z_i, \qquad \text{where } z_i > 0, \forall i. \qquad (5)$$

Chain self-entanglements take into account the "trace" of polymer chain, in addition to the monomer positions. An effective measure of entanglement complexity can be given in terms of the *probability distribution of overcrossings*, denoted by $\{A_N(n)\}$ [33]. This distribution measures the probability of producing a *two-dimensional projection* of the n-bead polymer with N "double points" (i.e., bond–bond "crossings"), averaged over all possible projections. The more "entangled" the chain, the higher is the probability that large overcrossing numbers dominate the projections. In contrast, a rodlike chain is unentangled [i.e., $A_0(n)$ is the largest contribution to the probability].

A single descriptor for the above distribution is the *mean number of overcrossings* $\overline{N}$. In simple words, $\overline{N}$ is the "effective" number of bond–bond crossings in an arbitrary projection of the grafted chain, *averaged over all directions in space.* For any arbitrary projection of a linear polymer configuration, the maximum possible number of overcrossings is $maxN = (n - 3)(n - 2)/2$ [33]. Depending on the shape of the conformation considered, most of the projections may yield low N values (if the polymer is swollen or unentangled) or high N values (if the polymer is entangled). The mean number of overcrossing, $\overline{N}$, will usually be much smaller than $maxN$ (cf. discussion in [27] and [33]). In practice, $\overline{N}$ is evaluated as an average over many randomized projections (e.g., 5×10^4) [24, 33].

If the ensemble of "accepted" chain configurations is denoted by $\{K_i\}$, then $\{D(K_i)\}$ is the set of

values accessible to a given shape descriptor. Since the sampled configurations are statistically independent, the configurationally averaged shape descriptors are computed as the simple mean within the $\{K_i\}$ ensemble. The configurational averages are denoted by $\langle D \rangle$.

For the objectives of this work, we focus mostly on the changes in entanglements during confinement, as characterized by $\langle \overline{N} \rangle$. Some exact and numerical properties are known for this descriptor in the case of long random walks [27, 34–36]. Below, we discuss the behavior of $\langle \overline{N} \rangle$ (and contrast it with that of $\langle R_G^2 \rangle^{1/2}$ and $\langle h \rangle$) as the chains are deformed by the approaching AFM-tip.

Dependence of Configurationally Averaged Shape Descriptors on Geometrical Confinement

Averaged shape-descriptor values were computed for various tip geometries, as specified by the disk radius ρ and the tip–surface separation L. For a descriptor D, the average $\langle D(\rho, L) \rangle$ is evaluated over chains with n and r_{ex} fixed. Its value for "free" grafted chains (i.e., with *no confinement* effects) is $\langle D \rangle_{free}$. As mentioned above, the confined chains reach $\langle D \rangle_{free}$ in two limit conditions, when the top is far away from the surface and when the tip is vanishingly thin, i.e.,

$$\lim_{\rho \to 0} \langle D(\rho, L) \rangle = \lim_{L \to \infty} \langle D(\rho, L) \rangle = \langle D \rangle_{free}. \quad (6)$$

Our simulations verify these limits within the accuracy allowed by the algorithm.

To understand the overall changes in molecular shape due to the presence of the tip, we discuss two cases separately: (A) the compression of grafted chains by tips with constant radius; and (B) confinement due to tips at constant distance to the surface, but variable radius.

COMPRESSION EFFECTS WITH VARIABLE *L*, AT CONSTANT ρ VALUES

The basic phenomenon discussed here is illustrated in Figure 2. In agreement with results in the literature for long chains with a stretching potential [20, 21], we find conformations where the chains escape from under the tip. As we show below, these "transitions" can be accompanied by distinctive changes in molecular shape.

First, it must be noted that only some molecular-shape descriptors are useful for following shape transitions. If one analyzes the mean heights of the chains, $\langle h \rangle$, only a continuous behavior is observed during compression. Figure 3 shows the results for the variation of $\langle h \rangle$ as a function of the tip–surface separation L, for various values of disk radius ρ. The tip with the smallest radius ($\rho = 3$ Å, curve a) causes small confinement effects. In this case, the mean height shows the smallest variation in terms of L. In contrast, the confinement effects are magnified for radii $\rho \geq 40$ Å (curves d and e). (In fact, the polymer mushroom is effectively confined to a slab for all L and $\rho \geq 40$ Å.) However, as the radius changes, $\langle h \rangle$ shows no distinctive features that can be associated with shape transitions.

Figure 4 shows a more interesting behavior when we monitor chain self-entanglements in terms of $\langle \overline{N} \rangle$. An analysis of Figure 4, reveals the following features:

- **(a)** Confinement effects on entanglements disappear for $L > 40$ Å (the free chain limit).
- **(b)** For all disk radii, $\langle \overline{N} \rangle$ shows a maximum at a particular tip–surface separation. The maximum is the largest when the confinement effects are maximized (large ρ) and becomes vanishingly small as confinement effects disappear (small ρ).

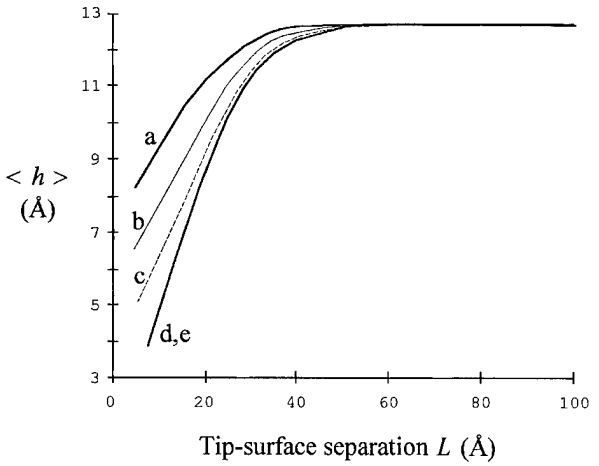


FIGURE 3. Variation in the configurationally averaged height of the grafted chains ⟨h⟩, as a function of tip–surface separation L, for various tip radii ρ. The labels stand for the following values of radius: (a) $\rho = 3$ Å; (b) $\rho = 11$ Å; (c) $\rho = 19$ Å; (d) $\rho = 40$ Å; (e) $\rho = 70$ Å. The last two curves are indistinguishable at the scale used. Error bars are omitted for clarity.

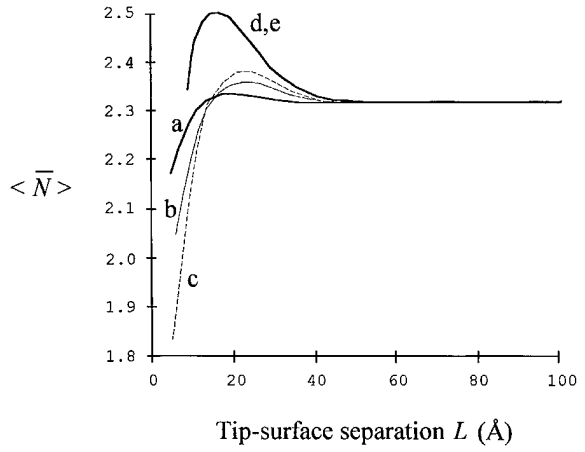


FIGURE 4. Variation in configurationally averaged mean overcrossing numbers for grafted chains, $\langle \overline{N} \rangle$, as a function of tip–surface separation L, for various tip radii ρ. The curve labels are the same as in Figure 3. Error bars are omitted for clarity.

(c) The tip–surface separation L leading to the maximum in $\langle \overline{N} \rangle$ changes with the radii ρ.

(d) When the compression effects are very strong (i.e., at very small L values for a fixed ρ), the mean overcrossing number decreases fast.

Recently, we discussed the occurrence of a maximum in self-entanglements for chains confined within a slab ($\rho \to \infty$) [24]. Using similar arguments, we can interpret some of the results above as follows:

(i) Within a slab ($\rho \to \infty$), compression can produce compact configurations. As L decreases, chains are "forced" to fold over themselves, thus increasing the complexity of entanglements.

(ii) As L decreases for large ρ, the configurational space accessible to the chains becomes smaller. Eventually, further compression squeezes the chains closer to the surface, thus preventing self-entanglements. As a result, $\langle \overline{N} \rangle$ diminishes under strong compression. In other words, $\langle \overline{N} \rangle$ must exhibit a maximum as function of L.

(iii) For smaller tip radii, e.g., $\rho < 40$ Å, the chains can access to a larger configurational space by "stretching" to the border of the tip and folding away from the disk (cf. Fig. 2). These "partly escaped" chains avoid compactification by the tip, thereby reducing the complexity of their entanglements. As a result, $\langle \overline{N} \rangle$ shows a smaller maximum than the one for large ρ.

(iv) For very small disk radii, the chains can "dodge" the tip for all L values, except when compression is extreme (L values close to l). These "fully escaped" chains effectively resemble the free grafted chains over a large range of L values.

The averaged molecular size, given in terms of the mean radius of gyration, $\langle R_G^2 \rangle^{1/2}$, parallels qualitatively the results of the mean number of overcrossings. Figure 5 shows the variation of $\langle R_G^2 \rangle^{1/2}$ as a function of L. Whereas $\langle \overline{N} \rangle$ exhibits a maximum, the radius of gyration exhibits a minimum during compression, confirming that chains become more compact. Note, however, that the position of the critical points are *not coincident*, i.e., maximum compactess and maximum entanglement complexity are *not* found simultaneously for the same tip geometry. (This agrees with the results for compression within slabs [24]). Therefore, the behavior of $\langle \overline{N} \rangle$ can provide new insights on shape transitions.

Summarizing, the presence of a maximum in $\langle \overline{N} \rangle$ for large ρ values is a indication of a "shape transition" between *compact entangled chains*, on the one hand, and *squeezed (minimally entangled) chains*, on the other. However, the shift of such a

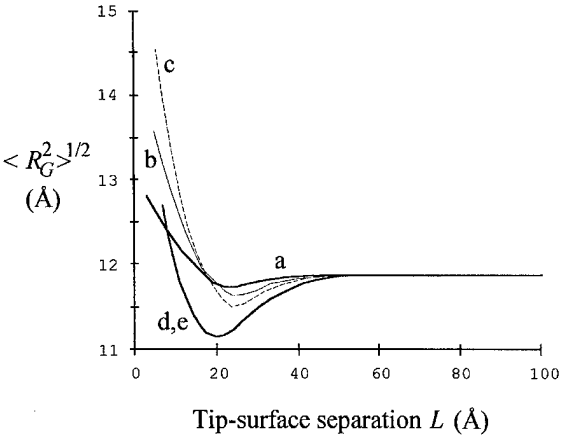


FIGURE 5. Variation in configurationally averaged radius of gyration for grafted chains, $\langle R_G^2 \rangle^{1/2}$, as a function of tip–surface separation L, for various tip radii ρ. The curve labels are the same as in Figure 3. Error bars are omitted for clarity.

maximum with ρ suggests a new regime, where chains reach intermediate compactness and entanglements through "escape transitions." To fully characterize this regime, we discuss below the behavior of $\langle \overline{N} \rangle$ as a function of the disk radius, at constant values of the tip–surface separation.

COMPRESSION EFFECTS WITH VARIABLE ρ, AT CONSTANT L VALUES

We consider now a "virtual" deformation, whereby the tip remains at a constant distance to the grafting surface while decreasing its radius at the base. The typical shape changes accompanying this "transformation" are displayed in Figure 6, for variable ρ and a small tip–surface separation ($L = 7$ Å).

Figure 6 illustrates how chains adopt flattened conformations at strong confinement (e.g., $\rho = 40$ Å and $\rho = 30$ Å). In this case, since L is very small, the chain cannot fold over itself and it is forced to stretch. However, since the disk is too wide (or, conversely, the chain is too short), only *few beads* can marginally "escape" the tip. We use the term "frustrated chains" to denote these configurations, where the polymer "fails" to escape the tip by any significant amount, even though the chains are stretched. (The term is used in only qualitative analogy to the concept of "frustration" in rugged potential energy surfaces [37], where conformations trapped in local minima are unable to escape to lower minima. In our case, "frustrated chains" cannot reach the entangled conformations that are characteristic of free grafted chains.)

The occurrence of "frustrated chain" configurations depends strongly on the values of L and ρ. For small disk radii ρ, most of the chain can effectively avoid the tip by adopting "escaped chain" configurations, in contrast to "frustrated chains" (cf. bottom of Fig. 6). On the other hand, if confinement is reduced by increasing the tip–surface separation, then chains will be able to fold over themselves. As a result, their mean configurations will resemble "confined chains" with high entanglement, rather than "escaped" or "frustrated" chains. In summary, we will expect the regime of "frustrated chains" to disappear, regardless of the tip radius, whenever the tip–surface separation is larger than some critical value L_C.

Our computer simulations convey these notions quantitatively. Figure 7 shows the configurationally averaged mean overcrossing numbers for the "transformation" in Figure 6. (The case $L = 7$ Å is the tightest confinement that we have been able to handle.) Despite the large error bars associated with configurational fluctuations, a rich behavior in $\langle \overline{N} \rangle$ is clear. The results in Figure 7 can be

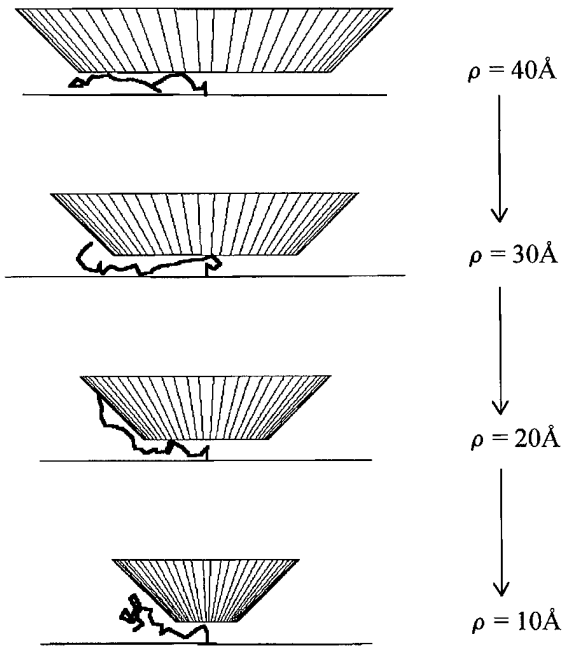


FIGURE 6. Typical deformations of grafted chains caused by a series of AFM-tips with variable radius ρ, at a constant tip–surface separation ($L = 7$ Å).

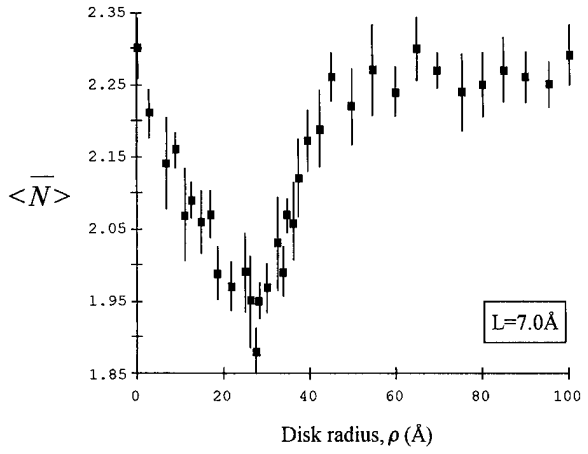


FIGURE 7. Variation in configurationally averaged mean overcrossing numbers for grafted chains, $\langle \overline{N} \rangle$, as a function of tip radius ρ, at a constant tip–surface separation ($L = 7$ Å). Error bars represent 95% confidence intervals.

summarized as follows:

(a) Chain entanglements are constant for $\rho > 50$ Å, where the chain is effectively confined within a slab. We find here "confined" conformations.

(b) Chain entanglements diminish when the disk radius decreases from 50 to ca. 30 Å, where they reach a minimum. In this case, the dominant chain conformations become *minimally entangled* by stretching to the border of the disk, where only some terminal beads can escape. We find here "frustrated chain" conformations.

(c) Chain entanglements increase again when the disk radius is reduced below ca. 30 Å. In this case, an increasingly larger section of the chain can escape the tip and "fold" on the outside. We find here "escaped chain" conformations.

Figure 8 shows the corresponding results for the variation in the chain mean radius of gyration under the same conditions. In this particular case, there is a perfect match between the behavior of $\langle \bar{N} \rangle$ and $\langle R_G^2 \rangle^{1/2}$. As the radius of the tip is reduced, the maximum in $\langle R_G^2 \rangle^{1/2}$ marks the transition from the stretched ("frustrated") configurations with large molecular size to the folded ("escaped") configurations that are more compact.

The presence of a minimum in $\langle \bar{N} \rangle$ vs. ρ is a characteristic of small L distances. Figure 7 can be contrasted with the behavior of chains at larger tip–surface distances. Figure 9 shows the dependence of $\langle \bar{N} \rangle$ vs. ρ over a range of L distances. (Error bars are omitted for clarity. The smoothed curves in Fig. 9 are polynomial fittings to the computed mean values in shape descriptors.) As L increases, the curves follow a qualitatively similar pattern until $L \approx 14$ Å. For $L > 14$ Å, $\langle \bar{N} \rangle$ *does not have a minimum* for the nonzero tip radius. In other words, the dominant configurations for $L >$ 14 Å pass directly from "confined chains" to "escaped chains." The critical tip–surface separation for this transition can thus be estimated at $L_C \approx 3.7l$, for the present chains where $l \approx 1.11 r_{ex}$. (The value of L_C will depend strongly on the excluded volume interaction.) Concluding, the shapes features represented by the minima in $\langle \bar{N}(\rho, L) \rangle$ vs. ρ appear to be specifically associated with the regime of "frustrated chain" configurations.

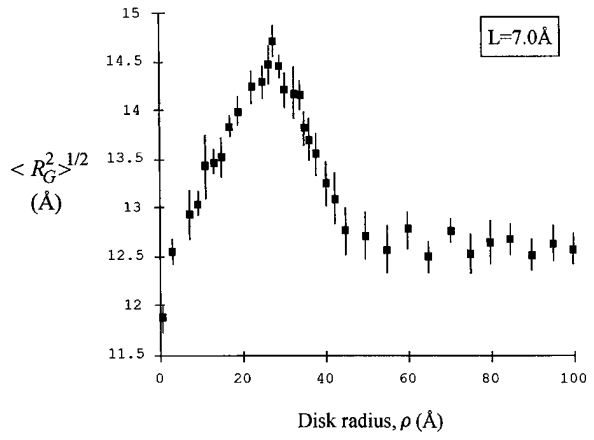


FIGURE 8. Variation in the configurationally averaged radius of gyration for grafted chains, $\langle R_G^2 \rangle^{1/2}$, as a function of tip radius ρ, at a constant tip–surface separation (L = 7 Å). Error bars represent 95% confidence intervals.

"PHASE DIAGRAM" FOR THE REGIMES OF ACCESSIBLE MOLECULAR SHAPES

The results above can be summarized by representing the molecular-shape features accessible to polymer mushrooms in a two-dimensional (ρ, L)-plot. We can regard this plot as the analog of a "phase diagram" for the configurations of a

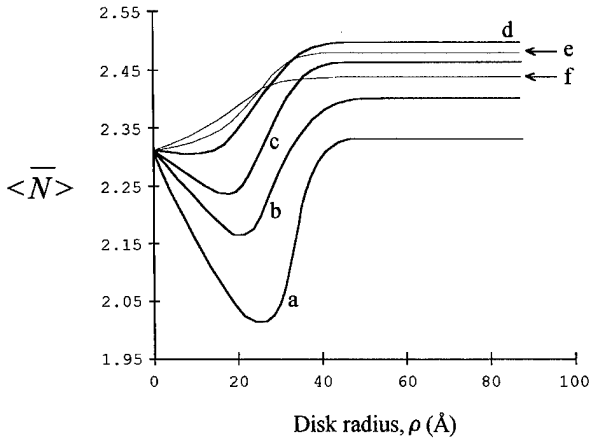


FIGURE 9. Variation in the configurationally averaged overcrossing numbers for grafted chains $\langle \bar{N} \rangle$, as a function of tip radius ρ, at various tip–surface separations. The labels stand for the following values of tip–surface separation: (a) L = 8 Å; (b) L = 10 Å; (c) L = 12 Å; (d) L = 14 Å; (e) L = 17.5 Å; (f) L = 22.5 Å. For clarity, the last two curves (e, f) are indicated by thin lines and error bars have been removed.

finite-size system. In this context, a descriptor of chain entanglements plays the role of an order parameter for labeling the "phases." [The analogy is only qualitative since the shape properties vary smoothly. The separation into sharp regions with distinct dominant conformations is somewhat arbitrary. In our convention, the boundaries are defined by the (ρ, L) values satisfying $\langle \overline{N}(\rho, L)\rangle = \langle \overline{N}\rangle_{free}$.]

Figure 10 shows all the results for $\langle \overline{N}(\rho, L)\rangle$. The global minimum is found at small L and intermediate ρ values, whereas the global maximum appears at large ρ and intermediate L values. The flat regions on this surface represent shapes similar to those of free grafted chains.

Using Figure 10, we can classify the configurations according to distinctive molecular-shape properties. The resulting "phase diagram" based on chain entanglements is shown in Figure 11. (A comparable, yet not identical, diagram can be given in terms of the radius of gyration.) Frustrated chains (with minimal entanglement) appear at $L < L_C$, whereas fully escaped chains (with low entanglement) can only be found at small ρ values. The separation between the escaped chains and the free chains (indicated by a dotted line) is artificial, since a faraway AFM-tip with small disk radius will not affect the polymer mushroom. The remaining boundary curves correspond to the tip geometries for which the mean molecular shape of the chains coincides with that of a free grafted mushroom [i.e., $\langle \overline{N}(\rho, L)\rangle = \langle \overline{N}\rangle_{free}$].

Figure 11 summarizes the results of this work. The "phase diagram" conveys the interplay between configurational and shape transitions due to variable confinement. The main features of this diagram should remain unaltered for longer chains (whenever the same repulsive potential is used) or for chains that are not perpendicularly grafted to the surface.

Further Comments and Conclusions

In this work, we have shown that chain self-entanglements can be used for monitoring the occurrence of configurational transitions (i.e., a change in the nature of the dominant configurations due to an external perturbation). Conceptually, the main result is the fact that the dominant configurations can indeed be classified into regimes (or "phases") by using the behavior of molecular-shape descriptors. The results in Figure 11 use mean overcrossing numbers as a descriptor. A similar analysis can be done by using other shape features, although "phase" boundaries will shift since distinct descriptors are generally uncorrelated.

The diagram in Figure 11 should be a valid qualitative guide to predict the behavior of chains interacting with obstacles. Note, however, that the nature and number of the "shape regimes" will change with the model chosen for the AFM-tip. For curved-surface tips, or tips with indentations,

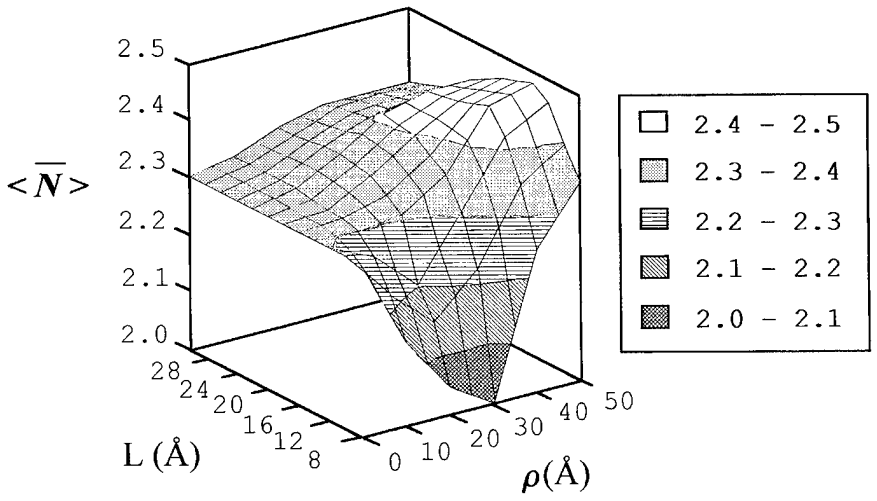


FIGURE 10. Dependence of the mean number of overcrossings on geometrical confinement over a wide range of values of tip radius ρ and tip–surface separation L.

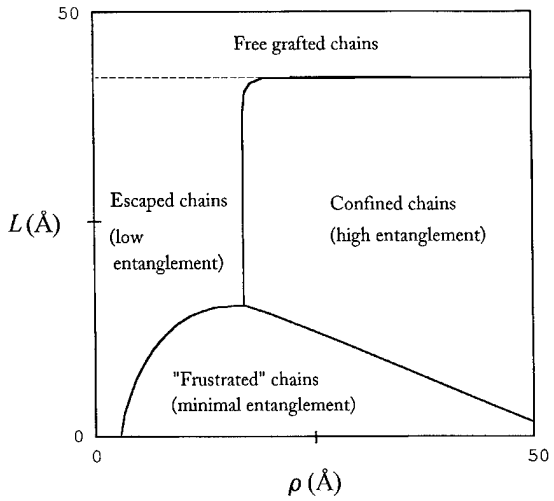


FIGURE 11. Qualitative configurational "phase" diagram indicating the molecular-shape regimes encountered during compression by a flat AFM-tip. The boundaries are estimated from the results in Figure 10, using the convention $\langle \bar{N}(\rho, L)\rangle = \langle \bar{N}\rangle_{\text{free}}$. The dotted line indicates that the distinction between free chains and "escaped" chains is blurred for large L and small ρ values.

a more complex pattern of shape transitions can be expected [21].

The present results from chain simulations complement previous work in the literature that is only valid for very long chains [20, 21]. Our classification of short-chain conformers according to dominant shape features could not have been done by using scaling arguments.

Our results contribute to a better understanding of "escape transitions" [20], since we have now shown that configurational changes analog to "escape transitions" can also be found in polymers with purely repulsive potentials. As discussed above, our configurational and shape transitions are strictly entropic phenomena. All "accepted" conformations have equal (zero) energy, as there is neither attraction between monomers or nor an energetic cost for stretching a chain. Nevertheless, the results show that "escape transitions" can still be recognized by the behavior of molecular-shape descriptors. Until now, these interesting phenomena had only been found before in more complicated polymer potentials [20, 21]. Note, however, that our model has no energy barriers and thus shape transitions will not exhibit hysteresis [21]. The behavior of chain self-entanglements under compression for realistic monomer–monomer interactions remains an interesting question open to study.

ACKNOWLEDGMENTS

I thank N. D. Grant (Sudbury) for her comments on the manuscript. This work was supported by the Fonds de Recherche de l'Université Laurentienne (FRUL) and a grant from the Natural Sciences and Engineering Research Council (NSERC) of Canada.

References

1. (a) I. Sanchez, Ed., *Physics of Polymer Surfaces and Interfaces* (Butterworth-Heinemann, Boston, 1992). (b) G. J. Fleer, M. A. Cohen-Stuart, J. M. H. M. Scheutjens, T. Cosgrove, and B. Vincent, *Polymers at Interfaces* (Chapman and Hall, London, 1993).
2. T. L. Kuhl, D. E. Leckband, D. D. Lasic, and J. N. Israelachvili, Biophys. J. **66**, 11479 (1994).
3. P.-G. de Gennes, *Scaling Concepts in Polymer Physics* (University Press, Ithaca, NY, 1985).
4. M. N. Barber, A. J. Guttmann, K. M. Middlemiss, G. M. Torrie, and S. G. Whittington, J. Phys. A **11**, 1833 (1978).
5. K. F. Freed, J. Chem. Phys. **79**, 3121 (1983).
6. A. Baumgärtner, in *Applications of the Monte Carlo Method in Statistical Physics*, K. Binder, Ed. (Springer-Verlag, Berlin, 1987), and references therein.
7. K. Binder, P.-Y. Lai, and J. Wittmer, Faraday Discuss. **98**, 97 (1994).
8. R. Hegger and P. Grassberger, J. Phys. A **27**, 4069 (1994).
9. L. Gutman and A. K. Chakraborty, J. Chem. Phys. **105**, 7842 (1996).
10. M. Daoud and P. G. de Gennes, J. Phys. (Paris) **38**, 85 (1977).
11. M. C. Tesi, E. J. Janse van Rensburg, E. Orlandini, and S. G. Whittington, J. Phys. A **27**, 347 (1994).
12. R. G. Winkler, A. Gerstmair, P. Reineker, T. Matsuda, and D. Y. Yoon, Int. J. Quantum Chem. **52**, 437 (1994).
13. P.-G. de Gennes, C. R. Acad. Sci. Paris Ser. IIb **320**, 85 (1995).
14. J. Baschnagel and K. Binder, Macromolecules **28**, 6808 (1995).
15. K. Binder, A. Milchev and J. Baschnagel, Annu. Rev. Mater. Sci. **26**, 107 (1996).
16. A. Milchev and K. Binder, J. Phys. II Fr. **6**, 21 (1996).
17. I. Teraoka, Prog. Polym. Sci. **21**, 89 (1996).
18. G. H. Peters and D. J. Tildesley, Phys. Rev. E **52**, 1882 (1995); *Ibid.* **54**, 5493 (1996).
19. P.-Y. Lai and C.-Y. Lai, Phys. Rev. E **54**, 6958 (1996).
20. G. Subramanian, D. R. M. Williams, and P. A. Pincus, Europhys. Lett. **29**, 285 (1995).
21. D. R. M. Williams and F. C. MacKintosh, J. Phys. II Fr. **5**, 1407 (1995).
22. A. Jaeckel and J. Dayantis, J. Phys. A **27**, 7719 (1994).

23. A. Milchev and K. Binder, J. Phys. II Fr. **5**, 1407 (1995).
24. G. A. Arteca, Int. J. Quantum Chem. (Symp. 30) **60**, 1515 (1996).
25. G. A. Arteca, J. Phys. Chem. **97**, 13831 (1993).
26. J. O. Hirschfelder, C. F. Curtiss, and R. B. Bird, *Molecular Theory of Gases and Liquids* (Wiley, New York, 1964), p. 551.
27. G. A. Arteca, Phys. Rev. E **49**, 2417 (1994).
28. M. P. Allen and D. J. Tildesley, *Computer Simulation of Liquids* (Oxford University Press, Oxford, 1987), p. 136.
29. W. H. Press, S. A. Teukolsky, W. T. Vetterling, and B. P. Flannery, *Numerical Recipes in Fortran* (Cambridge University Press, Cambridge, 1992), pp. 271–273.
30. P. L'Ecuyer, Commun. ACM **31**, 742 (1988).
31. G. A. Arteca, in *Reviews in Computational Chemistry*, K. B. Lipkowitz and D. B. Boyd, Eds., (VCH, New York, 1996), Vol. 9, pp. 191–253.
32. (a) G. A. Arteca, Biopolymers **35**, 393 (1995); (b) G. A. Arteca, Macromolecules, **29**, 7594 (1996).
33. G. A. Arteca, Biopolymers **33**, 1829 (1993).
34. E. Orlandini, M. C. Tesi, S. G. Whittington, D. W. Sumners, and E. J. Janse van Rensburg, J. Phys. A **27**, L 333 (1994).
35. G. A. Arteca, Phys. Rev. E **51**, 2600 (1995).
36. A. L. Kholodenko and D. P. Rolfsen, J. Phys. A **29**, 5677 (1996).
37. J. D. Bryngelson and P. G. Wolynes, Proc. Natl. Acad. Sci. U.S.A. **84**, 7524 (1987).

Real-Space Multigrid Methods for Large-Scale Electronic Structure Problems

J. BERNHOLC, E. L. BRIGGS, D. J. SULLIVAN, C. J. BRABEC, M. BUONGIORNO NARDELLI, K. RAPCEWICZ, C. ROLAND, M. WENSELL

Department of Physics, North Carolina State University, Raleigh, North Carolina 27696-8202

Received 8 April 1997; revised 29 July 1997; accepted 6 August 1997

ABSTRACT: We describe the development and applications of a new electronic structure method that uses a real-space grid as a basis. Multigrid techniques provide preconditioning and convergence acceleration at all length scales and therefore lead to particularly efficient algorithms. The salient points of our implementation include: (i) new compact discretization schemes in real space for systems with cubic, orthorhombic, and hexagonal symmetry and (ii) new multilevel algorithms for the iterative solution of Kohn–Sham and Poisson equations. The accuracy of the discretizations was tested by direct comparison with plane-wave calculations, when possible, and the results were in excellent agreement in all cases. These techniques are very suitable for use on massively parallel computers and in $O(N)$ methods. Tests on the Cray-T3D have shown nearly linear scaling of the execution time up to the maximum number of processors (512). The above methodology was tested on a large number of systems, such as the C_{60} molecule, diamond, Si and GaN supercells, and quantum molecular dynamics simulations for Si. Large-scale applications include a simulation of surface melting of Si and investigations of electronic and structural properties of surfaces, interfaces, and biomolecules. © 1997 John Wiley & Sons, Inc. Int J Quant Chem **65**: 531–543, 1997

Introduction

Over the course of the last several decades, plane-wave-based methods have been used to perform electronic structure calculations on a wide range of physical systems. The Car–Parrinello (CP) and other iterative methods [1, 2] have made such calculations possible for systems containing several hundred atoms [3]. While these methods have been very successful, several difficulties arise when they are extended to physical systems with large length scales or containing first-row or transition-metal atoms. Special tech-

Correspondence to: J. Bernholc.

© 1997 John Wiley & Sons, Inc.
CCC 0020-7608 / 97 / 050531-13

niques have been developed to handle some of these problems. Optimized pseudopotentials [4, 5], the augmented-wave method [6], plane waves in adaptive-coordinates [7–9], and preconditioning combined with conjugate-gradient techniques [10, 11] have had considerable success; however, these techniques are still constrained by the plane-wave basis, which requires periodic boundary conditions for every system and fast Fourier transforms (FFTs) to efficiently transform between real and reciprocal space. In particular, FFTs involve nonlocal operations that impose constraints on the adaptability of these algorithms to massively parallel computer architectures because they perform best on problems that can be divided into localized domains.

It has been appreciated for some time that there are potential advantages to performing electronic-structure calculations entirely in real space. Boundary conditions are not constrained to be periodic; this permits the use of nonperiodic boundary conditions for clusters and a combination of periodic and nonperiodic boundary conditions for surfaces. By employing nonuniform real-space grids, it is possible to add resolution locally, e.g., for a surface or cluster calculation. A basis that uses a high density of grid points in regions where the ions are located and a lower density of points in vacuum regions can lead to order of magnitude savings in the basis size and total computational effort [12]. More importantly, the use of a real-space basis opens up the possibility of using multigrid iterative techniques to obtain solutions of the Kohn–Sham equations. Multigrid methods [13], which provide automatic preconditioning on all length scales, can greatly reduce the number of iterations needed to converge the electronic wave functions. Furthermore, the real-space multigrid formulation does not involve long-range operations and is particularly suitable for parallelization and $O(N)$ algorithms [14, 15], because every operation can be partitioned into hierarchical real-space domains.

There have been a number of previous real-space grid-based electronic structure calculations. The finite-element method was applied by White et al. [16] to one-electron systems. They used both conjugate-gradient and multigrid acceleration to find the ground-state wave function. Two of the present authors [12] used nonuniform grids with locally enhanced regions in conjunction with multigrid acceleration to calculate the electronic properties of atomic and diatomic systems with nearly singular pseudopotentials. They verified that the preconditioning afforded by multigrid was effective in multilength-scale systems. Chelikowsky et al. [17] have used high-order finite-difference methods and soft nonlocal pseudopotentials on uniform grids to study the properties of Si and Ge clusters. The present authors have developed a real-space grid method with multigrid methods and tested it extensively against plane-wave results [18]. Other recent real-space work includes finite differencing on warped grids [19, 20], wavelet bases [21, 22], hierarchical nonlinear grids applied to diatomics [23], and full potential multigrid calculations for atoms and diatomics [24].

Real-Space Calculations

Several issues that are absent from plane-wave or orbital-based methods arise when using a real-space grid approach. In the former case the wave functions, potentials, and the electronic density are representable in explicit basis functions, and thus are known everywhere. In a real-space grid implementation, these quantities are known only at a discrete set of grid points, which can introduce a spurious dependence of the Kohn–Sham eigenvalues, the total energy, and the ionic forces on the positions of the ions with respect to the real-space grid. We have developed a set of techniques that can overcome these difficulties and can be used to compute accurate static and dynamical properties of large physical systems. In our formalism the wave functions, density, and potentials are directly represented on a three-dimensional real-space grid with linear spacing h_{grid} and number of mesh points N_{grid}. The ions are represented by soft-core norm-conserving pseudopotentials [25]. Exchange and correlation effects are treated using the local density approximation (LDA) of density functional theory.

For reasons of accuracy and computational efficiency, we discretize the Kohn–Sham equations in a generalized eigenvalue formulation:

$$A[\psi_n] + B[V_{\text{eff}}\psi_n] = \epsilon_n B[\psi_n]. \qquad (1)$$

A and B are the components of the *Mehrstellen* discretization [26], which is based on Hermite's generalization of Taylor's theorem. It uses a weighted sum of the wave function and potential values to improve the accuracy of the discretiza-

tion of the *entire* differential equation, not just the kinetic energy operator. The weights for the $O(h_{\text{grid}}^4)$ discretization are given in Table I. We have found that the fourth-order Mehrstellen discretization produces equivalent or better accuracy than the sixth-order central-finite-difference one. The higher accuracy of the Mehrstellen approach is achieved by using a nonseparable discretization and more local information (second nearest-neighbor points, for example).

We have found that pseudopotentials, especially the rather hard ones, must be smoothed before they are suitable for real space calculations. Smoothing is necessary to avoid high-frequency variation on the real-space mesh which reduces accuracy and slows convergence. This variation is absent from plane-wave calculations because the basis cuts off the large-G components of the potentials *exactly* [27]. To achieve this same cutoff effect in real space, we use the following filtering procedure: The radial pseudopotentials are Fourier-transformed to G space. They are multiplied by a cutoff function which decreases rapidly beyond $\pi/(\alpha h)$, where α is typically in the range 1.5-2.0. The filtered potentials are then back-transformed to real space. We have found that the Fourier-filtered pseudopotentials retain the accuracy of those used in plane-wave calculations.

To test the smoothness of the pseudopotentials, an isolated atom or a bulk system is displaced relative to the grid. The magnitude of the variation in total energy is a measure of smoothness of the pseudopotentials. In Figure 1 we show the change in the LDA energy of a carbon atom and a diamond supercell as a function of distance from a mesh point. In addition, the degeneracy pattern of the eigenvalues and the ionic forces are examined. If the pseudopotential is insufficiently smooth, the ionic forces in a symmetric lattice, for example, will not be small (vanish).

To facilitate comparisons with plane-wave calculations, we define an energy cutoff for the real-space calculation, $\pi^2/2h^2$ [Ry], to be equal to that

TABLE I
Mehrstellen discretization weights in 3D (h is the grid spacing).

Grid point	$6h^2$*A	6*B
Central	24	6
Nearest neighbors	−2	1
Second neighbors	−1	0

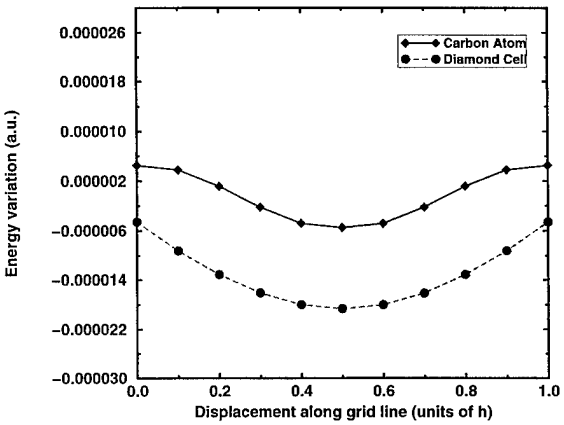


FIGURE 1. Variation of the total energy as a carbon atom and a 64-atom diamond supercell is displaced rigidly relative to the grid along a coordinate axis. The grid spacing h is 0.336 bohr.

of a plane-wave calculation that uses a FFT grid with the same spacing as the multigrid calculation [28].

To efficiently solve Eq. (1), we have used multigrid iteration techniques that accelerate convergence by employing a sequence of grids of varying resolutions. The final solution is obtained on a grid fine enough to accurately represent the pseudopotentials and the electronic wave functions. If the solution error is expanded in a Fourier series, it may be shown that iterations on any given grid level will quickly reduce the components of the error with wavelengths comparable to the grid spacing but are ineffective in reducing the components with wavelengths large relative to the grid spacing [13, 29]. The solution is to treat the lower frequency components on a sequence of auxiliary grids with progressively larger grid spacings, where the remaining errors appear as high-frequency components. This procedure provides excellent preconditioning for all length scales present in a system and leads to very rapid convergence rates. The operation count to converge one wave function with a fixed potential is $O(N_{\text{grid}})$, compared to $O(N_{\text{grid}} \log N_{\text{grid}})$ for FFT-based approaches [2].

To summarize, one self-consistent iteration consists of a multigrid step to solve Eq. (1), followed by the orthogonalization of the orbibals and an update of the electronic density. The components of the effective potential that depend on the density (Hartree and exchange-correlation) are then recomputed for the new density, and the process is

repeated until self-consistency is reached. The Hartree potential is computed by solving Poisson's equation using multigrid iterations on the corresponding Mehrstellen discretization. The nonlocal ionic pseudopotential is evaluated in real space using the Kleinman–Bylander [30] separable form. The operation count to converge one wave function with a fixed potential is $O(N_{grid})$, compared to $O(N_{grid} \log N_{grid})$ for FFT-based approaches [2]. In addition, all operations except orthogonalization are short-ranged, which allows for efficient parallelization and a natural implementation of $O(N)$ algorithms [14, 15].

Molecular Dynamics

Ab initio molecular dynamics (MD) simulations require accurate ionic forces so that higher-order integrators and large time steps can be used to achieve long simulation times. If the grid layout, whether uniform or nonuniform, does not change when the ions move, the Hellmann–Feynman (HF) force theorem [31] applies with no Pulay corrections [32]. However, the calculation of the HF forces on a real-space grid requires careful consideration of numerical errors because the derivative of even a filtered pseudopotential can introduce high-frequency components. The quality of our forces is sufficient, however, for even long simulations, as exemplified in Figure 2, which shows that the total energy for a 64-atom cell of bulk Si at 1100 K is conserved within 27 μeV per atom.

Parallelization

There are two apparent parallelization schemes for a real-space grid method. First, the orbitals could be distributed over processors and stored there. Its major advantage is that our high optimized serial code would require few changes. However, the orthogonalization of the orbitals would perform inefficiently because entire orbitals must be exchanged between processors. Our preferred scheme is data decomposition, where real-space domains are distributed over processors. Orthogonalization becomes sufficient because overlap integrals can be computed in two parts: the intraprocessor portion is fully parallel, and the interprocessor part sends only the intermediate sums between processors. Just as important, the

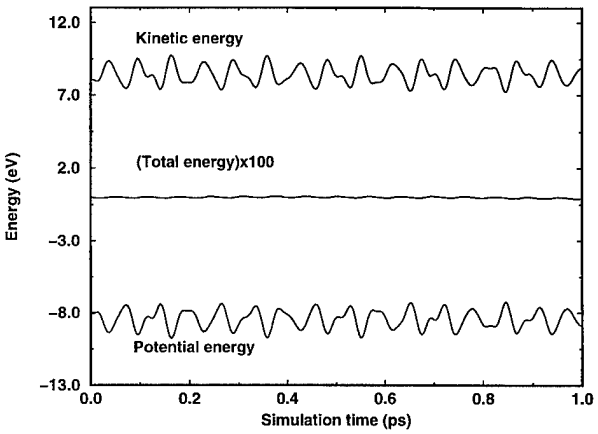


FIGURE 2. Potential, kinetic, and total energy of a molecular dynamics simulation of a 64-atom silicon cell at a temperature of 1100 K. Third-order Beeman–Verlet integration with an 80-a.u. time step was used for the integration of the ionic equations of motion. The total energy curve is multiplied by a factor of 100. The potential and total energies have been shifted by 251.171 a.u so that they could appear together.

compact nature of the Mehrstellen operator requires the exchange of only small amounts of data between nearest-neighbor processors. In tests of the code, ported from the Cray YMP-C90 to the massively parallel Cray T3D, we found nearly perfect load balancing (90%) on all systems tested. These tests used up to 512 processors.

Test Results

A significant advantage of the multigrid method is the speed of convergence to the electronic ground state for a given initial ionic configuration. For systems requiring a small energy cutoff or of small size, the speed advantage with respect to CP-based methods it not substantial. However, for systems requiring a large energy cutoff, or of large dimensions, this advantage—as measured in actual computational time—is typically an order of magnitude. This is because the maximum stable time step in the Car–Parrinello method must be much smaller than in the multigrid approach. Our initial tests of the real-space multigrid method were discussed previously [12, 18] and included a full comparison with established plane-wave results.

To illustrate the ability of the multigrid method to handle ill-conditioned systems, test calculations were performed on a 64-atom GaN cell in the

zinc-blende structure with the Ga $3d$ electrons in valence. A grid spacing of 0.14 bohr was used, which corresponds to an energy cutoff of 250 Ry in a plane-wave calculation. Only the Γ point was included in k-space sampling. Starting with random initial wave functions, only 75 self-consistent steps were required to converge the total energy. Recently, several calculations have been performed on GaN that explicitly included the d-electrons in valence; the multigrid results are in very good agreement with these calculations (see Table II).

In addition, the energy of formation of the Ga interstitial impurity in a 64-atom GaN supercell was calculated to be 7 eV. The ions were not relaxed at this 250-Ry cutoff in order to conserve computer resources. Instead, ionic coordinates from a fully relaxed Ga interstitial calculation with the Ga $3d$ electrons *in core* were used. As a check, the interstitial was also fully relaxed with the Ga $3d$ electrons in valence, but at a 160-Ry cutoff with a slightly softer pseudopotential. The maximum difference in ionic coordinates between the two relaxed structures was 0.1 Å.

The present results for the Ga interstitial confirm our previous values, obtained with the Ga $3d$ electrons *in core* [33]; namely, the Ga interstitial is one of the low-energy native defects in GaN. Recent experimental results indeed find indirect evidence for its presence, since Ga precipitates are formed upon annealing [34].

We have also studied the wurtzite phase of GaN in a 32-atom supercell with the d electrons in core. The discretization in the hexagonal plane is straightforward because the grid lines can be mapped onto a Cartesian plane. The Kohn–Sham eigenvalues computed by the real-space and plane-wave methods are in excellent agreement.

An isolated C_{60} molecule was selected as an example of a nonperiodic system. The simulation cell was a cube of length 23 bohrs and the grid spacing was 0.360 bohr. The initial ionic coordinates were generated using the classical Tersoff–Brenner potential [35], and the electronic wave functions were set to zero on the boundaries of the cell. After the convergence of the electronic system, the ions were relaxed using the same relaxation scheme as before. Two distinct bond lengths were found in the final structure, corresponding to the carbon–carbon single and double bonds. There were twice as many single bonds as double bonds, and the average double and single bond lengths were 1.39 and 1.44 Å, compared to 1.41 and 1.45 Å obtained in a previous CP calculation [36] for the C_{60} solid. The standard deviations of the bond-length distributions were on the order of 10^{-3} Å in both calculations. The experimental values for the solid are 1.40 and 1.45 Å, respectively.

Next, we examine the efficiency of multigrid acceleration. Table III illustrates the convergence properties as a function of grid resolution for an 8-atom diamond cell. The observed convergence rates are largely independent of the energy cutoff. The number of self-consistent field (SCF) steps required to converge the density is also nearly independent of the system size. At an equivalent cutoff of 35 Ry, the multigrid method required 17 steps to converge the total energy of the 8-atom diamond cell to a tolerance of 10^{-8}. When the same calculation was performed for a 64-atom cell only 20 SCF steps were needed.

Finally, we compare the convergence rates for four iterative-diagonalization schemes: steepest descents, multigrid, steepest descents with periodic subspace rotation, and multigrid with periodic subspace rotation. Subspace rotation (subspace diagonalization) speeds up iterative diagonalization schemes because it efficiently resolves exact or near degeneracies between orbitals.

TABLE II
Comparison of GaN results obtained with the Ga $3d$ electrons in valence.[a]

	Band gap	Cohesive energy
Full potential LMTO [56]	2.00	10.89
240 Ry, plane waves, 2-atom cell [57]	1.89	
Multigrid, 64-atom cell	1.88	10.64

[a] The multigrid calculation uses a 64-atom supercell, 250-Ry cutoff, and Γ point sampling. See text [eV].

TABLE III
Multigrid convergence tests in an 8-atom supercell.[a]

Grid spacing	Cutoff	Total energy	SCF steps
0.421	25.0	−44.87968	22
0.336	35.0	−45.03331	17
0.280	60.0	−45.06240	21
0.210	110.0	−45.06605	26

[a] Grid spacing [bohr], equivalent plane-wave cutoff [Ry], total energy [a.u.], and the number of steps to converge the density.

In the tests, the initial wave functions were randomly chosen, a worse-case scenario, and the time step was the same for each scheme. Ordinary multigrid rapidly decreases the error, but the convergence stalls after ~15 steps because the density is changing slowly. Periodic subspace rotation sorts out the small degeneracies between states, and when several unoccupied states are included in the calculation, it mixes in new information from the unoccupied sector. This greatly improves the convergence rate, even for steepest descents; see Figure 3.

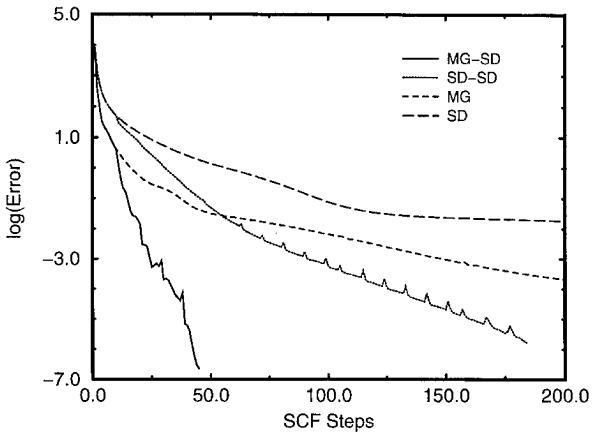


FIGURE 3. Convergence rates for a 64-atom diamond cell with a substitutional N impurity at a 63-Ry equivalent cut-off. The convergence rate, $\log_{10}(E - E_0)$, is plotted against the number of self-consistent field (SCF) steps. Random initial wave functions were used with a constant initial density. SD represents convergence rates for the steepest descents algorithm, MG is for multigrid, SD-SD is steepest descents with subspace diagonalizations, and MG-SD is multigrid with subspace diagonalizations.

Surfaces of Wurtzite GaN

The Perdew–Zunger parametrization [37] of the Ceperley–Alder form [38] of the exchange–correlation energy was chosen. Nonlocal, norm-conserving pseudopotentials [25, 39, 40] were included using the Kleinman–Bylander approach [30]. For gallium, a recently developed norm-conserving pseudopotential, which includes a nonlocal core correction [41] and permits an efficient description without the need for an explicit treatment of the *d*-valence electrons was used. For nitrogen, a standard pseudopotential with a neutral configuration as the atomic reference for all states was employed. These pseudopotentials have been demonstrated to reproduce accurately the bulk properties of GaN [42].

The calculated bulk properties are presented in Table IV. The theoretical lattice parameters of both the zinc-blende and wurtzite forms agree very well with experiment; a similar level of accuracy is expected for the surface and interface calculations described below. The cohesive energy of GaN and α-Ga is 10.42 and 3.4 eV, respectively. The binding energy of nitrogen molecule is 5.87 eV. The theoretical heat of formation of GaN is thus 1.15 eV, in good agreement with the experimental value of 1.14 eV.

The (0001) surface is a polar surface. The ideal surface has dangling bonds with charge distributions that are energetically unfavorable. If kinetically permitted, the surface atoms will relax and redistribute the "dangling-bond" charge density so as to satisfy the valences of all of the surface

TABLE IV
Calculated bulk properties of zinc-blende and wurtzite nitride semiconductors.[a]

	Zinc-blende		
	AlN	GaN	InN
a_0 (Å)	4.37 (4.38)	4.52 (4.5)	5.01 (4.98)
B_0 (MBar)	2.02 (2.02)	1.70 (1.90)	1.58 (1.37)
Wurtzite			
a (Å)	3.09 (3.11)	3.20 (3.19)	3.55 (3.54)
c/a	1.62 (1.60)	1.63 (1.63)	1.63 (1.61)
u (units of c)	0.378 (0.382)	0.376 (0.377)	0.375
B_0 (MBar)	1.99 (2.02)	1.69 (1.95, 2.37)	1.62 (1.26, 1.39)

[a] The values of the gap at the Γ-pt (E_Γ) and of the valence-band width (ΔE_{vbw}) are the LDA results. Note that the LDA indirect gap in zinc-blende A1N is 3.2 eV. Experimental values are in brackets and follow Ref. 52.

species. This can be achieved via structural relaxation (with a concomitant charge transfer between surface atoms). Recent experimental studies have revealed the presence of 2×2 reconstructions during growth [43]. In this study, we restrict our attention to these reconstructions on the gallium-terminated face.

We considered eight different 2×2 reconstructions, namely the ideal relaxed structure and gallium vacancy, nitrogen adatom, gallium adatom, and nitrogen-trimer, each on the T_3 and H_3 (hollow) sites; see Figures 4 and 5. We find that adatom reconstructions are the most energetically favorable of the studied reconstructions. In particular, in the gallium-rich case the gallium adatom on the T_3 site has the lowest energy, while in the nitrogen-rich case, the nitrogen adatom on the H_3 is the most stable.

The slabs contained four bilayers of GaN, three bilayers of which were relaxed. Relaxations in the third bilayer were negligible, indicating that a sufficiently thick slab was employed. Pseudo-hydrogen of charge 0.75 passivated the nitrogen-terminated face [44]. If the work functions of the two surfaces are different, then the periodic boundary conditions of the supercell enforce a common electrostatic potential in the vacuum and result in an unphysical change in the electric potential in the vacuum region equal to the difference between the two work functions. A large vacuum region of 10 Å served to reduce the size of this field. Calculations including explicitly a correction for this field did not show significant differences in the final equilibrium geometries [45]. An orthorhombic supercell with grid spacing of 0.21, 0.22, and 0.20 a.u. in the x, y, and z directions, respectively, was employed. Eight different reconstructions were studied using Γ-point sampling. For the lowest energy structures of each class, i.e., nitrogen adatom on H_3 site, nitrogen trimer on the T_3 site, etc., a further calculation using two k points in the irreducible Brillioun zone was carried out.

Figure 6 displays the relative surface energies for the five different reconstructions. Under gallium-rich conditions and for most of the range of the chemical potential, the lowest energy reconstruction is the gallium-adatom on the T_3 site; while under nitrogen-rich conditions, the reconstruction with the nitrogen-adatom on the H_3 site is preferred energetically.

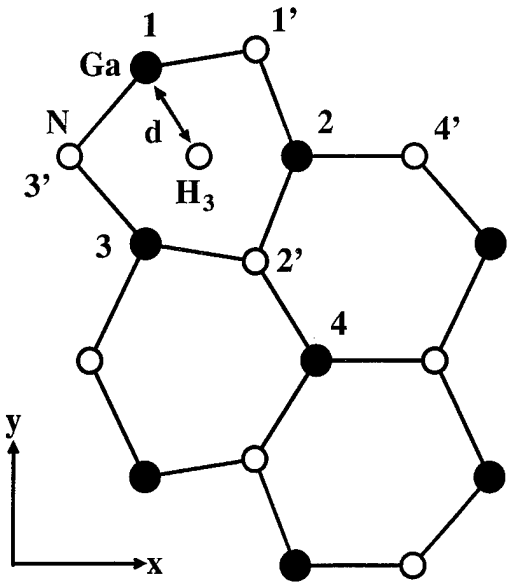


FIGURE 5. Schematic top view of the 2×2 nitrogen-adatom reconstruction on the (0001) surface of GaN. The nitrogen adatom sits above the hollow (H_3) site. The numbers denote gallium atoms on the surface, while the primed numbers denote nitrogen atoms in the first subsurface layer.

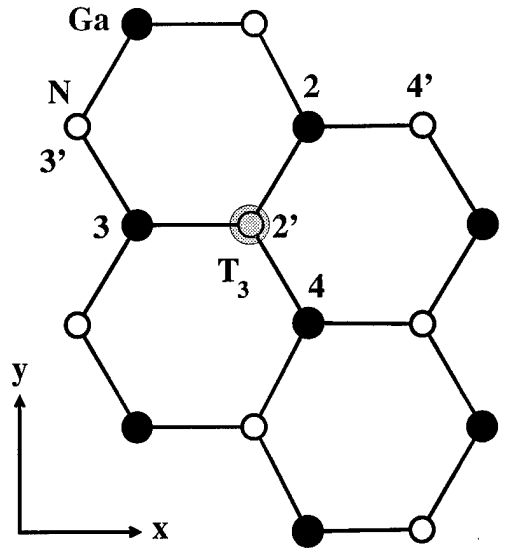


FIGURE 4. Schematic top view of the 2×2 gallium-adatom reconstruction on the (0001) surface of GaN. The gallium adatom (in gray) sits above a nitrogen in the second layer on the T_3 site. The numbers denote gallium atoms on the surface, while the primed numbers denote nitrogen atoms in the first subsurface layer.

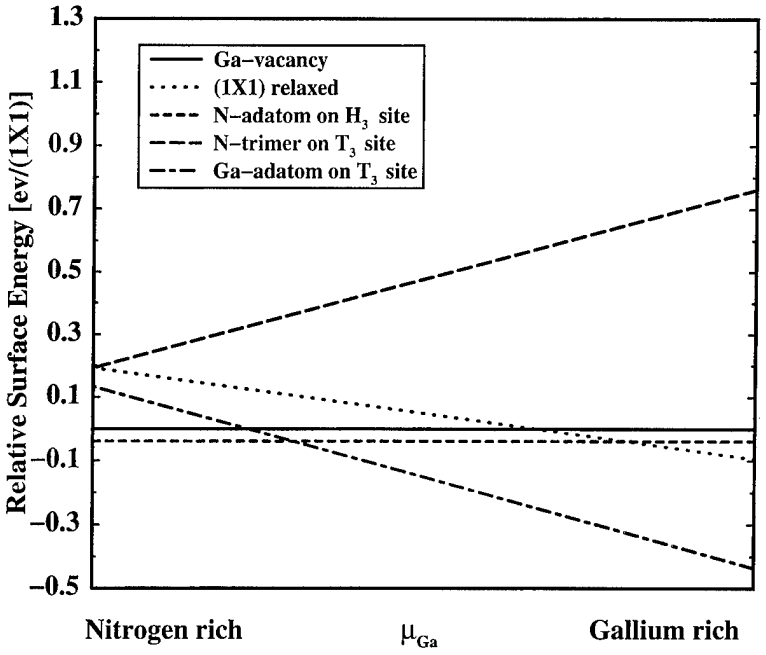


FIGURE 6. Formation energy vs. gallium chemical potential for the (0001) surface. The maximum chemical potential for N (Ga) is equal to the energy per atom calculated for N_2 (bulk Ga). Two k points are sampled in the irreducible Brillioun zone.

The gallium-adatom reconstruction is shown in Figure 4. The adatom sits on the T_3 site above the subsurface nitrogen atom; the gallium-nitrogen distance is 2.46 Å. The gallium-adatom surface-gallium bond-length is 2.40 Å which is very close to the Ga-dimer distance in α-gallium (2.44 Å). The bond angle between two gallium surface atoms and the adatom is 82°. The in-plane relaxation of the surface atoms is negligible; the only observed relaxation of the first bilayer is along the z direction. The three gallium atoms bonded to the adatom remain coplanar to a significant degree, while the remaining unbonded gallium surface atom relaxes into the slab. The proximity of the gallium adatom to the nitrogen subsurface atom lowers the electrostatic energy and makes this particular configuration energetically more favorable than the gallium adatom reconstruction with the adatom on the hollow site.

The nitrogen-adatom reconstruction is shown in Figure 5. The adatom sits on the hollow (H_3) site. The nitrogen-adatom surface-gallium bond-length is 2.0 Å and is very close to the Ga-N bond length distance in GaN bulk (1.96 Å). The bond angle between two gallium surface atoms and the nitrogen adatom is 89°. The relaxation perpendicular to the surface is very similar to that in the gallium-adatom reconstruction. This configuration is stabilized because it separates the nitrogen adatom from the subsurface nitrogen atom and thereby lowers the electrostatic repulsion.

Onset of Melting of Si (100) Surface

We now turn to the melting of the Si (100) surface. This is a classic problem, whose microscopic details are not well understood. This is particularly true of covalent materials like Si, whose surfaces are characterized by reconstructions, steps, islands, and other surface defects—all of which are expected to play a role in the microscopic aspects of the melting process. As a first step toward this goal, we have carried out simulations of the melting process of the Si (100) surface with finite-temperature ab initio methods. The temperature of the Si ions were controlled with a chain of five, linked Nose–Hoover thermostats [46]. Because the electrons are always quenched back onto the Born–Oppenheimer surface after every time step, no additional thermostat is needed for the electrons. The in-plane cells consisted of 16 atoms per layer and the basic time step of the simulation was 100 a.u.

The melting of the Si (100) surface has previously been investigated with classical molecular dynamics simulations [47], and the thermodynamics of melting has recently been investigated by ab initio techniques [48]. However, it is now known that classical potentials do not reproduce well several aspects of the melting process. Upon melting, Si goes from a fourfold coordinated semiconductor to a metallic liquid. The density of the liquid is about 10 percent higher than in the solid. The average coordination number is between 6 and 7, which is rather low for a metal. This low coordination number is indicative of persistent remnants of covalent bonding.

A relaxed six-layer slab of Si, with the bottom layer saturated by fixed H atoms, was heated up to 1500 K over a 1.5 ps period of time. Over the next 0.3 ps, the average temperature was raised to 1700 K, which is the melting temperature of bulk Si. Sample configurations as a function of time are shown in Figure 7.

We have characterized the structural, thermodynamic, and electronic properties changes that take place during the melting process. However, here we will only briefly summarize some of the main features, while a full description will be published elsewhere [49]. As the melting of the layers proceeds, there is a change in the density of the top layers as function of the vertical distance. While initially each of the layers is well separated and defined, the atomic density of the top layers becomes much more uniform at the end of the simulation time. During this time, the pair distribution function of the top four layers becomes much more liquidlike, with the second peak becoming essentially washed out. At the same time, the angular distribution function $g_3(\theta)$ changes by decreasing its large peak about the tetrahedral

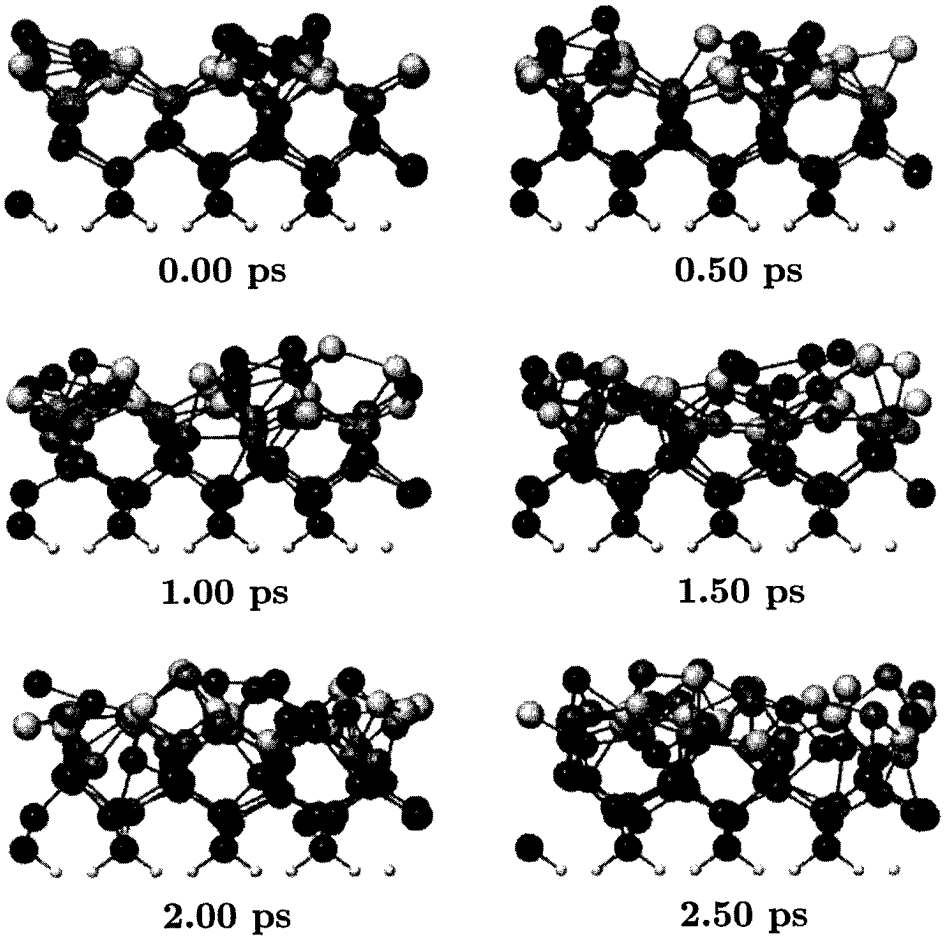


FIGURE 7. Side view of sample configurations of Si (100) surface at 1700 K as the top layers melt.

angle, broadening and developing a second peak in the 50–60° range, as shown in Figure 8. All of this is characteristic of a melted system. As a probe of the electronic properties, we have computed the local density of states for the bulk and liquid domains. These are compared in Figure 9. Note the relatively large buildup of states at the Fermi level for the liquid, characteristic of a metal, and the decrease in number of states for the bulk semiconductor.

Ongoing Work

ORDER-*N* REAL-SPACE IMPLEMENTATIONS

For very large systems, the complexity of the calculations increases as $O(N_{\text{atoms}}^3)$ in computer time due to orthogonalization, and the memory increases as $O(N_{\text{atoms}}^2)$. Several approaches that reduce both types of scaling behavior to $O(N_{\text{atoms}})$ have been proposed. These $O(N)$ methods rely on the assumption that physial properties are local, and that the orbitals [14] and/or the density matrix [15]—when localized in finite volumes about each atom—can describe the electron charge density, kinetic energy density, etc. to useful accuracy. More specifically, in most of the approaches the wave functions or the density are expanded in localized functions, usually atom- or bond-centered. The overlaps are then set to zero beyond a certain localization radius, and the size of this radius determines the accuracy. A detailed description of the methodology is beyond the scope of this work, but one can derive variational expressions in terms of these functions that lead to sparse matrix operations and $O(N)$ scaling. One should point out that only the range of the localized functions is predetermined, their shapes change during minimization. In the wave-function-based approaches, a useful analogy is to think of these orbitals as generalized Wannier functions; indeed, they become orthogonal at convergence. A recent review article provides an in-depth description of the various approaches [50]. In the quantum chemistry community there have been analogous developments aimed at achieving linear scaling in standard packages, which use Gaussian functions. To date, linear scaling has been achieved for the Coulomb part [51, 52], the exchange–correlation part within density functional theory [53], and most recently in the diagonalization part [54], following the Li–Nunes–Vanderbilt density-based approach.

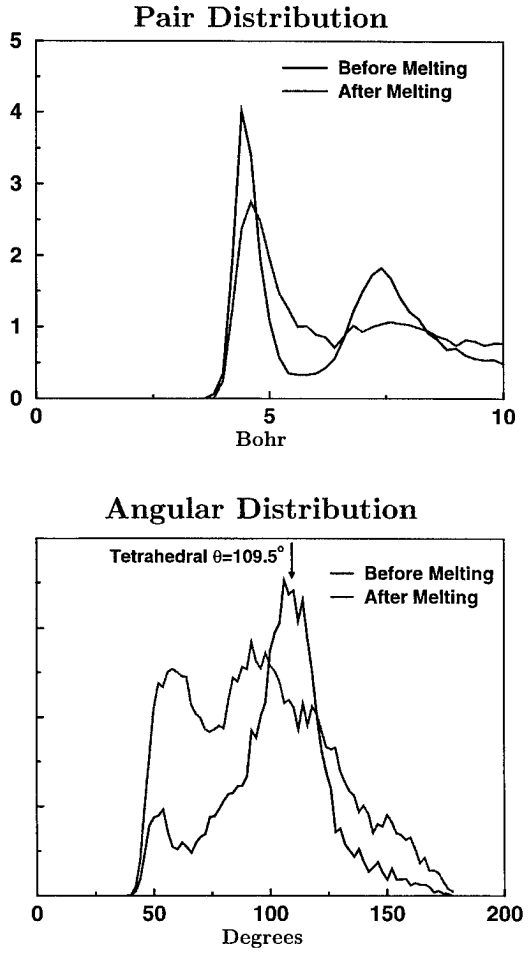


FIGURE 8. Angular correlation function before and after melting. Note the decrease in the large peak near the tetrahedral angle.

We have implemented a real-space self-consistent version of the Galli–Parrinello functional and tested it on 64- and 216-atom supercells of bulk Si. The Galli–Parrinello functional is variational, and the accuracy of the calculations depends strongly on the localization radius. In Table V, we show the errors per atom in the self-consistent total energy as a function of the radius. It is clear from the results that fairly large radii encompassing tens of atoms are necessary for an accurate description. We are currently testing other forms of $O(N)$ methods, comparing their accuracy and efficiency.

SOLVATED BIOMOLECULES

In collaboration with L. Pedersen (UNC-Chapel Hill), we are investigating the properties of a

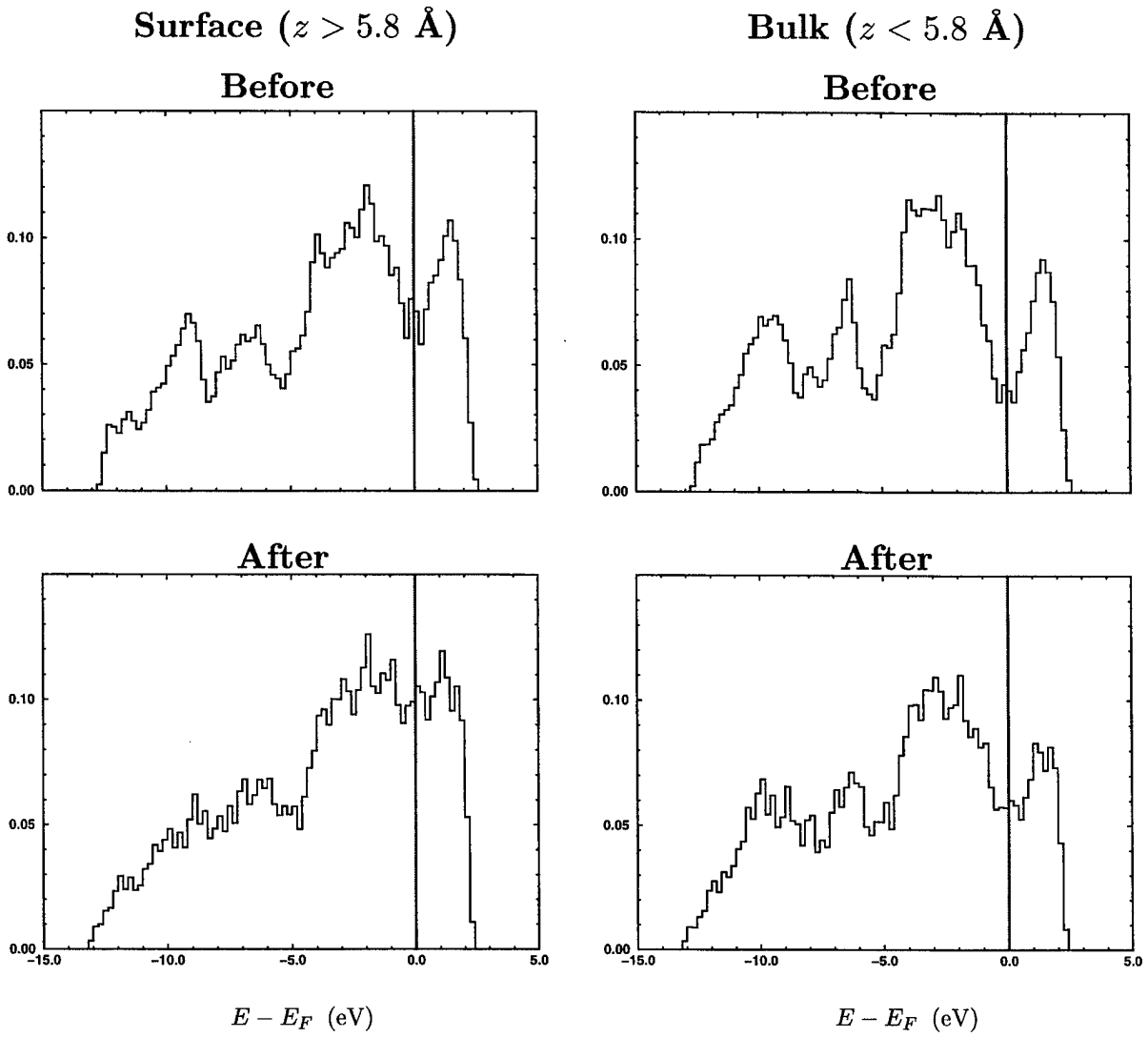


FIGURE 9. Local density of states in units of states per electron volt per atom after melting in the top layers and in the deeper "bulklike" region.

TABLE V
Error per atom due to localization in a self-consistent implementation of the *O(N)* Galli – Parinello functional.[a]

Localization radius (a.u.)	Error (eV / atom)
5.5	1.54
6.0	1.03
6.5	0.84
7.5	0.19
8.0	0.06
12.5	0.03

[a] See text.

protein associated with Alzheimer's disease, the amyloid β-peptide $C_{146}O_{45}N_{42}H_{210}$. The LDA calculations were performed on the Cray-T3D (128 or 256 processors), using a structure obtained from nuclear magnetic resonance (NMR) data that was refined by a molecular-mechanics force field program (AMBER). In Figure 10 we plot the electronic charge density of various parts of the protein. Presently, we are relaxing the system quantum mechanically in the presence of water, which is treated by a classical potential. We have also implemented the generalized gradient approximation to DFT (GGA) [55], which is known to improve the description of hydrogen bonding as well as the

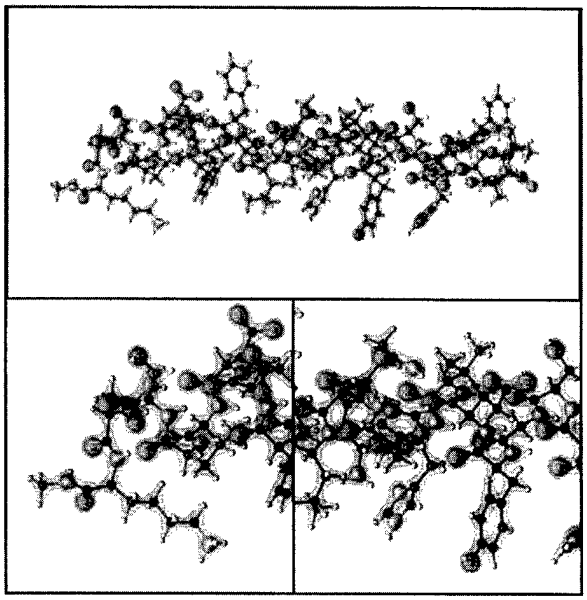


FIGURE 10. Three views of the electronic charge density of the amyloid β-peptide associated with Alzheimer's disease. The top view shows the entire molecule; the lower two views are close-ups of the first quarter and second third of the molecule, respectively.

values of the binding energies. In tests on an amino acid (phenylalanine), the GGA disassociation energy was lower by 7% than the LDA value of 142.59 eV.

Summary

We have developed a methodology for performing large-scale ab initio electronic structure calculations entirely in real space. By using highly efficient multigrid techniques to accelerate convergence rates, we are able to efficiently converge even difficult ill-conditioned systems, which require high-energy cut-offs or large length scales. The multigrid method is readily adaptable to parallel computer architectures, and an efficient parallel implementation was developed. The details of our implementation, which include new compact discretization schemes in real space for systems with cubic, orthorhombic, and hexagonal symmetry, and new multilevel algorithms for the iterative solution of Kohn–Sham equations, are described in Ref. [18]. This methodology was tested on a large number of systems, including the C_{60} molecule, diamond, Si and GaN supercells, and ab initio MD simulations. Further applications include a simulation of surface melting of Si, structural properties of a large amyloid β peptide ($C_{146}O_{45}N_{42}H_{210}$) implicated in Alzheimer's disease, and electronic and structural properties of GaN surfaces and $In_xGa_{1-x}N$ quantum wells. The accuracy of the method was also tested by direct comparison with plane-wave calculations, when possible, and the results were in excellent agreement in all cases.

ACKNOWLEDGMENTS

The preceding calculations were performed using the facilities of the Pittsburgh Supercomputer Center and the North Carolina Supercomputing Center.

References

1. R. Car and M. Parrinello, Phys. Rev. Lett. **55**, 2471 (1985).
2. For a recent review, see M. C. Payne, D. C. Allan, M. P. Teter, T. A. Arias, and J. D. Joannopoulos, Rev. Mod. Phys. **64**, 1045 (1992).
3. See, for example, I. Stich, M. C. Payne, R. D. King-Smith, and J.-S. Lin, Phys. Rev. Lett. **68**, 1351 (1992); K. D. Brommer, M. Needels, B. E. Larson, and J. D. Joannopoulos, *Ibid.* **68**, 1355 (1992); P. Boguslawski, Q.-M. Zhang, Z. Zhang, and J. Bernholc, *Ibid.* **72**, 3694 (1994).
4. D. Vanderbilt, Phys. Rev. B **41**, 7892 (1990).
5. A. M. Rappe, K. M. Rabe, E. Kaxiras, and J. D. Joannopoulos, Phys. Rev. B. **41**, 1227 (1990); J.-S. Lin, A. Qteish, M. C. Payne, V. Heine, *Ibid.* **47**, 4174 (1993); G. Li and S. Rabii, unpublished (1992).
6. P. E. Blöchl, Phys. Rev. B **41**, 5414 (1990).
7. F. Gygi, Europhys. Lett. **19**, 6617 (1992); F. Gygi, Phys. Rev. B **48**, 11692 (1993).
8. D. R. Hamann, Phys. Rev. B **51**, 7337 (1995); **51**, 9508 (1995).
9. A. Devenyi, K. Cho, T. A. Arias, and J. D. Joannopoulos, Phys. Rev. B **49**, 13373 (1994).
10. M. P. Teter, M. C. Payne, and D. C. Allan, Phys. Rev. B **40**, 12255 (1989).
11. T. A. Arias, M. C. Payne, and J. D. Joannopoulos, Phys. Rev. Lett. **69**, 1077 (1992); Phys. Rev. B **45**, 1538 (1992).
12. J. Bernholc, J.-Y. Yi, and D. J. Sullivan, Faraday Disc. Chem. Soc. **92**, 217 (1991).
13. A. Brandt, Math. Comp. **31**, 333 (1977); GMD Studien, **85**, 1 (1984).
14. W. Yang, Phys. Rev. Lett. **66**, 1438 (1991); G. Galli and M. Parrinello, *Ibid.* **69**, 3547 (1992); F. Mauri, G. Galli, and R. Car, Phys. Rev. B **47**, 9973 (1993); P. Ordejón, D. A. Drabold, M. P. Grumbach, and R. M. Martin, *Ibid.* **48**, 14646 (1993); J. Kim, F. Mauri, and G. Galli, Phys. Rev. B **52**, 1640 (1995); P. Ordejón, E. Artacho, and J. M. Soler, Phys. Rev. B **53**, R10441 (1996); and D. Sánchez-Portal, P. Ordejón, E. Artacho, and J. M. Soler, Int. J. Quant. Chem. **65**, 453 (1997).

15. S. Baroni and P. Giannozzi, Europhys. Lett. **17**, 547 (1992); X.-P. Li, R. Nunes, and D. Vanderbilt, Phys. Rev. B **47**, 10891 (1993); M. Daw, *Ibid.* **47**, 10895 (1993); W. Hierse and E. Stechel, *Ibid.* **50**, 17811 (1994); S. Goedecker and L. Colombo, Phys. Rev. Lett. **73**, 122 (1994); E. Hernandez and M. J. Gillan, Phys. Rev. B **51**, 10157 (1995); E. Hernandez, C. M. Goringe, and M. J. Gillan, *Ibid.* **53**, 7147 (1996).
16. S. R. White, J. W. Wilkins, and M. P. Teter, Phys. Rev. B **39**, 5819 (1989).
17. J. R. Chelikowsky, N. Troullier, and Y. Saad, Phys. Rev. Lett. **72**, 1240 (1994); J. R. Chelikowsky, N. Troullier, K. Wu, and Y. Saad, Phys. Rev. B **50**, 11355 (1994); X. Jing, N. Troullier, D. Dean, N. Binggeli, J. R. Chelikowsky, K. Wu, and Y. Saad, *Ibid.* **50**, 12234 (1994); J. R. Chelikowsky, X. Jing, K. Wu, and Y. Saad, *Ibid.* **53** 12071 (1996); X. Jing, N. Troullier, and J. R. Chelikowsky, Solid State Comm. **96**, 231 (1996).
18. E. L. Briggs, D. J. Sullivan, and J. Bernholc, Phys. Rev. B **52**, R5471 (1995); *Ibid.* **54**, 14362 (1996).
19. F. Gygi and G. Galli, Phys. Rev. B **52**, R2229 (1995).
20. G. Zumbach, N. A. Modine, and E. Kaxiras, Solid State Comm. **99**, 57 (1996).
21. K. Cho, T. A. Arias, J. D. Joannopoulos, and P. K. Lam, Phys. Rev. Lett. **71**, 1808 (1993).
22. S. Wei and M. Y. Chou, Phys. Rev. Lett. **76**, 2650 (1996).
23. E. J. Bylaska, S. R. Kohn, S. B. Baden, A. Edelman, R. Kawai, M. Elizabeth, G. Ong, and J. H. Weare, presented at the Sixth SIAM Conference on Parallel Processing for Scientific Computing, San Fransisco (1995).
24. K. A. Iyer, M. P. Merrick, and T. L. Beck, J. Chem. Phys. **103**, 227 (1995); T. L. Beck, K. A. Iyer, and M. P. Merrick, Proc. Sixth International Conference on Density Functional Theory, Paris (1995); and T. L. Beck, Int. J. Quant. Chem. **65**, 477 (1997).
25. D. R. Hamann, Phys. Rev. B **40**, 2980 (1989).
26. L. Collatz, *The Numerical Treatment of Differential Equations* (Springer, Berlin, 1960), p. 164.
27. To be precise, the LDA exchange-correlation potential is not represented exactly in a plane-wave basis because it is a nonlinear function of the density. However, its contribution to the high-frequency variation is small.
28. We assume that the electronic charge density is expanded with an energy cutoff twice as large as that of the wave functions.
29. W. L. Briggs, *A Multigrid Tutorial* (SIAM Books, Philadelphia, 1987).
30. L. Kleinman and D. M. Bylander, Phys. Rev. Lett. **48**, 1425 (1982).
31. H. Hellmann, *Einführung in die Quantenchemie* (Deuticke, Leipzig, 1937); R. P. Feynmann, Phys. Rev. **56**, 340 (1939).
32. P. Pulay, Mol. Phys. **17**, 197 (1969).
33. P. Boguslawski, E. L. Briggs, and J. Bernholc, Phys. Rev. B **51**, 17255 (1995).
34. Z. Lillenthal-Weber, presented at the 1995 MRS Fall Meeting, Boston, MA (1995).
35. J. Tersoff, Phys. Rev. Lett. **56**, 632 (1986); Phys. Rev. Lett. **61**, 2879 (1988); Phys. Rev. B **37**, 6991 (1988); D. W. Brenner, Phys. Rev. B **42**, 9458 (1990).
36. Q.-M. Zhang, J.-Y. Yi, and J. Bernholc, Phys. Rev. Lett. **66**, 2633 (1991).
37. J. Perdew and A. Zunger, Phys. Rev. B **23**, 5048 (1981).
38. D. Ceperley and B. Alder, Phys. Rev. Lett. **45** 566 (1980).
39. G. Bachelet, D. Hamann, and M. Schlüter, Phys. Rev. B **26**, 4199 (1982).
40. D. Hamann, M. Schlüter, and C. Chiang, Phys. Rev. Lett. **43**, 1494 (1979).
41. S. Louie, S. Froyen, and M. L. Cohen, Phys. Rev. B **26**, 1738 (1982).
42. M. Buongiorno Nardelli, K. Repcewicz and J. Bernholc, Phys. Rev. B **55**, R7323 (1997).
43. M. A. L. Johnson, Z. Yu, C. Boney, W. H. Rowland Jr., W. C. Hughes, J. W. Cook Jr., J. F. Schetzina, N. A. El-Masry, M. T. Leonard, H. S. Kong, and J. A. Edmond, MRS Proceedings, to appear.
44. K. Shiraishi, J. Phys. Soc. Jpn. **59**, 3455 (1990).
45. J. Neugebauer and M. Scheffler, Phys. Rev. B **46**, 16067 (1992).
46. S. Nose, J. Chem. Phys. **81**, 511 (1984); W. G. Hoover, Phys. Rev. A **31**, 1695 (1985); G. J. Martyna, M. L. Klein, and M. Tuckerman, J. Chem. Phys. **97**, 2635 (1992).
47. F. F. Abraham and J. Q. Broughton, Phys. Rev. Lett. **56**, 734 (1986).
48. S. Sugino and R. Car, Phys. Rev. Lett. **74**, 1823 (1995).
49. M. G. Wensell, E. L. Briggs, C. Roland, and J. Bernholc, to appear.
50. G. Galli, Cur. Opin. Solid State Mat. Sci **1**, 864 (1996).
51. C. A. White, B. G. Johnson, P. M. W. Gill, and M. Head-Gordon, Chem. Phys. Lett. **230**, 8 (1994); Chem. Phys. Lett. **253**, 268 (1996).
52. M. C. Strain, G. E. Scuseria, and M. J. Frisch, Science **271**, 51 (1996).
53. R. E. Stratmann, G. E. Scuseria, and M. J. Frisch, Chem. Phys. Lett. **257**, 213 (1996).
54. J. M. Millam and G. E. Scuseria, J. Chem. Phys. **106**, 5569 (1997).
55. A. D. Becke, J. Chem. Phys. **96**, 2155 (1992); J. P. Perdew, J. A. Chevary, S. H. Vosko, K. A. Jackson, M. R. Pederson, D. J. Singh, and C. Fiolhais, Phys. Rev. B **46**, 6671 (1992).
56. V. Fiorentini, M. Methfessel, and M. Scheffler, Phys. Rev. B **47**, 13353 (1993).
57. A. F. Wright and J. S. Nelson, Phys. Rev. B **50**, 2159 (1994); Phys. Rev. B **51**, 7866 (1995).

Relativistic Many-Body Perturbation Calculations for Zn and Cd and Their Singly Ionized Ions

YASUYUKI ISHIKAWA,[1] KONRAD KOC[2]

[1] *Department of Chemistry and The Chemical Physics Program, University of Puerto Rico, Rio Piedras Campus, P.O. Box 23346, San Juan, Puerto Rico 00931-3346*

[2] *Department of Physics, Pedagogical University, ul. Podchorążych 2, 30-084 Kraków, Poland*

Received 3 March 1997; accepted 20 March 1997

ABSTRACT: Relativistic correlation energies have been computed for the closed-shell ground states of Zn and Cd and their singly ionized open-shell ions by means of a recently developed relativistic many-body perturbation theory for open-shell multiplet states. All electrons were included in the correlation calculations. Analytic basis sets of Gaussian spinors are employed to expand the upper and lower components of the Dirac four spinors in closed- and open-shell matrix Dirac–Fock and relativistic many-body perturbation procedures. The ionization energies have been computed for the atoms, and the effects of relativity, electron correlation, and the nonadditive interplay of these effects on the ionization energies are analyzed. © 1997 John Wiley & Sons, Inc. Int J Quant Chem **65**: 545–554, 1997

Introduction

In heavy-atom systems, relativistic and electron correlation effects are large and strongly intertwined [1]. Therefore, accurate treatment of many-electron systems makes it necessary to go beyond the independent particle model to include both effects simultaneously. Fully relativistic many-body methods for atoms and molecules, which simultaneously account for both effects, are currently being developed and tested by several groups [2–16], using basis sets of either "local" or "global" functions. Three many-body techniques developed from nonrelativistic electronic structure theory have been successful in recovering correlation energy in relativistic treatments. They are relativistic many-body perturbation theory (MBPT) [2–6], relativistic configuration interaction (RCI) [7–12], and relativistic coupled-cluster (RCC) theory [13–16].

In recent studies [6], we have reported a state-specific relativistic MBPT for general open-shell systems in which our single Fock operator method [17] is employed to make a Møller–Plesset-type separation of the relativistic many-electron Hamiltonian. Relativistic correlation energies were com-

Correspondence to: Y. Ishikawa.

Contract grant sponsor: National Science Foundation.

© 1997 John Wiley & Sons, Inc.
CCC 0020-7608 / 97 / 050545-10

puted for the open-shell ground states of the Group IB and IIIA elements up to $Z = 79$ as well as their singly ionized closed-shell ions. The effects of relativity and electron correlation and the nonadditive interplay of these effects on their ionization energies (IE) were analyzed. The state-specific MBPT involves a full implementation of generalized Møller–Plesset perturbation theory [18] applied to general open-shell reference wave functions.

Relativistic effects are known to be important in the transition-metal atoms. The differential effects on the ionization energies of the first-row transition metals are as large as 0.5 eV in some cases [19, 20]. Therefore, even in the first-row transition metals, accurate determination of electronic structures requires approaches which can account for the nonadditive interplay of relativity and electron correlation. The purpose of the present study is to report on the application of our relativistic MBPT [6] to the Group IIB elements Zn and Cd and their singly ionized ions. In the next two sections, we outline our relativistic MBPT and its implementation with analytic basis set of G spinors (G for Gaussian after Grant [21]). In the last section, the results of matrix Dirac–Fock (DF) self-consistent field (SCF) and all-electron relativistic MBPT calculations on Zn and Cd and their singly ionized ions are presented. The effects of relativity and electron correlation and the nonadditive interplay of these effects on their IE are analyzed.

Relativistic Many-Body Perturbation Theory for Open-Shell Systems

In c-number theory, the effective many-body Hamiltonian most commonly used in relativistic atomic and moecular structure calculations is the no-pair Dirac–Coulomb (DC) Hamiltonian prescribed by Sucher [22] and Mittleman [23],

$$H_+^{DC} = \Sigma_i h_D(i) + \mathscr{L}_+ \left(\sum_{ij} 1/r_{ij} \right) \mathscr{L}_+ . \quad (1)$$

$\mathscr{L} = L_+(1)L_+(2)\ldots L_+(n)$, where $L_+(i)$ is the projection operator onto the space spanned by the positive-energy eigenfunctions of the matrix DF SCF equation [17]. The projection operator, $\mathscr{L}$, take into accouint the field-theoretic condition that the negative-energy states are filled and causes the projected DC Hamiltonian to have normalizable bound-state solutions. This approach is called the no-pair approximation [22] because virtual electron–positron pairs are not permitted in the intermediate states. h_D is a Dirac one-electron Hamiltonian:

$$h_D(i) = c\boldsymbol{\alpha}_i \cdot \mathbf{p}_i + (\beta - 1)c^2 + V_{\text{nuc}}(r_i). \quad (2)$$

Here $\boldsymbol{\alpha}$ and β are the 4×4 Dirac vector and scalar matrices, respectively. V_{nuc} is the nuclear potential, which for each nucleus takes the form

$$\begin{aligned} V_{\text{nuc}} &= -Z/r, \qquad r > R, \\ &= -(Z/2R)(3 - r^2/R^2), \qquad r \le R. \end{aligned} \quad (3)$$

The nuclei are modeled as spheres of uniform proton-charge distribution, Z the charge of nucleus. R is the radius of that nucleus and is related to the atomic mass, A, by $R = 2.2677 \times 10^{-5}\ A^{1/3}$. Adding the frequency-independent Breit interaction,

$$B_{12} = -1/2\left[\boldsymbol{\alpha}_1 \cdot \boldsymbol{\alpha}_2 + (\boldsymbol{\alpha}_1 \cdot \mathbf{r}_{12})(\boldsymbol{\alpha}_2 \cdot \mathbf{r}_{12})/r_{12}^2\right]/r_{12}, \quad (4)$$

to the electron–electron Coulomb interaction, in Coulomb gauge, results in the Coulomb–Breit potential which is correct to order α^2 [22, 23]. Addition of the Breit term yields the no-pair Dirac–Coulomb–Breit (DCB) Hamiltonian [22, 23]

$$H_+^{DCB} = \sum_i h_D(i) + \mathscr{L}_+ \left\{ \sum_{ij} (1/r_{ij} + B_{ij}) \right\} \mathscr{L}_+ , \quad (5)$$

which is approximately Lorentz covariant and increases the accuracy of calculated fine-structure splittings and inner-electron binding energies. Higher-order quantum electrodynamics (QED) effects appear first in order α^3 and are omitted.

The N-electron Hamiltonian, H, is partitioned into a model Hamiltonian H_0 and a perturbation V, such that $H = H_0 + V$. The zero-order Hamiltonian H_0 is arbitrary but should be chosen as close to the full Hammiltonian H as possible so that the perturbation series converges rapidly in low order. The zero-order Hamiltonian is usually chosen to be a sum of effective one-electron operators (Møller–Plesset partitioning [24]). In that form, all perturbation corrections describe electron correlation. For closed-shell systems, the best results have been obtained with Møller–Plesset partitioning. In the single Fock operator method of Koc and Ishikawa [17] relativistic MBPT for general open-shell multiplet states of atoms and molecules retains the essential aspects of Møller–Plesset per-

turbation theory. The theory providees a hierarchy of well-defined algorithms that allow one to calculate relativistic correlation corrections in noniterative steps and, in low order, yields a large fraction of the dynamical correlation. The no-pair DC Hamiltonian H_+^{DC} is

$$H_+^{DC} = H_0 + V, \tag{6}$$

where the unperturbed Hamiltonian H_0 is a sum of single DF SCF Fock operators R_0 [17] for closed- or open-shells:

$$H_0 = \sum_i R_0(i) \quad \text{and} \quad V = H_+^{DC} - \sum_i R_0(i), \tag{7}$$

and [6, 17]

$$R_0 = \mathscr{P}_c \mathscr{F}_c \mathscr{P}_c + \sum_{k(\in O)} \mathscr{P}_k \mathscr{F}_k \mathscr{P}_k + \mathscr{P}_v \mathscr{F}_c \mathscr{P}_v.$$

Here the mean-field operators, F_c and F_k, and the projection operators, $\mathscr{P}_c$, $\mathscr{P}_k$, and $\mathscr{P}_v$, have been defined in previous work [6, 17]. In this form of partitioning, all perturbation corrections describe relativistic electron correlation including the cross contribution between relativistic and correlation effects.

The exact many-electron wave function is expanded in configuration state functions (CSFs) $\{\Phi_i(\gamma_i JP);\ i = 1, 2, \ldots\}$ generated by single, double, triple, etc. excitations from the reference CSF, $\Phi_0(\gamma_0 JP)$. Individual CSFs are eigenfunctions of the total angular momentum and parity operators and are linear combinations of antisymmetrized products of positive-energy SCF spinors. The SCF spinors are mutually orthogonal, so the CSFs $\{\Phi_i(\gamma_i JP);\ i = 0, 1, 2, \ldots\}$ are also mutually orthogonal. The unperturbed Hamiltonian is diagonal in this space:

$$H_0 = \sum_i |\Phi_i(\gamma_i JP)\rangle E_i^{(0)} \langle \Phi_i(\gamma_i JP)| \tag{8}$$

so that

$$H_0|\Phi_i(\gamma_i JP)\rangle = E_i^{(0)}|\Phi_i(\gamma_i JP)\rangle \qquad (i = 0, 1, 2, \ldots) \tag{9}$$

$E_i^{(0)}$ is a sum of the SCF one-electron energies ε_q:

$$E_i^{(0)} = \sum_q \varepsilon_q N_q n_q[\Phi_i], \tag{10}$$

where the occupation number $N_q = 2j_q + 1$ and $n_q[\Phi_i]$ is the occupancy of the qth spinor in $\phi_i(\gamma_i JP)$.

Application of Rayleigh–Schrödinger perturbation theory provides order-by-order expressions of the perturbation series for the state approximated by $|\Phi_0(\gamma_0 JP)\rangle$ [6]:

$$\Psi = \Phi_0(\gamma_0 JP) + \Phi^{(1)}(JP) + \cdots, \tag{11}$$

$$E = E_0^{(0)} + E^{(1)} + E^{(2)} + E^{(3)} + \cdots, \tag{12}$$

where

$$\Phi^{(1)}(JP) = \sum_{i=1} \Phi_i(\gamma_i JP)\left\{V_{i0}(E_0 - E_i)^{-1}\right\}, \tag{13}$$

$$E_0^{(0)} + E^{(1)} = E_{SCF}, \tag{14}$$

$$E^{(2)} = \sum_{i=1} V_{0i} V_{i0} (E_0 - E_i)^{-1}, \tag{15}$$

$$E^{(3)} = \sum_{i,j=1} V_{0i} W_{ij} V_{j0} (E_0 - E_i)^{-1} (E_0 - E_j)^{-1}. \tag{16}$$

Here

$$V_{ij} = \langle \Phi_i(\gamma_i JP)|V|\Phi_j(\gamma_j JP)\rangle$$

and

$$W_{ij} = \langle \Phi_i(\gamma_i JP)|W|\Phi_j(\gamma_j JP)\rangle \qquad \text{with } W = V - E^{(1)}.$$

In this form, all the perturbation corrections beyond first-order describe relativistic electron correlation. Summation over the CSFs in Eqs. (13) through (16) are restricted to CSFs constructed from the positive-energy branch of the spinors, which effectively incorporates in the computational scheme the "no-pair" projection operator $\mathscr{L}_+$ of the DC and DCB Hamiltonians. Negative energy states, as part of the complete set of states, play a role in many-body calculations. However, contributions from the negative energy states due to creation of virtual electron-positron pairs are small [22], of the order α^3, and are neglected in the present study. Neglecting interactions with the filled negative-energy sea, i.e., neglecting virtual electron–positron pairs in summing the MBPT diagrams, we have a straightforward extension of nonrelativistic MBPT. In generalized Møller–Plesset formalism, the CSFs $\{\Phi_i(\gamma_i JP);\ i \neq 0\}$, generated by single excitations from the reference CSF, do not contribute to the second- and third-order energies because the singly excited CSFs, $\Phi_i(\gamma_i JP)$, generated by the SCF spinors, satisfy the generalized Brillouin theorem, $\langle \Phi_i(\gamma_i JP)|H_+^{DC}|\Phi_0(\gamma_0 JP)\rangle$

$= 0$. Thus $V_{i0} = 0$. CSFs generated by excitations higher than double also do not contribute to the second- and third-order energies, because for them $V_{i0} = 0$ and $H_{i0} = 0$.

Electron correlation effects are corrections to the independent electron approximation, and their importance depends on the choice of the approximation in which they are calculated. In nonrelativistic many-body calculations, the correlation energy, $E_{\mathrm{NR}}^{\mathrm{corr}}$ is defined as the difference between the exact eigenvalue of the N-electron Schrödinger Hamiltonian, $E_{\mathrm{NR}}^{\mathrm{exact}}$, and the nonrelativistic single-configuration Hartree–Fock (HF) energy, E_{HF} [25]:

$$E_{\mathrm{NR}}^{\mathrm{corr}} = E_{\mathrm{NR}}^{\mathrm{exact}} - E_{\mathrm{HF}}. \tag{17}$$

The nonrelativistic definition, Eq. (17), is based on the implicit assumption that it is easy to separate relativistic effects from an "exact" value of the total energy which contains both correlation and relativistic effects [25].

We employ in our MBPT calculations two different effective N-electron Hamiltonians, the no-pair DC Hamiltonian, Eq. (1), and the no-pair DCB Hamiltonian, Eq. (5). With respect to the two effective many-body Hamiltonians, we can define DCB correlation energy ($E_{\mathrm{DCB}}^{\mathrm{corr}}$) as the difference between the exact eigenvalue $E_{\mathrm{DCB}}^{\mathrm{exact}}$ of the DCB Hamiltonian, H_{+}^{DCB}, and the DF SCF energy (E_{SCF}), and DC correlation energy ($E_{\mathrm{DC}}^{\mathrm{corr}}$) as the difference between the exact eigenvalue ($E_{\mathrm{DC}}^{\mathrm{exact}}$) of the DC Hamiltonian, H_{+}^{DC}, and the DF SCF energy (E_{SCF}) [5, 6]:

$$E_{\mathrm{DCB}}^{\mathrm{corr}} = E_{\mathrm{DCB}}^{\mathrm{exact}} - E_{\mathrm{SCF}}, \tag{18}$$

$$E_{\mathrm{DC}}^{\mathrm{corr}} = E_{\mathrm{DC}}^{\mathrm{exact}} - E_{\mathrm{SCF}}. \tag{19}$$

The difference between the DCB correlation and the DC correlation, $E_{\mathrm{DCB}}^{\mathrm{corr}} - E_{\mathrm{DC}}^{\mathrm{corr}}$, is the relativistic many-body shift due to the low-frequency Breit interaction [5, 6].

Computation

The four-component atomic spinor, $\psi_{n\kappa m}$, is labeled by symmetry species κ and subspecies m, and

$$\psi_{n\kappa m}(r, \theta, \phi) = \frac{1}{r}\begin{bmatrix} P_{n\kappa}(r)\, X_{\kappa m}(\theta, \phi) \\ iQ_{n\kappa}(r)\, X_{-\kappa m}(\theta, \phi) \end{bmatrix} \tag{20}$$

with $P_{n\kappa}(r)$ and $Q_{n\kappa}(r)$ the large and small radial components, respectively, of the wave function. The four spinors are assumed to be orthonormal. In the matrix DF scheme, the radial functions are expanded in basis sets of analytic functions:

$$P_{n\kappa}(r) = \sum_i C_{n\kappa i}^{L} g_{\kappa i}^{L}(r) \tag{21}$$

and

$$Q_{n\kappa}(r) = \sum_i C_{n\kappa i}^{S} g_{\kappa i}^{S}(r), \tag{22}$$

where $\{C_{n\kappa i}^{L}\}$ and $\{C_{n\kappa i}^{S}\}$ are expansion coefficients for spinors of symmetry κ, and $\{g_{\kappa i}^{L}(r)\}$ and $\{g_{\kappa i}^{S}(r)\}$ are the large and small component basis sets, respectively.

The large radial component is expanded in a set of Gaussian-type functions (GTF) [5, 6, 9, 11, 12, 14, 15, 17]:

$$g_{\kappa i}^{L}(r) = A_{\kappa i}^{L} r^{n[\kappa]} \exp(-\zeta_{\kappa i} r^2) \tag{23}$$

with $n[\kappa] = -\kappa$ for $\kappa < 0$, and $n[\kappa] = \kappa + 1$ for $\kappa > 0$. $A_{\kappa i}^{L}$ is the normalization constant. The small component basis set $\{g_{\kappa i}^{S}(r)\}$ is constructed to satisfy the boundary condition associated with the finite nucleus of uniform proton charge distribution [1, 5, 6, 11, 15]. With the finite nucleus, GTF of integer power of r are especially appropriate basis functions because the finite nuclear boundary results in a solution which is Gaussian at the origin [1, 5, 6]. Basis functions which satisfy the nuclear boundary conditions are also automatically kinetically balanced [1, 5, 12]. Imposition of the boundary conditions results in particularly simple forms with spherical G spinors [1, 5, 6].

Matrix DF SCF and second-order relativistic MBPT calculations based on the no-pair Dirac–Coulomb Hamiltonian on the closed-shell ground $^1S_0$ state of Group IIB atoms, Zn and Cd, and the open-shell ground $^2S_{1/2}$ state of the singly ionized Zn^{1+} and Cd^{1+} ions employed large well-tempered basis sets [26] of G spinors. All electrons were included in the relativistic MBPT procedure to study the effects of relativity on electron correlation as well as the overall relativity and correlation contributions to the IE of the Group IIB atoms. The order of the partial-wave expansion ($L_{\max}$), the highest angular momentum of the spinors included in the virtual space, was $L_{\max} = 5$ throughout the study. The basis sets were $20s18p13d11f10g10h$ for zinc and $23s22p16d14f12g12h$ for cadmium. The well-tempered exponents were taken from the work of

Huzinaga and Klobukowski [26]. Table I shows the well-tempered basis set employed in the SCF and MBPT calculations on the neutral zinc atom and singly ionized zinc ion.

All-electron relativistic MBPT calculations were also performed that included the frequency-independent Breit interaction in the first and second orders of perturbation theory. These calculations were based on the no-pair Dirac–Coulomb–Breit Hamiltonian, H_+^{DCB}. The speed of light was taken to be 137.0359895 a.u. The nonrelativistic limit was simulated by setting the speed of light to 10^4 a.u. The nuclei were again modeled as spheres of uniform proton charge.

Results and Discussion

Table II displays the DF SCF energies E_{SCF}, second-order Dirac–Coulomb correlation energies, $E_{\mathrm{DC}}^{(2)}$, and first- and second-order Breit interaction energies, $B^{(1)}$ and $B^{(2)}$, for ground-state zinc, Zn^0, and Zn^{1+} in increasing order of partial-wave expansion. In each entry, the order of the partial-wave expansion, the DF SCF energy, and the relativistic MBPT energies are given in the first row. The values in parentheses in the second row are the nonrelativistic energies computed by setting $c = 10^4$.

TABLE I
Well-tempered exponents of the $20s18p13d11f10g10h$ G-spinor basis set employed in the DF SCF and RMBPT calculations of Zn^0 and Zn^{+1}.

	Symmetry					
Exponent	$s_{1/2}$	$p_{1/2,3/2}$	$d_{3/2,5/2}$	$f_{5/2,7/2}$	$g_{7/2,9/2}$	$h_{9/2,11/2}$
4250042.1	X					
663740.70	X					
144800.18	X	X				
38457.241	X	X				
11633.475	X	X				
3957.4984	X	X				
1508.8936	X	X				
624.94155	X	X	X			
272.06944	X	X	X	X		
121.77099	X	X	X	X	X	X
54.721784	X	X	X	X	X	X
24.885485	X	X	X	X	X	X
11.536923	X	X	X	X	X	X
5.2194206	X	X	X	X	X	X
2.3421989	X	X	X	X	X	X
1.0625147	X	X	X	X	X	X
0.46920953	X	X	X	X	X	X
0.18025741	X	X	X	X	X	X
0.08726504	X	X	X	X	X	X
0.04021766	X	X	X			

In the third column of Table II, we present the closed-shell DF SCF energies E_{SCF} for the ground $^1S_0(3d^{10}4s^2)$ state of Zn^0 as well as the open-shell DF SCF energies for the ground $^2S_{1/2}(3d^{10}4s^1)$ state of Zn^{1+}. The fourth column of the table gives the second-order Dirac–Coulomb correlation energies $E_{\mathrm{DC}}^{(2)}$ in increasing order of partial-wave expansion. The MBPT calculations were also performed with the frequency-independent Breit interaction included. The Breit interaction is introduced into the no-pair DC Hamiltonian, H_+^{DC}, by adding the frequency-independent Breit interaction, Eq. (4), to the instantaneous Coulomb interaction $1/r_{ij}$. In the fifth column we present the first-order Breit interaction energies, $B^{(1)}$. In the sixth column the second-order correlation corrections to the Breit interaction, $B^{(2)}$, are given in increasing order of partial-wave expansion. The $B^{(2)}$ are computed as the difference between the second-order correlation correction evaluated with the inclusion of B_{ij} in the effective electron–electron interaction and the second-order DC correlation correction, $E_{\mathrm{DC}}^{(2)}$. $B^{(2)}$ in correlation energies is the relativistic many-body shift that arises from incorporation of the frequency-independent Breit interaction into the effective two-body interaction.

The DF energies, -1794.61114 a.u., for the ground $^1S_0$ state Zn^0 atom, computed with a basis of $20s18p13d$ G spinors agree well with the corresponding numerical DF limit-1794.62 a.u. obtained with the numerical finite difference DF program of Desclaux [27]. The difference between relativistic DF SCF and its nonrelativistic limit for Zn^0, i.e., the relativistic energy lowering at the SCF level, is 16.76676 a.u.

Table II also shows the convergence patterns of the perturbation series in increasing partial-wave expansion. Because large G-spinor basis sets were employed to saturate the occupied and virtual spaces in each symmetry, the computed correlation energies have converged to at least four significant figures in each order of the partial-wave expansion. The convergence rates of the second-order Coulomb correlation correction with respect to partial-wave expansion are approximately the same for relativistic and nonrelativistic MBPT. The difference between the second-order Coulomb correlation correction $E_{\mathrm{DC}}^{(2)}$ at $c = 137.0359895$ and its

TABLE II
DF SCF and MBPT energies (a.u.) of the ground-state Zn^0 ($^1S_0$) and Zn^{+1} ($^2S_{1/2}$) in basis sets of increasing partial-wave expansion.[a]

L_{max}		E_{SCF}	$E_{DC}^{(2)}$	$B^{(1)}$	$B^{(2)}$	E_{tot}
2	Zn^0	−1794.61114	−0.96905	0.76145	−0.02037	−1794.83911
		(−1777.84438)	(−0.95893)			(−1778.80331)
	Zn^{+1}	−1794.32478	−0.93013	0.76134	−0.02036	−1794.51393
		(−1777.56381)	(−0.92134)			(−1778.48515)
3	Zn^0	−1794.61114	−1.42251	0.76145	−0.02342	−1795.29562
		(−1777.84438)	(−1.41104)			(−1779.25542)
	Zn^{+1}	−1794.32478	−1.36893	0.76134	−0.02341	−1794.95578
		(−1777.56381)	(−1.35949)			(−1778.92330)
4	Zn^0	−1794.61114	−1.56782	0.76145	−0.02447	−1795.44198
		(−1777.84438)	(−1.55679)			(−1779.40117)
	Zn^{+1}	−1794.32478	−1.51246	0.76134	−0.02446	−1795.10036
		(−1777.56381)	(−1.50351)			(−1779.06732)
5	Zn^0	−1794.61114	−1.62873	0.76145	−0.02502	−1795.50344
		(−1777.84438)	(−1.61799)			(−1779.46237)
	Zn^{+1}	−1794.32478	−1.57272	0.76134	−0.02501	−1795.16117
		(−1777.56381)	(−1.56418)			(−1779.12799)

[a] The values in parentheses are nonrelativistic energies computed by setting $c = 10^4$.

nonrelativistic limit ($c = 10^4$) is the relativistic DC many-body shift that arises from the use of relativistic single-particle states and the instantaneous Coulomb two-body interaction. The relativistic DC many-body shifts are relatively small for Zn^0 and Zn^{1+}, 0.01074 a.u. (0.292 eV) for Zn^0 and 0.00854 a.u. (0.232 eV) for Zn^{1+}, evaluated at $L_{max} = 5$. However, the effect on the IE of Zn^0 of the many-body shifts is significant because these values are noticeably different between Zn^0 and Zn^{1+}. For heavier systems, Au and Hg, the relativistic DC many-body shifts are an order of magnitude larger than that in Zn [5, 15].

We have summarized in Table III the IE for the ground $^1S_0$ state of the zinc atom obtained in partial-wave expansions up to $L_{max} = 5$. These IEs were computed by subtracting the total energy of Zn^0, from the last column of Table II, from that of Zn^{1+} in each order of the partial-wave expansion. The table illustrates the convergence pattern of the computed IE of Zn^0 in increasing partial-wave expansion. For comparison, we also list in the last row the experimental IE [28]. As the order of partial-wave expansion increases, the computed IE smoothly converges to approximately 9.32 eV. The experimental value is 9.39 eV [28]. The IE, 9.314 eV, computed by relativistic MBPT with the partial-wave expansion $L_{max} = 5$, has converged to within 0.01 eV of the extrapolated value ($L_{max} = \infty$) in the partial-wave expansion. The residual discrepancy of 0.07 eV between theory and experiment is due primarily to the truncation of MBPT at second order. The all-electron third-order correlation corrections for Zn^0 and Zn^{1+} are much more computationally demanding than the second-order, and are therefore neglected in the present study. The IE computed at the nonrelativistic limit, 9.099 eV, underestimates the experimental value by 0.3 eV because of the neglect of relativistic effects.

TABLE III
Computed ionization energy (eV) of Zn^0 in increasing partial-wave expansion.

	Ionization energy (eV)	
L_{max}	Relativistic	Nonrelativistic[a]
2	8.849	8.658
3	9.248	9.037
4	9.296	9.085
5	9.314	9.099
Experiment[b]	9.39	

[a] Nonrelativistic limit ($c = 10^4$).
[b] Experiment (Ref [28]).

When one compares experimental IEs of transition metals to those computed by nonrelativistic quantum chemical methods, one must correct for relativistic contributions. Martin and Hay [19] have calculated relativistic contributions to the experi-

mental ionization energies of transition metals at the DF level, assuming that electron correlation does not change the relativistic correction. Raghavachari and Trucks [20] modified the experimental IEs of transition metal atoms Sc through Zn by subtracting the relativistic corrections computed by Martin and Hay [19] from the experimental values. Their corrected "nonrelativistic" IE for Zn^0 is 9.23 eV, in good agreement with their estimate, 9.13 eV, computed by quadratic configuration interaction with single and double substitutions and perturbative triples (QCISD(T)). The corrected nonrelativistic IE, however, does not take into account the relativistic many-body shift. When this correction is accounted for, the agreement between them improves dramatically (see below).

Table IV displays the contribution at each order of perturbation theory to the ionization energy of Zn^0 computed at $L_{max} = 5$. These contributions were computed by subtracting the energy of Zn^0 from that of Zn^{1+} in each order of perturbation theory. Relativistic and nonrelativistic results are given, respectively, in the first and second rows. The third row gives, for each order, the difference between the relativistic and nonrelativistic contributions given, respectively, in the first and second rows. The second column gives the zero-order contribution, ΔE_{SCF}, to the ionization energy, relativistic and nonrelativistic, and their difference. The relativistic zero-order contribution 7.7923 eV, the so-called ΔSCF approximation to the IE, was computed by subtracting the DF SCF energy of Zn^0 from that of Zn^{1+}. The nonrelativistic zero-order contribution, 7.6347 eV, was computed by subtracting the nonrelativistic SCF energy of Zn^0 from that of Zn^{1+}. Both relativistic and nonrelativistic ΔSCF approaches significantly underestimate the ionization energy. Numerous nonrelativistic and relativistic SCF calculations have demonstrated that single-configuration SCF yields IE which are significantly lower than experimental, indicating that electron correlation effects are important. When the Coulomb correlation correction, $\Delta E_{DC}^{(2)} = 1.5241$ eV, the difference in the second-order DC correlation energies between Zn^{1+} and Zn^0 is taken into account, the computed IE dramatically improves. The effects of Breit interaction corrections on the computed IE, -0.00299 and 0.00027 eV, respectively, for $\Delta B^{(1)}$ and $\Delta B^{(2)}$, on the valence-shell electron IE of Zn^0, are negligible. The Breit interaction is a short-range interaction that primarily affects the inner-shell $s_{1/2}$ and $p_{1/2}$ electrons [5, 6].

Referring to the third row of Table IV, the largest relativistic correction to the nonrelativistic contribution to the ionization energy, 0.1576 eV, comes from the relativistic DF SCF. In an earlier study [19], Martin and Hay estimated this correction to be 0.16 eV, in agreement with our result. The effect of electron correlation on the relativistic corrections, i.e., the relativistic many-body shift, has not hitherto been available for the transition metals. The difference in relativistic many-body shifts between Zn^{1+} and Zn^0 (0.0599 eV) given in the third row of Table IV, which directly contributes to the IE, is approximately $\frac{2}{5}$ of the relativistic SCF contribution (0.1576 eV). The differential effect of relativistic DC correlation on the calculated relativistic corrections to the ionization energy is thus nonnegligible. The overall relativistic correction to the IE of the zinc atom is 0.215 eV. When this correction is subtracted from the experimental IE, one obtains 9.17 eV for the corrected nonrelativistic IE for Zn, in excellent agreement with the estimated nonrelativistic IE of 9.13 eV obtained by Raghavachari and Trucks [20]. The

TABLE IV

Contributions from each order of perturbation theory to the ionization energy (in eV) of ground state Zn^0 at $L_{max} = 5$.

$E(Zn^{+1})$-$E(Zn^0)$	ΔE_{SCF}	$\Delta E_{DC}^{(2)}$	$\Delta B^{(1)}$	$\Delta B^{(2)}$	Total (IE[b])
Relativistic	7.7923	1.5241	-0.0029_9	0.0002_7	9.314
Nonrelativistic	7.6347	1.4642	0.0	0.0	9.099
Diff. (Rel − Nonrel)	0.1576 (0.16)[a]	0.0599	-0.0029_9	0.0002_7	0.215

[a] Martin and Hay (Ref. [19]).
[b] Ionization energy.

residual discrepancy of ≈ 0.04 eV is primarily due to the truncation of partial wave to $L_{max} = 3$ in the nonrelativistic QCISD(T) calculations.

Table V displays the DF SCF energies E_{SCF}, second-order DC correlation energies $E_{DC}^{(2)}$, and first- and second-order Breit interaction energies, $B^{(1)}$ and $B^{(2)}$, for the ground $^1S_0$ state of the cadmium atom and its singly ionized Cd^{1+} ion obtained at $L_{max} = 5$. The relativistic many-body shift, $B^{(2)}$, increases dramatically from Zn to Cd. In going from Zn to Cd, the first- and second-order Breit interaction energies increase four- to fivefold, and the Breit interaction results in a significant modification of relativistic many-body effects. However, $B^{(1)}$ and $B^{(2)}$ are nearly identical for the neutral atoms and their singly ionized ions, and thus the valence-shell electron IE is almost entirely accounted for by the differences in DF energies, E_{SCF}, and the Coulomb correlation energies $E_{DC}^{(2)}$. Such is not the case with the elements of the fifth and higher rows, nor with highly ionized species [5, 6]. In highly ionized ions, $B^{(2)}$ is comparable in magnitude to the second-order Coulomb correlation correction. The differences in $B^{(1)}$, $B^{(2)}$, and $E_{DC}^{(2)}$ between an ion A^{n+} and $A^{(n+1)+}$ tend to affect the IE by similar amounts [5, 6].

As with Zn the large basis sets result in computed correlation energies that have converged to at least four significant figures in each order of the partial-wave expansion. The convergence rates of the second-order Coulomb correlation correction with respect to partial-wave expansion are approximately the same for relativistic and nonrelativistic MBPT. The relativistic DC mnay-body shifts are relatively small for Cd^0 and Cd^{1+}, i.e., 0.03530 a.u. (= 0.961 eV) for Cd^0 and 0.02984 a.u. (= 0.812 eV) for Cd^{1+} evaluated at $L_{max} = 5$. However, as with zinc, the effect on the IE of Cd^0 of the many-body shifts is significant because these values are noticeably different between Cd^0 and Cd^{1+}.

Table VI displays the contribution from each order of perturbation theory to the ionization energy of Cd^0 computed at $L_{max} = 5$. The table was constructed in a similar manner to Table IV. Relativistic and nonrelativistic results are given in the first and second rows, and the third row gives the difference between relativistic and nonrelativistic contributions. The second column gives the zero-order contribution, ΔE_{SCF}, to the ionization energy computed both relativistically and nonrelativistically and their difference. The ΔSCF approximation for IE, 7.3544 eV, was computed by subtracting the DF SCF energy of Cd^0 from that of Cd^{1+}. The nonrelativistic zero-order contribution 6.9264 eV was computed by subtracting the nonrelativistic SCF energy of Cd^0 from that of Cd^{1+}. As in the case of Zn, both relativistic and nonrelativistic ΔSCF approaches underestimate the ionization energy. When the Coulomb correlation correction $\Delta E_{DC}^{(2)} = 1.7309$ eV, the difference in the second-order DC correlation energies between Cd^{1+} and Cd^0, is taken into account, the computed IE improves. The differential effect of relativistic DC correlation on the calculated relativistic corrections to the ionization energy is nonnegligible. On the other hand, the effects of Breit interaction corrections on the computed IE, −0.00490 and 0.00027 eV, respectively, for $\Delta B^{(1)}$ and $\Delta B^{(2)}$, on the valence-shell electron IE of Cu^0 are still negligible in Cd. The IE at the nonrelativistic limit, 8.509 eV, underestimates the experimental value by 0.48 eV because of the neglect of relativistic effects. Referring to the third row of Table VI, the largest relativistic correction to the nonrelativistic contribution to the ionization energy, 0.4280 eV, comes from the relativistic DF SCF. The difference in relativistic many-body shifts between Cd^{1+} and Cd^0 (0.1486 eV) given in the third row of Table VI, which directly contributes to the IE, is approximately $\frac{1}{3}$ of the relativistic SCF contribution (0.4280

TABLE V
DF SCF and MBPT energies (a.u.) of the ground-state Cd^0 ($^1S_0$) and Cd^{+1} ($^2S_{1/2}$) computed with partial-wave expansion, $L_{max} = 5$.[a]

	E_{SCF}	$E_{DC}^{(2)}$	$B^{(1)}$	$B^{(2)}$	E_{tot}
Cd^0	−5593.32183	−2.57354	3.84216	−0.08161	−5592.13482
	(−5465.09882)	(−2.53824)			(−5467.63706)
Cd^{+1}	−5593.05156	−2.50993	3.84198	−0.08160	−5591.80111
	(−5464.84428)	(−2.48009)			(−5467.32437)

[a] The values in parentheses are nonrelativistic energies computed by setting $c = 10^4$.

TABLE VI
Contributions from each order of perturbation theory to the ionization energy of the ground state Cd^0 at $L_{max} = 5$ (in eV).

$E(Cd^{+1})$-$E(Cd^0)$	ΔE_{SCF}	$\Delta E_{DC}^{(2)}$	$\Delta B^{(1)}$	$\Delta B^{(2)}$	Total (IE[a])
Relativistic	7.3544	1.7309	−0.0049	0.0002_7	9.081
Nonrelativistic	6.9264	1.5823	0.0	0.0	8.509
Diff. (Rel − Nonrel)	0.4280	0.1486	−0.0049	0.0002_7	0.572

[a] Ionization energy

eV). The differential effect of relativistic DC correlation on the calculated relativistic corrections to the ionization energy is thus nonnegligible and larger than that in Zn. The overall relativistic correction to the IE of the cadmium atom is 0.572 eV.

We have summarized in Table VII the computed IEs for Zn and Cd. In the third column, the IEs computed in previous nonrelativistic and relativistic correlated calculations are shown. The experimental IEs are given in the last column. The IEs computed in this study agree with experiment. The discrepancies between the computed and observed IEs are within 0.1 eV for both Zn and Cd. The bulk of the error is due to truncation of the perturbation expansion at second order. Vijayakumar and Gopinathan [29] employed a relativistic correlated local density functional (RCΞ) method to calculate the IEs of atoms He through Zn. The computed IE of Zn by the RCΞ method is 8.41 eV, underestimating the experimental value by as much as 1 eV. Guo and Whitehead [30] computed the IE of Cd by generalized-exchange local-spin-density-functional method with relativistic corrections of the mass velocity and Darwin terms. The density functional method produces an IE for Cd (8.72 eV) in closer agreement with experiment (8.99 eV) than does Vijayakumar's RCΞ estimate for Zn.

TABLE VII
Ionization energies of Zn and Cd (eV).

	Ionization energy		
Atom	This work	Other work	Experiment[a]
Zn	9.314	8.41,[b] 9.13[c]	9.39
Cd	9.081	8.72[d]	8.99

[a] Moore's table (Ref. [28]).
[b] Vijayakumar and Gopinathan; relativitsic and correlated local-density Ξ method (Ref. [29]).
[c] Raghavachari and Trucks; nonrelativistic QCISD(T) (Ref. [20]).
[d] Guo and Whitehead; QR-LSD-GX-SIC-GWB method (Ref. [30]).

ACKNOWLEDGMENT

This work was supported in part by the National Science Foundation.

References

1. Y. Ishikawa and U. Kaldor, in *Computational Chemistry: Reviews of Current Trends*, Vol. 1, J. Leszczynski, Ed. (World Scientific, Singapore, 1996).
2. W. R. Johnson and J. Sapirstein, Phys. Rev. Lett. **57,** 1126 (1986); W. R. Johnson, M. Idrees, and J. Sapirstein, Phys. Rev. A **35,** 3218 (1987); W. R. Johnson, S. A. Blundell, and J. Sapirstein, Phys. Rev. A **37,** 307 (1988); *Ibid.* **42,** 1087 (1990); S. A. Blundell, J. Sapirstein, and W. R. Johnson, Phys. Rev. D **45,** 1602 (1992); S. A. Blundell, W. R. Johnson, and J. Sapirstein, Phys. Rev. A **37,** 2764 (1988); *Ibid.* **38,** 2699 (1988); *Ibid.* **42,** 1087 (1990); *Ibid.* **42,** 3751 (1990).
3. H. M. Quiney, I. P. Grant, and S. Wilson, Phys. Scr. **36,** 460 (1987); H. M. Quiney, I. P. Grant, and S. Wilson, in *Many-Body Methods in Quantum Chemistry* (Lecture Notes in Chemistry 52), U. Kaldor, Ed. (Springer, Berlin, 1989); H. M. Quiney, I. P. Grant, and S. Wilson, J. Phys. B **23,** L271 (1990).
4. K. Koc and J. Migdalek, J. Phys. B **23,** L5 (1990).
5. Y. Ishikawa, Phys. Rev. A **42,** 1142 (1990); Y. Ishikawa and H. M. Quiney, Phys. Rev. A **47,** 1732 (1993); Y. Ishikawa and K. Koc, Phys. Rev. A **50,** 4733 (1994).
6. Y. Ishikawa and K. Koc, Phys. Rev. A **53,** 3966 (1996); Phys. Rev. **A,** in press.
7. M. H. Chen, K. T. Cheng, and W. Johnson, Phys. Rev. A **47,** 3692 (1993).
8. D. R. Beck and Z. Cai, Phys. Rev. A **37,** 4481 (1988); D. R. Beck, *Ibid.* **37,** 1847 (1988); *Ibid.* **45,** 1399 (1992).
9. B. Hess, Phys. Rev. A **33,** 3742 (1986); G. Jansen and B. A. Hess, Phys. Rev. A **39,** 6016 (1989); R. Samzow, B. A. Hess, and G. Jansen, J. Chem. Phys. **96,** 1227 (1992); A Pizlo, G. Jansen, and B. A. Hess, J. Chem. Phys. **98,** 3945 (1993).
10. T. Kagawa, Y. Honda, and S. Kiyokawa, Phys. Rev. A **44,** 7092 (1991).

11. K. Koc, Y. Ishikawa, and T. Kagawa, Chem. Phys. Lett. **231,** 407 (1994); K. Koc, Y. Ishikawa, T. Kagawa, and Y.-K. Kim, Chem. Phys. Lett. **263,** 338 (1996).
12. P. J. C. Aerts and W. Nieuwpoort, Chem. Phys. Lett. **125,** 83 (1986); Int. J. Quant. Chem. Symp. **19,** 267 (1986); O. Visser, L. Visscher, P. J. C. Aerts, and W. C. Nieuwpoort, Theor. Chim. Acta **81,** 405 (1992).
13. E. Lindroth, Phys. Rev. A **37,** 316 (1988); E. Lindroth and S. Salomonson, Phys. Rev. A **41,** 4659 (1990); E. Lindroth, H. Persson, S. Salomonson, and A-M. Mårtensson-Pendrill, Phys. Rev. A **45,** 1493 (1992).
14. H. Sekino and R. J. Bartlett, Int. J. Quant. Chem. Symp. **24,** 241 (1990).
15. E. Eliav, U. Kaldor, and Y. Ishikawa, Phys. Rev. A **49,** 1724 (1994); *Ibid.* **50,** 1121 (1994); *Ibid.* **52,** 291 (1995); Phys. Rev. Lett. **74,** 1079 (1995).
16. S. A. Blundell, W. R. Johnson, Z. W. Liu, and J. Sapirstein, Phys. Rev. A **39,** 3768 (1989); **40,** 2233 (1989); S. A. Blundell, W. R. Johnson, and J. Sapirstein, Phys. Rev. A **43,** 3407 (1991).
17. K. Koc and Y. Ishikawa, Phys. Rev. A **49,** 794 (1994).
18. B. O. Roos, P. Linse, P. E. M. Siegbahn, and M. R. A. Blomberg, Chem. Phys. **66,** 197 (1982); K. Wolinski and P. Pulay, J. Chem. Phys. **90,** 3647 (1989); K. Hirao, Chem. Phys. Lett. **196** 397 (1992); *Ibid.* **201,** 59 (1993); R. B. Murphy and R. P. Messmer, J. Chem. Phys. **97,** 4170 (1992); I. Shavitt, presented at the 1992 Sanibel Symposium, St. Augustine, Florida, March 1992.
19. R. L. Martin and P. J. Hay, J. Chem. Phys. **75,** 4539 (1981).
20. K. Raghavachari and G. W. Trucks, J. Chem. Phys. **91,** 2457 (1989).
21. I. P. Grant, in *Relativistic, Quantum Electrodynamic, and Weak Interaction Effects in Atoms, Proceedings of the Conference on Relativistic, Quantum Eletrodynamic, and Weak Interaction Effects in Atoms*, W. R. Johnson, P. Mohr, and J. Sucher, Eds. AIP Conf. Proc. No. 189 (AIP, New York, 1989), p. 209.
22. J. Sucher, Phys. Rev. A **22,** 348 (1980); Phys. Scripta **36,** 271 (1987); J. Phys. B **21,** L585 (1988).
23. M. H. Mittleman, Phys. Rev. A **24,** 1167 (1981); *Ibid.* **4,** 893 (1971); *Ibid.* **5,** 2395 (1972).
24. C. Møller and M. S. Plesset, Phys. Rev. **46,** 618 (1934).
25. P. O. Löwdin, Adv. Chem. Phys. **2,** 207 (1959).
26. S. Huzinaga and M. Klobukowski, J. Mol. Struct. Theochem. **167,** 1 (1988); S. Huzinaga, M. Klobukowski, and H. Tatewaki, Can. J. Chem. **63,** 1812 (1985); S. Huzinaga and M. Klobukowski, Chem. Phys. Lett. **212,** 260 (1993).
27. J. P. Desclaux, Comput. Phys. Commun. **9,** 31 (1975).
28. C. E. Moore, *Atomic Energy Levels*, NSRDS-NBS No. 35 (U.S. Government Printing Office, Washington, DC , 1971).
29. M. Vijayakumar and M. S. Gopinathan, J. Chem. Phys. **97,** 6639 (1992).
30. Y. Guo and M. A. Whitehead, Phys. Rev. A **38,** 3166 (1988).

Hyperfine Structure Constants of $(d + s)^3$ States in La I and the Zr II and Hf II Isoelectronic Sequences

DONALD R. BECK

Physics Department, Michigan Technological University, Houghton, Michigan 49931

Received 2 March 1997; revised 18 June 1997; accepted 19 June 1997

ABSTRACT: Accurate results for hyperfine structure (HFS) constants of $(d + s)^n$ states often require the inclusion of both correlation and relativistic effects. Without these, Dirac–Fock HFS constants may have the wrong sign, the energies of uppermost d^n levels may be wrong by over 1 eV. Here, we demonstrate that these problems persist well into an isoelectronic sequence, and identify the principle configurations needed to achieve accurate results. © 1997 John Wiley & Sons, Inc. Int J Quant Chem **65**: 555–564, 1997

Introduction

Transition-metal atoms play important roles in catalysis, as impurities in plasma fusion devices, and as deep-level traps in semiconductors. Previously, properties of $(d + s)^n$ states of these species, which form many of the ground and low-lying excited states, have been rather poorly understood. Positions of d^n levels can be in error over 1 eV, independent particle hyperfine structure (HFS) constants can have the wrong sign, and little ab initio work has been done on their transition probabilities.

Project grant sponsor: Division of Chemical Sciences, Office of Energy Research, U.S. Department of Energy.
Project grant number: DE-FG02-92ER14282.

Our HFS work on these states, which began in 1992 [1], has established the need to accurately position the $d^{n-1}s$ levels relative to those from d^n and $d^{n-2}s^2$ in order to account for the HFS constants for the latter two configurations. We may interpret this as being due to the former normally having large HFS constants arising from the contact operator contributing at the zeroth-order (independent particle) level. Of course, in addition to positioning the levels correctly, the usual core polarization effects must be included.

Since relativistic effects associated with d, s electron interchanges may be several tenths of an electron volt [2], they can have an important impact on level positions and so must be included in any theoretical treatment. It is also necessary to treat d^n, $d^{n-1}s$, and $d^{n-2}s^2$ levels on an equal footing, so our theory must be a multireference

© 1997 John Wiley & Sons, Inc.
CCC 0020-7608 / 97 / 050555-10

one. Furthermore, when obtaining correlated wave functions for these levels, one can be involved with configurations possessing a few hundreds of eigenvectors, each constructed from several hundreds of Slater determinants. This calls for some innovative ways of reducing computational costs.

Methodology

The wave functions are generated from the Dirac–Coulomb Hamiltonian, with the Breit contribution, optionally, added as a perturbation. Multiconfigurational Dirac–Fock (MCDF) solutions obtained from Desclaux's program [3] are used as zeroth-order functions. There are generated from just $(d + s)^n$ levels. Correlation is introduced through relativistic configuration interaction (RCI); normally a first-order form is chosen, i.e., those configurations generated by making single or double excitations from outermost subshells of MCDF configurations. The question of what to use as one-electron functions for unoccupied (virtual) subshells is an important one, as poor choices may lead to (partial) variational collapse into the "positron sea." This can be avoided if the major and minor components of these functions are properly constrained (e.g., not allowed to vary separately). In our case, experience has demonstrated that use of relativistic screened (Z^*) hydrogenic functions avoid this problem, while at the same time providing an adequately converged series, if Z^* is chosen during the RCI process to minimize the energy for the root of interest.

Since much of our work deals with excited states, we prefer to work with moderately sized (< 7000) energy matrices, which we diagonalize using Weber and co-workers' [4] variant of the Davidson algorithm, to which we have added some improvements [5]. We thus want to use N electron functions which are eigenstates of J^2, J_z, and parity. Formerly, we used to generate eigenstates of J^2 by direct diagonalization of that matrix, but some of the correlation configurations can involve matrices of order several thousand, and we may need a few hundred eigenvectors. In our HFS studies, we have avoided this difficulty by splitting the configuration into two separate parts, each of which we make eigenstates of J^2 and J_z, and their "paste" the parts back together using standard vector coupling theory (sums of the product of the two section functions and a single $3j$ symbol are involved). The procedure is very fast and capable of dealing with large problems.

To further restrict the size of the energy matrix, we have automated a suggestion first made by Bunge [6] in a nonrelativistic study of the carbon atom. This recognizes that the N parents (eigenvectors) of a single configuration, generate matrix elements (with the zeroth-order function) involving M radial integrals, and that M is less than N, usually. In fact, in the transition metals and rare earths, M may be 10–1000 times smaller than N. Since the theory is first order in "form," a rotation of the original set of parents can be done, such that in the new set, there are only M parents which have a nonzero interaction with the reference function. The other $N - M$ functions can then be discarded, consistent with a first-order (in form) theory. Certain adjustments are made for the fact that our theory is relativistic, and multireference, but the approximation is both a good one (errors less than 200 cm^{-1}) and highly efficient. Further details of the methodology can be found in our Zr II paper [7].

COMPUTATIONAL STRATEGY

Our calculations begin by doing RCI calculations built from single and double excitations from the valence (e.g., $4d, 5s$ in Zr II) subshells into virtuals of symmetries s, p, d, g (one radial for each type). These excitations are significant contributors to energy differences, and sensitive to orthogonalization order (if core excitations are done first, it is difficult to recover energy loss from valence virtuals due to orthogonalization to core virtuals). Now the $4d$ and $5s$ radial functions can vary substantially between $(4d)^3$, $(4d)^2 5s$ and $4d(5s)^2$ configurations. To account for this, we do the MCDF calculation for the root of most interest (e.g., $(4d)^3 J = \frac{3}{2}$ was chosen in Zr II, as this was the subject of a recent measurement [7]), and use "Brillouin"-type excitations, viz. $4d \rightarrow vd$, $5s \rightarrow vs$ (and eventually $4p \rightarrow vp$) to improve the description of the other roots.

After the first set of valence virtuals is determined, a second set, associated with these same single and double valence excitations is added; this normally provides sufficient radial saturation

of the valence space. The larger triple excitations are also added in at this time.

In the next calculational layer, we begin to make single and double excitations form the shallow core, viz. the $4s$ and $4p$ subshells, adding in a third set of virtuals, with larger effective Z^* (determined during the RCI process). Important excitations include $4p \rightarrow vp + vf$, and $4s \rightarrow 5s + vs$, $4d + vd$. Decisions on what to include are based on the criteria that we are seeking energy contributions which are differentially large or make substantial contributions to HFS. These single excitations generally fall into both categories.

At this stage, errors in relative energy differences were still too large, on the order of a few tenths of an electron volt. We may reasonably expect the next most important corrections to come from the classes of excitations: $4p(4d + 5s) \rightarrow$, but in fact these have a differentially modest effect. Next, we looked at double excitations from $4p^6$. The most important of these, differentially, turn out to be $4p^2 \rightarrow 4d^2 + 4d\,vd$, which we may ascribe to (1) the fact that $l^2 \rightarrow (l + 1)^2$ are among the largest [8], and (2) Pauli exclusion effects are involved, i.e., the $4d$ subshells are already partially occupied, and this tends to reduce the contribution in varying amounts, depending on the occupancy of the $4d$ subshell for the level of interest. This finding is valid for all transition metal spectra studied to date, and was first noted in the Zr II work [7].

By using intermediate normalization $\langle \Phi | \Psi \rangle = 1$, where Φ is the zeroth-order function, and Ψ is the RCI function, it is possible to assign energy contributions to each correlation vector. These are collected in Table I, for Zr II for all configurations contributing 0.025 eV or more to at least one root. The excitations present in Table I reduce the average energy difference error to 0.075 eV ($\sim$ 600 cm^{-1}). On simpler systems, e.g., La II, we have reduced the error to 0.02 eV or $\sim$ 160 cm^{-1} [9].

Results

Zr II ISOELECTRONIC SEQUENCE

In this sequence, we avoid Y I because of the interpenetrating manifolds $5s^2 6s$ and $4d5s6s$ [10] which would increase the number of reference functions needed. In a relativistic treatment such as this, each J is a separate problem. We chose to study $J = \frac{3}{2}$ because it had the greatest number of reference functions (10), thus making it challenging, and because several $J = \frac{3}{2}$ levels were just being measured for Zr II [11]. Results for Zr II have already appeared [7, 11], but we reproduce them here in Table II, as this species can provide a benchmark for the other sequence members for which no HFS measurements exist. It can be seen that the average error for the RCI A results is 9.2%, in contrast to the Dirac–Fock (DF) values, for which two of the three results have the wrong sign. We also note that we are in agreement with the corrections of Kiess [12] to the Moore [10] energy levels.

In Table III we present results for the Nb III member of the $J = \frac{3}{2}$ isoelectronic sequence. For the five known energy differences [10], the theoretical error is 0.050 eV (410 cm^{-1}); note that we have predicted the positions of four new levels, not available from experiment [10, 13]. Though there is greater agreement between the DF and RCI results for A than in Zr II, there are still two levels exhibiting a sign reversal. The one and N electron basis sets used to generate the results are the same as that used for Zr II, with the obvious changes in radial functions (MCDF and virtuals, viz. Z^*).

In Table IV are presented the results for Mo IV $J = \frac{3}{2}$ using the same 1 and N electron basis sets (radial sets suitably adjusted). These calculations along isoelectronic sequences were considerably eased by the fact that almost the entire data sets (several thousand lines) could be reused from one member to the next. Here, the average error for the eight known [10, 14] energy levels is somewhat larger: 0.107 eV or 860 cm^{-1}, and just one new level has been identified. We may note that there is still one value of A for which the DF and RCI results have different signs.

THE Hf II ISOELECTRONIC SEQUENCE

Discussion of La I is postponed to the next section, as it is a thoroughly measured system and we have done calculations for several J's. The first member of the series considered here is Hf II, whose results are presented in Table V. The average error [10] for eight energy differences is 0.030 eV ($\sim$ 200 cm^{-1}). One new level is predicted, and three of the A's show large differences (sign or

TABLE I

Energy contributions in electron volts for Zr II, $J = \frac{3}{2}$. All signs reversed.

	Roots									
Basis	$4d^3$ ^2D	$4d^25s$ $+4d^3$ ^2P	$4d^3+$ $4d5s^2$ ^2D	$4d5s^2$ $+4d^3$ ^2D	$4d^3$ ^4P	$4d^25s$ ^4P	$4d^3+$ $4d^25s$ ^2P	$4d^25s$ ^2D	$4d^3$ ^4F	$4d^25s$ ^4F
$(4d+5s)^3$	−0.195	−1.041	−0.385	−0.140	0.010	0.002	0.993	0.738	0.014	0.008
$4d\,vp^2$	0.269	0.304	0.166	0.473	0.056	0.005	0.003	0.040	0.022	0.005
$4d\,vd^2$	0.339	0.011	0.228	0.002	0.192	0.002	0.216	−0.003	0.161	0.001
$4d\,vf^2$	0.571	0.054	0.395	0.010	0.351	0.000	0.338	−0.010	0.244	0.001
$4d\,vg^2$	0.069	0.008	0.044	0.000	0.021	0.000	0.021	−0.002	0.014	0.000
$4d\,vs\,vd$	0.000	0.061	0.006	0.000	0.000	0.047	0.000	0.044	0.000	0.048
$4d\,vp\,vf$	0.090	0.383	0.102	0.000	0.019	0.196	−0.031	0.214	0.041	0.192
$4d^2\,vs$	0.000	0.004	0.009	0.000	0.000	0.027	0.048	0.018	0.001	0.022
$4d^2\,vd$	0.024	0.063	0.066	0.036	0.091	0.016	0.075	0.006	0.084	0.004
$4d^2\,vg$	0.068	0.086	0.051	0.000	0.034	0.003	0.039	0.003	0.014	0.009
$5s\,vp^2$	0.000	0.014	0.000	0.097	0.000	0.034	0.000	0.009	0.000	0.000
$5s\,vd^2$	0.000	0.050	0.000	0.002	0.000	0.062	0.000	0.062	0.000	0.037
$5s\,vf^2$	0.000	0.164	0.000	0.016	0.000	0.172	0.000	0.127	0.000	0.058
$5s\,vs\,vd$	0.000	0.000	0.000	0.033	0.000	0.000	0.000	0.003	0.000	0.000
$5s\,vp\,vf$	0.000	0.000	0.000	0.227	0.000	0.000	0.000	−0.006	0.000	0.014
$4d\,5s\,vs$	0.004	0.000	−0.002	0.162	0.000	0.000	0.001	0.035	0.001	0.000
$4d\,5s\,vd$	0.000	0.561	0.010	0.047	0.000	0.316	−0.017	0.364	0.000	0.295
$4d\,5s\,vg$	0.012	0.000	−0.001	0.032	0.000	0.000	0.000	0.028	0.000	0.015
$5s^2\,vd$	0.000	0.000	0.000	0.434	0.000	0.000	0.000	−0.010	0.000	0.000
$4p^5\,vf\,4d^3$	0.911	0.034	1.003	0.000	1.109	0.021	1.010	0.021	1.166	0.020
$4p^5\,vf\,4d^25s$	0.022	0.853	0.020	0.054	0.020	0.852	0.023	0.805	0.019	0.899
$4p^5\,vf\,4d\,5s^2$	0.000	0.007	0.000	0.505	0.000	0.006	0.000	0.007	0.000	0.006
$4p^5\,vp\,4d^3$	0.012	0.040	0.016	0.000	0.030	0.042	0.021	0.056	0.035	0.084
$4p^5\,vp\,4d^25s$	0.000	0.067	0.002	0.092	0.004	0.067	0.004	0.081	0.005	0.079
$4p^5\,vp\,4d\,5s^2$	0.000	0.000	0.000	0.334	0.000	0.000	0.000	0.001	0.000	0.004
$4s\,vd\,4d^3$	0.049	0.014	0.036	0.000	0.042	0.005	0.032	0.002	0.022	0.006
$4s\,vd\,4d^25s$	0.025	0.056	0.034	0.015	0.026	0.041	0.001	0.020	0.026	0.018
$4p^4\,4d^5$	0.746	0.000	0.630	0.000	0.576	0.000	0.621	0.000	0.505	0.000
$4p^4\,4d^4\,5s$	0.000	0.757	0.001	0.000	0.000	0.754	−0.002	0.749	0.000	0.680
$4p^4\,4d^3\,5s^2$	0.005	0.000	0.002	0.876	0.001	0.000	0.001	−0.001	0.001	0.000
$4p^5\,4d^2\,vd\,vf$	0.062	0.011	0.070	0.000	0.070	0.012	0.074	0.012	0.075	0.012
$4p^5\,4d\,5s\,vd\,vf$	0.000	0.054	0.000	0.024	0.000	0.054	0.000	0.053	0.000	0.055
$4p^5\,5s^2\,vd\,vf$	0.000	0.000	0.000	0.029	0.000	0.000	0.000	0.000	0.000	0.000
$4s\,vs\,4d\,5s^2$	0.000	0.000	0.000	0.056	0.000	0.000	0.000	0.000	0.000	0.000
$4s\,4d^3\,5s$	0.001	0.062	0.004	0.004	0.005	0.061	0.004	0.045	0.006	0.016
$4s\,4d^4$	0.041	−0.005	0.063	0.000	0.057	0.002	0.042	0.003	0.016	0.002
$4p^5\,vp\,vd\,5s^2$	0.000	0.000	0.000	0.040	0.000	0.000	0.000	0.000	0.000	0.000
Total	3.136	2.721	2.576	3.516	2.718	2.846	3.520	3.553	2.473	2.623

TABLE II

Fine and hyperfine structure of Zr II, $J = \frac{3}{2}(d + s)^3$ states.

Level[a]		Energy (cm^{-1})		A (MHz)[b]		B (MHz) / $Q(b)$[b]	B (MHz)[b]
Config.	SLJ	Expt.[a]	Theory[b]	Theory[c]	Expt.	Theory[c]	Expt.
$4d^3$	^2D	27 699.96	29 066	−190.0		224.0	
$4d^3$	^2P	20 080.30	20 710	111.5	109.768	−138.4	33.716
				(−76.0)		(−33.9)	
$4d\,5s^2$	^2D	14 298.64	14 996	−114.7		−82.9	
$4d^3$	^2D	13 428.64	14 387	−66.8		165.1	
$4d^3$	^4P	9 742.80	10 072	134.1	110.177	−133.3	34.713
				(−56.4)		(−156.2)	
$4d^2\,5s$	^4P	7 736.02	8 209	−534.6		159.5	
$4d^2\,5s$	^2P	6 111.70	6 788	134.3		−132.2	
$4d^2\,5s$	^2D	4 248.30	5 084	190.3	199.250	−28.8	7.706
				(375.1)		(−83.8)	
$4d^3$	^4F	2 572.21	2 950	−298.0		−57.3	
$4d^2\,5s$	^4F	0.000	0	273.8		60.5	

[a] Labeling of levels is from Moore [10] as corrected by Kiess [12]. Experimental energy is also drawn from these sources.
[b] From previous work [11].
[c] Dirac–Fock results are given in parentheses.

TABLE III

Fine and hyperfine structure of Nb III, $J = \frac{3}{2}(d + s)^3$ states.[a]

Level		Energy (cm^{-1})		A (MHz)	B (MHz) / $Q(b)$
Config.	SLJ	Expt.[b]	Theory[c]	Theory[d]	Theory[d]
$4d\,5s^2$	^2D		71 816	937.7	355.9
				(710.0)	(326.5)
$4d^2\,5s$	^2P		44 448	−1012.2	−314.5
				(−965.6)	(−314.8)
$4d^2\,5s$	^2D	36 536	37 111	−1355.6	−114.0
				(−1526.7)	(−132.3)
$4d^2\,5s$	^4P	34 807	35 360	2401.4	255.7
				(2563.0)	(251.9)
$4d^3$	^2D		33 870	943.7	371.4
				(660.3)	(406.4)
$4d^2\,5s$	^4F	25 221	25 061	−1149.3	103.2
				(−1361.0)	(100.8)
$4d^3$	^2D		13 602	289.6	−42.78
				(427.4)	(−8.66)
$4d^3$	^2P	10 912	11 411	−47.82	−248.5
				(378.8)	(−271.2)
$4d^3$	^4P	8 608	8 864	−267.7	−215.8
				(310.4)	(−241.2)
$4d^3$	^4F	0.0	0.0	1128.0	−104.3
				(659.4)	(−114.9)

[a] $A = 92.90$, $Z = 41$, $I = \frac{9}{2}$, $\mu_I = 6.167$.
[b] From Iglesias [13].
[c] Uses same configurational basis set as Zr II, $J = \frac{3}{2}$.
[d] Dirac–Fock results are given in parentheses.

TABLE IV

Fine and hyperfine structure of Mo IV, $J = \frac{3}{2}(d + s)^3$ states.[a]

Level		Energy (cm^{-1})		A (MHz)	B (MHz) / $Q(b)$
Config.	SLJ	Expt.[b]	Theory[c]	Theory[d]	Theory[d]
$4d\,5s^2$	^2D		146 242	−342	501
				(−264)	(456)
$4d^2\,5s$	^2P	81 052	81 858	423	−446
				(387)	(−436)
$4d^2\,5s$	^2D	74 009	74 862	493	−170
				(510)	(−180)
$4d^2\,5s$	^4P	72 163	73 065	−871	350
				(−919)	(345)
$4d^2\,5s$	^4F	60 893	60 794	447	143
				(511)	(138)
$4d^3$	^2D	39 231	41 548	−272	524
				(−247)	(559)
$4d^3$	$^2D + {}^2P$	17 107	17 857	−106	10.9
				(−141)	(37.6)
$4d^3$	$^2P + {}^2D$	14 176	14 920	−86.0	−388
				(−162)	(−419)
$4d^3$	^4P	10 331	10 738	48.7	−315
				(−112)	(−340)
$4d^3$	^4F	0.0	0.0	−379	−151
				(−246)	(−161)

[a] $A = 95.94$, $Z = 42$, $I = \frac{5}{2}$, $\mu_I = -0.9133$.
[b] From Fernandez et al. [14].
[c] Uses same configurational basis set as Zr II, $J = \frac{3}{2}$.
[d] Dirac–Fock results are given in parentheses.

TABLE V
Fine and hyperfine structure of Hf II, $J = \frac{3}{2}(d + s)^3$ states.[a]

Level		Energy (cm^{-1})		A (MHz)	B (MHz) / $Q(b)$
Config.	SLJ	Expt.[b]	Theory[c]	Theory[d]	Theory[d]
$5d^3$	^2D		45 798	113.1 (104.0)	476.0 (533.0)
$5d^3$	^2P	37 324	37 198	−60.0 (48.6)	−99.9 (35.5)
$5d^3$	^2D	30 594	30 479	77.4 (81.7)	−337.0 (−361.0)
$5d^3$	^4P	27 285	26 958	−121.1 (43.0)	−290.0 (−308.0)
$5d^3$	^4F	18 897	18 395	140.8 (107.8)	−162.0 (−182.0)
$5d^2 6s$	^2P	17 830	17 478	−388.0 (−496.0)	−214.0 (−261.0)
$5d^2 6s$	^2D	14 359	14 446	−224.0 (−258.0)	−170.0 (−284.0)
$5d^2 6s$	^4P	12 920	12 815	638.0 (686.0)	320.0 (312.0)
$5d^2 6s$	^4F	3 644	3 336	−343.0 (−445.0)	193.0 (121.0)
$5d\,6s^2$	^2D	0	0	1.88 (117.3)	342.0 (458.0)

[a] $A = 178.49$, $Z = 72$, $I = \frac{7}{2}$, $\mu_I = 0.61$.
[b] From Moore [10].
[c] Uses same configurational basis set as Zr II, $J = \frac{3}{2}$.
[d] Dirac–Fock results are given in parentheses.

TABLE VI
Fine and hyperfine structure of Ta III, $J = \frac{3}{2}(d + s)^3$ states.[a]

Level		Energy (cm^{-1})		A (MHz)	B (MHz) / $Q(b)$
Config.	SLJ	Expt.[b]	Theory[c]	Theory[c]	Theory[c]
$5d^3$	^2D		42 299	478.9 (606.7)	679.1 (756.7)
$5d^2 6s$	^2P		38 054	−1140.0 (−1917.0)	−347.0 (−581.0)
$5d^2 6s + 5d^3$	^2D		30 834	−18.7 (678.0)	545.0 (687.0)
$5d^3 + 5d^2 6s + 5d 6s^2$	^2D		24 836	−415.3 (469.3)	−220.7 (−365.5)
$5d^2 6s$	$^4P + ^2P$		19 683	308.6 (357.7)	445.9 (474.0)
$5d^3$	$^4P + ^2P$		16 363	−165.1 (240.4)	−235.3 (−128.0)
$5d^3$	$^4P + ^2D$		13 402	−618.5 (337.0)	−295.2 (−470.0)
$5d^3$	$^2P + ^4P + ^4F$		7 814	−134.6 (357.0)	−279.6 (−413.0)
$5d^2 6s$	^4F		5 541	−1961.7 (−2433.1)	110.3 (120.7)
$5d^3$	^4F		0	926.7 (663.2)	−299.4 (−338.0)

[a] $A = 180.95$, $Z = 73$, $I = \frac{7}{2}$, $\mu_I = 2.36$.
[b] Uses same configuration basis set as Zr II, $J = \frac{3}{2}$.
[c] Dirac–Fock results are given in parentheses.

order of magnitude) between the DF and RCI results. Most of our tables also contain predictions for the electric quadruple constant, B, divided by the quadrupole moment, Q. One can either extract B, if Q is known [15], or if a measurement of B is available, as in Zr II [11], a determination of Q may be made.

In Table VI, we present our results for the Ta III member of this sequence. Since we were unable to find any experiment work on energy levels, our results constitute predictions for the relative positions of nine levels. In this case, there are five A's exhibiting substantial differences between DF and RCI results.

Table VII contains our results for the W IV member of this sequence. Again, there appears to be no available experiment, so nine new levels are predicted. Three A's exhibit sign changes between the DF and RCI value. Studies in the Zr II and Hf II sequences were terminated once we reached species of lesser technological interest (in our judgment); dramatic differences between at least a few RCI and DF A values are likely to persist beyond the ions reported here.

RESULTS FOR La I

La I has been well studied experimentally, for both energy differences [16] and HFS constants [17]. In addition to reporting results for $J = \frac{3}{2}$, we also did calculations for $J = \frac{7}{2}$ and $\frac{9}{2}$ as the ^2G HFS constants (B's), exhibit some substantial second-order (from A) contributions.

In Table VIII our results for $J = \frac{3}{2}$ are presented and compared to experiment. For eight energy differences, the average error is only 0.028 eV (227 cm^{-1}), and one new level is predicted. The largest errors are associated with the uppermost levels, which may suggest the presence of significant second-order electrostatic effects (see Discussion sec-

TABLE VII
Fine and hyperfine structure of W IV, $J = \frac{3}{2}(d + s)^3$ states.[a]

Level		Energy (cm^{-1})		A (MHz)
Config.	SLJ	Expt.[b]	Theory[c]	Theory[c]
$5d\,6s^2$	^2D		89 111	274.0 (316.0)
$5d^2\,6s$	^2P		66 789	−863.0 (−1018.0)
$5d^2\,6s$	^2D		53 377	−601.0 (−732.0)
$5d^2\,6s$	^4P		48 886	1458.0 (1551.0)
$5d^3$	^2D		47 207	299.0 (282.0)
$5d^2\,6s$	^4F		32 565	−1058.0 (−1172.0)
$5d^3$	^2P		26 313	−51.5 (145.0)
$5d^3$	$^4P + {}^2D$		19 578	−36.4 (158.0)
$5d^3$	$^4P + {}^2P$		11 113	−68.4 (160.0)
$5d^3$	^4F		0	458.0 (309.0)

[a] $A = 183.85$, $Z = 74$, $I = \frac{1}{2}$, $\mu_I = 0.117$.
[b] Uses same configurational basis set as Zr II, $J = \frac{3}{2}$.
[c] Dirac–Fock results are given in parentheses.

tion). The average error for the six measured A's is 10.3%, with the maximum error 19.0%. While there are no sign changes (DF vs. RCI) in these bottom six A's, the top two of them show large differences, and for two of the unmeasured A's there are sign changes. For the six B's, the average error is 32%, and the RCI values represent at best only a marginal improvement over DF values. For the smallest measured B (−6.00, we estimate a 12.4% correction from second-order HFS effects (see below).

The average energy difference errors for $J = \frac{7}{2}$ and $J = \frac{9}{2}$, shown in Table IX, are 0.17 and 0.13 eV, respectively (1350 and 1020 cm^{-1}). This is indicative that the basis set of Table I, so useful for $J = \frac{3}{2}$, needs improvement for these J's. Our more accurate studies on La II [9], Nb II [18], and Cs II [19] contain suggestions of what might be added. Comparing the A's, on the other hand, with observation [17] yields an average error of 11% for $J = \frac{7}{2}$ and 14% for $J = \frac{9}{2}$, which is comparable to our $J = \frac{3}{2}$ accuracy.

Both Tables VIII and IX contain results for B's, the electric quadrupole constants; those for the $5d^2 6s^2 G$'s involve large second order HFS effects which we discuss in the next section.

ELECTRIC QUADRUPOLE CONSTANTS FOR La $I, J = \frac{7}{2}, \frac{9}{2}$

When $|B/A| \ll 1$ and fine structure (FS) splittings are small, second-order contributions from A may be important; experiment measures net HFS, not individual poles (M_1, E_2). Lower-order poles (M_1) must be treated in high enough order so errors are smaller than those desired in the pole of interest. Based on the experimental work [17], the four levels with the largest discrepancies [B_{obs} vs. $B_{corrected}$] in La I are shown in Table X. Only the last two are of interest here, as we don't work on $J = \frac{5}{2}$. In Table X, the B_{obs} values are deduced from experiment without any second-order corrections as determined semi-empirically by fitting experiment [17]. This does not produce an entirely satisfactory fit to the directly observed frequencies [17].

The second-order correction may be expressed as in [17] as

$$\frac{\left|\langle {}^2G_{7/2}, F|H(M_1)|{}^2G_{9/2}, F\rangle\right|^2}{E\left({}^2G_{7/2}\right) - E\left({}^2G_{9/2}\right)},$$

where $H(M_1)$ is the relativistic magnetic dipole operator, and the denominator is the FS difference. In Ref. [17] this was initially evaluated at the MCDF level, but that yielded too small corrections. Here we show that the RCI second-order contribution is adequate to explain observation without having to introduce extra semi-empirically determined parameters.

In the spirit of Ref. [20], we may write the numerator as

$$W_{JJ'}(\text{MHz}) = (-1)^{I+F-J} \times \sqrt{I(I+1)(2I+1)J_>(J_>+1)(2J_>+1)} \times A_{JJ'} \begin{Bmatrix} I & J & F \\ J' & I & 1 \end{Bmatrix},$$

where

$$A_{JJ'} = 13074.7 \frac{\mu_I}{I\sqrt{J_>(J_>+1)}} \langle JJ|T_Q^{(1)}|J'J'\rangle.$$

Here μ_I is the magnetic dipole moment [15], $T_Q^{(1)}$ is the Qth component [$Q = J - J'$] of the relativistic magnetic dipole component and { } is a $6j$ symbol. The constant factor is a product of c and a factor to convert atomic units to megahertz. In evaluating $A_{JJ'}$ we take nonorthonormality effects fully into account [21]. Our RCI result for $A(5d^2 6s\ ^2G_{7/2}, 5d^2 6s\ ^2G_{9/2})$ is -504.8 MHz, whereas our MCDF value is $+343.7$ MHz.

Our RCI results for the electric quadrupole constants, using experimental [15] Q's are $B[5d^2 6s^2 G_{7/2}] = 112.6$ MHz and $B[5d^2 6s^2 G_{9/2}] = 108.3$ MHz. These results are obtained from the Zr II type bases, with $3p \rightarrow vp$ excitations added. These results are in good agreement with the semi-empirical B (corrected) values [17] which are, respectively, 111.512 and 127.571 MHz. These values appear in Table IX.

It is useful to look at what is happening in detail which we do in Table XI. By columns, these tables contain (1) the experimental energy differences (transitions between HFS levels), (2) experiment with the magnetic dipole contribution removed, using the observed A [labeled $\Delta E_{\text{expt}} - \delta\langle A_{\text{obs}}\mathbf{I}\cdot\mathbf{J}\rangle$], (3) the E_2 contribution obtained from our RCI B using first-order perturbation theory, B_{RCI}, (4) the second-order M_1 contributions using our RCI A, labeled $-\delta A^{(2)}$, and (5) a final column summing columns (3) and (4), Σ_{Th}. Experimental/theoretical discrepancies are obtained by comparing columns (2) and (5). It can be seen that the

TABLE VIII
Fine and hyperfine structure of ^{139}La I, $J = \frac{3}{2}(d+s)^3$ states.

Level		Energy (cm^{-1})		A (MHz)		B (MHz)[d]	
Config.	SLJ	Expt.[b]	Theory[c]	Theory[b]	Expt.[c]	Theory[b]	Expt.[c]
$5d^3$	^2D		27 680	212.6		36.4	
				(175.1)		(38.8)	
$5d^3$	^2P	21 037	21 614	−64.0		−14.1	
				(81.9)		(−1.03)	
$5d^3$	^2D	18 038	18 640	190.2		−24.3	
				(145.3)		(−23.3)	
$5d^3$	^4P	16 735	16 753	−231.8		−17.7	
				(68.1)		(−22.8)	
$5d^3$	^4F	12 431	12 361	391.8	445.0	−9.87	−16.07
				(176.15)		(−11.3)	
$5d^2 6s$	^2P	9 719	9 726	−530.7	−655.0	−24.2	−33.54
				(−188.96)		(−24.0)	
$5d^2 6s$	^2D	8 446	8 692	−422.9	−423.0	−4.45	−6.00[e]
				(−321.39)		(−16.2)	
$5d^2 6s$	^4P	7 491	7 556	842.6	930.0	25.0	34.72
				(844.26)		(22.9)	
$5d^2 6s$	^4F	2 668	2 436	−414.7	−480.0	10.7	16.34
				(−398.55)		(9.26)	
$5d\,6s^2$	^2D	0	0	129.7	141.0	29.9	44.78
				(111.23)		(31.8)	

[a] Experimental energy is taken from Martin et al. [16].
[b] This work. The values in parentheses are MCDF values taken from same reference as footnote [c].
[c] From Childs and Nielsen [17].
[d] Q is from Raghavan [15].
[e] Estimated second-order HFS contribution ~ 12.4% (see text).

TABLE IX

Fine and hyperfine structure of ^{139}La I, $J = \frac{7}{2}, \frac{9}{2}(d + s)^3$ states.

Level		Energy (cm^{-1})		A (MHz)		B (MHz)[d]	
Config.	SLJ	Expt.[b]	Theory[c]	Theory[b]	Expt.[c]	Theory[b]	Expt.[c]
$5d^3$	$^2F_{7/2}$	18 449	20 920	50.8 (187.0)		28.5	
$5d^3$	$^2G_{7/2}$	13 529	15 282	137.7 (182.8)		35.1	
$5d^3$	$^4F_{7/2}$	9 744	10 121	−18.2 (190.9)	−19	−19.3	−20.9
$5d^2 6s$	$^2G_{7/2}$	6 466	7 493	−253.7 (−189.7)	−292	113	112
$5d^2 6s$	$^2F_{7/2}$	4 558	5 659	−170.7 (81.9)	−197	37.5	40.3
$5d^2 6s$	$^4F_{7/2}$	0	0	411.3 (507.9)	463	17.9	16.1
$5d^3$	$^2H_{9/2}$	14 194	15 704	104 (125)		47.2	
$5d^3$	$^2G_{9/2}$	13 019	14 357	69 (131)		34.3	
$5d^3$	$^4F_{9/2}$	9 626	9 968	−53 (82)	−64	−20.6	−27.4
$5d^2 6s$	$^2G_{9/2}$	5 798	6 694	471 (432)	560	108	128
$5d^2 6s$	$^4F_{9/2}$	0	0	440 (451)	490	24.2	31.5

[a] Experimental energy is taken from Martin et al. [16].
[b] This work; RCI. The values in parentheses are MCDF values.
[c] From Childs and Nielsen [17]. All B's except those for $5d^3\,^4F$ are obtained using second-order HFS effects.

agreement is quite good; and that the second-order effects associated with M_1 can be an appreciable fraction of the first-order E_2 effects.

Discussion

A cautious error estimate for unmeasured A's might be 20–25% for RCI values, except for those below 50 MHz in magnitude. Errors for these might be 50–100%. These estimates are based, in part, in how A changes as the calculation proceeds. Although we have not emphasized, in detail, the importance of the relative positioning of $d^{n-1}s$ levels in this work, this is more thoroughly explored in the work on La II [9] and Cs II [19].

In general, uppermost levels exhibit large errors in energy positions and HFS constants. This is because these levels are closer in energy to "Rydberg" excited states than the lowest levels. Excita-

TABLE X

Experimental [17] results for HFS constants [B's] exhibiting significant second-order effects.

Level (cm^{-1})	Label		A (MHz)	B_{obs} (MHz)	$B_{corrected}$ (MHz)
3 010.002	$5d^2 6s$	$^4F_{5/2}$	300.563	10.873	7.800
9 183.797	$5d^2 6s$	$^2D_{5/2}$	876.319	−2.772	−5.404
9 919.821	$5d^2 6s$	$^2G_{9/2}$	559.812	202.638	127.571
9 960.904	$5d^2 6s$	$^2G_{7/2}$	−292.267	67.537	111.512

TABLE XI
La I $5d^2\,6s^2\,G$ electric quadrupole results (MHz) including second-order effects.[a]

Transition $F \rightarrow F'$	ΔE_{obs}	$\Delta E_{obs} - \langle A_{obs}\,\mathbf{I}\cdot\mathbf{J}\rangle$	B_{RCI}	$-\delta A^{(2)}$	Σ_{Th}
		$J = \frac{7}{2}\,A_{obs} = -292.267$ MHz			
7–6	−2016.965	28.904	46.44	−12.9	33.5
6–5	−1746.669	6.933	11.13	0	11.13
5–4	−1468.190	−6.855	−11.13	7.80	−3.33
4–3	−1182.851	−13.783	−22.08	11.3	−10.78
3–2	−891.992	−15.191	−24.37	11.4	−13.0
2–1	−596.977	−12.443	−20.3	9.05	−11.3
1–0	−299.185	−6.918	−10.4	4.95	−5.44
		$J = \frac{9}{2}\,A_{obs} = 559.812$ MHz			
8–7	4555.752	77.256	43.04	31.6	76.64
7–6	3943.948	25.264	14.07	12.9	27.0
6–5	3349.169	−9.703	−5.29	0	−5.29
5–4	2768.920	−30.14	−16.84	−7.80	−24.64
4–3	2200.726	−38.522	−21.5	−11.3	−32.8

[a] Entries are explained in text. Column 2 constitutes the experimental prediction and the last column constitutes the theoretical prediction.

tions from the core artificially pull all the $(d + s)^n$ levels away from these Rydberg levels, because they aren't given equivalent core correlation.

ACKNOWLEDGMENTS

Support from the Division of Chemical Sciences, Office of Energy Research, U.S. Department of Energy, Grant No. DE-FG02-92ER14282. Grateful acknowledgment is made to Bill Childs and Linda Young for helpful conversation on HFS constants and problems with La I (W.C.). Debasis Datta and Steve O'Malley are thanked for their work on related HFS projects.

References

1. D. R. Beck, Phys. Rev. A **45**, 1399 (1992).
2. R. L. Martin and P. J. Hay, J. Chem. Phys. **75**, 4539 (1981).
3. J. P. Desclaux, Comput. Phys. Commun. **9**, 31 (1975).
4. J. Weber, R. Lacroix, and G. Wanner, Comput. Chem. **4**, 55 (1980).
5. K. Dinov and D. R. Beck, Bull. Am. Phys. Soc. **38**, 1097 (1993).
6. A. Bunge, J. Chem. Phys. **53**, 20 (1970).
7. D. R. Beck and D. Datta, Phys. Rev. A **48**, 182 (1993).
8. K. Jankowski, P. Malinowski, and M. Polasik, J. Chem. Phys. **76**, 448 (1982).
9. D. Datta and D. R. Beck, Phys. Rev. A **52** 3622 (1995).
10. C. E. Moore, *Atomic Energy Levels*, Volume II, 1952, and Volume III, 1958, Circular National Bureau of Standards 467 (U.S. GPO, Washington, DC).
11. L. Young, C. A. Kurtz, D. R. Beck, and D. Datta, Phys. Rev. A **48**, 173 (1993).
12. C. C. Kiess, J. Opt. Soc. Am. **43**, 1024 (1953).
13. L. Iglesias, J. Opt. Soc. Am. **45**, 856 (1955).
14. M. T. Fernandez, I. Cabeza, L. Iglesias, O. Garcia-Riquelme, F. R. Rico, and V. Kaufman, Phys. Scr. **35**, 819 (1987).
15. P. Raghavan, At. Data Nucl. Data Tables **42**, 189 (1989).
16. W. C. Martin, R. Zalubas, and L. Hagan, *Atomic Energy Levels—The Rare Earths*, NSRDS-NBS60 (U.S. GPO, Washington, DC, 1978).
17. W. J. Childs and U. Nielsen, Phys. Rev. A **37**, 6 (1988).
18. L. Young, S. Hasegawa, C. Kurtz, D. Datta, and D. R. Beck, Phys. Rev. A **51**, 3534 (1995).
19. S. M. O'Malley and D. R. Beck, Phys. Rev. A **54**, 3894 (1996).
20. K. T. Cheng, J. E. Hardis, E. J. Dehm, and D. R. Beck, Phys. Rev. A **30**, 698 (1984).
21. Program RHFSOD, D. R. Beck, unpublished.

Scalar-Relativistic LCGTO DFT Calculations for Atoms Using the Douglas–Kroll Transformation

JONATHAN C. BOETTGER

Theoretical Division, Los Alamos National Laboratory, Los Alamos, New Mexico 87545

Received 1 March 1997; revised 29 April 1997; accepted 7 May 1997

ABSTRACT: Häberlen and Rösch (HR) demonstrated [Chem. Phys. Lett. **199**, 491 (1992)] the feasibility of performing scalar-relativistic, density functional theory (DFT) linear combination of Gaussian-type orbitals–fitting function (LCGTO-FF) calculations on clusters of atoms using an "incomplete" Douglas–Kroll transformation. Some of the approximations used in their multiatom calculations have not yet been fully explored for isolated atoms, especially the neglect of matrix elements involving vector products of the momentum and the use of fitting functions. In this investigation, scalar-relativistic LCGTO calculations (without fitting functions) were carried out at four levels of approximation, including that employed by HR, for four atoms: Ce, Au, Pb, and Pu. The results of these calculations suggest that the HR approximation should be applicable to atoms through the light actinides, so long as spin–orbit effects are unimportant. A comparison of very large basis-set results with results obtained using ordinary-size basis sets indicates that the valence (bonding) states from scalar-relativistic LCGTO-FF calculations should be no more sensitive to the orbital basis-set size than are their nonrelativistic counterparts. © 1997 John Wiley & Sons, Inc. Int J Quant Chem **65**: 565–574, 1997

Introduction

The linear combinations of Gaussian-type orbitals–fitting function (LCGTO-FF) technique is now used routinely to perform all-electron, full-potential, density functional theory (DFT) electronic structure calculations on a wide range of systems, including isolated clusters of atoms [1–3], 1D periodic polymer chains [4–6], 2D periodic ultrathin films [7–9], and 3D periodic crystalline solids [10–12]. This ability to treat localized (molecular) and periodically extended (crystalline) systems on an equal footing is one of the primary advantages of the LCGTO-FF method over other existing DFT electronic structure techniques. For example, the various linearized techniques used in solid-state physics (FLAPW, FLMTO, etc.) have

By acceptance of this article, the publisher recognizes that the U.S. Government retains a nonexclusive, royalty-free license to publish or reproduce the published form of this contribution, or to allow others to do so, for U.S. Government purposes.

Contract grant sponsor: U.S. Department of Energy.

© 1997 John Wiley & Sons, Inc.
CCC 0020-7608 / 97 / 050565-10

not yet been demonstrated to be useful tools for studying isolated clusters of atoms. Thus, the LCGTO-FF method is one of the few all-electron, full-potential methods that can be used to bridge the gap between quantum chemistry and solid-state physics. To this extent, the LCGTO-FF technique may be viewed as a "universal" band-structure technique.

One limitation of the LCGTO-FF method has been the difficulty associated with applying any fixed-basis method to heavy-atom systems, due to the lack of a stable method for incorporating relativistic corrections into such calculations [13]. Häberlen and Rösch [14–16] (HR) demonstrated the feasibility of performing scalar-relativistic LCGTO-FF calculations on clusters containing heavy atoms using an "incomplete" Douglas–Kroll [17] (DK) transformation (the HR approximation hereafter) that requires only a minimal increase in computational effort relative to the corresponding nonrelativistic calculation. The HR scalar-relativistic LCGTO-FF method (LCGTO-DF in their notation) has since been successfully applied to a number of heavy-atom systems [18–26]. This development is of great significance because it substantially increases the range of applicability for LCGTO-FF calculations.

Three aspects of the HR scalar-relativistic LCGTO-FF method have not yet been fully explored for isolated atoms: (1) the effect of neglecting all matrix elements involving vector products of the momentum; (2) the extent of sensitivity to the orbital basis-set size; and (3) the effect of using charge and exchange–correlation (XC) fitting functions in a scalar-relativistic calculation. In the current investigation, scalar-relativistic LCGTO calculations (without fitting functions) are carried out for four atoms (Ce, Au, Pb, and Pu) in an attempt to resolve these issues. In the next section, the scalar-relativistic LCGTO method is reviewed and the four approximations considered here are defined, including the HR approximation. Results are presented in the third section.

Scalar-Relativistic LCGTO DFT Method

The formulation of scalar-relativistic DFT used by HR [14] begins with the four-component Dirac–Kohn–Sham (DKS) equations [27]:

$$h^{(4)}_{DKS}\psi_i = \left[(c\boldsymbol{\alpha}\cdot\mathbf{p} + \beta mc^2) + v_{eff}\right]\psi_i = \epsilon_i\psi_i, \quad (1)$$

where

$$v_{eff} = v_n + v_c + v_{xc} \quad (2)$$

is the effective one-electron potential, composed of the nuclear potential v_n, the classical electronic Coulomb potential v_c, and the DFT XC potential v_{xc}. The eigenvalues of the DKS equations are unbounded, above and below, since they include both electron and positron degrees of freedom. For this reason, any attempt to solve the DKS equations variationally with a truncated basis set will lead to the so-called variational collapse problem, unless some specially designed collection of basis functions is used [13]. In principle, the electron and positron degrees of freedom in the DKS equations can be decoupled exactly to produce two sets of two-component equations whose eigenvalues are bounded [28]. The resulting second-order equations are, however, nonlinear in ϵ_i and are not amenable to solution with a matrix method. Both of these difficulties can be circumvented by performing some unitary transformation on the DKS equations that approximately decouples the electron and positron degrees of freedom while maintaining linearity. This is the approach followed by HR [14–16].

REDUCTION TO TWO-COMPONENT FORM

The approximate decoupling of the DKS equations into two sets of two-component equations begins with a free-particle Foldy–Wouthuysen [29] (FW) transformation using the unitary transformation operator

$$U_0 = A_p\left(1 + \beta R^{(4)}_p\right), \quad (3)$$

where

$$A_p = \left[\frac{E_p + mc^2}{2E_p}\right]^{1/2}, \quad (4)$$

$$R^{(4)}_p = K_p\boldsymbol{\alpha}\cdot\mathbf{p}, \quad (5)$$

$$K_p = c/\left(E_p + mc^2\right), \quad (6)$$

$$E_p = c(p^2 + m^2c^2)^{1/2}. \quad (7)$$

This transformation yields an alternative four-component equation

$$h^{(4)}_1\psi_i = [\,\beta E_p + \mathscr{E}_1 + \mathscr{O}_1]\psi_i = \epsilon_i\psi_i, \quad (8)$$

where $\mathscr{E}_1$ and $\mathscr{O}_1$ are even and odd operators with respect to commutation with β:

$$\mathscr{E}_1 = A_p\left[v_{eff} + R_p^{(4)} v_{eff} R_p^{(4)}\right] A_p \tag{9}$$

$$\mathscr{O}_1 = \beta A_p\left[R_p^{(4)} v_{eff} - v_{eff} R_p^{(4)}\right] A_p. \tag{10}$$

Note that, up to this point, no approximations have been made beyond those inherent in the original DKS equation.

It can be demonstrated that the even (odd) operators do not (do) couple the positive and negative kinetic-energy states of the free-particle DKS equation [30]. Equation (8) can then be reduced to an approximate two-component form by simply dropping the odd operator to get

$$h_{FPP}^{(2)} \phi_i = \epsilon_i \phi_i, \tag{11}$$

$$h_{FPP}^{(2)} = E_p + A_p\left[v_{eff} + R_p^{(2)} v_{eff} R_p^{(2)}\right] A_p,$$

where $R_p^{(2)}$ is the two-component equivalent of $R_p^{(4)}$,

$$R_p^{(2)} = K_p \boldsymbol{\sigma} \cdot \mathbf{p}. \tag{12}$$

This approximation is known as the free-particle projector (FPP) approximation because it can also be obtained by surrounding $h_{DKS}^{(4)}$ with free-particle projection operators, thereby forcing the electronic wave functions in the presence of v_{eff} to be constructed from a superposition of positive-energy free-particle states [30]. The FPP approximation should be reasonable if the effective potential is only weakly dependent on the position, a requirement that is clearly not satisfied near a nucleus.

The primary shortcoming of the FPP approximation is its total neglect of the mixing of positive and negative energy free-particle states induced by the presence of the odd operator $\mathscr{O}_1$ in $h_1^{(4)}$. An improved two-component equation can be obtained by performing another unitary transformation on $h_1^{(4)}$ that approximately eliminates $\mathscr{O}_1$. To this end, Douglas and Kroll [17] observed that the operator

$$U_1 = (1 + W^2)^{1/2} + W \tag{13}$$

will be unitary if W is anti-Hermitian. W can then be selected such that the transformation U_1 eliminates $\mathscr{O}_1$ from $h_1^{(4)}$ to first-order in W. Carrying out this procedure and expressing the integral operator W in momentum-space yields

$$W_{p,p'} = A_p(R_p - R_{p'}) A_{p'} v'_{p,p'}, \tag{14}$$

with

$$v'_{p,p'} = \frac{v_{eff}(\mathbf{p}, \mathbf{p}')}{E_p + E_{p'}}, \tag{15}$$

where $v_{eff}(\mathbf{p}, \mathbf{p}')$ is the momentum-space representation of v_{eff} and R_p is now assumed to take on its two- or four-component representation as needed. Applying U_1 to $h_1^{(4)}$, expanding the resulting operator to second-order in W, and dropping all higher-order odd operators yields the second-order DK equation [17, 31, 32]:

$$h_{EFP}^{(2)} \phi_i = \left[h_{FPP}^{(2)} - \frac{1}{2}\left(E_p W^2 + W^2 E_p + 2W E_p W\right)\right] \phi_i = \epsilon_i \phi_i. \tag{16}$$

This approximation is often referred to as the external-field projector (EFP) approximation because it effectively projects out the electronic solutions to the DKS equation for a particle moving in the external-field v_{eff}.

SCALAR-RELATIVITY

The approximate two-component equations presented above [Eqs. (11) and (16)] are fully relativistic, in the sense that they include mass-velocity, Darwin, and spin–orbit coupling corrections. A scalar-relativistic formulation is desired here to allow a direct comparison with previous work. In the FPP equation [Eq. (11)], the spin–orbit corrections are all contained in the term $A_p R_p v R_p A_p$. Using the standard properties of the Pauli matrices (σ), this term can be rewritten as

$$A_p R_p v R_p A_p = A_p K_p(\mathbf{p} \cdot v\mathbf{p} + i\boldsymbol{\sigma} \cdot \mathbf{p} \times v\mathbf{p}) K_p A_p. \tag{17}$$

The term involving $\mathbf{p} \cdot v\mathbf{p}$ is scalar-relativistic, whereas the term involving $\boldsymbol{\sigma} \cdot \mathbf{p} \times v\mathbf{p}$ is a spin–orbit coupling term. Thus, the scalar-relativistic FPP approximation does not require matrix elements of $\mathbf{p} \times v\mathbf{p}$.

Separating out the spin–orbit coupling terms for the EFP equation is somewhat more complicated because of the second-order terms in Eq. (16). The basic properties of the external-field correction terms can all be illustrated with the operator W^2.

Since the momentum-space operators in W commute, except for v', W^2 can be expressed as

$$W^2 = (A_p R_p v' R_p A_p)(A_p v' A_p) - (A_p v' A_p)\left(p^2 K_p^2\right)(A_p v' A_p) + (A_p v' A_p)(A_p R_p v' R_p A_p) - (A_p R_p v' R_p A_p)\left(p^2 K_p^2\right)^{-1}(A_p R_p v' R_p A_p). \quad (18)$$

The second term in this expression is scalar-relativistic as written. The first and third terms can be easily split into Darwin and spin–orbit coupling terms using Eq. (17). The last term is more complicated because it behaves like

$$(A_p R_p v' R_p A_p)^2 = \left[A_p K_p(\mathbf{p}\cdot v'\mathbf{p} + i\boldsymbol{\sigma}\cdot\mathbf{p}\times v'\mathbf{p})K_p A_p\right]^2. \quad (19)$$

Inspection of the rhs of Eq. (19) reveals that the squares of the individual factors in the parentheses are both scalar-relativistic, while their cross-products are spin–orbit coupling terms. Thus, even the scalar-relativistic version of the EFP approximation requires matrix elements of $\mathbf{p}\times v\mathbf{p}$. Throughout the remainder of this work, it will be assumed that all spin–orbit coupling terms in $h^{(2)}_{FPP}$ and $h^{(2)}_{EFP}$ are neglected.

INCOMPLETE TRANSFORMATIONS

The FPP and EFP equations both involve the operators E_p, A_p, and K_p. Although these operators are easy to work with in momentum-space, analytical evaluation of the GTO matrix elements for these operators has thus far proven to be impractical. This difficulty can be avoided by transforming the GTO basis set to an approximate momentum-space representation by diagonalizing the nonrelativistic kinetic-energy (KE) matrix [33]. First, the matrix elements of $\mathbf{p}\cdot v\mathbf{p}$ and $\mathbf{p}\times v\mathbf{p}$ (if needed) are evaluated along with the usual nonrelativistic matrix elements. Next, the nonrelativistic KE matrix is diagonalized to obtain approximate eigenfunctions of p^2 and the matrices are transformed to this approximate momentum space. The operators E_p, A_p, and K_p can then be constructed from the approximate p^2 eigenvalues. These basic components are used to form the complicated matrices, like $A_p R_p v' R_p A_p$, which are then back-transformed to the original basis set.

The approximate momentum-space representation becomes exact in the limit of a complete basis. Conversely, as the basis set is reduced, the approximate momentum-space representation can become a source of serious error. Hess [31] tested this approximation by calculating relativistic Hartree–Fock total and one-electron energies for Br ($Z = 35$) and Ag ($Z = 47$) using fairly large primitive basis sets that were contracted to obtain a wide range of basis-set sizes. Hess concluded that the results were sufficiently sensitive to warrant using the uncontracted basis sets whenever possible. (Jansen and Hess [32] carried out similar tests on Au [$Z = 79$] with contracted basis sets ranging from $13s9p6d1f$ to $17s12p8d4f$, but only studied the total energy variation in detail.) The requirement of a large basis set to ensure a good momentum-space representation conflicts with the obvious need to use rather heavily contracted orbital basis sets for heavy atoms to reduce the computational demands of such systems.

HR overcame this paradox by only applying the relativistic transformations associated with the FPP and EFP approximations to the one-electron portions of the DKS equations, i.e., the kinetic energy and nuclear potential. These incomplete transformations allow all of the relativistic matrix elements to be initially evaluated using the primitive GTO basis set and then transformed to a much smaller contracted basis set prior to beginning the iterative SCF cycle [15]. The more numerous two-electron integrals associated with v_c then only need to be evaluated for the smaller contracted basis set. These nuclear-only versions of the FPP and EFP approximations will be denoted as the FPPn and EFPn approximations, respectively. HR further reduced the complexity of the EFPn approximation by dropping all of the terms involving $\mathbf{p}\times v\mathbf{p}$; this then is the HR approximation.

COMPUTATIONAL DETAILS

To test the approximations discussed, an existing program for performing nonrelativistic LCGTO DFT calculations on atoms, without the use of fitting functions, (ATOM [34]) has been rewritten as a scalar-relativistic code (SATOM). In SATOM, each term in the effective one-electron potential (v_n, v_c, and v_{xc}) can be treated nonrelativistically (NR) or with one of three scalar-relativistic approximations, FPP, EFP without vector product terms,

or EFP with vector product terms. The HR approximation then corresponds to treating v_c and v_{xc} nonrelativistically and treating v_n with the EFP approximation without vector product terms.

Four atoms, spanning a wide range of atomic numbers, were studied here: Ce ($Z = 58$), Au ($Z = 79$), Pb ($Z = 82$), and Pu ($Z = 94$). In each case, LCGTO results have been obtained nonrelativistically and with four scalar-relativistic approximations: full EFP, EFPn, HR, and FPPn. For Ce and Pb, all calculations were carried out using the Xα LDA model ($\alpha = 0.7$) to allow direct comparison with previous LCGTO-FF and numerical results [16, 35]. For Au and Pu, the Hedin–Lundqvist [36] (HL) model was used to allow a comparison with numerical results obtained from a code written by Wills [37].

The present LCGTO calculations for Ce employed a high-quality $21s16p11d9f$ basis set described by Häberlen [16]. Unfortunately, no comparable quality basis sets have been published for Au, Pb, and Pu. For this reason, large $30s24p18d12f$ even-tempered basis sets were used for the three larger atoms. The (minimum:maximum) exponents of the s, p, d, and f parts of the large basis sets for Au and Pb were ($0.02{:}1 \times 10^8$), ($0.01{:}1 \times 10^5$), ($0.05{:}2 \times 10^4$), and ($0.1{:}2 \times 10^3$), respectively. For Pu, the limits for the d basis set were changed to ($0.02{:}1 \times 10^4$). To study the effects of basis-set size on the results, the calculations for Au and Pb were repeated with smaller basis sets. The small basis used for Au was a $20s15p11d6f$ basis derived from Gropen's [38] $19s14p10d5f$ basis by adding one exponent for each symmetry: s, 0.18; p, 0.20; d, 0.12; and f, 1.4. The small basis for Pb was the $20s17p11d6f$ basis employed by Knappe and Rösch [35] in their prototype scalar-relativistic LCGTO-FF calculations.

Results

The rich basis-set results for the NR and scalar-relativistic one-electron energies and total energies for Ce, Au, Pb, and Pu are compared with results from numerical calculations in Tables I–IV. In each case, the NR results are in excellent agreement, with the deepest core levels differing by no more than 0.5 eV and the total energies differing by no more than 0.3 Ry, demonstrating the high quality of the large basis sets. A careful inspection of Tables I–IV also reveals that, in each case, the EFP

TABLE I

Numerical and LCGTO results for the negatives of the nonrelativistic one-electron eigenvalues (in eV) and total energies (in Ry) are compared for paramagnetic Ce. Scalar-relativistic corrections to the nonrelativistic results are listed for various approximations. The numerical results are from [16]. The LCGTO results were calculated here with a $21s16p11d9f$ basis. All calculations used the Xα model with $\alpha = 0.7$.

	Nonrelativistic		Scalar-relativistic corrections				
	Num	LCGTO	Num	EFP	EFPn	HR	FPPn
1s	38286.20	38285.95	1932.93	1866.18	1838.04	1835.17	2723.95
2s	5956.84	5956.84	485.09	477.75	474.55	473.61	565.31
3s	1281.39	1281.41	105.83	104.38	103.83	103.54	121.63
4s	256.50	256.52	23.40	23.11	23.01	22.92	26.99
5s	36.54	36.57	3.45	3.42	3.41	3.39	4.04
6s	2.99	3.00	0.23	0.22	0.22	0.22	0.26
2p	5637.49	5637.49	133.70	133.25	130.98	136.38	131.86
3p	1142.79	1142.81	31.26	31.30	30.94	31.95	30.70
4p	204.75	204.78	5.51	5.53	5.48	5.68	5.29
5p	22.38	22.42	0.16	0.19	0.18	0.21	0.08
3d	883.62	883.62	−12.49	−12.64	−12.75	−12.96	−14.12
4d	113.76	113.77	−3.71	−3.69	−3.69	−3.75	−4.07
5d	3.08	3.07	−0.64	−0.62	−0.62	−0.62	−0.69
4f	8.58	8.61	−3.53	−3.49	−3.47	−3.51	−3.70
E	17134.59	17134.55	581.69	571.60	568.89	572.54	725.03

TABLE II

Numerical and LCGTO results for the negatives of the nonrelativistic one-electron eigenvalues (in eV) and total energies (in Ry) are compared for paramagnetic Au. Scalar-relativistic corrections to the nonrelativistic results are listed for various approximations. The LCGTO results were calculated here with a 30*s*24*p*18*d*12*f* basis. All calculations used the HL model.

	Nonrelativistic		Scalar-relativistic corrections				
	Num	LCGTO	Num	EFP	EFPn	HR	FPPn
1*s*	73021.73	73021.79	7617.36	7288.75	7200.23	7185.95	11173.46
2*s*	12187.55	12187.62	2034.09	1993.22	1982.11	1977.25	2428.50
3*s*	2852.37	2852.44	504.21	495.39	493.16	491.68	589.78
4*s*	600.78	600.81	127.28	125.13	124.64	124.21	148.83
5*s*	84.79	84.79	23.95	23.54	23.46	23.36	28.23
6*s*	4.51	4.51	1.67	1.64	1.63	1.64	2.00
2*p*	11720.50	11720.58	572.48	573.25	567.06	604.16	589.10
3*p*	2631.48	2631.58	166.33	167.40	166.14	174.19	170.19
4*p*	505.55	505.60	39.34	39.70	39.47	41.37	40.23
5*p*	54.55	54.55	5.50	5.59	5.56	5.88	5.62
3*d*	2217.99	2218.08	−16.42	−17.31	−17.91	−18.78	−22.61
4*d*	330.12	330.17	−4.70	−4.83	−4.88	−5.11	−6.07
5*d*	8.37	8.37	−1.17	−1.16	−1.16	−1.17	−1.31
4*f*	94.89	94.89	−13.22	−13.18	−13.14	−13.33	−13.96
E	35720.73	35720.65	2280.97	2237.68	2229.21	2253.88	2944.25

TABLE III

Numerical and LCGTO results for the negatives of the nonrelativistic one-electron eigenvalues (in eV) and total energies (in Ry) are compared for paramagnetic Pb. Scalar-relativistic corrections to the nonrelativistic results are listed for various approximations. The numerical results are from [35]. The LCGTO results were calculated here with a 30*s*24*p*18*d*12*f* basis. All calculations used the Xα model with $\alpha = 0.7$.

	Nonrelativistic		Scalar-relativistic corrections				
	Num	LCGTO	Num	EFP	EFPn	HR	FPPn
1*s*	78976.75	78976.27	8997.12	8640.22	8540.96	8523.55	13354.48
2*s*	13312.12	13312.11	2421.16	2377.64	2365.02	2358.97	2913.73
3*s*	3173.88	3173.94	604.04	594.37	591.82	589.92	711.34
4*s*	701.38	701.40	153.40	150.97	150.40	149.79	180.62
5*s*	113.91	113.91	29.86	29.34	29.25	29.07	35.49
6*s*	8.93	8.93	2.59	2.54	2.52	2.50	3.17
2*p*	12824.30	12824.31	668.90	677.78	670.84	717.56	699.65
3*p*	2940.72	2940.82	195.58	198.37	196.93	207.12	202.18
4*p*	598.97	599.03	45.18	46.29	46.02	48.44	46.86
5*p*	79.45	79.45	5.80	5.97	5.94	6.35	5.86
6*p*	3.13	3.13	−0.15	−0.14	−0.14	−0.13	−0.20
3*d*	2503.90	2503.99	−20.25	−21.07	−21.71	−22.82	−27.58
4*d*	409.46	409.51	−7.67	−7.79	−7.86	−8.20	−9.57
5*d*	23.86	23.86	−3.27	−3.27	−3.26	−3.33	−3.66
4*f*	152.37	152.36	−18.88	−18.91	−18.85	−19.18	−20.16
E	39055.40	39055.29	2705.40	2653.31	2643.97	2675.09	3513.16

TABLE IV

Numerical and LCGTO results for the negatives of the nonrelativistic one-electron eigenvalues (in eV) and total energies (in Ry) are compared for paramagnetic Pu. Scalar-relativistic corrections to the nonrelativistic results are listed for various approximations. The LCGTO results were calculated here with a 30*s*24*p*18*d*12*f* basis. All calculations used the HL model.

	Nonrelativistic		Scalar-relativistic corrections				
	Num	LCGTO	Num	EFP	EFPn	HR	FPPn
1*s*	104982.08	104982.29	17168.80	16343.22	16165.23	16128.81	26240.88
2*s*	18284.96	18285.20	4725.81	4615.31	4591.57	4578.44	5820.87
3*s*	4635.88	4636.15	1212.89	1187.79	1182.78	1178.49	1456.94
4*s*	1177.46	1177.62	329.99	323.28	322.05	320.59	395.44
5*s*	253.73	253.77	83.30	81.56	81.27	80.82	100.07
6*s*	35.23	35.24	14.02	13.65	13.60	13.50	17.10
7*s*	3.42	3.42	0.70	0.67	0.67	0.66	0.86
2*p*	17707.84	17708.08	1242.85	1257.35	1247.14	1356.24	1322.06
3*p*	4351.35	4351.64	378.01	383.73	381.35	405.97	396.19
4*p*	1045.15	1045.35	97.28	98.98	98.47	104.78	101.40
5*p*	201.82	201.88	20.77	21.19	21.09	22.58	21.44
6*p*	21.20	21.20	1.37	1.43	1.42	1.63	1.22
3*d*	3818.07	3818.34	−22.69	−25.11	−26.25	−28.45	−37.85
4*d*	797.72	797.90	−9.62	−10.11	−10.27	−11.03	−14.03
5*d*	110.79	110.82	−4.91	−5.01	−5.02	−5.21	−6.10
4*f*	453.88	453.95	−37.42	−37.54	−37.49	−38.32	−40.67
5*f*	8.43	8.41	−6.20	−6.22	−6.20	−6.29	−6.77
E	54004.24	54003.98	5106.93	4999.42	4983.10	5056.02	6828.79

approximation accounts for roughly 98% of the scalar-relativistic correction to the total energy and produces corrections to the core-state energies that are within 5% of the numerical results, with the exception of the Pu 3*d* energy. More importantly, the EFP approximation yields energies for the all-important valence states that are within a few hundredths of an eV of the values found in the numerical calculations. Using the simpler EFPn approximation in place of the EFP approximation produces a modest deterioration in the one-electron results that is concentrated in the chemically inert core states. On the other hand, the FPPn approximation is clearly inadequate for all four of the atoms considered. These observations are all in agreement with the results of earlier work on Ce [16] and Pb [35].

Analysis of the results obtained with the HR approximation is not so straightforward. For simplicity, focus on the Pu results in Table IV, since they exhibit the trends most clearly. The HR approximation has only a small effect on the relativistic corrections to the total energy and the *s* and *f* one-electron energies. (In fact, the shift in the total energy due to the HR approximation cancels some of the error already existing in the more rigorous EFP approximation.) For the *d*-state corrections, the HR approximation results in significantly larger percentage errors than does the EFPn approximation, but those errors represent only a small fraction of the orbital energies themselves. The most serious evidence for a potential problem with the HR approximation is in the relativistic corrections for the *p* states, for which the HR approximation gives even poorer results than does the simple FPPn approximation. To understand this, consider the vector product terms that are neglected in the HR approximation. For a spherical potential,

$$\mathbf{p} \times v\mathbf{p} = \frac{i}{r}\frac{dv}{dr}\mathbf{L}. \tag{20}$$

The radial factors in Eq. (20) blow up near the origin and, hence, will primarily affect states with small l values. At the same time, **L** will be zero for *s* states. Thus, the vector product terms, and the HR approximation, will primarily affect the *p* states, as observed. The HR approximation does not appear to have a significant effect on any of

the chemically active states for the four atoms under consideration. Given the similarity between the vector product terms being dropped in the HR approximation and the lowest-order spin–orbit coupling term in Eq. (17), the HR approximation should be valid for any system in which spin–orbit coupling is unimportant. At the same time, if spin–orbit coupling is required for a given system, there will be no advantage to using the HR approximation anyway.

The small basis set results for Au and Pb are given in Tables V and VI. Comparison of the large and small basis-set results for these two atoms reveals that the change in the basis set has a noticeable impact on the NR one-electron energies; note, in particular, the energy of the $5p$ state for Au, which is shifted by about 0.4 eV. It is also clear that the relativistic corrections to the total energy and the one-electron eigenvalues of the core states are sensitive to the basis-set size. Nevertheless, for the chemically active valence states, there is rather good agreement between the relativistic corrections obtained with the large and small basis sets. This suggests that the physical properties obtained with scalar-relativistic LCGTO calculations should be no more sensitive to the orbital basis set size than are their NR counterparts.

In Table VII, the current small basis LCGTO results for Pb are compared with previous LCGTO-FF calculations using the same orbital basis set and LDA model [35]. The LCGTO-FF work did not consider the full EFP approximation used here or the HR approximation; hence, results are only compared for the NR, EFPn, and FPPn approximations. There is very good agreement between the NR results, indicating that a good fitting function basis set was used in the earlier work. The differences between the scalar-relativistic LCGTO and LCGTO-FF results are significantly larger. Those differences are, however, once again concentrated in the chemically inert core states and should not pose any difficulties for multiatom calculations.

The three questions posed in the Introduction can now be answered as follows:

1. The neglect of matrix elements involving vector products of the momentum should not present any problems for systems in which the spin–orbit coupling is unimportant.

TABLE V

Numerical and LCGTO results for the negatives of the nonrelativistic one-electron eigenvalues (in eV) and total energies (in Ry) are compared for paramagnetic Au. Scalar-relativistic corrections to the nonrelativistic results are listed for various approximations. The LCGTO results were calculated here with a 20*s*15*p*11*d*6*f* basis. All calculations used the HL model.

	Nonrelativistic		Scalar-relativistic corrections				
	Num	LCGTO	Num	EFP	EFPn	HR	FPPn
1*s*	73021.73	73022.30	7617.36	7281.25	7192.75	7178.54	11117.51
2*s*	12187.55	12188.15	2034.09	1991.51	1980.41	1975.56	2419.90
3*s*	2852.37	2852.98	504.21	494.85	492.62	491.15	587.68
4*s*	600.78	601.40	127.28	124.87	124.38	123.95	148.15
5*s*	84.79	85.26	23.95	23.49	23.41	23.31	28.10
6*s*	4.51	4.53	1.67	1.65	1.64	1.64	2.00
2*p*	11720.50	11721.21	572.48	573.21	567.02	603.99	589.17
3*p*	2631.48	2632.12	166.33	167.29	166.03	174.04	170.10
4*p*	505.55	506.17	39.34	39.57	39.34	41.23	40.09
5*p*	54.55	54.95	5.50	5.54	5.51	5.83	5.56
3*d*	2217.99	2218.55	−16.42	−17.47	−18.02	−18.89	−22.68
4*d*	330.12	330.54	−4.70	−4.94	−4.99	−5.22	−6.19
5*d*	8.37	8.39	−1.17	−1.19	−1.18	−1.19	−1.33
4*f*	94.89	95.19	−13.22	−13.31	−13.26	−13.46	−14.10
E	35720.73	35719.90	2280.97	2236.13	2227.66	2252.24	2933.86

TABLE VI

Numerical and LCGTO results for the negatives of the nonrelativistic one-electron eigenvalues (in eV) and total energies (in Ry) are compared for paramagnetic Pb. Scalar-relativistic corrections to the nonrelativistic results are listed for various approximations. The numerical results are from [35]. The LCGTO results were calculated here with a 20s17p11d6f basis. All calculations used the Xα model with α = 0.7.

	Nonrelativistic		Scalar-relativistic corrections				
	Num	LCGTO	Num	EFP	EFPn	HR	FPPn
1s	78976.75	78976.79	8997.12	8631.51	8532.30	8515.90	13281.58
2s	13312.12	13312.67	2421.16	2376.22	2363.60	2357.86	2903.21
3s	3173.88	3174.49	604.04	593.93	591.38	589.58	708.83
4s	701.38	701.85	153.40	150.86	150.29	149.71	179.97
5s	113.91	114.25	29.86	29.37	29.27	29.10	35.42
6s	8.93	8.97	2.59	2.54	2.54	2.50	3.17
2p	12824.30	12824.82	668.90	675.69	668.75	713.45	695.88
3p	2940.72	2941.33	195.58	197.84	196.40	206.07	201.22
4p	598.97	599.44	45.18	46.17	45.89	48.18	46.63
5p	79.45	79.76	5.80	5.96	5.93	6.32	5.84
6p	3.13	3.12	−0.15	−0.14	−0.14	−0.13	−0.20
3d	2503.90	2504.49	−20.25	−20.86	−21.50	−22.54	−27.20
4d	409.46	409.79	−7.67	−7.74	−7.80	−8.12	−9.47
5d	23.86	23.92	−3.27	−3.23	−3.23	−3.29	−3.61
4f	152.37	152.61	−18.88	−18.88	−18.83	−19.13	−20.11
E	39055.40	39054.66	2705.40	2649.61	2640.28	2670.00	3496.23

TABLE VII

LCGTO and LCGTO-FF results for the negatives of the nonrelativistic one-electron eigenvalues (in eV) and total energies (in Ry) are compared for paramagnetic Pb. Scalar-relativistic corrections to the nonrelativistic results are listed for two approximations. The LCGTO-FF results are from [35] and are indicated by FF. All calculations used the 20s17p11d6f basis and the Xα model with α = 0.7.

	Nonrelativistic		Scalar-relativistic corrections			
	LCGTO	LCGTO-FF	EFPn	EFPn-FF	FPPn	FPPn-FF
1s	78976.79	78977.31	8532.30	8531.04	13281.58	13279.32
2s	13312.67	13312.75	2363.60	2363.22	2903.21	2902.52
3s	3174.49	3174.50	591.38	591.27	708.83	708.62
4s	701.85	701.84	150.29	150.26	179.97	179.91
5s	114.25	114.25	29.27	29.26	35.42	35.39
6s	8.97	8.97	2.54	2.53	3.17	3.16
2p	12824.82	12825.03	668.75	671.07	695.88	700.14
3p	2941.33	2941.38	196.40	197.03	201.22	202.36
4p	599.44	599.45	45.89	46.05	46.63	46.91
5p	79.76	79.75	5.93	5.87	5.84	5.90
6p	3.12	3.12	−0.14	−0.15	−0.20	−0.20
3d	2504.49	2504.50	−21.50	−21.60	−27.20	−27.38
4d	409.79	409.79	−7.80	−7.83	−9.47	−9.52
5d	23.92	23.92	−3.23	−3.24	−3.61	−3.62
4f	152.61	152.61	−18.83	−18.85	−20.11	−20.14
E	39054.66	39054.74	2640.28	2641.92	3496.23	3499.20

2. The valence (bonding) states from scalar-relativistic LCGTO calculations should be no more sensitive to orbital basis set size than are their NR counterparts.
3. Although the use of fitting functions has a somewhat larger impact on scalar-relativistic calculations than on NR calculations, this effect is confined to the deepest core levels and should not affect the properties that are of interest in most multiatom calculations.

ACKNOWLEDGMENTS

Helpful communications with N. Rösch are gratefully acknowledged. J. M. Wills is thanked for providing a copy of his numerical atom code. This work was supported by the U.S. Department of Energy.

References

1. B. I. Dunlap, J. W. D. Connolly, and J. R. Sabin, J. Chem. Phys. **71**, 3396 (1979); *Ibid.*, J. Chem. Phys. **71**, 4493 (1979).
2. B. I. Dunlap and N. Rösch, Adv. Quantum Chem. **21**, 317 (1990).
3. J. L. Ballester and B. I. Dunlap, Phys. Rev. A **45**, 7985 (1992).
4. J. W. Mintmire and C. T. White, Phys. Rev. Lett. **50**, 101 (1983); *Ibid.*, Phys. Rev. B **27**, 1447 (1983).
5. J. W. Mintmire and C. T. White, Phys. Rev. B **28**, 3283 (1983).
6. J. W. Mintmire, Phys. Rev. B **39**, 13350 (1989).
7. J. W. Mintmire, J. R. Sabin, and S. B. Trickey, Phys. Rev. B **26**, 1743 (1982).
8. J. C. Boettger, Internat. J. Quantum Chem. Symp. **27**, 147 (1993); also see J. C. Boettger and S. B. Trickey, Phys. Rev. B **32**, 1356 (1985).
9. U. Birkenheuer, J. C. Boettger, and N. Rösch, J. Chem. Phys. **100**, 6826 (1994).
10. J. C. Boettger, Int. J. Quantum Chem. Symp. **29**, 197 (1995).
11. J. C. Boettger and S. B. Trickey, Phys. Rev. B **51**, 15623 (1995).
12. J. C. Boettger, Phys. Rev. B **55**, 750 (1997).
13. W. Kutzelnigg, Int. J. Quantum Chem. **25**, 107 (1984).
14. N. Rösch and O. D. Häberlen, J. Chem. Phys. **96**, 6322 (1992).
15. O. D. Häberlen and N. Rösch, Chem. Phys. Lett. **199**, 491 (1992).
16. O. D. Häberlen, PhD Thesis (Technische Universität, Munich, 1993).
17. M. Douglas and N. M. Kroll, Ann. Phys. **82**, 89 (1974).
18. O. D. Häberlen, S. Chung, and N. Rösch, Int. J. Quantum Chem. Symp. **28**, 595 (1994).
19. O. D. Häberlen, H. Schmidbaur, and N. Rösch, J. Am. Chem. Soc. **116**, 8241 (1994).
20. S. Chung, S. Krüger, G. Pacchioni, and N. Rösch, J. Chem. Phys. **102**, 3695 (1995).
21. S. Chung, S. Krüger, S. P. Ruzankin, G. Pacchioni, and N. Rösch, Chem. Phys. Lett. **248**, 109 (1996).
22. A. L. Yakovlev, K. M. Neyman, G. M. Zhidomirov, and N. Rösch, J. Phys. Chem. **100**, 3482 (1996).
23. V. A. Nasluzov and N. Rösch, Chem. Phys. **210**, 413 (1996).
24. S. Chung, S. Krüger, H. Schmidbaur, and N. Rösch, Inorg. Chem. **35**, 5387 (1996).
25. U. Heiz, A. Vayloyan, E. Schumacher, C. Yeretzian, M. Stener, P. Gisdakis, and N. Rösch, J. Chem. Phys. **105**, 5574 (1996).
26. M. Mayer, O. D. Häberlen, and N. Rösch, Phys. Rev. A **54**, 4775 (1996).
27. M. V. Ramana and A. K. Rajagopal, Adv. Chem. Phys. **54**, 231 (1983).
28. See, e.g., Eq. (3) of K. G. Dyall, J. Chem. Phys. **100**, 2118 (1994).
29. L. L. Foldy and S. A. Wouthuysen, Phys. Rev. **78**, 29 (1950).
30. J. Sucher, Phys. Rev. A **22**, 348 (1980).
31. B. A. Hess, Phys. Rev. A **33**, 3742 (1986).
32. G. Jansen and B. A. Hess, Phys. Rev. A **39**, 6016 (1989).
33. B. A. Hess, R. J. Buenker, and P. Chandra, Int. J. Quantum Chem. **29**, 737 (1986).
34. J. C. Boettger, unpublished.
35. P. Knappe and N. Rösch, J. Chem. Phys. **92**, 1153 (1990).
36. L. Hedin and B. I. Lundqvist, J. Phys. C **4**, 2064 (1971).
37. J. M. Wills, unpublished.
38. O. Gropen, J. Comp. Chem. **8**, 982 (1987).

Correlated Relativistic Calculation of the Giant Resonance in the Gd^{3+} Absorption Spectrum

S. KOTOCHIGOVA,[1] H. LEVINE,[1] I. TUPITSYN[2]

[1] *National Institute of Standards and Technology, Gaithersburg, Maryland 20899*

[2] *Chemistry Institute, St. Petersburg University, 198 904 Stary Peterhoff, St. Petersburg, Russia*

Received 29 March 1997; revised 18 June 1997; accepted 19 June 1997

ABSTRACT: The aim of the present study is to extend the multiconfiguration Dirac–Fock approach to include spin polarization in order to study magnetically ordered systems. Routines handling time-dependent ionization phenomena adapted to multilevel and multichannel autoionization processes have been developed and used to describe the giant resonance in the Gd^{3+} absorption spectrum. In our calculation of the complete energy structure of $4d^9 4f^8$ configuration it is discovered that the majority of the oscillator strength associated with the $4d$–$4f$ transitions is limited to a relatively narrow spectral width, creating a giant resonance. Our calculations take account of the most important correlation effects, and the agreement with the experimentally observed giant resonance in gadolinium is quite good. © 1997 John Wiley & Sons, Inc. Int J Quant Chem **65**: 575–584, 1997

In this study, we demonstrate the applicability of the spin-polarized multiconfiguration Dirac–Fock (SPMCDF) formalism for an accurate description of magnetic dichroism in rare-earth atoms. The motivation for applying the SPMCDF method is our desire to use the exact form of the exchange potential essential for a correct calculation of the core spin polarization and ferromagnetism in general. As far as we know, our work is the first attempt to apply the Dirac–Fock formalism in combination with multiconfiguration effects [1] to describe magnetic dichroism on an atomic level. A multiconfiguration description enables one to introduce the multiple structure of relativistic terms with different total angular momenta. Moreover, this approach is designed to treat spin polarization and relativistic effects on the same footing by including the exchange potential dependence on the orientation of the electron spin. Magnetic dichroism in its circular and linear forms is caused by the reduced symmetry, compared to the paramagnetic state, due to the simultaneous effects of spin-orbit and spin polarization.

Besides being valuable in the study of ferromagnetic materials, magnetic dichroism also gives spectroscopic information about the electronic structure of free atoms and ions embedded in a

Correspondence to: S. Kotochigova.

© 1997 John Wiley & Sons, Inc.
CCC 0020-7608 / 97 / 050575-10

crystal. We have found that it is instructive to begin the study of magnetic dichroism assuming a free atom or ion. Moreover, there is experimental evidence that the total absorption cross section of rare-earth metals for photon energies near the $4d$ thresholds [2] is nearly identical with the corresponding quantity measured in the gas phase [3]. This motivates one to consider magnetic dichroism in an atomic model.

A number of relativistic theories have been developed recently to describe magnetic dichroism in magnetic solids [4–8] using the local density approximation. In particular, the $L_{2,3}$ edges of solid Gd have been studied within a multiple scattering formalism which includes finite lifetime effects for the excited states [9].

Here we consider a free Gd^{3+} ion, which has been obtained by removing the three valence electrons ($5d6s^2$) from the Gd atom. The remaining ion has a high-spin $4f^7$ state as the ground configuration. Spin polarization of the $4f$ orbital and as well as a large spin-orbit splitting of the $4d_{3/2}$ and $4d_{5/2}$ core hole states are essential ingredients for predicting strong magnetic dichroism in the Gd^{3+} spectrum. We wish to describe theoretically the transitions in Gd^{3+} from the ground $4d^{10}4f^{7\,8}S^0_{7/2}$ to the upper $4d^94f^8$ states. Experiment [10, 11] suggests that these transitions create the key features in the rare-earth atomic spectra: giant resonances. We will show that indeed the $4d$–$4f$ transitions of core electrons in the Gd^{3+} ion display resonance profiles similar to those obtained experimentally. Hence, for both rare-earth atoms and metals the strong overlap of the $4f$ and $4d$ orbitals makes the giant resonances an important proving ground for many-electron effects.

A decade ago considerable progress was made toward understanding the essence of giant resonances in absorption spectra of rare-earth elements. A compilation of review articles can be found [12]. In many cases, relativistic time-dependent local-density approximation (RTDLDA) [13] as well as random-phase approximation with exchange (RPAE) [14] and many-body perturbation theory (MBPT) [15] were applied successfully.

We focus particular attention on reproducing the Gd^{3+} total cross section in the 140- to 180-eV energy range. We want to demonstrate the formation of the giant resonance from the series of asymmetric absorption lines, all determined by $4d^{10}4f^7$–$4d^94f^8$ excitation, or otherwise mainly by $4d^94f^8$–$4d^94f^7\varepsilon f, 4d^{10}4f^6\varepsilon l$ autoionizing decays. The SPMCDF matrix elements and the resonance energies are used to solve time-dependent Floquet equations simulating the Gd^{3+} absorption cross section. This approach is a generalization of the theories of Fano [16] and Mies [17].

The study is organized as follows. In the first section a description of the SPMCDF theory is given. For the sake of completeness, a brief derivation of the relativistic formalism used to calculate autoionization and photoionization transition matrix elements is presented in the second section. The formalism of the time-dependent Floquet theory describing the appearance of the Fano-type resonances in absorption spectra is given in the third section. The absorption cross section and for circular and linear magnetic dichroism in Gd^{3+} spectrum are presented in the fourth section together with a comparison with experimental results [11].

Spin-Polarized Dirac–Fock Theory

The theory is modeled on the basis of the Dirac–Fock approximation with an exact description of the exchange potential. We have constructed the central-field spin-polarized Dirac-Fock (SPDF) equations by selecting all relativistic atomic orbitals in two groups with opposite directions of electron spin. The total energies have been taken as the center of gravity of relativistic terms. Averaging energies helps to break the *JJ* coupling and partly implement the *LS* coupling. We also use the fractional occupation of open relativistic suborbitals, so that the SPDF solutions can be reduced to the spin-polarized Hartree-Fock solutions in the limit of $c \to \infty$.

In the spin-polarized relativistic approximation, the radial parts $P(r)$ and $Q(r)$ of wave function become dependent on both the projections of the total angular momentum j_z (with quantum number m) and the electron spin μ. The solutions of these equations can be identified by the mixture of the quantum numbers m and μ, so it is hard to distinguish solutions related to a particular spin projection. To avoid construction of a large number of equations and to focus more on the spin-polarization effects, we assumed the radial functions $P(r)$ and $Q(r)$ to be independent of the quantum number m. This is justified because the

m splitting is much smaller than that of spin polarization.

The spin-polarization interaction mixes states with different total angular momenta j and creates new states, described by the linear combinations of $j_1 = l + \frac{1}{2}$ and $j_2 = l - \frac{1}{2}$ [20] for a given μ. We obtain from two relativistic orbitals, j_1 and j_2, two linear combinations by a unitary transformation. Coefficients in the linear combinations are found from the minimization of the total energy.

In this approximation, the atomic wave function $\psi(\mathbf{r})$ is a four-component Dirac spinor

$$\Psi(\mathbf{r}) = \frac{1}{r}\begin{pmatrix} P_\Lambda(r)\chi_{\kappa,m}(\hat{\mathbf{r}}) + P_{\hat{\Lambda}}(r)\chi_{-\kappa-1,m}(\hat{\mathbf{r}}) \\ iQ_\Lambda(r)\chi_{-\kappa,m}(\hat{\mathbf{r}}) + iQ_{\hat{\Lambda}}(r)\chi_{\kappa+1,m}(\hat{\mathbf{r}}) \end{pmatrix} \tag{1}$$

with $\Lambda = (\kappa, \mu)$, and $\hat{\Lambda} = (-\kappa - 1, \mu)$; $\chi_{\kappa,m}(\hat{\mathbf{r}})$ is a two-component spin-angular function (i.e., a Pauli spinor). P_Λ and Q_Λ are the large and small components of the wave function, respectively.

The quantum numbers κ (with $\kappa = \pm 1, \pm 2, \ldots$) are related to the orbital and total angular momentum quantum numbers l and j by

$$j = |\kappa| - \tfrac{1}{2}, \qquad l = j + s_\kappa/2, \qquad s_\kappa = \kappa/|\kappa|. \tag{2}$$

The set $\kappa = 1, 2, 3, \ldots$ is sometimes denoted as $p_{1/2}, d_{3/2}, f_{5/2}, \ldots$ and $\kappa = -1, -2, -3, \ldots$ corresponds to $s_{1/2}, p_{3/2}, d_{5/2}, \ldots$

The trial functions are then constructed from the wave functions $\psi(\mathbf{r})$ so that they belong to a given configuration $(n_1 l_1 \mu_1)^{q^1} \cdots (n_a l_a \mu_a)^{q^a}$. The former of these means that the set of one-electron functions (1) is made up of functions belonging to the spin-polarized subshells, where $q_1, \ldots, q_a$ are numbers of electrons with a specified direction of spin, belonging to the subshells $1, \ldots, a$.

Once the class of functions to be varied is chosen, the subsequent calculations are performed in two stages. In the first stage, μ-dependent expressions for the total energy are constructed for the centers of gravity of relativistic configurations. The second stage of the calculation involves a search for the extremals of the energy functional, which leads to a system of coupled differential equations

$$\begin{aligned}
\frac{dP_\Lambda}{dr} &= -\frac{\kappa}{r}P_\Lambda - \left(2c - \frac{\varepsilon_\Lambda}{2c} + \frac{Z - Y_\Lambda}{cr}\right)Q_\Lambda \\
&\quad - \frac{1}{r}X_\Lambda^P, \\
\frac{dQ_\Lambda}{dr} &= \frac{\kappa}{r}Q_\Lambda - \left(\frac{\varepsilon_\Lambda}{2c} + \frac{Z - Y_\Lambda}{cr}\right)P_\Lambda - \frac{1}{r}X_\Lambda^Q \\
\frac{dP_{\hat{\Lambda}}}{dr} &= -\frac{-\kappa - 1}{r}P_{\hat{\Lambda}} - \left(2c - \frac{\varepsilon_{\hat{\Lambda}}}{2c} + \frac{Z - Y_\Lambda}{cr}\right)Q_{\hat{\Lambda}} \\
&\quad - \frac{1}{r}X_{\hat{\Lambda}}^P, \\
\frac{dQ_{\hat{\Lambda}}}{dr} &= \frac{-\kappa - 1}{r}Q_{\hat{\Lambda}} - \left(\frac{\varepsilon_{\hat{\Lambda}}}{2c} + \frac{Z - Y_\Lambda}{cr}\right)P_{\hat{\Lambda}} \\
&\quad - \frac{1}{r}X_{\hat{\Lambda}}^Q,
\end{aligned} \tag{3}$$

where we have

$$\begin{aligned}
Y_\Lambda &= \sum_{\Lambda'}(q_{\Lambda'} - \delta_{\Lambda\Lambda'})Y^0_{\Lambda'\Lambda'} \\
&\quad + \sum_{\Lambda'}(1 + \delta_{\Lambda\Lambda'})\sum_{s>0}\frac{f^s_{\Lambda\Lambda'}}{q_\Lambda}Y^s_{\Lambda\Lambda'}, \\
X_\Lambda^P &= \frac{1}{c}\sum_{\Lambda'\neq\Lambda}\sum_s \frac{g^s_{\Lambda\Lambda'}}{q_\Lambda}Y^s_{\Lambda\Lambda'}Q_{\Lambda'} - r\sum_{\Lambda'\neq\Lambda}\frac{\lambda_{\Lambda\Lambda'}}{2cq_\Lambda}Q_{\Lambda'}, \\
X_\Lambda^Q &= \frac{1}{c}\sum_{\Lambda'\neq\Lambda}\sum_s \frac{g^s_{\Lambda\Lambda'}}{q_\Lambda}Y^s_{\Lambda\Lambda'}P_{\Lambda'} + r\sum_{\Lambda'\neq\Lambda}\frac{\lambda_{\Lambda\Lambda'}}{2cq_\Lambda}P_{\Lambda'}, \\
Y^s_{\Lambda\Lambda'} &= r\int\frac{r^s_<}{r^{s+1}_>}[P_\Lambda P_{\Lambda'} + Q_\Lambda Q_{\Lambda'}]\,dr',
\end{aligned} \tag{4}$$

and Z is the nuclear charge. Here, atomic units are used, i.e., $\hbar$, Planck's constant, the electron mass, the charge are numerically equal to 1. Indices Λ and Λ' label different atomic subshells in the SPDF approximation. The parameters ε and λ are the Lagrange multipliers when the normalization and orthogonalization conditions are taken into account. The functions f^s and g^s are defined by the electron orbital [18]. To solve Eq. (3) we apply the self-consistent field approximation. The ideas underlying the SPDF self-consistent field theory are similar to those in the Dirac-Fock (DF) theory. A numerical solution was performed by transforming the differential equations to a logarithmic scale $\rho = \ln r$. A uniform grid in ρ is taken between $\rho_{\min}$ and $\rho_{\max}$, corresponding with $r_{\min} = 0.1 \times e^{-4}/Z$ and $r_{\max} = 80$ a.u.

Since the interaction between an atom and the electromagnetic field is represented by a one-particle operator, the corresponding matrix element

can be written in the one-electron form

$$v_{\Lambda\Lambda'} = \langle \Psi_{\Lambda'} | \Pi_k | \Psi_\Lambda \rangle = \frac{1}{r}\left[\begin{pmatrix} P_{\Lambda'}\chi_{\kappa',m'} & |\Pi_k| & P_\Lambda \chi_{\kappa,m} \\ iQ_{\Lambda'}\chi_{-\kappa',m'} & & iQ_\Lambda \chi_{-\kappa,m} \end{pmatrix} + \begin{pmatrix} P_{\hat{\Lambda}'}\chi_{-\kappa'-1,m'} & |\Pi_k| & P_{\hat{\Lambda}}\chi_{-\kappa-1,m} \\ iQ_{\hat{\Lambda}'}\chi_{\kappa'+1,m'} & & iQ_{\hat{\Lambda}}\chi_{\kappa+1,m} \end{pmatrix} + \begin{pmatrix} P_{\hat{\Lambda}'}\chi_{-\kappa'-1,m'} & |\Pi_k| & P_\Lambda \chi_{\kappa,m} \\ iQ_{\hat{\Lambda}'}\chi_{\kappa'+1,m'} & & iQ_\Lambda \chi_{-\kappa,m} \end{pmatrix} + \begin{pmatrix} P_{\Lambda'}\chi_{\kappa',m'} & |\Pi_k| & P_{\hat{\Lambda}}\chi_{-\kappa-1,m} \\ iQ_{\Lambda'}\chi_{-k',m'} & & iQ_{\hat{\Lambda}}\chi_{\kappa+1,m} \end{pmatrix} \right], \quad (5)$$

where we have $\Pi_k = j_k(\omega/c, r)Y_{k\Delta m}$. The terms in the above expression can be written as radial and angular parts, for example,

$$\begin{pmatrix} P_{\Lambda'}\chi_{k',m'} & |\Pi_k| & P_\Lambda \chi_{\kappa,m} \\ iQ_{\Lambda'}\chi_{-k',m'} & & iQ_\Lambda \chi_{-\kappa,m} \end{pmatrix} = \sqrt{\frac{(2k+1)(2j_{\Lambda'}+1)}{(2j_\Lambda+1)}}\, C^{j_\Lambda m_\Lambda}_{j_{\Lambda'}m_{\Lambda'},k\Delta m} C^{j_\Lambda 1/2}_{k0,j_{\Lambda'}1/2} \times \sum_{\gamma=\pm 1} \langle R_\Lambda(\gamma)|j_k|R_{\Lambda'}(\gamma)\rangle, \quad (6)$$

where $C^{j_1 m_1}_{j_2 m_2, k\Delta m}$ are Clebsch–Gordan coefficients; $R(\gamma)$ is the radial part of a wave function, defined through the large $P_\Lambda(r)$ and small $Q_\Lambda(r)$ components of the wave function

$$\langle R_\Lambda(\gamma)|j_k|R_{\Lambda'}(\gamma)\rangle = \begin{cases} P_\Lambda(r) & \text{if } \gamma = 1 \\ Q_\Lambda(r) & \text{if } \gamma = -1, \end{cases} \quad (7)$$

with the condition that $(l_\Lambda + l_{\Lambda'} + k)$ is even, and j_k is a spherical Bessel function.

The total matrix element can be represented by a linear combination of the matrix elements in Eq. (5).

$$V_{ab} = \sum_{\Lambda\Lambda'} \sum_m c_\Lambda c_{\Lambda'} v_{\Lambda\Lambda'}, \quad (8)$$

where the matrix elements $v_{\Lambda\Lambda'}$ are generated by a one-electron dipole transition between states $\Lambda, \hat{\Lambda}$ and $\Lambda', \hat{\Lambda}'$, included as components in the initial and final levels, respectively. The coefficients c_Λ and $c_{\Lambda'}$ reflect the multiconfiguration character of terms and are determined by solving the multiconfiguration problem with the Dirac–Fock basis set (MCDF) [1]. In SPMCDF, the Dirac–Fock spin-polarized orbitals in Eq. (1) were used as the basis functions in Eqs. (5) and (8). The dipole selection rules for the different polarizations of external field are determined by the Clebsch–Gordan coefficients.

Transitions to the Continuum

The formalism for the calculation of photoionization matrix elements is similar to that between discrete levels. For the description of the continuum state we have limited ourselves to a single configuration as the correlation interaction between the continuum states is assumed to be negligible. The outer (free) electron with a well-defined orbital momentum and kinetic energy is considered to be moving in a core potential. The core potential is found by a SPDF calculation of the core orbitals in either the ground or excited state. A numerical integration leads to a continuum two-component wave function ϕ with the correct phase behavior. We matched the wave function ϕ to Coulomb functions between 10 and 20 a.u., with a charge appropriate for the remaining ion to normalize the wave functions. The Coulomb regular F and irregular G functions were calculated using continued fractions [19].

The many-body photoionization matrix elements of Eq. (8), assuming a single configuration for the continuum, reduces to

$$V_{a,\varepsilon i} = \sum_\Lambda \sum_m c_\Lambda v_{\Lambda,\varepsilon i}, \quad (9)$$

where a labels the initial discrete state, and i labels the core orbital. Here the label ε combines both the kinetic energy and the orbital angular momentum of the free electron. The one-electron matrix element $v_{\Lambda,\varepsilon i}$ is described by Eq. (5), but now calculated with continuum wave functions.

The autoionization matrix elements describe the transition between an autoionizing atomic state a and an ion, which need not be in the ground configuration, plus a free electron. This process involves separating two electrons in the outer shell

and is mediated by the Coulomb repulsion between those electrons. Within the Dirac–Fock framework each electron can be assigned an independent wave function. Calculating the many-electron autoionization matrix elements therefore reduces to the evaluation of two-electron matrix elements. If the electrons participating in the transition are labeled A and B for the atomic state a and C and D for the continuum configuration, where D defines the escaping electron, then the matrix element is given by

$$\begin{aligned}\langle AB|1/r_{12}|CD\rangle &= \sqrt{(2j_A+1)(2j_B+1)(2j_C+1)(2j_D+1)} \\ &\times \sum_\nu \frac{1}{(2\nu+1)^2} C^{\nu 0}_{j_A-1/2,\, j_C 1/2} \\ &\times C^{\nu 0}_{j_B-1/2,\, j_D 1/2} R^\nu(A,B,C,D) \\ &\times \sum_{m_A,m_B} \sum_{m_C,m_D} \sum_\alpha c_\alpha^{\mathrm{DF}} (-1)^{m_C+m_D+1} \\ &\times C^{\nu(m_A-m_C)}_{j_A m_A,\, j_C -m_C} C^{\nu(m_B-m_D)}_{j_B m_B,\, j_D -m_D}, \end{aligned} \tag{10}$$

where the c_α^{DF}'s describe the many-electron Dirac-Fock wave function in terms of Slater determinants. The radial integrals have the usual form

$$\begin{aligned} R^\nu(A,B,C,D) &= \int_0^\infty dr_1 \int_0^\infty dr_2 (P_A(r_1)P_C(r_1) + Q_A(r_1)Q_C(r_1)) \\ &\times \frac{r_<^\nu}{r_>^{\nu+1}} (P_B(r_2)P_D(r_2) + Q_B(r_2)Q_D(r_2)). \end{aligned} \tag{11}$$

The configuration interaction (CI) matrix element for autoionization is then subsequently found as a linear combination of these two electron matrix elements with coefficients given by the CI calculation for the a level.

Calculation of Absorption Cross Sections

The nature of giant resonances is complicated due to the simultaneous presence of a multiplet structure and discrete and continuum contributions. Any model for the frequency dependence of the resonances must have a discrete initial state ψ_0 and a number of final states embedded in the autoionizing region. Moreover, each final state is correlated to and interacts with its own continuum. The total wave function Ψ of such a system evolving under influence of a light field of frequency ω is represented as a linear combination of atomic wave functions, as calculated in the two preceding sections, which are either discrete ψ_k or continuum $\psi_{\varepsilon i}$ wave functions. Note that, in this section the subscripts $k, n = 0, 1, 2, \ldots$ label discrete states, while the subscript i labels the various continua, i.e., the various core orbitals, and ε is the kinetic energy of the free electron. Therefore, we have

$$\Psi = c_0(t)\psi_0 e^{i\omega t} + \sum_{k\neq 0} c_k(t)\psi_k + \sum_{i\in \text{continua}} \int d\varepsilon\, c_{\varepsilon i}(t)\psi_{\varepsilon i}, \tag{12}$$

where the coefficients c describe the light-induced mixing of states. The dynamics of the wave function is given by

$$i\frac{d\Psi}{dt} = H^f\Psi, \tag{13}$$

where H^f includes the atomic and relativistic atom-field interaction

$$H^f = H_0 - \sum_j \alpha_j \mathbf{A}_j(t), \tag{14}$$

$\mathbf{A}_j(t)$ is the relativistic vector potential of the external field, α_j is a Pauli matrix, and the sum j is taken over all electrons. Inserting Eq. (12) into Eq. (13), integrating over all electron coordinates $\mathbf{r}$, and using the rotating wave or resonant approximation to the time-dependent differential equations, the coefficients c are given by

$$\begin{aligned} i\frac{d}{dt}c_n(t) - E_n c_n(t) &= \sum_{k\neq n} c_k(t)V_{kn} + \sum_{i\in\text{continua}} \int d\varepsilon\, c_{\varepsilon i}(t)V_{\varepsilon i,n}, \\ i\frac{d}{dt}c_{\varepsilon i}(t) - E_{\varepsilon i}c_{\varepsilon i}(t) &= \sum_k c_k(t)V_{k,\varepsilon i}, \end{aligned} \tag{15}$$

where the index n denotes either the initial or final state and the energies E are the atomic energies except for the initial state where E_0 equals the initial atomic energy plus the photon energy ω.

The matrix elements V denote the coupling strength between the various levels. In fact, the $V_{\varepsilon i,k}$ lead to field-induced photoionization ($k = 0$) or autoionization ($k > 0$).

For the transition between the initial and upper state it follows that we have $V_{k=0,n} = d_{k=0,n}F$, where the d_{0n} are the dipole transition matrix elements and F the field strength. Similarly, for the field-induced photoionization, we have $V_{\varepsilon i,k=0} = d_{\varepsilon i,k=0}F$, where the $d_{\varepsilon i,0}$ denote dipole transition matrix elements into the continuum. On the other hand, the nonzero autoionizing matrix elements $V_{\varepsilon i,k}$ (for $k > 0$) are independent of the laser field and arise from CI. Moreover, the matrix elements V_{kn} for $k,n > 0$ can in principle be nonzero. This is due to the configuration interaction between two excited states. However, our level structure calculation has already taken those effects into account and thus we have $V_{kn} = 0$ for $k, n > 0$. Finally, as correlation between continua is weak, the matrix elements $V_{\varepsilon i,\varepsilon' i'}$ are negligibly small and therefore have been omitted from Eq. (15).

The major difficulty in solving Eq. (15) by straightforward integration over time t is caused by the kinetic energy ε. In fact, Eq. (15) forms an infinite set of coupled differential equations, which are complicated by the fact that the matrix elements $V_{\varepsilon i,k}$ have a weak dependence on ε such that any introduction of an energy cut-off will lead to a theory with poor convergence characteristics. Therefore we applied the Floquet approach which transforms the differential equations into a set of integral equations with the property that the integration over ε can be solved analytically. In the Floquet method the Laplace transformation

$$c_\rho(p) = \int_0^\infty dt\, c_\rho(t) e^{pt}, \tag{16}$$

where p is either k or ε_i, reduces Eq. (15) to the form,

$$\begin{aligned}
&[ip - E_n]c_n(p) - \sum_{k\neq n} c_k(p)V_{kn} \\
&\quad - \sum_{i\in\text{continua}} \int d\varepsilon\, c_{\varepsilon i}V_{\varepsilon i,n} = ic_n(0), \\
&[ip - E_{\varepsilon i}]c_{\varepsilon i} - \sum_k c_k(p)V_{k,\varepsilon i} = ic_{\varepsilon i}(0),
\end{aligned} \tag{17}$$

where $c_n(0)$ and $c_{\varepsilon i}(0)$ describe the population amplitudes of all levels at time $t = 0$, and are given by

$$c_0(0) = 1; \qquad c_k(0) = c_{\varepsilon i}(0) = 0 \tag{18}$$

for $k > 0$. In deriving Eq. (17), it is assumed that the autoionizing and CI matrix elements V are time-independent.

Equation (17) can be rewritten by eliminating $c_{\varepsilon i}$. The second equation of Eq. (17) gives

$$c_{\varepsilon i}(p) = \frac{\sum_k c_k(p)V_{k,\varepsilon i}}{ip - E_{\varepsilon i}} \tag{19}$$

and is inserted into the first equation of Eq. (17). The integral over ε can now be solved with Dirac's formula to give

$$\int d\varepsilon \frac{V_{k,\varepsilon i}V_{\varepsilon i,n}}{ip - E_{\varepsilon i}} = P - i\pi \tilde{V}_{k,\varepsilon_i}\tilde{V}_{\varepsilon i,n}, \tag{20}$$

where $\tilde{V}_{k,\varepsilon i}$ is a matrix element at the point $\varepsilon = -E_{\text{th},i} + ip$, where we have $E_{\varepsilon i} = E_{\text{th},i} + \varepsilon$, and $E_{\text{th},i}$ is the atomic energy at threshold. Because $V_{\varepsilon i,n}$ has weak energy dependence, the principal part P is small and will be neglected henceforth. Moreover, this weak dependence allows one to replace $\tilde{V}_{\varepsilon i,n}$ with its value at resonance when $E_{\varepsilon i} = E_n$. Therefore we get, for the discrete levels,

$$\begin{aligned}
&\left(ip - E_n + i\pi \sum_{i\in\text{continua}} |\tilde{V}_{\varepsilon i,n}|^2\right)c_n(p) \\
&\quad - \sum_{k\neq n}\left(V_{kn} - i\pi \sum_{i\in\text{continua}} \tilde{V}_{k,\varepsilon i}\tilde{V}_{\varepsilon i,n}\right) = ic_n(0).
\end{aligned} \tag{21}$$

For each p Eq. (21) forms a finite set of algebraic equations of form $(ip - \mathbf{A})c(p) = ic(0)$ over the discrete levels n, where $-\mathbf{A}$ denotes the matrix formed by the terms in Eq. (21), which are independent of p. In general, the solutions of the algebraic equations are given by

$$\begin{aligned}
c_n(p) &= \sum_k ic_k(0)(ip - \mathbf{A})^{-1}_{nk}, \\
(ip - \mathbf{A})^{-1}_{nk} &= \frac{D_{nk}(ip)}{D},
\end{aligned} \tag{22}$$

where $D_{kn}(ip)$ and D are the minors and the determinant of the matrix $(ip - \mathbf{A})$, respectively.

The inverse Laplace transformation of Eq. (22) gives us the time-dependent solutions of Eq. (21) and after some algebra we find

$$c_n(t) = i\sum_k \frac{D_{n0}(X_k)e^{X_k t}}{\Pi_{j\neq k}(X_k - x_j)}. \qquad (23)$$

From the population $P_n(t) = |c_n(t)|^2$ of a level, the partial photoabsorbtion cross section is found as

$$\sigma_n(\omega) = \frac{1}{\omega c} P_n(\tau)/(\tau F^2), \qquad (24)$$

where τ is the pulse duration and F the field strength. The method was originally developed for strong field applications [21].

Results

The absorption cross section of Gd^{3+} as a function of the photon energy is calculated using the resonant energies and the dipole matrix elements of transitions, from the ground state of the $4d^{10}4f^7$ configuration to the states of the $4d^94f^8$ configuration, which lie in the range of photon energies between 139 and 180 eV. The Gd^{3+} ground state is a high-spin state with seven aligned $4f$ electrons and zero orbital angular momentum, i.e., $^8S_{7/2}$. The absorption selection rule $\Delta J = \pm 1, 0$ permits transitions to states with total angular momentum $J' = \frac{5}{2}, \frac{7}{2}, \frac{9}{2}$.

The MCDF method [1] was applied to calculate initial and final states in the intermediate-coupling regime. The CI procedure included 7 relativistic configurations, belonging to the $4d^{10}4f^7$ configuration and describing the initial states and 14 relativistic configurations describing the final states of the $4d^94f^8$ configuration where seven and eight electrons were divided in all possible ways over the $4f_{5/2}$ and the $4f_{7/2}$ relativistic orbitals. Table I presents the resonant energies of the strongest lines in the Gd^{3+} spectrum which contribute to the giant resonance and correspond to transitions from the lowest level of the $4d^{10}4f^7$ configuration. Other lines (530 lines in the range between 140 and 160 eV) have strengths smaller by a factor of 2 or more.

The total absorption cross section is summed from three partial cross sections found for transitions to states with total angular momenta quantum numbers $J' = \frac{5}{2}, \frac{7}{2}, \frac{9}{2}$ of the $4d^94f^8$ configuration. Because there is no interference between channels belonging to different J', we solved the multichannel equations (21) for each J' separately.

TABLE I
Resonant energies of absorption lines used to construct the giant resonance in the Gd^{3+} spectrum.

J' of final state	Resonant energy in eV
$\frac{9}{2}$	140.444
$\frac{7}{2}$	141.856
$\frac{9}{2}$	144.424
$\frac{7}{2}$	144.537
$\frac{5}{2}$	144.622
$\frac{9}{2}$	144.787
$\frac{5}{2}$	153.990
$\frac{5}{2}$	154.028
$\frac{5}{2}$	154.092
$\frac{5}{2}$	154.129
$\frac{7}{2}$	154.972
$\frac{7}{2}$	155.052

For complex atomic systems, most of the autoionizing states have different core states and therefore decay to different continua. This plays an important role in the formation of the absorption spectrum of the Gd^{3+} ion.

Figure 1 presents the theoretical results for the absorption resonances induced by transitions to the three levels with $J' = \frac{9}{2}$, while Figure 2 shows the absorption lines of transitions from the ground state to states with $J' = \frac{7}{2}$ (four levels) and $J' = \frac{5}{2}$ states (five levels). The later transitions comprise considerably more oscillator strength than the J'

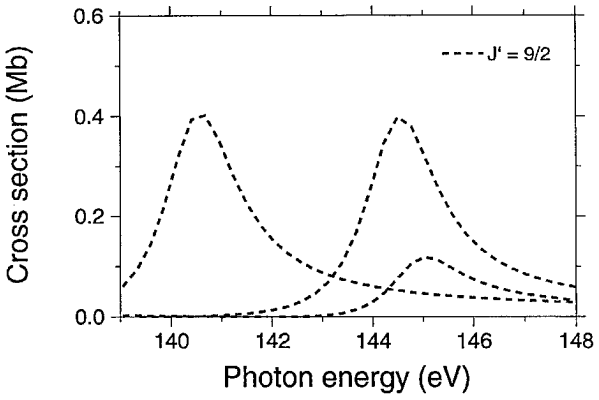


FIGURE 1. MCDF absorption cross section for $J = \frac{7}{2}$ to $J' = \frac{9}{2}$ resonant transitions between the ground state and states of the $4d^94f^8$ configuration.

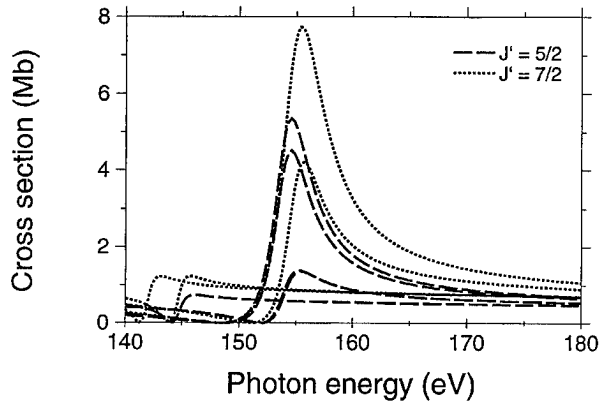


FIGURE 2. MCDF absorption cross section for $J = \frac{7}{2}$ to $J' = \frac{5}{2}, \frac{7}{2}$ resonant transitions between the ground state and states of the $4d^9 4f^8$ configuration.

$= \frac{9}{2}$ lines. The main reason for the significant differences in the cross sections and its strong dependence on J' can be found in the multiconfigurational distribution of the oscillator strengths among the levels of the $4d^9 4f^8$ configuration.

In the calculation, the full set of final states with the same total angular momentum J' are mixed; the results are plotted in Figure 3. The cross sections turn out to be given by the sums of the individual lines (cross sections are plotted in Figs. 1 and 2) to within 1%. The total cross section in Figure 3 determines the observable giant resonance. The maximum of this resonance lies at a higher photon energy (6.5 eV higher) than the experimental peak resonance at 148.86 eV [10, 11]. Figure 3 also displays several weak absorption lines preceding the giant resonance in the range from 140 to 146 eV. These satellites contain a small fraction of the oscillator strengths, but they are very characteristic features of the absorption spectrum, observed in core transitions of atomic gadolinium [10] and in solid gadolinium [11].

In order to compare the theoretical profile of Figure 3 (solid line) with the experimental resonance from [11], the theoretical cross section was shifted toward lower photon energies by 6.5 eV. The result is presented in Figure 4 together with the experimental profile. Since the experimental absorption cross section is given in relative units, we normalized it to our absolute theoretical total cross section to achieve the best comparison. Figure 4 shows that the MCDF calculation (solid line) describes the experimental spectrum (round dots) quite well. The giant resonance in both cases has a single Fano-type profile with almost the same width and asymmetry parameter q. The results indicate that the theoretical approach of the MCDF method is quite appropriate for an accurate description of the Gd absorption spectrum.

The MCDF results discussed above yield good agreement with the experiment, but do not include correlations due to spin polarization. However, this correlation is important in calculating magnetic dichroism. In order to introduce spin polarization we included in the model the alignment of all electron spins in the $4f^7$ orbital ($4f^5_{5/2}\uparrow\uparrow\uparrow\uparrow\uparrow\uparrow 4f^1_{7/2}\uparrow$) of the ground state of Gd^{3+}. The spin alignment of orbitals in the upper configuration $4d^9 4f^8$ is introduced as $4d^1_{5/2}\uparrow 4f^6_{5/2}\uparrow\uparrow\uparrow\uparrow\uparrow\uparrow 4f^2_{7/2}\uparrow\downarrow$. Spin polarization of the $4f$ orbital and

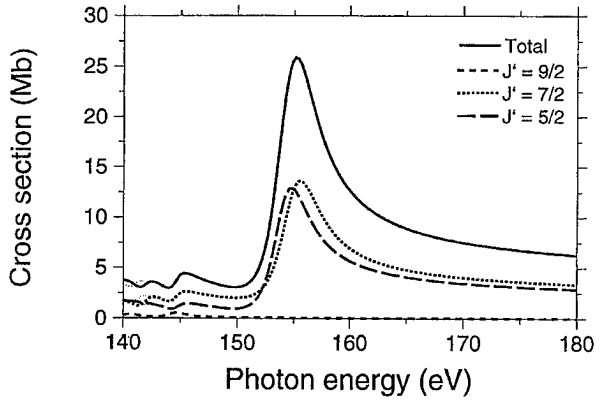


FIGURE 3. MCDF total absorption cross section for $J = \frac{7}{2}$ to $J' = \frac{5}{2}, \frac{7}{2}, \frac{9}{2}$ resonant transitions summed over final states (dashed lines) and the total absorption cross section (solid line).

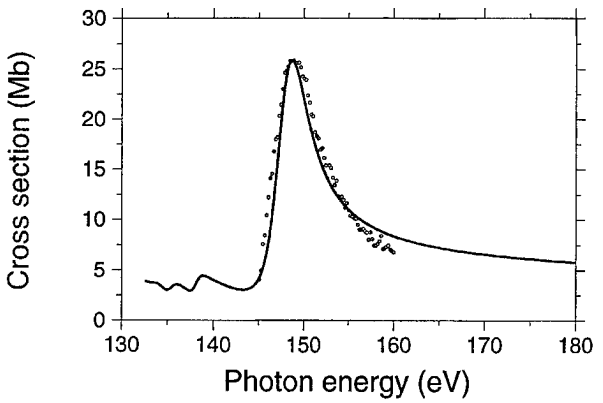


FIGURE 4. Theoretical (solid line) and experimental (open circles) total absorption cross section in Gd^{3+}. The theoretical cross section is shifted by 6.5 eV toward smaller photon energy.

the spin-orbit splittings of both $4d$ and $4f$ orbitals lead to the strong magnetic dichroism in Gd. In other words, magnetic dichroism appears when one can observe multiplet structure within the resonant profile. Our results show that the multiplet structure in Gd^{3+} is due to the fine splitting of final states.

In the spin-aligned model we consider transitions from the ground state with $J = \frac{7}{2}$ and $m_J = \frac{7}{2}$. First, we assume that the external field is either left- or right-circular-polarized. The selection rule $\Delta m = \pm 1$ for circular-polarized light allows transitions from the ground state to $J' = \frac{9}{2}$ levels only for left-circular-polarized light and to $J' = \frac{5}{2}, \frac{7}{2}, \frac{9}{2}$ levels with right-circular-polarized light. The pronounced polarization dependence of the calculated spectrum for left- and right-circular-polarized radiation can be seen in Figure 5.

The dashed lines in Figure 5 describe the total absorption cross section for left- and right-circular-polarization. The cross section for right-circular-polarized light is much higher than for left-circular-polarized light. The solid line in Figure 5 is the difference between the two cross sections and defines circular dichroism.

Linear dichroism, defined as the difference of the cross section for x-linear and z-linear polarized light, gives complementary information about Gd^{3+}. The cross section for x-linear polarized light is half of the sum of cross sections for left- and right-circular polarized transitions while the cross section for z-linear polarized light, with selection rule $\Delta m = 0$, allows transitions to $J' = \frac{7}{2}, \frac{9}{2}$, but not to $J' = \frac{5}{2}$ levels. The resulting spectra are shown in Figure 6.

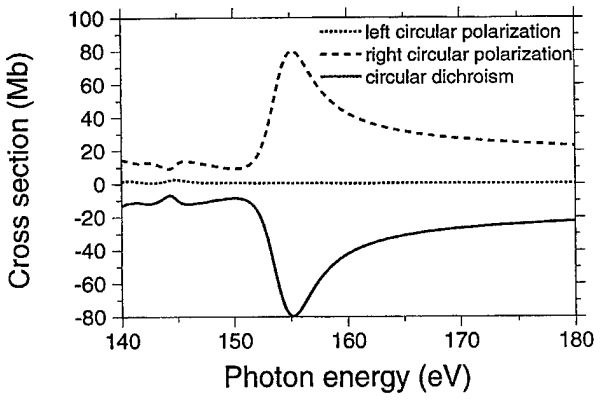


FIGURE 5. Total absorption cross section for left and right circular polarization (dashed lines), magnetic circular dichroism (solid line).

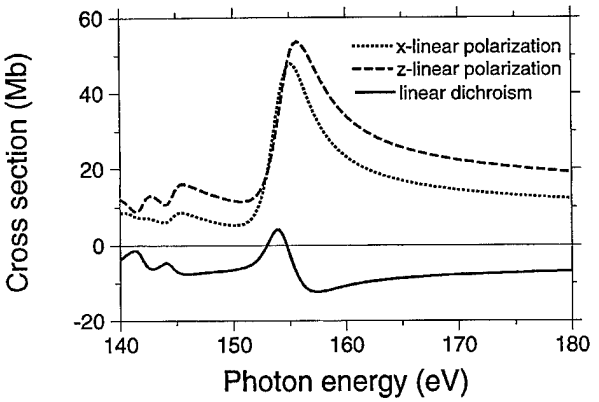


FIGURE 6. Total absorption cross section for x- and z-linear polarization (dashed lines), magnetic linear dichroism (solid line).

Conclusion

We have found from MCDF calculations that the giant resonance in the Gd^{3+} spectrum between 135 and 160 eV has multiplet structure. This structure is described by the spin-orbit splittings of the $4d^9 4f^8$ final configuration. Moreover, partial absorption asymmetric lines of different total angular momentum differ significantly. This allows the calculation of the dependence of the cross section on atomic and light polarization and thus the calculation of magnetic dichroism in Gd^{3+}.

Comparison of the theoretical and experimental results shows that we describe the resonance shape accurately, whereas the position of the resonance is obtained with a 4% accuracy. We believe that the distribution of the oscillator strengths will improve when additional correlation beyond CI with only the $4d^{10}4f^7$ and $4d^9 4f^8$ configurations is introduced.

The SPMCDF calculation of the absorption cross section in Gd^{3+} shows a strong dependence of the cross section on the polarization of light. The magnetic dichroism for the circular polarization is nearly maximal.

References

1. S. Kotochigova and I. Tupitsyn, Opt. Spectrosc. **60**, 4 (1986).
2. R. Haensel, P. Rabe, and B. Sonntag, Solid State Commun. **8**, 1845 (1970).
3. E. R. Radtke, J. Phys. B: At. Mol. Phys. **20**, L335 (1979).
4. W. Kohn and N. Rostoker, Phys. Rev. **94**, 1111 (1954).

5. D. D. Koelling and B. N. Harmon, J. Phys. C: Solid State Phys. **10**, 3106 (1977).
6. R. Feder, F. Rosicky, and B. Ackermann, Z. Phys. B–Cond. Mat. **52**, 31 (1983).
7. P. Strange, J. B. Staunton, and B. L. Gyorffy, J. Phys. C: Solid State Phys. **17**, 3355 (1984).
8. H. Ebert and R. Zeller, Phys. Rev. B **42**, 2744 (1990).
9. A. A. Ankudinov and J. J. Rehr, Phys. Rev. B **52**, 10214 (1995).
10. M. Richter, M. Mayer, M. Pahler, T. Prescher, E. V. Raven, B. Sonntag, and H.-E. Wetzel, Phys. Rev. A **40**, 7007 (1989).
11. O.-P. Sairanen and S. Aksela, J. Phys.: Cond. Mat. **4**, 3337 (1992).
12. J. P. Connerade, J. M. Esteva, and R. C. Karnatak, Eds., *Giant Resonances in Atoms, Molecules, and Solids* (Plenum, New York, 1987).
13. A. Zangwill, J. Phys. C: Solid State Phys. **20**, L627 (1988).
14. M. Ya. Amusia, S. I. Sheftel, and L. V. Chernysheva, Sov. Phys. Tech. Phys. **26**, 1444 (1981).
15. C. Pan, S. L. Carter, and H. P. Kelly, J. Phys. B: At. Mol. Phys. **20**, L335 (1987).
16. U. Fano, Phys. Rev. **124**, 1866 (1961).
17. F. H. Mies, Phys. Rev. **175**, 175 (1968).
18. H. A. Bethe and R. W. Jackiw, *Intermediate Quantum Mechanics*, 3rd ed (Benjamin, Menlopark, CA, 1986).
19. A. R. Barnett, D. H. Feng, J. W. Steed, and L. J. B. Goldfarb, Comput. Phys. Commun. **8**, 377 (1974).
20. P. Cortona, S. Doniach, and S. Sommers, Phys. Rev. A **31**, 2842 (1985).
21. S. Kotochigova, J. Opt. Soc. Am. B **9**, 1215 (1992).

Effective Potential for *e*-Atom Scattering by DCS Minimization at Intermediate Energies

JOSEPH M. PAIKEDAY
Southeast Missouri State University, Cape Girardeau, Missouri 63701

Received 3 March 1997; revised 7 August 1997; accepted 11 August 1997

ABSTRACT: The differential scattering cross section (DCS) for electrons scattered elastically by neon is studied using a model potential. The short-range part of the effective potential is represented by the Chebyshev approximation and the long-range polarization potential is represented by an energy-dependent function. The computed differential cross section obtained using the approximate effective interaction potential for electrons scattered by neon atoms in their ground state in the 50–100 eV energy range is compared with available published results. In the present study, a nonrelativistic Hartree–Fock wave function of the target atom is used to compute the short-range static part of the interaction potential and the parameters contained in the energy-dependent function are determined by the minimization of the DCS with respect to the angle and the incident energy. The resulting DCS in the angular range $2° < \Theta < 178°$ is found to be in good agreement with the available experimental and theoretical results in the intermediate energy range. © 1997 John Wiley & Sons, Inc. Int J Quant Chem **65:** 585–590, 1997

Introduction

The differential cross section of electrons scattered by atoms and selected molecules has been a topic of considerable interest as evidenced by a large number of experimental and theoretical work published over the last decade. The theoretical work has progressed mostly along the application of the *R*-matrix theory [1], while the semiempirical calculations based on the optical potential models [2] with or without adjustable parameters have increased over the last few years owing to their simplicity and the ease of computations leading to the differential scattering cross section (DCS) over a wide range of incident energy. In the present study, the model potential is based on the dipole polarizability α_d of the target atom and two parameters contained in the energy-dependent polarization potential determined by minimizing the DCS at the critical angle [3] with the condition that the computed integral cross section agrees with the experimental value of the integral cross section

Contract grant sponsor: Grants and Research Funding Committee of the Southeast Missouri State University.

© 1997 John Wiley & Sons, Inc.
CCC 0020-7608 / 97 / 050585-06

for two selected incident energies. The significance of the DCS minimum at the critical angle can be understood on the basis of the phenomenon of low-energy electron diffraction associated with the interaction between the incident electron and the atomic target. While the reported differential cross-section data for a given target atom varied from 5 to 13% depending on the incident energy, the integral cross section is known to have less uncertainty for most closed-shell atoms over the intermediate energy range. In the present study, the critical minima and the integral cross section of the computed DCS are shown to depend on the values of the parameters so that one can vary them to find the set that minimizes the DCS at the critical angle and corresponds to the correct integral cross section within the uncertainty of the experimental data. Using this set of parameters, the differential cross section for the target atom is computed over the energy range $20 < E < 500$ eV and the angular range $2° < \Theta < 180°$. The computed DCS are in good agreement with recently reported experimental and theoretical cross-section data for neon atoms over the intermediate energy range.

Approximation to the Effective Potential

The effective potential is constructed from the Hartree–Fock orbitals [4] of the target atom and is of the form given by

$$V_e = V_{ex}(r) + V_p(E, r) + (2Z/r)\sum_k \sum_n A_k P_n(r)\exp(-B_k r), \quad (1)$$

where $V_{ex}(r)$ and $V_p(E, r)$ are the exchange and polarization potentials, respectively, and the values of A_k and B_k ($k = 1, 2, \ldots, M$, $M < 10$) are determined from the Hartree–Fock wave function of the target atom. The approximate function representing the short-range part of the potential is then determined using the Chebyshev polynomials $T_n(x)$ given by

$$T_0(x) = 1, \quad T_1(x) = x, \quad T_2(x) = 2x^2 - 1. \quad (2a)$$

The higher-order functions can be generated with the recursion relation

$$T_{n+1}(x) = 2xT_n(x) - T_{n-1}(x). \quad (2b)$$

The coefficients C_j for the representation of the effective potential is computed from the following equation:

$$C_j = (2/N)\sum_k \mathrm{Log}_e\{(r_k/2Z)\langle\Phi_0|V(r_k)|\Phi_0\rangle\} \times T_{j-1}(x_k), \quad (2c)$$

where $x_k = \cos\{\pi(k - \frac{1}{2})/N\}$. The Chebyshev representation truncated to order M ($M < N$) is then given by ($k = 1$ to M in the sum)

$$V_0(r) = (2Z/r)\sum_n P_n(r)\exp\left\{\sum_k C_k T_{k-1}(r) - C_1/2\right\}. \quad (3)$$

In the approximating equation, several terms containing exponential and polynomial terms in the original function are reduced to fewer exponential terms of a sum of polynomials. This speeds up the DCS minimization code used in the present calculations. The operator $V(r_k)$ contained in the equation for C_j represents the Coulomb interaction between the incident electron and the target atom. In the present study, the Log(base e) of the original function is used due to its exponential variation for the Chebyshev representation using a value of $N = 30$ and the DCS is computed using the approximate function with $M = 9$. The exponential function is then used to reverse the basis representation of the Log of the original function for the computation of DCS. These coefficients are determined with the condition that the DCS computed from the original interaction agrees with the DCS obtained from the approximated potential within 1%. This has been found to be sufficiently accurate for the DCS minimization algorithm used in the present study.

Thus, the effective potential used in the present study is of the form

$$V_e(E, r) = V_{ex}(E, r) + V_p(E, r) + V_0(r). \quad (4)$$

Computation of Differential Cross Section

The effective interaction potential used in the present study is the sum of the short-range and the

energy-dependent long-range polarization terms given by

$$V(r) = \langle \Phi_0 | V_0(r, r_i) | \Phi_0 \rangle + \alpha_d / [r + f(A, B, E)]^4 + V_{ex}, \quad (5)$$

where Φ_0 is the ground-state Hartree–Fock [4] wave function of the target atom and V_0 contains the electron–electron and electron–nuclear potentials, α_d is the dipole polarizability of the target atom, and the parameters A and B contained in $f(A, B, E)$ are to be determined for the selected incident energy E (eV) of the electron. The form of the exchange potential V_{ex} is similar to the one used in an earlier calculation [5]. The differential scattering cross section $I(k, \Theta)$ is then computed from the scattering amplitude $f(k, \Theta)$ as a function of the wave number k and scattering angle Θ given by

$$f(k, \Theta) = (1/2ik) \sum_l (2l + 1) \times [\exp(2i\delta_l) - 1] P_l(\cos \Theta), \quad (6)$$

where the phase shifts δ_l are computed by solving the radial part of the Schrödinger equation for the angular momentum in the range $0 \leq l < 12$ using the Numerov algorithm [6] from which the zeros of the wave functions are used in the argument of Bessel and Neumann functions to compute the phase shifts accurate to four decimal places. For higher partial waves, the Born approximation is used for l in the range $11 < l < 30$ with a 32-point Gauss quadrature method for the numerical integration. The phase shifts for higher partial waves are computed using an analytical expression [7] for the phase shift in terms of integrals involving Bessel functions of fractional order for values of l up to 200. It has been found that for scattering angles $> 2°$ not more than 200 partial waves are needed for the DCS to converge to an accuracy of $\pm 0.1\%$. However, for angles less than 0.1°, it was found that more than 1000 partial waves were needed for convergence to the listed accuracy. All the computations were performed in double precision using an IBM4381. For scattering angles in the small-angle range, it was found that a faster algorithm was required to efficiently execute the minimization routine. For this, the electron–atom interaction was represented by a truncated least-square-fitted function containing fewer terms which substantially reduced the computing time of the forward scattering amplitude and the resulting integral cross section. For the higher partial waves, the approximation to the short-range interaction did not significantly affect the final results since the phase shifts depend mostly on the polarization potential. This enabled the determination of the approximate values of parameters A and B for helium and neon atoms that satisfy the specified conditions with a few minutes of computer time for each incident energy for a given target atom.

Discussion of Results

The variation of computed DCS with the parameters contained in the polarization potential $f(A, B, E)$ is shown in Figure 1. The plots numbered 1, 2, ... 6 are the DCS corresponding to the energy-dependent polarization potential with two parameters for an incident energy of 60 eV. For neon, the minimum of DCS occurs near 105° as seen in plot #1 and for smaller angles as the value of f is increased. The corresponding values of the computed integral cross section are shown in Table I. For the approximate determination of parameters A and B, the experimental values [8] of σ at 60 and 100 eV were used. Comparison of σ with other experimental values is shown in Figures 2

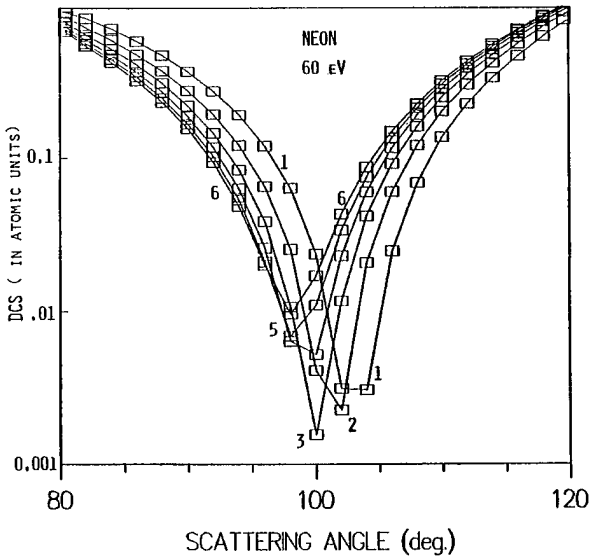


FIGURE 1. Plots numbered 1–6 showing the variation of computed DCS for e-neon scattering at 60 eV using the model potential for various values of $f(A, B, E)$ with $B = 0.00476$ and $A = 0.7$–1.5 in steps of 0.1 (DCS in units of a_0^2/ster).

TABLE I
Variation of integral cross section σ with $f(E)$ for neon at the incident energy E = 60 eV; experimental value[a] of $\sigma = 2.98 \pm 0.06$ (10^{-16} cm^2/ster).

Plot #	$f(E)$	σ
1	0.986	3.181
2	0.820	3.172
3	0.920	3.150
4	1.020	3.131
5	1.120	3.100
6	1.220	3.071

[a]Experimental data from [8].

and 3. The final values of A and B are determined by minimizing the DCS surface as shown in Figure 4 in the energy range $50 < E < 90$ eV and angular range $90 < \theta < 110°$. The contour plot shown in Figure 5 indicates that the critical values of the energy and angle are $E = 66$ eV and $\theta = 98°$. These are in good agreement with the experimental values of 65 eV and 101°, respectively. The values of the parameters are determined to be $A = 1.11$ and $B = 0.0036$. The computed values of σ for various incident energies are compared with the experimental values of Register et al. [8] and the R-matrix calculations of Fon et al. [1] as shown in Table II. The comparison between the present results and other theoretical and available experimental data is shown in Table III (50 eV) and Table IV (100 eV). The computed integral cross section for e-neon scattering for the incident energy of 30–200 eV and its comparison with experimental data are shown in Figure 2 and the computed differential cross sections at 100 eV compared with recent experimental and theoretical results for neon are shown in Figure 3.

The computed values of the DCS (open squares) are seen to be in good agreement with the experimental data and R-matrix calculations for scattering angles up to 140°. For larger angles, the model potential results seem to differ somewhat from the available theoretical data. For different target atoms, the present model calculations for the DCS are in good agreement with available published data except near the critical angles. It is possible that there is more uncertainty in the DCS near this region compared to those near the forward scattering angles. A more general function for $f(A, B, C, E)$ is being tested to determine the DCS near the critical angle for other atoms. The value of the computed critical angle has been found to be in good agreement with published data. The present model is being extended to argon, krypton, and xenon to determine the limitations of the effective interaction potential for the computation of the DCS in the intermediate energy range. In conclusion, the usefulness of the model potential used in the present study is for intermediate energies where a large number of partial waves are needed

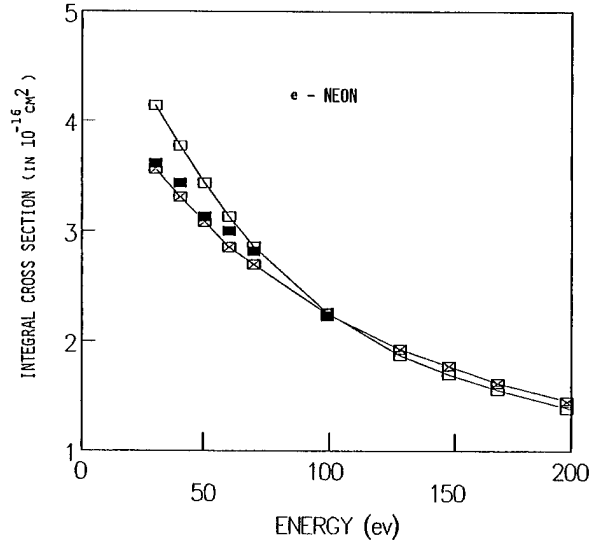


FIGURE 2. Comparison of the computed integral cross section for e-neon scattering for incident energy in the range 30–200: (□) results of this work; (■) experimental data; (⊠) R-matrix theory.

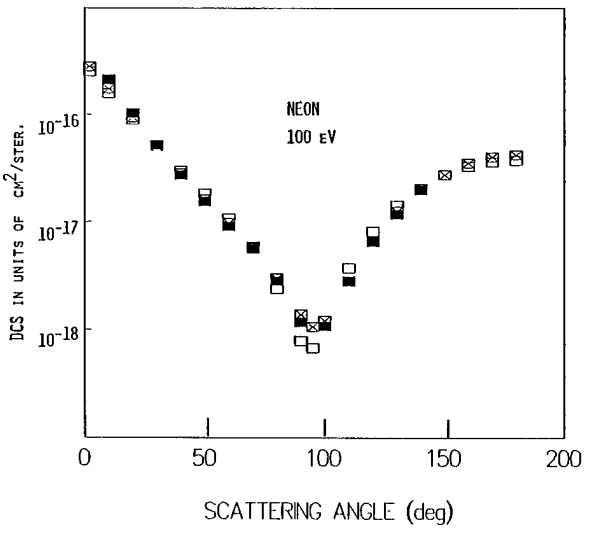


FIGURE 3. Comparison of the computed DCS (in units of cm^2/s) for e-neon scattering at an incident energy of 100 eV. Markers are same as in Figure 2.

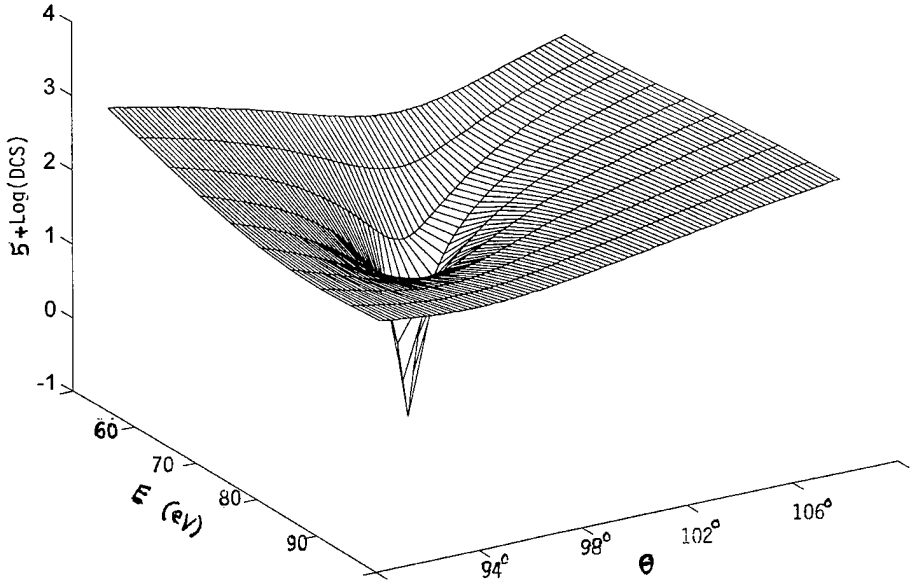


FIGURE 4. DCS surface (Log) for $50 < E < 80$ eV and $90 < \theta < 108°$ showing the minimum of DCS surface near $\theta = 98°$; $E = 66$ eV.

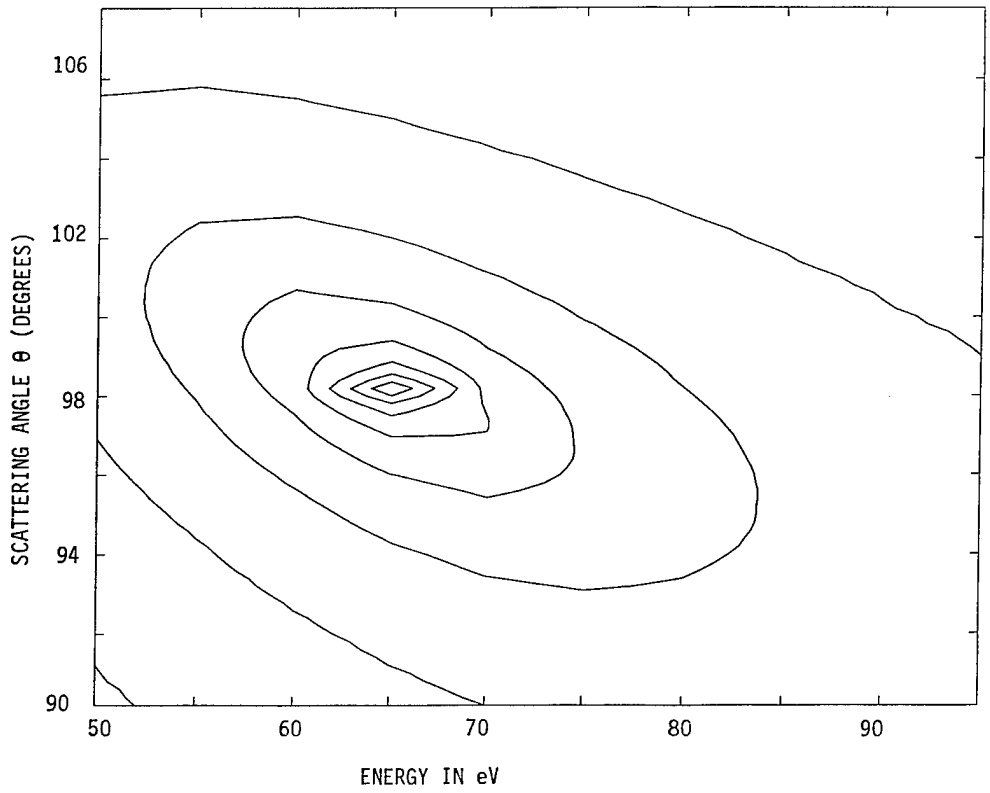


FIGURE 5. Contour plot corresponding to Figure 4.

TABLE II
Comparison of the computed cross section σ with experiment and *R*-matrix theory at various incident energies for neon atom; σ in units of (10^{-16} cm^2/ster).

E	σ^a	σ^b	σ^c
50	3.45	3.13	3.08
60	3.12	2.98	2.86
70	2.85	2.82	2.70
80	2.62	2.60	—
100	2.27	2.23	2.25
200	—		1.45

[a]Present results.
[b]Experimental values from [8].
[c]Theoretical values from [1].

TABLE III
Comparison of the differential cross section with experimental and other theoretical results for neon at 50 eV (units in a_0^2 / ster).

	Theory		Experiment
Angle Θ	Present	[9]	[8]
0	6.354	6.8582	
10	4.731	4.6057	
15	3.959	3.8401	4.182
20	3.329	3.1967	3.239
30	2.425	2.2424	2.100
40	1.838	1.6455	1.468
50	1.407	1.2717	1.139
60	1.031	0.9910	0.889
70	0.673	0.7209	0.643
80	0.352	0.4426	0.400
90	0.116	0.1919	0.168
100	0.016	0.0345	0.035
120	0.329	0.2424	0.268
140	1.193	1.1916	1.103
160	2.105	2.3315	
180	2.502	2.8406	

to obtain converged values of the DCS. For low energies, where a fewer number of partial waves will be sufficient for the convergence of the DCS, the close-coupling calculations have the advantage of being more accurate at all angles.

TABLE IV
Comparison of the differential cross section with experimental and other theoretical results for neon at 100 eV (units in a_0^2 / ster).

Angle Θ	Theory (Present)	Experiment [8]
10	6.515	7.605
20	3.630	3.699
30	1.969	1.843
40	1.104	0.968
50	0.661	0.553
60	0.405	0.324
70	0.228	0.199
80	0.105	0.100
90	0.042	0.042
100	0.051	0.039
120	0.299	0.229
140	0.758	0.700
160	1.195	
180	1.385	

ACKNOWLEDGMENT

The research was supported by grants received from the Grants and Research Funding Committee of the University.

References

1. W. C. Fon, K. A. Berrington, and A. Hibbert, J. Phys. B **14**, 323 (1981). R. P. McEachran and A. U. Stauffer, J. Phys. B **16**, 4023 (1983). A. Dasgupta and A. K. Bhatia, Phys. Rev. A **30**, 1241 (1984). H. P. Saha, Phys. Rev. A **39**, 5048 (1988).
2. W. Ihra and H. Friedrich, Phys. Rev. A **45**, 5278 (1992). D. Basu, S. K. Data, P. Kahn, and A. S. Ghosh, Phys. Rev. A **35**, 5255 (1987). A. W. Pangantiwar and R. Srivastava, Phys. Rev. A **40**, 2346 (1989). A. K. Jain and A. N. Tripathi, Phys. Rev. A **42**, 6912 (1990).
3. J. M. Wadehra, T. S. Stein, and W. E. Kauppila, Phys. Rev. A **29**, 2912 (1984).
4. C. F. Bunge and J. A. Barrientos, At. Data Nucl. Data Tab. **53**, 113 (1993). E. Clementi and C. Roetti, At. Data Nucl. Data Tab. **14**, 177 (1974).
5. R. Vanderporten, J. Phys. B **8**, 926 (1975). A. W. Pangantiwar and R. Srivastava, Phys. Rev. A **40**, 2346 (1989).
6. J. M. Paikeday, J. Chem. Phys. **65**, 397 (1976).
7. J. M. Paikeday, J. Chem. Phys. **65**, 397 (1976), Eqs. (3.14) and (3.15).
8. D. F. Register and S. Trajmar, Phys. Rev. A **29**, 1785 (1984). D. F. Register, S. Trajmar, and S. K. Srivastava, Phys. Rev. A **21**, 1134 (1980).
9. A. Dasgupta and A. K. Bhatia, Phys. Rev. A **30**, 1241 (1984).

Low-Energy Electron Scattering from a Model H_2 Potential Using Finite Elements in Two Dimensions

CHARLES A. WEATHERFORD, MEI DONG, BIDHAN C. SAHA

Physics Department, Florida A & M University, Tallahassee, Florida 32307

Received 3 March 1997; revised 11 July 1997; accepted 31 July 1997

ABSTRACT: The Schrödinger equation for the scattering of an electron by a hydrogen molecule is solved by the finite element method, in spherical coordinates, using fifth-order Hermite interpolating polynomials. The computational method is quite similar to the work of Shertzer and Botero [Phys. Rev. A **49**, 3673 (1994), and references therein]. However, to study large systems, an effective one-particle dynamical equation is defined, unlike the procedure of Shertzer and Botero. To illustrate the basic computational procedure, a model electron–H_2 interaction potential (static + exchange + polarization) is constructed and the K-matrix is calculated. A novel feature of the present method is the procedure for extracting the partial-wave amplitudes at a value of r, the size of which is fixed by the range of nonlocal potentials in the problem, and then propagating the scattering amplitudes out to an effective infinity where the converged K-matrix is determined. © 1997 John Wiley & Sons, Inc. Int J Quant Chem **65:** 591–600, 1997

Introduction

Low-energy electron–molecule scattering is a fundamental problem in molecular physics. An excellent review of the status of this field in 1980 can be found in the article by Lane [1]. An idea of the current status of the field can be obtained from a collection of articles appearing in a recent book [2]. In that book, a number of different methods are described for the solution of the low-energy electron–molecule scattering problem. As described in the article by Temkin and Weatherford [3], when the interaction is highly nonspherical, the use of angular momentum partial-waves is problematical in the region of close encounter between the electron and the molecule. At a large separation, partial-waves are more appropriate. Thus, Temkin and Weatherford, in a series of articles [4–7], described a solution method whereby the two-dimensional Schrödinger equation is directly discretized using finite differences. This was

Correspondence to: C. A. Weatherford.
Contract grant sponsor: Office of Naval Research.
Contract grant number: N00014-95-1-0614.
Contract grant sponsor: FAMU-Army High Performance Computing Research Center.
Contract grant number: DAAH04-95-C-0008.

© 1997 John Wiley & Sons, Inc.
CCC 0020-7608 / 97 / 050591-10

done within the context of time-independent scattering theory [1], and, thus, the partial differential equation was elliptic. They were considering electron–N_2 collisions where the cylindrical symmetry allows for the separation of the ϕ-variable, reducing the effective one-electron scattering equation to two coupled variables (r and θ). The scattering problem was solved in the frame of fixed nuclei (body frame). Thus, r describes the distance to the scattering electron and θ describes the angle of the scattering electron position vector with respect to the z axis (see Fig. 1).

In an independent development, Shertzer and co-workers [8–12] used the method of finite elements to discretize the Schrödinger equation for a number of important problems. In each case, they solved the Schrödinger equation explicitly as a few-body problem. The present work differs in that we are solving an effective one-body problem using finite elements in two dimensions (r, θ). This allows for the possibility of solving for the solution of electron scattering from much more complicated targets [1].

The K-matrix is a concise and computationally simple means of presenting the results of a scattering calculation using the method of partial differential equations. In the present work, the K-matrix is calculated for a model $e - H_2$ interaction potential, in spherical coordinates, which includes the static, exchange, and polarization potentials. The cylindrical symmetry is used to factor out the ϕ dependence, resulting in a two-dimensional elliptic partial differential equation. The scattering region is bounded by a quarter circle (see Fig. 1, where the scattering region is shown as a coordinate rectangle) at a value of $r = 10a_0$ where atomic units are used. The partial-wave amplitudes are extracted at that value of $r \equiv \rho$ and then the coupled ordinary differential scattering equations in r are propagated to an effective infinity where the K-matrix is determined [4,5].

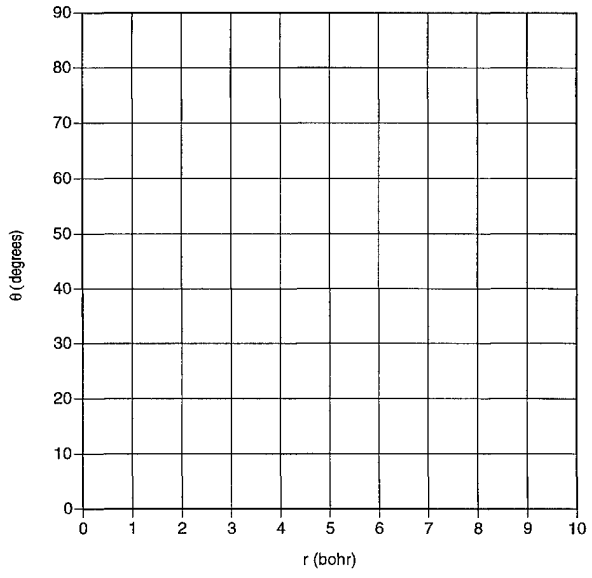


FIGURE 1. First quadrant of the $r - \theta$ plane deformed into a rectangle (PDE solution space).

In the next section, we describe the basic ideas of the finite element method that we are using. The third section describes the extraction of the partial-wave amplitudes and the propagation procedure. The fourth section describes the model H_2 potential. Finally, the fifth section gives the results and conclusions.

Finite Element Method

A short outline of the finite element method is presented below for the simple case of elastic scattering with local potentials—the generalization to inelastic multichannel scattering is straightforward but complicated: The time-independent Schrödinger equation for e^--molecule scattering using the fixed nuclei approximation (FNA) in 3D, using spherical coordinates (in atomic units), is

$$\left[\frac{\partial^2}{\partial r^2} + \frac{2}{r}\frac{\partial}{\partial r} + \frac{1}{r^2}\frac{\partial^2}{\partial \theta^2} + \frac{\cot\theta}{r^2}\frac{\partial}{\partial \theta} + \frac{1}{r^2 \sin^2\theta}\frac{\partial^2}{\partial \phi^2} + k^2\right]\Psi(r,\theta,\phi) = 2V(r,\theta,\phi)\Psi(r,\theta,\phi). \quad (1)$$

The homonuclear diatomic molecule is the simplest system for which nonspherical terms contribute to the scattering potential, so it will serve as the physical anchor for an otherwise computational study. When the energy of the incident electron is between 1 and 10 electron volts, the nonspherical structure of the molecule is particularly important. In such a situation, we use the axial symmetry of the molecule to reduce the Schrödinger equation to a two-dimensional partial differential equation. We assume for simplicity that the collision does not excite vibrational states of the molecule. Rotational excitations may be dealt with at the cross-section stage of the calculation in the usual adiabatic-nuclei manner [1].

The target molecule may be assumed to be oriented in a particular direction in space so we use the axis of symmetry of the molecule as the z-axis of our coordinate system (Fig. 2) and define a modified wave function ψ which is related to the true wave function Ψ for the projectile by

$$\Psi(r, \theta, \phi) = \psi^{(m)}(r, \theta)e^{im\phi}. \quad (2)$$

Note that we are using the nonreduced equation. The equation for $\psi^{(m)}(r, \theta)$ in atomic units is

$$\frac{\partial^2\psi^{(m)}}{\partial r^2} + \frac{2}{r}\frac{\partial\psi^{(m)}}{\partial r} + \frac{1}{r^2}\left\{cot(\theta)\frac{\partial\psi^{(m)}}{\partial\theta} + \frac{\partial^2\psi^{(m)}}{\partial\theta^2}\right\} + \left\{k^2 - 2V(r, \theta) - \frac{m^2}{r^2 sin(\theta)}\right\}\psi^{(m)} = 0, \quad (3)$$

where $V(r, \theta)$ is the scattering potential and k is the momentum of the projectile. A finite element approximation to this equation is solved on the domain $0 \le r \le \rho$, $0 \le \theta \le \pi/2$. The outer limit ρ is chosen to be sufficiently large that the scattered particle sees a nearly spherical potential at that distance and, for cases with a nonlocal potential, is greater than the range of the nonlocality. The range of θ was cut in half to take advantage of the symmetry of the molecule under reflections in the $x - y$ plane.

No radial boundary condition is set at $r = 0$. If we were solving the reduced equation, we would require that $\psi = 0$. We do set the derivative of ψ with respect to θ equal to zero at the origin ($\partial\psi/\partial\theta|_{r=0} = 0$). Even though we are solving an elliptic equation, which requires a specification of a boundary condition on all boundaries, we may avoid setting a boundary condition at individual points on the boundary as long as they are isolated. At $\theta = 0$, there are two possibilities: If m, the z-component of the orbital angular momentum, is nonzero, then $\psi = 0$; otherwise, $\partial\psi/\partial\theta = 0$. At $\theta = \pi/2$, the parity of the system dictates either that $u = 0$ or $\partial u/\partial\theta = 0$. At $r = \rho$, we impose the requirement that the incoming electron be in a state of well-defined orbital angular momentum, so that

$$\psi_l^{(m)}(\rho, \theta) = P_{lm}(cos\,\theta). \quad (4)$$

The parity of the associated Legendre function, $(-1)^{l+m}$, determines the choice of boundary condition at $\theta = \pi/2$. Although this parity is conserved by the scattered wave function, the value of l for the incident wave is not. Outgoing waves therefore contain a superposition of l, $l \pm 2$, $l \pm 4$, and so forth. The finite element discretization results in a matrix algebra problem:

$$\mathbf{A} \times \vec{X}_{lm} = \vec{B}_{lm}, \quad (5)$$

where $\mathbf{A}$ is the coefficient matrix; $\vec{X}_{lm}$, the solution vector at the grid points; and $\vec{B}_{lm}$, the vector of boundary values. Note that the solution and right-hand-sides are indexed by lm, the Legendre parameters from Eq. (4). Once the solution has been found, information about the scattering is extracted by matching it to the known asymptotic form [4] at $r_t < \rho$:

$$\psi_l^{(m)}(r_t, \theta) = \sum_{l'} P_{l'm}(cos\,\theta) \times \left[\frac{1}{r_t}S_{l'}(kr_t)J_{l'm,lm} + \frac{1}{r_t}C_{l'}(kr_t)N_{l'm,lm}\right] \quad (6)$$

and

$$\frac{\partial}{\partial r}\psi_l^{(m)}(r_t, \theta) = \sum_{l'} P_{l'm}(cos\,\theta) \times \left[\left(\frac{1}{r_t}\frac{\partial}{\partial r}S_{l'}(kr_t) - \frac{1}{r_t^2}S_{l'}(kr_t)\right)J_{l'm,lm} + \left(\frac{1}{r_t}\frac{\partial}{\partial r}C_{l'}(kr_t) - \frac{1}{r_t^2}C_{l'}(kr_t)\right)N_{l'm,lm}\right], \quad (7)$$

where l and m are the index and order of the Legendre function used in the boundary condition at large $r \equiv \rho$, and S and C are related to spherical

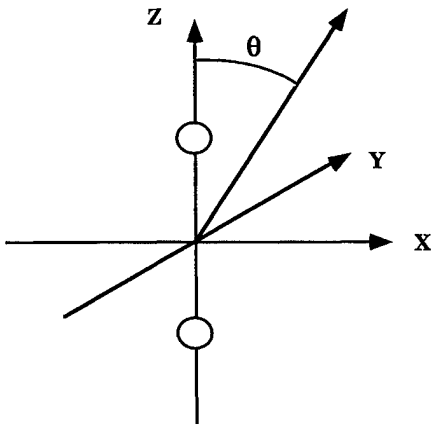


FIGURE 2. Spherical coordinate system for scattering from a diatomic molecule.

Bessel functions by $S_l = k^{1/2} r j_l$ and $C_l = -k^{1/2} r n_l$. Thus, j_l and n_l are the regular and irregular spherical Bessel function [13]. The coefficients **J** and **N** form matrices on the space of allowed values of orbital angular momentum. Note that **J** and **N** are diagonal in m because of the cylindrical symmetry. The validity of Eq. (7) can be established because of the Wronskian relation $S_l C_l' - S_l' C_l = -1$ (where the prime indicates differentiation with respect to r) and Leibnitz's rule with respect to the parametric differentiation of an integral. This latter point concerning parametric differentiation is a somewhat subtle point that is explainable only when viewed in light of the noniterative integral equation (NIEM) solution method [14,15]. We will not elaborate on the point now, but only say that it is well established [16].

The orthogonality of the Legendre functions may be used to project out a particular value of l. When this is done, the linear independence of the Bessel functions allows extraction of the unknown coefficients **J** and **N** from Eqs. (6) and (7) by a matrix inversion. This process must be done for each allowed value of l, e.g., each right-hand side of Eq. (5). However, the matrix **A** does not have to be redetermined since it is independent of the ρ boundary condition. The result is two matrices describing the transformation of an angular momentum eigenstate into a scattered wave. In principle, the dimension of the matrices is infinite, but, in practice, the finite range of the nonspherical potentials provides a cutoff. For an H_2 molecule, with a projectile energy below 10 eV, values of l less than 5 are all that are required. Hence, the matrices are at most 3×3. The K-matrix is defined by the equation

$$\psi_l^{(m)}(r, \theta) = \frac{1}{r} \sum_{l'} [S_{l'}(kr) + C_{l'}(kr) K_{l'l}] P_{l'm}(\cos\theta), \quad (8)$$

so $\mathbf{K} = \mathbf{N}\mathbf{J}^{-1}$, and the influence of the artificial imposition of an initial orbital state is removed. The diagonal elements of K are the tangents of the elastic-phase shifts, and the off-diagonal elements describe the coupling of states of different orbital angular momentum by the potential.

The method of finite elements is well described in [9,17] and references therein. We will give a short outline of the procedure. The procedure is

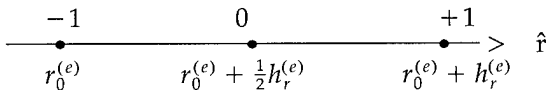
1. Divide solution space into nonoverlapping domains called "finite elements."
2. Define local basis functions within each element—in the present case, fifth-order Hermite polynomials.
3. Discretize in each element by the Galerkin method and implicitly form a global element matrix.
4. Form a global connected matrix by enforcing continuity of the solution and its derivatives across element boundaries.
5. Form a boundary reduced connected matrix and boundary vector; **A**; $\vec{B} \ni$

$$\mathbf{A}\vec{X} = \vec{B}. \quad (9)$$

6. Solve simultaneous equations by lower-upper factorization (LU) decomposition [17,18]:

$$\vec{X} = \mathbf{A}^{-1}\vec{\mathbf{B}}. \quad (10)$$

The method of Hermite interpolation is used [9]:



In terms of local variables x_i: $\{-1, 0, +1\}_{i=1}^{3}$,

$$\psi^{(e)}(x) = \sum_{i=1}^{6} \psi_i^{(e)} p_i(x), \quad (11)$$

where

$$\begin{bmatrix} \psi_1^{(e)} \\ \psi_2^{(e)} \\ \psi_3^{(e)} \\ \psi_4^{(e)} \\ \psi_5^{(e)} \\ \psi_6^{(e)} \end{bmatrix} = \begin{bmatrix} \psi^{(e)}(x_1) \\ \frac{\partial}{\partial x}\psi^{(e)}|_{x_1} \\ \psi^{(e)}(x_2) \\ \frac{\partial}{\partial x}\psi^{(e)}|_{x_2} \\ \psi^{(e)}(x_3) \\ \frac{\partial}{\partial x}\psi^{(e)}|_{x_3} \end{bmatrix} \quad (12)$$

and $p_i(x)$ is determined from

$$p_i(x) = \sum_{j=1}^{6} g_{ij} x^{j-1} \quad (13)$$

$$p_i(x_j) = \delta_{ij} \quad \text{for } i = 1,3,5 \quad \text{and} \quad j \in \{x_1, x_2, x_3\} \quad (14)$$

$$\frac{d}{dx}p_i(x)|_{x_j} = \delta_{ij} \quad \text{for } i = 2,4,6 \quad \text{and} \quad j \in \{x_1, x_2, x_3\}. \tag{15}$$

Let us write Eqs. (13) and (14) explicitly:

$$p_1(x) = g_{11} + g_{12}x + g_{13}x^2 + g_{14}x^3 + g_{15}x^4 + g_{16}x^5$$

$$\frac{d}{dx}p_2(x) = g_{22} + 2g_{23}x + 3g_{24}x^2 + 4g_{25}x^3 + 5g_{26}x^4$$

$$p_3(x) = g_{31} + g_{32}x + g_{33}x^2 + g_{34}x^3 + g_{35}x^4 + g_{36}x^5$$

$$\frac{d}{dx}p_4(x) = g_{42} + 2g_{43}x + 3g_{44}x^2 + 4g_{45}x^3 + 5g_{46}x^4$$

$$p_5(x) = g_{51} + g_{52}x + g_{53}x^2 + g_{54}x^3 + g_{55}x^4 + g_{56}x^5$$

$$\frac{d}{dx}p_6(x) = g_{62} + 2g_{63}x + 3g_{64}x^2 + 4g_{65}x^3 + 5g_{66}x^4.$$

We now implement conditions (14) and (15) and construct a matrix equation to be solved for g_{ij}:

$$\begin{bmatrix} g_{11} & g_{12} & g_{13} & g_{14} & g_{15} & g_{16} \\ g_{21} & g_{22} & g_{23} & g_{24} & g_{25} & g_{26} \\ g_{31} & g_{32} & g_{33} & g_{34} & g_{35} & g_{36} \\ g_{41} & g_{42} & g_{43} & g_{44} & g_{45} & g_{46} \\ g_{51} & g_{52} & g_{53} & g_{54} & g_{55} & g_{56} \\ g_{61} & g_{62} & g_{63} & g_{64} & g_{65} & g_{6t} \end{bmatrix} \times \begin{bmatrix} 1 & 0 & 1 & 0 & 1 & 0 \\ -1 & 1 & 0 & 1 & 1 & 1 \\ 1 & -2 & 0 & 0 & 1 & 2 \\ -1 & 3 & 0 & 0 & 1 & 3 \\ 1 & -4 & 0 & 0 & 1 & 4 \\ -1 & 5 & 0 & 0 & 1 & 5 \end{bmatrix} = \vec{1}. \tag{16}$$

The expression for $\psi^{(e)}$ in terms of global variables can now be written using

$$r = r_0^{(e)} + h_r^{(e)}\frac{(1+x)}{2}$$

$$x = -1 + \frac{2}{h_r^{(e)}}\left[r - r_0^{(e)}\right]. \tag{17}$$

To go to a global representation of (11), $\psi^{(e)}(r)$, it is not necessary to let $x \to r$ in $p_i(x)$. The global operators can be transformed to local operators which operate only on the piecewise continuous polynomials within each element:

$$\frac{d}{dr} = \frac{dx}{dr}\frac{d}{dx} = \frac{2}{h_r^{(e)}}\frac{d}{dx} \tag{18}$$

$$\frac{d^2}{dr^2} = \left[\frac{2}{h_r^{(e)}}\right]^2\frac{d^2}{dx^2}. \tag{19}$$

So, we can simply say that

$$\Psi^{(e)}(r) = \sum_{i=1}^{6}\psi_i^{(e)}p_i(x). \tag{20}$$

However, the problem with (17) is that $\psi_i^{(e)}$, for $i = 2,4,6$, represents derivatives of $\Psi^{(e)}(r)$ with respect to the local variable x and we need it to represent derivatives with respect to the global variable r:

$$\frac{\partial\psi^{(e)}(x)}{\partial x} = \frac{\partial r}{\partial x}\frac{\partial\psi^{(e)}(r)}{\partial r} = \frac{1}{2}h_r^{(e)}\frac{\partial\psi^{(e)}(r)}{\partial r}. \tag{21}$$

Thus,

$$\Psi^{(e)}(r) = \sum_{i=1,3,5}\psi_i^{(e)}p_i(x) + \sum_{i=2,4,6}\frac{1}{2}h_r^{(e)}\frac{\partial\psi^{(e)}(r)}{\partial r}p_i(x). \tag{22}$$

Let us now write

$$\Psi^{(e)}(r) = \sum_{i=1}^{6}\Psi_i^{(e)}P_i^{(e)}(x), \tag{23}$$

such that

$$\Psi_i^{(e)} = \begin{Bmatrix} \psi_i^{(e)} \\ \text{for } i = 1,3,5 \\ \left.\dfrac{\partial\psi^{(e)}(r)}{\partial r}\right|_{r_i = r_0^{(e)} + h_r^{(e)}\frac{(1+x_i)}{2}} \\ \text{for } i = 2,4,6 \end{Bmatrix} \tag{24}$$

and

$$P_i^{(e)}(x) = \begin{Bmatrix} p_i(x) & \text{for } i = 1,3,5 \\ h_r^{(e)}p_i(x) & \text{for } i = 2,4,6 \end{Bmatrix}. \tag{25}$$

Thus, the solution and its derivatives [see Eq. (12)] are extracted at each grid point in the solution space.

Partial-wave Amplitude Extraction and Propagation Procedure

The matrices **J** and **N** can be obtained from Eqs. (6) and (7), at $r = r_t$, as follows:

$$\begin{bmatrix} \mathbf{J}^{(m)}(r_t) \\ \mathbf{N}^{(m)}(r_t) \end{bmatrix} = \begin{bmatrix} \left[\frac{1}{r_t}\vec{\mathbf{S}}(r_t)\right] & \left[\frac{1}{r_t}\vec{\mathbf{C}}(r_t)\right] \\ \left[\frac{1}{r_t}\vec{\mathbf{S}}'(r_t) - \frac{1}{r_t^2}\vec{\mathbf{S}}(r_t)\right] & \left[\frac{1}{r_t}\vec{\mathbf{C}}(r_t) - \frac{1}{r_t^2}\vec{\mathbf{C}}(r_t)\right] \end{bmatrix}^{-1} \times \begin{bmatrix} \mathbf{F}^{(m)}(r_t) \\ \mathbf{F}'^{(m)}(r_t) \end{bmatrix}. \quad (26)$$

Note that the prime indicates differentiation with respect to r. Also, $\vec{\mathbf{S}}$ and $\vec{\mathbf{C}}$ indicate diagonal matrices. Note that the **F** and **F**′ are the terms within the large square brackets of Eqs. (6) and (7). Rewriting Eqs. (6) and (7) in terms of F and using the prime to indicate differentiation with respect to r (except when used on l'),

$$\psi_l^{(m)}(r_t, \theta) = \sum_{l'} P_{l'm}(\cos\theta) F_{l'l}^{(m)}(r_t) \quad (27)$$

$$\psi'^{(m)}_l(r_t, \theta) = \sum_{l'} P_{l'm}(\cos\theta) F'^{(m)}_{l'l}(r_t). \quad (28)$$

Then, using the orthogonality of the Legendre polynomials,

$$F_{l'l}^{(m)}(r_t) = \frac{(l'-m)!(l'+1/2)}{(l'+m)!}2 \times \int_0^{\pi/2} \sin(\theta)\, d\theta\, P_{l'm}(\cos\theta)\psi_l^{(m)}(r_t, \theta) \quad (29)$$

$$F'^{(m)}_{l'l}(r_t) = \frac{(l'-m)!(l'+1/2)}{(l'+m)!}2 \times \int_0^{\pi/2} \sin(\theta)\, d\theta\, P_{l'm}(\cos\theta)\psi_l'^{(m)}(r_t, \theta). \quad (30)$$

Let us drop the m label and switch to the reduced function f defined by $\mathbf{f} = r\mathbf{F}$. Let us also drop the l and l' label and switch to i and j. We thus have the matrix of partial-wave continuum orbitals **f** at $r = r_t$. Thus, from [14–16], we may write

$$\mathbf{f}(r) = \vec{\mathbf{S}}(r)\mathbf{J}(r) + \vec{\mathbf{C}}(r)\mathbf{N}(r), \quad (31)$$

where

$$J_{ij}(r) = \delta_{ij} + 2\int_0^r dx\, C_i(x) R_{ij}(x) \quad (32a)$$

$$N_{ij}(r) = 2\int_0^r dx\, S_i(x) R_{ij}(x), \quad (32b)$$

where

$$R_{ij}(r) = \sum_k V_{ik}(x) f_{ik}(x). \quad (33)$$

We are working with the unnormalized solution in the sense defined in [14]. Then, by using a trapezoidal integration rule with step size Δr, it can be shown that [16]

$$\mathbf{I}(r_i) = \mathbf{P}(r_i)\mathbf{I}(r_{i-1}), \quad (34)$$

where

$$\mathbf{I}(r) = \begin{bmatrix} \mathbf{J}(r) \\ \mathbf{N}(r) \end{bmatrix} \quad (35)$$

and

$$\mathbf{P}(r) = \vec{\mathbf{1}} + \Delta r\, \mathbf{M}(r) \quad (36)$$

and

$$\mathbf{M}(r) = 2\begin{bmatrix} +\vec{\mathbf{C}}(r)\mathbf{V}(r)\vec{\mathbf{S}}(r) & +\vec{\mathbf{C}}(r)\mathbf{V}(r)\vec{\mathbf{C}}(r) \\ -\vec{\mathbf{S}}(r)\mathbf{V}(r)\vec{\mathbf{S}}(r) & -\mathbf{S}(r)\mathbf{V}(r)\vec{\mathbf{C}}(r) \end{bmatrix}. \quad (37)$$

Thus, we may form

$$\mathbf{I}(r_\infty) = \mathbf{P} \times \mathbf{I}(r_i), \quad (38)$$

where, if $r_i = r_0$, the origin, then

$$\mathbf{I}(r_0) \equiv \begin{bmatrix} 1 \\ 0 \end{bmatrix}. \quad (39)$$

Otherwise, the value of $\mathbf{I}(r_i)$ is picked up from the partial differential equation (PDE) calculation and constructed using Eq. (35). Thus, we may propagate from the surface of the PDE sphere, out to an

approximate infinity. This is what we do in the present work. Thus,

$$\mathbf{P} = \mathbf{P}(r_f) \times \mathbf{P}(r_{[f-1]}) \times \cdots \times \mathbf{P}(r_i) \qquad (40)$$

and $\mathbf{P}(r_f) \equiv \mathbf{P}(r_\infty)$. Then,

$$\mathbf{K}(r_\infty) = \mathbf{N}(r_\infty) \times \mathbf{J}^{-1}(r_\infty). \qquad (41)$$

All the scattering information is contained in $\mathbf{K}(r_\infty)$. It is a real, symmetric matrix.

It should be pointed out that his propagation procedure is very similar to the procedure of the NIEM [14]. The NIEM propagated **f** instead of **I** and thus required unnecessary matrix multiplications. Therefore, this propagation is a very general solution algorithm and, in principle, could be used all the way into the origin. For the present problem under consideration, this works fine and is, in fact, used to check the accuracy of the results. For more general problems with highly nonspherical potentials, accuracy is lost because of the large number of partial-waves required near the origin and because of the large magnitude of the irregular spherical Bessel function $n_l(r)$ near the origin as compared with the regular spherical spherical Bessel function $j_l(r)$. We have therefore defined a computational procedure similar to the *R*-matrix method [19]. The difference is that we are breaking the *R*-matrix sphere up into elements and spanning each element with Hermite interpolating polynomials instead of basis function spanning the entire *R*-matrix sphere.

The Potentials

The potential energy function V in Eq. (3) represents the interaction of the projectile with the target molecule and is the source of the breaking of spherical symmetry. In principle, this interaction is highly complicated. A molecule is by no means a static, rigid body in the presence of an incoming electron, so a potential model is not strictly correct, but the practical usefulness of potentials in calculations is great enough to excuse the gross simplification of the scattering problem that they imply. The potentials involved in scattering from hydrogen molecules are approximations to three effects: the static electric moments of the molecule; the polarization of the molecule by the electric field of the projectile; and the substitution of an electron from the molecule for the projectile in the outgoing state, known as "exchange." An H_2 model was adopted in the present work, which mimics to some extent, the radial structure of the physical potentials and has angular properties which are expandable in the low-order Legendre polynomials of even parity. Actually, only three polynomials are needed because the potential, constructed below, contains only $l = 0, 2, 4$.

Because the hydrogen molecule is composed of identical atoms, the lowest-order multipole field seen by the projectile is the quadrupole term

$$V_Q(r, \theta) = \frac{q}{r^3} P_2(\cos\theta), \qquad (42)$$

where $Q = 0.49$ in atomic units. This form is valid for vales of r which are outside the molecule for all θ. At shorter ranges, the quadrupole potential is cut off by the usual exponential term $(1 - exp[-(r/a)^6])$ as a multiplier. The adjustable parameter a is set to 1, since no effort is made in the present work to fit experimental data. The static potential inside the molecule is represented by a Yukawa function of unit range and arbitrary strength, which is adjusted as necessary to give the correct order of magnitude for the *K*-matrix.

Polarization of the target is well known to include terms of both spherical and P_2 character [1]. The form used here is

$$V_p(r, \theta) = \frac{1}{2r^4}(1 - e^{(-r^6)})[a_0 + a_2 P_2(\cos\theta)], \qquad (43)$$

with $a_0 = 5.5$, and $a_2 = 1.4$.

The exchange potential used here is a crude form of the free-electron gas model. The basic idea here is that the electron in the target may be approximated by a degenerate Fermi gas whose density varies with position [1]. The exchange potential is proportional to the Fermi momentum at any point in space, giving

$$V_\chi(\vec{r}) = -\left(\frac{3}{2\pi}\right)[3\pi^2\beta(\vec{r})]. \qquad (44)$$

The electron density $\beta(\vec{r})$ is approximated by a simple sum,

$$\beta(r, \theta) = \frac{1}{4\pi} e^{-r}[1 + 1.3P_2(\cos\theta)], \qquad (45)$$

which has contours of constant density which resemble those of the sum of two hydrogen atoms

separated by 0.7 angstroms. The resulting potential can be approximated by a linear combination of Legendre polynomials, which is

$$V_\chi(r,\theta) = -0.8e^{-r/3}[0.97 + 0.43P_2(\cos\theta) + 0.1P_4(\cos\theta)]. \quad (46)$$

The "realistic" potential is a sum of these three terms.

The long-range quadrupole potential is the most important term in real scattering problems, but it does not vanish until a distance of 14 bohr radii from the molecule's center is reached. This was determined a posteriori, by searching for a region in which the K-matrix does depend on small changes in r_{max}. Such a long range requires a large number of radial points and, consequently, a long running time for the computer code. Although the convergence properties of the angular approximation are roughly independent of the quality of the radial approximation, this independence is valid only when the radial mesh is on the order of magnitude of the mesh which gives decent radial convergence. The P_2 terms in the polarization and exchange potentials are, in any case, expected to yield the same requirements on the angular mesh.

Results and Conclusions

Convergence of the K-matrix is determined in two way: The first takes advantage of the invariance of the K-matrix under time reversal to require that the K-matrix be symmetric. The second is that the value of an element of the of the K-matrix change with changes in the number of θ points in a manner which points clearly to an asymptotic limit. Now, in the present calculation, the radius of the PDE solution region was set at 10 bohr. The partial-wave amplitudes were extracted at the first grid point of the last element whose last grid point is ρ. The solution was then propagated to 70 bohr where the K-matrix was determined.

The matrices are not strictly symmetrical. When the scattering potential is spherical, the wave function should have the angular properties of the large-r boundary condition, all the way to the origin. This is true only when the boundary condition is for $l = 0$. When higher waves are used, each contains a contaminant of lower l values. This contamination decreases with each step in r away from the origin.

The second criterion makes an accurate graphical depiction of the convergence difficult. The convergence of almost all elements is monotonic, so the choice of a specific limit is arbitrary, yet it has a great impact on the perceived quality of the convergence. A systematic study of the convergence has not been done as a part of the present work. We set grid parameters which ensured accuracy to at least five significant figure in all of the K-matrix elements for $k = .1$, .5, and 1.0 au. The PDE r-grid used $\Delta r = 0.1$ bohr. The PDE θ-grid used $\Delta\theta = 10°$. The propagation step size was $\Delta r = 0.01$ bohr. The PDE (with propagation from 10 to 70 bohr) results are displayed in Tables I–III. The answers were checked by the propagation algorithm starting at the origin and going out to 70 bohr again using $\Delta r = 0.01$ bohr. The propagation algorithm actually produced K-matrix accuracy to 12 significant figures. All calculations were done using 64-bit arithmetic. Table IV shows the converged ($\rho = 70$ bohr) K-matrices as a function of the incident electron moment (k).

Figure 3, as well as the Σ_u contribution, compares the present Σ_g elastic cross sections, calcu-

TABLE I

***K*-matrix elements for $k = 0.1$ au in Σ_g symmetry; ρ is the value, in units of bohr, of r where the *K*-matrix was determined symmetric to the number of figures indicated.**

	$k = 0.1$ au					
ρ	$K(1,1)$	$K(1,2)$	$K(1,3)$	$K(2,2)$	$K(2,3)$	$K(3,3)$
10	−.39023E + 1	−.18534E + 0	−.43518E − 2	−.41619E − 2	−.10151E − 3	.47213E − 4
30	−.10282E + 1	−.71393E − 1	−.22522E − 2	.36462E − 1	.14096E − 2	.24640E − 2
50	−.10267E + 1	−.72195E − 1	−.22252E − 2	.36821E − 1	.98354E − 3	.24326E − 2
70	−.10267E + 1	−.72271E − 1	−.22363E − 2	.36769E − 1	.96741E − 3	.22941E − 2

TABLE II
Same as Table I except for k = 0.5 au.

	k = 0.5 au					
ρ	$K(1,1)$	$K(1,2)$	$K(1,3)$	$K(2,2)$	$K(2,3)$	$K(3,3)$
10	.25061E + 1	.61816E + 0	.77306E − 1	.16084E + 1	.23790E + 0	.63817E + 0
30	.34973E + 1	.10642E + 1	.12152E + 0	.21885E + 1	.30192E + 0	.76876E + 0
50	.34979E + 1	.10645E + 1	.12158E + 0	.21890E + 1	.30203E + 0	.76885E + 0
70	.34978E + 1	.10645E + 1	.12158E + 0	.21889E + 1	.30203E + 0	.76883E + 0

lated using [1]

$$\sigma = \frac{4\pi}{k^2} \sum_{l,l'} |T_{l,l'}|^2, \tag{47}$$

where

$$\mathbf{T} = \mathbf{1} - (\mathbf{1} + i\mathbf{K})(\mathbf{1} - i\mathbf{K})^{-1}, \tag{48}$$

and the total elastic cross-section calculation of Jain and Baluja [20] as well as the total experimental cross section of Hoffman et al. [21] It must be emphasized that the present calculation employs a model $e^- - H_2$ potential and, thus, the interesting agreement with the experimental results of Hoffman et al. is fortuitous. These results simply indicate that the model for the interaction potential has a realistic aspect to it.

The finite element method has been shown to be an effective numerical method for the solution of the time-independent electron–molecule scattering problem. The next step is to generalize to nonlocal potentials and coupled equations in order to treat real molecular targets realistically.

TABLE III
Same as Table I except for k = 1.0 au.

	k = 1.0 au					
ρ	$K(1,1)$	$K(1,2)$	$K(1,3)$	$K(2,2)$	$K(2,3)$	$K(3,3)$
10	.67237E + 0	.11579E + 0	.85839E − 2	.92080E + 0	.11500E + 0	.72282E + 0
30	.72882E + 0	.12633E + 0	.81894E − 2	.10158E + 1	.12908E + 0	.80166E + 0
50	.72888E + 0	.12632E + 0	.81858E − 2	.10159E + 1	.12908E + 0	.80172E + 0
70	.72887E + 0	.12632E + 0	.81852E − 2	.10159E + 1	.12908E + 0	.80171E + 0

TABLE IV
Converged K-matrix elements (ρ = 70 bohr) in Σ_g symmetry.

k	$K(1,1)$	$K(1,2)$	$K(1,3)$	$K(2,2)$	$K(2,3)$	$K(3,3)$
0.10	−.10267E + 1	−.72271E − 1	−.22363E − 2	.36769E − 1	.96741E − 3	.22941E − 2
0.25	−.3530E + 1	−.88189E + 0	−.68481E − 1	.79764E + 0	.80772E − 1	.19074E + 0
0.50	.34978E + 1	.10645E + 1	.12158E + 0	.21889E + 1	.30203E + 0	.76883E + 0
0.75	.12721E + 1	.27909E + 0	.26470E − 1	.14367E + 1	.20023E + 0	.88056E + 0
1.00	.72887E + 0	.12632E + 0	.81852E − 2	.10159E + 1	.12908E + 0	.80171E + 0
1.25	.45211E + 0	.67314E − 1	.26203E − 2	.75040E + 0	.86545E − 1	.68998E + 0
1.50	.27464E + 0	.36056E − 1	.52522E − 3	.56448E + 0	.59900E − 1	.58408E + 0
1.75	.15123E + 0	.15902E − 1	−.45278E − 3	.42410E + 0	.41872E − 1	.49046E + 0
2.00	.65783E − 1	.13066E − 2	−.10867E − 2	.31309E + 0	.28755E − 1	.40838E + 0
2.25	.11581E − 1	−.96914E − 2	−.16741E − 2	.22331E + 0	.18616E − 1	.33608E + 0
2.50	−.15535E − 1	−.17612E − 1	−.23247E − 2	.15070E + 0	.10418E − 1	.27204E + 0
2.75	−.20396E − 1	−.22432E − 1	−.30457E − 2	.93306E − 1	.36233E − 2	.21529E + 0
3.00	−.95865E − 2	−.24141E − 1	−.37803E − 2	.50201E − 1	−.20086E − 2	.16531E + 0

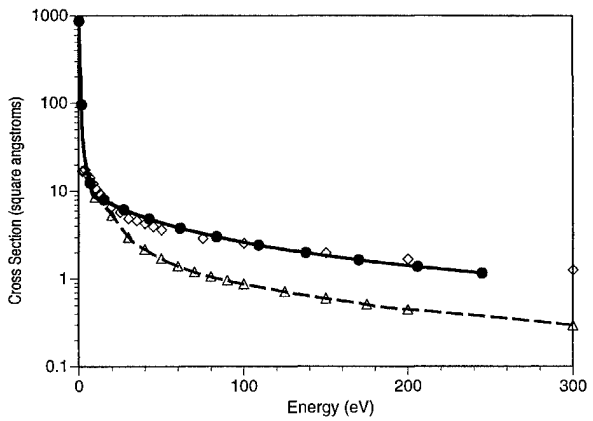


FIGURE 3. Cross section (●●●) present elastic $\Sigma_g + \Sigma_u$ cross section for H_2 model potential; (△ △ △) calculation of elastic cross section (Jain and Baluja [20]); (◇◇◇) experimental total cross section (Hoffman et al. [21]).

ACKNOWLEDGMENTS

This work was supported in part by the Office of Naval Research Contract N00014-95-1-0614 and by the FAMU-Army High Performance Computing Research Center under the auspices of the Department of the Army, Army Research Laboratory Cooperative Agreement DAAH04-95-2-0003/Contract Number DAAH04-95-C-0008, the content of which does not necessarily reflect the position or policy of the United States Army.

References

1. N. F. Lane, Rev. Mod. Phys. **52**, 29 (1980).
2. Computational Methods for Electron–Molecule Collisions, W. M. Huo and F. A. Gianturco, Eds., (Plenum, New York, 1995).
3. A. Temkin and C. A. Weatherford, in *Computational Methods for Electron–Molecule Collisions*, W. M. Huo and F. A. Gianturco, Eds. (Plenum, New York, 1995), p. 191.
4. C. A. Weatherford, K. Onda, and A. Temkin, Phys. Rev. A **31**, 3620 (1985).
5. C. A. Weatherford, F. B. Brown, and A. Temkin, Phys. Rev. A **35**, 4561 (1987).
6. A. Temkin, C. A. Weatherford, and E. C. Sullivan, in *Proceedings of the Sixteenth International Conference on the Physics of Electronic and Atomic Collisions*, New York, A. Herzenberg, Ed. (1989), (Invited Papers).
7. C. A. Weatherford and A. Temkin, Phys. Rev. A **49**, 2580 (1994).
8. F. S. Levin and J. Shertzer, Phys. Rev. A **32**, 3285 (1985).
9. L. R. Ram-Mohan, S. Saigal, D. Dossa, and J. Shertzer, Comp. Phys. **Jan / Feb**, 50 (1990).
10. T. C. Scott. J. Shertzer, and R. A. Moore, Phys. Rev. A **45**, 4393 (1992).
11. J. Shertzer and J. Botero, Phys. Rev. A **49**, 3673 (1994).
12. J. Ackermann, J. Shertzer, and P. Schmelcher, Phys. Rev. Lett. **78**, 199 (1997).
13. M. Abramowitz and I. Stegun, *Handbook of Mathematical Functions*, Dover, New York, 1970.
14. E. R. Smith and R. J. W. Henry, Phys. Rev. **55**, 442 (1977).
15. C. A. Weatherford and R. J. W. Henry, Can. J. Phys. A **7**, 1585 (1973).
16. C. A. Weatherford, in *Contributions in Mathematics and Natural Sciences*, H. W. Jones and C. B. Subrahmanyam, Eds. (Rose, Tallahassee, FL, 1986), p. 153.
17. K.-J. Bathe and E. L. Wilson, *Numerical Methods in Finite Element Analysis* (Prentice-Hall, Englewood Cliffs, NJ, 1976).
18. J. J. Dongarra, I. S. Duff, D. C. Sorensen, and H. A. van der Vorst, *Solving Linear Systems on Vector and Shared Memory Computers* (SIAM, Philadelphia, PA, 1993).
19. B. I. Schneider, in *Computational Methods for Electron–Molecule Collisions*, W. M. Huo and F. A. Gianturco, Eds. (Plenum, New York, 1995), p. 213 and references therein.
20. A. Jain and K. L. Baluja, Phys. Rev. **45**, 202 (1992).
21. K. R. Hoffman, M. S. Dababneh, Y.-F. Hsieh, W. E. Kauppila, V. Pol, J. H. Smart, and T. S. Stein, Phys. Rev. **25**, 1393 (1982).

Scattering by a Potential Separable in Ellipsoidal Coordinates

T. LEVITINA,* E. J. BRÄNDAS

Quantum Chemistry Group for Research in Atomic, Molecular and Solid State Physics, Uppsala University, Box 518, S-751 20 Uppsala, Sweden

Received 3 March 1997; revised 13 May 1997; accepted 14 May 1997

ABSTRACT: Some preliminary numerical studies of scattering by a potential separable in a general ellipsoidal coordinate system are presented. The associated scattering or far-field amplitudes are evaluated using expansions in radial and angle Lamé wave functions. Simple representations of the scattering matrix and the far-field amplitude are given as well as some preliminary figures of scattering data and related potential level surfaces. © 1997 John Wiley & Sons, Inc. Int J Quant Chem **65**: 601–608, 1997

Introduction

When separating the variables in terms of ellipsoidal coordinates (see Fig. 1), particular solutions of the Helmholtz equation are formed as products of the so-called angle and radial ellipsoidal (or Lamé) wave functions. For comparison, in case of a sphere, the products of the angle functions are the spherical harmonics, while the radial ones are the Bessel and Hankel functions.

A potentially very useful method to study, calculate, and analyze these ellipsoidal wave functions was presented, during the last 7–8 years, by the powerful Abramov School at the Department of Numerical Methods at the Computing Center of the Russian Academy of Sciences [1–3]. This work was, to a large extent, inspired by M. V. Fedoryuk, who investigated the fundamental properties of the ellipsoidal wave functions (see [4,5] and the literature cited therein). Furthermore, his articles [6,7] on acoustic scattering by a triaxial ellipsoid are also of great importance here, as he was the first to obtain the explicit form of the series expansions of scattering data in terms of ellipsoidal wave functions.

It should be noted in this context that we are not simply interested in the ellipsoidal wave functions as such, but we have, rather, a more general viewpoint in mind. For instance, one may apply the Fourier technique to solve the Schrödinger equation, thus arriving at a system of problems very similar to those arising in the study of the Helmholtz equation. In the particular case of the potential plotted in Figure 2, the angular functions

Correspondence to: E. J. Brändas.

* Permanent address: Department of Numerical Methods Computing Center of Russian Academy of Sciences Vavilova str.40, 117967 Moscow GSP-1, Russia.

Contract grant sponsor: Russian Foundation for Basic Research.

Contract grant number: 96-01-00951.

Contract grant sponsor: The Swedish Defense Research Establishment.

Contract grant number: FOA Project E6022.

© 1997 John Wiley & Sons, Inc.
CCC 0020-7608 / 97 / 050601-08

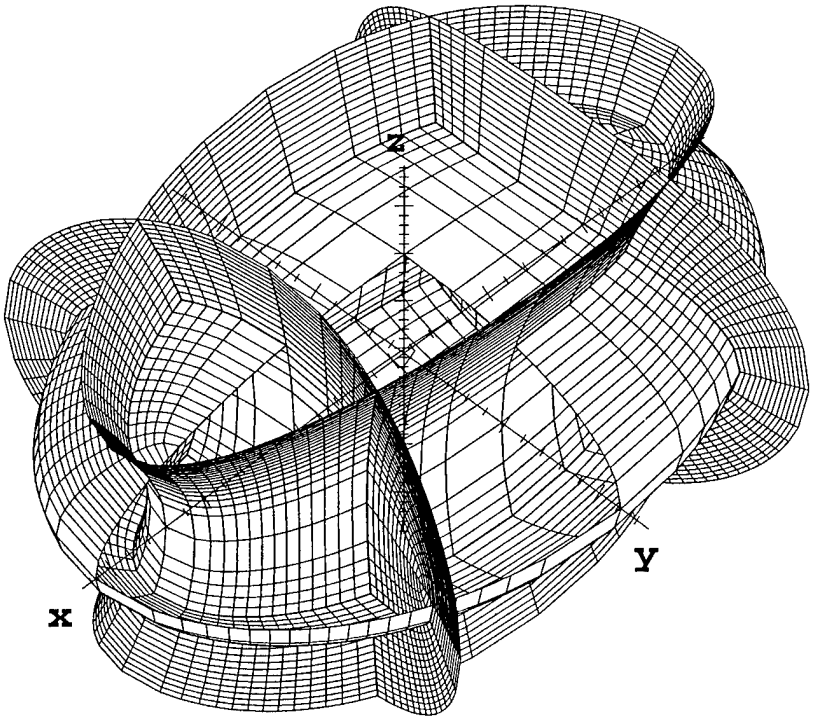


FIGURE 1. Examples of ellipsoidal coordinate surfaces. The grid is produced by the intersection of the coordinate surfaces. For more details, see text.

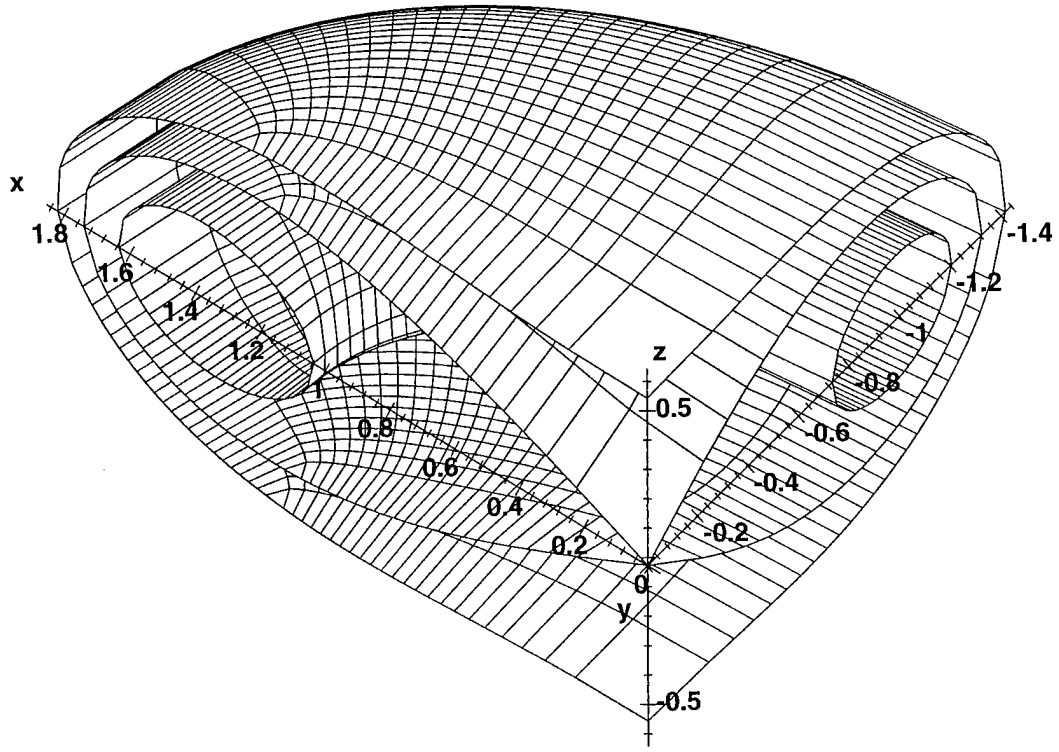


FIGURE 2. Equipotential surfaces of the potential $V(\xi_1, \xi_2, \xi_3) = \gamma_0 / [(\xi_3 - \xi_2)(\xi_3 - \xi_1)]$. Two adjacent octants are displayed to show the mirror symmetry of the potential.

will coincide with the angular ellipsoidal wave functions. The methods developed in [1–3] allow us to compute these perturbed ellipsoidal wave functions for an arbitrary potential separable in ellipsoidal coordinates and vanishing sufficiently fast at infinity and, more importantly, to represent scattering data in them. The present technique should also lead to many important applications to general problems in physics and chemistry, where the standard partial wave analysis may extend into the regime of thousands and more waves—obviously, by trying to manage a description of a system far from spherical symmetry.

In a recent contribution [8], we examined the shapes of the partial waves in an ellipsoidal representation using so-called $\rho\omega$-diagrams, where $\rho^2 = (a^2 - c^2)/(a^2 - b^2)$ and $\omega^2 = k^2(a^2 - b^2)$ are defined [see Eqs. (1)–(4) below]. It is easy to see that the flexibility offered by the ellipsoidal coordinate representation is obviously absent in the standard choices of coordinate systems.

We will here consider the scattering of particles by a potential which enables a separation of the variables in ellipsoidal coordinates, i.e., we look for the solution to the Schrödinger equation

$$\Delta\Psi + (k^2 - V(\boldsymbol{r}))\Psi = 0, \quad \vec{\mathbf{r}} \in \mathbb{R}^3 \qquad (1)$$

defined at infinity by

$$\Psi(\boldsymbol{r}, \boldsymbol{k}) \sim \exp i(\boldsymbol{k}, \boldsymbol{r}) + f(\boldsymbol{n}, \boldsymbol{n}_0)\frac{\exp(ikr)}{r}, \quad (r \to \infty) \qquad (2)$$

where $f(\boldsymbol{n}, \boldsymbol{n}_0)$ is the far-field or scattering amplitude, $\boldsymbol{n} = \boldsymbol{r}/r$ and $\boldsymbol{n}_0 = \boldsymbol{k}/k$. Our aim was to expand it in terms of the eigenfunctions of the Sturm–Liouville problem arising as a result of separation of variables in (1). In what follows, the variables introduced, in e.g., [1–3] are used.

Separation of Variables

Given $a > b > c > 0$, the ellipsoidal coordinate system is defined by

$$x^2/(a^2 + \eta) + y^2/(b^2 + \eta) + z^2/(c^2 + \eta) = 1,$$

or, going over to the dimensionless variables $\xi = (\eta + a^2)/(a^2 - b^2)$, being used further below, by

$$\frac{x^2}{(a^2 - b^2)\xi} + \frac{y^2}{(a^2 - b^2)(\xi - 1)} + \frac{z^2}{(a^2 - b^2)(\xi - \rho^2)} = 1. \qquad (3)$$

Here, we have denoted

$$\rho^2 = (a^2 - c^2)/(a^2 - b^2) > 1.$$

This equation defines a family of confocal surfaces specified by the variable ξ. To obtain a deeper understanding of the ellipsoidal coordinate system, one should contrast Figure 1 with Eq. (3). For each point (x, y, z), $xyz \neq 0$, the latter exhibits exactly three different roots, $\xi = \xi_1, \xi_2, \xi_3$, where $\xi_1 \in I_1 = (0; 1)$, $\xi_2 \in I_2 = (1; \rho^2)$, and $\xi_3 \in I_3 = (\rho^2; \infty)$. The equation $\xi_3 \equiv \xi_3^0 \in I_3$ defines an ellipsoid with the semiaxes $(a^2 - b^2)\xi_3^0 > (a^2 - b^2)(\xi_3^0 - 1) > (a^2 - b^2)(\xi_3^0 - \rho^2)$. As ξ_3 tends to $\rho^2 + 0$, ellipsoids degenerate into the part of the plane $z = 0$ bound by the focal ellipse $x^2/(a^2 - c^2) + y^2/(b^2 - c^2) = 1$. Setting $\xi_2 = \rho^2$, we obtain the part of the plane $z = 0$ complement to $\xi_3 = \rho^2$. As ξ_2 diminishes from ρ^2 to 1, the equation $\xi_2 = \xi_2^0$ specifies a hyperboloid of one sheet. As ξ_2 tends to $1 + 0$, hyperboloids degenerate to the part of the plane $y = 0$, enclosed between the branches of the focal hyperbola $x^2/(a^2 - b^2) - z^2/(b^2 - c^2) = 1$. The remaining part of the plane, which consists of two disjoined regions, containing foci of the hyperbola, is given by $\xi_1 = 1$. Starting from $\xi_1 = 1$, a family of hyperboloids of two sheets, each described by $\xi_1 = \xi_1^0$, tends to the plane $x = 0$, which coincides with the surface $\xi_1 = 0$.

The above three families of confocal surfaces form an orthogonal curvilinear coordinate system related to Cartesian coordinates within each octant (e.g., $x > 0$, $y > 0$, $z > 0$) by the one-to-one correspondence:

$$x^2 = (a^2 - b^2)\xi_1\xi_2\xi_3/\rho^2,$$
$$y^2 = -(a^2 - b^2)(\xi_1 - 1)(\xi_2 - 1) \times (\xi_3 - 1)/(\rho^2 - 1),$$
$$z^2 = (a^2 - b^2)(\xi_1 - \rho^2)(\xi_2 - \rho^2) \times (\xi_3 - \rho^2)/[(\rho^2 - 1)\rho^2].$$

In Figure 1, one can see the ellipsoidal coordinate surfaces of all possible types. Here, we cut off a one-eighth part of the ellipsoid to show the hyperboloids of both one and two sheets. It is readily seen that there is a point of intersection of all the plotted surfaces in each octant.

We now proceed as follows: Denote

$$L_j = \sqrt{f(\xi_j)}\,\frac{\partial}{\partial \xi_j}\left\{\sqrt{f(\xi_j)}\,\frac{\partial}{\partial \xi_j}\right\},$$

$$j = \overline{1,3}, \quad \text{with} \quad f(\xi) = \xi(\xi-1)(\xi-\rho^2),$$

$$\omega^2 = k^2(a^2 - b^2).$$

Then, in the newly introduced coordinates, the Lamé coefficients (see below) are $h_1^2 = (\xi_1 - \xi_2)(\xi_1 - \xi_3)(a^2 - b^2)/(4f(\xi_1))$ (h_2 and h_3 result from the above formula by a cyclic permutation of the indexes), with Eq. (1) taking the form

$$\{[(\xi_3 - \xi_2)L_1 + (\xi_1 - \xi_3)L_2 + (\xi_2 - \xi_1)L_3] + \tfrac{1}{4}(\xi_1 - \xi_2)(\xi_2 - \xi_3)(\xi_3 - \xi_1) \times [\omega^2 - V(\xi_1, \xi_2, \xi_3)]\}u(r) = 0. \quad (4)$$

In (4), we will admit a separable potential of the type

$$V(\xi_1, \xi_2, \xi_3) = [(\xi_3 - \xi_2)\alpha(\xi_1) + (\xi_1 - \xi_3)\beta(\xi_2) + (\xi_2 - \xi_1)\gamma(\xi_3)][(\xi_1 - \xi_2) \times (\xi_2 - \xi_3)(\xi_3 - \xi_1)]^{-1} \quad (5)$$

Here α, β, and γ are arbitrary functions. This is, in fact, the most general expression for such a potential [9].

By substituting a particular solution $\Psi(r) = \Lambda^{(1)}(\xi_1)\Lambda^{(2)}(\xi_2)\Lambda^{(3)}(\xi_3)$ into (1), we obtain three equations similar to the Lamé wave equations:

$$\sqrt{f(\xi_1)}\,\frac{d}{d\xi_1}\left\{\sqrt{f(\xi_1)}\,\frac{d\Lambda^{(1)}}{d\xi_1}\right\} + \tfrac{1}{4}[q(\xi_1, h, l, \omega) - \alpha(\xi_1)]\Lambda^{(1)} = 0, \quad 0 < \xi_1 < 1, \quad (6)$$

$$\sqrt{-f(\xi_2)}\,\frac{d}{d\xi_2}\left\{\sqrt{-f(\xi_2)}\,\frac{d\Lambda^{(2)}}{d\xi_2}\right\} - \tfrac{1}{4}[q(\xi_2, h, l, \omega) - \beta(\xi_2)]\Lambda^{(2)} = 0, \quad 1 < \xi_2 < \rho^2, \quad (7)$$

$$\sqrt{f(\xi_3)}\,\frac{d}{d\xi_3}\left\{\sqrt{f(\xi_3)}\,\frac{d\Lambda^{(3)}}{d\xi_3}\right\} + \tfrac{1}{4}[q(\xi_3, h, l, \omega) - \gamma(\xi_3)]\Lambda^{(3)} = 0, \quad \rho^2 < \xi_3 < \infty, \quad (8)$$

where h, l are the separation constants,

$$q(\xi, h, l, \omega) = h\rho^2 - l\rho^2\xi + \omega^2\xi^2.$$

Taking the symmetry of the problem into account, a particular solution of (1) must be either odd or even with respect to each coordinate plane. Since coordinate planes correspond to the ends of the intervals of the ellipsoidal coordinate variations, we find that

$$\begin{aligned}
&\text{either} \lim_{\xi_1 \to +0}\left(\sqrt{f(\xi_1)}\,\Lambda_1'(\xi_1)\right) = 0, \quad \text{or} \lim_{\xi_1 \to +0}\Lambda_1(\xi_1) = 0,\\
&\text{either} \lim_{\xi_1 \to 1-0}\left(\sqrt{f(\xi_1)}\,\Lambda_1'(\xi_1)\right) = 0, \quad \text{or} \lim_{\xi_1 \to 1-0}\Lambda_1(\xi_1) = 0,\\
&\text{either} \lim_{\xi_2 \to 1+0}\left(\sqrt{-f(\xi_2)}\,\Lambda_2'(\xi_2)\right) = 0, \quad \text{or} \lim_{\xi_2 \to 1+0}\Lambda_2(\xi_2) = 0,\\
&\text{either} \lim_{\xi_2 \to \rho^2-0}\left(\sqrt{-f(\xi_2)}\,\Lambda_2'(\xi_2)\right) = 0, \quad \text{or} \lim_{\xi_2 \to \rho^2-0}\Lambda_2(\xi_2) = 0,\\
&\text{either} \lim_{\xi_3 \to \rho^2+0}\left(\sqrt{f(\xi_3)}\,\Lambda_3'(\xi_3)\right) = 0, \quad \text{or} \lim_{\xi_3 \to \rho^2+0}\Lambda_3(\xi_3) = 0.
\end{aligned} \quad (9)$$

Here, we note that, in order to keep the same parity with respect to a coordinate plane, it is necessary that the boundary conditions for $\xi_1 \to 1 - 0$ and for $\xi_2 \to 1 + 0$ as well as for $\xi_2 \to \rho^2 - 0$ and for $\xi_3 \to \rho^2 + 0$ are identical. As in the case of ellipsoidal wave functions, the ends of the intervals I_j are singular points for (6)–(8). By a proper change of variables, one can, however, avoid these singularities [1, 3].

Thus, we obtain eight boundary value problems, each specified by a triplet of binary indexes (i_x, i_y, i_z), where $i_j = 0$ ($j = x, y, z$) for a particular solution $\Psi(r)$ of even parity with respect to the plane $j \equiv 0$ [see the left column of (9)], while

$i_j = 1$ $(j = x, y, z)$ corresponds to $\Psi(\boldsymbol{r})$ of odd parity with respect to $j \equiv 0$ [the right column of (9)]. Each particular solution can be extended smoothly over the whole space according to its parity properties [i.e., in accordance with (i_x, i_y, i_z)]. Given the set of boundary conditions represented by the triplet (i_x, i_y, i_z) and considering Eqs. (6) and (7) on the intervals $\xi_1 \in I_1$ and $\xi_2 \in I_2$, we will arrive at the following two-parameter Sturm–Liouville self-adjoint problem: We look for such a couple of values for $\{h, l\}$ that nontrivial solutions of (6) and (7) exist simultaneously on both intervals, satisfying the above-mentioned conditions corresponding to the triplet (i_x, i_y, i_z).

Let α and β be continuous. It can be proved that for any multi-index (m, n) there exists precisely one eigenvalue $(h, l)_n^m$ such that the corresponding solution to (6) oscillates m times within I_1, while the solution to (7) has $(n - m)$ zeroes inside I_2. Besides, this two-parameter problem is left-definite with respect to the vector $\boldsymbol{\mu} = (0, 1)$; hence, the eigenfunctions

$$\Xi_n^m(\xi_1, \xi_2) = \Lambda^{(1)}(\xi_1)\Lambda^{(2)}(\xi_2)$$

form a complete system on $\mathscr{L}^2(\Pi, \sigma)$, where $\Pi = I_1 \times I_2$ and

$$\sigma(\xi_1, \xi_2) = \tfrac{1}{4}(\xi_2 - \xi_1)[-f(\xi_1)f(\xi_2)]^{-1/2}$$

[10]. In passing, we note that the functions $\Xi_n^m(\xi_1, \xi_2)$, associated with distinct points of the spectrum, are orthogonal, with respect to the weight $\sigma(\xi_1, \xi_2)$, on Π. Extended according to the triplet (i_x, i_y, i_z) and normalized by

$$\int_\Pi \int [\Xi_n^m(\xi_1, \xi_2)]^2 \sigma(\xi_1, \xi_2)\, d\xi_1\, d\xi_2 = 1/8, \quad (10)$$

all the eigenfunctions for all sets (i_x, i_y, i_z) thus constitute an orthonormal basis in $\mathscr{L}^2(S, \sigma)$, where S is an arbitrary ellipsoid defined by $\xi_3 = \xi_3^* \in I_3$. The functions $\Xi_n^m(\xi_1, \xi_2)$ specified in this way are determined uniquely up to a sign. Any two functions $\Xi_n^m, \Xi_{n'}^{m'}$, with $m \neq m'$ and/or $n \neq n'$, are obviously orthogonal (if they are subject to the same boundary conditions, they are orthogonal on each part of S situated within a coordinate octant; otherwise, their inner product vanishes on S because they are of different parity).

The completeness of the function system, defined above, follows from the fact that each function from $\mathscr{L}^2(S)$ may be represented as a sum of eight terms of distinct parity with respect to coordinate planes:

$$u = v_0 + xv_1 + yv_2 + zv_3 + xyv_4 + xzv_5 + yzv_6 + xyzv_7$$

[here, $v_i = v_i(x^2, y^2, z^2)$]. One can therefore expand each term in the above equality as a series in the functions $\Xi_n^m(\xi_1, \xi_2)$ of the corresponding parity due to their completeness on $\mathscr{L}^2(\Pi, \sigma)$. The expansion holds for all coordinate octants and the sum of all the eight series yields then the expansion of the original function in terms of $\Xi_n^m(\xi_1, \xi_2)$ (for more details, see also [3]).

In [8], a natural way to classify these surface functions in relation to the conventional classification in the spherical case was proposed. The so-called $\rho\omega$-diagrams utilize the property that for small ω the shapes of the partial angular distribution are almost independent of the geometry of the problem and thus that the orbitals are close to the spherical case (see also [11]).

On I_3, a nontrivial solution to (8), subject to "the i_z boundary condition," exists for any h and l. If $\gamma(\xi_3) \sim \gamma_\infty \xi_3^q$ as $\xi_3 \to \infty$, with $q \leq 1$ (for simplicity), then (cf. the case of radial ellipsoidal functions) the behavior of such a solution at infinity is given by

$$\Lambda^{(3)}(\xi_3) = \frac{D}{\sqrt{\xi_3}} \sin\left(\omega\sqrt{\xi_3} + \Delta(l, h)\right) + \underline{O}\left(\frac{1}{\xi_3}\right), \quad \xi_3 \to \infty, \quad (11)$$

where D is of an arbitrary constant value (see below) and the phase $\Delta(l, h)$ expresses the influence of the potential on the scattered particle motion: If, e.g., $\alpha(\xi_1) = \beta(\xi_2) = \gamma(\xi_3) = 0$, then the functions $\Lambda_{m,n}^{(1)}(\xi_1)$, $\Lambda_{m,n}^{(2)}(\xi_2)$, and $\Lambda_{m,n}^{(3)}(\xi_3)$ coincide with the corresponding ellipsoidal wave functions with the phase $\Delta(l_n^m, h_n^m)$ given by

$$\Delta_n^m = \Delta(l_n^m, h_n^m) = -\pi[i_x + i_y + i_z]/2 \pmod{\pi}. \quad (12)$$

It is interesting to note that the last relation has not yet been proven thus far. Since we have only observed it in practical calculations [3], it still remains as a conjecture.

As for the asymptotical relation (11), the proof is analogous to the one used in [2] for the radial ellipsoidal wave functions. Calculations of the functions $\Lambda_{m,n}^{(1)}(\xi_1)$, $\Lambda_{m,n}^{(2)}(\xi_2)$, and $\Lambda_{m,n}^{(3)}(\xi_3)$ are carried out by applying previously developed

techniques to calculate ellipsoidal wave functions (see [1, 2]). The method for calculating the radial function [2] exploits the asymptotic behavior displayed in Eq. (11). Instead of computing the solution to Eq. (8), we integrated an auxiliary equation for a modified Prüfer angle, a modification equating the latter to $\Delta(l, h)$ at infinity. However, to speed up the calculations and to diminish the errors due to ODE numerical integration, we use additional terms of the radial function asymptotics, allowing us to reduce the integration interval (see [12, 13]).

Scattering Data Expansions

Following [14], we can now find the connection between the functions $\Xi(\xi_1, \xi_2)$ and the eigenfunctions of the scattering operator $\hat{S} = 1 + (ik/2\pi)\hat{f}$. We will further use the asymptotic representation of the particular solution $\Psi_n^m(\boldsymbol{r})$ in the form, putting $D = 1/\sqrt{\omega}$ [see (11)],

$$\Psi_n^m(\boldsymbol{r}) \sim \Xi_n^m(\xi_1, \xi_2)\frac{1}{2ikr}\{\exp[i(kr + \Delta_n^m)] - \exp[-i(kr + \Delta_n^m)]\}, \quad (r \to \infty). \quad (13)$$

Note that as ξ_3 tends to infinity the ellipsoidal coordinates as mentioned above approach the spherical ones, i.e.,

$$\xi_3(a^2 - b^2) \sim r^2 \quad (r \to \infty), \quad (14)$$

and (under the tradition of acoustics, θ is measured in relation to the large semiaxis which here happens to be the X-axis)

$$\begin{aligned} \xi_1\xi_2 &= \rho^2\cos^2\theta, \\ (\xi_1 - 1)(\xi_2 - 1) &= -(\rho^2 - 1)\sin^2\theta\cos^2\varphi, \\ (\xi_1 - \rho^2)(\xi_2 - \rho^2) &= \rho^2(\rho^2 - 1)\sin^2\theta\sin^2\varphi \end{aligned} \quad (15)$$

(see [6, 7] for more details).

The behavior of an arbitrary solution to (1) can now be expressed with the aid of the scattering operator $\hat{S}$ (defined on the unit sphere):

$$\Psi(\boldsymbol{r}, \boldsymbol{k}) \sim \frac{1}{2ikr}\{\exp(ikr)\hat{S}(\boldsymbol{n}, \boldsymbol{n}_0)F(-\boldsymbol{n}_0) - \exp(-ikr)F(\boldsymbol{n}_0)\}, \quad (r \to \infty), \quad (16)$$

where $F(\boldsymbol{n}_0)$ depends on the angles φ^0, θ^0 of the incidence direction.

Introducing the inversion (with respect to the origin) operator $\hat{I}$,

$$\hat{I}F(\boldsymbol{n}) = F(-\boldsymbol{n}),$$

we will, instead of (16), obtain

$$\Psi(\boldsymbol{r}, \boldsymbol{k}) \sim \frac{1}{2ikr}\{\exp(ikr)\hat{S}(\boldsymbol{n}, \boldsymbol{n}_0)\hat{I} - \exp(-ikr)\}F(\boldsymbol{n}_0), \quad (r \to \infty). \quad (17)$$

Rewriting (13) as

$$\Psi_n^m(\boldsymbol{r}) \sim \frac{1}{2ikr}\{\exp(ikr)\exp(2i\Delta_n^m) - \exp(-ikr)\} \times [\exp(-i\Delta_n^m)\Xi_n^m(\xi_1, \xi_2)], \quad (r \to \infty),$$

and comparing it with (17), we find that

$$F(\boldsymbol{n}_0) = \exp(-i\Delta_n^m)\Xi_n^m(\xi_1^0, \xi_2^0),$$

where ξ_1^0, ξ_2^0 are connected with the angles φ^0, θ^0 by (15) and with $\Xi_n^m(\xi_1, \xi_2)$ being the eigenfunction of $\hat{S}\hat{I}$:

$$\hat{S}\hat{I}\Xi_n^m(\xi_1^0, \xi_2^0) = \exp(2i\Delta_n^m)\Xi_n^m(\xi_1^0, \xi_2^0).$$

In view of Eq. (14) and since $\sigma(\xi_1, \xi_2) = \lim_{\xi_3 \to \infty}[h_1h_2/(a^2 - b^2)\xi_3]$, we have

$$\begin{aligned} &\int_0^{2\pi}\int_0^{\pi}[\Xi_n^m(\theta, \varphi)]^2 \sin\theta\, d\theta\, d\varphi \\ &\quad = \lim_{r\to\infty}\frac{1}{r^2}\int_{S_r}\int[\Xi_n^m(\boldsymbol{n})]^2\, dS \\ &\quad = \lim_{r\to\infty}\frac{1}{r^2}\int_{\xi_3 = \frac{r^2}{a^2-b^2}}\int[\Xi_n^m(\xi_1, \xi_2)]^2 \\ &\qquad \times h_1h_2\, d\xi_1\, d\xi_2 \\ &\quad = 8\int_{\Pi}\int[\Xi_n^m(\xi_1, \xi_2)]^2\sigma(\xi_1, \xi_2)\, d\xi_1\, d\xi_2 \end{aligned} \quad (18)$$

(here, S_r is a sphere of radius r). Thus, the matrix elements of the scattering operator in terms of the functions $\Xi_n^m(\xi_1, \xi_2)$ are (as the latter constitute an orthonormal system)

$$\begin{aligned} &\langle m, n|\,\hat{S}\,|m', n'\rangle \\ &\quad = \exp(2i\Delta_n^m)\langle m, n|\,\hat{I}\,|m', n'\rangle \\ &\quad = (-1)^{i'_x + i'_y + i'_z}\exp(2i\Delta_n^m)\langle m, n \mid m', n'\rangle \\ &\quad = (-1)^{i_x + i_y + i_z}\exp(2i\Delta_n^m) \\ &\qquad \times \delta_{m,m'}\delta_{n,n'}\delta_{(i_x, i_y, i_z)(i'_x, i'_y, i'_z)} \end{aligned}$$

or, written differently,

$$\hat{S}(\boldsymbol{n}, \boldsymbol{n}_0) = \sum_{(i_x, i_y, i_z)} \sum_{n=0}^{\infty} \sum_{m=0}^{n} \left[(-1)^{i_x+i_y+i_z} \exp(2i\Delta_n^m) \Xi_n^m(\xi_1, \xi_2) \Xi_n^m(\xi_1^0, \xi_2^0)\right]_{(i_x, i_y, i_z)}.$$

Therefore, the far-field or scattering amplitude is given by

$$f(\boldsymbol{n}, \boldsymbol{n}_0) = \frac{2\pi}{ik} \sum_{(i_x, i_y, i_z)} \sum_{n=0}^{\infty} \sum_{m=0}^{n} \left\{\left[(-1)^{i_x+i_y+i_z} \exp(2i\Delta_n^m) - 1\right] \Xi_n^m(\xi_1, \xi_2) \Xi_n^m(\xi_1^0, \xi_2^0)\right\}_{(i_x, i_y, i_z)}.$$

As a check, we note that for

$$\alpha(\xi_1) = \beta(\xi_2) = \gamma(\xi_3) = 0,$$

taking (12) into account, we get $f(\boldsymbol{n}, \boldsymbol{n}_0) = 0$.

Examples and Discussion

In Figure 2, we displayed a scattering potential, separable in ellipsoidal coordinates, given by the formula $V(\xi_1, \xi_2, \xi_3) = [\gamma_0/(\xi_3 - \xi_2)(\xi_3 - \xi_1)]$. As the potential goes to infinity, the corresponding equipotential surfaces approach the focal ellips (cf. the description of the ellipsoidal coordinate system). Far from the origin, the potential vanishes as r^{-4} and the corresponding equipotential surfaces approach a spherical shape. Generally, the shape of the equipotential surfaces does not depend on the value γ_0. We have here only plotted a quarter of each surface for three typical cases.

The corresponding numerical results are displayed in Figure 3. One can see here the examples of scattering diagrams, i.e., the plots $k\,|f(\boldsymbol{n}, \boldsymbol{n}_0)|$ for different incident directions: parallel to axis OX, parallel to axis OY, and parallel to axis OZ, from left to right. The parameter values are $\rho^2 = 2.0$, $\omega = 10.0$, and $\gamma_0 \rho^2 = -0.1$, the accuracy of the auxiliary ODE calculations is $\varepsilon = 10^{-6}$, and the maximum $n = 15$. We have not displayed the scattering amplitude for positive γ_0, since it will not give a large visual difference. In this particular case, the potential will only perturb the phase shift —a perturbation effect which is approximately linear. From the series expansion of $f(\boldsymbol{n}, \boldsymbol{n}_0)$, it follows that its absolute value does not depend on the sign of the potential. This means that within the linear domain the amplitudes in Figure 3 would

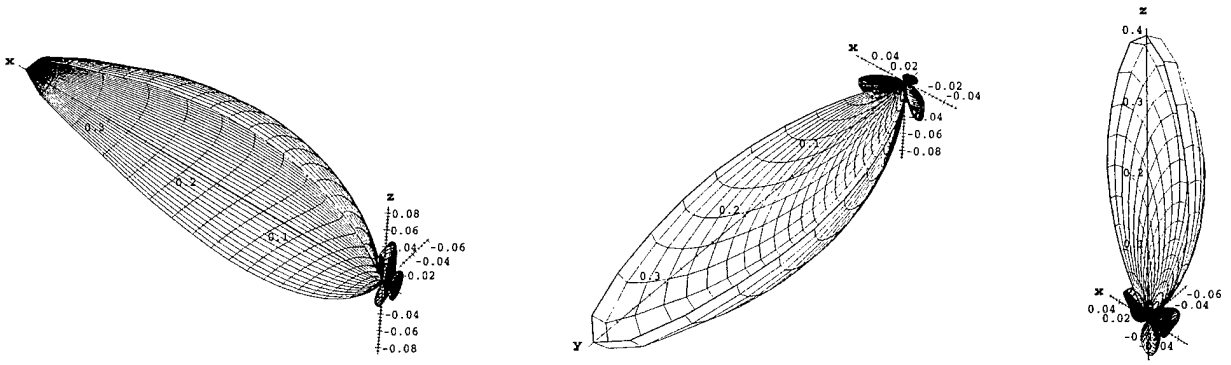


FIGURE 3. Examples of $k\,|f(\boldsymbol{n}, \boldsymbol{n}_0)|$ for the potential displayed in Figure 2. Various incident directions are shown from left to right.

naturally scale with the potential so that their shapes are preserved.

References

1. A. A. Abramov, A. L. Dyshko, N. B. Konyukhova, and T. V. Levitina, USSR Comput. Math. Math. Phys. **29**(3), 119 (1989).
2. A. A. Abramov, A. L. Dyshko, N. B. Konyukhova, and T. V. Levitina, USSR Comput. Math. Math. Phys. **31**(2), 25 (1991).
3. A. A. Abramov, A. L. Dyshko, N. B. Konyukhova, and T. V. Levitina, USSR Comput. Math. Math. Phys. **35**(9), 1103 (1995).
4. M. V. Fedoryuk, Izvest. Acad. Nauk SSSR, Ser. Matemat. **52**(4), 853 (1988).
5. M. V. Fedoryuk, Uspekhi Matemat. Nauk **44**(1/265), 123 (1989).
6. M. V. Fedoryuk, Diff. Uravneniya, **25**(11), 1990 (1989).
7. M. V. Fedoryuk, Akust. Zh. **34**(1), 160 (1988).
8. T. Levitina and E. J. Brändas, Int. J. Quantum Chem. Symp. **30**, 5 (1996).
9. L. P. Eisenhart, Phys. Rev. **74**(1), 87 (1948).
10. A. Källström and B. D. Sleeman, Proceed. R. Soc. Edin. **74A**, 145 (1974/75).
11. Yu, N. Demkov and V. S. Rudakov, Zh. Eksp. Teor. Fiz. **59**(6), 2035 (1970).
12. T. V. Levitina, Thesis (Vychisl. Tsentr Akad. Nauk SSSR, Moscow, 1991).
13. N. B. Konyukhova, S. Ye. Masalovich, and I. B. Staroverova, USSR Comput. Math. Math. Phys. **35**(3), 287 (1995).
14. I. V. Komarov, L. I. Ponomarev, and S. Yu. Slavyanov, *Spheroidal and Coulomb Spheroidal Functions* (Nauka, Moscow, 1976).

Transannular Interactions in S_8^{2+} and Se_8^{2+}: Reality or Artifact?

JERZY CIOSLOWSKI, XIANG GAO

Department of Chemistry and Supercomputer Computations Research Institute, Florida State University, Tallahassee, Florida 32306-3006

Received 1 March 1997; accepted 11 March 1997

ABSTRACT: Electronic structure calculations, carried out at the HF/6-311G*, MP2/6-311G*, and BLYP/6-311G* levels of theory, reveal an unexpectedly large influence of electron correlation on bonding in the octasulfur dication S_8^{2+}. Whereas a structure with a strong transannular bond linking two sulfur atoms with localized positive charges is predicted within the Hartree–Fock (HF) approximation, second-order Møller-Plesset (MP2) and Becke-Lee-Yang-Parr density functional (BLYP) calculations produce delocalized dications in which the transannular interactions are completely missing. Rigorous analysis of the computed electronic wave functions explains this phenomenon, which is also observed in the HF/TZVP and MP2/TZVP optimized geometries of Se_8^{2+}. In agreement with the experimental data, the *endo–exo* conformers are found to possess the lowest energies for the octachalcogen dications, in contrast to the corresponding neutral species in which steric interactions determine the relative energies, favoring the *exo–exo* ring conformations. None of the three theoretical approaches is capable of reproducing the experimental solid-state geometries of S_8^{2+} and Se_8^{2+}, which are almost certainly distorted to a large degree by the crystal packing and counterion effects. The results of the present study underscore the need for a concerted experimental and theoretical effort to provide the definitive answer to the question of transannular interactions in chalcogen compounds. © 1997 John Wiley & Sons, Inc. Int J Quant Chem 65: 609–616, 1997

Introduction

With its propensity to catenation (formation of homocyclic chains), sulfur occupies a unique place among the known elements. Combined with flexible packing in solid state, the large number of homocyclic compounds of sulfur gives rise to a multitude of allotropic modifications. So far, no fewer than 17 allotropes of sulfur, namely S_6, S_7 (4 modifications), S_8 (3 modifications), S_9 (2 modifications), S_{10}, S_{11}, S_{12}, S_{13}, S_{18} (2 conformers), and S_{20}, have been isolated in pure, crystalline form [1]. In fact, sulfur remains the element with the largest number of known allotropes, although

Correspondence to: J. Cioslowski.
Contract grant sponsor: National Science Foundation.
Contract grant number: CHE-9224806.

© 1997 John Wiley & Sons, Inc.
CCC 0020-7608 / 97 / 050609-08

this may change in the near future with the prospective discoveries of new fullerenes [2].

The most common form of sulfur is the octasulfur S_8 [1], which exists in three crystalline modifications, each composed of eight-membered rings possessing the *exo–exo* conformation [Fig. 1(a)] [3–5]. The monoclinic α-selenium and γ-selenium have analogous crystal structures [6, 7]. In contrast, salts containing the S_8^{2+} and Se_8^{2+} dications form crystals in which the chalcogen homocycles assume the less symmetrical *endo–exo* conformation [Fig. 1(b)] [8–11]. These salts are prepared by the oxidation of S_8 with a variety of reagents such as AsF_5 or SbF_5 [12]:

$$S_8 + 3XF_5 \rightarrow (S_8^{2+})(XF_6^-)_2 + XF_3, \qquad X = \text{As or Sb.} \quad (1)$$

The salts of the Se_8^{2+} dication can be obtained in a similar way [13].

The short intraring S_3–S_7 distance [Fig 1(b)] constitutes a prominent structural feature of the experimentally determined solid-state geometries of the S_8^{2+} dication. The proximity of these two atoms, which are found to be spaced by only ca. 2.9 Å [8, 9], has given rise to the speculation of transannular interactions operating across the sulfur octagons. Early theoretical studies have seemed to confirm the presence of such interactions. A short (R = 2.22 Å) transannular bond has been found in HF/STO-3G calculations on S_8^{2+} [14]. Although the properties of this bond have been analyzed, the discrepancy between the experimental and theoretical bond lengths has been neither explained nor even discussed. An even shorter bond (R = 2.060 Å) has been predicted by the MNDO method [15]. INDO calculations, carried out at the experimental geometries of the dications in question, have produced localized molecular orbitals spanning transannular bonds in S_8^{2+} and Se_8^{2+} [16]. For the latter species, no ab initio electronic structure studies have ever been reported.

The aforedescribed results clearly demonstrate the tendency of the Hartree–Fock (HF) method to grossly exaggerate the binding between the transannular atoms in the octachalcogen dications. It is therefore obvious that approximate treatments of electron correlation have to be invoked to provide a balanced description of bonding in these systems. Results of such a study are reported in this work. In particular, relative stabilities and geometries of the three conformers of the S_8^{2+} and Se_8^{2+} dications are predicted. The failures of the earlier calculations and the difficulties encountered in the present study are traced down to the unusual electronic structures of these species. The implications of the new predictions to the future experimental and theoretical work are discussed.

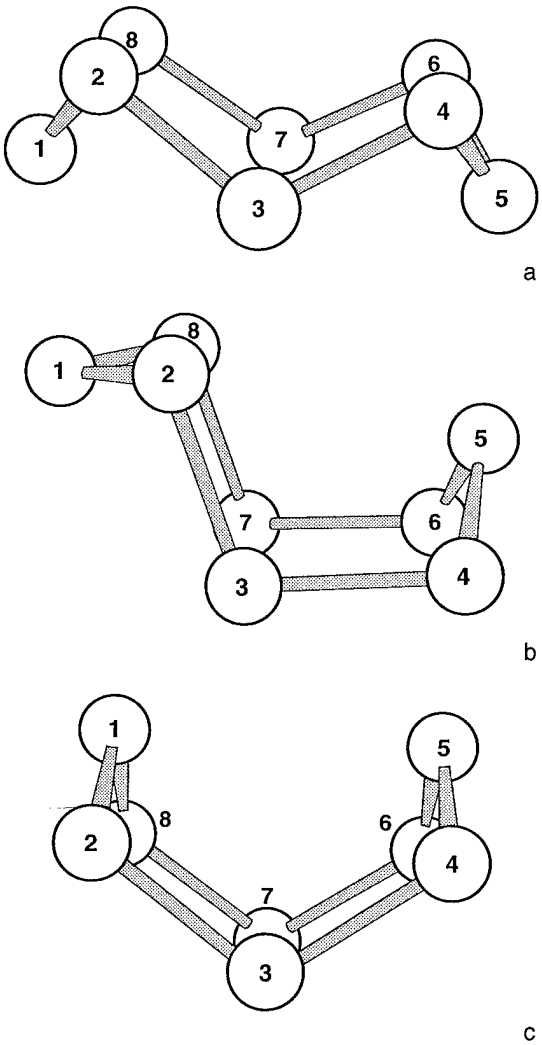


FIGURE 1. Three conformations of the eight-membered homocycles of sulfur and selenium: (a) *exo–exo*, (b) *endo–exo*, (c) *endo–endo*.

Details of Calculations

All the calculations described in this study were carried out with the GAUSSIAN G92/DFT system of programs [17] running on an SP2 cluster located at FSU/SCRI. For the sulfur homocycles, the basis

set of McLean and Chandler [18] augmented with polarization functions (as implemented under the name 6-311G* in GAUSSIAN 92/DFT) was used. Optimized geometries and vibrational frequencies were computed at the HF/6-311G*, MP2/6-311G* (frozen core), and BLYP/6-311G* levels of theory. Less extensive calculations were performed for the three conformers of Se_8 and Se_8^{2+}, geometries of which were optimized at the HF/TZVP and MP2/TZVP (frozen core) levels of theory [19]. The properties of atoms in the systems under study were determined with the algorithm described elsewhere [20]. The covalent bond orders [21] and the AOM-localized natural orbitals [22] were computed from the second-order Møller-Plesset (MP2) one-electron density matrices.

Results

Analysis of the data compiled in Table I leads to the conclusion that the stabilities of the individual conformers of S_8 and Se_8 are determined mostly by steric effects. This conclusion is borne out by two observations. First, the ordering of the relative energies follows that of the increasing crowding between the nonbonded chalcogen atoms, the *exo–exo* conformers being found the most stable and the *endo–endo* ones the least. Second, the computed energies barely change upon the inclusion of electron correlation effects, implying the predominance of interactions that are not specific to the electronic properties of any particular conformer. In contrast, the relative stabilities of the S_8^{2+} and Se_8^{2+} dications do not appear to be governed by steric crowding and are strongly affected by electron correlation, the *endo–exo* octacycles having the lowest energies at all levels of theory but the HF energy differences being too small to account for the experimental failure to observe the other two conformers.

The presence of unusual bonding in the dications under study is also hinted at by the relative magnitudes of the second adiabatic ionization potentials of the parent species (Table II). The computed MP2 and BLYP ionization potentials are significantly lower than their HF counterparts, despite the fact that the electron correlation effects tend to increase in importance with the number of electrons, in general stabilizing the neutral systems more than the doubly charged ones. As expected, Se_8 is predicted to undergo oxidation somewhat more readily than S_8.

TABLE I
Relative energies (kcal / mol) of the eight-membered homocycles of sulfur and selenium.[a]

Species	Conformation (symmetry)	Method HF	MP2	BLYP
S_8	*exo–exo* (D_{4d})	0.0	0.0	0.0
	endo–exo (C_s)	8.8	8.4	9.0
	endo–endo (D_{2d})	20.5	19.1	19.1
S_8^{2+}	*exo–exo* (C_{2v})	6.4	11.8	9.1
	endo–exo (C_s)	0.0	0.0	0.0
	endo–endo (C_{2v})	1.3	9.3	5.8
Se_8	*exo–exo* (D_{4d})	0.0	0.0	n/a
	endo–exo (C_s)	5.3	5.4	n/a
	endo–endo (D_{2d})	12.8	11.9	n/a
Se_8^{2+}	*exo–exo* (C_{2v})	2.9	9.7	n/a
	endo–exo (C_s)	0.0	0.0	n/a
	endo–endo (C_{2v})	1.5	3.5	n/a

[a] Zero-point energies not included.

The optimized geometries of the *exo–exo* conformers of the neutral species are in good agreement with the experimental solid-state data, though the bond lengths are consistently overestimated (Table III). This overestimation is especially pronounced at the BLYP/6-311G* level of theory (which also appears to slightly overestimate the bond angles) and is worse for Se_8 than for S_8. With better data lacking at present, these slight discrepancies can be attributed with equal probability to the basis-set incompleteness, crystal packing effects, and/or experimental errors.

The removal of two electrons from the *exo–exo* conformers of S_8 and Se_8 results in symmetry lowering from D_{4d} to C_{2v}. The distances between the formally nonbonded atoms 3 and 7 [Fig. 1(a)] become shorter, whereas those involving the 1–5 pairs increase (Table III). The ensuing unequiva-

TABLE II
Second adiabatic potentials (eV) of the S_8 and Se_8 molecules.

Species	Conformation	Method HF	MP2	BLYP
S_8	*exo–exo*	22.35	21.05	21.44
	endo–exo	21.69	20.18	20.65
	endo–endo	21.24	20.12	20.47
Se_8	*exo–exo*	20.80	19.39	n/a
	endo–exo	20.44	18.73	n/a
	endo–endo	20.19	18.60	n/a

TABLE III
Geometries of the *exo*–*exo* conformers of the eight-membered homocycles of sulfur and selenium.

Species	Method	Interatomic distances[a] (Å)				Bond angles[a] (°)		
		1–2	2–3	3–7	1–5	1–2–3	2–3–4	4–5–6
S_8	HF	2.069	2.069	4.719	4.719	107.4	107.4	107.4
	MP2	2.075	2.075	4.763	4.763	108.5	108.5	108.5
	BLYP	2.146	2.146	4.967	4.967	109.8	109.8	109.8
	exp.[b]	2.051	2.051	n/a	n/a	108.2	108.2	108.2
	exp.[c]	2.050	2.050	n/a	n/a	107.9	107.9	107.9
	exp.[d]	2.045	2.045	n/a	n/a	107.7	107.7	107.7
S_8^{2+}	HF	2.064	2.146	2.225	5.685	94.8	103.1	96.9
	MP2	2.093	2.081	3.328	5.423	99.8	105.6	92.7
	BLYP	2.154	2.160	3.134	5.670	98.1	106.7	95.3
Se_8	HF	2.391	2.391	5.406	5.406	106.1	106.1	106.1
	MP2	2.413	2.413	5.498	5.498	107.3	107.3	107.3
	exp.[e]	2.336	2.336	n/a	n/a	105.7	105.7	105.7
	exp.[f]	2.334	2.334	n/a	n/a	105.8	105.8	105.8
Se_8^{2+}	HF	2.394	2.497	2.492	6.634	95.2	101.4	96.5
	MP2	2.443	2.447	4.000	6.292	99.7	103.9	91.3

[a] See Fig. 1(a) for atom numbering.
[b] Symmetry-averaged X-ray structure of orthorhombic α-sulfur at 100 K [3].
[c] Symmetry-averaged X-ray structure of monoclinic β-sulfur at 113 K [4].
[d] Symmetry-averaged X-ray structure of monoclinic γ-sulfur [5].
[e] Symmetry-averaged X-ray structure of monoclinic α-selenium [6].
[f] Symmetry-averaged X-ray structure of monoclinic γ-selenium [7].

lence of chalcogen atoms produces three distinct bond angles and a pattern of short and long bonds that interleave in pairs. The computed geometries are extremely sensitive to the electron correlation effects, which equalize interatomic distances (including bond lengths) but appear to have somewhat less influence on the bond angles. Particularly drastic changes are observed for the 3–7 distances. Without the inclusion of electron correlation, these distances are predicted short enough to suggest the presence of strong transannular bonds possessing lengths comparable to those of the ordinary S–S and Se–Se links. On the other hand, both the MP2 and BLYP data seem to rule out such a possibility.

The shortening of distances between the nonbonded atoms (compare the 3–7 and 2–5 columns in Tables III and IV) observed upon going from the *exo–exo* to the *endo–exo* conformations of S_8 and Se_8 produces an increase in steric repulsions, which in turn results in a slight lengthening of bonds on average. Due to the lack of experimental data, neither this lengthening nor the concomitant bond alternation can be verified at present. On the other hand, experimentally determined geometries are available for the corresponding dications [8–11]. Examination of these geometries reveals the very poor performance of the Hartree–Fock method in predicting the strengths of the transannular interactions between the atoms in positions 3 and 7 in the *endo–exo* conformers of S_8^{2+} and Se_8^{2+}. Unfortunately, the approximate inclusion of electron correlation effects at the MP2 and BLYP levels of theory does not appear to bring the predicted bond lengths and angles into a closer agreement with their experimental counterparts. Although the computed MP2/6-311G* and BLYP/6-311G* S_3–S_7 distances in the *endo–exo* conformer of S_8^{2+} turn out to be very similar, they nevertheless deviate from the corresponding experimental value by roughly the same amount as the HF/6-311G* prediction does, the former deviation being positive and the latter negative.

The optimized geometries of the experimentally unknown *endo–endo* conformers [Fig. 1(c)] are listed in Table V. As mentioned above, the nonbonded pairs of atoms are positioned much closer in those conformers than in the *exo–exo* ones. In fact, the close proximity of the flag-pole atoms turns the D_{2d} *endo–endo* conformer of S_8 into a transition state at the HF/6-311G* and MP2/6-311G* levels of theory, although the correspond-

TABLE IV

Geometries of the *endo*–*exo* conformers of the eight-membered homocycles of sulfur and selenium.

Species and method		Interatomic distances[a] (Å)						Bond angles[a] (°)				
		1–2	2–3	3–4	4–5	3–7	2–5	1–2–3	2–3–4	3–4–5	4–5–6	8–1–2
S_8	HF	2.073	2.075	2.103	2.056	3.991	3.609	103.7	105.8	107.1	111.4	110.7
	MP2	2.081	2.072	2.125	2.056	4.147	3.583	104.2	105.5	106.7	113.2	112.1
	BLYP	2.166	2.105	2.240	2.115	4.623	3.775	106.5	107.8	108.1	116.7	113.0
S_8^{2+}	HF	2.060	2.140	2.106	2.069	2.235	3.816	95.1	107.5	98.3	95.8	96.3
	MP2	2.086	2.059	2.097	2.073	3.660	3.510	103.1	106.3	106.2	97.9	95.9
	BLYP	2.146	2.136	2.146	2.141	3.669	3.709	102.6	107.7	106.8	98.5	96.7
	exp.[b]	2.055	2.033	2.022	2.043	2.860	n/a	99.3	104.2	100.7	90.6	95.1
	exp.[c]	2.037	2.005	2.046	2.038	2.906	n/a	98.3	104.0	101.6	94.0	93.1
Se_8	HF	2.394	2.397	2.418	2.378	4.515	4.062	102.5	104.2	105.6	109.8	109.5
	MP2	2.416	2.415	2.455	2.396	4.767	4.019	103.1	103.3	104.8	112.0	111.2
Se_8^{2+}	HF	2.393	2.486	2.475	2.395	2.490	4.384	95.5	105.1	97.4	96.1	96.0
	MP2	2.433	2.428	2.477	2.425	4.763	3.938	104.4	103.6	105.8	102.3	96.0
	exp.[d]	2.32	2.31	2.35	2.30	2.84	n/a	95.2	101.3	98.2	93.3	89.8
	exp.[e]	2.300	2.295	2.319	2.312	2.905	n/a	94.6	102.4	99.1	92.7	90.0

[a] See Fig. 1(b) for atom numbering.
[b] Symmetry-averaged X-ray structure of (S_8^{2+}) $(AsF_6^-)_2$ [8].
[c] Symmetry-averaged X-ray structure of (S_8^{2+}) $(Sb_3F_{14}^-)$ (SbF_6^-) [9].
[d] Symmetry-averaged X-ray structure of (Se_8^{2+}) $(AlCl_4^-)_2$ [10].
[e] Symmetry-averaged X-ray structure of (Te_6^{4+}) (Se_8^{2+}) $(AsF_6^-)_6$ (SO_2) [11].

ing imaginary frequencies of $16i$ and $33i$ cm^{-1}, respectively, are too small to rule out the possibility of this system being actually a true minimum on the corresponding potential energy hypersurface. An analogous phenomenon is not observed for the *endo–endo* conformer of Se_8. At the MP2/6-311G* level of theory, the C_{2v} *endo–endo* conformer of S_8^{2+} is also a transition state with a small imaginary frequency of $41i$ cm^{-1}. Again, large differences between the HF and MP2 geometry predictions are found for S_8^{2+} and Se_8^{2+}.

In summary, all the three theoretical methods employed in this study are successful in predicting both the energetics and geometries of the neutral octachalcogen species. For the corresponding dications, the inclusion of electron correlation within the MP2 and BLYP approximations suffices to produce correct relative stabilities but fails to yield

TABLE V

Geometries of the *endo*–*endo* conformers of the eight-membered homocycles of sulfur and selenium.

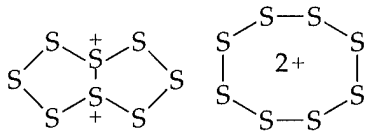
Species	Method	Interatomic distances[a] (Å)				Bond angles[a] (°)		
		1–2	2–3	3–7	1–5	1–2–3	2–3–4	4–5–6
S_8	HF	2.083	2.083	3.464	3.464	107.7	112.8	112.8
	MP2	2.091	2.091	3.459	3.459	106.7	113.3	113.3
	BLYP	2.162	2.162	3.686	3.686	107.2	115.6	115.6
S_8^{2+}	HF	2.065	2.118	2.201	3.665	100.3	117.0	96.1
	MP2	2.086	2.065	3.475	3.466	110.1	120.7	99.6
	BLYP	2.143	2.138	3.223	3.797	108.8	123.0	97.7
Se_8	HF	2.402	2.402	3.869	3.869	106.4	114.4	114.4
	MP2	2.428	2.428	3.866	3.866	104.9	112.0	112.0
Se_8^{2+}	HF	2.394	2.477	2.470	4.142	99.2	114.3	96.4
	MP2	2.411	2.437	6.418	4.804	116.5	120.6	115.4

[a] See Fig. 1(c) for atom numbering.

accurate geometries. This failure is particularly conspicuous for the distances between the atoms supposedly engaged in transannular interactions, for which the discrepancies between the "best" theoretical predictions and the experimental values are as large as 0.7 Å (Table IV)! These troublesomely large errors stem from a quite unusual coincidence of several unfavorable factors. First of all, the available experimental geometries [8–11] are of inferior quality by the contemporary standards. Even more importantly, the potential energy hypersurfaces of the dications in question are very flat in the directions corresponding to a lateral squashing of the rings. For example, in the *endo–exo* conformer of S_8^{2+}, the frequency of the *A'* vibration that involves predominantly the S_3–S_7 stretch is predicted to be equal 363 and 75 cm^{-1} at the HF/6-311G* and MP2/6-311G* levels of theory, respectively. Consequently, the across-the-ring distances are expected to be quite sensitive to small perturbations. With respect to the experimental data, this sensitivity implies a substantial influence of the crystal packing and counterion effects on the measured solid-state geometries. At the same time, relatively small errors in the computed energies and energy gradients are bound to translate into large deviations in the optimized intraring distances.

Rigorous analysis of the computed electronic wave functions elucidates the reasons behind the observed dramatic effects of electron correlation on bonding in the octachalcogen dications. The inspection of the AOM-localized natural orbitals (LNOs) in the *endo–endo* conformer of Se_8 reveals the presence of eight equivalent LNOs describing the Se–Se bonds (LNOs 129–136 in Table VI) in addition to two unequivalent lone-pair LNOs per each atom (LNOs 113–128). All of these LNOs are almost doubly occupied. The covalent bond orders equal 1.186 for the bonded pairs of atoms and 0.083 for the Se_3–Se_7 and Se_1–Se_5 nonbonded pairs. At the MP2/TZVP level of theory, the removal of two electrons from this system produces a delocalized dication, as indicated by the computed atomic charges of 0.1842 (Se_1 and Se_5), 0.2486 (Se_2, Se_4, Se_6, and Se_8), and 0.3186 (Se_3 and Se_7). The bond alternation observed in the optimized geometries (Table V) is reflected in the covalent bond orders of 1.229 (Se_1–Se_2, etc.) and 1.164 (Se_2–Se_3, etc.). At the same time, the covalent bond orders of 0.031 and 0.124, obtained for the Se_1–Se_5 and Se_3–Se_7 pairs of atoms, respectively, rule out the presence of any significant transannular interactions.

In principle, two qualitatively distinct types of bonding in the dications under study are possible. On one hand, the removal of two electrons from two lone-pair LNOs located across the ring may yield an orbital bonding of two chalcogen atoms with localized positive charges (as in structure **1**). Such bonding can easily overcome the strong electrostatic repulsion between the charges (the He_2^{2+} dication with R_{He-He} = 0.741 Å being a good example) [23]. On the other hand, the two electrons may come from several lone-pair LNOs, producing a dication with a delocalized positive charge (as in structure **2**).



1 **2**

In light of the above discussion, the exaggeration of transannular interactions observed within the Hartree–Fock approximation is attributable to an excessive localization of the positive charge. This spurious localization is readily explainable by the fact that the occupancies of the Hartree–Fock localized orbitals are restricted to either zero or two. In other words, the removal of two electrons from the lone-pair orbitals must produce either a

TABLE VI
MP2 / TZVP valence localized orbitals in the *endo–endo* conformer of Se_8.

Orbitals	Occup.	Loc. Num.	$-T$ (a.u.)	Description[a]
113–116	1.982	1.027	−3.713	Lone pairs of atoms 2, 4, 6, and 8 (98.7% loc.)
117–120	1.983	1.030	−3.682	Lone pairs of atoms 1, 3, 5, and 7 (98.5% loc.)
121–124	1.981	1.171	−2.175	Lone pairs of atoms 1, 3, 5, and 7 (92.3% loc.)
125–128	1.981	1.163	−2.151	Lone pairs of atoms 2, 4, 6, and 8 (92.6% loc.)
129–136	1.957	2.072	−2.112	Covalent Se–Se bonds (98.2% loc.)

[a]See Fig. 1(c) for atom numbering.

new bond or multicentric bonding orbitals, the latter possibility (which would be compatible with the structure **2**) being highly unlikely because of the angular misalignment of the lone pairs. On the other hand, fractional occupancies of LNOs are possible once electron correlation is turned on, favoring the delocalized picture of bonding. Such fractional occupancies are indeed observed in the MP2/TZVP LNOs of the *endo–endo* conformer of Se_8^{2+} (Table VII).

Almost certainly, the actual bonding in the S_8^{2+} and Se_8^{2+} dications is closer to that represented by structure **2** than to that portrayed by structure **1**. Consequently, because of the relatively low occupancies of the LNOs, the actual ground-state wave functions of these species are expected to possess considerable multiconfigurational character, necessitating the use of high-level treatments such as CAS SCF or CCSD(T) for quantitative predictions of electronic properties and geometries. Because of the computer hardware limitations, such calculations are not feasible at present. One should also note in passing that the electron correlation effects described in this work are quite unique, differing in their nature from the dispersive effects encountered in the description of the attractive closed-shell interactions between chalcogen atoms [24].

Conclusions

Transannular interactions in the octachalcogen dications pose a severe challenge to the modern techniques of computational quantum chemistry. The combination of flat potential energy hypersurfaces and unexpectedly large electron correlation effects renders the approximate approaches such as MP2 and BLYP inadequate for the prediction of the equilibrium geometries of these species. On the other hand, the relatively large size and low symmetry of the dications in question preclude the use of more sophisticated methods such as CAS SCF or CCSD(T) at present.

It is clear from the results reported in this study that the definitive answer to the question whether the transannular interactions in S_8^{2+} and Se_8^{2+} are indeed reality or just an artifact will ultimately require a coalescence of experimental and theoretical research. On the experimental front, precise gas-phase geometry determinations will be necessary in order to eliminate the ring distortions caused by the crystal packing effects and counterions. At the same time, large-scale ab initio electronic structure calculations involving comparisons among several high-level electron correlation treatments will have to be carried out.

The present work uncovers the reasons behind the failures of the previously published calculations to correctly predict the transannular chalcogen–chalcogen distances in the S_8^{2+} and Se_8^{2+} dications. The descriptions of bonding in these systems are completely different at the HF and correlated levels of theory, the latter appearing to be closer to reality. If present at all, the transannular interaction are weak and, stemming from a delicate balance between charge delocalization and localized bonding, certainly distinct from conventional bonds.

ACKNOWLEDGMENT

This work was partially supported by the National Science Foundation under the grant CHE-9224806.

TABLE VII
MP2 / TZVP valence localized orbitals in the *endo–endo* conformer of Se_8^{2+}.

Orbitals	Occup.	Loc. Num.	$-T$ (a.u.)	Description[a]
113–114	1.979	1.036	−3.714	Lone pairs of atoms 3 and 7 (98.3% loc.)
115–118	1.979	1.038	−3.681	Lone pairs of atoms 2, 4, 6, and 8 (98.2% loc.)
119–120	1.975	1.034	−3.671	Lone pairs of atoms 1 and 5 (98.4% loc.)
121–122	1.988	1.278	−2.181	Lone pairs of atoms 1 and 5 (88.3% loc.)
123–126	1.929	2.081	−2.158	2–3 (etc.) bonds (10.0% ion., 97.5% loc.)
127–130	1.926	2.094	−2.142	1–2 (etc.) bonds (6.1% ion., 97.5% loc.)
131–134	1.818	1.292	−2.178	Lone pairs of atoms 2, 4, 6, and 8 (87.8% loc.)
135–136	1.389	1.313	−2.243	Lone pairs of atoms 3 and 7 (87.0% loc.)

[a] See Fig. 1(c) for atom numbering.

References

1. R. Steudel, *Elemental Sulfur and Related Homocyclic Compounds and Ions, Studies in Inorganic Chemistry*, Vol. 5 (Elsevier, Amsterdam, 1984), pp. 3–37.
2. For a recent review of electronic structures of fullerenes see: J. Cioslowski, *Electronic Structure Calculations on Fullerenes and Their Derivatives* (Oxford University Press, New York, 1995).
3. P. Coppens, Y. W. Yang, R. H. Blessing, W. F. Cooper, and F. K. Larsen, J. Am. Chem. Soc. **99**, 760 (1977).
4. L. M. Goldsmith and C. E. Strouse, J. Am. Chem. Soc. **99**, 7580 (1977).
5. Y. Watanabe, Acta Cryst. B **30**, 1396 (1974).
6. P. Cherin and P. Unger, Acta Cryst. B **28**, 313 (1972).
7. O. Foss and V. Janickis, J. Chem. Soc. Dalton Trans., 624 (1980).
8. C. G. Davies, R. J. Gillespie, J. J. Park, and J. Passmore, Inorg. Chem. **10**, 2781 (1971).
9. R. Faggiani, R. J. Gillespie, J. F. Sawyer, and J. E. Vekris, Acta Cryst. C **45**, 1847 (1989).
10. R. K. McMullan, D. J. Prince, and J. D. Corbett, Inorg. Chem. **10**, 1749 (1971).
11. M. J. Collins, R. J. Gillespie, and J. F. Sawyer, Acta Cryst. C **44**, 405 (1988).
12. R. J. Gillespie, J. Passmore, P. K. Ummat, and O. C. Vaidya, Inorg. Chem. **10**, 1327 (1971).
13. R. J. Gillespie and J. Passmore, Acc. Chem. Res. **4**, 413 (1971).
14. T.-H. Tang, R. F. W. Bader, and P. J. MacDougall, Inorg. Chem. **24**, 2047 (1985).
15. N. C. Baird, J. Comp. Chem. **5**, 35 (1984).
16. K. Tanaka, T. Yamabe, H. Terama-e, and K. Fukui, Nouv. J. Chim. **3**, 379 (1979).
17. M. J. Frisch, G. W. Trucks, H. B. Schlegel, P. M. W. Gill, B. G. Johnson, M. W. Wong, J. B. Foresman, M. A. Robb, M. Head-Gordon, E. S. Replogle, R. Gomperts, J. L. Andres, K. Raghavachari, J. S. Binkley, C. Gonzalez, R. L. Martin, D. J. Fox, D. J. Defrees, J. Baker, J. J. P. Stewart, and J. A. Pople, GAUSSIAN 92/DFT, Revision G.3, GAUSSIAN, Inc., Pittsburgh, PA, 1993.
18. A. D. McLean and G. S. Chandler, J. Chem. Phys. **72**, 5639 (1980).
19. The TZVP basis set was downloaded from the database described in A. Schäfer, H. Horn, and R. Ahlrichs, J. Chem. Phys. **97**, 2571 (1992).
20. J. Cioslowski and B. B. Stefanov, Mol. Phys. **84**, 707 (1995).
21. J. Cioslowski and S. T. Mixon, J. Am. Chem. Soc. **113**, 4142 (1991).
22. J. Cioslowski, Int. J. Quant. Chem. **S24**, 15 (1990).
23. K. Lammertsma, P. V. R. Schleyer, and H. Schwarz, Angew. Chem. Int. Ed. Engl. **28**, 1321 (1989).
24. K. W. Klinkhammer and P. Pyykkö, Inorg. Chem. **34**, 4134 (1995).

Laser-Induced Alignment Dynamics in Multiphoton Dissociation of H_2^+

O. ATABEK

Laboratoire de Photophysique du CNRS, Bâtiment 210, Université Paris-Sud, Campus d'Orsay, 91405 Orsay Cedex, France

Received 1 March 1997; accepted 29 April 1997

ABSTRACT: Angular-resolved kinetic energy distributions of fragments resulting from dissociation induced by intense, short, linearly polarized laser pulses are calculated using an accurate three-dimensional Fourier transform method in spherical coordinates. The rotational excitation of the molecule leads, in general, to an alignment of the photofragments with respect to the field polarization vector. But, unexpectedly, increasing the field strength may also produce fewer aligned fragments at the higher kinetic energies of the multiphoton above the threshold dissociation spectrum. H_2^+ photodissociating by interaction with an Nd:YAG laser at $\lambda = 532$ nm and for intensities of 10–50 TW/cm^2 is taken as an illustrative example, for which some angular-resolved experimental spectra are available. A comprehensive interpretation is provided within the field-dressed Floquet picture by referring to two strong-field mechanisms, namely, the potential barrier lowering (also responsible for bond softening) and the nonadiabatic transitions (also responsible for the vibrational trapping). © 1997 John Wiley & Sons, Inc.
Int J Quant Chem **65**: 617–624, 1997

Introduction

Progress in laser technology producing very intense and short pulses has motivated a completely new formulation for the description of multiphoton dissociation dynamics of molecules [1]. Very complicated molecular behavior is observed as a response to the electromagnetic field. Repeated stimulated photon absorption and emission mechanisms lead to above-threshold dissociation (ATD), evidenced by the observation, in the fragment kinetic energy distributions, of peaks spaced by one quantum of the photon energy [2, 3]. In addition to *scalar* observables such as total or partial dissociation rates or the energy spectra of fragments, *vectorial* observables such as fragment angular distributions provide complementary views for a detailed understanding of the strong laser-induced dissociation dynamics. Two possibilities have so far been invoked for the interpretation of aligned fragments with respect to the

Contract grant sponsor: Institut du Développement et des Ressources en Informatique Scientifique I.D.R.I.S.
Contract grant number: 940425.

© 1997 John Wiley & Sons, Inc.
CCC 0020-7608 / 97 / 050617-08

field polarization vector, namely, an enhancement of the dissociation cross section for initially aligned molecules [2, 4, 5] or a dynamical alignment occurring during the fragmentation process as a consequence of the torque that the laser field exerts on the molecule [6–8]. The extensive use of one-dimensional models, where the fragmentation of diatomic molecules is merely described by a single degree of freedom, relies upon the first assumption [2, 9, 10]. The possibility of a dynamical alignment motivates the development of models where rotational degrees of freedom are fully included [11–14].

The most popular conviction so far experimentally supported by different observations is that, whatever the mechanism is, molecules subjected to an intense, linearly polarized laser radiation dissociate into fragments aligned with the polarization axis. There is, however, experimental evidence, on H_2^+ multiphoton dissociation, that protons are emitted along the polarization axis in narrow distributions, becoming broader as intensity increases [6]. The bond-softening (BS) mechanism resulting from laser-induced lowering of a potential energy barrier supports the interpretative scheme of the alignment process. More recently, we, conversely, pointed out that the vibrational trapping (VT) mechanism may be responsible for fragmentations occurring in a plane nearly orthogonal to the polarization axis [14]. This surprising prediction has been confirmed by quantum calculations on H_2^+ with an excitation wavelength of $\lambda = 80$ nm, producing a curve-crossing situation in a field-dressed molecule picture occurring at the left of the equilibrium position. The detailed understanding of such a mechanism involves very efficient trapping in all spatial directions except a direction quasi-perpendicular to the applied field where fragmentation may take place.

The aim of the present work was to understand another somewhat unexpected observation in H_2^+ of less aligned photofragments for stronger fields at a wavelength of $\lambda = 532$ nm [6], by calculating the angular-resolved kinetic energy spectra and interpreting them in terms of the interplay of field-induced chemical bond softening and hardening (trapping) mechanisms. The article is organized as follows: The next section provides a brief theoretical survey of a time-dependent quantum model where an initial (vibrational–rotational) state of H_2^+ is propagated on its two lowest electronic states, namely, $^2\Sigma_g^+$ and $^2\Sigma_u^+$. The linearly polarized laser imposes a privileged direction in the laboratory frame with respect to which the molecular axis is positioned. For short internuclear distances defining an inner region, a Fourier transform spectral method is used in spherical coordinates by combining a contact transformation with Dateo and Metiu's [13] grid approach for angular degrees of freedom. For the large distances of the outer region, an analytic approach, which is a three-dimensional generalization of Volkov-type solutions of [15], is adopted. The third section is devoted to the interpretation of the angular-resolved fragment kinetic energy spectra of H_2^+ irradiated by an intense pulse ($I = 10$–50 TW/cm^2) of $\lambda = 532$ nm delivered by a Nd:YAG laser source. Special attention is directed toward the understanding of the alignment properties of the experimental spectra of [6], in terms of multiphoton processes involving adiabatic potential energy barriers (BS situation) and nonadiabatic transitions (VT situations) affecting molecular dynamics during dissociation.

Theory

Our purpose was to solve the nuclear time-dependent Schrödinger equation on a Born–Oppenheimer level of approximation involving two electronic states labeled g (ground, $^2\Sigma_g^+$) and u (excited, $^2\Sigma_u^+$) following, for convenience, the standard symmetry notations of H_2^+:

$$i\hbar\hat{\mathbf{1}}\frac{d}{dt}\begin{pmatrix}\tilde{\psi}_g\\ \tilde{\psi}_u\end{pmatrix} = \hat{\mathbf{H}}\begin{pmatrix}\tilde{\psi}_g\\ \tilde{\psi}_u\end{pmatrix}, \tag{1}$$

where the total molecule-plus-field Hamiltonian is

$$\hat{\mathbf{H}} = \hat{\mathbf{1}}\left(\tilde{T}_R + \tilde{T}_\theta + \tilde{T}_\varphi\right) + \tilde{\mathbf{W}}(R, \theta; t), \tag{2}$$

1 being the identity matrix, and R, θ, and φ, the spherical coordinates of the internuclear vector $\vec{R}$ in the laboratory frame [14]. Kinetic terms are given by

$$\tilde{T}_R = -\frac{\hbar^2}{2mR^2}\frac{d}{dR}R^2\frac{d}{dR} \tag{3}$$

$$\tilde{T}_\theta = -\frac{\hbar^2}{2mR^2}\frac{1}{\sin\theta}\frac{d}{d\theta}\left(\sin\theta\frac{d}{d\theta}\right) \tag{4}$$

$$\tilde{T}_\varphi = -\frac{\hbar^2}{2mR^2}\frac{1}{\sin^2\theta}\frac{d^2}{d\varphi^2}, \tag{5}$$

where m represents the reduced mass. The radiative coupling written in the length gauge involves the scalar product of the dipole moment $\vec{\mu}$ (parallel to R for a $\Sigma \rightarrow \Sigma$ transition, as is the case of H_2^+) and the electric-field vector $\vec{\varepsilon}$ which is taken along the laboratory Z-axis:

$$\vec{\mu} \cdot \vec{\varepsilon} = \mu(R) \cos \theta \varepsilon(t) \cos \omega t. \tag{6}$$

The laser pulse carrier-wave frequency is ω and its envelope $\varepsilon(t)$ has a Gaussian shape:

$$\varepsilon(t) = \varepsilon_0 e^{-(t-t_0)^2/\tau^2} \tag{7}$$

of half-width τ. The potential part contains the field-free molecular potentials V as diagonal elements and the matter-field couplings as nondiagonal terms:

$$\tilde{W} = \begin{pmatrix} V_g(R) & -\mu(R)\cos\theta\varepsilon(t)\cos\omega t \\ -\mu(R)\cos\theta\varepsilon(t)\cos\omega t & V_u(R) \end{pmatrix} \tag{8}$$

As clear from Eq. (8), the motion associated with the azimuthal angle φ remains separated under the action of the φ-independent potential term and M_N, the Z-projection of the total rotational angular momentum N, is a good quantum number describing the invariance through rotation about the field-polarization vector. The potential-energy curves as well as the electronic transition moment are taken from Bunkin and Tugov's fit [16]. The initial state of H_2^+ ($^2\Sigma_g^+$) with an isotropic ensemble of *para*- and *ortho*-hydrogen in equilibrium involves two components with $N = 1$, $M_N = 0$ (statistical weight of 1/3), and $N = 1$, $M_N = \pm 1$ (statistical weight of 2/3), each of them having to be propagated separately and further combined using their respective weights [14].

Fourier transform methodology is one of the most popular approaches to solve Eq. (1), the angular variables being treated either by using basis-set expansions or grid techniques. This last approach has recently been significantly improved by Dateo and Metiu [13] with the implementation of a unitary Cayley scheme for T_θ combined with a Feit–Fleck split operator technique. The action of potential and kinetic operators on the wave function is evaluated through a combination of coordinate and momentum representations using an exponential Fourier transform for R and a cosine transform for θ. Although very accurate results are obtained for $M_N = 0$, it turns out that for $M_N = \pm 1$ the cosine transform, which, in principle, assumes even parity, may lead to some numerical unstabilities and inaccuracies in angular-resolved spectra (due to the nonzero derivatives of the $M_N = \pm 1$ wave function at $\theta = 0, \pi$) [17]. The contact transformation, defined by

$$\psi_{M_N}(R, \theta, \varphi; t) = \frac{1}{R\sqrt{\sin\theta}} e^{iM_N\varphi} \Phi_{M_N}(R, \theta; t), \tag{9}$$

is a way out of this difficulty; the numerical unstabilities related to the cosine transform performed on ψ_{M_N} can easily be removed by applying the procedure to Φ_{M_N}. The propagation technique, previously described [13, 14], is based on the repeated use of short-time propagators:

$$\Phi_{M_N}(R, \theta; t + dt) = \exp\left\{-\frac{i}{\hbar}\left[T_R + T_\theta + W_{M_N}(t)\right]dt\right\} \times \Phi_{M_N}(R, \theta; t), \tag{10}$$

where kinetic operators are merely

$$T_R = -\frac{\hbar^2}{2m}\frac{d^2}{dR^2} \tag{11}$$

$$T_\theta = -\frac{\hbar^2}{2m}\frac{1}{R^2}\frac{d^2}{d\theta^2} \tag{12}$$

and the effective potential is

$$W_{M_N}(R, \theta; t) = \tilde{W}(R, \theta; t) - \frac{\hbar^2}{2mR^2} + \frac{\hbar^2}{2mR^2}\frac{(M_N^2 - 1/4)}{\sin^2\theta}. \tag{13}$$

Since the three operators T_R, T_θ, and W_{M_N} do not commute, the exponential in [Eq. (10)] is split into five terms, using Moyal's formula [18] at the third-order approximation $O(\delta t^3)$.

The calculation of kinetic energy spectra involves, in principle, the propagation of the full wavepacket on very large grids, during the total pulse duration, such that the postpulse analysis leads to free-fragment properties. The overall procedure is very time-consuming, especially for a molecule as H_2^+ (odd charged homonuclear ion) due to its asymptotically divergent coupling with the field. To overcome this difficulty, the wave function is split into two regions: an internal and an asymptotic one. The latter is analyzed analyti-

cally by a three-dimensional generalization of the Volkov-type solutions of [15], while the above-mentioned numerical propagation is carried out on the former. Angular-resolved fragments probability distributions are then given by

$$\mathscr{P}(k,\theta)dk = \lim_{t\to\infty}\left[\left|\hat{\psi}_g^A(k,\theta;t)\right|^2 + \left|\hat{\psi}_u^A(k,\theta;t\right|^2\right]dk, \quad (14)$$

where $(t \to \infty)$ means that not only the laser pulse is switched off, but also that there is no outgoing continuum components of the inner part wavepacket. $\hat{\psi}_{g,u}^A$ represent the Fourier transform of the asymptotic region wavepacket components on the g and u channels, respectively.

Results

The angular-resolved fragments spectra are first analyzed with respect to their kinetic energy distributions. In the second step, the basic mechanisms leading to the alignment dynamics are presented and the part that they are playing is illustrated in some examples. Two strong-field intensities are considered, namely, 10^{13} and 5×10^{13} W/cm^2, at a wavelength of $\lambda = 532$ nm, with pulse rise and fall off times of $\tau = 30$ fs and the maximum at $t_0 = 75$ fs, in order to follow as closely as possible the experimental situation [6]. The field-dressed potential energy curves involved in the two main Floquet blocks are displayed in their diabatic and adiabatic representations in Figure 1. The adiabatic representation showing avoided curve-crossings results from the diagonalization of the radiative interaction for the intensity 10^{13} W/cm^2 and a fixed molecule-field orientation ($\theta = 0$ or π, which maximizes the coupling). The curve-crossing regions upon which the interpretation rests are indicated by rectangular boxes: X1 between the ground and the one-photon channels, X2 between the ground and the two-photon channels, and X3 between the two- and three-photon channels. Three initial vibrational states v of H_2^+ are taken into account, their energies corresponding to some specific situations with respect to the height of the adiabatic barrier. At the X1 avoided crossing $v = 2$ lies below and $v = 5$ above this barrier for both field strengths; as for $v = 4$, it lies above the barrier for the highest intensity and below for the lowest.

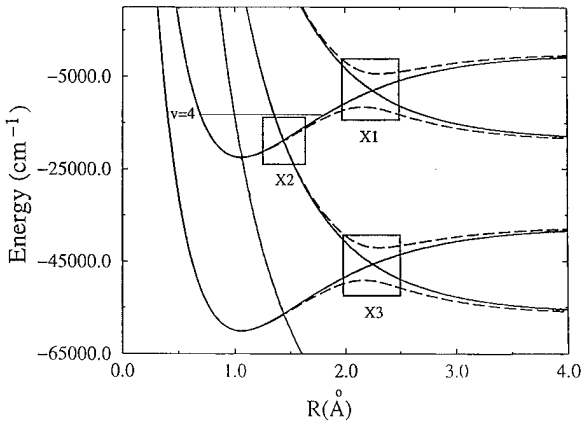


FIGURE 1. Field-dressed potential-energy curves of H_2^+ ($\lambda = 532$ nm), for an intensity of $I = 10^{13}$ W/cm^2, in the diabatic (solid lines) and adiabatic (broken lines) frames. Curve-crossing regions are outlined by rectangular boxes X1, X2, and X3. The energy of the $v = 4$ vibrational level is indicated by the thin horizontal line.

KINETIC ENERGY DISTRIBUTIONS

Three-dimensional viewgraphs of the spectra are given for $I = 10^{13}$ W/cm^2 in Figure 2. A behavior which is typical for ATD can be detected in terms of peaks, in the proton kinetic energy distributions, separated by the photon energy [2, 3]. The branching ratios (relative heights of the so-called one-, two- or three-photon peaks) reflect the energy positioning of the initial states. For $v = 2$, the potential barrier is too high at X1 for the dissociation to proceed by the absorption of a single photon. A third-order matter-field interaction at X2 gives rise to dissociation by absorbing two or three photons. For the intensity under consideration, an important nonadiabatic transition at X3 results in a competition between the two- and three-photon peaks. The situation is completely different for $v = 5$; the field-induced barrier lowering at X1 favors the single-photon process, with the one-photon peak in the spectra. The case of $v = 4$ is intermediate: There is still some competition between the barrier lowering (X1) and the nonadiabatic transition (X2) mechanisms, leading to a spectrum displaying three peaks with a major one-photon peak contribution.

ANGULAR DISTRIBUTIONS

Alignment processes are very sensitive to the dynamics which takes place at the crossing regions X1, X2, and X3. They are basically controlled

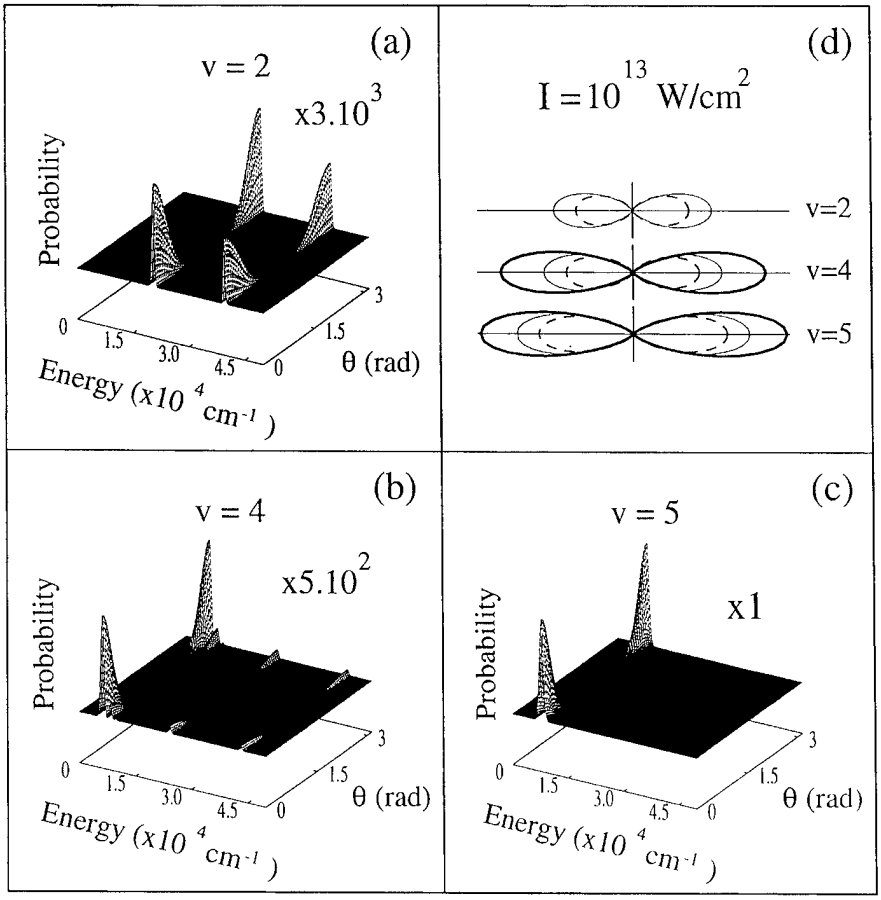


FIGURE 2. Angular-resolved kinetic energy spectra for the initial vibrational level $v = 2$ [panel (a)], $v = 4$ [panel (b)], and $v = 5$ [panel (c)] of H_2^+ irradiated by a $\lambda = 532$ nm laser delivering an intensity of $I = 10^{13}$ W/cm^2. Panel (d) gathers angular distributions in polar representation, for each v, of fragments contributing to the first photon peak (thick solid line) to the second photon peak (thin solid line) or the third photon peak (broken line).

by two mechanisms: the barrier lowering and the nonadiabatic transition. Let us examine them separately:

Barrier Lowering

In strong-field situations, the adiabatic potential barrier is lowered in an efficient way proportional to the radiative coupling, i.e., $\sqrt{I}\mu(R)\cos\theta$. For a given intensity, this lowering is much more important for $\cos\theta \sim 1$, i.e., for $\theta \sim 0$ or π. For $\cos\theta \sim 0$ ($\theta \sim \pi/2$), the high potential barrier is hardly penetrable. The torque, which is exerted by the laser on the molecule, allows the wavepacket to skirt around the potential barrier and find the minimum-energy pathway toward the dissociative valley (i.e., for directions close to $\theta = 0$ or π). In later steps, the large distance dynamics is no longer affected by an additional torque (due to the R^{-2} factor in T_θ [Eq. (12)]), such that the angular distribution is close to its value at the position X1 of the barrier, where alignment with the field ($\theta = 0$ or π) is favored.

Nonadiabatic Transition

In avoided crossing regions X2 and X3, the dynamics proceeds via a nonadiabatic jump from the upper attractive to the lower repulsive adiabatic surfaces. This is monitored by a nonadiabatic kinetic interstate coupling located at the avoided crossing point and presenting an amplitude maximum for $\theta \sim \pi/2$. We recall that strong radiative interactions in the diabatic frame, either for $\theta = 0$,

π or for high fields, correspond, accordingly, to small kinetic, nonadiabatic couplings responsible for the dissociation in the adiabatic frame. Finally, less aligned fragments are expected when nonadiabatic transitions are responsible for the dissociation.

In realistic situations, it is in the interplay of the two mechanisms that the interpretation is to be looked for. A direct consequence of the previous analysis remains, however, that the one-photon peak, resulting from the barrier-lowering mechanism (X1), leads to aligned fragments, whereas the two-photon peak resulting from a single nonadiabatic transition (X2) is characterized by less aligned fragments. The protons with a velocity distribution within the three-photon peak are even less aligned, as two nonadiabatic transitions (X2 and X3) are involved in their dynamics. This is clearly illustrated in Figure 2 for all three initial states $v = 2$, 4, or 5. Another direct consequence is the intensity dependence of the alignment. An increase in intensity produces more efficient barrier lowering, resulting in more aligned fragments when the leading mechanism is precisely the tunneling at X1. This can be seen in the angular distributions of the one-photon peaks of $v = 4$ and 5 displayed in Figure 3. Alignments are efficiently increased when going from 10^{13} to 5×10^{13} W/cm$^2 \cdot v = 5$, with an energy well above the adiabatic potential barriers for this range of intensities, is less sensitive to the tunneling mechanism. The increase in its alignment is much less than $v = 4$. Conversely, when nonadiabatic transitions monitor the dynamics, distributions are less aligned at high fields. This is the case for $v = 4$ and 5 in Figure 3 and corroborates the experimental observation of [6].

More detailed analysis is required for a thorough interpretation of some observations on the alignment patterns in terms of the role played by the initial vibrational state v or the intensity-dependent relative contribution of the initial angular distribution (i.e., $M_N = 0$ or ± 1). Two arguments can be invoked to support this analysis:

(i) Different initial vibrational states give rise to different kinetic energies during the dissociation process. A wavepacket issued from a high v presents a high kinetic energy distribution and feels the alignment effects of the X2 and X3 avoided crossing regions in a reduced way. It is also less sensitive to the long-range dynamics of the two-photon channel surface which tends to favor the $\theta \sim \pi/2$ direction for the fragmentation. This is why the fragments of a given kinetic energy (i.e., within a given peak) are more aligned for higher initial vibrational states. Figure 2 shows, precisely, that fragments contributing to the two-photon peak are more efficiently aligned for $v = 5$ than for

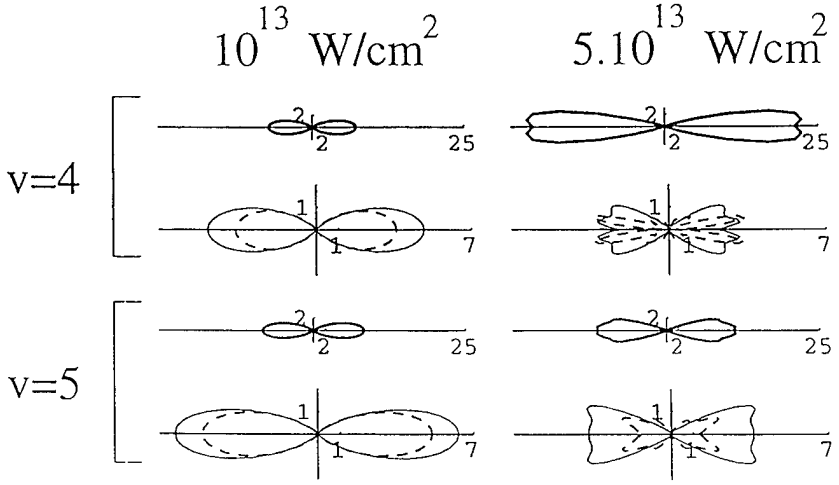


FIGURE 3. Angular distributions, in polar representation, of photons contributing to the first (thick solid line), second (thin solid line), or third photon peaks (broken line) and resulting from the photodissociation of H_2^+ ($v = 4$ and 5) for two field strengths $I = 10^{13}$ and 5×10^{13} W / cm^2 ($\lambda = 532$ nm). Note that the relative contributions of the three peaks to the angular distributions are different, the scales being indicated by the numbers (in arbitrary units) on the coordinate axis.

$v = 4$. The same observation is valid for the three-photon peak whose alignment increases with v.

(ii) To obtain results corresponding to an initial isotropic ensemble of molecules, an incoherent sum of two probabilities based on two initial angular distributions $Y_{10}(\theta, \varphi)$ (i.e., $M_N = 0$) and $Y_{11}(\theta, \varphi)$ (i.e., $M_N = \pm 1$) is to be performed [$Y_{N, M_N}(\theta, \varphi)$ designates the spherical harmonics and $Y_{1,-1}$ leads to the same result as Y_{11} because the total Hamiltonian does not depend upon the sign of M_N, as is clear from Eq. (13)]. Having in mind that Y_{10} behaves as $\cos\theta$ and Y_{11} as $\sin\theta$, the potential barrier, with a maximum at $\theta = \pi/2$, is hardly penetrable for Y_{11}. It is only for very strong fields that the barrier is lowered enough for the $M_N = \pm 1$ component to be in competition with the $M_N = 0$ component. The consequence is that for high intensities (or for vibrational levels above the barrier) fragments resulting from an initial Y_{11} distribution may significantly contribute to the spectrum, producing less aligned distribution patterns. This argument may also contribute to support the fact observed in Figure 3 that at high intensity, $I = 5 \times 10^{13}$ W/cm^2, the one-photon peak is less aligned for $v = 5$ than for $v = 4$ (the potential barrier is more transparent for the Y_{11} component of the higher-energy state $v = 5$ as compared to $v = 4$).

We finally note that the polar plots of some angular distributions show, at the high intensity of Figure 3, off-axis structures for both $v = 4$ and 5. Such structures have already been experimentally evidenced in similar contexts, i.e., in the angular distribution of the photoelectron ATI spectrum of xenon [19] and the angular distributions of O^+ and S^+ from dissociation of CO_2 or CS_2 [20]. In the latter case, an interpretation based on molecular pendular states arising from the large field-induced polarizabilities of these systems is given. In the former case, the mechanism which is invoked is rather close to the one monitoring the dissociation dynamics of the ATD regime. More precisely, the rings of the ionization dynamics are interpreted in terms of rescattering from the ion core of the tunneling component of the continuum wave function [19]. Here, it is the interferences (enhanced by the high-field intensity) between the short-distance nonadiabatic transition (responsible of the multiphoton excitation at X2) and the large distance tunneling (responsible of the dynamics at X1) which are at the origin of the mixing of Y_{10} and Y_{11} distributions and of bond softening and vibrational trapping mechanisms manifesting themselves as structures in the strongly anisotropic angular distributions of dissociation products.

As a word of conclusion, the widely discussed alignment of the fragments resulting from a multiphoton dissociation process is basically related to an adiabatic potential energy barrier lowering (which is also responsible for the bond softening). When using intense fields, there are, however, other mechanisms which also lead to dissociation, namely, the nonadiabatic transitions (as the ones involved in vibrational trapping). These transitions favor the $\theta = \pi/2$ direction in the dissociation dynamics. The most original finding is the possibility, at least for some wavelengths [14] or for some kinetic energies, to observe photofragments in a plane orthogonal to the polarization axis, a possibility enhanced by the high intensity. This is the first step aimed at the detailed interpretation of the intensity dependence of angular-resolved spectra and, in particular, to the understanding of some experimental observations of less aligned fragments with increasing field strength [6]. Work is in progress in our group for a more detailed study of the experimental data of [6].

ACKNOWLEDGMENT

I acknowledge a grant of computing time on a Cray C-98 from the Institut du Développement et des Ressources en Informatique Scientifique I.D.R.I.S. under Project No. 940425.

References

1. A. D. Bandrauk and S. C. Wallace, Eds., *Coherence Phenomena in Atoms and Molecules in Laser Fields*, Vol. 287, NATO Advanced Study Institute, Series B: Physics (Plenum, New York, 1992).
2. Ph. Bucksbaum, A. Zavriyev, H. G. Müller, and D. W. Schumacher, Phys. Rev. Lett. **64**, 1883 (1990).
3. A. Giusti-Suzor, X. He, O. Atabek, and F. H. Mies, Phys. Rev. Lett. **64**, 515 (1990).
4. B. Yang, M. Saeed, L. F. Di Mauro, A. Zavriyev, and Ph. Bucksbaum, Phys. Rev. A **44**, R1458 (1991).
5. K. Codling and J. L. Frasinski, J. Phys. B **26**, 783 (1993).

6. A. Zavriyev, Ph. Bucksbaum, H. G. Müller, and D. W. Schumacher, Phys. Rev. A **42**, 5500 (1990).
7. D. Normand, L. A. Lompré, and C. Cornaggia, J. Phys. B **25**, L497 (1992).
8. D. T. Strickland, Y. Beaudoin, P. Dietrich, and P. B. Corkum, Phys. Rev. Lett. **68**, 2755 (1992).
9. A. D. Bandrauk and M. H. Sink, J. Chem. Phys. **74**, 1110 (1981).
10. A. Giusti-Suzor and F. H. Mies, Phys. Rev. Lett. **68**, 3869 (1992).
11. E. E. Aubanel, J. M. Gauthier, and A. D. Bandrauk, Phys. Rev. A **48**, 2145 (1993). E. E. Aubanel, A. Conjusteau, and A. D. Bandrauk, Phys. Rev. A **48**, R4011 (1993).
12. E. Charron, A. Giusti-Suzor, and F. H. Mies, Phys. A **49**, R641 (1994).
13. C. E. Dateo and H. Metiu, J. Chem. Phys. **95**, 7392 (1991).
14. R. Numico, A. Keller, and O. Atabek, Phys. Rev. A **52**, 1298 (1995).
15. A. Keller, Phys. Rev. A **52**, 1450 (1995).
16. F. V. Bunkin and I. I. Tugov, Phys. Rev. A **8**, 601 (1973).
17. R. Numico, A. Keller, and O. Atabek, in preparation.
18. J. E. Moyal, Proc. Camb. Philos. Soc. **45**, 99 (1949).
19. B. Yang, K. J. Schafer, B. Walker, K. C. Kulander, P. Agostini, and L. F. Di Mauro, Phys. Rev. Lett. **71**, 3770 (1993).
20. G. Ravindra Kumar, P. Gross, C. P. Safvan, F. A. Rajgara, and D. Mathur, Phys. Rev. A **53**, 3098 (1996).

An Ab Initio Study of Oxygen Vacancies and Doping Process of Nb and Cr Atoms on TiO_2 (110) Surface Models

J. R. SAMBRANO,[1] J. ANDRÉS,[2] A. BELTRÁN,[2] F. R. SENSATO,[3] E. R. LEITE,[3] F. M. L. G. STAMATO, E. LONGO[3]

[1]*Departamento de Matemática, Universidade Estadual Paulista, C.P. 473, 17030 360 Bauru, SP, Brasil*

[2]*Departament de Ciències Experimentals, Universitat Jaume I, Apartat 224, 12080 Castelló, Spain*

[3]*LIEC, Departamento de Química, Universidade Federal de S. Carlos, C.P. 676, 13565 905 S. Carlos, SP, Brasil*

Received 27 March 1997; revised 11 August 1997; accepted 13 August 1997

ABSTRACT: We theoretically investigated how the formation of oxygen vacancies and the addition of niobium and chromium atoms as dopants modify the varistor properties of TiO_2. The calculations were carried out at the HF level using a contracted basis set, developed by Huzinaga et al., to represent the atomic centers on the (110) surface for the large $(TiO_2)_{15}$ cluster model. The change of the values for the net atomic charges and band gap after oxygen vacancy formation and the presence of dopants in the lattice are analyzed and discussed. It is shown that the formation of oxygen vacancies decreases the band gap while an opposite effect is found when dopants are located in the reduced surface. The theoretical results are compared with available experimental data. A plausible explanation of the varistor behavior of this system is proposed. © 1997 John Wiley & Sons, Inc. Int J Quant Chem **65:** 625–631, 1997

Key words: ab initio; oxygen vacancy; doping; titanium oxide surface; varistor ceramics

Correspondence to: J. R. Sambran.

Contract grant sponsor: Bancaixa-UJI.
Contract grant number: BP-9601.
Contract grant sponsors: CAPES/PICD (Brazil); FAPESP (Brazil); CNPq (Brazil).

© 1997 John Wiley & Sons, Inc.
CCC 0020-7608 / 97 / 050625-07

Introduction

In recent years, interest in the surface chemistry of metal oxides has rapidly grown. The enhanced attention is related to different types of catalytic reactions on oxide surfaces and the preparation of thin films of these materials with important technological applications [1–11]. Metal oxides, such as ZnO, SnO_2, and TiO_2, are materials with varistor properties that are used as semiconductor devices which present high nonlinearity between the current density and electric field, thus being suitable for transient voltage suppression [1–3]. Most of the chemistry of metal oxides is due to the presence of highly reactive defective sites such as cation or anion vacancies and/or a doping process by substitution of metal cations. As most of the surfaces studied experimentally contain defects resulting from preparation conditions or from ionic or electronic bombardment, one is led, after the theoretical study of ideal surfaces, to consider the case of surfaces containing defects. Once the vacancies are formed, their electronic nature can be changed by adding or removing electrons. Therefore, the electronic behavior is the key concept for understanding the operation.

In particular, different research groups [2–5] have studied doped TiO_2, ceramics having useful varistor properties, with nonlinearity coefficients (α) values in the range of $\alpha = 3$–12, α being defined by the relation $I = KV^{\alpha}$, where I is the current; V, the voltage; and K, a proportionality constant [8]. The presence of this potential barrier is due to the creation of defects formed during sintering of TiO_2 systems. The lack of lattice periodicity due to intrinsic defects leads to a high density of structural defects that can originate a potential barrier associated to a double space charge distribution and this phenomenon establishes variable resistance as a function of the applied electric field to the solid.

Understanding the chemical and physical properties of local active sites of metal oxides has a twofold interest: First, from a fundamental point of view, it is interesting to see which new features are induced by the presence of defects in the surface and how these surface defects are related to the bulk electronic and atomic structure. Second, the practical interest results from the numerous technological applications where they are used. Among these, varistor properties are probably the most important for us.

This is a collaborative project between experimental and theoretical research groups. Our increasing experimental efforts [7,8,12–14] can be accompanied by quantum chemical studies of local defects; among them, the cluster approach [5–17] is probably the most widely adopted and many successful applications of this model have been made on TiO_2 [18,19] and related systems [20–23]. The aim of this work was to use ab initio techniques to investigate the electronic structures of doped TiO_2 systems in order to understand, at the molecular level, the varistor properties of TiO_2 and to rationalize the role played by the oxygen vacancies and the substitution of Nb and Cr atoms, as dopants, replacing Ti atoms in the lattice.

The article is organized as follows: The model and method of calculation are summarized in the next section. The results and discussion are presented in the third section. A short section of conclusions closes this article.

Models and Method of Calculation

TiO_2 crystallizes in the rutile structure, which has tetragonal D_{4h}^{14} symmetry. There are two formula units per primitive unit cell, with the threefold-coordinated oxygen atoms forming a distorted octahedron around the titanium atoms [24]. This material has a relatively strong ionic character and its bulk valence band has a dominant O-p orbital character and the orbital composition of the lower conduction bands result from atomic Ti-3d states. Experimental analysis [25–28] shows that the (110) surface is the most stable face of TiO_2 and oxygen vacancies are by far the most frequently occurring defect. Therefore, we restrict ourselves here to the study of this structure the different types of defects and illustrate some basic aspects of the varistor phenomena. This face is a nonpolar surface that can be studied even in its bulk-derived experimental geometry. The rutile structure can be regarded as consisting of (110) planes of atoms containing both metal, Ti, and oxygen, O, atoms, separated by planes containing oxygen alone, so that the sequence of planes is O —Ti_2O_2—O—O—Ti_2O_2—O, etc. The entire crystal can then be built up of the symmetrical three-

plane O—Ti_2O_2—O units. We selected the large $(TiO_2)_{15}$ cluster model, shown in Figure 1, derived from the crystallographic data.

Models for the stoichiometric (110) surface of the titanium oxide surface in the oxidized and reduced forms, as well as doped with niobium and chromium atoms, were constructed in this work by using the usual repeating slab geometry. The following models were selected: $(TiO_2)_{15}$ **(I)** to represent the fully oxidized surface; $(TiO_2)_{14}TiO$ **(II)** and $(TiO_2)_{13}(TiO)_2$ **(III)** were made by removing one oxygen in position 16 and two oxygens in positions 16 and 17 from model **I**, respectively. $(TiO_2)_{13}(CrO)_2$ **(IV)** to represent the surface doped with the Cr atom in positions 14 and 14′ and $(TiO_2)_{13}(NbO)_2$ to represent the surface doped with the Nb atom in sites 3 and 3′ **(V)** and sites 1 and 1′ **(VI)**; $(TiO_2)_{11}(NbO)_2(CrO)_2$ corresponds to the surface simultaneously doped with the Nb atom in the 1 and 1′ sites and Cr in the 14 and 14′ sites **(VII)**. In model **VIII**, the Nb atom is placed in the 3 and 3′ sites, while the Cr atom is located in the 14 and 14′ sites, and in model **IX**, Nb is placed in the 14 and 14′ sites, while the Cr atom is located in the 1 and 1′ sites.

The calculations were carried out with the Gaussian94 package [29]. The ab initio Hartree–Fock (HF) level of the theory was employed with the contracted basis set for titanium (4322/42/3), oxygen (33/3), niobium (43333/433/43), and chromium (4322/42/3) atoms developed by Huzinaga et al. [30,31]. The orbital exponent and contraction coefficients of the atomic wave functions were determined by optimizing the total energies as explained in detail in a previous article of Sakai et al. [32]. All calculations were carried out in the ground singlet electronic state. HOMO–LUMO corresponds to the band gap value.

In addition, we try to determine how the boundary conditions can affect the different values of the band gap and net atomic charges of the different cluster models. The computational approach for the theoretical treatment is based on continuum models [33]: The cluster is embedded in a cavity while the environment, treated as a continuous medium having the same dielectric constant as the bulk system, is incorporated into the solute Hamiltonian as a perturbation. In this reaction-field approach, the bulk system is polarized by the environment. The electronic distribution of the cluster system polarizes the continuum which generates an electric field inside the cavity, which, in turn, affects the solute's geometry and electronic structure. The implementation of this

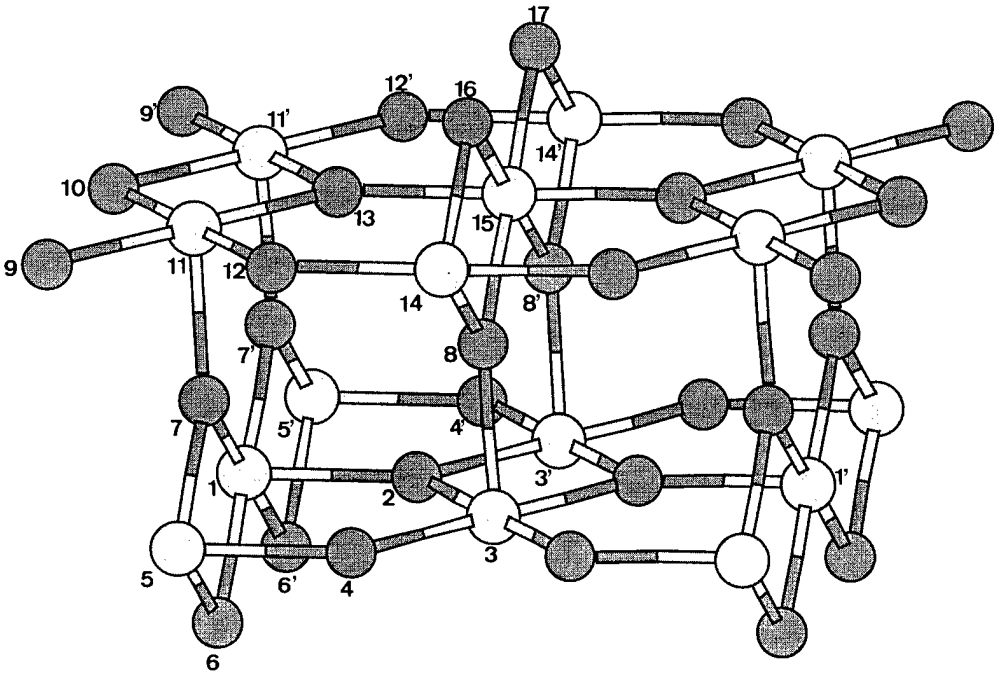


FIGURE 1. $(TiO_2)_{15}$ cluster model for the etoichiometric (110) surface. Black and gray circles represent oxygen and metal ions, respectively.

interaction scheme is achieved through the self-consistent reaction field method developed initially by Tapia [34,35]. In this work, we employed the continuum model of Rivail et al. [36–38] based on the use of cavities and a multipolar expansion of the solute electrostatic potential. Calculations were made using ellipsoidal cavities surrounded by a continuum of the dielectric constant (ε = 86.0, bulk TiO_2 rutile) and multipolar expansion up to order 6. An analysis and comparison between the results of the different cluster models obtained *in vacuo* and by taking into account a continuum representation of the environment show that the values of the band gap and net atomic charges are similar. For this reason, only the results given *in vacuo* are presented in this work.

Results and Discussion

Charges on atoms are calculated using the Mulliken population analysis. In addition, to improve the population representation, we selected the natural population analysis based on Weinhold's natural bond orbital (NBO) [39–41]. The Mulliken charges are always lower than the NBO, but similar trends are obtained with respect to the variation between pure (**I**) and doped (**IV**, **V**, **VI**, **VII**, **VIII**, and **IX**) clusters and clusters with vacancies (**II**, **III**). It seems difficult to discuss the absolute values of the charge on the individual Ti and O atoms; however, some useful information could be drawn from the results by comparing the charge on the atoms in the corresponding model.

The values of the net atomic charge and band gap for the nine models are presented in Table I. The results point out that the surface is reduced when oxygen vacancies are formed in the **II** and **III** models, with a corresponding decrease in the charge density of titanium, i.e., the Ti_{14} and Ti_{15} atoms decrease their positive charge whereas changes in the charge for more distant atoms are very small. This result can be represented by the following equation:

$$TiO_2 \overset{TiO_2}{\rightarrow} Ti''_{Ti} + V_o^{\cdot\cdot} + O_o^x + \tfrac{1}{2}O_2, \qquad (1)$$

in which the species Ti''_{Ti} are formed.

Therefore, the creation of intrinsic defects in the structure of titanium oxide promotes the reduction of the titanium atoms. The ab initio results reproduce, in a reasonable way, this redox reaction which occurs in *n*-type semiconductors such as TiO_2. As experimentally verified in our laboratory [7,8,12–14], there is a decreasing of the band gap value in the formation of *n*-type semiconductors, which is due to the $V_{\ddot{o}}$- and V_o-formed species. The results show that this effect is proportional to the increase of the concentration of the vacancies. The two-step reduction of the titanium atom can be rationalized on the basis of the simulation of one and two oxygen vacancies' formation. The percentual variation of the charge density of oxidized titanium to reduced titanium, Ti'_{14} and Ti_{15}, is around 40 and 6%, respectively, going from model **I** to model **II**. When the second vacancy is formed, Ti_{14} experiences a percentual reduction of 45% in the charge density. These results suggest the formation of the species Ti''_{Ti}. Marucco et al. [43] proposed that the defects induced by the reduction process in titanium dioxide are oxygen vacancies and interstitial titanium, their relative importance

TABLE I
Charge on titanium, oxygen, chromium, and niobium atoms and band gap (eV).

Atoms	I	II	III	IV	V	VI	VII	VIII	IX
$Ti_{(15)}$	1.70	1.60	1.46	1.49	1.37	1.31	1.07	1.42	1.51
$X_{(14)}$	1.56	1.60	0.87	0.97	1.19	1.22	1.15	1.20	1.07
$X_{(14')}$	1.56	0.94	0.87	0.97	1.19	1.22	1.15	1.20	1.07
$X_{(1)}$	1.71	1.62	1.55	1.70	1.63	1.60	1.61	1.62	1.32
$X_{(1')}$	1.71	1.62	1.55	1.70	1.63	1.60	1.61	1.62	1.32
$X_{(3)}$	1.73	1.64	1.71	1.77	1.68	1.73	1.67	1.57	1.75
$X_{(3')}$	1.73	1.74	1.71	1.77	1.68	1.73	1.67	1.57	1.75
Band gap	3.53	2.28	1.98	3.64	2.57	3.64	3.20	2.62	3.12

X is Ti, Nb, or Cr in the *x* and *x'* positions on the crystal cluster of TiO_2.

being governed mainly by temperature. Oxygen vacancies dominate below 1000°C. To interpret the electrical behavior, one can assume that an intermediate ion between Ti^{4+} and Ti^{2+}, the Ti^{3+} ion, can be formed during vacancy formation, according to the equation

$$2Ti_{Ti}^{x} + O_{o}^{x} \rightarrow 2Ti'_{Ti} + V_{\ddot{o}} + \tfrac{1}{2}O_2. \qquad (2)$$

This assumption is also in agreement with the experimental work of Watanabe et al. [9] which studied the reduction of the SnO_2 surface associated with the change of the valence state from Sn^{+4} to Sn^{+2}, which is similar to that observed in the TiO_2. These authors pointed out a decreasing of the band gap value associated with an increment of oxygen vacancies. On the basis of their results, they proposed the coexistence of an intermediate Sn_3O_4 structure in the reduced crystal (SnO_{2-x}), which characterizes the Sn^{3+} ion. In the present work, the substitution of the Ti atom by a metal, either Nb or Cr, should involve a change in the stoichiometric plane [O]—[TiO_2]—[O], with formal charges [2 −]—[4 +]—[2 −], by the planes [O]—[Cr_2O_2]—[O] or [O]—[Nb_2O_2]—[O], with formal charges [2 −]—[2 +]—[2 −] and [2 −]—[6 +]—[2 −], respectively. The results of Table I support this suggestion, showing the coexistence of two species with different charge densities in the site after reduction: the Ti^{+3} and the Ti^{+2} species.

After substitution of two Cr atoms for two Ti atoms, the **IV** model, the Ti_1 atoms increase their positive charge, around 10%, while the O_{12} atoms increase their negative charge. After substitution of two Nb atoms for two Ti atoms, the **V** model, Ti_5, Ti_{11}, and Ti_{15} atoms decrease their positive charge around 6%, while Ti_1 and Ti_{14} atoms increase their positive charge around 5 and 37%, respectively, and O_4 atoms decrease their negative charge while O_{12} atoms increase their negative charge. The double substitution of niobium and chromium atoms in Ti sites, the **VI** model, yields a decreasing of the positive charge for Ti_5, Ti_{11}, and Ti_{15} atoms, 4, 6, and 10%, respectively, while Ti_{14} atoms increase their positive charge about 40% and O_4 and O_{10} atoms increase their negative charge. For the **VII** model, Ti_3, Ti_{11}, and Ti_{15} atoms decrease their positive charge around 2, 4, and 27%, respectively, and O_9, O_{10}, and O_{12} atoms increase their negative charge while O_7 atoms decrease their negative charge. For the **VIII** model, Ti_1 atoms increase their positive charge about 5%, while O_{12} atoms increase their negative charge. For the **IX** model, Ti_{11} atoms decrease their positive charge about 9%, while Ti_{14} atoms increase their positive charge about 23%.

Table I presents the calculated values of the band gap, which shows the influence of vacancy formation and the presence of dopants on the surface of TiO_2. There is a partial oxidation when chromium substitutes titanium in the lattice and the species Cr'_{Ti} and $V_{\ddot{o}}$ are formed to preserve the electroneutrality, thus decreasing the conductivity of TiO_2. When the reduced TiO_2 is doped with chromium or niobium, the band gap value increases and TiO_2 becomes an *n*-type semiconductor when a vacancy is formed. Our results for the doped TiO_2 agree with the formation of an *n*-type semiconductor; however, this effect is highly dependent on the location of the dopant in the lattice. The band gap presents the lowest value when the doping process takes place in the Ti_3 or $Ti_{3'}$ (**V** and **VIII** models). Similar values of the band gap are found when two Cr atoms or two Nb atoms are located in position 14, 14′, or 1,1′, respectively (**IV** and **VI** models). There is a partial oxidation when Cr or Nb substitutes titanium in the lattice and the species X'_{Ti} (X = Cr, Nb) and V''_{O} are formed to preserve the electroneutrality, thus decreasing the conductivity of TiO_2. This result agrees with the experimental results of Gupta and Carlson [4] and Leite et al. [7] which characterize the degradation of the varistor. For example, the addition of Nb_2O_5 in small amounts to the TiO_2 system leads to an increase of the electronic conductivity in the TiO_2 lattice [13,14]. It is promoted by the formation of defects in the surface and in the interior of the grain, tending to electroneutralize mutually. The varistor behavior of TiO_2 can be explained by the introduction of defects in the crystal lattice that are responsible for the formation of Schottky-type potential barriers at the grain boundaries. By analogy with the atomic defect model proposed by Gupta and Carlson [4] for the ZnO varistor, the potential barrier is formed by intrinsic defects of TiO_2 (oxygen vacancy and interstitial ionized titanium atoms) and by extrinsic defects created by solid substitution of dopants and negative charges at the interface. To explain the adsorption of oxygen on the TiO_2 surface, Bueno et al. [8] proposed reactions 1 and 2 to be responsible for the formation of a potential barrier and, consequently, for the nonlinearity of TiO_2-based varistors.

Conclusions

We carried out an ab initio study on the TiO_2 system in order to rationalize our previous experimental results. The varistor properties of this material were analyzed taking into account the formation of oxygen vacancies and the presence of Nb and Cr as dopants in the lattice. Large cluster models were selected and a contracted basis set developed by Huzinaga et al. was used to represent the atomic centers. The specific details of the process may change at higher levels of theory (e.g., inclusion of correlation energy), but despite the approximate procedure of the calculations (e.g., band gap and Mulliken charges values obtained at HF level and embedding representation of cluster models) employed here, some important features were clarified. Taken together with the results of our previous experimental studies, the following conclusions can be drawn from the results reported in this study: (i) The ab initio calculations show that the formation of oxygen vacancies in TiO_2 leads to a decrease in the band gap value. (ii) Two different valence states of titanium may coexist, probably Ti^{+2} and Ti^{+3}. (iii) The band gap values are strongly affected by the doping process. (iv) The global analysis of the results agrees with the experimental data and the physical conception of the performance of the TiO_2 varistor. (v) Voltage barrier formation and degradation, associated with the band gap, can be explained by a redox reaction between atomic defects. This fact can be of relevance for the understanding of varistor properties of TiO_2 and related materials.

ACKNOWLEDGMENTS

This work was supported by research funds of the Bancaixa-UJI (Project BP-9601) and Brasilian Funding Agencies: CAPES/PICD, FAPESP, and CNPq. We are most indebted to the Servei d'Informàtica de la Universitat Jaume I for providing us with multiple computing facilities. The authors gratefully acknowledge Dr. I. Tuñon for technical support and useful comments on the continuum model calculations.

References

1. T. Masuyama, Jpn. J. Appl. Phys. **7**, 1294 (1968).
2. S. L. Yang and J. M. Wu, J. Mater. Res. **10**, 345 (1995).
3. M. Inamada, Jpn. J. Appl. Phys. **17**, 1 (1978).
4. T. K. Gupta and W. G. Carlson, J. Mater. Sci. **20**, 4091 (1985).
5. J. Pennewiss and B. Hoffmann, Mater. Lett. **40**, 219 (1990).
6. G. Sanon, R. Rup, and A. Mansingh, Phys. Rev. **44**, 5681 (1991).
7. E. R. Leite, J. A. Varela, and E. Longo, J. Mater. Sci. **27**, 5325 (1992).
8. P. R. Bueno, E. Camargo, E. Longo, E. Leite, S. A. Pianaro, and J. A. Varela, J. Mater. Sci. Lett. **15**, 2048 (1996).
9. Y. Watanabe, H. Endo, H. Semba, and M. Takata, J. Non-Cryst. Solids **178**, 84 (1994).
10. R. G. Egdell, A. Gulino, C. Rayden, G. Peacock, and P. Cox, J. Mater. Chem. **5**, 499 (1995).
11. K. I. Hadjiivanov and D. G. Klissurski, Chem. Soc. Rev. **25**, 61 (1996).
12. S. A. Pianaro, P. R. Bueno, E. Longo, and J. A. Varela, J. Mater. Sci. Lett. **14**, 692 (1995).
13. S. A. Pianaro, P. R. Bueno, E. Longo, and J. A. Varela, Appl. Pat. (June 1994) (Instituto Nacional de Propriedade Indultrial).
14. P. R. Bueno, S. A. Pianaro, E. C. Pereira, E. Longo, and J. A. Varela, submitted.
15. P. Jena, S. N. Khanna, and B. K. Rao, Eds. (Kluwer, Dordrecht, The Netherlands, 1992).
16. P. S. Bagus and G. Pacchioni, in *Cluster Models for Surface and Bulk Phenomena*, G. Pacchioni, P. S. Bagus and F. Parmigiani, Eds. (Plenum, New York, 1991), Vol. 283, Series B, p. 233.
17. L. G. M. Pettersson and T. Faxen, Theor. Chim. Acta. **83**, 345 (1993).
18. A. Hagfeldt, H. Siegbahn, S. E. Lindquist, and S. Lunell, Int. J. Quantum Chem. **44**, 477 (1992).
19. A. Hagfeldt, S. Lunell, and H. Siegbahn, Int. J. Quantum Chem. **49**, 97 (1994).
20. T. S. Rantala, V. Lantto, and T. T. Rantala, Phys. Scr. **T54**, 252 (1994).
21. J. B. L. Martins, E. Longo, and J. Andrés, Int. J. Quantum Chem. **27**, 643 (1993).
22. J. B. L. Martins, J. Andrés, E. Longo, and C. A. Taft, J. Mol. Struct. (Theochem) **330**, 301 (1995).
23. J. B. L. Martins, V. Moliner, J. Andrés, E. Longo, and C. A. Taft, J. Mol. Struct. (Theochem) **330**, 447 (1995).
24. J. Pennewiss and B. Hoffmann, Mater. Lett. **40**, 536 (1982).
25. V. M. Bermudez, Prog. Surf. Sci. **11**, 1 (1981).
26. G. Heiland and H. Lüth, in *The Chemical Physics of Solid Surfaces and Heterogeneous Catalysis*, D. A. King and D. D. Wooduff, Eds. (Elsevier, Amsterdam, 1984), Vol. III.
27. V. E. Henrich, Prog. Surf. Sci. **14**, 175 (1983).
28. V. E. Henrich, Rep. Prog. Phys. **48**, 11 (1985).
29. M. J. Frisch, G. W. Trucks, H. B. Schlegel, P. M. W. Gill, B. G. Johnson, M. A. Robb, J. R. Cheeseman, T. Keith, G. A. Peterson, J. A. Montgomery, K. Raghavachari, M. A. Al-Laham, V. G. Zakrzewski, J. V. Ortiz, J. B. Foresman, J. Cioslowski, B. B. Stefanov, A. Nanayakkara, M. Challacombe, C. Y. Peng, P. Y. Ayala, W. Chen, M. W. Wong, J. L. Andres, E. S. Replogle, R. Gomperts, R. L. Martin, D. J. Fox, J. S. Binkley, D. J. Defrees, J. Baker, J. P. Stewart, M.

Head-Gordon, C. Gonzalez, and J. A. Pople, *GAUSSIAN94, Revision B.1* (Gaussian, Inc., Pittsburgh, PA, 1995).

30. S. Huzinaga, Comput. Phys. Rep. **2**, 279 (1985).
31. S. Huzinaga, J. Andzelm, M. Klobukowski, E. R. Adzio-Andzelm, Y. Sakai, and H. Tatewaki, *Gaussian Basis Sets for Molecular Calculations* (Elsevier, Amsterdam, 1984).
32. Y. Sakai, H. Tatemaki, and S. Huzinaga, J. Comput. Chem. **3**, 6 (1982).
33. T. Tomasi and Persico, M. Chem. Rev. **94**, 2027 (1994).
34. O. Tapia and O. Goscinski, Mol. Phys. **29**, 1653 (1975).
35. O. Tapia, *Theoretical Models of Chemical Bonding*, Z. B. Maksic, Ed. (Springer-Verlag, Berlin, 1992, p. 435.
36. J. L. Rivail and D. Rinaldi, Chem. Phys. **18**, 233 (1976).
37. J. L. Rivail, D. Terryn, D. Rinaldi, and M. F. Ruiz-López, J. Mol. Struct. (Theochem) **120**, 387 (1985).
38. D. Rinaldi, J. L. Rivail, and N. J. Rguini, J. Comp. Chem. **13**, 675 (1992).
39. A. E. Reed, L. A. Curtiss, and F. Weinhold, Chem. Rev. **88**, 899 (1988).
40. J. E. Carpenter and F. Weinhold, J. Mol. Struct. (Theochem) **169**, 41 (1988).
41. J. P. Foster and F. Weinhold, J. Am. Chem. Soc. **102**, 7211 (1980).
42. A. E. Reed, R. B. Weinstock, and F. Weinhold, J. Chem. Phys. **83**, 735 (1985).
43. J. F. Marucco, J. Gaustron, and P. Lemasson, J. Phys. Chem. Sol. **42**, 363 (1981).

Ab Initio Calculations of the Magnetic Exchange Coupling in Sulfur-Bridged Binuclear Ni(II) Complexes

K. FINK, C. WANG, V. STAEMMLER

Lehrstuhl für Theoretische Chemie, Ruhr-Universität Bochum, D-44780 Bochum, Germany

Received 29 March 1997; revised 16 June 1997; accepted 19 June 1997

ABSTRACT: The geometry dependence of the exchange integrals and the total energies of sulfur-bridged complexes of the types $L_5NiSNiL_5$, $L_4NiS_2NiL_4$, and $L_3NiS_3NiL_3$ is studied by quantum chemical ab initio methods. The linear monobridged complex is antiferromagnetic, the bi- and triply-bridged complexes are ferromagnetic for NiSNi angles between 85° and 100° and antiferromagnetic for smaller and larger angles. The superexchange mechanism is analyzed, and a comparison with oxygen-bridged complexes and experimental data is performed. © 1997 John Wiley & Sons, Inc. Int J Quant Chem **65**: 633–641, 1997

Introduction

Though sulfur-bridged binuclear Ni(II) units are the active sites in some enzymes, e.g., urease [1–3], not much is known about the magnetic coupling of the spins at the two Ni^{2+} cations in S-bridged binuclear Ni(II) complexes of the general form $LNiS_nNiL$, $n = 1, 2, 3$, with one, two, or three sulfur bridges (L stands for any terminal ligands). In urease, it seems that the Ni(II) ions are all high spin and exhibit a weak antiferromagnetic coupling ($J = -6$ cm^{-1}) [1–3]. Trinuclear complexes of the form $LNiS_3NiS_3CoL$ and $LNiS_3NiS_3NiL$ with octahedrally coordinated Ni(II) ions have been recently synthesized by Beissel et al. [4]. The analysis of magnetic susceptibility measurements yielded values of about -30 cm^{-1} for the exchange coupling between two adjacent Ni(II) ions bridged by three S atoms (which, however, are not isolated S atoms or S^{2-} anions, but belong to the ligand system). Such values indicate that the antiferromagnetic coupling is stronger than in similar oxygen-bridged complexes, but it is not certain whether differences in the geometries, partial *d*-occupations of the sulfur atoms in the bridging unit or other reasons are the source for the stronger antiferromagnetism in S-bridged systems. One trinuclear sulfur-bridged nickel thiolate cluster with an almost planar Ni_3S_3 ring has been reported recently in the literature as

Correspondence to: V. Staemmler.

Contract grant sponsors: Deutsche Forschungsgemeinschaft, Ministerium für Wissenschaft und Forschung des Landes Nordrhein-Westfalen, and Fonds der Chemischen Industrie.

© 1997 John Wiley & Sons, Inc.
CCC 0020-7608 / 97 / 050633-09

well [5]. This complex, however, contains Ni^{2+} cations in square-planar coordination and is diamagnetic. To the best of our knowledge, no further bi- or trinuclear S-bridged Ni(II) complexes are known for which both X-ray structures and magnetic susceptibility data have been determined.

In a previous work [6] we have presented ab initio calculations for the exchange coupling in oxygen-bridged NiONi and NiO_2Ni systems, together with an analysis of the geometry dependence of the exchange integral J. The present work extends this study to S-bridged Ni(II) complexes of the form $LNiS_nNiL$, $n = 1, 2, 3$. Since the Ni–S distances vary considerably in different compounds, we analyzed the geometry dependence of the total energies and of the exchange integrals in the mono- and bibridged complexes and compared the results to those of oxygen-bridged complexes.

The study is organized as follows: The second section gives a brief description of the method of calculation. The third section contains the results for the linear monobridged complexes, the fourth and fifth sections those for the bi-bridged and triply-bridged complexes, respectively. The last section gives a short summary.

Method of Calculation

The present calculations have been performed in essentially the same way as in our previous study [6] on oxygen-bridged Ni(II) complexes. They consist of mainly three steps:

1. A self-consistent field (SCF) or, more precisely, a restricted open-shell Hartree–Fock (ROHF) calculation for the high-multiplicity state: For all complexes in this study this is a quintet state since the two Ni(II) ions, each of them with a d^8 configuration and a spatially nondegenerate $^3A_{2g}$ ($S = 1$) ground state in octahedral coordination, can be coupled to a quintet ($S = 2$), a triplet ($S = 1$), and a singlet ($S = 0$) state.
2. A full valence configuration interaction (VCI) calculation [7] using the ROHF orbitals of the first step, or alternatively a complete active space SCF (CASSCF) calculation [8] for all three states (quintet, triplet, singlet) simultaneously or for each of the states separately in order to reoptimize the orbitals for the triplet and singlet states. There is virtually no difference between these three treatments since the three electronic states are very close in energy. The active space for the VCI and CASSCF calculations consisted of the four e_g-type $3d$ atomic orbitals (AOs) at the two Ni atoms (for more details see Ref. [6].
3. Dynamic correlation effects are included on top of the VCI or CASSCF calculation by the multiconfiguration coupled electron pair approach (MC-CEPA) method [9]. We have always correlated the ten $3d$ AOs at the metal atoms and the $3s,3p$ valence orbitals at the bridging S atoms. In general, the averaged coupled pair functional (ACPF) variant of our MC-CEPA program [9] has been used, since this variant yields the most reliable values for the exchange splittings [6].

It has been found before [6, 10–12] that the inclusion of dynamic correlation effects is necessary if one wants to calculate reliable values for exchange integrals. The main reason is that the antiferromagnetic contribution, J_{AF}, to the total exchange integral J is determined by the extent to which "ionic" (charge transfer) configurations are mixed to the dominant "neutral" (covalent) ones in the VCI. As long as the ionic configurations are built up from orbitals which have been optimized for covalent states and no relaxation effects are accounted for, their energies are too high and consequently their contribution to J_{AF} is too small. In a separate study [10] we present "effective" CI calculations in which the VCI matrix is modified in such a way as to simulate these relaxation effects in an effective and cheap manner. In the present work we have simply scaled the antiferromagnetic contribution with a weighting factor, which has determined by a comparison between VCI and ACPF results. More details are given in the section on the bridged $L_4NiS_2NiL_4$ complex.

In order to save computer time, we have replaced the bulky terminal ligands, which are necessary in the experimental work to stabilize the rather unstable bi- and trinuclear complexes, by the He-like model ligands introduced in the earlier studies of this series [6, 11, 12]. In the present calculations the same parameters have been used as optimized before for the NiONi and NiO_2Ni complexes [6], i.e., an effective charge of 1.80 for the He-like model ligands L and a Ni–L distance

of 1.725 Å. In all complexes the number of terminal ligands was chosen in such a way that each metal ion had a full though distorted octahedral coordination.

The two Gaussian basis sets that have been used in the present calculations are summarized in Table I. The basis set for the model ligand is identical to the one optimized before for NiONi [6]. For Ni and S, the basis I has double zeta (DZ) quality, basis II has triple zeta plus polarization (TZP) quality.

Since the difference in the antiferromagnetic coupling through O and S bridges may be attributed to a partial d-occupation in the S^{2-} bridging ions, we have systematically varied the d exponent at the S-atom between 0.0 (no d functions) and 1.5 and monitored its influence on both the total energies and the value of J, i.e., the splitting between the lowest singlet, triplet, and quintet states. These tests have been performed for a linear NiSNi complex at a fixed Ni–S distance of 2.20 Å (i.e., slightly shorter than the equilibrium distance, compare next section) and for a bent NiS_2Ni complex in the vicinity of its SCF equilibrium structure with R(Ni–S) = 2.35 Å and ∠NiSNi = 90° (see fourth section). Basis set I was used for these tests. The results of these calculations can be summarized shortly as follows: The optimum value for the d exponent—as judged from the gain in the total energies—is about 0.2 at the CASSCF and 0.3 at the ACPF level. The gain in total energy is rather small at the CASSCF level ($\approx$ 0.020 a.u. for the linear NiSNi complex and $\approx$ 0.050 a.u. for NiS_2Ni), but large at the ACPF level ($\approx$ 0.120 a.u. for NiSNi; NiS_2Ni was not treated at this level). The J values, on the other hand, are hardly affected by the change of the d exponent: At the CASSCF level there is no noticeable influence of the d functions on J. This holds both for the NiSNi and the NiS_2Ni complexes, but for the bibridged complex with an NiSNi angle of 90° the antiferromagnetic part of the magnetic coupling is so small that statements concerning the d contribution are not conclusive. At the ACPF level, the contribution of the d AOs to J is in the order of 10% for the linear NiSNi unit.

The results of these basis tests indicate that the d orbitals at the bridging sulfur atoms do not directly influence the active orbitals, but are only needed for describing dynamic correlation and relaxation effects. All calculations reported in the next sections are performed with basis II and a d exponent of 0.3 (compare Table I).

Linear $L_5NiSNiL_5$ Complex

Table II contains our results for the total energy of the $^1A_{1g}$ ground state and for the exchange integral J in the linear monobridged $L_5NiSNiL_5$ complex, as functions of the Ni–S distance. Only the results of the ACPF variant of our MC-CEPA program [9] are included. As mentioned above, all metal $3d$ and the sulfur $3s3p$ orbitals have been correlated.

From the data of Table II one can conclude that the equilibrium distance amounts to 2.32 Å at the VCI (or SCF) level and is slightly shortened to 2.28 Å at the ACPF level. A direct comparison with experiment is not possible since no X-ray structure of a complex with a linear NiSNi bridge is known and since our calculations have been performed with the model ligands, which make the complex charge neutral. Bulky terminal ligands, effective

TABLE I
Gaussian basis sets for S-bridged binuclear Ni(II) complexes.

Atom	Type	Contraction	Ref.
		Basis I	
Ligand	TZ	$7s \rightarrow 3s(5,2^*1)$ (30.2, 9.8, 3.5, 1.4, 0.55, 0.17, 0.05)	6
Ni	DZ	$12s6p4d \rightarrow 7,5^*1; 4,2^*1; 2,2^*1$	13
S	DZ	$9s5p \rightarrow 4,5^*1; 2,3^*1 + 1s(0.1), 1p(0.1)$	14
		Basis II	
Ligand	TZ	As basis I	
Ni	TZP	$14s9p5d \rightarrow 10,4^*1; 6,3^*1; 3,2^*1 + s(0.35), f(2.0)$	15
S	TZP	$11s7p \rightarrow 5,6^*1; 4,3^*1 + 2s(1.0, 0.075), 2p(1.0, 0.075), 1d(0.3)$	14

TABLE II
VCI and ACPF results for the total energy and the exchange integral J in the linear $L_5NiSNiL_5$ complex.[ab]

R(Ni-S) Å	$E(^1A_{1g})$ a.u. VCI	$J_{0\to1}$ cm^{-1} VCI	$J_{1\to2}$ cm^{-1} VCI	$E(^1A_{1g})$ a.u. ACPF	$J_{0\to1}$ cm^{-1} ACPF	$J_{1\to2}$ cm^{-1} ACPF
2.20	−3433.083 115	−44.1	−45.2	−3433.657 409	−112.7	−116.2
2.25	.087 559	−39.1	−39.9	.659 846	−101.7	−104.5
2.30	.089 419	−34.5	−35.1	.659 905	−91.9	−94.0
2.35	.089 163	−30.5	−31.1	.658 081	−83.3	−84.9
2.40	0.87 171	−27.2	−27.5	.654 691	−76.2	−77.2

[a] L = He-like model ligand [6].
[b] $J_{0\to1} = 1/2[E(S=1) - E(S=0)]$; $J_{1\to2} = 1/4[E(S=2) - E(S=1)]$.

charges on the complexes, counter ions, etc. might have some influence on the exact value of the equilibrium distance, in particular since the potential curve is rather flat and its minimum is much less pronounced than, e.g., in $L_5NiONiL_5$ [6]. On the other hand, Ni–S distances of about 2.30 Å seem reasonable for octahedrally coordinated Ni atoms [1, 16, 17].

The exchange integral J is negative for all distances and decays nearly exponentially with increasing distance R, both at the VCI and the ACPF levels. As for the linear NiONi unit the J values at the ACPF level, i.e., after inclusion of dynamical correlation effects, are nearly a factor of 3 larger than at the VCI level. Again, we attribute this failure of the "active orbital" approach [18] to the fact that in the VCI or CASSCF treatments the energies of the charge transfer states are calculated with the unrelaxed orbitals optimized for the covalent ground state [10]. Finally, the splitting between the singlet ground state and the first excited triplet and quintet states shows a regular Landé pattern with a ratio 2:4, both in the VCI and ACPF treatments.

If we compare the absolute value of the exchange integral in the linear NiSNi unit (Table II) with our previous results for the NiONi bridge [6] at the respective equilibrium distances, we find that the antiferromagnetic coupling through the S bridge is slightly, but not substantially, larger than through the O bridge: For $L_5NiONiL_5$ at R(Ni–O) = 2.08 Å we found $J = -24$ cm^{-1} (VCI) and $J = -80$ cm^{-1} (best ACPF value) [6] while the corresponding values for the $L_5NiSNiL_5$ complex at R(Ni–S) = 2.30 Å are −35 and −94 cm^{-1}. This is again an indication that a partial occupation of the $3d$ AOs in the bridging sulfur atom is no important effect for the antiferromagnetic coupling through S bridges. It is more important that J depends quite sensitively on the Ni–S distance.

Bi-bridged $L_4NiS_2NiL_4$ Complex

Figure 1 contains contour plots for (a) the total energy of the lowest quintet state and (b) the exchange integral of the bi-bridged $L_4NiS_2NiL_4$ complex as functions of the Ni–S distance and the NiSNi angle, calculated at the VCI level with basis II without the f functions at the Ni atoms.

Figure 1(a) shows that the potential energy surface possesses a rather shallow minimum. At the VCI level the equilibrium geometry corresponds to a Ni-S distance of 2.41 Å and a NiSNi angle of 86.3°. The elongation of the Ni-S bond length as compared to the value for the NiSNi unit with a single linear sulfur bridge (2.32 Å, previous section) and the fact that the NiSNi bond angle is markedly below 90° indicate that the bulky S^{2-} anions try to avoid each other. The direct comparison with experimental data is again difficult, since most Ni(II) complexes with S-donor ligands have a square planar coordination [5, 17] and, again, our model ligands are not directly related to real ligands. However, bond angles between 85° and 94° have been reported for bi-bridged NiS_2Ni units [17]. On the other hand, the binuclear Ni(II) complex with two SPh bridges and octahedrally coordinated Ni(II) ions, as synthesized by Baidya et al. [16], exhibits much longer Ni–S distances (2.41 and 2.52 Å) and a larger NiSNi angle of 105.3°.

Figure 1(b) shows that the exchange integral changes sign just in the region of the minimum of the potential surface. The traditional explanation

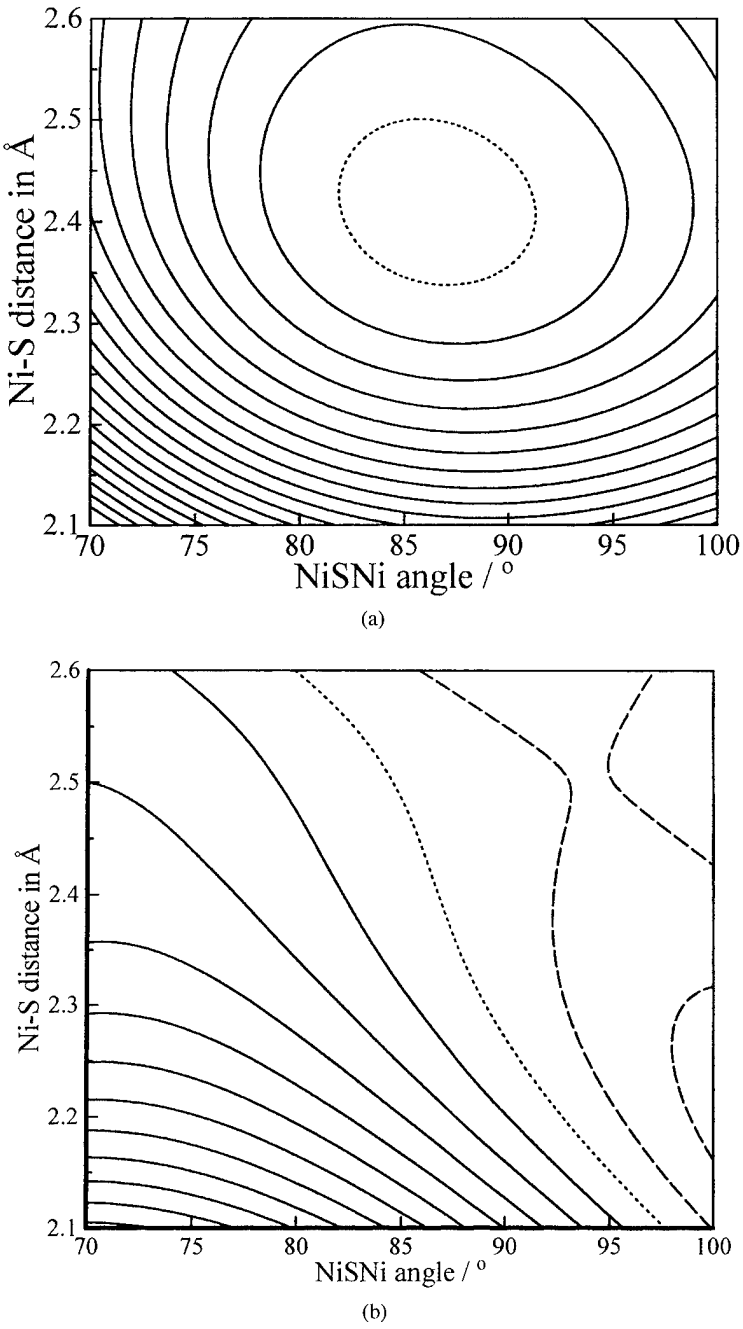


FIGURE 1. (a) Contour plot for the total energy of the lowest quintet state of the $L_4NiS_2NiL_4$ complex. ROHF, basis II without *f* functions at Ni. The lowest contour (dotted line) has an energy of −3826.225 a.u., the spacing of the contours is 0.010 a.u. = 26.24 kJ / mol. (b) Contour plot of the exchange integral in the $L_4NiS_2NiL_4$ complex. The spacing of the contours is 5 cm^{-1}; full contours represent negative, dashed ones positive values of *J*, the nodeline is dotted.

[6, 18, 19] is that the magnetic orbitals are orthogonal at an NiSNi angle of about 90° or slightly larger. The antiferromagnetic superexchange contribution in this region of the potential energy surface is therefore smaller than the direct coupling, hence the coupling is ferromagnetic in the region of about 85° to 100° [6] and antiferromagnetic for smaller and larger angles. This explanation is corroborated by the present calculations. Figure 1(b) shows that *J* is very sensitively depen-

dent on the geometry of the bridging unit, therefore an interpretation of experimental data for J is meaningless unless an X-ray structure is available.

As is well known [18], the exchange integral J consists of two contributions, the direct ferromagnetic exchange coupling, J_F, between the magnetic orbitals and the antiferromagnetic superexchange coupling, J_{AF}, which is caused by an admixture of ionic configurations to the predominantly covalent wave functions of the low-lying spin states [11]:

$$J = J_F + J_{AF}.$$

The ferromagnetic contribution J_F can be determined separately in a first step from a modified VCI calculation in which the active orbitals are localized, e.g., by a Boys localization procedure [20], and only the "neutral" (covalent) determinants, i.e., those determinants in which exactly two electrons occupy the localized e_g-type orbitals at each Ni center, are included. The "ionic" (charge transfer) determinants which are responsible for the superexchange coupling are thus excluded from the VCI and only the direct exchange coupling J_F between the localized magnetic orbitals is obtained. Of course, the value of J_F depends to a certain extent on the localization scheme.

In a second step, the full VCI calculation containing both neutral and ionic determinants is performed. It yields the total exchange splitting J, i.e., the sum of J_F and J_{AF}. However, as long as ROHF or CASSCF orbitals are used which have been optimized for the predominantly covalent low-lying spin states, J_F is described correctly but J_{AF} is largely underestimated. The reason is that the energies of the ionic states calculated with nonrelaxed covalent orbitals are much too high. CI calculations with single and double excitations into the full virtual space are necessary to properly account for the relaxation effects in the charge transfer states [10]. Our previous experience with ACPF and MC-CEPA calculations for various binuclear systems [6, 10–12] has shown that the antiferromagnetic contribution J_{AF} is enhanced by a factor of 2–3 after inclusion of dynamic correlation and relaxation effects. Stated differently, the relaxation effects lower the excitation energies of the charge transfer states by as much as a factor of 2 or even more.

In order to avoid the very time consuming ACPF calculations at every point of the two-dimensional potential energy surface for the $L_4NiS_2NiL_4$ complex, we have simply scaled the VCI result for the antiferromagnetic part J_{AF} by a scaling factor ξ, fixing J_F at its VCI value. ξ was determined semiempirically by comparing the VCI results and ACPF results at some preselected points. Table III shows that the ACPF results can be reasonably well simulated by a scaled VCI exchange interaction

$$J_{SC} = J_F + \xi J_{AF}$$

with a scaling factor $\xi = 2.0$.

Figure 2 shows a full two-dimensional contour plot of the scaled exchange integral J_{SC} using

TABLE III
Decomposition of the exchange integral J in the $L_4NiS_2NiL_4$ complex in a direct (J_F) and a superexchange (J_{AF}) contribution[a]

Distance[b]	NiSNi angle	J(VCI)[c]	J_F	J_{AF}	J_{SC}[d] $= J_F + 2*J_{AF}$	J(ACPF)[e]
2.0	90°	−47.52	24.80	−72.32	−119.83	
2.1	90°	−17.34	16.19	−33.52	−50.86	
2.2	90°	−4.17	11.08	−15.25	−19.42	−19.7
2.3	90°	0.99	7.74	−6.75	−5.76	
2.2	100°	9.44	14.43	−4.99	4.44	8.9
2.2	80°	−23.04	9.66	−32.70	−55.75	−50.3

[a] Basis II, without f functions, J in cm^{-1}.
[b] Ni–S distance in Å.
[c] J calculated at VCI level.
[d] The antiferromagnetic contribution to J was scaled by a factor of 2.0 to obtain good agreement with the ACPF results.
[e] ACPF results.

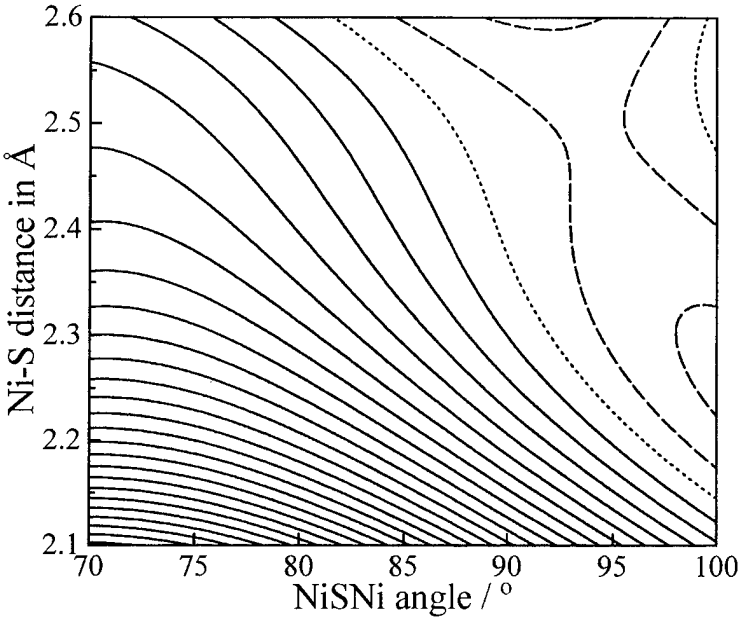


FIGURE 2. Same as Figure 1(b), the antiferromagnetic part of J was scaled by a factor of 2.0.

consistently $\xi = 2.0$. The comparison between the unmodified VCI results in Figure 1(b), and the scaled VCI results in Figure 2 shows that the ferromagnetic part of J remains unchanged while the antiferromagnetic part of J is strongly enhanced after the inclusion of dynamic correlation effects, either by real ACPF calculations or by the scaling of J_{AF}. Therefore, the region of positive values and the position of the node line are very similar in Figures 1(b) and 2, while the increase toward larger antiferromagnetic values of J for smaller Ni–S distances and bond angles is much steeper at the scaled VCI level.

The dependence of the exchange integral J on the Ni–S distance and on the NiSNi angle, found in the present study for $L_4NiS_2NiL_4$, is very similar to the behavior in the corresponding O-bridged $L_4NiO_2NiL_4$ complex [6].

$L_3NiS_3NiL_3$

We did not calculate full two-dimensional surfaces of the total energy and the exchange integral for the triply S-bridged complex $L_3NiS_3NiL_3$. The reason is that due to the use of the nearly charge neutral model ligands our $L_3NiS_3NiL_3$ complex has a total charge of -3.2 and no stable equilibrium geometry could be found. If the Ni-S distance is fixed to the experimental value of 2.36 Å observed by Beissel et al. [4] in the trinuclear NiS_3NiS_3Ni unit, the optimum NiSNi angle turns out to be smaller ($\approx 71°$) than the experimental equilibrium value (79° [4]). The electrostatic repulsion between the three negative S^{2-} anions is too large in our model and has to be reduced by using either singly charged SR^- anions or by adding reasonable counterions.

The behavior of J as a function of the Ni–S bond length and the NiSNi angle in the triply S-bridged $L_3NiS_3NiL_3$ complex is very similar to what was found before in the bibridged complex. This is nicely documented in Figure 3. From the similarity of the curves for the $L_4NiS_2NiL_4$ complex with an NiSNi angle of 80° and for $L_3NiS_3NiL_3$ at 79°, we conclude that the scaled VCI results for J as presented in Figure 2 for the bibridged complex can as well be used to predict the magneto-structural relations in triply S-bridged Ni(II) complexes.

At the experimental geometry (R(Ni–S) = 2.36 Å with an NiSNi angle of 79° [4]) we obtained $J = -9.5$ cm^{-1} with $J_F = 7.0$ cm^{-1} and $J_{AF} = -16.5$ cm^{-1}. If we again scale J_{AF} by a factor of 2,

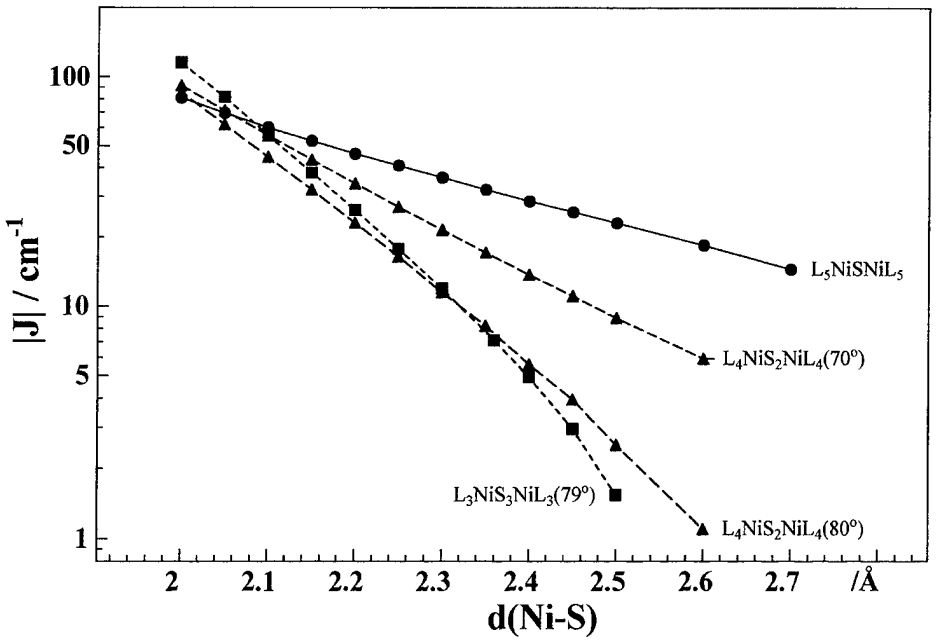


FIGURE 3. Exchange integral J as a function of the Ni–S distance in mono-, bi-, and triply S-bridged binuclear Ni(II) complexes. VCI level, basis II.

we obtained $J = J_F + 2J_{AF} = -26$ cm^{-1}, which is in agreement with the experimental value $J = -27.0$ cm^{-1}, reported by Beissel et al. for the trinuclear NiS_3NiS_3Ni complex [4].

Summary and Conclusions

In the present study we calculated the exchange integral J in mono-, bi-, and triply S-bridged binuclear Ni(II) complexes, we examined the geometry dependence of J and the total energy of the complexes, and compared the results to oxygen-bridged complexes. Inclusion of the $3d$ orbitals at the bridging sulfur ions lowers the total energy of the complexes, but has nearly no influence on J. The superexchange mechanism is the same as in oxygen-bridged complexes. Even the angular behavior of J is quite similar. The complexes are ferromagnetic for NiSNi angles between 85° and 100° and antiferromagnetic for smaller and larger angles.

In contrast to the oxygen-bridged Ni(II) complexes in which the Ni–O distances are quite similar in different compounds, the experimentally known values for Ni–S distances in different complexes with octahedrally coordinated Ni vary between 2.3 and 2.5 Å. This is caused by very shallow potential surfaces. Because of the strong geometry dependence of J and the change of its sign in the region of the minimum of the potential surfaces, the values for J will be different in different complexes.

In order to avoid the time-consuming ACPF calculations, we used a scaled VCI in which J_{AF} was weighted with a factor of 2. With this method we found very good agreement between our calculated value for J in a triply S-bridged complex and the experimental data of Beissel et al. [4].

ACKNOWLEDGMENTS

This study was financially supported by Deutsche Forschungsgemeinschaft, Ministerium für Wissenschaft und Forschung des Landes Nordrhein-Westfalen, and Fonds der Chemischen Industrie. One of us (C.W.) benefited from a grant of the Max-Buchner-Stifung. One of us (K.F.) is a member of the graduate college "Dynamische Prozesse an Festkörperoberflächen."

References

1. S. Wang, M. H. Lee, R. P. Hausinger, P. A. Clark, D. E. Wilcox, and R. A. Scott, Inorg. Chem. **33**, 1589 (1994).
2. P. A. Clark and D. E. Wilcox, Inorg. Chem. **28**, 1326 (1989).
3. E. P. Day, J. Peterson, M. Sendova, M. J. Todd, and R. P. Hausinger, Inorg. Chem. **32**, 634 (1993).

4. T. Beissel, T. Glaser, F. Kesting, K. Wieghardt, and B. Huber, Inorg. Chem. **35**, 3936 (1996).
5. A. Berkessel, J. W. Bats, M. Hüber, W. Haase, T. Neumann, and L. Seidel, Chem. Ber. **128**, 125 (1995).
6. C. Wang, K. Fink, and V. Staemmler, Chem. Phys. **192**, 25 (1995).
7. J. Wasilewski, Int. J. Quant. Chem. **36**, 503 (1989).
8. U. Meier and V. Staemmler, Theoret. Chim. Acta **76**, 95 (1989).
9. R. Fink and V. Staemmler, Theoret. Chim. Acta **87**, 129 (1993).
10. V. Staemmler, C. Wang, and K. Fink, to appear.
11. K. Fink, R. Fink, and V. Staemmler, Inorg. Chem. **33**, 6219 (1994).
12. C. Wang, K. Fink, and V. Staemmler, Chem. Phys. **201**, 87 (1995).
13. B. Roos, A. Veillard, and G. Vinot, Theoret. Chim. Acta **20**, 1 (1971).
14. S. Huzinaga, Approximate atomic functions. II. Preprint. University of Alberta, Edmonton, Canada, 1971.
15. A. J. H. Wachters, J. Chem. Phys. **52**, 1033 (1970).
16. N. Baidya, M. Olmstead, and P. K. Mascherak, Inorg. Chem. **30**, 929 (1991).
17. G. Sánchez, F. Ruiz, M. D. Santana, G. García, G. López, J. A. Hermoso, and M. Martinez-Ripoll, J. Chem. Soc., Dalton Trans., **1994**, 19.
18. O. Kahn, *Molecular Magnetism* (VCH Publishers, Weinheim, 1993).
19. P. J. Hay, J. C. Thibeault, and R. Hoffmann, J. Am. Chem. Soc. **97**, 4884 (1975).
20. J. M. Foster and S. F. Boys, Rev. Mod. Phys. **32**, 300 (1960).

Reaction Path for the Insertion Reaction of $SnCl_2$ into the Pt—Cl Bond: An Ab Initio Study

WILLIAM R. ROCHA, WAGNER B. DE ALMEIDA

Laboratório de Química Computacional e Modelagem Molecular, Depto. de Química, ICEX-UFMG, Belo Horizonte, MG 31270-901, Brazil

Received 11 March 1997; revised 16 April 1997; accepted 17 April 1997

ABSTRACT: The reaction pathway for the insertion reaction of $SnCl_2$ into the Pt—Cl bond on the *cis*-$Pt(Cl)_2(PH_3)_2$ compound was investigated at the ab initio MO level of theory. The optimized structure obtained for the transition state indicates that this reaction proceeds through a three-center transition state, and the formed intermediate *cis*-$Pt(Cl)(PH_3)_2(SnCl_3)$ easily isomerizes to the *trans*-$Pt(Cl)(PH_3)_2(SnCl_3)$ compound. The nature of the bonds was investigated with the charge decomposition analysis (CDA) method and this method indicates that the $SnCl_3$ group is a stronger *trans* director than is the PH_3 group. © 1997 John Wiley & Sons, Inc. Int J Quant Chem **65**: 643–650, 1997

Introduction

The hydroformilation of olefins catalyzed by platinum complexes in combination with group IV A metal halides is of great interest. These systems have been shown to be highly active and selective in hydroformilation of olefins and their catalytic activity is comparable to that industrially used and well-known rhodium catalyst [1]. As an example, catalyst precursors of the type *cis*-$Pt(Cl)_2(PR_3)_2$, when combined with $SnCl_2$, have been shown to be useful catalysts for the hydrogenation and hydroformilation of primary olefins [1b–1e]. Several questions related to this catalyst are still unclear or unanswered. For example, the fact that catalytic activity is observed only in the presence of $SnCl_2$ [2] suggest that the Pt—Sn bond plays a fundamental role in the catalytic cycle. Therefore, an understanding of the nature of the Pt—Sn bond is very important.

The ^{31}P and ^{195}Pt nuclear magnetic resonance (NMR) characterization of the complexes which arise in solution when $SnCl_2$ reacts with *cis*-$Pt(Cl)_2(PR_3)_2$ was studied by Pregosin and Sze [3]. The reaction scheme proposed by these authors (1)

Correspondence to: W. B. De Almeida.

Contract grant sponsor: CNPq (Conselho Nacional de Desenvolvimento Cietífico e Tecnológico).

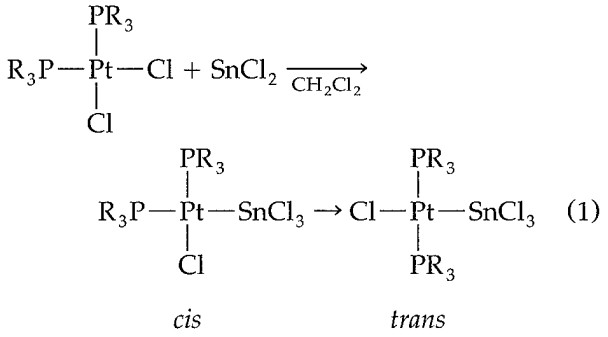
Contract grant sponsor: FAPEMIG (Fundação de Amparo à Pesquisa do Estado de Minas Gerais).

Contract grant sponsor: PADCT (Programa de Apoio ao Desenvolvimento Cintífico e Tecnológico.

Contract grant number: 62.0241/95.0.

© 1997 John Wiley & Sons, Inc.
CCC 0020-7608 / 97 / 050643-08

for this reaction indicates that the insertion of $SnCl_2$ into the platinum/chlorine bond in *cis*-$Pt(Cl)_2(PR_3)_2$ is followed by rapid isomerization:



SCHEME 1

Despite the fact that $^{31}PH\{^1H\}$- and ^{195}Pt-NMR spectroscopy of complexes containing platinum, tin, and phosphorus provide a sensitive probe for complex structures, questions related to the electronic nature of the Pt—Sn and Pt—P bonds are not answered directly by this method.

In this work, we investigated the reaction path for the insertion reaction of $SnCl_2$ into the Pt—Cl bond (Scheme **1** in gas phase and using R = H) at the *ab initio* level of theory. All the stationary points present on the potential energy surface (PES) for this reaction were located and the nature of the bonds between the ligands and the platinum atom were investigated. The *trans* effects of the $SnCl_3$ and PH_3 ligands are discussed and this may give some insight into how the elementary reactions (olefin insertion, carbon monoxide insertion, etc.), which take place in the catalytic cycle for hydroformilation of olefins, may proceed.

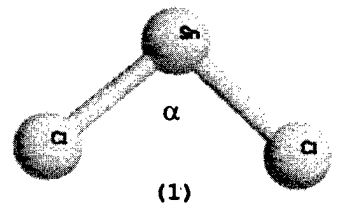
Method of Calculation

Full-symmetry unconstrained geometry optimizations were performed at the RHF level of theory using the ECP and valence basis sets of Stevens, Basch, Krauss, and Jasien (SBKJ) [4] for the Pt and Sn atoms, 6–31G* [5] basis sets for the P and Cl atoms, and a 3–21G [5] basis set for the hydrogen atoms. The tin atom can expand its valence shell and use *d* empty orbitals to form a back coordination of the type *d–d* with the platinum atom [6]. Therefore, to analyze the role of the *d* empty orbitals of the tin atom on the nature of the Pt—Sn bond, a set of five *d* polarization functions (α = 0.180) [7] were added to the Sn atom. The stationary points located on the PES were identified as minima (none imaginary frequencies) or transition states (characterized by having at least one imaginary frequency) through harmonic frequency calculation. To obtain better energetic results, we carried out second-order Møller–Plesset (MP2) perturbation theory single-point calculations on the RHF-optimized geometries with the same basis set. All calculations were carried out using the GAMESS96 [8] and GAUSSIAN94 [9] packages, at the Laboratorio de Quimica Computacional e Modelagem Molecular (LQC-MM), Departamento de Quimica, Universidade Federal de Minas Gerais (UFMG).

Results and Discussions

The optimized structural parameters obtained for the reactants [$SnCl_2$ **1** and *cis*-$Pt(Cl)_2(PH_3)_2$ **2**], transition state (**TS**), and the products *cis*-$Pt(Cl)(PH_3)_2(SnCl_3)$ **4** and *trans*-$Pt(Cl)(PH_3)_2(SnCl_3)$ **5**] are shown in Figure 1. The optimized angles of **2**, **4**, and **5** around the platinum atom are a little distorted from the expected optimal value of 90° for a d^8 square planar complex. The Pt—P bond distances predicted in our calculations are in good agreement with the experimentally observed Pt—P bond distances of 2.284 Å in $Pt(CH3)_2(PCH_3Ph_2)_2$ [10] and 2.303 Å in *trans*-Pt (H) $(SnCl_3)$ $(PPh_3)_2$ [11]. The Pt—Sn bond length of 2.604 Å in complex **4** and 2.576 Å in complex **5** are in good agreement with the experimental Pt—Sn values of 2.634 Å in *trans*-$Pt(SnCl_3)$ (COPh) $(PEt_3)_2$ [12], 2.601 Å in *trans*-$Pt(H)(SnCl_3)(PPh_3)_2$ [11], and 2.600 Å in *trans*-$Pt(H)(SnCl_3)(PCy_3)_2$ [13]. The Sn—Cl bond distances of 2.331 and 2.350 Å in complexes **4** and **5**, respectively (see Fig. 1), agrees with the experimental finding of 2.283–2.367 Å in the complex *trans*-$Pt(H)(SnCl_3)(PPH_3)_2$ [13]. The structural parameters calculated for the transition state (see Fig. 1) indicate that the formation of compound **4** occurs in a concerted way, where the Pt—Sn bond is forming and the Pt—Cl bond is breaking, leading to a three-center transition state.

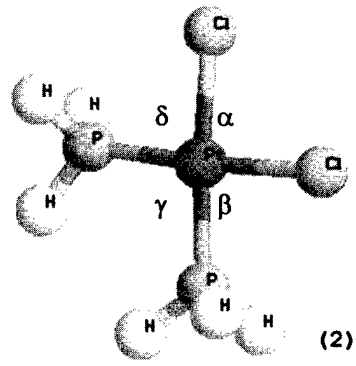
It is well known that bond distance is a very sensitive parameter in describing the *trans* influence, i.e., the ability of a ligand to labilyze the bond *trans* to it. If we compare the bond length of compounds **4** and **5** (see Fig. 1), it can be seen that the $SnCl_3$ group has a stronger *trans* influence than has the PH_3 group, because the Pt—Cl bond in compound **5** (2.411 Å), where the chlorine is



(1)

r(Sn-Cl) = 2.377

α = 97.851



(2)

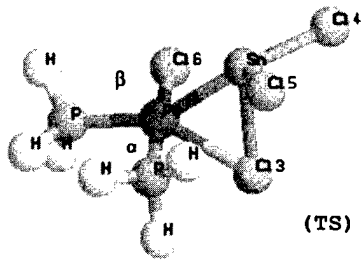
r(Pt-Cl) = 2.354

r(Pt-P) = 2.228

r(P-H) = 1.406

α = 92.413 β = 83.664

γ = 101.206 δ = 82.668



(TS)

r(Pt-Cl6) = 2.364

r(Pt-P) = 2.281(trans to $SnCl_3$)

r(Pt-P) = 2.340 (cis to $SnCl_3$)

r(Pt-Cl3) = 2.871

r(Pt-Sn) = 3.000

r(Sn-Cl4) = 2.421

θ(Pt-Sn-Cl3) = 61.099

θ(Sn-Cl3-Pt) = 66.186

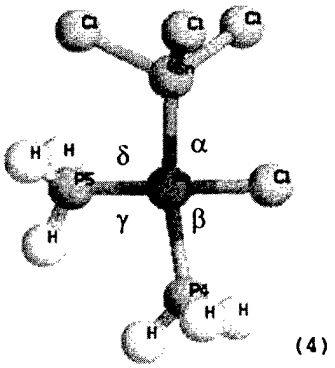
θ(Cl3-Pt-Sn) = 52.715

FIGURE 1. RFH-optimized structural parameters for the $SnCl_2$ (**1**), *trans*-$Pt(Cl)_2(PH_3)_2$ (**2**), transition state (**TS**), *cis*-$Pt(Cl)(PH_3)_2(SnCl_3)$ (**4**) and *trans*-$Pt(Cl)(PH_3)_2(SnCl)_3$ (**5**) molecules. Bond lengths in angstroms and bond angles in degrees.

trans to $SnCl_3$ group, is greater than is the Pt—Cl bond in compound **4** (2.373 Å) where the chlorine is *trans* to the PH_3 group. It can also be seen from Figure 1 that the Pt—P bond length *trans* to the $SnCl_3$ group in compound **4** (2.412 Å) is greater than is the Pt—P bond length in compound **2** (2.228 Å). This fact corroborates our assertion that $SnCl_3$ is a stronger *trans* director than is the PH_3 group.

The *trans* influence can qualitatively explain why the compound *cis*-$Pt(Cl)(PH_3)_2(SnCl_3)$, **4**, isomerizes to the *trans*-$Pt(Cl)(PH_3)_2(SnCl_3)$, **5**, compound. If the PH_3 ligand stays in a *trans* position in relation to the $SnCl_3$, these two groups will compete unevenly for the electron density from the Pt atom, so the Ph_3 group chooses to stay in a more favorable position *trans* to another PH_3 group in compound **5**. These qualitative arguments will be discussed in a quantitative way later.

The total energies obtained for compounds **1**–**5** are shown in Table I, and the energy diagram for the reaction is shown in Figure 2. As can be seen from Figure 2, the energetic trend is maintained for the reactants (**1** + **2**) and products (**4** and **5**) when an MP2 single-point calculation is per-



(4)

r(Pt-Cl) = 2.373

r(Pt-Sn) = 2.604

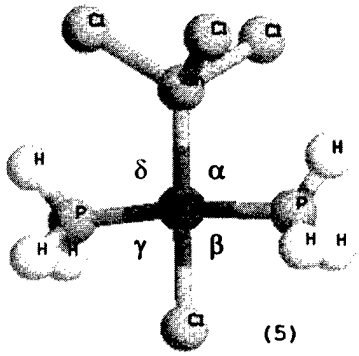
r(Pt-P4) = 2.412

r(Pt-P5) = 2.307

r(Sn-Cl) = 2.331

α = 85.467 β = 83.645

γ = 99.211 δ = 91.678



(5)

r(Pt-Cl) = 2.411

r(Pt-P) = 2.350

r(Pt-Sn) = 2.576

r(Sn-Cl) = 2.350

α = 91.880 β = 86.074

γ = 85.815 δ = 96.231

FIGURE 1. (continued)

formed on the RHF-optimized geometries. The formation of intermediate *cis*-$Pt(Cl)(PH_3)_2(SnCl_3)$, **4**, is favored by an amount of −37.5 kcal/mol and the occurrence of the isomerization *cis*-$Pt(Cl)(PH_3)_2(SnCl_3)$ → *trans*-$Pt(Cl)(PH_3)_2(SnCl_3)$ (**4** → **5**) is favored by −7.0 kcal/mol. The MP2 single-point calculation on the RHF-optimized geometry for the transition state (**TS**) structure gave an unexpected result −4.4 kcal/mol for the difference between the energies of the reactants and the transition state (see Table 1 and Fig. 2). What this result shows us is that the transition state is more stable than are the reactants, i.e., the $SnCl_2$ inserts into the Pt—Cl bond without a barrier. This result

TABLE I
Total energy values obtained for the stationary points on the potential energy surface (Fig. 1).

Compound	Energy (au) RHF[a]	MP2[b]
$SnCl_2$ (**1**)	−922.3586	−922.6748
$Pt(Cl)_2(PH_3)_2$ (**2**)	−1722.8362	−1723.4704
TS	−2645.1839	−2646.1522
cis-$Pt(Cl)(PH_3)_2(SnCl_3)$ (**4**)	−2645.2359	−2646.2050
trans-$Pt(Cl)(PH_3)_2(SnCl_3)$ (**5**)	−2645.2497	−2646.2161

[a] The basis set used is described in the Method of Calculation section.
[b] Single-point calculation at the RHF-optimized geometry.

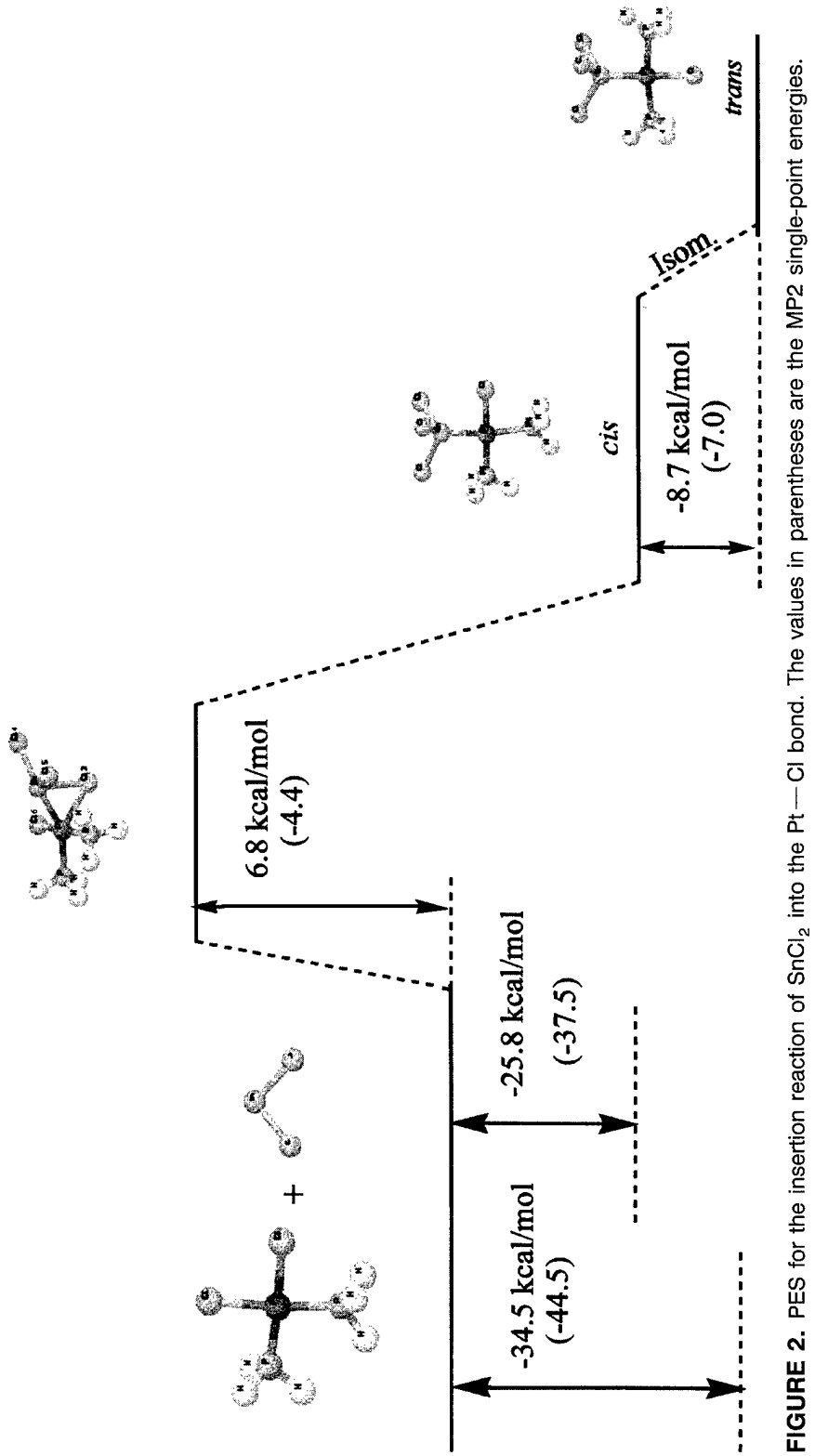


FIGURE 2. PES for the insertion reaction of $SnCl_2$ into the Pt—Cl bond. The values in parentheses are the MP2 single-point energies.

can be related to the fact that the formation of the **TS** occurs in a concerted way, where the Pt—Sn bond formation and Pt—Cl bond breaking occur at the same time. Therefore, the energy involved in the Pt—Sn bond formation is sufficiently high to stabilize the **TS** leading to an insertion without barrier.

Nature of the Bond

The nature of the bond in transition-metal complexes has gained much attention from the theoretical point of view since the appearance of the Dewar–Chatt–Duncanson model [14]. This model considers two factors responsible for stabilizing the bond in transition-metal complexes: the σ-donating interactions from the ligands to the metal and the π back donation from the metal to the ligands.

Several methods have appeared in the literature focusing on the evaluation of the energetic contribution to the bond energy as well as investigating the mixing of orbitals in the region of interaction between the metal and ligand. The construction of molecular orbitals in terms of fragment molecular orbitals was earlier employed by Fukui and co-workers [15] in a method called coupled fragment molecular orbital interaction for interacting systems. Bagus et al. [16] developed the constrained space orbital variation (CSOV), where the wave function of the complex is constructed from the molecular orbitals of the ligand and the metal atom. Ziegler and co-workers developed the extended transition state (ETS) method [17], based on the density functional formalism, which is similar to the CSOV method. More recently, Frenking and co-workers developed the charge decomposition analysis (CDA) [18] using fragment molecular orbitals. The CDA method consists of using linear combinations of fragment orbitals (LCFO) of properly chosen fragments A and B for the interpretation of the interactions in a molecule AB. The interaction is divided into three main contributions: (a) the mixing between the occupied orbitals of A and empty orbitals of B, which indicates the magnitude of electron donation from A to B (A $\rightarrow$ B), (b) the mixing between the occupied orbitals of B and the empty orbitals of A, which gives the extent of back donation, i.e., the electron donation from B to A (A $\leftarrow$ B), and (c) the mixing between the occupied orbitals of A and the occupied orbitals of B which indicates the extent of charge polarization in the region of bonding. Based on these points, the CDA method can be used as a quantitative view of the Dewar–Chatt–Duncanson model.

To analyze the nature of the bond in complexes *cis*-$Pt(Cl)(PH_3)_2(SnCl_3)$, **4**, and *trans*-$Pt(Cl)(PH_3)_2(SnCl_3)$, **5**, we used the CDA method, as implemented in the CDA 2.1 program [19]. The total amount of donation, back donation, and bond energy obtained by the CDA is shown in Table II. As can be seen, in all situations analyzed, the magnitude of donation from the PH_3 fragment to the $Pt(Cl)(PH_3)(SnCl_3)$ fragment is greater than is the magnitude of back donation, which indicates that the PH_3 is not a good π-acceptor. The other fact that contributes to the low extent of back donation in relation to the electron donation is that back donation is favored when there is an electron-rich metal, which is not the present case.

TABLE II

Total amount of donation, back donation, and bond energy for different chosen fragments A and B, obtained by the CDA method.

Fragment		Σ donation	Σ backdonation	Bond energy (kcal / mol)
A	B			
PH_3 [a]	$Pt(Cl)(PH_3)(SnCl_3)$	0.597 *e*	0.172 *e*	52.0
PH_3 [b]	$Pt(Cl)(PH_3)(SnCl_3)$	0.563 *e*	0.071 *e*	26.0
PH_3 [c]	$Pt(Cl)(PH_3)(SnCl_3)$	0.614 *e*	0.125 *e*	46.2

[a] PH_3 *cis* to $SnCl_3$ group in *cis*-$Pt(Cl)(PH_3)_2(SnCl_3)$, **4**, compound (see Fig. 1).
[b] PH_3 *trans* to $SnCl_3$ group in *cis*-$Pt(Cl)(PH_3)_2(SnCl_3)$, **4**, compound.
[c] PH_3 *trans* to another PH_3 group in compound *trans*-$Pt(Cl)(PH_3)_2(SnCl_3)$, **5**, compound (see Fig. 1).

The platinum atom is in a formal oxidation state of +2, assuming a d^8 configuration. Therefore, despite the fact that PH_3 is a poor π-acceptor ligand, the extent of back donation should be increased if we have a more electron-richer metal atom.

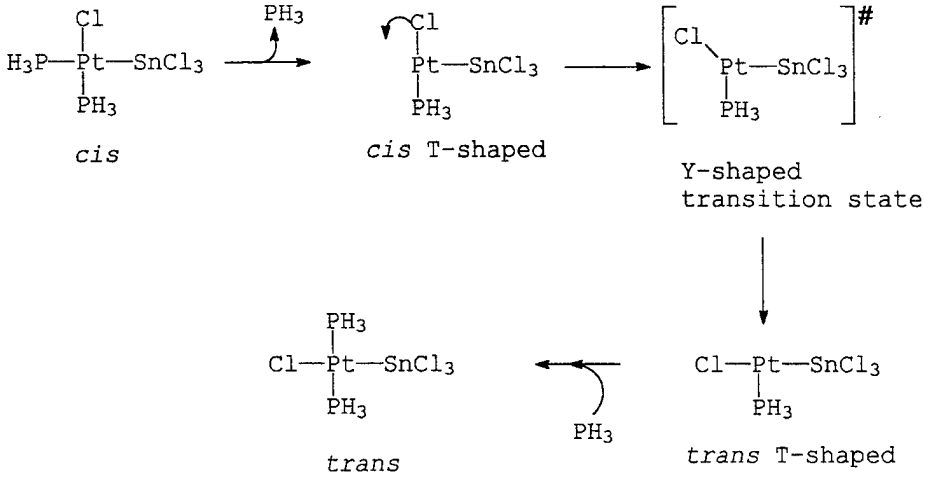
When we compare the extent of back donation of the two PH_3 groups in the *cis*-$Pt(Cl)(PH_3)_2(SnCl_3)$ complex, **4** (see Fig. 1 and Table II), the extent of back donation from the PH_3 group *trans* to the $SnCl_3$ is diminished, indicating that the $SnCl_3$ group is withdrawing electron density from the platinum atom, and this reduces the electron density available for donating to the PH_3 ligand. Based on this argument, the extent of back donation of the PH_3 *trans* to another PH_3 group in compound *trans*-$Pt(Cl)(PH_3)_2(SnCl_3)$, **5** (see Fig. 1), should be greater than the one found to the PH_3 group *trans* to $SnCl_3$ in complex **4** and less than the extent of back donation of the PH_3 group *cis* to the $SnCl_3$ group in compound **4** (see Fig. 1 and Table II). The results of CDA agree with these arguments as can be seen in Table II.

The Pt—P bond energy calculated for the PH_3 group *cis* to the $SnCl_3$ group (52.0 kcal/mol) is ca. 26 kcal/mol greater than is the Pt—P bond energy calculated for the PH_3 group *trans* to the $SnCl_3$ group (26.0 kcal/mol), as can be seen in Table II. This result provides a semiquantitative view of the *trans* effect of the $SnCl_3$ group, which, of course, could change if a correlated calculation is used to analyze the bond energy.

The occurrence of *cis* → *trans* isomerization in platinum (II) and Palladium (II) phosphine complexes is well known [20]. Three mechanisms can explain this reaction: the consecutive displacement mechanism [21], the Berry pseudorotation mechanism [20, 22], and the dissociative pathway [23]. In addition, changes of metal, ligand, solvent, or temperature can substantially affect the equilibrium. Therefore, the *cis*-$Pt(Cl)(PH3)_2(SnCl_3)_2$ → *trans*-$Pt(Cl)(PH_3)_2(SnCl_3)_2$ (**4** → **5**) isomerization reaction needs a more detailed study focusing on the solvent and ligand influence. A theoretical study on this isomerization reaction is already underway. Taking into account the strong *trans* influence of the $SnCl_3$ (Table II), as discussed before, can lead to a possible mechanism for the isomerization occurring in the gas phase. This may be a dissociative pathway through T-shaped three-coordinate intermediates, as is exemplified in Scheme 2 below. Some kinetic evidence for the intermediacy of a three-coordinate T-shaped species was obtained for *cis* and *trans*-$PdMe_2(PR_3)_2$ complexes [23].

Concluding Remarks

We studied the insertion reaction of $SnCl_2$ into the Pt—Cl bond and the resulting complex *cis*-$Pt(Cl)_2(PH_3)_2$ using ab initio MO methods. All the



SCHEME 2

stationary points located on the PES were fully optimized. The transition-state structure obtained indicates that the reaction proceeds through a three-center transition state. The optimized structures are in good agreement with experimental findings for similar systems. The analysis of the nature of the bonds showed that the $SnCl_3$ ligand is a stronger *trans* director than is the PH_3 group, and it is capable of weakening the Pt—P bond *trans* to it by ca. 26 kcal/mol. The amount of back donation of the PH_3 group is less than the donation, indicating that the PH_3 is not a good π-acceptor ligand. The results of the charge decomposition analysis gave us support to infer with the *cis*-$Pt(Cl)(PH_3)_2(SnCl_3)$ → *trans*-$Pt(Cl)(PH_3)_2(SnCl_3)$ isomerization reaction proceeds through a dissociative pathway with formation of T-shaped three-coordinate intermediates. We think that the information provided about this cocatalyst (strong *trans* influence of $SnCl_3$ and the formation of very stable compounds formed when tin interacts with platinum) is very important to study the elementary reactions for the hydroformilation of olefins using this heterobimetallic complex. Our group is currently investigating this catalytic cycle.

ACKNOWLEDGMENTS

The authors would like to thank the CNPq (Conselho Nacional de Desenvolvimento Científico e Tecnológico) for support. We are also grateful to Prof. Carlos A. L. Filgueiras and Dr. Wagner M. Teles for stimulating discussions. This work was partially supported by the FAPEMIG (Fundação de Amparo à Pesquisa do Estado de Minas Gerais) and the PADCT (Programa de Apoio ao Desenvolvimento Cintífinco e Tecnológico-Proc. No. 62.0241/95.0).

References

1. (a) C. Y. Hsu and M. Orchin, J. Am. Chem Soc. **97**, 3553 (1975). (b) G. Parrinelo and J. K. Stille, J. Am. Chem. Soc. **109**, 7122 (1987). (c) J. K. Stille and G. Parrinelo, J. Mol. Catal. **21**, 203, (1983). (d) L. Kollár, G. Parrinelo, and P. Pino, J. Organomet. Chem. **330**, 305 (1987). (e) L. Kollár, J. Bakos, I. Tóth, and B. Heil, J. Organomet. Chem. **350**, 277, (1988).
2. (a) R. Bardi, A. M. Piazzesi, G. Cavinato, P. Cavoli, and L. Toniolo, J. Organomet. Chem. **224**, 407 (1982). (b) R. Bard, A. M. Piazzesi, A. Del Pra, G. Cavinato, and L. Toniolo, J. Organomet. Chem. **234**, 107 (1982). (c) G. Cavinato and L. Toniolo, J. Organomet. Chem. **241**, 275 (1983).
3. P. Pregosin and N. Sze. Helv. Chim. Acta **61**, 1848 (1978).
4. (a) W. J. Stevens, H. Basch, and M. Krauss, J. Chem. Phys. **81**, 6026 (1984). (b) W. J. Stevens, H. Basch, M. Krauss, and P. Jasien, Can. J. Chem. **70**, 612 (1992).
5. W. J. Hehre, R. Ditchfield, and J. A. Pople, J. Chem. Phys. **56**, 2257 (1972).
6. L. D. Pettit, Q. Rev. 1 (1971).
7. A. Höllwarth, M. Böhme, S. Dapprich, A. W. Ehlers, A. Gobbi, V. Jonas, K. F. Köller, R. Stegmann, A. Veldkampe, and G. Frenking, Chem. Phys. Lett. **208**, 237 (1993).
8. M. W. Schmidt, K. K. Baldridge, J. A. Boatz, S. T. Elbert, M. S. Gordon, J. H. Jensen, S. Koseki, N. Matsunaga, K. A. Nguyen, S. J. Su, T. L. Windus, M. Dupuis, and J. A. Montgomery, GAMESS, J. Comp. Chem. **14**, 1347 (1993).
9. M. J. Frisch, G. W. Trucks, H. B. Schlegel, P. M. W. Gill, B. G. Johnson, M. A. Robb, J. R. Cheeseman, T. A. Keith, G. A. Petersson, J. A. Montgomery, K. Raghavachari, M. A. Al-Laham, V. G. Zakrzewski, L. V. Ortiz, J. B. Foresman, J. Cioslowski, B. B. Stefanov, A. Nanayaakkara, M. Challacombe, C. Y. Peng, P. Y. Ayala, W. Chen, M. W. Wong, J. L. Andres, E. S. Replogle, R. Gomperts, R. L. Martin, D. J. Fox, J. S. Binkley, D. J. Defrees, J. Baker, J. P. Stewart, M. Head-Gordon, C. Gonzalez and J. A. Pople, *GAUSSIAN 94 (Revision A.1)* (Gaussian, Inc., Pittsburgh, PA, 1995).
10. J. M. Wisner, T. J. Bartchak, J. A. Ibers, J. J. Low, and W. A. Goddard III, J. Am. Chem. Soc. **108**, 347 (1986).
11. M. Gómez, G. Muller, D. Sainz, and J. Sales, Organometallics **10**, 4036 (1991).
12. A. Albinati, U. N. Gunten, P. S. Pregosin, and H. J. Ruegg, J. Organomet. Chem. **295**, 239 (1985).
13. A. Del Pra, E. Forsellini, G. Bomberi, R. A. Michelin, and A. Ros, J. Chem. Soc., Dalton Trans. 1862 (1979).
14. (a) J. S. Dewar, Bull. Soc. Chim. Fr. **18**, C79 (1951). (b) J. Chatt and L. A. Duncanson, J. Chem. Soc. 2939 (1953).
15. (a) H. Fujimoto, S. Kato, S. Yamabe, and K. Fukui, J. Chem. Phys. **60**, 572 (1974). (b) S. Kato, H. Fujimoto, S. Yamabe, and K. Fukui, J. Am. Chem. Soc. **94**, 2024 (1974). (c) H. Fujimoto, N. Koga, and K. Fukui, J. Am. Chem. Soc. **103**, 7452 (1981).
16. (a) P. S. Bagus, K. Hermann, and C. W. Bauschlicher, J. Chem. Phys. **80**, 4378 (1984). (b) P. S. Bagus, K. Hermann, and C. W. Bauschlicher, J. Chem. Phys. **81**, 1966 (1984). (c) P. S. Bagus and F. Illas, J. Chem. Phys. **96**, 8962 (1992).
17. (a) T. Ziegler and A. Rauk, Theor. Chim. Acta **46**, 1 (1977). (b) E. J. Baerends and A. Rozendaal, NATO ASI **C176**, 159 (1986). (c) T. Ziegler, NATO ASI **C378**, 367 (1992).
18. (a) S. Dapprich and G. Frenking, J. Phys. Chem. **99**, 9352 (1995). (b) A. W. Ehlers, S. Dapprich, S. F. Vyboischikov, and G. Frenking, Organometallics **15**, 105 (1996).
19. S. Dapprich and G. Frenking, *CDA 2.1* (Marburg, 1994). internet: ftp/chemie.uni-marburg.de, login anonymous, directory pub/cda.
20. G. K. Anderson and R. J. Gross, Chem. Soc. Rev. **9**, 185 (1980).
21. F. Basolo and R. G. Pearson, *Mechanism of Inorganic Reactions*, 2nd ed. (Wiley, New York, 1967).
22. R. S. Berry, J. Chem. Phys. **32**, 933 (1960).
23. (a) F. Ozawa, T. Ito, Y. Nakamura, and A. Yamamoto, Bull. Chem. Soc. Jpn. **54**, 1868 (1981). (b) R. S. Paonessa and W. C. Trogler, J. Am. Chem. Soc. **104**, 3529 (1982).

Study of Ground and Excited States of Doped Polyacetylene

G. P. DAS, D. S. DUDIS

WL / MLBP, Wright Patterson Air Force Base, Ohio 45433

Received 5 March 1997; revised 17 July 1997; accepted 29 July 1997

ABSTRACT: Both theoretical and experimental studies in the past have indicated that the charge transport in doped polyacetylene is due primarily to traveling charged solitary waves along the polymer chain backbone accompanied by hopping from one chain to another. The conductivity in this model is still determined by a band gap. The nature of the ground and excited states of the doped system, however, is not fully understood. Previous ab initio calculations, based on transoctatetraene simulating transpolyacetylene interacting with a single iodine atom and also a fairly low level of basis set, have pointed to the possibility that, while the calculations at the Hartree–Fock level puts the charge-transfer state below the "covalent" state, the results are reversed when correlation is included. Apart from the basis-set inadequacy and the small size of the polyene considered in this study, it is also true that, in solution, iodine exists only as polyiodide ions I_3^-, I_5^-, etc. In this work, we address some of the above deficiencies of the model.
© 1997 John Wiley & Sons, Inc. Int J. Quant Chem **65:** 651–654, 1997

Introduction

The discovery [1, 2] that polyacetylene can be doped to near metallic conductivities, using donors, such as alkali metals, and acceptors, such as I_2 or AsF_5, as dopants has intensified interest in understanding the mechanism of charge transport in these materials. While qualitatively the conductivity is now firmly believed to result from charged solitary waves, as first proposed by Su, Schrieffer, and Heeger (SSH) [3], the description of the ground and excited states participating in the charge-transport process remains a theoretical challenge.

In a previous work, Das et al. [4] showed that if one simulates transpolyacetylene (*t*-PA) by transoctatetraene, the charge environment of a single iodine atom interacting with the polyene goes through a complete reversal as one goes from Hartree–Fock to a correlated calculation. While the Hartree–Fock ground state is a charge-transfer state with iodine acquiring close to a full electron at the expense of the polyene, the picture changes radically when correlation is included; the ground state now is essentially a neutral iodine interacting with the polyene, while the excited state is a

Correspondence to: G. P. Das.

© 1997 John Wiley & Sons, Inc.
CCC 0020-7608 / 97 / 050651-04

charge-transfer state $I^- + C_8H_{10}^+$. Based on this finding, it was proposed that the charge is transported by the electrons populating these excited states via excitons representing a "charged soliton" traveling along the length of the polymeric chains. A quantitative study of the time evolution of such processes was carried out, leading to a high diffusion mobility and, consequently, large conductivity.

The above study, however, is flawed by several deficiencies: First, the polyene considered is too small with potentially large end effects. Second, iodine in solution is found to exist only in clusters such as I_3 and I_5. Also, the basis set used in the above calculation may not be adequate to represent the charge-transfer states via-à-vis the neutral states even though the correlation level considered may have been right. Moreover, we neglected the effect of the neighboring polymer units, which is expected to be important since the separation between neighboring units (6–7A) is not large enough for the dopant system to interact solely with one unit. In what follows, we analyze all the above deficiencies except that of the basis set, which, because of the great complexity of the problem, we defer to a later work, retaining for the present the simplest basis used in our previous work, namely, the Hay–Wadt ECP basis for iodine and STO-3G for the rest.

Choice of Our Prototype System

Using I_3 instead of I increases the complexity of the analysis in several ways: First, we have a much larger number of valence electrons to deal with. Also, the determination of the ground and excited states has to take into account the fact that the geometry of I_3^- is very different from I_3 in addition to the large geometry change the polyene system undergoes. Since I_3 is really I2 + I and Hartree–Fock gives very poor results for the bonding in I_2 (usually predicting no binding at all), it is necessary that we employ all excitations involving all the valence electrons. At the Hay–Wadt level of the ECP basis, the various quantities of interest pertaining to the $I_2 + I$ problem is shown in Table I.

We shall consider $C_{12}H_{14}$ instead of C_8H_{14} in this work. This will ensure much smaller end effects when the dopant is a single iodine atom and is likely to be adequate for I_3.

TABLE I
ECP energies of atomic, diatomic, and triatomic iodine and their ions at the level of Hay – Wadt ECP basis set.

System	Energy (SCF) (Hartree)	Energy (MCSCF) (Hartree)
I	−11.15723	
I^-	−11.23469	
I_2	−22.31185	−22.34149
I_3	−33.43640	−33.48324
I_3^-	−33.59687	−33.61844
$I_2 + I$	−33.46908	−33.49872

Finally, adding to the above complexity, we have also to include in our discussion the interaction of the iodine molecule with both the adjacent polyene systems between which it finds itself. Thus, it will be necessary to calculate or estimate the interaction of the iodide ion if and when it forms not only with the polyene that it shares but also the neutral one on its other side.

General Computational Framework

The present calculations were performed using the GAMESS software with some important modifications. In our earlier work on the interaction of a solitary iodine atom with transoctatetraene, the active space selected for the CASSCF calculations consisted of the eight π valence and virtual orbitals on the polyene and three on the iodine atom. The geometry optimization using these CASSCF wave functions was a major effort but it was still well within the usual time and "economic" restrictions. In the present case, however, the active space needs to be enlarged to 21 orbitals (nine pertaining to the iodine atoms and 12 to the polyene π-space). This is too large an effort to be treated in a straightforward CASSCF framework, the number of configuration running to millions. We adopted a different scheme to be called the modified MP2 scheme (MMP2) to extract the correlation information.

For each state, we carry out the following steps: (a) We first construct the wave function for the state in question as a limited CASSCF involving only the Hartree–Fock occupied valence orbitals as the active space. In our case, this simply implies

inclusion of a single excitations into the only open shell available. The main purpose of using the CASSCF description is to retain the nature of the input orbitals through the SCF process for easy interpretability both for the "neutral" and "charge-transfer" states. (b) The bonding and antibonding π-orbitals are then localized. This is an important step and the details are found in [4]. This reduces the magnitude of the cross terms that are neglected in the present MP2 process. (c) A first-order CI is then performed using all single excitations into the given virtual space from the configurations generated in the first step. This step, by virtue of Brillouin's theorem, will not yield any significant contribution for the state that has been optimized via a CASSCF process described above. However, this will affect the state not optimized. (d) Now, pairwise correlation contributions are evaluated for each double excitation for both the ground and excited states. In all the calculations being reported here, we selected for our virtual space only the set of π-antibonding orbitals belonging to the polyene.

Results and Discussion

In Table II, we compare the results obtained from rigorous CASSCF calculations with those based on our approximate MMP2 model. Since the quantities of interest are the excitation energies of the states and not their absolute energies, it is evident that the approximate scheme is adequate for our purpose.

In Table III, the interaction potential of I_3 approaching the plane of $C_{12}H_{14}$ vertically is shown in the ground and excited states. No geometry reoptimization is carried out other than the fact that the geometry used for the charge-transfer state, which is the ground state at the uncorrelated level, is that of the cation $C_{12}H_{14}^+$. Similarly, the optimized geometry of neutral $C_{12}H_{14}$ is used for the covalent state, which is the midgap excited state at the Hartree–Fock level. The geometry of I3 was frozen at the minimum geometry of the ion I_3^-.

In Table IV, we show the RHF interaction energies of I_3^- in its linear optimized geometry as it approaches the plane of a neutral polyene molecule $C_{12}H_{14}$. In Table V, we show a balance sheet of energies based on our MMP2 calculations for I_3. Again, the geometries used for the neutral and charge-transfer states are those of $C_{12}H_{14}$ and $C_{12}H_{14}^+$, respectively. The charge-transfer-state energy is corrected upward because of a net repulsion from the neighboring polyene unit assumed

TABLE III

MMP2 energies vs. distance (R) of I_3 from the plane of the polyene $C_{12}H_{14}$; the length of I_3 is taken parallel to the polyene chain axis.

	Energy	
R (angstroms)	Ground state (Hartree)	Excited state (Hartree)
2.94	−490.43777	−490.38256
3.44	−490.45474	−490.39861
3.94	−490.45388	−490.40027
4.44	−490.44918	−490.39996

TABLE II

Comparison of rigorous CASSCf with MMP2: columns 2 and 4 represent the CASSCF results for the ground-state and first-excited-state energies, while columns 3 and 5 are the corresponding MMP2 results.

	Energy			
	Ground state		Excited state	
R (angstroms)	CASSCF (Hartree)	MMP2 (Hartree)	CASSCF (Hartree)	MMP2 (Hartree)
2.5	−316.23030	−316.18606	−316.17745	−316.12908
3.0	−316.23979	−316.20431	−316.19560	−316.15834
3.5	−316.23999	−316.20677	−316.19101	−316.16276
4.0	−316.23893	−316.20625	−316.18479	−316.15795
4.5	−316.23831	−316.20577	−316.17734	−316.15097

TABLE IV

Energies as I_3^- approaches the neutral $C_{12}H_{14}$; *R* is the perpendicular distance of of I_3^- from the plane of the polyene (the length of I_3 is taken parallel to the polyene chain axis).

R (angstrom)	RHF energy (Hartree)
2.94	−490.36435
3.44	−490.37127
3.94	−490.37145
4.44	−490.37144
	−490.40382

TABLE V

Balance sheet of energies of the charge-transfer and covalent states for the $I_3 + C_{12}H_{14}$ system calculated at the optimized geometries of $C_{12}H_{14}^+$ and $C_{12}H_{14}$, respectively.

	Energies	
	Charge-transfer state (Hartree)	Neutral state (Hartree)
MMP2 energy	−490.45474	−490.40027
Correlation error in I_3 and I_3^- and	−0.02157	−0.02964
Repulsive correction from neighbor	0.03255	−0.00227
Geometry correction		−0.03268
Total energy	−490.44376	−490.46486

separated from the first by 6.88 Å. The neutral-state energy is corrected downward since the lowest energy geometry of I_3 is readily iodine and I_2 well separated.

It is clear that within the approximation of the basis set used in this work as well as subject to the omission of "atomic" correlation corrections in the calculations our present model predicts that with I_3 as the dopant the energy of the charge-transfer state is slightly higher than that of the neutral state. When the atomic correlation terms are included, which essentially to improve the electron affinity of iodine by nearly 1 eV, these two states promise to be near-degenerate.

ACKNOWLEDGMENT

The present authors thankfully acknowledge many helpful discussions with Dr. A. T. Yeates.

References

1. H. Shirakawa, E. J. Louis, A. G. McDiarmid, C. K. Chiang, and A. J. Heeger, J. Chem. Soc. Commun. **1977**, 578 (1977).
2. A. J. Epstein and E. M. Cornwell, Eds., *Proceedings of the International Conference on Low-Dimensional Conductors*, Boulder, CO, Aug. 9–14, 1981 [Mol. Cryst. Liq. Cryst. 77 (1981); *Ibid.* 83 (1982).
3. W. P. Su, J. R. Schrieffer, and A. J. Heeger, Phys. Rev. Lett. **42**, 1698 (1979), *Ibid.*, Phys. Rev. B **22**, 2099 (1980).
4. G. P. Das, A. T. Yeates, and D. S. Dudis, Int. J. Quantum Chem. **59**, 251 (1996); *Ibid.* **60**, 1499 (1996).

Free and Hindered Rotations in Endohedral C_{60} Fullerene Complexes

J. HERNÁNDEZ-ROJAS, A. RUIZ, J. BRETÓN, J. M. GOMEZ LLORENTE

Departamento de Física Fundamental y Experimental, Universidad de La Laguna, 38205 Tenerife, Spain

Received 2 March 1997; accepted 5 March 1997

ABSTRACT: We propose a two-parameter model Hamiltonian to analyze the low-energy dynamics of endohedral C_{60} fullerene complexes such as $Li^+@C_{60}$, $Na^+@C_{60}$, $CO@C_{60}$, $LiF@C_{60}$, and $LiH@C_{60}$. The simplicity of the model is a direct consequence of very strong constraints imposed by both high symmetry and close confinement conditions, on the spherical anisotropy of the guest–cage interaction. In the parameter space region expanded by the selected systems, the guest low-energy dynamics undergo transitions from almost free rotations to more or less hindered rotations. These dynamics produce very particular features in the low-temperature rotational spectra, which can be taken, therefore, as fingerprints of a particular guest–cage interaction. © 1997 John Wiley & Sons, Inc. Int J Quant Chem **65:** 655–663, 1997

Key words: Fullerenes; endohedral complexes; rotational spectroscopy

Introduction

The recent discovery of the fullerenes has open a new field in science and technology, joining physicists and chemists in an effort to understand the many interesting possibilities that these new molecules offer, both in the gas and the fullerite solid phases. Among these possibilities we find those related with the use of these carbon aggregates as microscopic cavities to encapsulate atoms and even small molecules. Some experiments have succeeded in producing traces of metallofullerenes (Li, Na, K, Rb, Cs, Ca, Ba, La, ...) [1, 2], rare-gas fullerenes [3, 4], and diatomic fullerenes ($CO@C_{58}$) [5].

The solid phases of these endohedral complexes (endohedrally doped fullerites) become, in general, significantly more stable than the fullerites with

Correspondence to: J. M. Gomez Llorente.
Contract grant sponsor: Dirección General de Investigación.
Contract grant number: PB93-0578.
Contract grant sponsor: Consejería de Educación Cultura y Deportes del Gobierno de Canarias.
Contract grant number: PI 2/95.

© 1997 John Wiley & Sons, Inc.
CCC 0020-7608 / 97 / 050655-09

exohedral doping. On the other hand, the very interesting electric and magnetic properties that have been found in exohedral fullerites are also expected to occur in their endohedral counterparts. Moreover, very interesting applications have been suggested for these particular materials. As an example, we mention Cioslowski and Nanayakkara's proposal [6] for endohedral fullerites of polar molecules (CO, LiF, LiCl, NaF, NaCl), which may rotate more or less freely depending on the dipole–dipole interaction and on the temperature. These endohedral fullerites would "constitute a new class of ferroelectric materials and the first practical realization of ideal electric dipolar lattices," which could show low-temperature phase transitions between dipole ordered and disordered states. The transition temperatures estimated by these authors are in the range 25–60 K.

All these potential applications have stimulated many theoretical studies to elucidate the electronic structure of these compounds and the nature of the guest–cage interaction. The traditional theoretical methods of molecular physics and quantum chemistry have been proved to be very useful in establishing new results. Besides, great experimental efforts are currently devoted to obtain endohedral species in macroscopic quantities, and a very promising technique has been reported recently [7]. In the meanwhile, the results from these theoretical and experimental work have motivated further theoretical studies on dynamical aspects such as the rotational-vibrational motion of the confined species. These dynamics are going to affect some of the fullerite properties. For instance, a more accurate treatment of the phase transitions predicted by Cioslowski and Nanayakkara would require knowledge of this motion. Vibrational-rotational spectra are a primary source of information on these dynamics, but experimental data of this kind are not yet available.

Ab initio calculations for different trapped species have produced some sparse data on the guest–cage interaction; they provide mainly information on the equilibrium positions and vibrational frequencies for the confined atom or molecule. When the interaction is of physical nature, as may be the case when the guest species is a closed-shell atom or molecule, this may be fairly estimated using semiempirical electrostatic arguments. In this way analytical expressions have been proposed [8–11], which reproduce rather accurately [8, 9] the experimental and ab initio [12, 13] data. All this information on the nature of the guest–cage interaction has made possible several attempts to simulate theoretically the vibrational-rotational spectra of some endohedral fullerenes.

The first analyses [14–18] dealt with confined atoms and used a spherical representation of the atom–cage interaction in which the anisotropic terms were neglected. Within this approximation the rotational-vibrational spectrum for on-center endohedral fullerenes is reduced to that of an isotropic anharmonic three-dimensional (3D) oscillator [16, 17], and the corresponding spectrum for off-center fullerenes is that of an effective diatomic molecule [14, 15, 18]. The spherical representation of the atom–cage interaction is in general well justified for on-center atom complexes at low vibrational energies, but not for diatomic guests and off-center atoms. Classical trajectory studies for $Ne@C_{60}$ [19] and classical simulations of the dipole spectra of $Li^+@C_{60}$ [20] anticipated the relevance of the interaction anisotropy. This has been confirmed systematically by our group in a series of publications [21–25] in which we simulate dipole and Raman rotational-vibrational spectra for closed-shell confined atoms and diatomic molecules. We have found that the most significant manifestations of the interaction anisotropy appear in the low temperature ($T \sim 50$ K and lower) spectra. Low anisotropic interactions are found for the $CO@C_{60}$ and $Na^+@C_{60}$ complexes, whose spectra suggest the dominance of almost free rotations. The more anisotropic interactions of $Li^+@C_{60}$, $LiF@C_{60}$, and $LiH@C_{60}$ give rise to spectra, whose assignment requires the existence of librations and hindered rotations.

In this study we will show that all these spectra can be understood in terms of only two scaled parameters, which determine the relative magnitude of the anisotropic part of the guest–cage potential. We will consider isolated complexes, but many of our conclusions can be easily extended with little change to the corresponding fullerites. For completeness we will also review some of our previous results. In the following section we present an effective Hamiltonian describing the rotational motion of endohedral complexes of atoms and diatomic molecules. The third section is dedicated to a systematic analysis of the eigenvalue spectrum of this Hamiltonian as a function of the two scaled parameters. In the fourth section we show how to use this information in order to assign the features of the low-temperature rotational spectra. A further discussion and the main conclusions are presented in the last section.

Effective Scaled Rotational Hamiltonian

The different time scales involved in the dynamics of endohedral complexes of atoms and diatomic molecules can be used to obtain an effective Hamiltonian for the low-frequency motion in which we are interested. After separating the electronic degrees of freedom within the Born–Oppenheimer approximation, the next shorter time scales correspond to the cage, guest, and relative guest–cage vibrational motions [21–23]. At sufficiently low energies (up to $E \sim 150$ cm^{-1}) the complex will be in the ground state of these motions, and a good approximation describing the remaining dynamics can be provided by the effective rotational Hamiltonian [22, 23]

$$H_{\text{rot}} = \frac{1}{2I_c}\mathbf{K}^2 + \frac{\mathbf{l}^2}{2I_g} + V_{\text{eff}}(\alpha, \beta, \gamma; \theta, \phi), \quad (1)$$

where $\mathbf{K} = \mathbf{J} - \mathbf{l}$ is the cage angular momentum operator, which is the difference between the total angular momentum $\mathbf{J}$ and the angular momentum $\mathbf{l}$ associated with the motion of the confined atom or molecule. $I_c = \frac{2}{3}6OM_C R_C^2$ is the cage moment of inertia, with M_C being the carbon mass and R_C the cage radius (3.55 Å); I_g is the guest moment of inertia, and V_{eff} is an effective potential depending on the cage (Euler angles α, β, γ) and guest (θ, ϕ) orientations. This Hamiltonian represents two rotors coupled by kinetic and potential terms. I_g and V_{eff} are, in principle $\mathbf{l}^2$-dependent operators due to centrifugal distortion. However, this dependence has been found to be unimportant in all cases studied so far [21–23], and only very fine details depend on it; thus we will neglect it in the following analyses.

In Ref. [23] we established that this Hamiltonian is valid not only for confined atoms with large enough eccentricity in their equilibrium positions, but also for diatomic molecules with axial equilibrium configurations; in this case, the relative diatom–cage vibrational motion must also be in its ground state. The axial equilibrium configuration is found in all known examples of C_{60} endohedral complexes of diatomic molecules.

The relatively large value of the cage moment of inertia I_c makes a full quantal treatment of the cage rotation a hard task; for instance, the number of J values involved in the rotational spectra, even at the low temperature considered here would be very large (J up to ~ 300). However, this same large I_c value helps in providing further approximations. The simplest one assumes an infinite-mass cage, and leads to the Hamiltonian

$$H_{\text{im}} = \frac{B_e}{\hbar^2}\mathbf{l}^2 + V_{\text{eff}}(\theta, \phi), \quad (2)$$

where $B_e = \hbar^2/2I_g$ is the effective rotational constant. This depends on the equilibrium configuration of the guest species, which is practically determined by the spherically isotropic part of the guest–cage interaction [21, 22]. The B_e values calculated for our endohedral complexes are given in Table I.

It is known that there is a critical temperature, $T \sim 250$ K, in fullerites for the transition between nonrotating to almost free rotating fullerene molecules. For the low temperatures considered in this work, then, the motion of the fullerene molecules should be practically frozen, and the model in Eq. (2) would be then the adequate one. In this case V_{eff} should also account for additional interactions due to the crystal lattice. As will be discussed later, these additional terms are expected to be small when the density of empty cages in the fullerite is large enough.

If not fully quantally, the effects of the cage rotation can be included semiclassically with high reliability. This has been done for the determination of rotational spectra in Refs. [21–23]. It is assumed there that the C_{60} cage rotates freely with a classical and constant angular momentum. One then finds that the main features of these rotational spectra are already predicted by the Hamiltonian in Eq. (2). So we will concentrate our attention in the analysis of this simple model. The particular effects of the cage rotation will be discussed in the fourth section.

TABLE I
Rotational constant and scaled potential parameters for different endohedral complexes.

Guest	B_e (cm^{-1})	C_6^*	C_{10}^*
Li^+	1.45	78.77	80.22
Na^+	1.35	7.89	0.78
CO	1.78	5.46	0.22
LiH	1.82	53.65	30.76
LiF	1.27	80.94	31.58

The reliability of our theoretical analysis now depends on the accuracy of cage–guest effective potential surface V_{eff}, which belongs to the totally symmetric representation (A_g) of the I_h icosahedral group. As discussed in Ref. [22], confinement and symmetry constrain enormously the form of the potential. A natural expansion of the potential surface is done in spherical harmonics (L, M); then the C_{60} I_h symmetry restricts severely the L values participating in such an expansion ($L = 0, 6, 10, 12, \ldots$); furthermore, if electrostatic forces (dispersion-repulsion, cage polarization, etc.) dominate the interaction (as in the closed-shell ions and molecules considered in our work) the strong confinement will make such interaction rather smooth. As a result of all these constraints, it turns out that practically only $L = 0, 6$, and 10 manifolds are required in the expansion of the semiempirical expressions for V_{eff} (relative errors are $\sim 5\%$ at most). The $L = 0$ term is a constant; the $L = 6, 10$ manifolds are reducible representation of the I_h point group. When reduced, each one gives just one A_g representation. Therefore, we may accurately represent the effective interaction with the expression

$$V_{\text{eff}} = C_0 V_0 + C_6 V_6 + C_{10} V_{10}, \qquad (3)$$

where C_L are coefficients, and V_L represents the irreducible A_g representation coming from the L manifold; these functions are chosen to be real and normalized as $\int V_L^2 \, d\Omega = 1$. Some of their values are shown in Figure 1.

After scaling and redefining the energy origin, Eqs. (2) and (3) lead to the expression

$$H_{\text{im}}^* = \mathbf{l}^{*2} + C_6^* V_6 + C_{10}^* V_{10}, \qquad (4)$$

where $H_{\text{im}}^* = (H_{\text{im}} - C_0 V_0)/B_e$, $\mathbf{l}^* = \mathbf{l}/\hbar$, $C_n^* = C_n/B_e$. In conclusion, only the two parameters C_6^* and C_{10}^* determine the low-energy rotational dynamics in our model. Their values, for the systems selected in our work, are given in Table I.

A similar model has been proposed for the rotational dynamics of atom-spherical top van der Waals complexes [26], to represent situations opposite to ours, namely those in which the spherical top is much lighter than the atom. The meaning, range, and effect of these model parameters is thus quite different from ours.

Since the dimension of the parameter space of Hamiltonian (4) is just two, a systematic analysis of the effect of the anisotropy on the eigenvalue spectrum of this Hamiltonian can be readily carried out. This will be presented in the following section.

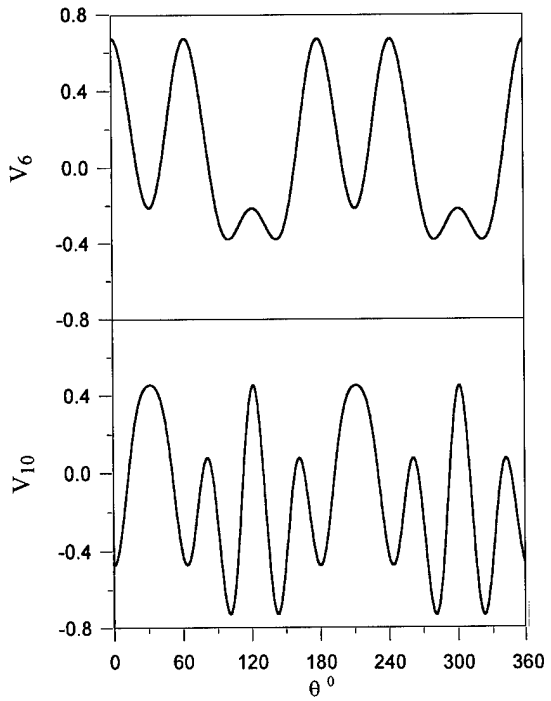


FIGURE 1. Values of the V_6 and V_{10} terms for the guest–cage interaction. They are given as a function of the polar angle θ for azimutal angle $\phi = 0$. The z axis has been chosen along the C_5 fullerene symmetry axis and one of the neighbor C_2 symmetry axis lies on xz plane. The first maximum in V_{10} corresponds to the middle of a short C—C bond and the second one to a long C—C bond. The four absolute minima in both panels correspond to the hexagon centers.

Analysis of the Rotational Eigenvalue Spectrum in the Parameter Space

Figure 2 presents the parameter space expanded by the endohedral complexes selected in our work. A different symbol indicates the position of each system. We will now study the evolution of the low-energy eigenvalues following the four straight lines drawn in this figure. The corresponding correlation diagrams are given in Figures 3–6. The spherical harmonic ($|l, m\rangle$) basis set has been used to diagonalize the scaled Hamiltonian in Eq. (4). Here, l values up to 30 have been included to get converged spectra. In Figure 3 we notice that the eigenvalue spectrum for $Na^+@C_{60}$ corresponds to

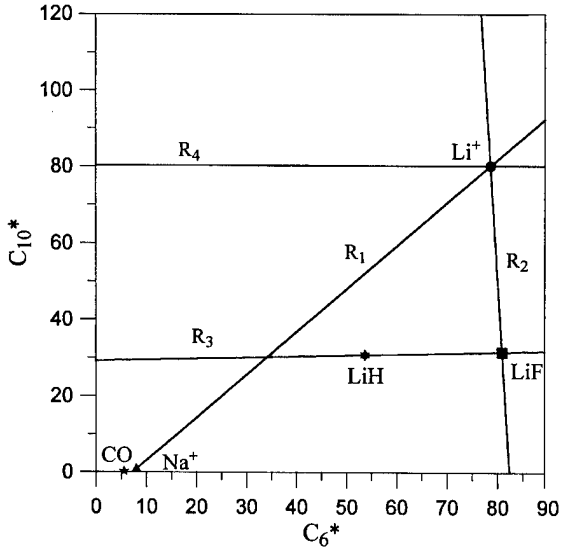


FIGURE 2. Parameter space of the model Hamiltonian in Eq. (4). Different symbols indicate the position of the endohedral complexes selected in our work. Along the lines drawn on this figure we have calculated the energy correlation diagrams in Figures 3 to 6.

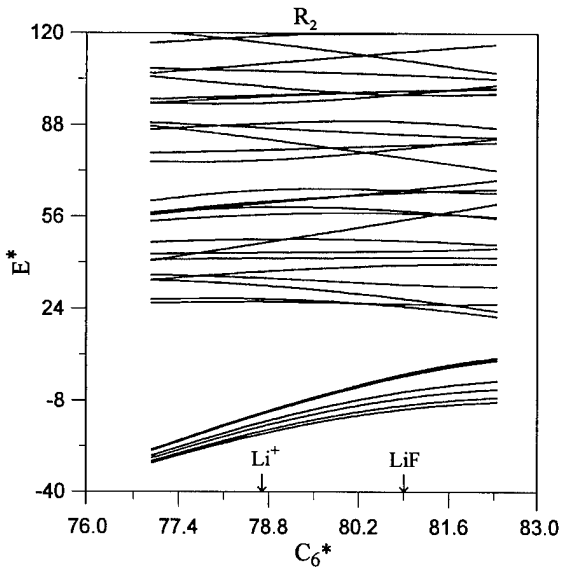


FIGURE 4. Energy correlation diagram as function of the C_6^* parameter calculated along the R_2 line in Figure 2.

that of a slightly perturbed free rotor. In particular, each l manifold splits according to the different irreducible representations of the I_h symmetry group, with practically no mixing between different l manifolds (basically the same spectrum is obtained for $CO@C_{60}$ [24, 27]).

In going from $Na^+@C_{60}$ to $Li^+@C_{60}$, mixing between different l manifolds increases and a single "quasi-band-gap" structure emerges at the bottom of the energy scale. The same structure appears in the eigenvalue spectrum of $LiH@C_{60}$ and $LiF@C_{60}$ (see Figs. 4 and 5), and of any system lying in parameter space expanded by these three

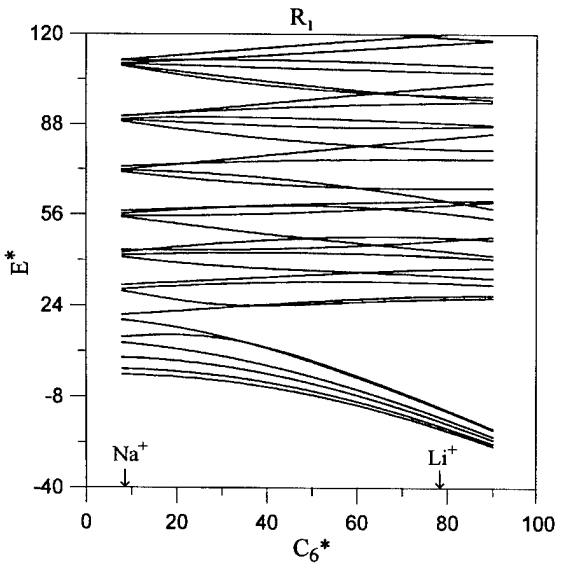


FIGURE 3. Energy correlation diagram as function of the C_6^* parameter calculated along the R_1 line in Figure 2.

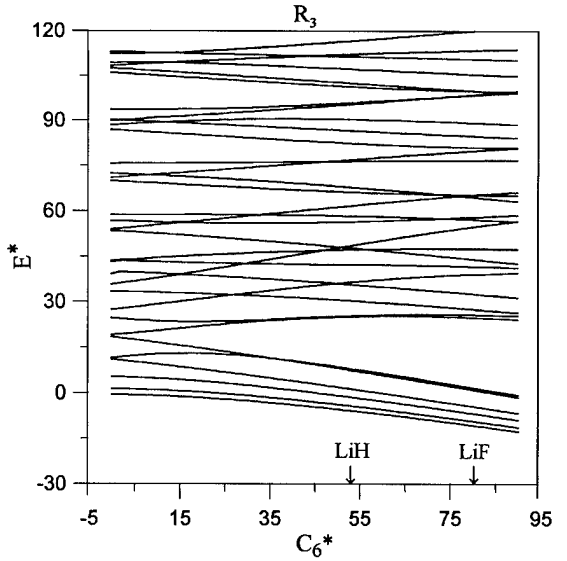


FIGURE 5. Energy correlation diagram as function of the C_6^* parameter calculated along the R_3 line in Figure 2.

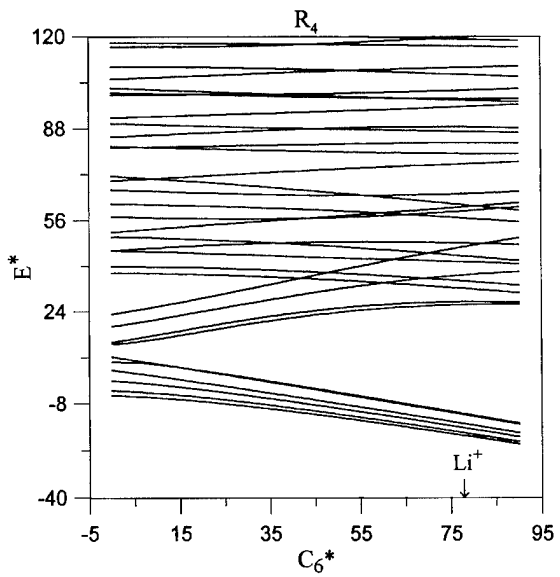


FIGURE 6. Energy correlation diagram as function of the C_6^* parameter calculated along the R_4 line in Figure 2.

complexes. Whenever the quasi-band is formed, it always contains 20 states grouped in the six I_h symmetry manifolds $A_g \oplus T_{1u} \oplus T_{2u} \oplus G_g \oplus G_u \oplus H_g$. This number coincides with the number of hexagon wells in the guest–cage potential surface. Thus the band represents trapping of the guest species in the hexagon wells (librational motion); tunneling connects different wells and accounts for the observed bandwidth. A look at the corresponding eigenfunctions confirms these conclusions: These states present the largest amplitudes around the hexagon wells of the potential [24, 25]. Above the gap, no other bands can be recognized in the eigenvalue spectra of any system lying in parameter space around and between the three anisotropic complexes; this is consistent with the fact that the hexagon well is not deep enough to support more than one quantum state; thus instead of additional bands, a kind of "quasi-continuum" of difficult assignment appears. The energy at which the quasi-continuum starts represents the onset of less-localized motion (hindered rotations). This result is confirmed by the delocalized character of the wave functions for states lying in this energy region. An exception to this rule appears in a set of 12 states, separated in the four symmetry species $A_g \oplus T_{1u} \oplus T_{2u} \oplus H_g$, whose wave functions present localization around the 12 pentagon centers. This localization is, however, not as perfect as the one found around the hexagon wells; some mixing takes place with delocalized states. Around the pentagon centers the guest–cage potential takes maximum values; a local minimum may exist but not deep enough to support a state. By decreasing the magnitude of the C_6^* parameter we can increase the depth of this well, which may now be able to support one state. This is what can be observed in Figure 6: a pentagon band emerges out of the manifold of delocalized states at low C_6^* values. When this band hides in the delocalized manifold of states, mixing takes place, but most of the pentagon character is preserved, except at the infrequent avoided crossings, where that character may be shared by another state. The whole situation is that of a kind of "quasi-resonance band." This is a quasi-band analog of the separatrix and saddle point quasi-resonances found in simple systems [28]. It is known that this localization phenomenon is quite stable and robust against perturbations, as can be confirmed in our case by the correlation diagrams.

At high enough energies mostly free rotations should dominate the dynamics; for instance, this happens in $Li^+@C_{60}$ for angular momentum quantum numbers higher than $l \sim 20$.

Examples of Rotational Spectra

The features of the eigenvalue spectrum and eigenfunctions analyzed in the previous section are going to determine the structure of the low-temperature rotational spectra, which may now be considered as fingerprint of a particular guest–cage interaction. Low-temperature dipole and Raman rotational spectra for these endohedral complexes have been calculated in Refs. [21–25]. As an example we present in Figures 7 and 8 the dipole spectra (T = 50 K) for the $Na^+@C_{60}$ and $Li^+@C_{60}$ complexes as a function of the reduced frequency $\omega^* = \hbar\omega/B_e$. These spectra are the result of a convolution with a Lorentzian whose full width at half maximum is $\Delta\omega^* = 0.2$. While panels (a) correspond to the infinite-mass cage model of Eq. (4), panels (b) present the effect to the cage rotation when this is treated semiclassically as indicated earlier. Note that the rotation of the cage enhances the free rotation of the low-anisotropy $Na^+@C_{60}$, and broadens the librational bands of the more anisotropic $Li^+@C_{60}$. This is a general result established in Refs. [22, 23]; there we showed that this opposite effect is the result of the competition

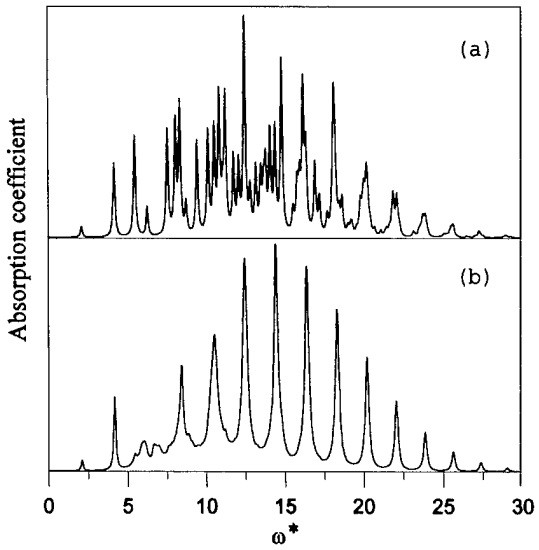


FIGURE 7. Dipole rotational spectra for $Na^+@C_{60}$ calculated at $T = 50$ K. Intensities, in arbitrary units, are given as a function of scaled frequencies. Panel (a) was obtained with the infinite-mass-cage Hamiltonian in Eq. (2). Panel (b) was calculated using a semiclassical approximation for the cage rotation (Ref. [23]). In all cases a Lorentzian of full width 0.2 has been used to convolute the spectrum.

between a centrifugal term that couples the guest rotation to the cage rotation and the anisotropic terms of the guest–cage interaction. When centrifugal coupling dominates over anisotropic potential coupling, the latter is effectively reduced; the result is a sharper rotational spectrum. On the contrary, if the anisotropic potential coupling dominates as in the librational bands, the cage rotation adds an extra broadening, which physically translates into a high tendency for the guest species to follow the cage rotation; as was shown in Refs. [22, 23], this rotational broadening can be accurately simulated by a smoothing of the infinite-mass-cage spectrum with a convoluting function whose width is the estimated cage-rotational broadening (~ 1.5 cm^{-1} at $T = 50$ K).

The spectrum for $Na^+@C_{60}$ confirms the almost free-rotor nature of its eigenvalue spectrum. It shows the $2B_e$ (just 2 in reduced units) oscillation typical of a diatomic molecule. Practically equal spectrum is obtained for $CO@C_{60}$. On the other extreme, the spectrum of $Li^+@C_{60}$ shows wide librational bands. The less intense half of the spectrum is basically due to transitions within the hexagon quasiband structure of the eigenvalue spectrum; the right and more intense half is caused by transition out of this band into the states lying above the gap. Most of the high-intensity lines can be assigned to transitions ending in one of the 12 states of the quasi-resonance pentagon band. This is due to the fact that the threshold for hindered rotation is determined by the high potential regions around the pentagon centers. The complexes $LiH@C_{60}$ and $LiF@C_{60}$ show similar features.

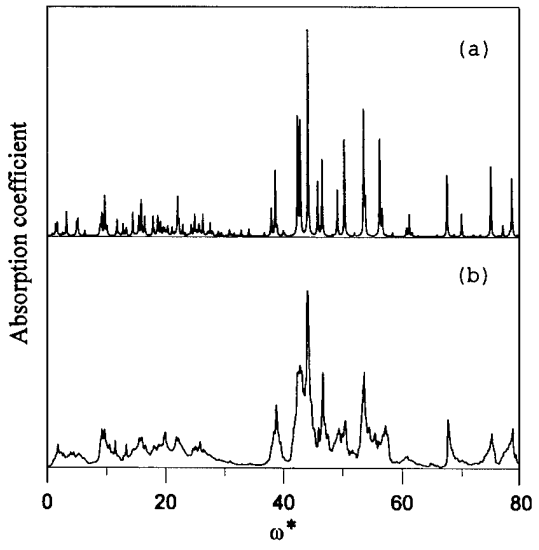


FIGURE 8. Same as Figure 7 for Li^+C_{60}.

Discussion and Conclusions

We have obtained a two-parameter scaled model Hamiltonian which may represent rather accurately the low-energy dynamics of endohedral C_{60} complexes of off-center atoms and small diatomic molecules. The simplicity of the model is a direct consequence of the high symmetry of the cage, the strong confinement conditions, and the mostly physical nature of the guest–cage interaction in the selected systems $Na^+@C_{60}$, $Li^+@C_{60}$, $CO@C_{60}$, $LiH@C_{60}$, $LiF@C_{60}$. This same simplicity has allowed us to perform a systematic analysis of the structure of the eigenvalue spectrum for the model in the parameter space relevant to those endohedral complexes. Energy correlation diagrams as a function of the parameters show transitions between basically two types of structures. On one side we have a parameter region around $Na^+@C_{60}$ and $CO@C_{60}$ complexes in which the model eigenvalue spectrum and the corresponding low-

temperature rotational spectra are like those of slightly perturbed free rotors. In the higher parameter region where $Li^+@C_{60}$, $LiH@C_{60}$, and $LiF@C_{60}$ lie, the effects of the guest–cage interaction anisotropy becomes more relevant; a potential well appears around the C_{60} hexagon centers deep enough to support a quantum state, which causes the appearance of a single quasi-band-gap structure at the bottom of the energy scale, whose states show large amplitudes at the hexagon wells. This band should therefore be associated with librational motion within these wells. Above the energy gap we find the threshold of hindered rotation and more delocalized states. Embedded in this region we have found a quasi-resonance band with states showing large amplitudes around the pentagon centers, which are, in general, regions of unstable equilibrium. By changing the relative magnitude of the model parameters one can stabilize this regions and convert the quasi-resonance-band into a quasi-band separated by energy gaps from the rest of the states. We have seen that the low temperature rotational spectra of the system in this region can be mostly assigned in terms of transitions within the hexagon band and out of this band into the pentagon quasi-resonance-band.

All this analysis has been carried out for a model that assumes that the cage rotation is frozen. However, we have seen that this rotation does not change the features in the rotational spectra which are related to the anisotropy of the guest–cage interaction, on the contrary, it sharpens the transition between the low and high anisotropy features. Actually one could realize rotating and nonrotating cage cases using endohedrally doped fullerites. First, take into account the fact that fullerites present a transition ($T \sim 250$ K) between a phase in which the rotation of the individual fullerene molecules is hindered and a phase in which this rotation is isotropically free, and that below $T \sim 90$ K all these motions are frozen [29]. If the density of doping is low enough, one can disregard the dipole–dipole interaction appearing between nonempty different cages; then the spherical anisotropy of the crystal field acting on a particular guest is going to be practically determined by its cage, since the distance between cages is relatively large (~ 10 Å). So, if we lower the temperature sufficiently ($T < 90$ K), we can realize our low-energy two-parameter model. Above the critical temperature for free cage rotation ($T \sim 250$ K) we should observe the effects of this rotation on the rotational-vibrational spectra, but the temperatures required would make necessary the use of a model which treats higher frequency motions not included in our simple model. The best low-temperature experimental realization of the rotating case could be done, of course, using gas-phase techniques.

Low-temperature spectra become, therefore, fingerprints of a particular guest–cage interaction, and thus a primary experimental source of information on this interaction. This interaction thus determines the low-energy rotational dynamics of the confined species, on which many of the properties of endohedral fullerites may depend, e.g., the critical temperatures (25–60 K) for the dipole-ordered phases predicted by Cioslowski and Nanayakkara [6].

The fact that the guest–cage interaction in complexes studied in our work has a dominantly physical nature allowed us to use semiempirical expressions for it. Strong confinement and symmetry constraints reduce enormously the effects of possible inaccuracies and thus increase the reliability of the calculations. We believe that these results could be valid as well for interaction of more chemical nature, i.e., these same strong constraints may reduce, also in this case, the number of relevant parameters to just the same two ones which come from the $L = 6$, 10 terms of the expansion of the potential in spherical harmonics. In this way on could extend our analysis to off-center complexes such $O@C_{60}$. In this case, an epoxy-type (C—O—C) bond has been suggested under the short C—C fullerene bond [20]. A situation like this can be produced with our model by choosing a negative C_{10}^* coefficient. Therefore, chemical interaction complexes would explore other regions of our two-parameter space. However, the higher librational frequencies expected for chemical bonding may make necessary the joint treatment of these modes with other vibrational modes which were excluded in our model.

ACKNOWLEDGMENTS

This work has been supported by grants from Dirección General de Investigación Científica Técnica (project no. PB93-0578) and from Consejería de Educación Cultura y Deportes del Gobierno de Canarias (project no. PI 2/95).

References

1. D. S. Bethune, R. D. Johnson, J. R. Salem, M. S. de Vries, and C. S. Yannoni, Nature **366**, 123 (1993).
2. H. Schwarz, T. Weiske, D. K. Böhme, and J. Hrušák. *Buckminsterfullerenes*, W. E. Billups and M. A. Ciufolini (eds.), Chapter 10 (VCH Publishers, New York, 1993).
3. M. Saunders, H. A. Jiménez-Vázquez, R. J. Cross, S. Mroczkowski, M. L. Gross, and D. E. Giblin, J. Am. Chem. Soc. **116**, 2193 (1994).
4. M. Saunders, H. A. Jiménez-Vázquez, R. J. Cross, and R. J. Poreda, Science **259**, 1428 (1993).
5. J. F. Christian, Z. Wan, and S. L. Anderson, Chem. Phys. Lett. **199**, 373 (1992).
6. J. Cioslowski and A. Nanayakkara, Phys. Rev. Lett. **69**, 2871 (1992).
7. R. Tellgmann, N. Krawez, S. H. Lin, I. V. Hertel, and E. E. B. Campbell, Nature **382**, 408 (1996).
8. J. Bretón, J. González-Platas, and C. Girardet, J. Chem. Phys. **99**, 4036 (1993).
9. J. Hernández-Rojas, J. Bretón, and J. M. Gomez Llorente, Chem. Phys. Lett. **222**, 88 (1994).
10. L. Pang and F. Brisse, J. Phys. Chem. **97**, 8562 (1993).
11. C. J. Williams, M. A. Whitehead, and L. Pang, J. Phys. Chem. **97**, 11652 (1993).
12. P. P. Schmidt, B. I. Dunlap, and C. T. White, J. Phys. Chem. **95**, 10537 (1991); J. L. Ballester and B. I. Dunlap, Phys. Rev. A **45**, 7985 (1992).
13. J. Cioslowski, J. Am. Chem. Soc. **113**, 4139 (1991).
14. G. W. Van Cleef, G. D. Renkes, and J. V. Coe, J. Chem. Phys. **98**, 860 (1993).
15. C. G. Joslin, J. Yang, C. G. Gray, S. Goldman, and J. D. Poll, Chem. Phys. Lett. **208**, 86 (1993).
16. C. G. Joslin, J. Yang, C. G. Gray, S. Goldman, and J. D. Poll, Chem. Phys. Lett. **211**, 587 (1993).
17. C. G. Joslin, J. Yang, C. G. Gray, S. Goldman, and J. D. Poll, Chem. Phys. Lett. **213**, 377 (1993).
18. C. G. Joslin, C. G. Gray, S. Goldman, J. Yang, and J. D. Poll, Chem. Phys. Lett. **215**, 144 (1993).
19. A. L. R. Bug, A. Wilson, and G. A. Voth, J. Phys. Chem. **96**, 7864 (1992).
20. Y. S. Li and D. Tománek, Chem. Phys. Lett. **221**, 453 (1994).
21. J. Hernández-Rojas, J. Bretón, and J. M. Gomez Llorente, Chem. Phys. Lett. **237**, 115 (1995).
22. J. Hernández-Rojas, J. Bretón, and J. M. Gomez Llorente, J. Chem. Phys. **104**, 1179 (1996).
23. J. Hernández-Rojas, J. Bretón, and J. M. Gomez Llorente, J. Chem. Phys. **104**, 5754 (1996).
24. J. Hernández-Rojas, J. Bretón, and J. M. Gomez Llorente, J. Chem. Phys. **105**, 4482 (1996).
25. J. Hernández-Rojas, J. Bretón, and J. M. Gomez Llorente, J. Phys. Chem. Solids, to appear.
26. J. M. Hutson and A. E. Thornley, J. Chem. Phys. **100**, 2505 (1994).
27. E. H. Olthof, A van der Avoird, and P. E. S. Wormer, J. Chem. Phys. **104**, 832 (1996).
28. O. Atabek, R. Lefebvre, M. Garcia Sucre, J. Gomez Llorente, and H. Taylor, Int. J. Quant. Chem. **40**, 2111 (1991); J. M. Gomez Llorente, F. Borondo, N. Berenger, and R. M. Benito, Chem. Phys. Lett. **192**, 430 (1992).
29. P. A. Heiney, The Fullerenes, H. W. Kroto, J. E. Fischer, and D. E. Cox (eds.) (Pergamon, Oxford, 1993), p. 163 and references therein.

Calculation of Frequency-Dependent Polarizabilities for Open-Shell Systems at the Second-Order Møller–Plesset Perturbation Theory Level Based on the Quasi-Energy Derivative Method

TAKAO KOBAYASHI,[1] KOTOKU SASAGANE,[2]
KIZASHI YAMAGUCHI[1]

[1]*Department of Chemistry, Graduate School of Science, Osaka University, Toyonaka, Osaka 560, Japan*
[2]*Department of Business Administration, Shinshu Junior College, Saku, Nagano 385, Japan*

Received 3 March 1997; revised 30 June 1997; accepted 19 July 1997

ABSTRACT: We extended the dynamic response theory in the Møller–Plesset perturbation theory (MPPT) based on the quasi-energy derivative (QED) method for closed-shell systems to that for open-shell systems. In this study we perform the calculations of frequency-dependent polarizabilities $\alpha(-\omega; \omega)$ for nondegenerate open-shell doublet systems (Li, Na, and K atoms and BeH, MgH, CaH, CN, and NH_2 molecules) in the second-order Møller–Plesset perturbation theory (MP2) starting with time-dependent restricted open-shell Hartree–Fock (TDROHF) approximation. © 1997 John Wiley & Sons, Inc. Int J Quant Chem **65**: 665–677, 1997

Introduction

With the rapid development of laser spectroscopy in experiment, the dynamic response properties are great topics in quantum chemistry now. For closed-shell systems, there are results of calculations of frequency-dependent polarizabilities and hyperpolarizabilities at the not only time-dependent Hartree–Fock (TDHF) level [1–3] but also correlated level [4–13] of theory. Sasagane, Aiga, and Itoh have proposed the quasi-energy derivative (QED) method, which is a more general method to define the dynamic response property [14]. In the QED method, the frequency-dependent polarizability is defined as

$$\alpha_{AB}(-\omega; \omega) = -\left.\frac{\partial^2 W(t)}{\partial \epsilon_A(-\omega)\, \partial \epsilon_B(\omega)}\right|_0, \quad (1)$$

Correspondence to: T. Kobayashi.

International Journal of Quantum Chemistry, Vol. 65, 665–677 (1997)
© 1997 John Wiley & Sons, Inc.
CCC 0020-7608 / 97 / 050665-13

where $W(t)$ is quasi-energy and $\epsilon_B(\omega)$ is the B-direction electric field strength of the $e^{-i\omega t}$ Fourier component. Aiga, Sasagane, and Itoh [15] have formulated the frequency-dependent polarizabilities and hyperpolarizabilities for closed-shell systems at the second-order Møller–Plesset perturbation theory (MP2) level based on the QED method and Aiga et al. [16] have calculated them with consideration of the existence of poles proper to many-body perturbation theory (MBPT) pointed out by Hättig and Heß [17].

On the other hand with respect to dynamic response properties for open-shell systems, there have been only a few reports, in contrast with the case of closed-shell systems. Hettema and Wormer [18] have calculated the frequency-dependent polarizabilities and determined van der Waals coefficients from frequency-dependent polarizabilities with imaginary frequency by the time-dependent restricted open-shell Hartree–Fock (TDROHF) method. Karna [19] has formulated a time-dependent spin-unrestricted Hartree–Fock (TDUHF) theory and has performed the calculations of dynamic nonlinear response properties (up to third order [$\beta(-\omega_\sigma; \omega_1, \omega_2)$]) by the TDUHF method. Pipin and Bishop [20] have calculated the dynamic polarizability of Li atoms by the sum-over-states (SOS) method based on the combined configuration interaction (CI) Hylleraas method. Very recently, Jaszuński and Rizzo [21] have presented the dynamic polarizabilities $\alpha(-\omega; \omega)$ and second hyperpolarizabilities for the dc-Kerr effect $\gamma(-\omega; \omega, 0, 0)$ of Li atoms by the time-dependent multiconfiguration self-consistent field (TDMCSCF, which has usually been referred to as MCTDHF) method. However, the frequency-dependent polarizabilities for open-shell systems at the correlated level of theory have not been reported yet with the exception of Li atoms. The calculations of polarizabilities for open-shell systems, except for Li atoms at the correlated level of theory, have been performed only in a static case by numerical energy derivative (finite-field) method [22–25]. Unfortunately, the dynamic response properties can be calculated only by analytical approach. However, it is also very important to estimate both the frequency dependency and electron correlation of polarizabilities for open-shell systems at the same time. We extended the dynamic response theory in the Møller–Plesset perturbation theory (MPPT) based on the QED method for closed-shell systems to that of open-shell systems [26].

In this work we perform the calculations of frequency-dependent polarizabilities for nondegenerate open-shell doublet systems (Li, Na, and K atoms and BeH, MgH, CaH, CN, and NH_2 molecules) at the TDROHF level and MP2 starting with TDROHF wave function (TDROHF + MP2) level based on the QED method and estimate the electron correlation contribution by MP2. There are some kinds of definitions of orbital energy in ROHF-based perturbation theory with respect to electron correlation. We employed the definition in open-shell perturbation theory 1 (OPT1), which has been proposed by Murray and Davidson [27, 28], as the diagonal blocks of Fock matrix (orbital energy matrix). These are the first calculations of frequency-dependent polarizabilities for open-shell systems except for Li atoms at the correlated level of theory.

Theory

In this section the dynamic response theory for open-shell systems at the MP2 level of theory based on the QED method [26] is briefly showed.

For convenience, we consider the high-spin open-shell systems. We use indices $\{i, j\}$, $\{p, q\}$, $\{a, b\}$, and $\{r, s\}$ to denote closed (doubly occupied), open (singly occupied), virtual, and arbitrary orbitals, respectively, and abbreviate "closed," "open," and "virtual" to "C," "O," and "V," respectively. The TDROHF wave function is approximated as a single determinant:

$$|\Phi_{\mathrm{TDROHF}}(t)\rangle = |\underbrace{\phi_i\bar{\phi}_i\phi_j\bar{\phi}_j\cdots}_{\text{closed}}\underbrace{\phi_p\phi_q\cdots}_{\text{open}}| = \exp[\kappa(t)]|\mathrm{ROHF}\rangle, \quad (2)$$

where

$$\kappa(t) = \sum_{rs}(\kappa_{rs}(t)E_{rs} - \kappa^*_{rs}(t)E^\dagger_{rs}) \quad (3)$$

and

$$E_{rs} = \sum_\sigma a^\dagger_{r\sigma}a_{s\sigma}, \qquad rs \in \{(\mathrm{VC}), (\mathrm{OC}), (\mathrm{VO})\}. \quad (4)$$

ϕ_r is the TDROHF orbital, E_{rs} is the generators of unitary group, $a^\dagger_{r\sigma}, a_{s\sigma}$ are creation and annihilation operators with the spin index σ. Here we introduce the following notation:

$$E_\lambda \equiv E_{rs}, \qquad \kappa_\lambda(t) \equiv \kappa_{rs}(t) \quad (5)$$

and

$$E_{-\lambda} \equiv E_{rs}^{\dagger}, \qquad \kappa_{-\lambda}(t) \equiv -\kappa_{rs}^{*}(t). \tag{6}$$

Then $\kappa(t)$ can be rewritten as

$$\kappa(t) = \sum_{\pm\lambda} \kappa_{\lambda}(t) E_{\lambda}. \tag{7}$$

In the following notation, we regard $|\mathrm{HF}\rangle$ as $|\mathrm{ROHF}\rangle$. Applying the time-dependent variational principle (TDVP) [29, 30] to $|\Phi_{\mathrm{TDROHF}}(t)\rangle$ in condition of the orthonormality of TDROHF orbitals, we obtain TDROHF equation in the first-quantized form in case that the definition in open-shell perturbation theory 1 (OPT1) proposed by Murray and Davidson [27, 28] is used as the diagonal blocks of Fock matrix (orbital energy matrix).

$$\left(F^{\mathrm{OPT1}} - i\frac{\partial}{\partial t}\right)|\phi_r\rangle = \sum_{s\in(C,O,V)} |\phi_s\rangle\theta_{sr}, \qquad r \in (C,O,V), \tag{8}$$

where

$$F^{\mathrm{OPT1}} = \sum_{I}\left[(1-\rho)F^{I}\rho_I + \rho_I F^{I}(1-\rho) + \rho_I F^{C}\rho_I\right] + \sum_{\substack{I,J \\ I\neq J}} \rho_I F^{CO}\rho_J + (1-\rho)F^{C}(1-\rho). \tag{9}$$

In Eq. (9), ρ_C, ρ_O, and ρ are defined as

$$\rho_C = \sum_{i\in C} |\phi_i\rangle\langle\phi_i|, \qquad \rho_O = \sum_{p\in O} |\phi_p\rangle\langle\phi_p|, \qquad \rho = \sum_{r\in C,O} |\phi_r\rangle\langle\phi_r| = \sum_{I} \rho_I \tag{10}$$

and $I(J)$ summation runs over all occupied (closed and open) space and F^C, F^O and F^{CO} are given by

$$F^{C} = h + 2J^{C} - K^{C} + J^{O} - \frac{K^{O}}{2}, \tag{11}$$

$$F^{O} = F^{C} - \frac{K^{O}}{2}, \tag{12}$$

$$F^{CO} = F^{C} + \frac{K^{O}}{2}, \tag{13}$$

where J^C and K^C are the Coulomb and exchange operators defined over the closed orbitals and J^O and K^O are the Coulomb and exchange operators defined over the open orbitals; h is the one-electron part of the Hamiltonian. F^{OPT1} can be expressed by matrix representation:

$$F^{\mathrm{OPT1}} = \begin{array}{c} \\ \mathscr{C} \\ \mathscr{O} \\ \mathscr{V} \end{array} \begin{array}{c} \begin{array}{ccc} \mathscr{C} & \mathscr{O} & \mathscr{V} \end{array} \\ \begin{pmatrix} (F^{C})_{CC} & (F^{CO})_{CO} & (F^{C})_{CV} \\ (F^{CO})_{OC} & (F^{C})_{OO} & (F^{O})_{OV} \\ (F^{C})_{VC} & (F^{O})_{VO} & (F^{C})_{VV} \end{pmatrix} \end{array}.$$

θ_{rs} can be written in the second quantized expression as

$$(CC)\quad \theta_{ij} = \left\langle \phi_i \middle| F^{C} - i\frac{\partial}{\partial t} \middle| \phi_j \right\rangle = \frac{1}{2}\sum_{\sigma}\langle \mathrm{HF}|\left[a_{j\sigma}^{\dagger}, \left[a_{i\sigma}, e^{-\kappa}\left(H - i\frac{\partial}{\partial t}\right)e^{\kappa}\right]\right]_{+}|\mathrm{HF}\rangle, \tag{14}$$

$$(OO)\quad \theta_{pq} = \left\langle \phi_p \middle| F^{C} - i\frac{\partial}{\partial t} \middle| \phi_q \right\rangle = \frac{1}{2}\sum_{\sigma}\langle \mathrm{HF}|\left[a_{q\sigma}^{\dagger}, \left[a_{p\sigma}, e^{-\kappa}\left(H - i\frac{\partial}{\partial t}\right)e^{\kappa}\right]\right]_{+}|\mathrm{HF}\rangle, \tag{15}$$

$$(VV)\quad \theta_{ab} = \left\langle \phi_a \middle| F^{C} - i\frac{\partial}{\partial t} \middle| \phi_b \right\rangle = \frac{1}{2}\sum_{\sigma}\langle \mathrm{HF}|\left[a_{b\sigma}^{\dagger}, \left[a_{a\sigma}, e^{-\kappa}\left(H - i\frac{\partial}{\partial t}\right)e^{\kappa}\right]\right]_{+}|\mathrm{HF}\rangle, \tag{16}$$

$$(CV)\quad \theta_{ia} = \left\langle \phi_i \middle| F^{C} - i\frac{\partial}{\partial t} \middle| \phi_a \right\rangle = \frac{1}{2}\langle \mathrm{HF}|\left[e^{-\kappa}\left(H - i\frac{\partial}{\partial t}\right)e^{\kappa}, E_{ai}\right]|\mathrm{HF}\rangle = 0, \tag{17}$$

$$(OV)\quad \theta_{pa} = \left\langle \phi_p \middle| F^{O} - i\frac{\partial}{\partial t} \middle| \phi_a \right\rangle = \langle \mathrm{HF}|\left[e^{-\kappa}\left(H - i\frac{\partial}{\partial t}\right)e^{\kappa}, E_{ap}\right]|\mathrm{HF}\rangle = 0, \tag{18}$$

$$(CO)\quad \theta_{ip} = \left\langle \phi_i \middle| F^{CO} - i\frac{\partial}{\partial t} \middle| \phi_p \right\rangle = \langle \mathrm{HF} | \left[e^{-\kappa} \left(H - i\frac{\partial}{\partial t} \right) e^{\kappa}, E_{pi} \right] | \mathrm{HF} \rangle = 0. \tag{19}$$

Equations (17), (18), and (19) are so-called Brillouin conditions. As the orbital mixing parameters in the same orbital blocks have no effects on variational principles, we can neglect them. Though we can get canonical TDROHF orbitals by diagonalizing the TDROHF orbital energy matrix, we use non-canonical TDROHF orbitals because of avoiding the possibility of singularity in the orbital mixing parameters in the same orbital blocks [15]. The zeroth-order Hamiltonian in OPT1 starting with TDROHF wave function becomes

$$H_0^{\mathrm{OPT1}} = \sum_{\mathrm{i}} F^{\mathrm{OPT1}}(\mathrm{i}) - i\frac{\partial}{\partial t}. \tag{20}$$

The time-dependent Schrödinger equation in which an overall time-dependent phase factor is isolated is given by

$$\left(H - i\frac{\partial}{\partial t} \right) |\Phi\rangle = |\Phi\rangle W(t), \tag{21}$$

where $W(t)$ is quasi-energy. The total Hamiltonian H is assumed to be written as

$$H = H_0 + H_1, \tag{22}$$

where H_0 is nonrelativistic Born–Oppenheimer electron Hamiltonian of the isolated system and time-dependent perturbed Hamiltonian H_1 is given as

$$H_1 = -\sum_{i=-n}^{n} \sum_{a=x,y,z} \epsilon_a(\omega_i) M_a \exp(-i\omega_i t). \tag{23}$$

M_a is an a-component of electric dipole moment operator and $\epsilon_a(\omega_i)$ is the electric field strength of $e^{-i\omega_i t}$ Fourier component. We assume a periodicity in H_1 as is known in many-mode Floquet theory [31].

In the MPPT starting with TDROHF wave function, Hamiltonian H is partitioned into

$$H = F + V, \tag{24}$$

where $F = \Sigma_i F^{\mathrm{OPT1}}(i)$. In Eq. (21), we introduce the perturbation expansions of $|\Phi\rangle$ and quasi-energy $W(t)$ with respect to V

$$|\Phi\rangle = \sum_{i=0}^{\infty} |\Phi_i\rangle = |\Phi_{\mathrm{TDROHF}}\rangle + \sum_{i=1}^{\infty} |\Phi_i\rangle, \tag{25}$$

$$W(t) = \sum_{i=0}^{\infty} W_i = W_{\mathrm{TDROHF}} + \sum_{i=2}^{\infty} W_i, \tag{26}$$

which result in the nth-order equations

$$\left(F - i\frac{\partial}{\partial t} - W_0 \right) |\Phi_n\rangle + V|\Phi_{n-1}\rangle = \sum_{i=0}^{n-1} |\Phi_i\rangle W_{n-i}, \qquad n \geq 1, \tag{27}$$

with the intermediate normalization condition $\langle \Phi_0 | \Phi \rangle = 1$. Writing $|\Phi_1\rangle$ as $|\Phi_1\rangle = \Sigma_K \exp(\kappa)|K\rangle t_K$ and multiplying Eq. (27) with $n = 1$ from the left by $\langle L|\exp(-\kappa)$, we obtain the equation for determining the amplitude t_K of the first-order MP wave function:

$$\sum_K G_{LK} t_K - i\dot{t}_L + \langle L | e^{-\kappa} V e^{\kappa} | \mathrm{HF} \rangle = 0, \tag{28}$$

where

$$G_{LK} = \langle L|G|K\rangle = \left\langle L \middle| \sum_{rs} \theta_{rs} E_{rs} - W_0 \middle| K \right\rangle, \tag{29}$$

$|K\rangle$ and $\langle L|$ are all doubly excited configuration state functions (CSFs) from |ROHF⟩ and ⟨ROHF|, respectively. The existence of $i\dot{t}_L$ in Eq. (28), which cause the poles proper to the MBPT, have been pointed out by Hättig and Heß [17]. Multiplying Eq. (27) with $n = 2$ from the left by $\langle \Phi_0| = \langle \mathrm{HF}|\exp(-\kappa)$, we obtain the MP2 quasi-energy correction

$$W_2 = \sum_K \langle \mathrm{HF} | e^{-\kappa} V e^{\kappa} | K \rangle t_K. \tag{30}$$

We introduce ζ_λ and $\bar{t}_L$, which are Lagrange multipliers for equations for the TDROHF orbital rotation parameters κ_λ and for the amplitudes t_K, respectively. Then the MP2 quasi-energy Lagrangian L is

$$L = W_{\mathrm{TDROHF}} + \sum_K \langle \mathrm{HF} | e^{-\kappa} V e^{\kappa} | K \rangle t_K + \sum_L \bar{t}_L \left\{ \sum_K G_{LK} t_K - i\dot{t}_L + \langle L | e^{-\kappa} V e^{\kappa} | \mathrm{HF} \rangle \right\} + \sum_{\pm\lambda} \zeta_\lambda \langle \mathrm{HF} | \left[E_\lambda, e^{-\kappa} \left(H - i\frac{\partial}{\partial t} \right) e^{\kappa} \right] | \mathrm{HF} \rangle. \tag{31}$$

The permanent electric dipole moment μ_A and frequency-dependent polarizability $\alpha_{AB}(-\omega;\omega)$ at the ROHF + MP2 level of theory based on the quasi-energy derivative method are defined as

$$\mu_A = -\left.\frac{\partial L(t)}{\partial \epsilon_A(0)}\right|_0, \tag{32}$$

$$\alpha_{AB}(-\omega;\omega) = -\left.\frac{\partial^2 L(t)}{\partial \epsilon_A(-\omega)\,\partial \epsilon_B(\omega)}\right|_0 \tag{33}$$

and explicitly given as

$$\mu_A = \langle \mathrm{HF}|M_A|\mathrm{HF}\rangle + \sum_{L,K} \bar{t}_L^{(0)} G_{LK}\{M_A\} t_K^{(0)} + \sum_{\pm\lambda} \zeta_\lambda^{(0)} \langle \mathrm{HF}|[\![E_\lambda, M_A]]|\mathrm{HF}\rangle, \tag{34}$$

$$\begin{aligned}\alpha_{AB}(-\omega;\omega) &= \langle \mathrm{HF}|\big[M_A, \kappa^B(\omega)\big]|\mathrm{HF}\rangle \\ &\quad - \sum_K \langle \mathrm{HF}|[\![V^{(0)}; \kappa^A(-\omega), \kappa^B(\omega)]|K\rangle t_K^{(0)} \\ &\quad - \sum_L \bar{t}_L^{(0)} \langle L|[\![V^{(0)}; \kappa^A(-\omega), \kappa^B(\omega)]|\mathrm{HF}\rangle \\ &\quad - \sum_{L,K} \bar{t}_L^{(0)} G_{LK}\{J^{AB}(-\omega,\omega)\} t_K^{(0)} \\ &\quad + \sum_K \bar{t}_K^A(-\omega)(G_{KK}^{(0)} - \omega) t_K^B(\omega) \\ &\quad + \sum_K \bar{t}_K^B(\omega)(G_{KK}^{(0)} + \omega) t_K^A(-\omega) \\ &\quad - \sum_{\pm\lambda} \zeta_\lambda^{(0)} \big\langle \mathrm{HF}\big|\big[E_\lambda, J^{AB}(-\omega,\omega)\big]\big|\mathrm{HF}\big\rangle,\end{aligned} \tag{35}$$

where M_A is an A component of electric dipole moment operator, and we have used the symmetric commutator

$$[A;B,C] = \tfrac{1}{2}([[A,B],C] + [[A,C],B]) \tag{36}$$

and have defined the following notations:

$$\begin{aligned}J^{AB}(-\omega,\omega) &= -\big[M_A, \kappa^B(\omega)\big] - \big[M_B, \kappa^A(-\omega)\big] \\ &\quad + \big[H_0; \kappa^A(-\omega), \kappa^B(\omega)\big] \\ &\quad + \omega[\kappa^A(-\omega), \kappa^B(\omega)]\end{aligned} \tag{37}$$

and

$$\begin{aligned}G_{LK}\{A\} &\equiv \frac{1}{2}\sum_{rs}\sum_{\sigma} \langle \mathrm{HF}|\big[a_{s\sigma}^\dagger, [a_{r\sigma}, A]\big]_+|\mathrm{HF}\rangle\langle L|E_{rs}|K\rangle \\ &\quad - \sum_{i\in C}\sum_{\sigma} \langle \mathrm{HF}|\big[a_{i\sigma}^\dagger, [a_{i\sigma}, A]\big]_+|\mathrm{HF}\rangle\langle L|K\rangle \\ &\quad - \frac{1}{2}\sum_{p\in O}\sum_{\sigma} \langle \mathrm{HF}|\big[a_{p\sigma}^\dagger, [a_{p\sigma}, A]\big]_+|\mathrm{HF}\rangle\langle L|K\rangle.\end{aligned} \tag{38}$$

In Eqs. (34) and (35), $t_K^{(0)}$, $\bar{t}_L^{(0)}$, and $\zeta_\lambda^{(0)}$ are the zeroth-order of t_K, $\bar{t}_L$, and ζ_λ; and $\kappa^A(\omega)$, $t_K^A(\omega)$, and $\bar{t}_L^A(\omega)$ are first-order of κ, t_K, and $\bar{t}_L$ in the perturbation expansion with respect to electric field, respectively. These amplitudes and multipliers are determined by the time-averaged variational condition for Lagrangian $\delta\{L\}_T = 0$. $V^{(0)}$ is the zeroth-order fluctuation potential.

Computational Details

The matrix elements in the second quantization language appearing in Eqs. (31) and (32) are calculated automatically by using the program [32] in the algebraic programming language REDUCE3. The program for calculation of frequency-dependent polarizability for open-shell system at the TDROHF + MP2 level of theory is connected to Sasagane's TDROHF program.

BASIS SETS

The primitive Gaussian basis sets for Li, Be, and H on MgH and BeH are derived from Sasagane's smooth-tempered basis sets $(14s)$, $(10s)$, and $(6s)$, respectively. A series of exponents in smooth-tempered basis set is given by $\zeta_k^{(N)}(\alpha,\beta,\gamma,\delta) = \alpha\beta^{k-1}\gamma^{\delta^{N-k}}$, $(k = 1,2,\ldots,N)$. We used the optimized parameter sets $(\alpha,\beta,\gamma,\delta) = (0.023455420, 2.3106846, 17.03123, 0.6247924)$ for Li, $(0.053619160, 2.7557931, 6.0954213, 0.50286011)$ for Be, and $(0.079899519, 2.6231810, 8.3605059, 0.56192361)$ for H on MgH and BeH. The diffuse/polarization functions $(5s14p/12d)$, $(3s9p/7d)$, and $(3s/7p)$ are added to the primitive basis sets for Li, Be, and H on MgH and BeH, respectively, and contracted to $[14s12p10d]$ for Li, $[9s7p5d]$ for Be, and $[6s5p]$ for H on MgH and BeH. The basis sets for Li, Be, and H on MgH and BeH are given in Table I. The primitive basis sets for Na, Mg, and K are derived

TABLE I
Smooth-tempered basis sets for Li, Be, and H.

Li [14*s*12*p*10*d*]			Be [9*s*7*p*5*d*]			H [6*s*5*p*]		
Type	Exponent	Coefficient	Type	Exponent	Coefficient	Type	Exponent	Coefficient
s	21385.428	0.00015000019	*s*	2996.0097	0.00087628616	*s*	82.969412	0.0025894488
	3194.5111	0.0011938157		442.62907	0.0068262223		12.476175	0.019972614
	711.25708	0.0063812155		102.22305	0.033436111		2.8198849	0.098435389
	203.21120	0.025844243		29.554163	0.12406540		0.80137208	0.33188081
	67.847365	0.088942149		9.5663893	0.34213598		0.25901324	0.64992411
	24.968615	0.26721810		3.2775362	0.60474561	*s*	82.969412	0.0018385256
	9.7649438	0.69035061	*s*	2996.0097	0.00069412747		12.476175	0.014297031
s	21385.428	0.00014407673		442.62907	0.0054235614		2.8198849	0.072945077
	3194.5111	0.0011474109		102.22305	0.026767969		0.80137208	0.27386902
	711.25708	0.0061324481		29.554163	0.10217944		0.25901324	0.72303267
	203.21120	0.024909655		9.5663893	0.30120542	*p*	2.8198849	0.0054112577
	67.847365	0.086074721		3.2775362	0.66381458		0.80137208	0.037682410
	24.968615	0.26250884	*s*	1.1554537	1.000000		0.25901324	0.20870216
	9.7649438	0.69744586	*p*	9.5663893	0.069383602		0.089993840	0.82404431
s	3.9668719	1.0000000		3.2775362	0.21148033	*s*	0.089993840	1.000000
p	24.968615	0.065800904		1.1554537	0.80594128	*p*	2.8198849	0.0049857914
	9.7649438	0.19389662	*sp*	0.41323385	1.000000		0.80137208	0.032937307
	3.9668719	0.80737986	*sp*	0.14885938	1.000000		0.25901324	0.20139597
sp	1.6502041	1.0000000	*d*	1.1554537	0.024542010		0.089993840	0.83219299
sp	0.69673783	1.0000000		0.41323385	0.17376192	*sp*	0.032564898	1.000000
d	3.9668719	0.057990397		0.14885938	0.87145372	*sp*	0.012055978	1.000000
	1.6502041	0.12960203	*spd*	0.053818796	1.000000	*sp*	0.0045209224	1.000000
	0.69673783	0.87849098	*spd*	0.019493284	1.000000			
spd	0.29691094	1.0000000	*spd*	0.0070669971	1.000000			
spd	0.12726174	1.0000000	*spd*	0.0025632172	1.000000			
spd	0.054744532	1.0000000						
spd	0.023602899	1.0000000						
spd	0.010190683	1.0000000						
spd	0.0044037687	1.0000000						
spd	0.0019040797	1.0000000						
spd	0.00082356019	1.0000000						
spd	0.00035628623	1.0000000						

from Partridge's uncontracted basis sets [33]. The Partridge's primitive basis sets (18*s*10*p*) for Na and Mg are contracted to [13*s*7*p*] by contracting (6*s*) with the six largest exponents in *s* functions to [1*s*] by using LCAO coefficients of 1*s* orbital in ROHF orbitals as the contraction coefficients and contracting (4*p*) with the four largest exponents in *p* functions to [1*p*] by using LCAO coefficients of 2*p* orbital in ROHF orbitals as the contraction coefficients. The contracted basis sets for Na and Mg [13*s*7*p*] are added by diffuse functions (2*s*5*p*) with exponents obtained from the smallest ones divided by 2.4. Then the polarization functions (10*d*) are added for Na with exponents (13.51565, 5.966856, 2.700045, 1.218512, 0.542187, 0.227413, 0.0948, 0.0395, 0.0165, 0.00685). For Mg, the polarization functions (5*d*) are added with exponents (7.753275, 1.614324, 0.302946, 0.0526, 0.00913). The Partridge's primitive basis set (20*s*12*p*) for K are contracted to [13*s*7*p*] by contracting (10*s*) with the 10 largest exponents in *s* functions to [3*s*] by using LCAO coefficients of 1*s*, 2*s*, and 3*s* orbitals in ROHF orbitals as the contraction coefficients and contracting (7*p*) with the seven largest exponents in *p* functions to [2*p*] by using LCAO coefficients of 2*p* and 3*p* orbitals in ROHF orbitals as the contraction coefficients. The contracted basis set for K [13*s*7*p*] is added by diffuse functions (2*s*4*p*) with exponents obtained from the smallest ones by divided by 2.5. The polarization functions (5*d*) are added for K with exponents (4.086109, 0.845487, 0.15171, 0.0243, 0.00388). Con-

sequently, the basis sets for Na, Mg, and K becomes [15*s*12*p*10*d*], [15*s*12*p*5*d*], and [15*s*11*p*5*d*], respectively. For H on CaH and NH_2, we employed Sadlej's polarized basis set [34] [3*s*2*p*] modified by Sasagane [16, 36]. For H on NH_2, the diffuse/polarization functions (1*s*/1*p*) which have *sp* exponent 0.010215 are added. For C and N, we used Sadlej's polarized basis sets [6*s*4*p*2*d*] modified by Sasagane with diffuse/polarization functions (1*s*1*p*/1*d*) in which *s* exponents are 0.014653 for C and 0.020168 for N and *pd* exponents are 0.012198 for C and 0.017337 for N. The basis sets for C, N, and H on CaH and NH_2 are shown in Table II. For Ca, Sadlej's original polarized basis set [9*s*7*p*2*d*] [35] are used.

GEOMETRIES

The calculations of dipole moments and dynamic polarizabilities of BeH, MgH, CaH, CN, and NH_2 are performed at the experimental equilibrium geometries [37, 38]. For BeH, MgH, CaH, and CN, R_{BeH} = 1.3431 Å, R_{MgH} = 1.7306 Å, R_{CaH} = 2.002 Å, and R_{CN} = 1.1718 Å. For NH_2, the *z* axis is C_{2v} axis, R_{NH} = 1.024 Å, and θ_{NHN} = 103.36°.

Results

In Table III, the experimental [39, 40] and other theoretical [20, 21, 22–25] values of static polarizabilities of Li, Na, and K atoms are given with our work. To our knowledge, no experimental values of dynamic polarizabilities of Li, Na, and K atoms have been reported. In Tables IV, V, and VI, the results of calculations of static and dynamic polarizabilities for Li, Na, and K atoms at the TDROHF and TDROHF + MP2 levels of theory are presented, respectively. The electron correlation contribution to the polarizabilities estimated by the second-order Møller–Plesset perturbation theory (MP2 contribution) is also shown. In Table IV, frequency-dependent polarizabilities for Li atom in

TABLE II
Modified Sadlej's polarized basis sets for C, N, and H.

C [7*s*5*p*3*d*]			N [7*s*5*p*3*d*]			H [3*s*2*p*][a]		
Type	Exponent	Coefficient	Type	Exponent	Coefficient	Type	Exponent	Coefficient
s	5240.6353	0.02235882	*s*	8104.0716	0.02229515	*s*	33.865014	0.008761077
	782.20480	0.1724634		1216.0215	0.1715770		5.094788	0.06542281
	178.35083	0.8672313		277.23428	0.8679323		1.158786	0.2928504
s	50.815942	0.3030337	*s*	78.904023	0.2899865		0.325840	0.7272122
	16.823562	0.7400231		25.874419	0.7525437	*s*	0.102741	1.000000
s	6.175776	0.6940676	*s*	9.346767	0.6700486	*s*	0.032395	1.000000
	2.418049	0.3400776		3.579794	0.3669701	*p*	1.158786	0.1864409
s	0.511900	1.000000	*s*	0.739610	1.000000		0.325840	0.8730840
s	0.156590	1.000000	*s*	0.222617	1.000000	*p*	0.102741	0.9764826
s	0.047901	1.000000	*s*	0.067006	1.000000		0.032395	0.03443044
s	0.014653	1.000000	*s*	0.020168	1.000000			
p	18.841800	0.03923992	*p*	26.868987	0.03948419			
	4.159240	0.2437874		5.991227	0.2486013			
	1.206710	0.8158682		1.750842	0.8111297			
p	0.385540	1.000000	*p*	0.560511	1.000000			
p	0.121940	1.000000	*p*	0.175948	1.000000			
p	0.038568	1.000000	*p*	0.055231	1.000000			
p	0.012198	1.000000	*p*	0.017337	1.000000			
d	1.206710	0.2679750	*d*	1.750842	0.2770034			
	0.385540	0.8199855		0.560511	0.8128187			
d	0.121940	0.6277424	*d*	0.175948	0.5974958			
	0.038568	0.4964327		0.055231	0.5295971			
d	0.012198	1.000000	*d*	0.017337	1.000000			

[a]For H on NH_2, the diffuse / polarization functions (1*s* / 1*p*) which have *sp* exponent 0.010215 are added.

TABLE III
Experimental and theoretical values of static polarizabilities of Li, Na, and K atoms (in a.u.).

	Li	Na	K
ROHF (this work)	170.13	190.55	416.27
ROHF + MP2 (this work)	165.01	165.88	285.23
PNO-CEPA	164.5 [22]	165.02 [23]	287.6 [23]
CI Hylleraas [20]	164.1		
MCSCF [21]	164.91		
UMP4 [24]	164.55		
UHF-CCSD(T) [25]	164.187		
Experimental values	164 ± 3 [39]	159.2 ± 3.4 [39]	292.8 ± 6.1 [39]
		164.6 ± 11.5 [40]	305.0 ± 21.6 [40]

TABLE IV
Frequency-dependent polarizabilities $\alpha(-\omega;\omega)$ of Li atoms (in a.u.).

	Frequency ω							
	0	0.005	0.010	0.015	0.020	0.025	0.030	0.035
TDROHF								
$\alpha(-\omega;\omega)$	170.13	171.07	173.95	178.97	186.52	197.22	212.11	232.92
TDROHF + MP2								
$\alpha(-\omega;\omega)$	165.01	165.90	168.63	173.38	180.52	190.61	204.61	224.09
CI Hylleraas [20]								
$\alpha(-\omega;\omega)$	164.1	165.0	167.7	172.4	179.5	189.6	203.4	222.8
TDMCSCF [21]								
$\alpha(-\omega;\omega)$	164.91	165.80	168.53	173.29				
MP2 contribution[a]								
$\alpha(-\omega;\omega)$	−5.121	−5.169	−5.319	−5.585	−5.996	−6.603	−7.494	−8.831
	−3.10%	−3.12%	−3.15%	−3.22%	−3.32%	−3.46%	−3.66%	−3.94%

[a]MP2 contribution is obtained after subtracting the TDROHF value from the TDROHF + MP2 value. The percentage is obtained by dividing the MP2 contribution with the TDROHF + MP2 value.

TABLE V
Frequency-dependent polarizabilities $\alpha(-\omega;\omega)$ of Na atoms (in a.u.).

	Frequency ω							
	0	0.005	0.010	0.015	0.020	0.025	0.030	0.035
TDROHF								
$\alpha(-\omega;\omega)$	190.55	191.48	194.32	199.25	206.58	216.86	230.90	250.05
TDROHF + MP2								
$\alpha(-\omega;\omega)$	165.88	166.57	168.66	172.27	177.58	184.88	194.64	207.51
MP2 contribution[a]								
$\alpha(-\omega;\omega)$	−24.67	−24.91	−25.65	−26.98	−29.01	−31.97	−36.26	−42.54
	−14.87%	−14.95%	−15.21%	−15.66%	−16.33%	−17.29%	−18.63%	−20.50%

[a]MP2 contribution is obtained after subtracting the TDROHF value from the TDROHF + MP2 value. The percentage is obtained by dividing the MP2 contribution with the TDROHF + MP2 value.

TABLE VI
Frequency-dependent polarizabilities $\alpha(-\omega; \omega)$ of K atoms (in a.u.).

	Frequency ω					
	0	0.005	0.010	0.015	0.020	0.025
TDROHF						
$\alpha(-\omega; \omega)$	416.27	420.50	433.71	457.71	496.22	556.55
TDROHF + MP2						
$\alpha(-\omega; \omega)$	285.23	286.71	291.18	298.59	308.58	319.49
MP2 contribution[a]						
$\alpha(-\omega; \omega)$	−131.05	−133.79	−142.53	−159.12	−187.64	−237.06
	−45.94%	−46.66%	−48.95%	−53.29%	−60.81%	−74.20%

[a]MP2 contribution is obtained after subtracting the TDROHF value from the TDROHF + MP2 value. The percentage is obtained by dividing the MP2 contribution with the TDROHF + MP2 value.

CI Hylleraas calculation by Pipin and Bishop [20] and those at the TDMCSCF level by Jaszuński and Rizzo [21] are shown with our work. Jaszuński and Rizzo used [13*s*11*p*9*d*5*f*] basis set and employed 5*s*4*p*2*d* as the orbitals in the active space to obtain the results of dynamic polarizabilities for Li atom shown in Table IV. Compared with the experimental and other theoretical values, the static polarizabilities of Li, Na, and K atoms at the ROHF + MP2 level give good corrections to those at the ROHF level. Moreover the frequency-dependent polarizabilities of Li atom at the TDROHF + MP2 level of theory are slightly higher than those in CI Hylleraas calculations by Pipin and Bishop and TDMCSCF calculations by Jaszuński and Rizzo but in good agreement with them. The calculations of frequency-dependent polarizabilities for Li atom at the TDROHF + MP2 level of theory are expected to give reliable results. On the other hand, no other theoretical values of dynamic polarizabilities of Na and K atoms have been reported. However, as the static limits of polarizabilities for Na and K atoms at the TDROHF + MP2 level of theory have very close values to the experimental values, the dynamic polarizabilities of Na and K atoms are also likely to give good results. In Tables VII, VIII, IX, X and XI, the results of calculations of dipole moments and static and dynamic polarizabilities for BeH, MgH, CaH, CN, and NH_2 at the ROHF and ROHF + MP2 levels of theory are presented with MP2 contribution, respectively. To our knowledge, no experimental and other theoretical values of static and dynamic polarizabilities for BeH, MgH, CaH, CN, and NH_2 have also been reported. So we cannot compare the calculations of frequency-dependent polarizabilities of those open-shell molecules at the TDROHF + MP2 level of theory with other results.

The percentage of MP2 contribution to dynamic polarizabilities $\alpha(-\omega; \omega)$ of Li, Na, and K atoms and average dynamic polarizabilities $\bar{\alpha}(-\omega; \omega)$ of BeH, MgH, CaH, and CN becomes greater as the frequency increases. The order of percentage of MP2 contribution to dynamic polarizabilities is Li < Na < K and BeH < MgH < CaH. The percentage of MP2 contribution to $\bar{\alpha}(-\omega; \omega)$ of NH_2 shows little change over the frequency range ω = 0–0.045 a.u., where the percentage is 8.55–8.57%.

Conclusion and Discussion

We presented the first calculations of frequency-dependent polarizabilities for open-shell systems except for Li atoms at the correlated level of theory. Compared with experimental [39, 40] and other calculations [20, 21, 22–25], the static polarizabilities of Li, Na, and K atoms at the ROHF + MP2 level give good corrections to those at the ROHF level. The dynamic polarizabilities of Li atoms at the TDROHF + MP2 level of theory are in good agreement with the previous calculations [20, 21]. As no experimental and other theoretical values of static and dynamic polarizabilities for BeH, MgH, CaH, CN, and NH_2 have also been reported, we cannot tell whether the calculations of frequency-dependent polarizabilities of those open-shell molecules at the TDROHF + MP2 level of theory are reliable or not at this time. However, the treatment of frequency-dependent polarizabilities by TDROHF + MP2 method is expected to be

TABLE VII
Dipole moments μ and frequency-dependent polarizabilities $\alpha(-\omega;\omega)$ of BeH (in a.u.).

	Frequency ω									
	0	0.005	0.010	0.015	0.020	0.025	0.030	0.035	0.040	0.045
ROHF										
μ_z	0.1096									
ROHF + MP2										
μ_z	0.1069									
TDROHF										
$\alpha_{xx}(-\omega;\omega)$	36.326	36.378	36.535	36.802	37.188	37.703	39.205	39.205	40.250	41.551
$\alpha_{zz}(-\omega;\omega)$	24.806	24.815	24.840	24.883	24.943	25.021	25.116	25.231	25.365	25.518
$\bar{\alpha}(-\omega;\omega)$[a]	32.486	32.523	32.637	32.829	33.106	33.476	33.950	34.547	35.288	36.207
TDROHF + MP2										
$\alpha_{xx}(-\omega;\omega)$	36.290	36.345	36.510	36.791	37.197	37.742	38.448	39.344	40.470	41.886
$\alpha_{zz}(-\omega;\omega)$	25.578	25.587	25.614	25.659	25.723	25.805	25.907	26.028	26.170	26.333
$\bar{\alpha}(-\omega;\omega)$[a]	32.719	32.759	32.878	33.080	33.372	33.763	34.268	34.905	35.703	36.702
MP2 contribution[b]										
$\alpha_{xx}(-\omega;\omega)$	−0.036	−0.033	−0.026	−0.011	0.009	0.039	0.081	0.139	0.220	0.335
	−0.10%	−0.09%	−0.07%	−0.03%	0.02%	0.10%	0.21%	0.35%	0.54%	0.80%
$\alpha_{zz}(-\omega;\omega)$	0.772	0.772	0.774	0.776	0.780	0.785	0.790	0.797	0.805	0.815
	3.02%	3.02%	3.02%	3.03%	3.03%	3.04%	3.05%	3.06%	3.08%	3.09%
$\bar{\alpha}(-\omega;\omega)$[a]	0.233	0.235	0.241	0.251	0.266	0.288	0.317	0.359	0.415	0.495
	0.91%	0.92%	0.94%	0.98%	1.03%	1.11%	1.23%	1.38%	1.59%	1.88%

[a] $\bar{\alpha} = \frac{1}{3}\alpha_{xx} + \frac{1}{3}\alpha_{zz}$.
[b] MP2 contribution is obtained after subtracting the TDROHF value from the TDROHF + MP2 value. The percentage is obtained by dividing the MP2 contribution with the TDROHF + MP2 value.

TABLE VIII
Dipole moments μ and frequency-dependent polarizabilities $\alpha(-\omega;\omega)$ of MgH (in a.u.).

	Frequency ω									
	0	0.005	0.010	0.015	0.020	0.025	0.030	0.035	0.040	0.045
ROHF										
μ_z	0.5862									
ROHF + MP2										
μ_z	0.5865									
TDROHF										
$\alpha_{xx}(-\omega;\omega)$	69.222	69.353	69.749	70.426	71.406	72.726	74.441	76.627	79.395	82.906
$\alpha_{zz}(-\omega;\omega)$	53.780	53.817	53.929	54.117	54.382	54.728	55.158	55.676	56.288	57.002
$\bar{\alpha}(-\omega;\omega)$[a]	64.075	64.174	64.476	64.989	65.731	66.727	68.013	69.643	71.693	74.271
TDROHF + MP2										
$\alpha_{xx}(-\omega;\omega)$	65.762	65.880	66.236	66.845	67.727	68.917	70.462	72.435	74.935	78.114
$\alpha_{zz}(-\omega;\omega)$	56.452	56.491	56.609	56.807	57.087	57.451	57.904	58.449	59.094	59.844
$\bar{\alpha}(-\omega;\omega)$[a]	62.658	62.750	63.027	63.499	64.181	65.095	66.276	67.773	69.655	72.024
MP2 contribution[b]										
$\alpha_{xx}(-\omega;\omega)$	−3.460	−3.473	−3.513	−3.580	−3.678	−3.809	−3.978	−4.192	−4.460	−4.793
	−5.26%	−5.27%	−5.30%	−5.36%	−5.43%	−5.53%	−5.65%	−5.79%	−5.95%	−6.14%
$\alpha_{zz}(-\omega;\omega)$	2.672	2.674	2.680	2.690	2.704	2.723	2.746	2.773	2.806	2.843
	4.73%	4.73%	4.73%	4.74%	4.74%	4.74%	4.74%	4.74%	4.75%	4.75%
$\bar{\alpha}(-\omega;\omega)$[a]	−1.416	−1.424	−1.449	−1.490	−1.551	−1.632	−1.737	−1.871	−2.038	−2.247
	−2.26%	−2.27%	−2.30%	−2.35%	−2.42%	−2.51%	−2.62%	−2.76%	−2.93%	−3.12%

[a] $\bar{\alpha} = \frac{2}{3}\alpha_{xx} + \frac{1}{3}\alpha_{zz}$.
[b] MP2 contribution is obtained after subtracting the TDROHF value from the TDROHF + MP2 value. The percentage is obtained by dividing the MP2 contribution with the TDROHF + MP2 value.

TABLE IX

Dipole moments μ and frequency-dependent polarizabilities $\alpha(-\omega; \omega)$ of CaH (in a.u.).

	Frequency ω							
	0	0.005	0.010	0.015	0.020	0.025	0.030	0.035
ROHF								
μ_z	0.8351							
ROHF + MP2								
μ_z	1.0168							
TDROHF								
$\alpha_{xx}(-\omega; \omega)$	176.63	177.48	180.10	184.68	191.57	201.37	215.10	234.45
$\alpha_{zz}(-\omega; \omega)$	102.00	102.19	102.78	103.78	105.23	107.16	109.65	112.79
$\bar{\alpha}(-\omega; \omega)$[a]	151.75	152.39	154.33	157.71	162.79	169.97	179.95	193.89
TDROHF + MP2								
$\alpha_{xx}(-\omega; \omega)$	149.93	150.48	152.18	155.12	159.46	165.47	173.56	184.33
$\alpha_{zz}(-\omega; \omega)$	103.15	103.34	103.90	104.86	106.24	108.09	110.46	113.44
$\bar{\alpha}(-\omega; \omega)$[a]	134.34	134.77	136.09	138.37	141.72	146.34	152.53	160.70
MP2 contribution[b]								
$\alpha_{xx}(-\omega; \omega)$	−26.70	−27.00	−27.92	−29.56	−32.11	−35.90	−41.54	−50.11
	−17.81%	−17.94%	−18.35%	−19.06%	−20.14%	−21.70%	−23.93%	−27.19%
$\alpha_{zz}(-\omega; \omega)$	1.16	1.15	1.12	1.08	1.02	0.927	0.810	0.656
	1.12%	1.11%	1.08%	1.03%	0.96%	0.86%	0.73%	0.58%
$\bar{\alpha}(-\omega; \omega)$[a]	−17.42	−17.62	−18.24	−19.35	−21.07	−23.63	−27.42	−33.19
	−12.97%	−13.07%	−13.40%	−13.98%	−14.87%	−16.14%	−17.98%	−20.65%

[a] $\bar{\alpha} = \frac{2}{3}\alpha_{xx} + \frac{1}{3}\alpha_{zz}$.

[b] MP2 contribution is obtained after subtracting the TDROHF value from the TDROHF + MP2 value. The percentage is obtained by dividing the MP2 contribution with the TDROHF + MP2 value.

TABLE X

Dipole moments μ and frequency-dependent polarizabilities $\alpha(-\omega; \omega)$ of CN (in a.u.).

	Frequency ω						
	0	0.005	0.010	0.015	0.020	0.025	0.030
ROHF							
μ_z	−0.9123						
ROHF + MP2							
μ_z	−0.5995						
TDROHF							
$\alpha_{xx}(-\omega; \omega)$	17.424	17.466	17.599	17.835	18.203	18.755	19.591
$\alpha_{zz}(-\omega; \omega)$	20.008	20.010	20.017	20.029	20.045	20.067	20.092
$\bar{\alpha}(-\omega; \omega)$[a]	18.285	18.314	18.405	18.566	18.817	19.192	19.758
TDROHF + MP2							
$\alpha_{xx}(-\omega; \omega)$	18.736	18.840	19.169	19.777	20.782	22.415	25.174
$\alpha_{zz}(-\omega; \omega)$	24.039	24.045	24.064	24.094	24.138	24.194	24.263
$\bar{\alpha}(-\omega; \omega)$[a]	20.504	20.575	20.800	21.216	21.900	23.008	24.870
MP2 contribution[b]							
$\alpha_{xx}(-\omega; \omega)$	1.312	1.373	1.570	1.943	2.579	3.660	5.583
	7.00%	7.29%	8.19%	9.82%	12.41%	16.32%	22.18%
$\alpha_{zz}(-\omega; \omega)$	4.031	4.035	4.046	4.065	4.092	4.127	4.170
	16.77%	16.78%	16.81%	16.87%	16.95%	17.06%	17.19%
$\bar{\alpha}(-\omega; \omega)$[a]	2.218	2.261	2.396	2.650	3.083	3.816	5.112
	10.82%	10.99%	11.52%	12.49%	14.08%	16.58%	20.56%

[a] $\bar{\alpha} = \frac{2}{3}\alpha_{xx} + \frac{1}{3}\alpha_{zz}$.

[b] MP2 contribution is obtained after subtracting the TDROHF value from the TDROHF + MP2 value. The percentage is obtained by dividing the MP2 contribution with the TDROHF + MP2 value.

TABLE XI
Dipole moments μ and frequency-dependent polarizabilities $\alpha(-\omega;\omega)$ of NH_2 (in a.u.).

	Frequency ω									
	0	0.005	0.010	0.015	0.020	0.025	0.030	0.035	0.040	0.045
ROHF										
μ_z	−0.7391									
ROHF + MP2										
μ_z	−0.7052									
TDROHF										
$\alpha_{xx}(-\omega;\omega)$	9.830	9.834	9.847	9.870	9.904	9.949	10.009	10.086	10.186	10.317
$\alpha_{yy}(-\omega;\omega)$	11.932	11.933	11.935	11.940	11.946	11.955	11.965	11.977	11.991	12.007
$\alpha_{zz}(-\omega;\omega)$	11.736	11.738	11.741	11.747	11.756	11.767	11.780	11.796	11.814	11.835
$\bar{\alpha}(-\omega;\omega)$[a]	11.166	11.168	11.175	11.186	11.202	11.224	11.251	11.286	11.330	11.386
TDROHF + MP2										
$\alpha_{xx}(-\omega;\omega)$	10.774	10.779	10.792	10.815	10.848	10.894	10.953	11.031	11.131	11.263
$\alpha_{yy}(-\omega;\omega)$	12.684	12.685	12.688	12.693	12.701	12.711	12.723	12.737	12.754	12.772
$\alpha_{zz}(-\omega;\omega)$	13.180	13.181	13.186	13.195	13.207	13.222	13.240	13.262	13.288	13.317
$\bar{\alpha}(-\omega;\omega)$[a]	12.212	12.215	12.222	12.234	12.252	12.275	12.306	12.343	12.391	12.451
MP2 contribution[b]										
$\alpha_{xx}(-\omega;\omega)$	0.945	0.945	0.945	0.945	0.945	0.944	0.944	0.945	0.945	0.946
	8.77%	8.76%	8.75%	8.73%	8.71%	8.67%	8.62%	8.56%	8.49%	8.40%
$\alpha_{yy}(-\omega;\omega)$	0.752	0.752	0.753	0.754	0.755	0.756	0.758	0.760	0.763	0.765
	5.93%	5.93%	5.93%	5.94%	5.94%	5.95%	5.96%	5.97%	5.98%	5.99%
$\alpha_{zz}(-\omega;\omega)$	1.443	1.444	1.445	1.447	1.451	1.455	1.460	1.467	1.474	1.482
	10.95%	10.95%	10.96%	10.97%	10.99%	11.01%	11.03%	11.06%	11.09%	11.13%
$\bar{\alpha}(-\omega;\omega)$[a]	1.047	1.047	1.047	1.049	1.050	1.052	1.054	1.057	1.061	1.065
	8.57%	8.57%	8.57%	8.57%	8.57%	8.57%	8.57%	8.56%	8.56%	8.55%

[a] $\bar{\alpha} = \frac{1}{3}(\alpha_{xx} + \alpha_{yy} + \alpha_{zz})$.
[b] MP2 contribution is obtained after subtracting the TDROHF value from the TDROHF + MP2 value. The percentage is obtained by dividing the MP2 contribution with the TDROHF + MP2 value.

valid for nondegenerate open-shell systems in which only dynamical pair correlation is significant, that is, TDROHF wave function is good as a reference state of Møller–Plesset perturbation theory.

In this calculation, OPT1 definition is used as the orbital energy matrix. There are some kinds of open-shell perturbation theory with respect to electron correlation by spin-unrestricted or restricted and the difference of definition of orbital energy. It is necessary to estimate the effect to response property by such differences in open-shell perturbation theory. In this study, we treated open-shell doublet systems for the calculation of dynamic polarizabilities at the TDROHF + MP2 level of theory. In the dynamic polarizability for open-shell system which has spin multiplicity more than triplet, the MBPT poles corresponding to the difference between (open + open) and (closed + closed) orbital energy ($\epsilon_p + \epsilon_q - \epsilon_i - \epsilon_j$) may exist, and they may be smaller than the first excited energy by spin-restricted open-shell random-phase approximation (RPA) or TDROHF since open orbital energy may be very close to closed orbital energy. In such a case, the first dispersion of dynamic polarizability exists before the first excited energy by RPA. However, such a MBPT pole has no physical meaning. That difficulty may be avoided by utilizing the arbitrarity of orbital energy.

ACKNOWLEDGMENT

All the computations were carried out on the IBM RS/6000 workstations. We are very grateful to Dr. Fumihiko Aiga for his much valuable advice. We thank Dr. Toshikazu Saitoh, Kazuhide Mori, and Motoyuki Shiga for helpful discussions. We would also like to thank Dr. Fumihiko Aiga and Motoyuki Shiga for supplying their program for calculation of dynamic polarizability of closed-shell system at the MP2 level of theory for us.

References

1. H. Sekino and R. J. Bartlett, J. Chem. Phys. **85**, 976 (1986).
2. J. E. Rice, R. D. Amos, S. M. Colwell, N. C. Handy, and J. Sanz, J. Chem. Phys. **93**, 8828 (1990).
3. S. P. Karna and M. Dupuis, Chem. Phys. Lett. **171**, 201 (1990); J. Comput. Chem. **12**, 487 (1991).
4. K. Sasagane, K. Mori, A. Ichihara, and R. Itoh, J. Chem. Phys. **92**, 3619 (1990).
5. P. Jørgensen, H. J. Aa. Jensen, and J. Olsen, J. Chem. Phys. **89**, 3654 (1988).
6. H. Hettema, H. J. Aa. Jensen, P. Jørgensen, and J. Olsen, J. Chem. Phys. **97**, 1174 (1992).
7. E. S. Nielsen, P. Jørgensen, and J. Oddershede, J. Chem. Phys. **73**, 6238 (1980).
8. P. E. S. Wormer and H. Hettema, J. Chem. Phys. **97**, 5592 (1992).
9. J. E. Rice and N. C. Handy, J. Chem. Phys. **94**, 4959 (1991).
10. J. E. Rice and N. C. Handy, Int. J. Quant. Chem. **43**, 91 (1992).
11. R. Kobayashi, H. Koch, and P. Jørgensen, Chem. Phys. Lett. **219**, 30 (1994).
12. J. F. Stanton and R. J. Bartlett, J. Chem. Phys. **99**, 5178 (1993).
13. B. Dutta, P. Sen, and D. Mukherjee, J. Phys. Chem. **99**, 6441 (1995).
14. K. Sasagane, F. Aiga, and R. Itoh, J. Chem. Phys. **99**, 3738 (1993).
15. F. Aiga, K. Sasagane, and R. Itoh, J. Chem. Phys. **99**, 3779 (1993).
16. F. Aiga and R. Itoh, Chem. Phys. Lett. **251**, 372 (1996); M. Shiga, F. Aiga, and K. Sasagane, submitted.
17. C. Hättig and B. A. Heß, Chem. Phys. Lett. **233**, 329 (1995).
18. H. Hettema and P. E. S. Wormer, J. Chem. Phys. **93**, 3389 (1990).
19. S. P. Karna, J. Chem. Phys. **104**, 6590 (1996).
20. J. Pipin and D. M. Bishop, Phys. Rev. A **45**, 2736 (1992).
21. M. Jaszuński and A. Rizzo, Int. J. Quant. Chem. **60**, 487 (1996).
22. H.-J. Werner and W. Meyer, Phys. Rev. A **13**, 13 (1976).
23. E.-A. Reinsch and W. Meyer, Phys. Rev. A **14**, 915 (1976).
24. G. Maroulis and A. J. Thakkar, J. Phys. B **22**, 915 (1989).
25. N. E. B. Kassimi and A. J. Thakkar, Phys. Rev. A **50**, 2948 (1994).
26. T. Kobayashi, K. Sasagane, and K. Yamaguchi, in preparation.
27. C. W. Murray and E. R. Davidson, Chem. Phys. Lett. **187**, 451 (1991).
28. C. W. Murray and E. R. Davidson, Int. J. Quant. Chem. **43**, 755 (1992).
29. P. W. Langhoff, S. T. Epstein, and M. Karplus, Rev. Mod. Phys. **44**, 602 (1972).
30. P. Kramer and M. Saraceno, *Geometry of the Time-dependent Variational Principle in Quantum Mechanics*, Lecture Notes in Physics, Vol. 140 (Springer, Berlin, 1981).
31. T.-S. Ho, S.-I. Chu, and J. V. Tietz, Chem. Phys. Lett. **96**, 464 (1983).
32. M. Gotoh, K. Mori, and R. Itoh, Int. J. Quant. Chem. **56**, 163 (1995).
33. H. Partridge, J. Chem. Phys. **87**, 6643 (1987); H. Partridge, J. Chem. Phys. **90**, 1043 (1989).
34. A. J. Sadlej, Coll. Czech. Chem. Commun. **53**, 1995 (1988).
35. A. Sadlej and M. Urban, J. Mol. Struct. (Theochem), **234**, 147 (1991).
36. K. Sasagane, in preparation.
37. G. Herzberg, *Molecular Spectra and Molecular Structure I. Spectra of Diatomic Molecules* (Van Nostrand, Toronto, 1966).
38. J. H. Callomon, E. Hirota, K. Kuchitsu, and W. J. Lafferty, Landolt-Börnstein Numerical Data and Functional Relationships in Science and Technology, New Series, II/7. In *Structure Data of Free Polyatomic Molecules*, K.-H. Hellwege and A. M. Hellwege, Eds. (Springer, Berlin, 1987).
39. R. W. Molof, H. L. Schwarz, T. M. Miller, and B. Bederson, Phys. Rev. A **10**, 1131 (1974).
40. W. D. Hall and J. C. Zorn, Phys. Rev. A **10**, 1141 (1974).

Electron Correlation Effects upon the Static (Hyper)polarizabilities of Push-Pull Conjugated Polyenes and Polyynes

DENIS JACQUEMIN,* BENOÎT CHAMPAGNE,† JEAN-MARIE ANDRÉ

Laboratoire de Chimie Théorique Appliquée, Facultés Universitaires Notre-Dame de la Paix, 61, rue de Bruxelles, B-5000 Namur, Belgium

Received 2 March 1997; revised 17 March 1997; accepted 20 March 1997

ABSTRACT: Ab initio calculations, including the electron correlation effects via the Møller–Plesset partitioning, of the static longitudinal polarizability (α_L), first and second hyperpolarizabilities (β_L and γ_L) of small push-pull molecules have been carried out with the 6-31G and 6-31G* basis sets. Two types of conjugated segment (polyacetylene and polyyne) were used as linker between the nitro and amino fragments, chosen as acceptor and donor groups. For small chains, the triply bonded structures lead to larger γ_L than the doubly bonded structures, although the α_L and β_L values order in the opposite direction. The second-order Møller–Plesset (MP2) corrections are essential to obtain correct estimates of the hyperpolarizabilities and are generally much larger than the MP3 and MP4 contributions. Geometry optimizations were carried out with both basis sets within the Hartree–Fock and MP2 schemes; the MP2 geometries lead to smaller bond length alternations and thus larger (hyper)polarizabilities. For α_L a careful choice of the geometry is more crucial than the use of polarization functions during the electronic state calculations; however, for the hyperpolarizabilities, both the geometry and the basis set are of importance. © 1997 John Wiley & Sons, Inc. Int J Quant Chem **65**: 679–688, 1997

Introduction

The nonlinear optical (NLO) properties of push-pull systems have been widely investigated, both theoretically and experimentally in the recent years. These molecules are composed of a conjugated segment end-capped by donor and acceptor groups. Numerous end groups and linkers were tested in order to obtain large NLO responses

*Research Assistant of the Belgian National Fund for Scientific Research.

†Research Associate of the Belgian National Fund for Scientific Research.

Correspondence to: D. Jacquemin.

Contract grant sponsor: FNRS-FRFC, Loterie Nationale.

Contract grant number: 9.4593.92.

Contract grant sponsor: FNRS, Action d'Impulsion à la Recherche Fondamentale of Belgian Ministry of Science.

Contract grant number: D.4511.93.

Contract grant sponsor: Belgian National Interuniversity Research Program.

Contract grant number: PAI/IUAP No. P3-049.

© 1997 John Wiley & Sons, Inc.
CCC 0020-7608 / 97 / 050679-10

(see the review article of Kanis et al. [1]). As shown by Sim et al. for the typical case of *p*-nitroaniline the electron correlation could lead to significant variations of the predicted NLO responses [2]. Indeed the inclusion of the second-order Møller–Plesset (MP2) correction gives, in comparison to the Hartree–Fock level, variations of +12%, +88% and +100% for the polarizability, the first and second hyperpolarizability, respectively. However, most of the ab initio calculations including the electron correlation effects have focused on small systems, and we refer the reader to the works of Shelton and Rice [3] and Bartlett and Sekino [4] for complete reviews of their (hyper)polarizability evaluations.

To maximize the longitudinal polarizability (α_L), first hyperpolarizability (β_L), and second hyperpolarizability (γ_L), a large electronic delocalization along the backbone of the molecule is needed; so, increasing the length of the linker in push-pull molecules leads to larger α_L, β_L, and γ_L values. In the case of β_L, the electronic asymmetry of the fragment is also of importance. Indeed, it was shown experimentally [5] and theoretically [6, 7] that β_L of a symmetric conjugated segment end-capped by donor and acceptor groups presents a saturation to a constant when the length of the linker increases. This is explained by the fact that the push-pull strength becomes *diluted* in the conjugated space for large chains. This saturation is even reproduced by the simple two-state picture, because the energy difference and the dipolar transition moment between the highest occupied and lowest unoccupied molecular orbitals (HOMO and LUMO) as well as the difference of dipole moment between the ground and excited states become constant for very large chains [1]. Nevertheless, the saturation regime is only reached for extended chains; for example, in the case of a α,ω-nitro,amino-polyacetylene systems, 18 carbon atoms are necessary in order to reach the inflection point (where the increase of β_L begins to slow down), whereas β_L is not yet constant for a chain containing 28 carbon atoms [7]. So the formula, $\beta_L = \kappa N^{\eta}$, which is generally used to fit the exponential grow of β_L with chain length (N), is only valid for small chain length and, in order to fit the global shape of the evolution of β_L, one has to use more elaborated functions [7, 8]. To compensate this drawback of a smaller β_L/N (longitudinal first hyperpolarizability per unit cell) for large chains, one could think of an asymmetric linker which will also contribute to the enhancement of β_L. If the use of such a segment prevents the saturation of β_L when chain length increases, it is however to the prejudice of a smaller electronic delocalization along the backbone (as shown, for small oligomers, by Tsunekawa et al. [9, 10]), and thus β_L of medium chains is smaller than for the corresponding symmetric linker [7]. Another idea is to bring more π electrons to the chain by using triply bonded structures. This has sometimes been proposed to optimize the NLO properties, although it has not produced experimental [11] or theoretical [1, 12, 13] larger β_L values than the corresponding doubly bonded structures with the exception of the smallest systems.

Correlated semi-empirical calculations of the evolution with chain length of β_L of push-pull systems have been performed recently; we refer the reader to Ref. [13] for a summary of these investigations. However, to our knowledge, no work has addressed the electron correlation effects on ab initio β_L in a series of oligomers of increasing size. Only a few recent calculations have addressed the electron correlation effects upon α_L and γ_L in oligomeric series. First calculations on model hydrogen chains have been carried out [14–16] and have shown that, in the case of an infinite chain, the ratio between the MP4 and coupled Hartree–Fock (CHF) α_L varies between .97 and .90 with the 6-311G** basis set, while the corresponding γ_L ratio is 1.31. For polyacetylene, polyyne, polypyrrole the ratios between the MP2 and CHF γ_L are 2.84, 8.0 and 2.2, respectively, with the 6-31G basis set [17, 18].

Our study is organized as followed. A brief presentation of the methods is given and followed by a detailed discussion of the results. In particular, comparisons with the nonsubstituted chains are carried out. Finally, we summarize and conclude.

Methodology

STATIC HYPERPOLARIZABILITIES

The application of a static uniform electric field (**E**) on a system leads to a reorganization of its charge distribution. This reorganization is characterized by representing either the dipole moment

($\boldsymbol{\mu}$) or the energy (ϵ) as a power series in **E**:

$$\boldsymbol{\mu} = \boldsymbol{\mu}_0 + \boldsymbol{\alpha} \cdot \mathbf{E} + \frac{1}{2!}\boldsymbol{\beta} : \mathbf{EE} + \frac{1}{3!}\boldsymbol{\gamma} \vdots \mathbf{EEE} + \cdots, \tag{1}$$

$$\epsilon = \epsilon_0 - \boldsymbol{\mu}_0 \cdot \mathbf{E} - \frac{1}{2!}\boldsymbol{\alpha} : \mathbf{EE} - \frac{1}{3!}\boldsymbol{\beta} \vdots \mathbf{EEE} - \cdots, \tag{2}$$

where ϵ_0 and $\boldsymbol{\mu}_0$ are the energy and the dipole moment of the molecule in the absence of an external electric field, respectively; $\boldsymbol{\alpha}$ is the electric dipole polarizability tensor which represents the linear response of the dipole moment to the external electric field. $\boldsymbol{\beta}$ and $\boldsymbol{\gamma}$ are the first and second hyperpolarizability tensors which correspond to the nonlinear phenomena. When the molecule is extended primarily in one direction, the longitudinal component of the (hyper)polarizabilities is the largest because the electrons are primarily delocalized along the backbone of the molecule. This is why we have restricted our investigation to this component.

If the Hellmann–Feymann [19, 20] theorem is fulfilled, i.e., if the wave functions are optimized variationally with respect to all parameters, the quantities in Eqs. (1) and (2) ($\boldsymbol{\mu}_0, \boldsymbol{\alpha}, \ldots$) are equivalent. This theorem is satisfied by Hartree–Fock (HF) wave functions, however it is not the case of the Møller–Plesset ones. Therefore, there exist two ways (leading to different numerical values) to compute the (hyper)polarizabilities; either via a differentiation of the field-dependent dipole moment or via a differentiation of the field-dependent energy, the last one being chosen in the present work.

MÖLLER–PLESSET PARTITIONING

Electron correlation corrections have been considered within the Møller–Plesset partitioning scheme [21] which leads to successive corrections (MP2, MP3,...) which are consistent with electron–electron interactions through second, third, etc. order. This technique presents the advantage to be size-consistent, i.e., to lead to the correct behavior when the size of the system increases. The total MP4 energy can be decomposed into different contributions:

$$\epsilon_{\mathrm{MP4}} = \epsilon_{\mathrm{HF}} + \epsilon_2^{\mathrm{D}} + \epsilon_3^{\mathrm{D}} + \epsilon_4^{\mathrm{S}} + \epsilon_4^{\mathrm{D}} + \epsilon_4^{\mathrm{T}} + \epsilon_4^{\mathrm{Q+R}}, \tag{3}$$

where the subscript characterizes the order of the electron–electron interactions, and the superscript describes the type of substitutions used in the intermediate states; S stands for single substitutions, D for double substitutions, T for triple substitutions. $\epsilon_4^{\mathrm{Q+R}}$ is the energy term coming from the disconnected quadruple substitutions and the associated renormalization. For P_L ($P_L = \alpha_L$, β_L, or γ_L), similar equations may be written:

$$P_{\mathrm{MP2}} = P_{\mathrm{HF}} + P_2^{\mathrm{D}}, \tag{4a}$$

$$P_{\mathrm{MP3}} = P_{\mathrm{MP2}} + P_3^{\mathrm{D}}, \tag{4b}$$

$$P_{\mathrm{MP4}} = P_{\mathrm{MP3}} + P_4, \tag{4c}$$

$$P_{\mathrm{MP4}} = P_{\mathrm{MP3}} + P_4^{\mathrm{S}} + P_4^{\mathrm{D}} + P_4^{\mathrm{T}} + P_4^{\mathrm{Q+R}}, \tag{4d}$$

where P_{MP4} is the MP4 value of P_L, while P_4 is the fourth-order correction to P_L, i.e., the value to be added to P_{MP3} to obtain P_{MP4}. Equations 4(a–d) permit to evaluate the relative importance of each type of excitations in the total P_{MP4} value. It is important to stress that all these terms are size consistent. The inclusion of the electron correlation requires the definition of an active space, i.e., a space where the electron substitutions occur. In our case, this space is the whole orbital space except for the core orbitals. When truncating Møller–Plesset schemes in that way, they are no more size consistent but, has shown in previous studies [22], the computed NLO properties are almost unaffected by this approximation.

FINITE-FIELD PROCEDURE

The NLO properties of the various molecules have been computed by adopting the finite-field (FF) method. This choice has been dictated by the lack of analytical techniques for computing the (hyper)polarizabilities within the Møller–Plesset schemes. In particular, we have considered the field dependence of the energy. So, the finite-difference expressions of the static (hyper)polarizabilities are given by:

$$\alpha_L^{0,k} = -\left[\frac{\partial^2 \epsilon(2^k E_L)}{\partial (2^k E_L)^2}\right]_{E_L = 0} \tag{5a}$$

$$= \lim_{E_L \to 0} \frac{2\epsilon(0) - \epsilon(-2^k E_L) - \epsilon(2^k E_L)}{(2^k E_L)^2}, \tag{5b}$$

$$\beta_L^{0,k} = -\left[\frac{\partial^3 \epsilon(2^k E_L)}{\partial(2^k E_L)^3}\right]_{E_L=0} \quad (5c)$$

$$= \lim_{E_L \to 0} \frac{\epsilon(-2^{k+1}E_L) - 2\epsilon(-2^k E_L) + 2\epsilon(2^k E_L) - \epsilon(2^{k+1}E_L)}{2(2^k E_L)^3}, \quad (5d)$$

$$\gamma_L^{0,k} = -\left[\frac{\partial^4 \epsilon(2^k E_L)}{\partial(2^k E_L)^4}\right]_{E_L=0} \quad (5e)$$

$$= \lim_{E_L \to 0} \frac{-\epsilon(-2^{k+1}E_L) + 4\epsilon(2^k E_L) - 6\epsilon(0) + 4\epsilon(-2^k E_L) - \epsilon(2^{k+1}E_L)}{(2^k E_L)^4}, \quad (5f)$$

where the basic field amplitude, E_L, is a chosen constant. k ($k = 0, 1, \ldots$) defines the lowest nonzero field amplitude used in each calculation. The field amplitudes are following a power of two pattern to permit the use of the Romberg procedure (see below). The 0 superscript stands for the zeroth iteration within the Romberg procedure. These equations are equivalent to those given by Sim et al. [2], if one takes into account the different definitions of β and γ in Eq. (2). Indeed, Sim and co-workers took an experimentalist's convention, developing the energy as: $\epsilon = \epsilon_0 - \boldsymbol{\mu}_0 \cdot \mathbf{E} - \frac{1}{2}\boldsymbol{\alpha}:\mathbf{EE} - \frac{1}{3}\boldsymbol{\beta}:\mathbf{EEE} - \cdots$.

Only the energies corresponding to different electric fields are necessary to use these FF formulas; however, this technique presents two major drawbacks: First, the energy has to be known at several different electric fields for the high-order hyperpolarizabilities; second, the errors associated with the numerical derivative formulas may not be negligible. In practice, the electric fields at which the energy is computed have to be small enough to satisfy the $E_L \to 0$ condition, to avoid SCF convergence problems, and to minimize high-order hyperpolarizability contaminations but large enough to obtain a sufficient number of significant digits in the numerical differentiation which is especially critical for the second hyperpolarizability.

The accuracy of the FF results is improved by the use of the Romberg's procedure [23], which removes the higher-order hyperpolarizability contaminations. Starting with the values obtained by using different k in the Eq. (5), one could systematically improve the hyperpolarizabilities values by applying the iterative formula [16]:*

$$P_L^{p,k} = \frac{4^p P_L^{p-1,k} - P_L^{p-1,k+1}}{4^p - 1}, \quad (6)$$

where p is the number of Romberg iterations. This improves the NLO property estimates to the prejudice of additional computational costs. During our calculations, we have chosen the following basic field amplitude: $E_L = 8.10^{-4}$ a.u. (1 a.u. of electric field = 5.1422 10^{11} V m^{-1}) and k takes the values 0, 1, 2, 3, and 4. This number of electric fields allows us to compute up to $\alpha_L^{4,0}$, $\beta_L^{3,0}$, and $\gamma_L^{3,0}$. As expected, γ_L is the most difficult quantity to calculate due to the high order of the numerical derivative used in Eq. (5); while the α_L values obtained after a unique Romberg's procedure are almost clear of any inaccuracies. In addition to this careful choice of the electric field amplitudes, the SCF convergence criterion has been tightened to 10^{-13} a.u. in the Gaussian94 program [24], which permits us to meet a $\sim 10^{-2}$ a.u. precision on the α_L, $\sim 10^{-1}$ a.u. on β_L, and $\sim 10^{1}$ a.u. on γ_L.

Results and Discussion

Two conjugated linkers [polyacetylene (PA) and polyyne (PY)] and two double-ζ basis sets are used in this work: 6-31G and 6-31G*. The 6-31G* basis is biased toward the representation of electron correlation rather than (hyper)polarizabilities, and generally it gives too small values for the (hyper)polarizabilities. It is difficult to predict which basis set will provide the more accurate correlated (hyper)polarizabilities estimates. It was shown in previous studies that the addition of p functions on the hydrogens of conjugated molecules is not crucial in order to obtain accurate estimates of the correlated longitudinal (hyper)polarizabilities values [18, 22]. This is related to the fact that the NLO responses of these systems are mainly due to the π-electron delocalization. For all systems, the geometry has been fully optimized at the Hartree–Fock and at the MP2 levels of approximation using thresholds corresponding to the tight keyword in the Gaussian94 program [24]. For the sake of simplicity, we do not present here the geometrical parameters obtained by those optimizations. We refer to the work of Tsunekawa and Yamaguchi [10] for a description

* In the Eq. (8) of Ref. [16], one should replace the numerator $4^p\gamma_L^{p-1,k} - \gamma_L^{p-1,k-1}$ by $4^p\gamma_L^{p-1,k} - \gamma_L^{p-1,k+1}$.

of the results of the RHF/6-31G (RHF = restricted HF) geometries of the doubly bonded structures.

Our results are displayed in Tables I, II, and III for the static longitudinal polarizability, first and second hyperpolarizabilities, respectively. Figures 1, 2, and 3 show the ratios between the different components of the total MP4 correction and the HF values; these results have been obtained for the RHF/6-31G optimized structures with the 6-31G basis set.

POLARIZABILITY

From Table I, it is clear that, for small chains, it is mostly the size rather than the nature of the conjugated segment that determines the α_L amplitude. Indeed, the differences in α_L values noticed when using triple bonds instead of double bonds is relatively small. Nevertheless, the PA-type linker gives always the largest α_L. α_2^D is more sensitive to the nature of the conjugated linker than α_{HF}. For small chains, this MP2 correction is always positive, i.e., it leads to an increase of α_L, the opposite being true for longer chains. The relative importance of the MP2 correction (α_2^D/α_{HF}) decreases with chain length (~ 9, 6 and 4% for the PA monomer, dimer, and trimer, respectively), see Figure 1. However, it is not clear that this trend will go on for longer chains. The MP3 and MP4 corrections are smaller than the MP2 one for PA oligomers; however, for the PY dimer α_4 is the largest component of the total Møller–Plesset correction. If α_3^D is negative (and decreases with increasing chain length, as shown on Fig. 1), the sign and the ratio α_3^D/α_4 varies a lot with the nature and length of the conjugated linker. In general the Hartree–Fock and MP4 results are in quite good agreement, and, in the case of the PA trimer, the correction is so negligible that it is not interesting to compute α_{MP4} compared to α_{HF}.

The ratios $\alpha_{MP4}/\alpha_{MP2}$ found by us are very close to the ones computed by Toto and co-workers [18] on nonsubstituted PA chains. For the dimer and trimer they found 0.981 and 0.969, respectively, while we have 0.982 and 0.970 using the 6-31G basis and the RHF/6-31G optimized struc-

TABLE I
Static longitudinal polarizability (a.u.) of NH_2-R-NO_2.[a]

R	Geometry	Basis	α_{HF}	α_{MP2}	α_{MP3}	α_{MP4}
CH=CH	HF/6-31G	6-31G	70.27	76.09	76.22	75.42
	MP2/6-31G	6-31G	75.89	83.31	83.23	81.43
	HF/6-31G	6-31G*	70.10	76.33	75.38	75.66
	MP2/6-31G	6-31G*	75.53	82.22	81.94	81.63
	HF/6-31G*	6-31G	66.54	71.74	71.37	71.44
	MP2/6-31G*	6-31G	71.69	78.06	77.91	77.04
	HF/6-31G*	6-31G*	66.63	72.29	71.08	71.93
	MP2/6-31G*	6-31G*	71.50	78.22	77.01	77.31
$(CH=CH)_2$	HF/6-31G	6-31G	144.45	152.99	150.93	150.24
	MP2/6-31G	6-31G	156.31	167.00	164.66	161.81
	HF/6-31G*	6-31G*	134.81	144.01	139.67	142.52
	MP2/6-31G*	6-31G*	146.88	158.26	154.05	155.53
$(CH=CH)_3$	HF/6-31G	6-31G	239.49	246.74	235.98	239.25
	MP2/6-31G	6-31G	263.21	271.92	260.49	260.32
	HF/6-31G*	6-31G*	221.26	233.16	220.36	
	MP2/6-31G*	6-31G*	248.79	263.47	250.50	
$(CH=CH)_4$	HF/6-31G	6-31G	358.96	354.49		
C≡C	HF/6-31G	6-31G	67.80	71.57	70.69	72.46
	MP2/6-31G	6-31G	74.60	78.38	78.00	78.99
	HF/6-31G*	6-31G*	65.28	70.46	68.53	71.11
	MP2/6-31G*	6-31G*	71.65	77.15	75.38	77.67
$(C\equiv C)_2$	HF/6-31G	6-31G	136.06	137.37	135.68	141.80
	MP2/6-31G	6-31G	151.14	150.28	150.39	155.23
$(C\equiv C)_3$	HF/6-31G	6-31G	221.89	217.27		

[a] 1 a.u. of polarizability = 1.6448×10^{-41} C^2 m^2 J^{-1}.

ture. However, the values of α_{MP2}/α_{HF} are different, as, for nonsubstituted PA, the polarizability always decreases when the electron correlation is included, while for substituted chains it is only the case for the tetramer (and most probably for longer chains). For the dimer, trimer, and tetramer Toto et al. [18] found 0.855, 0.831, and 0.816, respectively, while we have 1.06, 1.03, and 0.987 using the 6-31G basis and the RHF/6-31G geometry. Our chains are of course too small to show a convergence behavior.

The triple excitations contribute largely to the total MP4 correction; and in the case of the trimer, α_4^T is even larger than α_4, as shown by Figure 1. So the MP4(SDQ) values are not more accurate than the MP3 ones. This conclusion has been reached many times before for conjugated molecules [18, 22].

When optimizing at the MP2 level, the bond length alternation (BLA) decreases, i.e., the difference of bond length between single and double (or triple) bonds decreases and α_L increases ($\sim +7\%$). The addition of *d* polarization functions on the second-row atoms during the optimization process leads to an increase of the BLA and a decrease of α_L ($\sim -6\%$). In that respect, it is striking to note that for NH_2—CH=CH—NO_2, the difference between the MP4/6-31G//MP2/6-31G (finite-field calculation based on MP4 energies computed on the MP2 optimized geometry with the 6-31G basis set) and MP4/6-31G*//MP2/6-31G* α_L is mostly due to the variation of geometry and not to the addition of *d* functions during the FF calculations.

FIRST HYPERPOLARIZABILITY

Again for the first hyperpolarizability, the MP2 contribution to the total MP4 correction is by far the largest, and the ratio β_{MP2}/β_{HF} is relatively stable for a given conjugated linker, showing only small decrease with chain length. For the PA-like chains, this ratio is 2.70, 2.44, 2.26, and 2.25 for the monomer, dimer, trimer, and tetramer at the RHF/6-31G level (Fig. 2). It is striking to note that for the infinite chain this ratio is undetermined

TABLE II
Static longitudinal first hyperpolarizability (a.u.) of NH_2—R—NO_2.[a]

R	Geometry	Basis	β_{HF}	β_{MP2}	β_{MP3}	β_{MP4}
CH=CH	HF/6-31G	6-31G	−313.4	−846.9	−814.1	−824.0
	MP2/6-31G	6-31G	−379.2	−1095.7	−1017.2	−1058.4
	HF/6-31G	6-31G*	−246.4	−650.6	−600.1	−643.9
	MP2/6-31G	6-31G*	−308.5	−826.5	−769.7	−848.0
	HF/6-31G*	6-31G	−263.8	−706.9	−680.8	−688.0
	MP2/6-31G*	6-31G	−323.9	−902.2	−853.2	−874.1
	HF/6-31G*	6-31G*	−204.8	−544.4	−500.5	−537.7
	MP2/6-31G*	6-31G*	−256.5	−699.1	−634.1	−689.4
$(CH=CH)_2$	HF/6-31G	6-31G	−1494.1	−3649.9	−3713.5	−3700.4
	MP2/6-31G	6-31G	−1798.1	−4639.8	−4630.9	−4627.1
	HF/6-31G*	6-31G*	−1025.7	−2449.0	−2340.2	−2495.9
	MP2/6-31G*	6-31G*	−1266.2	−3139.3	−3022.1	−3184.7
$(CH=CH)_3$	HF/6-31G	6-31G	−4272.8	−9635.1	−9710.6	−9771.8
	MP2/6-31G	6-31G	−5219.2	−12438.7	−12513.5	−12397.7
	HF/6-31G*	6-31G*	−2951.5	−6558.7	−6137.6	
	MP2/6-31G*	6-31G*	−3811.4	−8844.8	−8567.7	
$(CH=CH)_4$	HF/6-31G	6-31G	−8168.6	−18459.1		
C≡C	HF/6-31G	6-31G	−524.7	−828.5	−822.8	−754.8
	MP2/6-31G	6-31G	−653.6	−1112.5	−1083.2	−988.1
	HF/6-31G*	6-31G*	−341.9	−528.9	−500.2	−490.8
	MP2/6-31G*	6-31G*	−456.4	−720.5	−687.9	−661.3
$(C≡C)_2$	HF/6-31G	6-31G	−1550.6	−2436.4	−2360.0	−2233.4
	MP2/6-31G	6-31G	−1999.1	−3311.8	−3199.5	−2931.5
$(C≡C)_3$	HF/6-31G	6-31G	−3057.0	−4651.8		

[a] 1 a.u. of first hyperpolarizability = 3.2063×10^{-53} C^3 m^3 J^{-2}.

TABLE III
Static longitudinal second hyperpolarizability (10^1 a.u.) of NH_2-R-NO_2.[a]

R	Geometry	Basis	γ_{HF}	γ_{MP2}	γ_{MP3}	γ_{MP4}
CH=CH	HF/6-31G	6-31G	742	1409	1419	2116
	MP2/6-31G	6-31G	1030	2035	2060	3207
	HF/6-31G	6-31G*	618	999	1014	1414
	MP2/6-31G	6-31G*	939	1600	1640	2317
	HF/6-31G*	6-31G	765	1555	1466	1988
	MP2/6-31G*	6-31G	866	1716	1689	2429
	HF/6-31G*	6-31G*	668	1217	1139	1484
	MP2/6-31G*	6-31G*	728	1248	1230	1707
$(CH=CH)_2$	HF/6-31G	6-31G	6660	17369	18092	21632
	MP2/6-31G	6-31G	8652	24123	24689	30515
	HF/6-31G*	6-31G*	4950	11790	11336	13605
	MP2/6-31G*	6-31G*	5784	14181	14056	17126
$(CH=CH)_3$	HF/6-31G	6-31G	34321	91241	94194	106614
	MP2/6-31G	6-31G	43544	125193	129089	147598
	HF/6-31G*	6-31G*	24463	59672	56391	
	MP2/6-31G*	6-31G*	29629	76354	76241	
$(CH=CH)_4$	HF/6-31G	6-31G	99351	269353		
C≡C	HF/6-31G	6-31G	1982	3864	3706	4146
	MP2/6-31G	6-31G	2553	5405	5156	5787
	HF/6-31G*	6-31G*	1382	2544	2270	2711
	MP2/6-31G*	6-31G*	1776	3270	3035	3525
$(C\equiv C)_2$	HF/6-31G	6-31G	11234	22117	20392	22757
	MP2/6-31G	6-31G	14162	31220	28811	31577
$(C\equiv C)_3$	HF/6-31G	6-31G	31400	61949		

[a] 1 a.u. of second hyperpolarizability = 6.2352×10^{-65} C^4 m^4 J^{-3}.

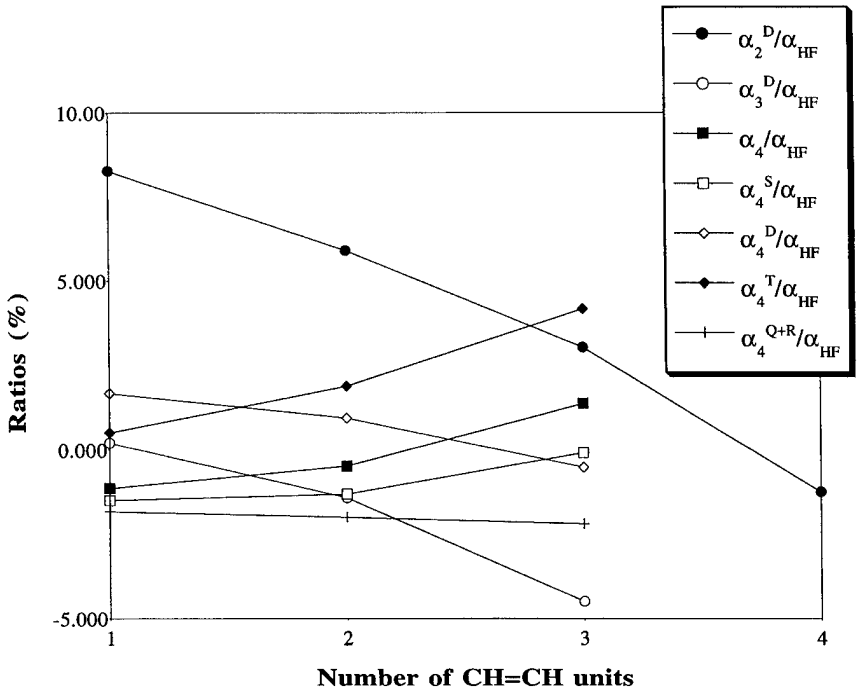


FIGURE 1. Ratios between the Møller–Plesset corrections and the Hartree–Fock static polarizability values for α,ω-nitro,amino polyene chains. These results have been obtained with the 6-31G basis set on the RHF/6-31G optimized structures.

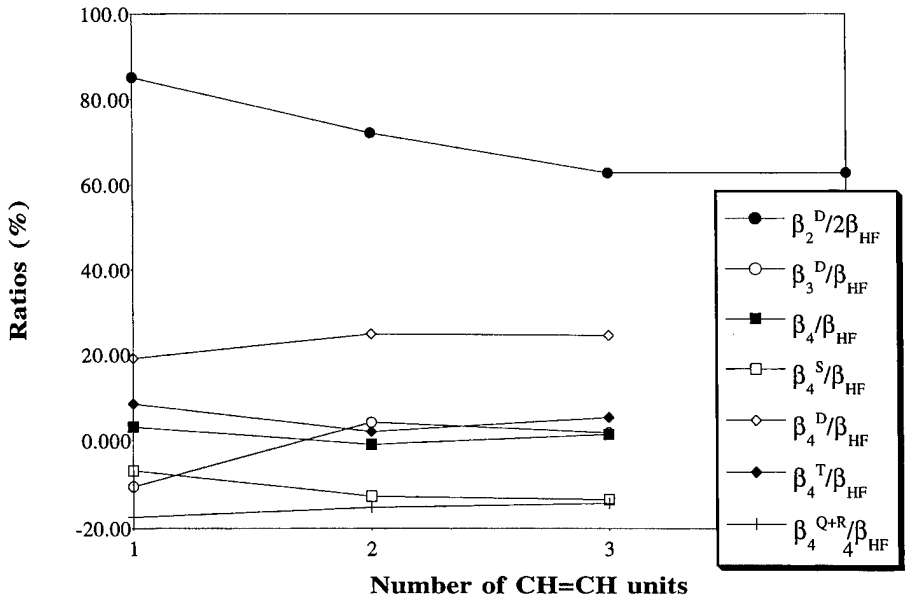


FIGURE 2. Ratios between the Møller–Plesset corrections and the Hartree–Fock static first hyperpolarizability values for α,ω-nitro,amino polyene chains. These results have been obtained with the 6-31G basis set on the RHF / 6-31G optimized structures. The β_2^D / β_{HF} ratio has been divided by a factor 2 for the purpose of visibility.

because the PA has a zero β_L. For comparison the ratio found, by a similar method, is 1.62 for the *p*-nitro-aniline [2] and −4.48 for the polymethineimine (PMI) dimer [22]. (These PMI oligomers are similar to PA, but half of the carbon atoms are replaced by nitrogen atoms.) This ratio slightly increases when the geometry optimization is carried out at the MP2 level, as a result of the larger electronic delocalization along the backbone but is almost the same for both basis sets. For PA, with the 6-31G basis set, we have $|\beta_3^D| > |\beta_4|$, but their relative sign changes as a function of the geometry, the basis set, as well as the length of the conjugated segment. However, with the same basis set, in PY chains the opposite is true: $|\beta_3^D| < |\beta_4|$. The contribution of the triple excitations to the total MP4 correction is generally large: $|\beta_4^T| > |\beta_4|$. Moreover it is striking to note the relative stability with chain length of most of the ratios drawn at Figure 2.

Note the importance of the electron correlation corrections in the ordering of the doubly versus triply bonded structures. Indeed, for the monomer and dimer, the β_{MP4} values order in the opposite direction to β_{HF} ones; while the ordering given by the MP2 or MP3 technique changes as a function of the basis set and the geometry used. However, for the trimer, it becomes clear, even at HF level, that the PA linker leads to larger β_L.

Under a geometry optimization at the MP2 level, the β_L values increase significantly (from +20 to +40%) compared to the values obtained on the corresponding HF optimized geometry. The addition of polarization functions on the carbon atoms leads to a decrease of β_L (from −30 to −40%). This basis set effect can be divided into two components: a direct one, coming from the variation of the computed property, and an indirect one, coming from the change on geometry. Although, for NH_2—CH=CH—NO_2 both components are important (which was not the case for the polarizability) and have the same sign, the sum does not reproduce exactly the *full* 6-31G* results, showing that they are not purely additive.

SECOND HYPERPOLARIZABILITY

In the computation of γ_L, similarly to β_L, the MP2 correction is of more importance, and generally, one can notice, on Figure 3 that $\gamma_2^D > \gamma_{HF}$. Moreover, the ratio γ_{MP2}/γ_{HF} increases with chain length, which goes in opposition to the nonsubstituted PA chains. For the monomer, dimer, trimer, and tetramer of nonsubstituted PA, Toto and co-

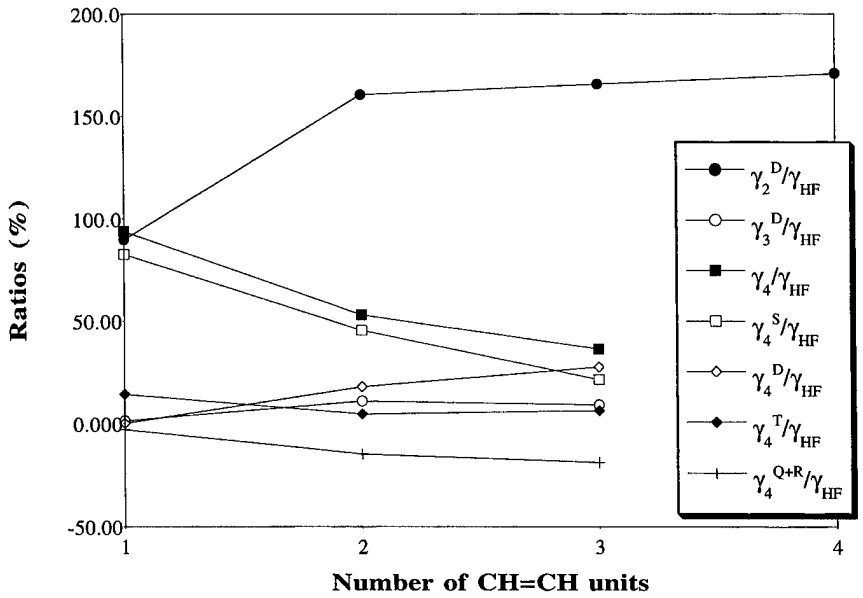


FIGURE 3. Ratios between the Møller–Plesset corrections and the Hartree–Fock static second hyperpolarizability values for α,ω-nitro,amino polyene chains. These results have been obtained with the 6-31G basis set on the RHF / 6-31G optimized structure.

workers [18] found the ratio to be 3.05, 2.20, 2.00, and 1.92, respectively, while we have 1.90, 2.61, 2.66, and 2.71 using the 6-31G basis and the RHF/6-31G geometry. For small chains γ_4 has a magnitude comparable to γ_2^D for the CH=CH fragment, but the relative importance of the fourth-order correction decreases with increasing chain length. Indeed, γ_4/γ_{HF} decreases when shifting from the dimer to the trimer, while γ_2^D/γ_{HF} still increases (see Fig. 3). γ_3^D changes of sign according to the linker studied but is smaller by one order of magnitude than both γ_2^D and γ_4. In the case of γ_L the triple excitations do not contribute largely to the total MP4 correction, and thus the relatively cheap MP4(SDQ) method may be accurate.

The substituted PY monomer and dimer present large γ_L values in comparison to the corresponding substituted PA molecules. This means that the largest polarizability does not systematically lead to the largest second hyperpolarizability; although for long chains this is going to be true. The ratio γ_{MP2}/γ_{HF} (each being computed at the corresponding 6-31G optimized geometry) of the substituted (nonsubstituted) PY dimer is 2.78 (2.27, see Ref. [17]).

The effects of the geometry and the basis set on γ_L are comparable to the ones noticed for α_L and β_L, i.e., the MP2 geometry leads to larger γ_L values; the addition of polarization function to smaller one. Like β_L, the amplitude of γ_L depends on the geometry and the basis set used during the FF calculations.

Conclusions and Outlook

We have carried out Møller–Plesset calculations of the static polarizability, first and second hyperpolarizabilities of polyacetylene and polyyne linkers end-capped by nitro and amino groups. The MP2 correction, which leads to significant increases of the hyperpolarizability estimates, is generally much larger than the MP3 and MP4 ones, except in the cases of the second hyperpolarizability of small PA chains and of the polarizability of the PY dimer. If the absolute values of NLO properties are very different for substituted or nonsubstituted chains, the ratios P_{MP2}/P_{HF} (and especially P_{MP4}/P_{MP2}) are quite close, especially for medium-size oligomers. PA linkers always lead to larger static (hyper)polarizabilities than the PY chains, except in the case of γ_L of small oligomers. For α_L and β_L, P_{MP2}/P_{HF} decreases with increasing chain length, while for γ_L this ratio increases.

Under optimization at the MP2 level, the bond length alternation decreases, and thus the (hyper)polarizabilities increase; while the addition of *d* polarization functions on the second-row atoms decreases the NLO estimates.

In our calculations we have neglected the vibrational contribution to the (hyper)polarizabilities; however, these contributions may be of importance, as recently reviewed [25]. For example, it was shown that the static vibrational contributions to β_L is more than twice the electronic contributions for the small NO_2—$(CH{=}CH)_N$—NH_2 chains at the RHF/6-31G level within the double harmonic approximation. To our knowledge, no Møller–Plesset correction of the vibrational first hyperpolarizability has been computed yet for such push-pull systems, and it is still impossible to know how the relative weight of the vibrational contributions will change when electron correlation corrections are included.

Calculations including the electron correlation at the MP2 level of substituted PA oligomers of medium and large size are now carried out in our laboratory in order to address the saturation behavior.

ACKNOWLEDGMENTS

The authors are indebted to Prof. B. Kirtman for careful reading of the manuscript. D. J. and B. C. thank the Belgian National Fund for Scientific Research for their Research assistant and Research associate position, respectively. All calculations have been performed on the IBM RS6000 cluster of the Namur Scientific Computing Facility (Namur-SCF). The authors gratefully acknowledge the financial support of the FNRS-FRFC, the Loterie Nationale for the convention No. IVo.2.4159.97, and the Belgian National Interuniversity Research Program on Sciences of Interfacial and Mesoscopic Structures (PAI/IUAP No. P4/10).

References

1. D. R. Kanis, M. A. Ratner, and T. J. Marks, Chem. Rev. **94**, 195 (1994).
2. F. Sim, S. Chin, M. Dupuis, and J. E. Rice, J. Phys. Chem. **97**, 1158 (1993).
3. D. P. Shelton and J. E. Rice, Chem. Rev. **94**, 3 (1994).
4. R. J. Bartlett and H. Sekino, in *Nonlinear Optical Materials: Theory and Modeling*, Sashi P. Karna and Alan T. Yeates, Eds., (ACS Symposium Series No. 628, Washington, DC, 1996), pp. 23–57.
5. M. Blanchard-Desce, C. Runser, A. Fort, M. Barzoukas, J. M. Lehn, V. Bloy, and V. Alain, Chem. Phys. **199**, 253 (1995).
6. J. O. Morley, V. J. Docherty, and D. Pugh, J. Chem. Soc. Perkin Trans. 2, 1351 (1987).
7. D. Jacquemin, B. Champagne, J. M. André, and B. Kirtman, submitted.
8. B. Champagne, D. Jacquemin, J. M. André, and B. Kirtman, J. Phys. Chem. **101**, 3158 (1997).
9. T. Tsunekawa and K. Yamaguchi, Chem. Phys. Lett. **190**, 533 (1992).
10. T. Tsunekawa and K. Yamaguchi, J. Phys. Chem. **96**, 10268 (1992).
11. M. Barzoukas, M. Blanchard-Desce, D. Josse, J. M. Lehn, and J. Zyss, Chem. Phys. **133**, 323 (1989).
12. J. O. Morely, J. Phys. Chem. **99**, 10166 (1995).
13. I. D. L. Albert, J. O. Morley, and D. Pugh, J. Phys. Chem. A **101**, 1763 (1997).
14. B. Champagne, D. H. Mosley, M. Vračko, and J. M. André, Phys. Rev. A **52**, 178 (1995).
15. B. Champagne, D. H. Mosley, M. Vračko, and J. M. André, Phys. Rev. A **52**, 1039 (1995).
16. B. Champagne and D. H. Mosley, J. Chem. Phys. **105**, 3592 (1996).
17. J. L. Toto, T. T. Toto, and C. P. de Melo, Chem. Phys. Lett. **245**, 660 (1995).
18. T. T. Toto, J. L. Toto, C. P. de Melo, M. Hasan, and B. Kirtman, Chem. Phys. Lett. **244**, 59 (1995).
19. Hellmann, *Die Entfürhung in die Quantenchemie* (Deuticke, Leipzig, 1937).
20. R. P. Feynmann, Phys. Rev. **36**, 340 (1939).
21. C. Møller and M. S. Plesset, Phys. Rev. **46**, 618 (1934).
22. D. Jacquemin, B. Champagne, and J. M. André, J. Mol. Struct. (THEOCHEM), to appear.
23. H. Rutihauser, Numer. Matematik **5**, 48 (1963).
24. M. J. Frisch et al., *GAUSSIAN 94, Revision B.1*, Gaussian Inc., Carnegie-Mellon University, Pittsburg, PA, 1995.
25. B. Kirtman and B. Champagne, Int. Rev. Phys. Chem., to appear.

Vibrational Versus Electronic First Hyperpolarizabilities of Mono- and Disubstituted Benzenes: An Ab Initio Coupled Hartree–Fock Investigation

BENOÎT CHAMPAGNE*

Laboratoire de Chimie Théorique Appliquée, Facultés Universitaires Notre-Dame de la Paix, 61, rue de Bruxelles, B-5000 Namur, Belgium

Received 2 March 1997; revised 24 April 1997; accepted 24 April 1997

ABSTRACT: Static electronic and vibrational longitudinal first hyperpolarizabilities ($\beta_L^e(0)$ and $\beta_L^v(0)$) of a series of mono- and disubstituted benzenes were calculated at the Hartree–Fock 6-31G level by using coupled Hartree–Fock and the double harmonic oscillator approximations, respectively. Although the $\beta_L^v(0)/\beta_L^e(0)$ ratio is slightly larger than unity and rather constant with respect to the substituent(s), it turns out, for the monosubstituted compounds, that the variations of $\beta_L^e(0)$ upon substitution can be most accounted for by the mesomeric effects, whereas for $\beta_L^v(0)$, the inductive effects are also of importance. © 1997 John Wiley & Sons, Inc. Int J Quant Chem **65**: 689–696, 1997

Introduction

Quantum chemical evaluations of the polarizabilities (α), first and second hyperpolarizabilities (β and γ), and their interpretation in terms of structure–property relationships help in the design of new compounds for nonlinear optical (NLO) applications [1]. Recently, particular attention has been given to the vibrational contributions to these properties [2]. In fact, although the application of an external electric field induces simultaneous distortions of the electron and nuclear motions, in the clamped nucleus or canonical treatment, one considers that the field acts sequentially on the electron and nuclear motions [3–4]. This leads to the distinction between the electronic (α^e, β^e, and γ^e) and vibrational (α^v, β^v, and γ^v) (hyper)polarizabilities. The present study copes with the evaluation of the electronic and vibrational static longitudinal first hyperpolarizabilities [$\beta_L^e(0)$ and $\beta_L^v(0)$] of a series of mono- and disubstituted benzenes. Since the first investigations have

*Research Associate of the National Fund for Scientific Research (Belgium).

Contract grant sponsor: FNRS-FRFC.
Contract grant number: 9.4593.92.
Contract grant sponsor: FNRS.
Contract grant number: D.4511.93.
Contract grant sponsor: Belgian National Interuniversity Research Program.
Contract grant number: PAI/IUAP No. P3-049.

© 1997 John Wiley & Sons, Inc.
CCC 0020-7608 / 97 / 050689-08

demonstrated that β_L^v can be substantial for conjugated molecules in the static limit [2], it can be optimized to maximize the dc-Pockels (dc-P) and optical rectification (OR) responses. At optical frequencies, the vibrational component to the second harmonic generation (SHG) response is negligible. A similar strategy has already been followed for 20 years now for the electronic counterpart as reviewed by Kanis et al. [5].

Zerbi and co-workers [6–8] found that, for many second-order conjugated molecules, the calculated static electronic and vibrational hyperpolarizabilities are very similar. Using experimental data, they concluded that β^v/β^e is close to unity. In the latter case, the vibrational first hyperpolarizability is evaluated from infrared and Raman absorption spectra, whereas electric field-induced SHG (EFISHG) measurements give the electronic counterpart which—to be correct—would have been required to be extrapolated to zero frequency. Consequently, they argued that such a coincidence is not fortuitous and that β^v and β^e are just two manifestations of the same underlying physical phenomenon. They made the connection with the strong electron–phonon coupling along the coordinate which is associated with the variation of the bond-length alternation (BLA). A first quantitative demonstration of their assumption was recently elaborated on by Castiglioni et al. [9]. However, in addition to its restriction to the two-state approximation for computing β^e, whereas β^v is evaluated at the double harmonic oscillator approximation by neglecting all the modes but the BLA mode, their approach neglects an important contribution [10]. The rationalization of the β^v/β^e ratio value is even made more difficult by a few recent results concerning push–pull conjugated materials which demonstrate the dependence of the β^v/β^e ratio upon both the chain length and the nature of the linker [2].

This lack of satisfactory quantitative justification for the relationship between β^v and β^e in these conjugated systems makes the subject very attractive. In the present study, the relationship between β^v and β^e [particularly between $\beta_L^e(0)$ and $\beta_L^v(0)$] is tackled from another side, i.e., the $\beta_L^e(0)$ and $\beta_L^v(0)$ quantities are analyzed in terms of both the *inductive* and the *mesomeric* substituent constants. Then, these relationships to simple physical concepts are compared. A similar approach was followed by Hehre et al. [11] to study the charge distributions and nuclear magnetic shifts in a series of monosubstituted benzenes and in *m*- and *p*-substituted fluorobenzenes. In addition, a few investigations of second-order NLO materials have demonstrated that a satisfactory linear dependence relates β^e to the σ_p parameters (see below for their description). These experimental or theoretical investigations of mono- and disubstituted benzenes [12], stilbenes [12, 13], polyenes [14], and polymethineimines [14] showed that this approach could be used by the organic chemists to elaborate new promising materials for NLO and to predict their properties from the nature and positions of the donors and acceptors. This work is organized as follows: The next section briefly summarizes the methodological and computational aspects, the third section presents the results and elaborates an interpretation, whereas we conclude in the fourth section.

Methodological and Computational Aspects

The $\beta_L^e(0)$ values were evaluated at the coupled Hartree–Fock (CHF) [15] level with the split-valence 6-31G basis set [16]. This approach, which is equivalent to a Hartree–Fock finite-field procedure, takes explicitly into account the field-induced electron reorganizational effects. On the other hand, the vibrational counterpart, $\beta_L^v(0)$, is obtained at the RHF/6-31G level within the double harmonic oscillator approximation [17–19] and reads

$$\beta_L^v(0) = [\,\mu\alpha]^{0,0}_{L;\,\omega=0} = 3\sum_a \left(\frac{\partial \mu_L}{\partial Q_a}\right)_0 \left(\frac{\partial \alpha_L}{\partial Q_a}\right)_0 \Big/ \omega_a^2, \tag{1}$$

where 0, 0 indicates that no electrical or mechanical anharmonicity is included. The sum runs over all the vibrational normal modes of frequency ω_a. The $(\partial P_L/\partial Q_a)_0$ with $P_L = \mu_L$, α_L, which are the derivatives of the property with respect to the normal coordinate Q_a, are evaluated at the equilibrium geometry.

For optical processes, both β_L^v and β_L^e are modulated, although in very different ways. Indeed, the frequency dispersion of β_L^e has been shown to follow the relation [20]

$$\beta_L^e(-\omega_\sigma;\,\omega_1,\,\omega_2) = \beta_L^e(0)\left[1 + A\omega_L^2 + B\omega_L^4 + \cdots\right], \tag{2}$$

where $\omega_\sigma = \omega_1 + \omega_2$ and $\omega_L^2 = \omega_\sigma^2 + \omega_1^2 + \omega_2^2$. A and B are parameters depending upon the molecule, but only B depends upon the NLO process. On the other hand, by adopting the enhanced [21] or infinite-frequency [22] approximation which relies on the fact that the optical frequencies are at least one order of magnitude larger than the vibrational ones, one obtains

$$\beta_L^v(-\omega;\omega,0)_{\omega\to\infty} = \beta_L^v(0;\omega,-\omega)_{\omega\to\infty} = \tfrac{1}{3}[\mu\alpha]^{0,0}_{L;\omega=0} \quad (3)$$

$$\beta_L^v(-2\omega;\omega,\omega)_{\omega\to\infty} = 0. \quad (4)$$

In other words, for SHG, β_L^v is negligible, whereas for the dc-P and OR effects, it amounts to 1/3 of the static quantity. This point is obviously of importance for optimizing the responses according to the NLO process.

All the β calculations were performed with the Gaussian94 program [23] on the RHF/6-31G-optimized structures. A tight convergence threshold on the residual forces was adopted to meet a satisfactory accuracy in computing the $(\partial P_L/\partial Q_a)_0$ values. The 6-31G atomic basis set was employed because it is known to be reasonably accurate for evaluating the hyperpolarizabilities of push–pull conjugated systems [5]. Addressing electron correlation corrections is left for future investigations. For these second-order NLO materials, a few calculations have already revealed that the inclusion of electron correlation effects leads to a 15–50% increase in β_L^e, whereas, to our knowledge, it has not yet been addressed for β_L^v. Further computational details on these calculations can be found in [24]. The molecules have been oriented such that the C_1 and C_4 atoms belong to the z- or longitudinal axis. Since our purpose consists of relating β^e and β^v to the substituent constants, only the $\beta_{zzz} = \beta_L$ tensor component was analyzed. It is striking to note that for weak donor or acceptor groups β_L is not necessarily the dominant tensor component, whereas in the case of the resonant D/A pairs, β_L is always dominant.

Results and Discussion

The μ_L, $\beta_L^e(0)$, and $\beta_L^v(0)$ values are listed in Tables I and II for the mono- and disubstituted benzenes, respectively, whereas Table III gives the various σ parameters employed in this study. As shown in the previous investigations [12–14], different types of σ parameters have proven to be adequate for reproducing the β^e variations. Most often, the *para* substituent constants (σ_p, σ_p^+, σ_p^-) are employed. The empirical σ_p parameters were originally related by Hammett to the variation of the dissociation constant of *p*-substituted acids, the benzoic acids in water at 25°C being the refer-

TABLE I

RHF/6-31G longitudinal component of the dipole moment and the static electronic and vibrational first hyperpolarizability as a function of the substituent in monosubstituted benzenes.

R	μ_L	β_L^e	β_L^v
OCH_3	0.044	126.1	96.8
OH	−0.225	143.4	43.1
$N(CH_3)_2$	0.688	297.4	180.8
NH_2	0.573	259.2	112.5
F	−0.965	108.3	−59.1
CH_3	0.130	44.8	23.4
CH_2CH_3	0.116	−12.4	8.0
$CHCH_2$	−0.059	−37.5	−61.1
CCH	−0.264	−23.9	40.7
SH	−0.752	28.5	16.1
Cl	−1.076	134.3	−210.1
SiH_3	−0.363	−119.1	−236.9
CN	−1.914	−56.1	−56.0
CF_3	−1.606	35.0	−205.3
CHO	−1.262	−197.3	−358.8
$COCH_3$	−0.939	−197.7	−229.2
CO_2H	−0.745	−205.5	−308.1
NO_2	−2.294	−269.7	−311.3

All the values are given in au. (1.0 au of dipole moment = 8.4783610^{-30} cm = 2.541765 Debye; 1.0 au of first hyperpolarizability = 3.2063×10^{-53} C^3 m^3 J^{-2} = 8.641×10^{-33} esu).

TABLE II

RHF/6-31G longitudinal component of the dipole moment and the static electronic and vibrational first hyperpolarizability as a function of the substituent in disubstituted benzenes (all values in au).

R, R'	μ_L	β_L^e	β_L^v
CHO, CH_3	1.478	366.6	518.1
CHO, F	0.282	335.0	344.6
CHO, OH	1.146	517.7	607.8
CHO, NH_2	2.124	928.0	1014.8
NO_2, CH_3	2.548	500.7	492.3
NO_2, F	1.329	408.9	298.5
NO_2, OH	2.222	672.4	704.6
NO_2, NH_2	3.230	1262.8	1351.6

TABLE III
The inductive (σ_I) and mesomeric (σ_R^0, $\sigma_R^{+/-}$) substituent constants.

R	σ_I	σ_R^0	$\sigma_R^{+/-}$
OCH_3	0.29	−0.44	
OH	0.25	−0.41	−1.17
$N(CH_3)_2$	0.12	−0.53	
NH_2	0.11	−0.48	−1.41
F	0.51	−0.33	−0.58
CH_3	−0.03	−0.10	−0.28
CH_2CH_3	−0.02	−0.12	
$CHCH_2$	0.06	−0.07	
CCH	0.20	0.03	
SH	0.29	−0.20	
Cl	0.48	−0.21	
SiH_3	0.05	0.09	
CN	0.57	0.08	
CF_3	0.42	0.07	
CHO	0.25	0.27	0.79
$COCH_3$	0.26	0.15	
CO_2H	0.32	0.29	
NO_2	0.68	0.19	0.56

The σ_R^0 are the unbiased values associated with nonconjugated reaction centers, whereas the $\sigma_R^{+/-}$ are the dual values which express the enhanced mesomeric interaction of a donor (σ_R^+) with an acceptor or of an acceptor (σ_R^-) with a donor. Values taken from [25].

ence [25]. Obviously, these σ_p parameters involve both *inductive* and *mesomeric* effects, whereas the latter ones are overestimated for medium/strong donor substituents because they interact resonantly with the acceptor acid group. This is why unbiased (σ_p^0) and dual (σ_p^+, σ_p^-) parameters are required to express the extreme behaviors. Indeed, on the one hand, the σ_p^0 parameters characterize substituents which do not interact with the reactive center, whereas, on the other hand, the σ_p^+ (σ_p^-) parameters include the enhancement of the donor (acceptor) character due to its resonant interaction with an acceptor (donor) substituent in the *para* position [25]. A further refinement of this parametrization is accomplished by the splitting of the different σ_p into mesomeric or resonant (σ_R) and inductive or electrostatic (σ_I) parts. The σ_I do not depend upon the presence or not of other interacting substituents, whereas there exist unbiased and dual σ_R constants [25]. In our case, the distinction between the σ_I and σ_R effects is of importance. We have considered the unbiased σ_R^0 values for the monosubstituted benzenes, whereas for the disubstituted constants, the dual $\sigma_R^{+/-}$ parameters have been employed. Two important comments are needed before deducing σ-relations and comparing these with previous studies. First, as mentioned by Exner [25], there are errors in the substituent constants which are not always unequivocally determined. These errors originate from both the experimental data and their subsequent theoretical manipulations such as these in deriving the σ_R constants. Second, the $\sigma_R^{+/-}$ values are often considered to be equivalent to $\sigma_p^{+/-}$ values because the resonant effect is dominant, neglecting the importance of the inductive effects such as in the case of the NO_2 group.

Figure 1 shows that the $\beta_L^v(0)/\beta_L^e(0)$ ratio is rather constant with respect to the nature and number of the substituents, the deviation being associated mainly with the monosubstituted compounds. The slightly larger amplitude of $\beta_L^v(0)$ with respect to $\beta_L^e(0)$ was first analyzed in terms of their dependence upon σ_R^0 (Figs. 2 and 3). The least-squares fittings,

$$\beta_L^e(0) = -51.5 - 572.5\sigma_R^0 \qquad R = 0.93 \quad (5)$$

$$\beta_L^v(0) = -134.3 - 524.6\sigma_R^0 \qquad R = 0.84, \quad (6)$$

show that the variations in $\beta_L^e(0)$ can be better accounted for by the mesomeric effects than can the corresponding variations in $\beta_L^v(0)$. Indeed, the correlation coefficient is closer to unity for $\beta_L^e(0)$ and the constant term of the line, which obviously should be equal to zero, is smaller. The removal of this constant term leads to poorer fittings of which the correlation coefficient is equal to 0.88 and 0.28 for $\beta_L^e(0)$ and $\beta_L^v(0)$, respectively. The corresponding standard deviation of the errors is equal to 66 and 136 au. This good description of the $\beta_L^e(0)$ variations in terms of σ_R^0 is in agreement with the fact that the charge-transfer (β_{ct}) contribution to $\beta_L^e(0)$ is known to be by far the largest component, the remaining term (β_{add}) being associated to the inductive effects. The largest deviations of the calculated $\beta_L^e(0)$ from the linear fitting estimates concern the CF_3 and NO_2 groups, i.e., substituents with small σ_R^0 with respect to σ_I. This dominance of β_{ct} is even more pronounced for the *D/A*-disubstituted compounds [26–27]. In what concerns $\beta_L^v(0)$, the CH_3, CCH, Cl, and CN substituents present the largest deviations from the linear fitting. In a similar way, for μ_L, the least-squares fitting to σ_R^0 is poor:

$$\mu_L = -0.80 - 2.04\sigma_R^0 \qquad R = 0.64. \quad (7)$$

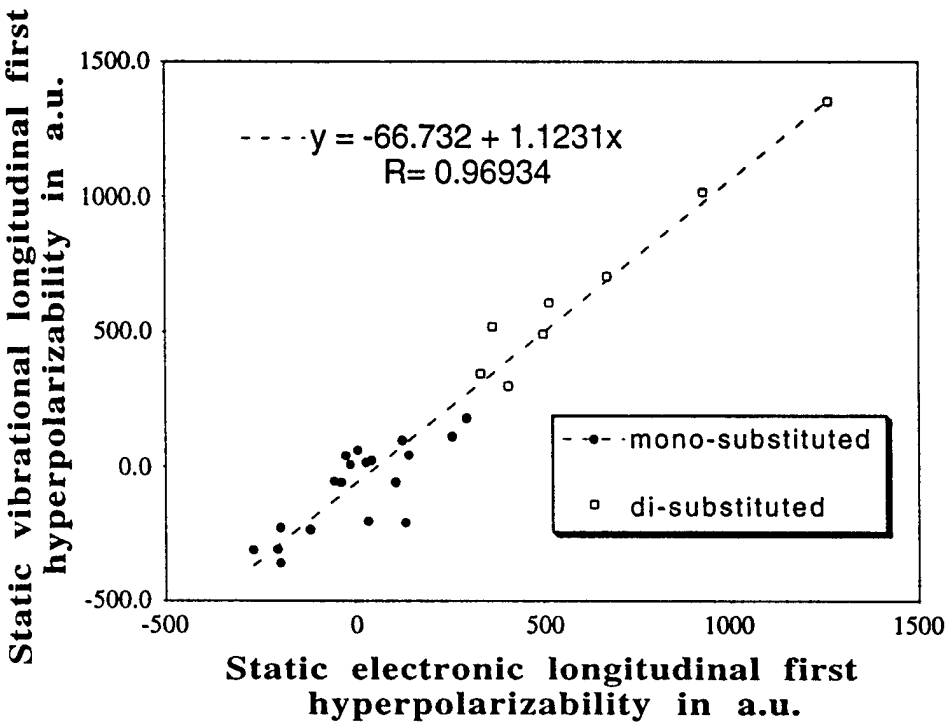


FIGURE 1. Plot of the RHF / 6-31G $\beta_L^v(0)$ vs. $\beta_L^e(0)$ for the mono- and disubstituted benzenes.

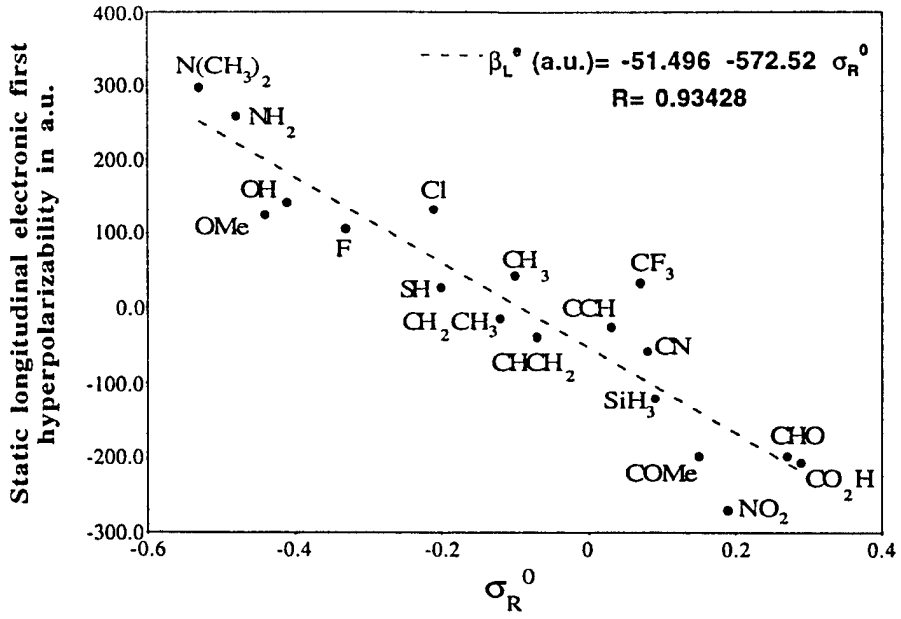


FIGURE 2. CHF / 6-31G $\beta_L^e(0)$ values as a function of σ_R^0.

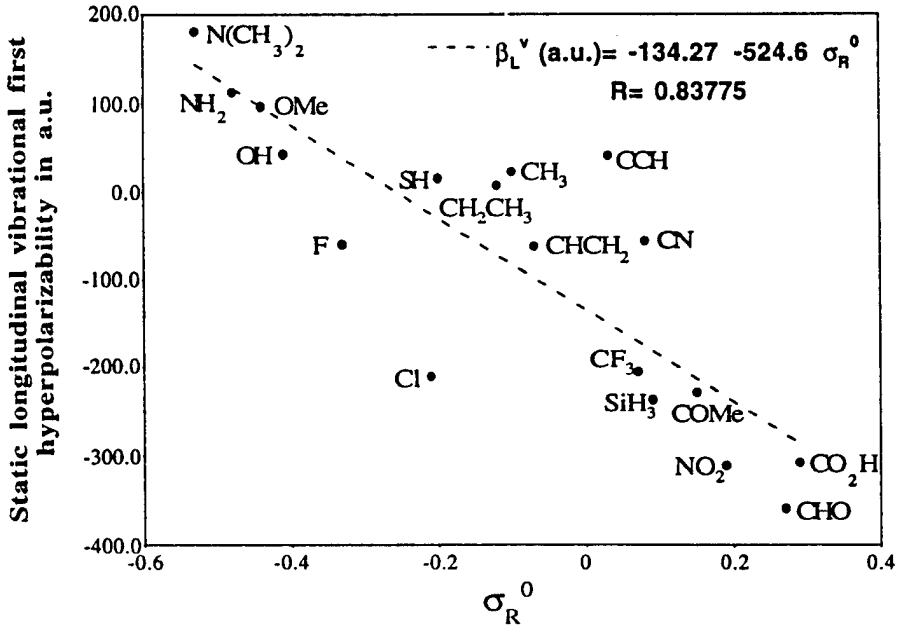


FIGURE 3. RHF / 6-31G double harmonic $\beta_L^v(0)$ values as a function of σ_R^0.

With the relation to σ_R^0 being insufficient in several instances, the role of σ_I needs to be assessed. To make it, one can assume that any property, P, depends linearly upon both σ_I and σ_R^0 according to

$$P = \rho_I \sigma_I + \rho_R \sigma_R^0. \tag{8}$$

The ρ_I and ρ_R factors which depend upon the investigated property are determined by a least-squares fitting procedure. One then obtains

$$\beta_L^e(0) = -127.5\sigma_I - 530.7\sigma_R^0 \tag{9}$$

$$\beta_L^v(0) = -376.1\sigma_I - 424.1\sigma_R^0 \tag{10}$$

$$\mu_L = -2.88\sigma_I - 1.56\sigma_R^0. \tag{11}$$

These results support our first idea that the inductive effects have a larger impact on $\beta_L^v(0)$ than on $\beta_L^e(0)$, whereas they are dominant for μ_L. They also indicate that for such monosubstituted benzenes $\beta_L^v(0)$ and $\beta_L^e(0)$ are not determined by the same underlying phenomena. The standard deviation of the errors which measures the goodness of these fittings is equal to 61, 87, and 0.27 au for $\beta_L^e(0)$, $\beta_L^v(0)$, and μ_L, respectively, showing a clear improvement over the simple linear fitting for $\beta_L^v(0)$ and μ_L, whereas for $\beta_L^e(0)$, both fittings are of equivalent quality. Most of the significant deviations from Eqs. (9)–(11) can be attributed to the particular nature of the substituents. For the CHO and SiH_3 groups, the $\beta_L^v(0)$ values are poorly reproduced as could be understood from their large intrinsic contributions. For Cl but also SiH_3, a part of the deviation can certainly be attributed to the lack of *d*-functions on the Cl and Si atoms. Moreover, the $\beta_L^v(0)$ estimates for the cyano- and acetylenobenzenes are of relatively poorer quality than for the other substituents. In the case of $\beta_L^e(0)$, the estimates for the CF_3- and CH_2CH_3-substituted benzenes are particularly bad due to both a large deviation and a wrong sign. Obviously, improvements of these fitting relations would be obtained by adopting higher-level quantum chemical methods, i.e., including electron correlation corrections and using a larger atomic basis set.

Nevertheless, these global double linear relationships deserve to be considered in the design of NLO materials and particularly for their help in determining the factors which influence the vibrational and electronic first hyperpolarizabilities. Indeed, there was no a priori reason to expect a linear relation between the $\beta_L(0)$'s and the substituent constants which are related to variations of chemical reaction constants.

Then, an interesting point consists of estimating from Eqs. (9)–(11) the $\beta_L^e(0)$, $\beta_L^v(0)$, and μ_L values of the substituted compounds and comparing these to the calculated ones. For the disubstituted benzenes, the substituent effect is represented by the difference of their individual constants, the coop-

erative or resonant effects being accounted for by taking $\sigma_R^{+/-}$ in the place of σ_R^0. One can directly see inconsistencies between these estimates and the calculations. In particular, the $\beta_L(0)$'s of the NH_2-substituted compounds are much larger than these of the parent OH-substituted systems although the corresponding changes in σ_R^+/σ_I are rather small. In addition, for the $\beta_L^e(0)$ of the CH_3- and F-substituted systems, these estimated values overestimate the calculated ones. It is our feeling that these prediction errors are related to the difficulty of knowing $\sigma_R^{+/-}$. Indeed, there is no reason why these values would be the same for the solvolysis of cumyl chlorides in 90% aqueous acetone and for β quantities. In other words, contrary to the unbiased constants, the dual parameters can be easily considered dependent upon the strength of the resonantly interacting group. In this regard, it seems obvious that the NH_2 group resonantly interacts much more strongly with the acceptor group than does the OH group.

The nonnegligible deviations from the linear relation obtained by Ulman [13] and the interpretation given by Cheng et al. [12] of the σ-dependence of the EFISHG β values demonstrate also that the dual parameters are not determined in an absolute way. Indeed, Cheng et al. obtained linear relations with different slopes for the *para*-substituted nitro- and methoxybenzenes. On the other hand, Jacquemin et al. [14] obtained a very good correlation constant for polyenes and polymethineimines substituted by strong or weak donors and acceptors. However, it is striking to note that, in the latter, the same standard geometry was adopted for the linker in order to address the electronic effects of the substituents, neglecting, therefore, the consequences on the linker geometry. Accordingly, the NO_2/NH_2 pair significantly transforms the aromatic benzene ring into a partially quinonoid structure [24].

Synopsis and Outlooks

This RHF/6-31G study points out that the $\beta_L^v(0)/\beta_L^e(0)$ ratio for mono- and disubstituted benzenes is rather constant with respect to the nature of the substituent(s) and is slightly larger than unity. With the lack of electron correlation and anharmonicity corrections preventing us from making a better estimate, these results are in agreement with the observation of Zerbi and coworkers [6–8] who found experimentally and theoretically that $\beta_L^v(0)$ and $\beta_L^e(-2\omega; \omega, \omega)$ are of the same amplitude. However, the analysis of the dependence of $\beta_L^v(0)$ and $\beta_L^e(0)$ upon the mesomeric and inductive substituent constants in the monosubstituted benzenes exhibits different behaviors. $\beta_L^e(0)$ can mostly be described by the unbiased mesomeric constants (σ_R^0), whereas its vibrational counterpart also depends upon the inductive constants (σ_I). Moreover, the intrinsic contribution of the substituent is generally larger for $\beta_L^v(0)$ than for $\beta_L^e(0)$.

Nevertheless, it is important to note that, at optical frequencies, this $\beta_L^v(0)/\beta_L^e(0)$ ratio decreases to about 0.3 as a consequence of both the dispersion-induced increase of β_L^e and the decrease of β_L^v by a factor of 3 as determined in the infinite-frequency double harmonic oscillator level of approximation. On the grounds of the recent results concerning α, ω nitroamino polyenes, polyynes, and polythiophenes which show that the $\beta_L^v(0)/\beta_L^e(0)$ ratio ranges between 1.1 and 2.8 according to the length and nature of the conjugated linker, further investigations of these substituent effects would deserve to be carried out to address, from the chemical point of view, the value of the $\beta_L^v(0)/\beta_L^e(0)$ ratio.

ACKNOWLEDGMENTS

B. C. thanks the Belgian National Fund for Scientific Research for his research associate position, Prof. J. M. André for continuous support, and Prof. B. Kirtman, Prof. D. M. Bishop, and D. Jacquemin for stimulating discussions. The calculations were performed on the IBM RS6000 cluster of the Namur Scientific Computing Facility (Namur-SCF) and the author also gratefully acknowledges the financial support of the FNRS-FRFC, the "Loterie Nationale" for the Convention No. 9.4593.92, the FNRS within the framework of the "Action d'Impulsion à la Recherche Fondamentale" of the Belgian Ministry of Science under the Convention D.4511.93, and the Belgian National Interuniversity Research Program on "Sciences of Interfacial and Mesoscopic Structures" (PAI/IUAP No. P3-049).

References

1. (a) D. S. Chemla and J. Zyss, Eds., *Organic Materials for Nonlinear Optics* (Academic Press, New York, 1987), Vols. I

and II. (b) P. Prasad and D. J. Williams, *Introduction to Nonlinear Optical Effects in Molecules and Polymers* (Wiley, New York, 1991). (c) R. W. Boyd, *Nonlinear Optics* (Academic Press, New York, 1992). (d) P. O. Löwdin, Ed., Int. J. Quantum Chem., special issue on Molecular Nonlinear Optics **43**(1) (1992). (e) J. Zyss, Ed., *Molecular Nonlinear Optics, Materials, Physics, and Devices* (Academic Press, New York, 1993). (f) J. Michl, Ed., Chem. Rev., thematic issue on Optical Nonlinearities in Chemistry **94**(1) (1994). (g) D. M. Bishop, Adv. Quantum Chem. **25**, 1 (1994). (h) S. P. Karna and A. T. Yeates, Eds., *Theoretical and Computational Modeling of NLO and Electronic Materials*, ACS Symposium Series (American Chemical Society, New York, 1995).

2. B. Kirtman and B. Champagne, Int. Rev. Phys. Chem. (in press).
3. D. M. Bishop, Rev. Mod. Phys. **62**, 343 (1990).
4. D. M. Bishop, B. Kirtman, and B. Champagne, submitted.
5. D. R. Kanis, M. A. Ratner, and T. J. Marks, in ref. 1f, p. 195.
6. M. Del Zoppo, C. Castiglioni, and G. Zerbi, Nonlin. Opt. **9**, 73 (1995).
7. P. Zuliani, M. Del Zoppo, C. Castiglioni, G. Zerbi, S. R. Marder, and J. W. Perry, J. Chem. Phys. **103**, 9935 (1995).
8. P. Zuliani, M. Del Zoppo, C. Castiglioni, G. Zerbi, C. Andraud, T. Brotin, and A. Collet, J. Phys. Chem. **99**, 16242 (1995).
9. C. Castiglioni, M. Del Zoppo, and G. Zerbi, Phys. Rev. B **53**, 13319 (1996).
10. D. M. Bishop and B. Kirtman, Phys. Rev. B (in press).
11. W. J. Hehre, R. W. Taft, and R. D. Topsom, Prog. Phys. Org. Chem. **12**, 159 (1976).
12. L. T. Cheng, W. Tam, S. H. Stevenson, G. R. Meredith, G. Rikken, and S. R. Marder, J. Phys. Chem. **95**, 10631 (1991).
13. A. Ulman, J. Phys. Chem. **92**, 2385 (1988).
14. D. Jacquemin, B. Champagne, and J. M. André, Synth. Met. **80**, 205 (1996).
15. C. E. Dykstra and P. G. Jasien, Chem. Phys. Lett. **109**, 388 (1984). H. Sekino and R. J. Bartlett, J. Chem. Phys. **85**, 976 (1986). S. P. Karna and M. Dupuis, J. Comp. Chem. **12**, 487 (1991), and references therein.
16. W. J. Hehre, R. Ditchfield, and J. A. Pople, J. Chem. Phys. **56**, 2257 (1972).
17. B. Kirtman and D. M. Bishop, Chem. Phys. Lett. **175**, 601 (1990).
18. D. M. Bishop and B. Kirtman, J. Chem. Phys. **95**, 2646 (1991).
19. D. M. Bishop and B. Kirtman, J. Chem. Phys. **97**, 5255 (1992).
20. D. M. Bishop, J. Chem. Phys. **95**, 5489 (1991). D. M. Bishop and D. W. De Kee, J. Chem. Phys. **104**, 9876 (1996); *Ibid.* **105**, 8247 (1996).
21. D. S. Elliott and J. F. Ward, Mol. Phys. **51**, 45 (1984).
22. D. M. Bishop, M. Hasan, and B. Kirtman, J. Chem. Phys. **103**, 4157 (1995).
23. M. J. Frisch, G. W. Trucks, H. B. Schlegel, P. M. W. Gill, B. G. Johnson, M. A. Robb, J. R. Cheeseman, T. Keith, G. A. Petersson, J. A. Montgomery, K. Raghavachari, M. A. Al-Laham, V. G. Zakrzewski, J. V. Ortiz, J. B. Foresman, J. Cioslowski, B. B. Stefanov, A. Nanayakkara, M. Challacombe, C. Y. Peng, P. Y. Ayala, W. Chen, M. W. Wong, J. L. Andres, E. S. Replogle, R. Gomperts, R. L. Martin, D. J. Fox, J. S. Binkley, D. J. DeFrees, J. Baker, J. P. Stewart, M. Head-Gordon, C. Gonzalez, and J. A. Pople, *Gaussian 94, Revision B.1* (Carnegie-Mellon University, Pittsburgh, PA, 1995).
24. B. Champagne, Chem. Phys. Lett. **261**, 57 (1996).
25. O. Exner, in *Correlation Analysis in Chemistry*, N. B. Chapman and J. Shorter, Eds. (Plenum Press, New York, 1978), Chap. 10, p. 439.
26. J. L. Oudar and D. S. Chemla, J. Chem. Phys. **66**, 2664 (1977).
27. J. Zyss, J. Chem. Phys. **70**, 3341 (1979).

Theoretical Studies of Second Hyperpolarizability by Path Integral Method: Effects of External Magnetic Field

HIDEMI NAGAO,[1,*] KOJI OHTA,[1] MASAYOSHI NAKANO,[2] KIZASHI YAMAGUCHI[2]

[1]*Department of Optical Materials, Osaka National Research Institute, Ikeda, Osaka 563, Japan*
[2]*Department of Chemistry, Graduate School of Science, Osaka University, Toyonaka, Osaka 560, Japan*

Received 2 March 1997; revised 1 August 1997; accepted 6 August 1997

ABSTRACT: Explicit expressions of polarizability and hyperpolarizability are formulated by a path integral method in terms of the generalized coherent states of the Thouless parametrization. A novel scheme is shown for calculating the molecular properties including total energy, and the Monte Carlo method using the metropolis algorithm is utilized for performing the actual calculations. As a simple example, the hydrogen molecule is examined to demonstrate performances of the present scheme. We discuss improvement of the accuracy of the (hyper)polarizabilities depending on the number of the division for the partition function and also the behaviors of the (hyper)polarizability for the external magnetic field. We compare the present results with those obtained by the conventional molecular orbital theory. © 1997 John Wiley & Sons, Inc. Int J Quant Chem **65**: 697–707, 1997

Introduction

In the context of quantum chemical calculations of the static (hyper)polarizabilities, we have two main approaches, i.e., the perturbation techniques and the derivative techniques. In the perturbation techniques, the perturbation energy is usually expressed as the summation over electronic states (sum over states [SOS]). The hyperpolarizability has been calculated by the perturbative approach with various approximate models [1–5]. The most useful advantage of the SOS technique in terms of the analysis of the nonlinear optical response is that it allows one to obtain a physical picture as to which excited states play a significant role in the response. On the other hand, the derivative techniques rely on the fact that the static

Correspondence to: H. Nagao.
* *Present address:* Institute for Molecular Science, Myodaiji, Okazaki 444, Japan.

© 1997 John Wiley & Sons, Inc.
CCC 0020-7608 / 97 / 050697-11

(hyper)polarizability tensor components can be obtained as first- (second-, third-) order derivatives of a given dipole moment component with respect to the electric field. Those derivatives can be evaluated numerically or analytically within the coupled Hartree–Fock scheme. The finite-field (FF) approach is used for the numerical procedure, originally proposed by Cohen and Roothaan [6], where the molecular Hamiltonian explicitly includes a finite electric-field-dependent term. Several Hartree–Fock self-consistent-field or post-Hartree–Fock calculations need to be performed for different numerical values of the electric field. The total energy or dipole moment as a function of the different field values is then differentiated numerically.

Many calculations of static (hyper)polarizabilities of several interesting materials have been reported. These results suggest that it is important to calculate them considering the effect of electron correlation using sufficiently large basis sets [7]. In particular, the second hyperpolarizability value, γ, is very dependent on these factors. However, an accurate and practical computational method for determining the sensitive physical properties to the electron correlation of quantum many-body systems is still under study.

In the last decades, there have been several attempts to apply the path integral method to calculating physical properties, with success for simple systems. The path integral was first introduced by Feynman [8–10]. The theory has been successfully applied to many problems [11–15] in quantum mechanics. Because the path integral is expressed as multidimensional integrals with a huge number of variables, we cannot directly compute this integration by ordinary ways of numerical integrations. Therefore, a statistical method such as the Monte Carlo (MC) method [16–22] is attempted for the integrations. The standard approach to the Monte Carlo simulation of field theory has been established through Feynman's path integral formulation. It is necessary to work at an imaginary time so that the integrands of the path integrals do not oscillate. It is also necessary to work with systems having a finite extent in both space and imaginary time. This is equivalent to finite temperature statistical mechanics.

Recently, we also applied the path integral method to the many-electron systems in quantum chemistry [23–27]. The path integral formulation of the partition function was presented in terms of the LCAO coefficients or the Thouless parameterization. We presented numerical calculations [28–31] of the ensemble average of the total energy and the magnetization by means of the MC method. We already reported briefly the numerical results of the calculations of the (hyper)polarizability for a H_3^+ system [32].

In this article, we show dependencies of the (hyper)polarizability on the external magnetic field for a hydrogen molecule using our path integral expressed by the generalized coherent state, where our model Hamiltonian includes the ab initio Hamiltonian and the electric- and magnetic-field-dependent terms. We also discuss relations between (hyper)polarizability and spin states.

Theory

To apply a path integral method to molecular systems, the path integral formulation of the partition function is derived by using the generalized coherent states. The Slater determinant $|Z\rangle$ is written in terms of complex coefficients $Z_{ph}^{\sigma\rho}$ as

$$|Z\rangle = \det(1 + Z^+Z)^{-\frac{1}{2}} \times \exp\left[\sum_{\sigma,\,\rho=\alpha,\beta}\sum_{p=1}^{M-N_\sigma}\sum_{h=1}^{N_\rho} Z_{ph}^{\sigma\rho} a_{p\sigma}^+ a_{h\rho}\right]|\phi\rangle \tag{1}$$

$$= \det(1 + Z^+Z)^{-\frac{1}{2}} \times \prod_{\rho=\alpha,\beta}\prod_{h=1}^{N_\rho}\left(a_{h\rho}^+ + \sum_{\sigma=\alpha,\beta}\sum_{p=1}^{M-N_\sigma} Z_{ph}^{\sigma\rho} a_{p\sigma}^+\right)|0\rangle, \tag{2}$$

where $|\phi\rangle$ is a Slater determinant composed of N orbitals (hole-orbitals), N_σ means the number of hole–orbitals with a spin σ, and N is $N_\alpha + N_\beta$. M is the number of the base. The p labels denote the particle orbitals that are orthogonal to the hole orbitals h, and Z is a matrix whose elements are $Z_{ph}^{\sigma\rho}$. $a_{i\sigma}^+$ ($a_{i\sigma}$) is the creation (annihilation) operator for the i-th orbital. These operators also obey the anticommutation relation.

The partition function Ξ is written as

$$\Xi = Tr[e^{-\beta H}]. \tag{3}$$

The symbol Tr indicates a trace operation, and $\beta = (k_B T)^{-1}$ with the Boltzmann constant k_B and a temperature of T Kelvin.

A path integral representation of the partition function in terms of the generalized coherent states

yields

$$\Xi = \int \prod_{k=1}^{n} d\xi(Z_k)\langle Z_k|Z_{k-1}\rangle \times \exp\left[-\tau \sum_{l=1}^{n} H(Z_l^*, Z_{l-1})\right], \quad (4)$$

with

$$|Z_0\rangle = |Z_n\rangle, \quad (5)$$

where

$$d\xi(Z) = c\prod_{\sigma\rho} \prod_{p=1}^{M-N_\sigma} \prod_{h=1}^{N_\rho} \frac{dZ_{ph}^{\sigma\rho *}\, dZ_{ph}^{\sigma\rho}}{2\pi i} \times |\det(1 + Z^+Z)|^N \quad (6)$$

and

$$H(Z_k^*, Z_{k-1}) = \langle Z_k|H|Z_{k-1}\rangle. \quad (7)$$

$\tau = \beta/n$. n is the number of the divisions, which is used as the parameter of the actual calculation of physical properties. From expression (4), we will derive an expression of the ensemble average of an operator such as the total energy or the dipole moment.

MODEL HAMILTONIAN

To apply the path integral expressed by the generalized coherent states to the quantum chemistry, we consider the ab initio Hamiltonian including electric- and magnetic-field dependent terms for molecular systems. In the Born–Oppenheimer approximation, the Hamiltonian is written as

$$H = H_0 + H_I + H_{II}, \quad (8)$$

where

$$H_0 = \sum_{\sigma=\alpha,\beta} \sum_{i,j=1}^{M} h_{ij}^{\sigma} a_{i\sigma}^{+} a_{j\sigma} + \frac{1}{2} \sum_{\sigma,\rho=\alpha,\beta} \sum_{i,j,k,l=1}^{M} V_{ijkl}^{\sigma\rho\rho\sigma} a_{i\sigma}^{+} a_{j\rho}^{+} a_{k\rho} a_{l\sigma}, \quad (9)$$

$$H_I = -\sum_{\sigma=\alpha,\beta} \mathbf{F}\cdot\mu_{ij}^{\sigma} a_{i\sigma}^{+} a_{j\sigma}, \quad (10)$$

$$H_{II} = -2\mu_0 \mathbf{H}_0 \sum_{i=1}^{M} S_{iz}, \quad (11)$$

$$h_{ij}^{\sigma} = \int d\mathbf{r}\, \varphi_{i\sigma}^{*}(\mathbf{r}) \left[-\frac{\nabla^2}{2m} - \sum_{a=1}^{N_a} \frac{Z_a}{|\mathbf{r} - \mathbf{R}_a|}\right] \varphi_{j\sigma}(\mathbf{r}), \quad (12)$$

$$V_{ijkl}^{\sigma\rho\rho\sigma} = \int d\mathbf{r}\, d\mathbf{r}'\, \varphi_{i\sigma}^{*}(\mathbf{r})\varphi_{j\rho}^{*}(\mathbf{r}') \frac{1}{|r - r'|} \varphi_{k\rho}(\mathbf{r}')\varphi_{l\sigma}(\mathbf{r}), \quad (13)$$

and

$$\mu_{ij}^{\sigma} = \int dr\, \varphi_{i\sigma}^{*}(\mathbf{r})\mu\varphi_{j\sigma}(\mathbf{r}). \quad (14)$$

In Eq. (9), the first term represents the kinetic and the nuclear–electron interaction part and the second one represents the electronic interaction part. H_I and H_{II} are the electric-field-dependent term and the Zeeman Hamiltonian, respectively. μ is the dipole moment, and $\mathbf{F}$ indicates the electric field. μ_0 and h_0 indicate the magnetic moment and the static external magnetic field, respectively. Here, we introduce an orthogonal basis set $\{\varphi_i(\mathbf{r})\}$ such as a Hartree–Fock (HF) molecular orbital (MO). Therefore, $a_{i\sigma}^{+}$ ($a_{i\sigma}$) becomes the creation (annihilation) operator for the i-th MO. S_{iz} indicates a z-component of the spin angular momentum at the i-th site. In Eq. (13), $\mathbf{R}_a$ is a spatial coordinate of the a-th nucleus, and N_a, the number of the nucleus. Z_a indicates the positive electron charge of the a-th nucleus.

We derive the matrix elements $\langle Z_k|H|Z_{k-1}\rangle$ of the Hamiltonian in Eq. (8):

$$H(Z_k^*, Z_{k-1}) = H_0(Z_k^*, Z_{k-1}) + H_I(Z_k^*, Z_{k-1}) + H_{II}(Z_k^*, Z_{k-1}). \quad (15)$$

ENSEMBLE AVERAGE

The ensemble average of any operator O can be calculated:

$$\langle\langle O\rangle\rangle = \frac{\mathrm{Tr}[Oe^{-\beta H}]}{\mathrm{Tr}[e^{-\beta H}]} \quad (16)$$

$$= \frac{\int \prod_{k=1}^{n} d\xi(Z_k)\langle Z_k|Z_{k-1}\rangle \times e^{-\tau\sum_{l=1}^{n} H(Z_l^*, Z_{l-1})} \frac{1}{n} \sum_{m=1}^{n} \langle Z_m|O|Z_{m-1}\rangle}{\int \prod_{k=1}^{n} d\xi(Z_k)\langle Z_k|Z_{k-1}\rangle e^{-\tau\sum_{l=1}^{n} H(Z_l^*, Z_{l-1})}}. \quad (17)$$

In this article, we numerically calculate the ensemble average of the total energy $\langle\langle H \rangle\rangle$ or that of the dipole moment $\langle\langle \mu \rangle\rangle$.

It is impossible to directly calculate the ensemble average of physical properties in Eq. (17) with the matrix elements of the Hamiltonian in Eq. (15), because a huge amount of integral variables is generated. Therefore, the above integral is approximated by other numerical methods such as the Monte Carlo method.

Static (Hyper)polarizabilities

We consider a Hamiltonian written as

$$H = H' - \mathbf{F} \cdot \mu, \tag{18}$$

where H' is the addition of the ab initio Hamiltonian and the Zeeman Hamiltonian. If the second term is the perturbation term applied to the molecular system, the (hyper)polarizabilities are derived in terms of the perturbation procedure. Let us consider the molecule symmetric with respect to the x-direction. Then, the expression of the ensemble average of the dipole moment, $\langle\langle \mu_\nu \rangle\langle$ ($\nu = x, y, z$), becomes

$$\langle\langle \mu_\nu \rangle\rangle = \frac{\mathrm{Tr}\left[\mu_\nu e^{-\beta H'} \right]}{\mathrm{Tr}\left[e^{-\beta H'} \right]}. \tag{19}$$

According to the procedure of the linear response theory, we obtain an expression for $\langle\langle O_{1x} \rangle\rangle$ to the first order in the dipole moment μ_ν:

$$\langle\langle O_{1x} \rangle\rangle = \sum_{\nu = x, y, z} \frac{\int_0^\beta d\lambda \, \mathrm{Tr}\left[e^{-(\beta-\lambda)H'} \mu_\nu e^{-\lambda H'} \mu_x \right]}{\mathrm{Tr}\left[e^{-\beta H'} \right]} F_\nu - \beta \sum_{\nu = x, y, z} \frac{\mathrm{Tr}\left[e^{-\beta H'} \mu_\nu \right]}{\mathrm{Tr}\left[e^{-\beta H'} \right]} \frac{\mathrm{Tr}\left[e^{-\beta H'} \mu_x \right]}{\mathrm{Tr}\left[e^{-\beta H'} \right]} F_\nu. \tag{20}$$

Therefore, the polarizability α_{xx} is derived by

$$\langle\langle \alpha_{xx} \rangle\rangle = \frac{\partial \langle\langle O_{1x} \rangle\rangle}{\partial F_x}. \tag{21}$$

Similar to the above procedure, we finally have an explicit expression of the hyperpolarizability γ_{xxxx}:

$$\begin{aligned} \langle\langle O_{3x} \rangle\rangle &= \sum_{\nu_1, \nu_2, \nu_3} \int_0^\beta d\lambda \int_0^\lambda d\lambda' \int_0^{\lambda'} d\lambda'' \\ &\times \mathrm{Tr}\left[e^{-(\beta-\lambda)H'} \mu_{\nu_1} e^{-(\lambda-\lambda')H'} \mu_{\nu_2} \right. \\ &\left. \times e^{-(\lambda'-\lambda'')H'} \mu_{\nu_3} e^{-\lambda'' H'} \mu_x \right] \\ &\times F_{\nu_1} F_{\nu_2} F_{\nu_3} / \mathrm{Tr}\left[e^{-\beta H'} \right] \\ &- \sum_{\nu_1, \nu_2, \nu_3} \int_0^\beta d\lambda \, \mathrm{Tr}\left[e^{-(\beta-\lambda)H'} \mu_{\nu_1} e^{-\lambda H'} \mu_x \right] \\ &\times F_{\nu_1} / \mathrm{Tr}\left[e^{-\beta H'} \right] \int_0^\beta d\lambda \int_0^\lambda d\lambda' \\ &\times \mathrm{Tr}\left[e^{-(\beta-\lambda)H'} \mu_{\nu_2} e^{-(\lambda-\lambda')H'} \mu_{\nu_3} e^{-\lambda' H'} \right] \\ &\times F_{\nu_2} F_{\nu_3} / \mathrm{Tr}\left[e^{-\beta H'} \right], \end{aligned} \tag{22}$$

$$\langle\langle \gamma_{xxxx} \rangle\rangle = \frac{1}{6} \frac{\partial^3 \langle\langle O_{3x} \rangle\rangle}{\partial F_x \, \partial F_x \, \partial F_x}. \tag{23}$$

It may be easily shown that these expressions are equal to those obtained from the conventional perturbation theories of, e.g., the SOS method and so on.

Numerical Example

In this section we discuss the performances of numerical calculations of the ensemble average of the physical property by a Monte Carlo method based on this method. A novel numerical scheme is presented. The simplest example of a hydrogen molecule is examined. Results by this scheme are compared with those obtained from the conventional MO method.

CALCULATING SCHEME AND MONTE CARLO PROCEDURE

Figure 1 illustrates a numerical scheme to calculate the ensemble average of the physical property by a Monte Carlo method. We need the matrix elements, h_{ij}^σ and $V_{ijkl}^{\sigma\rho\rho\sigma}$, between orbitals in each term of Eqs. (12) and (13). Because our initial coherent state is constructed by the HF orbitals, matrix elements based on the HF orbitals must be

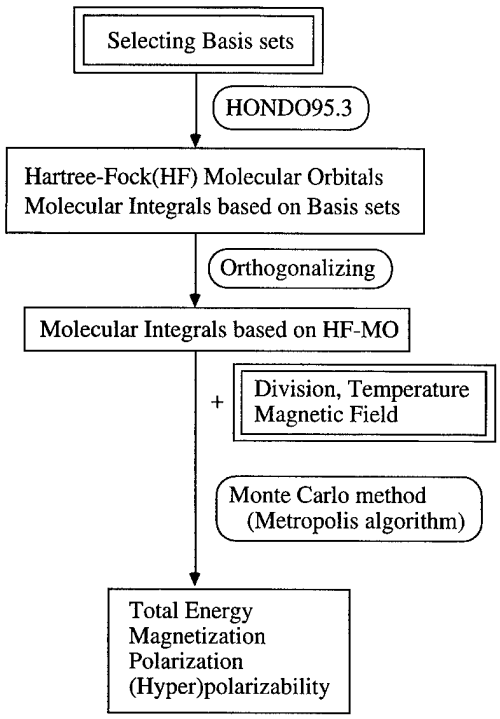


FIGURE 1. Scheme for calculating physical properties.

generated. First, the HF molecular orbitals and the molecular integrals based on a basis set are obtained from HF calculations using the HONDO95.3 program package [33]. Second, we convert them into the molecular integrals based on the HF orbitals orthogonal to each other. Finally, the ensemble average of the physical property is calculated using the above molecular integrals, the number of the division n for the partition function, and a temperature based on a metropolis algorithm. The random number with the density $|\det(1 + Z^{+}Z)|^{N}$ of the probability is generated by the rejection method. To avoid the negative sign problem, a reweighting method is attempted [34].

EXAMPLE

As a numerical example, first, the total energy is calculated for a hydrogen molecule. The results are compared with those obtained from the conventional molecular orbital theory. Next, the calculation results of the (hyper)polarizabilities are shown for the hydrogen molecule. Here, the dependence of the values on the number of the divisions is discussed. Dependence on the external magnetic field is also discussed.

Total Energy and Dipole Moment Without External Magnetic Field

We consider a hydrogen molecule with an atomic distance of 1.46 au as shown in Figure 2. All calculations were carried using the 4-31G basis set. Figure 3 and Table I show the ensemble average of the total energy vs. the number of the divisions for the partition function at temperature of 1 K. For 10^4 divisions, the ensemble average of the total energy becomes -1.1406 ± 0.0033 au. As shown in Table I, the CCSD total energy, which is equivalent to the full-CI energy in the case of the two-electron system, obtained by Gaussian 92 [35] is -1.15127 au. The total energy is expected to be equal to that of full-CI when the number of divisions becomes large. We also show the ensemble average of the dipole moment under the same condition in Figure 4. These results suggest that for the infinite divisions for the partition function at lower temperature calculations by the MC method cause errors. We expect that the ensemble average of the dipole moment value for each division number n will vanish at higher temperature. Note that the accuracy of calculations by the MC method is generally proportional to the square root of the number of the divisions. It means that precise calculations by the MC method takes us a long time. For this reason, the calculations for 10^4 divisions were carried out to obtain qualitative effects of these physical properties. It is necessary to investigate further these effects with larger number of the divisions, n, and temperature for the quantitative study of these physical properties.

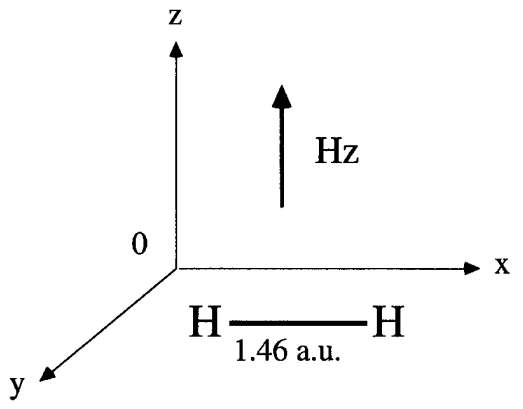


FIGURE 2. Employed model system of a hydrogen molecule.

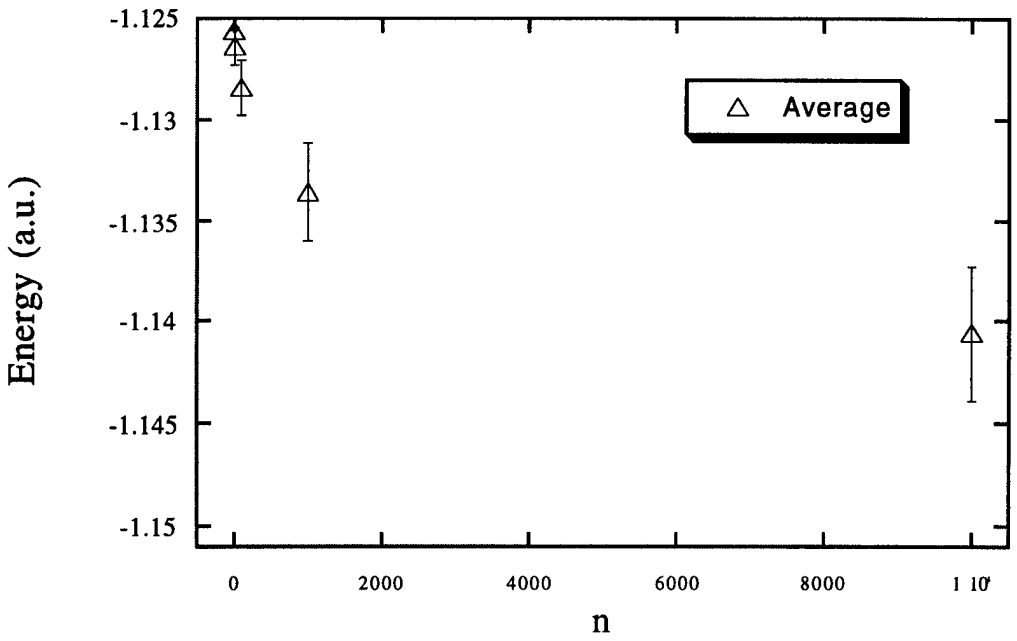


FIGURE 3. Total energy vs. the number of divisions for the partition function.

(Hyper)polarizabilities Without External Magnetic Field

From Eqs. (21)–(24), α_{xx} and γ_{xxxx} are calculated in terms of the MC method. The present calculations were performed using the 4-31G basis set under a condition of a temperature of 1 K. The α_{xx} and γ_{xxxx} values are also calculated for the H_2 molecule by the FF method with Gaussian 92. These calculations were made using the numerical derivative of the total energy with respect to the applied electric field. The results at HF and other correlation levels are shown in Tables II–IV. The

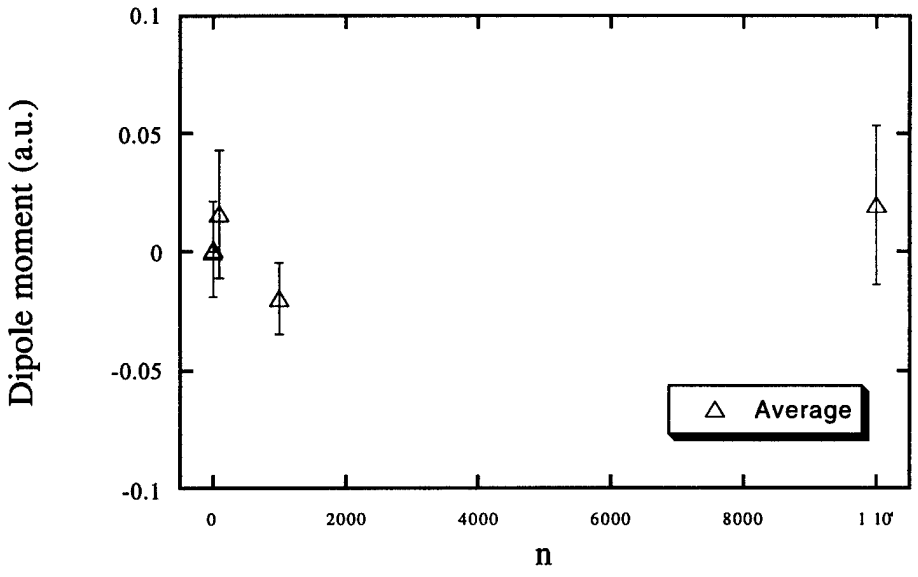


FIGURE 4. Dipole moment vs. division number.

TABLE I
Total energy.

MC method		MO method	
n	Total energy (au)	Method	Total energy (au)
1	-1.1256 ± 0	HF	-1.126
10	-1.1264 ± 0.0009	MP2	-1.143
100	-1.1285 ± 0.0014	MP3	-1.149
1000	-1.1336 ± 0.0024	MP4DQ	-1.150
10,000	-1.1406 ± 0.0033	MP4SDQ	-1.150
		CCSD	-1.151

TABLE III
Hyperpolarizability.

MC method		FF method	
n	γ_{xxxx} (au)	Method	γ_{xxxx} (au)
1	-22.603 ± 0.000	HF	-22.00
10	-19.456 ± 1.976	MP2	-17.39
100	-12.492 ± 3.150	MP3	-12.79
1000	-10.979 ± 1.207	MP4DQ	-9.59
10,000	-9.707 ± 1.069	MP4SDQ	-10.21
		CCSD	-8.72

polarizability α_{xx} for each division number in the MC method is shown in Figure 5 and Table II. For the division number of 10^4, the α_{xx} value becomes 6.675 ± 0.180 au. On the other hand, the CCSD method gives 6.407 au. As for the total energy value, we can also expect that by using a larger division number the polarizability value will vary from that with the HF calculation to that with the full-CI. Similarly, the hyperpolarizability γ_{xxxx} also shows a tendency similar to other physical properties, which becomes the exact value at the limit of infinite division number as expected from Figure 6 and Table III.

(Hyper)polarizabilities Under External Magnetic Field

We calculate the (hyper)polarizability of the hydrogen molecule under the external magnetic field. These calculations were carried out using 4-31G basis set under a condition of division number of 10^3 and temperature of 1 K. First, the variation of the α_{xx} value with the magnetic field is shown in Figure 7 and Table IV. When the magnetic field is in the region from 0.0 to 1.5 au, the α_{xx} value becomes about 6 au. However, when the magnetic field is over 2.0 au, the α_{xx} value suddenly decreases to about 3 au. This result can be explained as follows: As shown schematically in Figure 8, triplet energy level splits into three distinct levels by the external magnetic field (Zeeman splitting). Over the critical magnetic field, the lowest one of the three levels becomes lower than the singlet energy level (spin crossover). The sudden decrease in the polarizability described above may reflect

TABLE II
Polarizability.

MC method		FF method	
n	α_{xx} (au)	Method	α_{xx} (au)
1	6.962 ± 0.000	HF	6.924
10	6.988 ± 0.121	MP2	6.665
100	6.845 ± 0.151	MP3	6.516
1000	6.785 ± 0.091	MP4DQ	6.440
10,000	6.675 ± 0.180	MP4SDQ	6.449
		CCSD	6.407

TABLE IV
Polarizability: (a) polarizability vs. magnetic field; (b) polarizability for the singlet or triplet spin state.

(a)

MC method	
HZ	α_{xx} (au)
0.0	6.899 ± 0.036
0.5	7.175 ± 0.429
1.0	6.576 ± 0.295
1.5	6.763 ± 0.610
2.0	3.207 ± 0.505
2.5	3.370 ± 0.295
3.0	3.303 ± 0.155

(b)

FF method	α_{xx} (au)	
Method	Singlet	Triplet
HF	6.924	3.322
MP2	6.665	3.297
MP3	6.516	3.288
MP4DQ	6.440	3.285
MP4SDQ	6.449	3.285
CCSD	6.407	3.283

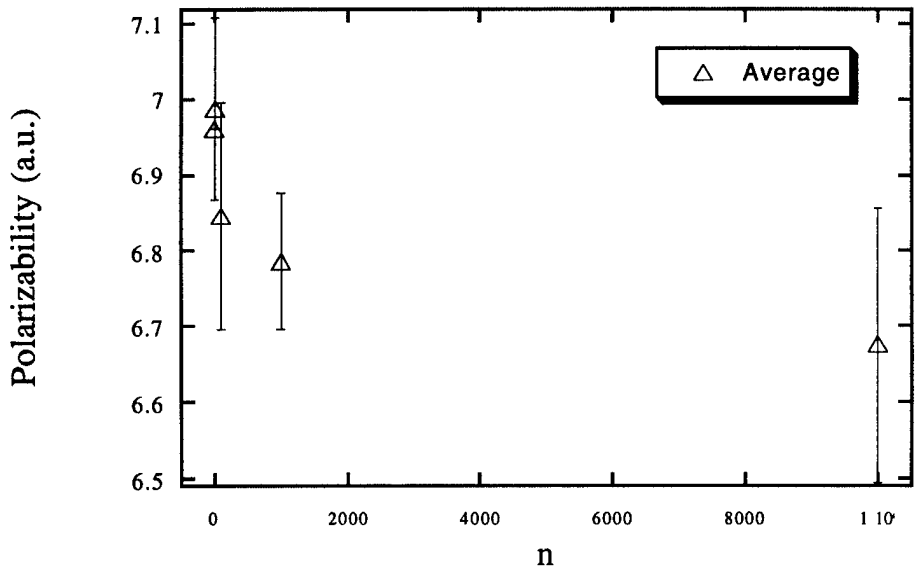


FIGURE 5. Polarizability vs. division number.

this transition of the ground state. This explanation is also supported by the results of independent calculations of α_{xx} values for singlet and triplet states by the FF method shown in Table IV. Calculated results for the hyperpolarizability γ_{xxxx} are shown in Figure 9 and Table V. When the magnetic field is in the region from 0.0 to 1.0 au, the γ_{xxxx} value is around -11 au. On the other hand, the γ_{xxxx} value becomes larger at the region over the magnetic field of 1.0 au. The singlet and triplet γ_{xxxx} values by the FF method are -8.72 and 42.24 au, respectively, as shown in Table V. The increase in the γ_{xxxx} values also can be considered to be the result of the transition of the ground state

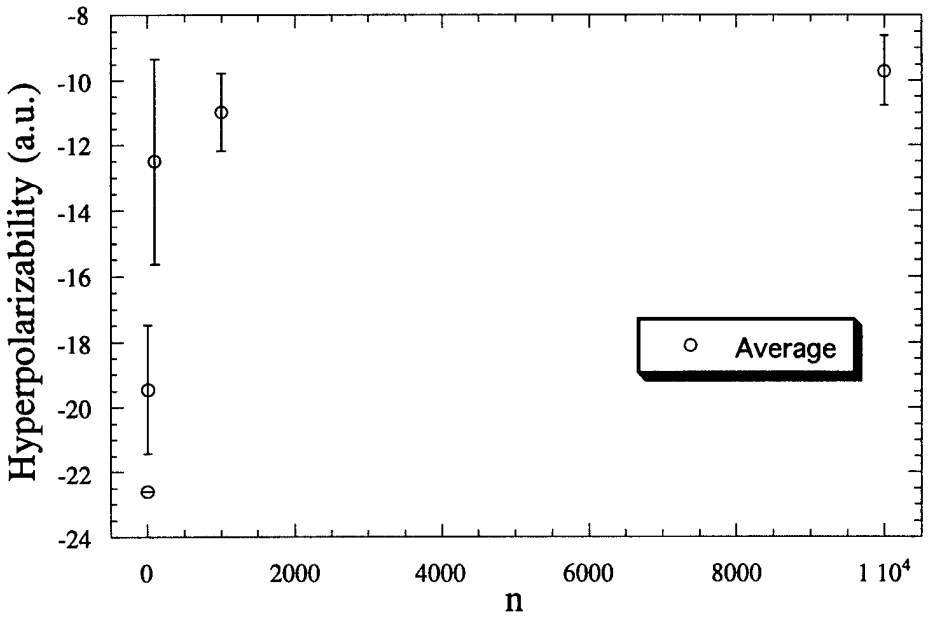


FIGURE 6. Hyperpolarizability vs. division number.

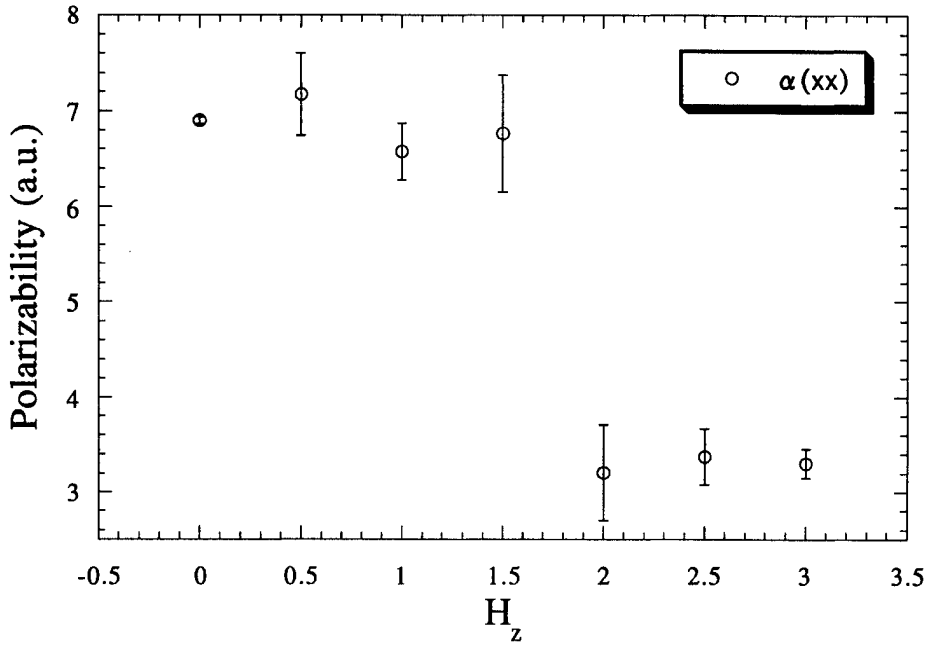


FIGURE 7. Polarizability vs. static magnetic field.

TABLE V
Hyperpolarizability: (a) Hyperpolarizability vs. magnetic field; (b) hyperpolarizabilities for the singlet and triplet spin states.

(a)

MC metho	
Hz	γ_{xxxx} (au)
0.0	−11.492 ± 1.214
0.5	−13.672 ± 4.288
1.0	−11.004 ± 2.940
1.5	−8.797 ± 4.677
2.0	−1.922 ± 6.991
2.5	5.047 ± 10.684
3.0	8.239 ± 14.021

(b)

FF method	γ_{xxxx} (au)	
Method	Singlet	Triplet
HF	−22.00	39.47
MP2	−17.39	41.24
MP3	−12.79	41.95
MP4DQ	−9.59	42.15
MP4SDQ	−10.21	42.02
CCSD	−8.72	42.24

between different spin states. These results qualitatively show that the (hyper)polarizability under the external magnetic field is explained in terms of the relative stability of the singlet and triplet states. Note that the γ_{xxxx} value by the MC method in the region over the magnetic field of 2.5 au is less than that of the triplet state by the FF method because of using the division number of 10^3. For more precise calculations, the division number should be larger than 10^3.

Concluding Remarks

We presented a path integral formulation and the scheme to calculate the ensemble average of

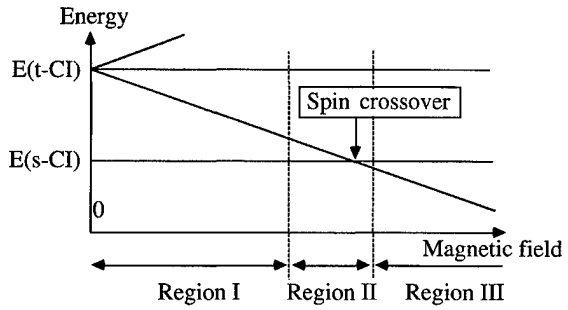


FIGURE 8. Zeeman split and spin crossover.

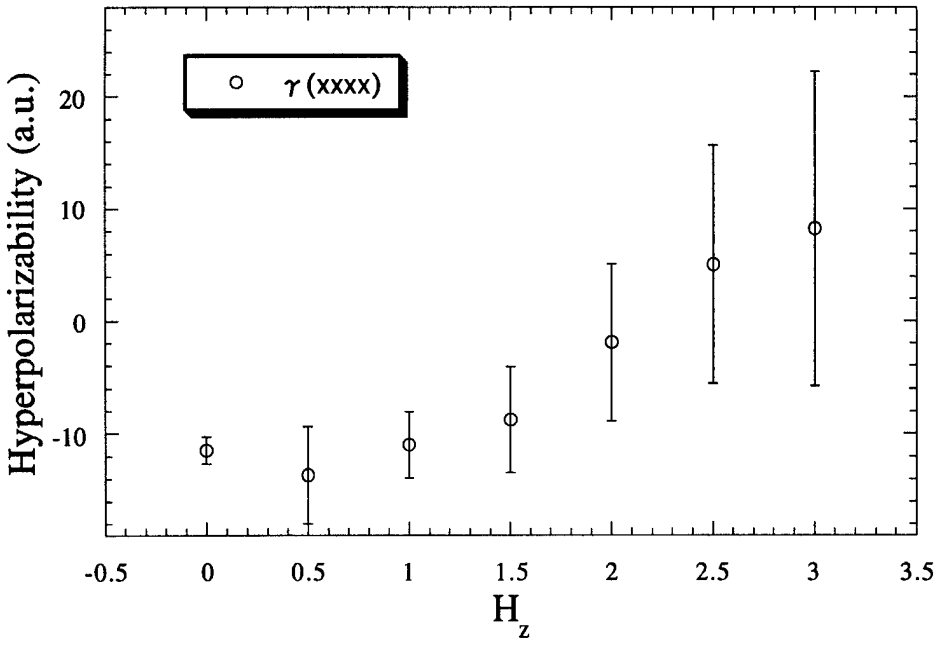


FIGURE 9. Hyperpolarizability vs. static magnetic field.

physical properties in terms of the Monte Carlo method. We applied our method to calculations of total energy, dipole moment, and static (hyper)polarizability of a hydrogen molecule. The qualitative dependence of those physical properties on the number of divisions for the partition function was shown, which indicates that various properties will converge to an exact value at the limit of larger division number. The qualitative dependence of physical properties on the external field is also shown. It is found that the static (hyper)polarizability value varies around the spin crossover. Our method can be a useful tool for investigating such phenomena as the property change under the transition process. In next step, we will reform our scheme to yield more quantitative results for investigating larger systems, chemical catastrophe (dissociation), and so on.

ACKNOWLEDGMENTS

The authors would like to thank Prof. K. Nishikawa, Dr. H. Kawabe, and Dr. M. Kikuchi for their continued encouragement and helpful discussions throughout this work. We also wish to express our grateful acknowledgment to Prof. W. Mori, Dr. S. Takeda, Dr. M. Okumura, and Mr. T. Kawakami for our instructive discussions.

References

1. B. M. Pierce, J. Chem. Phys. **91**, 791 (1989).
2. W. A. Parkinson and M. C. Zerner, J. Chem. Phys. **94**, 478 (1991).
3. J. O. Morley, Int. J. Quantum Chem. **46**, 19 (1993).
4. J. O. Morley, J. Phys. Chem. **99**, 1923 (1995).
5. M. Nakano and K. Yamaguchi, Chem. Phys. Lett. **206**, 285 (1993).
6. H. D. Cohen and C. C. J. Roothaan, J. Chem. Phys. **43**, S34 (1965).
7. K. Ohta, T. Fukumi, and T. Sakaguchi, Nonlinear Opt. **6**, 215 (1994).
8. R. P. Feynman, Rev. Mod. Phys. **20**, 367 (1948).
9. R. P. Feynman, Phys. Rev. **76**, 769 (1949).
10. R. P. Feynman, Phys. Rev. **80**, 40 (1950).
11. J. P. Blaizot and H. Orland, Phys. Rev. **24**, 1740 (1981).
12. R. P. Feynman and A. R. Hibbs, *Quantum Mechanics and Path Integrals* (McGraw-Hill, New York, 1965).
13. L. H. Ryder, *Quantum Field Theory* (Cambridge University Press, London, 1984).
14. J. W. Negele and H. Orland, *Quantum Many-Particle Systems* (Addison-Wesley, Reading, MA, 1988).
15. J-P. Blaizot and G. Ripka, *Quantum Theory of Finite Systems* (Massachusetts Institute of Technology, Boston, MA, 1986).
16. M. Suzuki, Ed., *Quantum Monte Carlo Method in Condensed Matter Physics* (World Scientific, Singapore, 1993).
17. M. Suzuki, Prog. Theor. Phys. **56**, 1454 (1976).
18. M. Suzuki, Commun. Math. Phys. **51**, 183 (1976).
19. H. F. Trotter, Proc. Am. Math. **10**, 545 (1959).

20. N. Metropolis, A. W. Rosenbuth, M. N. Rosenbluth, A. H. Teller, and E. Teller, J. Chem. Phys. **21**, 1087 (1953).
21. J. M. Hammersley and D. C. Handscomb, *Monte Carlo Methods* (Methuen, London, 1964).
22. K. Binder, *Phase Transitions and Critical Phenomena*, C. Domb and M. S. Green, Eds. (Academic Press, New York, 1976), Vol. 5b.
23. H. Nagao, K. Nishikawa, and S. Aono, Chem. Phys. Lett. **190**, 97 (1992).
24. H. Nagao, K. Nishikawa, and S. Aono, Chem. Phys. Lett. **215**, 5 (1993).
25. H. Kawabe, K. Nishikawa, and S. Aono, Int. J. Quantum Chem. Phys. Lett. **215**, 5 (1993).
25. H. Kawabe, K. Nishikawa, and S. Aono, Int. J. Quantum Chem. **51**, 265 (1994).
26. H. Kawabe, H. Nagao, and K. Nishikawa, Int. J. Quantum Chem. **59**, 457 (1996).
27. H. Kawabe, H. Nagao, and K. Nishikawa, Int. J. Quantum Chem. Quantum Chem. Symp. **30**, 11 (1996).
28. H. Nagao, Y. Shigeta, H. Kawabe, T. Kawakami, K. Nishikawa, and K. Yamaguchi, J. Chem. Phys. (in press).
29. H. Nagao, H. Kawabe, T. Kawakami, M. Okumura, W. Mori, K. Nishikawa, and K. Yamaguchi, Mol. Cryst. Liq. Cryst. **286**, 171 (1996).
30. T. Kawakami, H. Nagao, K. Ueda, W. Mori, and K. Yamaguchi, Mol. Cryst. Liq. Cryst. **286**, 177 (1996).
31. T. Kawakami, H. Nagao, W. Mori, and K. Yamaguchi, Syn. Met. **85**, 1753 (1997).
32. H. Nagao, M. Nakano, S. Yamada, K. Ohta, and K. Yamaguchi, Syn. Met. **85**, 1159 (1997).
33. M. Dupuis, A. Marquez, and E. R. Davidson, *HONDO 95.3 from CHEM-Station* (IBM Corp., Neighborhood Road, Kingston, NY. 12401, 1995).
34. H. Kawabe, K. Kodama, H. Nagao, and K. Nishikawa, Int. J. Quantum Chem. (in press).
35. M. J. Frisch, G. W. Trucks, M. Head-Gordon, P. M. W. Gill, M. W. Wong, J. B. Foresman, B. G. Johnson, H. B. Schlegel, M. A. Robb, E. S. Replogle, R. Gomperts, J. L. Andres, K. Rahgavachari, J. S. Binkley, C. Gonzalez, R. L. Martin, D. J. Fox, D. J. Defrees, J. Baker, J. J. P. Stewart, and J. A. Pople, *Gaussian 92* (Gaussian, Inc., Pittsburgh, PA, 1992).

C—H ··· O and N—H ··· O Hydrogen Bonds in Liquid Amides Investigated by Monte Carlo Simulation

JOÃO M. MARQUES CORDEIRO

Departamento de Fisica e Quimica, Faculdade de Engenharia de Ilha Solteira—UNESP, Av. Brasil, 56, 15.385-000, Ilha Solteira, SP, Brazil

Received 3 March 1997; revised 19 June 1997

ABSTRACT: Monte Carlo simulations of liquid formamide, *N*-methylformamide (MF), and *N,N*-dimethylformamide (DMF) have been performed in the isothermal and isobaric ensemble at 298 K and 1 atm, aiming to investigate the C—H ··· O and N—H ··· O hydrogen bonds. The interaction energy was calculated using the classical 6-12 Lennard-Jones pairwise potential plus a Coulomb term on a rigid six-site molecular model with the potential parameters being optimized in this work. Theoretical values obtained for heat of vaporization and liquid densities are in good agreement with the experimental data. The radial distribution function [RDF, $g(r)$] obtained compare well with R-X diffraction data available. The RDF and molecular mechanics (MM2) minimization show that the C—H ··· O interaction has a significant role in the structure of the three liquids. These results are supported by ab initio calculations. This interaction is particularly important in the structure of MF. The intensity of the N—H ··· O hydrogen bond is greater in the MF than formamide. This could explain some anomalous properties verified in MF. © 1997 John Wiley & Sons, Inc. Int J Quant Chem **65**: 709–717, 1997

Key words: Monte Carlo simulation; amides; hydrogen bond; radial distribution functions

Introduction

Liquids have particularly interested the chemistry community due to their fundamental role in chemical and biological processes. Therefore, the study of their properties have attracted a good deal of attention, in spite of the difficulties involved. In the last decade, computational methods such as molecular dynamics and Monte Carlo (MC) have become popular tools in this task [1–4]. These methodologies have shown to be specially useful to investigate some structural aspects related with the liquid state. Nevertheless, the success of the investigation is strongly dependent on

© 1997 John Wiley & Sons, Inc.
CCC 0020-7608 / 97 / 050709-09

the availability of intermolecular potential functions that yield a reasonable model for the liquid. In recent years, we have undertaken a theoretical investigation on the liquid properties emphasizing the liquid structure and solute–solvent interactions in binary mixtures [5]. The concept of hydrogen bond (H bond) has been fundamental in understanding the interaction between molecules, especially in aqueous systems. However, as yet, many aspects of this type of nonbonded interaction are not well known, in spite of all the work that has been done in that area. One point of dispute is the possibility of the C—H ··· O interaction be considered as H bond [6]. Taylor and Kennard have provided conclusive evidence of the existence of this interaction in crystals, in which the lengths of the C ··· O distance are between 3.0 and 4.0Å, and the C—H ··· O angle ranges between 90° and 180° [7]. The energy of this interaction is small (2.0–20 kJ/mol) [6], but there is little doubt that it has important implications in chemistry, biochemistry, and crystal engineering, especially when strong O—H ··· O and N—H ··· O H bonds are absent [6, 8]. C—H ··· O bonds may even distort the geometry of the strong H bond in specific instances. Anomalies in strong H bond patterns of certain crystal structures are explained on the basis of the interplay of strong and weak H bonds [8]. In general, the strength and effectiveness of C—H ··· O H bond depends on the C—H carbon acidity [9] and on the O atom basicity [10], which is enhanced by cooperative effects. The criteria for the significance of a particular C—H ··· O geometry have also been the subject of some discussion. Recent analysis has shown that angular characteristics of the larger C—H ··· O contacts (C ··· O 3.5–4.0 Å) and their effects on crystal structures resemble those with shorter contacts (3.0–3.5 Å) [6]. It should be emphasized that the C—H ··· O bond is not really a van der Waals contact but is essentially electrostatic. Therefore, since its strength falls off slower with distance than the usual van der Waals interaction, it is conceivable at distances equal to or larger than the van der Waals limit [8]. Thus, even long C ··· O separations (about 4.0 Å) must be considered, and one can expect that these weak H bonds have orienting effects on molecules, influencing in liquid structure.

Another type of H bond that plays a master role in biological chemistry is the N—H ··· O=C H bond. However, some aspects of its structure are not yet well understood. Bertolasi and co-workers have shown that the range of the N ··· O distance is between 2.7 and 3.3 Å, while the N—H ··· O angle ranges between 144° and 175° [11]. The authors have concluded that the resonance is the most important factor determining the strength of the interaction and is responsible by the strong H bonds formed.

The main goal of this study is to investigate the patterns of this interactions in liquid phase using computer simulations. For that purpose we have performed MC simulations [12] of the simplest liquid amides, like formamide, *N*-methylformamide, and *N,N*-dimethylformamide (DMF). Those molecules contain a carbonyl C—H group that could form C—H ··· O bond, and two of them also have a O=C—N—H group that could form an N—H ··· O=C bond. In the latest case the main feature is the capability of this group to present resonance. Besides, it is possible to investigate the role of the substitution on the donor capability of the amine group.

Molecular Models

A MC investigation using optimized potential for liquid simulations (OPLS) force field parameters [13] on a five-site model and a molecular dynamics simulation with test-particle model potential [14] on a six-site model has been published for formamide. Monte Carlo [13] and molecular dynamics [15] simulations have been performed for a five-site model of DMF using OPLS potentials. More recently, molecular dynamics simulation on the three liquids has been published using six-sites model in which the structure factors for the liquids were explored and compared with the experimental ones [16]. Having in mind our main purpose in this work, we have optimized a six-site model for those three liquids (the methyl groups are treated as a monatomic site) such that the H ··· O interaction in C—H ··· O can be studied. This parametrization is also important to investigate the behavior of the aldehydic hydrogen in the amide–water solutions. In order to clarify the site–site intermolecular correlation obtained by the plots of the radial distribution function, we have investigated the dimer formation in the gas phase at molecular mechanics (MM2) level [17]. The molecules were modeled as rigid structures and therefore intramolecular relaxation effects are not

considered. As it is known these molecules do not present rotation around the C—M bond due to the resonance verified in the peptide bond. The molecular geometry parameters for the three molecules were taken from the Jorgensen and Swenson (JS) study [13]. The potential parameters were optimized for formamide and DMF and accordingly used in MF. The Lennard-Jones parameters used for aldehydic hydrogen were those developed by Hagler and Liphson [18] while the rest were optimized using those reported by JS [10] as a starting trial set. The comparison with the experimental values of density and heat of vaporization (ΔH_v) was the criterion used to optimize these parameters. The charge distribution was optimized to yield a dipole moment around 15–20% greater than the one in the gas phase. This procedure has been used as a criterion to compensate for neglecting polarization effects in fluid simulations [13, 19, 20]. In formamide we have started with the charges published by Hagler and Liphson [18] (the point charges on amine sites are very similar to those used by JS [13]). For the DMF we have used the aldehydic charges obtained for formamide and the charges published by JS for the amine group [13]. The optimization of the charges was made such that the aldehydic and amine groups were set to be zero. I kept the charge distribution on the aldehydic group the same for all studied molecules and changed only the charges on the amine group. All the approximations above are criteria to minimize the number of potential parameters. In Table I, I present the potential parameters used for the simulations of the three amides. The results from this work attest the quality of the Lennard-Jones potential parameters reported by JS [13].

A calculation of the partial charges was made with 6-31G* basis set using the CHELPG procedure included in the Gaussian 92 program [21] as discussed elsewhere [22], maintaining fixed our molecular geometries. In Table II, I present the results obtained in this work.

It is noticed that the charges calculated with the CHELPG method are somewhat different from those I have used in the simulation. The main difference is in the charges of the carbonylic carbon and the nitrogen. However, the dipole moments are quite similar in both calculations. Therefore, I conclude that the dipole moment plays an important role in the experimentally observed ΔH_v and liquid densities. It is interesting to notice that the derivation of partial charges from molecular orbital calculations depends on the various assumptions in the molecular orbital theories, while that optimized by MC simulations depends on the fitting of experimental results with the intermolecular force field used.

Computational Aspects

INTERMOLECULAR POTENTIAL FUNCTION

To determine the potential topology, the energy E_{ab} between molecules **a** and **b** has been represented by a sum of Coulomb and Lennard-Jones potentials centered on the sites:

$$E_{ab} = \sum_{ij} \left[A_{ij}/r_{ij}^{12} - B_{ij}/r_{ij}^{6} + q_i q_j / r_{ij} \right], \quad (1)$$

where r_{ij} is the distance between site i in **a** and site j in **b** and q_i and q_j are fractional point charges located on i and j molecular sites (it has been supposed that the electrostatic contribution to the intermolecular potential is suitable repre-

TABLE I
Potential parameters for the amides used in this work.

Sites	q	σ (Å)	ε (kcal / mol)
	Formamide ($\mu = 4.2D$)		
C	0.34	3.75	0.105
O	−0.46	2.96	0.21
H(C)	0.12	2.75	0.038
N	−0.830	3.25	0.17
H(N)	0.415	0.00	0.00
	MF ($\mu = 4.3D$)		
C	0.34	3.75	0.105
O	−0.46	2.96	0.21
H(C)	0.12	2.75	0.038
N	−0.70	3.25	0.14
Me	0.285	3.80	0.13
H(N)	0.415	0.00	0.00
	DMF ($\mu = 4.4D$)		
C	0.34	3.75	0.105
O	−0.46	2.96	0.21
Hc	0.12	2.75	0.038
N	−0.57	3.25	0.14 (0.17)
Me	0.285	3.80	0.13 (0.17)

The values between brackets are those reported by Jorgensen and Swenson [13]. The unit of μ in Debye (the values are those ones obtained with the charges presented).

TABLE II
Partial charges located on the amides sites obtained with 6-31G* basis functions.

Formamide (μ = 4.34)	MF (μ = 4.34)	DMF (μ = 4.35)
C = 0.752	C = 0.565	C = 0.463
O = −0.630	O = −0.586	O = −0.595
H(C) = −0.003	H(C) = 0.017	H(C) = 0.051
N = −0.970	N = −0.544	N = −0.143
H(N) = 0.401	H(N) = 0.303	CH_3 = 0.153
H(N) = 0.449	CH_3 = 0.246	CH_3 = 0.072

Unit of μ in Debye.

sented by fractional charges located on the molecular sites). For each site k, the parameters A_{kk} and B_{kk} were given by $A_{kk} = 4\varepsilon_k\sigma_k^{12}$ and $B_{kk} = 4\varepsilon_k\sigma_k^6$, where ε_k and σ_k are the Lennard-Jones parameters for the kth site. Parameters A_{ij} and B_{ij} for a nondiagonal interaction $[i,j]$ were obtained using the geometric combining rules $A_{ij} = (A_{ii}A_{jj})^{1/2}$ and $B_{ij} = (B_{ii}B_{jj})^{1/2}$ [23]. This approach has been frequently used in this field of study. In an earlier work we have shown that the difference in the results obtained using the geometric combining rule above and well-know Lorentz-Berthelot rule is negligible [5].

MONTE CARLO SIMULATIONS

MC simulations were carried out in the isothermal and isobaric *ensemble* at 298.15 K and internal pressure 1 atm, employing Metropolis importance sampling [24] and cubic box boundary conditions. All the systems investigated have consisted of 256 monomers in a cubic cell. In our earlier work we have demonstrated that the number of molecules in the box, does not imply significant changes in the results obtained [5]. In the calculation of configurational energy using Eq. (1), the Coulombic term was calculated with Ewald sum [23]. Starting from the initial distribution of monomers, a new configuration was generated by randomly translating and rotating a randomly chosen molecule along Cartesian coordinates. Ranges for translations and rotations of the monomers and volume changes were adjusted to yield an acceptance/trial ratio of about 0.45 for new configurations. After a volume movement the coordinates of the center of mass of all molecules in the reference box were scaled in an usual way [23]. Each calculation started with an equilibration phase of 1.2×10^6 configurations following by an average segment consisting of 8×10^6 configurations. Statistical uncertainties were calculated from separate averages over blocks of 2×10^5 configurations. The calculations were carried out on Silicon Graphics Power 4D and IMB RISC 6000 workstations.

Results and Discussion

THERMODYNAMIC

In Table III, I show the thermodynamic results obtained for the three amides. The results agree very well with those reported by JS for formamide and DMF [13] and a good agreement is noted between theoretical and experimental values. As already discussed above, the potential parameters

TABLE III
Values of thermodynamics properties of the pure liquids.[a]

Liquid	ΔH_v	$-E_i$	$\bar{V}$	ρ
This work				
Formamide	14.79 ± 0.02	14.20 ± 0.02	40.93	1.10 ± 0.003
MF	13.77 ± 0.02	13.18 ± 0.02	59.32	1.00 ± 0.003
DMF	11.40 ± 0.03	10.81 ± 0.03	78.54	0.93 ± 0.003
Experimental values[b]				
Formamide	14.70	14.11 ± 0.02	39.89	1.13
MF	13.77	13.18 ± 0.02	57.56	1.02
DMF	11.10	10.51 ± 0.03	77.66	0.94

[a] Heat of vaporization (ΔH_v) and intermolecular energy (E_i) in kcal / mol. The heat of vaporization was estimated by $\Delta H_v = -E_i + RT$. Mole volume ($\bar{V}$) in cm^3 / mol (the experimental one is calculated with experimental, density and molecular weight). Density (ρ) in g / cm^3.
[b] ΔH_v and ρ obtained from Ref. [25].

were optimized for formamide and DMF and used in methylformamide. As one can notice, these parameters reproduce well the experimental thermodynamic properties of the liquids.

RADIAL DISTRIBUTION FUNCTIONS AND HYDROGEN BOND

Formamide

The radial distribution functions (RDF) computed for formamide are shown in Figure 1. Qualitatively, our results are similar to those reported by JS [13]. The small differences in the height of some peaks can be attributed to differences in the charges located on the sites. The closest intermolecular correlation verified in the RDF is between the oxygen and the hydrogen atoms bonded to nitrogen located at 1.9 Å. This correlation has been verified by different experimental techniques and reported earlier by Kalman and co-workers [26]. It is also very close to the smaller distance reported by Bertolasi and co-workers to the H bond in the molecules investigated by them [11]. In the same way, the N—O correlation at 2.9 Å also agrees with the distance determined experimentally by Kalman and co-workers [26], and it is in the range of distances reported by Bertolasi and co-workers to the N—H ··· O=C H bond [11]. According to these authors, these distances are characteristic of a strong H bond between the molecules and are verified preferentially in molecules that present resonance. It is clear from the height and the peak positions of the two amine hydrogen that there is no strong preference between them in the hydrogen bond formation.

Figure 2 shows the only two dimers found with the minimization procedures that agree with the $g(r)$ plots. The legend show the most important geometric parameters to our discussion. As one can observe, the $g(r)$ plots are a combination of these dimers. This is an indication of the existence of both of them in the liquid. This coexistence is stressed by the O/H(C) RDF which presents two significant peaks at 2.9 and 4.9 Å. The form of the N/N $g(r)$ is also due to the coexistence of both dimers in the liquid. The N—H ··· O angle in dimer **a** is roughly 157°, which agrees with the values reported by Bertolasi and co-workers for the N ··· O distance verified in this correlation [11]. Ohtaki and co-workers have optimized formamide dimers with ab initio LCGO–MO–SCF with a minimum base set $(2s/1p)$ [27]. They have obtained that the cyclic dimer is the most stable, which is also the case in our study, but the authors have concluded that the trans dimer is more probably in the liquid because this dimer favors the formation of open chains, which stabilize the liquid. Those authors have also optimized the dimer forming H bonds between oxygen and aldehydic hydrogen and have founded that this dimer presents a small stability with the equilibrium distance O—H of 3.2 Å, which is very close to the first maximum of the O/H(C) RDF observed in Figure 1. The C ··· O lengths and C—H ··· O angles reported here also agree with the values presented by Desiraju [6] as characteristic of C—H ··· O H bonds. Then the results are consistent with the existence of the C—H ··· O H bond in the liquid formamide. This correlation must contribute to increases the stability of the trans dimer (dimer **a**). Then, our six-site

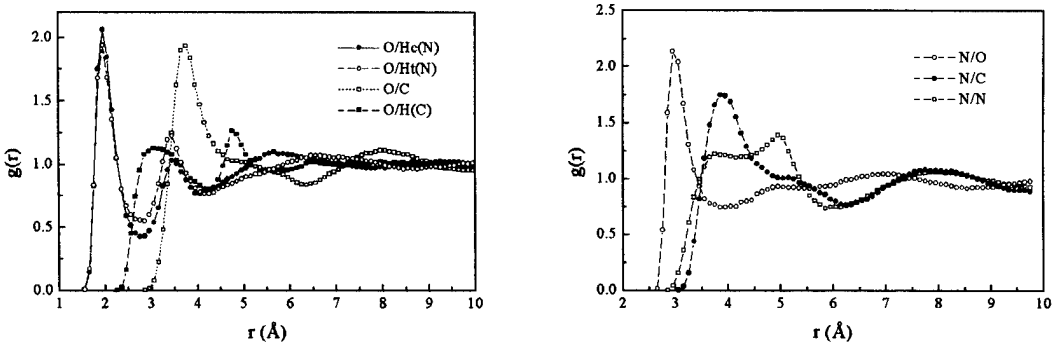


FIGURE 1. Plots of radial distribution function for formamide. H_c and H_t are the aminic hydrogens *cis* and *trans* to the oxygen, respectively.

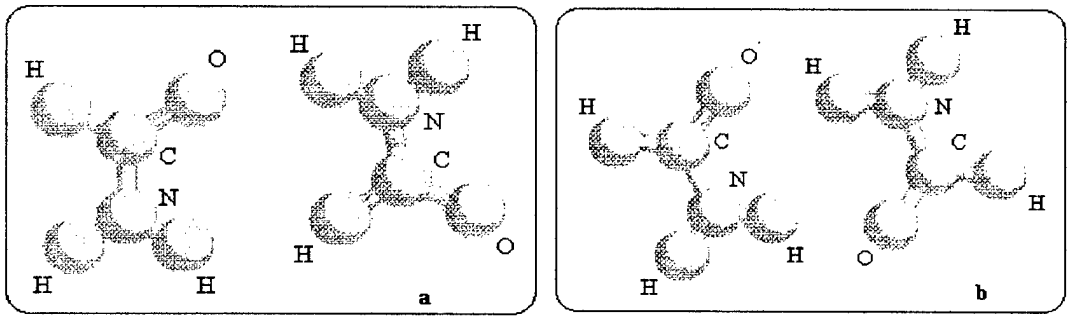


FIGURE 2. The two formamide dimers optimized at MM2 level that agree with $g(r)$. Geometric parameters of dimer **a**: r(O / Ht) = 2.0 Å; r(O / Hc) = 3.6 Å; r(O / N) = 3.0 Å; r(O / C) = 3.5 Å; r(O / H(C)) = 3.0; COH angle = 152°; NHO angle = 148.6°; CHO angle = 102.6°. Geometric parameters of dimer **b**: r(O / Ht) = 3.9 Å; r(O / Hc) = 2.0 Å (for the two H-bond); r(O / N) = 3.0 Å; r(O / C) = 3.8 Å; COH angle = 120° (for the two H-bond); NHO angle = 178°. H_c and H_t are the aminic hydrogens *cis* and *trans* to the oxygen, respectively.

model can identify the two types of correlation discussed in the introduction present in liquid formamide. Based in this work and in the early ones [13, 27], we consider that the structure of the liquid formamide consists of the two dimers showed in the Figure 2. Given the discussion above, I consider the position that the formamide is formed of flexible chains of dimer **a** with cyclic dimers "immersed" in it [27] seems to be reliable.

N,N-Dimethylformamide

Unlike the formamide, no distinct peak has been verified in X-ray study of DMF [28]. As a consequence, there is more interest in simulating this liquid since, of course, it forms a condensed phase. In Figure 3 is shown the RDF computed for the liquid. Qualitatively, the $g(r)$ graphs obtained here are equivalent to those obtained by JS [13]. As in the case of formamide, there are little differences in the height of the peaks, which can be attributed to differences in the charges located on the sites. The present $g(r)$ results show a greater definition for the shoulders in the oxygen–carbon correlation then in the JS study [13], as consequence of the fact that I recognize C and H as different sites instead of a single site. The $g(r)$ plots show that the shortest intermolecular distance in liquid phase is not between oxygen and methyl groups, as was reported in the JS study [13], but between oxygen and the aldehydic hydrogen. Figure 4 presents the two dimers found for which the atom–atom distances better reproduce the $g(r)$ plots obtained. From these dimers it is clear that there is a significant correlation between oxygen and the hydrogen bonded to the carbonyl group. This correlation must contribute for the correlation between oxygen and trans methyl to be more intense than oxygen and cis methyl. The first peak in the correlation oxygen–carbon occurs in the dimer involv-

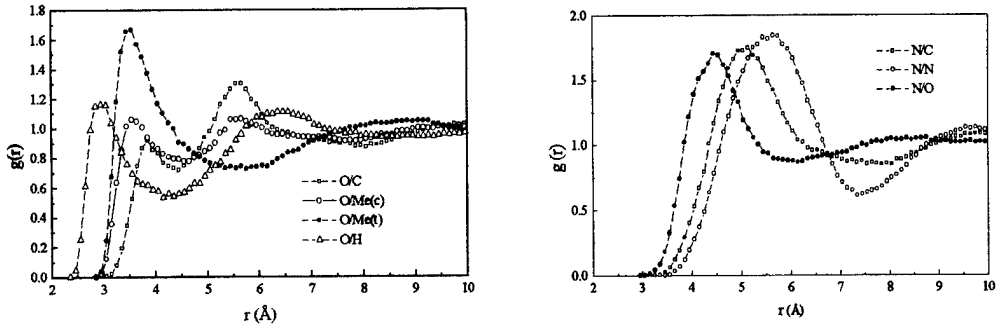


FIGURE 3. Plots of radial distribution function for *N*, *N*-dimethylformamide. Me(c) and and Me(t) are the aminic methyls *cis* and *trans* to the oxygen, respectively.

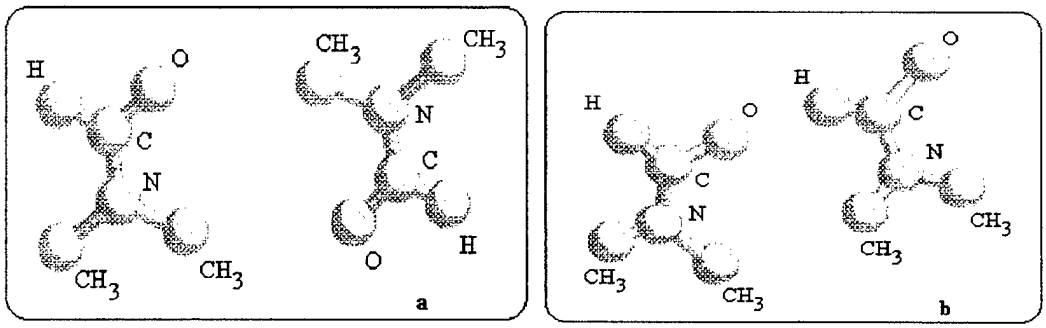


FIGURE 4. The two DMF dimers optimized at MM2 level that agree with the $g(r)$ plots. Geometric parameters of the dimer **a**: r(O / Me(c)) = 3.5 Å; r(O / C) = 5.4 Å; r(O / H) = 6.5 Å; r(N / C) = 5.0 Å; r(N / N) = 5.7 Å; r(O / N) = 4.7 Å; C(CH_3)O angle = 158°. Geometric parameters of the dimer **b**: r(O / Me(t)) = 3.5 Å; r(O / C) = 3.8 Å; r(O / H) = 2.8 Å; r(N / C) = 5.3 Å; r(N / N) = 5.8 Å; r(O / N) = 4.0 Å; COH angle = 143°; CHO angle = 144°. Me(c) and Me(t) are the aminic methyls *cis* and *trans* to the oxygen, respectively.

ing the oxygen–hydrogen correlation while the peak at 5.5 Å is due to the dimer involving the cis methyl. The second peak in the O/C correlation, more intense than the first peak, is a clear indication of the existence of two different dimers in the liquid bulk. Also in this case, the C ··· O lengths and C—H ··· O angles reported for dimer **b** agree with the values presented by Desiraju as being characteristics of C—H ··· O hydrogen bonds [6]. Ohtaki and co-workers [28] have made an ab initio MO–SCF calculation for the dimer bonded by C=O—H(C) and found a stabilization energy of −4.3 kcal/mol and a bond distance O—H of 3.2 Å. Based in the Desiraju study [6] and in the hydrogen bond energy of water (7.2–9.6 kcal/mol), this energy seems to be too high. Our results show that the distance of this interaction is also lower than that reported by those authors [28]. One should keep in mind that we are comparing results for liquids with ab initio results for the gas phase. The existence of these two dimers in the liquid phase agrees with the structure proposed by Ohtaki and co-workers [28, 29] of a random distribution of molecular dipole orientation.

N-Methylformamide

In the simulation of these molecules we have two possibilities for the position of the methyl and hydrogen sites of the amine group. Each one can be cis or trans to oxygen. The hydrogen trans conformer is predicted to be 4.2–5 kJ/mol more stable than the cis one. Experimentally the relative concentration of the cis conformer is found to be around 10%, which is in agreement with the stabilization energy [30]. In this work, I have modeled the molecule with the hydrogen trans to the oxygen. Figure 5 shows the RDF graphs obtained for

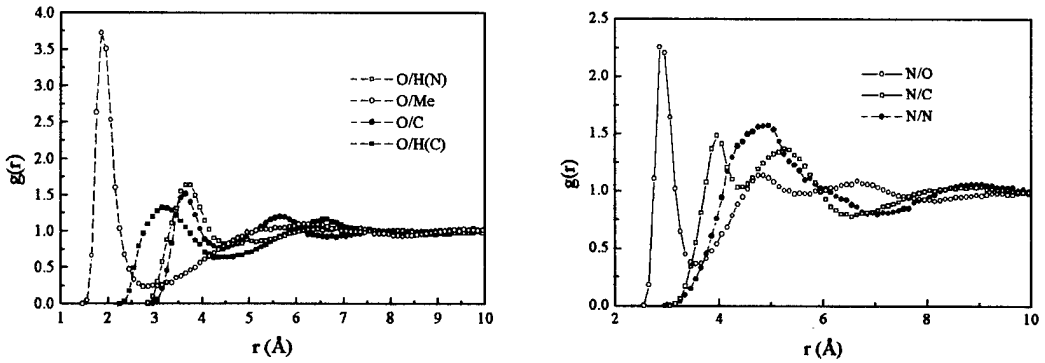


FIGURE 5. Plots of radial distribution function for methylformamide.

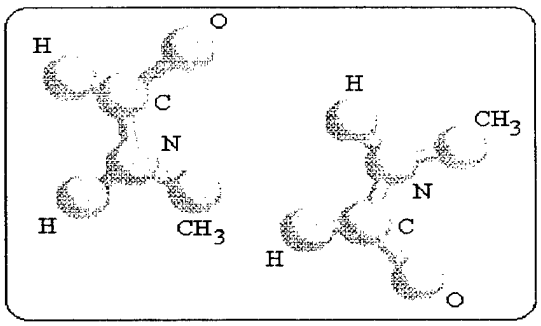


FIGURE 6. Methylformamide dimer optimized at MM2 level. Geometric parameters of the dimer: r(O–H(N)) = 2.0 Å; r(O–CH_3) = 3.6 Å; r(O–C) = 3.4 Å; r(O–H(C)) = 3.0 Å; r(N–O) = 2.9 Å; r(N–C) = 3.9 Å, 4.7 Å; N–H ··· O angle = 156°; C–H ··· O angle = 104°.

this liquid, and Figure 6 shows the only dimer that we succeeded to optimize that agrees with the RDF graphs presented.

Thus for this liquid, the intermolecular interaction between oxygen–amine hydrogen with hydrogen bond formation prevails. The O ··· H(N) and N ··· O distance and N—H ··· O angle agree with this [8]. The weak correlation between oxygen and hydrogen bonded to the carbonyl around 3 Å must contribute to the dimer stabilization. The O ··· H(C) length and C—H ··· O angle agree with that reported by Desiraju for the H bond between this atom [6]. It is interesting to notice that the substitution of a hydrogen by a methyl group from formamide to MF make the aminic hydrogen in MF more acidic than in the formamide, due to the stabilization of the methyl group in the change of nitrogen from sp^3 to sp^2. Then the O ··· H(N) hydrogen bond must be stronger. This dimer agrees with the structure proposed by Ohtaki and co-workers [31] and Neuefeind and co-workers [32] of linear chains with preferred parallel orientation of the molecular moment.

Conclusions

Clearly the properties of formamide and *N*-methylformamide are a consequence of the hydrogen bond between oxygen and aminic hydrogen. DMF does not present this correlation. *N*-methylformamide presents an O ··· H(N) H bond stronger than formamide, with the consequence than the aminic hydrogen is more acidic in the first one. So, MF must be more structured around this hydrogen bond than formamide. Other properties to be noticed are the melting and boiling points of formamide, MF, and DMF which are 2.55 and 111°C, −3.86 and 185°C, and −60.48 and 155°C, respectively [25]. Then, clearly MF presents an anomalous behavior, a consequence of a greater structuration of the liquid phase in which the O ··· H(N) plays a very important role. On other hand, formamide and DMF are completely soluble in water, while MF is not [25]. The more intense correlation in DMF is between the oxygen and methyl group located in the trans position with respect to oxygen, but the O ··· H(C) is the closest. Ab initio calculations on the dimer stabilization energy of oxygen–aldehydic hydrogen interaction from formamide and DMF give values of −2.0 and −4.3 kcal/mol, respectively [26, 27]. This correlation in DMF is more stable than in the other two liquids and must have a greater significance in the liquid structure. In all studied liquids, the length, angles, and energetic analysis made on the O ··· H(C) permit the conclusion, based in the Desiraju study [6], that there is hydrogen bond formation in the liquids. Liquid formamide is made of flexible chains in which are immersed cyclic dimers. Liquid DMF is constituted of two dimers roughly dispersed in the liquid phase. MF is constituted of linear chains of one dimer only.

References

1. K. D. Gibson and H. A. Scheraga, J. Comp. Chem. **11,** 468 (1990).
2. W. L. Jorgensen, Chem.-Org. Chem. **4,** 91 (1991).
3. T. P. Strastsma and J. A. McCammon, Ann. Rev. Phys. Chem. **43,** 407 (1992).
4. B. M. Ladanyi and M. S. Skaf, Ann. Rev. Phys. Chem. **44,** 335. (1993).
5. L. C. G. Freitas and J. M. M. Cordeiro, J. Mol. Struct. (Theochem). **335,** 189 (1995). See also A. L. L. Sinoti, J. R. S. Politi, and L. C. G. Freitas, J. Braz. Chem. Soc. **7,** 133, (1996).
6. G. R. Desiraju, Acc. Chem. Res. **24,** 290 (1991).
7. R. Taylor and O. Kennard, J. Am. Chem. Soc. **104,** 5063 (1986).
8. G. R. Desiraju, Angew. Chem. Int. Ed. Ing. **34,** 2311 (1995).
9. G. R. Desiraju, J. Chem. Soc. Chem. Commun. 179 (1989), 454 (1990).
10. T. Steiner, J. Chem. Soc. Chem. Commun. 2341 (1994).
11. V. Bertolasi, P. Gilli, V. Ferretti, and G. Gilli, Acta Cryst. **B51,** 1004 (1995).
12. DIADORIM Fortran code by L. C. G. Freitas, Theoretical Chemistry Lab., Dept. of Chemistry, UFSCar, S. Carlos, SP, Brazil.

13. W. L. Jorgensen and C. J. Swenson, J. Am. Chem. Soc. **107,** 569 (1985).
14. K. P. Sagarik and R. Ahlrichs, J. Chem. Phys. **86,** 5117 (1987).
15. S. Yashonath and C. N. Rao, Chem. Phys. **155,** 351 (1991).
16. P. C. Schoester, M. D. Zeidler, T. Radnai, and P. A. Bopp, Z. Naturf. **50a,** 38 (1995).
17. PCModel program, Serena Software, Bloomington, IN 40402-3026, USA.
18. A. T. Hagler, E. Huler, and S. Lifson, J. Am. Chem. Soc. **96,** 5319 (1975).
19. B. G. Rao and U. C. Singh, J. Am. Chem. Soc. **112,** 3803 (1990).
20. M. E. Cournier and W. L. Jorgensen, Mol. Phys. **51,** 119 (1984).
21. M. J. Frish and a series of authors, Gaussian 92, revision A, Gaussian Inc., Pittsburgh, PA, 1992.
22. H. A. Carlson, T. B. Nguyen, M. Orosco, and W. L. Jorgensen, J. Comp. Chem. **14,** 1240 (1993).
23. M. P. Allen and D. J. Tildesley, *Computer Simulations of Liquids,* (Oxford University Press, Oxford, 1987).
24. N. Metropolis. A. W. Rosembluth, M. N. Rosembluth, A. H. Teller, and E. Teller, J. Chem. Phys. **21,** 108 (1953).
25. D. R. Lide, Ed. *CRC Handbook of Physics and Chemistry,* 73rd edition (CRC Press, Cleveland, Ohio, 1992).
26. E. Kalman, I. Serke, G. Palinkas, M. D. Zeidler, F. J. Wiesmann, H. Bertagnolli, and P. Chieuz, Z. Naturforsh, **38A,** 231 (1983).
27. H. Ohtaki, A. Funaki, B. M. Rode, and G. J. Reibnegger, Bull. Chem. Soc. Jpn. **56,** 2116 (1983).
28. H. Ohtaki, S. Itoh, T. Yamagushi, S. Ishiguro, and B. M. Rode, Bull. Chem. Soc. Jpn. **56,** 3406 (1983).
29. T. Radnai, S. Itoh, and H. Ohtaki, Bull. Chem. Soc. Jpn. **61,** 3845 (1988).
30. A. C. Fantoni and W. Caminati, J. Chem. Soc., Faraday Trans. **92,** 343 (1996).
31. H. Ohtaki, S. Itoh, and B. M. Rode, Bull. Chem. Soc. Jpn. **59,** 271 (1986).
32. J. Neuefeind, P. Chieux, and M. D. Zeidler, Mol. Phys. **76,** 143 (1992).

Understanding the Mechanism of the Addition of Organomagnesium Reagents to 2-Hydroxypropanal: An Ab Initio Molecular Orbital Analysis

MÓNICA OLIVA, VICENT S. SAFONT, JUAN ANDRÉS, RAQUEL CASTILLO, VICENTE MOLINER

Departament de Ciències Experimentals, Universitat Jaume I, Box 224, 12080 Castelló, Spain

Received 2 March 1997; revised 2 May 1997; accepted 6 May 1997

ABSTRACT: The molecular mechanism for the gas-phase addition of organomagnesium reagents: CH_3MgCl, $2CH_3MgCl$, $(CH_3)_2Mg$, and $(CH_3)_2Mg$ plus Cl_2Mg, to 2-hydroxypropanal as a model of chiral α-alkoxy carbonyl compounds is investigated at the 6-31G* basis-set level of calculation. An extensive exploration of the reactive potential energy surface was carried out in order to locate and characterize the stationary points. The geometry of stationary points and the harmonic vibrational frequencies, transition vectors, and electronic structure of the transition structures were obtained. The theoretical results are analyzed, discussed, and compared with previous theoretical and available experimental data. The first step corresponds to the exothermic formation of the chelate complexes without an energy barrier. These stationary points correspond to puckered five-membered rings, determining the stereochemistry of the global process, which is retained throughout the reaction pathway. For the reactions of one equivalent of an organomagnesium compound [CH_3MgCl or $(CH_3)_2Mg$], the second step for the intramolecular mechanism is associated to the C—C bond formation via 1,3-migration of the nucleophilic methyl group from the organomagnesium compound to the carbonyl carbon and the corresponding transition structure can be described as a four-membered ring, the *anti* attack being the most favorable pathway. CH_3MgCl is a more powerful quelant agent than is the $(CH_3)_2Mg$ system. Therefore, the reaction pathway associated to the nucleophilic attack of CH_3MgCl + 2-hydroxypropanal presents a larger barrier height than that of $(CH_3)_2Mg$ + 2-hydroxypropanal addition. The inclusion of a second equivalent corresponding to the $2CH_3MgCl$ and $(CH_3)_2Mg$ + Cl_2Mg systems yields an intermolecular mechanism, the barrier height decreases, and

Correspondence to: M. Oliva.

Contract grant sponsor: Ministerio de Ecucación y Ciencia (DGICYT).

Contract grant number: PB93-0661.

© 1997 John Wiley & Sons, Inc.

CCC 0020-7608 / 97 / 050719-10

the process can be considered as an assisted intermolecular mechanism: The first equivalent forms the chelate structure and the second one carries out the nucleophilic addition to the carbonyl group. The most favorable pathway corresponds to an intermolecular mechanism via an *anti* attack for the addition of $2CH_3MgCl$. © 1997 John Wiley & Sons, Inc. Int J Quant Chem **65**: 719–728, 1997

Key words: chelate complex; organomagnesium reagents; chiral α-alkoxy carbonyl compounds; enantioselective additions; intra- and intermolecular mechanisms

Introduction

During the last several years, there has been a notable increase in research on organomagnesium alkylation reactions [1–3]. Detailed knowledge of such reactions is relevant not only for the understanding of the addition mechanism but also for the development of enantioselective synthesis via the presence of chiral centers, since the latter is necessary to avoid formation of undesirable diastereoisomers. Face-selective nucleophilic addition of Grignard reagents to a trigonal carbon such a carbonyl group may create a new chiral center of high diastereoisomeric or enantiomeric purity with practical significance in synthetic organic chemistry [3–7]. However, there is still no general agreement concerning the nature of the molecular mechanism for this type of chemical reaction [1–3, 8–10].

Explaining experimental behavior has been a challenging problem in theoretical physical chemistry. The quantum mechanical techniques are used to characterize the potential energy surface (PES) representing a chemical reaction [11, 12]. The analysis of this PES provides molecular geometries, vibrational frequencies for reactants, products, intermediates, and transition structures (TSs). From these data, the barrier heights and rate constants for the reaction pathways connecting the reactants with the products via the corresponding TSs can be calculated. An understanding of the nature of the TS for a reaction can be valuable for practical as well as theoretical reasons. We are engaged in a research program to explore new possibilities in asymmetric synthesis from both experimental and theoretical viewpoints. We describe herein our theoretical work on the analysis of nucleophilic addition of organomagnesium reagents [CH_3MgCl, $2CH_3MgCl$,$(CH_3)_2Mg$ and $(CH_3)_2Mg$ plus Cl_2Mg] to 2-hydroxypropanal in the gas phase as a model of chiral α-alkoxy carbonyl compounds. The main objective is the characterization of the reactive potential energy surface, to obtain the nature of the molecular mechanism for these chemical reactions and to rationalize experimental observations.

Methods and Models

The calculations were performed with the GAUSSIAN94 program [13]. The ab initio calculations were made at the HF/6-31G* [14–18] level. This basis-set representation yields reasonable results in related theoretical studies [4, 19–22].

The exact characterization of the TSs was achieved by using a simple algorithm [23–26], in which the coordinates describing the system are separated into two sets: the control space, which is responsible for the unique negative eigenvalue in the respective force constant matrix associated with the transition vector (TV) [27], and the complementary space, which includes the remaining coordinates. The geometry optimizations were carried out alternatively on each subspace, one at a time, until a stationary structure was obtained. Finally, a complete analytical optimization was achieved for the whole space of all variables. The Berny analytical gradient optimization routines [28, 29] were used. The nature of each stationary point was checked by diagonalizing the mass-weighted Hessian matrix to determine the number of imaginary frequencies (zero for local minima and one for the TS). The TSs were verified to be the right ones by tracing the intrinsic reaction coordinate (IRC) [30] path from each TS to the two lower-energy structures it connects by using the second-order González–Schlegel integration method [31, 32]. In the present work, the CH_3MgCl (**I**), $2CH_3MgCl$ (**II**), $(CH_3)_2Mg$ (**III**), and $(CH_3)_2Mg + Cl_2Mg$ (**IV**) organomagnesium reagents were selected while the 2-hydroxypropanal compound was employed to represent the chiral α-alkoxy carbonyl compounds.

Results and Discussion

To discriminate between alternative reaction channels, a characterization of the PESs including the location of stationary points is essential. An extensive exploration of the different PESs has rendered two minima (chelate complexes and products) and one TS. The addition of CH_3MgCl to the carbonyl group of 2-hydroxypropanal has rendered two competitive reaction channels: the *anti* and *syn* attacks. The corresponding chelate complexes, **ICha** and **IChs**, TSs associated with the 1,3-migration of the methyl group, **ITSa** and **ITSs**, and the corresponding products, **IPa** and **IPs**, respectively, are localized on the PES. A schematic representation of the structures of these stationary points is shown in Figure 1.

The stationary points for the addition of two equivalents of organomagnesium reagents, $2CH_3MgCl$, to 2-hydroxypropanal are depicted in Figure 2. The addition processes take place along an intermolecular mechanism via attack on *anti* and metal-chelated *anti* conformations, **IIChaa**, **IITSaa**, and **IIPaa**; attack on *anti* and metal-chelated *syn* conformation, **IIChas**, **IITSas**, and **IIPas**; attack on *syn* and metal chelated *anti* conformation, **IIChsa**, **IITSsa**, and **IIPsa**; and attack on *syn* and metal-chelated syn conformation, **IIChss**, **IITSss**, and **IIPss**, respectively.

The pathways corresponding with the addition process of $(CH_3)_2Mg$ to 2-hydroxypropanal render six stationary points along *anti* and *syn* chelation processes, **IIICha**, **IIIChs**, **IIITSa**, **IIITSs**, **IIIPa**, and **IIIPs**, as shown in Figure 3. Finally, an intermolecular process corresponding to the addition of

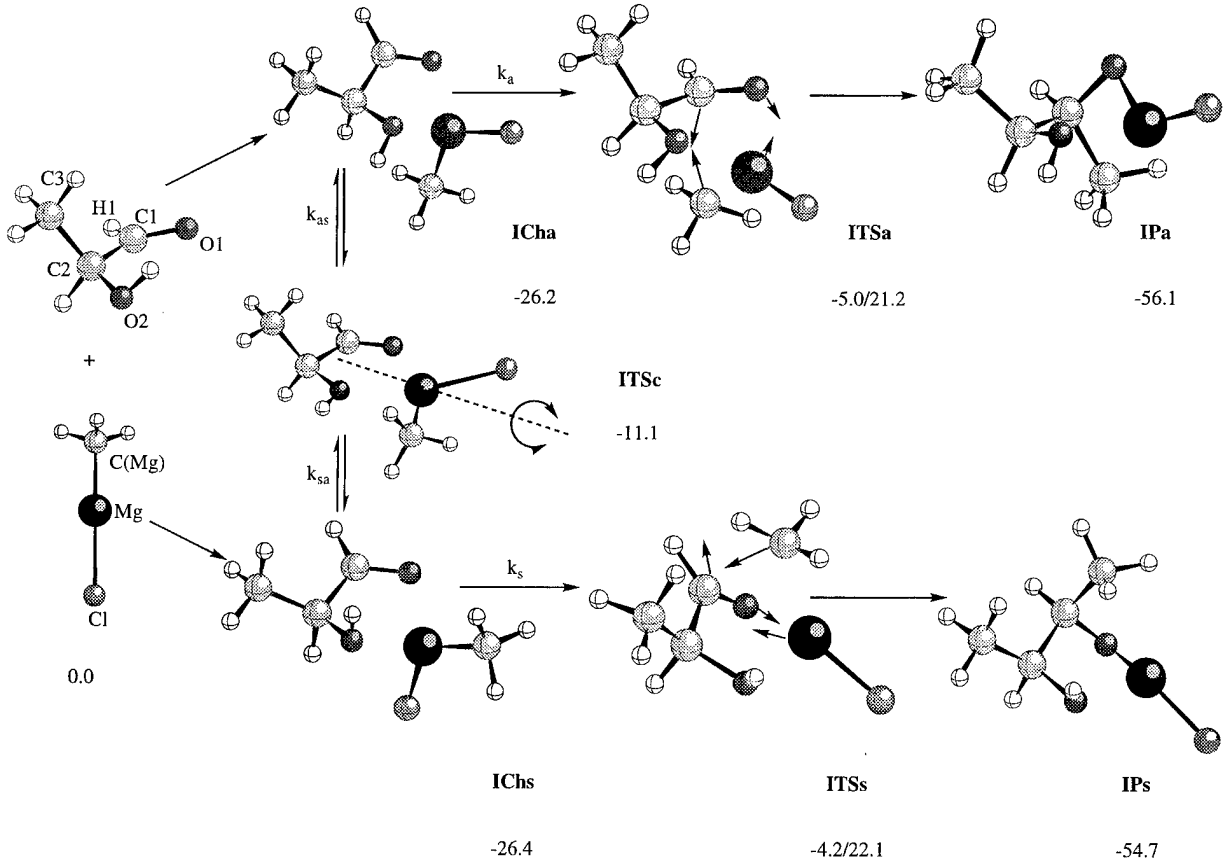


FIGURE 1. Reactants, chelate complexes, TSs, and product structures for the *anti* (upper path) and *syn* (lower path) addition of CH_3MgCl to 2-hydroxypropanal. Relative energies, including zero-point energies and thermal corrections, in kcal / mol, to reactants (total energy = −965.439246 au) and barrier heights, in kcal / mol (after the slash). The arrows on the TSs represent the reaction coordinate vectors. The atom labels are included.

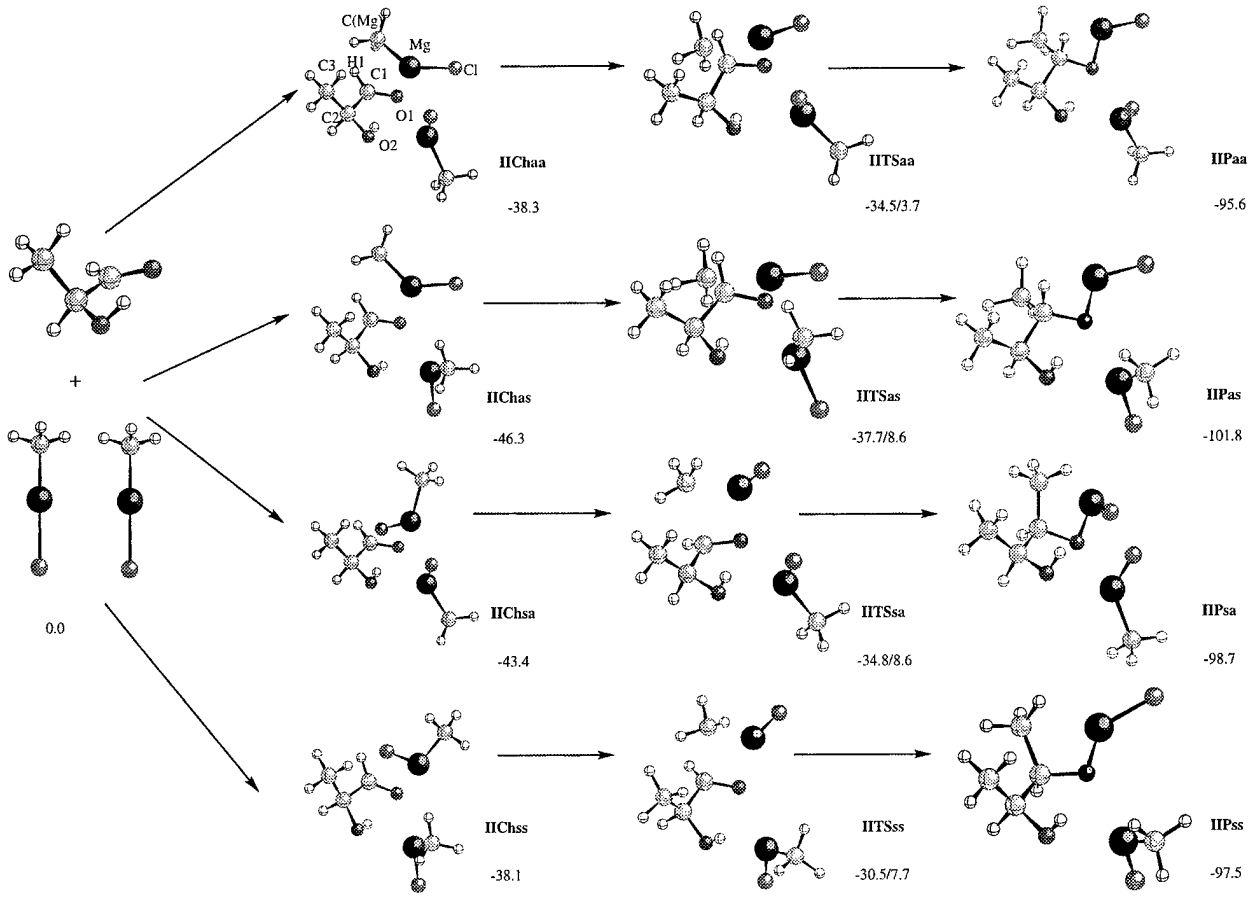


FIGURE 2. (a) Reactants, chelate complex, TSs, and products for the *anti* and *syn* addition of two equivalents of CH_3MgCl to 2-hydroxypropanal. Relative energies, including zero-point energies and thermal corrections, in kcal / mol, to reactants (total energy = −1664.166056 au) and barrier heights, in kcal / mol, (after the slash).

$(CH_3)_2Mg + Cl_2Mg$ to 2-hydroxypropanal was considered. In this case, the molecule of Cl_2Mg forms the chelate structure and the molecule of $(CH_3)_2Mg$ carried out the nucleophilic attack on the carbonyl group. The corresponding stationary points are presented in Figure 4: **IVCha, IVChs, IVTSa, IVTSs, IVPa,** and **IVPs.**

A schematic representation of the structures of the stationary points is shown in Figures 1–4. The completely optimized geometries are available from the authors on request. An analysis of the results reveals slight differences depending on the model system. The chelate structures are puckered five-membered rings; the metal is coordinated to the lone pair of the carbonyl oxygen and the methoxy oxygen is not pyramidalized. Similar structures have been found for related chelates using X-ray methods [33] and related theoretical calculations [4, 34, 35]. There is a correlation between reactivity and stereoselectivity that demonstrates the mechanistic importance of chelation, the chelate structure being maintained throughout the reaction path.

The intramolecular conversion of the chelate complex to the product takes place via the corresponding TS with retention of the chelate configuration. For CH_3MgCl and $(CH_3)_2Mg$ systems, the nucleophilic methyl group of the organomagnesium compound is located over or above the chelate ring in the TS structure. The steric interactions with the α-substituted group, CH_2R_3, are avoided in the case of *anti* attack, which is consistently favored.

The inclusion of a second CH_3MgCl molecule yields an assisted intermolecular mechanism, where the first molecule forms the chelate structure and the second CH_3MgCl molecule carries out the nucleophilic addition to the carbonyl group.

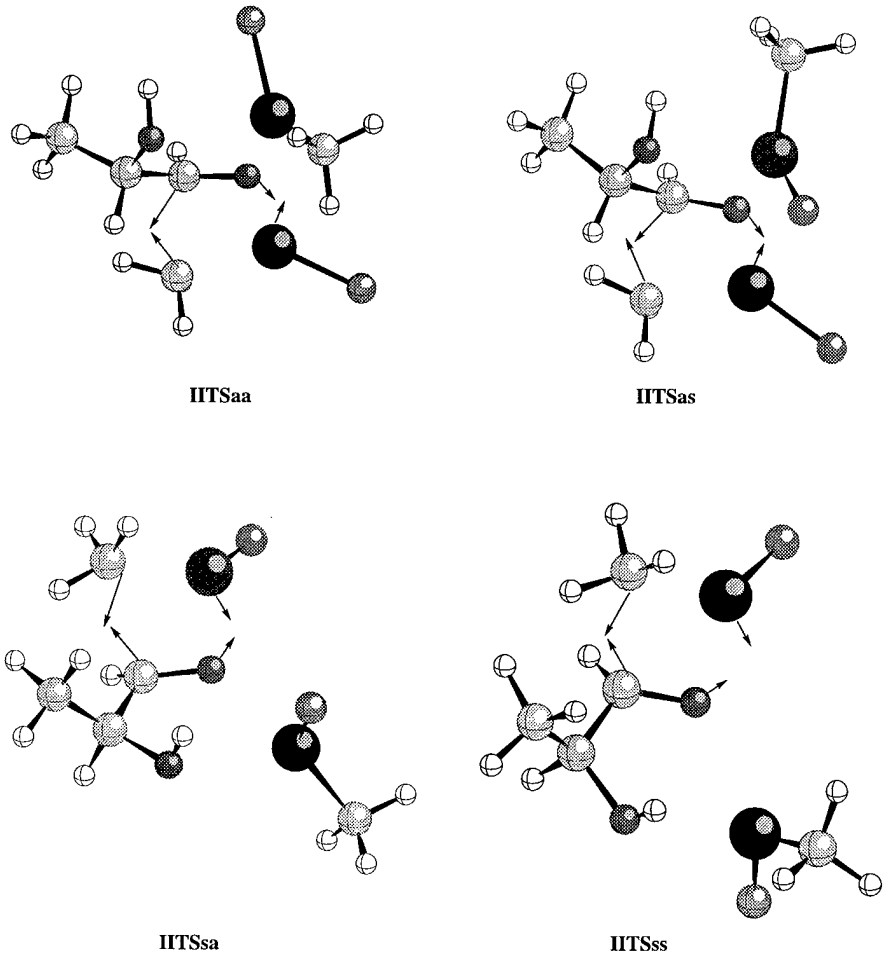


FIGURE 2. (b) A schematic representation of the TSs for the *anti* and *syn* addition of two equivalents of CH_3MgCl to 2-hydroxypropanal. The arrows on the TSs represent the reaction coordinate vectors. The atom labels are included.

This fact is in agreement with experimental data reported by Reetz et al. [36].

The addition of CH_3MgCl to 2-hydroxypropanal presents a barrier height of 21–22 kcal/mol, the products being the most stable species (28–30 kcal/mol below the chelate complexes). In this case, both methods render that the *anti* attack is the most favorable pathway. The ratio between the product obtained by means of an *anti* attack with respect to that obtained by a *syn* attack was calculated in our early work [37] assuming a Boltzmann's distribution of the TS leading to the two diastereomers. However, the presence of a transition structure controlling the interconversion between both chelate complexes, **TSc**, on the PES opens up the possibility of an equilibrium between both chelate complexes, and according to the Curtin–Hammett principle [38–40], the product ratio is therefore not determined by the relative energies of the TSs with respect to their corresponding chelate complexes but, instead, depends primarily on the relative energy of the two TSs with respect to each other. In this case, a complete kinetic analysis gives [22, 41] the following product ratio equation:

$$\frac{[\mathbf{IPa}]}{[\mathbf{IPs}]} = \frac{k_a}{k_s}\left[\frac{k_{sa}(1 + (\sum e^{-\Delta E_{ICha}/RT}/\sum e^{-\Delta E_{IChs}/RT})) + k_s \sum e^{-\Delta E_{ICha}/RT}/\sum e^{-\Delta E_{IChs}/RT}}{k_{as}(1 + (\sum e^{-\Delta E_{ICha}/RT}/\sum e^{-\Delta E_{IChs}/RT})) + k_a}\right] \quad (1)$$

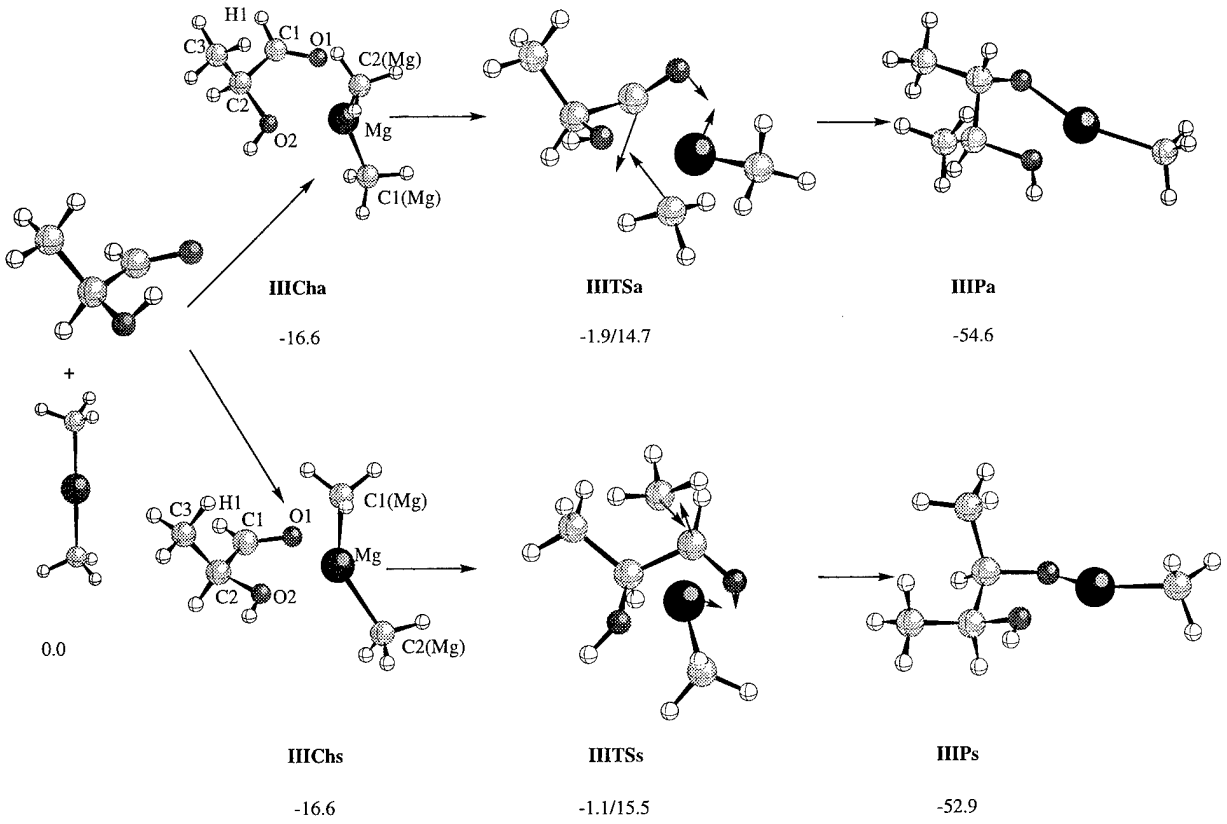


FIGURE 3. Reactants, chelate complexes, TSs, and products for the *anti* (upper path) and *syn* (lower path) addition of $(CH_3)_2Mg$ to 2-hydroxypropanal. Relative energies, including zero-point energies and thermal corrections, in kcal / mol, to reactants (total energy = −545.435254 au) and barrier heights, in kcal / mol (after the slash). The arrows on the TSs represent the reaction coordinate vectors.

To do such calculations, the rate constants k_a, k_s, k_{as}, and k_{sa} (Fig. 1) must be found. this can be achieved by means of the TS theory (TST) [42–44], assuming that the transmission coefficient is equal to 1. A pressure and temperature of 1 atm and 195.15 K was taken in the S and k calculations, respectively. The product ratio for the diastereomers obtained by means of the *anti* attack of the organomagnesium reagent methyl group with respect to those obtained by means of a *syn* attack is 89:11. Using MP2/6-31G*, the activation barriers associated to **ITSa** and **ITSs** are significantly reduced from the HF/6-31G* results (ca. 5–6 kcal/mol), having very similar values. As a consequence, a decrease in stereoselectivity is sensed (68:32). This is corrected by using the correlation energy obtained at the MP3 level (87:13). This fact can be related to the known tendency of MP2 calculations to overcorrect the too high HF results and shows that MP2 calculations overestimate the effect of the electron correlation energy on the TSs with respect to that of the reactants, in agreement with previous studies of related Diels–Alder reactions [45–51].

The TV renders very concisely the essentials of the chemical process under study. The corresponding components of TV for the variables defining the reaction coordinate vectors are depicted in Figures 1–4 and are available from the authors upon request. The TSs are well associated with forming/breaking bonds, as can be seen from the main components of the TVs. The results provide good hints for a qualitative and semiquantitative analysis.

An analysis of the TV shows that the major components are C1—C(Mg), C(Mg)—Mg, C1–O1, and Mg—O1 distances, the C1—C(Mg) distance being the most important. The minimal set of coordinates capable of producing the TS are these variables. This result is obtained after reducing the size of the control space followed by the diagonalization of the corresponding Hessian matrix. It is

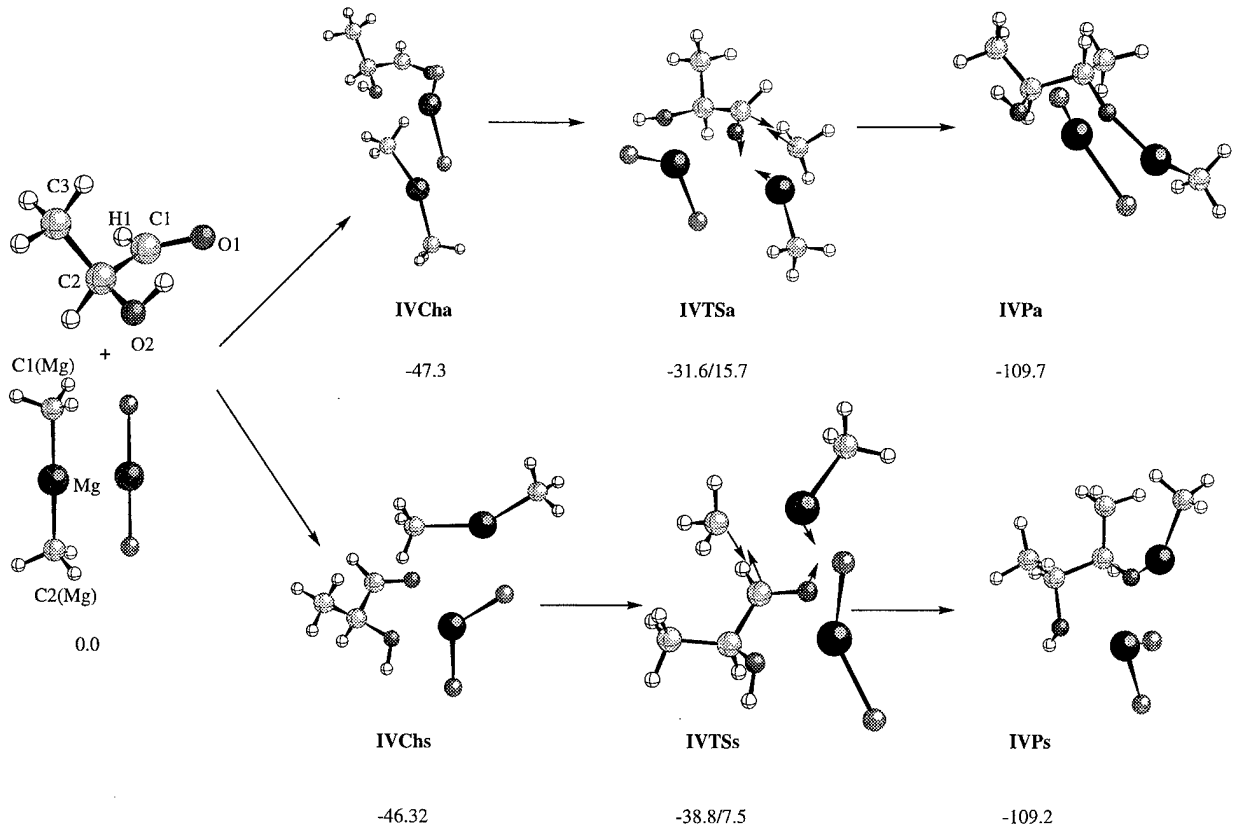


FIGURE 4. Reactants, chelate complexes, TSs, and products for the *anti* (upper path) and *syn* (lower path) addition of $(CH_3)_2Mg$ plus Cl_2Mg to 2-hydroxypropanal. Relative energies, including zero-point energies and thermal corrections, in kcal / mol, to reactants (total energy = −1664.157711 au) and barrier heights, in kcal / mol (after the slash). The arrows on the TSs represent the reaction coordinate vectors.

important to note that while the atoms participating in the control space are always the same, those in the complementary space are not. If these latter do not modulate in first order the force constants in the control space, the TV is invariant. The invariance is to be understood in terms of preservation of the reactive fluctuation patterns associated with the chemical interconversion processes. One of the interesting results obtained is a sort of geometric invariance of the fragments participating in a TS geometry. This fact has been found by us [25, 26, 52] and other workers [53]. Structural invariance of the TS structure fragments is an important result from the technical viewpoint. It helps setting up the search of TSs.

In the case of the addition of two equivalents of CH_3MgCl to the carbonyl group of the 2-hydroxypropanal, the barrier heights are predicted to be lower than in the 1:1 stoichiometry case (3–9 kcal/mol), the *anti* attack on the *anti* chelate being the most favorable pathway. The ratio between the products obtained by means of *anti* attacks with respect to those obtained by *syn* attacks can be calculated assuming a Boltzmann distribution of the TSs leading to the two diastereoisomers, by using the following equation [54]:

$$anti/syn = \sum e^{-\Delta E_a/RT} \Big/ \sum e^{-\Delta E_s/RT}, \quad (2)$$

where *anti* and *syn* refer to the TS conformation and ΔE_a and ΔE_s are the relative energies (with the zero-point vibrational energies and temperature corrections) of the TSs for the *anti* and *syn* attacks, respectively, with respect to the corresponding chelate complexes. The product ratio obtained (> 99:1, *anti*:*syn*) agrees very well with the experimental ratio, obtained by Carda et al. [55]. The corresponding TVs for the variables defining the control space are shown in Figure 2(b). These TVs are well associated with forming/breaking bonds, C1—C(Mg), C(Mg)—Mg, C1—O1, and Mg —O1, as can be seen from their main components.

The barrier heights for the addition of $(CH_3)_2Mg$ to 2-hydroxypropanal are lower than in the case of the addition of 1 equiv of CH_3MgCl but higher than in the intermolecular processes (2 equiv of CH_3MgCl). The barrier heights are 14–16 kcal/mol, the products being the most stable species (36–38 kcal/mol below the chelate complexes). In this case, we find that the *anti* attack is the most favorable pathway, with a lower energy barrier and a larger stability for the products than for the *syn* attack. The product ratio is calculated by Eq. (2), yielding 89:11 *anti/syn*. The corresponding TVs for the variables defining the control space are shown in Figure 3. These TVs are well associated with forming/breaking bonds, C1—C1(Mg), C1(Mg)—Mg, C1—O1, and Mg—O1, as can be seen from the main components.

Since Grignard reagents are an equilibrium mixture of CH_3MgCl, $(CH_3)_2Mg$, and Cl_2Mg, all of which can react with chiral α-alkoxy carbonyl compounds, we have considered the addition with $(CH_3)_2Mg + Cl_2Mg$. In this case, the latter system forms the chelate intermediate and the former one carries out the nucleophilic attack. The barrier heights for the addition of $(CH_3)_2Mg + Cl_2Mg$ to 2-hydroxypropanal are lower than in the case of the addition of 1:1 CH_3MgCl and $(CH_3)_2Mg$, but higher than in the intermolecular processes (2:1 of $2CH_3MgCl$). The barrier height is 7–16 kcal/mol, the products being the most stable species (62–63 kcal/mol below the chelate complexes). In this case, the *syn* attack is the most favorable path way with a lower energy barrier and greater stability for the products than for the *anti* attack. The product ratio is calculated by Eq. (2) and is > 99:1 *syn/anti*. The corresponding TVs for the variables defining the control space are shown in Figure 4. The TVs are well associated with the forming/breaking bonds, C1—C1(Mg), C1(Mg)—Mg, C1—O1, and Mg—O1, as can be seen from the main components.

In Figure 5, the stationary points belonging to the different reaction pathways of the addition

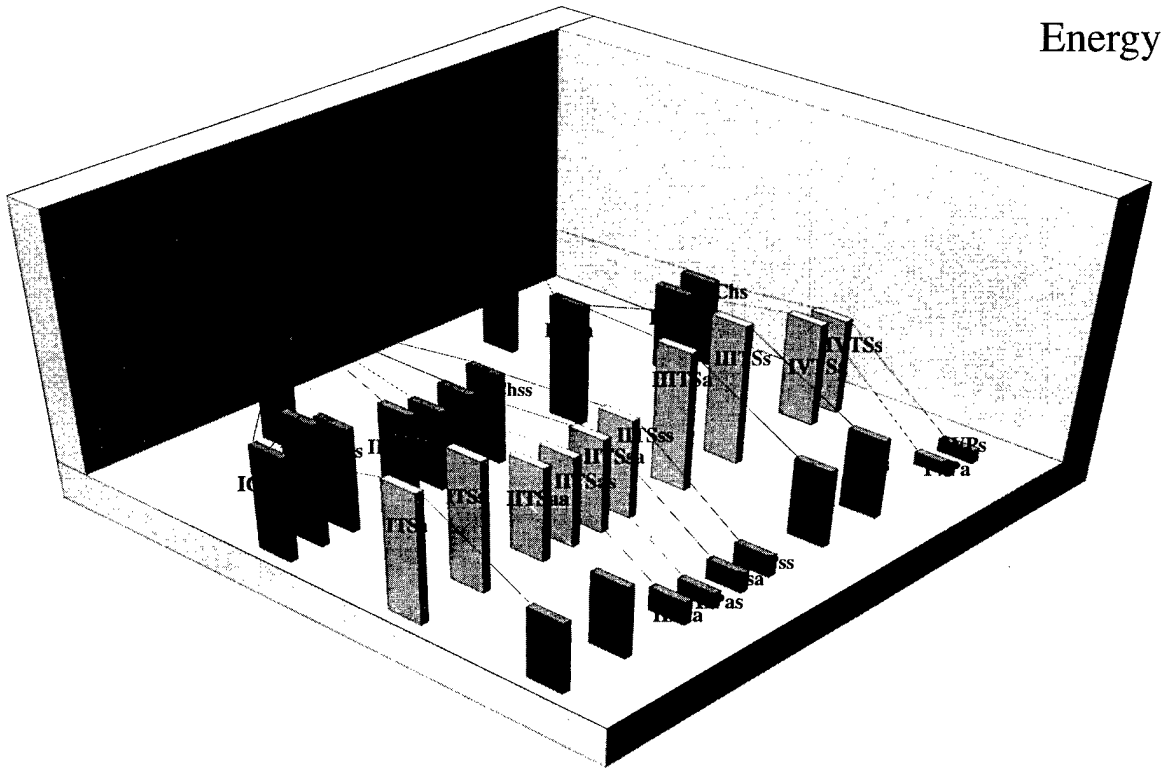


FIGURE 5. A schematic view of the reaction pathways studied in this work. **R1** corresponds with the addition of CH_3MgCl to 2-hydroxypropanal while **R2** is associated with the reaction of $(CH_3)_2Mg$ plus Cl_2Mg and 2-hydroxypropanal. The names of the different stationary points appearing along the reaction pathways are defined in the text. **IIICh** represents **IIICha** and **IIIChs**, which have the same energy and roughly the same structure.

processes are schematically depicted. In this representation, a global perspective of the reactive PES is summarized in order to compare the different molecular mechanisms found in this work.

Conclusions

Quantum chemical characterization of TSs may be rationalized to discuss molecular mechanisms for organic reactions. The theory of nucleophilic addition of organometallic reagents to carbonyl compounds is still a much debated subject, particularly with respect to the origin of stereoselectivity. The following factors are found to be dominant in the molecular mechanism for the carbonyl addition of organomagnesium reagents to chiral α-alkoxy carbonyl compounds:

(i) The formation of *syn* and *anti* chelate complexes is an exothermic process in the gas phase, corresponding to the first step in the addition process, and takes place without an energy barrier. The magnesium is coordinated to the lone pair of the carbonyl oxygen and to the methoxy oxygen. The chelate complexes can be described as puckered five-membered rings.

(ii) *syn* and *anti* chelate intermediates determine the stereochemistry of the addition process, maintaining the conformation throughout the reaction pathway.

(iii) The C—C bond-forming stage, corresponding to the 1,3-intramolecular migration from chelate complex to products, is the second and rate-limiting step for the addition process. The corresponding transition structures are four-membered rings and the most favorable pathway is the *anti* attack.

(iv) The inclusion of a second molecule of an organomagnesium reagent decreases the barrier height and the process can be described as an assisted intermolecular mechanism: The first molecule forms the chelate structure and the second molecule carries out the nucleophilic addition to the carbonyl group.

(v) The reaction pathway for the nucleophilic attack of CH_3MgCl + 2-hydroxypropanal has a barrier height larger than the $(CH_3)_2Mg$ + 2-hydroxypropanal addition. CH_3MgCl is a more powerful quelant agent than is $(CH_3)_2Mg$.

(vi) The most favorable pathway corresponds to an *anti* attack via an intermolecular-assisted mechanism for the addition of $2CH_3MgCl$. These theoretical results are in agreement with the experimental data of Reetz et al. [36] and with the diastereoisomeric excess obtained by Carda et al. [55].

(vii) The inclusion of the solvent effects into the calculation can lead to a better (qualitative) description of the product ratio. However, studies with similar systems [4] show that polarity effects on the structures and energies of the reactions are rather small.

ACKNOWLEDGMENTS

This work was supported by research funds provided by the Ministerio de Educación y Ciencia, DGICYT (Project PB93-0661). Calculations were performed on an IBM RS6000 workstation of the Departament de Ciències Experimentals and on two Silicon Graphics Power Challenge L of the Servei d'Informàtica of the Universitat Jaume I. We are indebted to these centers for providing us with computer capabilities. M. O. thanks the Ministerio de Educación y Ciencia for an FPI fellowship. R. C. thanks Silicon-Graphics for a fellowship.

References

1. M. T. Reetz, Acc. Chem. Res. **26**, 462 (1993).
2. M. T. Reetz, Angew. Chem., Int. Ed. Engl. **23**, 556 (1984).
3. X. Chen, E. R. Hortelano, E. L. Eliel, and S. V. Frye, J. Am. Chem. Soc. **114**, 1778 (1992).
4. S. Mori, M. Nakamura, E. Nakamura, N. Koga, and K. Morokuma, J. Am. Chem. Soc. **117**, 5055 (1995).
5. S. S. Wong and M. N. Paddon-Row, J. Chem. Soc., Chem Commun. 327 (1991).
6. J. M. Coxon, K. N. Houk, and R. T. Luibrand, J. Org. Chem. **60**, 418 (1995).
7. S. V. Frye and E. L. Eliel, J. Am. Chem. Soc. **110**, 484 (1988).
8. M. T. Reetz, S. Stanchev, and H. Haning, Tetrahedron **48**, 6813 (1992).
9. K. Mead and T. L. Macdonald, J. Org. Chem. **50**, 422 (1985).
10. N. T. Anh, Top. Curr. Chem. **88**, 145 (1980).
11. P. N. Skancke, Acta Chem. Scand. **47**, 629 (1993).
12. I. H. Williams, Chem. Soc. Rev. 277 (1993).

13. M. J. Frisch, G. W. Trucks, H. B. Schlegel, P. M. W. Gill, B. G. Johnson, M. A. Robb, J. R. Cheeseman, T. Keith, G. A. Peterson, J. A. Montgomery, K. Raghavachari, M. A. Al-Laham, V. G. Zakrzewski, J. V. Ortiz, J. B. Foresman, J. Cioslowski, B. B. Stefanov, A. Nanayakkara, M. Challacombe, C. Y. Peng, P. Y. Ayala, W. Chen, M. W. Wong, J. L. Andres, E. S. Replogle, R. Gomperts, R. L. Martin, D. J. Fox, J. S. Binkley, D. J. Defrees, J. Baker, J. P. Stewart, M. Head-Gordon, C. Gonzalez, and J. A. Pople, *GAUSSIAN94, Revision B.1* (Gaussian, Inc., Pittsburgh, PA, 1995).
14. R. Ditchfield, W. J. Hehre, and J. A. Pople, J. Chem. Phys. **54**, 724 (1971).
15. W. J. Hehre, R. Ditchfield, and J. A. Pople, J. Chem. Phys. **56**, 2257 (1972).
16. P. C. Hariharan and J. A. Pople, Mol. Phys. **27**, 209 (1974).
17. P. C. Hariharan and J. A. Pople, Theor. Chim. Acta **28**, 213 (1973).
18. M. S. Gordon, Chem. Phys. Lett. **76**, 163 (1980).
19. J. Andrés, J. J. Queralt, V. S. Safont, M. Canle, and J. A. Santaballa, J. Phys. Org. Chem. **9**, 371 (1996).
20. J. Andrés, J. J. Queralt, V. S. Safont, M. Canle, and J. A. Santaballa, J. Phys. Chem. **100**, 3561 (1996).
21. J. J. Queralt, V. S. Safont, V. Moliner, and J. Andrés, Theor. Chim. Acta **94**, 247 (1996).
22. V. S. Safont, V. Moliner, M. Oliva, R. Castillo, L. R. Domingo, and J. Andrés, J. Mol. Struct. (Theochem), in press.
23. O. Tapia and J. Andres, Chem. Phys. Lett. **109**, 471 (1984).
24. J. Andres, R. Cárdenas, E. Silla, and O. Tapia, J. Am. Chem. Soc. **110**, 666 (1988).
25. O. Tapia, J. Andres, and V. S. Safont, J. Chem. Soc., Faraday Trans. **90**, 2365 (1994).
26. O. Tapia, J. Andres, and V. S. Safont, J. Phys. Chem. **98**, 4821 (1994).
27. J. W. McIver, Jr., Acc. Chem. Res. **7**, 72 (1974).
28. H. B. Schlegel, J. Comput. Chem. **3**, 214 (1982).
29. H. B. Schlegel, J. Chem. Phys. **77**, 3676 (1982).
30. K. Fukui, J. Phys. Chem. **74**, 4161 (1970).
31. C. González and H. B. Schlegel, J. Phys. Chem. **94**, 5523 (1990).
32. C. González and H. B. Schlegel, J. Chem. Phys. **95**, 5853 (1991).
33. M. T. Reetz, K. Harms, and W. Reif, Tetrahedron Lett. **29**, 5881 (1988).
34. V. Jonas, G. Frenking, and M. T. Reetz, Organometallics **12**, 2111 (1993).
35. M. Nakamura, E. Nakamura, N. Koga, and K. Morokuma, J. Chem. Soc., Faraday Trans. **90**, 1789 (1994).
36. M. T. Reetz, B. Raguse, and T. Seiz, Tetrahedron **49**, 8561 (1993).
37. V. S. Safont, V. Moliner, M. Oliva, R. Castillo, J. Andrés, F. González, and M. Carda, J. Org. Chem. **61**, 3467 (1996).
38. D. Y. Curtin, Rec. Chem. Prog. **15**, 111 (1954).
39. P. I. Pollak and D. Y. Curtin, J. Am. Chem. Soc. **72**, 961 (1950).
40. L. P. Hammett, *Physical Organic Chemistry* (McGraw-Hill, New York, 1970).
41. J. I. Seeman, Chem. Rev. **83**, 83 (1983).
42. K. J. Glasstone, K. J. Laidler, and H. Eyring, *The Theory of Rate Processes* (McGraw-Hill, New York, 1941).
43. K. J. Laidler, *Theories of Chemical Reaction Rates* (McGraw-Hill, New York, 1969).
44. G. Herzberg, *Molecular Spectra and Molecular Structure* (Van Nostrand, Princeton, NJ, 1945).
45. K. N. Houk, R. J. Loncharich, J. F. Blake, and W. J. Jorgensen, J. Am. Chem. Soc. **111**, 9172 (1989).
46. W. L. Jorgensen, D. Lim, and J. F. Blake, J. Am. Chem. Soc. **115**, 2936 (1993).
47. R. D. Bach, J. J. W. McDouall, and H. B. Schlegel, J. Org. Chem. **54**, 2931 (1989).
48. S. M. Bachrach and M. Liu, J. Org. Chem. **57**, 6736 (1992).
49. S. M. Bachrach, J. Org. Chem. **59**, 5027 (1994).
50. B. Jursic and Z. Zdravkovski, J. Chem. Soc., Perkin Trans 2 1223 (1995).
51. Y. Li and K. N. Houk, J. Am. Chem. Soc. **115**, 7478 (1993).
52. J. Andres, V. Moliner, J. Krechl, J. L. Domingo, and M. T. Picher, J. Am. Chem. Soc. **117**, 8807 (1995).
53. A. Yliniemla, H. Konschin, C. Neagu, A. Pajunen, T. Hase, G. Brunow, and O. Teleman, J. Am. Chem. Soc. **117**, 5120 (1995).
54. G. Frenking, K. F. Köhler, and M. T. Reetz, Tetrahedron **47**, 9005 (1991).
55. M. Carda, F. González, S. Rodríguez, and J. A. Marco, Tetrahedron: Asym. **4**, 1799 (1993).

A Semiempirical Study on the Ring-Opening Process for the Cyclopropanone, 2,2-Dimethylcyclopropanone, *trans*-2,3-Di-*tert*-Butylcyclopropanone, and Spiro(bicyclo[2.2.1]heptane-2.1′-cyclopropan)-2′-one Systems in Solution

R. CASTILLO, J. ANDRÉS, V. MOLINER, V. S. SAFONT, M. OLIVA
Departament de Ciències Experimentals, Universitat Jaume I, Box 224, 12080 Castelló, Spain

Received 2 March 1997; revised 3 April 1997; accepted 8 April 1997

ABSTRACT: The molecular mechanisms for the ring openings of cyclopropanone, 2,2-dimethylcyclopropanone, *trans*-2,3-di-*tert*-butylcyclopropanone, and spiro(bicyclo[2.2.1]heptane-2.1′-cyclopropan)-2′-one systems were studied at the PM3 semiempirical level in the gas phase and including solvent effects. The behavior of the solvent polarity was considered by using the SCRF polarizable continuum method. Six solvents were selected: hexane, ether, tetrahydrofuran, pyridine, acetone, and acetonitrile. An extensive exploration of the potential energy surface using analytical gradient techniques allows the characterization of stationary points associated to the stereomutation conversion. Along a disrotatory ring-opening mechanism, cyclopropanone, 2,2-dimethylcyclopropanone and *trans*-2,3-di-*tert*-butylcyclopropanone are intraconverted via an oxyallyl intermediate. The epimeric forms of the spiro(bicyclo[2.2.1]heptane-2.1′-cyclopropan)-2′-one intraconvert along two competitive pathways correspond to two-step processes by a disrotatory ring-opening mechanism. Two oxyallyl intermediates and four transition structures were obtained and the corresponding transition vectors are associated to the carbon–carbon bond-breaking process and the dihedral angle measuring the conrotatory movement of the plane defined by the three carbon atoms of the cyclopropanone ring. The oxyallyl intermediates and the transition structures for the four model systems present similar structures and energies and they are located on a rather

Correspondence to: R. Castillo.
Contract grant sponsor: Ministerio de Educación, DG1CYT.
Contract grant number: PB93-0661.

© 1997 John Wiley & Sons, Inc.
CCC 0020-7608 / 97 / 050729-10

flat region. The analysis of the theoretical results shows that the solvent reaction field decreases the energy barriers for the ring-opening processes and a stabilization of the oxyallyl intermediates takes place. The calculated relative barrier heights are in good agreement with the experimental data available, and the trends in the kinetics can be explained primarily by steric interactions. Nevertheless, for the spiro(bicyclo[2.2.1]heptane-2.1'-cyclopropan)-2'-one system, it is necessary to include a specific interaction of a discrete molecule of the nucleophilic solvent on the quantum mechanical representation to explain the experimental behavior. © 1997 John Wiley & Sons, Inc. Int J Quant Chem **65**: 729–738, 1997

Introduction

Stereomutation rearrangements involving cyclopropanone systems has been the subject of continuous interest from experimental and theoretical viewpoints [1–7]. The molecular mechanism corresponding to the ring-opening process via oxyallyl intermediates is a common reaction with important applications in organic synthesis [8–10]. Numerous theoretical studies have been reported on this type of stereomutation [5, 11–16], many of them for the purpose of elucidating the nature of the ring-opening process [1, 2, 4, 5, 7, 11 16]. In particular, the cyclopropanone ring can be postulated as a reactive intermediate in the Favorskii rearrangement [10, 17–21]. Recently, we reported quantum chemical calculations on the mechanism of the Favorskii reaction [22]. In addition, some efforts have been devoted in our laboratory to the theoretical treatment of solvent effects in chemical reactivity studies [23–25]. The results indicate that the activation energies and relative rate constants can be estimated with good accuracy at a high level of theory, but more important for organic chemists, even simple calculations at moderate levels of theory, such as semiempirical procedures, give useful information of the solvent effects on the molecular mechanism for different chemical rearrangements. Calculations of the properties of stationary points located on the reactive potential energy surface (PES) of great complexity can be characterized by using semiempirical molecular orbital theory. We tried to determine the reaction mechanisms and how the solute–solvent interactions can affect the different barrier heights and the relative energies of reactants, possible intermediates, transition structures (TSs) and products on PES.

Solvent effects or, more generally, environmental effects can be accounted for by two different approaches: adding discrete solvent molecules around the subsystem of interest, the supermolecule approach, or placing them in a cavity surrounded by a continuum approach [26–28]. In the first approach, specific solvent effects are successfully represented, while in the second, nonspecific and long-range interactions are appropriately included. In the continuum models [26], the solute is embedded in a cavity, while the solvent, treated as a continuous medium, characterized by some macroscopic properties, e.g., the same dielectric constant as that of the bulk liquid, is incorporated into the solute Hamiltonian as a perturbation. In this reaction field approach, the bulk medium is polarized by the solute molecules. The electronic distribution of the solute polarizes the continuum which generates an electric field inside the cavity, which, in turn, affects the solute's geometry and electronic structure. This is a convenient model for describing electrostatic interactions due to the solvent polarity while short-range interactions are not correctly represented by this method. The implementation of this interaction scheme is achieved through the self-consistent reaction field method developed initially by Tapia et al. [29, 30].

Kinetic data for stereomutation on cyclopropanone systems derive from experimental results in the solution phase [1–4, 6, 7], which is often obtained with a great deal of effort. Substitution on the cyclopropane ring has subtle influences on the kinetics for ring cleavage and the origin of these kinetic effects is not clear. We describe herein a complementary theoretical analysis carried out with a PM3 semiempirical procedure to study the ring opening of various substituted cyclopropanone systems, which have generated considerable interest among organic and physical chemists due to important mechanistic roles that have been discerned but not entirely elucidated [1–7, 12–17]. It is of considerable interest to know the energy profiles of the corresponding reaction pathways in

the gas phase and in the presence of different solvents. This computational investigation contributes to a better understanding of the stereomutation via a ring-opening process, being the main objective the characterization of the reactive potential energy surface in the gas phase including the environmental effects and thus to obtain the nature of the molecular mechanism and to rationalize the experimental observations.

Computational Methods and Models

PM3 semiempirical calculations [31] were carried out with the GAUSSIAN94 package of programs [32]. The PESs were calculated in detail to ensure that all relevant stationary points were located and properly characterized. The exact location of the TSs was achieved by using an algorithm [33–35] in which the coordinates describing the system are separated into two sets: the control space, which is responsible for the unique negative eigenvalue in the respective force constants matrix, and the remaining coordinates set, which is called complementary space. The geometry optimizations were carried out alternatively on each subspace, one at a time, until a stationary structure was obtained. Finally, a complete analytical optimization of the TS was achieved with an "eigenvalue following" optimization method [36, 37] for all variables.

The intrinsic reaction coordinate (IRC) [38] pathways, from the TSs down to the two lower-energy structures, were traced using the second-order González–Schlegel integration method [39, 40] in order to verify that each saddle point links the two putative minima. The requested convergence on the density matrix was 10^{-9} atomic units and the threshold value of maximum displacement was 0.0018 Å and that of maximum force was 0.00045 Hartree/bohr using the Berny analytical gradient optimization routine [41, 42]. The nature of each stationary point was checked by diagonalizing the Hessian matrix to determine the number of imaginary frequencies (zero for the local minima and one for the TSs). The unique imaginary frequency associated with the transition vector (TV) [43] of the different TSs was analyzed.

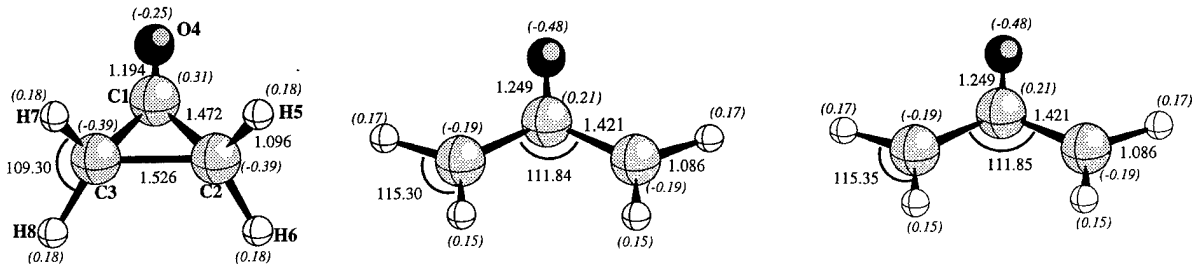
The energies of the stationary structures on the PES including solvent effects was calculated at the PM3 semiempirical level using the Conductor-like Screening Model (COSMO) option [44] included in the MOPAC93 package program [45]. This COSMO model, proposed by Klamt and Schüürmann [44], calculates the electrostatic solvation energy by representing the solute charge distribution as a set of point charges and dipoles in the neglect differential diatomic overlap formalism. The cavity chosen for the calculations was the solvent-excluded surface obtained by overlapping spheres. The liquid is assimilated to a continuum characterized by its dielectric constant. Six solvents were selected: hexane, ether, tetrahydrofuran, pyridine, acetone, and acetonitrile.

Four systems were studied: cyclopropanone (**C**), 2,2-dimethylcyclopropanone (**D**), *trans*-2,3-di-*tert*-butylcyclopropanone (**T**), and spiro(bicyclo[2.2.1] heptane-2.1′-cyclopropan)-2′-one (**S**) in the gas phase and in six different solvents: hexane, ether, tetrahydrofuran, pyridine, acetone, and acetonitrile.

Results and Discussion

An extensive exploration of the PES by means of the PM3 method was carried out in order to asses the different stationary points related to the ring-opening process. The geometries of cyclopropanone (**C**), 2,2-dimethylcyclopropanone (**D**), and *trans*-2,3-di-*tert*-butylcyclopropanone (**T**), as well as the corresponding oxyallyl structures and transition structures are illustrated in Figures 1–3, respectively. For the spiro(bicyclo[2.2.1]heptane-2.1′-cyclopropan)-2′-one system (**S**), two reaction pathways depicted corresponding to the two possible disrotatory ring-opening processes for this steromutation were characterized; for this system, two oxyallyl intermediates and four TSs were located. The structures associated to the stationary points of both channels are illustrated in Figure 4. The labels of the structures corresponding to TSs and oxyallyl intermediates are designed by the letters **TS** and **I**, respectively. The stationary points are distinguished from each other by appending the label **C**, **D**, **T**, or **S**. For the **S** system, the two reactive channels are designed by the letters **A** and **B**, and the numbers **1** and **2**, for both steps of the two stepwise mechanisms. Thus, the localized stationary points are: **S**, **TS-SA1**, **TS-SB1**, **I-SA**, **I-SB**, **TS-SA2**, **TS-SB2**, and **S′**.

The most relevant geometrical parameters of the stationary points obtained for the different systems are depicted in Figures 1–4. Optimized geometries



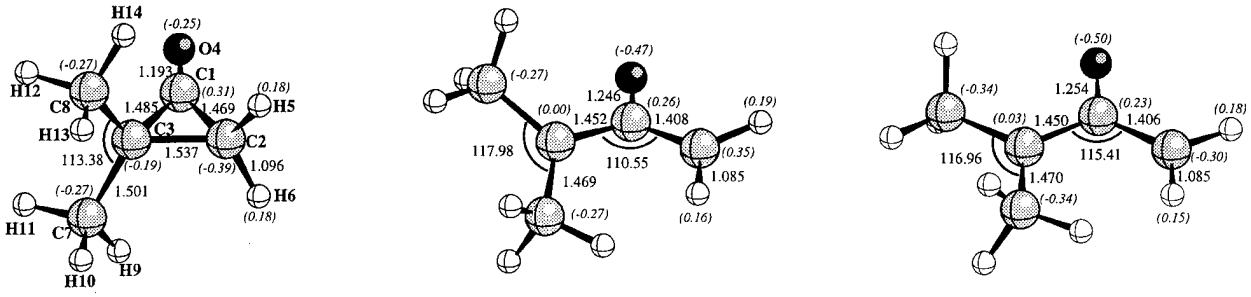
<C2C1C3 = 62.48
<C1C2C3 = 58.75
μ = 0.87 D
E = -0.005724 (0.00)

C2-C3= 2.353
<O4-C1-C2-H5= 0.0
<H7-C3-C2-H5= 0.0
μ = 1.97 D
E = 0.085156 (57.03)

C2-C3= 2.354
<O4-C1-C2-H5 = 0.49
<H7-C3-C2-H5 = 0.0
μ = 1.97 D
E = 0.085155 (57.03)

FIGURE 1. Representation of the optimized geometries for the stationary points: cyclopropanone, TS for disrotatory ring opening, and oxyallyl intermediate. Distances in angstroms and bond angles in degrees. Values in italics (in parentheses) are net atomic charges.

of all structures are available from the authors on request. For **C**, the optimized structure agrees with the experimental data obtained by Nelson and Pierce [46] from a microwave analysis and the computed geometries obtained by Lim et al. [5] at the (4/4)CASSCF/6-31G* calculation level. The TSs and the oxyallyl intermediates are located on a very flat region of the PES. On going from cyclopropanone to the TSs or oxyallyl intermediate, the electronic charge redistribution shows that an excess of negative charge is developed on the carbonyl carbon atom and to a lesser extent on the peripheral carbon atoms (see Figs. 1–4). Some interesting observations emerge from the Mulliken population analysis [47]. There is no change in the Mulliken charges between the TSs and oxyallyl



<C2-C1-C3 = 62.68
<O4-C1-C2-H5 =
<H5-C2-C1-H6 =
μ = 0.88 D
E = -0.029321 (0.00)

C2-C3 = 2.351
<O4-C1-C2-H5 = 10.62
<H5-C2-C1-H6 = 181.17
μ = 2.07 D
E = 0.042899 (45.32)

C2-C3 = 2.355
<O4-C1-C2-H5 = 0.35
<H5-C2-C1-H6 = 180.22
μ = 2.15 D
E = 0.042741 (45.22)

FIGURE 2. Representation of the optimized geometries for the stationary points: 2,2-dimethylcyclopropanone, TS for disrotatory ring opening, and oxyallyl intermediate. Distances in angstroms and bond angles in degrees. Values in italics (in parentheses) are net atomic charges.

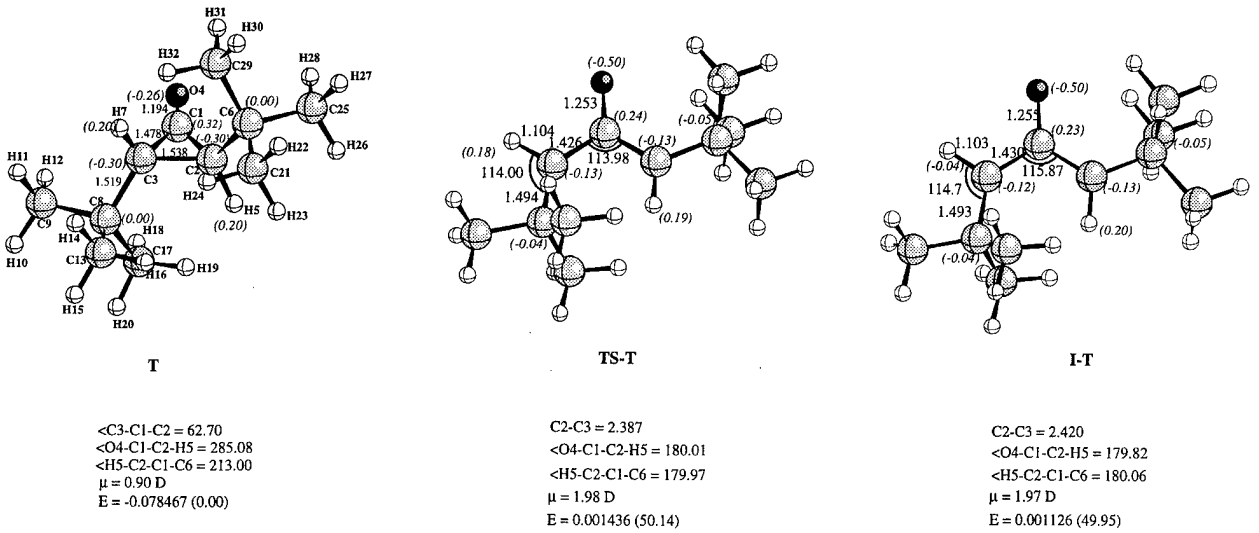


FIGURE 3. Representation of the optimized geometries for the stationary points: *trans*-2,3-di-*tert*-butylcyclopropanone, TS for disrotatory ring opening, and oxyallyl intermediate. Distances in angstroms and bond angles in degrees. Values in italics (in parentheses) are net atomic charges.

intermediates. The imaginary frequency for the TSs **TS-C**, **TS-D**, and **TS-T** are 131.8i, 65.4i, and 70.3i cm^{-1}, respectively. For model **S**, the TSs **TS-SA1**, **TS-SB1**, **TS-SA2**, and **TS-SB2** present the following imaginary frequency values: 64.4i, 54.9i, 78.0i, and 49.0i cm^{-1}, respectively. The corresponding TVs are associated to a disrotatory ring opening, as expected. These four TSs yield similar optimized geometrical parameters and energies. The predicted energy barrier between the cyclopropanone systems and TSs are in the range of 45.3–57.0 kcal/mol. For the simple model **C**, calculations at high level of theory [5] show a barrier height of 32.4 kcal/mol. As expected, the PM3 results tends to overestimate this barrier. However, our goal was to rationalize the experimental behavior of this stereomutation process for more complex systems in various solvents.

The TSs are energetically and structurally very similar to oxyallyl intermediates. The principal differences are the rotation of α-carbon atoms of the cyclopropanone rings, in the range 0.1–20.4°, out of plane in the TS, and the C—O distance of the carbonyl group that increases in the range of 0.052–0.060 Å, on going from cyclopropanone systems to oxyallyl intermediates. The energy differences between the TSs and oxyallyls intermediates are less than 0.2 kcal/mol. These structures can be described as diradicals with a strong carbon–oxygen double bond and an electron mainly localized on the terminal carbon atoms. An analysis of the barrier energies shows that the rate of the interconversion processes follows the order **S** > **D** > **T** > **C**. This order can be explained by two additive effects—(i) Hyperconjugative effects: Alkyl substitution strongly stabilizes the TS or the oxyallyl intermediate for the ring-opening process. This hyperconjugative stabilization is more effective by the norbornane, **S** system, than by the *tert*-butyl groups, methyl groups, and hydrogen atoms in the **T**, **D**, and **C** systems, respectively. (ii) The size of the steric hindrances of this reaction on going from the cyclopropanones to the TSs corresponding to the ring-opening process: In a disrotatory mechanism, ring opening of the **T** system forces a tertiary alkyl group into a 1,3-*cis* allylic interaction with a hydrogen atom in the ring-opened oxyallyl intermediate. For the **D** system, this repulsive interaction is less hindered and takes place between two hydrogen atoms. In contrast, due to the presence of the rigid norbornane ring in the **S** system, the rotation movement around C2–C3 and C3–C4 bonds is smaller than are those of freely rotating analogs and the 1,3-*cis*-allylic interaction involves the ring hydrogen and the oxyallyl hydrogen. Consequently, a substantial promotion of the stereomutation process can be expected.

The next step in our investigation is the study of the solvent effects on the basic features of the stereomutation reaction and we are now in a position to compare our results with those of Greene et al. [1, 2] for the **T** system, Cordes and Berson [4,

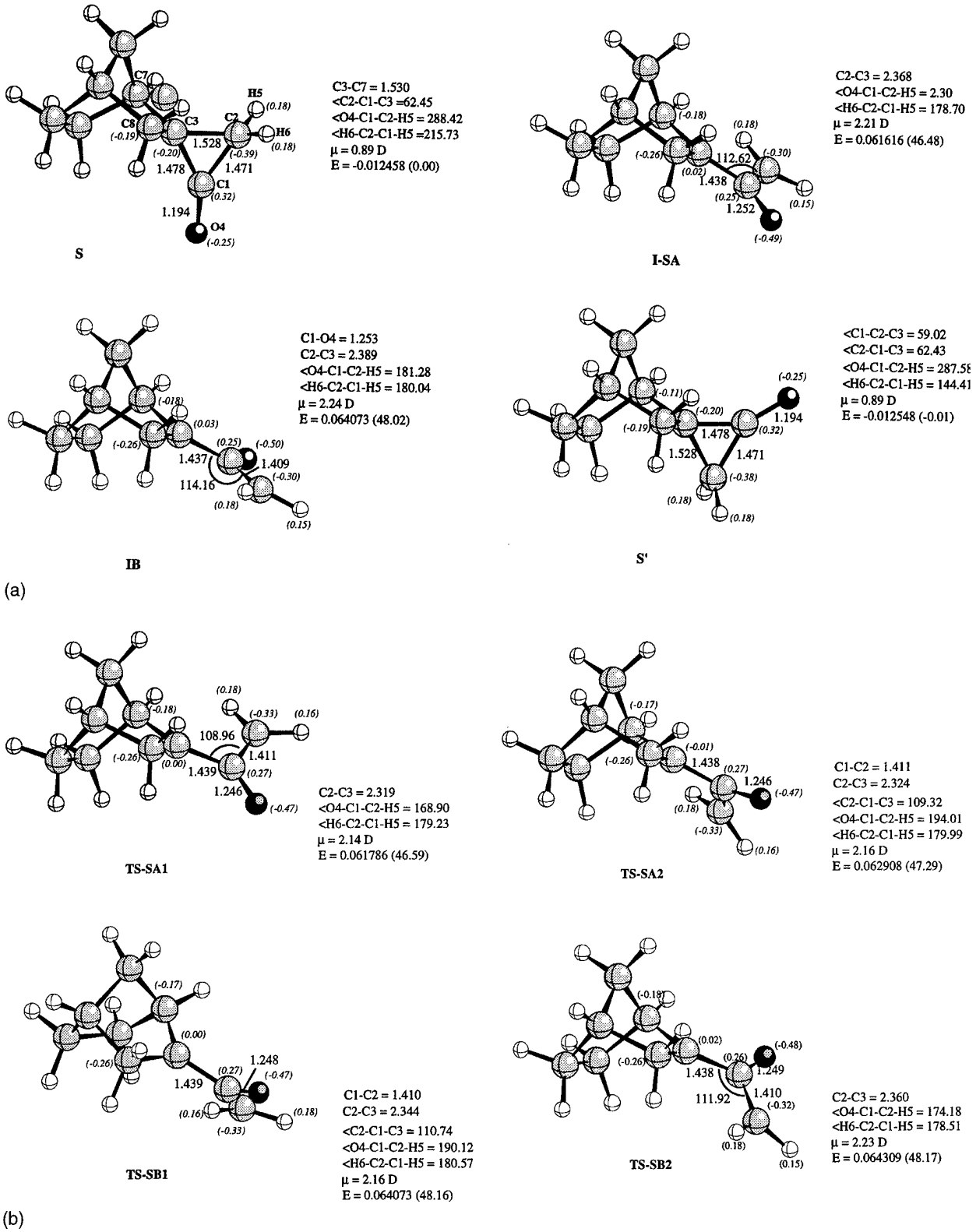


FIGURE 4. Representation of the optimized geometries for the stationary points: spiro(bicyclo[2.2.1]heptane-2.1′-cyclopropan)-2′-one, TS for disrotatory ring opening, and oxyallyl intermediate. Distances in angstroms and bond angles in degrees. Values in italics (in parentheses) are net atomic charges.

7] for the **S** system, and the theoretical work of Lim et al. [5] on the **C** and **D** systems. The relative barrier heights vs. the solvatochromic parameter $E_T(30)$ (Dimroth–Reichardt parameter) [48–51] for the six solvents are depicted in Figure 5. As could be expected from the electrostatic data, TSs and oxyallyl intermediates present identical solvation effects; however, preferential solvation of these stationary points would be expected due to that they are more polar than are the cyclopropanone ground-state systems. It should be noted that the dipole moments are increased in the range of 1.07–1.34 D upon the ring opening of the corresponding cyclopropanones for the four model systems. This is an indication that solvation influences the stability of these structures to a different extent. An analysis of the results shows that the negative of the relative barrier height increases on going from the nonpolar hexane to the polar acetonitrile solvent. A change to a more polar solvent will increase the reaction rate due to that TSs are more polar than are the initial cyclopropanone systems. The low values of these relative energies for the steromutations in solution reflect the diradical rather than the zwitterionic nature of the oxyallyls, while the presence of a zwitterion is accompanied by much larger solvent effects [49]. Additionally, our results are in reasonable agreement with the Monte Carlo simulations reported by Lim et al. [5] for the **C** and **D** models. This fact supports the use of the PM3 semiempirical procedure to study the steromutation processes in solution.

In Figure 6, a comparison between our results and experimental data for the **S** [4, 7] system is given. The values of the relative barrier heights vs. the E_T (30) for the spirocyclopropanone **S** are not correlated with the experimental data for the **T** system or with the values theoretically predicted for the more simple **D** and **C** models. In particular, Cordes and Benson [7] found that the rate of stereomutation in the **S** system is slower in ether and in acetone than in hexane and in methylene chloride. This deceleration was explained by Cordes and Benson [7] in terms of a nucleophilic association of these solvents with the carbonyl group in the cyclopropanone ring, leading to a ground-state stabilization. Reaction field representation of solvent effects is a convenient model for describing electrostatic interactions due to the solvent polarity. However, short-range interactions are not correctly represented by this method. Therefore, to understand the role played by specific and nonspecific

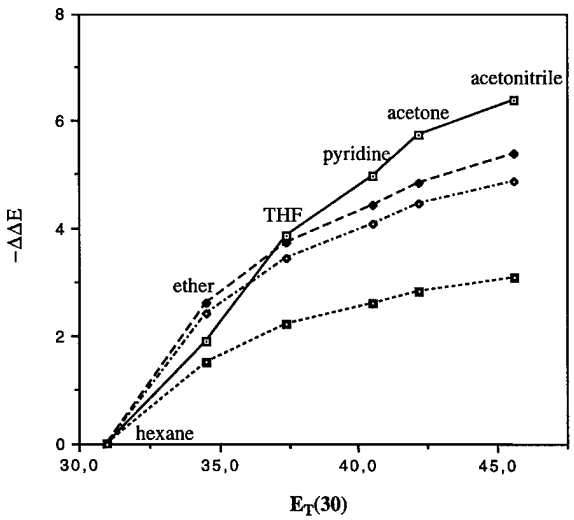


FIGURE 5. Relative barrier heights (kcal / mol) for the ring-opening process vs. solvent parameter $E_T(30)$ (Dimroth–Reichardt term). The ordinate shows the negative of the barrier height relative to that in hexane taken as zero. (——) Cyclopropanone; (- - - -) 2,2-dimethylcyclopropanone; (····) *trans*-2,3-di-*tert*-butylcyclopropanone; (-·-·) spiro(bicyclo[2.2.1]heptane-2.1′-cyclopropan)-2′-one.

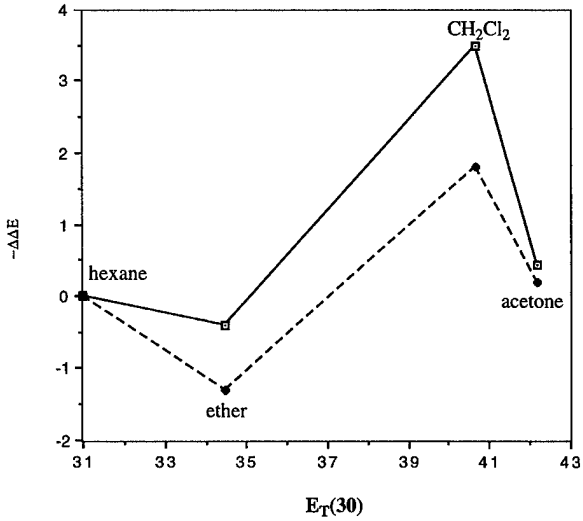


FIGURE 6. Relative barrier heights (kcal / mol) for the stereomutation process vs. solvent parameter $E_T(30)$ (Dimroth–Reichardt term) for the spiro(bicyclo[2.2.1]heptane-2.1′-cyclopropan)-2′-one system. (- - - -) Experimental values reported by Cordes and Berson (these authors used the free energy of activation) [7]. (——) Theoretical data including specific interaction in the nucleophilic solvent.

solute–solvent interactions in the stereomutation process of the **S** system in solution and understanding how nucleophilic solvents alter the barrier height for the ring opening, we studied the reaction including a single discrete molecule of the nucleophilic solvents.

The apparent contradiction between experiment and theory could be overcome taking into account a single molecule of nucleophilic solvents in the quantum mechanical treatment. Thus, to explore this aspect, specific interactions between the nitrogen or oxygen lone pairs of the nucleophilic solvents (ether and acetone) and the vulnerable carbonyl carbon of the cyclopropanone ring were considered. Following the extensive crystal structure studies of Bürgi et al. [52–54] and previous analysis by Cordes et al. [7, 55], a model in which the distance between the oxygen atom and the carbon atom of the cyclopropanone ring, O···C=O, is fixed to a value of 2.6 Å (near van der Waals contact) and O···C=O angles of 98° (a reasonable Bürgi–Dunitz angle) was selected. The minima and the TSs were also located in the presence of this additional solvent molecule with an arrangement depicted in Figure 7. The analysis of the results, presented in Figure 6, shows that this extra stabilization (2.8 and 4.0 kcal/mol for ether and acetone solvent, respectively) is more favorable in the cyclopropanone ring systems than in the TSs or oxyallyl intermediates, because the con-

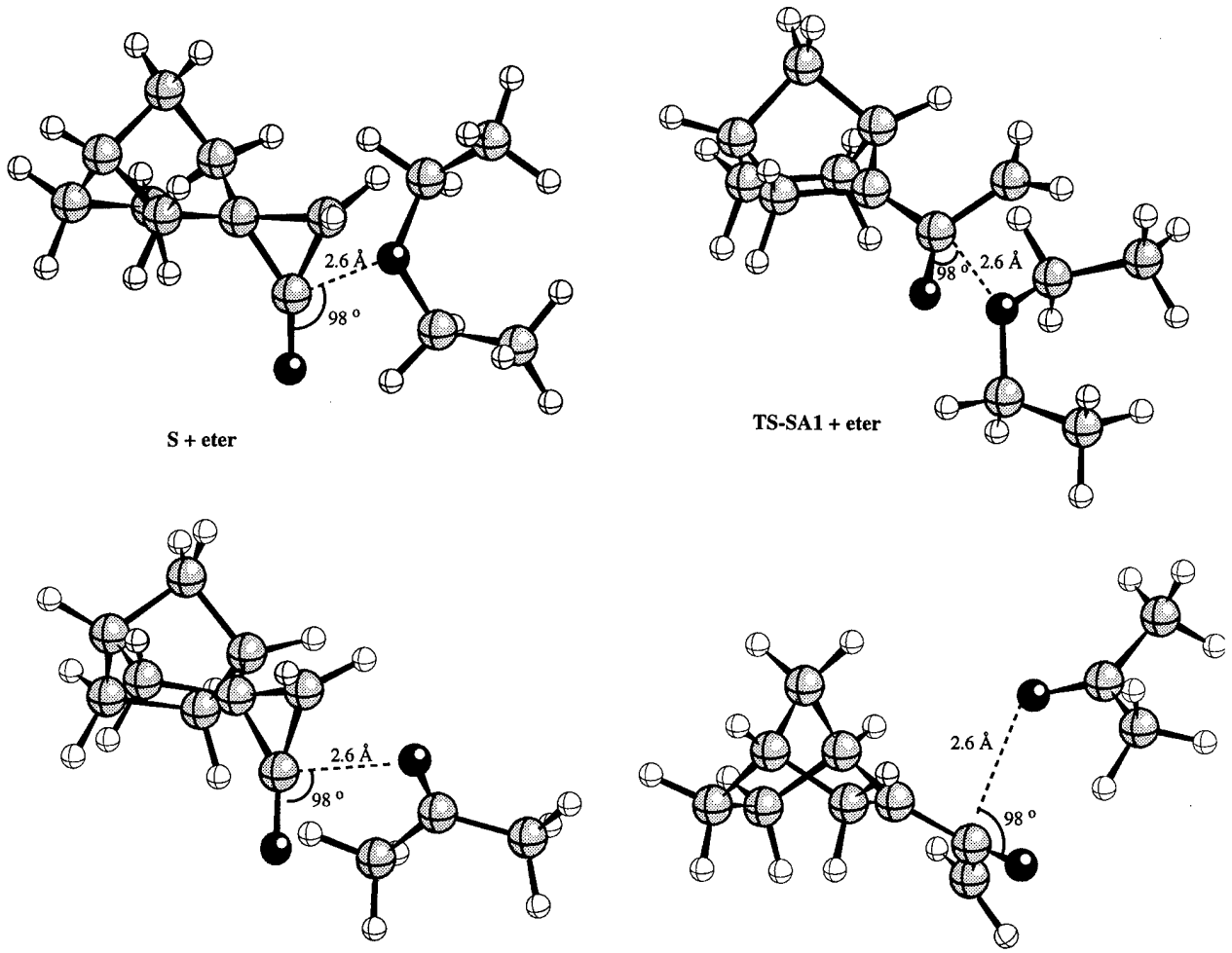


FIGURE 7. A schematic view of the optimized geometries for the spiro(bicyclo[2.2.1]heptane-2.1′-cyclopropan)-2′-one system interacting with a single molecule of the nucleophilic solvent: (a) ether; (b) acetone. The distance between the oxygen atom of the solvent and the carbonyl carbon of the cyclopropanone ring was fixed at 2.6 Å and the angle (<oxygen atom–carbonyl carbon–carbonyl oxygen) was fixed at 98°. Distances in angstroms and bond angles in degrees.

centrated charge in the ground state becomes dispersed in the TSs. This result is in good agreement with the experimental data. In contrast, the racemization of the **T** system has not an anomalous behavior in nucleophilic solvents due to the presence of *tert*-butyl groups, preventing the formation of this interaction.

Conclusions

In this work, we carried out a PM3 theoretical study of the solvent effects along the reaction profiles on the corresponding PES for the ring-opening process of the cyclopropanone, 2,2-dimethylcyclopropanone, *trans*-2,3-di-*tert*-butylcyclopropanone, and spiro(bicyclo[2.2.1]heptane-2.1'-cyclopropan)-2'-one systems. The polarizable continuum model and the inclusion of a discrete molecule of nucleophilic solvents are used to introduce solvent effects. The continuum and discrete solvent models offer a complementary view of the nature of solute–solvent interactions. The specific details of the process may change at higher levels of theory (e.g., ab initio, inclusion of correlation energy), but despite the approximate procedure of the calculations employed here, some important features were clarified. The following conclusions can be drawn from the results reported in this study:

(i) The stereomutation processes take place via an oxyallyl intermediate along a disrotatory ring-opening mechanism. The corresponding TSs and oxyallyl intermediates are structurally and energetically related.

(ii) The oxyallyl intermediates and the TSs for the four model systems are shallow minima on a rather flat region, indicating the proximity of the oxyallyls to the transition structures for the ring-opening processes.

(iii) The solvent reaction field decreases the energy barriers for the stereomutation processes and a stabilization of the oxyallyl intermediates takes place. A good agreement between the theoretical results and experimental data is found.

(iv) For the stereomutation of the spiro(bicyclo [2.2.1]heptane-2.1'-cyclopropan)-2'-one system, the inclusion of one discrete molecule of the nucleophilic solvents forming an specific interaction between the lone pairs of ether, acetone, acetonitrile, pyridine, or tetrahydrofuran molecules and the carbonyl group of the cyclopropanone ring is able to explain the experimental data. This discrete molecule plays an active role in the stereomutation process, showing that this interaction is more favorable with the carbonyl group of the cyclopropanone system than is the TS for the ring opening or the oxyallyl intermediate.

ACKNOWLEDGMENTS

This work was supported by research funds of the Ministerio de Educación, DGICYT (Project PB93-0661). We are most indebted to the Servei d'Informàtica de la Universitat Jaume I for providing us with multiple computing facilities. M. O. thanks the Ministerio de Educación y Ciencia for an FPI fellowship. R. C. thanks Silicon-Graphics for a fellowship.

References

1. D. B. Sclove, J. F. Pazos, R. L. Camp, and F. D. Greene, J. Am. Chem. Soc. **92**, 7488 (1970).
2. F. D. Greene, R. L. Camp, L. Kim, J. F. Pazos, D. B. Sclove, and C. Wilkerson, Proc. Int. Cong. Pure Appl. Chem. 23rd **2**, 325 (1971).
3. A. Liberles, A. Greenberg, and A. Lesk, J. Am. Chem. Soc. **37**, 8685 (1972).
4. M. H. J. Cordes and J. A. Berson, J. Am. Chem. Soc. **114**, 11010 (1992).
5. D. Lim, D. A. Hrovat, W. T. Borden, and W. L. Jorgensen, J. Am. Chem. Soc. **116**, 3494 (1994).
6. T. S. Sorensen and F. Sun, J. Am. Chem. Soc. **117**, 5592 (1995).
7. M. H. J. Cordes and J. A. Berson, J. Am. Chem. Soc. **118**, 6241 (1996).
8. N. J. Turro, Acc. Chem. Res. **2**, 25 (1969).
9. T. H. Chan and B. S. Ong, Tetrahedron **36**, 2269 (1980).
10. P. J. Chenier, J. Chem. Ed. **55**, 286 (1978).
11. L. J, Schadd, B. A. Hess, and R. Zahradnik, J. Org. Chem. **46**, 1991 (1981).
12. J. V. Ortiz, J. Org. Chem. **48**, 4744 (1983).
13. P. M. Lahti, A. R. Rossi, and J. A. Berson, J. Am. Chem. Soc. **107**, 2273 (1985).
14. Y. Osamura, W. T. Borden, and K. Morokuma, J. Am. Chem. Soc. **1984**, 5112 (1984).
15. M. B. Coolidge, K. Yamashita, K. Morokuma, and W. T. Borden, J. Am. Chem. Soc. **112**, 1751 (1990).
16. A. S. Ichimura, P. M. Lahti, and A. R. Matlin, J. Am. Chem. Soc. **112**, 2868 (1990).
17. R. L. Camp and F. D. Greene, J. Am. Chem. Soc. **90**, 7349 (1968).

18. H. H. Wasserman, D. R. Berdahl, and T.-J. Lu, *The Chemistry of the Cyclopropyl Group* (Wiley, New York, 1987).
19. D. H. Hunter, J. B. Stothers, and E. W. Warnhoff, in *Rearrangements in Ground and Excited States*, Vol. 1, P. de Mayo, Ed. (Academic Press, New York, 1980), pp. 391–470.
20. A. Baretta and B. Waegell, React. Intermed. **2**, 527 (1982).
21. J. March, *Advanced Organic Chemistry* (Wiley, New York, 1992).
22. V. Moliner, R. Castillo, V. S. Safont, M. Oliva, S. Bohm, I. Tuñón, and J. Andrés, J. Am. Chem. Soc. **119**, 1941 (1997).
23. J. Andrés, S. Bohm, V. Moliner, E. Silla, and I. Tuñón, J. Phys. Chem. **98**, 6955 (1994).
24. I. Tuñón, E. Silla, and J. Bertrán, J. Chem. Soc., Faraday Trans. **90**, 1757 (1994).
25. L. R. Domingo, M. T. Picher, J. Andrés, V. Moliner, and V. S. Safont, Tetrahedron **52**, 10693 (1996).
26. T. Tomasi and M. Persico, Chem. Rev. **94**, 2027 (1994).
27. C. J. Cramer and D. G. Truhlar, in *Solvent Effects and Chemical Reactivity*, O. Tapia and J. Bertran, Eds. (Kluwer, Dordrecht, 1996), pp. 1–80.
28. O. Tapia, J. Andrés, and F. L. M. G. Stamato, in *Solvent Effects and Chemical Reactivity*, O. Tapia and J. Bertran, Eds. (Kluwer, Dordrecht, 1996), pp. 283–361.
29. O. Tapia and O. Goscinski, Mol. Phys. **29**, 1653 (1975).
30. O. Tapia, in *Theoretical Models of Chemical Bonding*, Z. B. Maksic, Ed. (Springer-Verlag, Berlin, 1992), p. 435.
31. 31. J. P. Stewart, *J. Comp. Chem.* **10**, 209 (1989).
32. M. J. Frisch, G. W. Trucks, H. B. Schlegel, P. M. W. Gill, B. G. Johnson, M. A. Robb, J. R. Cheeseman, T. Keith, G. A. Petersson, J. A. Montgomery, K. Raghavachari, M. A. Al-Laham, V. G. Zakrzewski, J. V. Ortiz, J. B. Foresman, J. Cioslowski, B. B. Stefanov, A. Nanayakkara, M. Challacombe, C. Y. Peng, P. Y. Ayala, W. Chen, M. W. Wong, J. L. Andres, E. S. Replogle, R. Gomperts, R. L. Martin, D. J. Fox, J. S. Binkley, D. J. Defrees, J. Baker, J. P. Stewart, M. Head-Gordon, C. Gonzalez, and J. A. Pople, *Gaussian 94* (Gaussian, Inc., Pittsburgh, PA, 1994).
33. O. Tapia and J. Andres, Chem. Phys. Lett. **109**, 471 (1984).
34. J. Andrés, V. Moliner, and V. S. Safont, J. Chem. Soc., Faraday Trans. **90**, 1703 (1994).
35. O. Tapia, J. Andrés, and V. S. Safont, J. Chem. Soc., Faraday Trans. **90**, 2365 (1994).
36. J. Baker, *J. Comput. Chem.* **7**, 385 (1986).
37. J. Baker, *J. Comput. Chem.* **8**, 563 (1987).
38. K. Fukui, *J. Phys. Chem.* **74**, 4161 (1970).
39. C. Gonzalez and H. B. Schlegel, J. Phys. Chem. **94**, 5523 (1990).
40. C. Gonzalez and H. B. Schlegel, J. Chem. Phys. **95**, 5853 (1991).
41. H. B. Schlegel, J. Comp. Chem. **3**, 214 (1982).
42. H. B. Schlegel, J. Chem. Phys. **77**, 3676 (1982).
43. J. W. J. McIver, Acc. Chem. Res. **7**, 72 (1974).
44. A. Klamt and G. Schüürmann, J. Chem. Phys. **2**, 799 (1993).
45. J. J. P. Stewart, MOPAC93 (Fujitsu Corp. Ltd., Tokyo).
46. R. Nelson and L. Pierce, J. Mol. Spectrosc. **18**, 344 (1965).
47. R. S. Mulliken, J. Chem. Phys. **23**, 1833 (1955).
48. E. Kosower, *Physical Organic Chemistry* (Wiley, New York, 1968), Chap. 2.6.
49. C. Reichardt, *Solvents and Solvent Effects in Organic Chemistry* (VCH, Wienheim, 1988).
50. C. Reichardt, Justus Liebigs Ann. Chem. **752**, 64 (1971).
51. C. Reichardt and K. Dimroth, Fortschr. Chem. Forsch. **11**, 1 (1968).
52. H. B. Bürgi, J. D. Dunitz, and E. Shefter, J. Am. Chem. Soc. **95**, 5065 (1973).
53. H. B. Bürgi, J. D. Dunitz, and E. Shefter, Acta Crystallogr. B **30**, 1517 (1974).
54. H. B. Bürgi and J. D. Dunitz, Acc. Chem. Res. **16**, 153 (1983).
55. M. H. J. Cordes, S. de Gala, and J. A. Berson, J. Am. Chem. Soc. **116**, 11161 (1994).

Ab Initio Studies on the Ziegler–Natta Polymerization Mechanisms of Ethylene and Propylene. Role of Cocatalysis and Stereoregulation

SHOGO SAKAI

Department of Information Systems Engineering, Faculty of Engineering, Osaka Sangyo University, Daito 574 Japan

Received 2 March 1997; revised 22 April 1997; accepted 22 April 1997

ABSTRACT: As a model of olefin polymerization for a heterogeneous Ziegler–Natta catalyst, the mechanisms of the insertion of ethylene and propylene into R-Ti-$(Cl_2AlH_2)_2^+$ (R = CH_3, C_3H_7) are studied by ab initio self-consistent field (SCF) methods and many-body perturbation theory. The structures of the reactant, the intermediate, the transition state, and the product are optimized by the Hartree–Fock molecular orbital calculation level. The reactions are classified into two steps: the first forms of olefin–Ti π complex, and the second step is the carbon–carbon bond formation through the pull–push mechanisms. The cocatalysis play a role in facilitating the pull–push mechanism with the Al–Cl bonds alternation. For the insertion reaction of propylene, the four-type conformations for attacking of propylene (two primary forms: methyl-substituted carbon attacks to the carbon side of Ti–C bond; two secondary forms: methyl-substituted carbon attack to Ti atom) are studied. For the complex formation, the secondary forms are more stable in energy than the primary forms. For the transition state, the primary forms are more stable in energy than the secondary forms. © 1997 John Wiley & Sons, Inc. Int J Quant Chem **65**: 739–747, 1997

Introduction

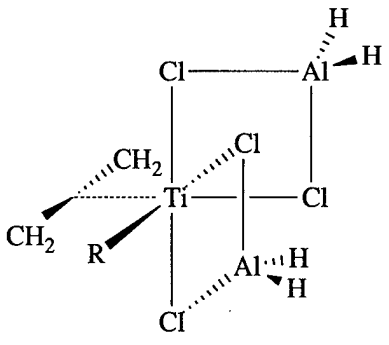
It is widely known that Ziegler–Natta catalysis polymerization is one of the most important industrial polymerization reaction, and many experimental studies have been reported [1–10]. The manufacture for Ziegler–Natta type polymerization is based on heterogeneous catalyst which have become highly selective and efficient. Classical Ziegler catalysts are heterogeneous with the polymerization taking place on dislocations and edges of $TiCl_4$ crystals. Heterogeneous titanium-based Ziegler catalysts are more versatile; they are able to polymerize propene with a very high degree of stereoselectivity and catalyze the copolymerization of ethylene with higher alk-1-enes such as hex-1-

Contract grant sponsor: Sangyo Institute of Osaka Sangyo University.

© 1997 John Wiley & Sons, Inc.
CCC 0020-7608 / 97 / 050739-09

ene, important for the production of flexible, nonbrittle polymers for use as films and in packaging. Although there are successful processes which give rise to a wide range of polymer products, the diversity of active sites in heterogeneous catalysts leads to an uneven degree of comonomer incorporation, with a high incorporation rate in short chains, and little incorporation in the high-molecular-weight fraction, a drawback where metallocenes offer particular promise. In 1959 Breslow and Newburg [11] suggested for their $[TiCl_2Cp_2]AlClEt_2$ system that the transition metal is first alkylated and then forms a halide-bridged binuclear complex which is capable of reaction with ethylene. In spectroscopic study of the formation of ion pair in Cp_2TiCl_2 and $MeAlCl_2$ system, both groups of Long [12] and Eisch [9] did not observe the ions ($Cp_2TiCH_3^+$ and $AlCl_4^-$). The possibility that Cp_2TiCl_2:Cl_2AlCH_3 might be the active catalysts is ruled out by the ultraviolet (UV) studied of Long [12] and the kinetic studies of Fink [13]. Eisch and co-workers [14] by H, C, and Al nuclear magnetic resonance (NMR) spectroscopy, also concluded that the ion pair $[(Cp_2TiCH_2SiMe_3)^+—AlCl_4^-$: included Ti–Cl–Al bridged bond] in $Cp_2Ti(Cl)CH_2SiMe_3$ and $AlCl_3$ system are effective catalysts for the polymerization of ethylene.

For the generic mechanism of olefin insertion of the Cossee mechanism [10] has been accepted widely as the most plausible. The first step is olefin coordination to a vacant site of Ti atom. In the second step olefin is inserted into the Ti–C bond through a four-membered cyclic transition state. Many theoretical studies of Ziegler–Zatta catalysis polymerization have been reported. Most of these studies discuss the reaction mechanism in Ziegler–Natta polymerization based on Cossee's model. Cossee's model was treated with semiempirical self-consistent field (SCF) molecular orbital (MO) methods by Armstrong and co-workers [15] and by Novaro and co-workers [16]. Their results suggested that the Ziegler–Natta mechanism might be explained by a concerted motion of the olefin and alkyl group that would bring about a transition from octahedral coordination to a trigonal-bipyramidal coordination for the Ti atom. This view was also confirmed with the ab initio SCF MO method by Clementi and co-workers [17, 18]. Balazs and Johnson [19] demonstrated the reaction $CH_3TiCl_4 + C_2H_4$ by using a SCF-X_α-SW MO method. The interaction between C_2H_4 and $CH_3TiCl_2^+$ was examined by ab initio MO methods [20, 21] and by density functional methods [22]. In the more realistic systems of homogeneous catalysis (including Cp), hydrozirconation of ethylene and acetylene by $Cp_2Zr(H)Cl$ and (or) $Cp_2TiCH_3^+$ was studied by ab initio MO methods [23, 24]. The insertions of ethylene into $Cp_2ZrCH_3^+$ and $(SiH_2Cp_2)ZrCH_3^+$ were also treated by ab initio MO method [25] and by density functional methods [26–28]. The stereotacticity of zirconium metallocene Ziegler–Natta propylene polymerization catalysis was studied using a combination of ab initio MO method and empirical force field molecular mechanics techniques [29–34]. However, above theoretical studies did not reported for the mechanism of cocatalysis of Ziegler–Natta polymerization. The present author has proposed the fundamental carbon–carbon bond formation mechanisms with a simple model of Cossee type in a previous study [35]. The proposed mechanisms were on the basis of electronic pull–push process: the electrons in the Ti–R bond move to the region of new carbon–carbon bond formation, and π electrons of ethylene move to the region of new Ti–carbon bond formation. These mechanisms were the same as those of alumination reaction of olefin as shown in our previous studies [36, 37]. In the study [35], the role of cocatalysis for the Ziegler–Natta type reaction was also reported on the basis of the classical model ($CH_3TiCl_4AlH_2 + H_2C=CH_2$). For this model, it was clarified that the cocatalysis play a role in facilitating the pull–push mechanism through the Al–Cl bond alternation. Although we clarified entirely the role of cocatalysis for the model, we could not explain the stereotacticity for polymerization on the basis of the model. Consequently, for the explanation of the role of cocatalysis and the stereoreguration for the heterogeneous Ziegler–Natta polymerization, the present author proposes a new model as the following:



This model is more realistic compared with the previous one. For our model of olefin polymerization, a heterogeneous as well as homogeneous catalysis has been adopted.

In this study, two subjects are reported. The first is the role of cocatalysis for olefin insertion mechanism. The second is the stereoregulation of propylene polymerization on the basis of our model.

Method of Calculation

The basis sets used for Ti atom through the study were 3-21G of Dobbs and Hehre [38]. For C, H, Cl, and Al atoms the standard 3-21G basis functions [39, 40] were used. The set is denoted at the following sections as BS-I. For better energies the 6-31G(d) basis functions [41, 42] for carbon atom and the $(8s/4p/3d)$ contracted functions [43] for Ti atom were used, denoted as BS-II. All equilibrium- and transition-state geometries were determined by the use of analytically calculated energy gradients with Hartree–Fock (HF) wave functions. The stationary points were identified as the equilibrium or the saddle point by examining the calculated normal vibrational frequencies. The force constant matrix and thereby the vibrational frequencies were calculated by analytical second-derivative procedures [44, 45], and zero-point vibrational energy corrections were obtained at this level. Additional calculations were performed to obtain improved energy comparisons—the calculations at the HF-optimized structures with electron correlation incorporated through the second- and third-order Møller–Plesset (MP2 and MP3) perturbation theory [46–50].

Ab initio molecular orbital calculations were carried out by using the GAUSSIAN94 program [51].

Results and Discussion

INSERTION OF ETHYLENE INTO $H_3CTi(Cl_2AlH_2)_2^+$ AND ROLE OF COCATALYSIS

The stationary point geometries of reactant, complex, transition state, and product for $(Cl_2AlH_2)_2TiCH_3^+ + H_2C{=}CH_2$ reaction are illustrated in Figure 1. For all stationary points, Ti, Cl^c, Cl^d, and three carbon atoms are almost in the same plane. The stationary point geometry of reactant has a C_s symmetry. The C_s symmetry plane bisects each angle of Cl^a–Ti–Cl^c and Cl^b–Ti–Cl^d, and is in the plane of Ti–C–H^a. For the reactant conformation, there are two possible spaces for approaching of olefin: Cl^a–Ti–C–Cl^c and Cl^b–Ti–C–Cl^d spaces. The space of Cl^a–Ti–C–Cl^c is more wide than the space of Cl^b–Ti–C–Cl^d from the comparison of the angels of $Cl^cTiC(H_3)$ and $Cl^dTiC(H_3)$. The Cl^c–Ti (and Cl^a–Ti) bond length is a little shorter than the Cl^d–Ti (and Cl^b–Ti) bond length. The difference between Cl^c–Ti and Cl^d–Ti bond lengths, however, is only 0.019 Å in length. Consequently, the space of Cl^a–Ti–C–Cl^c is favorable for the approaching of olefin.

For the π complex, C^β carbon in ethylene interacts stronger with the Ti atom than the C^α carbon, because of the repulsion of C^α and Cl^c atom (or Ti–Cl^c bond). In the catalysis part, the bond between Ti atom and Cl^c becomes longer by 0.321 Å in length than that in the reactant. Because the Cl^c atom moves to the reverse side of methyl-Ti bond for Ti atom during the complex formation. The longer Ti–Cl^c leads to be the shorter Cl^c–Al bond, the longer Cl^b–Al bond, and the shorter Ti–Cl^b bond in comparison with those of the reactant. Accordingly, this part (Ti, Cl^c, Al, and Cl^b) is a complex between Cl^c–AlH_2 and Ti–Cl^b. On the other hand, the variation of Ti–Cl^d bond for the π complex formation is small (only 0.03 Å in length). As a result, the one side of cocatalysis is active for the π-complex formation and the other is not active.

For the transition state, the Ti–Cl^c bond becomes shorter in length than that of the π complex. This behavior facilitates the bond breaking of Ti–$C(H_3)$. Because the insertion mechanism is the pull–push as shown in our previous work [35, 36], the electrons of Ti–$C(H_3)$ bond move to the region of new C–C bond formation and original π electrons of ethylene part move to the region of the new C–Ti bond formation. Accordingly, the approach of Cl^c to Ti atom facilitates the moving of the electrons of Ti–$C(H_3)$ bond region. On the other side, the Ti–Cl^d bond length becomes longer than that of the π complex. This behavior facilitates moving the π electrons of the ethylene part easily to the new C–Ti bond formation region (the reverse side of Ti–Cl^d bond for Ti atom).

For the product, polymer grows up for the more wide space of Cl–Ti–Cl. The mechanism of cocatalysis is shown in Figure 2. From the figure, the bonds alternation for Cl–Al and Ti–Cl bond occurs

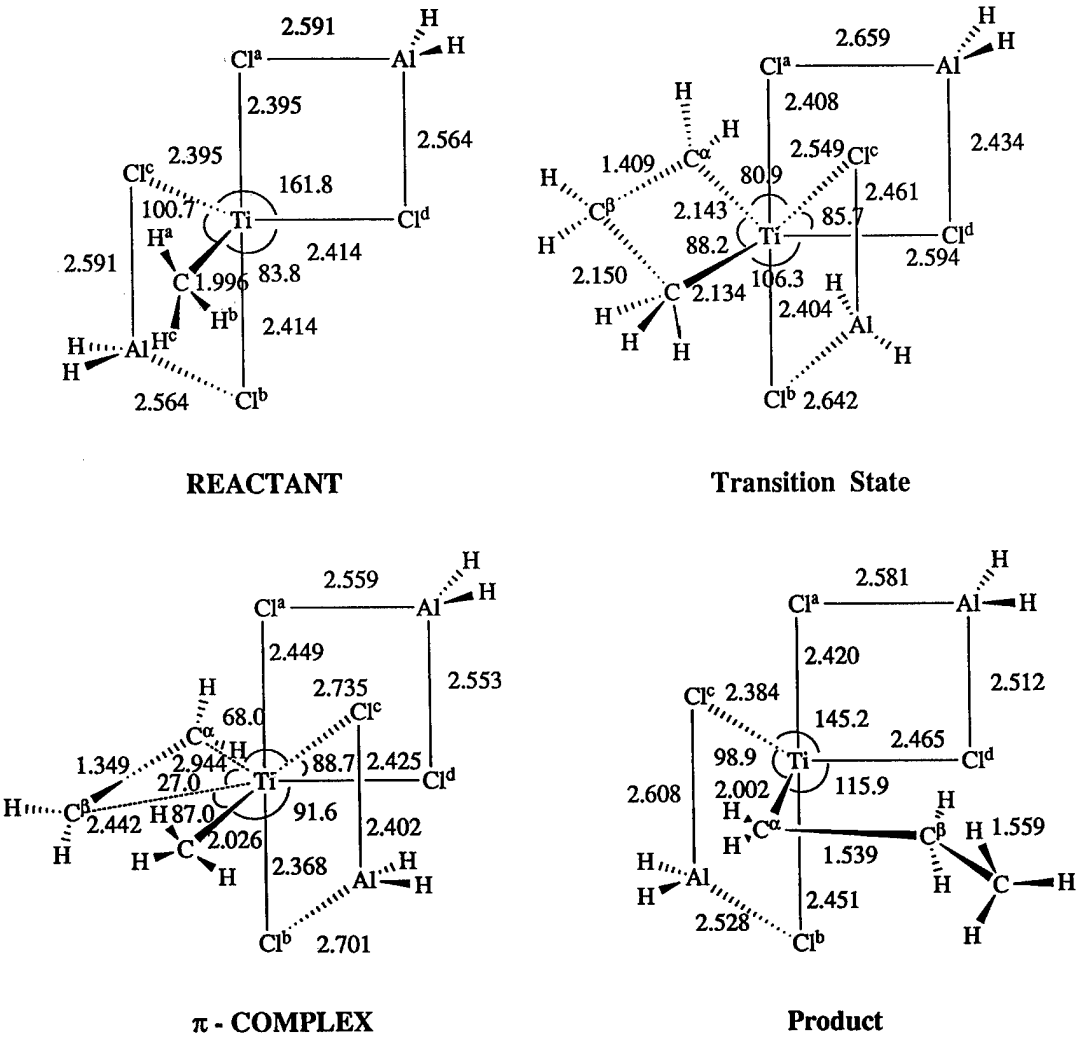


FIGURE 1. HF/BS-I optimized geometries of reactant, π complex, transition state, and product for reaction $H_3CTi(Cl_2AlH_2)_2^+ + H_2C{=}CH_2$. Distances and angles are in angstrom and degrees, respectively.

during the one process of polymerization. It is also considered that this is the reaction of olefin insertion into $H_3C{-}TiCl_2^+$ plus cocatalysis $(ClAlH_2)_2$. Many theoretical works [22, 30] treated the insertion of ethylene into $H_3C{-}TiCl_2^+$ as a model of the homogeneous catalysis of $[Cp_2TiCH_3]^+$. The potential energy surface of $H_3CTiCl_2^+$ ethylene is different from that of our system. For $Cl_2TiCH_3^+ +$ ethylene, the complexation energy at the π complex is over 40 kcal/mol. On the other hand, the complexation energy of our system is about 10 kcal/mol. The large difference of the complexation energies comes from the distribution of the positive charge by the cocatalysis. The influence of the complexation energy on the charge distribution can be seen for the other homogeneous systems. The π complexation energy for $Cp_2TiCH_3^+ +$ ethylene was proposed by Wess and co-workers [24]: -5.3 kcal/mol for the HF calculation and -23.7 kcal/mol for the MP2 calculation level. Yoshida and co-workers [25] proposed the π complexation energy for $H_2SiCp_2TiCH_3^+ +$ ethylene by various methods: -13.0 kcal/mol for the HF calculation, -28.6 kcal/mol for the MP2 calculation, -20.9 kcal/mol for the MP3 calculation, and -21.9 kcal/mol for QCISD calculation levels. For these homogeneous systems, the π complexation energies by the HF calculation are almost the same to

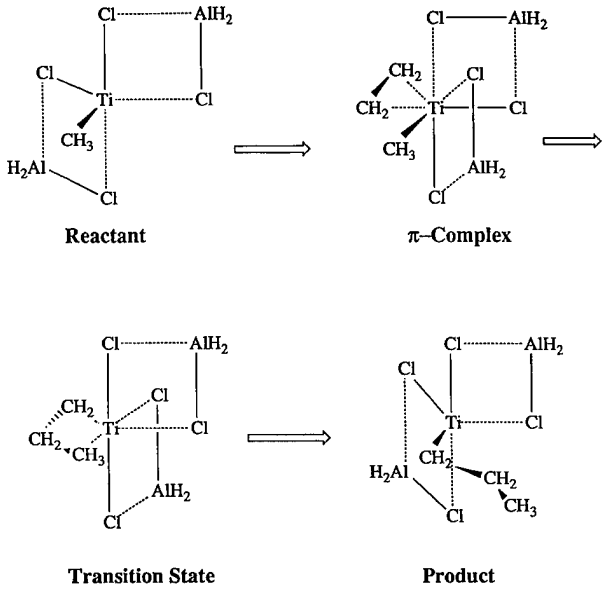


FIGURE 1. Continued.

Chart 1

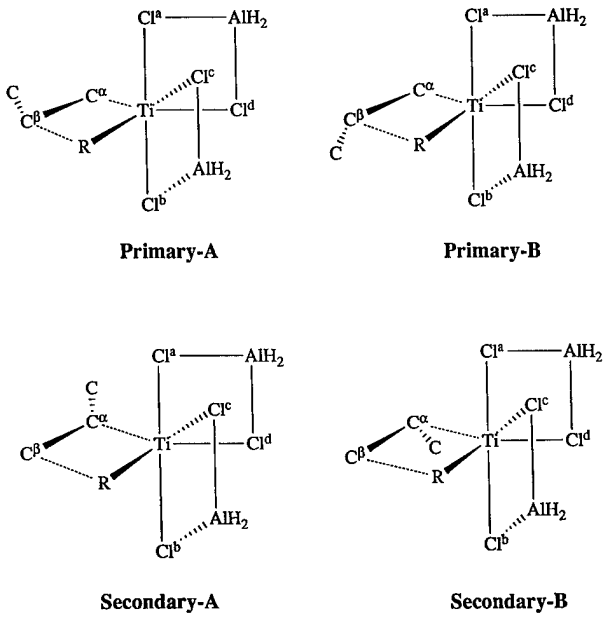


FIGURE 2. Mechanism of olefin insertion into Ti–CH_3 bond of $H_3CTi(Cl_2AlH_2)_2^+$.

the value for our system. Yoshida and co-workers pointed out that the calculation values for their system are far from convergence in the perturbation series. Accordingly the difference between the calculated π complexation energies by the HF and by the MP2 levels is quite large (15.6 kcal/mol) for the homogeneous system. For our system, the difference of the π complexation energies by the HF and by the MP2 calculations is only 4.2 kcal/mol. The ethylene binding energy for $H_2SiCp_2TiCH_3^+$ is 21.9 kcal/mol (best value), and is the middle value of those for $Cl_2TiCH_3^+$ and for our system.

For the activation energy at the transition state —the energy is given relative to the π complex of [Ti]–CH_3^+ and ethylene—13.8 kcal/mol for the HF calculation and 4.3 kcal/mol for the MP2 calculation level for $Cl_2TiCH_3^+$ system were proposed [30]. For the $H_2SiCp_2TiCH_3^+$ system [25], 14.3 kcal/mol for the HF calculation, 1.3 kcal/mol for the MP2 calculation, 10.9 kcal/mol for the MP3 calculation, and 7.1 kcal/mol for the RQCISD calculation levels were proposed. The activation energies from the π complex for our system is 9.3 kcal/mol for the HF calculation, 0 kcal/mol for the MP2 calculation, and 3 kcal/mol for the MP3 calculation levels. The activation energy barrier height for our system is about 7–2 kcal/mol lower than those for the other homogeneous systems. It is considered that this energy difference comes from the energy reduced by the cocatalysis. This low-energy barrier corresponds to the fact that the reaction of heterogeneous catalysis is more active than that of homogeneous catalysis.

ISOTACTIC STEREOREGULATION IN PROPYLENE POLYMERIZATION

For evaluation of regio- and stereoregulatory capabilities, we have to compare the four possible conformations for π complex and transition state shown in Chart 1 the differences in the geometry and the total energy. The four π complexes and four transition-state geometries, primary A, primary B, secondary A, and secondary B shown in Chart 1, for propylene insertion into $H_3C—Ti(Cl_2AlH_2)_2^+$ have been optimized by the HF/BS-I method. The some geometry parameters and the relative energies, relative to primary A for all the case, are summarized in Table II.

For π complex, the difference of the distances of Ti–C (C^α and C^β) bonds are drastic for the conformations of the primary and secondary. This comes from the π-electron distribution of propylene. Namely the unsubstituted carbon in propylene has more π-electron density than methyl-substituted carbon. It is widely known that the π complex is formed with the interaction between the empty

TABLE I
Relative energies from the reactant for ethylene polymerization and propylene polymerization (kcal / mol).

Method	HF / BS-I	MP2 / BS-I	HF / BS-II	MP2 / BS-II	MP3 / BS-II
Ethylene $+H_3CTi(Cl_2AlH_2)_2$					
Reactant	0.0	0.0	0.0	0.0	0.0
π Complex	−13.1	−14.4	−8.7	−12.9	−11.3
Transition state	−2.2	−12.1	0.6	−13.7	−8.3
Product	−31.6	−31.6	−30.4	−34.5	−34.3
Propylene $+H_3CTi(Cl_2AlH_2)_2$					
Reactant	0.0	0.0	0.0	0.0	
π Complex					
Primary A	−18.5	−20.2	−13.6	−19.3	
Primary B	−18.9	−19.9	−14.0	−19.0	
Secondary A	−20.9	−20.4	−16.3	−19.5	
Secondary B	−20.6	−20.5	−15.7	−19.5	
Transition state					
Primary A	−5.9	−16.0	−1.9	−18.0	
Primary B	−6.3	−16.6	−2.0	−18.1	
Secondary A	−3.0	−14.0	1.2	−14.1	
Secondary B	−2.8	−14.0	1.9	−13.9	

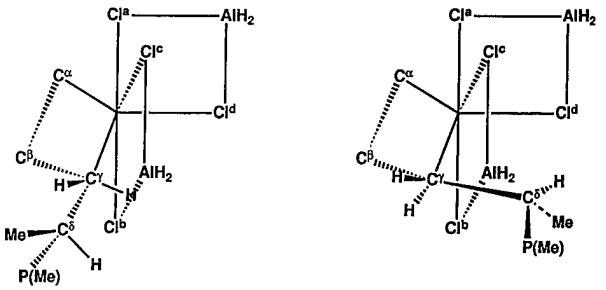
orbital of transition metal and π orbital of olefin. Consequently, the unsubstituted carbon interacts stronger with Ti atom than the methyl-substituted carbon. The differences between the total energies of the primary and secondary conformations for the HF and MP2 calculation levels are 2 and 0.2–0.3 kcal/mol, respectively. The conformations of the secondary are a little favorable in energy to compare with those of the primary. The energy difference, however, is very small, and the stereo-regulation of the product is not decided probably by the formation of the π complex. The conformation of the secondary is similar to that of the ethylene insertion. The energy difference between A and B for both of the primary and secondary is little (under 1 kcal/mol). The π complexation energy for propylene is about 7–8 kcal/mol more stable than that for the ethylene. The difference of these complexation energies for both systems comes from the π-electron distribution with methyl-substitution group. As the results, the π complexation energy have more influence for the electronic part of the methyl-substitution group than that for the steric part.

TABLE II
Ti – C bond distance and the relative energy from primary A geometry for propylene polymerization.

	Bond distance (Å)					Relative energy (kcal / mol)			
	$Ti-C^{\alpha}$	$Ti-C^{\beta}$	$Ti-C(H_3)$	$C^{\alpha}-C^{\beta}$	$C^{\beta}-C(H_3)$	HF / BS-I	MP2 / BS-I	HF / BS-II	MP2 / BS-II
Complex									
Primary A	2.355	3.001	2.034	1.361	3.055	0.0	0.0	0.0	0.0
Primary B	2.348	3.029	2.029	1.361	3.213	−0.38	0.27	−0.40	0.30
Secondary A	3.008	2.325	2.026	1.369	3.047	−2.47	−0.19	−2.71	−0.28
Secondary B	3.003	2.327	2.025	1.367	3.053	−2.10	−0.27	−2.17	−0.20
Transition state									
Primary A	2.092	2.540	2.139	1.432	2.108	0.0	0.0	0.0	0.0
Primary B	2.092	2.537	2.141	1.431	2.105	−0.37	−0.61	−0.12	−0.11
Secondary A	2.195	2.512	2.121	1.406	2.172	2.89	1.92	3.08	3.96
Secondary B	2.199	2.511	2.116	1.406	2.174	3.14	2.00	3.79	4.14

For the transition state, the Ti–C^{α} bond lengths of the primary conformations are about 0.1 Å shorter than those of the secondary. From the comparison of the geometry parameters between the primary and secondary conformations, the primary conformations are earlier transition states than the secondary conformations. The conformations of the primary are about 3–4 kcal/mol more stable in energy than those of the secondary at both calculation levels of the HF and MP2. The difference of activation energy barrier heights between the primary and the secondary conformations comes from the π electrons distribution with methyl-substituted group. As described above, the unsubstituted carbon in propylene has much π-electron density. Consequently, the reaction path of the secondary conformation is unfavorable for the pull–push mechanism; the electrons in the Ti-R bond move to the region of new carbon–carbon bond formation and the electrons of π bond move to the region of new Ti–C bond formation. Namely the electron distribution of propylene for the secondary conformations has reverse effects for the electron movement along the reaction path. The energy differences between A and B for both primary and secondary conformations are also under 1 kcal/mol. The energy difference between primary A and primary B should determine isotactic stereoregulation for the product. From the small energy difference, it is concluded that the isotacticity is not decided for the initiation step of polymerization. This conclusion corresponds to the results [34] for propylene insertion to transition metal (Ti, Zr, and Hf)–C bond for homogeneous catalysis systems by ab initio MO–MM (molecular mechanics) method. They concluded the stereoselectivity is decided after the first propylene insertion from the results of the MM calculations. The stereoregulation via direct ligand–olefin interaction for their catalyst is not significant. Accordingly the stereoselectivity is decided by steric energies between monomer and polymer. However, their calculation is the MM and included only steric effects (not electronic effects).

In order to study the steric and electronic effects of polymer by ab initio molecular orbital calculation level, the transition states for the second step, as shown in Figure 3, were calculated. In Figure 3, conformation I indicates the polymer part $C^{\delta}HM_2$, spreads to the outside of the space of $Cl^bTiCl^dC^{\gamma}$. Conformation II indicates the polymer part spreads to the inside of the space of $Cl^bTiCl^dC^{\gamma}$. For these



Conformation (I) **Conformation (II)**

FIGURE 3. Conformations of polymer part at the transition state for reaction of $(CH_3)_2CHCH_2Ti(Cl_2AlH_2)_2^+$ and propylene.

two conformations of polymer part, the transition states of eight types (primary A-I, A-II, B-I, and B-II, and secondary A-I, A-II, B-I, and B-II) were calculated. These eight conformations are real transition states and have one negative eigenvalue for their force constant matrix. The relative energies for these eight transition state are listed in Table III. The energy difference between the primary A-I and A-II is only 0.7 kcal/mol at the MP2 calculation. The energy of the primary B-II is almost the same to that of the primary A-I. However, the primary B-I is about 5 kcal/mol higher in energy than the primary A-I. The value of 5 kcal/mol indicates the static repulsion energy between the methyl groups of propylene and polymer part. The primary B-II is about 5 kcal/mol more stable in energy than the primary B-I. If the space of Cl^bTiCl^d is crowded with other catalysis (maybe

TABLE III
Relative energy from primary A-I conformation for the second step of propylene polymerization.

	Relative energy (kcal / mol)	
	HF / BS-I	MP2 / BS-I
Transition state		
Primary A-I	0.0	0.0
Primary A-II	0.88	0.69
Primary B-I	5.27	4.61
Primary B-II	0.51	−0.23
Secondary A-I	1.63	3.75
Secondary A-II	2.32	4.26
Secondary B-I	2.28	4.01
Secondary B-II	1.97	3.49

this assumption indicates a realistic heterogeneous catalysis), the conformation II types are unstable in the energy. All secondary types are about 4 kcal/mol more unstable in energy than the primary A-I. This reason comes from the electronic distribution of propylene as mentioned above. The insertion is the pull–push mechanism, and π electrons of monomer have to move new Ti-C bond region through the transition state. Consequently, the regioselectivity of reaction is controlled by the static repulsion between the methyl groups of monomer and of the first unit in polymer for the primary types, and is controlled by the electronic effects (the π electrons distribution of monomer) for the secondary types. As a result, the reaction path of the primary A-I type leads to the isotactic sequence.

Conclusions

The mechanisms of the insertion of ethylene and propylene into R-Ti$(Cl_2AlH_2)_2^+$ (R = CH_3 and C_3H_7) were studied by ab initio MO methods. Our treated catalytic system is one kind of a edge model of $TiCl_4$ crystals for heterogeneous Ziegler–Natta catalysts. The reactions are classified into two steps: the formation of olefin–Ti π complex and olefin insertion through the pull–push mechanism. For the π-complex formation step, one side of cocatalysis works actively to weak the Ti–CH_3 bond. For the olefin insertion step, the cocatalysis works to break the old Ti–CH_3 bond, and the other side of cocatalysis works to form a new Ti–C bond. As the results, the cocatalysis play a role in facilitating the pull–push mechanism through the Al–Cl bonds alternation.

For the initial step of the propylene polymerization, four types of conformation were studied for each π complex and for each transition state: primary A, primary B, secondary A, and secondary B. For the π-complex formation, the secondary conformations are a little favorable in energy to compare with those of the primary. The energy difference, however, is only 0.2–0.3 kcal/mol by the MP2 calculation and about 2 kcal/mol by the HF calculation level. Accordingly, the π complex does not decide probably the stereoregulation of the product. For the transition state, the primary conformations are favorable by about 4 kcal/mol in energy to compare with those of the secondary. The energy difference between the primary conformations A and B is only 0.3 kcal/mol by the MP2 level. Therefore, the isotacticity is not decided at the initiation step of polymerization.

The transition states for the second step of polymerization were calculated by the HF/BS-I calculation level. All secondary types of the transition states are about 4 kcal/mol higher in energy than the primary A-I. Conformation II for the primary types has almost the same energy to the primary A-I. However, if the space of $Cl^bTiCl^dC^\gamma$ is crowded with other catalysis, all conformations of type II are unstable in energy. Accordingly, the transition state of the primary B is about 5 kcal/mol higher than that of the primary A. The most stable structure, the primary A-I, leads to the isotactic type product.

As mentioned, the role of the cocatalysis for the pull–push mechanism and the isotacticity for propylene polymerization could be shown on the basis of our model of the Ziegler–Natta type catalysis. It is considered that the role of cocatlysis and the mechanisms of the isotacticity polymerization can be extended to the case of the homogeneous catalysis system.

ACKNOWLEDGMENT

The present research is supported in part by Grant-Aid for Scientific Research on Priority Area "Theory of Chemical Reactions" from the Ministry of Education, Science and Culture. This work is also supported in part by the Grant-Aid for Special Research from the Sangyo Institute of Osaka Sangyo University, for which I express my gratitude. The computer time was made available by the Computer Center of the Institute for Molecular Science (IMS), and all of them are grateful acknowledged.

References

1. K. Ziegler, E. Holzkamp, H. Breil, and H. Martin Angew. Chem. **67**, 541 (1955).
2. T. Natta, Macromol. Chem. **16**, 213 (1955).
3. K. J. Ivin, J. J. Rooney, and C. D. Stewart, J. Chem. Soc., Commun. 604 (1978).
4. T. J. Katz and S. J. Lee, J. Am. Chem. Soc. **102**, 422 (1980).
5. J. S. Uppal, D. E. Johnson, and R. H. Staley, J. Am. Chem. Soc. **103**, 508 (1981).
6. J. Soto, M. L. Steigerwald, and R. H. Grubbs, J. Am. Chem. Soc. **104**, 4479 (1982).
7. T. C. Clarke and C. S. Yannomic, J. Am. Chem. Soc. **105**, 7787 (1983).

8. L. Clawson, J. Soto, S. L. Buchwald, M. L. Steigerwald, and R. H. Grubbs, J. Am. Chem. Soc. **107**, 3377 (1985).
9. J. J. Eisch, A. M. Piotrowski, S. K. Brownstein, E. J. Gabe, and F. L. Lee, J. Am. Chem. Soc. **107**, 7219 (1985).
10. P. J. Cossee, J. Catal. 80 (1964).
11. D. S. Breslow and N. R. Newburg, J. Am. Chem. Soc. **81**, 81 (1959).
12. W. P. Long, J. Am. Chem. Soc. **81**, 5312 (1959).
13. G. Fink and W. Zoller, Makromol. Chem. **182**, 2365 (1981).
14. J. Eisch, K K. Caldwell, S. Werner and C. Krujer, Organomet. Chem. **10**, 3417 (1991).
15. D. R. Armstrong, P. G. Perkins, and J. J. P. Stewart, J. Chem. Soc., Dalton Trans. 1972 (1972).
16. O. Novaro, S. Chow, and P. Magnouat, J. Catal. **41**, 91 (1976).
17. G. Giuuchi, E. Clementi, M. E. Ruiz-Vizcaya, and O. Novaro, Chem. Phys. Lett. **49**, 8 (1977).
18. O. Novaro, E. Blaisten-Barojas, E. Clementi, G. Giunchi, and M. E. Ruiz-Vizcaya, J. Chem. Phys. **68**, 2337 (1978).
19. A. C. Balazs and K. H. Johnson, J. Chem. Phys. **77**, 3148 (1982).
20. H. Fujimoto, T. Yamasaki, H. Mizutani, and N. Koga, J. Am. Chem. Soc. **107**, 6157, (1985).
21. H. Kawamura-Kuribayashi, N. Koga, and K. Morokuma, J. Am. Chem. Soc. **114**, 2359 (1992).
22. L. Fan, D. Harrison, L. Deng, T. K. Woo, D. Swerhone, and T. Ziegler, Can J. Chem. **73**, 989 (1995).
23. J. Endo, N. Koga, and K. Morokuma, Organomet. **12**, 2777 (1993).
24. H. Weiss, M. Ehrig, and R. Ahlrichs, J. Am. Chem. Soc. **116**, 4919 (1994).
25. T. Yoshida, N. Koga, and K. Morokuma, Organomet. **14**, 746 (1995).
26. T. K. Woo, L. Fan, and T. Ziegler, Organomet. **13**, 2252 (1994).
27. J. C. W. Lohrenz, T. K. Woo, L. Fan, and T. Ziegler, Organomet. Chem. **497**, 91 (1995).
28. L. Fan, D. Harrison, T. K. Woo, and T. Ziegler, Organomet. **14**, 2018 (1995).
29. L. A. Castonguay and A. K. Rappe, J. Am. Chem. Soc. **114**, 5832 (1992).
30. H. Kawamaura-Kuribayashi, N. Koga, and K. Morokuma, J. Am. Chem. Soc. **114**, 2359 (1992).
31. H. Kawamura-Kuribayashi, N. Koga, and K. Morokuma, J. Am. Chem. Soc., **114**, 8694 (1992).
32. E. P. Bierwagen, J. E. Bercaw, and W. A. Goddard, J. Am. Chem. Soc. **116**, 1481 (1994).
33. G. Guerra, L. Cavallo, G. Moscardi, M. Vacatello, and P. Corradini, J. Am. Chem. Soc. **116**, 2988 (1994).
34. T. Yoshida, N. Koga, and K. Morokuma, Organomet. **15**, 766 (1996).
35. S. Sakai, J. Phys. Chem. 98, 12053 (1994).
36. S. Sakai, J. Phys. Chem. **95**, 175 (1991).
37. S. Sakai, J. Phys. Chem. **95**, 7089 (1991).
38. K. D. Dobbs and W. J. Hehre, J. Comput. Chem. **8**, 861 (1987).
39. J. S. Binkley, J. A. Pople, and W. J. Hehre, J. Am. Chem. Soc. **102**, 1980 (1980).
40. M. S. Gordon, J. S. Binkley, J. A. Pople, W. J. Pietro, and W. J. Hehre, J. Am. Chem. Soc. **104**, 2997 (1982).
41. P. C. Hariharan and J. A. Pople, Mol. Phys. **27**, 209 (1974).
42. M. M. Francl, W. J. Pietro, W. J. Hehre, J. S. Binkley, M. S. Gordon, D. J. DeFrees, and J. A. Pople, J. Chem. Phys. **77**, 3654 (1982).
43. L. Gianolio and E. Clementi, Gass. Chim. Ital. **110**, 179 (1980).
44. J. A. Pople, J. S. Binkley and R. Seeger, Int. J. Quant. Chem. **9**, 229 (1975).
45. J. A. Pople, R. Krishnan, H. B. Schegel, and J. S. Binkley, Int. J. Quant. Chem. **S13**, 225 (1979).
46. C. Møller and M. S. Plesset, Phys. Rev. **46**, 618 (1934).
47. J. S. Binkley and J. A. Pople, Int. J. Quant. Chem. **9**, 229 (1975).
48. J. A. Pople, J. S. Binkley, and R. Seeger, Int. J. Quant. Chem. **S10**, 1 (1976).
49. R. Krishnan and J. A. Pople, Int. J. Quant. Chem. **14**, 91 (1978).
50. R. Krishnan, M. J. Frisch, and J. A. Pople, J. Chem. Phys. **72**, 4244 (1980).
51. K. J. Frisch, G. W. Trucks, H. B. Schlegel, P. M. W. Gill, B. G. Johnson, M. A. Robb, J. R. Cheseman, T. A. Keith, G. A. Petersson, J. A. Montgomery, K. Raghavachari, M. A. Al-Laham, V. G. Zakrzewski, J. V. Ortiz, J. B. Foresman, J. Cislowski, B. B. Stefanov, A. Nanyakkara, M. Challacombe, C. Y. Peng, P. Y. Ayala, W. Chen, M. W. Wong, J. L. Andres, E. S. Replogle, R. Comperts, R. L. Martin, D. J. Fox, J. S. Binkley, D. J. DeFrees, J. Baker, J. P. Stewart, M. Head-Gordon, C. Gonzalez, and J. A. Pople. GAUSSIAN94, Gaussian, Inc., Pittsburgh, PA, 1995.

Systematic Study of the Lowest Energy States of Au_n ($n = 1-4$) Using DFT

JORGE M. SEMINARIO AND JAMES M. TOUR

Department of Chemistry and Biochemistry, University of South Carolina, Columbia, South Carolina 29208

Received 29 March 1997; revised 15 July 1997; accepted 19 July 1997

ABSTRACT: A density functional theory study of Au, Au_2, Au_3, and Au_4 is performed focusing on the study of gold tips or contacts of interest in investigations of molecular-scale electronics. The ground state for the four systems corresponds to the one with the lowest multiplicity, and the ordering of energies follows the multiplicity in all cases. It is found that the tetrahedral geometry of Au_4 is not the preferred one for the lowest spin states with neutral charge, but is the preferred one for charged systems. The ionization potential and electron affinities for the four systems were also obtained. A qualitative interpretation of the Kohn–Sham highest occupied molecular orbital (HOMO) and lowest unoccupied molecular orbital (LUMO) orbitals is given based on the present calculations. © 1997 John Wiley & Sons, Inc. Int J Quant Chem **65**: 749–758, 1997

Introduction

The development of scanning tunneling microscopy (STM) techniques has enormously triggered the possibilities of using organic chemistry as the fundamental complement for semiconductors [1]. This may allow the fabrication of logical circuits at the level of single molecules [2]. These studies require the precise knowledge of the effect of the STM tips or contacts on these molecules. One of the major metals used as tips or contacts for the development of molecular-level electronic circuits is gold. In some cases, small gold clusters are the preferred material for measurements of current–voltage characteristics [3]. Other interest centers on the measurements of electrical resistance of wires composed of single atoms, and previous studies have been performed with xenon [4]. Therefore, in this study we have decided to focus on the characteristics of small gold clusters that could represent the tips or contacts in experiments of molecular conductance. These contacts could be small enough to form one-atom-point contacts. In addition, the interactions of gold clusters with single molecules must be studied in order to understand and design systems for single-molecule electronics. There are several experimental techniques such as molecular beams that allow the synthesis and characterization of clusters of a defined size. Several studies have been able to determine, theoretically and exper-

Correspondence to: J. M. Seminario.
Contract grant sponsor: Advanced Research Projects Agency.

© 1997 John Wiley & Sons, Inc.
CCC 0020-7608 / 97 / 050749-10

imentally, dissociation energies, ionization potentials, and chemical reactivity for some gold clusters [5–17]. The study of gold clusters is interesting because clusters combine both the properties of metallic surfaces and metallic compounds. The goal of this contribution is to study and determine the basic properties of the lowest states of gold monomer, dimer, trimer, and tetramer using the best theoretical tools available at present, and at the same time, to determine a proper tool to study much larger clusters and gold complexes of interest for molecular-scale electronics.

Theory

We have used density functional theory (DFT) techniques [18–24] combined with effective core potentials [25]. Presently, this seems to be the most powerful combination of tools to deal with relatively large numbers of big atoms. The basis set used for the gold atom is the Los Alamos National Laboratory's (LANL) set for effective core potentials (ECP) of double-ζ type [26–28]. The use of DFT is fully justified due to the fact that is an ab initio tool able to deal with a broad variety of systems. Several successful applications of DFT have been reported using the so-called hybrid functionals, where a portion of the exchange is calculated as a fully nonlocal functional of the wave function of an auxiliary noninteracting system of electrons. Since this resembles the exchange in the Hartree–Fock (HF) procedure (actually in any wave function procedure), it is common to refer to this functional, or procedure, as a DFT–HF hybrid. However, we have to consider that the so-called exchange is being calculated using a noninteractive wave function whose density, but not its wave function, corresponds to the real system. A detailed analysis and their theoretical rigor was recently reviewed [29]. The functional that we used is the B3PW91 [30–33]. All calculations were performed using the Gaussian-94 program [34]. All geometry optimizations were performed via the Berny algorithm in redundant internal coordinates [35]. The thresholds for convergency were 0.00045 atomic units (a.u.) and 0.0003 a.u. for the maximum force and root mean square (RMS) force, respectively. The self-consistency of the noninteractive wave function was performed with a requested convergence on the density matrix of 10^{-8}, and 10^{-6} for the RMS and maximum density matrix error between iterations, respectively. These settings provide correct energies of, at least, five decimal figures and geometries of approximately three decimal figures. On the other hand, the use of the pseudopotentials with relativistic corrections have been widely demonstrated to be a good compromise with the alternative use of full-electron procedures. This reduces the required computational effort without loss of accuracy [36].

Results and Discussions

Table I shows the results for the lowest state of each spin symmetry of the gold atom. The predicted ground state is a doublet, and this result is

TABLE I
Results for the gold monomer (1 Ha = 27.2114eV).[a]

Multiplicity	Energy (H_a)	Energy (eV)	Experimental (eV)
Doublet (Au)	−135.48424 (0.00)		
Quartet (Au)	−135.22896 (6.95)		
Sextet (Au)	−134.84610 (17.36)		
Octet (Au)	−134.37500 (30.18)		
Singlet (Au^-)	−135.56147		
Triplet (Au^-)	−135.45921		
Singlet (Au^+)	−135.14100		
Triplet (Au^+)	−135.03201		
IP of Au		9.34[b]	9.22
EA of Au		2.10[b]	2.31
KS–HOMO Au		−6.77	
KS–LUMO Au		−4.60	

[a] Relative energies in parentheses (eV).
[b] Relativistic MRSDCI / (13*s*11*p*5*D*4*f*) yielded IP = 9.04 eV and EA = 2.11 eV [9].

in agreement with the experimental observation [37]. The ordering of the higher spin states follows the predicted trend. In order to calculate the ionization potential (IP) and electron affinity (EA) of the gold atom, we also studied the positive and negative ions of gold. These results are also in excellent agreement with the experimental values, and they are slightly better than expensive relativistic multireference single-double configuration interaction (MRSDCI) calculations using larger basis sets [9]. Table I also shows the Kohn–Sham (KS) highest occupied molecular orbital (HOMO) and lowest unoccupied molecular orbital (LUMO) energies of the Au atom. They are plotted in Figure 1 where the Δ values are shown from the negative of the HOMO level to the IP, and from the negative of the LUMO level to the EA. These Δ values are 2.57 and 2.50 eV for the HOMO and LUMO, respectively. These values correspond to the electron contribution to the energy in the adiabatic integral [38, 39] of the Kohn–Sham [40] procedure:

$$\int_0^1 \langle \Psi_\lambda | V_{ee} | \Psi_\lambda \rangle \, d\lambda,$$

resulting from the reorganization of the electron density after the electron ejection or capture.

Table II shows the results for the gold dimer. The ground state is a singlet with a bond length of

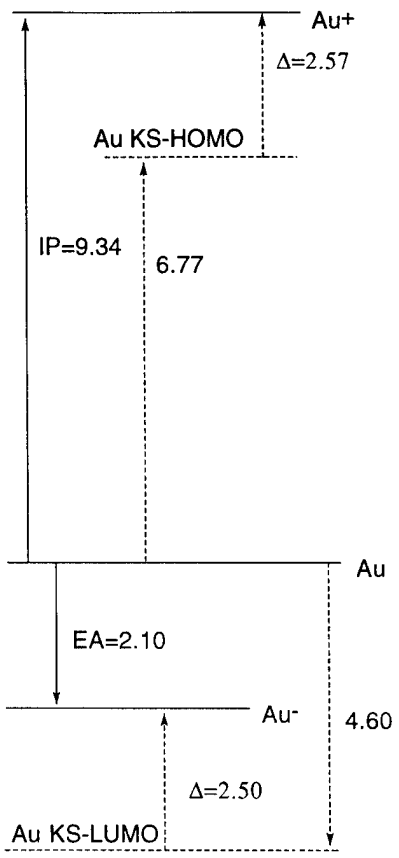


FIGURE 1. Energy levels for the Au atom (in eV)

TABLE II
Results for the gold dimer (D_e is calculated with respect to two doublet monomers).[a]

Multiplicity	Energy (H_a)	Bond Length (A)	Energy (eV)	D_e (eV)
Singlet Au_2 $^1\Sigma_g$	−271.03845	2.547	0.00	1.90
		(2.472)		(2.30)
		[2.549]		[2.22]DHK BLYP
		[2.556]		[2.19]Pauli BP
		[2.517]		[2.26]ZORA-BP
		[2.515]		[2.29]DKH BP
		[2.513]		[2.54]DKH PW
		[2.54]		[1.86]ARPR-CEPA
		[2.54]		[2.13]RPP-QCI(T)
Triplet Au_2 $^3\Sigma_u$	−270.97384	2.961	1.76	0.15
Quintet Au_2	−270.76759	2.638	7.37	−5.47
Septet Au_2	−270.49636	2.502	14.75	−12.85
Doublet Au_3^- $^2\Sigma_u$	−271.11149	2.695		
Doublet Au_3^+ $^2\Sigma_g$	−270.69432	2.675		
EA of Au_2			1.99	
			(1.94)	
IP of Au_2			9.36	

[a] Experimental values are in parentheses. Other calculations [17] are shown in square brackets.

2.547 Å and an atomization energy of 1.90 eV with respect to two gold ground-state atoms. This is followed by a triplet state at 1.76 eV of separation and with a weak bond of only 0.15 eV. The lowest quintet and lowest septet were also calculated. They show stable structures with a bond length of 2.695 and 2.675 Å, respectively. In addition, we have also analyzed the positive and negative ions in order to obtain IP and EA of the ground-state gold dimer. These calculations yielded 9.36 and 1.99 eV, respectively, practically the same values as for the monomer. The EA is in excellent agreement with the experimental value of 1.94 eV [12–14]. We were not able to find an experimental value for the IP of Au_2. The bond dissociation energy (D_e) of 1.90 eV is in fairly good agreement with the reported experimental values of 2.30 eV [41] and 2.33 eV [10, 11]. The bond length is slightly overestimated by 0.077 Å. However, our results are in closer agreement with a direct perturbation relativistic DFT procedure [16] which reported a D_e of 2.04 eV and a bond length of 2.58 Å. Several calculations on Au_2 have recently been reported [17] and they are listed in Table II.

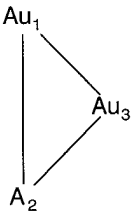
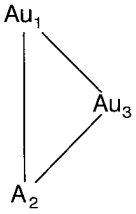
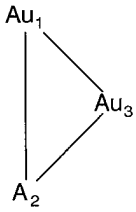
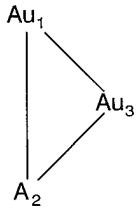
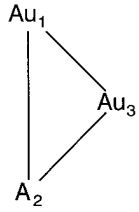
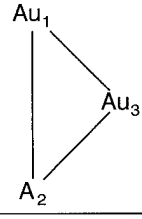
Table III shows the results for the trimer. The lowest doublet, quartet, and sextet were calculated. As with the monomer and dimer, the ordering of energies follows the multiplicity. As per our goal, resembling the STM tip implies the search for local minima with a triangular structure. Therefore, all our geometry optimizations started with a triangular structure. In addition, the search was extended to the positive and negative singlets and triplets. Except for the negative singlet of Au_3^- that yielded a linear structure, all the other geometries were triangular. For the charged ions, the singlets were lower in energy than the triplets. The quartet was the only neutral structure to have D_{3h} symmetry and correspond to the one with the longest bond length. The doublet and triplet are stable with respect to dissociation into three ground-state Au atoms by 2.79 and 0.48 eV, respectively. The sextet is unstable by 7.41 eV. Only the singlet is stable with respect to a monomer plus dimer system by 0.88 eV.

Table IV shows the results for the tetramer. The search for local minima was started with an almost tetrahedral structure with no constraints on its symmetry (C_1 symmetry). The ordering of energies was again the same as their multiplicities; however, no tetrahedral geometry was found for the lowest singlet and triplet. The lowest quintet corresponds to a tetrahedral structure at 3.16 eV above the singlet. The singlet ended up planar in a triangular arrangement connecting the fourth gold atom in one of the vertices. The triplet afforded an almost perfect square with a puckered angle of 12.9° and 0.81 eV above the singlet, and an additional search constrained to D_{4h} symmetry yielded practically the same energy as the puckered one. The quintet was a tetrahedron. Interestingly, the three structures are stable with respect to four gold atoms in their ground state by 4.96, 4.15, and 1.80 eV, respectively. The singlet and triplet are stable with respect to two dimers by 1.15 and 0.34 eV, respectively. The quintet is unstable by 2.01 eV. The singlet and triplet are also stable with respect to a ground-state trimer and a monomer while the quintet is not stable. We can also observe from Tables II–IV that the bond length of the doublet negative tetramer is in very close agreement with the experimental Au–Au gold distance in the Au(100) (1 × 1) surface. [15].

Structural and Electronic Analysis

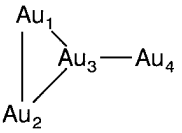
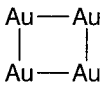
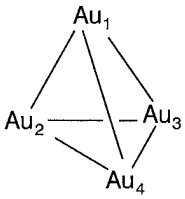
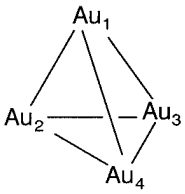
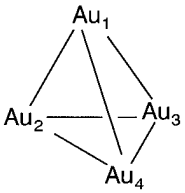
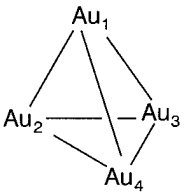
The point contacts of gold clusters are of paramount importance for single-molecule electronic studies. To our knowledge, there are no ab initio studies dealing with the use of clusters as the contacts for single molecules. Most previous studies dealt with surfaces. Shown in Figure 1 are the electronic levels for the gold atom in its ground state. The ground state of gold is used as the reference to compare with the energy of its positive and negative ions. The negative of the KS HOMO and LUMO of the ground state of the gold atom are also shown. The KS orbitals correspond to a system of fictitious noninteracting electrons with a density identical to the real system. Therefore, the negative of the HOMO energy corresponds to the energy increase of the system when this fictitious orbital stops being part of the noninteracting system due to the hypothetically instantaneous ejection of one electron in the real system. The loss of one electron implies an electron relaxation in the real and noninteractive systems that has, as a consequence, an increase in the total energy of the positive ion. This excess (Δ) is dominated by the electron–electron repulsion, which grows more than the kinetic and nuclear–electron energies combined. Similarly, the insertion of an electron in the real system causes the LUMO of the noninteractive system of the neutral atom to be

TABLE III
Results for the gold trimer.[a]

System	Energy, H_a (eV)	Geometry (Å and °)			Structure
$Au_3\ ^2B_2C_v$	−406.55521 (0.00)	2.642 69.4	2.642 55.3	3.007 55.3	
$Au_3\ ^4A_1D_{3h}$	−406.47020 (2.31)	2.966			
$Au_3\ ^6B_1C_{2v}$	−406.28273 (7.41)	2.695 66.9	2.695 56.5	2.972 56.5	
$Au_3^-\ ^3A_1D_{3h}$	−406.64609 (−2.47)	2.787			
$Au_3^-\ ^1A_1D_{\infty h}$	−406.69050 (−3.68)	2.623			$Au_1 - Au_2 - Au_3$
$Au_3^+\ ^1A_1D_{3h}$	−406.29524 (7.07)	2.674			
$Au_3^+\ ^3A_1C_{2v}$	−406.19806 (9.72)	3.090 50.4	3.090 64.8	2.631 64.8	

[a]When electronic state and symmetry of the optimized system do not correspond with the initial state the latter is indicated.

TABLE IV
Results for the gold tetramer.[a]

System	Energy, H_a	Energy (eV)	Geometry (Å and °)	Structure
$^1A_1$ C_{2v} Au_4	−542.11914	0.00	1–3, 2–3 = 2.761 1–2 = 2.608 3–4 = 2.560	
$^3A_{1g}$ D_{4h} Au_4	−542.08941	0.81	2.684[b]	
$^5B_1$ D_{2d} Au_4	−542.00314	3.16	1–2, 3–4 = 2.979 1–3, 1–4 2–3 2–4 = 2.733	
Doublet Au_4^-	−542.17039	−1.39	1–3 = 2.827 3–4 2.282 1–4 = 2.828 1–2 = 2.877 2–4 = 2.885 2–3 = 2.893	
Doublet Au_4^+	−541.81813	8.19[c]	1–3 = 2.955 1–4 = 2.943 2–3 = 2.922 2–4 = 2.912 1–2 = 2.626 3–4 = 2.626	
Quartet Au_4^-	−542.17848	−1.61	1–3 = 2.848 1–4 = 2.851 2–3 = 2.851 2–4 = 2.852 1–2 = 2.852 3–4 = 2.848	
Quartet Au_4^+	No convergence			

[a]All initial geometries were almost perfect tetrahedrons.
[b]A similar geometrical and isoenergetic conformation with a puckered angle of 12.9 was also found.
[c]A lower energy structure with C_{2v} planar symmetry (rombic) was found with energy of −541.8205 a.u.

occupied and, therefore, instantaneously reducing the energy by an amount equivalent to the negative of the LUMO energy. Since the electrons become denser due to the presence of the excess electron, the relaxation of the electrons will tend to spread out the electronic charge. As in the case of the positive ion, an increase in the total energy results. As expected from a physical interpretation of the KS orbitals, the subtraction of the HOMO energy from the total energy of the neutral system will yield an underestimation of the IP. Furthermore, the addition of the LUMO energy to the

neutral atom will yield an underestimation of the energy of the negative ion. Relaxation effects will produce an increase of the energies in both cases.

Therefore, DFT presents a better qualitative and quantitative picture than HF theory where, in most cases, the LUMO energy is always positive [42] and thus contrary to a real physical situation. Since the virtual KS orbitals describe electrons moving in the field of $N - 1$ electrons, they therefore lack the artificial upward shift of the Hartree–Fock virtual orbitals [43]. In addition, using an exact functional, the HOMO energy is the exact ionization energy since this energy depends only upon the asymptotic decay of the density [44]. For further details on the Kohn–Sham orbitals see, for instance, Refs. [21, 23] and the works cited within. It is important to mention that relaxation energy defined here has contributions from the potential and kinetic energies. The potential energy arises from the nuclear–electron and electron–electron interactions and are incorporated into Δ, which is formed by the contributions of the T, V_{ee} and V_{ne} energies. Therefore, when an electron leaves the neutral system, at that instant, the V_{ee} and T lower the total energy and the V_{ne} increases the total energy. Then, in the relaxation process, the V_{ne} has more effect than the $V_{ee} + T$ energy. Conversely, when an electron enters into the neutral system to form the negative ion, at that instant the $V_{ee} + T$ energy increases, therefore increasing the total energy. Accordingly, the V_{ne} increases in its absolute value, thus lowering the total energy. In this situation, the $V_{ee} + T$ term has a dominant effect. These ideas are in disagreement with another study using the local density approximation (LDA), which claims that the so-called relaxation and correlation effects cancel, thus Koopman's theorem can be used for the outer orbitals [45].

Table V summarizes the energetic results for the four gold systems. The HOMO and LUMO energies follow the trend and qualitative behavior of the monomer. For the dimer and trimer, the effects of geometry relaxation have to be considered, and basically the IP and EA tend to be in the same range of values as the cluster increases in size. This has strong implications in the estimation of Fermi levels for gold obtained from small clusters calculations. We also noticed that a tetrahedral geometry is not allowed with low spin and neutral charge. In addition, results in Table V yield a perfect qualitative interpretation of the Kohn–Sham HOMO and LUMO, allowing us to express the energy of the cation and anion with respect to the energy

TABLE V
Ionization potentials (IP), electron affinities (EA), Kohn – Sham (KS) HOMO and LUMO energies of Au, Au_2, and Au_3 in eV.[a]

	Au_1	Au_2	Au_3
IP	9.34	9.36	7.07
$-\varepsilon_{HOMO}$	6.77	7.19	5.40
Δ_{HOMO}	2.57	2.17	1.57
EA	2.10	1.99	2.47
$-\varepsilon_{LUMO}$	4.60	3.79	3.81
Δ_{LUMO}	2.50	1.80	1.34

[a] We have not used the Au_4 because no ground-state system with tetrahedral symmetry was found.

of the neutral, which can be written in KS–DFT as (see for instance Ref. [46])

$$E = T_s + V_{ne} + \int_1^0 \langle \Psi_\lambda | V_{ee} | \Psi_\lambda \rangle \, d\lambda,$$

and using the KS orbital energies, as

$$E = \sum_1^n \varepsilon_i + \int_0^1 \langle \Psi_\lambda | V_{ee} | \Psi_\lambda \rangle \, d\lambda.$$

Therefore, the energy of the cation is

$$E^{(+)} = \left\{ \sum_1^n \varepsilon_i - \varepsilon_{HOMO} + \Delta_{HOMO}^{\text{non int}} \right\} + \left\{ \int_0^1 \langle \Psi_\lambda | V_{ee} | \Psi_\lambda \rangle \, d\lambda - \Delta_{HOMO}^{\text{adiaba}} \right\}.$$

and the energy of the anion

$$E^{(-)} = \left\{ \sum_1^n \varepsilon_i + \varepsilon_{LUMO} - \Delta_{LUMO}^{\text{non int}} \right\} + \left\{ \int_0^1 \langle \psi_\lambda | V_{ee} | \Psi_\lambda \rangle \, d\lambda + \Delta_{LUMO}^{\text{adiaba}} \right\}.$$

Thus

$$\Delta_{HOMO} = \Delta_{HOMO}^{\text{non int}} - \Delta_{HOMO}^{\text{adiaba}}$$

and

$$\Delta_{LUMO} = -\Delta_{LUMO}^{\text{non int}} + \Delta_{LUMO}^{\text{adiaba}}.$$

Since Δ_{HOMO} and Δ_{LUMO} are always positive, the noninteracting changes predominate over the adiabatic changes when the system looses one electron, and the opposite happens when an electron is gained by the system.

An analysis of the HOMO and LUMO orbitals also helps in explaining the geometrical structure of the gold tetramers. The dimer and trimer structures are straightforwardly understood. Figure 2 shows the HOMO and LUMO orbitals for the singlet, triplet, and quintet lowest states of Au_4. We see that in the planar structure of the singlet, the HOMO is localized on the gold atom outside of the triangle and the LUMO is localized on the base of the triangle. Therefore, electron conduction will be preferred when one electron enters from the base and one electron ejects from the tip. The reverse would be less preferred and probably only possible through a tunnel effect as in the STM. This logical way to interpret conductivity in molecules needs to be analyzed further since it would be instrumental for the design of molecular circuits. The HOMO and LUMO corresponding to the ground state of the planar tetramer are also show in Figure 2. In addition we have plotted the HOMO and LUMO of the nonoptimized tetramer with a T_d symmetry. Clearly, the HOMO of the nonoptimized tetramer indicates that this corresponds to an antibonding orbital and therefore no stable structure is found. The D_{4h} point group used here can end up on a T_d or a D_{4h} structure on

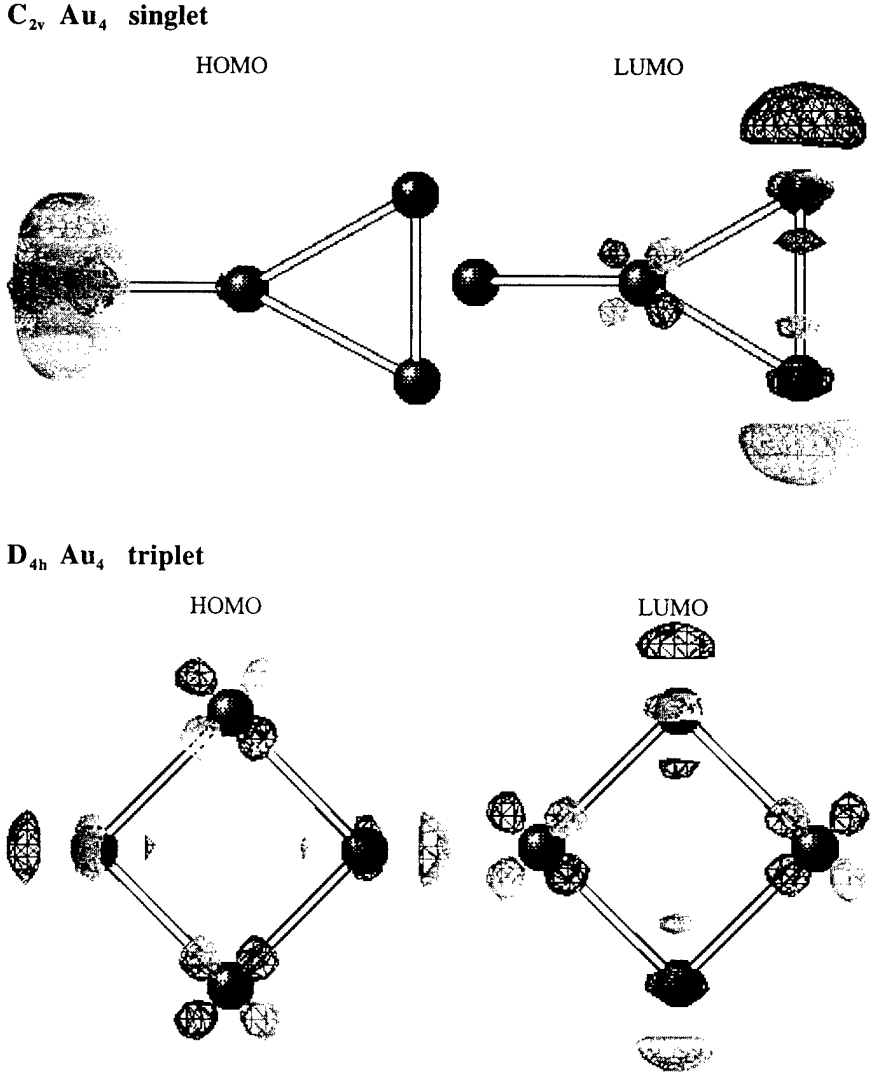


FIGURE 2. HOMO and LUMO orbitals for the optimized lowest singlet, triplet, and quintet states of Au_4 as well as for the nonoptimized triplet of T_d symmetry.

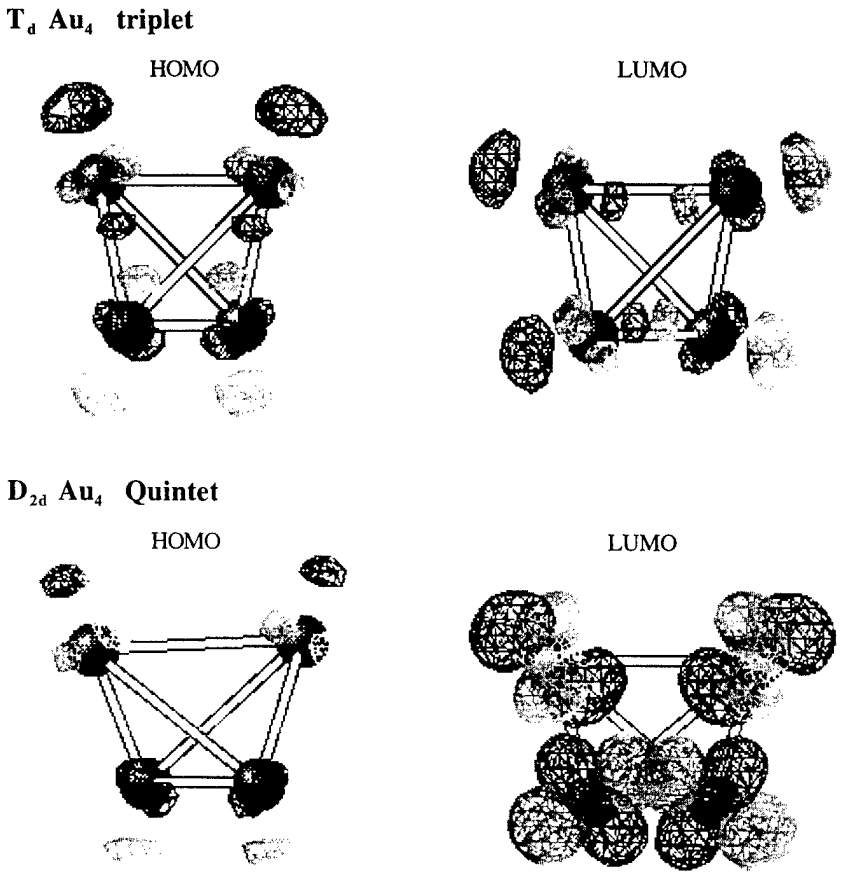


FIGURE 2. Continued

the other end. The preferred symmetry is the D_{4h}. The HOMO and LUMO of the lowest quintet state is also shown in the figure. Although this structure has reached a local extremum, it cannot be realistically considered because it corresponds to an artifact of the procedure; since several of the alpha-occupied orbitals are above several of the beta-unoccupied orbitals. The orbital analysis allows us to conclude that there is no possibility of having a tetrahedral geometry for the gold tetramer due to the instability associated with the asymetric electronic occupation of degenerate orbitals in the T_d structure of Au_4 because there is a distortion pathway that will lower the electronic energy of the molecule yielding a removal of the orbital degeneracy. In this case, the distortion can reduce the T_d symmetry to C_{2v}, D_{4h}, or D_{2d} point groups. Although strictly associated initially with the instability of a degenerate electronic state [47], the above distortion is also known as a Jahn–Teller effect [48]. All orbitals presented in Figure 2 corresponds to contours of $\pm 0.07/\text{bohr}^{3/2}$, i.e., contours of $\frac{1}{2}\%$ probability per cubic Bohr or in classical terms, contours corresponding to a electronic density of 0.005 electrons per cubic Bohr.

ACKNOWLEDGMENTS

We greatly appreciate the help of A. G. Zacarias for her help in several aspects of this work. We also thank the Advanced Research Projects Agency for support of this work.

References

1. L. A. Bumm, J. J. Arnold, M. T. Cygan, T. D. Dunbar, T. P. Burgin, L. Jones II, D. L. Allara, J. M. Tour, and P. S. Weiss, Science **271**, 1705 (1996).
2. R. Wu, J. S. Schumm, D. L. Pearson, and J. M. Tour, J. Org. Chem. **61**, 6906 (1997).
3. R. P. Andres, T. Bein, M. Dorogi, S. Feng, J. I. Henderson, C. P. Kubiak, W. Mahoney, R. G. Osifchin, and R. Reifenberger, Science **272**, 1323 (1996).

4. A. Yazdani, D. M. Eigler, and N. D. Lang, Science **272**, 1921 (1996).
5. D. Cvetko, A. Lausi, A. Morgante, F. Tommasini, P. Cortona, and M. G. Dondi, J. Chem. Phys. **100**, 2052 (1994).
6. V. Kellö and A. J. Sadłej, J. Chem. Phys. **103**, 2991 (1995).
7. S. S. Lin, B. Strauss, and A. Kant, J. Chem. Phys. **51**, 2282 (1969).
8. C. E. Moore, *Table of Atomic Energy Levels* (U.S. National Bureau of Standards, Washington, D.C., 1971).
9. A. Pislo, G. Jansen, and B. A. Jess, J. Chem. Phys. **98**, 3945 (1993).
10. G. A. Bishea and M. D. Morse, Chem. Phys. Lett. **171**, 430 (1990).
11. A. Kowalski, M. Czaikowski, and W. H. Breckenridge, Chem. Phys. Lett. **119**, 368 (1985).
12. J. Ho, K. M. Ervin, and W. C. Lineberger, J. Chem. Phys. **93**, 6987 (1990).
13. D. G. Leopold, J. Ho, and W. C. Lineberger, J. Chem. Phys. **86**, 1715 (1987).
14. C. L. Pettiete, S. H. Yang, M. J. Craycraft, J. Conceicao, R. T. Laaksonen, O. Cheshnovsky, and R. E. Smalley, J. Chem. Phys. **88**, 5377 (1988).
15. E. Lang, W. Grimm, and K. Heinz, Surf. Sci. **117**, 169 (1982).
16. C. van Wüllen, J. Chem. Phys. **103**, 3589 (1995).
17. N. Rösch, S. Kruger, M. Mayer, and V. A. Nasluzov, in *Recent Developments and Applications of Modern Density Functional Theory*, J. M. Seminario, Ed. (Elsevier, Amsterdam, 1996), p. 497.
18. J. M. Seminario and P. Politzer, *Density Functional Theory: A Tool for Chemistry*, (Elsevier, Amsterdam, 1995).
19. J. M. Seminario, *Recent Developments in Modern Density Functional Theory*, (Elsevier, Amsterdam, 1996).
20. D. P. Chong, *Recent Advances in Density Functional Theory (Part I)* (World Scientific, Singapore, 1995).
21. R. G. Parr and W. Yang, *Density Functional Theory of Atoms and Molecules* (Oxford University Press, Oxford, 1989).
22. E. S. Kryachko and E. Ludeña, *Energy Density Functional Theory of Many-electron Systems* (Academic, New York, 1990).
23. R. M. Dreizler and E. K. U. Gross, *Density Functional Theory* (Springer, Berlin, 1990).
24. J. K. Labanowski and J. W. Andzelm, *Density Functional Methods in Chemistry* (Springer, New York, 1991).
25. T. H. Dunning Jr and P. J. Hay, in *Modern Theoretical Chemistry*, H. F. Shaefer III, Ed. (Plenum, New York, 1976), p. 1.
26. P. J. Hay and W. R. Wadt, J. Chem. Phys. **82**, 270 (1985).
27. W. R. Wadt and P. J. Hay, J. Chem. Phys. **82**, 284 (1985).
28. P. J. Hay and W. R. Wadt, J. Chem. Phys. **82**, 299 (1985).
29. A. Görling and M. Levy, J. Chem. Phys. **106**, 2675 (1997).
30. A. D. Becke, J. Chem. Phys. **98**, 5648 (1993).
31. J. P. Perdew, in *Electronic Structure of Solids*, P. Ziesche and H. Eschrig, Eds. (Akademie, Berlin, 1991), p. 11.
32. J. P. Perdew, J. A. Chevary, S. H. Vosko, K. A. Jackson, M. R. Pederson, D. J. Singh, and C. Fiolhais, Phys. Rev. B **46**, 6671 (1992).
33. J. P. Perdew and Y. Wang, Phys. Rev. B **45**, 13244 (1992).
34. M. J. Frisch, G. W. Trucks, H. B. Schlegel, P. M. W. Gill, B. G. Johnson, M. A. Robb, J. R. Cheeseman, T. Keith, G. A. Petersson, J. A. Montgomery, K. Raghavachari, M. A. Al-Laham, V. G. Zakrzewski, J. V. Ortiz, J. B. Foresman, J. Ciolowski, B. B. Stefanov, A. Nenayakkara, M. Challacombe, C. Y. Peng, P. Y Ayala, W. Chen, M. W. Wong, J. L. Andres, E. S. Replogle, R. Gomperts, R. L. Martin, D. J. Fox, J. S. Binkley, D. J. Defrees, J. Baker, J. P. Stewart, M. Head-Gordon, C. Gonzalez, and J. A. Pople, Gaussian 94, Revision E.1, Gaussian, Inc., Pittsburgh, PA, 1996.
35. C. Peng, P. Y. Ayala, H. B. Schlegel, and M. J. Frisch, J. Comp. Chem., in preparation.
36. K. M. Neyman, G. Pacchioni, and N. Rösch, in *Recent Developments and Applications of Modern Density Functional Theory*, J. M. Seminario, Ed. (Elsevier, Amsterdam, 1996), p. 569.
37. G. Herzberg, *Atomic Spectra and Atomic Structure* (Dover, New York, 1945).
38. J. Harris and R. O. Jones, J. Phys. F **4**, 1170 (1974).
39. D. C. Langreth and J. P. Perdew, Solid State Commun. **17**, 425 (1975).
40. W. Kohn and L. J. Sham, Phys. Rev **140**, A1133 (1965).
41. K. P. Huber and G. Herzberg, *Molecular Spectra and Molecular Structure* (Van Nostrand Reinhold, New York, 1979).
42. A. Szabo and N. S. Ostlund, *Modern Quantum Chemistry* (Dover, New York, 1996).
43. C. F. Guerra, O. Visser, J. G. Snijders, G. teVelde, and E. J. Baerends, in *Methods and Techniques in Computational Chemistry: METECC-95*, E. Clementi and G. Corongiu, Eds. (MOTECC, Cagliara, 1995).
44. M. Levy, in *Recent Developments and Applications of Modern Density Functional Theory*, J. M. Seminario, Ed. (Elsevier, Amsterdam, 1996).
45. M. Vijayakumar and M. S. Gopinathan, J. Chem. Phys. **103**, 6575 (1995).
46. J. M. Seminario, in *Modern Density Functional Theory: A Tool for Chemistry*, J. M. Seminario and P. Politzer, Eds. (Elsevier, Amsterdam, 1995).
47. H. A. Jahn and E. Teller, Proc. Roy. Soc. A **161**, 220 (1937).
48. J. K. Burdett, *Chemical Bonding in Solidas* (Oxford University Press, New York, 1995).

Ab Initio Prediction of the Geometry and IR Frequencies of the Mono- and Dihydrated Complexes of the Oxo-amino-Tautomers of Guanine

LEONID GORB,* JERZY LESZCZYNSKI

Department of Chemistry, Jackson State University P.O. Box 17910, 1325 J. R. L. Lynch Street, Jackson, Mississippi 39217

Received 29 March 1997; revised 3 June 1997; accepted 3 June 1997

ABSTRACT: The results of ab initio post-Hartree–Fock study of the molecular structures, relative stabilities, and Hartree–Fock level calculations of IR frequencies and intensities for mono- and dihydrated oxo-amino-tautomers of guanine are reported. The geometries of the local minima were optimized without symmetry restrictions at the second-order Møller–Plesset perturbation theory. The standard 6-31 G(*d*) basis set was used. Local minima were verified by calculations of the matrix of energy second derivatives [Hessian at the HF/6-31 G(*d*) level]. The single-point calculations were also performed at the MP4(SDQ)/6-31G(*d*)//MP2/6–31G(*d*) and MP2/6-31++G(d, p)//MP2/6-31G(*d*) levels of theory. The total energies were corrected for the zero-point energy contributions scaled by a factor of 0.9. The structural parameters of mono- and dihydrated complexes were analyzed and related to the characteristics of hydrogen bonds. We found that the interaction of guanine tautomers with two water molecules changes the order of the gas-phase stability: 7GUA ≈ 9GUA into the order which corresponds to the stability of the guanine tautomers in the polar solvent: 9GUA ≫ 7GUA. The predicted IR HF/6-31G(*d*) level frequencies and intensities are presented. © 1997 John Wiley & Sons, Inc. Int J Quant Chem **65:** 759–765, 1997

Correspondence to: J. Leszczynski.

* Permanent address: Institute of Water and Colloid Chemistry of the National Academy of Sciences, 42 Vernadsky av., Kiev-142, 252680 Ukraine.

Contract grant sponsor: NSF.

Contract grant number: OSR-945285.

Contract grant sponsor: Office of Naval Research.

Contract grant number: N00014-95-0049.

Contract grant sponsor: Army Research Office and the University of Minnesota.

Contract grant numbers: DAAH04-95-2-003; DAAH94-95-C-008.

© 1997 John Wiley & Sons, Inc.
CCC 0020-7608 / 97 / 050759-07

Introduction

The structural characteristics of the isolated DNA and RNA bases and the prototypic molecules have been the subject of extensive spectroscopic studies in recent years. Most of the structural characteristics have been obtained using infrared spectroscopy and high-resolution microwave studies. These investigations are always more relevant if they are performed in parallel with ab initio quantum chemical calculations, which, at the correlated level with sufficiently large basis sets, are able to reproduce such structural characteristics as geometry and IR frequencies with the same accuracy as those of experiments (see e.g., [1]). Examples of such spectroscopic investigations coupled with ab initio quantum chemical calculations can be found in [2].

Currently, the focus of these combined investigations is strongly shifted toward the study of isolated intermolecular complexes with water molecules. It is so natural because the hydration of the DNA and RNA bases plays a special role in determining the three-dimensional structure of these kinds of biopolymers. The available literature on this subject consists of investigations of only the pyrimidine type of DNA bases and their prototypic molecules [3]. To fill the gap formed by a lack of investigations of hydrated puring bases, we initiated ab initio calculations of the two tautomers of guanine: the oxo-amino form of the N(9)H tautomer (9GUA) and the oxo-amino form of the N(7)H tautomer (7GUA), which are the lowest minima on the potential surface of isolated guanine tautomers [4].

Before discussing the objective of this article, justification for considering the mono- and dihydrated species of guanine tautomers is in order. We are interested only in the cyclic forms of these complexes because of the existence of both experimental and theoretical data which support the idea that similar structures are the most important minima on the potential surface of the water–DNA base complexes:

(i) According to the X-ray data of guanidine monohydrate [5], the water molecule is located in the vicinity of the carbonyl oxygen;

(ii) according to the calculations of formamide and acetamide–water complexes [6, 7], the $>C{=}O\cdots H_2O\cdots HN<$ bifurcated structure is really the global minimum; and

(iii) recently, it was concluded from the studies of rotationally resolved fluorescence excitation spectrum [3a, b] that the mono- and dihydrated complexes of pyridone have the same geometrical structure as that assumed for the 7(9)GUA $\cdot H_2O$ and the 7(9)GUA $\cdot 2H_2O$ species in this study.

The purpose of this article was to provide accurate theoretical data for the studied species. The following properties of the mono- and dihydrated guanine species are predicted: (1) the geometry and rotational constants of the mono- and dihydrated 7(9)GUA species; (2) the stability of these complexes and a comparison with the stability of isolated species; and (3) IR frequencies of mono- and dihydrated 7(9)GUA species and a comparison with the spectra of isolated components.

Computational Methods

The ab initio LCAO-MO method [8] was used to study the interaction of guanine tautomers with water molecules. The calculations were carried out with the Gaussian-92 program [9]. The standard 6-31G(d) basis set was used. All the geometries were optimized without symmetry restrictions (C_1 symmetry was assumed) by the gradient procedure [10] initially at the HF level and subsequently at the second-order Møller–Plesset perturbation theory [11]. Local minima were verified by establishing that the matrix of energy second derivatives (Hessian) [at the HF/6-31G(d) level] has only positive eigenvalues. The single-point calculations were performed at the MP4(SDQ)/6-31G(d)//MP2/6-31G(d) and MP2/6-31 + + G(d, p)//MP2/6-31G(d) levels of theory. The total energies were corrected for the HF/6-31G(d) level with a zero-point energy contribution scaled by a factor of 0.9.

Results

The calculated geometrical parameters for mono- and dihydrated complexes of 7(9)GUA are presented in Figure 1. Tables I and II present the computed rotational constants along with selected intermolecular parameters for 7(9)GUA $\cdot H_2O$ and 7(9)GUA $\cdot 2H_2O$. The data corresponding to the

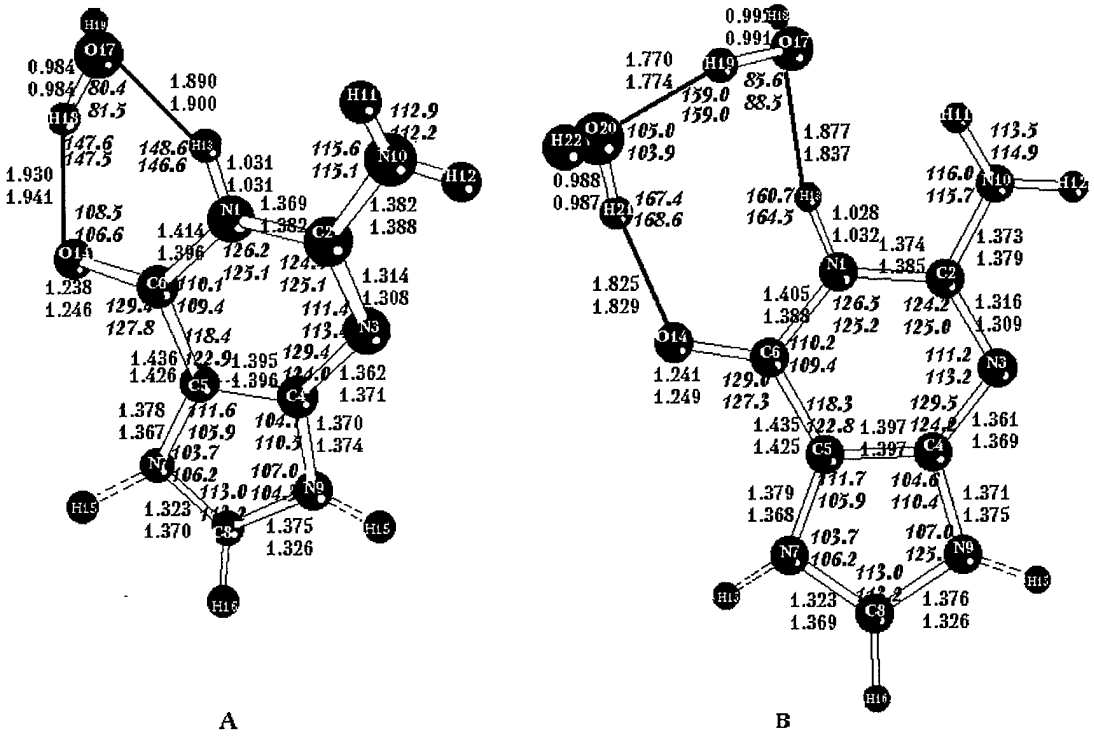


FIGURE 1. Structural parameters of mono- and dihydrated oxo-amino-guanine complexes. (A) Up indexes: monohydrated oxo-amino-N(9)H guanine; down indexes: monohydrated oxo-amino-N(7)H guanine. (B) Up indexes: dihydrated oxo-amino-N(9)H guanine; down indexes: dihydrated oxo-amino-N(7)H guanine.

relative stability of isolated and hydrated guanine species together with computed dipole moments are collected in Table III. The computed IR frequencies are given in Tables IV and V.

Discussion

GEOMETRY OF 7(9)GUA · H_2O AND 7(9)GUA · 2 H_2O SPECIES

An analysis of the structural parameters in hydrogen-bonded systems A—H ··· B, where A and B are heavy atoms which are involved in hydrogen bonding, is crucial for an understanding of the reasons for proton transfer in DNA bases. According to the classification of nearly linear hydrogen bonds [12] (AHB more than 165°), the very low values of the proton-transfer barriers take place when the A—B distance is less than 2.5 Å (A and B are oxygens and/or nitrogens atoms). In this case, the two heavy atoms are so close to each

TABLE I
MP2 / 6-31G(*d*) rotational constant (A, B, C, GHz) and selected intermolecular parameters (Å) for the monohydrated 7(9)-guanine complexes.

	9GUA · H_2O	7GUA · H_2O
A	1.47278	1.46761
B	0.74504	0.74764
C	0.49581	0.49647
$RN_{10}O_{17}$	2.822	2.811
$RO_{14}O_{17}$	2.818	2.820

TABLE II
MP2 / 6-31G(*d*) rotational constant (A, B, C, GHz) and selected intermolecular parameters (Å) for the dihydrated 7(9)-guanine complexes.

	9GUA · H_2O	7GUA · H_2O
A	1.23260	1.22306
B	0.524809	0.52490
C	0.37245	0.37073
$RN_{10}O_{17}$	2.868	2.845
$RO_{17}O^{1}_{20}$	2.719	2.752
$RO_{14}O_{20}$	2.794	2.804

The O—O distance in $(H_2O)_2$ is 2.915 Å at the MP2/6-31G(*d*) level of theory.

TABLE III
Relative stability (kJ mol^{-1}) and dipole moments (D) of guanine tautomers and their mono- and dihydrated species.

Species	MP4(SDQ)/ 6-31G(*d*)// MP2/ 6-31G(*d*)	MP2/ 6-31++G(*d*)// MP2/ 6-31G(*d*)	MP2/ G-31G(*d*)// MP2/ 6-31G(*d*)	μ[a]
9GUA	0.0	0.0	0.0	7.0
7GUA	1.6	1.8	−0.2	1.6
9GUA · H_2O	0.0	0.0	0.0	5.7
7GUA · H_2O	−4.1	0.5	−2.3	1.6
9GUA · $2H_2O$	0.0	0.0	0.0	4.9
7GUA · $2H_2O$	6.8	2.7	4.8	2.8

[a]Evaluated from MP2-optimized geometry using HF density.

other that the zero-point energy level could appear even under the barrier. In the case of the A—B distance between 2.8 and 3.0 Å, the value of the proton-transfer barrier is much higher. This observation is the reference point for our analysis of the structural data (Fig. 1 and Tables I and II) of mono- and dihydrated tautomers of 9(7) guanine.

According to the data of previous theoretical studies and experimental observations [3a, b], the influence of the interaction with one and/or two water molecules on the bond distances and bond angles of prototypic molecules manifests itself mainly in the region of intermolecular hydrogen bonding. Our data (see Fig. 1 and Tables I and II) completely confirm this point. All other structural parameters of the heterocyclic rings are vitually the same [except for the N_1—C_6 "single" bond of 9(7)GUA tautomers which is also under the influence of hydrogen bonding] and depend only on the chemical structure of tautomers.

The addition of the second water molecule makes a noticeable change in the geometrical structure of the hydrogen-bonded complexes. All of them become much more linear compared to the monohydrated complexes; the distance between O_{14} and O_{20} of dihydrated complexes is much shorter than the corresponding distance O_{14}—O_{17} of the monohydrated complexes. Also, the distance between O_{17} and O_{20} is much shorter than the interatomic distance in a free water dimer (see data in Tables I and II). All the observed trends for the 9(7)GUA · H_2O and 9(7)GUA · $2H_2O$ complexes are congruous with the available experimental and calculated [3a, b] data of the mono- and dihydrated complexes of pyridone. Thus, based on geometrical characteristics, one might expect that the participation of two water molecules in a proton-transfer reaction between the N_1 and O_{14} atoms of the guanine molecule could be more favorable than is the participation of only one water molecule.

RELATIVE STABILITIES

The relative stabilities of the isolated and solvated guanine tautomers have been predicted by different levels of theory up to an MP4(SDQ)/6-311 + + G(*d*, *p*)//MP2/6-31G(*d*) approximation [13]. In Table III, the calculated stabilities of isolated tautomers are in complete agreement with the data in [13].

Our present discussion will concentrate on an evaluation of the relative stability of the hydrated complexes. For the isolated tautomers of guanine, the following stability pattern is established:

$$7\text{GUA} \approx 9\text{GUA}. \qquad (1)$$

This relationship (1) corresponds well with the available experimental data for the species in the gas phase [4]. According to the data of experimental IR studies, 7GUA is probably the most stable tautomer. The tendency for the 7GUA form of guanine monohydrates to stabilize exists. Based on the data presented in Table III, the same stability pattern in obtained for complexes of guanine with one water molecule:

$$7\text{GUA} \cdot H_2O \approx 9\text{GUA} \cdot H_2O. \qquad (2)$$

The described peculiarity of monohydrated complexes is changed for the dihydrated isolated com-

TABLE IV
Calculated IR frequences (FREQ, in cm^{-1}) and absolute intensities (INT, km mol^{-1}) for 9-guanine species.

9-Guanine		9GUA · H_2O		9GUA · $2H_2O$	
FREQ	INT	FREQ	INT	FREQ	INT
152	6	50	6	34	4
180	2	110	18	57	1
218	10	153	2	59	4
339	17	167	1	147	18
355	93	186	6	157	4
366	7	218	25	164	1
392	1	247	90	192	4
522	7	351	6	199	100
573	43	370	38	220	12
576	109	381	63	237	4
608	293	387	73	315	129
654	109	398	59	356	9
679	8	526	57	367	11
721	10	562	256	385	1
729	30	576	196	391	7
790	60	581	57	430	27
823	13	676	256	496	349
871	90	690	196	533	9
908	15	719	2	550	91
969	4	735	31	575	168
1033	11	771	2	584	6
1147	13	815	48	680	176
1162	12	865	6	700	142
1192	22	894	202	719	6
1251	21	909	40	736	54
1282	59	970	5	777	9
1425	5	1032	13	819	22
1457	54	1158	15	830	353
1478	62	1162	7	870	63
1535	22	1206	10	905	26
1577	8	1262	10	922	180
1687	26	1288	70	969	5
1736	112	1428	11	1032	15
1781	464	1466	11	1158	17
1792	111	1513	189	1162	6
1842	536	1536	16	1219	7
1999	901	1578	9	1266	5
3452	4	1702	45	1295	71
3814	69	1743	76	1430	17
3849	76	1787	305	1465	11
3909	112	1797	148	1505	151
3927	56	1840	638	1536	26
		1854	111	1572	16
		1959	1001	1704	44
		3451	5	1745	59
		3732	305	1786	304
		3820	90	1804	144
		3908	114	1838	796
		3937	61	1856	89
		3968	217	1866	99
		4144	125	1938	1073
				3450	5
				3761	278
				3811	168
				3887	379
				3909	125
				3930	637
				3944	71
				4132	110
				4145	135

plexes which display the quite usual tendency to approach the stability of fully hydrated species:

$$9GUA \cdot 2H_2O > 7GUA \cdot 2H_2O.$$

IR FREQUENCIES

The present IR frequencies are intended to guide experimental investigators in the study of the title species. As can be expected from the calculated data, it is clear that the major differences between the spectra of isolated species and complexes are the intermolecular vibration modes (50–300 cm^{-1}) and the valence *sym* and *antisym* OH and NH vibrations (3400–4100 cm^{-1}). The predicted shifts of vibrational frequencies upon the complexation can be applied to an identification of these species in the isolated-matrix experiments. Although the HF/6-31G(*d*) level harmonic frequencies overestimate the experimentally observed unharmonic spectrum by approximately 10%, the differences between predicted and observed shifts are usually not larger than 10–20 cm^{-1}.

Conclusion

In this article, the stability, the harmonic IR frequencies, and the structural parameters at the post-Hartree–Fock level are revealed. The principal conclusions from this study are the following:

1. The structural parameters of mono- and dihydrated oxo-amino-guanine tautomers calculated at the MP2/6-31G* level permits the

TABLE V
Calculated IR frequences (FREQ, in cm^{-1}) and absolute intensities (INT, km mol^{-1}) for 7-guanine species.

7-Guanine		7GUA · H_2O		7GUA · $2H_2O$	
FREQ	INT	FREQ	INT	FREQ	INT
160	22	49	2	33	1
169	6	111	11	57	2
213	3	158	20	59	1
324	1	174	1	147	10
344	110	192	5	160	7
366	1	251	59	167	11
406	1	287	74	180	4
509	133	333	41	202	114
523	3	352	24	219	7
586	5	387	31	235	3
644	84	394	53	317	134
669	205	422	118	345	33
685	56	451	71	365	4
702	44	544	16	385	4
733	21	583	276	399	1
814	51	608	30	433	43
824	49	665	172	484	138
869	100	680	1	508	74
907	14	694	150	526	104
1027	4	746	25	553	294
1041	1	778	1	594	13
1135	19	832	21	678	197
1203	5	848	161	691	2
1223	40	896	87	699	104
1259	14	908	43	741	41
1306	85	1027	6	798	9
1408	25	1050	3	811	10
1452	19	1143	41	836	346
1482	83	1194	57	869	63
1547	233	1229	17	905	14
1607	64	1259	28	925	187
1650	3	1336	78	1033	3
1710	1	1369	65	1038	1
1755	304	1461	113	1151	20
1804	72	1504	186	1211	21
1854	602	1551	208	1234	16
1970	1003	1591	251	1265	13
3450	6	1619	84	1319	67
3799	56	1673	169	1410	45
3851	79	1702	60	1469	5
3908	49	1787	618	1502	192
3913	142	1812	128	1547	191
		1832	156	1608	74
		1871	508	1661	66
		3443	7	1720	29
		3825	51	1756	166
		3835	608	1811	46
		3922	135	1849	843
		3944	46	1855	129
		3987	311	1864	67
		4144	156	1917	1132
				3447	7
				3734	381
				3811	116
				3893	348
				3917	131
				3934	711
				3937	10
				4134	111
				4146	136

TABLE V
(Continued)

classification of the intermolecular hydrogen bonds as rather weak.

2. It is found that the interaction of guanine tautomers with two water molecules changes the order of gas-phase stability (7GUA 9GUA) into the order which corresponds to the stability of the guanine tautomers in a polar solvent (9GUA ≫ 7GUA).
3. The main difference in the calculated IR frequences of isolated, monohydrated, and dihydrated species are found in the region of valence *sym* and *antisym* vibrations of OH and NH bonds and in the region related to the intermolecular vibrations.

ACKNOWLEDGMENTS

The authors thank the Mississippi Center for Supercomputing Research for computational facilities. This work was facilitated by NSF Grant No. OSR-945285, by the Office of Naval Research Grant No. N00014-95-1-0049, and by a contract (DAAL 03-89-0038) between the Army Research Office and the University of Minnesota for the Army High Performance Computing Research Center under the auspices of the Department of the Army, Army Research Laboratory cooperative agreement No. DAAH04-95-2-0003/contract no. DAAH04-95-C-008. The policy of the government and no official endorsement should be inferred.

References

1. L. Goodman, J. Leszczynski, and T. Kundu, J. Am. Chem. Soc. **115**, 11991 (1993).
2. (a) S. Szczepaniak, M. Szczesniak, W. Szajda, W. B. Person, and J. Leszczynski, Can J. Chem. **69**, 1705 (1991); (b) M. J. Nowak, L. Lapinski, J. Fulara, A. Les, and L. Adamowicz, J. Phys. Chem. **96**, 1562 (1992); (c) K. Szczepaniak, W. B. Person, J. Leszczynski, and J. Kwiatkowski, Postepy Biochem. **41**, 300 (1995); (d) J. Florian, V. Baumruk, and J. Leszczynski, J. Phys. Chem. **100**, 5578 (1996); (e) H. Vranken, J. Smets, G. Maes, L. Lapinski, M. J. Nowak, and L. Adamowicz, Spectrochim. Acta A **50**, 875 (1994).
3. (a) A. Held and D. W. Pratt, J. Am. Chem. Soc. **115**, 9708 (1993); (b) J. Del Bene, J. Phys. Chem. **98**, 5902 (1994); (c) A. Sobolewski and L. Adamowicz, J. Chem. Phys. **102**, 5708 (1995); (d) F. Buyl, J. Smets, G. Maes, and L. Adamowicz, J. Phys. Chem, **99**, 14967 (1995); (e) J. Smets, L. Adamowicz, and G. Maes, J. Phys. Chem. **99**, 6387 (1995); (f) J. Smets, L. Adamowicz, and G. Maes, J. Phys. Chem. **100**, 6434 (1996).
4. (a) K. Szczepaniak and M. Szczesniak, J. Mol. Struct. **156**, 29 (1987); (b) J. Leszczynski, Chem. Phys. Lett. **174**, 347, (1990); (c) M. J. Nowak, L. Lapinski, J. S. Kwiatkowski, and J. Leszczynski, in *Current Trends in Computational Chemistry*, J. Leszczynski, Ed. (World Scientific, Singapore, 1997), Vol. 2, p. 140.
5. U. Thewald, C. E. Bugg, and R. E. Marsh, Acta Crystallogr. B **27**, 2358 (1971).
6. (a) X.-C. Wang, J. Nichols, M. Feyereisen, M. Gutowski, J. Boatz, D. J. Haymet, and J. Simons, J. Phys. Chem. (1991); **95**, 10419; (b) P. G. Jasien and W. J. Stevens, **84**, 3271 (1986); (c) S. Scheiner and L. Wang, J. Am. Chem. Soc. **115**, 1958 (1993); (d) J. Pranata, G. D. Davis, J. Phys. Chem. **99**, 14340 (1995); (e) H. B. Schlegel, P. Gund, and E. M. Fluder, **104**, 5347 (1982).
7. (a) H. Guo and M. Karplus, J. Phys. Chem. **98**, 7104 (1994); (b) D. A. Dixon and K. D. Dobbs, J. Phys. Chem. **98**, 13436 (1994).
8. See, e.g., W. H. Hehre, L. Radom, P. v. Schleyer, and J. A. Pople, *Ab Initio Molecular Orbital Theory* (Wiley, New York, 1986).
9. M. J. Frish, G. W. Trucks, M. Head-Gordon, P. M. W. Gill, M. W. Wong, J. B. Foresman, H. B. Johnson, H. B. Schlegel, M. A. Robb, E. S. Replogle, R. Gomperts, J. L. Andres, K. Reghavachari, J. S. Binkley, C. Gonzalez, R. L. Martin, D. J. Fox, D. J. DeFrees, J. Baker, J. J. J. Stewart, J. A. Pople, *GAUSSIAN 92, Revision D* (Gaussian Inc., Pittsburgh, 1992).
10. H. B. Schlegel, J. Comp. Chem. **3**, 314 (1982).
11. C. Møller and M. S. Plesset, Phys. Rev. **46**, 618 (1934).
12. W. W. Cleland and M. M. Kreevoy, Science **264**, 1887 (1994).
13. C. Colominas, F. J. Luque, and M. Orozco, J. Am. Chem. Soc. **118**, 6811 (1996).

A Molecular Orbital Study of the Dimerization Process of Vinyl Monomers

M. A. MORA

Departamento de Química, Universidad Autónoma Metropolitana, Campus Iztapalapa, Mexico, D.F., CP. 09300

Received 8 April 1997; revised 1 August 1997; accepted 6 August 1997

ABSTRACT: Molecular orbital calculations were carried out for the dimerization step in the polymerization process of vinyl acetate and styrene through free radicals and ionic mechanisms. The calculations were performed for monomers, dimers, their positive and negative ions, and free radicals. The minimum-energy geometry is achieved in all cases, the geometrical and electronic parameters are analyzed, a dimerization reaction pathway is proposed, and the heats of polymerization obtained are in excellent agreement with experimental data. © 1997 John Wiley & Sons, Inc. Int J Quant Chem 65: 767–785, 1997

Introduction

In polymers, the sequence distribution, tacticity, and, in general, the intramolecular structure are important, because they may suply information about the monomer addition process, e.g., about the preference of monomers to add in the iso- or syndiotactic configuration [1,2]. Moreover, knowledge about the intramolecular structure is of paramount importance for the understanding of the relations between structure and polymer properties [3] and there is significant interest in characterizing polymeric materials, especially blends at the molecular level. This interest is due, in part, to the tremendous technological importance of polymer blends. The bulk, macroscopic properties of such materials are determined by the microscopic structure that, in turn, is critically dependent upon the degree of molecular mixing between the blend components. The peculiar properties of polymer materials arise from differences between the thermodynamic interactions in systems containing macromolecules and those systems of only small molecules.

The nature of intermolecular interaction determines the microscopic structure in any condensed-phase system. However, when the system contains macromolecules, there is additional complexity due the intramolecular considerations; the number of configurations available to a polymer chain, although restricted by covalent bond geometries, is vast. Thus, the morphology of a

International Journal of Quantum Chemistry, Vol. 65, 767–785 (1997)
© 1997 John Wiley & Sons, Inc.
CCC 0020-7608 / 97 / 050767-19

chain involves the interplay between the interactions of the polymer with its environment and the possible chain conformations. Since the interactions between the chains of a polymer may play an important role in defining the ultimate properties of these polymers, it is desirable to investigate quantitatively the structure of isolated polymer chains. The geometry of the dimers may be important in defining the interactions between neighboring chains of the polymer and in the monomer addition mechanism. To understand better the geometry of these dimers, model compounds of poly(vinyl acetate) and polystyrene were investigated.

In this work, we used vinyl acetate (VA) and styrene (ST) dimer bond dissociation energies to model the reverse reaction of a chain-growth polymerization, predicting the heat of polymerization. Also, we investigated the evolution of the conformations and the binding process when a monomer approaches the active species, an ion or a free radical. In other words, we explored a reaction coordinate.

We present results of semiempirical and ab initio molecular orbital calculations for 2,4-diacetate butane as a model compound of poly(VA) and 2,4-diphenylbutane as model substance of PS. All calculations were performed with the system of programs Gaussian94 [4]. Two levels of theory were used: semiempirical calculations with the Austin model 1 Hamiltonian (AM1) [5] and self-consistent-field calculations using unrestricted open-shell Hartree–Fock wave functions (UHF) [6] with two different Gaussian orbital basis sets: 3-21G* [7] and 6-31G* [8].

Using geometrical parameters obtained with ab initio methods for small systems, the geometry optimization of bigger molecules could be carried out using semiempirical methods like AM1 without unduly high computer and memory requirements. The AM1 method embodies the approximations that are inherent to the neglect of diatomic differential overlap (NDDO) formalism [9] and overcome the major weakness of the modified neglect of differential overlap (MNDO) method [10] on which it is based. It is known that AM1 pro-

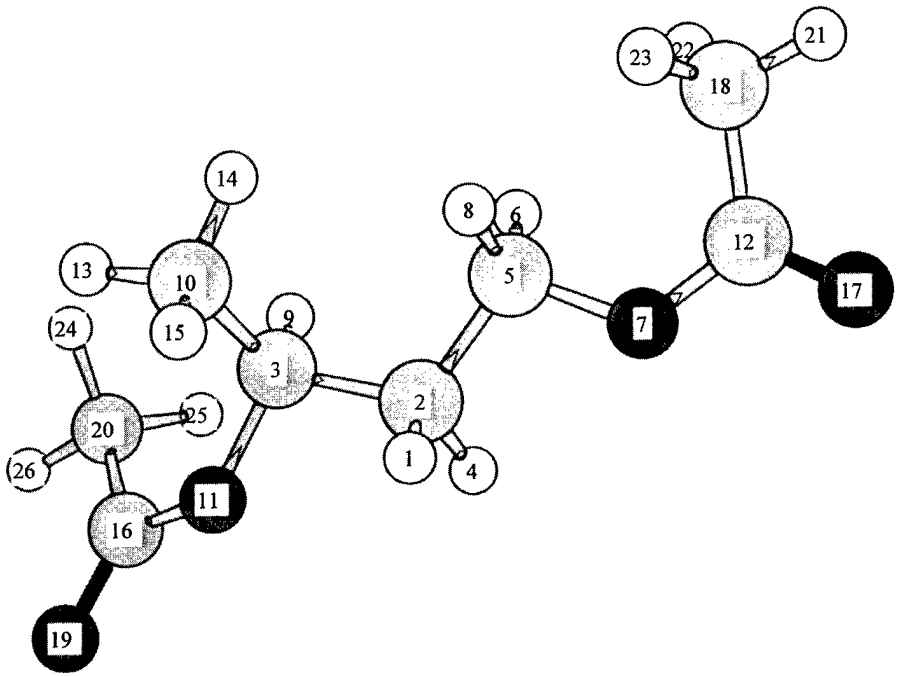


FIGURE 1. Dimer of VA; structure optimized with the HF / 6-31G* basis set. The numbering is used throughout the text.

duces fairly accurate equilibrium geometries, orbital orderings, and partial charges [11].

Methodology

The minimum-energy conformation for the monomers of VA and ST were obtained in a previous work [12]. Taking as a basis those geometries, model compounds to represent dimers were formed; in each case, the initial geometry corresponds to an isotactic all-*trans* conformation.

With those geometries, an optimization process was initiated. In the first step, full-optimization calculations were made for each dimer to find the global minimum. With the resulting geometries, rotational barriers were calculated, taking as rotation axes the skeletal bonds between heavy atoms. The torsion angles were changed with increments of 20° in each particular case. For each point, all the non-hydrogen geometrical parameters were varied simultaneously.

To form the free radical of each dimer, one hydrogen atom was removed from the optimized VA dimer and ST dimer models, and by assigning a positive or negative charge, the corresponding cations or anion were formed. These processes were made with the optimization of the geometrical parameters for the atoms nearest to the site where the hydrogen atom was removed. In the next step, the bond between monomeric units was broken; it was done by changing the C_2—C_3 (see Fig. 1) bond distance for the VA dimeric species and the C_4—C_6 (see Fig. 6) bond distance for the ST dimeric species. This bond enlargement was made in steps of 0.2 Å from the equilibrium distances to 4.5 Å. In this step, two types of calculation were made: In the first, only the geometrical parameters of the atoms nearest to the bond-breaking site were optimized, and in the second one, all the geometrical parameters were optimized. A schematic view of the process is

$$\begin{aligned}
&\text{(a)}\quad \mathrm{A{-}A} \rightarrow \mathrm{A{-}A^{\cdot}} + \mathrm{H^{\cdot}} \\
&\text{(b)}\quad \mathrm{A{-}A^{\cdot}} \rightarrow \mathrm{A} + \mathrm{A^{\cdot}} \\
&\text{(c)}\quad \mathrm{A{-}A^{+}} \rightarrow \mathrm{A} + \mathrm{A^{+}} \qquad (1) \\
&\text{(d)}\quad \mathrm{A{-}A^{-}} \rightarrow \mathrm{A} + \mathrm{A^{-}},
\end{aligned}$$

where A—A represents a dimer molecule formed by two monomers of A, A— $A^{\cdot}$ is the free radical of the dimer, A—A^{+} is a cationic dimer, and A—A^{-} is an anionic dimer.

The minimum-energy conformation and total energy for the different monomeric (A, $A^{\cdot}$, A^{+}, A^{-}) and dimeric (A—A, A— $A^{\cdot}$, A—A^{+}, A—A^{-}) species were found by allowing all atoms to move. The bond dissociation energy can be calculated in two different ways: as the difference between the sum of the calculated total energies for the right-side species in its minimum-energy conformation and the total energy of the left-side compound also in its minimum energy conformation, and from the potential energy curves for the dissociation of VA and ST dimeric species [Eqs. (Ib)–(Id)], taking the difference between the energy of the optimized dimeric species (initial point in the curve) and the energy value where the curve becomes asymptotic.

TABLE I
Dimer of VA *z*-matrix input for the Gaussian-94 program; the numbers on the atoms correspond to Figure 1.

Dimer of VA						
H						
C	1	R2				
C	2	R3	1	A3		
H	2	R4	1	A4	3	D4
C	2	R5	1	A5	3	D5
H	5	R6	2	A6	1	D6
O	5	R7	2	A7	6	D7
H	5	R8	2	A8	6	D8
H	3	R9	2	A9	1	D9
C	3	R10	2	A10	9	D10
O	3	R11	2	A11	9	D11
C	7	R12	5	A12	2	D12
H	10	R13	3	A13	2	D13
H	10	R14	3	A14	13	D14
H	10	R15	3	A15	13	D15
C	11	R16	3	A16	2	D16
O	12	R17	7	A17	5	D17
C	12	R18	7	A18	17	D18
O	16	R19	11	A19	3	D19
C	16	R20	11	A20	19	D20
H	18	R21	12	A21	7	D21
H	18	R22	12	A22	21	D22
H	18	R23	12	A23	21	D23
H	20	R24	16	A24	11	D24
H	20	R25	16	A25	24	D25
H	20	R26	16	A26	24	D26

The heat of dissociation obtained in this way must be the negative of the polymerization heat in terms of monomer unit added. The minimum-energy geometry and the total energy for each radical, cation, and anion and monomeric and dimeric species were found by full optimization.

Results and Discussion

VINYL ACETATE

In previous studies of the VA monomer [12], we reported an energetically more favorable conformation. Using that geometry, the dimer of VA was formed. This model compound has the vinyl groups in a parallel position perpendicular to the skeletal sequence, and this conformation corresponds to an isotactic all-*trans*. The various atoms have been numbered (Fig. 1) and will hereafter be referred to by these numbers. With this initial geometry, a calculation changing simultaneously all the geometric parameters was made. With this new geometry and taking the bond C_2—C_5 as the axis of rotation, the rotational barrier was calculated from 0° to 360° with angle increments of 20°; 0° corresponds to having the bond C_5—C_7 *cis* to the bond C_2—C_3. In each point, the position of the acetate groups atoms was optimized. From this rotational barrier, the minimum-energy conformation was taken as the initial one for the next rotational barrier calculation, this time through the bond C_2—C_3. Optimization of the geometrical parameters for the atoms neighboring this bond was made. Again, with the new minimum-energy conformation, a full-optimization calculation was carried out. Table I defines the notation we use for the internal coordinates of the VA dimer in the format of the z-matrix input for the program Gaussian 94. The UHF/6-31G*-optimized values of the intermolecular distances, *Rj*, the bond angles, *Aj*, and the dihedral angles, *Dj*, are given in Tables II, III, and IV, respectively. The first two

TABLE II
Internuclear distances for the different dimeric species of VA, calculated with the UHF / 6-31G(*d*) method.

	Initial parameters	Optimized parameters	Anion	Cation	Free radical
R2	1.08105	1.084	1.0884	1.0817	1.0846
R3	1.52795	1.5269	1.5366	1.5431	1.5268
R4	1.0815	1.0835	1.0898	1.0932	1.0885
R5	1.52584	1.5211	1.4954	1.473	1.4959
R6	1.0837	1.0857	1.0761	1.0816	1.0783
R7	1.44419	1.4118	1.3928	1.2428	1.3696
R8	1.08037	1.0826			
R9	1.08208	1.083	1.0866	1.0839	1.0831
R10	1.52993	1.5237	1.5296	1.5237	1.5228
R11	1.4502	1.4202	1.3786	1.3976	1.4196
R12	1.36113	1.3365	1.3295	1.5175	1.3455
R13	1.08371	1.0844	1.0804	1.0823	1.0846
R14	1.08271	1.085	1.0908	1.0883	1.0845
R15	1.08225	1.0842	1.0893	1.0836	1.084
R16	1.36081	1.3354	1.486	1.3618	1.3353
R17	1.1968	1.1826	1.1876	1.1522	1.1803
R18	1.51217	1.5117	1.511	1.4847	1.5092
R19	1.19753	1.1832	1.2647	1.1745	1.1832
R20	1.51332	1.5131	1.5217	1.5086	1.513
R21	1.07769	1.079	1.0801	1.0794	1.0792
R22	1.08359	1.0841	1.084	1.0834	1.0848
R23	1.08314	1.0844	1.0828	1.0834	1.0834
R24	1.08328	1.0836	1.0885	1.0835	1.0835
R25	1.08254	1.0847	1.0948	1.0851	1.0848
R26	1.07822	1.079	1.0875	1.0787	1.079!

TABLE III
Bond angles for the different dimeric species of VA, calculated with the UHF / 6-31G(*d*) method.

	Initial parameters	Optimized parameters	Anion	Cation	Free radical
A3	109.20119	109.3892	109.5052	111.3468	109.4869
A4	107.68760	107.0329	106.1593	107.4943	106.5460
A5	109.67980	109.5263	110.0410	110.3933	109.3951
A6	110.86996	110.6728	120.5230	122.9585	119.9846
A7	105.08688	106.4235	117.4401	120.6877	112.5518
A8	111.52025	111.2892			
A9	110.00961	108.8651	108.8560	109.0228	108.8957
A10	113.59662	114.0690	112.3991	111.9307	113.2548
A11	104.15747	105.1302	107.0583	102.8399	105.3686
A12	124.38530	123.3404	122.2633	119.8762	123.1970
A13	110.80390	110.8378	107.6032	110.7637	111.0958
A14	111.23519	111.3142	112.5814	111.4145	110.9288
A15	109.16586	110.2305	110.2342	110.3348	109.9922
A16	125.74818	125.2239	114.661	125.4188	125.1943
A17	119.24141	119.1289	119.7086	116.5776	118.7749
A18	116.88147	118.1824	117.5256	107.7608	117.6845
A19	119.29680	119.0126	116.6171	117.5297	119.0181
A20	117.31459	118.8165	104.436	118.3378	118.7979
A21	107.87529	107.9146	108.1808	108.3815	107.9812
A22	111.03209	111.4270	110.5046	109.4000	110.6888
A23	110.86750	111.0104	111.1130	109.3901	111.2064
A24	111.64095	112.0892	112.1481	112.2392	112.1051
A25	110.65525	110.7329	111.3839	110.7128	110.7063
A26	107.61335	107.5731	109.1456	107.5398	107.5774

column data correspond to the initial (AM1-optimized) and UHF/6-31G*-optimized values for the VA dimer, respectively. The last three data columns give the UHF/6-31G*-optimized parameters values for the anion, cation, and free-radical dimeric species. By adopting the convention given by Flory and coworkers [13], the final geometry corresponds to a *tg* conformation. Figure 1 shows the VA dimer final conformation.

With the minimum-energy conformation for the dimer obtained in this way, the bond distance C_5—H_8 was changed by increments of 0.2 Å from the equilibrium value to 5 Å. This bond enlargement is equivalent to the dimer dissociation in one hydrogen and one dimer free radical. This dissociation process was made with optimization of the geometrical parameters for the atoms nearest to the bond which is being broken. In Table III it is possible appreciate how the bond angles C_2—C_5—O_7 and C_2—C_5—H_6 change from almost tetrahedral in the initial conformation to almost trigonal when the system is dissociated, and in Table V, how the electronic densities for the atoms neighboring C_5 are substantially changed. With the dimer free-radical geometry obtained this way and the program parameter charge made equal to zero, one, or minus one, the geometries and heats of formation were obtained for the free-radical, cation, and anion dimeric species, respectively.

For each one of these three species, the C_2—C_3 bond distance was changed from the equilibrium value to 4.2 Å with increments of 0.3 Å. Figure 2 shows the UHF/3-21G* potential energy curves obtained for the dissociation of the dimeric species. The dissociation products are one monomer and one ionic or free-radical monomeric species. Around the distance of 2.0 Å, the energy is a maximum, which means that the dimeric species are dissociated and the C_2—C_3 bond is almost broken. However, between 2.0 and 4 Å, some attractive interactions occur principally between

TABLE IV
Dihedral angles for the different dimeric species of VA, calculated with the UHF / 6-31G(*d*) method.

Atom	Initial parameters	Optimized parameters	Anion	Cation	Free radical
D4	−118.03805	−117.3563	−116.4926	−118.5230	−117.2242
D5	124.37077	125.3241	125.3115	128.0308	124.1003
D6	−177.00407	−176.0425	−167.6353	−165.8375	−166.8072
D7	−119.10359	−119.5823	−141.3371	−177.6376	−141.3146
D8	121.47613	120.4413			
D9	−179.21453	−177.4649	−181.4689	−176.8852	−180.4869
D10	−124.41414	−122.9400	−119.3468	−122.5343	−122.6618
D11	118.08135	117.7678	119.0362	118.2071	117.8713
D12	−178.27760	−177.9501	−95.9448	−182.6225	−167.3026
D13	−175.48810	−174.8035	−178.4848	−176.9629	−177.8408
D14	−120.13487	−119.7525	−120.2503	−119.3246	−120.1987
D15	119.16572	119.4663	118.6905	119.5042	119.5933
D16	−151.51809	−146.3294	−145.8997	−150.9679	−147.3915
D17	−178.93995	−178.8368	−182.3227	−359.1194	−175.9514
D18	−179.80448	−179.8345	−180.9907	−180.0441	−179.6381
D19	−166.59531	−171.7614	−28.5634	−171.9048	−171.9182
D20	−178.31833	−178.4059	−134.4832	−178.1465	−178.3473
D21	−179.42262	−178.4141	−179.1716	−179.9199	−186.8656
D22	119.81004	120.029	120.3031	120.6593	119.2167
D23	−119.65612	−119.6049	−120.6860	−120.6502	−120.7299
D24	−62.28269	−58.5701	−51.6634	−58.0384	−58.2904
D25	120.90497	120.7807	120.8520	121.2944	120.7116
D26	−119.74459	−120.1251	−120.4455	−119.9548	−120.1626

O_7 and the hydrogens H_1 and H_4. In Tables II–IV are the geometrical parameters obtained for the dimer anion, cation, and free radical of the dissociated VA dimer. Notice the geometry adopted by the monomeric species.

Figures 3 and 4 show the evolution of the Mulliken and electrostatic potential net atomic charges calculated for the skeletal atoms as a function of the C_2—C_3 bond distance for the cation of the dimer when calculated with the UHF/3-21G(*d*) method. It is necessary to point out the sign and magnitude of the charges on the C_3 and C_5 atoms. In the final state, C_3 has a positive net atomic charge because when the C_2—C_3 bond is broken a monomeric cation with an electron-deficient carbon atom is formed. The cationic character is on C_3. On the other hand, the other dissociation product is a monomeric unit with a double bond between C_2 and C_5. This double bond is evident from the net atomic charges on the C_2 and C_5 atoms which have Mulliken atomic charge negative values. Figure 4 shows how the atomic charge values calculated from the electrostatic potential have almost the same behavior in respect to the C_2—C_3 bond distance. The geometrical parameters for the dimeric species, neutral, anionic, cationic, and free radical, of the VA are shown in Tables II–IV. Notice the monomer geometry which is planar and the nonplanar geometry for the monomeric species. Figure 5 shows for the free-radical dimer the geometry adopted by the dissociation products.

The process in the opposite direction must be a dimerization process, which may be interpreted as the propagation step in a polymerization mechanism. The heats of polymerization calculated for VA from the potential energy curves are −18.627 kcal/mol for the anionic mechanism, −31.778 kcal/mol for the cationic mechanism, and −23.022 kcal/mol for the free-radical mechanism; the experimental value from the literature [14] is −21.0 kcal/mol.

TABLE V

Total atomic charges from Mulliken population analysis for the dimeric species of VA, calculated with the UHF / 6-31G(*d*) method.

Atom	VA	VA anion	VA cation	VA free radical
1 H	0.205172	0.147594	0.287148	0.287148
2 C	−0.332017	−0.357533	−0.476120	−0.476120
3 H	0.144219	0.245764	0.154746	0.154746
4 C	0.207229	0.181474	0.290899	0.290899
5 H	−0.002987	0.120137	0.400659	0.400659
6 C	0.159126	0.173557	0.318052	0.318052
7 H	−0.609809	−0.597995	−0.514816	−0.514816
8 C	0.167823			
9 H	0.167434	0.146838	0.193760	0.193760
10 H	−0.498400	−0.492737	−0.511565	−0.511565
11 C	−0.623438	−0.735056	−0.634492	−0.634492
12 C	0.774221	0.770519	0.751987	0.751987
13 C	0.176504	0.218369	0.223286	0.223286
14 H	0.161408	0.090427	0.154930	0.154930
15 H	0.192680	0.113955	0.215910	0.215910
16 C	0.776163	0.509799	0.769270	0.769270
17 C	−0.526482	−0.561445	−0.399745	−0.399745
18 C	−0.621054	−0.610418	−0.579832	−0.579832
19 H	−0.528501	−0.790477	−0.478013	−0.478013
20 H	−0.624681	−0.492259	−0.629457	−0.629457
21 H	0.229435	0.196462	0.276367	0.276367
22 H	0.192066	0.196666	0.262972	0.262972
23 H	0.195782	0.215863	0.263654	0.263654
24 H	0.190545	0.100517	0.197866	0.197866
25 H	0.197787	0.099525	0.202732	0.202732
26 H	0.229773	0.110453	0.259804	0.259804

STYRENE

Table VI defines the notation used for the internal coordinates of the ST dimer in the format of the *z*-matrix. The optimized values of the internuclear distances, *Rj*, the bond angles, *Aj*, and the dihedral angles, *Dj*, are given in Tables VII, VIII, and IX, respectively. In the first and second columns are, respectively, the AM1- and UHF/6-31G*-optimized parameter values for the dimer of styrene. The last three data columns give the UHF/3-21G*-optimized parameters for the anion, cation, and free radical of the ST dimer. The atomic numbering is presented in Figure 6.

The curves of the C_4—C_6 bond distance vs. the UHF/3-21G* energy for the dissociation of the three species of styrene are shown in Figure 7. There, the three curves present a maximum between 2.1 and 2.4 Å, and every one has a different form. The curve corresponding to the ST cation shows asymptotic behavior from 2.5 Å, which means that the C_4—C_6 bond is broken, forming a styrene monomer with a double bond between the C_6 and the C_{11} atoms and an ST monomer cation. Figure 8 shows the dissociation products. The cationic character of the dimer can be appreciated in Figure 9 by the net atomic charge on the carbon atoms 4 and 11 before and after the dimer dissociation. The free-radical curve reaches its asymptotical behavior at approximately 2.8 Å. The dissociation products of the dimer anion are a monomeric anion and a monomer. The net atomic charge on C_{11} is from −0.5 at the equilibrium distance value to around −0.2 for distances greater than 2.8 Å. On the other hand, the net atomic charge on C_4 is from almost zero to −0.55. This fact confirms that in this case, again, the dissociation is undertaken given the above-mentioned products.

When the C_4—C_6 bond is breaking, there are changes in the bond and dihedral angles of the atoms C_8 and H_7 which are bonded to C_4. Figure

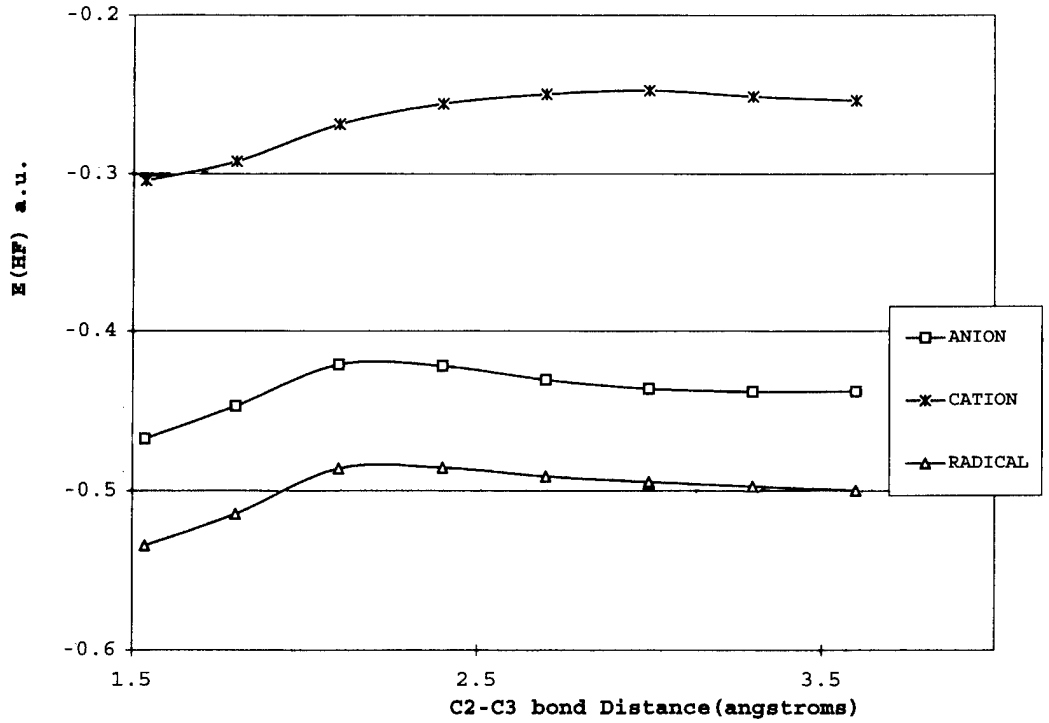


FIGURE 2. Potential energy curve for the VA dimeric species, calculated with the UHF / 3-21G* model chemistry. The zero energy corresponds to 606.0 au.

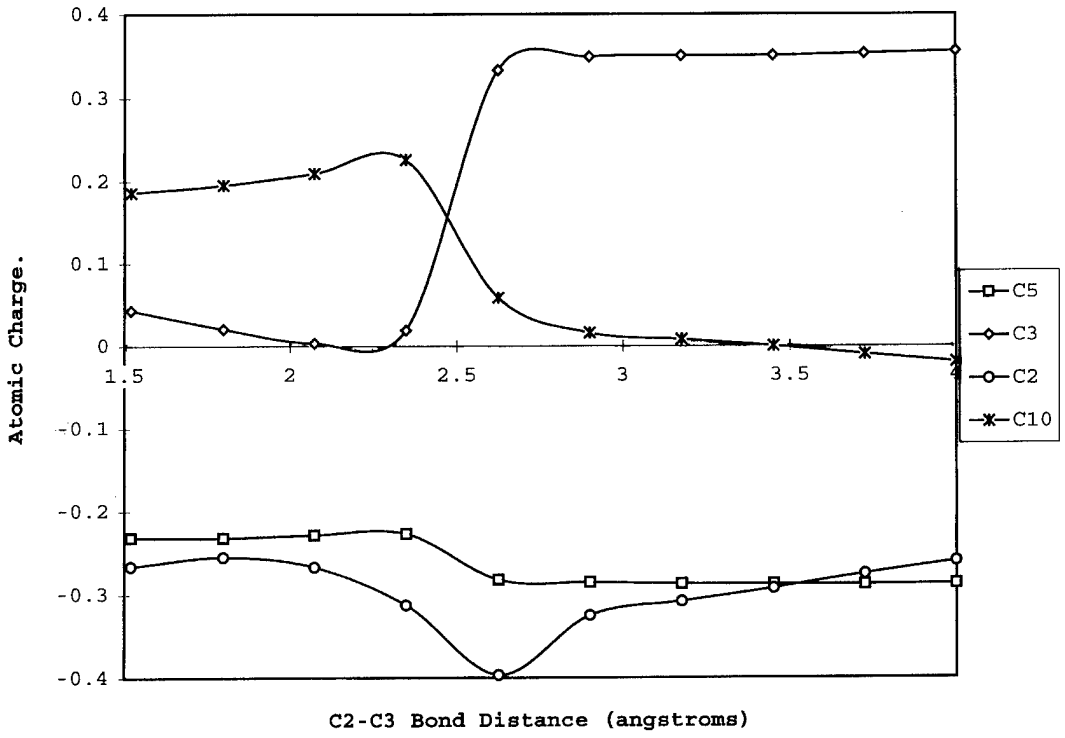


FIGURE 3. Change of the Mulliken net atomic charges for the main-chain atoms during the dissociation of the VA cation of the dimer, calculated at the UHF / 3-21G* level of theory.

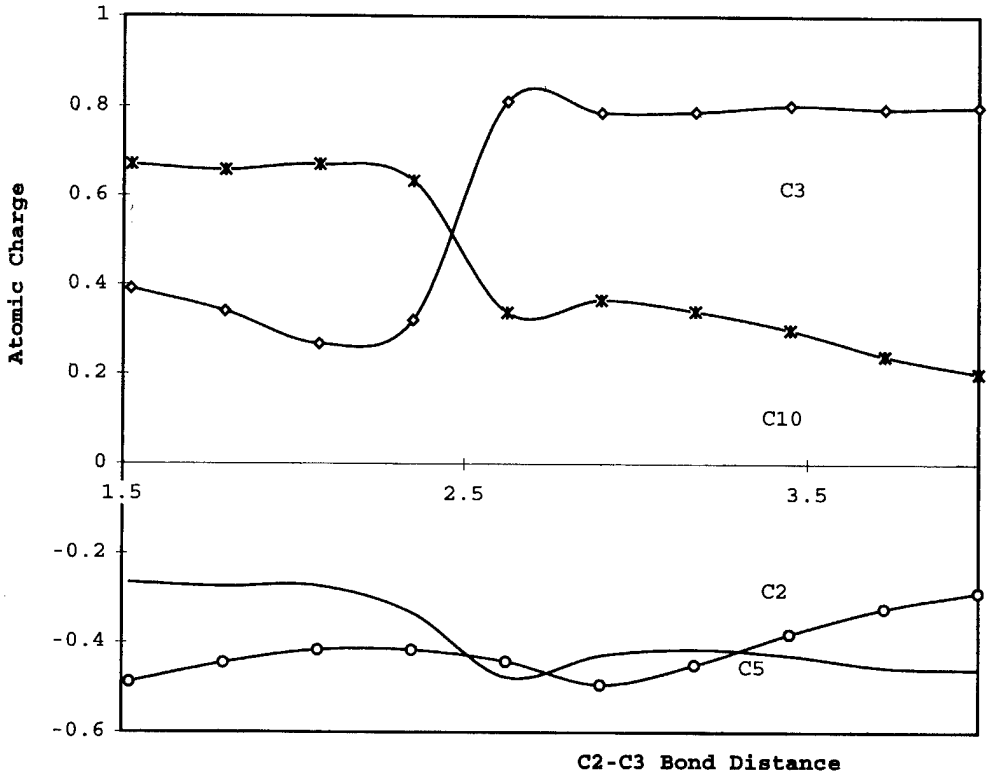


FIGURE 4. Change of the electrostatic potential net atomic charges for the main-chain atoms during the dissociation of the VA cation of the dimer, calculated at the UHF / 3-21G* level of theory.

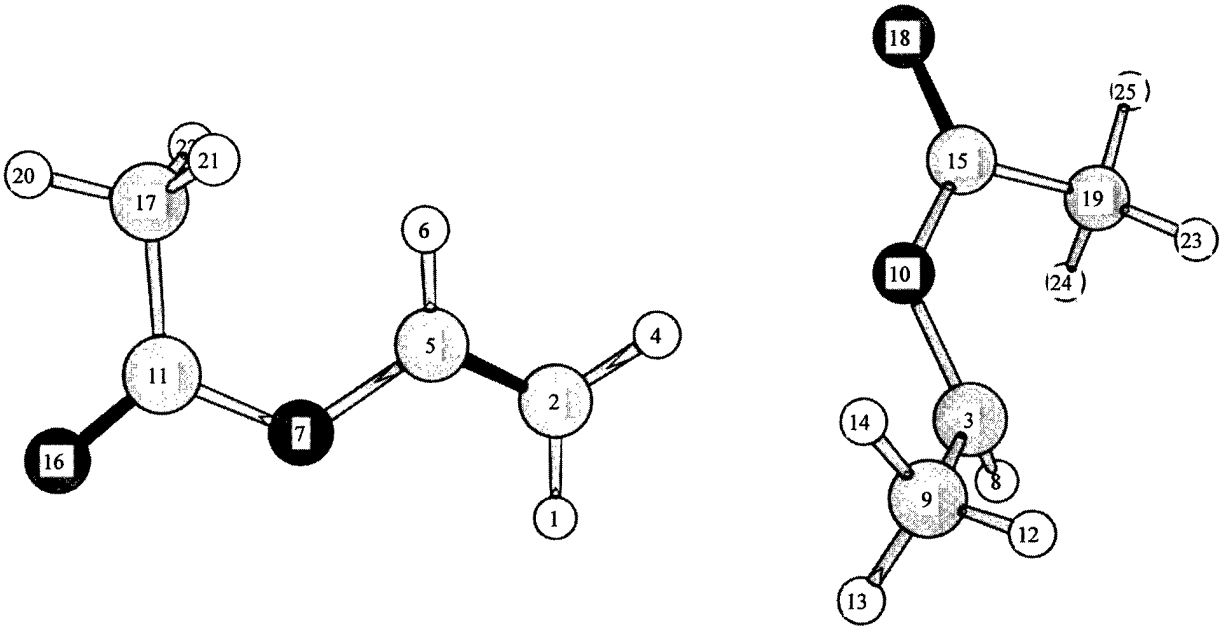


FIGURE 5. Dissociation products of the VA free radical of the dimer, obtained at the UHF / 3-21G* level of theory.

TABLE VI
ST z-matrix input for the Gaussian-94 program; the numbering of the atoms correspond to Figure 6.

H							
C	1	R2					
H	2	R3	1	A3			
C	2	R4	1	A4	3	D4	0
H	2	R5	1	A5	3	D5	0
C	4	R6	2	A6	1	D6	0
H	4	R7	2	A7	6	D7	0
C	4	R8	2	A8	6	D8	0
H	6	R9	4	A9	2	D9	0
H	6	R10	4	A10	9	D10	0
C	6	R11	4	A11	9	D11	0
C	8	R12	4	A12	2	D12	0
C	8	R13	4	A13	12	D13	0
H	11	R14	6	A14	4	D14	0
H	11	R15	6	A15	14	D15	0
C	11	R16	6	A16	14	D16	0
C	13	417	8	A17	4	E17	0
C	12	R18	8	A18	4	D18	0
H	12	R19	8	A19	18	D19	0
H	13	R20	8	A20	17	D20	0
C	17	R21	13	A21	8	D21	0
H	17	R22	13	A22	21	D22	0
H	18	R23	12	A23	8	D23	0
C	16	R24	11	A24	6	D24	0
C	16	R25	11	A25	24	D25	0
H	21	R26	17	A26	13	E26	0
C	25	R27	16	A27	11	D27	0
C	24	R28	16	A28	11	D28	0
H	24	R29	16	A29	28	D29	0
H	25	R30	16	A30	27	D30	0
C	27	R31	25	A31	16	D31	0
H	27	R32	25	A32	31	D32	0
H	28	R33	24	A33	16	D33	0
H	31	R34	27	A34	25	D34	0

10 shows how the bond angles of the C_6, C_8, H_7, H_{10}, and C_{11} atoms change from almost tetrahedral to trigonal values. The variation of the bond angle defined by C_2—C_4—C_6 is represented by the lowest curve in Figure 10. This curve and the curves in Figure 11 provide information about the trajectory followed by the monomer when it is moving away from the other fragment. Such changes are because on C_4 and C_6 a hybridization change is occurring from SP_3 to SP_2. Figure 12 shows the change of the total overlap population on the bonds of the main chain as a function of the bond distance. There it is possible to appreciate a change from a single to a double bond between the C_6 and C_{11} atoms. Also, between C_4 and C_6, there is a change from a characteristic value of a single bond to a zero total overlap population value when this bond has been broken. The change in the C_6 bond angle from 112 Å to almost 90 Å shows the trajectory followed by the monomer cation when it is approaching the molecular monomer. Figure 8 presents the dissociation products.

The energy difference between products and reagents [see Eq. (1)] could be a measure of the polymerization heat. From the dissociation curves, the calculated values for ST are −16.31, −19.45, and −21.34 kcal/mol for the anionic, cationic, and free-radical mechanism, respectively. The values calculated for the cationic species are in excellent agreement with the experimental value which is −16.7 kcal/mol [15,16].

Conclusions

For VA and ST, we optimized the geometry of monomers and dimers in their neutral, cationic, anionic, and free-radical forms. The heats of polymerization obtained from the dissociation process are in good agreement with the values reported in the literature. With the methods used in this work, it is possible to appreciate the rearrangement of the electronic density. In all the cases where a bond rupture or formation (ionization and dimerization) occurred, changes in the hybridization of the atoms directly involved in such processes were observed.

From the energy differences for the process of dimerization, it is possible to see that for the VA the anionic mechanism seems to be the most feasible one, followed by the free radicals. The more-favored mechanism for ST is the anionic followed by the cationic. This order of polymerization is in excellent agreement with the Schildknecht classification [17].

The results enable us to postulate that heats of polymerization can be reasonably estimated by ab initio quantum mechanical calculations. Many possibilities may be suggested for the reaction pathway followed by the monomer in their approach to the other species, but only one path is possible in the dissociation process. The path which we are proposing is the dimerization path for ST and VA.

TABLE VII

Internuclear distances for the different dimeric species of styrene, calculated with the UHF / 6-31G(*d*) and UHF / 3-21G* methods.

	Initial parameters	Optimized parameters	Anion	Cation	Free radical
R2	1.08313	1.0845	1.087351	1.085147	1.082979
R3	1.08376	1.0859	1.084398	1.082008	1.084316
R4	1.54506	1.5365	1.548771	1.541442	1.541876
R5	1.08437	1.0847	1.083480	1.081592	1.084130
R6	1.54822	1.5415	1.565072	1.592307	1.560874
R7	1.0857	1.0875	1.087424	1.082980	1.083802
R8	1.524	1.523	1.512671	1.517996	1.521031
R9	1.08331	1.086	1.083338	1.079065	1.083519
R10	1.08414	1.0871	1.083540	1.081076	1.084238
R11	1.5496	1.5372	1.510959	1.476950	1.509654
R12	1.39065	1.3935	1.465396	1.399079	1.399970
R13	1.38684	1.3893	1.384125	1.395863	1.397356
R14	1.08352	1.0846			
R15	1.08539	1.0871	1.076574	1.076165	1.074842
R16	1.51699	1.6146	1.409728	1.383034	1.410167
R17	1.38483	1.3872	1.389970	1.393763	1.393798
R18	1.38284	1.3837	1.394176	1.391641	1.391450
R19	1.07168	1.0757	1.074704	1.073076	1.071672
R20	1.07365	1.0764	1.082014	1.073428	1.073298
R21	1.38267	1.3831	1.456959	1.391121	1.392209
R22	1.07227	1.0758	1.074224	1.071714	1.072019
R23	1.07202	1.0758	1.080686	1.071540	1.072622
R24	1.38826	1.3903	1.428397	1.421720	1.427760
R25	1.38713	1.3908	1.428047	1.421996	1.427277
R26	1.07112	1.0754	1.075916	1.070472	1.072221
R27	1.38324	1.3851	1.390244	1.364232	1.389586
R28	1.38389	1.3856	1.388108	1.367788	1.387982
R29	1.07367	1.0768	1.073511	1.073147	1.073661
R30	1.07377	1.0768	1.070176	1.070342	1.071485
R31	1.38479	1.3855	1.402132	1.396969	1.401893
R32	1.07259	1.0757	1.073199	1.069944	1.072030
R33	1.072	1.0758	1.073939	1.069775	1.072197
R34	1.0713	1.0754	1.072277	1.070921	1.072131

TABLE VIII

Bond angles for the different dimeric species of ST, calculated with the UHF / 6-31G(*d*) and UHF / 3-21G* methods.

	Initial parameters	Optimized parameters	Anion	Cation	Free radical
A3	108.33837	107.7667	108.787	108.644	110.504
A4	111.21367	111.4655	111.976	111.722	108.427
A5	108.10089	107.6871	108.791	107.786	111.214
A6	112.17282	122.9059	109.928	111.643	108.076
A7	108.11570	107.2820	107.699	108.915	111.382
A8	110.49859	111.2918	112.138	112.551	108.608
A9	108.76368	108.5197	107.480	108.076	108.428
A10	109.62103	109.8119	107.938	107.689	112.622
A11	113.64087	114.3750	114.024	109.519	121.499
A12	121.19954	121.5492	120.837	121.427	120.421
A13	120.48590	120.4949	121.337	119.796	117.560
A14	110.12286	110.1620			
A15	109.14581	109.1545	117.966	116.240	124.834
A16	110.65706	112.3793	125.044	127.225	121.026
A17	121.04501	121.2240	123.675	120.617	120.847
A18	120.83009	121.0439	118.444	120.390	119.901
A19	119.93723	119.9504	120.941	120.520	119.400
A20	119.46750	119.4909	118.015	119.900	120.091
A21	120.13621	120.1610	118.221	120.0460	119.780
A22	119.76853	119.7094	120.924	119.755	119.777
A23	119.76843	119.6806	118.159	119.723	119.896
A24	120.63336	120.8650	120.366	118.895	123.000
A25	120.70228	120.8867	122.670	122.381	120.277
A26	120.32113	120.3923	120.420	120.212	120.995
A27	120.81487	120.9931	120.957	120.179	121.364
A28	120.75128	121.0002	121.503	120.585	118.672
A29	119.53357	119.5145	118.575	119.108	119.625
A30	119.45174	119.5118	119.215	119.852	120.672
A31	120.12089	120.1800	120.856	119.721	119.577
A32	119.86709	119.7680	119.449	120.517	119.801
A33	119.82719	119.7669	119.860	120.665	120.237
A34	120.18628	120.2854	120.313	119.193	

TABLE IX

Dihedral angles for the different dimeric species of ST, calculated with the UHF / 6-31G(*d*) and UHF / 3-21G* methods.

	Initial parameters	Optimized parameters	Anion	Cation	Free radical
D4	−121.79377	−122.5815	121.771	−123.139	−121.644
D5	117.06081	115.9720	117.265	116.908	117.271
D6	62.09327	62.6393	56.961	65.152	60.288
D7	−118.90094	−117.9309	−116.470	−118.285	−117.901
D8	123.61427	125.5284	123.991	121.429	123.633
D9	172.42559	174.3642	174.229	175.667	173.099
D10	−116.94578	−115.6387	−114.803	117.712	−115.854
D11	120.83665	121.3542	123.273	122.755	123.011
D12	−62.04618	−61.8644	−60.204	−54.350	−60.001
D13	−179.74842	−179.8569	−179.021	−179.694	−179.184
D14	61.72438	62.4989			
D15	−117.86062	−116.7008	94.894	88.511	94.818
D16	121.17856	121.7599	−177.612	−177.834	−177.681
D17	179.79928	179.8637	179.136	179.804	179.304
D18	−179.77884	−179.8371	−179.140	−179.670	−179.275
D19	179.91523	179.9692	−179.789	−179.533	−179.949
D20	−179.99439	−180.0385	179.836	179.180	179.839
D21	−0.05688	−0.016	−0.092	−0.140	−0.113
D22	179.95525	180.0192	179.779	179.726	179.984
D23	179.93643	179.9625	−179.989	−179.749	179.972
D24	−90.34242	−91.1110	179.493(	−182.503	178.103
D25	177.99809	178.6660	179.775	179.912	179.842
D26	179.98703	180.0002	−179.949	179.912	179.978
D27	−178.02109	−178.556	−179.508	179.595	−179.866
D28	178.02595	178.5297	179.477	179.552	179.862
D29	179.68947	179.7631	−179.970(	179.579	−179.918
D30	−179.85802	−179.7743	−179.371	−179.715	179.758
D31	−0.00875	−0.0313	−0.058	0.928	−0.020
D32	−179.84312	−179.7941	−179.720	179.527	179.913
D33	179.84029	179.8574	−179.915	−179.395	179.961
D34	−179.89313	−179.8424	179.985	179.380	−179.936

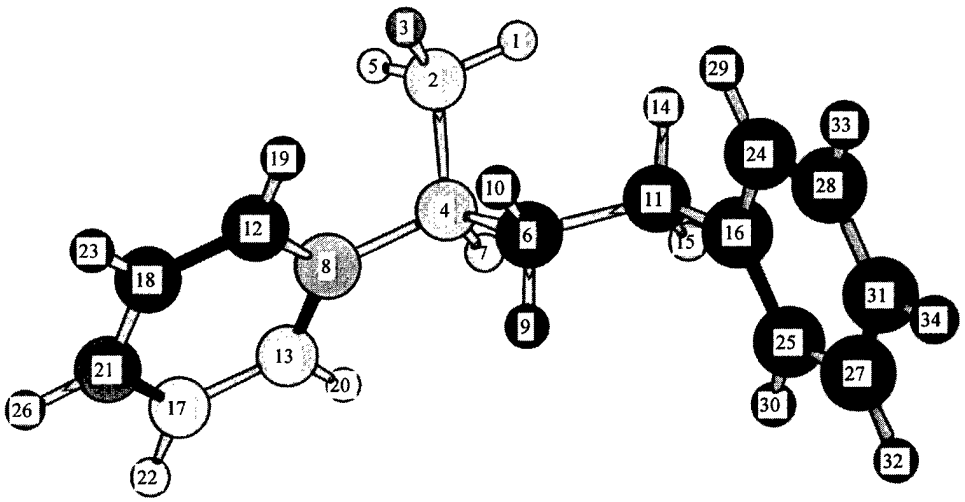


FIGURE 6. Dimer of ST; optimized structure with the HF / 6-31G* method, showing the numbering used throughout the text.

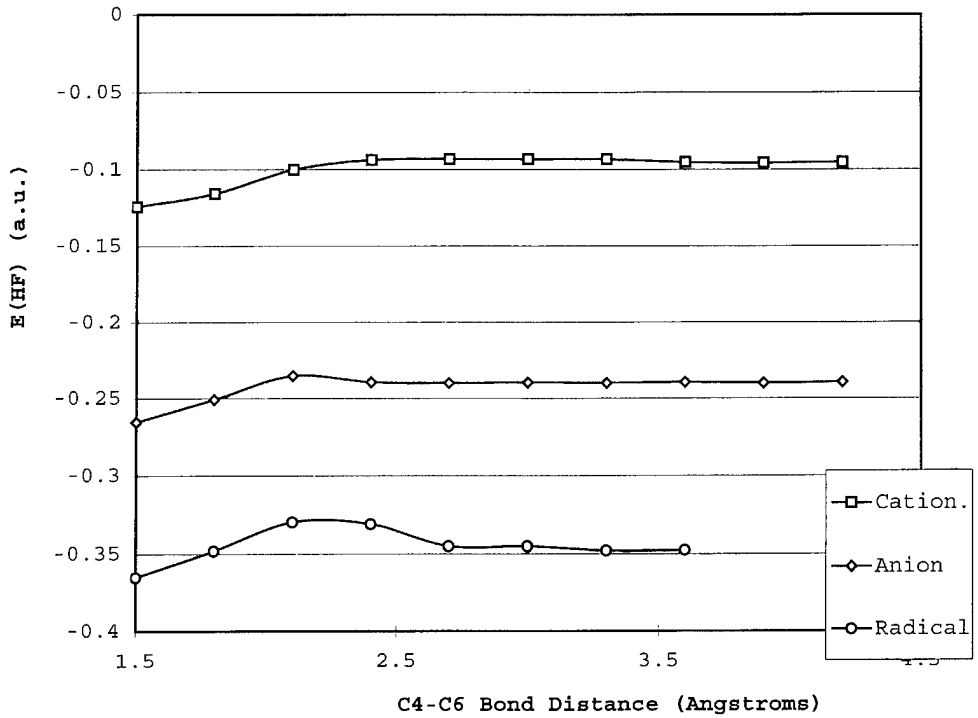


FIGURE 7. Potential energy curve for the dimeric species of ST, calculated with the UHF / 3-21G* model chemistry. The zero energy corresponds to 612.0 au.

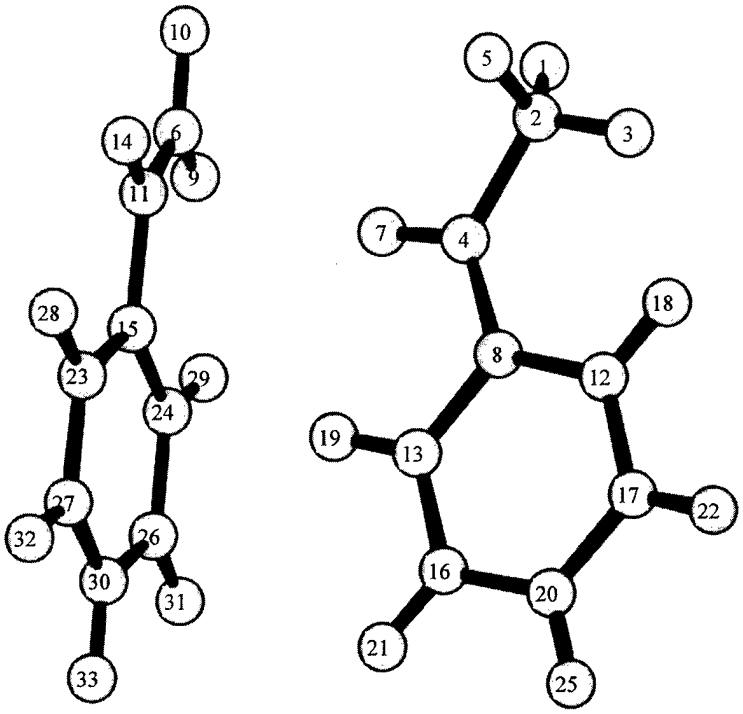


FIGURE 8. Dissociation products of the dimer free radical of ST, obtained at the UHF / 3-21G* level of theory.

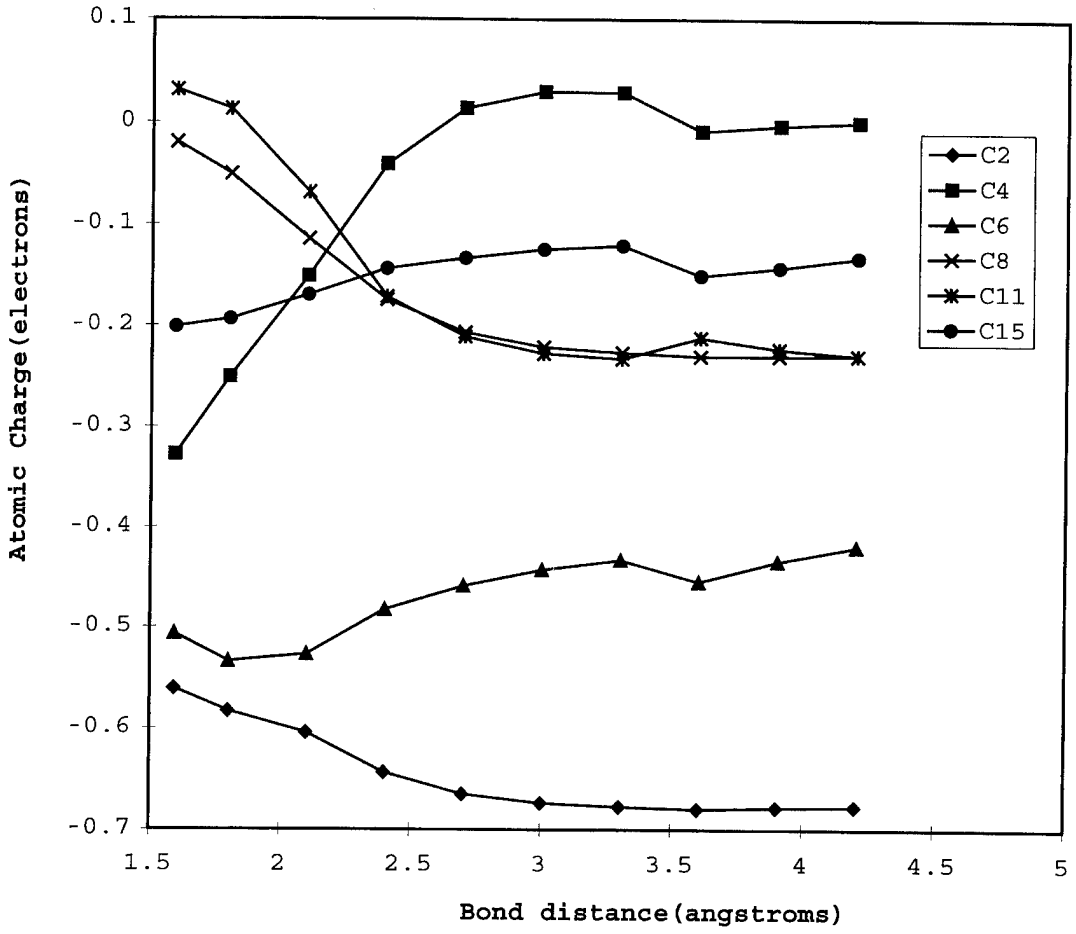


FIGURE 9. Change of the Mulliken net atomic charges for some relevant carbon atoms of the ST cation of the dimer during the dissociation.

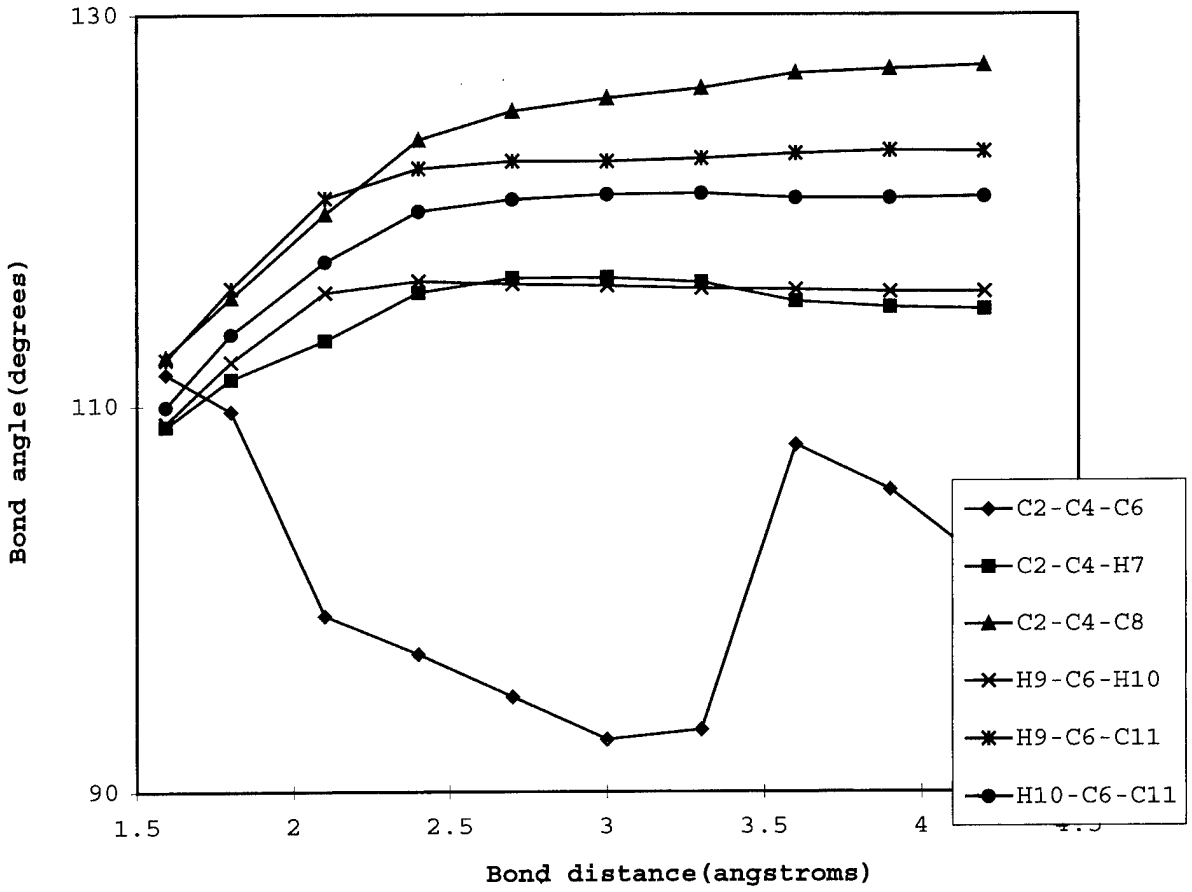


FIGURE 10. Step-by-step evolution of some relevant bond angles during the dissociation of the ST cation of the dimer.

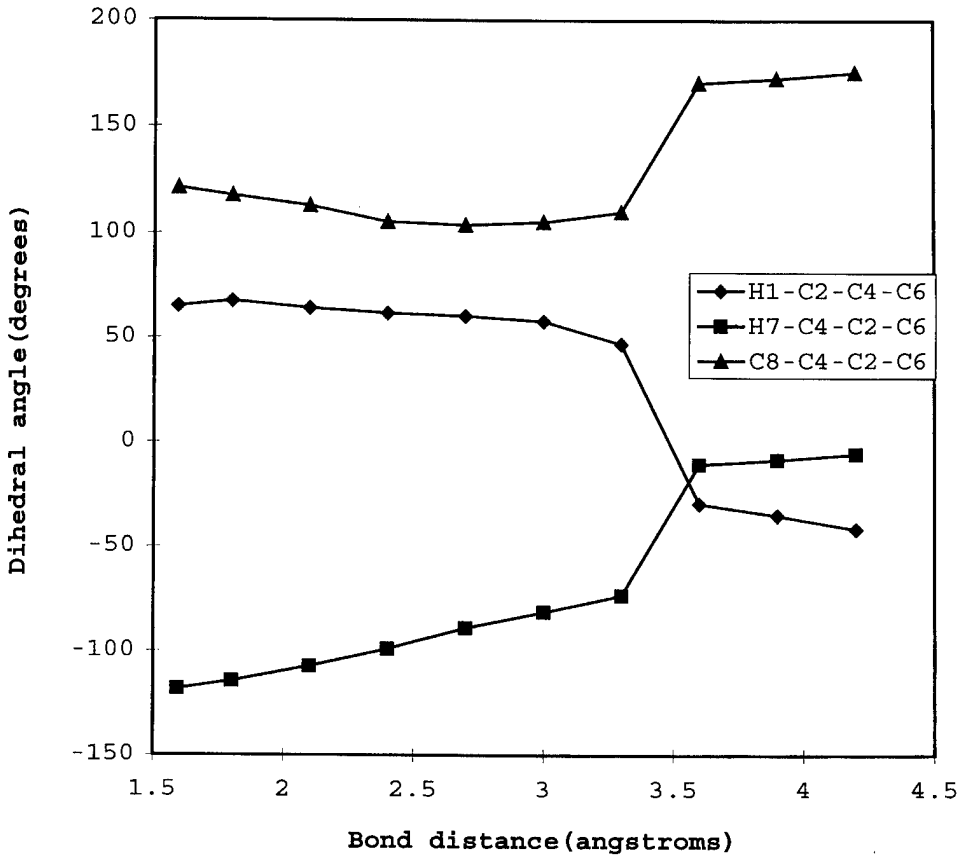


FIGURE 11. Dihedral angles vs. C4 — C6 bond distance during the dissociation of the ST cation of the dimer.

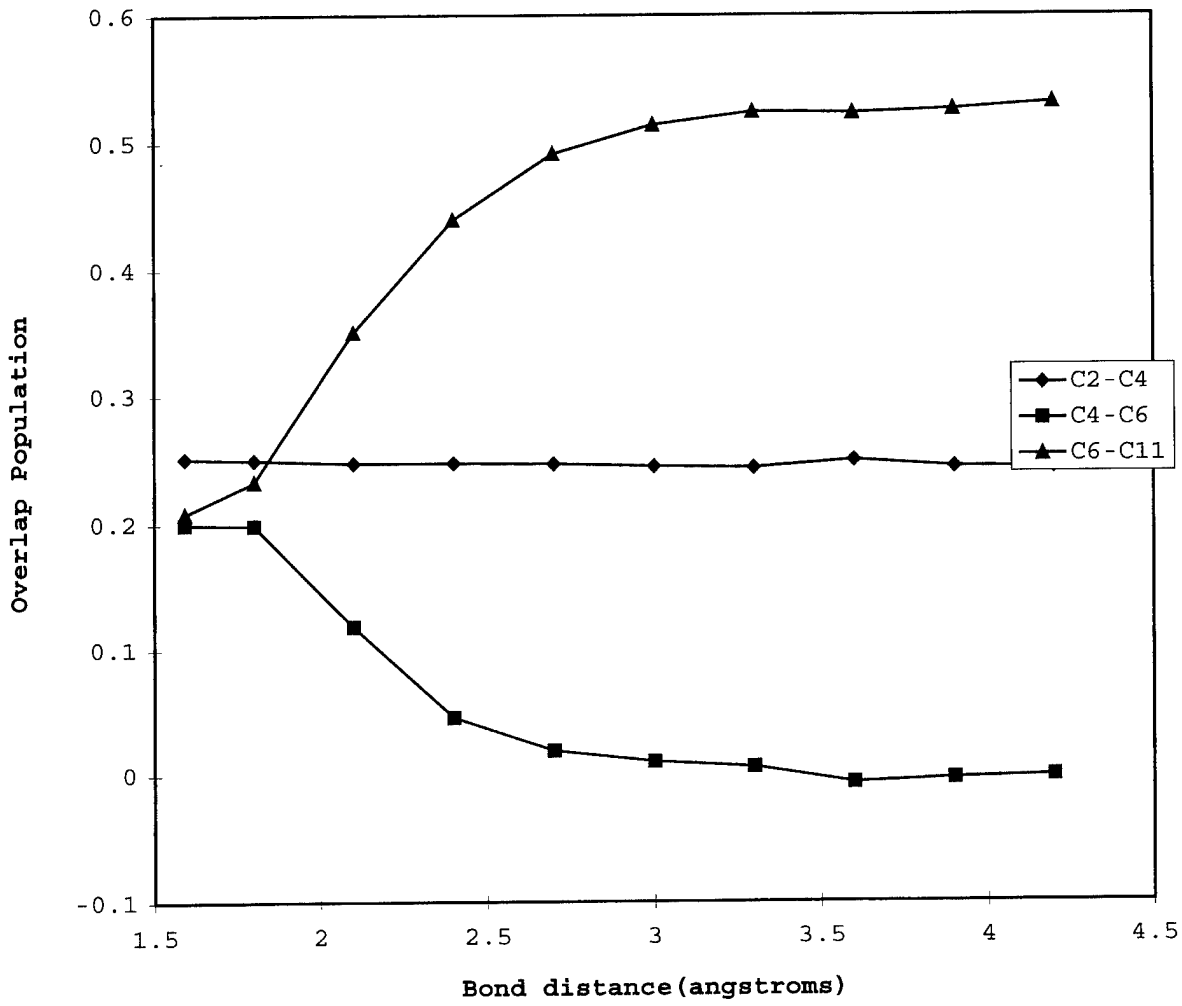


FIGURE 12. Bond distance vs. half of the total overlap population calculated for the ST cation of the dimer.

References

1. J. L. Koening, *Chemical Microstructure of Polymer Chains* (Wiley, New York, 1980).
2. H. L. Frish, G. L. Mallows, F. Hestley, and F. A. Bovey, *Macromolecules* **1**, 553 (1968).
3. C. H. Pichot, M. Llauro, and Q. Pham, *J. Polym. Sci., Polym. Chem. Ed.* **19**, 2619 (1981).
4. M. J. Frisch, G. W. Trucks, H. B. Schlegel, P. M. W. Gill, B. G. Johnson, M. A. Robb, J. R. Cheeseman, T. Keith, G. A. Petersson, J. A. Montgomery, K. Raghavachari, M. A. Al-Laham, V. G. Zakrzewski, J. V. Ortiz, J. B. Foresman, J. Cioslowski, B. B. Stefanov, A. Nanayakkara, M. Challacombe, C. Y. Peng, P. Y. Ayala, W. Chen, M. W. Wong, J. L. Andres, E. S. Replogle, R. Gomperts, R. L. Martin, D. J. Fox, J. S. Binkley, D. J. Defrees, J. Baker, J. P. Stewart, M. Head-Gordon, C. Gonzalez, and J. A. Pople, *Gaussian 94, Revision D.4* (Gaussian, Inc., Pittsburgh, PA, 1995).
5. M. J. S. Dewar, E. G. Zoeblisch, E. F. Ealy, and J. J. P. Stewart, *J. Am. Chem. Soc.* **107**, 3902 (1985).
6. J. A. Pople and R. K. Nesbet, *J. Chem. Phys.* **22**, 571 (1959).
7. J. S. Binkley, J. A. Pople, and W. J. Here, J. Am. Chem. Soc. **102**, 939 (1980); M. S. Gordon, J. S. Binkley, J. A. Pople, W. J. Pietro, and W. J. Here, J. Am. Chem. Soc. **104**, 2797 (1982); W. J. Pietro, M. M. Francl, W. J. Here, D. J. Defrees, J. A. Pople, and J. S. Binkley, J. Am. Chem. Soc. **104**, 5039 (1982); K. D. Dobbs and W. J. Here, J. Comp. Chem. **7**, **369** (1986); K. D. Dobbs and W. J. Here, J. Comp. Chem. **8**, 861 (1987); K. D. Dobbs and W. J. Here, J. Comp. Chem. **8**, 880 (1987).
8. R. Ditchfield, W. J. Hehre, and J. A. Pople, J. Chem. Phys. **54** 724 (1971); W. J. Hehre, R. Ditchfield, and A. Pople, J. Chem. Phys. **56**, 2257 (1972); P. C. Hariharan and J. A.

Pople, Mol. Phys. **27**, 209 (1974); M. S. Gordan, Chem. Phys. Lett. **76**, 163 (1908); P. C. Hariharan and J. A. Pople, Theor. Chim. Acta **28**, 213 (1973).

9. M. J. S. Dewar, *The Molecular Orbital Theory of Organic Chemistry* (McGraw-Hill, New York, 1969).
10. M. J. S. Dewar and W. Thiel, J. Am. Chem. Soc. **99**, 4899 (1977); *Ibid.* **99**, 4907 (1977); J. J. P. Stewart and M. J. S. Dewar, MOPAC 4.0, QCPE #455 (Bloomington, IN, 1987).
11. M. J. S. Dewar and D. M. Storch, J. Am. Chem. Soc. **107**, 3898 (1985).
12. M. A. Mora, M. Rubio, and R. Salcedo, Polymer **34**, 5143 (1993).
13. P. J. Flory, P. R. Sundararajan, and L. C. DeBolt, J. Am. Chem. Soc. **96**, 5015 (1974).
14. F. Rodriguez, *Principles of Polymer Sy stems* (McGraw-Hill, New York, 1982); P. J. Flory, *Principles of Polymer Chemistry* (Cornell University Press, Ithaca, NY, London, 1978).
15. R. M. Joshy, B. J. Zwolinski, in *Vinyl Polymerizations*, George E. Ham, Ed. (Marcel Dekker, New York, 1967), Vol. 1, Chap. 8.
16. P. J. Flory, *Principles of Polymer Chemistry* (Cornell University Press, Ithaca, NY, 1953), p. 254.
17. C. E. Schildknecht, S. T. Gross, H. R. Davison, J. M. Lambert, and A. O. Zoss, *Ind. Eng. Chem.* **40**, 2014 (1948).

CASSCF, MP2, and CASMP2 Studies on Addition Reaction of Singlet Molecular Oxygen to Ethylene Molecule

YASUNORI YOSHIOKA,[1] TSUNAKI TSUNESADA,[1] KIZASHI YAMAGUCHI,[1] ISAO SAITO[2]

[1]*Department of Chemistry, Graduate School of Science, Osaka University, Toyonaka, Osaka 560, Japan*
[2]*Department of Synthetic Chemistry and Biological Chemistry, Graduate School of Engineering, Kyoto University, Sakyo-ku, Kyoto 606, Japan, CREST*

Received 5 March 1997; accepted 12 March 1997

ABSTRACT: The reaction mechanism and relative stabilities of the intermediates and transition states in the reaction of $^1O_2$ plus ethylene molecule using ab initio molecular orbital (MO) theories at several levels of theory with the correction of the nondynamic and dynamic electron correlation effects were systematically investigated. Full geometry optimizations of the corresponding biradical (BR) intermediates, perepoxide (PE) and 1,2-dioxetane (DO) were performed by complete-active-space CASSCF{2,2}/6-31G* method with nondynamic electron correlation effect and Møller-Plesset MP2/6-31G* method with dynamic electron correlation effect. For the 1,4-biradical intermediates, new gauche-type ^{1}BR state was found at both CASSCF and MP2 levels, corresponding to the transition state of the rotation motion of the O_2 moiety. It was found from the intrinsic-reaction-coordinate (IRC) study that another gauche-type ^{1}BR transition state connects smoothly to the reactant system $^1O_2 + H_2C = CH_2$ and the gauche minimum ^{1}BR state, showing that the reaction through the 1,4-biradical intermediates initially proceeds through the gauche transition state to form the gauche minimum ^{1}BR state, following that the free rotation of O_2 moiety occurs due to the energy barrier less than 4.0 kcal/mol. The stability of the perepoxide is surprisingly sensitive to the levels of the theory and the basis sets employed. The coupled-cluster methods, CCSD and CCSD(T), gave the reasonable stabilities of 1,4-biradical intermediates, perepoxide, and dioxetane as a reaction product. From the results of the CCSD and CCSD(T) methods, the reaction of $^1O_2 + H_2C = CH_2$ proceeds by a two-step mechanism through the 1,4-biradical intermediates rather than through the perepoxide. © 1997 John Wiley & Sons, Inc. Int J Quant Chem **65**: 787–801, 1997

Correspondence to: Y. Yoshioka.
Contract grant sponsor: CREST.

© 1997 John Wiley & Sons, Inc.
CCC 0020-7608 / 97 / 050787-15

The additions of the singlet molecular oxygen to various types of the olefin derivatives have been extensively studied over 30 years [1, 2]. A large number of accumulated data suggested three types of the reaction modes: (I) 1,2-addition to give 1,2-dioxetane; (II) ene reaction to give carbonyl fragments and allylic hydroperoxides; (III) 1,4-addition to give endperoxides. For these reaction modes, the following five mechanisms are suggested as shown schematically in Figure 1: (i) concerted mechanism which proceeds without well-defined intermediates; (ii) mechanism through a homopolar biradical (BR) intermediates; (iii) mechanism through a zwitterionic (ZW) intermediates; (iv) mechanism through a one-electron transfer (ET) biradical intermediates; (v) mechanism through a perepoxide (PE) intermediates [3, 4]. The experimental studies on the reaction mechanisms [3, 4] have clarified that energy differences between these reaction mechanisms are not so large even in a gas phase and highly dependent on the chemical conditions such as solvent polarity employed. Several reaction mechanism are, then, operative in each reaction mode.

On the other hand, theoretical studies [5, 6] showed that the reacting complexes between molecular oxygen and various olefins are regarded as typical quasi-degenerate systems in energy. This indicates that the reaction complexes are very sensitive for introducing substituents and/or changing reaction conditions such as solvents, and interconversion of reaction mechanisms easily occurs. This also suggests the possibility that the relative stabilities of electronic states on the reaction pathway are highly sensitive to the level of the theory with and without correlation effects and basis sets employed.

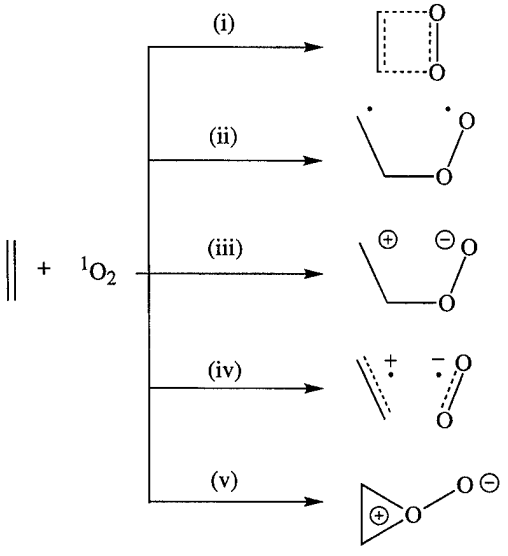


FIGURE 1. Typical five reaction mechanisms of singlet oxygen molecule and ethylene derivatives.

Harding and Goddard supported the biradical mechanism such as CH_2CH_2OO with extensive calculations at the GVB-CI level with a double-ζ plus polarization (DZP) basis set [7]. The perepoxide were located as a minimum with higher energy than biradical minimum by about 8 kcal/mol. On the basis of the MINDO/3 level of theory, Dewar et al. studied the reaction of O_2 with various substituted alkenes [8]. They found, in the case of ethene itself, that the reaction proceeds through a polar perepoxide, which in turn rearranges to 1,2-dioxetane in a rate-determining step.

Hotokka et al. have performed the calculations of reaction intermediates and transition states optimized with constraints of the symmetry and geometry at the level of CASSCF and CCI, concluding that the formation of the perepoxide intermediate is easier than passing through a C_s syn-biradical pathway [9]. Robb and co-workers suggested from the calculations at the level of CASSCF{6,6}/4-31G that the 1,2-dioxetane-forming reaction is described as a two-step reaction which proceeds through a gauche biradical intermediate [10]. It is, however, noteworthy that these theoretical results may not be conclusive because the CASSCF do not involve the correction of the dynamic electron correlation. In fact, the heat of the 1,2-dioxetane formation is too small (12.8 [9] and 4.0 [10b] kcal/mol) compared with the value from thermochemical estimation (30 kcal/mol). These theoretical results, therefore, show that the reaction mechanism is still not conclusive for the reaction mode as well as the experimental data.

In this article, we systematically investigate the reaction mechanism and relative stabilities of the intermediates and transition states in the reaction of ethylene molecule plus $^1O_2$ using ab initio molecular orbital (MO) theories at several calculational levels with the correction of the nondynamic and dynamic electron correlation effects [11, 12]. Full geometry optimizations of the corresponding BR intermediates, PE, and 1,2-dioxetane (DO) are performed by CASSCF{2,2}/6-31G* level with nondynamic electron correlation effect and Hartree–Fock [HF; restricted (R) or unrestricted (U)]

MP2/6-31G* level with dynamic electron correlation effect. The relative stabilities of the reaction intermediates and transition states are estimated again by the approximately spin-projected but size-consistent UHF scheme (APUHF) [13], the approximate spin projection scheme (APUMP2 and APUMP4) [6], and the RHF or UHF coupled-cluster [(R or U)CCSD and (R or U)CCSD(T)] [6d, 14] methods, CASMP2 [15] method, and CASPT2 [12] method at the optimized geometries using the same 6-31G* basis set. The reaction mechanisms through 1,4-biradical intermediates and perepoxide will be discussed and suggested. The program package Gaussian 94 [15] was employed to evaluate the above.

Calculational Procedures

Calculations for the singlet biradical intermediates were carried out at UHF, UHF natural orbital (UNO) CASSCF [16, 17] and UMP2 [18] levels of theory with 6-31G* basis set. As described in the previous works [19] the RHF is not suitable for estimating the electronic structures of the species in the singlet biradical states due to the triplet instability [13]. The singly occupied MOs (SOMO) with radical characteristics are, then, induced by mixing highest occupied (HO) and lowest unoccupied (LU) MOs of the RHF solution, resulting in the different orbitals for different spins (DODS) MO picture by the singlet UHF solution. The singlet DODS solution constructed is not a pure eigenfunction of the spin angular momentum due to the contamination from triplet excited wave function. The removement of the contamination result in the approximately spin-projected UHF (APUHF) [13]. The correlation correction by the APUHF method for the case of tricentric biradical such as O_3, CH_2NHCH_2, CH_2OO, OCH_2O, and CH_2CH_2O gives the simple relation as follows [19a]:

$$^1\phi_{\text{UNO CASCI}\{2,2\}} \cong {}^1\phi_{\text{APUHF}} \cong {}^1\phi_{\text{UNO CASSCF}\{2,2\}}. \quad (1)$$

Similarly, UMP2 is not also a pure spin state with the contamination from higher excited states. The approximate spin projection to the singlet state gives the APUMP2 wave function. As described in a previous work [19b], the APUMP2 method is simply related by the CASMP2 method from the behavior of potential energy curve for the rotation of the ethylene molecule, as follows:

$$^1\phi_{\text{UNO CASMP2}\{2,2\}} = {}^1\phi_{\text{APUMP2}} + \Delta, \quad (2)$$

where Δ is term corresponding to the orbital relaxation energy.

The geometry optimizations for the singlet biradical species were carried out by two different procedures: (i) the natural orbitals are constructed by DODS MOs obtained, following that the UNO CASSCF{2,2} calculations were performed in an active space of two SOMOs and two biradical electrons to include the nondynamic electron correlation effect and (ii) UMP2 calculations were performed by using DODS MOs of the UHF solution to include the dynamic electron correlation effect [11]. The usual RHF picture was used for CASSCF{2,2} and MP2 (RMP2) to calculate the singlet closed-shell species such as perepoxide, 1,2-dioxetane, and so on.

All geometrical parameters of the reaction intermediates and transition states were fully optimized by the above two methods without constraints of the symmetry and geometry. For the stationary point, the vibrational frequency analyses were carried out to clarify the intermediate, transition state (TS) or higher-order saddle point on the potential energy surface. The relative stabilities of the reaction intermediates and transition states are estimated again by the APUHF, APUMP2,APUMP4, UCCSD, UCCSD(T), CASMP2, and CASPT2 methods at the optimized geometries.

Results and Discussion

REACTANTS

The geometry optimizations of O_2 ($^1\Delta_g$) at the CASSCF{2,2}/6-31G* level gives the O—O bond distances of 1.210 Å, being in quite good agreement with the experimental value of 1.216 Å [20a]. The O—O bond distance of CASSCF{2,2}/6-31G* is smaller by 0.048 Å than 1.258 Å of CASSCF/4-31G by Robb et al. [10b]. For the triplet O_2 ($^3\Sigma_g$), the O—O bond distances were estimated to be 1.168 and 1.247 Å by CASSCF{2,2} and UMP2, respectively, being smaller by 0.040 Å and longer by 0.039 Å than the experimental value of 1.208 Å. The $^1\Delta_g$ state at CASSCF{2,2} level is higher in energy by 0.62 eV (14.2 kcal/mol) than the $^3\Sigma_g$ state, being quite smaller than the experimental value of 1.07 eV.

In the ethylene molecule, the RMP2/6-31G* method gives the optimized geometrical parameters of 1.336 Å for C—C bond distance, 1.085 Å for C—H, and 121.7° for C—C—H bond angle, being in quite reasonable agreement with the experimental values [20b] of 1.330 Å, 1.076 Å, and 121.7°, respectively.

REACTION PATHWAY THROUGH 1,4-BIRADICAL INTERMEDIATES

Optimized 1,4-Biradical Intermediates

The $(2s + 2s)$-type attacks of singlet molecular oxygen ($^1O_2$) to ethylene molecule have the possibility to provide intermediates with 1,4-biradical orbitals on terminal carbon and oxygen atoms in the *s*-cis type of the coplanar geometry. Four types of the singlet BR intermediates are expected by the rotation of the terminal methylene group and/or oxygen atom, that is, $^1\sigma\sigma$-, $^1\sigma\pi$-, $^1\pi\sigma$-, and $^1\pi\pi$-BR intermediates. The C—O bond cleavage of 1,2-dioxetane (DO) leads the $^1\sigma\sigma$-BR intermediate with σ-type radical orbital on terminal carbon atom and σ-type radical orbital on another terminal oxygen atom. The $^1\sigma\sigma$-BR intermediate has higher energy by 12.9 kcal/mol than $^1\sigma\pi$-BR at APUHF/4-31G level, and the $^1\pi\sigma$-BR state is also more unstable by 13.3 kcal/mol [21]. Though the $^1\pi\pi$-BR state is comparable in energy with the $^1\sigma\pi$-BR state [21], the terminal methylene group is rotated by 90° in the $^1\pi\pi$-BR state. This means that the reaction to 1,2-dioxetane proceeds through the energy barrier due to the rotation of the terminal methylene group. In this study, we investigated the $^1\sigma\pi$-BR states as the reaction intermediates to the 1,2-dioxetane. Although only *s*-cis conformation is noted, the *s*-trans and gauche conformations are equally possible for 1,4-peroxy biradicals. Full geometry optimizations of the corresponding *s*-cis conformation, the *s*-trans and gauche conformations were carried out at the levels of CASSCF{2,2}/6-31G* and UMP2/6-31G*.

Four optimized structures with the geometries of *s*-cis, two gauche's, and *s*-trans types in the $^1\sigma\pi$ BR state were found by UMP2/6-31G* and CASSCF{2,2}/6-31G* methods. Their conformations with optimized geometrical parameters are shown in Figure 2. Their relative stabilities to the gauche-type ^{1}BR(G1) state are summarized in Table I. The corresponding values by the CASSCF/4-31G method by Robb et al. [10b] are also given for comparison.

As can be seen from Table I, the most stable structures of the singlet BR state is the gauche-type BR(G1), which was optimized by both UMP2/6-31G* and CASSCF{2,2}/6-31G* methods. This state is a real local minimum (stationary point) on the potential energy surface with all positive eigenvalues of Hessian matrix (ν_{min} = 65 cm^{-1} by UMP2 method), being in good agreement with the result of Robb et al. [10b]. The bond distances of C—O and O—O given by UMP2 are slightly larger than those by CASSCF{2,2}, while the C—C bond distance of UMP2 is slightly shorter than that of CASSCF{2,2}. These tendencies are observed in another three optimized structures. For the bond distances of O—O and C—O, 1.310 and 1.472 Å of UMP2 and 1.301 and 1.432 Å of CASSCF{2,2} using the 6-31G* basis set are quite shorter than 1.376 and 1.530 Å of CASSCF{6,6}/4-31G by Robb et al. [10b]. These differences may be due to the inclusion of the polarization functions and the use of unrestricted natural orbital (UNO) for the CASSCF method. The twisted angles (82.8° and 87.1°) of O—O—C—C by both UMP2 and CASSCF{2,2} are slightly larger than 79.6° of Robb et al. [10b].

Next, the stationary point is the *s*-trans $^1\sigma\pi$-BR state with higher energy by only 0.6 and 0.3 kcal/mol than the most stable gauche-type BR(G1) state by UMP2/6-31G* and CASSCF{2,2}/6-31G* methods, respectively. This state possesses the lowest vibrational frequencies of 21 cm^{-1} at UMP2/6-31G* level, indicating that the $^1\sigma\pi$-BR stationary point is really a shallow minimum on the potential energy surface. These results are also in quite good agreement with the results of Robb et al. [10b]. The bond distances of O—O, C—O, and C—C are quite similar to the values of the most stable gauche-type BR(G1) state at both UMP2/6-31G* and CASSCF{2,2}/6-31G* levels. The O—O and C—O bond distances are also shorter by 0.071–0.095 Å compared with those of Robb et al. [10b].

Each of UMP2/6-31G* and CASSCF{2,2}/6-31G* methods gives two transition states, the saddle point on the potential energy surface, with one negative eigenvalue of Hessian matrix; one is a *s*-cis $^1\sigma\pi$-BR state and another is a gauche ^{1}BR(G2) state. The *s*-cis $^1\sigma\pi$-BR state has higher energy by 2.5 and 3.5 kcal/mol than those of the most stable gauche-type BR(G1) state at UMP2/6-31G* and CASSCF{2,2}/6-31G* levels, respectively, compared with 2.0 kcal/mol of Robb et al. [10b]. Robb et al. found three optimized geometries with the structures of *s*-cis-type 1,4-biradical conforma-

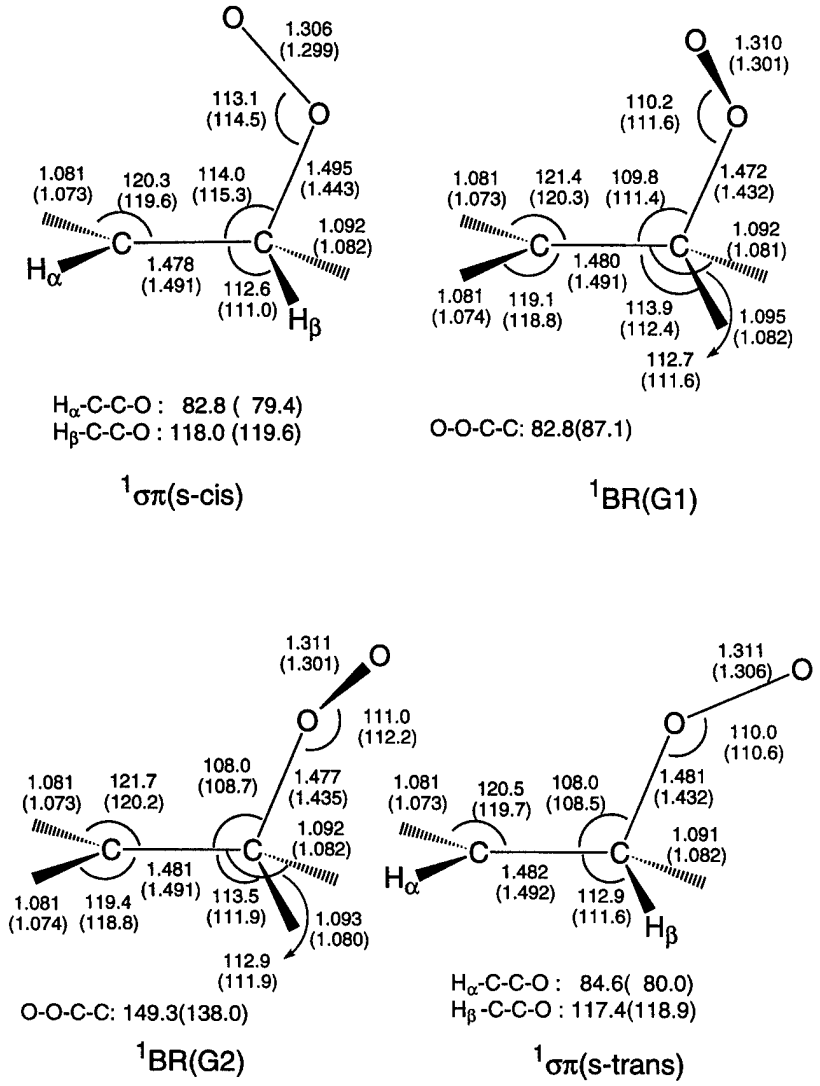


FIGURE 2. Optimized geometrical parameters of the singlet biradical states obtained by UMP2 / 6-31G* method and UNO CASSCF{2,2} / 6-31G* method in parenthesis.

tions; one is obtained by both 4-31G and STO-3G basis sets using CASSCF method; others are given by only STO-3G basis set. Two structures, which are the second-order saddle points on the Π3 and Π4 energy surface (Fig. 5 in Ref. [10b]), have the C—O bond distances of 1.842 Å (1.874 Å by 4-31G) and 1.759 Å given by STO-3G basis set employed, being quite different from our results of 1.478 Å (UMP2) and 1.491 Å (CASSCF). Robb et al. [10b] also showed that the third structure with the C—O bond distance of 1.538 Å by STO-3G is a local minimum on the Π3 energy surface. This structure corresponds to our structure. Their conclusion is, however, in conflict with our result that the *s*-cis $^1\sigma\pi$-BR state is the saddle point on the potential energy surface, namely the transition state. The *s*-cis $^1\sigma\pi$-BR and gauche-type BR(G2) states have really imaginary frequencies of $125i$ and $44i$ cm^{-1} at UMP2/6-31G* level, respectively.

It should be also noted that the gauche-type BR(G2) state obtained here is far from the C_1 gauche first-order saddle point given by Robb et al. [10b] in the molecular geometry and relative stability to the gauche-type ^{1}BR(G1) state. The C—O distances are 1.472 and 1.432 Å and the relative energies to most stable gauche-type BR(G1) state are estimated to be 0.7 kcal/mol by both UMP2/6-31G* and CASSCF{2,2}/6-31G*, while

TABLE I
Relative stabilities (kcal / mol) of optimized structures of reactants, reaction intermediates, transition states, and products.

States \ Methods	CASSCF{2,2}	MP2	CASSCF[a]
$O_2(^1\Delta_g) + H_2C = CH_2$	−18.1		−22.8 (−17.7)
$O_2(^3\Sigma_g) + H_2C = CH_2$	−32.3	−30.1	
$^1\sigma\pi$BR (*s*-cis)	3.5	2.5	(2.0)
^{1}BR (gauche1)	0.0[b]	0.0[c]	0.0 (0.0)
^{1}BR (gauche2)	0.7	0.7	
$^1\sigma\pi$BR (*s*-trans)	0.3	0.6	0.6 (0.4)
^{1}BR (gauche TS)		19.9	6.7 (11.1)
$^1\sigma\pi$BR (*s*-trans SP2)[d]	18.7[e]	21.0	9.6 (12.1)
Perepoxide (PE)	3.2	−0.6	−39.0 (32.3)
PE (SP2)[d]	44.4	12.9	−25.4 (45.4)
Dioxetane (^{1}DO)	−51.8[f]	−51.5	−26.8 (−41.8)[h]
^{1}DO (TS)	−51.8[g]	−50.8	
$2H_2C = O$	−84.5[i]	−105.0	

[a] CASSCF / 4-31G and (CASSCF / STO-3G) in Ref. [10b] of Robb et al.
[b] Total energy is −227.598231 a.u.
[c] Total energy is −228.168207 a.u.
[d] SP2 means a second-order saddle point.
[e] CASSCF{2,2} value at the geometry optimized by CASSCF{4,4}.
[f] Total energy is −227.680865 a.u.
[g] Total energy is −227.680805 a.u.
[h] C_{2v} symmetry not C_2.
[i] The formaldehyde dimer with C−C distance of 10 Å was calculated.

Robb et al. [10b] gave the C—O distance of 1.850 Å and the relative energy of 6.7 kcal/mol by 4-31G basis set. This shows that the present gauche-type BR(G2) state is apparently different from the transition state leading to 1,2-dioxetane suggested by Robb et al. [10b], even if the gauche-type BR(G2) state has single negative eigenvalue of the Hessian matrix.

The potential energy curves of the singlet BR states for C—O rotation at UMP2 and CASSCF levels are depicted in Figure 3. Four singlet BR states obtained here are smoothly connected, indicating that the present gauche-type BR(G2) state is apparently the transition state of the rotation motion of 1,4-biradical states. The rotational energy barriers are within 3.5 kcal/mol, showing that the free rotation easily occurs in the singlet state. The carbon–carbon bond distances of four structures are fallen into small regions from 1.478 to 1.482 Å, being larger than 1.336 Å of ethylene molecule at RMP/6-31G* level. This indicates that the radical characteristics on a terminal carbon atom with cleavage of π bonding orbital is kept throughout the rotation motion. Similarly, the oxygen–oxygen bond distances of 1.306, 1.310, 1.311, and 1.311 Å are longer than 1.208 Å ($X^3\Sigma_g^-$) and 1.216 Å ($a^1\Delta_g$) of oxygen molecule estimated by the experiment, reflecting the biradical characteristics on terminal oxygen atom. The C—O distances are between 1.472 and 1.495 Å for the rotation motion. The UMP2 method gives longer distances than the CASSCF{2,2} method due to inclusion of dynamic electron correlation effects except for C—C distance of *s*-trans $^1\sigma\pi$-BR state.

Relative Stabilities of 1,4-Biradical Intermediates at Various Calculational Levels

Table II summarizes the relative stabilities of four 1,4-biradical states estimated by various levels of theory based on the geometries optimized by UNO CASSCF{2,2} and UMP2 method using 6-31G* basis set. The UMP4 with higher-order correlation correction indicates that the most stable 1,4-biradical state is the gauche-type BR(G1) state at the geometries optimized by both CASSCF{2,2} and UMP2 methods. The relative stabilities of four states gives the same ordering to those of UMP2 levels, indicating that BR(G1) and $^1\sigma\pi$-BR (*s*-trans) states are the local minimum and BR(G2) and $^1\sigma\pi$-BR (*s*-cis) are the first-order saddle points on the potential energy surface.

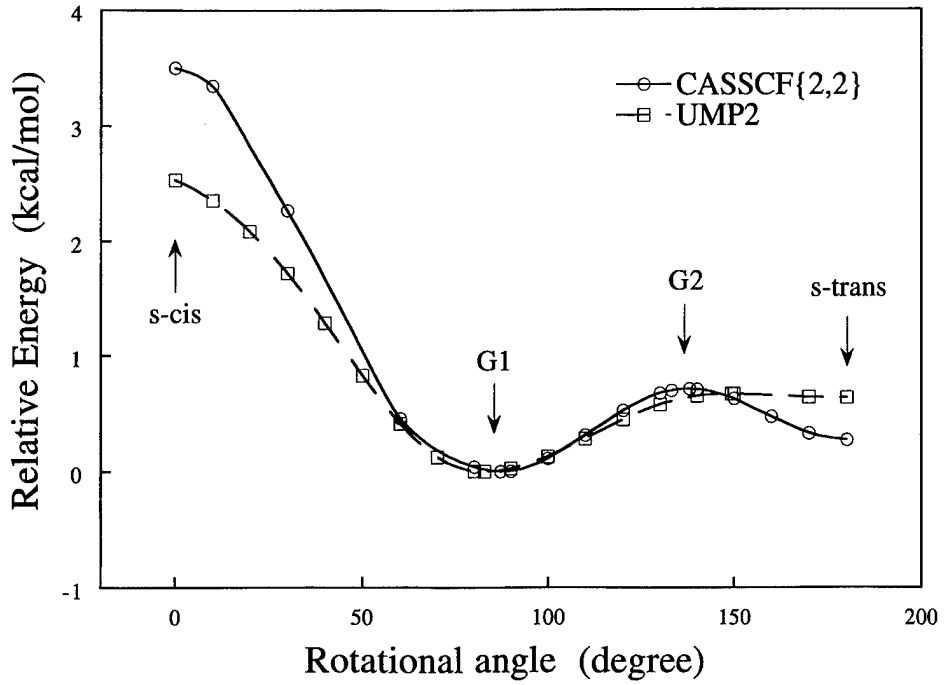


FIGURE 3. Potential energy curves of the singlet biradical states for the rotation of C—C—O—O estimated by UMP2/6-31G* and UNO CASSCF{2,2}/6-31G* methods.

The approximately spin-projected (AP)UHF and (AP)UMPn levels are constructed by removing the contamination of the triplet exited wave function. The APUHF gives the same ordering of the relative stabilities at four biradical states with the geometries optimized by CASSCF{2,2} and UMP2 methods. As is shown in Eq. (1), and presented in the previous work [19], the APUHF gave the correlation correction nearly equal to those of the CASCI{2,2} and CASSCF{2,2} in the case of tri-

TABLE II

Relative stabilities (kcal/mol) of four 1,4-biradical intermediates estimated by various levels of theory based on the geometries optimized by CASSCF{2,2} and UMP2 using 6-31G* basis set.

States Geom \ Methods	$^1\sigma\pi$BR (s-cis)		^{1}BR (G1)[a]		^{1}BR (G2)[a]		$^1\sigma\pi$BR (s-trans)	
	CASSCF	UMP2	CASSCF	UMP2[b]	CASSCF	UMP2	CASSCF	UMP2
UHF	2.11	3.08	−0.81	0.0	−0.18	0.36	−0.97	−0.08
APUHF	2.64	3.73	−0.56	0.0	0.12	0.85	−0.30	0.68
CASSCF	2.50	3.62	−1.00	0.0	−0.29	0.74	−0.73	0.33
UMP2	3.53	2.53	1.07	0.0	1.67	0.67	−1.61	0.64
APUMP2	4.38	3.52	1.26	0.0	1.90	1.31	2.53	1.68
UMP4	3.99	2.59	1.44	0.0	2.18	0.72	2.00	0.65
APUMP4	4.88	3.61	1.58	0.0	2.41	1.40	2.98	1.76
CCSD	4.07	2.86	1.27	0.0	2.08	0.70	1.65	0.50
CCSD(T)	4.31	2.78	1.53	0.0	2.36	0.75	2.02	0.58
CASMP2	3.97	3.16	1.08	0.0	1.75	1.06	2.01	1.20
CASPT2	10.34	9.48	−0.33	0.0	1.17	4.93	8.48	7.59

[a] Gauche geometry, G1 is a local minimum and G2 is a transition state.

[b] Total energies in units of a.u. are −227.606549 for UHF, −227.606588 for APUHF, −227.596633 for CASSCF, −228.168207 for UMP2, −228.168429 for APUMP2, −228.224839 for UMP4, −228.225177 for APUMP4, −228.212413 for CCSD, −228.229669 for CCSD(T), −228.175792 for CASMP2, and −228.193027 for CASPT2.

centric biradical intermediates such as O_3, CH_2NHCH_2, CH_2OO, OCH_2O, and CH_2CH_2O. It seems that these relationships are also supported in the case of tetracentric biradical species.

However, the APUMPn ($n = 2, 4$) gives the reversed stabilities that the gauche-type BR(G2) state is more stable than the *s*-trans $^1\sigma\pi$-BR state, conflicting with above results that the *s*-trans $^1\sigma\pi$-BR state is the local minimum and the gauche-type BR(G2) state is the first-order saddle point on the potential energy surface. These results show that the approximately spin-projected (AP) procedure is, in some cases, not effective for describing the energy differences of the energetically quasi-degenerate chemical system. This may be due to fact that the APUMPn methods include the small contribution of the higher excited states than triplet excited state. The APUMPn methods should be carefully used to describe the chemical systems and intermediates with strong biradical character as well as APUHF.

Two coupled-cluster CCSD and CCSD(T) methods with dynamic electron correlation show that the relative stabilities of four 1,4-biradical state give the same ordering to those optimized by CASSCF{2,2} and UMP2 methods. The energy gaps between four BR states fall into within a few kcal/mol, giving the reasonable chemical pictures.

However, in the CASMP2 method, the characteristics of four states such as minimum and transition state on the potential energy surface are lost as well as the APUMP2 and APUMP4 methods, indicating that the inclusion treatment of the dynamic electron correlation based on the CASSCF wave function is not effective for 1,4-biradical species. The behaviors of the CASMP2 and APUMP2 methods support the relationship given in Eq. (2). Though the CASPT2 method gives larger energy gaps between four 1,4-biradical states than the CASMP2, the CASPT2 has similar tendencies on the characteristics of the potential energy surface to the CASMP2.

From Table II, following conclusions are described for the chemical systems which are quasi-degenerate in energy and have the strong biradical character. The dynamic electron correlation is essentially necessary to elucidate the electronic structures. The inclusion of the dynamic electron correlation should be done carefully and adequately. The geometry optimization should be done to represent the energetics in quasi-degenerate chemical system and the electronic structures with the biradical character even if the high-quality method is employed.

Transition States with 1,4-Biradical Characteristics

Figure 4 shows optimized geometry of the C_1 gauche transition state with just one imaginary frequency of 1191*i* cm-1 at UMP2/6-31G* level. These structures are corresponding to the transition state given by the CASSCF calculation of Robb et al. [10b]. As is indicated in Table I, the relative energies of 19.9 kcal/mol at UMP2 level is larger than 6.7 kcal/mol of Robb et al. [10b]. The C—C and C—O bond distances of 1.373 and 1.873 Å are shorter by only 0.028 Å and longer by only 0.023 Å of Robb et al. [10b], being similar tendencies in the case of the 1,4-biradical states.

Robb et al. [10b] indicated the qualitative description of the potential energy surfaces (Fig. 5 in Ref. [10b]). They described that the gauche TS is connected to the gauche 1,4-biradical minimum (G1). They also suggested that the avoided crossing corresponding to the closure of the gauche 1,4-biradical minimum to 1,2-dioxetane exists and the transition state is located far from the gauche TS obtained. However, they did not discuss the path from the gauche TS to the 1,2-dioxetane molecule concretely.

The intrinsic-reaction-coordinate (IRC) calculation was performed to elucidate the characteristics of the gauche transition state. Figure 5 shows the

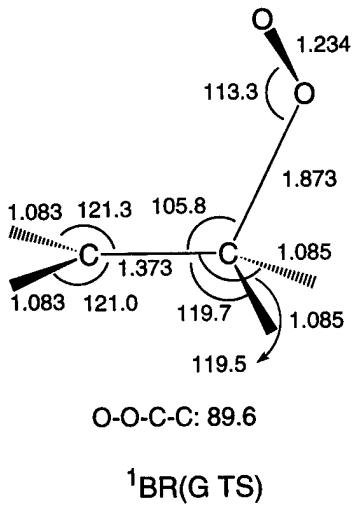


FIGURE 4. Optimized geometrical parameters of the C_1 gauche transition state obtained by UMP2/6-31G* method.

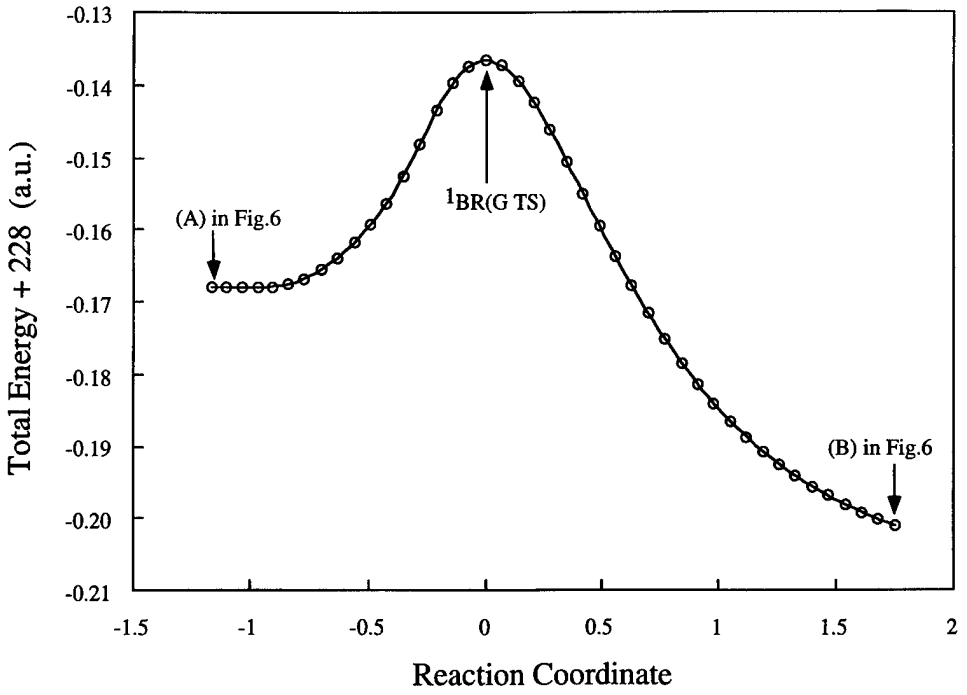


FIGURE 5. Energy variation from the gauche transition state along the intrinsic reaction coordinate using UMP2 / 6-31G* method.

energy variation from the gauche transition state along the intrinsic reaction coordinate. The energy profile smoothly connects to both directions of two different states. The geometries on the terminal points of the reverse and forward directions of intrinsic reaction coordinate are depicted in Figure 6. It is found from Fig. 6(a) that the geometry obtained from the reverse direction is almost equal to that of the gauche ^{1}BR minimum shown in Figure 2, indicating that the gauche transition state

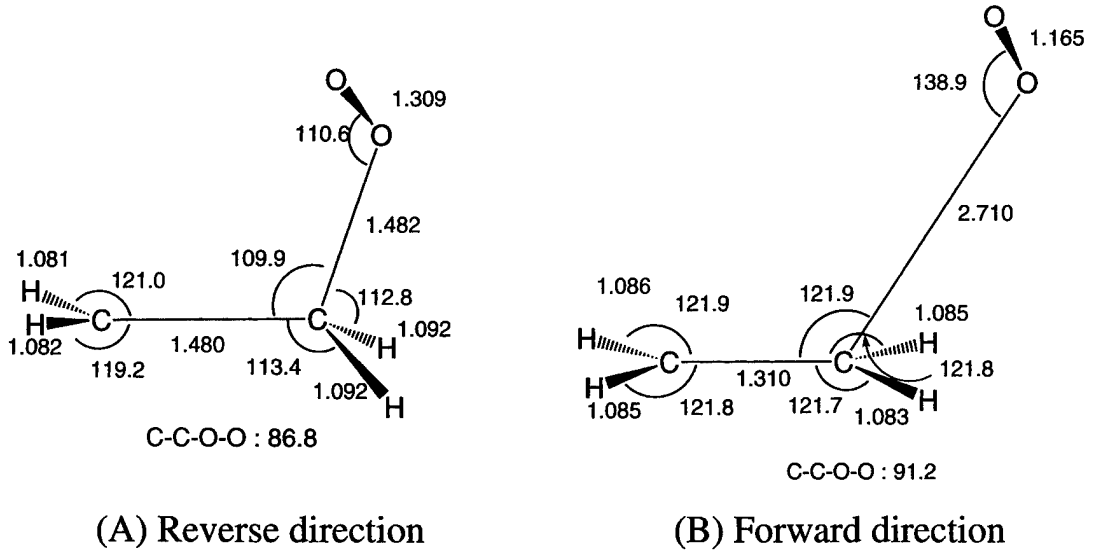


FIGURE 6. Geometrical parameters of the states obtained by the intrinsic reaction coordinate calculation from the C_1 gauche transition state using the UMP2 / 6-31G* method: (a) reverse direction, (b) forward direction.

is smoothly connected to the gauche ^{1}BR state. Figure 6(b) represents the geometry obtained from the forward direction. The C—O distance is 2.710 Å, being quite longer as a chemical bonding. The C—C bond distance in the ethylene moiety is 1.310 Å, being nearly equal to 1.336 Å of the ethylene molecule optimized by RMP2/6-31G* method. Apparently, the C_1 gauche transition state has a reaction path to connect with the dissociation limit of $^1O_2 + H_2C = CH_2$.

The reaction of $^1O_2 + H_2C = CH_2$ through the 1,4-biradical intermediates initially proceeds through the C_1 gauche transition state to form the gauche ^{1}BR minimum state, following that the free rotation of O_2 moiety along the C—O bond axis occurs due to the energy barrier less than 4.0 kcal/mol. The free rotation brings about the possibility to form the 1,2-dioxetane molecule.

The transition state corresponding to the gauche ^{1}BR(G TS) state was not found at the UNO CASSCF{2,2} level. The occupation numbers of the UNOs are 1.998, 1.874, 1.052, 0.948, 0.126, and 0.002 for HOMO − 2, HOMO − 1, HOMO, LUMO, LUMO + 1, LUMO + 2, respectively, showing that the active space in CASSCF should be composed of four orbitals and four electrons at least. However, at the UNO CASSCF{4,4} level, the transition state corresponding to the ^{1}BR(G TS) state was not also found. This indicates that the wide active space with more orbitals and more electrons may be necessary [19]. On the contrary, the occupation numbers of the gauche minimum ^{1}BR state are given by 1.998, 1.996, 1.063, 0.937, 0.004, and 0.002 at above same ordering, showing that two radical orbitals are concentrated to HOMO and LUMO. Similarly, for the *s*-cis $^1\sigma\pi$-BR state, the occupation numbers of HOMO − 1, HOMO, LUMO, and LUMO + 1 are 1.997, 1.0, 1.0, and 0.003, even the transition state of the rotation motion. In the previous work of tricentric bisdesmiphiles such as O_3, CH_2OCH_2, CH_2ONH, and HNOO [19a], it was shown that the CASSCF{2,2} method, in which the occupation numbers of only HOMO and LUMO suggest the radical orbitals, gives the qualitatively and quantitatively correct description of the singlet $\pi\pi$-radical states. Therefore, the active space of two orbitals and two electrons are reasonable to represent the 1,4-biradical states except for the case of the gauche ^{1}BR transition state.

Another optimum state with the *s*-trans geometry was found as shown in Figure 7. This structure corresponds to the C_s anti-first-order saddle point of Robb et al. [10b]. Our structures obtained by

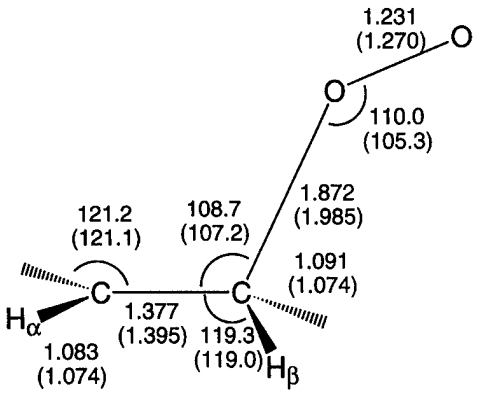


FIGURE 7. Optimized geometrical parameters of the *s*-trans-type second-order saddle point obtained by UMP2 / 6-31G* method and UNO CASSCF{4,4} / 6-31G* method in parenthesis.

UMP2/6-31G* are, however, a second-order saddle point on the potential energy surface with two imaginary frequencies of 1267*i* and 37*i* cm^{-1}. The total energy is decreased with rotation of the oxygen molecule along the C—O bond axis, approaching to the C_1 gauche transition state of the first-order saddle point.

The geometrical parameters of CASSCF shown in Figure 7 is obtained by the active space of four orbitals and four electrons, since the optimized geometry was not found at the CASSCF{2,2} level. The relative energy in Table I was estimated by the CASSCF{2,2} method at the geometry optimized by the CASSCF{4,4} method. The occupation numbers of the *s*-trans ^{1}BR(SP2) state are given by 1.997, 1.832, 1.0, 1.0, 0.168, and 0.003 at same ordering to the above, while the occupation numbers of the *s*-trans minimum ^{1}BR state are 1.997, 1.0, 1.0, and 0.003 for HOMO − 1, HOMO, LUMO, and LUMO + 1, respectively.

REACTION PATHWAY THROUGH PEREPOXIDE INTERMEDIATES

As shown in Figure 8, two optimized structures of the perepoxide type were found at both RMP2/6-31G* and CASSCF{2,2}/6-31G* levels. One (a) is a true minimum on the potential energy surface, another (b) is a second-order saddle point. These behaviors are very similar to those of CASSCF/4-31G and STO-3G by Robb et al. [10b].

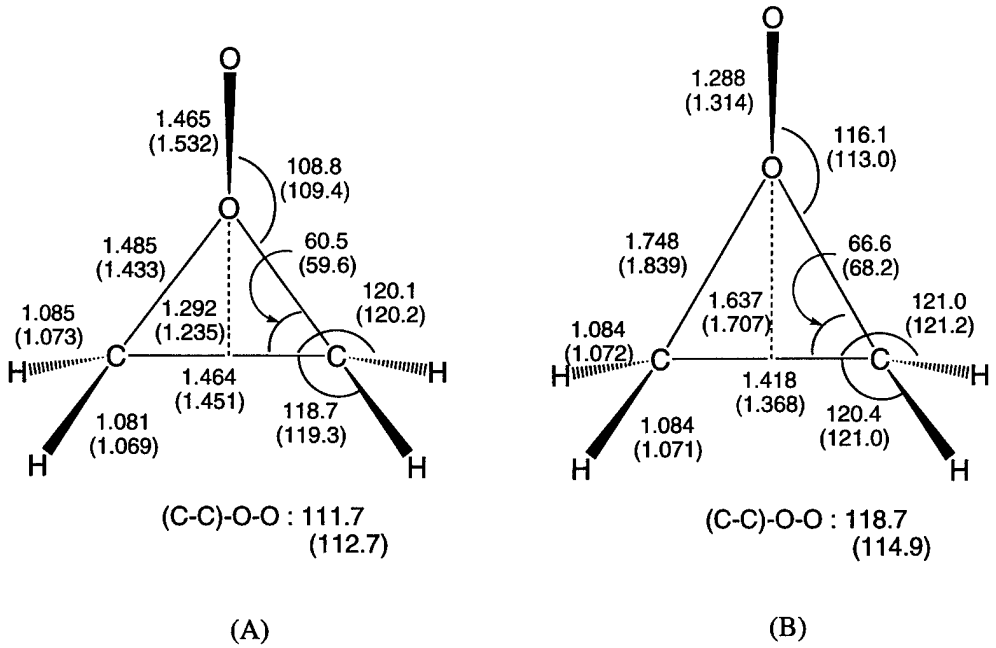


FIGURE 8. Optimized geometrical parameters of (a) perepoxide and (b) perepoxide-like (second-order saddle point) obtained by UMP2 / 6-31G* method and CASSCF{2,2} / 6-31G* method in parenthesis.

However, the geometrical parameters obtained are quite different from each other even at the CASSCF levels. For the minimum C_s perepoxide, the CASSCF{2,2} gives the shorter bond distances; for example, 1.433 Å of C—O and 1.532 Å of O—O for 1.559 and 1.634 Å of Robb et al. [10b], respectively. The RMP2 method, which gives a longer C—O bond distance and shorter O—O bond distance than those of the CASSCF method, has also similar tendencies. On the other hand, for the second-order saddle point, the MP2 method gives the bond distances of 1.748 and 1.288 Å of C—O and O—O, CASSCF/4-31G gives 1.821 and 1.467 Å, respectively.

As can be seen from Table I, the relative stabilities of the perepoxide based on the gauche minimum ^{1}BR state are surprisingly conflicting each other at the calculational levels and basis sets employed. The minimum basis set by CASSCF gives positive relative energy, the double-zeta basis set gives negative one, and the inclusion of the *d*-polarization switches the sign back to positive, giving the relative energy nearly equal to the gauche minimum ^{1}BR state. By the correction of the dynamic electron correlation, the stability of the perepoxide falls into the compatibility with the gauche minimum ^{1}BR state.

The perepoxidic intermediates have been studied by semiempirical and ab initio molecular orbital works. The CNDO/2 study [22] suggested that the perepoxide was a quasi-intermediate with the shallow minimum on the potential energy surface. It is also suggested by the MINDO/3 study [8] that the reaction of $^1O_2 + H_2C = CH_2$ proceeds through the perepoxide rather than the 1,4-biradical intermediates. The MNDO study [10b] indicated that the perepoxide is a local minimum on the potential energy surface with the higher energy by 32.6 kcal/mol than the dissociation limit of $^1O_2 + H_2C = CH_2$. On the other hand, the extensive calculations at the GVB-CI level with the DZP basis set by Harding and Goddard [7] supported the biradical mechanism from the result that the perepoxide was located as a minimum with higher energy than biradical minimum by about 8 kcal/mol. The ab initio MO MCSCF and CCI study of Roos et al. [9] concluded that the perepoxide is a preferable reaction pathway rather the 1,4-biradical intermediates. At last, we can see the results by Robb [10b] shown in Table I.

It is apparent from above discussion that the stability of the perepoxide is very sensitive to the basis sets and calculational levels employed in describing the electronic structure. This means that

the relative stability to the 1,4-biradical states and the reasonable reaction pathway are not conclusive within the previous investigations and our calculational levels, indicating that more high-quality calculational levels are necessary to elucidate the clear reaction mechanism of $^1O_2 + H_2C = CH_2$. These will be discussed later in this text.

1,2-DIOXETANE AS THE REACTION PRODUCT

Figure 9 shows the most stable geometries of 1,2-dioxetane optimized at both RMP2/6-31G* and CASSCF{2,2}/6-31G* levels with all positive vibrational frequencies. This structure has the C_2 symmetry with twisted angles of 19.2° and 10.1° at RMP2 and CASSCF levels, respectively, being consistent with that of Robb et al. [23]. On the other hand, the RHF/6-31G* gives the structure with C_{2v} symmetry as a local minimum on the potential energy surface with the lowest positive frequency of 54 cm^{-1}, as shown in Figure 10. The RMP2 and CASSCF methods have also the similar structures shown in Figure 10. These states are, however, the first-order saddle point with single imaginary frequency and have higher energy by 0.68 and 0.01 kcal/mol than the state of the C_2 symmetry at RMP2 and CASSCF levels, respectively, indicating that the C—O bonds in the ground state of the 1,2-dioxetane swing alternately.

As shown in Table I, the relative stability between the ^{1}BR(G1) and the 1,2-dioxetane at the CASSCF{2,2}/6-31G* level gives comparable value to that at the MP2/6-31G* level, being quite different from 27 kcal/mol of CASSCF/4-31G by Robb et al. [10b]. The heat of 1,2-dioxetane formation at CASSCF{2,2} level is estimated to be 33.7 kcal/mol compared with 12.8 [9] and 4.0 [10b] kcal/mol, being reasonable value with 30 kcal/mol of thermochemical estimation. This indicates that the polarization function and correlation effect play important roles for describing the electronic structure of the 1,2-dioxetane.

Robb et al. [23] studied the reaction mechanism of the chemiluminescent decomposition of 1,2-dioxetane by using CASSCF/4-31G method. They gave the relative energies between 1,2-dioxetane and two formaldehydes by 57.1 kcal/mol at CASSCF level and 61.4 kcal/mol at MP2 level using the optimized geometries of CASSCF. As is shown in Table I, our relative energy is 32.7 kcal/mol by CASSCF{2,2}/6-31G* method, being smaller than their CASSCF results. However, the relative energy of 53.5 kcal/mol at the MP2/6-31G* level is comparable with their result. Since discussion of the decomposition of 1,2-dioxetane is not part of this study, the investigation of this problem should be left in future.

From Figures 9 and 10, the carbon–carbon bond distance of 1,2-dioxetane at the MP2 level is given by 1.509 Å, which is shorter than the standard single-bond length of C—C single bond. The oxygen–oxygen bond distance is 1.521 Å, being quite longer than 1.421 Å given by geometry optimiza-

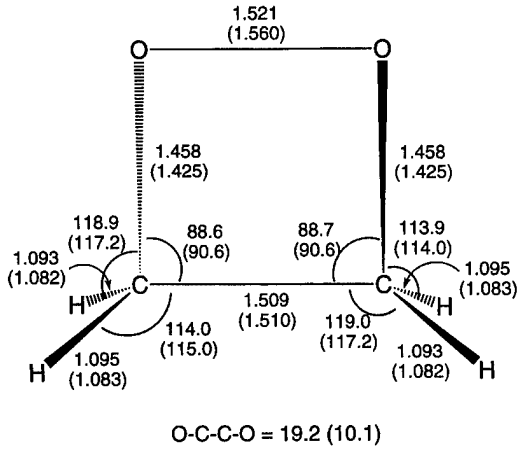


FIGURE 9. Optimized geometrical parameters of 1,2-dioxetane with C_2 symmetry obtained by RMP2 / 6-31G* method and CASSCF{2,2} / 6-31G* method in parenthesis.

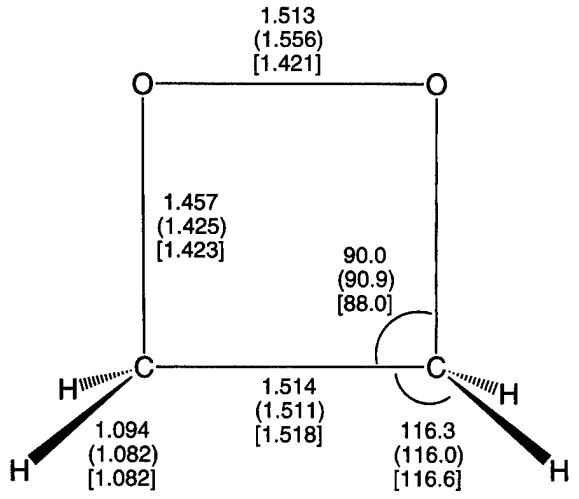


FIGURE 10. Optimized geometrical parameters of 1,2-dioxetane with C_{2v} symmetry obtained by RMP2/6-31G*, CASSCF{2,2} / 6-31G* in parenthesis, and RHF/6-31G* in square brackets.

tion of RHF/6-31G*, indicating that the correlation effect plays an important role to describe the electronic structure of 1,2-dioxetane. The carbon–oxygen bond distance also changes from 1.423 to 1.458 Å by inclusion of correlation effects.

RELATIVE STABILITIES OF REACTION INTERMEDIATES AT VARIOUS CALCULATIONAL LEVELS

Table III summarizes the relative energies of reaction intermediates, transition state, and products estimated by various levels of theories using the geometries optimized at the MP2/6-31G* level. The relative energies of the perepoxide are surprisingly sensitive to the calculational levels of theories.

Compared with the energy barrier height of 18.0 kcal/mol from ^{1}BR(G1) to ^{1}BR(G TS) by the UHF method, the APUHF method increases to 28.2 kcal/mol, while the CASSCF method with the nondynamic electron correlation does not almost increase, that is, 19.9 kcal/mol. Though the dynamic electron correlation is important to describe more precisely the singlet biradical states, the relative energies of UMP2 and UMP4 are not almost changed. The relative energy by the APUHF, APUMP2, and APUMP4 methods are largely increased as well as the CASMP2. The coupled-cluster methods decrease the barrier height to 9.9 and 6.7 kcal/mol by CCSD and CCSD(T), respectively.

On the other hand, as is shown in Table III, the perepoxide is largely fluctuated by the calculational levels. Compared with results of the RHF method, the nondynamic and dynamic electron correlation decreases the relative energies between ^{1}BR(G1) state and the perepoxide. At the MP2 and MP4 levels, the stabilities of the perepoxide are compatible with the ^{1}BR(G1) state. The coupled-cluster method unstabilized the perepoxide to 6–8 kcal/mol.

The relative stabilities of the 1,2-dioxetane are not so sensitive to the calculational levels, falling into between 40 and 52 kcal/mol. However, the CASMP2 method decreases it to about 33 kcal/mol. The energy differences between DO and two formaldehyde are nearly equal to 50–60 kcal/mol except for the CASSCF and CASMP2 methods.

It is apparent from Table III that the reaction pathways from the singlet oxygen plus ethylene to 1,2-dioxetane will be differently described by the calculational levels. In the UHF and CASSCF methods, the reaction pathway through 1,4-biradical states is preferable rather than through the perepoxide intermediate due to the greater stability of the BR state than the perepoxide. At the MP2 level, though the transition state from ^{1}BR(G1) state or perepoxide to the 1,2-dioxetane is not found, two reaction pathways might be competitive with each other. At the coupled-cluster method, the ^{1}BR(TS) state and the perepoxide, which is a local minimum on the potential energy surface, are iso-energetics, indicating that the possibility of reaching the singlet BR(G1) state is higher than the perepoxide intermediate.

As was examined previously [6d, 13, 19a] a potential energy curve for the dissociation process of covalent bond in a bicentric system is divided

TABLE III
Relative stabilities (kcal / mol) of reaction intermediates estimated by various levels of theory based on the geometries optimized by RMP2 or UMP2 using 6-31G* basis set.

Methods \ States	^{1}BR (G1)[a]	^{1}BR (G TS)	Perepoxide	DO	$2H_2C=O$
R(U)HF	0.0	18.0	30.4	−11.5	−75.7
APUHF	0.0	28.2			
CASSCF	0.0	19.9	4.9	−51.0	−82.1[b]
R(U)MP2	0.0	19.9	−0.6	−51.5	−105.0
APUMP2	0.0	34.6			
R(U)MP4	0.0	16.4	2.2	−46.9	−99.9
APUMP4	0.0	29.3			
CCSD	0.0	9.9	8.1	−40.9	−93.7
CCSD(T)	0.0	6.7	5.7	−43.5	−95.1
CASMP2	0.0	35.5	−4.6	−33.4	−109.3[b]
CASPT2	0.0	17.0	5.0	−42.9	−100.6[b]

[a] Total energies are given in footnote in Table II.
[b] The formaldehyde dimer with C — C distance of 10 Å was calculated.

into three characteristic regions: (I) stable region, (II) intermediate (transition) region, and (III) unstable (magnetic) region. As is well known, the full configuration interaction (FCI) provides a reasonable potential curve over the whole region. The RHF and RMP methods can be applied to species in region I, but they usually give an unreasonable result in region III. The RHF coupled-cluster (RCC) method is suitable to species in region I, usually reliable in region II, and unreasonable in region III. On the other hand, the UHF method provides a proper dissociation curve, but it suffers the so-called spin contamination error, giving the higher energy than FCI over the whole region. The UMPn method provides the potential curve close to FCI, but usually fails for the description of species in region II. However, the potential curve and wave function presented by the UHF coupled-cluster (UCC) should be very close to that by FCI if the exponential part is taken to involve sufficient higher excitation operators. In fact, the spin contamination errors on the potential curve were not serious even at the truncated UCCSD(T) level in the bicentric systems examined before [14].

It seems, therefore, that the coupled-cluster method is reliable and necessary to describe the reactions including the unstable or radical intermediate. The perepoxide and 1,2-dioxetane constructed of the covalent bond should be located in region I, while the singlet biradical intermediates and transition state with strong biradical characteristics are in region III. Therefore, the coupled-cluster method is reliable and necessary to describe the reactions, including the unstable or radical intermediate. It is concluded from Table III that the singlet oxygen reaction to ethylene molecule will proceed by a two-step mechanism through 1,4-biradical intermediates, though the transition state should be located by coupled-cluster treatment or more sophisticated method.

Conclusion

The reaction mechanism and relative stabilities of the intermediates and transition states in the reaction of ethylene molecule plus $^1O_2$ using ab initio MO theories at several levels of theory with the correction of the nondynamic and dynamic electron correlation effects were systematically investigated. Full geometry optimizations of the corresponding biradical (BR) intermediates, perepoxide (PE), and 1,2-dioxetane (DO) were performed by CASSCF{2,2}/6-31G* method with nondynamic electron correlation effect and RHF or UHF (R or U)MP2/6-31G* method with dynamic electron correlation effect.

Four optimized geometries of *s*-cis, two gauche's, and *s*-trans types in the ^{1}BR states were found by both UMP2/6-31G* and CASSCF {2,2}/6-31G* methods, possessing biradical characteristics with terminal methylene moiety and terminal oxygen atom. One of two gauche's and *s*-trans types are local minimums on the potential energy surface. For the rotation around the C—O bond axis, four ^{1}BR states are smoothly connected with the rotation barrier less than 4 kcal/mol, indicating that the free rotation easily occurs in the singlet state. One of two gauche types, which was found as a new geometry of 1,4-biradical singlet state, and *s*-cis-type geometry are the transition states of the rotation motion.

The C_1 gauche geometry was also found as a transition state on the potential surface. The IRC study showed that it connects smoothly to the gauche ^{1}BR minimum state for the reverse direction and the dissociation limit of $^1O_2 + H_2C = CH_2$ for the forward direction. It is, therefore, concluded that the reaction of $^1O_2 + H_2C = CH_2$ through the 1,4-biradical intermediates initially proceeds through the C_1 gauche transition state to form the gauche ^{1}BR minimum state, following that the free rotation of O_2 moiety along the C—O bond axis occurs due to the energy barrier less than 4 kcal/mol.

The relative stabilities of four 1,4-biradical states, the transition states, perepoxide, and 1,2-dioxetane were estimated again by the APUHF [13], APUMPn (n = 2, 4) [6], CCSD, CCSD(T) [6d, 14], CASMP2 [15], and CASPT2 [12] methods at the geometries optimized at both CASSCF{2,2}/6-31G and MP2/6-31G* levels. The APUHF gives the same ordering of the relative stabilities for four 1,4-biradical states at the geometries optimized by CASSCF{2,2} and UMP2 methods, while the APUMP (n = 2, 4) provides the reverse stabilities for 1,4-biradical states. It may be, therefore, noted that both APUHF and APUMP methods are suitable and unsuitable to describe the qualitative pictures of the species and quantitative pictures, respectively. The description of the perepoxide is very sensitive for basis sets employed and levels of theory, causing the difficulties determining the reaction mechanism of $^1O_2 + H_2C = CH_2$. For the description of the 1,2-dioxetane, the correction of

the dynamic electron correlation such as MP2 treatment is necessary at least.

As is mentioned in the previous section, the RHF coupled-cluster (RCC) method is suitable for species in the stable region I and usually reliable in intermediate region II. The potential curve and wave function presented by the UHF coupled-cluster (UCC) should be very close to that by FCI over the whole regions [6d, 12]. It seems, therefore, that the CCSD and CCSD(T) methods are necessary to elucidate the reaction mechanism including the unstable and radical intermediates. From the data of the CCSD and CCSD(T) methods, the reaction of $^1O_2 + H_2C = CH_2$ proceeds by a two-step mechanism through the 1,4-biradical intermediates rather than through the perepoxide.

ACKNOWLEDGMENT

This work has been supported by Core Research for Evolutional Science and Technology (CREST) of Japan Science and Technology Corporation (JST).

References

1. (a) D. R. Kearns, Chem. Rev. **71**, 395 (1971); (b) A. A. Frimer, Chem. Rev. **79**, 359 (1979); (c) M. Balci, Chem. Rev. **81**, 91 (1981).
2. (a) H. H. Wasserman and R. W. Murray, Eds., *Singlet Oxygen* (Academic, New York, 1979); (b) M. A. J. Rogers and E. L. Powers, *Oxygen and Cyx Radicals in Chemistry and Biology* (Academic, New York, 1981); (c) A. A. Frimer, Ed., *Singlet Oxygen, Vols I–IV* (CRC Press, Boca Raton, FL, 1985).
3. (a) C. S. Foote, Acc. Chem. Rev. **1**, 104 (1968); (b) G. B. Schuster, Chem. Rev. **12**, 366 (1979); (c) L. M. Stephenson, M. J. Grdine, and M. Orfanopoulos, Acc. Chem. Res. **13**, 419 (1980).
4. A. A. Gorman, I. Hambert, B. Space, and M. C. Standen, J. Am. Chem. Soc. **110**, 8053 (1988).
5. B. H. Brandow, Adv. Quant. Chem. **10**, 187 (1977).
6. (a) K. Yamaguchi, Y. Yoshioka, and T. Fueno, Chem. Phys. Lett. **46**, 360 (1977); (b) K. Yamaguchi, Y. Yoshioka, K. Takatsuka, and T. Fueno, Theoret. Chim. Acta, **48**, 185 (1978); (c) K. Yamaguchi, Y. Takahara, T. Fueno, and K. N. Houk, Theoret. Chim. Acta, **73**, 337 (1988); (d) S. Yamanaka, M. Okumura, M. Nakano, and K. Yamaguchi, J. Mol. Struct. (Theochem), **310**, 205 (1994).
7. (a) L. B. Harding and W. A. Goddard III, J. Am. Chem. Soc. **99**, 4520 (1977); (b) L. B. Harding and W. A. Goddard III, Tetrahedron Lett. **8**, 747 (1978); (c) L. B. Harding and W. A. Goddard III, J. Am. Chem. Soc. **102**, 439 (1980).
8. (a) M. J. S. Dewar, Chem. Br. **11**, 97 (1975); (b) M. J. S. Dewar and W. Thiel, J. Am. Chem. Scc. **97**, 3978 (1975); (c) M. J. S. Dewar, A. C. Griffin, W. Thiel, and I. J. Turchi, Ibid., **97**, 4439 (1975).
9. M. Hotokka, B. Roos, and P. Siegbahn, J. Am. Chem. Soc. **105**, 5263 (1983).
10. (a) B. Bernardi, A. B. Bottoni, M. Olivucci, M. A. Robb, H. B. Schelegel, and G. Tonachini, J. Am. Chem. Soc. **110**, 5993 (1988); (b) G. Tonachini, H. B. Schlegel, F. Bernardi, and M. A. Robb, J. Am. Chem. Soc. **112**, 483 (1990).
11. W. T. Borden and E. R. Davidson, Acc. Chem. Res. **29**, 67 (1996).
12. (a) M. Dupuis, A. Marquez, and E. R. Davidson, HONDO 95.3 from CHEM Station, 1995, IBM Corporation, Neighborhood Road, Kingston, NY 12401; (b) P. M. Kozlowski and E. R. Davidson, J. Chem. Phys. **100**, 3672 (1994).
13. (a) K. Yamaguchi, Chem. Phys. Lett. **33**, 330 (1975); (b) K. Yamaguchi, Chem. Phys. Lett. **35**, 230 (1975).
14. (a) K. Yamaguchi, Int. J. Quant. Chem. Sym. **14**, 269 (1980); (b) S. Yamanaka, M. Okumura, K. Yamaguchi, and K. Hirao, Chem. Phys. Lett. **225**, 213 (1994); (c) S. Yamanaka, M. Okumura, H. Nagao, and K. Yamaguchi, Chem. Phys. Lett. **233**, 88 (1995).
15. M. J. Frisch, G. W. Trucks, H. B. Schlegel, P. M. W. Gill, B. G. Johnson, M. A. Robb, J. R. Cheeseman, T. A. Keith, G. A. Petersson, J. A. Montgomery, K. Raghavachari, M. A. Al-Laham, V. G. Zakrewski, J. V. Ortiz, J. B. Foresman, J. Cioslowski, B. B. Stefanov, A. Nanayakkara, M. Challacombe, C. Y. Peng, P. Y. Ayala, W. Chen, M. W. Wong, J. L. Andres, E. S. Replogle, R. Gomperts, R. L. Martin, D. J. Fox, J. S. Binkley, D. J. Defrees, J. Baker, J. P. Stewart, M. Head-Gordon, C. Gonzalez, and J. A. Pople, Gaussian, Inc., Pittsburgh, PA, 1995.
16. B. Roos, Int. J. Quant. Chem. Sym. **14**, 175 (1980).
17. (a) P. Pulay and T. P. Hamilton, J. Chem. Phys. **88**, 4926 (1988); (b) J. M. Bofill and P. Pulay, J. Chem. Phys. **90**, 3657 (1989).
18. (a) K. J. Bartlett and G. D. Purvis, Int. J. Quant. Chem. **14**, 561 (1978); (b) J. A. Pople, K. Krishnan, H. B. Schlegel, and J. B. Binkley, Int. J. Quant. Chem. **14**, 545 (1978); (c) L. T. Redmon, G. D. Purvis III, and R. J. Bartlett, J. Chem. Phys. **72**, 986 (1980); (d) R. J. Bartlett and G. O. Purvis III, Phys. Scr. **21**, 225 (1980); (e) B. H. Brandow, Rev. Mod. Phys. **39**, 771 (1967); (f) L. T. Redmon and R. J. Bartlett, J. Chem. Phys. **67**, 2290 (1977).
19. (a) Y. Yoshioka, D. Yamaki, G. Maruta, T. Tunesada, K. Takada, T. Noro, and K. Yamaguchi, Bull. Chem. Soc. Jpn. **69**, 3395 (1996); (b) Y. Yoshioka, D. Yamaki, S. Kiribayashi, T. Tunesada, M. Nishino, K. Yamaguchi, and M. Mizuno, Electr. J. Theoret. Chem., submitted.
20. (a) G. Herzberg, Diatomic Molecules, 2nd ed. (Van Nostrand, Princeton, NJ, 1950); (b) J. H. Callomon, E. Hirota, K. Kuchitsu, W. J. Lafferty, A. K. Maki, and C. S. Pote, Structure Data on Free Polyatomic Molecules, Numerical Data and Function Relationship in Science and Technology, Landolt-Bornstein New Series, K. H. Ellwege, Ed. (Springer-Verlag, Berlin, 1976), Vol. 7.
21. (a) K. Yamaguchi, in Singlet Oxygen III, A. A. Frimer Ed. (CRC Press, Boca Raton, FL, 1985), p. 119; (b) Y. Yoshioka, T. Kawakami, S. Yamada, M. Nishino, K. Yamaguchi, and I. Saito, in preparation.
22. (a) S. Inagaki, S. Yamabe, H. Fujimoto, and K. Fukui, Bull. Chem. Soc. Jpn. **45**, 3510 (1972); (b) S. Inagaki and K. Fukui, J. Am. Chem. Soc. **97**, 7480 (1973).
23. M. Reguero, F. Bernadi, A. Bottoni, M. Olivucci, and M. A. Robb, J. Am. Chem. Soc. **113**, 1566 (1991).

Quantum Chemical Study of the Molecular Dynamics of Hydrated Li^+ and Be^{2+} Cations

GERHARD BISCHOF,[1] ALEXANDER SILBERNAGL,[1] KERSTI HERMANSSON,[2] MICHAEL PROBST[1,2]

[1] *Institute of General and Inorganic Chemistry, Innsbruck University, Innrain 52a, A-6020 Innsbruck, Austria*

[2] *Inorganic Chemistry, The Ångstrøm Laboratory, Uppsala University, Box 538, S-75121 Uppsala, Sweden*

Received 29 March 1997; accepted 11 August 1997

ABSTRACT: Molecular dynamics simulations of clusters of Li^+ and Be^{2+} cations with up to 12 water molecules were performed calculating the particle trajectories using Hartree–Fock-derived forces. It was found that independent of the starting configuration tetrahedral clusters are obtained in less than 1 ps. Only for Li^+ clusters, transition states with five and three water molecules are found. We discuss the structures of the clusters and the vibrational dynamics of the water molecules and compare them with other ab initio simulations, with simulations using analytical potential functions, and with static calculations. Water-dissociation (hydrogen transfer) reactions which take place at elevated temperatures were investigated. © 1997 John Wiley & Sons, Inc. Int J Quant Chem **65**: 803–816, 1997

Introduction

The hydration of ions plays a key role in many processes occurring in solution chemistry and is of great importance in many areas of physics, biochemistry, and biology. The molecular dynamics (MD) method has established itself as a valuable tool to obtain insight into the properties of aqueous solutions and hydrated ions at a microscopic level [1–3].

In this article, we report structural and dynamical results from MD simulations of clusters of Li^+ and Be^{2+} cations with water molecules. Many-body effects were incorporated into the simulation by using energies and forces from Hartree–Fock wave functions to propagate the trajectories. Due to the strong interactions caused by the small and

Correspondence to: M. Probst.
Contract grant sponsor: Austrian FWF.
Contract grant numbers: P10106-MOB, P9010-MOB.
Contract grant sponsor: Swedish Natural Science Research Council.

© 1997 John Wiley & Sons, Inc.
CCC 0020-7608 / 97 / 050803-14

highly charged cation, aqueous Be^{2+} clusters are ideal systems for studying strong nonadditive interactions. Comparisons are made with clusters of the singly charged Li^+ cation for which nonadditive effects are less important but for which only a few theoretical studies on clusters exist.

Experimental [4–6], quantum chemical [7–9], and simulation [6, 10, 11] studies on aqueous salt solutions containing Be^{2+} all report or predict a coordination number of four for not-too-concentrated solutions. For example, O-NMR [5] experiments on a $Be(ClO_4)_2$ solution at 295 K gave a coordination number of 4.1 ± 0.2.

It has been shown by ab initio calculations of clusters [7–9] that the high charge density on the Be^{2+} ion leads to strong nonadditive interactions. A comparison of classical molecular dynamics simulations with pair potentials only and with three-body effects incorporated [10, 11] showed that in correctly determining the coordination number nonadditive interactions play a crucial role.

Recently, calculations on $Be^{2+}(H_2O)_n$ systems were also carried out using the so-called Car–Parinello (CP) molecular dynamics method by Marx et al. [12–14]. Their results are compared with our findings in more detail in the subsequent sections.

Li^+ ions in water were among the first molecular liquids studied in computer simulations [15] and there exist many MD simulation studies of Li ions in various concentrations [16–18]. While the coordination number of Li^+ in dilute aqueous solutions is still inconclusive, most of the newer studies assume a sixfold coordination to be most likely.

In the following sections we discuss at first the details of our calculations. Then, structural properties of the clusters, simulation experiments performed in order to study the dissociation of water molecules, and vibrational properties are discussed. Finally, we compare the method used in the present work with alternative ones and summarize our conclusions.

Details of Calculations

In most MD simulations, analytical potentials are employed to derive the interparticle forces and most of the analytical potentials assume a pairwise additivity of the interactions, at least between unbonded atoms. While this is often a good approximation, it becomes inaccurate or even fails in cases where effects like polarization, charge transfer, or bond-breaking/bond formation are relevant. In principle, analytical potentials can be constructed to account also for such effects and many efforts have been made along these lines [19–22]. An alternative that became viable in recent time is to employ quantum chemical methods to treat the system as a whole when calculating the forces acting on the particles.

For the MD simulations reported here, the particle trajectories were calculated via forces from Hartree–Fock Hamiltonians with small basis sets. The wave function was optimized at every time step. The equations of motion were solved using a velocity-Verlet algorithm [23] and all degrees of freedom were kept active. For the constant-temperature simulations, the Berendsen thermostat [24] was used. A time step of 0.3 fs was sufficient to resolve also the hydrogen motions and a typical MD run was performed for 6000 time steps, corresponding to 1.8 ps elapsed time. One time step of a complex with 12 water molecules took about 180 s on a single MIPS 8000 processor of an SGI power challenge computer. The time is almost exclusively spent in the force calculation while the time for obtaining the new positions and velocities is negligible. The forces were obtained from a slightly modified Gaussian 94 computer code [25] which we interfaced to our MD routines.

THEORETICAL LEVEL

In principle, any suitable wave function—or density functional-based method for which energy gradients are available—can be used in an ab initio MD approach. We decided to work at the Hartree–Fock (HF) level since for the systems studied here electron correlation plays a minor role and a comparison of the computer codes accessible to us showed the calculations of forces to be about twice as fast for HF as for density functional-based methods like B3LYP [26, 27] or for MP2. Density functionals without gradient correction are considerably faster but they fail to reproduce hydrogen bonding correctly.

To be able to handle systems with two hydration shells, we are restricted to use rather small basis sets. For a comparison of basis-set quality, we carried out geometry optimizations on the systems $Be^{2+}(H_2O)_n$ ($n = 1$–4) and list the results in

Table I. (The binding energy per water molecule is given by $\Delta E = [E([Be(OH_2)_n]^{2+}) - E(Be^{2+}) - nE(H_2O)]/n$).

The CEP [29] basis set in single-zeta contraction compares energetically well with larger ones. On the HF level, it gives ΔE values of −136.6, −129.6, −116.3, and −103.1 kcal/mol for the mono- to tetrahydrates, compared with, e.g., −135.6, −128.0, −107.9, and −96.3 kcal/mol for the "DZP" basis set and it is (accidentally) even closer to the 6-311G** basis at the MP2 level (−147.3, −136.7, −119.0, and −103.2 kcal/mol). We found that small double-zeta basis sets like 3-21G give binding energies somewhat too high.

Table I also shows that the CEP basis set in a single-zeta contraction leads to Be—O distances about 0.07 Å too long. Also, the O—H distances are slightly too long. These errors stay constant during the series of hydrates. The use of CEP in a double-zeta contraction would have improved these distances at the expense of a fivefold increase of computing time. The H—O—H angle is in good agreement with more expensive basis sets and methods. We finally decided to use the CEP basis set in a single-zeta contraction for the MD simulations. Table II lists the results for the $Li^+(H_2O)_n$ (n = 1–4) clusters with the CEP basis set. Table III shows the harmonic vibrational frequencies for $Be^{2+}(H_2O)_n$ (n = 1–4) compared to two other basis sets and methods. The shifts in the O—H stretching vibrations are the largest for n = 1 and decrease then with increasing charge transfer to the cation. Most relevant are the differences between the O—H stretching vibrations of the isolated H_2O molecule and the fourfold coordinated clusters. For the CEP basis set, the slight average upshift of the symmetric (~ 10 cm^{-1}) and the large downshift of the asymmetric stretching mode (~ -290 cm^{-1}) are in reasonable agreement with the 3-21G values and also with shifts found

TABLE I
Binding energies and optimized geometries of $Be^{2+}(H_2O)_n$ with n = 1–4.

Method and basis set		n	r_{O-H} (Å)	∠HOH (degree)	r_{Be-O} (Å)	ΔE (kcal/mol)	Ref.
HF	CEP-4G	1	1.033	107.5	1.635	−136.6	This
		2	1.027	108.3	1.644	−129.6	work
		3	1.020	108.9	1.682	−116.2	
		4	1.014	108.8	1.736	−103.1	
HF	DZP	1	0.976	108.0	1.536	−135.6	[7]
		2	0.968	108.3	1.537	−128.0	
		3	0.961	107.9	1.613	−107.9	
		4	0.956	108.0	1.662	−96.3	
HF	3-21G	1	0.999	108.7	1.517	−169.2	[8]
		2	0.991	109.6	1.533	−158.0	
		3	0.981	110.2	1.585	−140.0	
		4	0.975	110.6	1.645	−123.1	
HF	3-21G*	1	0.999	108.0	1.503	−161.3	[8]
		2	0.990	108.4	1.528	−149.0	
		3	0.980	108.4	1.580	−130.8	
		4	0.974	108.2	1.648	−114.1	
DFT	Plane wave basis set +ECP	1	0.991	108.0	1.490	−149.6	[12]
		2	0.982	108.7	1.525	−140.2	
		3	0.974	108.6	1.585	−127.9	
		4	0.970	108.6	1.668	−117.7	
MP2	6-311G**	1	0.991	108.0	1.507	−147.3	[28]
		2	0.983	108.1	1.526	−136.7	
		3	0.974	107.8	1.579	−119.0	
		4	0.970	107.0	1.668	−103.2	

TABLE II
Hartree–Fock energies and optimized geometries of $Li^+(H_2O)_n$ with n = 1–4 (CEP basis set).

n	r_{O-H} (Å)	∠HOH (degree)	r_{Li-O} (Å)	ΔE (kcal / mol)
1 (C_{2v})	1.0090	107.2	1.945	−41.7
2 (D_{2d})	1.0081	107.5	1.961	−39.9
3 (D_3)	1.0074	107.9	1.994	−36.6
4 (D_{2d})	1.0067	108.0	2.043	−32.9

for other cations [31]. Interestingly, the reported shifts from the DFT calculations with a plane-wave basis set [12] are zero.

Structural Results

In contrast to Be^{2+} where tetrahedral coordination is expected if nonadditive effects are incorporated in the simulations, this is not so clear for Li^+. For example, a neutron diffraction study of a 3.57 m LiCl solution resulted in a coordination number of 5.5 ± 0.3 [32] and MD simulations of aqueous solutions at different concentrations but with pair potentials also seem to indicate that in infinitely diluted systems an octahedral tetrahedral coordination is preferred [16–18]. On the other hand, simulations on the system Li^+/H_2O with nonadditive potentials [33, 34] resulted in tetrahedral coordination of the cation.

We performed simulations with different initial configurations. Independent of the initial state, tetrahedrally coordinated complexes are obtained. The same starting configurations for $Be^{2+}(H_2O)_n$ and $Li^+(H_2O)_n$ (n = 6, 8, 10, 12) were used. The simulations were performed at 300 K using a Berendsen thermostat [24] for equilibration.

Figure 1 shows the different starting configurations of the Be^{2+} clusters. In the center of the figure, a representative configuration resulting from the simulations is shown. The tetrahedral coordination of the oxygen atoms of the inner-shell water molecules (plotted in black) can be seen clearly. This particular configuration originates from the initial structure $Be^{2+}(H_2O)_2(H_2O)_8$ (c) but the other three starting configurations would

TABLE III
Harmonic frequencies of the most important modes in the $Be^{2+}(H_2O)_n$ clusters with n = 0–4.

	H_2O			n = 1			n = 2			n = 3			n = 4		
Mode	CEP (this work)	3-21G [8]	Plane wave [12]	CEP (this work)	3-21G [8]	Plane wave [12]	CEP (this work)	3-21G [8]	Plane wave [12]	CEP (this work)	3-21G [8]	Plane wave [12]	CEP (this work)	3-21G [8]	Plane wave [12]
Be—(OH_2) bending				888–913	944–955	710–816	831–905	866–950	640–840	718–912	751–938	580–740	636–783	657–785	490–600
Be—O stretch				963	1126	1060	1213	1376	1210	1028	1129	980	877–982	1007–1018	830
H—O—H bending	1727	1799	1610	1752	1820	1700	1754	1824–1827	1730	1761–1764	1834–1840	1730	1767–1783	1830–1840	1730
O—H sym. str.	3900	3812	3710	3676	3500	3490	3742	3588–3610	3600	3835–3853	3703–3726	3680	3903–3919	3775–3796	3710
O—H asym. str.	4246	3945	3830	3709	3511	3520	3803	3630	3620	3933–3935	3764–3966	3750	4033–3936	3853–3857	3830

The experimental values for H_2O are 1595, 3657, and 3756 cm^{-1} for the anharmonic and 1648, 3832, and 3943 cm^{-1} for the harmonic frequencies [30]. For the larger complexes, the lowest and highest frequency of a set of modes are given, if available.

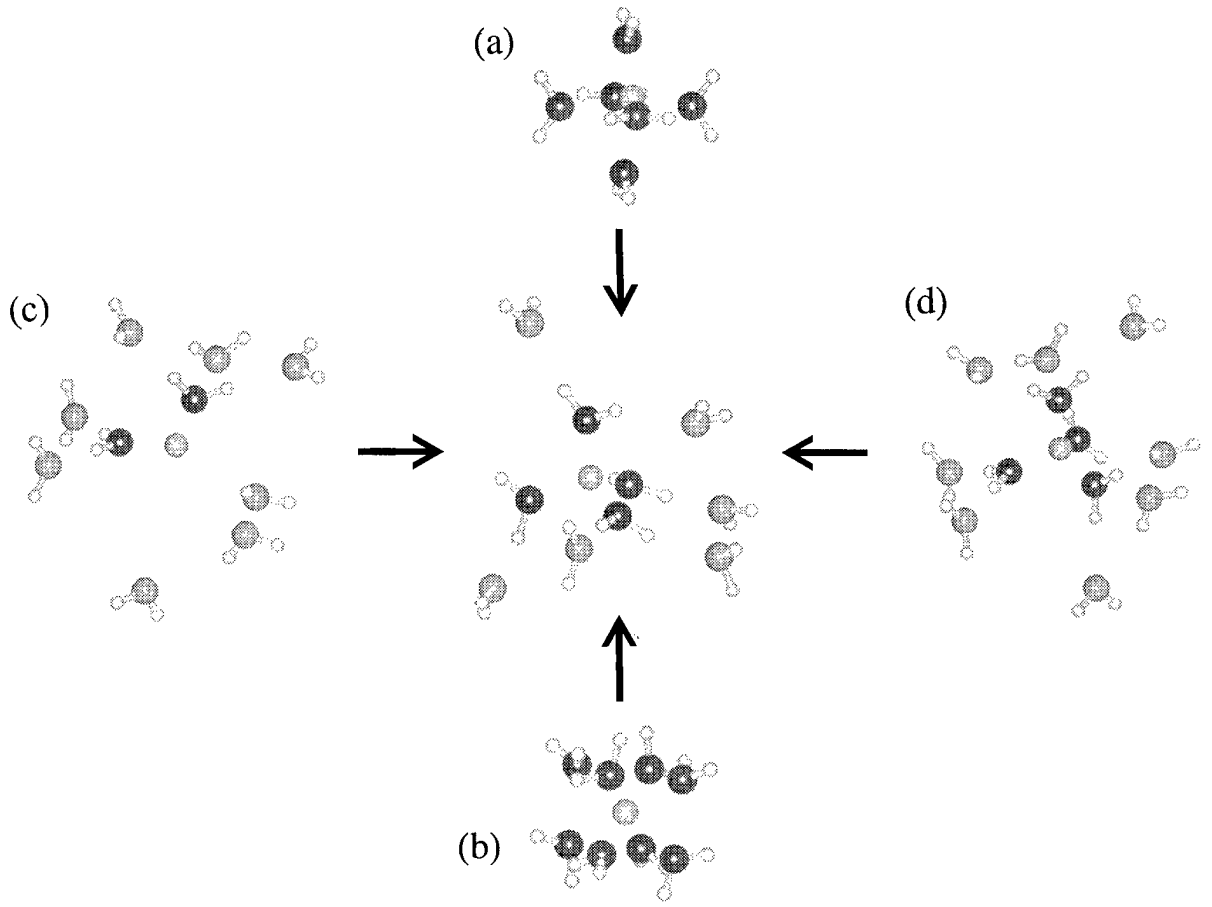


FIGURE 1. Different starting configurations of the Be^{2+} (respectively, Li^+)–water clusters: (a) $Be^{2+}(H_2O)_6$; (b) $Be^{2+}(H_2O)_8$; (c) $Be^{2+}(H_2O)_2(H_2O)_8$; (d) $Be^{2+}(H_2O)_4(H_2O)_8$; (center) a typical $Be^{2+}(H_2O)_{12}$ configuration resulting from (c). Black spheres represent oxygen atoms of water molecules in the first hydration shell.

lead to similar final configurations (as is symbolized by the four arrows in Fig. 1), qualitatively only differing in the number of second-shell water molecules. Configurations with Li^+ as a central cation, on average, show the same fourfold coordination.

First, we discuss the simulations involving beryllium, then the ones with lithium cation:

Be

(a) The initial configuration denoted (a) in Figure 1 is a $Be^{2+}(H_2O)_6$ cluster which was obtained from the T_h symmetrically optimized geometry [8] and which was also used in [12]. There, it was found that, starting from an octahedral cluster at 20 K, a fourfold hydrated structure is obtained after 0.2 ps. We found that a similar tetrahedral structure is reached after 0.1 ps (by slightly displacing the cation from the origin, we had removed the symmetry from the system). Then, we carried out equivalent simulations with $Be^{2+}(H_2O)_8$ (b), a hexahedral initial configuration (eight water molecules cubically arranged in the first shell), with $Be^{2+}(H_2O)_{10}$ (c), two water molecules in the first shell and eight in the second and with $Be^{2+}(H_2O)_{12}$ (d), four water molecules in the first and eight water molecules in the second shell. All these simulations resulted in fourfold coordinated first hydration shells after similar times (~ 0.1 ps). No exchange of water molecules between the first and the second hydration shell was observed after this time.

A quantitative picture of the solution structure can be obtained from the radial distribution functions. In the following discussion, we refer to $Be^{2+}(H_2O)_{12}$ unless mentioned otherwise. Because finite clusters are investigated, the radial distribu-

tion functions are not normalized by r^{-2}, as is usually done for periodic systems. The first maximum of $g_{Be-O}(r)$ at 1.72 Å (Fig. 2, solid line) can be compared to 1.65 Å [13] (CP simulation) and 1.75 Å (MD study with a threebody potential [11]). The value obtained from the X-ray diffraction study [6] of a 5.3 molal aqueous $BeCl_2$ solution is 1.67 Å. The Be—O distances in crystals with fourfold coordinated Be^{2+} ions are shorter and lie between 1.60 and 1.63 Å [35]. Considering that the CEP basis set leads to an overestimation of the Be—O distance of about 0.07 Å (Table I), the values from X-ray [6] and the CP simulation [13] are probably more accurate than in the MD study [11] and are consistent with our data. The peak maximum of 1.72 Å can further be compared with the values of the optimized cluster with (1.714 Å, Table IV) and without (1.736 Å) the eight second-shell water molecules, showing that the dynamic motion has a smaller influence on the average Be—O distance than on the second hydration shell.

The second maximum of g_{Be-O} at 4.07 Å deviates more from the potential minimum at 3.957 Å. For the three systems with fewer water molecules, values between 3.6 and 4.4 Å are obtained. The first and second peaks of g_{Be-O} are completely separated and are well defined, similar to what was found in the MD study [11] with periodic boundaries. These data cannot be compared further to the CP simulation study [13] because the small periodic box of about 10 Å containing 31 water molecules in [13] already disturbs the second hydration shell, leading to an unstructured $g_{Be-O}(r)$ curve beyond 3.5 Å.

The Be—H distribution function has its first maximum at 2.42 Å (Fig. 2, dotted lines). This is again about 0.07 Å more than the value obtained in [13]. It is again close to the values of the potential minimum (2.457 Å), indicating that the water molecules in our simulation are, on average, only slightly tilted away from a planar Be—H_2O subconfiguration.

The integral values are also plotted in figure 2 for O and H and show the expected plateaus for 4 and 12 oxygen atoms or 8 and 24 hydrogens, respectively. The distribution of the H—O—H angles for the first and second hydration shell have maxima at 111.5° and 108.3°, respectively (optimized values: 109.9° and 108.1°) and thus show that the angle is little influenced by the cation. The distribution of the intramolecular O—H distances in the first shell (Fig. 3, solid line) gives a peak with a maximum between 1.00 and 1.04 Å, nearly symmetrically around the potential minimum of 1.023 Å. Compared to an isolated H_2O molecule, the bonds are elongated by about 0.01 Å. The

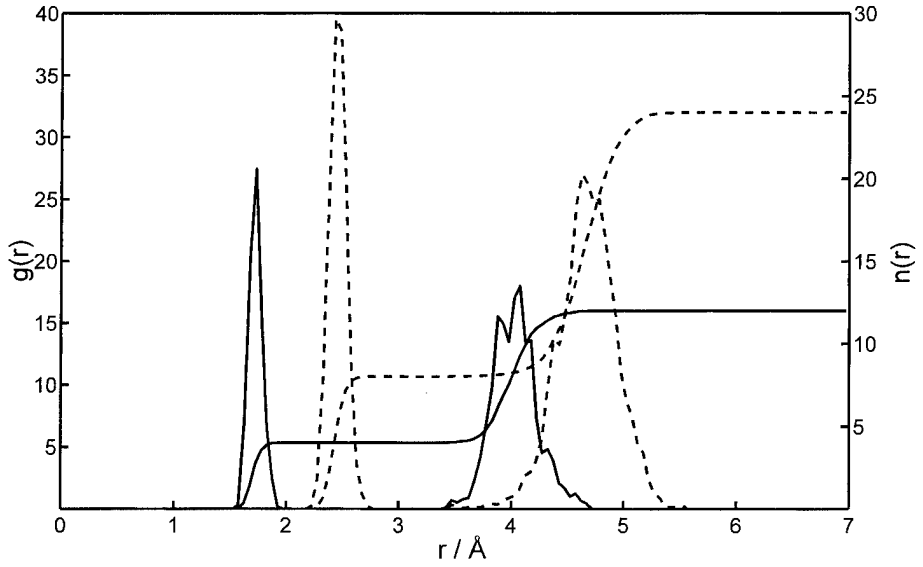


FIGURE 2. Be—O radial distribution function $g_{Be-O}(r)$ with running coordination number $n_{Be-O}(r)$ (solid curves) and Be—H radial distribution function $g_{Be-H}(r)$ with running coordation number $n_{Be-H}(r)$ (dotted curves) of $Be^{2+}(H_2O)_{12}$.

TABLE IV
Optimized geometries of the $Be^{2+}(H_2O)_4(H_2O)_8$ and the $Li^+(H_2O)_4(H_2O)_8$ clusters (HF with CEP basis set).

	r_{O-H} (Å)	∠HOH (degree)	r_{Be-O} (Å)
$Be^{2+}(H_2O)_4(H_2O)_8$			
First shell	1.023	109.9	1.714
Second shell	1.012	108.1	3.957
$Li^{2+}(H_2O)_4(H_2O)_8$			
First shell	1.008	108.3	2.033
Second shell	1.011	108.0	4.476

average distance between the oxygens in the first and second hydration shell in our the simulation (2.35 Å) is about 0.1 Å longer than the optimized value (2.243 Å), indicating a large dynamic contribution.

Li

Simulations with the Li^+ ion were performed with the same set of starting configurations as described above. A tetrahedrally hydrated Li^+ ion emerges as the most stable subsystem but its formation is much slower than for Be^{2+} and we observed "transition states" with different coordination numbers in the initial states of the simulations. It took between 0.45 ps [from $Li^+(H_2O)_2(H_2O)_8$] and 0.70 ps [from $Li^+(H_2O)_8$] until the tetrahedral complex was formed.

Figure 4 shows two examples of intermediate structures: (a) The complex with a threefold coordinated Li^+ was formed from the $Li^+(H_2O)_6$ cluster after 0.16 ps. (b) A complex with five water molecules was formed from $Li^+(H_2O)_2(H_2O)_8$ after 0.25 ps. Similar complexes with three- and

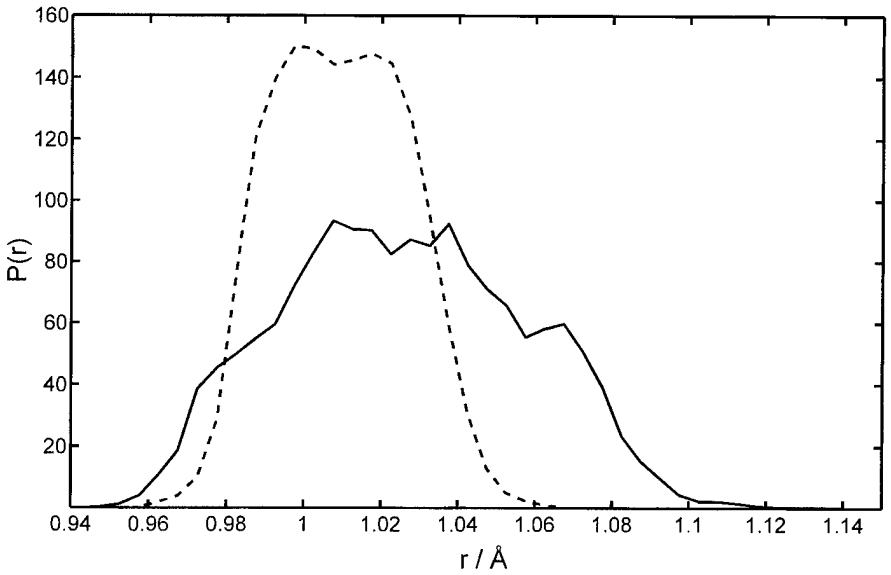


FIGURE 3. Distribution of the intramolecular O—H distances in the first hydration shells of $Be^{2+}(H_2O)_{12}$ (solid curve) and $Li^+(H_2O)_{12}$ (dotted curve).

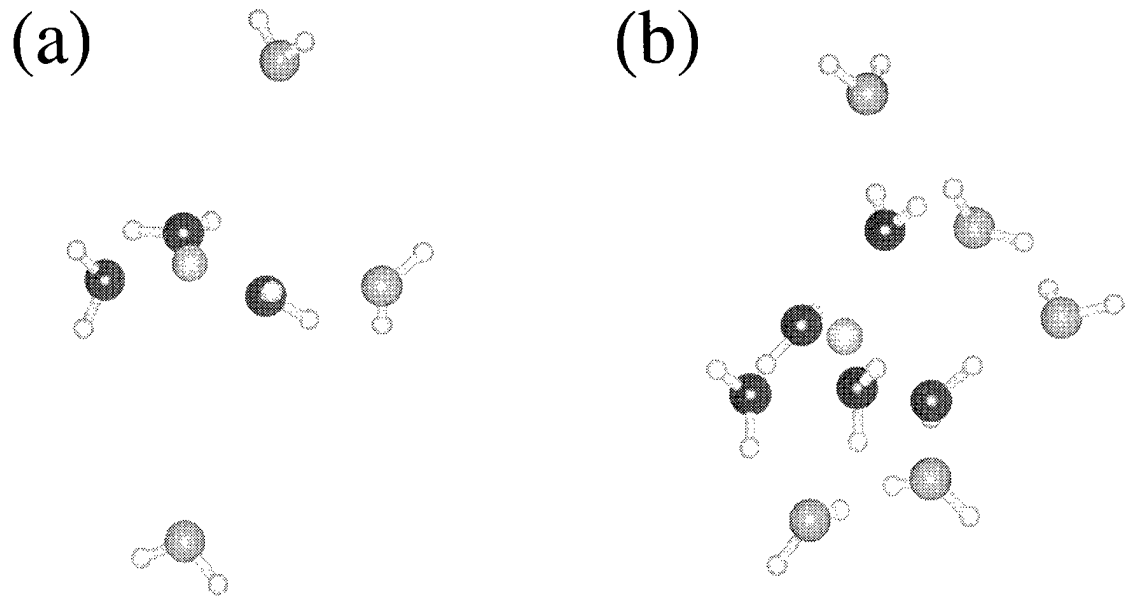


FIGURE 4. Snapshots of (a) an intermediate state with threefold coordinated Li^+ after simulating for 0.16 ps from the $Li^+(H_2O)_6$ configuration and (b) an intermediate state with fivefold coordinated Li^+ after simulating for 0.25 ps starting from $Li^+(H_2O)_2(H_2O)_8$.

fivefold coordination were also found for the other starting configurations. Since we used no periodic boundary conditions or any potentials confining the particles in the simulations, water molecules can—and will finally—evaporate from the second hydration shell. In the Be^{2+}/H_2O system, the strong attraction of the water molecules makes this a process too slow to be observed, but for Li^+/H_2O, such evaporation is observed in all simulations.

Figure 5 shows the radial distribution functions $g_{Li-O}(r)$ and $g_{Li-H}(r)$ for $Li^+(H_2O)_4(H_2O)_8$. The first peak of the Li—O distance distribution has its maximum at 2.08 Å. The corresponding value of the potential minimum is 2.03 Å (Table IV). In simulations studies with nonadditive potentials [33, 34], values of 1.98 and 2.0 Å were found. The Li—O distances are about 0.35 Å longer than the Be—O distances, which directly reflects the different ionic radii of the ions (Li^+: 0.59 Å vs. Be^{2+}: 0.27 Å) and shows that the ion–water attraction and not the water–water repulsion are dominating. The $g(r)$ curves decrease nearly to zero between their first- and second-shell maxima. The first peak again integrates to four.

The second hydration shell of Li^+ leads to a broad peak between 4.0 and 5.0 Å with a maximum at 4.57 Å (potential minimum: 4.48 Å). The tail of the function is caused by the slowly evaporating water molecules. The maximum of g_{Li-H} is located at 2.72 Å. This is about 0.15 Å longer than that found in a simulation carried out with pair potentials and periodic boundaries [36]. From our geometry optimization, a value of 2.75 Å is obtained. The maxima of the distribution of the H—O—H angle are found at 108.5° and 107.5° for first and second shells, respectively.

The intramolecular O—H distance distribution (Fig. 3, dashed line) has its maximum between 0.993 and 1.020 Å for the first-shell water molecules. They are thus slightly less elongated than in the complexes with Be^{2+}.

The distance between the oxygens in the first and second hydration shell from the simulation is about 0.05 Å longer than between the corresponding potential minima. While this is only about half of the value found for Be^{2+}, it is still a large deviation.

Dissociation of Water Molecules

Be^{2+} can cause abstraction of hydrogen from water molecules, giving $BeOH^+$. This is the reason why solutions of Be^{2+} salts are acidic (a 0.5 molal solution of $BeCl_2$ has an approximate pH value of

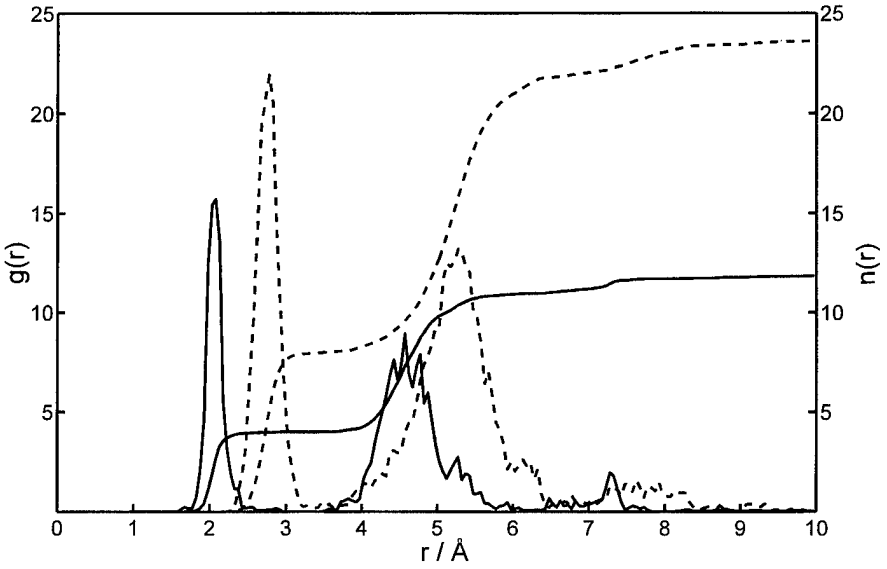


FIGURE 5. Li—O radial distribution function $g_{Li-O}(r)$ with running coordination number $n_{Li-O}(r)$ (solid curves) and Li—H radial distribution function $g_{Li-H}(r)$ with running coordination number $n_{Li-H}(r)$ (dotted curves) of $Li^+(H_2O)_{12}$.

3.5). Ab initio MD allows the simulation of such dissociation reactions. At room temperature, this reaction is rather infrequent in the liquid phase and will be even more so in small clusters. In the case of elevated temperatures, however, the reaction takes place more rapidly. We performed the following experiments:

(a) Starting from $Be^{2+}(H_2O)_8$ with velocities corresponding to 20 K, we found water dissociation according to

$$Be^{2+}(H_2O)_8 \rightarrow Be^+(H_2O)_2OH + H_3O^+ + 4\,H_2O$$

after about 0.17 ps. The potential energy at the beginning of the simulation led to a temperature of about 2000 K during this time. A typical configuration of the products is shown in Figure 6.

(b) The acidity of Be^{2+} can be expected to be much higher if it is not saturated with four (or more) water molecules. Indeed, a small model system consisting of one molecule of water in the first hydration shell and one hydrogen bonded to the first one reacts after 0.3 ps at 300 K according to

$$Be^{2+}(OH_2)OH_2 \rightarrow BeOH^+ + H_3O^+.$$

(c) MD simulations starting with the equilibrated $Be^{2+}(H_2O)_4(H_2O)_8$ configuration were performed at different temperatures with intervals of about 1000 K. At 5000 K, we observed water dissociation after 0.45 ps.

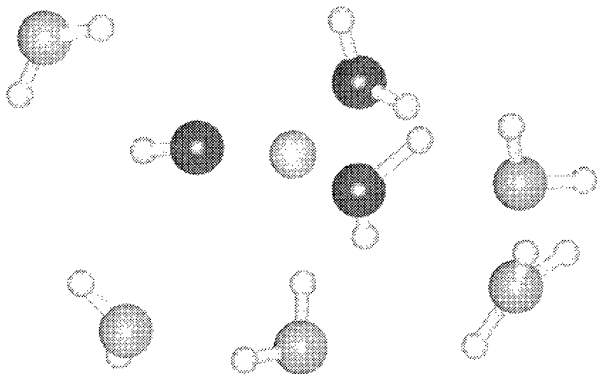


FIGURE 6. Typical configuration after dissociation of a water molecule from the $Be^{2+}(H_2O)_8$ cluster after 0.45 ps simulation time.

Figure 7 shows the distance between the hydrogen atom which is being transferred and both of the oxygen atoms involved in the dissociation reaction. At start of the simulation, this hydrogen and the oxygen atom of the water molecule, which will be protonated, are about 6 Å apart (light curve). The hydrogen exchange at 0.45 ps happens within about two cycles of the O—H vibrations and no protonated water dimer with a shared hydrogen or a similar species is formed. The vibra-

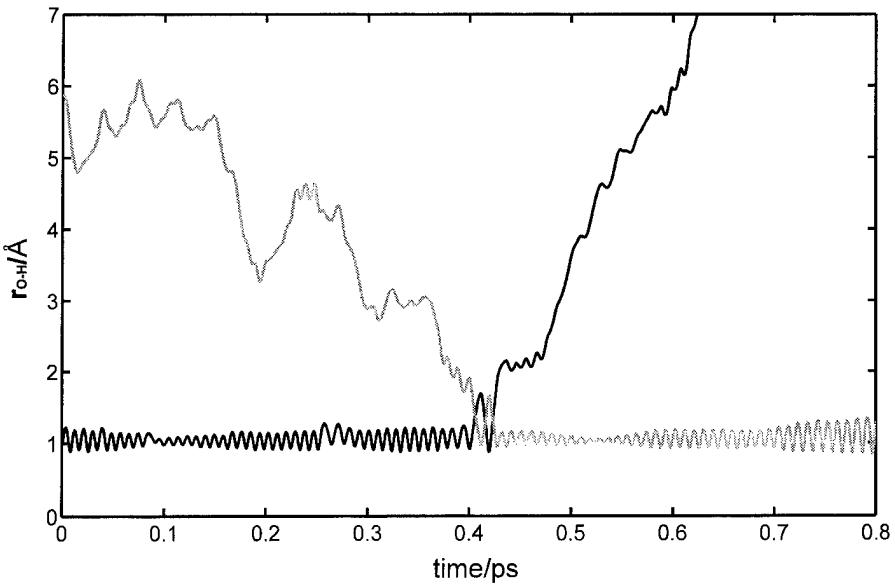


FIGURE 7. Hydrogen transfer in $Be^{2+}(H_2O)_{12}$ at high temperatures. The distance between a hydrogen atom and the oxygen atom in the same water molecule (black curve) and the oxygen atom to which the hydrogen is transferred (light curve) are shown as a function of time.

tional amplitudes of the old and the new O—H bonds are similar. After the transfer, the two fragments, OH^- (as part of $BeOH^+$) and H_3O^+, immediately move away from each other. While these nonequilibrium simulation experiments on water dissociation are clearly not statistically representative for water dissociation, in general, in clusters or in the liquid phase, there are only a few cases where such events have been observed in simulation studies.

Vibrational Dynamics of the Water Molecules

From an experimental point of view, the shifts of the O—H vibrations of water molecules which become members of ionic clusters or hydration shells are highly interesting since they allow one to probe the molecular environment [37].

From equilibrated $Be^{2+}(H_2O)_4(H_2O)_8$ and $Li^+(H_2O)_4(H_2O)_8$ clusters, simulations of about 5000 time steps each were performed. The velocities at every time step were used to calculate the vibrational modes. The results are listed in Table V. The vibrations of an isolated water molecule calculated from a room-temperature MD trajectory include anharmonic contributions but differ only by a few wave numbers from harmonic values obtained from the matrix of second derivatives at equilibrium geometry. It can be seen from Table V that even for Be^{2+}—H_2O the difference is small compared to the frequency shift upon complexation.

The MD frequency shift of the asymmetric O—H stretching mode for the $Be^{2+}(H_2O)_4$ system is -543 cm^{-1} and the one of the symmetric O—H stretching mode is -244 cm^{-1}. The corresponding harmonic values are -537 and -224 cm^{-1}. For comparison, a Hartree–Fock study of Mg^{2+}—H_2O and Al^{3+}—H_2O [31] gave O—H (decoupled) frequency shifts of 220 cm^{-1} for Mg^{2+} and 670 cm^{-1} for Al^{3+}. It seems reasonable that the OH shift resulting from the Be^{2+} ion is located between the values of Mg^{2+} and Al^{3+}.

In contrast to the Be^{2+} ion, Li^+ causes no such strong frequency shift of the OH stretching modes compared to the single water OH stretching modes (symmetric stretch: $+54$ cm^{-1}; asymmetric stretch: -54 cm^{-1}) The corresponding value in [31] was -70 cm^{-1} (O—H uncoupled).

These test calculations serve as a basis for interpreting the results for larger clusters. In Figure 8, the power spectra $I(\nu)$ as calculated from the velocity vectors $v(t)$ of the atoms are plotted (intensities are arbitrary and do not reflect IR intensities; $\mathcal{F}$ denotes the Fourier transform; this formula is equivalent to calculating the Fourier

TABLE V

Molecular dynamics-derived and harmonic frequencies (in cm^{-1}) of the isolated water molecule and water in the Be^{2+}/H_2O and Li^+/H_2O systems with 1 and 12 water molecules (the given frequencies refer to the molecules in bold typeface).

		H—O—H bending	O—H sym. stretch	O—H asym. stretch
H_2O	Harmonic	1727	3900	4246
H_2O	MD	1736	3906	4232
Be^{2+}**OH_2**	Harmonic	1752	3676	3709
Be^{2+}**OH_2**	MD	1736	3662	3689
Li^+**OH_2**	Harmonic	1782	3955	4152
Li^+**OH_2**	MD	1790	3960	4178
Be^{2+}**$(H_2O)_4$**$(H_2O)_8$	Harmonic	1845	3696	3725
Be^{2+}**$(H_2O)_4$**$(H_2O)_8$	MD	1845	3689	3710
$Be^{2+}(H_2O)_4$**$(H_2O)_8$**	Harmonic	1743	3912	4211
$Be^{2+}(H_2O)_4$**$(H_2O)_8$**	MD	1736	3900	4198
Li^+**$(H_2O)_4$**$(H_2O)_8$	Harmonic	1792	3952	4141
Li^+**$(H_2O)_4$**$(H_2O)_8$	MD	1790	3981	4239
$Li^+(H_2O)_4$**$(H_2O)_8$**	Harmonic	1729	3913	4242
$Li^+(H_2O)_4$**$(H_2O)_8$**	MD	1763	3927	4252

transform of the velocity autocorrelation function):

$$I(\nu) \sim |\mathcal{F}(v(t)) \cdot \mathcal{F}(v(-t))|.$$

Since no splitting into symmetric and asymmetric modes is visible, the following procedure [38] was employed to separate them: If the hydrogen velocities relative to the oxygen velocities are projected onto the O—H bonds, their sums and differences should correspond to the symmetric and asymmetric modes. For Figure 8 and Table V, this scheme is used to separate the modes. It can be seen that their maxima nearly coincide.

The first-shell bending mode appears at 1845 cm^{-1}. For the second shell, the bending mode is

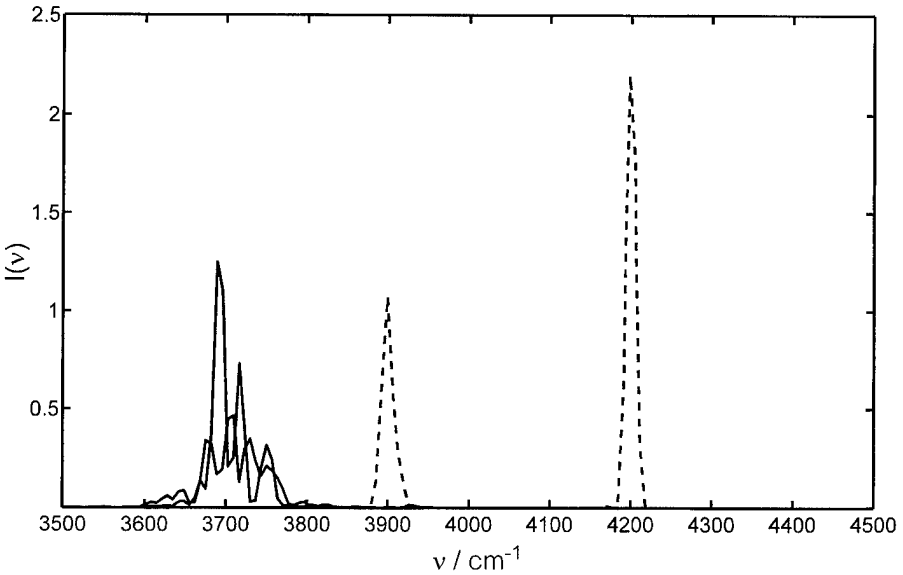


FIGURE 8. Power spectra of the symmetric and asymmetric O—H stretching modes of the water molecules in the first (solid curves) and second (dashed curves) hydration shells of $Be^{2+}(H_2O)_{12}$.

located at 1736 cm^{-1}; the symmetric O—H stretching mode, at 3900 cm^{-1}, and the asymmetric OH stretching mode, at 4198 cm^{-1} (Table V). The frequency shift between the two shells is thus 211 cm^{-1} for the symmetric O—H stretching mode and 488 cm^{-1} for the asymmetric stretching mode. The O—H modes of the second shell agree within a few wavenumbers with the OH stretching modes of an isolated water molecule.

Figure 9 shows the power spectrum for $Li^+(H_2O)_4(H_2O)_8$. The symmetric O—H stretching mode of the first shell is located at 3981 cm^{-1}, and the asymmetric stretching mode, at 4239 cm^{-1} (Table V). The second-shell frequencies are just slightly different (3927 and 4259 cm^{-1}, respectively). There is no strong frequency shift of the OH stretching modes between the two shells in contrast to the Be^{2+} system. It could perhaps have been expected that the agreement between harmonic frequencies and simulation-derived values is less close for the larger complexes than, i.e., for the more rigid monohydrates. However, as can be seen from Table V, at least for the O—H modes, this is not the case.

Summary and Conclusions

The data presented show that many but not all qualitative aspects of hydrated Be^{2+} clusters can approximately be derived from optimized geometries. However, without the corresponding simulations, this fact would not have been easy to conclude. Besides providing the statistical distributions, the MD simulations show the occurrence of intermediate coordination states in Li^+ clusters and the dynamical effect on the distance of the two hydration shells. The simulations involving hydrogen transfer indicate that it would be possible to study statistical features of these reactions by performing simulations with an extended set of systematically varying initial conditions. The evolution of the Li^+ clusters from their initial configurations shows that in aqueous clusters of this cation the most stable hydration number of four can easily be disturbed.

We found MD simulations with forces derived from ab initio wave functions to be a practical method for studying these systems. While this method is traditionally used for geometry optimization, it is not applied as often as the so-called Car–Parrinello (CP) scheme for molecular dynamics. In the latter, the electron density is traditionally expanded in a plane-wave basis set. More characteristically, however, the orbital coefficients are treated as part of the coordinates and the combined gradient of the orbital coeofficients and of the nuclear coordinates with respect to the energy is used for propagating the system.

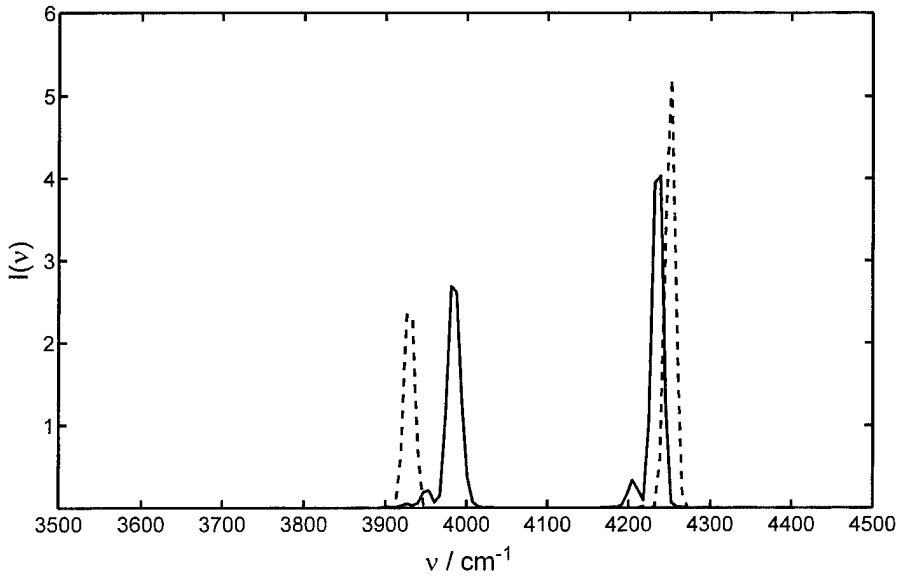


FIGURE 9. Power spectra of the symmetric and asymmetric O—H stretching modes of the water molecules in the first (solid curves) and second (dashed curves) hydration shells of $Li^+(H_2O)_{12}$.

At first it might seem that using the optimized wave function must be slower since iterations are needed at every time step, but this disadvantage is partially alleviated by the possibility of using a larger time step, since the electronic degrees of freedom must be combined with rather low fictitious masses which also complicate frequency calculations. The time step used in the present work (0.3 ps) is at least twice as large as the one typically employed in CP simulations. A second argument why the CP method could be advantageous is its reportedly better energy conservation [39]. Indeed, for perfect energy conservation, extremely accurate nuclear forces are necessary and they might be difficult to obtain from a wave function optimized to some threshold criterion than from the set of generalized coordinates. We did not, however, observe any problems related to this circumstance.

From a pragmatic point of view, it seems that for the simulation of periodic systems there is presently no alternative to using plane waves as a basis set. For nonperiodic systems, simple "hierarchical" MD simulation schemes like the one we used here, where the wave function is optimized at every step and its gradient calculated, might be equally economic. Finally, it shall be mentioned that there exist also successful attempts to combine Hartree–Fock-type calculations with the generalized coordinate treatment [40] as well as the "opposite" combination, using plane-wave basis sets within a traditional DFT scheme [41].

ACKNOWLEDGMENTS

Financial support from the Austrian FWF (Projects P10106-MOB and P9010-MOB) is gratefully acknowledged. M. P. and K. H. acknowledge support from the Swedish Natural Science Research Council.

References

1. K. Heinzinger, Physica B **131B**, 196 (1985); K. Heinzinger, in *Water-Biomolecule Interactions*, M. Palma, M. Palma-Vittorelli, and F. Parak, Eds. (SIF, Bologna, 1993), p. 23.
2. P. Bopp, Pure Appl. Chem. **59**, 1071 (1987).
3. R. W. Impey, P. A. Madden, and I. R. McDonald, J. Phys. Chem. **87**, 5071 (1983).
4. C. Pigenet, J. Raman Spectrosc. **13**, 66 (1982).
5. A. Pittet, G. Elbaze, L. Helm, and A. E. Merbach, Inorg. Chem. **29**, 1936 (1990).
6. T. Yamaguchi, H. Ohtaki, E. Spohr, G. Palinkas, K. Heinzinger, and M. Probst, Z. Naturforsch. **41a**, 1175 (1986).
7. M. Probst, J. P. Limtrakul, and B. Rode, Chem. Phys. Lett. **132**, 370 (1986).
8. K. Hashimoto, N. Yoda, and S. Iwata, Chem. Phys. **116**, 193 (1987).
9. K. Hashimoto and S. Iwata, J. Phys. Chem. **93**, 2165 (1989).
10. M. Probst, E. Spohr, and K. Heinzinger, Chem. Phys. Lett. **161**, 405 (1989).
11. M. Probst, E. Spohr, K. Heinzinger, and P. Bopp, Mole. Simul. **7**, 43 (1991).
12. D. Marx, J. Hutter, and M. Parinello, Chem. Phys. Lett. **241**, 457 (1995).
13. D. Marx, M. Sprik, and M. Parinello, submitted.
14. D. Marx, E. S. Fois, and M. Parinello, Int. J. Quantum Chem. **57**, 655 (1996).
15. E. Clementi and R. Barsotti, Chem. Phys. Lett. **59**, 101 (1978).
16. P. Bopp, I. Okada, H. Ohtaki, and K. Heinzinger, Z. Naturforsch. **40a**, 116 (1985).
17. K. Tanaka, N. Ogita, Y. Tamura, I. Okada, H. Ohtaki, G. Pálinkás, E. Spohr, and K. Heinzinger, Z. Naturforsch. **42a**, 29 (1987).
18. Y. Tamura, K. Tanaka, E. Spohr, and K. Heinzinger, Z. Naturforsch. **43a**, 1103 (1988).
19. U. Niesar, G. Corongiu, E. Clementi, G. Kneller, and D. Bhattacharya, J. Phys. Chem. **94**, 7949 (1990).
20. J. A. C. Rullmann and P. T. van Duijnen, Mol. Phys. **63**, 451 (1988).
21. A. Wallqvist, Chem. Phys. **148**, 439 (1990).
22. G. Corongiu, Int. J. Quantum Chem. **42**, 1209 (1992).
23. M. P. Allen and D. J. Tildesley, *Computer Simulations of Liquids* (Clarendon Press, Oxford, 1987), p. 78ff.
24. H. J. Berendsen, J. P. M. Postma, W. F. van Gunsteren, A. DiNola, and J. R. Haak, J. Chem. Phys. **81**, 3684 (1984).
25. M. J. Frisch, G. W. Trucks, H. B. Schlegel, P. M. W. Gill, B. G. Johnson, M. A. Robb, J. R. Cheeseman, T. Keith, G. A. Petersson, J. A. Montgomery K. Raghavachari, M. A. Al-Laham, V. G. Zakrzewski, J. V. Ortiz, J. B. Foresman, C. Y. Peng, P. Y. Ayala, W. Chen, M. W. Wong, J. L. Andres, E. S. Replogle, R. Gomperts, R. L. Martin, D. J. Fox, J. S. Binkley, D. J. Defrees, J. Baker, J. P. Stewart, M. Head-Gordon, C. Gonzalez, and J. A. Pople, *Gaussian 94, Revision 8.3* (Gaussian, Inc., Pittsburgh PA, 1995).
26. A. D. Becke, J. Chem. Phys. **98**, 5648 (1993).
27. C. Lee, W. Yang, and R. G. Parr, Phys. Rev. B **37**, 785 (1988).
28. W. J. Pietro, M. M. Francl, W. J. Hehre, D. J. Defrees, J. A. Pople, and J. S. Binkley, J. Am. Chem. Soc. **104**, 5039 (1982).
29. W. J. Stevens, H. Basch, and M. Krauss, J. Chem. Phys. **81**, 6026 (1984).
30. W. S. Benedict, N. Gailar, and E. K. Plyer, J. Chem. Phys. **24**, 1139 (1956).

31. M. Probst and K. Hermansson, J. Chem. Phys. **96**, 8895 (1992).
32. J. R. Newsome, G. W. Neilson, and J. E. Enderby, J. Phys. C **13**, L923 (1980).
33. P. Cieplak and P. A. Kollman, J. Chem. Phys. **86**, 6393 (1987).
34. L. X. Dang, J. Chem. Phys. **96**, 6970 (1992).
35. M. A. Lee, N. W. Winter, and W. H. Casey, J. Phys. Chem. **98**, 8641 (1994).
36. R. W. Impey, P. A. Madden, and I. R. McDonald, J. Phys. Chem. **87**, 5071 (1983).
37. O. Kristiansson, A. Eriksson, and J. Lindgren, Acts Chem. Scand. A **38**, 609 (1984); *Ibid.* **38**, 613 (1984).
38. E. Spohr, G. Pálinkás, K. Heinzinger, P. Bopp, and M. Probst, J. Phys. Chem. **92**, 6754 (1988).
39. K. Remler and P. Madden, Mol. Phys. **70**, 921 (1990).
40. B. Hartke and E. Carter, J. Chem. Phys. **97**, 6569 (1992); *Ibid.*, Chem. Phys. Lett. **189**, 358 (1992).
41. H.-P. Cheng, J. Chem. Phys. **105**, 6844 (1986).

Vibrational Analysis of $TeCl_4$. II. A Hartree–Fock, MP2, and Density Functional Study

ATTILA KOVÁCS,[1] GÁBOR I. CSONKA[2]

[1] *Research Group for Technical Analytical Chemistry of the Hungarian Academy of Sciences at the Institute of General and Analytical Chemistry of the Budapest Technical University, H-1521 Budapest, Hungary*

[2] *Department of Inorganic Chemistry of the Budapest Technical University, H-1521 Budapest, Hungary*

Received 1 March 1997; accepted 7 March 1997

ABSTRACT: The geometry and vibrational spectrum of $TeCl_4$ was calculated with various quantum chemical methods [Hartree–Fock, second-order Møller-Plesset (MP2) and generalized gradient approximation density functional theory (GGA-DFT)]. Five different basis-set combinations were tested: the relativistic effective core potentials with double-zeta split valence basis (RECP) of Hay & Wadt (HW) and Stevens et al. (CEP); the above RECP basis sets extended with polarization functions for Te and using a 6-31G* basis for Cl (HW* and CEP*); a medium-size all-electron basis set (ALL). The quality of the calculated data was assessed by comparison with recent experimental results. The Hartree-Fock method combined with the HW and CEP basis sets provided a very good approximation of the experimental vibrational spectra. The quality of the results is comparable to those of the best methods (MP2, B3-P, B3-PW with HW* and CEP* and B3-LYP, B3-P, B3-PW with the ALL basis set). However, the HW and CEP basis sets provided very poor geometry and vibrational frequencies when they were used in combination with any correlated method in this work. Similarly, the DFT methods using Becke's 1988 exchange functional (B-LYP, B-P, B-PW) without the inclusion of the exact exchange let to very poor results with the basis sets used in this study. © 1997 John Wiley & Sons, Inc. Int J Quant Chem **65**: 817–826, 1997

Contract grant sponsor: Hungarian Scientific Research Foundation.

Contract grant number: F022170.

© 1997 John Wiley & Sons, Inc.
CCC 0020-7608 / 97 / 050817-10

Introduction

Vibrational data are of great importance at various fields of chemistry and physics such as molecular mechanics and molecular dynamics, statistical thermodynamics, gas electron diffraction analysis, etc. However, their experimental determination for inorganic molecules is difficult. High temperatures, long path lengths, and sensitive detectors are needed to detect the (often low-intense) vibrational bands of the low-volatile compounds. Additionally, the interpretation of the high-temperature spectra is hampered by the broad rotational contours, hot bands, and possible presence of other components in the gas phase (decomposition and association products). Hence, results from other techniques such as matrix isolation spectroscopy and theoretical methods are acknowledged to extend the high-temperature experimental data.

The quantum chemical calculations have been successfully applied for the interpretation and prediction of vibrational spectra of organic compounds [1]. However, the application for inorganic molecules is more difficult. First of all, these latter molecules are usually built up out of heavier elements, rendering the computations with all-electron basis sets very expensive. Furthermore, the errors arising from the neglect of relativistic effects are important from the fourth row of the periodic table. These two problems can be solved by using relativistic effective core potentials (RECP) [2–8], which are extensively used in Hartree-Fock (HF) and post-HF calculations.

The density functional (DFT) methods are known to provide good estimates of the vibrational spectra of organic compounds. Recent DFT studies of transition-metal complexes also have shown promising agreement with the experimental infrared (IR) frequencies and intensities [9, 10]. However less information is available about the performance of the DFT methods with effective core potentials. The use of DFT functionals with ECPs generated previously from Hartree–Fock atomic calculations is not free of problems. Since the exchange and correlational functionals are nonlinear in the density, the core and valence densities are not strictly separable. Hence, the use of ECPs generated from HF calculations should be carefully tested for their applicability in DFT work. Promising results have been published recently by Russo et al. [11]. Investigating a small but representative set of transition-metal compounds [ScF_3, TiF_4, VF_5, TiO, $Ni(CO)_4$, CuF], they found that the RECPs of Hay and Wadt [2–4] can be used in DFT methods, as well.

In the present study we test the performance of currently most successful generalized gradient approximation (GGA) and hybrid DFT methods using effective core potentials as compared to Hartree–Fock and second-order Møller-Plesset (MP2) methods as well as to all-electron basis sets.

The tellurium tetrachloride molecule was chosen as a model for this study. Its molecular geometry (determined by gas electron diffraction) and experimental vibrational spectra are known from a recent study [12]. The $TeCl_4$ molecule has a trigonal bipyramid structure with a vacant equatorial position (C_{2v} symmetry). The molecular geometry is in accordance with the valence-shell electron-pair repulsion (VSEPR) theory [13]. Characteristics are the axial Te—Cl bonds being longer than the equatorial bonds and the axial chlorines being slightly bent toward the equatorial ones. Concerning the vibrational data, eight of the nine fundamentals of $TeCl_4$ were found in the experimental specta and a good estimate [based on a scaled quantum mechanical (SQM) [14] force field] is available for the unobserved A_2 (ν_4) mode [12].

Computational Details

Geometries, Cartesian harmonic force constants, and IR intensities of $TeCl_4$ were calculated at the HF, MP2 [15], and DFT levels of theory using the Gaussian 94 program [16]. Six exchange-correlation density functionals were employed in the present study: Becke's 1988 (B) [17] and Becke's three parameter (B3) [18] gradient-corrected exchange functionals were combined with the Lee–Yang–Parr (LYP) [19], Perdew (P) [20], and Perdew–Wang (PW) [21] correlation functionals. The default grid (75,302) implemented in the Gaussian 94 program was used in the DFT calculations. We used five different basis set combinations:

1. HW: the Hay & Wadt RECPs with double-zeta valence basis sets for both Cl and Te [3]
2. CEP: the RECPs of Stevens et al. and the corresponding double-zeta valence basis sets for both Cl and Te [5, 6]
3. HW*: the 6-31G(d) basis set for chlorine and the Hay & Wadt RECP with double-zeta va-

lence basis set [3] extended with a single set of *d*-type polarization functions [22] for tellurium

4. CEP*: the 6-31G(d) basis set for chlorine and the RECP of Stevens et al. with double-zeta valence basis set [6] extended with a single set of *d*-type polarization functions [22] for tellurium
5. ALL (all-electron basis set): the standard 6-31G(d) basis set for chlorine and a 3-21G(d) basis [23] for tellurium

Harmonic vibrational frequencies and IR intensities were computed for the fully optimized geometries. The first derivatives of the potential energy with respect to the nuclear coordinates were calculated analytically at all quantum chemical levels. The second derivatives were obtained analytically for the all-electron basis set and numerically for the RECP basis sets.

Results and Discussion

GEOMETRY

The computed geometrical parameters of $TeCl_4$ obtained at various levels of theory are compared to the experimental geometry in Table I.

The DFT methods containing Becke's 1988 exchange functional (B-LYP, B-P, and B-PW) with the most economic HW and CEP basis sets found the T_d geometry as a single minimum on the *potential energy surface*. All the other calculations converged to the right C_{2v} structure resulting longer axial Te—Cl bonds with respect to the equatorial ones in accordance with the experimental data. The methods resulting in false geometries were omitted from the further studies.

Figures 1(a) and 1(b) show the deviations between the calculated and experimental geometrical parameters. The most significant difference between the computed results is the very poor performance of the HW and CEP basis sets for the bond distances [cf. Fig. 1(a)].

The calculated bond lengths are longer than the experimental ones, with one exception of the HF/HW* result for the Te—Cl_{eq} bond. In general, the computations underestimate the Cl_{eq}—Te—Cl_{eq} bond angle, however, differ in the character of the Cl_{ax}—Te—Cl_{eq} angle (cf. Table I). The experimental tilt of the axial chlorines toward the equatorial ones is reproduced by the HF and MP2 methods (except the MP2/CEP level) and by the B3-type DFT/ALL calculations. In all the other cases no tilt, or a small opposite tilt, was obtained. The latter bond angle is generally overestimated by the various methods, except the HF with all the basis sets and the MP2/ALL [cf. Fig. 1(b)]. The deviations for all the geometrical parameters are generally larger than the experimental errors.

In general, the computed bond lengths and the Cl_{ax}—Te—Cl_{eq} angle increase in the order HF < MP2 < B3-P ~ B3-PW < B3-LYP < B-P ~ B-PW < B-LYP. [The only significant deviation from this trend was found for the bond lengths obtained at the MP2/HW and CEP levels; cf. Fig. 1(a)]. We note that similar behavior has been found earlier for C—C and C—O bond lengths of sugars and 1,2-ethanediol [24, 25]. The computed Cl_{eq}—Te—Cl_{eq} bond angle varies in a narrower range. The above trend, but with negative sign (because of the underestimating character of the computations), can be recognized, except for the results obtained by using the ALL basis set.

Summing up, the experimental geometry of $TeCl_4$ is best reproduced by the HF and MP2 methods. The DFT methods provided poorer results, especially those that contain the B-type exchange functional. The HW*, CEP*, and ALL basis sets are of similar quality, HW* being slightly superior; the HW and CEP basis sets are much poorer.

FREQUENCIES

The observed and computed fundamentals of $TeCl_4$ are compiled in Table II. The deviations between selected computed and the experimental frequencies are shown in Figure 2. We present here the results obtained at various levels of theory using the HW and HW* basis sets. They resemble the results obtained with the other related basis sets (HW to CEP, HW* to CEP* and ALL). The following trend can be observed: The B3-type DFT/HW and B-type DFT/HW* frequencies are considerably underestimated, while the HF and MP2/HW* ones are overestimated. The HF/HW and most of the B3-type DFT/HW* frequencies vary around the experimental values. We note the significant underestimation of the ν_8 and ν_9 stretching fundamentals by the DFT calculations. The computed frequencies increase in the order B-LYP < B-P ~ B-PW < B3-LYP < B3-PW ~ B3-P < MP2 < HF. This trend is just the opposite to that seen for most of the geometrical parameters (cf. Fig. 1).

TABLE I
Molecular geometry of $TeCl_4$.

Basis[a]	Method	Bond length (Å)		Bond angle (deg)		
		Te — Cl_{ax}	Te — Cl_{eq}	Cl_{ax} — Te — Cl_{ax}	Cl_{eq} — Te — Cl_{eq}	Cl_{ax} — Te — Cl_{eq}
	Exp.[b]	2.430(6)	2.298(6)	175.9(6)	103.0(7)	88.7[c]
HW	HF	2.537	2.409	172.8	101.4	87.7
	MP2	2.588	2.468	177.8	100.5	89.3
	B-LYP[d]	2.585		109.5		
	B-P[d]	2.568		109.5		
	B-PW[d]	2.566		109.5		
	B3-LYP	2.578	2.481	174.3	99.3	91.9
	B3-P	2.559	2.463	176.6	99.6	90.9
	B3-PW	2.560	2.466	177.6	99.9	90.8
CEP	HF	2.568	2.431	174.4	100.6	88.2
	MP2	2.626	2.501	177.9	98.6	90.7
	B-LYP[d]	2.607		109.5		
	B-P[d]	2.587		109.5		
	B-PW[d]	2.586		109.5		
	B3-LYP	2.600	2.505	171.0	98.7	92.9
	B3-P	2.579	2.486	174.8	99.2	91.7
	B3-PW	2.583	2.491	173.9	99.1	92.0
HW*	HF	2.440	2.290	175.2	100.7	88.1
	MP2	2.441	2.313	176.6	100.2	88.9
	B-LYP	2.507	2.389	172.5	99.4	92.4
	B-P	2.485	2.369	174.6	99.5	91.7
	B-PW	2.479	2.367	175.9	100.0	91.3
	B3-LYP	2.472	2.346	179.0	100.1	90.4
	B3-P	2.453	2.330	179.6	100.2	89.9
	B3-PW	2.455	2.333	179.8	100.1	89.9
CEP*	HF	2.461	2.313	175.5	100.6	88.5
	MP2	2.463	2.339	176.8	100.4	89.0
	B-LYP	2.522	2.415	172.2	99.9	92.5
	B-P	2.500	2.395	174.9	100.1	91.6
	B-PW	2.499	2.393	174.9	100.1	91.7
	B3-LYP	2.491	2.371	178.8	100.2	90.4
	B3-P	2.471	2.354	179.7	100.3	89.9
	B3-PW	2.475	2.357	179.8	100.3	90.1
ALL	HF	2.449	2.317	173.5	100.7	87.9
	MP2	2.448	2.338	174.7	100.5	88.3
	B-LYP	2.509	2.410	178.5	102.3	90.4
	B-P	2.481	2.383	179.6	102.2	89.9
	B-PW	2.480	2.382	179.8	102.1	89.9
	B3-LYP	2.477	2.368	177.8	101.7	89.3
	B3-P	2.452	2.345	176.8	101.5	89.0
	B3-PW	2.456	2.348	176.9	101.5	89.0

[a] For details of basis sets HW, CEP, HW*, CEP*, and ALL see text.
[b] From a gas electron diffraction study, Ref. [12], r_a values.
[c] Calculated from the data given in Ref. [12].
[d] The computed geometry has tetrahedral symmetry.

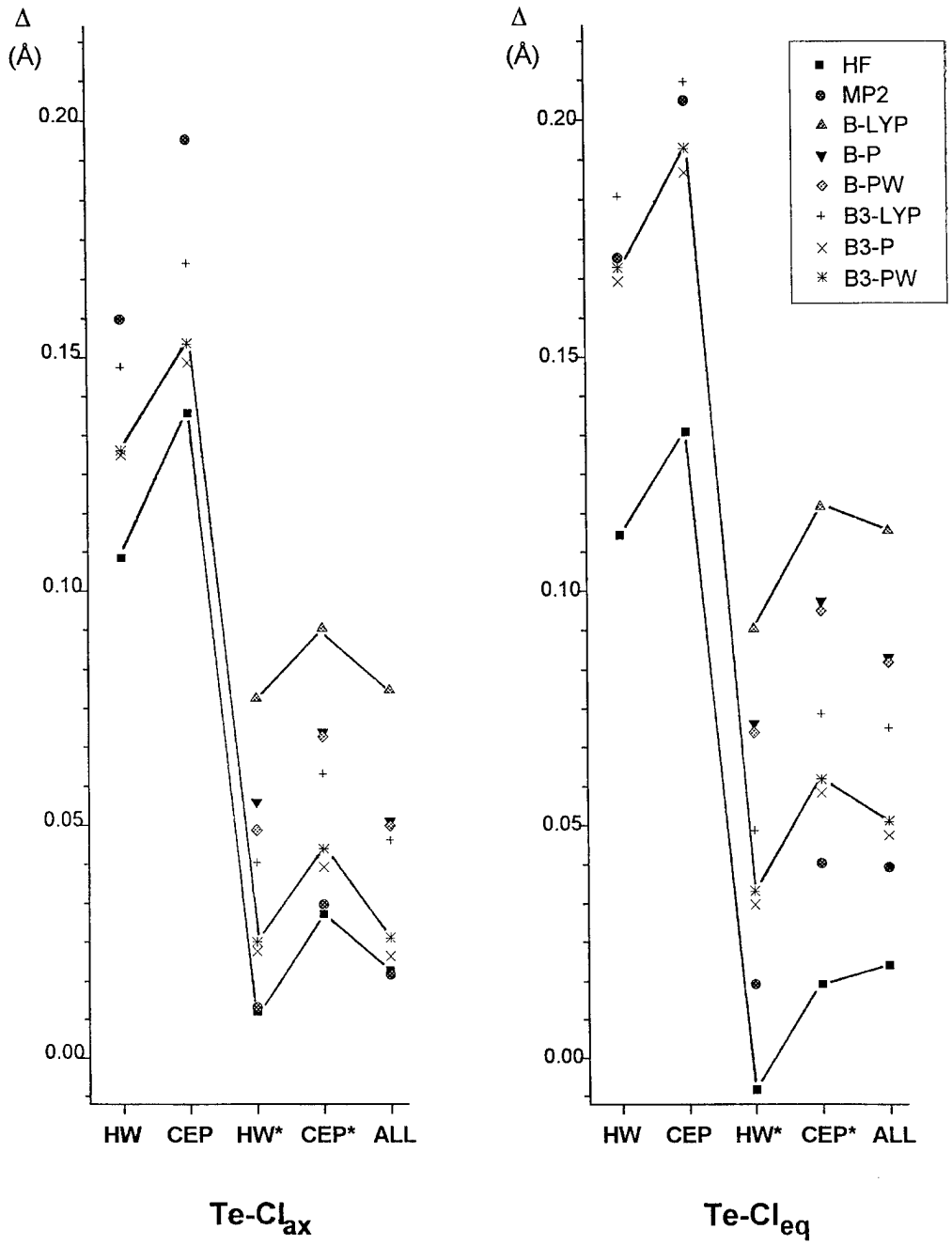


FIGURE 1a. Deviations between computed and experimental geometrical parameters: (a) bond lengths; (b) bond angles.

The performance* of the computational levels can be assessed and compared by the root-mean-square (rms) and maximal deviations between the experimental and theoretical frequencies (Fig. 3).† The rms deviations are scattered within the 8–53 cm^{-1} range, while the maximal deviations (absolute values) vary from 15 to 80 cm^{-1}.

* By performance we mean here how the different theoretical levels are able to estimate the experimental (anharmonic) vibrational spectra. We do not intend to investigate the quality of the calculated harmonic frequencies.

† The ν_4 mode was not involved in the evaluation of these deviations.

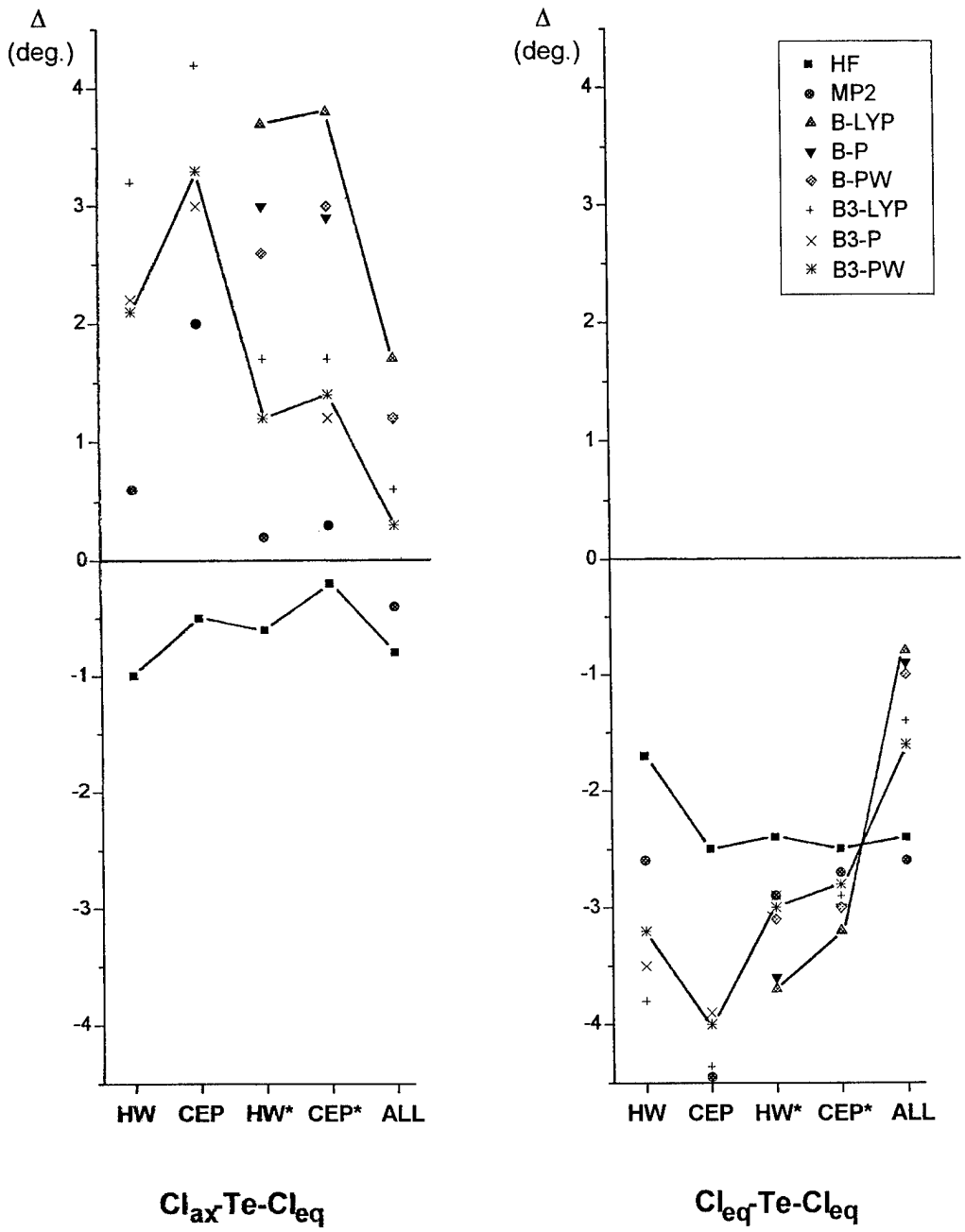


FIGURE 1b. (continued)

On Figure 3 a significant trend can be observed for both the theoretical levels and the basis sets, a trend which is reflected at both the rms and maximal deviations.

The performance of the HW and CEP basis sets used with the correlated methods is very poor, however, it is surprisingly good with the Hartree-Fock theory. The HF/HW level belongs even to the best methods. The HW*, CEP*, and ALL basis sets performed well with the MP2 and B3-type DFT levels, while about two–three times larger deviations can be observed for the results obtained at the B-type DFT calculations. It is noteworthy that the MP2/HW* and CEP* frequencies are in very good agreement with the experimental data, however, the agreement worsened using the all-electron (ALL) basis set. Here the B3-type DFT levels are definitely superior. We note also the

TABLE II

Experimental and calculated fundamentals (cm^{-1}) and calculated IR intensities ($km\ mol^{-1}$) of $TeCl_4$.

Basis[a]	Method	ν_1	ν_2	ν_3	ν_4	ν_5	ν_6	ν_7	ν_8	ν_9	rms dev.	max. dev.
	Exp.[b]	72	104	158	(150[c] ± 10)	165	290	312	378	382		
HW	HF	73 (3)	107 (13)	150 (19)	160 (0)	174 (8)	285 (1)	307 (224)	366 (21)	359 (9)	10.5	21
	MP2	57 (3)	82 (9)	125 (11)	133 (0)	147 (4)	254 (1)	299 (145)	319 (24)	315 (10)	38.0	67
	B3-LYP	50 (3)	61 (6)	109 (6)	113 (0)	128 (2)	258 (4)	300 (129)	308 (33)	309 (14)	46.8	73
	B3-P	52 (2)	67 (6)	133 (7)	118 (0)	133 (2)	265 (4)	309 (134)	320 (34)	321 (15)	37.3	61
	B3-PW	53 (2)	68 (6)	111 (7)	121 (0)	135 (3)	266 (4)	310 (133)	316 (35)	318 (13)	40.8	64
CEP	HF	73 (4)	102 (13)	147 (18)	153 (0)	168 (6)	271 (1)	300 (279)	365 (22)	354 (11)	15.4	28
	MP2	54 (4)	69 (8)	117 (8)	121 (0)	135 (2)	238 (2)	294 (162)	303 (29)	306 (14)	48.2	76
	B3-LYP	40 (3)	54 (5)	103 (4)	108 (0)	123 (1)	250 (6)	300 (154)	298 (38)	306 (16)	52.7	80
	B3-P	48 (3)	63 (6)	108 (6)	115 (0)	130 (2)	258 (6)	310 (161)	309 (41)	317 (16)	44.7	69
	B3-PW	47 (3)	61 (6)	107 (6)	115 (0)	130 (2)	257 (6)	308 (160)	307 (40)	315 (16)	46.0	71
HW*	HF	96 (3)	128 (10)	181 (14)	184 (0)	201 (10)	301 (2)	306 (341)	408 (60)	415 (23)	25.3	36
	MP2[b]	85 (2)	113 (7)	163 (9)	166 (0)	183 (5)	291 (3)	322 (256)	376 (59)	385 (21)	9.4	18
	B-LYP	65 (2)	72 (4)	126 (4)	127 (0)	146 (1)	258 (8)	290 (186)	315 (62)	326 (22)	37.2	63
	B-P	67 (2)	79 (4)	131 (5)	134 (0)	153 (1)	270 (7)	303 (194)	331 (64)	341 (23)	27.1	47
	B-PW	70 (1)	86 (4)	132 (5)	137 (0)	155 (2)	271 (7)	305 (196)	330 (64)	342 (22)	26.0	48
	B3-LYP	72 (2)	95 (5)	145 (7)	149 (0)	167 (2)	275 (5)	305 (229)	345 (62)	357 (22)	16.7	33
	B3-P	73 (2)	100 (6)	149 (7)	154 (0)	172 (3)	286 (5)	317 (234)	358 (65)	370 (22)	9.6	20
	B3-PW	78 (2)	100 (6)	150 (7)	153 (0)	171 (3)	284 (5)	315 (234)	357 (64)	369 (22)	10.0	21
CEP*	HF	92 (3)	122 (9)	177 (15)	176 (0)	195 (8)	304 (2)	314 (353)	400 (61)	407 (25)	20.3	30
	MP2	80 (2)	107 (7)	158 (10)	158 (0)	175 (5)	291 (3)	328 (256)	368 (59)	376 (22)	8.4	16
	B-LYP	59 (2)	73 (3)	118 (4)	122 (0)	139 (1)	262 (8)	299 (183)	309 (60)	320 (22)	40.3	69
	B-P	64 (2)	79 (4)	124 (5)	128 (0)	146 (2)	273 (8)	312 (194)	325 (64)	335 (22)	30.6	53
	B-PW	64 (2)	80 (4)	126 (5)	130 (0)	147 (2)	273 (8)	312 (196)	326 (64)	336 (22)	29.8	52
	B3-LYP	72 (2)	92 (5)	141 (7)	142 (0)	160 (2)	277 (6)	313 (229)	340 (62)	352 (22)	19.3	38
	B3-P	74 (2)	96 (5)	145 (8)	147 (0)	164 (3)	288 (5)	324 (237)	354 (65)	365 (23)	12.5	24
	B3-PW	74 (2)	95 (5)	145 (8)	146 (0)	164 (3)	286 (6)	322 (237)	352 (65)	363 (23)	13.3	26
ALL	HF	96 (2)	131 (8)	181 (13)	183 (0)	200 (11)	307 (2)	327 (326)	411 (64)	416 (26)	27.0	35
	MP2	86 (1)	119 (6)	166 (9)	167 (0)	184 (6)	299 (3)	341 (252)	384 (62)	389 (23)	15.2	29
	B-LYP	52 (2)	80 (4)	125 (5)	138 (0)	155 (1)	238 (3)	267 (197)	335 (65)	338 (23)	36.5	52
	B-P	64 (1)	95 (4)	135 (5)	147 (0)	164 (2)	266 (4)	301 (205)	353 (67)	355 (23)	18.5	27
	B-PW	73 (1)	99 (4)	139 (5)	142 (0)	157 (3)	279 (6)	321 (207)	341 (68)	348 (23)	19.9	37
	B3-LYP	70 (2)	104 (5)	146 (7)	155 (0)	172 (3)	275 (4)	309 (233)	365 (66)	369 (23)	9.8	15
	B3-P	74 (1)	111 (5)	152 (7)	161 (0)	177 (4)	294 (4)	332 (239)	380 (68)	384 (24)	9.1	20
	B3-PW	79 (1)	112 (5)	154 (7)	156 (0)	171 (5)	293 (4)	333 (238)	364 (68)	375 (24)	10.4	21

[a] For details of basis sets HW, CEP, HW*, CEP*, and ALL see text.
[b] From Ref. [12].
[c] SQM value using the MP2 / HW* harmonic force field.

significant improvement of the results obtained at the B3-LYP level used with the ALL basis set compared to those with HW* and CEP*. The results of the B3-P and B3-PW levels used with CEP* worsened somewhat compared to those using the HW* basis and to MP2/CEP*. The performance of the Hartree–Fock theory with these three larger basis sets is similar to that of the B-type DFT methods.

The best agreement between the experimental and computed frequencies was obtained at the MP2/CEP* level, however, only slightly worse are the HF/HW, the MP2, B3-P and B3-PW/HW*, and the B3-P, B3-LYP and B3-PW/ALL results (rms deviation less than 11 cm^{-1}, maximal deviation not exceeding 21 cm^{-1}).

The computed vibrational data of $TeCl_4$ are suitable to assist the assignment of the bands in

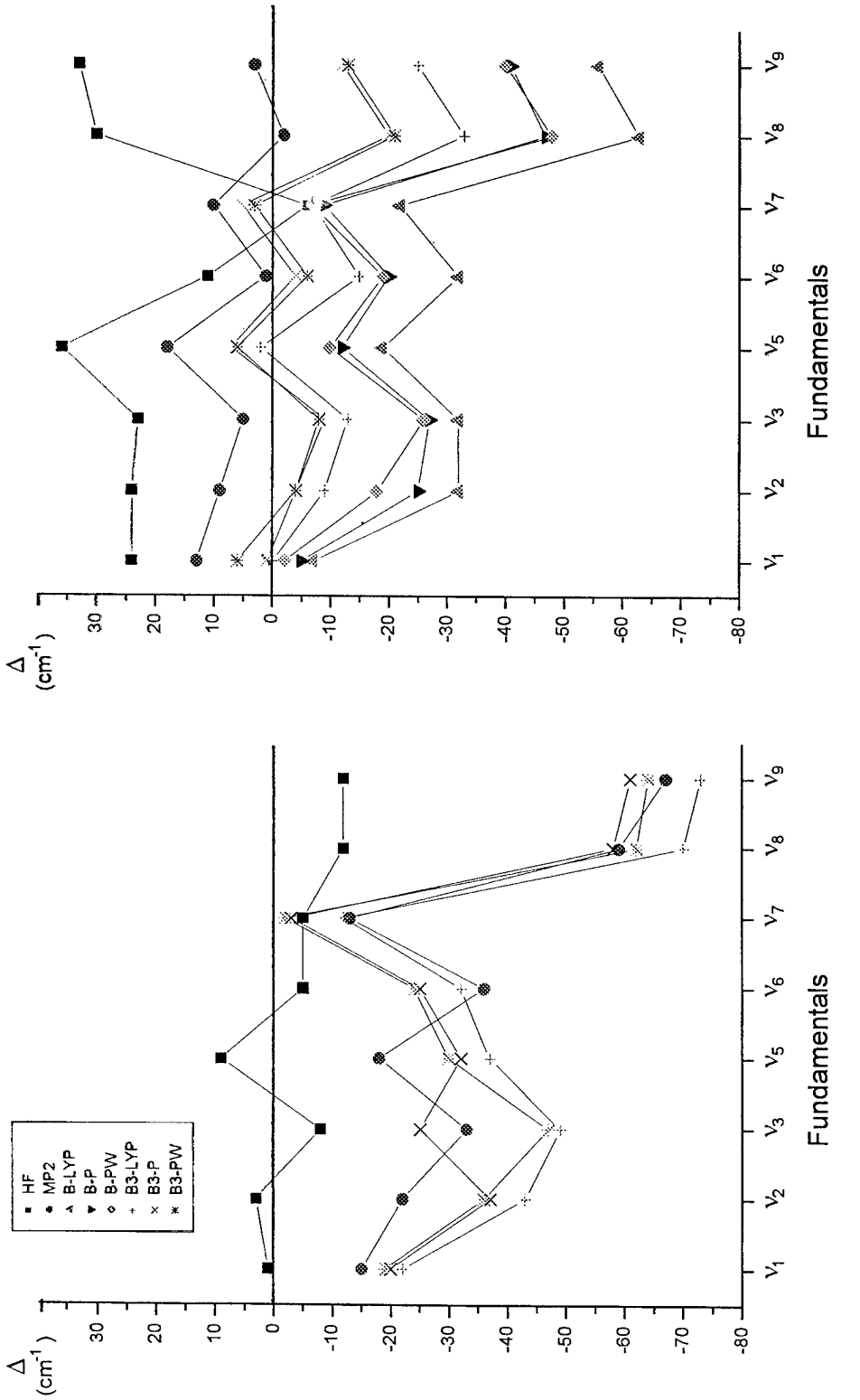


FIGURE 2. Deviations between calculated and experimental vibrational frequencies obtained at various levels of theory using basis sets (a) HW and (b) HW*.

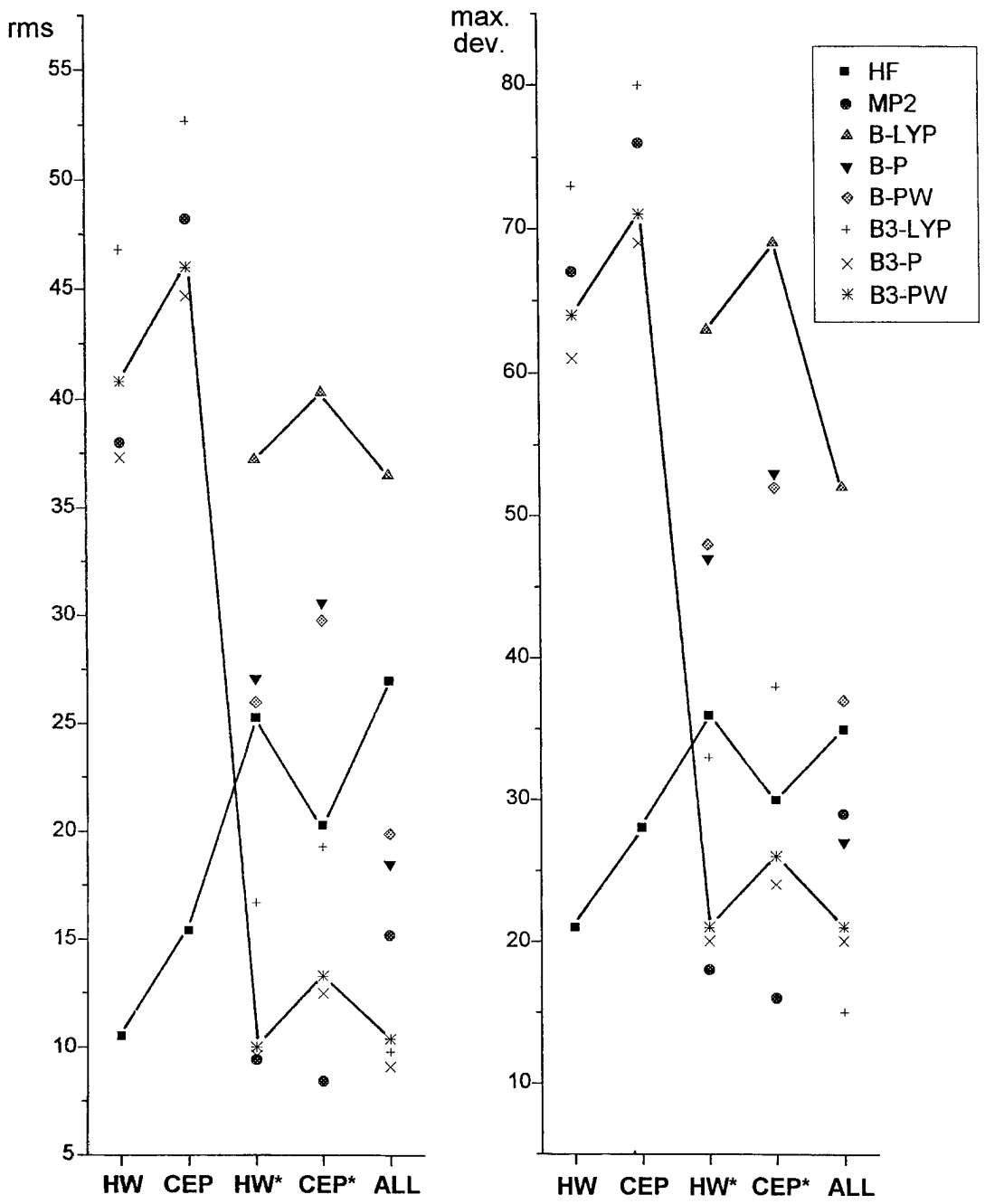


FIGURE 3. (a) Rms and (b) maximal deviations (absolute values) between the calculated and experimental vibrational frequencies.

the experimental spectra (cf. Table II). The stretching fundamentals can be assigned unambiguously by the computed IR intensities. In most cases the relative sequence of the frequencies is in accord with the experimental observations, and only the computed ν_8 and ν_9 stretching fundamentals are interchanged at the HF/HW, HF/CEP, and MP2/HW levels as well as the calculated ν_7 and ν_8 modes at the B3-P and B3-PW/CEP levels. The deformation modes have similar (small) computed

IR intensities, and the relative order of their frequencies agrees with that of the experimental ones. The unobserved ν_4 mode was positioned between ν_3 and ν_5 by all the quantum chemical calculations except for B3-P/HW and HF/CEP*, however the experimental values of these fundamentals are also very close [12].

Conclusions

1. The molecular geometry of $TeCl_4$ is best reproduced at the HF and MP2 levels using the HW*, CEP*, and ALL basis sets. The density functional methods gave rise to poorer results, especially those using Becke's 1988 exchange functional. The RECP basis sets (HW and CEP) provided poor results, especially for the bond distances.
2. Generally, the vibrational frequencies calculated by the MP2 and B3-type DFT methods with basis sets HW*, CEP*, and ALL (except MP2/ALL and B3-LYP/HW* and CEP*) as well as at the HF/HW level are in good accord with the experimental data. The agreement is good enough to assist the assignment of the measured vibrational spectra.
3. The HW and CEP basis sets compensate effectively the errors of the HF method for $TeCl_4$. The HW* and CEP* basis sets are best combined with MP2, B3-P and B3-PW. Regarding the all-electron basis set a combination with the B3-type DFT methods is superior.
4. Based on their performance and cost effectiveness the methods using relativistic effective core potentials are advantageous for large-scale computations.

ACKNOWLEDGMENT

This research has been supported by the Hungarian Scientific Research Foundation (OTKA, No. F 022170).

References

1. B. A. Hess, Jr., J. Schaad, P. Cársky, and R. Zahradník, Chem. Rev. **86**, 709 (1986).
2. P. J. Hay and W. R. Wadt, J. Chem. Phys. **82**, 270 (1985).
3. W. R. Wadt and P. J. Hay, J. Chem. Phys. **82**, 284 (1985).
4. P. J. Hay and W. R. Wadt, J. Chem. Phys. **82**, 299 (1985).
5. W. J. Stevens, H. Basch, and M. Krauss, J. Chem. Phys. **81**, 6026 (1984).
6. W. J. Stevens, M. Krauss, H. Basch, and P. G. Jasien, Can. J. Chem. **70**, 612 (1992).
7. L. F. Pacios and P. A. Christiansen, J. Chem. Phys. **82**, 2664 (1985).
8. M. M. Hurley, L. F. Pacios, P. A. Christiansen, R. B. Ross, and W. C. Ermler, J. Chem. Phys. **84**, 6840 (1986).
9. L. Fan and T. Ziegler, J. Phys. Chem. **96**, 6937 (1992).
10. R. Fournier and I. Pápai, in *Recent Advances in Density Functional Methods, Part 1.*, D. Chong, Ed. (World Scientific, Singapore, 1995).
11. T. V. Russo, R. L. Martin, and P. J. Hay, J. Phys. Chem. **99**, 17085 (1995).
12. A. Kovács, K.-G. Martinsen, and R. J. M. Konings, J. Chem. Soc. Dalton Trans., 1037 (1997).
13. R. J. Gillespie and I. Hargittai, *The VSEPR Model of Molecular Geometry* (Allyn and Bacon, Boston, 1991).
14. P. Pulay, G. Fogarasi, G. Pongor, J. E. Boggs, and A. Vargha, J. Am. Chem. Soc. **105**, 7073 (1983).
15. C. Møller and M. S. Plesset, Phys. Rev. **46**, 618 (1934).
16. M. J. Frisch, G. W. Trucks, H. B. Schlegel, P. M. W. Gill, B. G. Johnson, M. A. Robb, J. R. Cheeseman, T. Keith, G. A. Petersson, J. A. Montgomery, K. Raghavachari, M. A. Al-Laham, V. G. Zakrezewski, J. V. Ortiz, J. B. Foresman, J. Cioslowski, B. B. Stefanov, A. Nanayakkara, M. Challacombe, C. Y. Peng, P. Y. Ayala, W. Chen, M. W. Wong, J. L. Andres, E. S. Replogle, R. Gomperts, R. L. Martin, D. J. Fox, J. S. Binkley, D. J. DeFrees, J. Baker, J. J. P. Stewart, M. Head-Gordon, C. Gonzalez, and J. A. Pople, Gaussian 94, Revision B.2, Gaussian, Inc., Pittsburgh, PA, 1995.
17. A. D. Becke, Phys. Rev. A. **38**, 3098 (1988).
18. A. D. Becke, J. Chem. Phys. **98**, 5648 (1993).
19. C. Lee, W. Yang, and R. G. Parr, Phys. Rev. B **37**, 785 (1988).
20. J. P. Perdew, Phys. Rev. B **33**, 8822 (1986).
21. J. P. Perdew and Y. Wang, Phys. Rev. B **45**, 13244 (1992).
22. B. A. Smart and C. H. Schiesser, J. Comp. Chem. **16**, 1055 (1995).
23. K. D. Dobbs and W. J. Hehre, J. Comp. Chem. **7**, 359 (1986).
24. G. I. Csonka and I. G. Csizmadia, Chem. Phys. Lett. **243**, 419 (1995).
25. G. I. Csonka, K. Éliás, and I. G. Csizmadia, Chem. Phys. Lett. **257**, 49 (1996).

Computation of Vibrational Frequencies for Adsorbates on Surfaces

JOHN D. HEAD

Department of Chemistry, University of Hawaii, 2545 The Mall, Honolulu, Hawaii 96822

Received 2 March 1997; revised 6 May 1997; accepted 7 May 1997

ABSTRACT: A general strategy for computing the vibrational frequencies of adsorbates on surfaces is presented. Rather than use numerical fits to the surface energy, we advocate diagonalizing a mass weighted energy second-derivative matrix. The computation of energy derivatives has several advantages: It facilitates a more accurate treatment of the adsorbate/substrate mass ratios. The normal modes of the surface vibrations are given automatically in the diagonalization step. Finally, a major advantage of using energy derivatives is that they provide estimates of the range of the adsorbate/substrate interactions which can be used to ensure that the frequency values are converged. We illustrate the strategy for cluster calculations which simulate the H/Al(100), O/Al(111), H_2O/Al(111), and Al/Si(111) surfaces. © 1997 John Wiley & Sons, Inc. Int J Quant Chem **65**: 827–838, 1997

Introduction

High-resolution electron energy loss spectroscopy (HREELS) [1, 2] and reflection adsorption infrared spectroscopy (RAIRS) [1, 3] are vibrational spectroscopic techniques which now play a valuable role in identifying and characterizing structural information on adsorbates, such as reactive intermediates, on surfaces. Generally, symmetry arguments coupled with experimental experience from related better-understood systems enables vibrational assignments to be correlated with a specific atomic or molecular adsorbate at a particular surface site. Unfortunately, this empirical approach does not always facilitate an unambiguous assignment of the adsorbate identity and structure to the data. For example, we have recently argued that water molecularly adsorbs on the Al(111) surface at low temperatures [4, 5], while the experimental HREELS data was originally interpreted with water dissociation taking place [6]. Our argument was based on ab initio cluster calculations where we computed the geometry and vibrational frequencies for the chemisorbed water. We were able to show that the two high-frequency vibrational modes observed at 3450 and 3720 cm^{-1} by HREELS could be assigned, respectively, to H-bonded and non-H-bonded OH stretches in water [5] and did not require the presence of a hydroxyl group on the Al(111) surface as proposed earlier [6].

There have been a large number of ab initio calculations used to predict vibrational frequencies for molecules. Such calculations are powerful be-

© 1997 John Wiley & Sons, Inc.
CCC 0020-7608 / 97 / 050827-12

cause they can readily provide useful vibrational information about both well and poorly characterized molecular structures. A useful overview of the accuracy of the vibrational frequencies computed by Hartree–Fock (HF), Møller–Plesset (MP2), and density functional theory (DFT) was given recently by Scott and Radom [7] for a series of small polyatomic molecules containing up to four heavy atoms. Ab initio vibrational frequency calculations for quite large molecules have also been reported. For example, Pulay and co-workers recently published DFT calculations which computed vibrational frequencies for free-base porphyrin [8]. However, the computational requirements of vibrational calculations must obviously scale rapidly with system size, making their use in analyzing adsorbates on surfaces challenging. Cluster calculations are one of the common techniques for theoretically investigating adsorption on surfaces. The cluster approach assumes that the dominant chemical interactions are local in nature and tend to involve only a few of the substrate atoms close to the adsorbate [9]. It is the local nature of the adsorbate interactions that enables a reduction in the computational effort since only a subset of vibrational modes of the cluster need to be calculated. Apart from some recent calculations involving relatively small clusters which have obtained adsorbate vibrational frequencies by explicitly computing a second derivative matrix [10, 11], the usual approach to computing the adsorbate vibrational frequencies has been by making numerical fits to the variation in the total energy of the cluster as the adsorbate atoms are displaced along expected normal mode directions [12]. This energy-fitting procedure has also been used for slab calculations [13]. The calculations treat the substrate mass as being infinitely larger than that of the adsorbate, but, as we show below, this can lead to large errors in the adsorbate frequencies. In addition to the substrate mass approximation, the energy-fitting procedure requires some approximation to the form of the normal modes when considering a polyatomic adsorbate. For example, both Rösch and Bagus et al. obtained a stretching frequency for CO adsorbed on a surface by fixing the CO center of mass at the equilibrium distance above the surface and fitting to the energy variation with CO distance [12]. To avoid making assumptions about the form of the normal modes, we have started computing vibrational frequencies for an adsorbate on a cluster by diagonalizing the mass-weighted energy second-derivative matrix computed for a subset of atoms composing the cluster. In the case of a single adatom, the energy-fit procedure and the energy second derivatives for the adatom alone result in identical adsorbate vibrational frequencies. A disadvantage of our strategy over numerical fits is that the more computationally demanding energy derivatives now need to be calculated. However, by computing estimates of the energy second derivatives between the adsorbate and substrate and using a frequency correction formula, originally proposed by Black [14], one can more realistically incorporate the adsorbate/substrate mass ratio into the frequency calculation. The frequency correction formula also provides a guide to the spatial extent of the adsorbate interactions with the substrate and provides a convergence check on the necessary cluster size.

In this article, we illustrate strategies for computing more physically realistic adsorbate vibrational frequencies by considering H, O, and water adsorbates on Al surfaces and for an Al adatom on the Si(111) surface. In the next section, we describe how the cluster calculations were performed and how the vibrational frequencies were computed from the mass-weighted energy second-derivative matrix and the frequency correction formula. In the third section of the article, we present results and discuss the adsorbate vibrations for each of the four systems. We first show that, as expected, due to the H adatoms having the smallest adsorbate-to-substrate mass ratio, H adsorption on the Al(100) surface is the most straightforward system to theoretically treat. We find substantial frequency correction terms, owing to the larger 0.59 O-to-Al mass ratio, to occur when using the energy second-derivative matrix to compute the vibrational frequencies for a single O adatom on the Al(111) surface. The size of the O frequency correction terms becomes much smaller if a larger second derivative matrix is formed using additional second derivatives from the nearby substrate atoms. We find an Al_3O subcluster to produce O vibrations consistent with the corrected O-only frequency calculation. We also consider different-sized subclusters in the frequency calculations for water adsorbed on the Al(111) surface. An important feature about the adsorbed water frequency calculations is that we do not need to make any assumptions about the form of the adsorbate normal modes since they are given automatically by the diagonalization procedure. However, vibrational calculations at the SCF level on molecules are well known to overestimate the frequencies

and we go on to show for the H_2O/Al(111) surface, using energy-fitting procedures, how the normal modes obtained at an initial level of theory can be used to obtain estimates of the vibrational frequencies at a higher level of theory. In the Al/Si(111) system, we show that the frequency correction formula is still a useful tool for identifying adsorbate and substrate localized vibrations even though the Al-to-Si mass ratio is 0.96 and the adsorbate frequency values are overlapped by vibrations from the Si substrate. Concluding remarks are given in the final section of the article.

Method

In our previous work, we used cluster calculations to simulate the H/Al(100) [15], O/Al(111) [16, 17], water/Al(111) [4, 5], and Al/Si(111) [18] surfaces. We found that the general features of the adsorption can often be reliably modeled by taking the set of central substrate atoms which interact most strongly with the adsorbate atoms and surrounding them by a complete shell of neighboring substrate atoms having the same geometry as in the extended surface. For example, in our study of the H/Al(100) surface, we used the Al_9(5,4)H and Al_{14}(8,6)H clusters, with one and two central Al atoms, to simulate H adsorption at the four-fold on-top and two-fold bridging sites, respectively, where the (5,4) and (8,6) notation refers to the number of substrate atoms in each cluster layer. We ignore edge effects for the Al clusters, while in the Si calculations we follow the usual practice of terminating the Si dangling bonds at the cluster edges with H atoms. The Al cluster atoms are constrained to appropriate fcc lattice positions using the bulk lattice parameter of 4.05 Å [19] except in the water/Al(111) calculations where we allow surface relaxation effects for the central Al atoms. In our simulation of the Al/Si(111) surface, we found the inclusion of substrate relaxation effects to be essential in order to obtain a stable adsorption site which agrees with the experimentally observed surface structure and we constrained the outer Si atoms at their experimental Si bulk lattice positions [20].

All the cluster calculations were performed using the GAMESS [21] computer program. The equilibrium adsorbate geometry is found by partially optimizing the clusters' total energy while constraining most of the substrate atoms to their extended surface positions [22]. The adsorbate partial geometry optimizations and vibrational frequency calculations utilize energy gradients and these computations are performed at the restricted closed and open Hartree–Fock level. We also discuss some single geometry cluster energies computed using restricted second-order Møller–Plesset theory [23]. The Hay and Wadt effective core potential (ECP) and its double zeta valence basis set $[3s3p]/(2s2p)$ was used for Al and Si [24]. In the Al/Si(111) clusters, d-polarization functions were also added to the basis sets for the Al adatom and its neighboring Si atoms. The Dunning and Hay split valence basis $[4s]/(2s)$ was used for H [25]. The Dunning and Hay split valence basis set augmented with a d-polarization and a diffuse p-function $[9s6p1d]/(3s3p1d)$ was used for O [25]. More complete details on the calculations are given in our earlier work [4, 5, 15–18].

Computing the complete set of vibrational frequencies for larger clusters rapidly becomes a demanding task and would produce a number of vibrational modes associated with cluster edge effects which are not strictly relevant to the experimental characterization of the adsorbate. For this reason, in both cluster and slab calculations, a more economical approach is to fit the cluster energy to some potential energy surface for a select number of vibrational modes involving the adsorbate [12]. A typical application of this procedure was used by Jacobsen et al. [13] in their slab calculations to obtain O vibrational frequencies ν on the Al(111) surface using the quadratic fitting formula

$$\hbar\omega = h\nu = \hbar\sqrt{\frac{2\Delta E}{M_{\text{eff}}\Delta b^2}}\,, \tag{1}$$

where ΔE is the energy change when the O atom is displaced by a distance Δb from the minimum. Jacobsen et al. took M_{eff} to be the mass of the adatom and made the common approximation that the substrate has infinite mass. Another difficulty with this fitting approach is deciding which direction to take the Δb displacement when dealing with polyatomic adsorbates [12]. We encountered this problem in our water/Al(111) cluster calculations and we started to compute the adsorbate vibrational frequencies and relevant normal modes by diagonalizing subblocks of the mass-weighted energy second-derivative matrix [4, 5].

Forming the mass-weighted energy second-derivative matrix either analytically or numerically as finite differences of the energy gradients is the routine quantum chemical technique for computing vibrational frequencies of molecules [26]. However, to keep the calculations tractable and since we are only interested in a subset of the possible cluster frequencies, we only form the mass-weighted second-derivative matrix for a fragment of the atoms in the cluster. In block form, the full mass-weighted force constant matrix is

$$\mathbf{K} = \begin{pmatrix} \mathbf{K}_{AA} & \mathbf{K}_{AS} \\ \mathbf{K}_{SA} & \mathbf{K}_{SS} \end{pmatrix}, \tag{2}$$

where A labels the adsorbate set of atoms used in the second-derivative matrix formation and S are the remaining substrate atoms composing the cluster. The A subset may also include some substrate atoms, but these atoms should be chosen to preserve the symmetry of the adsorbate vibrational modes. The i-th row of the force constant matrix is initially calculated by taking the finite difference of the analytical gradient $\mathbf{g}$ vector by displacing the atom with the j-th coordinate in the A set to give

$$K_{ij} = \frac{1}{\sqrt{m_i m_j}} \frac{\partial^2 E}{\partial q_i \, \partial q_j} = \frac{1}{\sqrt{m_i m_j}} \frac{\Delta g_i}{\Delta q_j}, \tag{3}$$

where $\Delta\mathbf{g} = \mathbf{g}(\Delta q_j) - \mathbf{g}(0)$ and m_i is the mass of the nucleus associated with coordinate i. Equation (3) can also be written in terms of taking $\pm\Delta q_j$ displacements so that a more symmetrical force constant matrix is produced. Similarly, when i and j are both elements of A, an improved force constant block should result from averaging K_{ij} and K_{ji}. Equation (3) also facilitates making an estimate of the $\mathbf{K}_{AS}$ force constant block provided that the gradient vector $\mathbf{g}$ is computed for all the atoms in the cluster.

Once the $\mathbf{K}_{AA}$ block of the force constant matrix is formed, the adsorbate vibrational frequencies ω are obtained by diagonalizing $\mathbf{K}_{AA}$. As expected, we find for a single atom adsorbate the $\mathbf{K}_{AA}$ diagonalization and the curve-fitting procedure implied by Eq. (1) produce identical frequencies. For polyatomic adsorbates, such as water on the Al(111) surface, the diagonalization of the adsorbate force constant block, $\mathbf{K}_{AA}$, produces both the adsorbate vibrational frequencies and the relevant normal modes. However, restricting the A set to just adsorbate atoms means that the frequency calculations are still treating the substrate as having infinite mass. Furthermore, these frequency calculations do not give any indication as to whether any significant interactions between the adsorbate and the substrate are being neglected.

However, by calculating energy gradients and forming the off-diagonal $\mathbf{K}_{AS}$ block enables an estimate to the convergence of the frequency calculations to be made. Transforming the mass-weighted second-derivative matrix $\mathbf{K}$ so that the separate adsorbate and surface blocks are diagonalized

$$\tilde{\mathbf{K}} = \begin{pmatrix} \boldsymbol{\omega}^2 & \tilde{\mathbf{K}}_{AS} \\ \tilde{\mathbf{K}}_{SA} & \boldsymbol{\Omega}^2 \end{pmatrix} \tag{4}$$

where ideally the $\boldsymbol{\Omega}^2$ eigenvalues would correspond to surface phonons, the off-diagonal force constant matrix block $\tilde{\mathbf{K}}_{AS}$ should be small when the adsorbate vibrational frequencies are strongly localized and decoupled from the substrate. Following an approach originally suggested by Black [14], an estimate of the corrected adsorbate vibrational frequencies can be obtained from

$$\begin{aligned} (\omega_i^{\mathrm{cor}})^2 &= \omega_i^2 + \sum_j \frac{\left(\tilde{K}_{AS}\right)_{ij}^2}{\omega_i^2 - \Omega_j^2} \\ &\approx \omega_i^2 + \frac{1}{\omega_i^2} \sum_j \left(\tilde{K}_{AS}\right)_{ij}^2, \end{aligned} \tag{5}$$

where the approximation in the last formula assumes that $\omega_i \gg \Omega_M$, the maximum phonon frequency of the substrate. Equation (5) can be derived by applying a simple perturbation theory argument to Eq. (4) or by using the more elaborate continued fraction technique originally used by Black [14]. Bulk Al has a maximum phonon frequency of approximately 300 cm^{-1} [27], suggesting that only small corrections should be found for high adsorbate frequency modes. Much higher-frequency phonon modes exist for the Al/Si(111) surface but we still find Eq. (5) useful because it provides a measure of how small the off-diagonal $\tilde{\mathbf{K}}_{AS}$ block is becoming. In the next section, we demonstrate how Eq. (5) generally serves as a useful guide to the convergence and reliability of the frequency values computed for surface vibrations.

Results and Discussion

H/AL(100) RESULTS

In Table I, we present the vibrational frequencies for H adsorption at an on-top and a bridging site on clusters which simulate the Al(100) surface. EELS experiments by Paul found bands at 1750 and 1125 cm^{-1} which were assigned to H vibrations at the on-top and bridging sites [28]. The general EELS selection rule is that only adsorbate vibrations normal to the surface are observed. However, it should be noted the EELS band at 1750 cm^{-1} may not be simply associated with H adsorbed at an on-top site since the intensity band grows simultaneously with a peak at 750 cm^{-1}. In our earlier cluster calculations [15], by assuming the form of the H atom normal modes and using energy fits, we argued the origin of the 1750 and 750 cm^{-1} peaks to be due to two H at neighboring on-top sites. However, by following the procedure outlined in this article and obtaining the adsorbate normal modes by diagonalizing the mass-weighted second-derivative matrix for the 2 H atoms, we found a strong coupling between the surface normal and parallel H modes. This surface normal and parallel modes coupling contradicts our earlier assumption and makes our previous analysis no longer valid. At present, we do not fully understand the origin of the two peaks at 1750 and 750 cm^{-1} and more work is in progress. Nevertheless, as indicated in Table I, our computed surface normal vibrations are in very good agreement with the two high-frequency bands observed in the EELS experiments. Hjelmberg, in substrate perturbed jellium calculations, also computed 1694 and 1048 cm^{-1} for the on-top and bridge sites, respectively [29]. As expected, due to the small H-to-Al mass ratio, we find the frequencies corrected using Eq. (5) to differ only slightly from their uncorrected values. The largest corrections occur for the H x and y surface parallel modes at the on-top site where Eq. (5) is not strictly valid since the uncorrected frequency, 233 cm^{-1}, is less than the Al maximum phonon frequency. Our H/Al(100) cluster calculations demonstrate that vibrational frequencies for adsorbates with low masses can be reliably obtained using total energy-fitting procedures provided, of course, the correct normal mode associated with the adsorbate is known.

TABLE I

Vibrational frequencies computed using clusters which simulate the H / Al(100) and O / Al(111) surfaces; the z direction is normal to the surface and all frequencies are in cm^{-1}.

Adsorption site and cluster	Al—X distance (Å)	Vibrational frequency		Assignment
		Uncorrected	Corrected	
On-top	1.630	1737	1767	H z
$Al_9(5,4)H$		233	289	H x
		233	289	H y
Bridge	1.832	1095	1106	H z
$Al_{14}(8,6)H$		778	793	H x in-plane
		526	532	H y out-of-plane
		O only		
Three-fold open	1.788	595	708	O x
$Al_{18}(12,6)O$		594	703	O y
		393	577	O z
		Al_3O		
		713	717	O x
		712	716	O y
		607	610	O z
		213	280	Al_3O x frus. tran.
		211	281	Al_3O y frus. tran.
		205	334	Al_3O z frus. tran.
		⋮	⋮	Al—Al vibrations

O/Al(111) RESULTS

The investigation of O adsorption on the Al(111) surface has been a surprising challenge to surface science [30]. HREELS experiments at low O coverage find peaks in two regions at 545–650 and 800–850 cm^{-1} [31–34]. In agreement with the recent work of others [35–37], we have performed cluster calculations which show the 545–650 cm^{-1} HREELS band to correlate with normal vibrations of O above the surface at threefold open or fcc sites and the 800–850 cm^{-1} band to correlate with symmetric combinations of horizontal vibrations from two or more O at neighboring threefold fcc sites which become HREELS-allowed [17]. In Table I, we list results for the frequency calculations for a single O atom on the Al_{18}(12,6) cluster. The uncorrected frequencies are obtained by diagonalizing the mass-weighted energy second-derivative matrix formed for O only and for the Al_3O subcluster consisting of O and its three nearest Al neighbors. The uncorrected frequency calculations ignore the O-to-Al mass ratio of 0.59 and treat the substrate mass as infinite to produce an O surface normal vibration in poor agreement with the experimental values. Similar O vibrational results were obtained by Jacobsen et al. using the numerical fitting procedure given by Eq. (1) in their slab calculations [13]. For a slab with a 0.25 O monolayer coverage, Jacobsen et al. computed 411 and 427 cm^{-1} for the surface normal and parallel O vibrations. Their surface normal vibration 411 cm^{-1} value matches very closely our O only result. By performing the frequency calculations with the mass-weighted energy second-derivative matrix formed for Al_3O subcluster, the O vibrations are shifted to much higher frequency and we obtain a surface normal O mode which is much more consistent with the HREELS values. The O-only frequencies after correction with Eq. (5) are in very close agreement with the three high frequencies computed for the Al_3O subcluster. Diagonalizing the Al_3O second-derivative matrix results in 12 frequencies altogether; we have listed only the six highest frequencies in Table I since the nine low-frequency modes are mostly associated with Al—Al vibrations and the frequency correction formula [Eq. (5)] is no longer valid. Further support that the Al_3O subcluster results in more realistic frequencies than the O-only calculations comes from Eq. (5), which corrects the three high-frequency modes by 4 cm^{-1} or less. These small Al_3O subcluster frequency corrections suggest that the most important surface interactions responsible for O vibrations are between the O and the three neighboring Al atoms and that the adsorbate frequency values are essentially converged when the second-derivative matrix formed for the Al_3O subcluster is used. We have tested this frequency convergence idea further by performing frequency calculations for larger subcluster sizes for O adsorbed on a single layer Al_{18} cluster having a central Al_6 subcluster surrounded by all the neighboring Al atoms in the Al(111) surface layer. We verified that the O frequencies computed with an Al_3O subcluster are converged by obtaining the same O frequencies with the Al_6O subcluster [17].

To summarize, these cluster calculations which simulate the O/Al(111) surface demonstrate that caution is needed with energy-fitting procedures to obtain adsorbate vibrational frequencies when the adsorbate to substrate mass ratio is significant. The O-only frequency calculation shows that useful estimates of the adsorbate-to-substrate mass effect can be obtained from the correction formula given by Eq. (5). Equation (5) corrections to the adsorbate frequencies become small when the subcluster *A* block includes all the dominant adsorbate-to-substrate interactions.

H_2O/Al(111) RESULTS

Table II summarizes the results of frequency calculations for water adsorbed at an on-top site on the Al(111) surface using the $Al_{15}(10,5)H_2O$ cluster shown in Figure 1. The Al_{15}(10,5) cluster consists of two central Al atoms surrounded by the complete set of 13 nearest neighbors from the first and second layers of the (111) surface of the Al fcc lattice. We used the Al_{15} cluster in our earlier work to explore water adsorption at the on-top and bridging sites and found the on-top site to be preferred. The frequency calculations are performed by diagonalizing the mass-weighted energy second-derivative matrix for H_2O only and the Al_2H_2O subcluster. Not surprisingly, because of their weak interaction with Al surface, the frequencies for OH stretches and H—O—H bending mode are the same for both the H_2O only and Al_2H_2O subcluster. A Mulliken population analysis does show charge transfer from the water H atoms to the Al surface, which is probably responsible for the adsorbed OH stretches being red-shifted from the 4237 and 4102 cm^{-1} stretch frequencies computed for free water using the same basis set [4, 5]. The free-water bending frequency

TABLE II

Vibrational frequencies for H_2O adsorbed at an on-top site on the Al(111) surface using the $Al_{15}(10,5)H_2O$ cluster.

	H_2O only		Al_2H_2O		MP2		
Mode	Uncorrected	Corrected	Uncorrected	Corrected	Frequency	δ (Å)	Assignments
1	4174	4174	4174	4174	4186	0.001	Antisym. OH str.
2	4053	4053	4053	4053	3749	0.018	Sym. OH stretch
3	1800	1800	1800	1800	1606	0.001	H—O—H bend
4	575	583	584	584	620	0.099	In-plane H_2O rock
5	243	298	317	319	232	0.021	Al—O stretch
6			295	302			In-plane Al—Al str.
7	200	220	236	352			H_2O frust. rot.
8			203	247			H_2O frust. rot.
9			185	250			H_2O frust. rot.
10			166	266			Al mode
11			138	252			Al—Al trans.
12			119	146			z frust. trans.
13	91	156	84	191			H_2O frust. rot.
14	84	121	76	98			x frust. trans.
15	61	279	57	404			y frust. trans.

The uncorrected frequencies are computed by using H_2O only and the Al_2H_2O subcluster at the Hartree–Fock level. Estimates of MP2 frequencies are obtained by performing numerical fits along the normal modes computed for the H_2O-only calculations. The shift in the MP2 minimum from the original SCF geometry along each normal mode is given by δ. All frequencies are in cm^{-1}.

at 1802 cm^{-1} is unaffected by the surface adsorption. Relatively small differences between the uncorrected and corrected frequencies start to appear for modes 4 and 5. Mode 4 is a frustrated water rotation where the water does an in-plane rock above the Al atom and the small frequency correction from Eq. (5) suggests that it is more correctly treated with the Al_2H_2O subcluster. Mode 5 corresponds to the Al—O stretching mode and Eq. (5) in the H_2O-only frequency calculation produces a fairly large correction term since, again, we are not treating the substrate mass correctly. The corrected frequency from the Al_2H_2O subcluster calculation shows that mode 5 is now probably converged, even though Eq. (5) should not be expected to be very accurate for such a low-frequency value. In our earlier work [5], we assigned the water symmetric stretch, the bending frequency, the in-plane rock, and the Al—O stretch to the HREELS peaks experimentally observed at 3770, 1645, 775, and 325 cm^{-1}, respectively, for the submonolayer coverage with 5.4×10^{14} water molecules/cm^2 [6].

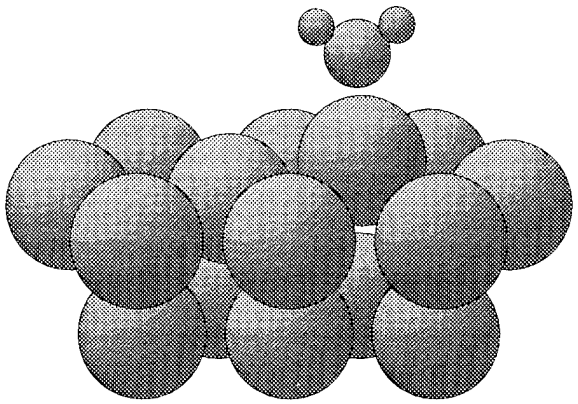


FIGURE 1. The $Al_{15}(10,5)H_2O$ cluster with the water preferentially adsorbed atop an Al atom. This cluster geometry was obtained by a partial geometry optimization which included the water and the two central Al cluster atoms.

The frequency correction formula [Eq. (5)] serves as a useful check on the convergence of the adsorbed water frequencies on the Al(111) surface. The small frequency corrections found for the four highest-frequency modes could be used as an argument that numerical fitting procedures would also give adequate frequencies for the adsorbed water. However, gradient information is needed before the argument for simply performing numerical fit calculations can be made. Furthermore, the numerical fitting procedure would require an assumed form for the adsorbed water normal modes

and the advantage of our approach is that we avoid making any assumptions by diagonalizing the mass-weighted energy second-derivative matrix obtained at the SCF level. Unfortunately, SCF calculations are well known to overestimate vibrational frequencies of molecules by 10–13% [7]. The trends in the SCF frequencies computed for adsorbates on surfaces has not been rigorously quantified, but one way to obtain improved frequency values is to use the SCF normal modes with small Eq. (5) corrections as displacement directions for numerical fits to the cluster energies calculated at a higher level of theory. In Table II, we list the adsorbed water frequencies obtained by fitting to the MP2 energy variation along the normal modes calculated in the H_2O only SCF calculations. We do find the MP2 symmetric OH stretch and H—O—H bending frequencies to be in much closer agreement with the HREELS vibrations observed at 3770 and 1650 cm^{-1}. The parameter δ in Table II gives the displacement along each normal mode between the SCF and MP2 minimum energies and this gives some indication as to whether the optimized MP2 adsorbate geometry is significantly different from the SCF minimum. We find that the largest δ displacement occurs for the in-plane H_2O rock mode. Hence, for the modes having small δ values, the relatively straightforward SCF vibrational calculation combined with Eq. (5) provides some justification for obtaining the water on Al(111) vibrational frequencies using numerical fits at the MP2 level without having to perform the more computationally demanding MP2 energy-gradient calculation.

Al/Si(111) RESULTS

The interaction of Al with the Si surface has been extensively investigated both experimentally and theoretically, and for a more extensive review of the literature, we refer the reader to our recent cluster calculations for this surface [18]. On surfaces with up to $\frac{1}{3}$ ML Al coverage, scanning tunneling microscopy experiments [38] and slab calculations [39] indicate that the adatom preferentially adsorbs at a T_4 site where the Al bonds to three first-layer Si atoms and is directly above a Si atom from the second layer rather than the H_3 site where the second layer Si atom is absent. Surprisingly, cluster calculations at the Hartree–Fock level found Al adsorption at the T_1 site, where the Al atom is adsorbed atop a single Si atom, to be more stable than is adsorption at either of the T_4 or H_3 sites. The Al adsorption induces a Si(111) surface relaxation and our work shows these relaxation effects can be simulated providing that the cluster is large enough and the energy is computed at beyond the Hartree–Fock level. We were able to show that the largest relaxation effects occur at the T_4 site, resulting in an Al adsorption energy 5 kcal/mol more stable than adsorption at the H_3 site and considerably more stable than adsorption at the T_4 site. However, we only obtained this result for the T_4 site after the partial geometry optimization of the $AlSi_5$ subcluster in the $AlSi_{26}H_{24}$ cluster and computing MP2 energy corrections [18]. Some of the previous cluster calculations have also attempted to calculate Al adsorption frequencies even though the Al-to-Si mass ratio is 0.96 [40]. Kelly et al. in HREELS experiments on the Al/Si(111) surface found peaks at 525 and 450 cm^{-1} [41]. Kelly et al. noted that their interpretation of the two peaks is complicated by the closeness of a peak due to the clean Si(111)2 × 1 surface and by the similarity of the Al and Si masses. To clarify the origin of the 525 and 450 cm^{-1} peaks, Kelly et al. also investigated In adsorption on the Si surface and again found peaks at 525 and 450 cm^{-1}, suggesting that the Al adsorption results in two new peaks due to localized substrate phonons.

To explore the limits of calculating adsorbate vibrational frequencies, we investigated computing the Al—Si vibrations using the partially optimized $Si_{22}H_{21}Al$ and $Si_{26}H_{24}Al$ clusters described previously [18] which simulate Al adsorption atop the T_1 and threefold T_4 sites, respectively. Since previous cluster calculations have suggested that the preferred Al adsorption is at either the T_1 or the T_4 sites, we did not perform vibrational calculations on the H_3 site [18]. The partially optimized T_1 Si_4Al and T_4 Si_5Al subcluster fragments from the larger clusters are shown in Figure 2. In Tables III and IV, we present the Hartree–Fock vibrational frequencies obtained by diagonalizing the mass-weighted energy second-derivative matrix for differently sized subclusters at the two sites. Tables III and IV show that the Si phonon frequencies overlap the Al—Si vibrations and the approximate form of Eq. (5) is no longer valid, and for this reason, we list a Δ value equaling the amount of the correction which would be obtained if Eq. (5) was still correct. Our Al-only frequency calculations give essentially the same values as obtained by Illas et al. who obtained 237 cm^{-1} at the T_1 and 313 cm^{-1} at T_4 sites [40]. In the fre-

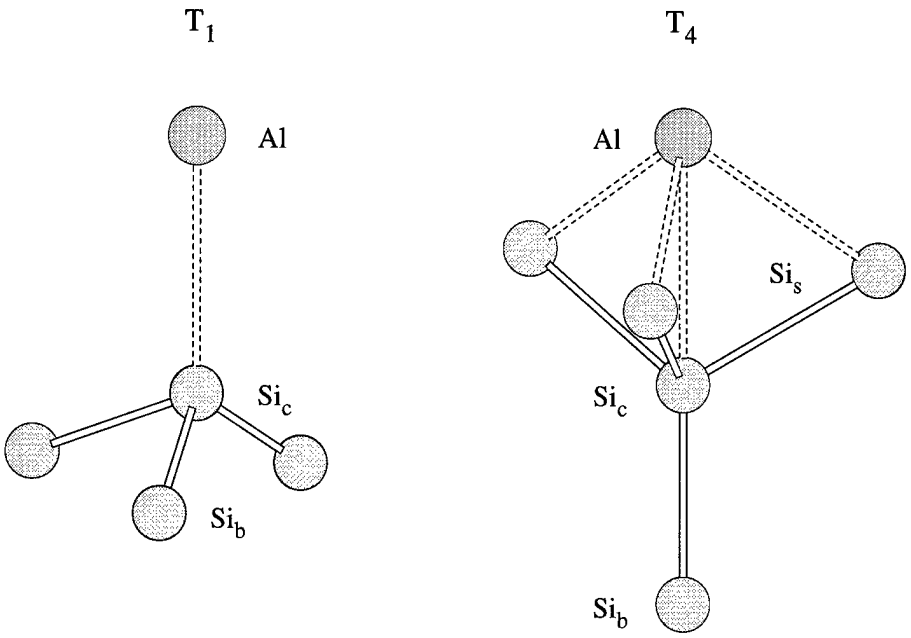


FIGURE 2. The Si_4Al and Si_5Al subclusters used in the frequency calculations for the T_1 and T_4 sites. The atom labels Si_c, Si_b, and Si_s correspond to the central, bulklike, and surface Si atoms referenced in Tables III and IV.

quency calculation for the T_1 site using the Si_4Al subcluster, the surface normal Al—Si stretching frequency shifts to 335 cm^{-1}, as predicted by Eq. (5). However, this shift agreement has to be fortuitous since Δ is still 77 cm^{-1} for the new stretch frequency value. Although we do not expect Eq. (5) to be very reliable for the Al/Si(111) surface, the correction factors Δ do still serve as a useful guide to whether the frequencies are converged. The three highest frequencies have the smallest Δ

TABLE III
Vibrational frequencies for Al adsorption at the T_1 site on the Si(111) surface using the $Si_{22}H_{21}Al$ cluster.

	Al only		Si_4Al		
Mode	Frequency	Δ	Frequency	Δ	Assignments
1			509	26	x Si_{cen}
2			508	26	y Si_{cen}
3			466	31	z Si_{cen}
4			425	69	Si_{bulk}
5			425	69	Si_{bulk}
6			404	75	Si_{bulk}
7			400	81	Si_{bulk}
8			368	85	Si_{bulk}
9			368	85	Si_{bulk}
10	239	96	335	77	Al—Si z str.
11			233	174	x Si_{cen}
12			233	174	y Si_{cen}
13			148	100	Al—Si z trans.
14	51	49	50	59	Al x
15	51	49	50	59	Al y

The uncorrected frequencies are computed by using Al only and the Si_4Al subcluster. All frequencies are in cm^{-1} and Δ is frequency correction from Eq. (5).

TABLE IV
Vibrational frequencies for Al adsorption at the T_4 site on the Si(111) surface using the $Si_{26}H_{24}Al$ cluster.

	Al only		Si_4Al		Si_5Al		
Mode	Frequency	Δ	Frequency	Δ	Frequency	Δ	Assignments
1			585	39	641	7	Si_{cen}—Si_{bulk} str.
2			484	21	485	23	Si_{cen}—Si_{surf} *x* str.
3			484	21	485	23	Si_{cen}—Si_{surf} *y* str.
4					454	99	Si_{bulk} *x*
5					453	98	Si_{bulk} *y*
6			426	42	444	49	Si_{surf}
7			416	64	416	64	Si_{surf}
8			416	64	416	64	Si_{surf}
9					371	80	Si_{bulk} *z*
10			369	81	369	80	Si_{surf}
11			337	23	336	24	Si_{surf}
12			337	23	336	24	Si_{surf}
13	317	85	308	26	306	21	Al—Si_{cen} *z* str.
14			212	144	210	146	Si_{cen}
15			212	144	210	146	Si_{cen}
16	260	95	196	76	196	76	*x* Al
17	259	95	196	76	196	76	*y* Al
18			231	128	184	109	Al—Si_{cen} *z* trans.

The uncorrected frequencies are computed by using Al only and the Si_4Al and Si_5Al subclusters. All frequencies are in cm^{-1} and Δ is frequency correction from Eq. (5).

correction factors in Table III and correspond to vibrational modes for the central Si atom directly underneath the Al adatom which is also bonded to the three bulklike Si atoms in the Si_4Al subcluster. The three bulk Si atoms in the Si_4Al subcluster each have three nearest neighbors not included in the Si_4Al subcluster, and as a result, their Δ values are larger. It is worth noting that the surface normal vibration for the central Si atom at 466 cm^{-1} agrees remarkably well with the 450 cm^{-1} peak observed in the HREELS experiments by Kelly et al. [41].

Similar trends in the frequency-correction term Δ are found in Table IV for the T_4 site. The Si_4Al subcluster does not include the Si_{bulk} atom from the third layer of the Si(111) surface. From both the Si_4Al and Si_5Al subclusters, the Al adatom surface normal vibration appears to be converging to a frequency of 306 cm^{-1} and is not that much different from the frequency calculated in the Al-only calculation. The convergence of the highest-frequency mode, which is associated with the central Si directly underneath Al and above the Si_{bulk} atom, is more sensitive to the subcluster size used and improves tremendously on going to the Si_5Al subcluster. We suspect that this surface normal highest-frequency mode could be responsible for the 525 cm^{-1} peak observed in HREELS, although our SCF frequency value is much too large. The small Δ value computed for this mode suggests that it might be valid to use the Si_5Al subcluster normal modes to perform a numerical fit to the MP2 energy and this work is in progress. Overall, these Al/Si(111) cluster calculations show that while Eq. (5) is not valid for computing adsorbate frequency correction terms, Eq. (5) can still serve as a useful guide to the convergence of the frequency of surface vibrations.

Conclusions

We have presented a general strategy for computing vibrational frequencies for adsorbates on surfaces. Rather than use numerical fitting methods, we advocate using a scheme which involves energy-gradient calculations. The initial vibrational frequencies are obtained by diagonalizing a mass-weighted energy second-derivative matrix formed for a subcluster of atoms from the surface. The diagonalization avoids having to make assumptions on the form of the adsorbate normal

modes. Furthermore, the energy gradients facilitate making estimates of the influence of the adsorbate/substrate mass ratio through the frequency-correction formula given by Eq. (5). Equation (5) produces only small frequency-correction terms for the H/Al(100) surface since the H-to-Al substrate mass ratio is small. For the O/Al(111) surface, we find larger frequency corrections, and these are accurate providing that the frequency value of interest is greater than the maximum phonon frequency of the substrate. However, as we show for H_2O/Al(111) and Al/Si(111) surfaces, even when the surface vibration frequency does not exceed the maximum substrate phonon frequency value, Eq. (5) still serves as a useful guide for checking if the frequency of a surface normal mode is converged. Once the frequency of surface normal mode has been shown to converge, one can then resort to numerical fitting methods and obtain the adsorbate vibrational frequency at a higher level of theory where the gradient calculation is more prohibitively expensive.

ACKNOWLEDGMENTS

We are grateful for the generous use of the IBM SP2 at the Maui High Performance Computer Center.

References

1. D. P. Woodruff and T. A. Delchar, *Modern Techniques of Surface Science*, 2nd ed. (University Press, Cambridge, 1994).
2. H. Ibach and D. L. Mills, *Electron Energy Loss Spectroscopy and Surface Vibrations* (Academic Press, New York, 1982).
3. Y. J. Chabal, Surf. Sci. Rep. **8**, 211 (1988).
4. S. Jin and J. D. Head, Surf. Sci. **318**, 204 (1994).
5. M. D. Calvin, J. D. Head, and S. Jin, Surf. Sci. **345**, 161 (1996).
6. J. E. Crowell, J. G. Chen, D. M. Hercules, and J. T. Yates, Jr., J. Chem. Phys. **86**, 5804 (1987); J. G. Chen, P. Basu, L. Ng, and J. T. Yates, Jr., Surf. Sci. **194**, 397 (1988).
7. A. P. Scott and L. Radom, J. Phys. Chem. **100**, 16502 (1996).
8. P. M. Kozlowski, A. A. Jarzecki, and P. Pulay, J. Phys. Chem. **100**, 7007 (1996); P. M. Kozlowski, A. A. Jarzecki, P. Pulay, X. Li, and M. Z. Zgierski, J. Phys. Chem. **100**, 13985 (1996).
9. G. Pacchioni, P. S. Bagus, and F. Parmigiani, Eds. *Cluster Models for Surface and Bulk Phenomena* (Plenum, New York, 1992).
10. M. Staufer, K. M. Neyman, P. Jakob, V. A. Nasluzov, D. Menzel, and N. Rösch, Surf. Sci. **369**, 300 (1996).
11. R. Konečný and D. J. Doren, J. Phys. Chem. **106**, 2426 (1996).
12. For example, in G. Pacchioni, P. S. Bagus, and F. Parmigiani, Eds., *Cluster Models for Surface and Bulk Phenomena* (Plenum, New York, 1992), the following papers obtain adsorbate vibrational frequencies by performing numerical fits to the cluster energy: P. S. Bagus and G. Pacchioni, pp. 233, 305; N. Rösch, p. 251; F. Illas, J. M. Ricart, J. Rubio, J. Casanovas, and L. Roset, p. 333; R. Fournier, N. Russo, D. R. Salahub, and M. Toscano, p. 433.
13. J. Jacobsen, B. Hammer, K. W. Jacobsen, and J. K. Nørskov, Phys. Rev. B **52**, 14954 (1995).
14. J. E. Black, Surf. Sci. **100**, 555 (1980); J. E. Black, in *Vibrations at Surfaces*, R. Caudano, R. Gilles, and A. A. Lucas, Eds. (Plenum, New York, 1981), p. 57; J. E. Black, B. Laks, and D. L. Mills, Phys. Rev. B **22**, 1818 (1980).
15. J. D. Head, Chem. Phys. Lett. **190**, 417 (1992).
16. J. D. Head, in *Cluster Models for Surface and Bulk Phenomena*, G. Pacchioni, P. S. Bagus, and F. Parmigiani, Eds. (Plenum, New York, 1992), p. 415.
17. J. D. Head, Surf. Sci., to appear.
18. V. Kairys and J. D. Head, Surf. Sci. **380**, 283 (1997).
19. N. W. Ashcroft and N. D. Mermin, *Solid State Physics* (Holt, New York, 1976).
20. D. R. Lide, Ed., *CRC Handbook of Chemistry and Physics*, 71st ed. (CRC Press, Boca Raton, Florida, 1990).
21. M. W. Schmidt, K. K. Baldridge, J. A. Boatz, S. T. Elbert, M. S. Gordon, J. H. Jensen, S. Koseki, N. Matsunaga, K. A. Nguyen, S. Su, T. L. Windus, M. Dupuis and J. A. Montgomery, Jr., *GAMESS, The General Atomic and Molecular Electronic Structure System*, J. Comput. Chem. **14**, 1347 (1993).
22. J. D. Head, J. Comp. Chem. **11**, 67 (1990).
23. P. J. Knowles, J. S. Andrews, R. D. Amos, N. C. Handy, and J. A. Pople, Chem. Phys. Lett. **186**, 130 (1991); W. J. Lauderdale, J. F. Stanton, J. Gauss, J. D. Watts, and R. J. Bartlett, Chem. Phys. Lett. **187**, 21 (1991).
24. P. J. Hay and W. R. Wadt, J. Chem. Phys. **82**, 270 (1985).
25. T. H. Dunning and P. J. Hay, in *Modern Theoretical Chemistry*, H. F. Schaefer, Ed. (Plenum, New York, 1977), Vol. 3, p. 1.
26. G. Fogarasi and P. Pulay, in *Vibrational Spectra and Structure*, J. R. Durig, Ed. (Elsevier, Amsterdam, 1985), Vol. 14, p. 125; B. A. Hess, Jr., L. J. Schaad, P. Cársky, and R. Zahradník, Chem. Rev. **86**, 709 (1986).
27. P. K. Lam and M. L. Cohen, Phys. Rev. B **25**, 6139 (1982).
28. J. Paul, Phys. Rev. B **37**, 6164 (1988).
29. H. Hjelmberg, Surf. Sci. **81**, 539 (1979).
30. I. P. Batra and L. Kleinman, J. Electron Spectrosc. Relat. Phenom. **33**, 175 (1984).
31. J. L. Erskine and R. L. Strong, Phys. Rev. B **25**, 5347 (1982).
32. R. L. Strong, B. Firey, F. W. deWette, and J. L. Erskine, J. Electron Spectrosc. Relat. Phenom. **29**, 187 (1983).
33. C. Astadi, P. Geng, and K. Jacobi, J. Electron Spectrosc. Relat. Phenom. **44**, 175 (1987).

34. J. E. Crowell, J. G. Chen, and J. T. Yates, Surf. Sci. **165**, 37 (1986); J. G. Chen, J. E. Crowell, and J. T. Yates, J. Chem. Phys. **84**, 5906 (1986).
35. P. S. Bagus, C. R. Brundle, F. Illas, F. Parmigiani, and G. Polzonetti, Phys. Rev. B **44**, 9025 (1991).
36. H. Brune, J. Wintterlin, J. Trost, G. Ertl, J. Wiechers, and R. J. Behm, J. Chem. Phys. **99**, 2128 (1993).
37. B. G. Frederick, M. B. Lee, and N. V. Richardson, Surf. Sci. **348**, L71 (1996).
38. R. J. Hamers, Phys. Rev. B **40**, 1657 (1989).
39. J. E. Northrup, Phys. Rev. Lett. **53**, 683 (1984).
40. F. Illas, J. M. Ricart, J. Rubio, J. Casanovas, and L. Roset, in *Cluster Models for Surface and Bulk Phenomena*, G. Pacchioni, P. S. Bagus, and F. Parmigiani, Eds. (Plenum, New York, 1992), p. 333; J. Rubio, F. Illas, and J. M. Ricart, Phys. Rev. B **38**, 10700 (1988).
41. M. K. Kelly, G. Margaritondo, J. Anderson, D. J. Frankel, and G. J. Lapeyre, J. Vac. Sci. Technol. A **4**, 1396 (1986).

Theoretical Studies on the Catalytic Activity of Ag Surface for the Oxidation of Olefins

HIROSHI NAKATSUJI,[1,2,3] ZHEN-MING HU,[1] HIROMI NAKAI[1,*]

[1]*Department of Synthetic Chemistry and Biological Chemistry, Graduate School of Engineering, Kyoto University, Sakyo-ku, Kyoto 606-01, Japan*

[2]*Department of Applied Chemistry, Graduate School of Engineering, University of Tokyo, Hongo, Tokyo 113, Japan*

[3]*Institute for Fundamental Chemistry, 34-4, Takano-Nishihirakicho, Sakyo-ku, Kyoto 606, Japan*

Received 2 March 1997; accepted 14 March 1997

ABSTRACT: Systematic theoretical studies for the mechanisms of the epoxidation and complete oxidation of ethylene and propylene over silver surface as well as the reactivity and the stability of oxygen species on Cu, Ag, and Au surfaces have been presented. The dipped adcluster model (DAM) combined with the ab initio Hartree–Fock (HF), second-order Møller-Plesset (MP2), and SAC/SAC-CI (symmetry-adapted cluster/configuration interaction) methods are used. These studies clarify the origin of silver as a unique effective catalyst for the epoxidation of ethylene and the different mechanisms for the oxidation of olefins over silver surface. For the epoxidation of ethylene, the superoxide O_2^-, which is molecularly adsorbed in bent end-on geometry on the silver surface, is the active species. The origin of the unique catalytic activity of silver for the epoxidation of ethylene is due to its ability to adsorb oxygen as the superoxide species. Such an adsorbed species cannot be stable or exist on Cu and Au surfaces. For the oxidation of propylene, both reaction mechanisms initiated by the activation of olefinic carbon and by the activation of the allyl hydrogen exist. The activation of the allyl hydrogen is the origin of the complete oxidation of some olefins over silver surface. The present results not only let us have a better understanding of the reaction mechanisms of olefins over silver surface but also supply a basic idea for the new catalyst design of the epoxidation reaction. © 1997 John Wiley & Sons, Inc. Int J Quant Chem **65**: 839–855, 1997

* *Present address*: Department of Chemistry, School of Science and Engineering, Waseda University, Ohkubo 3-4-1, Shinjuku-ku, Tokyo 169, Japan.

Correspondence to: H. Nakatsuji.

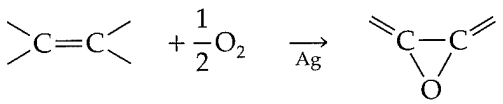
Contract grant sponsor: Japanese Ministry of Education, Science, and Culture and the New Energy and Industrial Technology Development Organization (NEDO).

© 1997 John Wiley & Sons, Inc.
CCC 0020-7608 / 97 / 050839-17

Key words: Reaction mechanism; epoxidation; combustion; catalytic activity of silver, copper, and gold; superoxide; atomic oxygen; propylene; ethylene; dipped adcluster model (DAM); SAC/SAC-CI method; ab initio Hartree–Fock (HF) and second-order Møller-Plesset (MP2) methods

Introduction

The heterogeneous selective oxidation of olefins to epoxides on silver



olefin epoxide (1)

is an exceedingly important industrial catalytic reaction, and as such has received long and extensive study [1–7]. One particularly interesting aspect of the epoxidation reaction is its uniqueness: Not only is silver a uniquely effective catalyst for heterogeneous epoxidation but also ethylene is the only hydrocarbon which may be epoxidized with high selectivity. Actually, silver catalysts are used in industry to produce several million tons of ethylene oxide yearly [1–4]. Recent experimental studies show that, except for ethylene, only a few olefins such as styrene [8, 9], 3,3-dimethylbutene [10], norbornene [11], and butadiene may be epoxidized over silver with high selectivity. In contrast, other olefins such as propylene, butenes, and pentenes are epoxidized over silver but with extremely low selectivity [12–16].

During the past 20 years, many studies [12–24] have been devoted to getting a better understanding of the epoxidation reaction mechanism. However, the origin of this unique catalytic activity of silver has not yet been clarified, and also the mechanistic details of the epoxidation and that of the competing combustion to carbon dioxygen and water are far from understood. One of the main questions about the mechanism of ethylene oxidation is the roles of the adsorbed molecular and atomic oxygen. Both mechanisms involving molecular oxygen [12–18] and atomic oxygen [19–23] as the active species have been suggested. It has been suggested that the uniqueness of silver is associated with its ability to adsorb oxygen as the superoxide species [24]. More direct evidence for molecular oxygen as the active species has been obtained by several studies: e.g., only complete oxidation occurs when N_2O pulse which gives atomically adsorbed oxygen is used, but the epoxidation reaction occurs when O_2 pulse which gives molecularly adsorbed oxygen, at least initially, is used [25]. The mechanism assuming atomic oxygen as an active species was suggested from the experimental data that only atomically adsorbed oxygen exist at high temperature in an industrial condition, since molecular oxygen desorbs or dissociates. The assumption that molecular and atomic oxygens cause the partial and total oxidation reactions, respectively, gives an upper limit for the selectivity of 6/7. Recent experiments giving higher selectivity than 6/7 [26] imply that the atomic oxygen may at least pay an important role for the epoxidation of ethylene.

Theoretical studies have done much less for the epoxidation reaction of olefins. Though a few works [27–30] studying the epoxidation mechanism of ethylene have ever been published, less discussions were presented [27, 30] for the oxidation of propylene, and the calculations did not explicitly include the surface contribution. The main difficult problem still remaining in the theoretical studies is how to describe chemisorption species and calculate adsorption energy correctly based on a selected small cluster. This may be why no ab initio theoretical study for the full reaction pathway and the associated energy diagrams of the epoxidation reaction of olefins has been reported.

In a series of our previous studies [31–37], a theoretical model, named the dipped adcluster model (DAM) [31–33], has been proposed to study chemisorptions and surface reactions by involving the interactions between bulk metal and admolecules with consideration of the electron transfer between them and the image force correction. Such an interaction is found to be very important for studying the chemisorptions and the reactions of the oxygen on a metal surface, and even a small DAM could be used to give correct electronic

structures and reliable adsorption energies in contrast to the cluster model. Previous studies [34–36] for the chemisorption of oxygen on a silver surface showed that the molecularly adsorbed oxygen exists in two stable geometries; i.e., an end-on (bent) structure in an on-top site and a side-on structure in a bridge site. The ground state in the former geometry is superoxide, which is expected to be more electronically favorable for the reaction with ethylene [36].

In this work, we present a brief account of our recent systematic studies on the catalytic activity of silver surface for the oxidation of olefins. We will try to address the following three questions: (1) What species of surface oxygen is responsible for the ethylene epoxidation? (2) Why is silver a unique catalyst for the epoxidation? (3) Why do higher olefins mainly process complete oxidation on the same silver catalyst? We performed the ab initio Hartree–Fock (HF), second-order Møller-Plesset (MP2), and the SAC (symmetry-adapted cluster)/SAC-CI (configuration interaction) calculations with the use of the DAM. More details are seen in the literature [38–40].

Epoxidation Mechanism of Ethylene on Silver Surface

In this section we give an account of our research on the mechanism of the epoxidation of ethylene on a silver surface [38]. The energy diagrams of the reactions of ethylene with both molecularly adsorbed and atomically adsorbed oxygens on a Ag surface are studied. The Eley-Rideal mode, namely the reaction between the adsorbed oxygen species and a gaseous ethylene is assumed. The DAM was used to include the effects of the bulk metal such as the electron transfer between adcluster and surface and the image force. Geometry optimizations for calculating the reaction path were performed using the ab initio unrestricted Hartree–Fock (UHF) method and the energies at the optimized geometries were calculated by the MP2 methods including the image force correction. The Gaussian basis set used is of double-zeta accuracy, and some additional functions were added for improvement. They are shown to reproduce well the known geometries and the energetics of the reactions [38]. The model adclusters used in the present study are the molecularly adsorbed end-on (bent) form in an on-top site and the atomically adsorbed on-top structure.

REACTIONS WITH MOLECULARLY ADSORBED OXYGEN

Epoxide Formation

We first study the epoxidation reaction of ethylene with the molecularly adsorbed superoxide on a silver surface. For the formation of ethylene oxide, the reaction takes place by an initial interaction of the oxygen with one of the carbon in ethylene [5, 6]. Figure 1 shows the obtained favorable initial attack of ethylene to superoxide species adsorbed on the silver surface. Starting from this geometry, we optimized the geometries of the intermediates and the transition states (TSs) along the reaction pathway. The optimized geometries and energy diagrams are shown in Figure 2. The reaction proceeds from the left to the right, and the energy is in kcal/mol relative to the free system, i.e., $Ag_2 + O_2 + C_2H_4$.

Figure 2 shows a two-step mechanism of the reactions. The first step of this reaction is the adsorption of molecular O_2 on Ag surface in which one electron is transferred from the bulk metal to the adcluster, i.e., $n = 1$. The transferred electron mainly occupies the out-of-plane p^* orbital of O_2, and the in-plane p^* molecular orbital (MO) of O_2 remains singly occupied. The ground state for the end-on adsorption of O_2 is the superoxide. The adsorption energy of superoxide is calculated to be

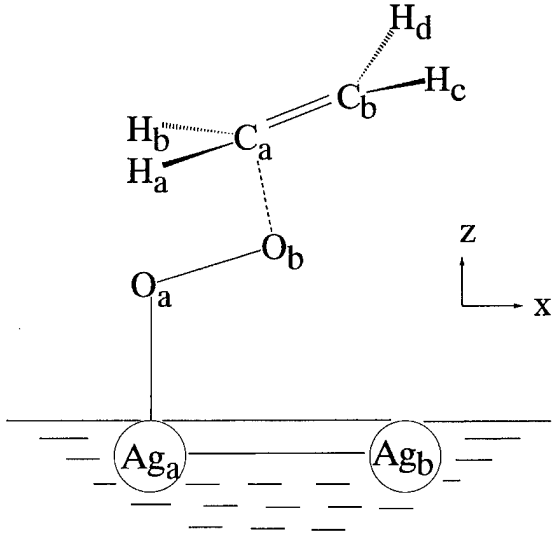


FIGURE 1. Model adcluster used. Geometries were optimized in the Cs symmetry except for the Ag—Ag distance and the O_a—Ag—Ag angle fixed at 2.8894 Å and the 90.0°, respectively.

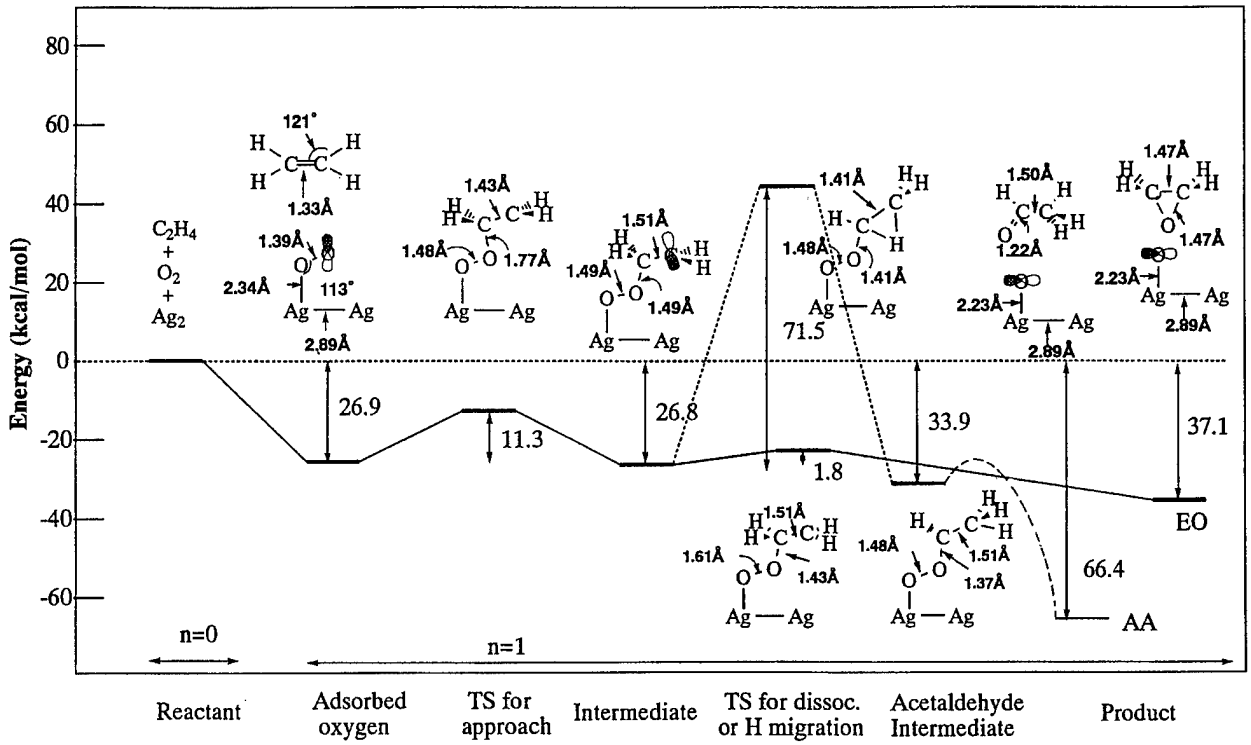


FIGURE 2. Energy diagram for the reaction between ethylene and molecularly adsorbed superoxide on Ag surface. The route leading to ethylene oxide (EO) and acetaldehyde (AA) are shown by the solid and broken lines, respectively.

7.4 kcal/mol at the UHF level and 26.9 kcal/mol at the MP2 level. The experimental molecular adsorption energies are 9.2, 9.3, and 24.1 kcal/mol for the Ag(111) [18], Ag(110) [18], and electrolytic Ag [41] surfaces, respectively. The next step is the attack of ethylene onto the terminal oxygen atom O_b which is more reactive than the inside one O_a, leading to the TS and the intermediate with the energy barrier of 11.3 kcal/mol. The energy level of the intermediate is similar to that of initial step. In the TS the σ bond between O_b and C_a is formed and the in-plane p bond of O_2 and the p bond of C_2 are broken. The geometry parameters at every step clearly reflect the reaction processing along the reaction path [38].

When the intermediate is produced, the formation of ethylene oxide is an easy path as shown by the real line, leaving an atomic oxygen on the Ag surface. The calculated heat of reaction is 37.1 kcal/mol. The energy diagram given in Figure 2 shows that the reaction leading to ethylene oxide proceeds very smoothly: The reaction is exothermic, there are no very high barriers, and there are no too stable intermediates. We therefore conclude that the epoxide formation reaction from the superoxide species on a silver surface proceeds very smoothly. We note that the exothermicity of the overall reaction is partially due to the formation of the atomically adsorbed oxygen on the silver surface.

Acetaldehyde Formation

We next study the formation process of acetaldehyde from ethylene and molecularly adsorbed superoxide on the Ag surface. In Figure 2, the path is given by the broken line. When acetaldehyde is produced, it is further oxidized to CO_2 and H_2O by combustion in the presence of adsorbed oxygen, and therefore it is an intermediate in the complete oxidation process [42].

The formation of acetaldehyde starts from the intermediate shown in the center of Figure 2: up to it the reaction path is common to the epoxidation reaction. H_a bound to C_a in the intermediate migrates to C_b, giving a stable conformation denoted as acetaldehyde intermediate in Figure 2. However, the energy barrier for this H_a migration is as high as 71.5 kcal/mol. This step is therefore energetically forbidden. This is a reason for the high

selectivity of the epoxide formation process starting from the superoxide species summarized in the preceding section.

Effect of Silver Surface

The effect of the silver surface may be twofold: One is to provide a reactive species adsorbed on the surface, and the other is to provide electrons to the reaction site as considered in the DAM. Figure 3 shows the energy diagram for the reaction between ethylene and gaseous oxygen without the silver surface. Two energy diagrams correspond to the calculations with $n = 1$ and $n = 0$. The former involves an excess electron but the latter is neutral. For $n = 1$, we used the optimized geometries shown in Figure 2, and, for $n = 0$, we performed the geometry optimization for the present purpose. The geometries illustrated in the upper and lower sides correspond to those for $n = 0$ and $n = 1$, respectively. For $n = 0$, the O—O distance is calculated to be 1.37 Å for the intermediate, which is smaller than the corresponding value 1.49 Å for $n = 1$. The same is true for all the intermediates and TSs.

Comparing Figure 3 with Figure 2, we clearly see the catalytic activity of the silver surface for the epoxidation reaction. Without the surface, the reaction is endothermic and the pathway has a large barrier. Electron transfer ($n = 1$) certainly reduces the barrier, but the direct interaction with the actual silver atoms on the surface is quite important. Clearly, the exothermicity of the reaction shown in Figure 2 is due to the formation of the atomically adsorbed oxygen on the surface.

REACTIONS WITH ATOMICALLY ADSORBED OXYGEN

When ethylene oxide is ejected out of the Ag surface, the atomically adsorbed oxygen O^- is left on the surface. It is also produced by the dissociative adsorption of O_2 on the surface, and the dissociative state is more stable than the molecular adsorption state. In our calculation, the dissociated oxygen has its singly occupied orbital in the $2p$ orbital parallel to the surface.

Figure 4 shows the energy diagram for the reaction of ethylene with the atomically adsorbed oxygen on the Ag surface. When ethylene attacks

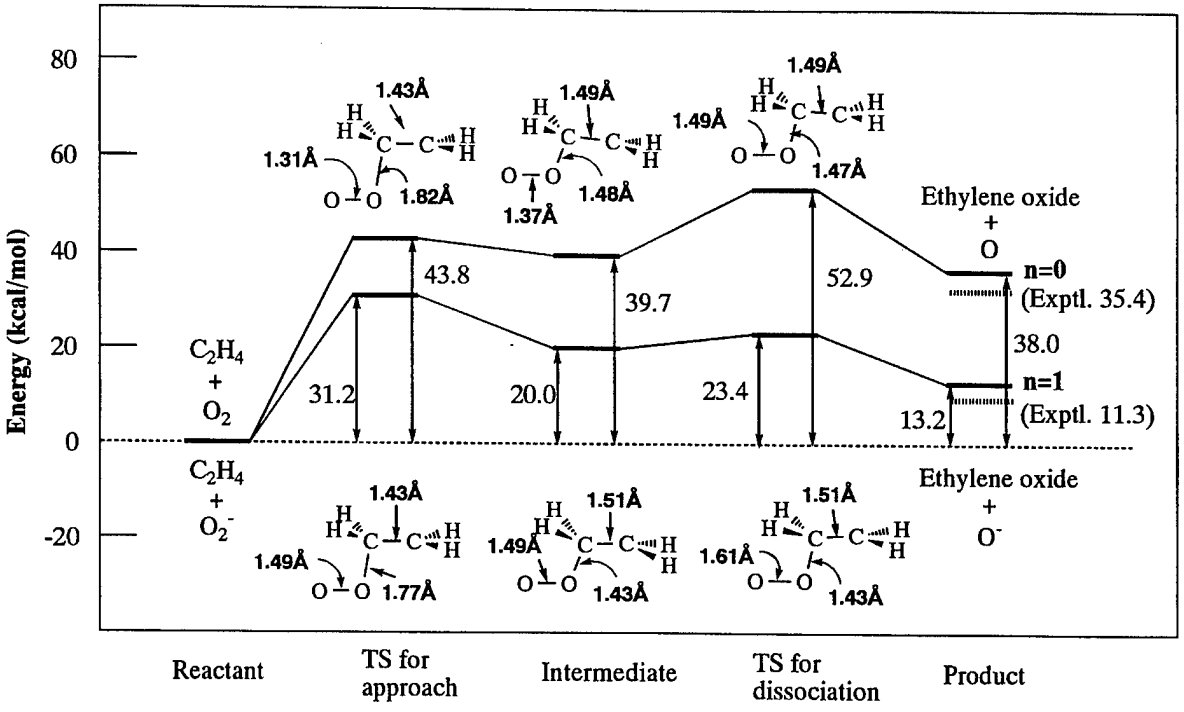


FIGURE 3. Energy diagram for the reactions between ethylene and gaseous oxygens [neutral O_2 ($n = 0$) and O_2 anion ($n = 1$)]. The upper geometries are for $n = 0$, and the lower geometries for $n = 1$.

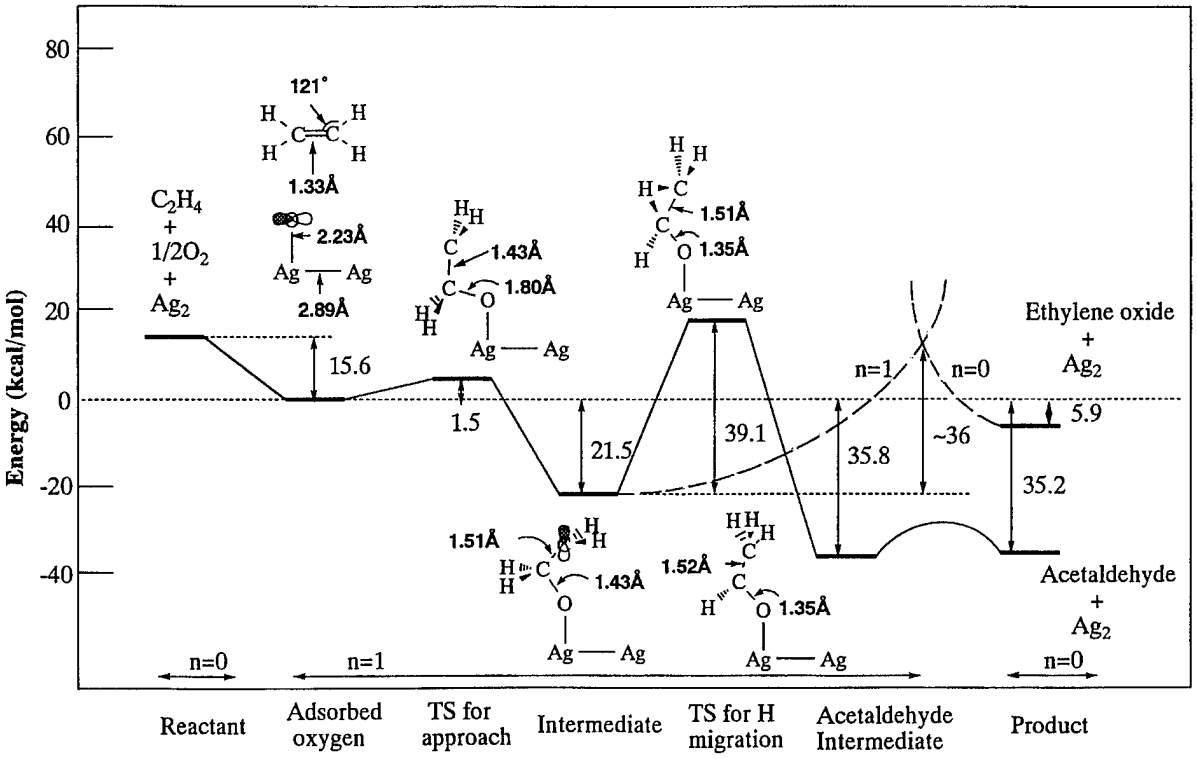


FIGURE 4. Energy diagram for the reaction between ethylene and atomically adsorbed oxygen on Ag surface.

atomic oxygen on the surface, the most favorable approach is to form the C_a—O_a bond as illustrated in Figure 4. It is similar to the approach of ethylene to the superoxide species shown in Figure 2. The calculated energy barrier from the adsorbed oxygen to the intermediate is, however, as small as 1.5 kcal/mol, reflecting the reactivity of the atomic oxygen.

The next step from this intermediate is very important, since it determines the selectivity of the atomically adsorbed oxygen. If C_b attacks the oxygen to form the C_b—O_a bond, ethylene oxide is formed. If C_b attacks another C—H bond, causing the hydrogen migration, acetaldehyde is a product, which is an intermediate for the complete oxidation product.

For the hydrogen migration reaction, the barrier was calculated to be 39.1 kcal/mol, which is high but lower than the barrier, 71.5 kcal/mol, of the reaction in which the superoxide species was involved (see Fig. 2). This process were calculated using the adcluster with $n = 1$. Unfortunately, the structure of the TS to form the C_b—O_a bond could not be determined by the geometry optimization procedure using both of the $n = 1$ and $n = 0$ adclusters. If the pathway from the intermediate to ethylene oxide is one step, it is a quite interesting step since it involves both geometrical changes and *one electron back-transfer* from the admolecule to the bulk metal. In the DAM picture, the intermediate in Figure 4 is neutrally described with $n = 1$, i.e., with one additional electron supplied from the bulk metal to the adcluster, but the product, ethylene oxide plus Ag_2 should be neutral, i.e., $n = 0$. Therefore, we calculated two potential curves, one starting from the intermediate and the other from ethylene oxide plus Ag_2 using $n = 1$ and $n = 0$, respectively. All the geometrical parameters were assumed to change linearly, except for the Ag—O distance, which was fixed to 2.180 Å.

The potential curve for $n = 1$ increases monotonically from the intermediate to the product, while the curve for $n = 0$ also increases monotonically from ethylene oxide and Ag_2 to the intermediate, and the two energy curves cross. The energy difference between the crossing point and the intermediate is about 36 kcal/mol, which may be considered as the energy barrier of this process. Namely at this TS, one electron is transferred back to the metal.

The selectivity giving either ethylene oxide or acetaldehyde would be dependent on the heights of the barriers of the two processes and on the stabilities of the two products. The calculated energy barriers for the two processes are similar, 39.1 and about 36 kcal/mol, respectively. On the other hand, the energy difference between the two products and the intermediate are +15.6 and −13.7 kcal/mol, respectively, which means endothermicity and exothermicity from the intermediate, respectively. From the above data alone, it is difficult to decide which is a preferential process, though the acetaldehyde formation may be favorable for the exothermicity. However, it may be said that both ethylene oxide and acetaldehyde are formed from ethylene and atomically adsorbed oxygen on the Ag surface. Furthermore, this fact is very important since it would be a reason for the experimental maximum selectivity more than 6/7 [5–7].

OVERALL MECHANISM OF EPOXIDATION OF ETHYLENE

We summarize here our results on the mechanism of the epoxidation of ethylene on a silver surface. The calculated energy barriers and the heats of the reactions are summarized in Table I. The primarily important species for the epoxidation of ethylene on a silver surface is the superoxide O_2^- which is molecularly adsorbed on the surface in the bent end-on geometry. Ethylene attacks the terminal oxygen atom of the superoxide, as shown in Figure 1, with the barrier of about 11 kcal/mol, and then the reaction proceeds quite smoothly leading to ethylene oxide as shown in Figure 2. The overall reaction is exothermic by 37 kcal/mol from $C_2H_4 + O_2$ + Ag surface or by 10 kcal/mol from C_2H_4 + superoxide on Ag surface. The second exothermicity is due to the larger adsorption energy of the atomic oxygen than that of the superoxide.

On the contrary, the complete oxidation of ethylene from the superoxide species is forbidden due to the existence of the large barrier (72 kcal/mol) in the hydrogen migration step, though this reaction is largely exothermic by 66 kcal/mol from the initial compounds or by 40 kcal/mol from the superoxide on Ag and C_2H_4. When silver surface does not exist, the epoxidation reaction is a very unfavorable reaction having a high-energy barrier and endothermicity. Thus, the epoxidation of ethylene by the superoxide on the Ag surface is highly efficient and selective.

The atomically adsorbed oxygen, which is left on the surface after completion of the epoxidation reaction by the superoxide or which may exist by the dissociative adsorption of O_2 on the surface, has two reaction channels leading to ethylene oxide and to complete oxidation. The selectivity here seems to be small and both products would be obtained. This would be the reason why some experiments reach the selectivity larger than 6/7.

In the process leading to ethylene oxide, the electron back-transfer from the reaction adsorbate complex to the metal surface should be important and related to the barrier. We note that both electron acceptor and donor may work to reduce the barrier of the electron transfer step: They work to stabilize the $n = 1$ and $n = 0$ curves, respectively. The effects of Ce and halogen as promoters of catalyst are well known experimentally [5–7]. We

TABLE I

Comparison of the energy barrier and the heat of reaction for the epoxidation and acetaldehyde formation by the molecularly and atomically adsorbed oxygens (kcal / mol).

Reaction	Energy barrier	Heat of reaction[a]
Molecularly adsorbed oxygen		
$O_2(a) / Ag + C_2H_4 \rightarrow C_2H_4O + O(a) / Ag$	11.3	10.2
$O_2(a) / Ag + C_2H_4 \rightarrow CH_3CHO + O(a) / Ag$	71.5	39.5
Atomically adsorbed oxygen		
$O(a) / Ag + C_2H_4 \rightarrow C_2H_4O + Ag$	~36	21.5 (24.7)
$O(a) / Ag + C_2H_4 \rightarrow CH_3CHO + Ag$	39.1	50.8 (52.3)
Without Ag surface		
$O_2^- + C_2H_4 \rightarrow O^- + C_2H_4O$	31.2	−13.2 (−11.3)
$O_2 + C_2H_4 \rightarrow O + C_2H_4O$	52.9	−38.0 (−35.4)

[a] Values in parentheses show the experimental values.

speculate that these promoters act in this electron-transfer step. Design of the promoter or co-catalyst, which is effective to this electron-transfer step, is of crucial importance since it would be a key for raising up the selectivity over 6/7.

Activation of O_2 on Cu, Ag, and Au Surfaces

The experimental results show that silver is a unique catalyst for the epoxidation of ethylene. However, it is not yet well understood why only silver is so exceptional. In the former section, we showed that the superoxide species adsorbed in the end-on form on a Ag surface is very active and selective for the epoxidation reaction. Aiming to clarify the reason why only silver is an effective catalyst for the epoxidation of ethylene, in this section, we perform a comparable study for the chemisorption and activation of oxygen on Cu, Ag, and Au surfaces.

We take M_2O_2 (M = Cu, Ag, Au) as adclusters. Both electronic structures and the reactivity of the molecular end-on and side-on adsorptions are studied. The geometries of the molecular end-on and side-on species are optimized at the UHF level. The relative stabilities of the adsorbed species is studied by SAC/SAC-CI method [43–45], since the roles of lower ground and excited states are quite important in this kind of surface electronic processes [34–36]. The DAM [31–33] is again adopted to investigate the electron transferability of these surfaces.

REACTIVITY AND STABILITY OF SUPEROXIDE SPECIES

Figure 5 shows an illustration of the geometries of the end-on and side-on forms. The calculations are performed by assuming one-electron transfer

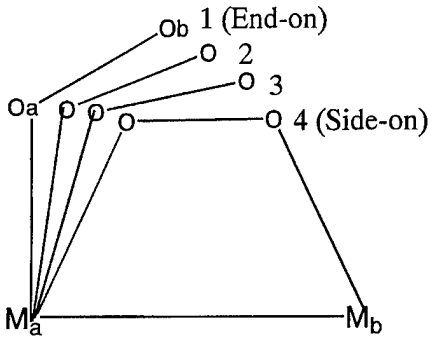


FIGURE 5. Illustration of the geometrical conversion from end-on (#1) to side-on (#4) forms. The M—M (M = Cu, Ag, and Au) distances were fixed at the lattice constants.

from the bulk to the adcluster occurs. The optimized O—O distances are 1.36–1.38 Å in the end-on form, which are close to or slightly greater than that of a free O_2 anion (1.35 Å) [46], and that in the side-on form are all about 1.51 Å. The calculated Cu—O distance are shorter than the Au—O and Ag—O distances, reflecting a large adsorption energy and a short lattice constant of Cu.

The calculated electronic structure of O_2 in the end-on and side-on adsorption forms is superoxide O_2^- and peroxide O_2^{2-}, respectively. Table II shows the net charge and frontier density (or spin population), which are related to the reactivity of the superoxide species. In all three species, the net charges on the inside (O_a) and outside (O_b) oxygen atoms are calculated to be about −0.6 and −0.15, respectively, while the outside oxygen atoms have a frontier density of about 0.86, which is much larger than that of the inside oxygen atoms (about 0.12). This shows that the outside oxygen is much more reactive than the inside one and that the former is not so negative as the latter one, the same result as that reported before [36] for a linear Ag—O—O system. Actually, in the epoxidation reaction with ethylene, the oxygen that reacts with

TABLE II
Net charge and frontier density of the end-on superoxide species on Cu, Ag, and Au surfaces.

	Net charge				Frontier density			
System[a]	M_a	M_b	O_a	O_b	M_a	M_b	O_a	O_b
Cu_2O_2	+0.060	−0.271	−0.643	−0.146	0.007	0.002	0.133	0.858
Ag_2O_2	+0.058	−0.295	−0.605	−0.158	0.014	0.003	0.119	0.864
Au_2O_2	+0.095	−0.285	−0.644	−0.166	0.007	0.002	0.116	0.876

[a]The geometry of the end-on form is shown in Fig. 1.

ethylene is the outside one as shown in the above section. Based on the analyses of the net charge and the frontier density, similar reactivity is expected for the end-on superoxide species on Cu, Ag, and Au surfaces.

The reactivities of the superoxide species on Cu, Ag, and Au surface for ethylene are also very similar [39]. The differences among Cu, Ag, and Au surfaces are small, if the superoxide species exists on the metal surfaces. Large observed differences in the catalytic activity of these metal surfaces are therefore attributed to the different stabilities of the adsorbed oxygen species, particularly the stability of the superoxide species.

Next, we examine a conversion from the end-on to the side-on geometries. This process accompanies a conversion from the superoxide to the peroxide, since the ground state of the end-on and side-on species are the superoxide and peroxide, respectively, as shown in some details in this section. Thus, the method to be used here should be able to describe both ground and excited states in a good accuracy. For this purpose, the HF method is inadequate, we use the SAC/SAC-CI method [43–45]. The geometries optimized at the HF level are used for the end-on (#1) and side-on (#4) forms, respectively. The intermediate geometries #2 and #3, which are illustrated in Figure 5, are approximated as a linear function of the OMM angle.

Figure 6 shows the potential energy curves (PECs) calculated for the conversion process between the end-on and side-on forms on the Cu, Ag, and Au surfaces. In the end-on geometry, the superoxide ($^2B_2$) is always the ground state, but in the side-on geometry, the ground state is the peroxide species ($^2A_1$). The superoxide species with the $^2A_2$ symmetry is less important since it never becomes the ground state in this conversion process. In the $^2B_2$ superoxide, the in-plane π^* orbital of oxygen is singly occupied while the out-of-plane π^* orbital is doubly occupied. These occupations are reversed in the $^2A_2$ state. The crossing of the PECs of the superoxide and peroxide occurs between the end-on and side-on geometries.

Relative stabilities of the superoxide and peroxide in the end-on and side-on geometries and the barrier of the conversion are quite important for understanding the catalytic activities of metals for the epoxidation of ethylene. Such information is given in Figure 6. In the end-on form, the superoxide species is more stable than the peroxide species: the energy difference is about 20 kcal/mol for Ag

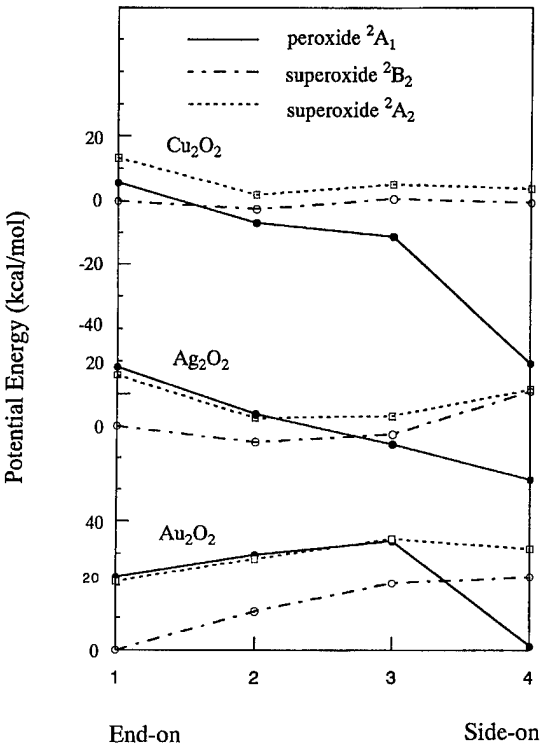


FIGURE 6. Potential energy curves calculated by the SAC / SAC-CI method for the conversion between the end-on (#1) and side-on (#4) adsorption states in the lowest three states of the Cu_2O_2, Ag_2O_2, and Au_2O_2 adclusters with $n = 1$.

and Au and 5 kcal/mol for Cu. In the side-on form, the peroxide species is more stable than the superoxide species: The energy difference is 50.1, 27.6, 21.2 kcal/mol for Cu, Ag, and Au, respectively. The energy difference between the end-on superoxide and the side-on peroxide is 50.8, 23.1, and −1.2 kcal/mol for Cu, Ag, and Au, respectively. On the Cu surface, the superoxide species in the end-on form easily converts into the peroxide species in the side-on form because of a large stabilization energy and for a lack of the barrier: The lifetime of the end-on superoxide species should be very short on the Cu surface. On the other hand, an energy barrier of about 20 kcal/mol is calculated for the conversion on Au. On the Ag surface, the end-on superoxide should have a considerable lifetime as seen from the PECs shown in Figure 6. Based on the above results, we can conclude that the reason for the nonselectivity of Cu for the epoxidation of ethylene is due to the absence of the stable adsorbed superoxide species. However, for Au, the results obtained from Figure

6 does not give a clear explanation for its inability of this reaction. As far as one-electron transfer from the bulk metal into the adcluster occurs for Cu, Ag, and Au, the reactivity of the superoxide on these metals should be similar.

ELECTRON TRANSFERABILITY OF Cu, Ag, AND Au

The results listed in the preceding section show that the oxygen superoxide species adsorbed on Au surface has essentially the same reactivity as those on Cu and Ag surfaces. The stabilities of the molecularly adsorbed oxygen species are mainly due to the electron-transfer effect from the bulk metal as already shown previously for silver [34–36] and palladium [31, 32]. The chemical potentials (work functions) of the Cu, Ag, and Au surfaces are 4.48, 4.52, and 5.37 eV for the (110) surfaces, 4.94, 4.74, and 5.31 eV for the (111) surfaces, and 4.59, 4.64, and 5.47 eV for the (100) surfaces [47]. The Cu surface is expected to have similar properties to the Ag surface. However, it is not clear whether the electron transfer also occurs for the Au surface. We therefore investigate here the $E(n)$ curves of the M_2—O_2 systems in the DAM in order to clarify why Au cannot be a good catalyst for the epoxidation of ethylene.

Figure 7 is a display of the $E(n)$ curves, namely the energy of the adcluster calculated as a function of n. It was calculated with the use of the highest spin coupling model [39]. The optimized end-on geometries of M_2O_2 adclusters are adopted since they are the most stable geometries of the superoxide adsorbed species. The $E(n)$ curves are upper convex, and at $n = 1.0$, the systems are more stable than at $n = 0.0$, and the order of stability is $Cu_2O_2 > Ag_2O_2 > Au_2O_2$. According to DAM [31], the electron transfer would occur between the adcluster and the bulk metal when the chemical potential of the adcluster becomes equal to the chemical potential of the solid surface, i.e., $\partial E(n)/\partial n = -\mu$. For Cu_2O_2 and Ag_2O_2 systems, the tangents of the $E(n)$ curves become equal with the experimental chemical potentials at about $n = 0.9$. Therefore, from the concept of DAM [31], one electron should flow from the Cu and Ag bulk metals into the adcluster after some barrier. This is the case we used to study the activation of O_2 on the surfaces shown in the preceding section. However, for the Au_2O_2 system, though the energy at

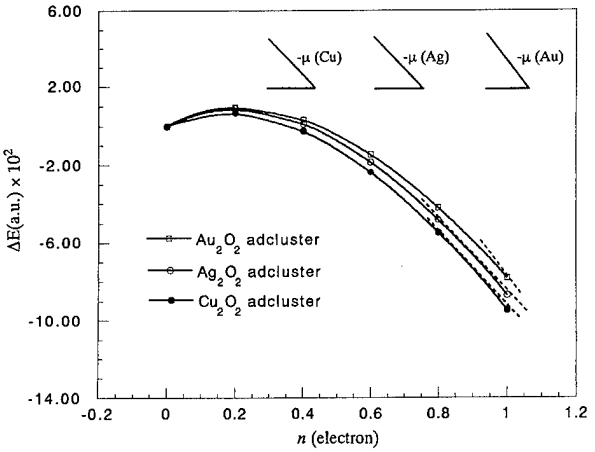


FIGURE 7. $E(n)$ curves for the Cu_2O_2, Ag_2O_2, and Au_2O_2 adclusters in the highest spin coupling model at the optimized end-on geometries.

$n = 1.0$ is lower than that at $n = 0.0$, the tangent of the $E(n)$ curve is still smaller than the experimental chemical potential. Therefore, different from Cu and Ag metals, one-electron flow does not occur from the Au metal into the adcluster. This point of the Au surface is essentially different from the other metals and should be the reason why the molecularly adsorbed oxygen species cannot exist on the clean gold surface. Thus, the inactivity of the gold surface for the oxygen is explained by the DAM as being due to its poor donating property.

The chemical potential of Au is much larger than those of Cu and Ag. We note that this difference is attributed actually to the relativistic effect in gold [48, 49]. The importance of the relativistic effects to the valence-electron properties such as chemical shift has been recently clarified in this laboratory [50–52].

We further note that the electron flow is difficult to occur between the clean gold metal and the adcluster because it does not satisfy the condition clarified by the DAM [31]. However, as the energy at $n = 1.0$ is lower than that at $n = 0.0$, the electron transfer can be realized if the chemical potentials μ of the gold metal can be lowered by an addition of promoters, etc. Experimentally, the recent works performed by Haruta et al. [53, 54] show that gold is remarkably active for the oxidation of CO and hydrocarbons when it is supported on suitable metal oxides. This may be explained by such effect of the metal-oxide support.

BRIEF SUMMARY

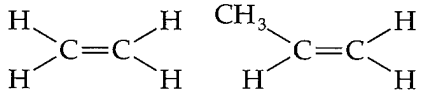
The electron transfer from metal to O_2 is a key factor for the chemisorption of oxygen on a metal surface, as shown previously [32–37]. The differences in the relative stabilities of different oxygen species on different metal surfaces are attributed to the differences in the electron-donating ability. The present DAM calculations show that, for Cu and Ag surfaces, one-electron transfer from the bulk metal into the adcluster occurs after some barriers. On the other hand, electron transfer is difficult to occur for the Au surface since the gold surface has the higher work function. This is why molecular adsorption of O_2 does not occur on the Au surface.

On Cu surface, peroxide is much more stable than superoxide, and there is essentially no barrier for the conversion from superoxide to peroxide, so that the lifetime of the superoxide species should be too short to react with ethylene. On Ag surface, however, the superoxide species would have considerable lifetime on the surface. On Au surface, the superoxide species does not exist because the molecular adsorption of O_2 does not occur due to the difficulty of the electron transfer from the clean bulk metal. We think that this difference in the stabilities of the end-on superoxide species on Cu, Ag, and Au surfaces is a reason of the observed difference in the catalytic activity of these metals for the epoxidation of ethylene.

The above conclusion for the origin of the different catalytic activity of Cu, Ag, and Au surfaces for the epoxidation of ethylene suggests a possibility of making a new catalyst for this reaction. The key is an appropriate lifetime of the end-on superoxide species on the metal. Silver realizes it without any special modification. However, if one can realize such superoxide species on some metals using some modification, we think that the essential factor is realized.

Oxidation Mechanism of Propylene on Silver Surface

Though silver is an effective catalyst for the epoxidation of ethylene (85–87% conversion) [5–7], it is a very poor catalyst for the epoxidation of propylene (2–5% conversion) [12–16]. A relatively small substitution of hydrogen with methyl group,



causes such a drastic change of the reaction. It is interesting to understand why. To know the difference of the oxidation mechanism between ethylene and propylene will lead to a better understanding of the general oxidation mechanism of other olefins on silver surface. Further, in the chemical industry, propylene oxide is an important material, so that to know why silver is so poor for the conversion of propylene to propylene oxide is a starting point for a design of a new effective catalyst. This section is a summary of our recent study on the oxidation mechanism of propylene [40].

Two possible reasons may be considered for the difference in the reaction of ethylene and propylene on a silver surface. One possibility is that the reaction routes are the same but the methyl substituent causes a large change in the barrier height and/or in the stability of the intermediates in the course of the reaction. Another possibility is that an entirely different reaction route comes out for the existence of the methyl group. We have investigated these two possibilities. As in the case of ethylene, we study the reactions of the two active oxygen species on a silver surface: the molecularly adsorbed superoxide species and the dissociatively adsorbed atomic oxygen species.

The calculational methods are the same as those discussed in the second section. The DAM [31–33] was used to include the effect of the bulk metal such as the electron transfer and the image force. The basis sets are the same as before, and the geometries of the reactants, intermediates, transition states, and the products were optimized by the Hartree–Fock method and the energies were calculated by the MP2 method in order to include the effects of electron correlations.

ATTACK ON OLEFINIC CARBON

We first study the reaction route, which is essentially the same as that of ethylene [38]: The reaction starts from the interaction between the adsorbed oxygen and the doubly bonded carbon atom of propylene. Figure 8 is an illustration of the adcluster for the initial interaction of propylene

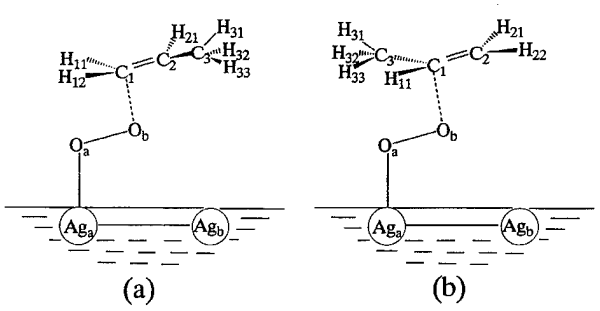
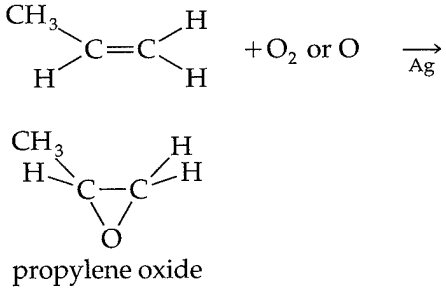
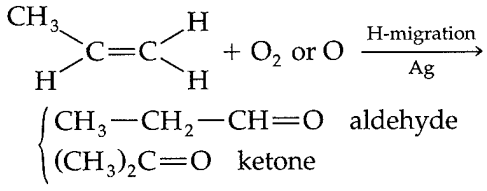


FIGURE 8. Model adclusters for the olefinic carbon attack mechanism: (a) on the terminal olefinic carbon, (b) on the central olefinic carbon.

with the superoxide species. Since two carbons in propylene are different, two different attacks were considered. The interaction with atomic oxygen was similarly considered. The reaction may process as follows:



(2)



(3)

In (3), aldehyde is a product of the terminal C attack and ketone is a product of the central C attack, and they are further oxidized to CO_2 and H_2O.

Figure 9 shows the optimized geometries and the energy diagrams for the reaction of the molecularly adsorbed oxygen with the terminal C of propylene. It is similar to Figure 2 for the reaction with ethylene: The substitution of one hydrogen with methyl group does not cause a large change for the reaction route and the energetics. In this reaction mechanism, the route going to propylene oxide should be quite smooth without any high-energy barrier and without any too stable intermediate, while the route leading to the aldehyde should be essentially blocked up by the existence of a high-energy barrier in the hydrogen migration step. The diagram for the reaction of the superoxide with the central carbon atom of propylene [Fig. 8(b)] was similar to Figure 9 [40]. Thus, if the reaction proceeds along this reaction route, propylene oxide should be produced in high selectivity due to the catalytic activity of the superoxide

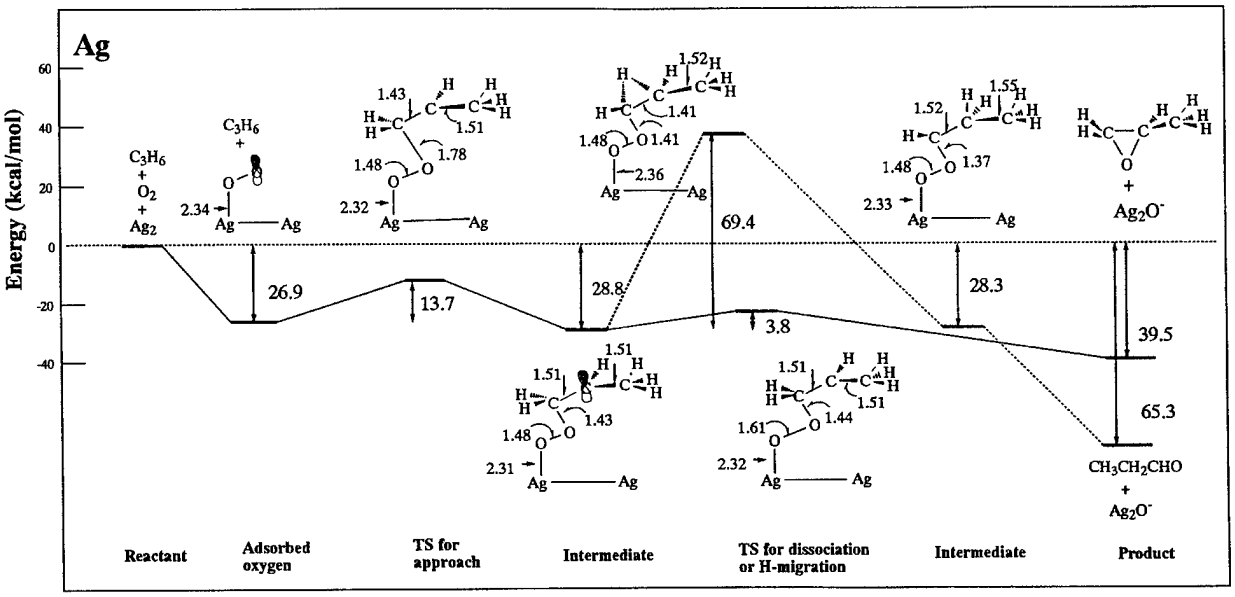


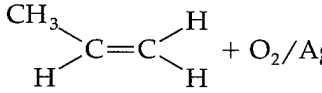
FIGURE 9. Energy diagram for the reaction between the terminal carbon atom of propylene and the molecularly adsorbed superoxide on a Ag surface. The route leading to propylene oxide and aldehyde are shown by the solid and broken lines, respectively.

species adsorbed on silver. Also, for the reaction with atomically adsorbed oxygen, a similar conclusion as that of ethylene may be obtained as the reaction route and the energy diagrams of propylene are similar to ethylene [38].

The results shown above mean that if the reaction proceeds through the oxygen attack on the olefinic carbon of propylene, silver should be as good a catalyst as for ethylene for the epoxidation. However, this result contradicts with the experimental observation that the conversion of propylene into propylene oxide is only 2–5% on the silver catalyst [12–17]. We therefore examine another possibility that a reaction route entirely different from those of ethylene may exist. Since propylene has a methyl group, but ethylene does not, we next examine the reaction route involving the reaction of this methyl group with the reactive oxygen on a silver surface.

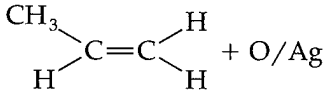
ATTACK ON ALLYLIC HYDROGEN

Propylene is different from ethylene by an existence of a methyl group. We examine here the reaction route involving the reaction of this methyl group with the superoxide and the atomic oxygen on a silver surface. Figure 10 shows the initial attack of the superoxide [Fig. 10(a)] and atomic oxygen [Fig. 10(b)] on the methyl hydrogen, and the reactions process as follows:



$$\rightarrow CH_2{-}CH{-}CH_2/Ag + H{-}O{-}O/Ag \quad (4)$$

$$\rightarrow CH_2{-}CH{-}CH_2/Ag + O/Ag + HO/Ag \quad (5)$$



$$\rightarrow CH_2{-}CH{-}CH_2/Ag + HO/Ag \quad (6)$$

These reactions produce the allyl intermediate adsorbed on the silver surface, which is oxidized further to CO_2 and H_2O. Since allyl radical or anion is a rather stable intermediate, this reaction route is feasible.

Figure 11 shows the optimized reaction route for the attack of superoxide on the methyl hydrogen of propylene as given by (4) and (5). The present result was added to the previous one for

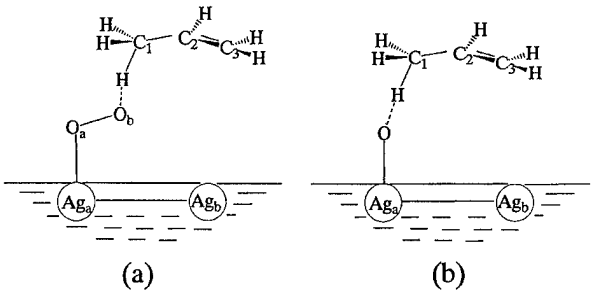


FIGURE 10. Model adclusters for the allylic H attack mechanism: (a) reaction with molecularly adsorbed superoxide species, (b) reaction with atomically adsorbed oxygen.

the carbon attack given in Figure 9. The optimized geometries of the intermediates and the transition states for the present H attack are given in the lower side, while those for the previous C attack are given on the upper side. The energy levels of the intermediates and the transition states for the present reaction route are lower than those of the previous one. The barrier for the attack on the methyl hydrogen was calculated to be 10.8 kcal/mol, which is lower than the barrier for the carbon attack, 13.7 kcal/mol, and then the system becomes allyl intermediate and the hydroperoxy group adsorbed on silver [Eq. (4)]. This intermediate is also more stable than the previous one, but the hydroperoxy group is unstable and further converted into OH and O as given by Eq. (5): The barrier in this step is only 2.8 kcal/mol and the stabilization energy is as large as 42.6 kcal/mol. When two-site interaction between allyl and silver surface is further allowed, the system is further stabilized by 18.1 kcal/mol. Thus, the reaction route starting from the allylic H attack is always lower than that starting from the olefinic C attack, so that the reactions represented by Eqs. (4) and (5) should proceed more easily than the reactions given by Eqs. (2) and (3).

We next examine the similar reaction given by Eq. (6) involving the atomic oxygen adsorbed on silver. Figure 12 shows the optimized reaction route and its energetics. The lower figures give the optimized geometries for the allylic H attack and the upper ones for the olefinic C attack. The barrier for the allylic H attack is essentially zero: only 0.1 kcal/mol. The allyl intermediate is more stable than the intermediate of the previous C attack: when two-site interaction between allyl and silver surface is allowed, it is further stabilized by 18.1 kcal/mol. Thus, again, for the atomic oxygen on

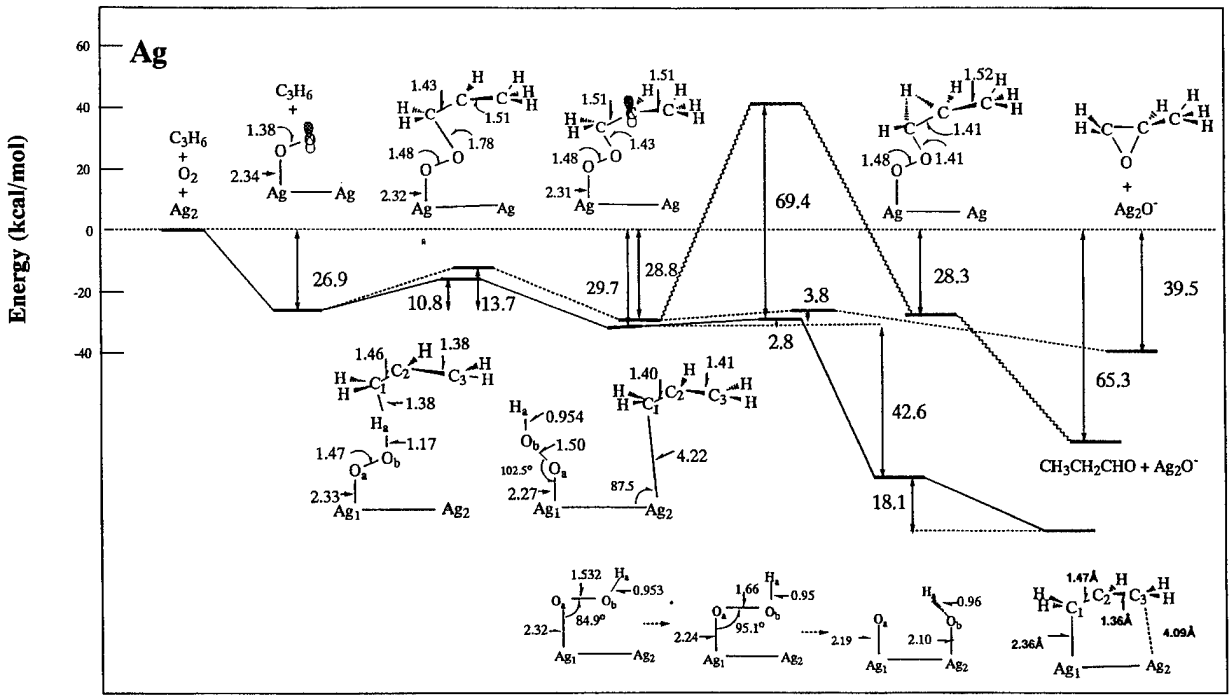


FIGURE 11. Comparison of the energy diagrams for the reactions between propylene and the molecularly adsorbed oxygen. The route for the allylic H attack is shown by the solid line, and those for the carbon attack are shown by the broken and waved lines.

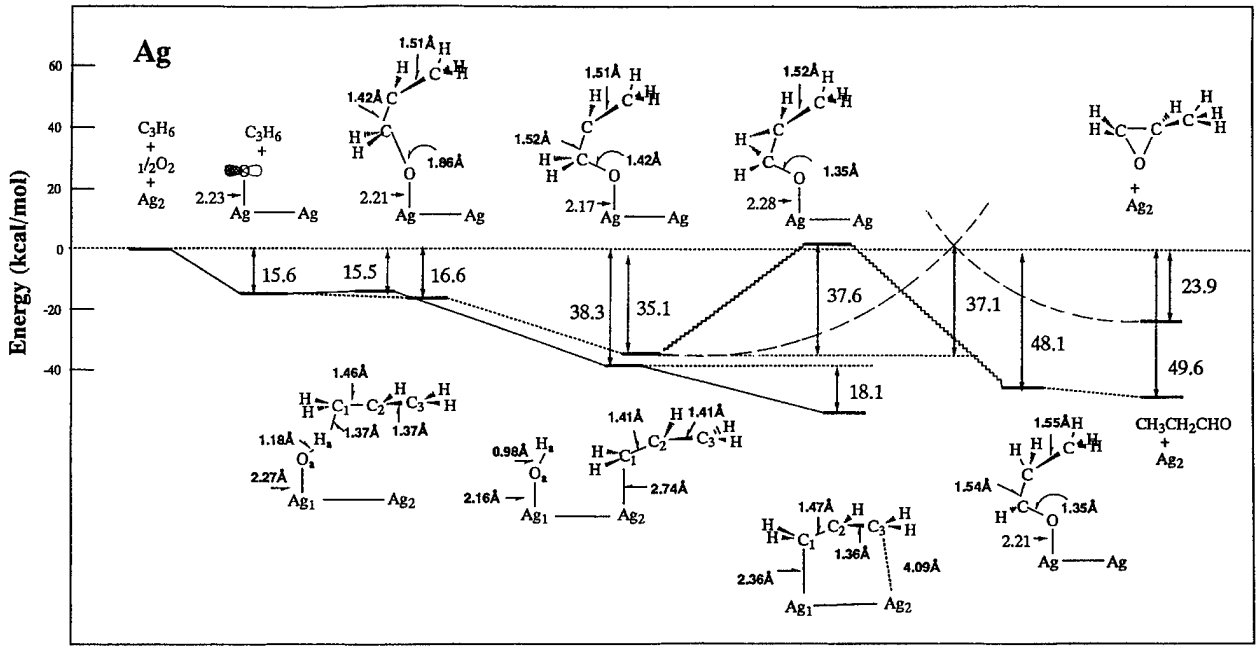


FIGURE 12. Comparison of the energy diagrams for the two reactions between propylene and the atomically adsorbed oxygen on a Ag surface.

the silver surface, the allylic H attack is an easier reaction than the olefinic C attack. The allyl intermediate thus produced is stable on the silver surface so that it will be further attacked by the oxygen species on the surface and would finally be converted into CO_2 and H_2O.

Thus, for both superoxide and atomic oxygen on a silver surface, the reaction starting from the allylic H attack proceeds more easily than the one starting from the olefinic C attack. Therefore, the conversion to propylene oxide does not effectively occur on a silver surface.

The origin of the activation of this allyl hydrogen is due to the stability of the preceding adsorbed allyl intermediate. We have investigated the nature of the allyl intermediate adsorbed on a silver surface. Figure 13 shows the optimized geometry of the allyl intermediate on Ag_2 calculated with $n = 0$ and $n = 1$. We see that the adsorption energy is larger with $n = 1$ than with $n = 0$, indicating that the allyl species on silver is actually an allyl anion species. Actually, the charge on the allyl group was -0.52 for $n = 1$, while it was -0.27 in the case of $n = 0$. The existence of the anion allyl species on silver surface had been suggested experimentally by Madix et al. [23] to be the intermediate leading to the complete oxidation.

BRIEF SUMMARY

Figure 14 is a summary of the reaction mechanism of propylene on a silver surface. The allylic hydrogen is more reactive than the olefinic carbon, due to the stability of the allyl anion species on the silver surface, so that propylene is converted to allyl intermediate and further converted to CO_2 and H_2O. If an olefin does not have an allylic hydrogen, like ethylene, styrene, etc., it is converted to epoxide in high selectivity. Even if it has an allylic hydrogen but the allyl intermediate is not stable like in norbornene, the route leading to epoxide is more preferable. This explains the selectivity of the silver surface for the epoxidation reactions of olefins.

We note that the present results clearly show that the route leading to propylene oxide also exists on a silver surface. However, it is not the most favorable reaction path. The selectivity is just between 2 and 5% experimentally. Since propylene oxide is an important material in chemical industry, it is interesting whether we can block up the route leading to the allylic intermediate.

Concluding Remarks

We reported, in this study, the mechanisms of the epoxidation and complete oxidation reaction of propylene on a silver surface and the stabilities and activities of the oxygen species adsorbed on Cu, Ag, and Au surfaces. We performed the (U)HF, MP2, and SAC/SAC-CI calculations with the use of the DAM which involved the interaction between bulk metal and admolecules with consideration of electron transfer and image force correction.

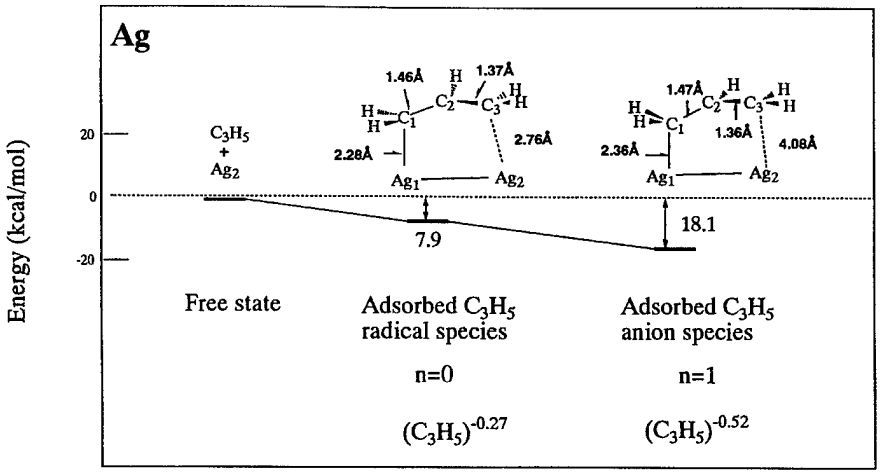


FIGURE 13. Stability of the allyl species adsorbed on Ag_2 cluster in the neutral ($n = 0$) and anion ($n = 1$) adcluster states.

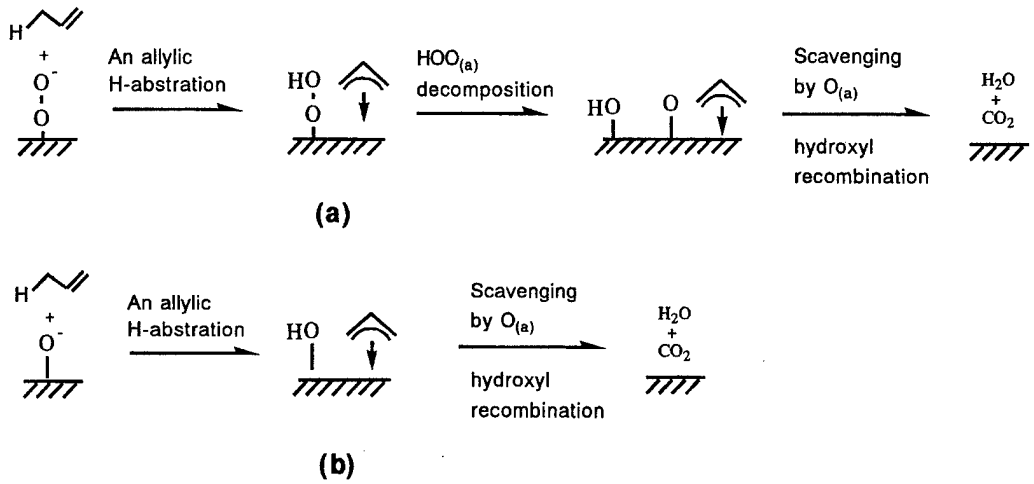


FIGURE 14. Mechanism of the complete oxidation of propylene over a silver surface; (a) with molecularly adsorbed oxygen, (b) with atomically adsorbed oxygen.

For the epoxidation of ethylene, the active species is the superoxide, which is molecularly adsorbed on the surface in the bent end-on geometry. Ethylene attacks the terminal oxygen atom of the superoxide leading to ethylene oxide quite smoothly. The importance of the silver surface is quite evident. On the other hand, the atomically adsorbed oxygen species is not selective: Both epoxidation and complete oxidation products would be obtained. However, to promote the selectivity of the atomically adsorbed species will certainly promote the total selectivity to epoxidation product. In the process leading to ethylene oxide, the electron back-transfer from the reaction adsorbate complex to the metal surface should be important.

The origin of the catalytic activity of the silver surface is due to its ability to stabilize the superoxide species. On Cu surfaces, peroxide is much more stable than superoxide, so that the lifetime of the superoxide species should be too short to react with ethylene. On Au surfaces, the superoxide species does not exist because the molecular adsorption of O_2 does not occur due to the difficulty of the electron transfer from the clean bulk metal.

For the oxidation of propylene on silver surface, two competitive mechanisms exist. The dominant mechanism for the epoxidation of olefins is initiated by the activation of the olefinic carbon. The dominant mechanism for the complete oxidation of propylene is due to the activation of the allylic C—H bond. The latter is more favorable due to the formation of the stable adsorbed allyl intermediate, which is the motivation force for the complete oxidation of propylene.

We note that the proposed two competitive mechanisms not only reflect the difference between ethylene and propylene but also explain rather well the available experimental facts for the epoxidation and complete oxidation of olefins. Therefore, it reflects a general mechanism to understand the oxidation of olefins over silver surface.

ACKNOWLEDGMENTS

Some calculations were performed using the computers at the Institute for Molecular Science. Part of this study was supported by a Grant-in-Aid for Scientific Research from the Japanese Ministry of Education, Science, and Culture and by the New Energy and Industrial Technology Development Organization (NEDO).

References

1. R. A. van Santen and H. P. C. E. Kuipers, Adv. Catal. **35**, 265 (1987).
2. W. M. H. Sachtler, C. Backx, and R. A. van Santen, Cat. Rev. Sci. Eng. **23**, 127 (1981).
3. X. E. Verykios, F. P. Stein, and R. W. Coughlin, Cat. Rev. Sci. Eng. **22**, 197 (1980).
4. K. A. Jørgensen, Chem. Rev. **89**, 431 (1989).
5. A. Ayame, in *Series of Lectures on Catalysis VII, Fundamental Industrial Catalytic Reactions*, Murakami Y, Ed. (Catalytic Society of Japan, Tokyo, 1985), pp. 170–185, in Japanese.

6. A. Ayame and H. Kanoh, Shokubai **20**, 381 (1978), in Japanese.
7. H. Miura, A. Ayame, H. Kanoh, K. Miyahara, and I. Toyoshima, Shinku **25**, 302 (1982).
8. Y. Murakomo and K. Tanaka, Nippon Kagaku Kaishi **11**, 1603 (1977).
9. S. Hawker, C. Mukoid, J. P. S. Badyal, and R. M. Lambert, Surf. Sci. **219**, L615 (1989).
10. C. Mukoid, S. Hawker, J. P. S. Badyal, and R. M. Lambert, Catal. Lett. **4**, 57 (1990).
11. J. T. Roberts and R. J. Madix, J. Am. Chem. Soc. **110**, 8540 (1988).
12. N. W. Cant and W. K. J. Hall, J. Catal. **52**, 81 (1978).
13. M. Imachi, M. Egashira, R. L. Kuczkowski, and N. W. Cant, J. Catal. **70**, 177 (1981).
14. C. Henriques, M. F. Portela, C. Mazzocchia, and E. Guglielminotti, *New Frontiers in Catalysis*, L. Guczi et al., Eds. (Elsevier, Amsterdam, 1993), p. 1995.
15. P. V. Geenen, H. J. Boss, and G. T. Pott, J. Catal. **77**, 499 (1982).
16. M. Akimoto, K. Ichikawa, and E. Echigoya, J. Catal. **76**, 333 (1982).
17. C. T. Campbell, J. Catal. **157**, 43 (1985); **99**, 28 (1986).
18. C. T. Campbell and M. T. Paffett, Surf. Sci. **143**, 517 (1984); **177**, 417 (1986).
19. E. L. Force and A. T. Bell, J. Catal. **38**, 440 (1975); **40**, 356 (1975).
20. R. B. Grant and R. M. Lambert, J. Catal. **92**, 364 (1985).
21. J. T. Gleaves, A. G. Sault, R. J. Madix, and J. R. Ebner, J. Catal. **121**, 202 (1990).
22. M. A. Barteau and R. J. Madix, J. Am. Chem. Soc. **105**, 344 (1983).
23. J. T. Roberts, R. J. Madix, and W. W. Crew, J. Catal. **141**, 300 (1993).
24. H. H. Voge and C. R. Adams, Advan. Catal. **17**, 151 (1967).
25. M. Kobayashi, M. Yamamoto, and H. Kobayashi, *Proc. 6th. Intern. Congr. Catal.* A24, 1976; M. Kobayashi, *Catalysis Under Transient Conditions*, A. T. Bell and L. L. Hegedus, Eds. (ACS, Washington, DC, 1982), p. 209.
26. J. Deng, J. Yang, S. Zhang, and X. Yuan, J. Catal. **138**, 395 (1992).
27. E. A. Carter and W. A. Goddard, J. Catal. **112**, 80 (1988); Surf. Sci. **209**, 243 (1989).
28. P. J. van den Hoek, E. J. Baerends, and R. A. van Santen, J. Phys. Chem. **93**, 6469 (1989).
29. K. A. Jørgenson and R. Hoffmann, J. Phys. Chem. **94**, 3046 (1990).
30. S. Beran, P. Jiru, B. Wichterlova, and R. Zahradnik, *Proc. Sixth Int. Cobgr. Catal.* **1**, 324 (1997).
31. H. Nakatsuji, J. Chem. Phys. **87**, 4995 (1987).
32. H. Nakatsuji, H. Nakai, and Y. Fukunishi, J. Chem. Phys. **95**, 640 (1991).
33. H. Nakatsuji, Proc. Surf. Sci. **54**, 1 (1997).
34. H. Nakatsuji and H. Nakai, Chem. Phys. Lett. **174**, 283 (1990).
35. H. Nakatsuji and H. Nakai, J. Chem. Phys. **98**, 2423 (1993).
36. H. Nakatsuji and H. Nakai, Can. J. Chem. **70**, 404 (1992).
37. H. Nakatsuji, Int. J. Quant. Chem. **42**, 725 (1992).
38. H. Nakatsuji, H. Nakai, K. Ikeda, and Y. Yamamoto, Surf. Sci., in press.
39. H. Nakatsuji, Z. M. Hu, H. Nakai, and K. Ikeda, Surf. Sci., in press.
40. Z. M. Hu, H. Nakai, and H. Nakatsuji, Surf. Sci., submitted.
41. X. Bao, J. Deng, and S. Dong, Surf. Sci. **163**, 444 (1985).
42. L. Ya. Margolis, Adv. Catal. **14**, 4289 (1963).
43. H. Nakatsuji and K. Hirao, J. Chem. Phys. **68**, 2053 (1978).
44. H. Nakatsuji, Chem. Phys. Lett. **59**, 362 (1978); **67**, 329 (1979).
45. H. Nakatsuji, in *Computational Chemistry—Reviews of Current Trends*, J. Leszczynski, Eds. (World Scientific, London, 1997).
46. P. H. Krupenie, J. Phys. Chem. Ref. Data **1**, 423 (1972).
47. *Handbook of Chemistry and Physics*, R. C. Weast et al., Eds. (CRC Press, Cleveland, 1984–1985).
48. E. Eliav, U. Kaldor, and Y. Ishikawa, Phys. Rev. A **49**, 1724 (1994).
49. U. Kaldor and B. A. Hess, Chem. Phys. Lett. **230**, 1 (1994).
50. H. Nakatsuji, H. Takashima, and M. Hada, Chem. Phys. Lett. **233**, 13; 95 (1995).
51. C. C. Ballard, M. Hada, H. Kaneko, and H. Nakatsuji, Chem. Phys. Lett. **254**, 170 (1996).
52. H. Nakatsuji, M. Hada, H. Kaneko, and C. C. Ballard, Chem. Phys. Lett. **255**, 195 (1996).
53. M. Haruta, S. Tsubota, T. Kobayashi, M. Kageyama, M. Genet, and B. Delmon, J. Catal. **144**, 175 (1993).
54. T. Hayashi and M. Haruta, Shokubai 37 (1995) 72, in Japanese; M. Haruta, Chem. Eng. **59**, 168 (1995), in Japanese.

Simulations of Laser-Assisted Field Emission Within the Local Density Approximation of Kohn–Sham Density-Functional Theory

MARK J. HAGMANN

Department of Electrical and Computer Engineering, Florida International University, Miami, Florida 33199

Received 3 March 1997; revised 16 May 1997; accepted 22 May 1997

ABSTRACT: We have developed procedures for determining the potential, electron density, and current at a planar metal surface with an applied static field in vacuum. These calculations are made using density-functional theory within the local density approximation (LDA) for the Kohn–Sham exchange and correlation. Several different techniques were compared including the use of different expressions for the exchange and correlation energies. The steady-state response of field emission to a laser is found using Floquet methods to solve the dipole approximation of the time-dependent Schrödinger equation with the static potential obtained from density-functional theory. These simulations show that there is a resonance in the response that causes a significant increase in the tunneling current. This resonance occurs for electrons that are promoted above the barrier by absorbing quanta from the laser when the line integral of the momentum between the turning points is equal to $h/2$. © 1997 John Wiley & Sons, Inc. Int J Quant Chem **65**: 857–865, 1997

Introduction

Photofield emission [1, 2], the study of the energy distribution of electrons emitted from a metal surface subjected to an intense static electric field plus a weaker radiation field, is used to characterize the surface density of states in metals. Lee and Robbins [3] measured the time dependence of the total current from a field emitter when the laser beam was chopped with an electromechanical shutter. They found that under conditions that are typical of the photofield studies, the rise time of the current is approximately 1 ms. They showed by analysis that the thermal relaxation time is within one order of magnitude of the rise time, which they measured. Thus, Lee and Robbins concluded that the laser-induced increase in the current is primarily the result of tip heating, and this raises doubt regarding much of the published photofield data. However, few references

© 1997 John Wiley & Sons, Inc.
CCC 0020-7608 / 97 / 050857-09

have been made to this study by Lee and Robbins, and thermal effects are not mentioned in many of the subsequent photofield studies.

It is the purpose of this study to use numerical simulations based on the local density approximation of Kohn–Sham density-functional theory to examine the nonthermal effects of laser-assisted field emission in order to clarify the mechanism for photofield emission. A number of different methods have been used to model laser-assisted field emission, but most of these are one-particle solutions [4–6] in which the time-dependent Schrödinger equation is solved for a specified approximation of the potential, and all of the effects of electron–electron interactions are neglected. A many-particle approach [7, 8] that is based on nonequilibrium Green's functions [9] shows considerable promise, but we chose to use density-functional theory [10, 11] in the present study because we consider this procedure to be better understood due to a longer and more extensive history of application.

Analysis

The density-functional formalism, which was introduced by Hohenberg, Kohn, and Sham [12, 13], is a many-particle approach in which the properties of a system (such as a metal surface) are determined as functions of only the electron density $n(x)$. We use a jellium model in which the positive ions within the metal half-space ($x < 0$) are replaced by a uniform positive charge background with density $n_+(x)$. The many-particle problem of determining the potential and electron density at a metal surface may be solved through density-functional theory by finding a consistent solution for the following set of four equations:

$$\frac{-\hbar^2}{2m}\frac{\partial^2\psi_I}{\partial x^2} + (\phi(x) + V_{xc}(n))\psi_I = E_I\psi_I, \quad (1)$$

$$n(x) = \sum_{I=1}^{N} |\psi_I(x)|^2, \quad (2)$$

$$\phi(x) = \frac{e}{\varepsilon_0}\int_{-\infty}^{x} [n_+(x') - n(x')](x' - x)\,dx', \quad (3)$$

$$V_{xc}(n) = \frac{-e^2 n^{1/3}}{4\pi\varepsilon_0}\left[0.985 + \frac{0.946 + 8.92a_0 n^{1/3}}{\left[1 + 12.6a_0 n^{1/3}\right]^2}\right]. \quad (4)$$

Here, the one-particle Schrödinger equation (1) is solved to determine the wave functions for a series of energies E_i representing the distribution of normal energies in the metal. The electron density $n(x)$ is determined by normalizing the summation of the probability densities in Eq. (2). The Coulomb portion of the effective potential required in Eq. (1) is determined by integration of Poisson's equation as shown in Eq. (3), in which it is assumed that the Coulomb potential and electric field are zero deep within the metal. A number of different methods have been used to approximate the exchange-correlation contribution to the effective potential [14–16]. In most calculations we have used the Wigner interpolation form as shown in Eq. (4), which was derived using the local density approximation (LDA), but we have also tested an approximation by Gell-Mann and Brueckner [16] which is more appropriate for high electron densities. More exact calculations have shown [17] that, for an electron at a jellium edge, the Fermi hole calculated within the LDA approximates the exact hole. Thus, the corresponding LDA force field at the surface is fairly accurate; thus it is reasonable to use this approximation in simulating field emission. Conventional mks units are used in place of atomic units throughout this work, so that Eq. (4) contains the symbol a_0 denoting the Bohr radius, which is approximately 0.052917 nm.

Solutions for Static Problems

In static problems we solve the system of Eqs. (1)–(4) by means of iteration. We begin by approximating the effective potential that is required in Eq. (1) by using either the Fowler–Nordheim model [18] or a closed-form approximation of a variational solution [19]. The numerically efficient method of back-propagation [20] is used to solve the Schrödinger equation without forming a matrix. The solutions are obtained for a large number of energies E_I (for $I = 1$ to N) to simulate the distribution of normal energies which was derived by Modinos [21].

We have used two different methods to introduce an applied static field into the formulation of Eqs. (1)–(4) in order to simulate field emission from a metal surface, and we have found that these two methods give identical results. In the first approach the normalization of the electron density in Eq. (2) is adjusted so that there is a net

charge within the descretized region, and the magnitude of this charge will produce the specified value of the applied static field. In this method the applied static field does not appear explicitly in the calculations. In the second approach the normalization of the electron density in Eq. (2) is adjusted so that the descretized region is neutral, and the applied static field is specified throughout the entire space including the metal. All of the examples in this article are for tungsten metal. We have assumed that tungsten has a density of 19.30 g/cm^3 and that there are 6 free electrons per atom. Thus, we assume a Fermi energy of 19.1 eV, a bulk electronic density of $3.79 \times 10^{29}/mtr^3$ (0.0562 in atomic units), and a Wigner-Seitz radius of 0.0857 nm (1.62 bohrs).

Figures 1 and 2 show the potential barrier and the electron density at a tungsten surface with applied static fields of 5 and 2 V/nm, respectively. In both of these figures the dashed curves represent the potential barrier for the Fowler–Nordheim model [18], which requires specifying the work function (4.5 eV) and includes a correction from image theory. The results of our iterative calculations are shown as solid curves for the potential barrier, and dotted curves for the electron density. The iterative solutions for these two figures required under relaxation for convergence, so that at each step in the iterations the potential was updated by setting $V_{I+1}(x) = \alpha V_I(x) + (1 - \alpha)V_{I-1}(x)$. A relaxation factor ($\alpha$) of 0.001 was used in the iterations with a total of 200 energies. A total of 1000 intervals was used on the x axis to descretize a length of 2 nm of metal and 6.5 nm of vacuum with an increment of $\Delta x = 0.0085$ nm.

The iterative static density-functional solutions for the potential that are shown in Figures 1 and 2 converge with consistent results as the depth of the metal that is discretized is varied from 2 to 8 nm, the number of electron energies is changed from 50 to 1000, and the number of intervals is varied from 200 to 1500. The upper values given for these parameters are practical limits for calculations with a personal computer. The length of vacuum that is descretized must be increased for very low values of the applied static field so that the potential at the far end of the grid is well below the Fermi level. There was no significant change when the calculations for Figures 1 and 2 were repeated using the approximation by Gell-Mann and Brueckner [16] in place of the Wigner interpolation form for the exchange-correlation contribution to the effective potential as shown in Eq. (4). Figures 1 and 2 show that both the height

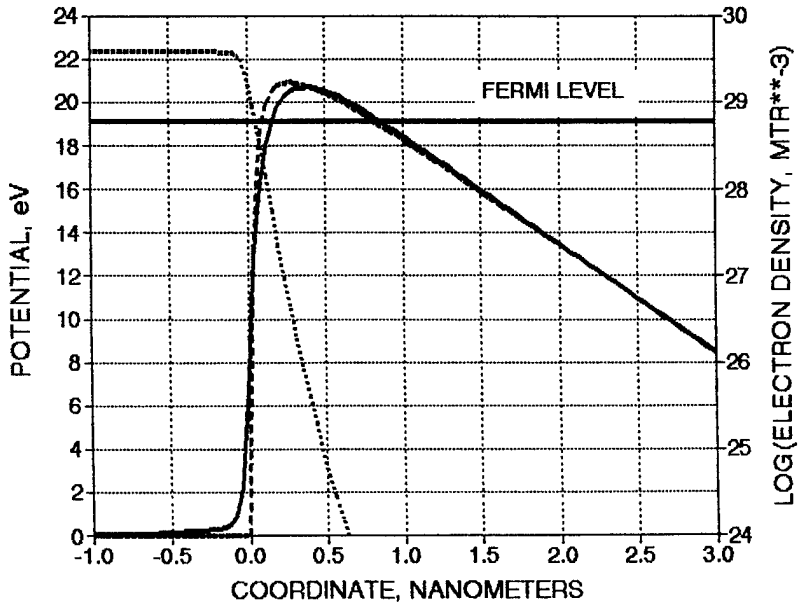


FIGURE 1. Potential barrier and electron density at a tungsten surface with a static field of 5 V/nm. The potential and electron density are represented by a solid curve and a dotted curve, respectively. The dashed curve is the potential for the Fowler–Nordheim model.

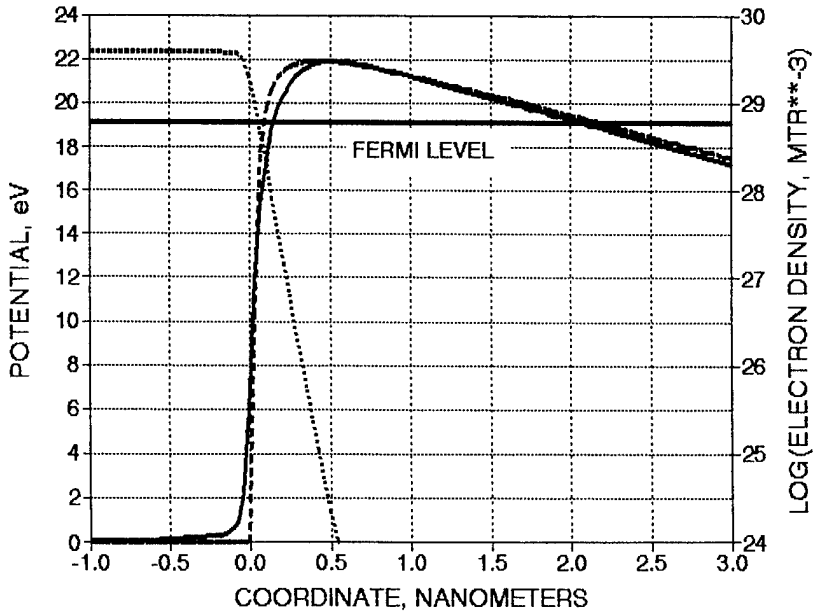


FIGURE 2. Potential barrier and electron density at a tungsten surface with a static field of 2 V/nm. The potential and electron density are represented by a solid curve and a dotted curve, respectively. The dashed curve is the potential for the Fowler–Nordheim model.

of the barrier and the length of the tunneling region are decreased, thus increasing the current, as the applied static field is increased.

Figure 3 shows the maximum height of the potential barrier at a tungsten surface as a function of the applied static field. Values obtained using the Fowler–Nordheim model are shown with a solid curve, and the results of our iterative calculations are shown as solid squares connected with a dashed curve. As in the first two figures, the iterative calculations were made using a relaxation factor of 0.001, a total of 200 energies, and a depth

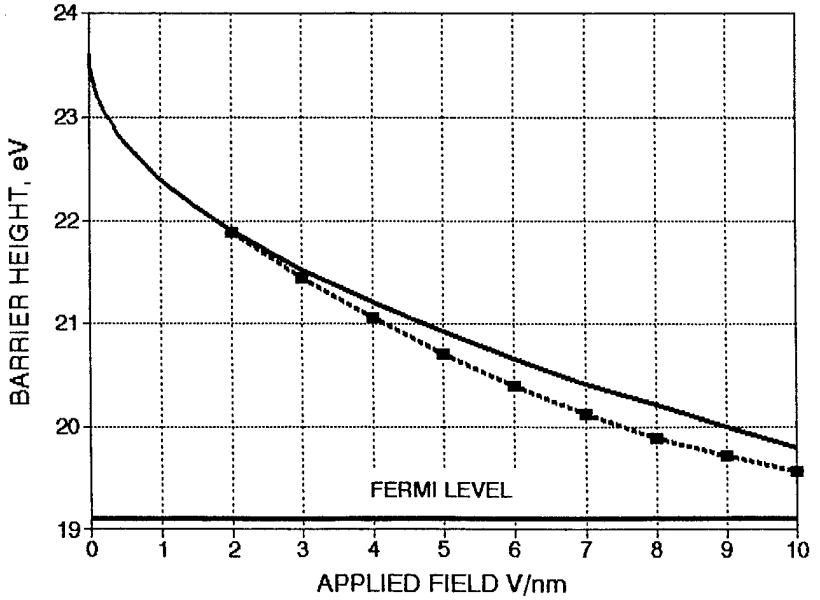


FIGURE 3. Barrier height at a tungsten surface as a function of the applied static field. Iterative solutions are shown as solid squares connected by a dashed curve, and the solid curve is for the Fowler–Nordheim model.

of 2 nm of metal. The results in Figure 3 appear to show that there is fairly good agreement between density-functional theory and the Fowler–Nordheim model. However, it may be seen in Figures 1 and 2 that while the maximum height of the barrier may be in good agreement for the two models, the peak is moved closer to the surface and the length of the tunneling region is increased with the Fowler–Nordheim model. Thus, we conclude that the value of the tunneling current would be underestimated with the Fowler–Nordheim model.

Steady-State Response of Field Emission to a Laser

We begin by replacing Eq. (1) with the dipole approximation [22] for the one-dimensional time-dependent Schrödinger equation for a static potential plus a radiation field:

$$\frac{-\hbar^2}{2m}\frac{\partial^2\Psi_I}{\partial x^2} + [V_0 + exE_0\cos(\omega t)]\Psi_I = i\hbar\frac{\partial\Psi_I}{\partial t}, \tag{5}$$

where the radiation is polarized in the axial direction, and the static potential V_0 and the magnitude of the electric vector of the optical field E_0 may be functions of x. Floquet's theorem [23] may be used to write the solution of Eq. (5) in the following form:

$$\Psi_I = \sum_{-\infty}^{\infty} \psi_{I,N}\exp[-i(\mathrm{E}_I + N\hbar\omega)t/\hbar], \tag{6}$$

where the $\psi_{I,N}$ are functions of x that must be determined. We have shown previously [6] that consistency of Eqs. (5) and (6) for arbitrary values of time requires that the following ordinary differential equation is satisfied:

$$\frac{-\hbar^2}{2m}\frac{d^2\psi_{I,N}}{dx^2} + [V_0 - E_I - N\hbar\omega]\psi_{I,N} + \tfrac{1}{2}[\psi_{I,N-1} + \psi_{I,N+1}]xE_0 = 0. \tag{7}$$

We have used several different methods [24] to solve Eq. (5). In the first procedure, which is the one used for the examples in this study, shooting methods [25] are used to solve the system of simultaneous ordinary differential equations resulting from Eq. (7). We require that each wave function $\psi_{I,N}$ is consistent with a single plane wave having the appropriate energy incident upon the barrier, but a full spectrum of energies is required for the reflected and transmitted waves. Recursion is used with finite difference approximations to march through the barrier, thus determining the wave function at the far side of the barrier as functions of the known incident wave and the unknown reflected waves at the near side. Consistency of the transmitted wave function with only outgoing transmitted waves is enforced which results in a numerical solution for the wave functions at all points in space. This is an extension of the numerically efficient method of back-propagation [20], which we use to solve the Schrödinger equation for static problems.

It is possible to replace Eq. (2) with a double summation over the indices I and N to determine the electron density as a function of position and time, and to replace Eq. (3) with an expression for the time-dependent scalar potential. However, it is not clear as to what should be used in place of Eq. (4) to determine the time-dependent exchange-correlation contribution to the effective potential. Several different formulations have been presented to extend the static density-functional theory to a time-dependent formulation [26–30], but we have not yet implemented any of them. In particular, we are concerned that the random phase approximation (RPA) may not be valid at optical frequencies. Others have used an adiabatic approximation [31, 32] in which they assume that the dynamic solution is equivalent to a sequence of static solutions that are obtained for various times during a cycle of the optical signal. The adiabatic approximation has been used to determine optical second harmonic generation with metals. However, we feel that it is difficult to justify this approach, except in the far infrared spectrum, because it neglects all effects of the exchange of photons with the optical source, a mechanism which is evident in Eqs. (6) and (7).

As a first approach to the time-dependent problem, we have simulated the steady-state response of field emission to a laser by assuming that the time-averaged response by the electrons is the same as for the static problem, and the effects of the time-dependent response are included in the motion of the plasma which causes screening of the radiation field. Dominance of the static response may be seen in that even with a laser power flux density of 10^{10} W/m^2, with a typical applied static field of 5 V/nm, the optical electric field is 0.055 percent of the static field. Thus, we

use density-functional theory to determine the effective potential considering only the static field, and then solve Eq. (5) allowing for the exponential decay of the optical field caused by screening within the metal. Others have used hydrodynamic models to simulate the interaction of an intense laser pulse with a metal, and they have used the Drude approximation to determine the frequency dependence of the complex conductivity in order to estimate the penetration of optical fields into the metal [33]. We also use the Drude model [34], and thus we assume that the depth into the metal at which the optical fields decay by $1/e$ is given by

$$\delta = \frac{1}{\sqrt{\varepsilon_0 \mu_0 \left(\omega_p^2 - \omega^2\right)}}, \tag{8}$$

where ω_p, the plasma frequency, corresponds to a wavelength of 54.3 nm for tungsten. For example, the depth of penetration in tungsten is 8.65, 8.66, and 10.3 nm at wavelengths of 10 μm, 1μm, and 100 nm, respectively. We have found that the results of our calculations are independent of the depth of metal that is descretized when this depth is 80 nm or greater, so a depth of 100 nm was used in each of the following examples which simulate the steady-state response of field emission to a laser.

Figure 4 shows the ratio of the tunneling current with a laser to that with no laser as a function of the optical wavelength for electrons with normal energies of 0.95, 0.96, 0.97, 0.98, 0.99, and 1.00 (from top to base of the figure) of the Fermi level. The calculations were made for a tungsten surface with an applied static field of 5 V/nm and a laser power flux density of 10^{10} W/m^2.

A resonance in which the current is significantly increased by the laser may be seen in each curve of Figure 4. The mechanism for this resonance is reinforcement of the wave function by reflections at the turning points. Thus, the resonance occurs for electrons that are promoted above the barrier by absorbing quanta from the optical field when the line integral of the momentum between the turning points is equal to $h/2$, where h is Planck's constant. It may be seen in Figure 3 that with an applied static field of 5 V/nm a single photon at 730 nm has sufficient energy to promote an electron at the Fermi level to an energy above the potential barrier. For the special case of a square barrier the resonance requires that the barrier length is an integral multiple of one-half the De Broglie wavelength for electrons that are promoted above the barrier by absorbing single photons [35]. This relation of the barrier length to the De Broglie wavelength is also the criterion for the transmission coefficient to be maximum for the static problem in which the energy of a particle is above a square barrier [36]. For square barriers we find

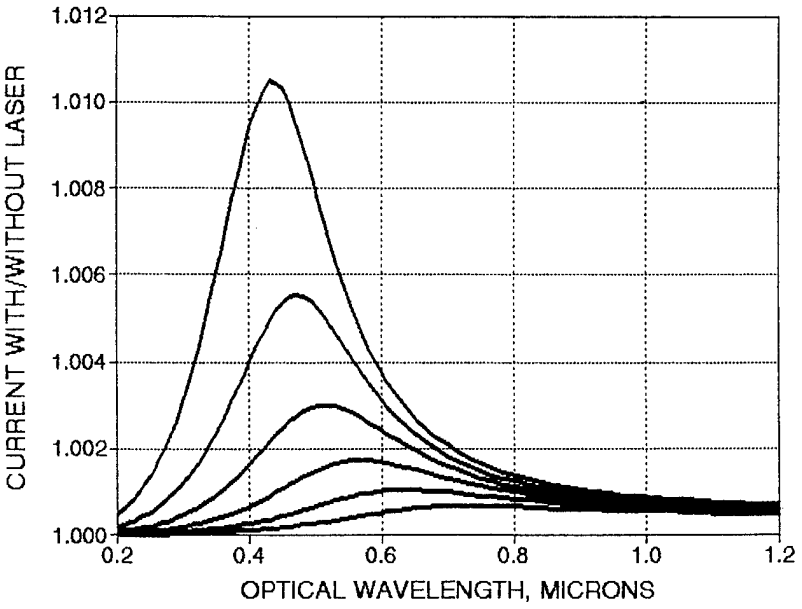


FIGURE 4. Current ratio with / without a laser vs. optical wavelength for electrons with normal energies of 0.95, 0.96, 0.97, 0.98, 0.99, and 1.00 (top to base) ε_F in tungsten with a static field of 5 V/nm and an optical flux of 10^{10} W/m^2.

that the resonance has multiple sharp peaks [35] instead of the single broad peak that is seen in each curve of Figure 5. These differences are consistent with results for the static problem [36] and are attributed to the decreased definition of the turning points when there are no discontinuities in the potential [37].

Figure 5 shows the ratio of the tunneling current with a laser to that with no laser as a function of the optical wavelength allowing for the full distribution of energies in the metal at temperatures of −273, 200, 1000, 1500, and 2000°C, for the curves from the top to the base of the figure, respectively. The calculations were made for a tungsten surface with an applied static field of 5 V/nm and a laser power flux density of 10^{10} W/m^2. The resonance is more prominent at lower temperatures, and this may be understood because of the more narrow distribution of energies. We have repeated the calculation for 200°C using the Fowler–Nordheim model for the potential barrier. The results are similar, but the static current density is reduced by 22%, and the resonance has a current enhancement of 0.227% at a wavelength of 337 nm instead of 0.242% at 416 nm. Each of these changes may be attributed to the somewhat greater length and height of the barrier with the Fowler–Nordheim model.

Figure 6 shows the ratio of the tunneling current with a laser to that with no laser as a function of the optical wavelength for a tungsten surface at 200°C with a laser power flux density of 10^{10} W/m^2. The value of the applied static field is 4.1, 4.3, 4.5, 4.7, 5.0, and 5.5 V/nm, for the curves from the top to the base of the figure, respectively. This figure shows that as the applied static field is reduced, the resonance shifts to a shorter wavelength, but there is also an increased response at longer wavelengths. We find that in the limit as the applied static field is reduced to values much less than 4.0 V/nm the behavior approaches that of the photoelectric effect, that is, a sharp all-to-nothing transition in the transmission occurs at a single wavelength. This may be understood because, for weak applied static fields, the height and length of the barrier are so large that the probability of tunneling is negligible so that transmission requires promotion above the barrier by the sustained absorption of a photon.

Discussion

Our results agree with experimental data from photofield studies in that the increase in the emitted current that is caused by a laser is proportional to the laser power flux density, maximum for polarization normal to the emitting metal surface, and from the electrons that absorb a single photon. However, it is generally assumed that the spectral

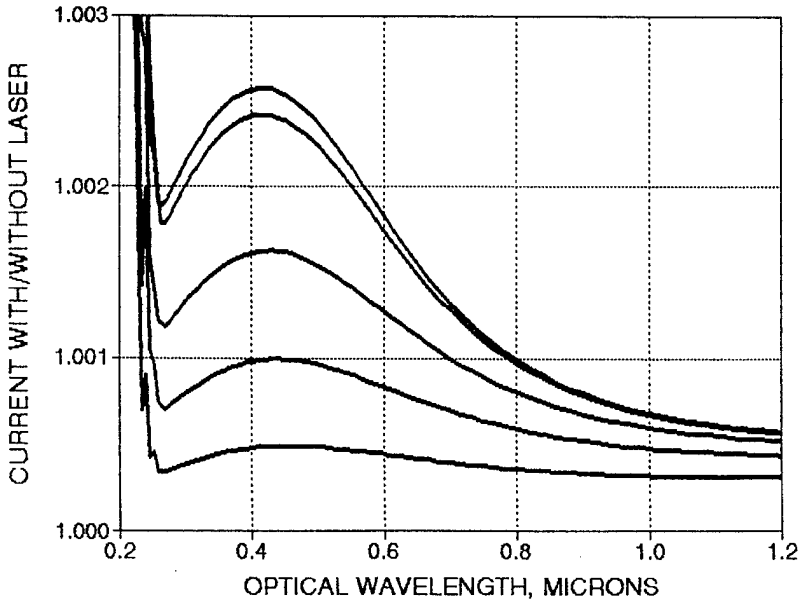


FIGURE 5. Current ratio with / without a laser vs. optical wavelength for tungsten at −273, 200, 1000, 1500, and 2000°C (top to base) with a static field of 5 V/nm and an optical flux of 10^{10} W/m^2.

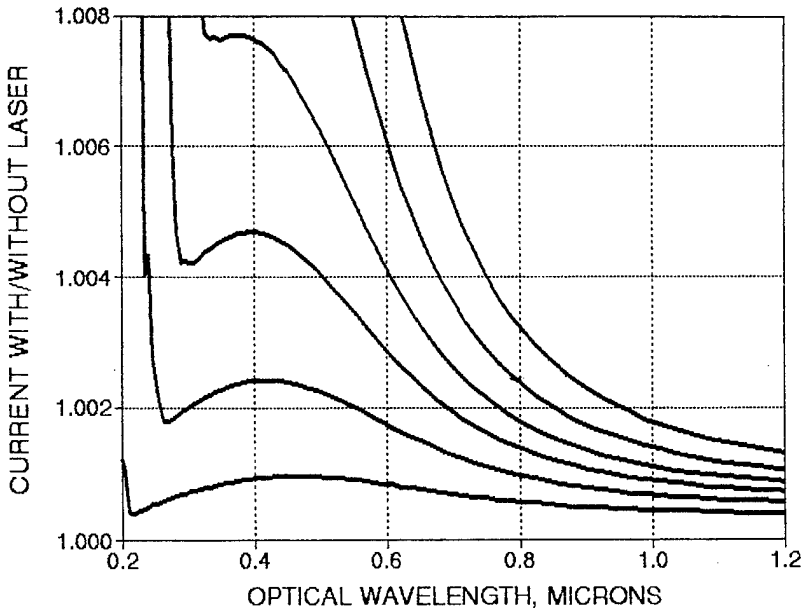


FIGURE 6. Current ratio with / without a laser vs. optical wavelength for tungsten at 200°C with static fields of 4.1, 4.3, 4.5, 4.7, 5.0, and 5.5 V/nm (top to base) and an optical flux of 10^{10} W/m^2.

response of photofield emission is rather simple; strongest for illumination near the blue end of the visible spectrum and virtually undetectable at longer wavelengths. By contrast, our simulations suggest that the spectral response is more complex, and that it is quite sensitive to the value of the applied static field. We believe that this difference may be caused by (1) the focus of photofield studies being on electron energy distributions rather than the spectral response, and (2) the presence of thermal effects in the data. Our results suggest that the nonthermal effects which we have simulated occur on a time scale on the order of 10 fs so that these effects could be separated from thermal effects by using lasers that are amplitude modulated at radio frequencies in photofield studies.

ACKNOWLEDGMENT

We acknowledge helpful suggestions by N. D. Lang, H. F. Gray, and J. L. Shaw.

References

1. S. Jaskólka, T. Radon, E. V. Chulkov, and O. S. Koroleva, Vacuum **46**, 449 (1995).
2. S. Mogren and R. Reifenberger, Surf. Sci. **254**, 169 (1991).
3. M. J. G. Lee and E. S. Robins, J. Appl. Phys. **65**, 1699 (1989).
4. M. Y. Sumetskii, Sov. Tech. Phys. Lett. **11**, 448 (1985).
5. N. M. Miskovsky, S. H. Park, P. H. Cutler, and T. E. Sullivan, J. Vac. Sci. Technol. B **12**, 2148 (1994).
6. M. J. Hagmann, J. Vac. Sci. Technol. B **13**, 1348 (1995).
7. C. Caroli, D. Lederer-Rozenblatt, B. Roulet, and D. Saint-James, Phys. Rev. B **10**, 861 (1974).
8. A. Levy Yeyati and F. Flores, J. Phys.: Condens. Matter **4**, 7341 (1992).
9. L. V. Keldysh, Sov. Phys. JETP **20**, 1018 (1965).
10. N. D. Lang, in *Solid State Physics*, Vol. 28, H. Ehrenreich, F. Seitz and D. Turnbull, Eds. (Academic Press, New York, 1973), pp. 225–300.
11. V. Sahni, in *Topics in Current Chemistry*, Vol. 181, R. F. Nalewajski, Ed. (Springer, Berlin, 1996), pp. 1–39.
12. P. Hohenberg and W. Kohn, Phys. Rev. B **136**, 864 (1964).
13. W. Kohn and L. J. Sham, Phys. Rev. A **140**, 1133 (1965).
14. J. P. Perdew and A. Zunger, Phys. Rev. B **23**, 5048 (1981).
15. S. H. Vosko, L. Wilk, and M. Nusair, Can. J. Physics **58**, 1200 (1980).
16. M. Gell-Mann and K. A. Brueckner, Phys. Rev. **106**, 364 (1957).
17. V. Sahni, in *Recent Advances in Density Functional Methods, Part I*, D. P. Chong, Ed. (World Scientific, Singapore, 1995), pp. 79–128.
18. R. H. Fowler and L. Nordheim, Proc. R. Soc. London, A **119**, 173 (1928); L. Nordheim, Proc. R. Soc. London, A **121**, 626 (1928).
19. P. G. Dzhavakhidze, A. A. Kornyshev, and G. I. Tsitsuashvili, Solid State Commun. **52**, 401 (1984).
20. T. M. Kalotas and A. R. Lee, Am. J. Phys. **59**, 48 (1991).
21. A. Modinos, *Field, Thermionic, and Secondary Electron Emission Spectroscopy* (Plenum, New York, 1984), pp. 1–9.
22. F. H. M. Faisal, *Theory of Multiphoton Processes* (Plenum, New York, 1987), pp. 8–10.

23. A. Pimpale, S. Holloway, and R. J. Smith, J. Phys. A **24**, 3533 (1991).
24. M. J. Hagmann, Int. J. Quant. Chem. **56**, Quant. Symp. Issue No. 29, 289 (1995).
25. H. B. Keller, *Numerical Methods for Two-Point Boundary-Value Problems* (Dover, New York, 1992), pp. 39–71.
26. A. Liebsch and W. L. Schaich, Phys. Rev. B **40**, 5401 (1989).
27. A. Zangwill and P. Soven, Phys. Rev. A **21**, 1561 (1980).
28. M. J. Stott and E. Zaremba, Phys. Rev. A **21**, 12 (1980).
29. G. D. Mahan, Phys. Rev. A **22**, 1780 (1980).
30. E. K. U. Gross, J. F. Dobson, and M. Petersilka, in *Topics in Current Chemistry*, Vol. 181, R. F. Nalewajski, Ed. (Springer, Berlin, 1996), pp. 81–172.
31. G. Nagy and D. Roy, Surf. Sci. **320**, 7 (1994).
32. P. G. Dzhavakhidze, A. A. Kornyshev, A. Liebsch, and M. Urbakh, Phys. Rev. B **45**, 9339 (1992).
33. A. Ng, P. Celliers, A. Forsman, R. M. More, Y. T. Lee, F. Perrot, M. W. C. Dharma-wardana, and G. A. Rinker, Phys. Rev. Lett. **72**, 3351 (1994).
34. N. W. Ashcroft and N. D. Mermin, *Solid State Physics* (W. B. Saunders, Philadelphia, 1976), pp. 2–27.
35. M. J. Hagmann, J. Appl. Phys. **78**, 25 (1995).
36. L. I. Schiff, *Quantum Mechanics* (McGraw-Hill, New York, 3rd ed., 1968), pp. 101–104.
37. C. W. Leming and A. Van Smith, Am. J. Phys. **59**, 441 (1991).

Theoretical Calculation of Carbon Clusters

ESTHER AGACINO VALDES,[1] PABLO DE LA MORA,[2] MIGUEL CASTRO,[3] JAIME KELLER[1]

[1]*Centro de Investigaciones Teoricas, Facultad de Estudios Superiores Cuautitlan, U.N.A.M., Cuautitlan Izcalli 54740, Edo. México, México*
[2]*Dpto. de Física, Facultad de Ciencias, U.N.A.M., Ciudad Universitaria 04510, México D.F.*
[3]*Facultad de Química, U.N.A.M., Ciudad Universitaria 04510, México D.F.*

Received 2 March 1997; revised 3 July 1997; accepted 22 July 1997

ABSTRACT: Structural parameters and energy have been calculated for C_{1-3} and C_9 clusters using density functional theory through the deMon program. The C_{1-3} clusters were fully optimized using deMon; different basis sets were tested in order to choose the suitable one to be used in the C_9 clusters. In the case of C_2 the results were compared with experimental values. DZVP2 basis was selected because it always gave the closest value to the experimental data. The C_9 carbon clusters were designed in relation to C(100) diamond surface. The energies of the nonrelaxed and relaxed surfaces with and without hydrogen were calculated. In the same way CH_3-relaxed and CH_2-relaxed species were calculated. The diamond growth mechanism proposed in the literature was evaluated by an energy analysis. The C—CH_3 distance is reported. © 1997 John Wiley & Sons, Inc. Int J Quant Chem **65**: 867–875, 1997

Introduction

Diamond surface has attracted a lot of attention because of the technological applications in thin films grown by chemical vapor deposition (CVD) techniques [1]. Many experimental and theoretical studies have been made over the last decades. Nowadays several ideas have been suggested about the characteristics of the diamond surface, the mechanism of diamond growth and the precursor agent of this chemisorption process.

Correspondence to: E. Agacino Valdes.

Although the first theoretical studies of diamond surfaces focussed in (111) surface, at the present, it is known that the (100) face is prevalent in diamond growth under conventional CVD conditions [2]. This orientation has the lowest density defect, making it more appropriate for electronic applications.

Density functional theory (DFT) will be applied to the study of the energies involved in the relaxation and chemisorption process of C(100) diamond surface to grow thin film; to do this, C_9 carbon clusters resembling the C(100) diamond surface will be used. Before, small carbon clusters C_{1-3} were calculated using different basis sets in

© 1997 John Wiley & Sons, Inc.
CCC 0020-7608 / 97 / 050867-09

order to select an adequate one to be used in C_9 carbon clusters.

Method and Methodology

In this work, the code deMon based in density functional theory was used. This program implements the linear combinations of Gaussian-type orbitals (LCGTO-DF) [3]. These methods have been described extensively. The calculations were made in local spin density approximation (LSDA).

The geometries of the $C_{1\text{-}3}$ clusters and C_9 (non-relaxed hydrogenated, relaxed, and relaxed hydrogenated) were fully optimized by deMon, but in other C_9-carbon clusters only the adsorbed species (CH_3 and CH_2) were optimized. The starting geometry for the surface cluster was taken from other calculations involving surface models [4] and therefore it was kept frozen.

For the small carbon clusters ($C_{1\text{-}2}$), four basis sets were tested: STO-3G(33/3), DZVP(621/41/1*), DZVP2(721/51/1*), and TZVP(7111/411/1*). The results of the C_2 cluster were compared with experimental and theoretical data. The basis set which produced the best compromise between bond energy and bond distance was chosen as suitable to be used in C_9 carbon clusters.

C ATOM

It is known that a carbon atom has a $(2s^2 2p^2)$ ^3P ground state with two unpaired electrons. The excited state $(2s^1 2p^3)$ is ^5S, with four unpaired electrons which explain the tetravalency of this element and all the chemistry of the hydrocarbons.

Table I shows the calculated total energy of the singlet and triplet states. Notice that, in agreement with the experimental evidence, the triplet state is the most stable species, but the computed difference between singlet and triplet states is only about 5×10^{-2} for all the basis considered. It is a very low value compared with experimental one. The DZVP2 basis together with TZVP and DZVP gave the closest energy value in relation to the experiments.

C_2 MOLECULE

Dicarbon molecule has eight valence electrons, and the molecular orbital theory establishes a $KK(\sigma_g 2s)^2(\sigma_u^* 2s)^2(\pi_u 2p)^4$ electronic configuration

TABLE I
Total energies for a carbon atom.

	E_T (hartrees)	
Basis set	Singlet	Triplet
STO-3G	−36.89954	−36.95530
DZVP	−37.41906	−37.46365
DZVP2	−37.42278	−37.46727
TZVP	—	−37.46729
[5]	—	−37.68
[6]	—	−37.6886

which corresponds to a $^1\Sigma_g^+$ ground state. A $(\pi_u 2p)^3(\sigma_g 2p)^1$ external electronic configuration is the $^3\Pi_u$ excited state. The spectrum of this molecule has been extensively studied and at the beginning it was found that the Mulliken bands (which arise from the $^1\Sigma_g^+$ lower state) appeared at comparable intensity with the Swan bands (which arise from the $^3\Pi_u$ lower state). These results raise the question about which state is the ground state [7]. Today, Ballik and Ramsay's [8] observations have fixed $^1\Sigma_g^+$ at 0.075 eV below $^3\Pi_u$, and $^1\Sigma_g^+$ is the ground state for only a small margin.

Fougere and Nesbet [9] have studied the electronic structure of this molecule over the range $R_e = 1.5a_0$ to $8.0a_0$ using different Slater-type orbitals basis sets and two different levels of configuration interaction. The best calculations obtained by Fougere and Nesbet were 1.2855 Å and 6.76 eV for the $^1\Sigma_g^+$ state; for the triplet state the best bond energy result (5.45 eV) was not the best equilibrium distance (1.3937 Å) because another calculation gave 4.00 eV and 1.3261 Å, respectively. As it can be seen, the $^1\Sigma_g^+$ state is predicted as the ground state. At the present 6.25 ± 0.2 eV [10] and 6.12 eV [11] are recognized as the best experimental values of C_2 bond energies.

Tables II and III show the total energies and the bond lengths computed for the triplet and the singlet state and the experimental results cited above. Other calculations are also tabulated.

It is important to notice that the total energies calculated in both two states $^1\Sigma_g^+$ and $^3\Pi_u$ are very close; this is the reason for which the determination of the ground state has been controversial [12].

The DZVP2 basis gives the best bond energy in comparison to experimental and theoretical results. For the bond length the DZVP2 basis is not the best, in this case TZVP basis is better, but since the differences in bond lengths are of the order of

TABLE II
Total energies for a $^1\Sigma_g^+$ state in dicarbon molecule.

Basis set	E_T (hartrees)	r_0 (Å)	D_0 (eV)
STO-3G	−74.21381	1.2637	8.25
DZVP	−75.18474	1.2734	7.01
DZVP2	75.18873	1.2786	6.92
TZVP	75.19739	1.2518	7.15
[9]	—	1.2855	6.76
[10]	—	1.243	6.25 ± 0.2
[11]	—	1.242	6.12
[13]	—	1.2422	6.36
[14]	75.531	1.252	6.24

2%, this parameter is not as important as the energy, and DZVP2 basis is the most suitable to be used. These results are in agreement with considerations about a best description C_2 ground state must use a large configuration mixing in its ground state, therefore, the results can be improved using an extended basis [15].

C_3 MOLECULE

The C_3 molecule is just barely linear as is indicated by its very small bending frequency (63 cm^{-1}). Although Douglas [16] has established that C_3 is linear, others say that this molecule might be slightly nonlinear [17]. Liskow et al. [18] have made self-consistent field (SCF) and configuration mixing calculations and found that a reasonably large basis set, including *d* functions, is necessary to account the small bending frequency, but the configuration mixing procedure is not needed; they computed the orbital energies as a function of the angle at ~ 1.27 Å of distance and found that the larger basis predicts C_3 to be linear, in agreement the experiment. Perić Radić [19] also studied the ground state and the first two excited states of C_3 which are experimentally known; they used a

TABLE III
Total energies for a $^3\Pi_u$ state in dicarbon molecule.

Basis set	E_T (hartrees)	r_0 (Å)	D_0 (eV)
STO-3G	−74.21701	1.3371	8.34
DZVP	−75.20247	1.3197	7.49
DZVP2	75.20554	1.3235	7.37
TZVP	75.21277	1.3081	7.57
[9]	—	1.3937	5.45
[10]	—	—	6.17
[14]	75.551	1.318	6.16

TABLE IV
Total energies for a lineal tricarbon molecule.

Basis set	E_T (hartrees)	r_0 (Å)	D_0 (eV)
STO-3G	−111.51367	1.334	17.67
DZVP	−112.98469	1.309	16.19
DZVP2	−112.98888	1.3132	16.01
TZVP	−113.00586	1.2962	16.47
[18]	−113.38082	1.328	—
[20]	—	—	13.97

multiconfiguration SCF, plus extensive configuration mixing calculation and their results were in agreement with experiment. Both authors found the $^1\Sigma_g^+$ state is the ground state.

Different geometrical possibilities were calculated for the singlet and triplet state: linear, nonlinear, and a triangle (cycle). These last two geometries, when fully optimized transform to the linear geometry. Table IV presents these results. The singlet was always the predicted ground state. The $^1\Sigma_g^+$ state is the ground state, in agreement with the experimental evidences. As in the case of the dicarbon molecule, DZVP2 was the best in bond energies, but for the bond length TZVP gave the best result.

Since the bond distance differences are small, but not the energy differences, the DZVP2 basis, which gave the bond energy closest to the experimental data, was used to model the C_9 carbon clusters.

C_9 CARBON CLUSTERS

Figure 1(a) shows a *bcc* unit cell (a = 3.567 Å) of diamond; notice that the C(100) surface has successive parallel chains in (110) direction. When the surface is formed, the lack of saturation of the surface carbons induce a relaxation process. Hamza et al. [21] found that raising the temperature to 1300 K, C(100) surface produces a LEED pattern made up of two domains with 2×1 symmetry; forming a π symmetric dimer bond between two surface carbon atoms of two consecutive chains [Figure 1(b)] [22]. Atomic force microscopy (AFM) [23] and scanning tunneling microscopy [4] has also evidenced the C(100) 2×1 surface reconstruction. It is the most accepted geometry, at least in experimental conditions of diamond growth.

The structure of a hydrogenated surface has been under discussion for many years; the mono-

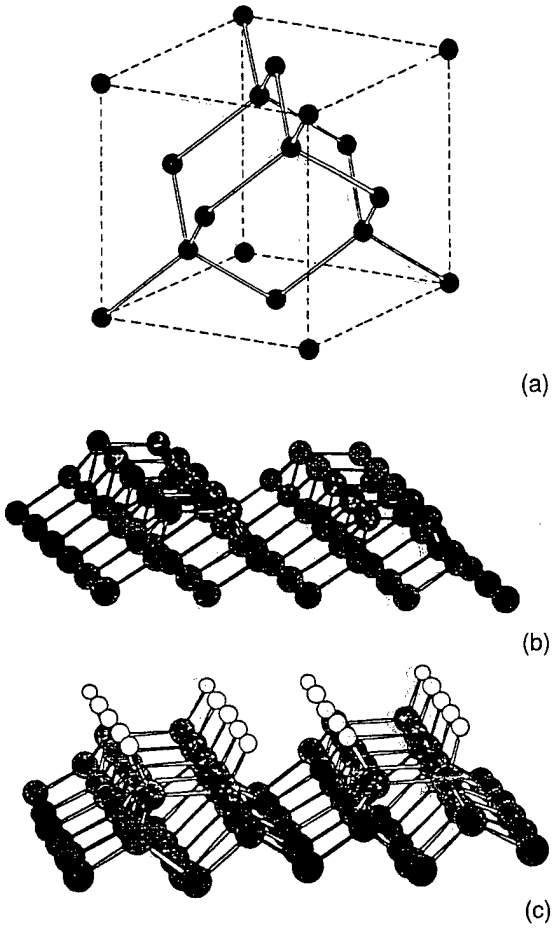


FIGURE 1. (a) Unitary cell of diamond (Ref. [1]); (b) relaxed surface C(100) 2 × 1; (c) monohydrogenated surface diamond C(100) 2 × 1.

hydrogenated, dihydrogenated, and alternating structures have been evaluated to establish the most stable one. Thomas et al. [24] report that atomic hydrogen doses do not remove the 2 × 1 LEED pattern even after doses equivalent to 100 monolayers of hydrogen. Using HREELS and LEED techniques, Thomas et al. [24] reported the monohydrogenated dimer row surface as the most stable. No evidence was observed for other species even after a large atomic hydrogen exposure.

The symmetric dimer with monohydride termination [Figure 1(c)] is the most likely structure. Therefore, the dihydrogen and alternating configurations were not considered. This is consistent with theoretical calculations [25].

Several authors have used the cluster approach to study the chemisorption process involved in C(100) diamond growth. It is based in the generally accepted idea that the chemisorption process is a localized phenomenon of orbital interaction. C_9 is the best carbon cluster for studying the reconstructed C(100) diamond surface.

One of the first C_9 carbon cluster calculations was made by Verwoerd [26]. He studied the reconstruction of both the clean Si(100) and C(100) surfaces and the process of hydrogen chemisorption onto these two surfaces by a semiempirical method and using a C_9 carbon cluster [27]. Starting from the ideal parameters, Verwoerd made a whole optimization using a semiempirical MNDO method. For clean and monohydrogenated reconstructed C(100) surfaces, he predicted a symmetric dimer; the C–C distances calculated for these dimers were 1.43 and 1.67 Å, respectively. The dihydride structure was predicted as unstable (C–C distance in the dimer of 0.74 Å), because of the repulsive interaction between the electron densities of the two hydrogens. Taking a C_9 carbon cluster model similar to Verwoerd's, we calculated the relaxed and nonrelaxed surfaces, with and without chemisorbed hydrogens and with CH_2 and CH_3 adsorbed. Verwoerd reported 3.09 eV for relaxation energy and 4.39 eV for binding energy of hydrogen. Mehandru and Anderson [25b] obtained 2.52 and 4.39 eV, respectively. They use semiempirical methods, but Mehandru and Anderson use a cluster larger than Verwoerd.

An interesting work that combined STM images and theoretical calculations of molecular dynamics in a semiempirical DFT was made by Frauenheim et al. [4]. They used a supercell of 126 carbon atoms for C(001) surface and reported a symmetric dimer with a distance of 1.41 Å for a clean surface and 1.50 Å for a monohydrogenated surface. Other details of the structural parameters of Frauenheim et al. [4] are presented in Table V. We took their relaxed structural parameters.

TABLE V
Relaxed structural parameters of C_9 carbon clusters (Ref. [4]).

Surf. struct.	Bond lengths (Å)	Bond angles (deg)
C(100) 2 × 1	(1-1) 1.41	1-1-2 = 109
	(1-2) 1.50	2-1-2 = 113.7
C(100) 2 × 1:H	(1-2) 1.07	1-2-2 = 112
	(2-2) 1.58	1-2-3 = 113
		2-2-3 = 104

The C_9 carbon cluster was constructed considering two consecutive diagonal chains [see the *bcc* unitary cell in Figure 1(a)], with two more layers below. The dimensions of the cluster correspond to the diagonal (2.5223 Å) in the *bcc* unit cell. As in the unit cell, the cluster has four layers with an interlayer spacing which is 1/4 of the lattice constant of the *bcc* cell. Table VI presents the Cartesian coordinates of the nonrelaxed C_9 carbon cluster taken from the *bcc* cell parameters [Fig. 2(a)]; Figures 2(b) and 2(c) present the corresponding relaxed and relaxed hydrogenated structures using Table V parameters as the starting point.

In order to saturate the valencies of the nonsurface carbons, 12 virtual hydrogens have been used;

TABLE VI
Cartesian coordinates of the nonrelaxed C_9-carbon clusters.

Atom	X	Y	Z
C_1	0.0000	0.0000	0.0000
C_2	1.2612	0.0000	0.8918
C_3	2.5223	0.0000	0.0000
C_4	0.0000	2.5223	0.0000
C_5	1.2612	2.5223	0.8918
C_6	2.5223	2.5223	0.0000
C_7	0.0000	1.2612	−0.8918
C_8	1.2612	1.2612	−1.7835
C_9	2.5223	1.2612	−0.8918

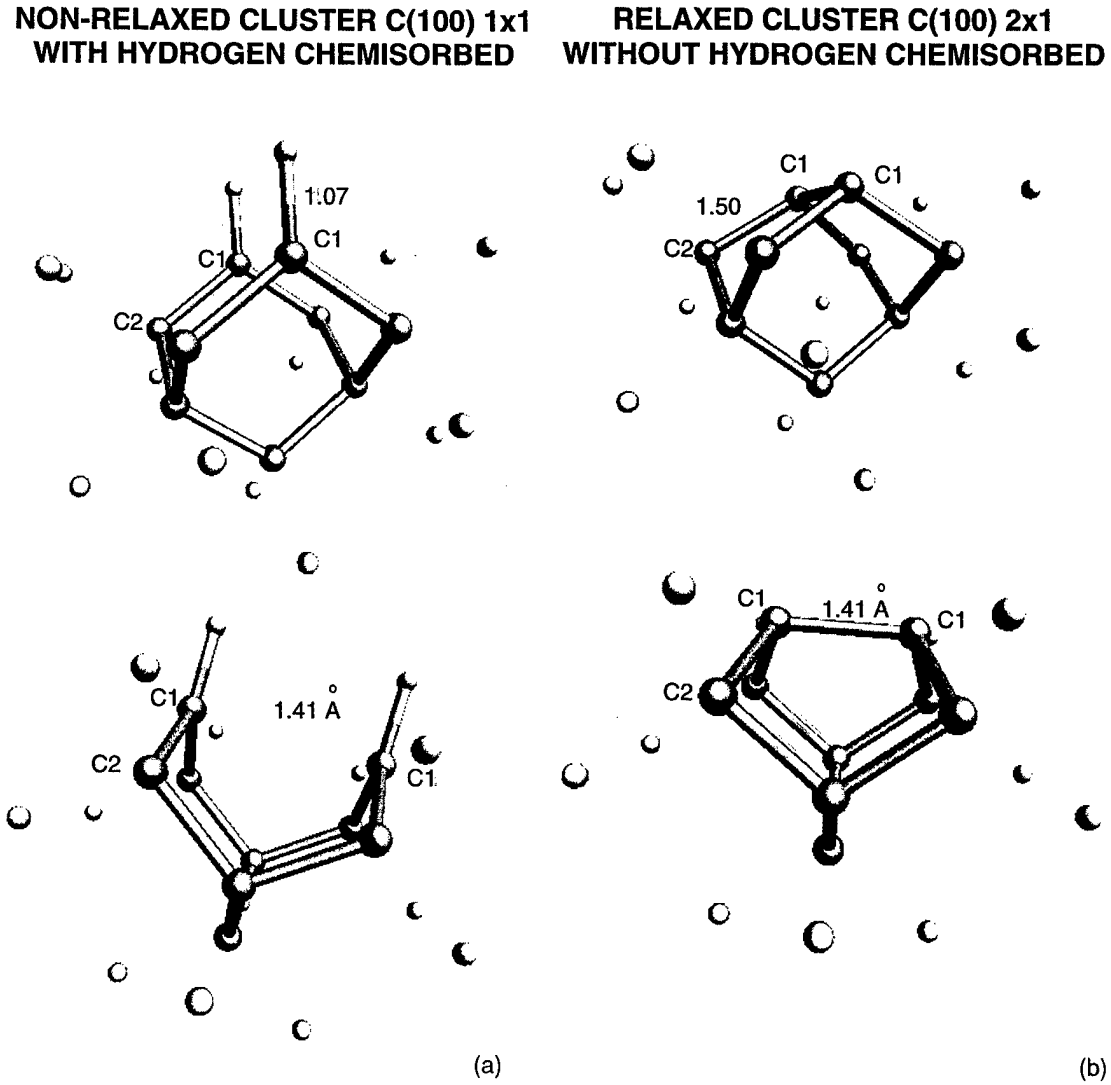


FIGURE 2. Geometrical structure of carbon clusters: (a) hydrogen nonrelaxed; (b) relaxed; and (c) relaxed monohydrogenated.

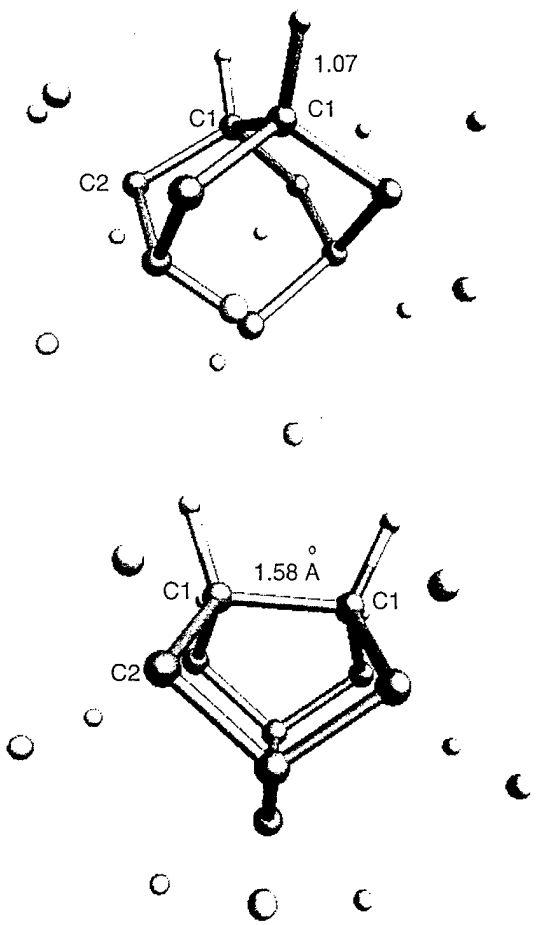


FIGURE 2. (continued)

Table VII shows the total energies computed for nonrelaxed hydrogen, relaxed, and relaxed monohydrogenated C_9 carbon cluster and the energies involved in the relaxation and hydrogen chemisorption process.

The experimental results are qualitatively reproduced. The relaxation process produces a stabilization of the cluster, but notice that the presence of hydrogen stabilizes it too much. The computed relaxation energy is smaller than that calculated by Verwoerd [26] and Mehandru-Andersen [25b].

Methyl Adsorption and Growth of the First Layer of Diamond

Because of the unique properties of diamond, great efforts have been put into the synthesis of this material to be used in advanced materials applications. The first attempt to obtain diamond was in 1955, but the process required high pressures and temperatures. After 1955 a great number of investigators began to explore the possibility of synthesizing diamond at low pressure and temperature, that is, in the region of its metastability. The chemical vapor deposition (CVD) technique of diamond films was a reality in 1958, but the growth rates were very slow and graphitic carbon was deposited simultaneously; hydrogen was necessary to remove the graphitic phase.

In 1975, Deryagin's group [28] reported the use of a gas activation technique which resulted in dramatic increases in diamond growth rates, while eliminating much of the graphitic deposition. Starting in the 1980s many reports were published of successful diamond growth in low pressure using new gas activation techniques.

It is now well established that diamond can be deposited at low pressures (from 1 to 10^{-2} atm.) and temperatures between 700 and 1000° C using the CVD technique. In this technique, a mixture of methane and ~ 98% of hydrogen is activated by passing it through a plasma or a hot filament; this process produces atomic hydrogen and carbon radicals, and the deposition of these species over the diamond surface produces the growth of diamond and graphitic phases. A highly preferential etching of the graphitic phases is produced by atomic hydrogen [1].

Although different small hydrocarbon fragments have been analyzed as possible precursor species in diamond growth, at present it is ac-

TABLE VII
Total energies for the nonrelaxed and the relaxed cluster, with and without hydrogen.

C_9 cluster	Nonrelaxed + 2H	Relaxed	Relaxed + 2H
E_{total} (hartrees)	−348.10161	−346.95654	−348.23939
$E_{relax.}$ (eV) $= E_{(relaxed+2H)} - (E_{nonrelaxed+2H})$		−3.75	
$E_{quims.\,(H)}$ (eV) $= 1/2E_{(relaxed+2H)} - E_{(relaxed)}$		−4.49	

cepted that CH_3 is the dominant growth species [29].

Mehandru and Anderson [25b] calculated CH_2 and CH_3 energy barriers in the presence of the hydrogen vacancies on the monohydrogenated surface and reported for CH_2 and CH_3, a C–CH_2 and C–CH_3 of 1.48 and 1.59, respectively; the corresponding binding energies are 4.38 and 3.38 eV in the most stable sites. We have calculated the energy of C_9–H, CH_3, C_9–H, CH_2^*, and C_9–2H, CH_2 using the deMon program.

Five steps in the growth mechanism were considered as suggested by Garrison et al. [30]: (1) A hydrogen leaves the surface and a radical site is formed. (2) The methyl radical is adsorbed over a radical site. (3) A second hydrogen belonging to methyl radical leaves the surface and a methylen radical is formed. (4) The dimer bond is broken by a methylene group; a methyliden group and a radical site are formed. (5) A methyliden group attacks the radical site and a bridge-methylene structure is formed. A new layer of diamond has been produced and the hydrogens of the methylene group can be substituted for new methyl radicals that arrive to the surface.

The calculated energies confirm that, in the mechanism suggested by Garrison et al. [30], step 3 is an activated process that produces an intermediate radical state. Table VIII presents the results and Figure 3 presents a scheme of this process. Another interesting point in the mechanism is step 4. The problem is whether the methylen group will attack the dimer bond or will displace the top hydrogen. In order to choose between these two possibilities, an electrostatic potential calculation was made for the C_9–H, CH_2 structure. Figure 4 presents the electrostatic potential curves in the plane bisecting the dimer for this structure.

TABLE VIII

Total energies for the relaxed cluster with methyl and methylene species adsorbed and energy changes involved in the steps of the mechanism.

	C_9–H, CH_3	C_9–H, CH_2
E_{total} (hartrees)	−386.51	−385.54
$dC_{surf} - C_{ads}$ (Å)	1.53	—

Steps	ΔE / eV
Step 1	+0.01
Step 2	+0.5
Step 3	−0.69
Step 4	−0.002
Step 5	+0.89

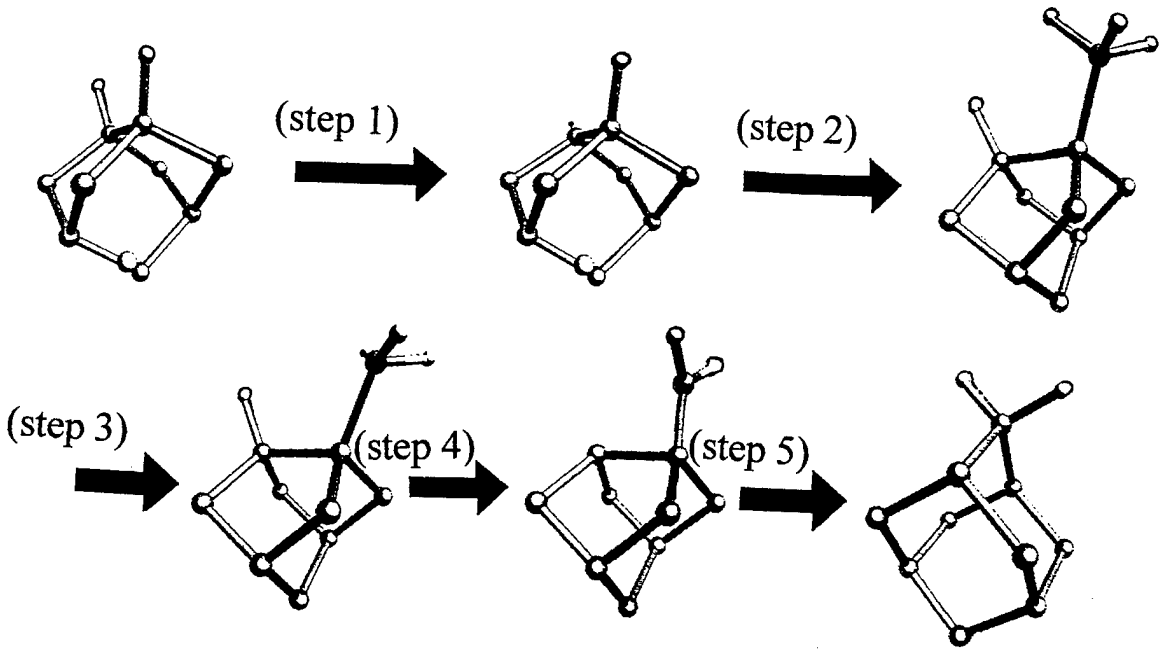


FIGURE 3. Steps 1 and 2 of the reaction mechanism.

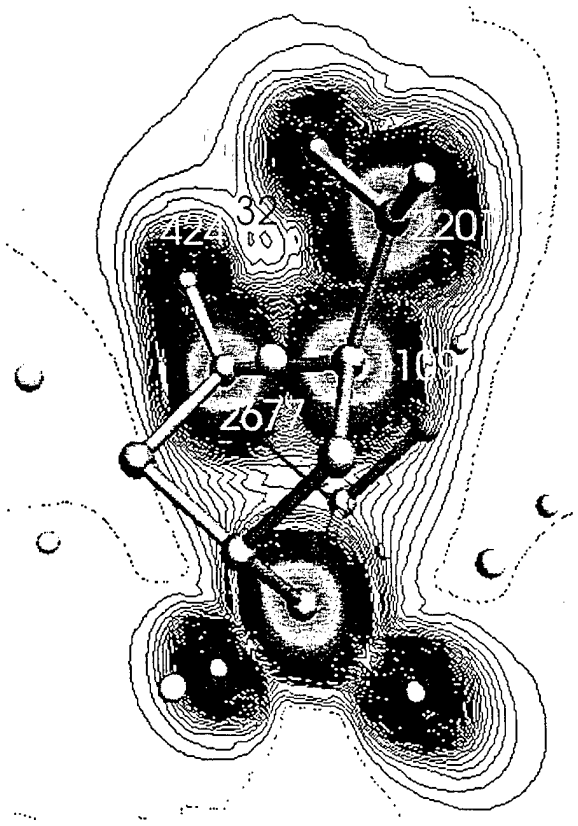


FIGURE 4. Electrostatic potential curves in the plane bisecting the C_9–H, CH_2 cluster.

The electrostatic potential curves predict that the methylen group look for interaction with the dimer rather than for the top hydrogen. Then, step 4 is potentially possible: The methylen group breaks the dimer bond and it does not displace the top hydrogen.

Conclusions

A full optimization of C_9 cluster predicts the relaxation of the C(100) surface as the most stable and confirm the important role of Hydrogen in the stabilization of this surface.

The energy involved in the step 2 is negative and the intermediate C_9–H, CH_2 has a barrier energy of 34.08 eV. The electrostatic potential shown the step 4 is potentially possible. In order to improve the results quantitatively, a partial optimization of clusters larger than C_9 are being calculated.

ACKNOWLEDGMENTS

We thank Prof. Dennis Salahub for allowing us to use the KS-deMon code. Support from projects DGAPA-UNAM (IN-101295, SC-007096, SC-007697), and CONACYT (4880-E) is gratefully acknowledged. This work was done using the Cray YMP4/464 at UNAM.

References

1. K. E. Spear, J. Am. Chem. Soc. **72**, 171 (1989).
2. T. Tsuno, T. Imai, Y. Nishibayashi, K. Hamada, and N. Fujimori, Jpn. J. Appl. Phys. **30**, 1063 (1991).
3. R. G. Parr and W. Yang, *Density Functional Theory of Atoms and Molecules* (Oxford Univ. Press, Oxford, 1989); D. R. Sahalub, Adv. Chem. Phys. **69**, 447 (1987); A. St. Amant and D. R. Sahalub, Chem. Phys. Lett. **169**, 387 (1990); D. R. Sahalub, R. Fournier, P. Mlynarski, I. Papai, A. St. Amant, and J. Ushio, *Theory and Applications of Density Functional Approaches in Chemistry*, J. Labanowsky and J. Andzelm, Eds. (Springer, New York, 1991), p. 77.
4. Th. Frauenheim, V. Stephen, P. Blaudeck, D. Porezag, H.-G. Busmann, W. Zimmermann-Edling, and S. Lauer, Phys. Rev. **B48**, 18189 (1993).
5. R. K. Nesbet, J. Chem. Phys. **40**, 3619 (1964).
6. J. S. Sims and S. Hagstrom, Phys. Rev. **A4**, 908 (1971).
7. R. G. W. Norrish, G. Porter, and B. A. Thrush, Nature, **169**, 582 (1952).
8. E. A. Ballik and D. A. Ramsay, J. Chem. Phys. **29**, 1418 (1958); E. A. Ballik and D. A. Ramsay, J. Chem. Phys. **31**, 1128 (1959).
9. P. F. Fouguere and R. K. Nesbet, J. Chem. Phys. **44**, 285 (1966).
10. L. Brewer, W. T. Hicks, and O. H. Krikoin, J. Chem. Phys. **36**, 182 (1962).
11. J. Drowart, R. P. Burns, G. DeMaría, and M. G. Inghram, J. Chem. Phys. **31**, 1131 (1959).
12. G. Herzberg, *Molecular Spectra and Molecular Structure*, Vol. IV, 2nd ed. (VNB, New York, 1950).
13. S. M. Read and J. T. Vanderslice, J. Chem. Phys. **36**, 2366 (1962); E. A. Ballik and D. A. Ramsay, Astrophys. J. **137**, 1127 (1963).
14. G. Verhaegen, J. Chem. Phys. **49**, 4696 (1968).
15. R. S. Mulliken and W. C. Ermler, Diatomic Molecules (Academic, New York, 1977), pp. 138–162.
16. A. E. Douglas, Astrophys. J. **114**, 466 (1951).
17. L. Gausset, G. Herzberg, A. Laigerqvist, and A. Rosen, Discuss. Faraday Soc. **35**, 113 (1963); Astrophys. J. **142**, 45 (1965).
18. D. H. Liskow, Ch. F. Bender, and H. F. Schaefer, J. Chem. Phys. **56**, 5075 (1972).
19. J. Perić Radić, J. Römelt, S. D. Peyerimhoff, and R. J. Buenker, Chem. Phys. Lett. **50**, 344 (1977).
20. J. Kordis and K. A. Gingerich, J. Chem. Phys. **58**, 5058 (1972).

21. A. V. Hamza, G. D. Kubiak, and R. H. Stulen, Surf. Sci. **227**, 35 (1990); P. G. Lurie and J. M. Wilso, Surf. Sci. **65**, 453 (1977).

22. H. Kawarada, Surf. Sci. Reports, **26**, 205 (1996).

23. L. F. Sutcu, C. J. Chu, M. S. Thomson, R. H. Hauge, J. L. Margrave, and M. P. D'Evelyn, Appl. Phys. Lett. **71**, 5930 (1992); L. F. Sutcu, M. S. Thomson, C. J. Chu, R. H. Hauge, and J. L. Margrave, Appl. Phys. Lett. **60**, 1685 (1992).

24. R. E. Thomas, R. A. Rudder, and R. J. Markunas, J. Vac. Sci., Tech. **A10**, 2451 (1992).

25. (a) Y. L. Yang and M. P. D'Evelyn, J. Am. Chem. Soc. **114**, 2796 (1992); Y. L. Yang and M. P. D'Evelyn, J. Vac. Sci. Tech. **A10**, 978 (1992); (b) S. P. Mehandru and A. B. Anderson, Surf. Sci., **248**, 369 (1991); (c) Z. Jing and J. L. Whitten, Surf. Sci. **314**, 300 (1994).

26. W. S. Verwoerd, Surf. Sci. **103**, 404 (1981).

27. W. S. Verwoerd, Surf. Sci. **108**, 153 (1981).

28. B. V. Derjaguin and D. B. Fedoseev, Sci. Am. **233**, 102 (1975).

29. L. R. Martin and M. W. Hill, Appl. Phys. Lett. **55**, 2248 (1989).

30. B. G. Garrison, E. J. Dawnkaski, D. Srivastava, and D. W. Brenner, Science **255**, 835 (1992).

Spin-Averaged Hartree–Fock Procedure for Spectroscopic Calculations: The Absorption Spectrum of Mn^{2+} in ZnS Crystals

KRASSIMIR K. STAVREV, MICHAEL C. ZERNER

Quantum Theory Project, University of Florida, Gainesville, Florida 32611-8435

Received 25 February 1997; revised 1 June 1997; accepted 1 June 1997

ABSTRACT: A spin-averaged Hartree–Fock (SAHF) procedure is examined within the framework of the configuration-averaged methodology proposed earlier. The SAHF method produces reasonable total energies and can be successfully used for the calculation of electronic spectra, especially in the cases of marked energy separation between the spin states. An example is given with the spectroscopy of Mn^{2+} ions in the ZnS crystal where the SAHF procedure provides a more accurate interpretation of the electronic spectrum than that obtained by other self-consistent-field methods. © 1997 John Wiley & Sons, Inc. Int J Quant Chem **65**: 877–884, 1997

Introduction

The applications of quantum chemical methodologies to investigations of open-shell transition-metal (TM) systems are complicated by the large number of spin states often associated with such systems. The number of spin states in an open-shell system depends on the number of open-shell orbitals and electrons. In general, the number of microstates available to an open-shell system is given by Eq. (1), with N and m the numbers of open-shell electrons and spatial orbitals, respectively;

$$\binom{2m}{N} = \frac{(2m)!}{N!(2m-N)!} \tag{1}$$

and the number of states for a given multiplicity

Correspondence to: M. C. Zerner.
Contract grant sponsor: Office of Naval Research.
Contract grant sponsor: National Science Foundation.
Contract grant number: CHE-9312651.

© 1997 John Wiley & Sons, Inc.
CCC 0020-7608 / 97 / 050877-08

by [1]

$$N_{m,N}(S) = \binom{m}{(2S+N)/2}\binom{m}{(N-2S)/2} - \binom{m}{(2S+N+2)/2} \times \binom{m}{(N-2S-2)/2} \quad (2)$$

$$N_{m,N}(S) = M_{m,N}(S) - M_{m,N}(S+1), \quad (3)$$

with n_α = number of α spin electrons, $n_\alpha \geq n_\beta$, and $S = \frac{1}{2}(n_\alpha - n_\beta)$; $N = n_\alpha + n_\beta$ and it is understood that the second term in Eq. (2) is zero should $(N + 2S + 2) > 2m$. Note that $(N + 2S)/2 = n_\alpha$ and $(N - 2S)/2 = n_\beta$. The first term in Eq. (3) is the number of times n_α electrons can be arranged in m α-spin orbitals multiplied by the number of times n_β that electrons can be arranged in m β-spin orbitals. The second term subtracts from the first those microstates that have the value $S_z = S$ but that belong to multiplicities greater than S.

In the case of a single TM center, several hundreds of possible states can arise and this number grows quickly to 10^5–10^6 for TM dimers, 10^{11}–10^{12} for systems with four metals, etc. This large number of possible states can create a large number of states close in energy to the lowest-energy state and often prevents the self-consistent-field (SCF) convergence, leading also to spatial or spin instabilities and thus invalidating the pure spin description of the system. The calculation of the ground state is, therefore, a difficult task and requires a special approach to the treatment of molecules with a large number of open shells.

Previous work on TM systems has demonstrated that an iterative configuration averaged Hartree–Fock (CAHF) procedure [1] is suitable for the description of electronic properties and geometric characteristics of metal clusters [2–7]. The CAHF procedure has been compared with other methods which also average over multiplets and effective degeneracies, and the CAHF reliability has been demonstrated especially for molecular systems with extensive open shells [2]. The CAHF operator was developed within the restricted open-shell Hartree–Fock (ROHF) approximation and generalized for systems with an arbitrary number of electrons and open-shell orbitals [2, 3]. For this purpose, a Fock operator for the averaged energy of a configuration is considered. The energies and the orbitals from such an operator can be used to form a reference for a subsequent spin projection to obtain the pure spin states using, e.g., Rumer diagrams [1, 8, 9] or unitary group techniques [10, 11]. Subsequent configuration interaction (CI) can also be performed with such conveniently obtained orbitals, allowing for a proper check of the ground state and a refinement of the total wave function and its properties.

It was the aim of this work to present a further development of the CAHF theory that allows for a better approach to the spin-state problem through a selection of the configuration-averaged states by a spin eigenvalue. This leads to a smaller and significantly simplified pool of possible states and can present a better reference for the subsequent CI. An example is given with the spectroscopy of the Mn^{2+} ion in the ZnS lattice where the new approach is compared with the ROHF calculations performed previously on the same system [12] using the ZINDO program and the INDO/S Hamiltonian [13].

Theory

In general, we are trying to calculate the average energy of a system with N electrons in m spatial orbitals. The number of possible microstates is given by Eq. (1). We assume that the states are described by spin and spatially adapted linear combinations of Slater determinants, $|\phi_1 \phi_2 \ldots \phi_N|$ constructed from a set of orthonormal spin orbitals $\{\phi_i\}$, $\langle \phi_i | \phi_j \rangle = \delta_{ij}$.

The number of determinants of N electrons in m spatial orbitals, when one of the orbitals ϕ_i is doubly occupied, given by

$$\binom{2m-2}{N-2}. \quad (4)$$

Since each such determinant yields the Coulomb integrals J_{ii} in the expression for its energy, this is also the number of J_{ii} integrals that appear in all possible determinants [Eq. (1)].

Accordingly, for $i \neq j$, the number of J_{ij} integrals that appears in all possible determinants is

given by

$$4\binom{2m-2}{N-2}. \tag{5}$$

as the electrons in ϕ_i and ϕ_j can be of α and β spin independently. The general Coulomb integral, J_{ij}, is defined as

$$J_{ij} = \iint d\tau(1)\, d\tau(2)\phi_i^*(1)\phi_j^*(2)(1/r_{12})\phi_i(1)\phi_j(2). \tag{6}$$

In a simple fashion, the number of exchange integrals, K_{ij}, when considering all possible determinants of Eq. (1), is given by

$$2\binom{2m-2}{N-2}, \tag{7}$$

with

$$K_{ij} = \iint d\tau(1)\, d\tau(2)\phi_i^*(1)\phi_j^*(2)(1/r_{12})\phi_i(2)\phi_j(1). \tag{8}$$

In this case, both ϕ_i and ϕ_j need to be of α or β spin, respectively, for the factor 2 rather than the 4 of Eq. (5). The average total energy of the open-shell is then obtained through averaging over the total number of integrals for all possible states. This leads to

$$E_{ave}(open) = \frac{N}{m}\sum_n h_n + \frac{N(N-1)}{2m(2m-1)} \times\left[\sum_n J_{nn} + 2\sum_{n<p}(2J_{np} - K_{np})\right]. \tag{9}$$

To use the ROHF operator [14], the energy must be cast in the form of

$$E = 2\sum_i h_i + \sum_{i,j}(2J_{ij} - K_{ij}) + \sum_m n_m h_m + \frac{1}{4}\sum_\mu\sum_\nu\sum_{p\in\mu}\sum_{n\in\nu} n_\mu n_\nu(2a_{\mu\nu}J_{pn} - b_{\mu\nu}K_{pn}) + \frac{1}{2}\sum_{i,p} n_p(2J_{ip} - K_{ip}). \tag{10}$$

The first two terms in Eq. (10) account for contributions from electrons in the closed shell orbitals, the next two are those for open-shell contributions to the energy, and the last term gives the coupling between the closed and the open shells. Here, i and j stand for the doubly occupied closed-shell orbitals, and p and n label the open-shell orbitals with fractional occupations n_μ and n_ν belonging to open shells μ and ν, respectively. In the general case, p and n refer to individual orbitals, and each μ and ν define a separate open-shell Fock operator. Most often, sets of orbitals having the same vector coupling coefficients, a and b in Eq. (9), are grouped together into shells described by the same open-shell operator [1, 14]. Comparing Eq. (9) with (10) gives the vector coupling coefficients for a given open shell r, with fractional occupation $n_r = N_r/m_r$:

$$a_{rr} = b_{rr} = \frac{2m_r(N_r - 1)}{N_r(2m_r - 1)}. \tag{11}$$

The vector coupling coefficients between the different open shells are equal to 1:

$$a_{rs} = b_{rs} = 1. \tag{12}$$

The configuration average thus obtained is a mix of various states with different total spin. This spin contamination is generic for the CAHF and typically presents a difficulty in the determination of the pure spin state specified in the ROHF calculations. When a fraction of the total CAHF states is selected by the total spin, one obtains a significantly smaller range of configurations; we further refer to them as spin-averaged states [see Eq. (2)]. This spin-averaged Hartree–Fock (SAHF) procedure, similar to the CAHF methodology, operates in the reduced manifold of spin-eigenstates within a given configuration, leaving unsampled (in the average) a large number of unwanted configurations.

For the SAHF, the vector coupling coefficients have the following form:

$$a(S, m, N) = \frac{m}{(m^2-1)N^2} \times\left[mN(N-1) + \frac{N(N-4)}{2} + 2S(S+1)\right] \tag{13}$$

$$b(S,m,N) = \frac{m^2}{(m^2-1)N^2} \times \left[\frac{2N}{m}(N-1) + N(N-4) + 4S(S+1)\right]. \quad (14)$$

To derive Eq. (14) (perhaps there is a simpler way!), we consider four cases and the genealogical construction of spin states [1]. Each case gives rise to the occurrence of at least one Coulomb integral. In case one, there is one up-spin electron in both orbitals ϕ_i and ϕ_j. Such a triplet-coupled pair gives rise to $J_{ij} - K_{ij}$ and occurs multiplied by the number of times the remaining determinant can couple to give an eigenstate of spin eigenvalue S [more correctly, S^2 eigenvalue of $S(S+1)$]. If $S \geq 1$, this is $(N_{m-2,N-2}(S-1) + N_{m-2,N-2}(S) + N_{m-2,N-2}(S+1))$ times [see Eq. (2)]. If $S = 1/2$, the multiplicative factor is $(N_{m-2,N-2}(S) + N_{m-2,N-2}(S+1))$, and if $S = 0$, $N_{m-2,N-2}(S)$ (from the addition rule of angular momentum, $S = |S+1|, |S+1|-1, \ldots |S-1|$). A second case has an up-spin electron in ϕ_i and a down-spin in ϕ_j, forming an $(\alpha\beta - \beta\alpha)/\sqrt{2}$ singlet-coupled pair. Such a pair contributes $J_{ij} + K_{ij}$ and occurs $N_{m-2,N-2}(S)$ times. The third case contains two electrons in ϕ_i and one in ϕ_j or visa versa. Each such situation contributes $2(2J_{ij} - K_{ij})$ and occurs $(N_{m-2,N-3}(S+1/2) + N_{m-2,N-2}(S-1/2))$ times if $S \geq 1/2$ or $N_{m-2,N-2}(S)$ if $S = 0$. Finally, the case of two electrons in each of these orbitals contributes $4J_{ij} - 2K_{ij}$ and occurs $N_{m-2,N-4}(S)$ times. Combining these terms and dividing by $N_{m,N}(S)$, which is very tedious and best done symbolically, yields the average number of J's and K's. Interestingly, the special cases delineated above take care of themselves providing that the binomial terms in Eq. (2) with an ill-defined argument are set equal to zero. The comparison is then made with Eq. (10) with all open-shell fractional occupancy $n_\mu = n_i = N/m$ to obtain the a_{ij} and b_{ij} of Eqs. (13) and (14).

J_{ii} occurs $N_{m-1,N-2}(S)$ times, whereas, of course, two electrons in one orbital contribute no K_{ii}. In comparing with Eq. (10), however, J_{ii} occurs $n_i n_i\,(2a_{ii} - b_{ii})/4$ times (since $J_{ii} = K_{ii}$), allowing the same expression to be used for a_{ii} as for a_{ij} and for b_{ii} as for b_{ij}, $i \neq j$, and, thus, the SAHF procedure is characterized by a single open-shell operator as it was for the CAHF procedure. The advantages of the SAHF approach are illustrated in the next section.

Application

We illustrate the SAHF approach for the case of two electrons in two orbitals, which is represented by the six microstates shown in Figure 1. The average energy obtained by the CAHF method over all the six states is then split within the SAHF framework into two pieces, corresponding to the three possible singlets (Fig. 2) and the triplet states that form this configuration. Figure 1 shows two possible ways to obtain the averaged energies, through the averaging over all the individual microstates (left block) or through the pure spin states (on the right). The results are the same as shown in the figure.

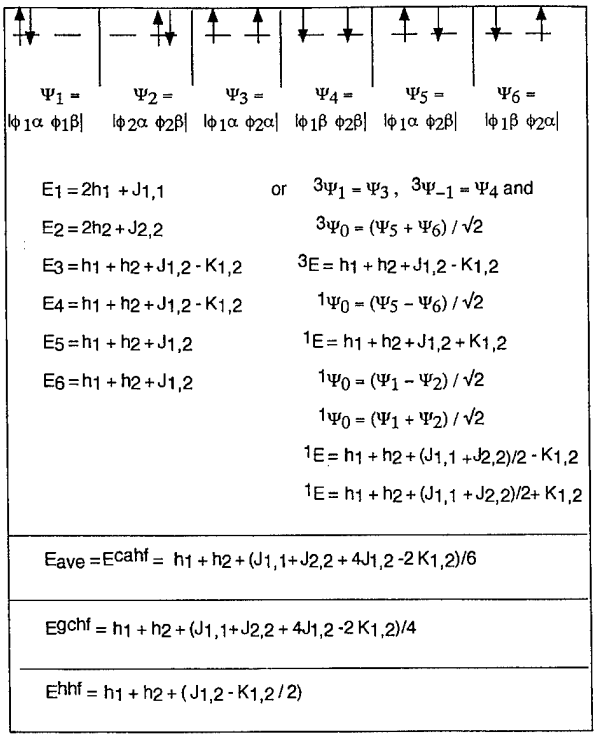


FIGURE 1. Configuration averaging illustrated for the simplest case of two electrons in two spatial orbitals. *h* stands for the one-electron terms in the energy expressions; *J* and *K* are the Coulomb and the exchange integrals, respectively. At the bottom of the table, the CAHF energy is compound with other averaging procedures, such as "grand canonical Hartree–Fock" (gchf) and "hyper-Hartree–Fock" (hhf) ([15] and [16], respectively).

The relative energies obtained by various methods for the similar case of a d^8 TM ion in an octahedral ligand field (two electrons in the upper doubly degenerate e_g orbitals, d_{z^2} and $d_{x^2-y^2}$) are depicted in Figure 3. On the right side of Figure 3, the CI energies of the ground-state triplet and the first two excited-state singlets that originate from the three dominant configurations are shown. We see that the open-shell triplet and singlet SCF calculations, ROHF-3 and ROHF-1, respectively, represent a good reference for the corresponding lower-lying spin states. SAHF-1 gives closer energy for the higher-lying singlet than the other methods. In all the cases, RHF is a poor reference for either singlet or triplet states. Upon projection, the CAHF produces higher energies for the ground-state triplet and singlets, but is a good reference for higher-lying triplets, as, e.g., those originating from mixed (t_{2g}, e_g) configurations, not included in any of the SCF schemes shown here. Note that the ROHF-3 and SAHF-3 correspond to the same triplet state which is unique, (see also Fig. 1).

We conclude from these simple considerations that configuration-averaging models provide a good reference for the spectroscopic CI calculations. The advantages offered by the SAHF ap-

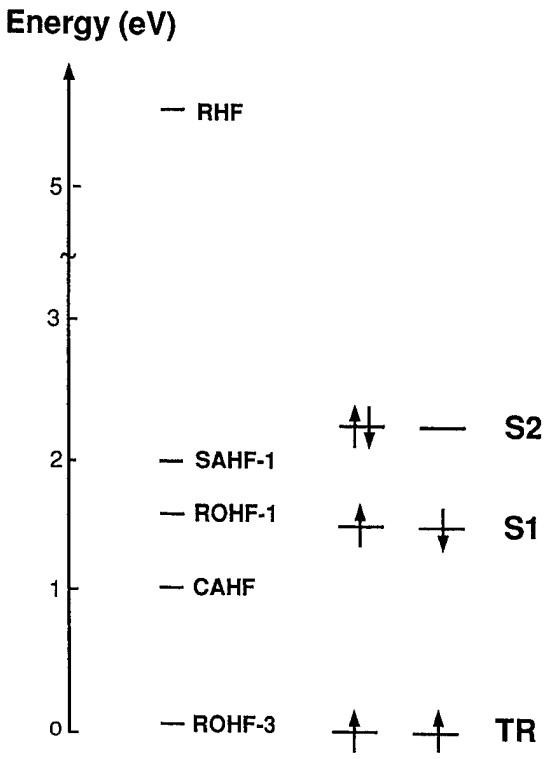


FIGURE 3. Relative energies of the states produced by various SCF methods (left) compared with the CI energies for the three lowest states originating from d^2 configuration (right).

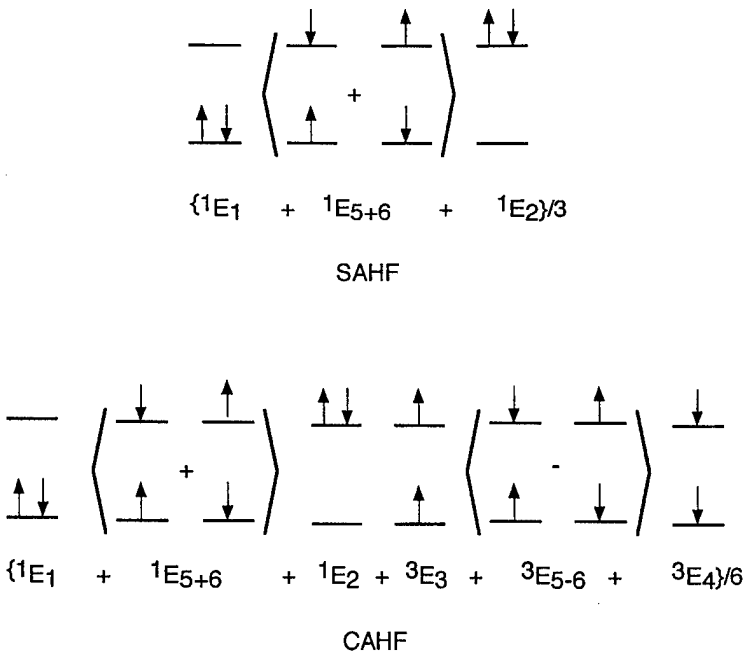


FIGURE 2. Comparison between the SAHF and CAHF in the case of two electrons in two orbitals. The numbering corresponds to the pictures on top of Figure 1.

proach can be demonstrated with relative ease in the cases where there is a distinct separation between the ground and the excited spin states. We illustrate this idea with the examination of the electronic spectrum of a d^5 ion in a cubic crystal field (Fig. 4), which has an unique sextet ground-state $^6A_1$ originating from the high-spin $e^2t_2^3$ configuration in a tetrahedral field.

The electronic spectrum of ZnS:Mn has been thoroughly investigated in the last several decades [17–24]. Five distinct bands have been observed in the visible region corresponding to d–d transitions from the $^6A_1$ ground state to the manifold of quartet states originating from the configurations $e^y t_2^{5-y}$, with $y = 1$–4. The t_2^5 configuration contributes to to the doublet excited states and requires excitation of two electrons from the ground

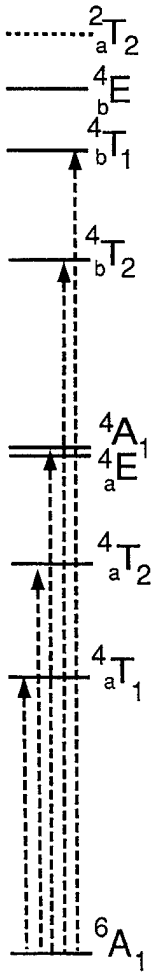


FIGURE 4. Term level diagram for a d^5 ion in a cubic ligand field and the sextet–quartet transitions related to the ZnS:Mn absorption spectrum.

$e^2t_2^3$ configuration. This requires a double spin-flip during the electronic transition and imposes a strict spin prohibition on such bands. Doublet states are, therefore, considered unlikely to contribute measurably to the d–d absorption spectrum of ZnS:Mn.

In a previous work [12], we calculated the d–d bands of the ZnS:Mn spectrum using the ROHF ground state as a reference for the subsequent CI that forms the quartet states using the spectroscopic intermediate neglect of differential overlap (INDO/S) model [13]. We applied the same approach here using the SAHF states as a reference. The results are given in Table I. We see that the level of accuracy is considerably improved by the SAHF method and the average error decreases to the level of the vibrational broadening of the spectroscopic bands: 0.14 eV. Following the SAHF calculations, the $^4A_1$ level is again calculated *above* the ^4E state by 160 cm^{-1}, as compared to the 100 cm^{-1} that we calculated earlier using the ROHF approximation [12]. The relative positioning of these two states is controversial [18, 20]: The first doublet state that we calculate using CI single and double excitations is at 3.72 eV, beyond the observable spectroscopic range for ZnS with a band gap absorption starting at nearly 3.6 eV. Therefore, the possible contribution of doublet states to the ZnS:Mn electronic spectrum should be ruled out.

TABLE I
Calculated and experimental band energies (eV) for ZnS:Mn; ab initio and experimental data are taken from [22].

Transition	Ab initio[a]	ROHF[b]	This work	Experiment
$^6A_1 \rightarrow a^4T_1$	2.68	2.72	2.61	2.34
$\rightarrow a^4T_2$	2.83	2.76	2.68	2.49
$\rightarrow a^4E$	2.96	2.78	2.69	2.67
$\rightarrow {}^4A_1$	2.96	2.78	2.71	2.67
$\rightarrow b^4T_2$	3.31	3.18	3.07	2.89
$\rightarrow b^4T_1$	3.39	3.47	3.15	3.19
$\rightarrow b^4E$	3.52	3.56	3.46	—
Average absolute error	0.31	0.24	0.12	

[a] MR-CIS calculations employing Watcher's (14, 9, 5) basis with extra diffuse functions for Mn (14, 11, 6) [8, 7, 4] and Roos–Siegbahn's (10, 6) [7, 4] basis for S; from [25].
[b] ROHF stands for transition energies calculated using ROHF sextet state as a reference for the subsequent configuration interaction (see [2]).

The absorption spectrum is essentially reproduced from sextet-to-quartet d–d excitations and the agreement with the experiment (see [24]) is improved significantly by the SAHF procedure.

The SAHF procedure is the same as the ROHF approximation for the case of maximum multiplicity, i.e., $S = s_z = m$. It appears that it is a reasonable starting position for any CI of the multiplicity over which the average is taken, but need not to be the best average for the cases of lower multiplicity. Returning for the moment to the case of two electrons in two orbitals, the singlet average contains $|\phi_i\bar{\phi}_i|$, $[|\phi_i\bar{\phi}_j| - |\bar{\phi}_i\phi_j|]/\sqrt{2}$ and $|\phi_j\bar{\phi}_j|$. The $|\phi_j\bar{\phi}_j|$ state may be of such high energy as to render the average orbitals obtained not as good for the lowest-lying singlets as that for the CAHF case of Figure 1, since the energy there is lowered by including the three triplet states in this average (see, e.g., Fig. 2). Indeed, in such cases, it can be difficult to converge the SCF.

It is interesting also to develop an operator that presents the average of a given multiplicity for an open-shell structure of N electrons in $m = N$ orbitals. This would be the case, e.g., of the singlets or the triplets possible from ψ_3 through ψ_6 of Figure 1. There are

$$N(S) = 1 \qquad \text{with } S = S_{max} = N/2$$

$$N(S) = \binom{N}{(2S+N)/2} - \binom{N}{(2S+N+2)/2} \qquad \text{with } S < S_{max} \quad (15)$$

such states (one singlet, and one triplet for ψ_3 through ψ_6 of Figure 1). Thus, the coupling coefficients are obtained in the form

$$\begin{aligned} 2a_{ii} = b_{ii}, \quad a_{ij} = 1 \qquad & \text{all} \quad i, j \\ b_{ii} = 2 \qquad & \text{all} \quad i \\ b_{ij} = 2\big[\eta_\beta(\eta_\beta - 1) + \eta_\alpha(\eta_\alpha - 1) & \\ -2\eta_\alpha\eta_\beta/N(S)\big]/m(m-1) \qquad & \text{all} \quad i \neq j. \end{aligned} \quad (16)$$

This development, unfortunately, generates a different operator for each orbital; for example, in the common case of the ROHF singlet operator for two electrons in two orbitals, this is two open-shell operators. Such an approach quickly becomes unwieldy. For the case of antiferromagnetic spin coupling, however, where electrons of a given spin are "frozen" in the corresponding orbitals of a given center, say C and D, this approach again becomes simple, leading to

$$\begin{aligned} a_{ij} = 1 \qquad & \text{all} \quad i, j \\ b_{ij} = 2 \quad i \in C(\uparrow), \quad & j \in D(\uparrow); \quad \text{or} \\ i \in C(\downarrow), \quad & j \in D(\downarrow) \\ b_{ij} = 0 \qquad & \text{otherwise.} \end{aligned} \quad (17)$$

This leads to two open-shell operators, one for all up-spin domains, $C(\uparrow)$ and $D(\uparrow)$, and one for the down-spin spin domains, $C(\downarrow)$ and $D(\downarrow)$:

$$\mathbf{A} = \mathbf{I} = \begin{pmatrix} \mathbf{I} & \mathbf{I} \\ \mathbf{I} & \mathbf{I} \end{pmatrix} \Big/ \begin{pmatrix} \mathbf{I} & \mathbf{I} \\ \mathbf{I} & \mathbf{I} \end{pmatrix}; \qquad \mathbf{B} = \begin{pmatrix} 2\mathbf{I} & \mathbf{0} \\ \mathbf{0} & 2\mathbf{I} \end{pmatrix}. \quad (18)$$

For this to be useful, the orbitals must be localized, as they often are for d orbitals in open-shell situations, and electrons of up- and down-spin must be assigned to different domains as well as specifying the overall S_z value, i.e., $A(\uparrow)$, $B(\downarrow)$, $C(\uparrow)\ldots$. This operator has been used several times by us with good success [26].

ACKNOWLEDGMENTS

This work was supported in part through a grant from the Office of Naval Research and through a grant from the National Science Foundation, CHE-9312651.

References

1. R. Pauncz, *Spin Eigenfunctions* (Plenum Press, New York, 1979).
2. M. C. Zerner Int. J. Quantum Chem. **35**, 567 (1989), and references therein.
3. M. Kotzian, N. Rösch, and M. C. Zerner, Theor. Chim. Acta **81**, 201 (1992).
4. G. L. Estiu and M. C. Zerner, Int. J. Quantum Chem. Symp. **27**, 195 (1993).
5. G. L. Estiu and M. C. Zerner, J. Phys. Chem. **98**, 4793 (1994).
6. G. L. Estiu and M. C. Zerner, J. Phys. Chem. **98**, 9972 (1994).
7. K. K. Stavrev and M. C. Zerner, Chem. Res. J. **2**, 83 (1996).
8. I. L. Cooper and R. McWeeny, J. Chem. Phys. **45**, 226 (1966); See also R. McWeeny, *Methods in Molecular Quantum Mechanics*, 2nd ed. (Academic Press, San Diego, 1989).
9. B. Sutcliffe, J. Chem. Phys. **45**, 235 (1966).
10. B. Brooks and H. Schaefer, J. Chem. Phys. **70**, 5092 (1979).
11. J. Paldus, Phys. Rev. A **14**, 1620 (1976).
12. K. K. Stavrev and M. C. Zerner J. Chem. Phys. **102**, 34 (1995).
13. M. C. Zerner, ZINDO, a semiempirical program package (Quantum Theory Project, University of Florida, Gainesville,

FL); see, also, M. C. Zerner, G. H. Loew, R. Kirchner, and U. Müller-Westerhoff, J. Am. Chem. Soc. **102**, 589 (1980); J. E. Ridley and M. C. Zerner, Theor. Chim. Acta **32**, 118 (1973); A. D. Bacon and M. C. Zerner, Theor. Chim. Acta **53**, 21 (1979).

14. W. D. Edwards and M. C. Zerner, Theor. Chim. Acta **72**, 347 (1987).
15. S. F. Abdulnur, J. Lindenberg, Y. Öhrn and P. W. Thulstrup, Phys. Rev. A **6**, 889 (1972); P. Jorgensen and Y. Öhrn, Phys. Rev. A **8**, 112 (1973).
16. J. C. Slater, J. B. Mann, T. M. Wilson, and J. H. Wood, Phys. Rev. **184**, 672 (1969); D. R. Hartree, Proc. Camb. Philos. Soc. **24**, 89 (1928).
17. H.-E. Ğumlich and J. Lumin, **23**, 73 (1981), and references therein.
18. R. Parrot and C. Blanchard, Phys. Rev. B **6**, 3992 (1972).
19. P. Koidl, Phys. Stat. Sol. B **74**, 477 (1976).
20. A. Fazzio, M. J. Caldas, and A. Zunger, Phys. Rev. B **30**, 3430, (1984).
21. R. Parrot, C. Naud, F. Gendron, C. Porte, and D. Boulanger, J. Chem. Phys. **87**, 1463 (1987).
22. R. Parrot, A. Geoffroy, C. Naud, W. Busse, and H.-E. Gumlich, Phys. Rev. B **23**, 5288 (1988).
23. J. Dreyhsig and J. W. Allen, J. Phys. Condens. Mat. **1**, 1087 (1989).
24. J. W. Richardson and G. J. M. Janssen, Phys. Rev. B **39**, 4958 (1989).
25. G. J. M. Janssen, PhD Thesis (Groningen University, The Netherlands, 1986).
26. M. G. Cory, K. K. Stavrev, and M. C. Zerner, Int. J. Quantum Chem. **63**, 781 (1997).

Calculation of the Absorption Spectrum of Benzene in Condensed Phase. A Study of the Solvent Effects

KALINE COUTINHO,[1] SYLVIO CANUTO,[1] M. C. ZERNER[2]

[1] *Instituto de Física, Universidade de São Paulo, CP 66318, 05315-970 São Paulo, SP, Brazil*

[2] *Quantum Theory Project, University of Florida, Gainesville, Florida 32611*

Received 3 March 1997; revised 23 April 1997; accepted 29 April 1997

ABSTRACT: The red shift of the first absorption band of benzene in the condensed phase is calculated. The solid-phase calculations are performed using the experimental crystal structure. For the liquid two different approaches are considered. One is the herringbone structure suggested by X-ray experiments, and the other uses supermolecules generated by Monte Carlo simulation. Attention is given to the contribution of the usual parallel and T-shape conformations of the benzene dimers obtained in the simulation. Comparison with experiment shows a relatively poor result for the herringbone structure and good agreement for the supermolecular structures generated by the simulation.
© 1997 John Wiley & Sons, Inc. Int J Quant Chem **65**: 885–891, 1997

Introduction

In this study we calculate and analyze the red shift of the first absorption band of benzene in the condensed phase as compared to the gas phase. The interest in the structure [1] and spectra of clusters and condensed-phase benzene is related to several topics of interest in chemistry, physics, and biology. It naturally relates to the importance of the interaction between aromatic π-systems. This present study also relates to our interest in solvent effects in molecular absorption spectroscopy [2, 3]. For the calculation of the solvatochromic shift of liquid benzene, we use two structures. One is the well-known herringbone structure [4] and the other is a disordered structure obtained from Monte Carlo (MC) simulation. For completeness, we also consider the first absorption transition of the solid benzene. All quantum mechanical calculations are made using the INDO/CIS model [5] as implemented in the ZINDO program [6], and we use the so-called supermolecular (SM) approach. In the case of the solid and the herringbone structure of the liquid, two configurations are used (Fig. 1). In the first we use 14 benzene molecules both for the solid and the liquid, as seen in Figure 1(a) (top). In the second, we use only 13 benzene molecules.

Correspondence to: S. Canuto.

Contract grant sponsors: CNPq, FAPESP, and Office of Naval Research.

© 1997 John Wiley & Sons, Inc.
CCC 0020-7608 / 97 / 050885-07

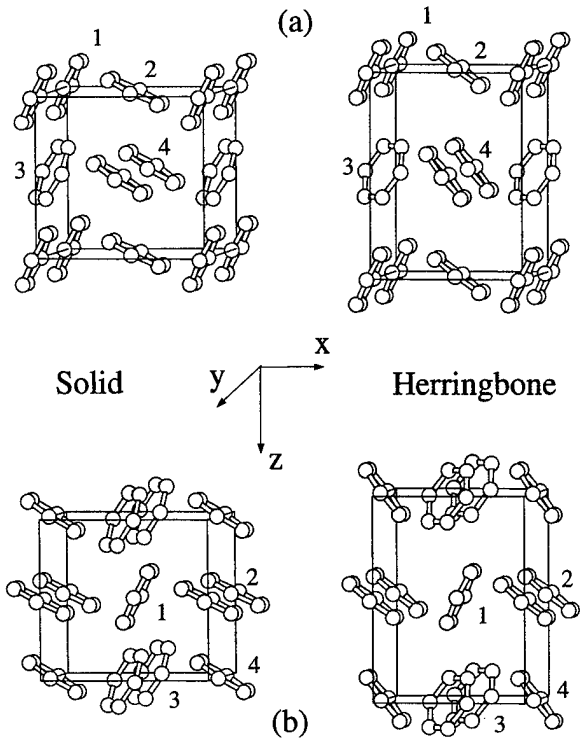


FIGURE 1. Crystalline and the herringbone structures of solid and liquid benzene. The top figures show 14 benzene molecules. The bottom figures show instead 13 molecules and includes one bulk benzene in the center. Molecules 1, 2, 3, and 4 generate the unit cell as defined by Narten [4].

This corresponds to including one benzene and its 12 nearest neighbors of the well-known P*bca* space group [4]. This second case, as seen in Figure 1(b) (bottom), as opposed to the first case, includes a central benzene molecule to represent the "bulk." Calculations are then performed at these four structures but in each case using a fixed geometry.

For the case of the disordered liquid benzene the structures generated by the MC simulation [7] are used. Each SM is composed of 14 benzene molecules. As we shall see, this corresponds to including the first coordination shell as obtained from the radial distribution function (RDF). In addition, however, several SM calculations are performed. The actual number of SM structures used takes into account the statistical correlation between MC structures. The final excitation energy is obtained averaging over the transition energies obtained for each structure. A comparison of these different procedures will be made.

Monte Carlo Simulation

The MC simulation is performed using standard procedures for the Metropolis sampling technique [8] in the canonical ensemble, where the number of molecules N, the volume V, and the temperature T are fixed. As usual, periodic boundary conditions in a cubic box [9] are used. In our simulation, we use 125 molecules of benzene. The volume of the cubic box is determined by the experimental density of the liquid, $\rho = 0.8990$ g/cm^3 [10], and the temperature is $T = 25$°C. There has been much discussion about the quadrupolar interaction of benzene and its relation to the structure [11] (see next section). In our theoretical experiments, we are willing to generate a disordered structure for the liquid. Therefore, the benzene molecules interact only by the Lennard-Jones potential:

$$U_{ab} = \sum_{i}^{\text{on } a} \sum_{j}^{\text{on } b} 4\varepsilon_{ij}\left[\left(\frac{\sigma_{ij}}{r_{ij}}\right)^{12} - \left(\frac{\sigma_{ij}}{r_{ij}}\right)^{6}\right], \quad (1)$$

where Σ^a is the sum over the atoms of molecule a, Σ^b is the sum over the atoms of molecule b, r_{ij} is the distance between atoms i and j, $\varepsilon_{ij} = \sqrt{\varepsilon_i \varepsilon_j}$, $\sigma_{ij} = \sqrt{\sigma_i \sigma_j}$, and σ_i and ε_i are the parameters of atom i. The potential parameters used were developed by Jorgensen and co-workers [12]: $\sigma_C = 3.75$ Å, $\varepsilon_C = 0.11$ kcal/mol, and $\sigma_H = \varepsilon_H = 0$. As the environment of the liquid system has no significant effect on the conformational equilibrium for the benzene molecule [4, 14], we consider, in the simulation, rigid conformations of the benzene molecules in the D_{6h} structure with $r_{CC} = 1.40$ Å, $r_{CH} = 1.088$ Å, and all angles $\theta = 120°$. We recognize that distortions of the benzene structure would lead to considerably enhanced intensity of the forbidden $^1B_{2u}$ transition we examine. We do not believe, however, that the position of the band maximum will be much effected [15].

In the calculation of the pairwise energy, each molecule interacts with all other molecules within a center-of-mass separation that is smaller than the cutoff radius $r_c = 13.11$ Å. For separations larger than r_c, we use the long-range correction of the potential energy [13]. Over the 125 benzene molecules included in the simulation, each molecule interacts effectively with ~ 60 neighbors.

The initial configuration is generated randomly, considering the position and the orientation of

each molecule. A new configuration, or one MC step, is generated by selecting all molecules sequentially and trying to translate it in all the Cartesian directions and also rotate it around a randomly chosen axis. The maximum allowed displacement of the molecules is auto-adjusted after 50 MC steps to give an acceptance rate of new configurations around 50%. The maximum rotation angle is fixed during the simulation in $\delta\theta = \pm 15°$. The full simulation [7] involves a thermalization stage of about 5000 MC steps followed by an averaging stage of 48,000 MC steps. During the averaging stage some thermodynamical properties, as the internal energy and the heat capacity at constant volume, are calculated, and they are in complete agreement with that calculated by Jorgensen and co-workers [12]. The radial distribution function is also calculated during the averaging stage in the simulation.

Results and Discussions

The structure of the liquid benzene has been of interest for many years. Ever since the X-ray study of Narten [4], the herringbone structure is believed to prevail. This structure is illustrated in Figure 1 along with the known experimental structure of solid benzene. In the case of the benzene dimer the interest is basically related to the relative stabilization of the parallel and T-shape structure [16]. A herringbone structure for the dimer has also been proposed [17]. More recent studies [18] have indicated that a parallel-displaced configuration seems to be more stable than the T-shape favorite structure for the dimer. It seems clear from all these studies that the parallel-displaced, T-shape, and T-shape-displaced structures are very close in energy.

From these considerations it seems appropriate to consider SM calculations of the liquid benzene with all these possibilities, not only the herringbone structure. Thus several structures generated by the MC simulation will be used. As these structures are statistically correlated, we will select structures that are separated by a certain number of MC steps. This number results from the time correlation function and the statistical inefficiency analysis [19]. In fact, we select structures that are separated by twice the correlation time ($2\mathcal{T}$), obtained after the integration of the time correlation function. Clearly, "time" here should mean MC step. The calculated time correlation function, $C(t)$, and the statistical inefficiency, s, for the energies of the liquid benzene structures are shown in Figure 2. The calculated $C(t)$ function gives the correlation time value of $\mathcal{T} \sim 400$ *steps*. This is related to the statistical inefficiency and the relation $s \approx 2\mathcal{T}$ holds. Thus we use only MC structures that are separated by 800 MC steps. As the entire simulation took 48,000 MC steps, only 60 are statistically relevant and used in our studies.

Figure 3 shows a comparison between the calculated RDF from the MC simulation and the experimental RDF of Narten [4]. As can be seen, the overall agreement between these two results is very good. The results show a first broad peak ranging from 3.0 to 7.6 Å. Integration of this peak gives the coordination number of $N_s = 12.5$. This theoretical result is of interest in two different aspects. First, the experimental result of Narten gives $N_s = 12$, in close agreement with our theoretical value. This suggests that N_s is not enough to uniquely characterize the liquid as having a herringbone structure. The second aspect is of more technical interest. $N_s = 12.5$ signifies that, on the average, each benzene molecule has 13 (rounding off) neighbors and therefore the supermolecule should have 14 molecules. Hence all three systems, including the solid and the herringbone, will be calculated with the same number of molecules. The difference is, however, that in the case of the MC liquid a total of 60 SM quantum mechanical calculations are performed.

In all cases the excitation energy to the $B_{2u}(\pi - \pi^*)$ state of benzene is calculated including all the $e_{1g} \rightarrow e_{2u}$ transitions of each individual benzene; that is, from 28 occupied molecular orbitals into 28 molecular orbitals of the virtual space.

Table I summarizes the calculated numerical results and compares them with the experimental values for the red shift of benzene in condensed phase.

Figure 4 shows the calculated result for the excitation energy of the MC liquid together with the final average (-306 cm^{-1}) and the experimental [20] (-320 cm^{-1}) values for the shift compared to the gas phase. It should be noted that the shift for an individual structure may differ by a few hundreds of cm^{-1}, but the "ensemble average" final result is in very good agreement with the experimental result. It is interesting to analyze, wherever possible, the contribution of the individual benzene molecules. This is, of course, not always possible. However, we note that in many

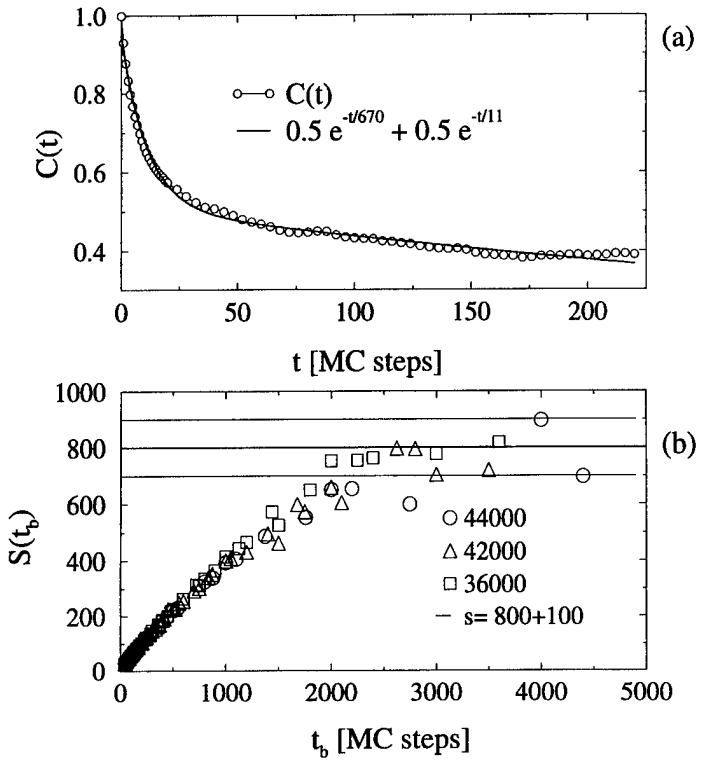


FIGURE 2. Time correlation function (top) and the statistical inefficiency (bottom) of the MC simulation. See text.

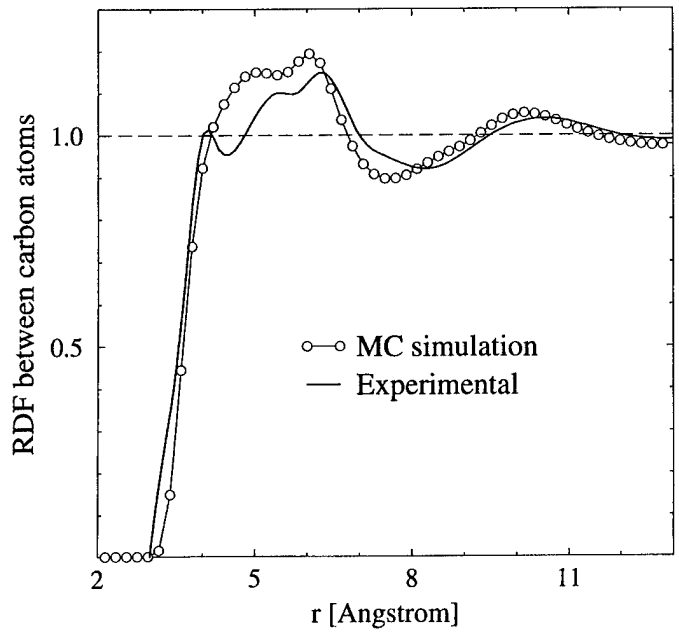


FIGURE 3. Comparison of the calculated and experimental [4] carbon–carbon radial distribution function of the liquid benzene.

TABLE I

Summary of the calculated and experimental results for the $B_{2u}(\pi - \pi^*)$ energy shift (cm^{-1}) in the absorption spectra of benzene in condensed phases.[a]

System	N	$\Delta E_{calc.}$	$\Delta E_{exp.}$ [20]
Gas	1	0	0
Solid[b]	13	−260	−260 ± 30
	14	−240	
Liquid (herringbone)[c]	13	−100	−320 ± 30
	14	−60	
Liquid (herringbone)[d]	13	−100	−320 ± 30
	14	−40	
Liquid (MC)[e]	14	−306	−320 ± 30

[a] N is the number of molecules included in the quantum calculations.
[b] Lattice parameters [4] (7.460, 9.666, 7.034) in Å.
[c] Density of 0.874 g / cm^3 corresponding to the lattice parameters [4] (6.75, 9.74, 9.03) in Å.
[d] Density of 0.899 g / cm^3 (used in the MC simulation) corresponding to the lattice parameters (6.75, 9.74, 8.78) in Å.
[e] Average value over 60 SM structures.

structures the transition is somewhat localized in two benzene molecules. Interesting enough, these two molecules are found to be in well-known conformations, like the T-shape-displaced and the parallel-displaced (see Fig. 5 for illustration). Therefore we now look at systems composed of

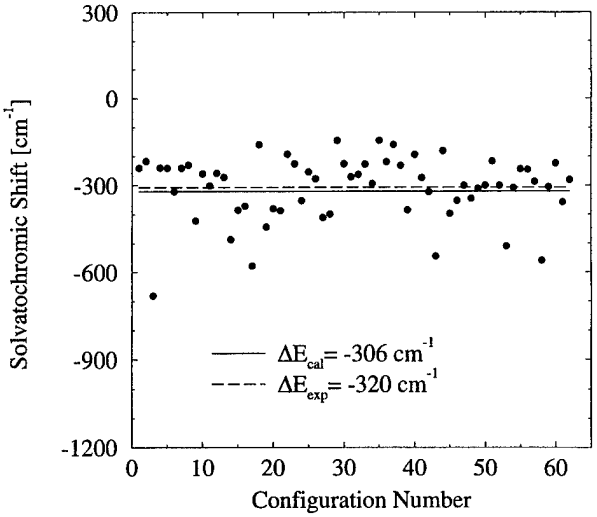


FIGURE 4. Calculated red shift obtained from the disordered MC structures of the liquid benzene. Also shown is the average value (solid line) and the experimental result (dashed line).

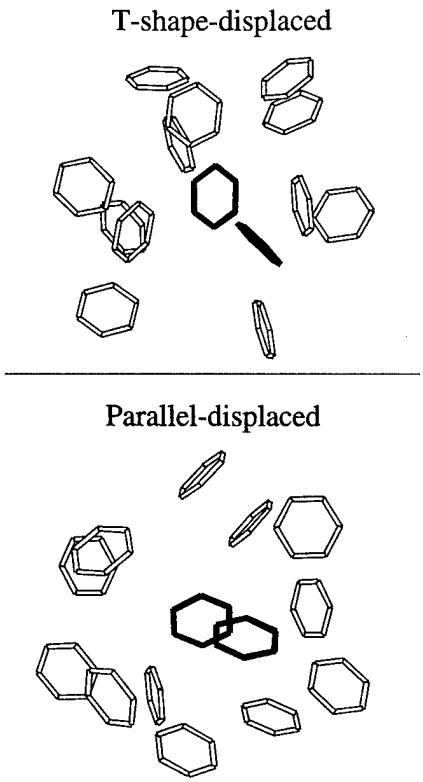


FIGURE 5. Illustration of MC structures showing the T-shape, displaced, and parallel-displaced dimer conformations. These dimers give a large contribution to the total red shift. See text and Table II.

only two benzene molecules. We find from the MC simulation that ~ 25% of the benzenes have the nearest neighbor within an angle between 0 and 20°, corresponding to the parallel and parallel-displaced conformations of the dimer. Similarly, ~ 15% have its nearest neighbor within an angle between 70 and 90°, corresponding to the T-shape, T-shape-displaced, and L-shape conformations. The average contribution of these "ordered" dimer conformations is compared, in Table II, with the result obtained using all dimers generated in the Monte Carlo simulation irrespective of the angle. Dimers alone are not able to give a good result for the red shift, but it is clear that those ordered dimer conformations make contributions that are significant. We note, in particular, that these parallel conformations give larger shifts than the perpendicular ones. This seems to suggest that these ordered dimer conformations of benzene are of importance in understanding the spectroscopic red shift of the liquid phase.

TABLE II
Summary of the average contribution of different dimer conformations to the calculated shift for the $B_{2u}(\pi - \pi^*)$ absorption transition of liquid benzene.[a]

System	N	$\Delta E_{calc.}$ (cm^{-1})
MC T-shape	2	−98
MC T-shape-displaced and L-shape	2	−135
MC parallel	2	−179
MC parallel-displaced	2	−197
MC dimer	2	−103
MC supermolecule	14	−306

[a] N is the number of molecules included in the quantum calculations.

In the case of the herringbone structure with 14 molecules, the calculated shift is too small, only $-60\ cm^{-1}$. This discrepancy, however, is not found in the similar structure of the solid. In this case the calculated result is $-240\ cm^{-1}$ in good agreement with the experimental value of $-260\ cm^{-1}$ [20].

A possible deficiency of the use of the herringbone structure shown in Figure 1(a) is that there is no benzene molecule in the center of the box to represent the "bulk." To look at this we have used the structures shown in Figure 1(b) for the herringbone and the solid. The calculated results, however, changed only from the previous -60 to $-100\ cm^{-1}$ showing only slight improvement. For the solid it changed from the previous -240 to $-260\ cm^{-1}$, bringing the shift to a better agreement with the experimental result.

Summary and Conclusions

In this work we have calculated the red shift of the first absorption band of benzene in the condensed phase. The herringbone structure used for the liquid gives a red shift that is only 15–25% of the experimental value. In turn, the use of a disordered liquid obtained from Monte Carlo simulation gives a red shift that is in very good agreement with experiments. In this disordered liquid most of the usual structures of the benzene dimer, such as the parallel, parallel-displaced, T-shape, T-shape-displaced, etc., are included naturally, but there is little long-range order. The calculated red shift for crystalline benzene is also in very good agreement with the experimental shift.

ACKNOWLEDGMENTS

This work is supported in part by grants from CNPq and FAPESP and from the Office of Naval Research.

References

1. I. Pettersson and T. Liljefors, *J. Comput. Chem.* **8**, 1139 (1987); N. L. Allinger and J. H. Lii, *J. Comput. Chem.* **8**, 1146 (1987); X. Shi and L. S. Bartell, *J. Phys. Chem.* **92**, 5667 (1988); L. S. Bartell, L. R. Sharkey, and X. Shi, *J. Am. Chem. Soc.* **110**, 7006 (1988).
2. C. Reichardt, *Solvents and Solvent Effects in Organic Chemistry* (Verlag-Chemie, Weinheim, 1979); E. S. Amis and J. F. Hinton, *Solvent Effects on Chemical Phenomena*, Vol. 1 (Academic Press, New York, 1973); P. Beak, *Acc. Chem Res.* **10**, 186 (1977); M. F. Nicol, *Solvent Effects on Electronic Spectra, App. Spectr. Rev.* **8**, 183 (1974); N. S. Bayliss and E. G. McRae, *J. Phys. Chem.* **58**, 1002 (1954); A. Warshel, *Computer Modeling of Chemical Reactions in Enzymes and Solutions* (Wiley, New York, 1991); J. Tomasi and M. Persico, *Chem Rev.* **94**, 2027 (1994); C. J. Cramer and D. G. Truhlar, in *Reviews in Computational Chemistry*, Vol. 6, D. B. Boyd and K. B. Lipkowitz, Eds. (VCH, New York, 1995); J. Gao, *Acc. Chem. Res.* **29**, 298 (1996).
3. K. Coutinho and S. Canuto, *Adv. Quantum Chem.* **28**, 89 (1997); N. Rösch and M. C. Zerner, *J. Phys. Chem.* **98**, 5817 (1994); M. Karelson and M. C. Zerner, *J. Phys. Chem.* **96**, 6949 (1992); M. A. Thompson and M. C. Zerner, *J. Am. Chem. Soc.* **113**, 8210 (1991).
4. A. H. Narten, *J. Chem. Phys.* **48** (1968) 1630; A. H. Narten, *J. Chem. Phys.* **67** (1977) 2102.
5. J. Ridley and M. C. Zerner, *Theor. Chim. Acta* **32**, 111, (1973).
6. ZINDO: A semi-empirical program package, M. C. Zerner, University of Florida, Gainesville, FL 32611.
7. DICE: A Monte Carlo program for molecular liquid simulation, K. Coutinho and S. Canuto, University of São Paulo, Brazil.
8. N. Metropolis, A. W. Rosenbluth, M. N. Rosenbluth, A. H. Teller, *J. Chem. Phys.* **21**, 1087 (1953).
9. M. P. Allen and D. J. Tildesley, *Computer Simulation of Liquids* (Clarendon Press, Boca Raton, FL, 1987).
10. *CRC Handbook of Chemistry and Physics*, 64th ed. (CRC Press, 1983–1984).
11. W. L. Jorgensen and D. L. Severance, *J. Am. Chem. Soc.* **112**, 4768 (1990).
12. W. L. Jorgensen, J. Chandrasekhar, and J. D. Madura, *J. Am. Chem. Soc.* **106**, 6638 (1984).
13. W. L. Jorgensen, R. C. Binring, Jr., and B. Bigot, *J. Am. Chem. Soc.* **103**, 4393 (1981).
14. W. L. Jorgensen, *J. Phys. Chem.* **87**, 5304 (1983).
15. G. Pearl, M. C. Zerner, A. Broo, and J. McKelvey, in progress.
16. K. C. Jandra, J. C. Hemminger, J. S. Winn, S. E. Novick, S. J. Harris, and W. J. Klemperer, *J. Chem. Phys.* **63**, 1419 (1975); J. M. Steed, T. A. Dixon, and W. J. Klemperer, *J. Chem.*

Phys. **70**, 4940 (1979); G. Karlström, P. Linse, A. Wallqvist, and B. Jönsson, *J. Am. Chem. Soc.* **105**, 3777 (1983); P. Hobza, H. L. Selzle, and E. W. Schlag, *J. Chem. Phys.* **93**, 5893 (1990).

17. D. E. Williams, *Acta Cryst.* **A36**, 715 (1980); M. Schamer and E. R. Bernstein, *J. Chem. Phys.* **82**, 3722 (1985).
18. P. Hobza, H. L. Selzle, and E. W. Schlag, *J. Am. Chem. Soc.* **116**, 3500 (1994); P. Hobza, H. L. Selzle, and E. W. Schlag, *Chem. Rev.* **94**, 1767 (1994).
19. K. Coutinho, M. J. de Oliveira, and S. Canuto, to appear.
20. T. Inagaki, *J. Chem. Phys.* **57** (1972) 2526; V. L. Broude, *Sov. Phys. Usp.* **4**, 584 (1962).

Structure of the Correlation–Kinetic Component of the Kohn–Sham Exchange Potential in Atoms and at Metal Surfaces

ALEXANDER SOLOMATIN, VIRAHT SAHNI

Department of Physics, Brooklyn College of the City University of New York, 2900 Bedford Avenue, Brooklyn, New York 11210 and The Graduate School and University Center of the City University of New York, 33 West 42nd Street, New York, New York 10036

Received 2 March 1997; revised 2 May 1997; accepted 6 May 1997

ABSTRACT: The Kohn–Sham density functional theory "exchange" potential $v_x(\mathbf{r}) = \delta E_x^{KS}[\rho]/\delta\rho(\mathbf{r})$, where $E_x^{KS}[\rho]$ is the "exchange" energy functional, is composed of a component representative of Pauli correlations and one that constitutes *part* of the correlation contribution to the kinetic energy. The Pauli term is the work done $W_x^{KS}(\mathbf{r})$ in the field $\mathscr{E}_x^{KS}(\mathbf{r})$ obtained by Coulomb's law from the Fermi hole charge distribution constructed from the Kohn–Sham orbitals. The correlation–kinetic term is the work done $W_{t_c}^{(1)}(\mathbf{r})$ in the field $\mathbf{Z}_{t_c}^{(1)}(\mathbf{r})$ derived from the kinetic-energy–density tensor involving the first-order correction to the Kohn–Sham single-particle density matrix. The sum of these fields is conservative, so that the total work done is path-independent. There is no explicit correlation–kinetic contribution to the "exchange" energy $E_x^{KS}[\rho]$. Its contribution is manifested via the Kohn–Sham orbitals generated via the potential $v_x(\mathbf{r})$. The functional $E_x^{KS}[\rho]$ is thus expressed in virial form entirely in terms of the Pauli field $\mathscr{E}_x^{KS}(\mathbf{r})$. In this article, we determine and study the structure of the correlation–kinetic component field $\mathbf{Z}_{t_c}^{(1)}(\mathbf{r})$ and work $W_{t_c}^{(1)}(\mathbf{r})$ for the nonuniform electron density system in atoms and at metal surfaces. © 1997 John Wiley & Sons, Inc. Int J Quant Chem **65**: 893–906, 1997

Introduction

The Kohn–Sham [1] (KS) density functional theory [2, 3] "exchange–correlation" energy functional $E_{xc}^{KS}[\rho]$ of the density $\rho(\mathbf{r})$ and its functional derivative (potential) $v_{xc}(\mathbf{r}) = \delta E_{xc}^{KS}[\rho]/\delta\rho(\mathbf{r})$ incorporate correlations due to the Pauli exclusion principle and Coulomb repulsion as well as the correlation contribution to the kinetic energy. The functional and derivative also have a rigorous physical interpretation [4–7] in which they are described more insightfully in terms of these correlations. The interpretation involves a field $\mathscr{R}(\mathbf{r})$, which, in turn, is a sum of two fields. The first of these $\mathscr{E}_{xc}(\mathbf{r})$ accounts for Pauli and Coulomb

Correspondence to: V. Sahni.

Contract grant sponsor: Research Foundation of the City University of New York.

© 1997 John Wiley & Sons, Inc.
CCC 0020-7608 / 97 / 050893-14

correlations and is determined by Coulomb's law from its source which is the quantum mechanical Fermi–Coulomb hole charge distribution. The second $\mathbf{Z}_{t_c}(\mathbf{r})$ accounts for the correlation–kinetic contribution, and its source is the difference between the kinetic-energy–density tensors for the Kohn–Sham noninteracting and Schrödinger interacting systems. The corresponding field is the derivative of the resulting tensor. The functional derivative $v_{xc}(\mathbf{r})$ is the sum of the work $W_{xc}(\mathbf{r})$ and $W_{t_c}(\mathbf{r})$ done in the fields $\mathscr{E}_{xc}(\mathbf{r})$ and $\mathbf{Z}_{t_c}(\mathbf{r})$, respectively. Since the field $\mathscr{R}(\mathbf{r})$ is conservative, the sum of the work done is path-independent. The quantum mechanical exchange–correlation $E_{xc}[\rho]$ and correlation–kinetic $T_c[\rho]$ energy components of the functional $E_{xc}^{\mathrm{KS}}[\rho]$ can also be expressed in virial form in terms of the respective fields $\mathscr{E}_{xc}(\mathbf{r})$ and $\mathbf{Z}_{t_c}(\mathbf{r})$ which give rise to them. (As in Schrödinger theory, there is no self-interaction in the physical description [4, 5] of the Kohn–Sham theory electron-interaction energy functional and its derivative.)

In a similar vein, the KS theory "exchange" energy $E_x^{\mathrm{KS}}[\rho]$, and its functional derivative $v_x(\mathbf{r}) = \delta E_x^{\mathrm{KS}}[\rho]/\delta\rho(\mathbf{r})$, can also be described [8] in terms of a field representative of Pauli correlations and one representing *part* of the correlation–kinetic effect. Further, within the density functional theory representation [3, 9] of Hartree–Fock (HF) theory, it is also possible to define [5, 10] an "exchange" energy functional $E_x^{\mathrm{KSHF}}[\rho]$ and potential $v_x^{\mathrm{HF}}(\mathbf{r}) = \delta E_x^{\mathrm{KSHF}}[\rho]/\delta\rho(\mathbf{r})$, whereby the HF density and energy are obtained. This functional and derivative can also be described [4, 5, 10] in terms of a field representative of Pauli correlations as well as one representing the corresponding correlation–kinetic effects. Finally, in exchange-only [11, 12] density functional theory, the corresponding "exchange" energy functional $E_x^{\mathrm{OPM}}[\rho]$ and potential $v_x^{\mathrm{OPM}}(\mathbf{r})$ are defined [11] as those of the optimized potential method [13] (OPM). Once again, this energy and potential can be described [14] in terms of a field representative of Pauli correlations and one representing kinetic effects. The sum of these fields is again conservative. In each of the above cases, the field which accounts for Pauli correlations is obtained by Coulomb's law from a Fermi hole charge distribution. The resulting potential is then the work done to move an electron in the field. This field and potential have been studied previously [6, 15–21] for atoms and metal surfaces and their structure for these nonuniform density systems understood. The definitions of the corresponding kinetic components differ, but the fields and potentials are all derived in the same manner from kinetic-energy–density tensors. In this article, we determine and study the structure of the kinetic component of the KS "exchange" potential as applied to atoms and metal surfaces.

We begin in the next section by defining the "exchange" energy functionals and potentials for the cases discussed above. Although, in principle, the KS, HF, and OPM orbitals are different, in practice, their differences are minimal in that the structure of the corresponding local "exchange" potentials is essentially equivalent. In our calculations on atoms (third section), we, therefore, assume the KS "exchange" potential and orbitals to be those of the optimized potential method. For the metal surface calculations (fourth section), we employ an accurate representation of the KS "exchange" potential derived [18, 19] via restricted differentiation of the functional $E_x^{\mathrm{KS}}[\rho]$. This potential does, however, have the exact [22–24] structure of the KS "exchange" potential both in the asymptotic vacuum and metal bulk regions. A summary of the results and concluding remarks are made in the fifth section.

Definitions of "Exchange" Energy Functionals and Potentials in Terms of Fields

In this section, we define the "exchange" energy functional and potential in terms of fields within (a) the Kohn–Sham theory of the fully interacting system, (b) the Kohn–Sham theory representation of Hartree–Fock theory, and (c) the exchange-only Kohn–Sham theory.

KOHN–SHAM THEORY

In KS theory, the "exchange" potential $v_x(\mathbf{r})$, which is the derivative of the functional $E_x^{\mathrm{KS}}[\rho]$, is [8] the sum of a Pauli $W_x^{\mathrm{KS}}(\mathbf{r})$ and correlation–kinetic $W_{t_c}^{(1)}(\mathbf{r})$ component:

$$v_x(\mathbf{r}) = \frac{\delta E_x^{\mathrm{KS}}[\rho]}{\delta\rho(\mathbf{r})} = W_x^{\mathrm{KS}}(\mathbf{r}) - W_{t_c}^{(1)}(\mathbf{r}). \quad (1)$$

Here, $W_x^{\mathrm{KS}}(\mathbf{r})$ is the work done to move an electron in the field $\mathscr{E}_x^{\mathrm{KS}}(\mathbf{r})$ determined via Coulomb's law

from the Fermi hole charge $\rho_x^{KS}(\mathbf{r}, \mathbf{r}')$. Thus,

$$W_x^{KS}(\mathbf{r}) = -\int_\infty^{\mathbf{r}} \mathscr{E}_x^{KS}(\mathbf{r}') \cdot d\mathbf{l}', \tag{2}$$

where

$$\mathscr{E}_x^{KS}(\mathbf{r}) = \int \frac{\rho_x^{KS}(\mathbf{r}, \mathbf{r}')(\mathbf{r} - \mathbf{r}')}{|\mathbf{r} - \mathbf{r}'|^3} d\mathbf{r}'. \tag{3}$$

In turn, the Fermi hole $\rho_x^{KS}(\mathbf{r}, \mathbf{r}')$ at $\mathbf{r}'$ for an electron at $\mathbf{r}$ is defined in terms of the idempotent Dirac density matrix $\gamma_s(\mathbf{r}, \mathbf{r}')$ constructed with the KS orbitals $\psi_i(\mathbf{r})$ as

$$\rho_x^{KS}(\mathbf{r}, \mathbf{r}') = -|\gamma_s(\mathbf{r}, \mathbf{r}')|^2 / 2\rho(\mathbf{r}), \tag{4}$$

where

$$\gamma_s(\mathbf{r}, \mathbf{r}') = \sum_i \psi_i^*(\mathbf{r}) \psi_i(\mathbf{r}'), \tag{5}$$

such that $\gamma_s(\mathbf{r}, \mathbf{r}) = \rho(\mathbf{r})$. The work $W_{t_c}^{(1)}(\mathbf{r})$ is that done to move an electron in the field $\mathbf{Z}_{t_c}^{(1)}(\mathbf{r})$:

$$W_{t_c}^{(1)}(\mathbf{r}) = -\int_\infty^{\mathbf{r}} \mathbf{Z}_{t_c}^{(1)}(\mathbf{r}') \cdot d\mathbf{l}', \tag{6}$$

where

$$\mathbf{Z}_{t_c}^{(1)}(\mathbf{r}) = \frac{\mathbf{z}(\mathbf{r}; [\gamma_1^c])}{\rho(\mathbf{r})}. \tag{7}$$

The field $\mathbf{Z}_{t_c}^{(1)}(\mathbf{r})$ is further defined in terms of a field $\mathbf{z}(\mathbf{r}; [\gamma_1^c])$ whose component $z_\alpha(\mathbf{r})$ is derived from the kinetic-energy–density tensor $t_{\alpha\beta}(\mathbf{r}; [\gamma_1^c])$ as

$$z_\alpha(\mathbf{r}; [\gamma_1^c]) = 2 \sum_{\beta=1}^{3} \frac{\partial}{\partial r_\beta} t_{\alpha\beta}(\mathbf{r}; [\gamma_1^c]), \tag{8}$$

where

$$t_{\alpha\beta}(\mathbf{r}; [\gamma_1^c]) = \frac{1}{4} \left(\frac{\partial^2}{\partial r'_\alpha \partial r''_\beta} + \frac{\partial^2}{\partial r'_\beta \partial r''_\alpha} \right) \gamma_1^c(\mathbf{r}', \mathbf{r}'')|_{\mathbf{r}' = \mathbf{r}'' = \mathbf{r}}, \tag{9}$$

and $\gamma_1^c(\mathbf{r}, \mathbf{r}')$ is the first-order correction to the KS density matrix $\gamma_s(\mathbf{r}, \mathbf{r}')$ as obtained via perturbation theory by an expansion of the system wave function in terms of the electron-interaction coupling constant. The sum of the work $[W_x^{KS}(\mathbf{r}) - W_{t_c}^{(1)}(\mathbf{r})]$ is path-independent since $\nabla \times [\mathscr{E}_x^{KS}(\mathbf{r}) - \mathbf{Z}_{t_c}^{(1)}(\mathbf{r})] = 0$. The expression for the exchange potential $v_x(\mathbf{r})$ of Eq. (1) is *exact* [8], because it incorporates *all* terms linear in the coupling constant. Higher-order perturbation theory leads to the correlation component of the KS energy and potential.

There is no explicit correlation–kinetic contribution [8] to the KS "exchange" energy $E_x^{KS}[\rho]$. The contribution, however, is manifested indirectly via the KS orbitals $\psi_i(\mathbf{r})$, so that $E_x^{KS}[\rho]$, which is also related to its functional derivative $v_x(\mathbf{r})$ by the virial theorem [25], is expressed [4] entirely in terms of the field $\mathscr{E}_x^{KS}(\mathbf{r})$ as

$$E_x^{KS}[\rho] = \frac{1}{2} \int\int \frac{\rho(\mathbf{r}) \rho_x^{KS}(\mathbf{r}, \mathbf{r}')}{|\mathbf{r} - \mathbf{r}'|} d\mathbf{r}\, d\mathbf{r}', \tag{10}$$

$$= -\int \rho(\mathbf{r}) \mathbf{r} \cdot \nabla v_x(\mathbf{r})\, d\mathbf{r}, \tag{11}$$

$$= \int \rho(\mathbf{r}) \mathbf{r} \cdot \mathscr{E}_x^{KS}(\mathbf{r})\, d\mathbf{r}, \tag{12}$$

with

$$\int \rho(\mathbf{r}) \mathbf{r} \cdot \mathbf{Z}_{t_c}^{(1)}(\mathbf{r})\, d\mathbf{r} = 0. \tag{13}$$

KOHN–SHAM REPRESENTATION OF HARTREE–FOCK THEORY

The KS "exchange" energy functional $E_x^{KSHF}[\rho]$ which leads to the HF theory ground-state energy and density is defined as [4, 5, 10]

$$E_x^{KSHF}[\rho] = E_x^{HF}[\rho; \gamma^{HF}] + T_c^{HF}[\rho], \tag{14}$$

where $E_x^{HF}[\rho; \gamma^{HF}]$ is the HF theory exchange energy determined from the idempotent Dirac density matrix $\gamma^{HF}(\mathbf{r}, \mathbf{r}')$ constructed from the HF orbitals $\phi_i^{HF}(\mathbf{r})$. [The definitions of these properties are the same as Eqs. (4), (5), and (10) with $\psi_i(\mathbf{r})$ replaced by $\phi_i^{HF}(\mathbf{r})$.] The correlation–kinetic energy $T_c^{HF}[\rho]$ is defined as

$$T_c^{HF}[\rho] = T^{HF}[\rho] - T_s[\rho], \tag{15}$$

where $T^{HF}[\rho]$ is the HF theory kinetic energy, and $T_s[\rho]$, the kinetic energy of noninteracting fermions obtained from orbitals of the KS equation which leads to the HF theory density and energy.

The exchange energy $E_x^{HF}[\rho; \gamma^{HF}]$ component is defined in terms of an electric field $\mathscr{E}_x^{HF}(\mathbf{r})$ derived via Coulomb's law from the HF theory Fermi hole $\rho_x^{HF}(\mathbf{r}, \mathbf{r}')$ in the same manner as Eq. (12).

The correlation–kinetic energy $T_c^{HF}[\rho]$ component is expressed in terms of a field $\mathbf{Z}_{t_c}^{HF}(\mathbf{r})$ as

$$T_c^{HF}[\rho] = \frac{1}{2}\int d\mathbf{r}\rho(\mathbf{r})\mathbf{r}\cdot\mathbf{Z}_{t_c}^{HF}(\mathbf{r}), \qquad (16)$$

where

$$\mathbf{Z}_{t_c}^{HF}(\mathbf{r}) = \frac{1}{\rho(\mathbf{r})}\left[\mathbf{z}(\mathbf{r};[\gamma_s^{HF}]) - \mathbf{z}(\mathbf{r};[\gamma^{HF}])\right], \quad (17)$$

the field $\mathbf{z}(\mathbf{r})$ is as defined by Eqs. (8) and (9), and $\gamma_s^{HF}(\mathbf{r},\mathbf{r}')$ is the idempotent density matrix constructed from the orbitals of the KS equation which leads to the HF density and energy.

The KS exchange potential $v_x^{HF}(\mathbf{r})$ which generates the HF theory density and energy is

$$v_x^{HF}(\mathbf{r}) = \frac{\delta E_x^{KSHF}[\rho]}{\delta\rho(\mathbf{r})} = W_x^{HF}(\mathbf{r}) + W_{t_c}^{HF}(\mathbf{r}), \quad (18)$$

where $W_x^{HF}(\mathbf{r})$ and $W_{t_c}^{HF}(\mathbf{r})$ are, respectively, the work done in the fields $\mathscr{E}_x^{HF}(\mathbf{r})$ and $\mathbf{Z}_{t_c}^{HF}(\mathbf{r})$. [See Eqs. (2) and (6).] Once again, the sum of the work $[W_x^{HF}(\mathbf{r}) + W_{t_c}^{HF}(\mathbf{r})]$ is path-independent since $\nabla \times [\mathscr{E}_x^{HF}(\mathbf{r}) + \mathbf{Z}_{t_c}^{HF}(\mathbf{r})] = 0$.

KOHN–SHAM EXCHANGE-ONLY THEORY

The exchange-only [11, 12] version of KS theory corresponds to the optimized potential method [13] (OPM). The resulting exchange energy $E_x^{OPM}[\rho;\gamma_s^{OPM}]$ and potential $v_x^{OPM}(\mathbf{r})$ are determined by a self-consistent solution of the OPM integral and differential equations. The exchange energy is obtained through Eq. (10) via the Fermi hole $\rho_x^{OPM}(\mathbf{r},\mathbf{r}')$ or density matrix $\gamma_s^{OPM}(\mathbf{r},\mathbf{r}')$ constructed from the OPM orbitals $\phi_i^{OPM}(\mathbf{r})$. The potential $v_x^{OPM}(\mathbf{r})$ may be expressed as [14]

$$v_x^{OPM}(\mathbf{r}) = W_x(\mathbf{r}) + W_{t_s}(\mathbf{r}), \qquad (19)$$

where $W_x(\mathbf{r})$ is the work done in the field $\mathscr{E}_x(\mathbf{r})$ determined via Coulomb's law [see Eq. (2)] from the Fermi hole $\rho_x(\mathbf{r},\mathbf{r}')$ constructed from the orbitals $\phi_i^{WF}(\mathbf{r})$ of the Work Formalism [21, 26] (WF) differential equation. [This equation is the same as the KS differential equation with $v_{xc}(\mathbf{r})$ replaced by $W_x(\mathbf{r})$.] With $\gamma_s^{WF}(\mathbf{r},\mathbf{r}')$, the corresponding idempotent density matrix, the work $W_{t_s}(\mathbf{r})$ is that done in the field $\mathbf{Z}_{t_s}(\mathbf{r})$, where

$$\mathbf{Z}_{t_s}(\mathbf{r}) = \frac{1}{\rho(\mathbf{r})}\left[\mathbf{z}(\mathbf{r};[\gamma_s^{OPM}]) - \mathbf{z}(\mathbf{r};[\gamma_s^{WF}])\right] \quad (20)$$

and where the field $\mathbf{z}(\mathbf{r})$ is as defined previously in terms of the appropriate kinetic-energy–density tensor. [See Eqs. (8) and (9).] In this exchange-only case, the virial theorem [25] leads to the energy relation

$$E_x^{OPM}[\rho;\gamma_s^{OPM}] - E_x^{WF}[\rho;\gamma_s^{WF}] = \int \rho(\mathbf{r})\mathbf{r}\cdot\mathbf{Z}_{t_s}(\mathbf{r})\,d\mathbf{r}. \quad (21)$$

We note that in the derivation of Eq. (19) it is assumed that the OPM and WF densities are equivalent, which is essentially the case for both finite and extended systems. However, the off-diagonal elements of $\gamma_s^{OPM}(\mathbf{r},\mathbf{r}')$ and $\gamma_s^{WF}(\mathbf{r},\mathbf{r}')$ are not assumed to be equivalent so that the field $\mathbf{Z}_{t_s}(\mathbf{r})$ is finite. Furthermore, the work $W_x(\mathbf{r})$ and $W_{t_s}(\mathbf{r})$ are separately path-independent.

To summarize, the exchange potential of KS theory [Eq. (1)] and that of its representation of HF theory [Eq. (18)] and of the OPM [Eq. (19)] are all composed of two components. The first, representative of Pauli correlations, is the work done in a field determined by Coulomb's law from the Fermi hole charge constructed with the corresponding orbitals. The second, representative of correlation–kinetic effects, is the work done in a field determined from a corresponding kinetic-energy–density tensor.

Structure of Correlation–Kinetic Field and Potential in Atoms

To determine an accurate representation of the correlation–kinetic field $\mathbf{Z}_{t_c}^{(1)}(\mathbf{r})$ and potential $W_{t_c}^{(1)}(\mathbf{r})$ in atoms, we assume the KS exchange potential $v_x(\mathbf{r})$ to be that of the optimized potential method $v_x^{OPM}(\mathbf{r})$. We then determine the work $W_x(\mathbf{r})$ by a self-consistent solution of the Work Formalism differential equation. In other words, we assume the "exchange" problem to be defined by the case described by Eq. (19). We, however, refer to the potentials $v_x^{OPM}(\mathbf{r})$ and $W_x(\mathbf{r})$ as the KS exchange potential $v_x(\mathbf{r})$ and its Pauli component $W_x^{KS}(\mathbf{r})$, respectively, since, as noted, the difference between the two sets of potentials is minimal. The differences $[\nabla v_x(\mathbf{r}) - \mathscr{E}_x^{KS}(\mathbf{r})]$ and $[v_x(\mathbf{r}) - W_x^{KS}(\mathbf{r})]$

are then the correlation–kinetic field $\mathbf{Z}_{t_c}^{(1)}(\mathbf{r})$ and potential $W_{t_c}^{(1)}(\mathbf{r})$, respectively.

In Figures 1 and 2, we plot the Pauli component field $\mathscr{E}_x^{\mathrm{KS}}(r)$ due to the Fermi hole charge for Ne and Ar atoms. Note the shell structure as exhibited by the field and the fact that it exists primarily within the K-shell, becoming less significant in the outer shells, decaying asymptotically as $-1/r^2$. In Figures 3 and 4, we plot the corresponding correlation–kinetic component field $Z_{t_c}^{(1)}(r)$ for these atoms. In these graphs, we also indicated the radial probability density, so that it is evident that the field $Z_{t_c}^{(1)}(r)$ exists principally in the intershell region and is oscillatory there. Furthermore, the magnitude of this field is greatest in the region between the K and L shells, becoming much smaller in the outer intershell regions. The field $Z_{t_c}^{(1)}(r)$ is also short-ranged in comparison to the Pauli field $\mathscr{E}_x^{\mathrm{KS}}(r)$, vanishing at about the commencement of the outermost occupied shell. It is also interesting to note that there is a small component of this field present in the interior of the atom. Finally, observe that the field $Z_{t_c}^{(1)}(r)$ is much smaller, about a fifth of the magnitude of the Pauli field $\mathscr{E}_x^{\mathrm{KS}}(r)$.

In Figures 5 and 6, we plot the Pauli $W_x^{\mathrm{KS}}(r)$ and correlation–kinetic $W_{t_c}^{(1)}(r)$ components of the KS "exchange" potential $v_x(r)$ for Ne and Ar, respectively. As known [6], the Pauli component $W_x^{\mathrm{KS}}(r)$ exhibits a shell structure and is monotonic with a positive slope since the field $\mathscr{E}_x^{\mathrm{KS}}(r)$ is negative throughout space. It decays asymptotically as $-1/r$ in the classically forbidden region as does $v_x(r)$. Since the correlation–kinetic field $Z_{t_c}^{(1)}(r)$ is oscillatory and exists in the intershell regions, the corresponding potential $W_{t_c}^{(1)}(r)$ exhibits a dip in these regions, vanishing well within the outermost occupied shell. It is this correlation–kinetic component which then gives rise to the well-known bumps of the KS potential $v_x(r)$ in the

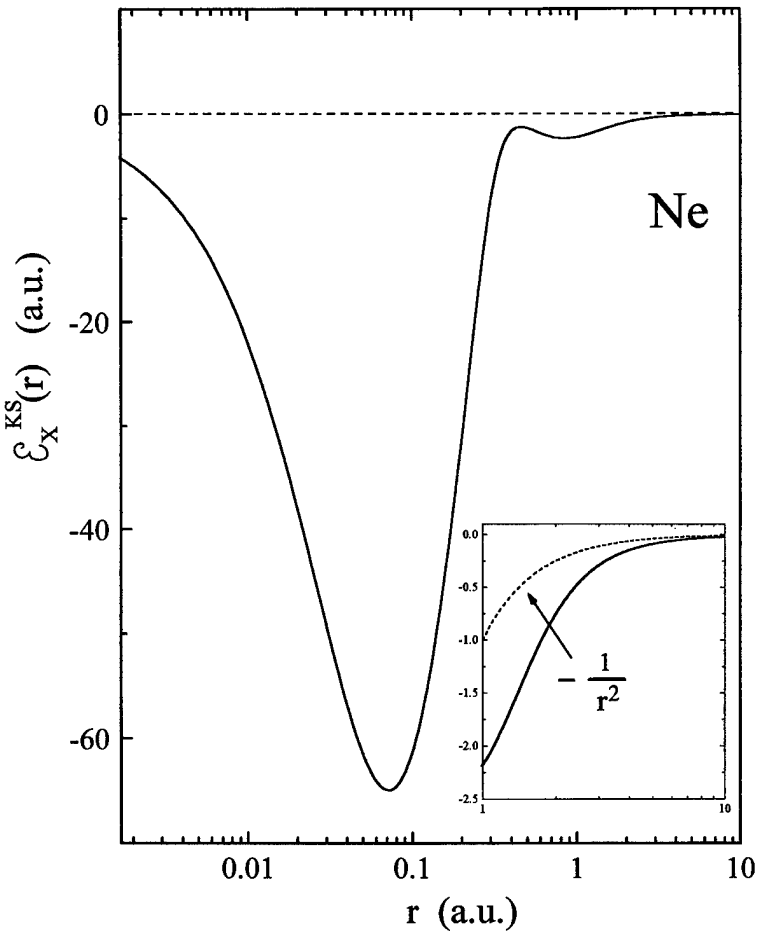


FIGURE 1. The Pauli component field $\mathscr{E}_x^{\mathrm{KS}}(r)$ for the Ne atom.

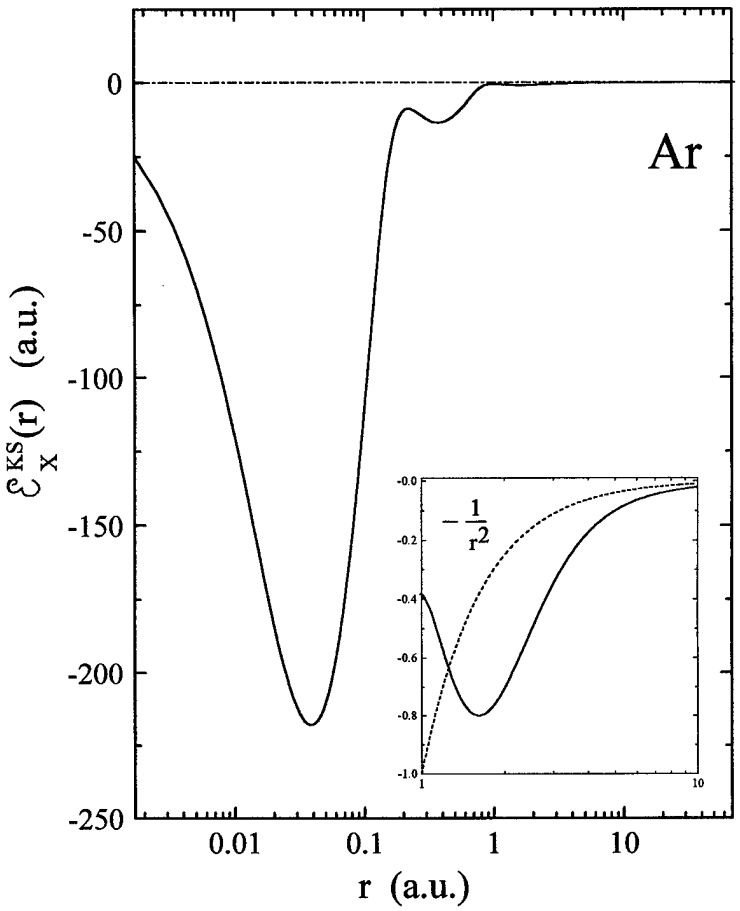


FIGURE 2. The Pauli component field $\mathcal{E}_x^{KS}(r)$ for the Ar atom.

intershell regions. Again, we note that there is a small component of this potential in the interior of atoms. Finally, observe that $W_{t_c}^{(1)}(r)$ is an order of magnitude smaller than the Pauli potential $W_x^{KS}(r)$. Thus, the correlation–kinetic effects contributing to the KS potential $v_x(r)$ are small. As such, it is justified to represent the potential $v_x(r)$ in finite systems by its Pauli component $W_x^{KS}(r)$. The high accuracy of this approximation with regard to total ground- and excited-state energies, ionization potentials, and electron affinities has been demonstrated in the literature [4, 5, 15, 21, 26].

Structure of Correlation-Kinetic Field and Potential at Metal Surfaces

For the jellium [27] and structureless pseudopotential [28] models of a metal surface, there is translational symmetry in the plane parallel to the surface and the effective potential of the electrons is local. Thus, the KS orbitals are of the form

$$\psi_{\mathbf{k}}(\mathbf{r}) = \sqrt{\frac{2}{V}}\, e^{i\mathbf{k}_{\parallel}\cdot\mathbf{x}_{\parallel}} \phi_k(x), \qquad (22)$$

where $(\mathbf{k}_{\parallel}, \mathbf{x}_{\parallel})$ are the momentum and position vectors parallel to the surface, and (k, x), the components perpendicular to it. The metal is assumed to occupy the negative half-space. For these models, the *exact* asymptotic structure of the KS "exchange" potential $v_x(\mathbf{r})$ and of its Pauli component $W_x^{KS}(\mathbf{r})$ in the classically forbidden vacuum region has been determined [20, 22–24]. The *analytical* expressions for these structures which are valid for *fully self-consistently* determined orbitals show both potentials to decay in an $-x^{-1}$ image-potential-like manner, but with different decay coefficients which depend upon the metal Fermi energy and surface barrier height. Thus [see Eq. (1)], the asymptotic

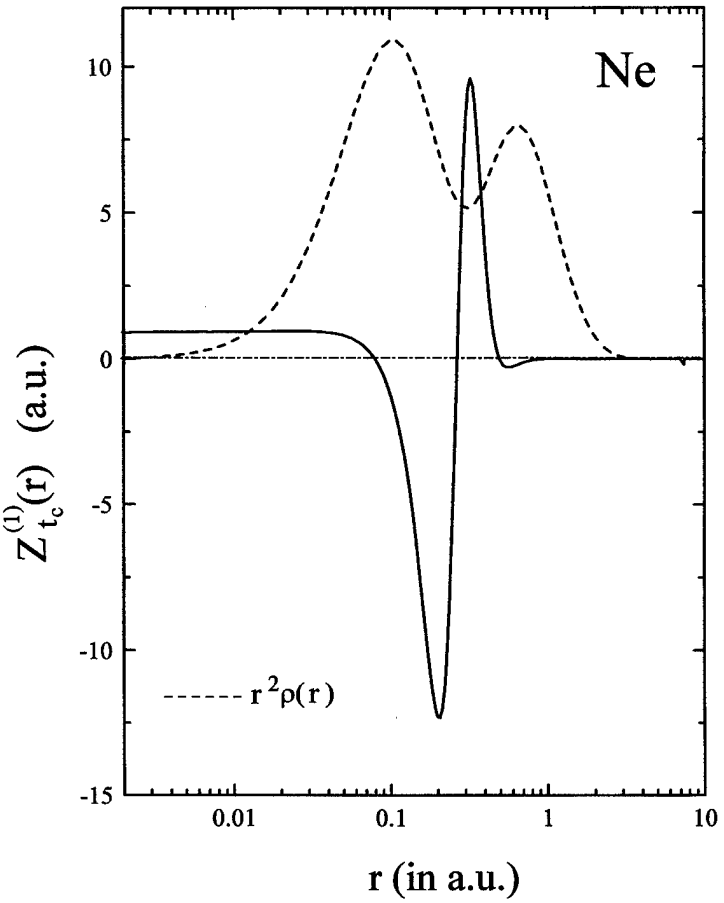


FIGURE 3. The correlation–kinetic component field $Z^{(1)}_{t_c}(r)$ for the Ne atom. The radial probability density is plotted as the dashed line.

structure of the correlation–kinetic component $W^{(1)}_{t_c}(\mathbf{r})$ is also known *exactly* to decay as

$$W^{(1)}_{t_c}(x) \underset{x\to\infty}{=} \frac{\alpha^{(1)}_{t_c}(\beta)}{x}, \tag{23}$$

where the decay coefficient is

$$\alpha^{(1)}_{t_c}(\beta) = \frac{\beta^2-1}{2\beta^2}\left[1 - 2\frac{\beta^2-2}{\beta^2} - \frac{4}{\pi\sqrt{\beta^2-1}} \times\left\{1 + \frac{4-3\beta^2}{\beta^2}\ln(\beta^2-1)\right\}\right] \tag{24}$$

and where $\beta^2 = W/\epsilon_F$, with W the barrier height, $\epsilon_F = k_F^2/2$ the Fermi energy, $k_F = 1/\alpha r_s$ the Fermi momentum, $\alpha^{-1} = (9\pi/4)^{1/3}$, and r_s the Wigner–Seitz radius. The asymptotic value of the KS "exchange" potential in the metal bulk is also known to be exactly

$$v_x(x) \underset{x\to-\infty}{=} -k_F/\pi.$$

For the KS "exchange" potential $v_x(\mathbf{r})$, we employ an accurate representation of it derived [18, 19] by restricted differentiation of the energy functional $E_x^{\mathrm{KS}}[\rho]$. The resulting expression $v_x^{(0)}(\mathbf{r})$ for the potential which is in terms of the density $\rho(\mathbf{r})$ and Slater potential [29] $V_x^S(\mathbf{r})$ is

$$v_x^{(0)}(\mathbf{r}) = \frac{1}{2d\rho(\mathbf{r})/dk_F}\frac{d}{dk_F}(\rho(\mathbf{r})V_x^S(\mathbf{r})), \tag{25}$$

where $V_x^S(\mathbf{r})$ is defined as

$$V_x^S(\mathbf{r}) = \int \frac{\rho_x^{\mathrm{KS}}(\mathbf{r},\mathbf{r}')}{|\mathbf{r}-\mathbf{r}'|}\,d\mathbf{r}'. \tag{26}$$

Thus, the potential $v_x^{(0)}(\mathbf{r})$ incorporates the intrinsic nonlocality of the problem through the dynamic

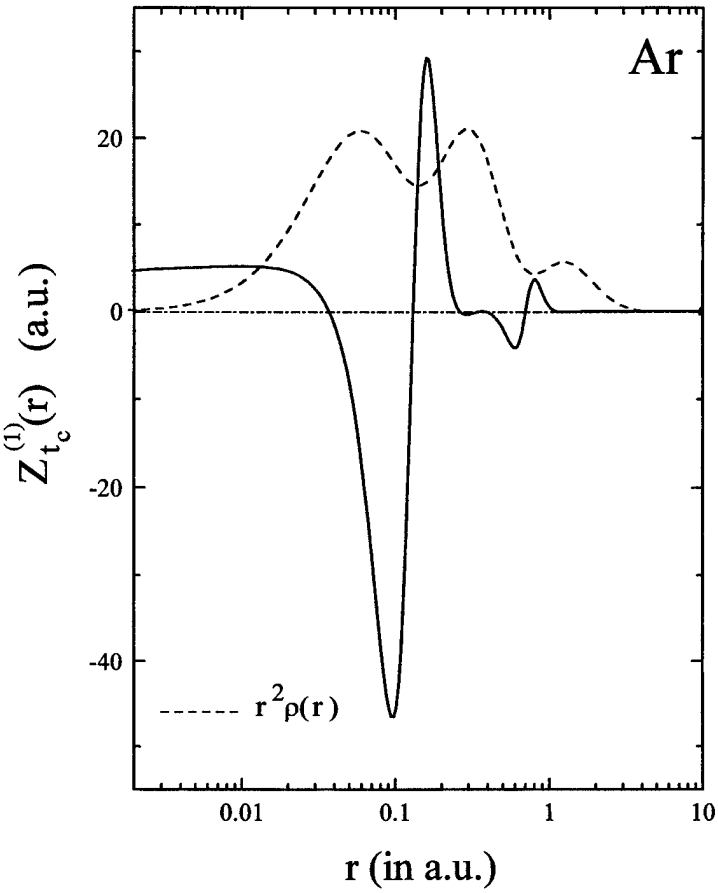


FIGURE 4. The correlation–kinetic component field $Z_{t_c}^{(1)}(r)$ for the Ne atom. The radial probability density is plotted as the dashed line.

Fermi hole charge. It also possesses [18, 22, 24] the correct asymptotic structure of $v_x(\mathbf{r})$ in both the asymptotic vacuum and metal–bulk regions.

Now for the orbitals of Eq. (22), the expression for the Slater potential in dimensionless coordinates normalized to the Fermi momentum is [22–24]

$$\frac{V_x^S(z)}{(3k_F/2\pi)} = -\frac{4}{\pi\rho_n(z)} \times \int_0^1 dk' \int_0^{k'} dk \phi_k^*(z)\phi_{k'}(z) G(k, k'; z), \quad (27)$$

where

$$G(k, k'; z) = \pi\lambda'^2 \int_0^{(\lambda^2-\lambda'^2)^{1/2}} dq J(q, z) + \int_{\lambda-\lambda'}^{\lambda+\lambda'} dq J(q, z)\{S_\lambda(q) + S_{\lambda'}(q)\},$$

$$J(q, z) = 2\int_{-\infty}^{\infty} dz' e^{-q|z-z'|}\phi_k(z')\phi_{k'}^*(z'),$$

$$S_\lambda(q) = \lambda^2 \tan^{-1}\frac{(\lambda^2 - X_\lambda^2)^{1/2}}{X_\lambda} - X_\lambda(\lambda^2 - X_\lambda^2)^{1/2},$$

$$S_{\lambda'}(q) = S_\lambda(q)|_{\lambda\to\lambda'},$$

$$X_{\lambda,\lambda'}(q) = \frac{1}{2}\left(q \pm \frac{\lambda^2 - \lambda'^2}{q}\right)$$

and where $\rho_n(z)$ is the density normalized to the bulk value $\bar{\rho} = k_F^3/3\pi^2$:

$$\rho_n(z) = 3\int_0^1 (1 - k^2)|\phi_k(z)|^2 dk. \quad (28)$$

In these equations, $\lambda = (1 - k^2)^{1/2}$, $\lambda' = (1 - k'^2)^{1/2}$, and $z = k_F x$. The expression for the Pauli

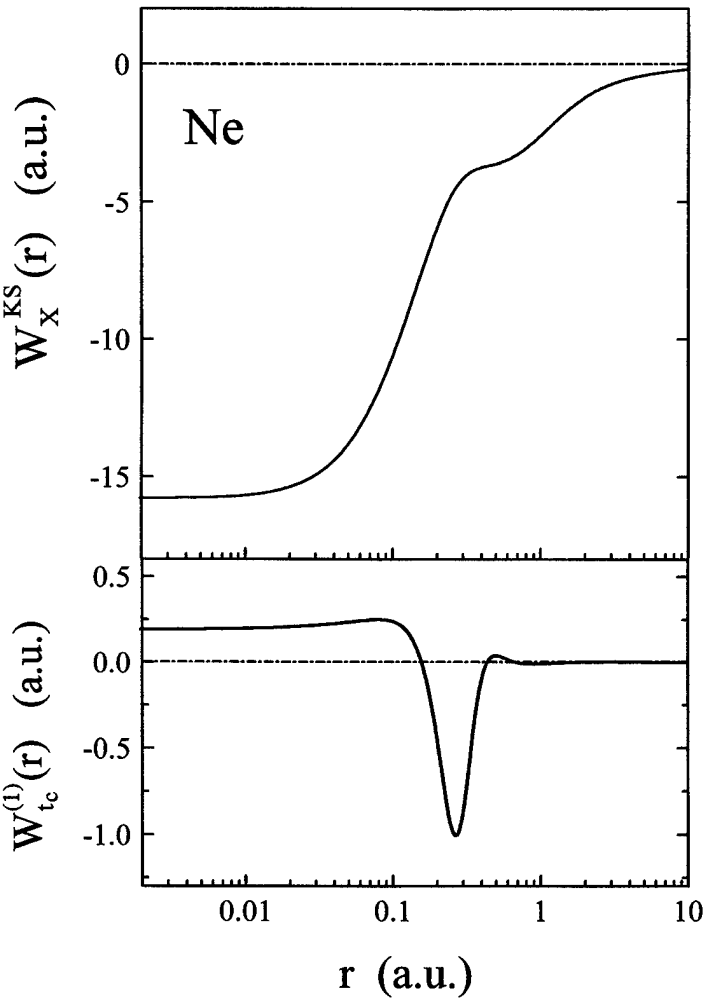


FIGURE 5. The Pauli $W_x^{KS}(r)$ and correlation–kinetic $W_{t_c}^{(1)}(r)$ potentials for the Ne atom.

component field $\mathscr{E}_x^{KS}(\mathbf{r})$ is [20]

$$\frac{\mathscr{E}_x^{KS}(z)}{(3k_F^2/2\pi)} = -\frac{4}{\pi\rho_n(z)} \times \int_0^1 dk' \int_0^{k'} dk \phi_k^*(z)\phi_{k'}(z)H(k,k';z), \quad (29)$$

where

$$H(k,k';z) = \pi\lambda'^2 \int_0^{(\lambda^2-\lambda'^2)^{1/2}} dqqM(q,z) + \int_{\lambda-\lambda'}^{\lambda+\lambda'} dqqM(q,z)\{S_\lambda(q) + S_{\lambda'}(q)\},$$

$$M(q,z) = 2\int_{-\infty}^{\infty} dz' sgn(z-z')e^{-q|z-z'|}\phi_k(z')\phi_k^*(z').$$

The work done $W_x^{KS}(z)$ is then

$$\frac{W_x^{KS}(z)}{(3k_F/2\pi)} = -\int_\infty^z \frac{\mathscr{E}_x^{KS}(z')}{(3k_F^2/2\pi)} dz'. \quad (30)$$

For orbitals generated by model effective potentials, the spatial integrals $J(q,z)$ and $M(q,z)$ above can be determined analytically. Thus, for such orbitals, the Slater potential $V_x^S(z)$ and the field $\mathscr{E}_x^{KS}(z)$ are then *entirely* in terms of finite-region momentum-space integrals and therefore easily determined for *all*-electron positions throughout space.

The expressions for the Slater potential $V_x^S(z)$ of Eq. (27) and of the work $W_x^{KS}(z)$ of Eq. (30) are valid for arbitrary orbitals $\phi_k(z)$. In our calculations, we employ those of the jellium and finite-linear-potential model [30] of a metal surface. The

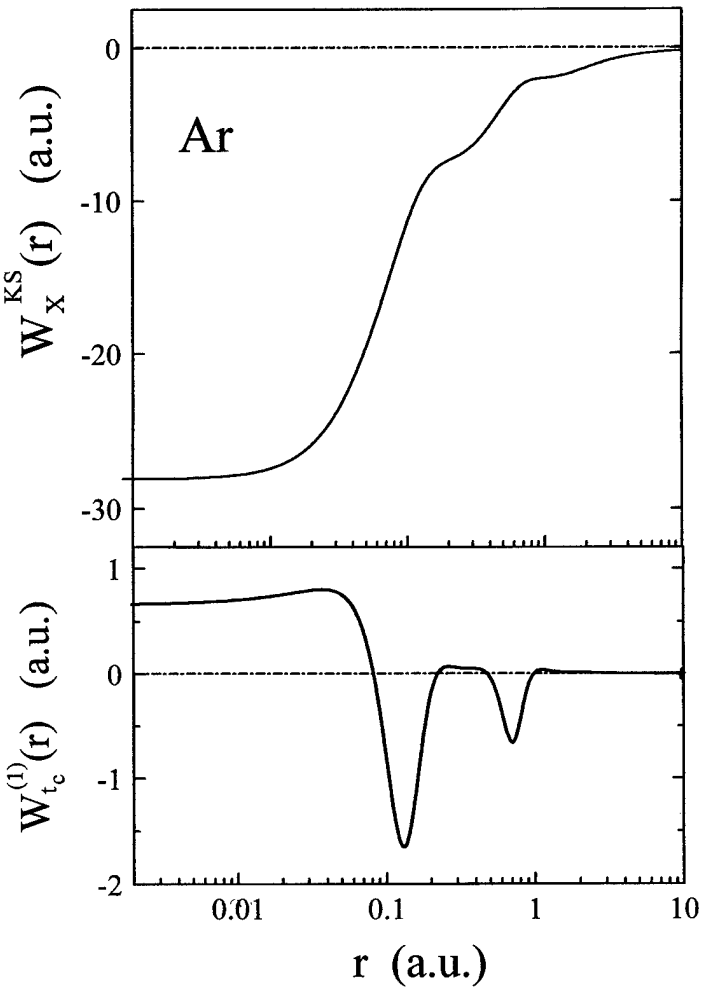


FIGURE 6. The Pauli $W_x^{KS}(r)$ and correlation–kinetic $W_{t_c}^{(1)}(r)$ potentials for the Ar atom.

advantage of employing these orbitals is that they are semianalytical and lead to results essentially equivalent [17] to those of fully self-consistent calculations. Furthermore, as noted above, the integrals $J(q, z)$ and $M(q, z)$ can then be obtained analytically. The KS effective potential for this model is

$$v_{eff}(z) = Fz[\theta(z) - \theta(z - z_b)] + W\theta(z - z_b), \tag{31}$$

for which the orbitals $\phi_k(z)$ are

$$\begin{aligned}\phi_k(z) = \sin[kz + \delta(k)]\theta(-z) \\ + [B_k\, Ai(\zeta_k) + C_k\, Bi(\zeta_k)] \\ \times [\theta(z) - \theta(z - z_b)] \\ + D_k \exp(-\kappa_k z)\theta(z - z_b),\end{aligned} \tag{32}$$

where $k = \sqrt{2E}$, $\kappa_k = \sqrt{2(W - E)}$, $\zeta_k = zz_F^{-1/3} - \zeta_0$, $\zeta_0 = k^2 z_F^{2/3}$, $F = (k_F^2/2)/z_F$, $z_F = (k_F^2/2)z_b/W$, E is the energy, W is the barrier height, and $Ai(\zeta_k)$ and $Bi(\zeta_k)$ are the Airy functions. The phase factor $\delta(k)$ and the coefficients B_k, C_k, and D_k are determined by the requirement of continuity of the wave function and its logarithmic derivative at $z = 0$ and $z = z_b$.

The correlation–kinetic component field $Z_{t_c}^{(1)}(z)$ and potential $W_{t_c}^{(1)}(z)$ are determined in a manner similar to that for atoms, except that the *same* orbitals $\phi_k(z)$ are employed in the calculation of the potentials $v_x^{(0)}(z)$ and $W_x^{KS}(z)$. In Figures 7 and 8, we plot for Li metal ($r_s = 3.24$) the Pauli $\mathscr{E}_x^{KS}(z)$ and correlation–kinetic $Z_{t_c}^{(1)}(z)$ fields, respectively, employing the orbitals of Eq. (32). The relationship between r_s and β is determined via energy minimization in the local density approximation. The

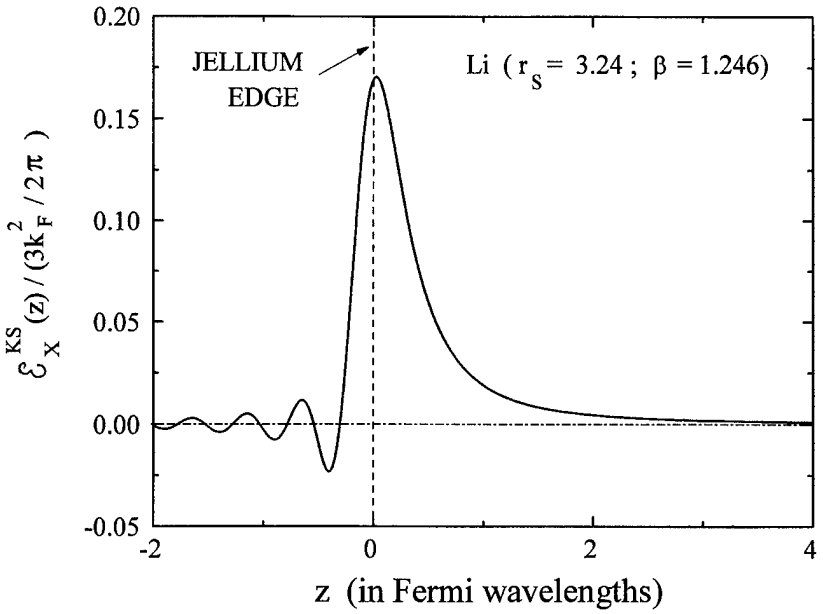


FIGURE 7. The Pauli component field $\mathscr{E}_x^{KS}(z)$ at the surface of the Li metal.

corresponding value of $\beta = 1.246$. (See Appendix of [17].) [The field $\mathscr{E}_x^{KS}(z)$ is also plotted elsewhere [16, 17, 20] for $r_s = 2.0$ and 6.0. For purposes of completeness, we include it here for Li metal.] Observe that both fields are concentrated in the surface region and possess the requisite Bardeen–Friedel [27] oscillations in the metal bulk. However, as in the atomic case, the correlation–kinetic field is an order of magnitude weaker than is the Pauli field. Observe that both fields decay many Fermi wavelengths into the vacuum region. (For Li metal, one Fermi wavelength is 5.61 Å.) The correctness of the asymptotic structure of the field $Z_{t_c}^{(1)}(z)$ in the vacuum region is demonstrated in

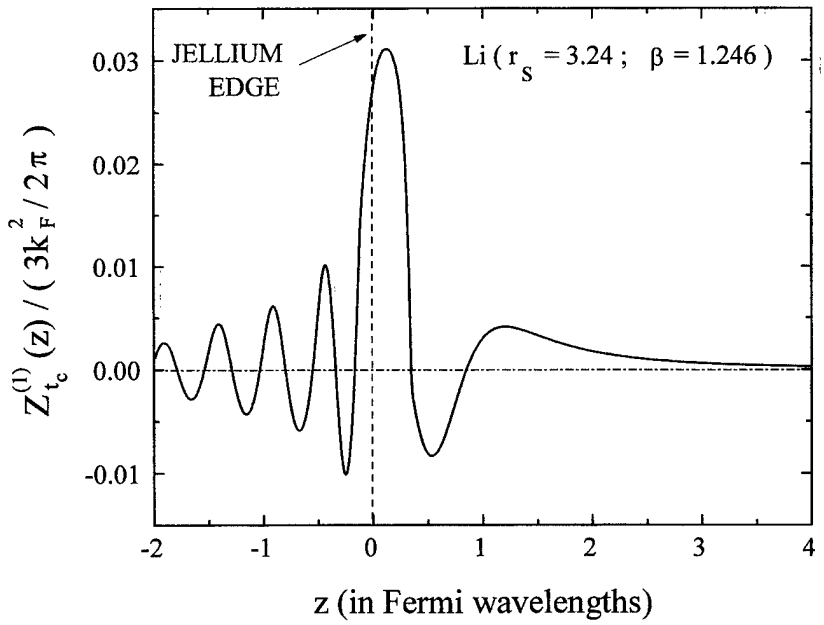


FIGURE 8. The correlation–kinetic field $Z_{t_c}^{(1)}(z)$ at the surface of the Li metal.

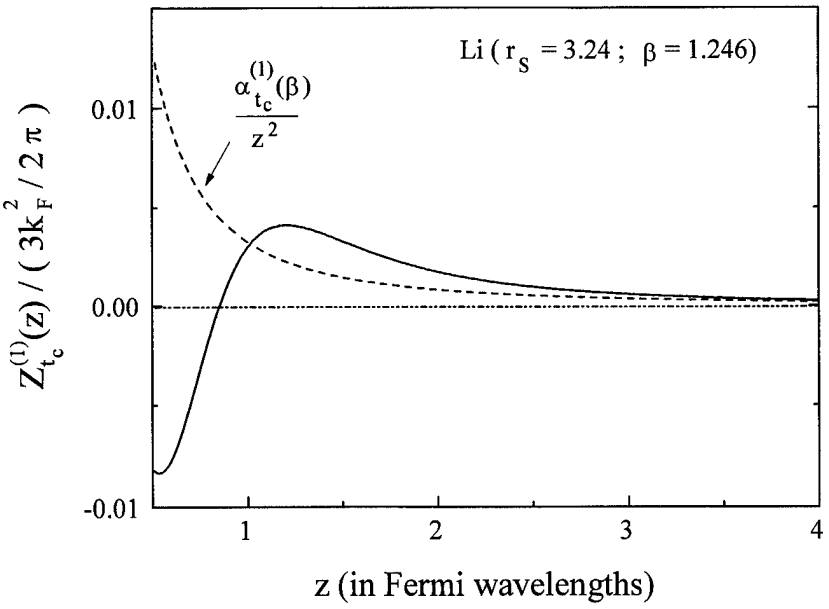


FIGURE 9. Comparison of the asymptotic structure of the correlation–kinetic field $Z_{t_c}^{(1)}(z)$ at the surface of the Li metal with its exact analytical asymptotic structure $\alpha_{t_c}^{(1)}(\beta)/z^2$.

Figure 9 where the exact analytical structure $\alpha_{t_c}^{(1)}(\beta)/z^2$ is also plotted. The calculated and exact structures can be observed to have merged at a distance of about four Fermi wavelengths from the surface.

In Figure 10, we plot the approximate KS exchange potential $v_x^{(0)}(z)$ and the work done $W_x^{KS}(z)$. The potential $v_x^{(0)}(z)$ which possesses the exact [22–24] asymptotic structure of the KS exchange potential $v_x(z)$ in the vacuum region achieves this

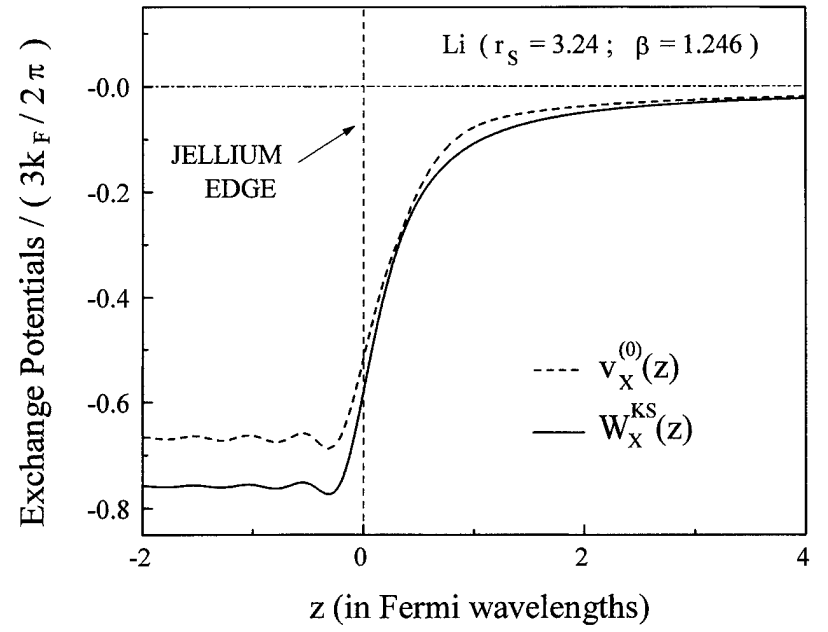


FIGURE 10. The approximation $v_x^{(0)}(z)$ to the Kohn–Sham exchange potential as determined by Eq. (25). The Pauli component $W_x^{KS}(z)$ of Eq. (30) is also plotted.

limit by about one Fermi wavelength from the surface. As is evident from the figure, it also has the correct limiting value of $-2/3$ (in units of $3k_F/2\pi$) of $v_x(z)$ in the metal bulk. The asymptotic structure of $W_x^{KS}(z)$ in the vacuum differs from that of the KS potential $v_x(z)$ as has been shown [20] analytically. The limiting value of $W_x^{KS}(z)$ in the metal bulk is also different [20], being -0.757 (in units of $3k_F/2\pi$) for Li metal. The resulting correlation–kinetic potential component $W_{t_c}^{(1)}(z)$ is plotted in Figure 11. Note that this potential is entirely positive and possesses the correct asymptotic structure of Eq. (23) in the vacuum. The potentials $v_x^{(0)}(z)$, $W_x^{KS}(z)$, and $W_{t_c}^{(1)}(z)$ all exhibit the Bardeen–Friedel oscillations within the metal. Once again, the potential $W_{t_c}^{(1)}(z)$ is an order of magnitude smaller than $W_x^{KS}(z)$. However, as the asymptotic structure of the KS potential $v_x(z)$ and its Pauli component $W_x^{KS}(z)$ differ in both the vacuum and metal bulk regions, the significance of the correlation–kinetic term $W_{t_c}^{(1)}(z)$ should be greater in the metal surface case than it is for atoms.

Conclusions and Summary

The KS "exchange" potential $v_x(\mathbf{r})$ is composed of a term $W_x^{KS}(\mathbf{r})$ representative of Pauli correlations and another $W_{t_c}^{(1)}(\mathbf{r})$ which constitutes part of the correlation–kinetic effects. These components of the potential $v_x(\mathbf{r})$ arise, respectively, from fields $\mathscr{E}_x^{KS}(\mathbf{r})$ and $\mathbf{Z}_{t_c}^{(1)}(\mathbf{r})$ representative of these correlations. In this article, we studied the structure of the correlation–kinetic field $\mathbf{Z}_{t_c}^{(1)}(\mathbf{r})$ and potential $W_{t_c}^{(1)}(\mathbf{r})$ as applied to finite atomic and extended metal surface systems. For these systems, this field and potential are about an order of magnitude smaller than the corresponding Pauli components. In atoms, the field $\mathbf{Z}_{t_c}^{(1)}(\mathbf{r})$ exists principally in the intershell regions and is oscillatory there. This then gives rise to a trough in the resulting potential $W_{t_c}^{(1)}(\mathbf{r})$ in these regions. Since the Pauli component $W_x^{KS}(\mathbf{r})$ is monotonic with a positive slope everywhere, the intershell bumps of the KS potential $v_x(\mathbf{r})$ can now be understood to be entirely a consequence of correlation–kinetic effects. Although there is a small component of the field $\mathbf{Z}_{t_c}^{(1)}(\mathbf{r})$ in the deep interior of atoms, this field is *short-ranged*, vanishing within the last occupied shell. The asymptotic structure $-1/r$ of $v_x(\mathbf{r})$ in the classically forbidden region is therefore due entirely to its Pauli component $W_x^{KS}(\mathbf{r})$. Since the field $\mathbf{Z}_{t_c}^{(1)}(\mathbf{r})$ in atoms is small and short-ranged, the KS potential $v_x(\mathbf{r})$ can be approximated accurately by its Pauli component $W_x^{KS}(\mathbf{r})$. This is borne out in the literature [4, 15]. For example, total ground-state energies of atoms with this approximation lie within 25 ppm of those of the OPM, being within 5 ppm for atoms heavier than Kr.

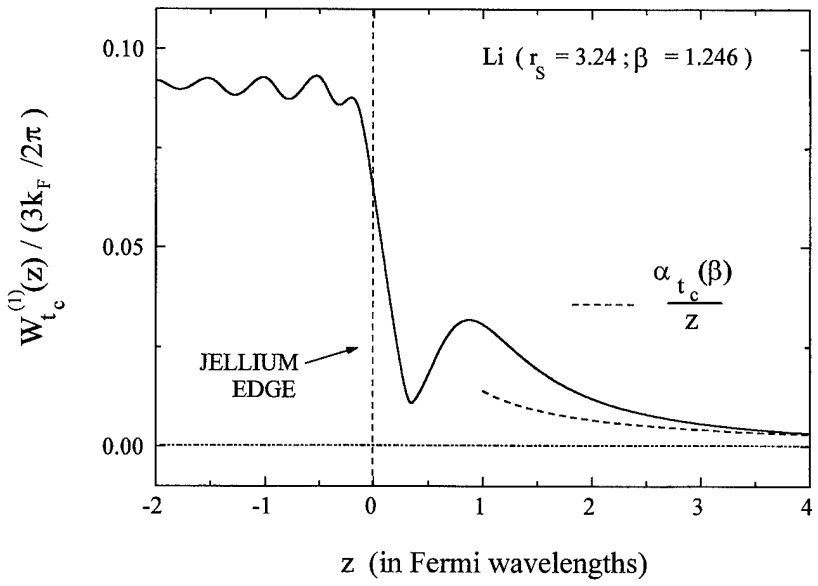


FIGURE 11. The correlation–kinetic component $W_{t_c}^{(1)}(z)$ of the approximate Kohn–Sham exchange potential $v_x^{(0)}(z)$. The function of $\alpha_{t_c}^{(1)}(\beta)/z$ is also plotted.

At a metal surface, the correlation–kinetic field $\mathbf{Z}_{t_c}^{(1)}(\mathbf{r})$ is concentrated mainly in the surface region. The field, however, is *long-ranged*. It decays asymptotically in the vacuum as [20] $\alpha_{t_c}^{(1)}/x^2$, with the coefficient $\alpha_{t_c}^{(1)}$ dependent upon the metal Fermi energy and surface barrier height. It also extends deep into the metal, exhibiting the requisite Bardeen–Friedel oscillations there. The resulting correlation–kinetic potential $W_{t_c}^{(1)}(\mathbf{r})$ is therefore also long-ranged in the vacuum with a structure of $(\alpha_{t_c}^{(1)}/x)$. Further, it too exhibits the Bardeen–Friedel oscillations in the metal and has a finite positive limiting value in the metal bulk. The Pauli component $W_x^{\mathrm{KS}}(\mathbf{r})$ is also long-ranged [20], with an $-x^{-1}$ image-potential-like structure in the vacuum similar to that of the KS potential $v_x(\mathbf{r})$, but with a decay coefficient that is different. In the metal bulk, $W_x^{\mathrm{KS}}(\mathbf{r})$ also has a finite (negative) limiting value which is close to but less than that of $v_x(\mathbf{r})$ which is $-k_F/\pi$. Thus, although the contribution of $v_x(\mathbf{r})$ to properties such as the surface energy and work function will be due principally to its Pauli component, we expect the correlation–kinetic contribution in this instant not to be insignificant. The long-range of both the Pauli and correlation–kinetic components of $v_x(\mathbf{r})$ in the vacuum is also of significance from the perspective of various surface probes such as the scanning-tunneling microscope as well as for the interaction of electrons, ions, and positrons with the surface.

ACKNOWLEDGMENT

This work was supported in part by a grant from the Research Foundation of the City University of New York.

References

1. W. Kohn and L. J. Sham, Phys. Rev. A **140**, 1133 (1965).
2. P. Hohenberg and W. Kohn, Phys. Rev. B **136**, 864 (1964).
3. R. G. Parr and W. Yang, *Density Functional Theory of Atoms and Molecules* (Oxford University Press, Oxford, 1989); R. M. Dreizler and E. K. U. Gross, *Density Functional Theory* (Springer-Verlag, Berlin, 1990); N. H. March, *Electron Density Theory of Atoms and Molecules* (Academic Press, London, 1992).
4. V. Sahni, in *Density Functional Theory III*, R. Nalewajski, Ed. [Top. Curr. Chem. **182**, 1 (1996)] (Springer-Verlag, Heidelberg, 1996).
5. V. Sahni, Phys. Rev. A **55**, 1846 (1997).
6. M. K. Harbola and V. Sahni, Phys. Rev. Lett. **62**, 489 (1989); V. Sahni and M. K. Harbola, Int. J. Quantum Chem. Symp. **24**, 569 (1990); M. K. Harbola and V. Sahni, J. Chem. Ed. **70**, 920 (1993). M. Slamet, V. Sahni, and M. K. Harbola, Phys. Rev. A **49**, 809 (1994); M. K. Harbola, M. Slamet, and V. Sahni, Phys. Lett. A **157**, 60 (1991).
7. A. Holas and N. H. March, Phys. Rev. A **51**, 2040 (1995).
8. M. Levy and N. H. March, Phys. Rev. A **55**, 1885 (1997).
9. M. Levy, Proc. Natl. Acad. Sci. U.S.A. **76**, 6062 (1979); P. W. Payne, J. Chem. Phys. **71**, 490 (1979); A. Holas, N. H. March, Y. Takahashi, and C. Zhang, Phys. Rev. A **48**, 2708 (1993).
10. A. Holas and N. H. March, in *Density Functional Theory I*, R. Nalewajski, Ed. [Top. Curr. Chem. **180**, 57 (1996)] (Springer-Verlag, Heidelberg, 1996).
11. V. Sahni, J. Gruenebaum, and J. P. Perdew, Phys. Rev. B **26**, 4371 (1982).
12. V. Sahni and M. Levy, Phys. Rev. B **33**, 3869 (1986); S. B. Trickey, Phys. Rev. B **30**, 3523 (1984); J. P. Perdew and M. R. Norman, Phys. Rev. B **30**, 3525 (1984).
13. R. T. Sharp and G. K. Horton, Phys. Rev. **30**, 317 (1953); J. D. Talman and W. F. Shadwick, Phys. Rev. A **14**, 36 (1976).
14. M. Slamet and V. Sahni, Bull. Am. Phys. Soc. **42**, 674 (1997); *Ibid.*, in preparation.
15. V. Sahni, Y. Li, and M. K. Harbola, Phys. Rev. A **45**, 1434 (1992); Y. Li, M. K. Harbola, J. B. Krieger, and V. Sahni, Phys. Rev. A **40**, 6084 (1989).
16. M. K. Harbola and V. Sahni, Phys. Rev. B **39**, 10437 (1989).
17. V. Sahni, Surf. Sci. **213**, 226 (1989).
18. A. Solomatin, V. Sahni, and N. H. March, Phys. Rev. B **49**, 16856 (1994).
19. A. Solomatin and V. Sahni, Int. J. Quantum Chem. Symp. **29**, 31 (1995).
20. A. Solomatin and V. Sahni, submitted.
21. V. Sahni, in *Structure and Dynamics of Atoms and Molecules: Conceptual Trends*, J. L. Calais and E. Kryachko, Eds. (Kluwer, Dordrecht, 1995), and references therein.
22. A. Solomatin and V. Sahni, Phys. Lett. A **212**, 263 (1996).
23. A. Solomatin and V. Sahni, Phys. Rev. B **56**, 3655 (1997).
24. A. Solomatin and V. Sahni, Ann. Phys. **259**, 97 (1997).
25. M. Levy and J. P. Perdew, Phys. Rev. A **32**, 2010 (1985).
26. V. Sahni, Int. J. Quantum Chem. **53**, 591 (1995).
27. J. Bardeen, Phys. Rev. **49**, 653 (1936).
28. J. P. Perdew, Prog. Surf. Sci. **48**, 245 (1995); J. P. Perdew, H. Q. Tran, and E. D. Smith, Phys. Rev. B **42**, 11627 (1990); H. B. Shore and J. H. Rose, Phys. Rev. Lett. **66**, 2519 (1991).
29. J. C. Slater, Phys. Rev. **81**, 385 (1951).
30. V. Sahni, C. Q. Ma, and J. S. Flamholz, Phys. Rev. B **18**, 3931 (1978).

Forces Between Atoms and Atomic Planes in Condensed Metallic Phases and in Semiconducting Silicon

N. H. MARCH
Oxford University, Oxford, England

Received 3 March 1997; accepted 11 August 1997

ABSTRACT: Density functional theory for the pair potential in liquid Na near melting is first compared with that extracted by liquid structure inversion. All the main features are in quantitative agreement. Quantum chemical representations of metallic crystalline energies are then treated as a function of local coordination number and near-neighbor distance. K and Cu are especially referred to, in different lattice structures. Finally, the Tersoff potential based on density functional theory is discussed in relation to the cleavage force in ideal crystalline Si, and is related to bond breaking. © 1997 John Wiley & Sons, Inc. Int J Quant Chem **65**: 907–917, 1997

Background

The search for force fields in condensed matter goes back to at least the so-called rigid-ion model in the 1930s. The idea was, say for a simple metal crystal like Na or Al, to settle on a model for the charge density to associate with a particular nucleus, the superposition of which on each nucleus would lead to the periodic density in the crystal. But the screened ion was to be chosen judiciously so that as the ions vibrated about their equilibrium lattice positions the blobs of localized charge density moved rigidly with the nuclei. This was understood at that time to imply pair forces between nuclei. This idea was formalized in the 1960s through pseudopotential theory. The essential equation embodying these approaches can then be written for the internal energy E as

$$E = E_\Omega + \sum_{i<j} \phi(r_{ij}, \Omega). \qquad (1)$$

Thus, the energy is divided into two parts: a volume-dependent part E_Ω, with Ω denoting specifically the atomic volume, and a pair potential contribution ϕ, which is itself density-dependent as explicitly noted in writing Eq. (1). Clearly, Eq. (1) is valuable for comparing, say, crystalline phases in which atomic rearrangements are made at a constant volume. In the next section, density functional theory (DFT) will be used, in the manner of Perrot and March [1], to obtain the pair potential

Correspondence to: N. H. March at 6 Northcroft Road, Egham, Surrey, TW20 0DU, England.

This article was prepared specifically for a session on "Density Functional Theory and Intermolecular Forces."

Contract grant sponsor: ONR.

© 1997 John Wiley & Sons, Inc.
CCC 0020-7608 / 97 / 050907-11

$\phi(r)$ in the liquid phase of metallic Na, just above its freezing point. Reference will also be made, but now briefly, to both K and Be. However, emphasis will be placed on the fact that, for Na, contact can be established with an "experimental potential" derived by inverting the measured liquid structure factor $S(q)$, derived from either X-ray or neutron diffraction experiments. To date, this has not proved possible for K and Be, although, in the former case, X-ray diffraction data are available in the work of Greenfield et al. [2].

Attention will then move in the third section to a different type of representation of the ground-state energy of crystals, namely, through direct appeal to the dependence on local coordination. This approach goes back at least to the formulation of Poshusta and Klein [3] and was worked out in the alkali metals by Malrieu et al. [4]. The specific form to be discussed in the third section follows directly the work of March et al. [5]. Instead of Eq. (1) for a crystal with a coordination number and near-neighbor distance r_0, one writes

$$E(c, r_0) = \frac{1}{2} cR(r_0) - f(c)g(r_0), \qquad (2)$$

where it is of the essence of the method that $R(r_0)$ and $g(r_0)$ are determined explicitly by free-space dimer potential-energy curves. The detailed forms to be chosen for the functions R, g, and f are discussed in the third section. Then, in a similar vein, the directionally bonded Si crystal will be discussed, the example taken being the Tersoff potential [6] which is fitted to the density functional calculations of Yin and Cohen [7]. The type of description used in the third section is, in fact, characteristic of the so-called glue models of interatomic forces used by solid-state theorists. The Tersoff potential will be illustrated specifically by using it to calculate the cleavage force in Si, following the very recent work of Matthai and March [8]. We must note here, however, that there is already a body of work in which high-precision, all-electron, local spin density approximation (LSDA) calculations on films and slabs (especially metals) exist, from which cleavage energies can be deduced. At least some of these calculations have reported what amounts to the first derivative of the energy with respect to the interplanar distance (see, e.g., Boettger et al. [9], Rösch et al. [10], Smith et al. [11], Gay et al. [12], and others).

Then, in the fourth section, some attention is given, reverting back to the type of philosophy underlying the old rigid-ion model, to the precise formulation of lattice dynamics in relation to force fields, via DFT. Since phonon dispersion relations turn out to be described in terms of two densities, obviously, that of the perfect periodic crystal and also the change due to "freezing in" a phonon, one cannot only formulate a correct "vector rigid-ion" model in lattice dynamics but also one can, but now in the elastic region only, formulate the cleavage force in terms of phonon dispersion relations, as in the original work of Zaremba [13], which was extended by Kohn and Yaniv [14]. With this as background to the present review, let us turn immediately to discuss the calculation of the pair potential entering Eq. (1) for metallic Na in the liquid phase, just above its freezing point.

Density Functional Theory (DFT) of Pair Potentials in Simple *sp* Liquid Metals, Especially Na Near Freezing

The treatment below follows closely that of Perrot and March [1]. These workers adopted, essentially, within DFT, the philosophy of the rigid-ion model referred to above. Their building block was therefore the screening charge around a single Na^+ ion plunged into a bath of conduction electrons precisely equal to that in liquid metal Na near freezing. This screening charge was calculated by DFT, from the Kohn–Sham equations using a local density approximation (LDA). Figure 1 shows that the total charge $Q(r)$ enclosed within a sphere of radius r centered on the Na nucleus is approaching the asymptotic value of unity at large r. This is a requirement imposed by the fact that long-range electric fields cannot exist in a metallic medium. The so-called Friedel oscillations in the screening charge are in evidence; they fall off grossly as $\cos(2k_f r)/r^3$, with $2k_f$ denoting the diameter of the Fermi sphere, determined, in turn, by the mean conduction electron density into which the metal ion Na^+ is plunged.

Perrot and March then assumed that the ground-state electron density of the two-center problem is the superposition of the one-center densities. They thereby calculated the change in kinetic energy, $\Delta T(R)$ say, as the pair of screened ions brought from infinite separation to the specified internuclear separation R. This change in kinetic energy is naturally calculated from the Kohn–Sham wave functions. One also must calcu-

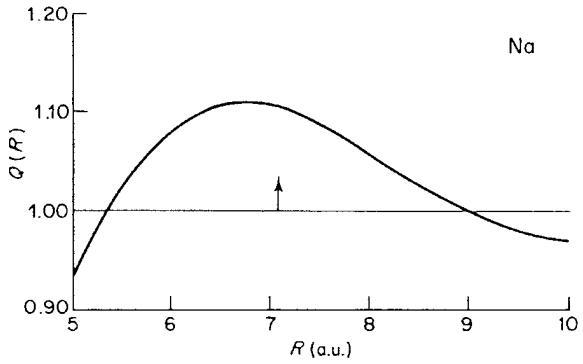


FIGURE 1. Integrated displaced charge $Q(r)$ contained with a sphere of radius r centered on a Na^+ ion embedded in an initially uniform electron gas of density equal to the conduction electron density in liquid metal near freezing. Note that (a) $Q(r) \rightarrow 1$ for perfect screening of the monovalent ion Na^+ in this conducting medium and (b) the corresponding pair potential $\phi(r)$ given by Perrot and March [1] have a prominent turning point at the position marked by the arrow (see also Fig. 2).

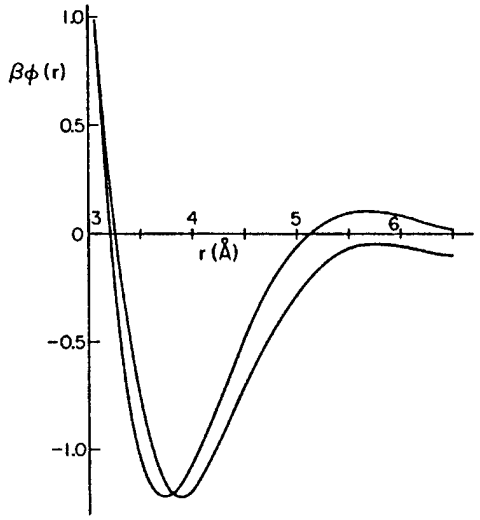


FIGURE 2. Pair potentials $\phi(r)$ in liquid Na just above freezing point, in units of $k_B T_m = \beta^{-1}$, with T_m the melting temperature. Upper curve at large r: DFT $\phi(r)$; lower curve at large r: "diffraction" potential obtained by Reatto [17] by inverting liquid structure factor $S(q)$ measured using X-rays by Greenfield et al. [2].

late the potential energy change $\Delta U(R)$ in assembling the pair from infinite separation. This latter quantity is, in fact, determined solely by the total charge $Q(r)$ defined above.

To be more specific, Perrot and March showed from DFT based on the superposition density that if one denotes the kinetic energy change $\Delta T(R)$, plus exchange and correlation energy change in LDA, by the sum $\Delta G(R)$, then the basic equation for the pair potential has the structure

$$\phi(R) = \Delta G(R) + \Delta U(R). \tag{3}$$

As already remarked, the quantity $\Delta U(R)$ is specified uniquely in terms of $Q(R)$. The reader requiring fuller details is referred to the articles of Perrot and March [1]. Their pair potential obtained using LDA for the exchange–correlation potential $V_{xc}(r)$ in the Kohn–Sham equations is shown for Na liquid metal at freezing in the upper curve at large r in Figure 2. We note briefly that a similar pair potential was derived for divalent liquid Be metal [1] and subsequently also for liquid metal K [15].

COMPARISON OF DFT PAIR POTENTIAL FOR Na WITH DIFFRACTION POTENTIAL FROM LIQUID STRUCTURE FACTOR INVERSION

The purpose of this section is to outline the way in which this DFT pair potential for liquid Na can be brought into direct contact with an "experimental" diffraction potential. The idea of inverting the experimentally measured liquid structure factor $S(q)$ goes back to the proposal of Johnson and March [16]. These workers pointed out that a pair potential $\phi(r)$ could be extracted, at least in principle, from the force equations of the BGY classical statistical mechanical hierarchy. If we write for the (classical) nuclei in a liquid metal near freezing the pair distribution function $g(r_{12})$, essentially, the Fourier transform of the measured structure factor $S(q)$, in the Boltzmann form

$$g(r_{12}) = \exp(-U(r_{12})/k_B T), \tag{4}$$

where $U(r_{12})$ is the potential of mean force and k_B is Boltzmann's constant, then the force equation reads

$$-\frac{\partial U(r_{12})}{\partial \mathbf{r}_1} = -\frac{\partial \phi(r_{12})}{\partial \mathbf{r}_1} - \int \frac{g^{(3)}(\mathbf{r}_1, \mathbf{r}_2, \mathbf{r}_3)}{g(r_{12})} \frac{\partial \phi(r_{13})}{\partial \mathbf{r}_1} d\mathbf{r}_3. \tag{5}$$

This equation is readily interpreted. The left-hand side is evidently the total force on atom 1. The right-hand side expresses this as a sum of two parts: The first is the direct pair interaction from a second atom at distance r_{12} from atom 1. The second term comes from the force exerted by an

atom at r_3, weighted with the probability g^3/g, where $g^{(3)}$ is the three-atom correlation function, while $g(r_{12})$ in the denominator takes care of the fact that there is certainly a second atom at distance r_{12} from atom 1. In early work [16], $g^{(3)}$ had to be approximated (e.g., as a product of three $g(r)$'s), and this was uncontrolled. However, Reatto et al. [17] brought the scheme to full fruition for Na by using computer simulation to bypass the need to approximate the three-particle correlation function, and their pair potential for liquid Na near freezing is compared with the density functional pair potential of Perrot and March [1] in Figure 2. Although small quantitative differences exist, it is remarkable that all the main features of the diffraction potential are reflected in the DFT $\phi(r)$. This is made plain in Table I, where the principal features of the DFT potential are compared with those of the diffraction potential. We stress that there were no adjustable parameters in the DFT calculation, the input merely being the valence of unity for Na, the experimental density of the liquid at freezing, and, of course, the LDA approximation to $V_{xc}(r)$ inserted into the Kohn–Sham equations.

It is worth adding here that the asymptotic form of $\phi(r)$ has subsequently been studied further in the work of Blazej and March [18]. These workers took the "spherical" blobs of screening charge around the pair of ions at separation R and allowed the blobs to float off the nuclei, although remaining undeformed. They then show that a correction to the usual asymptotic form of $\phi(r)$ results, to yield the result

$$\phi(r) = \frac{A\cos(2k_f r + \alpha)}{r^3} - \frac{B}{r^4} : r \to 0. \quad (6)$$

In Eq. (6), A denotes the amplitude of the Friedel oscillatory form and α is a phase shift. Blazej and March displayed the form of the next term as proportional to r^{-4}. However, more work has to be done on the range of validity of Eq. (6), which probably will come into its own at larger separation r than is plotted in Figure 2. The generalization of Eq. (6) to forces between a pair of atoms outside a metal surface has been given by Blazej et al. [19].

We turn from this discussion of pair potentials within the framework of Eq. (1) to the very different quantum chemical model expressed in Eq. (2). Of course, the present use of Eq. (2) is for crystal lattices with different local coordination c, while a merit of Eq. (1) in the above context was that it could be applied not only to long-range ordered assemblies but also to condensed metallic phases with short-range order.

Coordination Number-dependent Force Fields

COLD METAL CRYSTALS

March et al. [5] very recently used a near-neighbor Heisenberg Hamiltonian approach, based on results of Malrieu et al. [4] for alkali and noble metals to set up a coordination number-dependent pair potential $\phi(r, c)$, with c denoting the coordination number. The Heisenberg Hamiltonian used is basically characterized by properties of the free-space dimer, say Na_2 in the alkalis or Cu_2 in the noble metal. Both ground-state and triplet-state potential-energy curves are, however, now involved—the latter presenting some practical difficulties for DFT, which is still mainly useful as a ground-state theory (see, however, Theophilou [20]).

Let us follow these brief comments by summarizing the quantitative results of Malrieu et al. [4] for three (say alkali) metal structures: fcc, bcc, and simple cubic (sc). One then has for the cohesive energy $E_c(r_0)$ at near-neighbor distance r_0, with

TABLE I
Principal features of DFT potential compared with "experimental" diffraction potential for liquid Na near freezing.

Positions of turning points and nodes (Å)	Principal minimum	First maximum	Second minimum	First node
DFT[a] $\phi(r)$	3.73	5.67	7.37	3.20
Diffraction[b] $\phi(r)$	3.9	5.76	7.44	3.3

[a]Perrot and March [1].
[b]Reatto [17].

the coefficients of R and g in Eq. (2) taken from [4]:

$$\text{(i)}\quad \text{fcc}(c=12): E_{12}(r_0) = 6R(r_0) - 4g(r_0) \quad (7)$$

$$\text{(ii)}\quad \text{bcc}(c=8): E_8(r_0) = 4R(r_0) - 4g(r_0)$$

$$\text{(iii)}\quad \text{sc}(c=6): E_6(r_0) = 3R(r_0) - 3g(r_0)$$

Within the philosophy of this work (compare also the Tersoff work [6] on Si), March et al. [5] effected an approximate generalization of Eqs. (7) to read

$$E_c(r_0) = \frac{1}{2}cR(r_0) - f(c)g(r_0). \quad (8)$$

The form of the first term on the right-hand side of Eq. (8) may be motivated as a simple additive sum of the interactions between nearest-neighbor pairs. The "correction" term involving the coordination number-dependent function $f(c)$ is less easy to justify, although there are formulas given in Malrieu et al. accurate through second-order of perturbation theory. In Eq. (8) as applied to metallic Na say, $R(r_0)$ is the triplet $^3\Sigma_u$ potential curve of the free-space dimer, while $g(r_0)$ represents the "exchange" part. $g(r_0)$ is precisely one-half of the difference between the triplet $^3\Sigma_u$ and the singlet $^1\Sigma_g$ potential-energy curves. March et al. noted that, given these potential-energy curves (say from DFT), the procedure set out fully by Carlsson et al. [21] can then be used to derive a pair potential $\phi(r, c)$ having the shape

$$\phi_c(r) = c\phi_1(r) - f(c)\phi_2(r). \quad (9)$$

Concerning the function $f(c)$, it is relevant here to note, following March et al. [5], that Robertson et al. [22] took a fixed near-neighbor distance r_0 equal to that in fcc Al and performed DFT calculations as a function of the coordination number. They can fit their results for the energy $E(r_0)$ by writing

$$E(r_0) = cA_1 + c^{1/2}A_2. \quad (10)$$

While it must not be assumed that the $c^{1/2}$ fit will work away from their r_0, the sublinear dependence of $f(c)$ in Eq. (8) is already evident (but now for Na say) from Eq. (7).

DFT AND TERSOFF POTENTIAL FOR Si

We turn from *sp* metals, with essentially nondirectional bonding, to covalently bonded Si. The focus will be the work of Tersoff [6], who presented convincing evidence that the atomic coordination number c is the main variable determining the now directional bonding properties of Si in different structures.

The central idea that the bond order, a measure of bond strength, depends upon the local environment can already be found in the study of Abell [23]. He argued that an atom with numerous neighbors makes weaker chemical bonds than an atom will with only a few neighbors. For more recent work on bond-order potentials, the reader may refer to Alinaghian et al. [24], where extensive references are given.

What we must stress in the present context is that the above ideas have been made fully quantitative for Si using DFT. Thus, the work of Yin and Cohen [7] is based on self-consistent pseudopotential calculations using LDA. From their work ([7]; see also Tersoff [6]), we constructed Table II which records DFT values for the cohesive energy of Si with different atomic coordination numbers. Both cohesive energy/bond and per atom are collected in Table II. As to the former case, the first show row of this table shows a clear, monotonic decrease as the coordination number increases, which is a quantitative account for Si of the arguments of Abell [23]. The cohesive energy per atom, in contrast, goes through a maximum as the coordination number c increases through diamond, leveling off at higher values of c.

Below, we focus on the use of the Tersoff potential for Si, constructed to embody almost all the DFT results in Table II, for calculating the cleavage

TABLE II
DFT values for cohesive energy of Si (in eV).[a]

	Dimer	Graphite	Diamond	Simple cubic	fcc
Cohesive energy / bond	3.2	2.6	2.3	1.4	0.7
Cohesive energy / atom	1.6	3.9	4.7	4.3	4.1

[a] Constructed from Yin and Cohen [7]; see also Tersoff [6].

force as a function of interplanar separation [8]. But two points should be made first in this connection: First, there are, as the author himself emphasizes, overly soft bond-angle forces in Tersoff's parametrization of the DFT results. He himself stresses the need for an improved treatment of bond-angle forces (see, again, the recent study of Alinaghian et al. [24]). Second, Tersoff [6] also emphasized the merits of his potential as applied to Si(100) and Si(111) surfaces: These are a focal point of the study of Matthai and March [8] to be summarized later.

Cleavage Force Between Planes of Atoms in *sp* Metals and in Si

JELLIUM MODEL FOR *sp* METALS: ELASTIC REGIME

We shall refer to the phonon theory below to summarize the way to calculate the cleavage force in the elastic regime from appropriate dispersion relations, following Zaremba [13] and Kohn and Yaniv [14]. However, let us first obtain for simple *sp* metals the gross variation of the cleavage force $F(z)$ in the elastic regime, where

$$F(z) = Az, \tag{11}$$

with z the interplanar separation. The work of March and Paranjape [25] used the simplest DFT, namely, the linearized Thomas–Fermi (TF) approximation, combined with a semi-infinite jellium approach to obtain (see also Heinrichs [26])

$$A = t/r_s^{11/2}, \tag{12}$$

with r_s the mean interelectron separation, related to density n_0 by $n_0 = 3/4\pi r_s^3$. Their value of the constant t was refined (and substantially increased) according to the subsequent work of Streitenberger [27] who gave the result

$$t = 0.229\frac{\hbar e}{m^{1/2}}. \tag{13}$$

Having summarized this simple approach to treat the elastic regime in *sp* metals, we note that the same model can be used on a jellium cylinder to predict size effects in atomic force microscopy (see the Appendix). Let us turn next to the recent work on the cleavage force in ideal Si crystal, treated by Matthai and March [8].

POSITION AND HEIGHT OF MAXIMUM IN CLEAVAGE FORCE $F(z)$ FOR Si: RELATION TO BOND BREAKING

Matthai and March [8] discussed the cleavage force in a model of Si with a chemically bonded force field. In their model, a cleaved piece of Si has parallel faces at separation $a + z$, with a the original interplanar spacing perpendicular to the cleavage plane.

These workers then presented an estimate for a block of Si of the maximum value of $F(z)$ and its position, z_{max} say, using the coordination-dependent interatomic potential of Tersoff [6], already discussed above.

Matthai and March considered two cases (see also Fig. 3):

(i) a Si(111) surface, with one bond cut and

(ii) a Si(100) surface, with breaking of two bonds.

The modeling of the surface was carried out by having 12 planes of movable atoms on top of a fixed substrate. The system was allowed to relax by molecular dynamics. The atoms on the surface planes were held fixed, with the remainder permitted to relax. As the energy $E(z)$ is a function of the separation z of atoms in the two surface planes, the cleavage force $F(z)$ then is given by

$$F(z) = \frac{dE(z)}{dz}. \tag{14}$$

The form of $E(z)$ obtained by Matthai and March is shown in Figure 4.

The maximum in cases (i) and (ii) occurs when z lies between 0.8 and 0.95 of the original interplanar separation a. To gain insight, Matthai and March considered the H_2 molecule as it is pulled apart from its equilibrium-internuclear separation, R_e say. Using the Coulson–Fischer wave function [28], designed to allow a "transition" from a delocalized molecular orbital (LCAO) behavior at R_e to a (unsymmetrized) Heitler–London character at large internuclear separation R, Matthai and March pointed out that after extension of $0.6R_e$ from the equilibrium separation the LCAO MO is no longer the lowest-energy state, the electrons becoming localized. We identify this "transition" with bond breaking. From Figure 4, we see that the situation

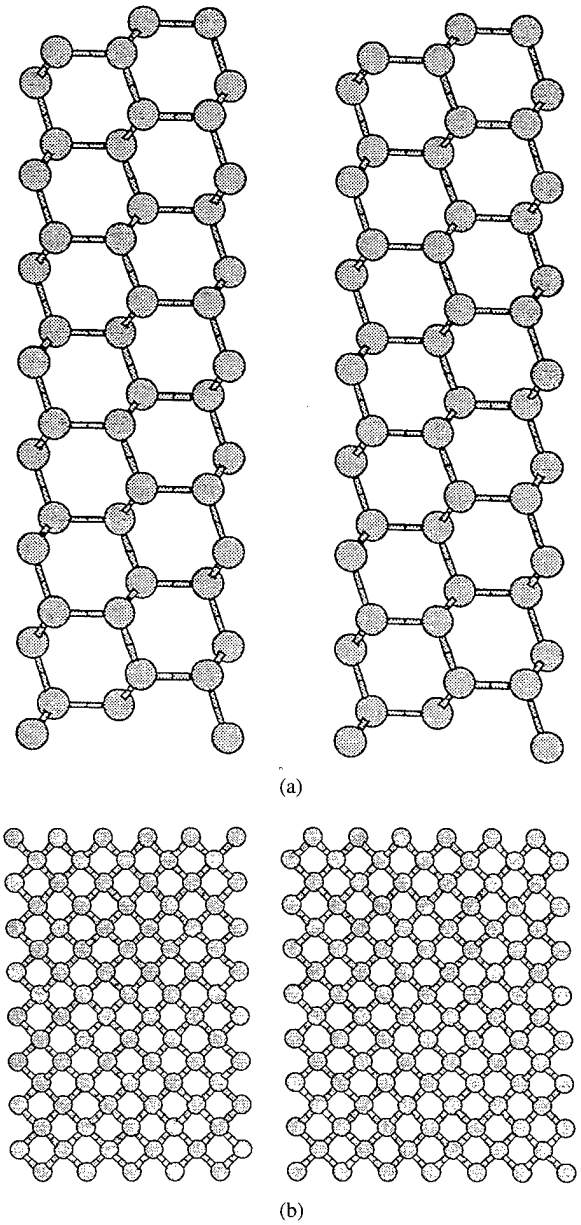


FIGURE 3. Si(111) surface with one bond cut; (b) Si(100) surface with breaking of two bonds. (After Matthai and March [8].)

is only quantitatively different for Si, a somewhat larger extension now being required for bond breaking. Of course, this treatment is restricted to ideal crystalline Si: In real materials, defects will lead to important changes from such ideal behavior.

We turn to the area of lattice dynamics, where some precise statements relating to interatomic forces can be made.

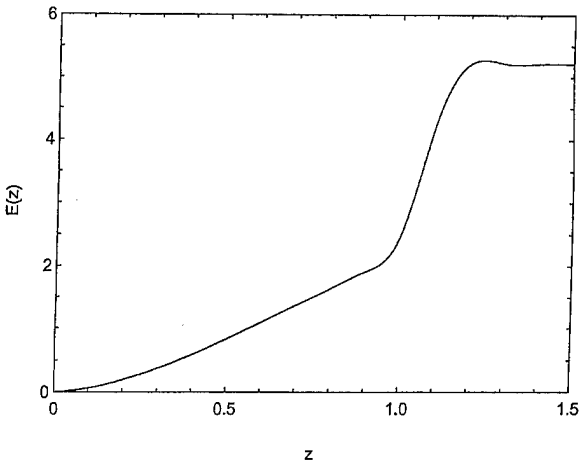


FIGURE 4. Energy $E(z)$ as a function of separation z of atoms in two surface planes of Si. Cleavage force $F(z)$ is then to be obtained from Eq. (14). (After Matthai and March [8].)

Phonon Theory in Conducting Crystals, Including Cleavage Force in Elastic Region

We start with simple metals and adopt the treatment of Jones and March [29]. For pair potentials, one has an equivalent "rigid-ion" model (see first section) in which the ground-state density $\rho(\mathbf{r})$ in the presence of a phonon frozen into the lattice is given by

$$\rho(\mathbf{r}) = \sum \sigma(|\mathbf{r} - l - \mathbf{u}_l|), \qquad (15)$$

where l are the direct lattice vectors and $\mathbf{u}_l$ denote the small displacements from the lattice positions due to the frozen phonon. The spherical localized "blobs" $\sigma(r)$, centered on each nucleus in the perturbed lattice, are assumed to move "rigidly," i.e., without deformation, as the ions suffer small displacements from their equilibrium lattice positions l_n.

Jones and March [29] showed, from the concepts of DFT, that while the above is, of course, approximate, although a good approximation for bcc Na metal from the earlier discussion of liquid Na near freezing, a vector rigid-ion picture is formally exact for phonon theory. Thus, one writes for the first-order density change $\rho_1(\mathbf{r})$ when the ions are moved by small displacements $\mathbf{u}_l$ from the sites l,

following Jones and March,

$$\rho_1(\mathbf{r}) = \sum_l \mathbf{u}_l \cdot \frac{\partial \rho(\mathbf{r})}{\partial \mathbf{u}_l}. \quad (16)$$

This change is given by linear response theory as

$$\rho_1(\mathbf{r}, E) = \int \Delta V^{(1)}(\mathbf{r}') F(\mathbf{r}\mathbf{r}' E)\, d\mathbf{r}', \quad (17)$$

where (see, e.g., Stoddart et al. [30]) F can be calculated from the one-body periodic potential $V(\mathbf{r})$ of DFT from

$$\frac{\partial F}{\partial E} = 2Re\left[G_0(\mathbf{r}\mathbf{r}_1 E_+)\frac{\partial \rho_0(\mathbf{r}_1 \mathbf{r} E)}{\partial E}\right], \quad (18)$$

where G_0 is the perfect lattice Green function while $\rho_0(\mathbf{r}\mathbf{r}'E)$ is a Dirac (idempotent) density matrix whose diagonal element $\rho_0(\mathbf{r})$ is the exact crystal density.

One can (Jones and March [29]) express the change in the one-body potential $\Delta V^{(1)}(\mathbf{r}_1)$ in Eq. (17) due to "freezing in a phonon" as

$$\Delta V^{(1)} = \Delta V^{(1)}_{electrostatic} + \int U(\mathbf{r}\mathbf{r}')\rho_1(\mathbf{r}')\, d\mathbf{r}'. \quad (19)$$

Writing Eq. (16) next as

$$\rho_1(\mathbf{r}) = \sum_l \mathbf{u}_l \cdot R_l(\mathbf{r}), \quad (20)$$

Jones and March demonstrated that $\mathbf{R}_l(\mathbf{r}) = \mathbf{R}(\mathbf{r} - l)$ and they obtained an integral equation for $\mathbf{R}(\mathbf{r})$ from DFT. This was solved approximately for Al and for Si (Claesson et al. [31]). The relation to the "rigid-ion" model, or pair potential theory, was fully discussed by Jones and March [29] and also the way phonon dispersion curves can be calculated.

FERMI SURFACE IN METALS AND LONG-RANGE FORCES

Flores et al. [32] used the above formulation to treat the effect of Fermi surface topology on long-range oscillatory interactions in metals, generalizing the results for simple *sp* metals discussed earlier in this article. When, for instance, there are necks on the Fermi surface, obvious anisotropic effects arise, and in certain directions, an interaction energy–oscillatory function/r, with r the range of the interaction, can occur, contrasted with $\cos 2k_F r/r^3$ in simple metals.

The writer (March [33]) has emphasized a related point, namely, that the one-body potential of DFT, $V_{xc}(\mathbf{r})$, plus $U(\mathbf{r}\mathbf{r}')$ discussed above, are sufficient to map out the Kohn [34] anomaly in the lattice vibrations. This will then yield the correct Fermi surface. Direct use of the one-electron eigenvalues from the solution of the Kohn–Sham equations with potential $V(\mathbf{r})$ does not, on the other hand, give the correct Fermi surface, as pointed out by Gunnarsson and Schönhammer [35].

ELASTIC REGIME OF CLEAVAGE FORCE IN TERMS OF PHONON THEORY

We return briefly at this point to the elastic regime of the cleavage force $F(z)$, where $F(z) = Az$. The work of Zaremba [13] and Kohn and Yaniv [14] gave A explicitly in terms of the phonon dispersion relations in the perfect lattice before cleavage and this is a very precise route for the calculation of the constant A. One expects nearly free-electron metals to regain grossly $A \propto r_s^{-11/2}$ as obtained by March and Paranjape [25] as well as in the later work of Streitenberger [27]. We stress that all the above is within the context of DFT, although in constructing $\Delta V^{(1)}$ appearing in Eqs. (17) and (19), Jones and March emphasized that one requires the "exchange–correlation" functional $U(\mathbf{r}\mathbf{r}')$, which transcends knowledge of the one-body potential of DFT. Thus, to complete the phonon calculation, as Jones and March [29] proved, one also needs the further functional derivative

$$U(\mathbf{r}, \mathbf{r}') = \frac{\delta V_{xc}(\mathbf{r})}{\delta \rho(\mathbf{r}')}, \quad (21)$$

with $V_{xc}(\mathbf{r})$ the usual exchange–correlation potential of DFT. Claesson et al. [31] discussed approximate forms of F and U for (a) Al and (b) Si and the interested reader is referred to their article for the detailed forms. However, it is noteworthy that a shell model treatment of Si is equivalent to a factorization of the response function $F(\mathbf{r}, \mathbf{r}')$, which, of course, affords great simplification.

Summary and Future Directions

Different DFT approaches have been discussed for treating interatomic force laws in condensed

metallic phases and for dealing with interplanar interactions in suitably cleaved crystals. It has been stressed in the latter case that the calculations presented here are for "ideal" materials. Naturally, defects will have to be incorporated before the theoretical predictions can be brought into direct contact with observation.

Returning to the central Eqs. (1) and (2), for simple liquid metals such as Na near freezing, contact has been made between a DFT pair potential calculated from first principles using LDA and that extracted using only classical statistical mechanics to invert the measured liquid structure factor $S(q)$. As Figure 1 and Table I show, the agreement is already rather remarkable, although some purely quantitative differences remain. As this article was nearing completion, work by Rajagopalan and Srivastava [36] appeared on liquid Cu. This was used subsequently by March and Ray [37] to compare it with the density functional calculations of Carlsson et al. [21], who extracted a pair potential for Cu. March and Ray [37] also used the coordination number representation (2) for Cu to extend the Carlsson et al. work on fcc Cu to give $E(c, r_0)$ also for bcc, sc, and diamond structures, but for these latter cases, to our knowledge, there is not as yet DFT work for comparison. For the simpler *sp* metal K, however, Rubio and March [38] very recently brought the DFT calculations for a variety of structures (in LDA) into contact with the quantum chemical model (2). However, they used semiempirical representations of the singlet and triplet potential-energy curves for the K_2 dimer. While the $^1\Sigma_g$ potential-energy curve is obviously accessible through DFT, more problems exist in calculating the triplet curve from DFT, but approaches such as that set out by Theophilou [20] and later developments should be studied further in the context of the quantum chemical representation (2).

Finally, phonon theory has been posed here in density functional language, with illustrative examples given for Al and Si crystals and also for the cleavage force following [13, 14]. The Appendix treats size effects on the cleavage force in nearly free-electron metals and the establishment of a self-consistent field from the simplest DFT for future studies of such size influences. Atomic force microscopy may, perhaps, in the future, throw further light on the relevance of such studies to real materials, e.g., Si and W [39, 40].

Appendix: Size Dependence of Cleavage Force Between Parallel Planar Jellium Metal Surfaces

Razavy et al. [41] very recently discussed size effects in the jellium model already referred to in the main text. As there, the simplest DFT, namely, the linearized Thomas–Fermi (TF) model, was employed. The force between two parallel planar conducting cylinders of infinite extension was considered by these workers.

In such a system, with cylindrical symmetry, the main achievement was to establish the self-consistent field analytically, by solving the linearized TF equation

$$\frac{\partial^2 V}{\partial \rho^2} + \rho^{-1}\frac{\partial V}{\partial \rho} + \frac{\partial^2 V}{\partial z^2} = q^2 V, \qquad \text{(A1)}$$

with q^{-1} the TF screening length. Separating the variables through

$$V(\rho, z) = F(\rho)Z(z) \qquad \text{(A2)}$$

leads to two differential equations:

$$\frac{d^2 Z}{dz^2} = -p^2 Z \qquad \text{(A3)}$$

and

$$\frac{d^2 F}{d\rho^2} + \rho^{-1}\frac{dF}{d\rho} = (p^2 + q^2)F, \qquad \text{(A4)}$$

with p being a real separation constant. Specifying regions I and II as within the two semi-infinite jellium cylinders, Razavy et al. [41] found in these regions

$$V(\rho, z) = \int_{-\infty}^{\infty} C(p)\cos pz I_0[Q(p)\rho]\, dp, \quad \rho < R, \qquad \text{(A5)}$$

with R the radius of the cylinders and I_0 the usual Bessel function. To specify $C(p)$, Razavy et al. [41] matched V in Eq. (A5) to the electrostatic potential in region III, where this denotes the whole region outside the two jellium semi-infinite cylinders, including the gap of width d between them.

The energy stored in the electrostatic field was then calculated as the sum of two terms, ΔE_1 *and*

ΔE_2, and the force F from

$$F = \frac{\partial \Delta E_1}{\partial d} + \frac{\partial \Delta E_2}{\partial d}. \qquad \text{(A6)}$$

Razavy et al. showed that the first term is independent of d, while all the dependence of ΔE_2 on d can be subsumed within the simple factor $\sin(kd/2)$, with k a Fourier transform variable. It would be of obvious interest if this size dependence predicted by the simplest DFT could be tested using the atomic force microscope and work along these lines is in progress (see Allegrini et al. [40]).

In concluding this Appendix, it is worth commenting that the work of Razavy et al. discussed above makes available an (of course, approximate) self-consistent field as a function of cleavage separation d. In the future, this may well afford a "zeroth-order" field to use in solving the Kohn–Sham equations in cylindrical symmetry for a cleaved jellium cylinder. Of course, an LDA contribution to $V(r)$, namely, $V_{xc}(r)$ would have to be added, since the TF approximation used by Razavy et al. [41] does not include exchange and correlation.

ACKNOWLEDGMENTS

The writer owes to Professor D. Micha his grateful thanks for stimulating and motivating this article and for generous travel support. The opportunity to complete the article came as a result of a visit to the group of Professor J. A. Alonso in the latter part of 1996. Professor Alonso and his colleagues are thanked here for a very fruitful stay in a most interactive environment and for generous hospitality. The work relating to mechanical properties of conducting crystals was supported by ONR and, in particular, Dr. Peter Schmidt is thanked for much help and his continuing support. The award by the Leverhulme Trust of an Emeritus Fellowship for work on density functional theory is gratefully acknowledged. Finally, the writer is indebted to the referee for numerous critical yet constructive comments which have improved the presentation of this review.

References

1. F. Perrot and N. H. March, Phys. Rev. A **41**, 4521 (1990); *Ibid.*, Phys. Rev. A **42**, 4884 (1990).
2. A. Greenfield, J. Wellendorf, and N. Wiser, Phys. Rev. A **4**, 1607 (1971).
3. R. D. Poshusta and D. J. Klein, Phys. Rev. Lett. **48**, 1555 (1982).
4. J. P. Malrieu, D. Maynau, and J. P. Daudey, Phys. Rev. B **30**, 1817 (1984).
5. N. H. March, M. P. Tosi, and D. J. Klein, Phys. Rev. **52**, 9115 (1995).
6. J. Tersoff, Phys. Rev. B **37**, 6991 (1988); *Ibid.*, Phys. Rev. B **39**, 5566 (1989).
7. M. T. Yin and M. L. Cohen, Phys. Rev. B **24**, 2303 (1981); *Ibid.*, Phys. Rev. B **26**, 5668 (1982).
8. C. C. Matthai and N. H. March, J. Phys. Chem. Solids **58**, 765 (1997).
9. J. Boettger, Int. J. Quantum Chem. Symp. **27**, 147 (1993); see also J. Boettger and S. B. Trickey, Phys. Rev. B **32**, 1356 (1985).
10. N. Rösch, U. Birkenheuer, and J. Boettger, J. Chem. Phys. **100**, 6826 (1994).
11. J. R. Smith, J. E. Raynolds, D. J. Srolovitz, and G.-L. Zhao, (Material Research Society, Pittsburgh, PA, 1996), p. 177.
12. J. G. Gay, J. R. Smith, and F. J. Arlinghaus, Phys. Rev. B **21**, 2201 (1980).
13. E. Zaremba, Solid State Commun. **23**, 347 (1979).
14. W. Kohn and A. Yaniv, Phys. Rev. B **20**, 4948 (1979).
15. M. W. Johnson, N. H. March, F. Perrot, and A. K. Ray, Philos. Mag. **69**, 965 (1994).
16. M. D. Johnson and N. H. March, Phys. Lett. **3**, 313 (1963).
17. See, e.g., L. Reatto, Philos. Mag. A **58**, 37 (1988), and references therein.
18. M. Blazej and N. H. March, Phys. Rev. E **48**, 1782 (1993).
19. M. Blazej, N. H. March, and F. Flores, Mol. Phys. **86**, 951 (1995).
20. A. K. Theophilou, Philos. Mag. B **69**, 771 (1994).
21. A. E. Carlsson, C. D. Gelatt, and H. Ehrenreich, Philos. Mag. **41**, 241 (1980).
22. I. J. Robertson, V. Heine, and M. C. Payne, Phys. Rev. Lett. **70**, 1944 (1993).
23. G. C. Abell, Phys. Rev. B **31**, 6184 (1985).
24. P. Alinaghian, S. R. Nishitari, and D. G. Pettifor, Philos. Mag. B **69**, 889 (1994).
25. N. H. March and B. V. Paranjape, Phys. Rev. B **30**, 3131 (1984).
26. J. Heinrichs, Phys. Rev. B **32**, 4232 (1996).
27. P. Streitenberger, Phys. Stat. Sol. B **135**, 321 (1986).
28. C. A. Coulson and I. Fischer, Philos. Mag. **40**, 386 (1949).
29. W. Jones and N. H. March, Proc. R. Soc. A **317**, 359 (1970).
30. J. C. Stoddart, N. H. March, and M. J. Stott, Phys. Rev. **186**, 683 (1969).
31. A. Claesson, W. Jones, G. G. Chell, and N. H. March, Int. J. Quantum Chem. Symp. **7**, 629 (1973).
32. F. Flores, N. H. March, Y. Ohmura, and A. M. Stoneham, J. Phys. Chem. Sol. **40**, 531 (1979).
33. N. H. March, Phys. Rev. B **38**, 10067 (1988).

34. W. Kohn, Phys. Rev. Lett. **2**, 393 (1959).
35. O. Gunnarsson and K. Schönhammer, Phys. Rev. B **37**, 3128 (1988).
36. R. Rajagopalan and K. Srinavasa Rao, Phys. Rev. E **55**, 4423 (1997).
37. N. H. March and A. K. Ray, Phys. Chem. Liq. (in press).
38. A. Rubio and N. H. March, Phys. Rev. B, (in press).
39. G. Binnig, C. F. Quate, and Ch. Gerber, Phys. Rev. Lett. **56**, 930 (1986).
40. See also a preliminary report by M. Allegrini, R. Gucciardi, M. Labardi, and N. H. March, presented at NATO Workshop on Atomic Force Microscopy (June 1996).
41. M. Razavy, N. H. March, and B. V. Paranjape, Phys. Rev. B **54**, 4492 (1996).

A Theoretical Study of the Electronic Structure of Transition-Element Carbides M_nC (M = Fe, Ni, Cu, n = 1, 5; and M = Ti, n = 1, 7) and Their Interactions with an O Atom by DFT Methods

RAMÓN M. SOSA, PATRICIA GARDIOL, GERARDO BELTRAME

Institute of Physics, Faculty of Engineering, Avda. Julio Herrera y Reissig 565, Montevideo 11300, Uruguay and Institute of Physics, Faculty of Sciences, Tristán Narvaja 1674, Montevideo 10773, Uruguay

Received 1 March 1997; revised 29 May 1997; accepted 2 June 1997

ABSTRACT: Electronic structures and properties of carbides MC, M_5C (M = Fe, Ni, Cu), and TiC and Ti_7C were studied using density functional methods (DF), particularly the local density approach (LDA) with the Vosko–Wilk–Nusair (VWN) correlation functional, the generalized gradient approximation (GGA) of Becke and Perdew (using Becke's 1988 exchange functional and Perdew's 1986 correlation functional —BP86), and the ADF program of Baerends et al. In the first part of this report, we studied equilibrium geometries and dissociation energies for the process MC → M + C involving the doublet ground state for M = Cu, singlet and triplet states for M = Ni, and triplet and quintuplet states for M = Fe, Ti. Charge distributions by population analysis, dipole moments, and vibrational frequencies were also evaluated. All calculations were done using triple-zeta basis sets, with frozen-core orbitals and the GGA corrections. In the second part of this report, we consider the doublet states of Cu_5C and singlet and triplet states of Ni_5C, taking planar and nonplanar models for the M_5 clusters. The triplet and quintuplet states of Fe_5C were studied with a nonplanar model for the Fe_5 cluster, whereas in the case of the triplet and quintuplet states of Ti_7C, a Ti_7 planar model was chosen. Optimization of the position of the C atom in the cluster, dissociation energies, distribution of charges in the molecule, and dipolar moments were also analyzed, and

Correspondence to: R. M. Sosa.

Contract grant sponsor: CONICYT (Consejo Nacional de Investigaciones Científicas y Tecnológicas) of Uruguay.

International Journal of Quantum Chemistry, Vol. 65, 919–928 (1997)

© 1997 John Wiley & Sons, Inc.

CCC 0020-7608 / 97 / 050919-10

comparisons with the results obtained for the corresponding carbides (MC) were made. These results, together with the ones of the corresponding carbonyls—that have previously been done by the same methodology—provide us with an interesting comparison of the M—C bond dissociation energy in carbides and carbonyls. Calculations of the C—O bond dissociation energies for the MCO and M_nCO compounds were also performed. © 1997 John Wiley & Sons, Inc. Int J Quant Chem 65: 919–928, 1997

Introduction

Carbonyls and carbides (and also carbenes) of transition elements are a very important class of compounds for several reasons: One of these is that carbonyls are considered to be the first step in the reaction of CO with H_2, catalyzed by transition elements (Fischer–Tropsch synthesis). From the industrial point of view, this is of paramount importance due to the large number of chemicals that can be obtained from it.

The initial step of the chain of reactions is the chemisorption by materials which contain such elements. The simplest model for these materials is one atom, which is where the importance of the MCO compounds lies. Carbides (MC) are obtained by cleavage of the C—O bond from carbonyls, and carbenes (MCH_2) are obtained by hydrogenation of the carbides or carbonyls. In previous reports [1–3], we considered carbonyls and carbenes of Ti, Ni, Fe, and Cu using DFT methods. In this report, we focus on carbides as a complementary study.

As a further step, it is natural to consider—as suitable models for real materials—clusters or crystals of the elements involved and to use the appropriate computational techniques. To compare the results obtained in the MC and M_nC calculations, we must use the same computational level in both cases. Therefore, the cluster size cannot be too large.

These calculations should provide accurate predictions, at least for the equilibrium molecular geometries, dissociation energies, and vibrational frequencies. For this reason, we studied—besides the MC compounds—the M_5C structure with symmetry C_{4v} (for M = Ni, Fe, Cu) and Ti_7C with symmetry C_{6v}. They all involve transition-atom clusters with geometries taken from their crystals.

The transition elements considered in this report (Ti, Cu, Ni, and Fe) present quite different difficulties. Cu is the simplest because of its electronic structure, as compared to Ni, Fe, and Ti; Ni is the most difficult. We focused our interest in the geometrical and energetical aspects of the systems under consideration.

Methods

The calculations reported in this article are based on the Kohn–Sham approach to density functional theory (DFT) [4], with the methodology of Baerends et al. The program used was ADF (version 2.0.1) [5].

The density functional, also called the exchange-and-correlation (XC) functional, consists of a local part (the local density approach, LDA) and a so-called gradient correction (the generalized gradient approximation, GGA). Initially, the LDA used for the calculation of the exchange energy Ex(LDA) was the one proposed by Slater [6] ($X\alpha$ approximation), but a version that also includes a correlation part—the one used in this report—is that proposed by Vosko, Wilk, and Nusair (VWN) [7].

The GGA introduces terms depending on the gradient of the electron density that account for the inhomogeneities necessary to describe the nonuniform electron gas in the case of atomic and molecular systems. GGA corrections are the sum of two terms: exchange and correlation. The introduction of these, sometimes called nonlocal corrections, significantly improve the results of the calculation of several properties, such as bond energies, molecular geometries, and dipole moments.

We have several possibilities using the ADF program with the GGA correction calculations. The one used in this report is due to Becke [8] for the exchange term and that of Perdew [9] for the correlation. The method is called, accordingly, LDA/BP.

We used the Slater-type orbital (STO) basis set for the atomic orbitals (AO), which are internally stored in the ADF program. We selected the one called IV, which is a triple basis set with polarization.

Integrals involving electronic density (such as Coulomb potentials) were evaluated using these auxiliary bases and then taking linear combinations of these integrals. The coefficients of these linear combinations were evaluated in each SCF cycle.

The matrix elements of the overlap and Fock matrices were calculated by numerical integration. The success of DFT methods—such as the one implemented in ADF—is due, among other reasons, to the existence of accurate and very efficient numerical methods for the calculation of integrals using STO functions [10].

Instead of calculating total energies, as most methods do, ADF calculates bond energies according to Ziegler's procedure [11]. These bond energies are the difference between the total energy of a molecule (or atom) and those of the atoms (or fragments) in established reference states.

Optimization of the M—C bond length at the LDA/BP level was done for all the compounds considered in this report. In all cases, the lowest energy of the M and C fragments were obtained, and the adiabatic M—C bond dissociation energy was calculated in every case using the sum-of-fragments energies (E_{sof}) and the energy at the equilibrium geometry of the MC compounds. Mulliken population analysis was carried out, and the charge distribution in the molecule and the related dipole moment were obtained, as well as the vibrational frequencies of the normal modes.

Regarding the M_5C compounds, we have two possibilities for the M_5 clusters: Ni and Cu crystals have fcc (face-centered cubic) elementary cells, whereas Fe has a bcc (body-centered cubic) and Ti has an hcp (hexagonal close-packed) one. In the Ni and Cu cases, we selected two cluster models. The first one, called "planar" and symbolized by (5, 0), had all five atoms located on the vertices of a square and its center. This would correspond to the top face of the elementary cell. The other, called "hollow" and symbolized by (4, 1), was formed by taking the four-center atoms of the lateral faces of the cube and the fifth atom on the center of the bottom face, thus forming a square pyramid with the four M atoms at the corners of the base and the fifth M atom at the top. This was the only one employed in the case of Fe. We are using the nomenclature given by Post and Baerends [12].

The geometry of these clusters was taken from experimental crystal data. The distance from the center of the square to one of the M atoms was 2.54 Å in the case of Cu, 2.50 Å in the case of Ni, and 2.03 Å in the case of Fe, and for Ti, the center of the hexagon was 2.91 Å from the other Ti atoms.

The central M atom in (5, 0), which we will call M_1, was displaced from the M_4 plane a distance equal to 1.80 Å for the Cu_5 (4, 1) cluster and 1.77 Å for the Ni_5 (4, 1) cluster. In the case of the Fe_5 cluster, the distance from Fe_1 to the Fe_4 plane was 1.44 Å.

All calculations were carried out at the unrestricted approximation level. We checked the electronic configuration after SCF convergence in order to see if the LUMO orbital was lower in energy than was the HOMO, both for α and β spin. Every time we found this not to be the case, we changed the configuration accordingly, verifying the decrease in energy and continuing until the lowest energy was attained. In some cases of difficult convergence, we had to resort to the level-shifting technique, increasing the energy of the virtual orbitals a little bit (in some cases up to 0.5 au).

Results and Discussion

All calculations reported in this article were done at the LDA/BP level. It is well known [13, 14] that predictions for molecular geometries are improved when GGA corrections—such as BP—are included in the LDA methodology, resulting in values very close to experimental ones. In general, DFT methods are superior to Hartree–Fock (HF) ones, particularly for metal–ligand bond lengths.

CO CASE

One of the objectives of this article was to evaluate the dissociation energy of the C—O bond when the carbonyl group is attached to one or several transition-element atoms and then to compare this value to that of the free CO molecule. In that way, we can rationalize the action that different metal catalysts may have on reactions that involve the cleavage of that particular bond.

For the free CO molecule, the C—O bond energy obtained—with an optimized C—O bond distance of 1.1394 Å—was −0.540653 au. For the fragments O (triplet), O (singlet), and C (singlet), the bond energies were −0.057444, −0.00875, and −0.000206 au, respectively. Therefore, the sum of the lowest bond energies for the resulting frag-

ments of the dissociation of CO was E_{sof} [C(1) + O(3)] = −0.057650 au, which gave us a value for the (adiabatic) dissociation energy equal to 303 kcal/mol.

We found in the literature [15] an experimental value of 11.09 eV (256 kcal/mol) for this dissociation energy and a C—O bond distance of 1.127 Å. In [16], a calculated value of 277 kcal/mol is reported, as well as a bond distance of 1.127 Å. They also provided an experimental value of 259 kcal/mol, so our result is about 44 kcal/mol too high (17% higher). As far as bond distance is concerned, the agreement is satisfactory.

We calculated values for the CO dissociation energy and bond distance using different bases and DFT parameterizations. These values were in good agreement with the ones just referred to.

In any case, since we focus our interest on energy differences to be able to assess the influence of the nature and number of the different metal clusters bonded to the CO molecule on the C—O bond dissociation energy, we used in our calculations the value just quoted (303 kcal/mol).

MC AND MCO (M = Ti, Fe, Ni, Cu) CASES

In Table I, we show the bond energies (in atomic units) for the optimized distances d(MC) as well as the adiabatic dissociation energies and electronic configurations of the different carbides MC. We evaluated these dissociation energies by subtracting from the bond energies the ones corresponding to the M and C atoms in the configurations and multiplicities that yield the lowest energies.

The bond energies for the different atoms that we used to calculate the E_{sof} are given below:

Doublet	Cu	(2 3 5/1 3 5)(s^1d^{10})	−0.009972 au
Triplet	Ni	(2 3 5/1 3 4)(s^1d^9)	−0.021278 au
Quintuplet	Fe	(2 3 5/2 3 1)(s^2d^6)	−0.137846 au
Quintuplet	Ti	(2 3 3/1 3 0)(s^1d^3)	−0.042003 au
Singlet	C	(1 1 0/1 1 0)(s^2p^2)	−0.000206 au

In Table II, we provide values for the equilibrium geometries, bond energies, and dissociation energies of the M—C bonds of the carbonyls given in [1] (for the Fe, Ni, and Cu compounds) and [2] (for the Ti compounds). We also included, under the column ΔD_e, the difference between the values of the M—C bond dissociation energies in the carbide and the corresponding carbonyl. This difference can be easily shown to be identical to the difference between the values of the C—O bond dissociation energy in free CO and the carbonyls, a key quantity in this report. This reduction is very important, since it shows the decrease in energy needed to dissociate the carbonyl—i.e., to break the C—O bond—when going from free CO to CO bonded to a metallic ligand. It explains why in catalytic processes, and especially in heterogeneous catalysis with transition elements, reactions whose rate-determining step involve the cleavage of that particular bond are enhanced compared to their noncatalyzed counterparts. The corresponding electronic configurations for the carbonyls are the ones detailed in the publications just referenced, so we shall not repeat them here.

TABLE I
MC compounds.

Molecule	d	E	D_e	Configuration	E_{sof}
CuC(2)	1.799	−0.154060	90.3	(5 5 2/5 4 2)	−0.010178
NiC(1)	1.624	−0.246783	141.4	(5 4 2/5 4 2)	−0.021484
NiC(3)	1.625	−0.230529	131.2	(5 5 2/4 4 2)	−0.021484
FeC(3)	1.565	−0.386087	155.6	(5 4 2/4 4 1)	−0.138052
FeC(5)	1.628	−0.357984	138.0	(5 5 2/4 4 0)	−0.138052
TiC(3)	1.679	−0.279043	148.6	(5 4 0/3 4 0)	−0.042209
TiC(5)	1.829	−0.244165	126.7	(5 4 1/3 3 0)	−0.042209

d: M—C distance (Å); E: bond energy (au); D_e: adiabatic bond dissociation energy (kcal/mol); E_{sof}: sum of fragments energy (au).

TABLE II
MCO compounds.

Molecule	d(MC)	d(CO)	a(MCO)	E	D_e	ΔD_e	D'_e
CuCO(2)	1.903	1.160	136.8	−0.575241	15.4	75	228.2
NiCO(1)	1.661	1.167	180.0	−0.659746	61.4	80	223.1
NiCO(3)	1.861	1.164	142.5	−0.605833	27.5	104	199.5
FeCO(3)	1.698	1.173	180.0	−0.753609	47.1	109	194.6
FeCO(5)	1.864	1.166	163.7	−0.741656	39.6	98	204.7
TiCO(3)	2.013	1.171	180.0	−0.626791	27.7	121	182.2
TiCO(5)	2.034	1.171	180.0	−0.653341	44.4	82	220.7

d(MC): M—C distance (Å); d(CO): C—O distance (Å); a(MCO): MCO angle (degrees); E: bond energy (au); D_e: M—C bond dissociation energy (kcal/mol); ΔD_e: difference between D_e values from Tables I and II (kcal/mol); D'_e: C—O bond dissociation energy (kcal/mol).

The interaction energies for MC + O correspond to dissociation energies of the C—O bond in the reverse reaction, i.e., MCO → MC + O. These values are obtained by adding the energy of O(3) (−0.057444 au) to the one of the corresponding carbide and then subtracting the energy of the carbonyl, listed in Table II. The optimized distance for the carbide was used; therefore, the result corresponds to the adiabatic dissociation energy D'_e.

It is interesting to compare the optimized distances M—C for the corresponding carbides (Table I) and carbonyls (Table II). In every case, we see a reduction in that distance when going from the carbonyl to the carbide. This is to be expected, since the strength of the C—M bond increases when only the M atom is the one bonded to the C atom, compared to the case when there is also a C—O bond involved. According to Tables I and II, this reduction goes from 0.037 Å for NiC(1) to 0.334 Å for TiC(3).

In the same fashion, we see a concomitant increase in the dissociation energy of the M—C bond when going from the carbonyl to the corresponding carbide, i.e., it is more difficult to remove the C atom from the metal surface when it is present as a carbide than as a carbonyl. This increase, which is presented under the column ΔD_e in Table II, also reaches its maximum at TiC(3).

For NiC, like NiCO, the singlet state turns out to be more stable than is the triplet. The differences in the distances d(Ni—C) are 0.037 Å for the singlet and 0.236 Å (much greater) for the triplet. Note that the distances d(Ni—C) in the case of the carbides are almost the same, whereas they are significantly larger for the triplet in the case of the carbonyls.

The reduction in D_e is 80 kcal/mol (similar to that of CuCO) for the ground state (singlet), but it increases to 104 kcal/mol for the excited state (triplet). When we go onto FeC, we see that—in the same manner as in FeCO—the triplet state is more stable than is the quintuplet and the values of $\Delta D'_e$ are 109 and 98 kcal/mol, respectively. For TiC, we find the triplet state to be more stable than is the quintuplet, as opposed to the corresponding carbonyls.

According to these values, the compound in which the C—O bond is strongest (of the ones considered here) is CuCO(2), followed closely by NiCO(1) and TiCO(5). On the other hand, it is weakest in TiCO(3), followed by FeCO(3). If we consider ground states only, then the weakest C—O bond is the one in FeCO(3), followed by TiCO(5) and NiCO(1). The strongest bond is still that of CuCO(2).

In Table III, we tabulate the charge transfer, dipole moment, and overlap for the carbide species, obtained via a Mulliken population analysis of the different compounds listed. Appropriate values for the carbonyls are also included. We observe an important charge transfer from the metal atoms to carbon, which—for the ground states—oscillates between 0.29 au for NiC(1) and 0.40 au for TiC(3). These values are always slightly higher for the corresponding excited states. The same order is obeyed by the dipole moments, as is to be expected. When compared to the carbonyls, we see

TABLE III
MC compounds.

Molecule	q	q'	μ	S	S'	$f(I)$	$f'(I')$
CuC(2)	0.3164	0.1032	2.433	0.37	0.28	621 (0.5)	386 (7)
NiC(1)	0.2868	0.1376	1.983	0.43	0.42	928 (25)	617 (0.2)
NiC(3)	0.3248	0.1132	2.752	0.43	0.33	877 (26)	460 (9)
FeC(3)	0.3412	0.1939	2.471	0.45	0.40	962 (57)	574 (26)
FeC(5)	0.3977	0.1896	3.013	0.46	0.37	887 (42)	462 (6)
TiC(3)	0.3969	0.2951	3.151	0.51	0.33	982 (83)	431 (10)
TiC(5)	0.4082	0.2675	3.265	0.37	0.34	865 (52)	402 (25)

q: Atomic charge transferred from the M to the C atom; μ: dipole moment (D); S: total M—C overlap; f: vibrational frequency (cm^{-1}); I: intensity (km / mol). Primed quantities refer to the corresponding carbonyl.

that the charge transfer is fairly smaller than in the carbide case, but follows essentially the same order.

In the same table, we display the vibrational frequencies and intensities of the M—C bonds for the carbides MC (f) and for the carbonyls MCO (f') (the latter were taken from [1, 2]). We can infer from them that there is a marked increase in the vibrational frequency of the M—C stretching mode when going from the carbonyl to the carbide (which goes from 235 cm^{-1} for CuC(2) to 551 cm^{-1} for TiC(3), concomitant with a reduction in the M—C bond distance.

For the ground states of NiC, FeC, and TiC, the frequencies are fairly close to one another and significantly greater than that of CuC. This denotes stronger M—C bonds in those compounds, in agreement with the dissociation energies given in Table I. The overlaps follow a similar trend.

In the case of TiC, comparing the triplet ground state to the excited quintuplet, we see that the vibrational frequency of the M—C bond in the first is significantly larger than in the second. This is also true for the dissociation energies (Table I).

M_nC AND M_nCO ($n = 5$ FOR M = Fe, Ni, Cu; $n = 7$ FOR M = Ti) CASES

In Table IV, like in Table I, we show the equilibrium geometries and bond energies of the carbide species with the C atom in the field of the M_n clusters as well as their adiabatic dissociation ener-

TABLE IV
M_nC compounds.

Molecule	d	E	D_e	Configuration	E_{sof}
$Cu_5C(2)(5, 0)$	1.750	−0.393986	93.7	(11 3 7 4 25 / 11 3 7 4 24)	−0.244523
$Cu_5C(2)(4, 1)$	0.05	−0.425183	157.4	(12 3 7 4 24 / 11 3 7 4 24)	−0.174142
$Ni_5C(1)(5, 0)$	1.625	−0.606384	145.8	(11 3 6 3 24 / 10 3 6 3 24)	−0.373782
$Ni_5C(1)(4, 1)$	−0.050†	−0.587068	183.8	(11 2 7 4 23 / 10 3 6 4 24)	−0.293903
$Ni_5C(3)(5, 0)$	1.65	−0.611966	149.3	(11 2 7 4 24 / 11 3 6 4 22)	−0.373782
$Ni_5C(3)(4, 1)$	−0.10†	−0.595919	189.4	(10 3 7 4 24 / 10 3 6 4 23)	−0.293903
$Fe_5C(3)(4, 1)$	0.50	−1.274801	186.0	(11 2 4 5 21 / 10 2 3 6 20)	−0.978150
$Fe_5C(5)(4, 1)$	0.40	−1.281033	189.9	(11 2 4 5 22 / 10 2 3 5 20)	−0.978150
$Ti_7C(3)(7, 0)$	1.82	−1.086318	129.9	(10 1 3 3 1 5 13 / 10 1 3 3 16 10)	−0.878152
$Ti_7C(5)(7, 0)$	1.79	−1.101740	139.5	(10 1 3 3 16 13 / 10 1 3 2 16 10)	−0.878152

d: M_1—C distance (Å); †: negative distances indicate central atom M_1 and C atom are on the same side of the M_4 plane; E: bond energy (au); D_e: bond dissociation energy (kcal / mol); E_{sof}: sum of fragments energy (au).

gies. To calculate these dissociation energies, one must know the bond energies for the M_n clusters in their configurations of minimum energy, which are listed below:

$Cu_5(5,0)$	(10 3 7 4 24/10 3 7 4 23)	−0.244317 au
$Cu_5(4,1)$	(10 3 7 4 24/10 3 7 4 23)	−0.173936 au
$Ni_5(5,0)$	(9 3 7 4 22/9 2 7 4 23)	−0.373576 au
$Ni_5(4,1)$	(9 3 7 4 22/9 2 7 4 23)	−0.293697 au
$Fe_5(4,1)$	(8 3 3 6 22/10 1 3 6 18)	−0.977944 au
$Ti_7(7,0)$	(9 1 3 3 16 12/8 1 3 2 16 10)	−0.878946 au

Adding to these energies the one of the C atom (which has already been quoted as −0.000206 au), we get the sum of fragments energy E_{sof}, shown in Table IV. Similarly, in Table V, we show the equilibrium geometries, bond energies, and dissociation energies of the M_n—C bond for the carbonyls, which have also been given in [1] for M = Fe, Ni, Cu and in [2] for M = Ti. These are obtained from the sum of fragments energy given above and the energy of CO at the equilibrium distance (1.139 Å), which is −0.540653 au. We also provide values for the sum of fragments (M_n and CO) energy, E_{sof}, but do not include the corresponding electronic configurations because they have already been given in prior reports, the only exception being those of the Ti clusters. These are (11 1 3 3 18 12/11 1 3 3 18 10) and (11 1 3 3 18 13/11 1 3 2 18 20) for $Ti_7CO(3)(7,0)$ and $Ti_7CO(5)(7,0)$, respectively. Note that the values reported in this table were calculated after optimization of the C—O distance, unlike in earlier publications [1].

Cu_5C Case

Let us consider first the Cu_5C cluster and its corresponding carbonyl in both (5,0) and (4,1) geometries.

Cu_5CO is more stable in the geometry (5,0) by 47 kcal/mol, whereas Cu_5C is more stable in the (4,1) geometry by 20 kcal/mol. The Cu_1—C distance in Cu_5C (5,0) is 1.750 Å, 0.049 Å smaller than in CuC. The dissociation energy of the Cu_5C bond is 93.7 kcal/mol, 3.4 kcal/mol greater than in the former case. In this way, we see that the interaction of CuC with the square ring Cu_4 brings about a strengthening of the C—Cu_5 bond.

When compared to the corresponding carbonyls, we see—in the (5,0) case—a reduction in the Cu—C distance: from 0.225 to 0.104 Å, which shows a greater interaction between the C atom and the Cu_5 group than between the C and the Cu atoms. The adiabatic dissociation energy of the C—O bond, D_e, is concomitantly reduced with respect to the CuCO case (from 228 to 215 kcal/mol).

In the case of the (4,1) cluster, we observe an equilibrium distance of 0.05 Å to the center of the square (on the opposite side relative to the C atom), and since the Cu_1 atom is 1.80 Å away from the Cu_4 plane, the distance Cu_1—C is 1.85 Å, just a little greater than the one in CuC (1.80 Å, Table I). However, here we have the influence of the Cu_4 ring, which increases considerably the dissociation energy of the Cu_5—C bond with respect to the (5,0) case, going from 93.7 to 157.4 kcal/mol. Thus, as the Cu_4 ring approaches the C atom, the intensity of the C-cluster bond is considerably enhanced

TABLE V
M_nCO compounds.

Molecule	d	d(CO)	E	E_{sof}	D_e	D'_e	ΔD_e	Diff.
$Cu_5CO(2)(5,0)$	1.975	1.160	−0.794584	−0.784970	6.03	215.3	87.8	12.9
$Cu_5CO(2)(4,1)$	1.70	1.15	−0.719414	−0.714589	3.03	148.6	154.5	79.7
$Ni_5CO(1)(5,0)$	1.70	1.17	−0.950188	−0.914229	22.55	179.7	123.4	43.4
$Ni_5CO(1)(4,1)$	0.02	1.23	−0.876046	−0.834350	26.16	145.3	157.8	77.8
$Ni_5CO(3)(5,0)$	1.75	1.17	−0.958880	−0.914229	28.02	181.6	121.4	17.8
$Ni_5CO(3)(4,1)$	0.05	1.22	−0.856103	−0.834350	13.65	127.2	175.9	72.2
$Fe_5CO(3)(4,1)$	1.05	1.22	−1.547066	−1.518597	17.86	134.8	168.3	59.8
$Fe_5CO(5)(4,1)$	0.90	1.25	−1.592293	−1.518597	46.24	159.3	143.8	45.4
$Ti_7CO(3)(7,0)$	2.00	1.16	−1.472449	−1.419599	33.16	206.3	96.8	−24.1
$Ti_7CO(5)(7,0)$	2.05	1.19	−1.484859	−1.419599	40.95	204.4	98.7	16.4

d: M_1—C distance (Å); d(CO): C—O distance (Å); E: bond energy (au); E_{sof}: sum of fragments energy (au); D_e: M_n—C bond dissociation energy (kcal/mol); D'_e: C—O bond dissociation energy (kcal/mol); Diff.: difference between ΔD_e values between Tables II and V (kcal/mol).

when going from (5, 0) to (4, 1). As for the dissociation energy of the C—O bond (D_e'), it shows the opposite change: it gets reduced from 215 to 149 kcal/mol.

Ni_5C Case

Let us now consider the Ni_5C case. Here, we have four different cases to analyze: singlet and triplet combined with (5, 0) and (4, 1) geometries. According to Table V, the triplet state is more stable than is the singlet by 3.5 kcal/mol for the (5, 0) case and by 5.6 kcal/mol for the (4, 1) case. This differs from the NiC case, where the singlet is more stable than is the triplet by 10.2 kcal/mol.

The dissociation energies D_e for the bonds Ni—C and Ni_5—C show tendencies similar to the ones of Cu. For the singlet, it increases slightly (from 141 to 146 kcal/mol) in the (5, 0) case and strongly (to 184 kcal/mol) in the (4, 1) case.

For the triplet, we have similar values, amounting to 18.1 and 58.2 kcal/mol increments. Thus, the interaction of the Ni_4 ring with the NiC carbide is similar to that of the Cu case.

Now, let us look at the corresponding carbonyls. In the case of NiCO, the singlet is more stable than is the triplet by 34 kcal/mol, according to Table II. In the case of Ni_5CO, the singlet is still more stable in the (4, 1) case, but the triplet is the more stable one when the structure is of the (5, 0) type. It is observed, then, that in going from NiCO to Ni_5CO, the difference in energy between the two multiplicities is reduced, being inverted in the (5, 0) case.

The reduction of the C—O bond dissociation energy amounts to 43 and 78 kcal/mol in the case of the singlet when going from NiCO(1) to Ni_5CO(5, 0) and Ni_5CO(4, 1), respectively. In the triplet case, we observe reductions of 18 and 72 kcal/mol when going from NiCO(3) to Ni_5CO(3)(5, 0) and Ni_5CO(3)(4, 1), respectively.

In [17], values are reported for compounds similar to the ones that are the subject of this study, but of the form Ni(5, 4) and Ni(4, 5) as well as Ni(5, 0) (in the nomenclature we are using). For Ni(4, 5), distances in the order of 0.1–0.3 Å are mentioned, not too different from the values found in the present report (0.05 and 0.10 Å, singlet and triplet, respectively). As for the Ni_n—C bond dissociation energies, they report a calculated value of 265 kcal/mol and an experimental one of 170 kcal/mol. The latter is in excellent agreement with our values (184 kcal/mol for the singlet and 189 kcal/mol for the triplet). However, in the (5, 0) case, their calculated value for the Ni_1—C distance is 1.18 Å, substantially smaller than ours (1.625 Å), and a bond dissociation energy of 117 kcal/mol, whereas our values are 146 kcal/mol for the singlet and 149 kcal/mol for the triplet.

Fe_5C Case

In the case of Fe_5C, we have only the (4, 1) geometry for the cluster and the triplet and quintuplet states. Regarding the carbide species, we see that—according to Table IV—the quintuplet is more stable than is the triplet by 3.9 kcal/mol, unlike the FeC case, where the triplet is more stable than is the quintuplet by 17.6 kcal/mol. This shows the great influence that the Fe_4 ring has over the FeC species, which is also reflected by the fact that the C atom is almost in the Fe_4 plane.

As in prior cases, let us consider the influence that the Fe_4 group has over the Fe_5—C bond dissociation energy in the carbides and over the C—O bond in the carbonyls. We observe an increment in the former energy in the case of the triplet, going from 155.6 (FeC) to 186.0 kcal/mol (Fe_5C). In the case of the quintuplet, the corresponding change is from 138.0 to 189.9 kcal/mol. Once again, the strengthening of the Fe—C bond by the action of the Fe_4 ring is clearly manifested.

If we focus on the C—O bond dissociation energy, we infer—from Tables II and V—that in the case of the triplet it diminishes by 59.8 kcal/mol. In the case of the quintuplet, the corresponding reduction is 45.4 kcal/mol. The influence of the Fe_4 ring on the FeCO species is found to strengthen the interaction of the Fe atom with the metallic cluster and weaken the C—O bond.

In [18], the compound $Fe_5C(CO)_{15}$ was considered. It has three carbonyl groups per Fe atom, and it is the first carbide cluster reported in the literature, being the most similar one to our Fe_5C. The only information that is provided about this carbide is the distance from the C atom to the Fe_4 plane, which is estimated as being 0.08 Å. Our value is 0.40 Å, which is much larger, but one should keep in mind the differences between the two compounds.

Ti_7C Case

Lastly, let us consider the Ti carbides and carbonyls. Here, we focused only on the (7, 0) geometry of the cluster. From Table IV, we see that in the case of Ti_7C the quintuplet is more stable than is the triplet by 9.6 kcal/mol. This is quite the opposite of TiC, where the triplet is more stable by 21.9 kcal/mol, as in the Fe cases. When we move onto the corresponding carbonyl compounds, we find the quintuplet to be more stable in both cases, the differences being 7.8 kcal/mol for Ti_7CO and 16.7 kcal/mol for TiCO.

In the case of $Ti_7C(5)$, which is the ground state, there is a 12.8 kcal/mol increment with respect to the (excited) state TiC(5). This change is similar to those already seen in planar cases.

However, if we consider $Ti_7C(3)$ (excited state), there is a 18.7 kcal/mol reduction in the Ti—C bond dissociation energy. This is an anomalous case, since it means that the interaction of the Ti_6 ring with the TiC carbide strengthens the C–metal bond for the ground state, but not for the excited state.

We have a similar situation for the C—O bond in the case of the carbonyls. In the quintuplet, the C—O bond dissociation energy decreases by 16.3 kcal/mol when going from TiCO(5) to $Ti_7CO(5)$. In this case, both states are ground states. In the triplet, we have again an anomalous case, since the C—O bond dissociation energy increases by 24.1 kcal/mol.

When we concentrate on the values of charge transfer, we see that in the Cu and Ni compounds there is a marked increase (as shown in Table VI) when going from the (5, 0) to the (4, 1) geometry, whereas a reduction is observed in the dipole moments. In the (5, 0) and (7, 0) cases, this charge transfer is similar to those of the carbides MC, listed in Table III.

For the charge distribution analysis, we will consider a typical case only. Choosing Cu_5C as an example, a population analysis gives us for the atoms on the vertices of the square a positive charge of 0.1030 au, whereas that on the central one is −0.1586 au. This leaves a total charge for the cluster of 0.2535 au, which is the net electronic charge transferred to the C atom. In the (4, 1) case, each Cu atom on a vertex carries a positive charge not too different from that of the previous case (0.1126 au), but the fifth Cu atom now bears a positive charge as well (0.1278 au), which results in a larger positive charge on the cluster (0.5782 au).

TABLE VI
M_nC compounds.

Molecule	q	μ
$Cu_5C(2)$ (5, 0)	0.2535	1.335
$Cu_5C(2)$ (4, 1)	0.5782	0.313
$Ni_5C(1)$ (5, 0)	0.3494	1.781
$Ni_5C(1)$ (4, 1)	0.6035	0.403
$Ni_5C(3)$ (5, 0)	0.3208	1.565
$Ni_5C(3)$ (4, 1)	0.5695	0.142
$Fe_5C(3)$ (4, 1)	0.4786	0.868
$Fe_5C(5)$ (4, 1)	0.5507	0.755
$Ti_7C(3)$ (7, 0)	0.4049	0.988
$Ti_7C(5)$ (7, 0)	0.4141	0.935

q: Electronic charge transferred from M_n to C (au). μ: dipole moment (D).

Conclusions

1. For the carbides considered in this report, the most stable states are the singlet for NiC and the triplets for FeC and TiC, which is quite similar to the corresponding carbonyl compounds, except for TiCO, where the quintuplet is more stable than is the triplet.
2. M—C bond lengths are significantly reduced when going from the carbonyls to the corresponding carbides, whereas bond dissociation energies increase in like manner.
3. There is a sizable reduction in the dissociation energy of the C—O bond of the carbonyls with respect to the free CO molecule.
4. In the case of the M—C carbides, we observe an important charge transfer from the metal atom to the C atom, which varies between 0.30 and 0.40 electronic charge units.
5. The stretching frequencies for the M—C bonds of the MC carbides increase, as is to be expected, in the same order as bond dissociation energies. These values are considerably higher than the ones of the corresponding carbonyls.
6. Considering now the M_nC carbides, we find the following results: First, for Cu_5C, the geometry of the (4, 1) cluster is more stable than is the (5, 0) one, as opposed to the car-

bonyl case. Ni_5C, however, shows higher stability for the (5, 0) geometry, and at the same time, the triplet becomes slightly more stable than is the singlet. NiC displays the opposite behavior. In the case of Fe_5C, the quintuplet is more stable than is the triplet, in a similar way to that of the corresponding carbonyls and unlike TiC, where the triplet is more stable than is the quintuplet. For Ti_7C, and also for Ti_7CO, the quintuplet is more stable than is the triplet. We find the opposite order for TiC.

7. Looking now at the dissociation energy of the C—O bond in the M_nCO compounds, we notice a reduction with respect to the corresponding MCO compounds. This reduction is moderate for the planar geometries, but significantly greater for the nonplanar ones. This means that the C—O bond is weakened considerably by the influence of the M_4 group (M = Cu, Ni, Fe). In the case of Ti_7CO, we find a similar reduction in the C—O bond energy (compared to TiCO), but this is only so in the ground quintuplet state, since in the excited triplet state, we find an increase in that energy.

ACKNOWLEDGMENT

Financial support from CONICYT (Consejo Nacional de Investigaciones Científicas y Tecnológicas) of Uruguay is gratefully acknowledged.

References

1. R. M. Sosa and P. Gardiol, Int. J. Quantum Chem.: Quantum Chem. Symp. **30**, 1429 (1996).
2. R. M. Sosa and P. Gardiol, Int. J. Quantum Chem. (in press).
3. R. M. Sosa and P. Gardiol, J. Mol. Struct. (Theochem) (in press).
4. W. Kohn and L. J. Sham, Phys. Rev. A **140**, 1133 (1965).
5. ADF 2.0.1, SCM, Theoretical Chemistry (Wrije Universiteit, Amsterdam); E. J. Baerends, D. E. Ellis, and P. Ross, Chem. Phys. **2**, 41 (1973); G. te Velde and E. J. Baerends, J. Comp. Phys. **99**, 84 (1992) (There is a newer release: ADF 2.1, December, 1996).
6. J. C. Slater, Phys. Rev. **81**, 381 (1952).
7. S. J. Vosko, L. Wilk, and M. Nusair, Can. J. Phys. **58**, 1200 (1980).
8. A. D. Becke, Phys. Rev. A **38**, 3098 (1988).
9. J. P. Perdew, Phys. Rev. B **33**, 8822 (1986); Errata: **34**, 7406 (1986).
10. P. M. Boerrigter, G. te Velde, and E. J. Baerends, *Int. J. Quantum Chem.* **33**, 87 (1988).
11. T. Ziegler and A. Rauk, Theor. Chem. Acta **46**, 1 (1977).
12. D. Post and E. J. Baerends, J. Chem. Phys. **78**, 5663 (1983).
13. L. Fang and T. Ziegler, J. Chem. Phys. **95**, 7401 (1991).
14. T. Ziegler, Chem. Rev. **91**, 651 (1991).
15. K. P. Huber and G. Herzberg, *Constants of Diatomic Molecules* (Van Nostrand Reinhold, New York, 1979).
16. B. I. Dunlap, H. L. Yu, and P. R. Antoniewicz, Phys. Rev. A **25**(1), 25 (1982).
17. R. Fournier, N. Russo, D. R. Salahub, and M. Toscano in *Cluster Models for Surface and Bulk Phenomena*, G. Pacchioni, P. S. Bagus, and F. Parmigianni, Eds., NATO ASI Series, Series B, Phys. Vol. 283 (Plenum, New York, 1992), p. 433.
18. M. Tachikawa and E. L. Muetterties, Progress Inorg. Chem. **28**, 203 (1981).

Density Matrix Methods for Semiconductor Coulomb Dynamics

JAMES W. DUFTY,[1] CHANG SUB KIM,[2] MICHAEL BONITZ,[3] ROLF BINDER[4]

[1]*Department of Physics, University of Florida, Gainesville, Florida 32611*
[2]*Department of Physics, Chonnam National University, Kwangju 500-757, South Korea*
[3]*Universität Rostock, Fachbereich Physik, Universitätsplatz 3, Rostock 18051, Germany*
[4]*Optical Sciences Center, University of Arizona, Tucson, Arizona 85721*

Received 29 March 1997; revised 28 April 1997; accepted 8 May 1997

ABSTRACT: Current experiments on semiconductor devices using femtosecond lasers provide new theoretical challenges for the description of charge carrier dynamics. Among the new features of such experiments are states driven very far from equilibrium and probes on time scales short compared to scattering and other characteristic material relaxation times. Standard many-body methods must be modified and extended to accommodate these features. We propose that the quantum hierarchy for reduced density operators is an ideal formulation of such initial value problems and describe how the dominant effects of exchange and charge correlations can be accounted for in a simple and physically transparent closure of the hierarchy of equations. The transformations, approximations, and interpretation can be accomplished independent of any particular matrix representation. Decomposition into kinetic equations for band occupation densities and polarization densities follows in a straightforward way after the many-body problem has been brought under control. © 1997 John Wiley & Sons, Inc. Int J Quant Chem **65**: 929–940, 1997

Correspondence to: J. W. Dufty.
Contract grant sponsor: NSF.
Contract grant numbers: INT 9414072; PHY 9312723.
Contract grant sponsors: KOSEF; KRF.

© 1997 John Wiley & Sons, Inc.
CCC 0020-7608 / 97 / 050929-12

Introduction

For the past decade, the fabrication of ultrasmall devices and associated developments in laser technology for exploration of their properties have raised important theoretical questions, both conceptual and practical. In particular, the short times sampled in femtosecond laser studies and the wealth of potential information from different initial preparations call for a description of Coulomb kinetics (e.g., electrons and holes) far from equilibrium, extending from initial times to times long compared to the characteristic collision times and dephasing times [1, 2]. Such theoretical considerations already have been explored in other contexts, such as transport in simple classical liquids and plasmas [3] and for nuclear matter [4], but their experimental relevance in these cases has been less compelling. The objective here is to formulate the problem of Coulomb kinetics in terms of the fundamental exact first two hierarchy equations for the one- and two-particle reduced density operators. Practical applications result from an approximate closure of the two-particle equation subject to important constraints on acceptable approximations associated with conservation laws, representability, stationary solutions, and quantum statistics. These structural properties are independent of considerations of classical or quantum effects and do not rely on the matrix representation appropriate to the specific problem. The theoretical analysis of a given approximation occurs at the compact abstract level for greatest simplicity and generality and in a formulation that allows exploitation of previous work on classical systems.

This approach is illustrated for a simple two-band model of a semiconductor, to show how corrections to the semiconductor Bloch equations can be constructed to include the effects of scattering and dynamic screening. In this discussion, only electron–electron and electron–laser interactions are considered; the lattice is presumed to be rigid. A simple closure approximation including exact three-particle exchange correlations and all residual pair correlations is indicated and its content discussed. Solution of the two-particle equation gives the two-particle reduced density operator as a functional of the one-particle density operator. Use of this result in the first hierarchy equation for the one-particle density operator gives a closed kinetic equation. The resulting non-Markovian kinetic equation describes the evolution of an arbitrary initial preparation from asymptotically short times to the long-time Boltzmann limit. The short time evolution includes the buildup of dynamical screening (polarization effects); at long times, the Boltzmann scattering rates are determined from the full T-matrix rather than from the weak coupling Born approximation.

In this brief presentation, only the theoretical structure and method are described as an overview of the general approach to carrier dynamics. More detailed calculations based on the approximation suggested here are in progress.

Reduced Density Operators and Hierarchy

We consider N electrons interacting with a rigid ionic lattice, with overall charge neutrality. The electrons interact with the lattice and with each other via bare Coulomb potentials. In addition, they interact with a classical (i.e., many photon) transverse electric field, $\mathbf{E}(t)$ via a dipole interaction. The Hamiltonian for the system is then

$$H(t) = H_0 + U + U_{ext}(t), \qquad H_0 = \sum_{i=1}^{N} h_0(i) \quad (1)$$

$$U = \frac{1}{2}\sum_{i\neq j}^{N} V(i,j), \qquad U_{ext} = -\mu\cdot\mathbf{E}(t), \quad (2)$$

where $h_0(i)$ is the single-particle Bloch Hamiltonian for interaction of electron i with the lattice, $V(i, j)$ is the Coulomb potential for interaction of electrons i, j, and $\mu = \sum_{i=1}^{N} \mu(i)$ is the total dipole moment due to all electrons. The external field $\mathbf{E}(t)$ characterizes the laser field, which may have a very short time scale in some pump experiments, but may also represent a longer time driving field with a duration comparable to various dephasing mechanisms. The details of this field are not important for the formal considerations here, but can play a role in the numerical method used to solve the equations. The eigenvalue problem for the Bloch Hamiltonian is described by

$$h_0\psi_\alpha(\mathbf{k}) = \epsilon_\alpha(\mathbf{k})\psi_\alpha(\mathbf{k}), \quad (3)$$

where α denotes the band index, and $\mathbf{k}$, the momentum quantum number (here and in the following we set $\hbar = 1$).

The initial state of the system is defined by an N-particle density operator, $\rho(1,\ldots,N)$. This could be the Gibbs distribution if the electron–lattice system is initially in equilibrium, but it is not necessary to specify its form at this point. Implicit in the definition of the density matrix is an N-particle symmetrization operator so that a representation of its matrix elements in terms of unsymmetrized products of single particle states is possible [5]. This is an important feature that will be exploited in the next section to extract the exchange correlation of the reduced density operators associated with $\rho(1,\ldots,N)$. The time evolution of the density operator is governed by the Liouville–von Neumann equation

$$\partial_t \rho(t) + i[H(t), \rho(t)] = 0. \tag{4}$$

The reduced density operators for m particles are defined by

$$f^{(m)}(1,\ldots,m;t) = N^m Tr_{m+1\ldots N}\rho(t). \tag{5}$$

The notation on the right side indicates a trace over the degrees of freedom associated with particles $m+1$ through N. More precisely, in matrix representation, it denotes summation over the diagonal quantum numbers for these particles. The reduced density operators $f^{(m)}$ inherit an M-particle symmetrization operator from the corresponding N-particle symmetrization operator in ρ. The BBGKY (Born, Bogoliubov, Green, Kirkwood, Yvon) hierarchy equations [5,6] for the time dependence of the reduced distribution functions now follow directly from a partial trace of the Liouville–von Neumann equation,

$$\begin{aligned}\partial_t f^{(m)}(1,\ldots,m;t) &+ \sum_{i=1}^{m} i\big[(h_0(i) - \mu(i)\cdot\mathbf{E}(t)),\\ &f^{(m)}(1,\ldots,m;t)\big]\\ &+ \sum_{i\neq j}^{m} i[V(i,j), f^{(m)}(1,\ldots,m;t)]\\ &= -\sum_{i=1}^{m} Tr_{m+1} i[V(i,m+1),\\ &f^{(m+1)}(1,\ldots,m+1;t)].\end{aligned} \tag{6}$$

The left side of this equation is just the Liouville–von Neumann equation for m isolated particles. The right side expresses a coupling to the other degrees of freedom through the Coulomb interactions. In the following, it will be sufficient to consider only the cases with $m = 1$ and 2,

$$\begin{aligned}\partial_t f^{(1)}(1;t) &+ i[H(1;t), f^{(1)}(1;t)]\\ &+ Tr_2 i[V(1,2), f^{(2)}(1,2;t)] = 0\end{aligned} \tag{7}$$

$$\begin{aligned}\partial_t f^{(2)}(1,2;t) &+ i[H(1,2;t), f^{(2)}(1,2;t)]\\ &+ \sum_{i=1}^{2} Tr_3 i[V(i,3), f^{(3)}(1,2,3;t)] = 0,\end{aligned} \tag{8}$$

where the single-particle and two-particle Hamiltonians are given by

$$\begin{aligned}H(1;t) &= h_0(1) - \mu(1)\cdot\mathbf{E}(t) \qquad H(1,2;t)\\ &= \sum_{i=1}^{2}(h_0(i) - \mu(i)\cdot\mathbf{E}(t)) + V(1,2).\end{aligned} \tag{9}$$

These equations are exact but formal since they are not closed in terms of $f^{(1)}$ and $f^{(2)}$ alone. It is necessary to construct a suitable approximation that expresses $f^{(3)}$ as a functional of $f^{(1)}$ and $f^{(2)}$. Then Eqs. (7) and (8) provide the means to calculate $f^{(1)}$ and $f^{(2)}$. In particular, if the equation for $f^{(2)}$ is solved as a functional of $f^{(1)}$, i.e.,

$$f^{(2)}(1,2;t) = F^{(2)}(1,2;t \mid f^{(1)}), \tag{10}$$

then use of this solution in the first hierarchy Eq. (7) provides a closed *kinetic equation* for $f^{(1)}$:

$$\begin{aligned}\partial_t f^{(1)}(1;t) &+ i[H(1;t), f^{(1)}(1;t)]\\ &+ Tr_2 i[V(1,2), F^{(2)}(1,2;t \mid f^{(1)})] = 0.\end{aligned} \tag{11}$$

This is the approach proposed here for obtaining the appropriate kinetic equation for charge carriers. The procedure is representation-independent, and as a first-order equation in time, it is appropriately posed as an initial value problem. This is in contrast to the alternative nonequilibrium Keldysh Green's function method which requires a detailed reconstruction of the specified initial conditions from an artificial past history [7].

Exact Exchange Effects and Correlations

There are two important sources of correlations among the charge carriers. One is due to the long-range Coulomb interaction, while the other is due to the exchange symmetry among particles of the

same species. It is useful to extract explicitly the dominant effects due to exchange symmetry by identifying the exchange operators implicit in the definitions of the reduced density operators. This will allow a more controlled identification of the residual correlations due to Coulomb interactions. The two- and three-particle reduced density operators are expressed as

$$f^{(2)}(1,2;t) \equiv \tilde{f}^{(2)}(1,2;t)\mathscr{S}(1,2) = \mathscr{S}(1,2)\tilde{f}^{(2)}(1,2;t) \quad (12)$$

$$f^{(3)}(1,2,3;t) \equiv \tilde{f}^{(3)}(1,2,3;t)\mathscr{S}(1,2,3) = \mathscr{S}(1,2,3)\tilde{f}^{(3)}(1,2,3;t), \quad (13)$$

where $\mathscr{S}(1,2)$ and $\mathscr{S}(1,2,3)$ are the two- and three-particle antisymmetrization operators that convert product states for two and three electrons into antisymmetric states, respectively. Such symmetrization factors occur necessarily from the definition of the underlying N-particle density matrix. The last equality follows from the permutation symmetry of the reduced density operators and of the symmetrization operators. Next, the correlation operators associated with $\tilde{f}^{(2)}(1,2;t)$ and $\tilde{f}^{(3)}(1,2,3;t)$ are introduced:

$$\tilde{f}^{(2)}(1,2;t) \equiv f^{(1)}(1;t)f^{(1)}(2;t) + \bar{g}(1,2;t) \quad (14)$$

$$\tilde{f}^{(3)}(1,2,3;t) \equiv f^{(1)}(1;t)f^{(1)}(2;t)f^{(1)}(3;t) + f^{(1)}(1;t)\bar{g}(2,3;t) + f^{(1)}(2;t)\bar{g}(1,3;t) + f^{(1)}(3;t)\bar{g}(1,2;t) + \bar{g}(1,2,3;t). \quad (15)$$

Since the symmetrization operators have been extracted explicitly in (12) and (13), the correlation functions $\bar{g}(1,2;t)$ and $\bar{g}(1,2,3;t)$ are primarily measures of correlations due to the Coulomb interactions. Conversely, even when there are no correlations in $\tilde{f}^{(2)}(1,2;t)$ and $\tilde{f}^{(3)}(1,2,3;t)$, the distribution functions $f^{(2)}(1,2;t)$ and $f^{(3)}(1,2,3;t)$ have two- and three-particle correlations induced by the antisymmetrization operators. Therefore, it is useful to rewrite the first two hierarchy equations in terms of $\bar{g}(1,2;t)$ and $\bar{g}(1,2,3;t)$. The first equation becomes

$$\partial_t f^{(1)}(1;t) + i[H(1;t), f^{(1)}(1;t)] + Tr_2 i\left[V_s(1,2), f^{(1)}(1;t)f^{(1)}(2;t)\right] + Tr_2 i[V_s(1,2), \bar{g}(1,2;t)] = 0, \quad (16)$$

where $V_s(1,2) \equiv V(1,2)\mathscr{S}(1,2)$ is the pair potential with exchange effects. The left side of this equation is recognized as generating the time-dependent Hartree–Fock dynamics so the equation becomes

$$\partial_t f^{(1)}(1;t) + i\left[H_{hf}(1;t), f^{(1)}(1;t)\right] = -Tr_2 i[V_s(1,2), \bar{g}(1,2;t)], \quad (17)$$

where the Hartree–Fock Hamiltonian is

$$H_{hf}(1;t) = H(1;t) + V_{hf}(1;t),$$
$$V_{hf}(1;t) \equiv Tr_2 f^{(1)}(2;t)V_s(1,2). \quad (18)$$

This is the expected result: The mean-field Hartree–Fock dynamics is modified by a coupling to other electrons due to the presence of Coulomb correlations.

The equation for the correlations, $\bar{g}(1,2;t)$, follows from the second hierarchy equation. The effects of the symmetrization operators are evaluated in detail in the Appendix leading to the exact equation for $\bar{g}(1,2;t)$:

$$\begin{aligned}\partial_t \bar{g}(1,2;t) &+ i\left[\hat{H}(1,2;t)\bar{g}(1,2;t) - \bar{g}(1,2;t)\hat{H}^{\dagger}(1,2;t)\right] \\ &+ Tr_3 i\left\{\left[V_s(1,3), f^{(1)}(1;t)\right]\times\bar{g}(2,3;t)\mathscr{S}(2,3) + \left[V_s(2,3), f^{(1)}(2;t)\right]\times\bar{g}(1,3;t)\mathscr{S}(1,3)\right\} \\ &= -i\left\{\hat{V}(1,2;t)f^{(1)}(1;t)f^{(1)}(2;t) - f^{(1)}(1;t)f^{(1)}(2;t)\hat{V}^{\dagger}(1,2;t)\right\} \\ &- \sum_{j=1}^{2} Tr_3 i[V(j,3), \bar{g}(1,2,3;t)\times(1 - P_{13} - P_{23})], \end{aligned} \quad (19)$$

with the definitions

$$\hat{H}(1,2;t) = H_{hf}(1;t) + H_{hf}(2;t) + \hat{V}(1,2;t) \quad (20)$$

$$\hat{V}(1,2;t) \equiv \{1 - f^{(1)}(1;t) - f^{(1)}(2;t)\}V(1,2). \quad (21)$$

The first two terms on the left side describe pair dynamics generated by the Hamiltonian $\hat{H}(1,2;t)$. This Hamiltonian differs from $H(1,2)$ in two important ways: First, the single-particle energies are renormalized to the mean-field Hartree–Fock energies. Second, the pair potential is modified

by the prefactor $\{1 - f^{(1)}(1;t) - f^{(1)}(2;t)\}$ describing "blocking" effects of the statistics. To see this, note that $\{1 - f^{(1)}(1;t) - f^{(1)}(2;t)\} = \{h^{(1)}(1;t)h^{(1)}(2;t) - f^{(1)}(1;t)f^{(1)}(2;t)\}$, where $h^{(1)}(1;t) = 1 - f^{(1)}(1;t)$ is the "hole" occupancy. Thus, the matrix elements of $\hat{V}(1,2;t)$ are restricted according to the occupation of carrier density in the nonequilibrium state. Both the blocking and mean-field effects in $\hat{H}(1,2;t)$ account for significant many-particle correlations in this effective pair dynamics. The third and fourth terms on the left side describe polarization or screening effects that are essential for a proper treatment of the long-ranged Coulomb interactions. In the classical limit, these are the linearized Vlasov operators leading to the Debye–Hückel dynamic screening and pair correlations. Here, these operators generate the random phase or chain approximation including exchange effects. The first term on the right side of (20) is a source of correlations due to the "commutator" of $\hat{V}(1,2;t)$ with the uncorrelated pair operator $f^{(1)}(1;t)f^{(1)}(2;t)$; equivalently, the time derivative of the uncorrelated state is correlated due to the Coulomb interactions. Here, this source of correlations is due to the pair interaction including blocking effects. Finally, all residual many-body effects are contained in the last term on the right side describing three-particle correlations not associated solely with three-particle exchange effects.

Equations (17) and (20) are still exact and fully equivalent to Eqs. (7) and (8). However, the analysis of the exchange effects and the transformation to the correlation functions provides a form in which the dominant mean field, polarization, and blocking effects are made explicit. This is a more convenient form for introduction of appropriate approximations or application to specific problems.

Bloch Representation

The above analysis has used only the abstract operator form of the reduced density operators and associated hierarchy equations. Specific applications require a particular matrix representation. For example, a fully ionized plasma might best be described in terms of single-particle momentum states. To show the relationship of the density matrix approach to the standard equations of semiconductor physics, we consider a representation using Bloch states $\psi_{\alpha\mathbf{k}}(\mathbf{r}) = \langle \mathbf{r} \mid \alpha\mathbf{k}\rangle$, $h(1) \mid \alpha\mathbf{k}\rangle = \epsilon_\alpha(\mathbf{k}) \mid \alpha\mathbf{k}\rangle$. Only the first hierarchy equation will be considered; the analysis for the second equation is similar:

$$\partial_t f^{(1)}(1;t) + i\left[H_{hf}(1;t), f^{(1)}(1;t)\right] + C(1;t) = 0, \tag{22}$$

where $C(1;t)$ is the "collision" operator due to pair correlations

$$C(1;t) = Tr_2 i[V_s(1,2), \bar{g}(1,2;t)]. \tag{23}$$

The band occupation densities, $n_\alpha(\mathbf{k};t)$, and the polarization densities, $p_{\alpha\alpha'}(\mathbf{k};t)$, are defined by

$$n_\alpha(\mathbf{k};t) \equiv \langle \alpha\mathbf{k} \mid f^{(1)}(t) \mid \alpha\mathbf{k}\rangle$$
$$p_{\alpha\alpha'}(\mathbf{k};t) \equiv \langle \alpha\mathbf{k} \mid f^{(1)}(t) \mid \alpha'\mathbf{k}\rangle, \tag{24}$$

where the band indices $\alpha \neq \alpha'$ in the definition of the polarization density $p_{\alpha\alpha'}(\mathbf{k};t)$. To simplify the discussion, we consider the case of only two bands (conduction and valence). Also, we consider only homogeneous states, so that the one-particle density matrix is diagonal in the wave vector, $\mathbf{k}$. The equations are then found to be

$$\partial_t n_\alpha(\mathbf{k};t) - 2\mathrm{Im}\left\{\langle \alpha\mathbf{k} \mid H_{hf}(1;t) \mid \alpha'\mathbf{k}\rangle p_{\alpha'\alpha}(\mathbf{k};t)\right\} + C_{\alpha\alpha}(\mathbf{k};t) = 0 \tag{25}$$

$$\partial_t p_{\alpha\alpha'}(\mathbf{k};t) + i\left[\langle \alpha\mathbf{k} \mid H_{hf}(1;t) \mid \alpha\mathbf{k}\rangle - \langle \alpha'\mathbf{k} \mid H_{hf}(1;t) \mid \alpha'\mathbf{k}\rangle\right] p_{\alpha\alpha'}(\mathbf{k};t) + i\langle \alpha\mathbf{k} \mid H_{hf}(1;t) \mid \alpha'\mathbf{k}\rangle \times [n_{\alpha'}(\mathbf{k};t) - n_\alpha(\mathbf{k};t)] + C_{\alpha\alpha'}(\mathbf{k};t) = 0, \tag{26}$$

where it is understood that $\alpha \neq \alpha'$. The matrix elements in these equations are easily evaluated:

$$\langle \alpha\mathbf{k} \mid H_{hf}(1;t) \mid \nu\mathbf{k}\rangle = \epsilon_\alpha(\mathbf{k})\delta_{\alpha,\nu} + \langle \alpha\mathbf{k} \mid V_{hf} \mid \nu\mathbf{k}\rangle - \mathbf{E}(t)\cdot\mu_{\alpha\nu}, \tag{27}$$

where $\mu_{\alpha\nu}(\mathbf{k}) \equiv \langle \alpha\mathbf{k} \mid \mu \mid \nu\mathbf{k}\rangle$. Equations (25) and (26) then become

$$\partial_t n_\alpha(\mathbf{k};t) - 2\mathrm{Im}\left\{\left[\langle \alpha\mathbf{k} \mid V_{hf} \mid \alpha'\mathbf{k}\rangle - \mathbf{E}(t)\cdot\mu_{\alpha\alpha'}\right] \times p_{\alpha'\alpha}(\mathbf{k};t)\right\} + C_{\alpha\alpha}(\mathbf{k};t) = 0 \tag{28}$$

$$\partial_t p_{\alpha\alpha'}(\mathbf{k};t) + i\left[\langle \alpha\mathbf{k} \mid H_{hf}(1;t) \mid \alpha\mathbf{k}\rangle - \langle \alpha'\mathbf{k} \mid H_{hf}(1;t) \mid \alpha'\mathbf{k}\rangle\right] p_{\alpha\alpha'}(\mathbf{k};t) + i\left[\langle \alpha\mathbf{k} \mid V_{hf} \mid \alpha'\mathbf{k}\rangle - \mathbf{E}(t)\cdot\mu_{\alpha\alpha'}\right] \times (n_{\alpha'}(\mathbf{k};t) - n_\alpha(\mathbf{k};t)) + C_{\alpha\alpha'}(\mathbf{k};t) = 0. \tag{29}$$

The matrix elements of the Hartree–Fock potential are easily evaluated and the resulting equations for $n_\alpha(\mathbf{k};t)$ and $p_{\alpha\alpha'}(\mathbf{k};t)$ are found to be

$$\begin{aligned}
&\partial_t n_c(\mathbf{k};t) + 2\mathrm{Im}(\mathbf{E}(t)\cdot\mu_{cv}p_{vc}(\mathbf{k};t)) \\
&\quad + 2\mathrm{Im}\sum_{\mathbf{q}}\tilde{V}(q)[\,n_c(\mathbf{k}+\mathbf{q};t)I_{cc}(\mathbf{k},-\mathbf{q}) \\
&\quad \times I^*_{vc}(\mathbf{k},-\mathbf{q}) + n_v(\mathbf{k}+\mathbf{q};t) \\
&\quad \times I_{cv}(\mathbf{k},-\mathbf{q})I^*_{vv}(\mathbf{k},-\mathbf{q}) \\
&\quad + p_{cv}(\mathbf{k}+\mathbf{q};t)I_{cc}(\mathbf{k},-\mathbf{q})I^*_{vv}(\mathbf{k},-\mathbf{q}) \\
&\quad + p_{vc}(\mathbf{k}+\mathbf{q};t)I_{cv}(\mathbf{k},-\mathbf{q})I^*_{vc}(\mathbf{k},-\mathbf{q})]\,p_{vc}(\mathbf{k};t) \\
&\quad + C_{cc}(\mathbf{k};t) = 0 \qquad (30)\\
&\partial_t p_{cv}(\mathbf{k};t) + i(\epsilon_c(\mathbf{k}) - \epsilon_v(\mathbf{k}) - \mathbf{E}(t) \\
&\quad \cdot[\,\mu_{cc} - \mu_{vv}])p_{cv}(\mathbf{k};t) \\
&\quad - i\sum_{\mathbf{q}}\tilde{V}(q)\Big[\,n_c(\mathbf{k}+\mathbf{q};t) \\
&\quad \times\big(|I_{cc}(\mathbf{k},-\mathbf{q})|^2 - |I_{vc}(\mathbf{k},-\mathbf{q})|^2\big) \\
&\quad + n_v(\mathbf{k}+\mathbf{q};t)\big(|I_{cv}(\mathbf{k},-\mathbf{q})|^2 - |I_{vv}(\mathbf{k},-\mathbf{q})|^2\big) \\
&\quad + 2p_{cv}(\mathbf{k}+\mathbf{q};t)\mathrm{Re}(I_{cc}(\mathbf{k},-\mathbf{q})I^*_{cv}(\mathbf{k},-\mathbf{q}) \\
&\quad - I_{vc}(\mathbf{k},-\mathbf{q})I^*_{vv}(\mathbf{k},-\mathbf{q}))]\,p_{cv}(\mathbf{k};t) \\
&\quad - i\Big\{\sum_{\mathbf{q}}\tilde{V}(q)[\,n_c(\mathbf{k}+\mathbf{q};t) \\
&\quad \times I_{cc}(\mathbf{k},-\mathbf{q})I^*_{vc}(\mathbf{k},-\mathbf{q}) + n_v(\mathbf{k}+\mathbf{q};t) \\
&\quad \times I_{cv}(\mathbf{k},-\mathbf{q})I^*_{vv}(\mathbf{k},-\mathbf{q}) \\
&\quad + p_{cv}(\mathbf{k}+\mathbf{q};t) \\
&\quad \times I_{cc}(\mathbf{k},-\mathbf{q})I^*_{vv}(\mathbf{k},-\mathbf{q}) + p_{vc}(\mathbf{k}+\mathbf{q};t) \\
&\quad \times I_{cv}(\mathbf{k},-\mathbf{q})I^*_{vc}(\mathbf{k},-\mathbf{q})] \\
&\quad + \mathbf{E}(t)\cdot\mu_{cv}\Big\} \\
&\quad \times(n_v(\mathbf{k};t) - n_c(\mathbf{k};t)) + C_{cv}(\mathbf{k};t) = 0. \qquad (31)
\end{aligned}$$

Here, $I_{\alpha\alpha'}(\mathbf{k},\mathbf{q})$ arises from the Coulomb matrix elements

$$\begin{aligned}
&\langle\alpha_1\mathbf{k}_1;\alpha_2\mathbf{k}_2|V|\alpha'_2\mathbf{k}'_2;\alpha'_1\mathbf{k}'_1\rangle \\
&\quad = \delta_{\mathbf{k}'_1+\mathbf{k}'_2,\mathbf{k}_1+\mathbf{k}_2}\sum_{\mathbf{q}}\tilde{V}(q)\delta_{\mathbf{k}'_1,\mathbf{k}_1+\mathbf{q}} \\
&\qquad \times I_{\alpha_1\alpha'_1}(\mathbf{k}_1,-\mathbf{q})I_{\alpha_2\alpha'_2}(\mathbf{k}_2,\mathbf{q}) \qquad (32)
\end{aligned}$$

$$\begin{aligned}
I_{\alpha\alpha'}(\mathbf{k},\mathbf{q}) &\equiv \int d\mathbf{r}\,e^{i\mathbf{q}\cdot\mathbf{r}}\psi^*_{\alpha\mathbf{k}}(\mathbf{r})\psi_{\alpha'\mathbf{k}-\mathbf{q}}(\mathbf{r}) \\
&= I^*_{\alpha'\alpha}(\mathbf{k}-\mathbf{q},-\mathbf{q}) \qquad (33)
\end{aligned}$$

and $\tilde{V}(q)$ is the Fourier-transformed pair potential. The valence and conduction occupation numbers are related by $n_c(\mathbf{k};t) + n_q(\mathbf{k};t) = \text{constant}$, and the polarization densities are related by $p_{cv} = p_{vc}\dagger$. These are the most general hierarchy equations.

The matrix elements $C_{\alpha\alpha'}(\mathbf{k};t)$ describe both inter- and intraband collisions and can be expressed in terms of the matrix elements of the correlation function $\bar{g}(1,2;t)$ using (23)

$$\begin{aligned}
&C_{\alpha\alpha'}(\mathbf{k};t) \\
&\quad = \langle\alpha\mathbf{k}|\{Tr_2 i[\,V_s(1,2),\bar{g}(1,2;t)]\}|\alpha'\mathbf{k}\rangle \\
&\quad = i\sum_{\mathbf{k}_1,\mathbf{k}_2,\mathbf{k}_3}\sum_{\nu_1,\nu_2,\nu_3}\{\langle\alpha\mathbf{k};\nu_1\mathbf{k}_1|V_s|\nu_2\mathbf{k}_2;\nu_3\mathbf{k}_3\rangle \\
&\qquad \times\langle\nu_2\mathbf{k}_2;\nu_3\mathbf{k}_3|\bar{g}|\alpha'\mathbf{k};\nu_1\mathbf{k}_1\rangle \\
&\qquad - \langle\alpha\mathbf{k};\nu_1\mathbf{k}_1|\bar{g}|\nu_2\mathbf{k}_2;\nu_3\mathbf{k}_3\rangle \\
&\qquad \times\langle\nu_2\mathbf{k}_2;\nu_3\mathbf{k}_3|V_s|\alpha'\mathbf{k};\nu_1\mathbf{k}_1\rangle\}. \qquad (34)
\end{aligned}$$

Further reduction follows from substitution of the Coulomb matrix element (32).

In practice, the relevant values of $\mathbf{q}$ may be sufficiently small to justify the approximation $I_{\alpha,\nu}(\mathbf{k},\mathbf{q}) \to I_{\alpha\nu}(\mathbf{k},0) = \delta_{\alpha,\nu}$. Then, these equations simplify to the usual forms

$$\begin{aligned}
&\partial_t n_c(\mathbf{k};t) + 2\mathrm{Im}(\mathbf{E}(t)\cdot\mu_{cv}p_{vc}(\mathbf{k};t)) \\
&\quad + 2\mathrm{Im}\sum_{\mathbf{q}}\tilde{V}(q)p_{cv}(\mathbf{k}+\mathbf{q};t)p_{vc}(\mathbf{k};t) \\
&\quad + C_{cc}(\mathbf{k};t) = 0 \qquad (35)\\
&\partial_t p_{cv}(\mathbf{k};t) + i(\epsilon_c(\mathbf{k}) - \epsilon_v(\mathbf{k}) - \mathbf{E}(t) \\
&\quad \cdot[\,\mu_{\alpha\alpha} - \mu_{\alpha'\alpha'}])p_{cv}(\mathbf{k};t) \\
&\quad - i\sum_{\mathbf{q}}\tilde{V}(q)[\,n_c(\mathbf{k}+\mathbf{q};t) - n_v(\mathbf{k}+\mathbf{q};t)] \\
&\quad \times p_{cv}(\mathbf{k};t) \\
&\quad - i\Big\{\sum_{\mathbf{q}}\tilde{V}(q)p_{cv}(\mathbf{k}+\mathbf{q};t) + \mathbf{E}(t)\cdot\mu_{cv}\Big\} \\
&\quad \times(n_v(\mathbf{k};t) - n_c(\mathbf{k};t)) \\
&\quad + C_{cv}(\mathbf{k};t) = 0, \qquad (36)
\end{aligned}$$

with the collision matrix elements

$$C_{cc}(\mathbf{k};t) = -2\mathrm{Im}\sum_{\mathbf{q}\neq 0,\mathbf{k}_1}\tilde{V}(q)\times\{\langle c\mathbf{k}-\mathbf{q};c\mathbf{k}_1+\mathbf{q}|\bar{g}|c\mathbf{k};c\mathbf{k}_1\rangle + \langle c\mathbf{k}-\mathbf{q};v\mathbf{k}_1+\mathbf{q}|\bar{g}|c\mathbf{k};v\mathbf{k}_1\rangle - \langle c\mathbf{k}_1+\mathbf{q};c\mathbf{k}-\mathbf{q}|\bar{g}|c\mathbf{k};c\mathbf{k}_1\rangle - \langle v\mathbf{k}_1+\mathbf{q};c\mathbf{k}-\mathbf{q}|\bar{g}|c\mathbf{k};v\mathbf{k}_1\rangle\} \quad (37)$$

$$C_{cv}(\mathbf{k};t) = -2\mathrm{Im}\sum_{\mathbf{q}\neq 0,\mathbf{k}_1}\tilde{V}(q)\times\{\langle c\mathbf{k}-\mathbf{q};c\mathbf{k}_1+\mathbf{q}|\bar{g}|v\mathbf{k};c\mathbf{k}_1\rangle + \langle c\mathbf{k}-\mathbf{q};v\mathbf{k}_1+\mathbf{q}|\bar{g}|v\mathbf{k};v\mathbf{k}_1\rangle\} - \sum_{\mathbf{q}\neq 0,\mathbf{k}_1}\tilde{V}(q)\{\langle c\mathbf{k}_1+\mathbf{q};c\mathbf{k}-\mathbf{q}|\bar{g}|v\mathbf{k};c\mathbf{k}_1\rangle + \langle v\mathbf{k}_1+\mathbf{q};c\mathbf{k}-\mathbf{q}|\bar{g}|v\mathbf{k};v\mathbf{k}_1\rangle - \langle c\mathbf{k};c\mathbf{k}_1|\bar{g}|c\mathbf{k}_1+\mathbf{q};v\mathbf{k}-\mathbf{q}\rangle - \langle c\mathbf{k};v\mathbf{k}_1|\bar{g}|v\mathbf{k}_1+\mathbf{q};v\mathbf{k}-\mathbf{q}\rangle\}. \quad (38)$$

Aside from the small $\mathbf{q}$ limitation of the Coulomb matrix elements, the above equations are still exact. The detailed dependence of $C_{\alpha\alpha'}(\mathbf{k};t)$ on $n_\alpha(\mathbf{k};t)$ and $p_{\alpha\alpha'}(\mathbf{k};t)$ requires specification of $\bar{g}(1,2;t)$ as a functional of $f^{(1)}(1;t)$. This follows from an approximate solution to Eq. (19). To illustrate the procedure, consider the weak coupling limit in which $\bar{g}(1,2;t)$ is evaluated to first order in the Coulomb interactions. Since $\bar{g}(1,2,3;t)$ occurs in (19) multiplied by $V(1,2)$, it is sufficient to evaluate $\bar{g}(1,2,3;t)$ to zeroth order in the potential. However, since the correlations due to statistics have already been extracted, the three-particle correlation function vanishes to this order. Also, since the source term on the right side is of first order in the potential, then $\bar{g}(1,2;t)$ also is of first order. Thus, all explicit dependence on $V(1,2)$ can be neglected on the left side of the equation, leading to the weak coupling equation

$$\partial_t\bar{g}(1,2;t) + i[(H(1)+H(2)),\bar{g}(1,2;t)] = -i\{\hat{V}(1,2;t)f^{(1)}(1;t)f^{(1)}(2;t) - f^{(1)}(1;t)f^{(1)}(2;t)\hat{V}^\dagger(1,2;t)\}, \quad (39)$$

with the solution

$$\bar{g}(1,2;t) = e^{-i(H(1)+H(2))t}\bar{g}(1,2;0)e^{i(H(1)+H(2))t} - i\int_0^t d\tau e^{i(H(1)+H(2))(t-\tau)}\times\{\hat{V}(1,2;\tau)f^{(1)}(1;\tau)f^{(1)}(2;\tau) - f^{(1)}(1;\tau)\times f^{(1)}(2;\tau)\hat{V}^\dagger(1,2;\tau)\}e^{i(H(1)+H(2))(t-\tau)}. \quad (40)$$

Since the Hamiltonian $H(1)$ is diagonal in the Bloch representation, it is straightforward to calculate the matrix elements of $\bar{g}(1,2;t)$ given by (40) and obtain the collision operator as a quartic function of the occupation numbers [recall $\hat{V}(1,2;t) \equiv \{1-f^{(1)}(1;t)-f^{(1)}(2;t)\}V(1,2)$]. The result is a generalization of the Born–Boltzmann collision operator, extended to include the effects of initial correlations and non-Markovian effects at short times. In the long time limit, it becomes exactly the Uhlenbeck–Boltzmann collision operator with scattering calculated in the Born approximation. An improved approximation appropriate for most current experimental conditions is described in the next section, where strong scattering and polarization effects are accounted for as well.

Pair Correlation Approximation

The exact transformed hierarchy Eq. (19) for $\bar{g}(1,2;t)$ is an appropriate form for the introduction of approximations since it makes explicit the physical mechanisms for renormalized single-particle states, blocking in the pair dynamics, and dynamic screening. The approximations entail some statement about the three-particle correlations in $\bar{g}(1,2,3;t)$. More specifically, the approximation should give $\bar{g}(1,2,3;t)$ in terms of the pair correlations and one-particle distribution function, so that the first two hierarchy equations become closed equations for $f^{(1)}(1;t)$ and $\bar{g}(1,2;t)$. The formal solution to the second equation provides the functional in (10) required for a kinetic equation

$$F^{(2)}(1,2;t\,|\,f^{(1)}) = \{f^{(1)}(1;t)f^{(1)}(2;t) + \bar{g}(1,2;t\,|\,f^{(1)})\}\mathscr{S}(1,2). \quad (41)$$

In general, there is no small parameter on which to base a systematic expansion. However, there are exact structural properties of the hierarchy equation that impose important constraints on the class of approximations considered acceptable. For example, the single-particle reduced density operator is representable as a trace over the two-particle reduced density operator, $Nf^{(1)}(1;t) = Tr_2 f^{(2)}(1,2;t)$ and, therefore, the exact first hierarchy equation for $f^{(1)}(1;t)$ should result from a partial trace over any acceptable approximate closure of the second hierarchy equation. Additional constraints follow from the invariance of the hierarchy equations under symmetry transformations derived from the Hamiltonian (e.g., rotations, translations, Galilean boosts). An important consequence of these invariances is the local conservation laws for mass, energy, and momentum. Constraints imposed by the requirement of exact conservation laws are discussed in [5, 8, 9]. Other constraints can be included as well. For example, if the reduced density operators for the equilibrium state are known, it can be required that they are also solutions to the approximate hierarchy equations. In this way, the class of approximations can be assured to have the most important properties of the exact hierarchy in a context that does not imply weak coupling or other small parameter limits.

For long-range Coulomb interactions, it is important to describe screening effects. This is included explicitly on the right side of (20), as are the mean field Hartree–Fock-renormalized single-particle energies and the Pauli blocking effects for the pair potential. Thus, all of the important mechanisms appear in this form even before considering three-particle correlations in $\bar{g}(1,2,3;t)$. Furthermore, it is shown in [5] that *any* choice for $\bar{g}(1,2,3;t)$ that is Hermitian and pairwise symmetric in the particle labels preserves both the representability of $f^{(1)}$ and the exact conservation laws. Consequently, we suggest that the residual three-particle correlations described by $\bar{g}(1,2,3;t)$ can be neglected entirely, except for the conditions of very strong coupling. The resulting approximation preserves the exact local conservation laws for mass, energy, and momentum and is time reversal invariant. It contains strong collision effects (ladder diagrams) through the dependence on the potential in $\hat{H}(1,2;t)$ and dynamical polarization effects in the random-phase approximation (ring diagrams). There are no a priori limitations on the time scale in this approximation so that a uniform treatment of the initial value problem is possible.

With this approximation, Eq. (19) becomes a closed equation for $\bar{g}(1,2;t)$ in terms of $f^{(1)}(1;t)$, with the form

$$(\partial_t - L(1,2;t))\bar{g}(1,2;t) = -i\big[\hat{V}(1,2;t)f^{(1)}(1;t)f^{(1)}(2;t) - f^{(1)}(1;t)f^{(1)}(2;t)\hat{V}^\dagger(1,2;t)\big]. \quad (42)$$

The formal solution provides the functional in (10) required for a kinetic equation

$$F^{(2)}(1,2;t\,|\,f^{(1)}) = \{f^{(1)}(1;t)f^{(1)}(2;t) + \bar{g}(1,2;t\,|\,f^{(1)})\}\mathscr{S}(1,2), \quad (43)$$

$$\bar{g}(1,2;t\,|\,f^{(1)}) = \mathrm{Tr}_{34}U(1,2,3,4;t,t_0)\bar{g}(3,4;t_0) - i\mathrm{Tr}_{34}\int_{t_0}^{t}d\bar{t}\,U(1,2,3,4;t,\bar{t}) \times\big[\hat{V}(3,4;\bar{t})f^{(1)}(3;\bar{t})f^{(1)}(4;\bar{t}) - f^{(1)}(3;\bar{t})f^{(1)}(4;\bar{t})\hat{V}^\dagger(3,4;\bar{t})\big]. \quad (44)$$

Here, $U(1,2,3,4;t,t_0)$ is the two-particle propagator associated with the generator $L(2,2;t)$. Its form and reduction to familiar quantities such as scattering matrices and dielectric functions will be discussed elsewhere [10] and only the structural features noted here. The first term on the right side of (44) gives the pair dynamics due to initial correlations determined from the system preparation. The second term describes the correlation buildup even in the absence of such initial correlations. Both contributions can be of equal importance for initial value problems at short times.

The collision operator in the kinetic Eq. (22) reflects these two contributions:

$$C(1;t) = -i\mathrm{Tr}_2[V_s(1,2),\bar{g}(1,2;t)] = I^c(1;t) + I(1;t) \quad (45)$$

$$I^c(1;t) = -i\mathrm{Tr}_{234}[V_s(1,2), U(1,2,3,4;t,t_0)\bar{g}(3,4;t_0)] \quad (46)$$

$$I(1;t) = -i\mathrm{Tr}_{234}\int_{t_0}^{t}d\bar{t}\big[V_s(1,2),U(1,2,3,4;t,\bar{t}) \times\{\hat{V}(3,4;\bar{t})f^{(1)}(3;\bar{t})f^{(1)}(4;t) - f^{(1)}(3;\bar{t})f^{(1)}(4;\bar{t})\hat{V}^\dagger(3,4;\bar{t})\}\big]. \quad (47)$$

The Hartree–Fock dynamics is modified at short times by the conditions of the initial preparation through $I_1^c(t)$. The other modification is independent of the initial preparation and represents the buildup of scattering effects. The term $I(1;t)$ grows from zero to an asymptotic value $I(1;\infty)$, while the initial correlations term $I_1^c(t)$ is expected to decrease to zero for most physical preparations. This initial transient period represents the transition from time scales short compared to the scattering time up to times long enough for completed collisions. On the long time scale, $C(1;t) \rightarrow I(1;\infty)$ and the kinetic equation takes the usual Markov form. In this limit, a Boltzmann–Uhlenbeck form is obtained with scattering determined by the full T-matrix [11]. During the transient period, the incomplete scattering is described by an effective potential with dynamical screening ranging from Coulomb at short times to fully screened at long times.

Discussion

The objective of this presentation has been to give an overview of an approach to formulating practical kinetic theories for charged particle dynamics, with the potential for application to current and proposed experiments on semiconductors using femtosecond lasers to prepare and probe the charges. The new features of such experiments requiring reconsideration of standard kinetic theory are states far from equilibrium and the inclusion of short time scales. The approach here formulates the description in terms of the exact hierarchy for the one- and two-particle reduced density operators. These operators determine most directly the relevant observables of interest. There are two components to the analysis. First, an exact transformation of the first two hierarchy equations is performed to isolate the strong correlations due to quantum statistics from correlations due to the Coulomb forces. This description in terms of the excess correlations also makes explicit the mean-field effects associated with Hartree–Fock renormalization of the single-particle energies and the dominant polarization effects necessary to account for screening of the long-range Coulomb forces. As a single-time Markovian first-order set of differential equations, the description is formulated as an initial value problem, appropriate for the experimental conditions of interest. The second component of the analysis is an approximate closure of the second hierarchy equation, with the three-particle correlations expressed as explicit functionals of the two-particle correlations and the one-particle reduced density operator. The resulting approximation transforms the first two hierarchy equations into a closed set of coupled equations to determine the one-particle-reduced density operator and the two-particle correlations. Finally, a last step is possible where the approximate second hierarchy equation is solved formally to give the two-particle correlations in terms of the one-particle density operator. Use of this result in the exact first hierarchy equation gives a closed kinetic equation for the one-particle density operator. While the coupled pair of equations for the correlations and one-particle distribution is local in time (Markovian), the reduced kinetic theory description in terms of the one-particle distribution alone is necessarily nonlocal in time. This latter feature is essential for a proper treatment of relaxation and transport at short times.

The transformation of the hierarchy and resulting explicit representation of the most important physical mechanisms simplifies the choice of approximations considerably. Additional constraints are associated with the exact relationship on one- and two-particle reduced density operators, the exact conservation laws, and the existence of stationary states (equilibrium, in the absence of driving fields). It is proposed in the fifth section that these constraints are satisfied by an approximation obtained by neglecting $\bar{g}(1,2,3;t)$. The resulting approximate equations retain all of the desired physical mechanisms and time scales, excluding only conditions of strong Coulomb coupling. The detailed solution to the equation for the pair correlations is essentially an effective two-body problem and will be discussed elsewhere.

The analysis of the hierarchy and considerations leading to this approximation occurs at the abstract operator level and does not require explicit attention to the detailed structure of the physical system considered (e.g., the number of bands) and additional processes are easily accounted for at this abstract level. Having completed the many-body analysis, the physical properties of interest follow directly from an appropriate matrix representation of the operator equations, so that manipulation of complex notation is deferred to this late stage. Of course, the final measure of any approach is the ability to describe interesting new

phenomena in quantitative applications. We hope to report on such results in the near future.

ACKNOWLEDGMENTS

This research was supported by NSF Grants INT 9414072 and PHY 9312723 and by KOSEF and KRF through the Nondirected Research Fund.

Appendix: Transformation of the Hierarchy Equations

Define a superoperator, $\mathscr{P}_{12}$, that exchanges the labels of particles 1 and 2 in all operators to its right:

$$\mathscr{P}_{12}\, X(1,2) = X(2,1). \tag{48}$$

This operator should not be confused with the permutation operator defined over quantum states, P_{12}, that permutes the quantum labels of the states. The second equation of the BBGKY hierarchy then can be written in the compact form:

$$\begin{aligned}&\partial_t f^{(2)}(1,2;t) + i[\,H(1,2;t), f^{(2)}(1,2;t)] \\ &\quad + (1+\mathscr{P}_{12})Tr_3 i[\,V(1,3)f^{(3)}(1,2,3;t) - hc] \\ &\quad = 0,\end{aligned} \tag{49}$$

where *hc* indicates the Hermitian conjugate of the preceding term in the brackets. The objective of this Appendix is to show how the exchange effects in the definitions of $f^{(2)}(1,2;t)$ and $f^{(3)}(1,2,3;t)$ can be evaluated exactly to give the Hartree–Fock energies, the blocking factors in the pair potential, and the linear operators responsible for polarization effects. Substitution of (14) into (49) and use of the first hierarchy equation gives

$$\begin{aligned}&\mathscr{S}(1,2)\{\partial_t \bar{g}^{(2)}(1,2;t) + i[\,H(1,2;t), \bar{g}^{(2)}(1,2;t)] \\ &\quad + i[\,V(1,2;t), f^{(1)}(1;t)f^{(1)}(2;t)]\} \\ &\quad - \mathscr{S}(1,2)(1+\mathscr{P}_{12})Tr_3 i[\,V(1,3)\bar{f}^{(2)}(1,3;t) \\ &\quad \times f^{(1)}(2;t)\mathscr{S}(1,3) - hc] \\ &\quad + (1+\mathscr{P}_{12})Tr_3 i \\ &\quad \times [\,V(1,3)\bar{f}^{(3)}(1,2,3;t) \\ &\quad \times \mathscr{S}(1,2,3) - hc] = 0.\end{aligned} \tag{50}$$

First, note that the last term can be written with an overall prefactor of $\mathscr{S}(1,2)$ as well using the identity $\mathscr{S}(1,2,3) = (1 - P_{13} - P_{23})\mathscr{S}(1,2)$ and the fact that $\mathscr{S}(1,2)$ commutes with any symmetric two-particle operator. Consequently, the overall operator $\mathscr{S}(1,2)$ in (51) can be factored out, leaving the simpler result:

$$\begin{aligned}&\partial_t \bar{g}^{(2)}(1,2;t) + i[\,H(1,2;t)\bar{g}^{(2)}(1,2;t)] \\ &\quad + i[\,V(1,2;t), f^{(1)}(1;t)f^{(1)}(2;t)] \\ &\quad - (1+\mathscr{P}_{12})Tr_3 i[\,V(1,3)\bar{f}^{(2)}(1,3;t) \\ &\quad \times f^{(1)}(2;t)\mathscr{S}(1,3) - hc] \\ &\quad + (1+\mathscr{P}_{12})Tr_3 i \\ &\quad \times \big[\,V(1,3)\bar{f}^{(3)}(1,2,3;t)(1 - P_{13} - P_{23}) - hc\big] \\ &\quad = 0.\end{aligned} \tag{51}$$

Next, represent $\bar{f}^{(3)}(1,2,3;t)$ in the last term using (15) in the equivalent form

$$\begin{aligned}&\bar{f}^{(3)}(1,2,3;t) \\ &\quad = \bar{f}^{(2)}(1,3;t)f^{(1)}(2;t) + f^{(1)}(1;t)\bar{g}(2,3;t) \\ &\quad + f^{(1)}(3;t)\bar{g}(1,2;t) + \bar{g}(1,2,3;t)\end{aligned}$$

to obtain

$$\begin{aligned}&V(1,3)\bar{f}^{(3)}(1,2,3;t)(1 - P_{13} - P_{23}) \\ &\quad = V(1,3)\bar{f}^{(2)}(1,3;t)f^{(1)}(2;t)(\mathscr{S}(1,3) - P_{23}) \\ &\quad + V(1,3)\{\bar{g}(2,3;t)f^{(1)}(1;t) \\ &\quad + \bar{g}(1,2;t)f^{(1)}(3) \\ &\quad + \bar{g}(1,2,3;t)\}(1 - P_{13} - P_{23}).\end{aligned} \tag{52}$$

The contribution proportional to $\mathscr{S}(1,3)$ cancels the terms on the second line of (51) and the equation for $\bar{g}^{(2)}(1,2;t)$ becomes

$$\begin{aligned}&\partial_t \bar{g}^{(2)}(1,2;t) + i[\,H(1,2;t), \bar{g}^{(2)}(1,2;t)] \\ &\quad + i[\,V(1,2;t), f^{(1)}(1;t)f^{(1)}(2;t)] \\ &\quad - (1+\mathscr{P}_{12})Tr_3 i\big[\,V(1,3)\bar{f}^{(2)}(1,3;t) \\ &\quad \times f^{(1)}(2;t)P_{23} - hc\big] \\ &\quad + (1+\mathscr{P}_{12})Tr_3 i\big[\,V(1,3) \\ &\quad \times \{\bar{g}(2,3;t)f^{(1)}(1;t) + \bar{g}(1,2;t)f^{(1)}(3)\} \\ &\quad \times (1 - P_{13} - P_{23}) - hc\big] \\ &\quad + (1+\mathscr{P}_{12})Tr_3 i\big[\,V(1,3)\bar{g}^{(3)}(1,2,3;t) \\ &\quad \times (1 - P_{13} - P_{23}) - hc\big] = 0.\end{aligned} \tag{53}$$

The fourth term on the left side can be simplified using the identities

$$P_{23}P_{23} = 1, \qquad Tr_3 P_{23} = 1,$$
$$P_{23}X(1,2,3)P_{23} = X(1,3,2) \tag{54}$$

to write

$$\begin{aligned}
&Tr_3 V(1,3)\tilde{f}^{(2)}(1,3;t)f^{(1)}(2;t)P_{23} \\
&\quad = Tr_3 P_{23}P_{23}V(1,3)\tilde{f}^{(2)}(1,3;t)f^{(1)}(2;t)P_{23} \\
&\quad = Tr_2 P_{23}V(1,2)\tilde{f}^{(2)}(1,2;t)f^{(1)}(3;t) \\
&\quad = Tr_3 f^{(1)}(3;t)P_{23}V(1,2)\tilde{f}^{(2)}(1,2;t) \\
&\quad = Tr_3 P_{23}P_{23}f^{(1)}(3;t)P_{23}V(1,2)\tilde{f}^{(2)}(1,2;t) \\
&\quad = Tr_3 P_{23}f^{(1)}(2;t)V(1,2)\tilde{f}^{(2)}(1,2;t) \\
&\quad = f^{(1)}(2;t)V(1,2)\tilde{f}^{(2)}(1,2;t).
\end{aligned} \tag{55}$$

The second equation of the BBGKY hierarchy now becomes

$$\begin{aligned}
&\partial_t \bar{g}(1,2;t) + i[(H(1;t) + H(2;t)), \bar{g}^{(2)}(1,2;t)] \\
&\quad + i\left[\hat{V}(1,2;t)\bar{g}(1,2;t) - hc\right] \\
&\quad + (1 + \mathscr{P}_{12})Tr_3 i\left[V(1,3)\{\bar{g}(2,3;t)f^{(1)}(1;t) \right. \\
&\quad \left. + \bar{g}(1,2;t)f^{(1)}(3)\}(1 - P_{13} - P_{23}) - hc\right] \\
&\quad + i\left[\hat{V}(1,2;t)f^{(1)}(1;t)f^{(1)}(2;t) \right. \\
&\quad \left. - f^{(1)}(1;t)f^{(1)}(2;t)\hat{V}^{\dagger}(1,2;t)\right] \\
&\quad + (1 + \mathscr{P}_{12})Tr_3 i\left[V(1,3)\bar{g}^{(3)}(1,2,3;t) \right. \\
&\quad \left. \times(1 - P_{13} - P_{23}) - hc\right] = 0,
\end{aligned} \tag{56}$$

with the definition

$$\hat{V}(1,2;t) \equiv [1 - f^{(1)}(1;t) - f^{(1)}(2;t)]V(1,2). \tag{57}$$

This shows clearly the origin of the Pauli blocking factor in the pair potential.

The remaining exchange terms in the second line of (56) can be analyzed in a similar way:

$$\begin{aligned}
&Tr_3 V(1,3)[\bar{g}(2,3;t)f^{(1)}(1;t) \\
&\quad + \bar{g}(1,2;t)f^{(1)}(3)](1 - P_{13} - P_{23}) \\
&\quad = Tr_3 V(1,3)\left[\bar{g}(1,2;t)f^{(1)}(3) \right. \\
&\quad \left. - \bar{g}(2,3;t)f^{(1)}(1;t)P_{13}\right] \\
&\quad + Tr_3 V(1,3)\left[\bar{g}(2,3;t)f^{(1)}(1;t)(1 - P_{23}) \right. \\
&\quad \left. - \bar{g}(1,2;t)f^{(1)}(3)(P_{13} + P_{23})\right] \\
&\quad = Tr_3 V(1,3)\left[\bar{g}(1,2;t)f^{(1)}(3) \right. \\
&\quad \left. - P_{13}P_{13}\bar{g}(2,3;t)f^{(1)}(1;t)P_{13}\right] \\
&\quad + Tr_3 V(1,3)\left[\bar{g}(2,3;t)f^{(1)}(1;t)(1 - P_{23}) \right. \\
&\quad \left. - P_{13}P_{13}\bar{g}(1,2;t)f^{(1)}(3)P_{13}(1 + P_{13}P_{23})\right] \\
&\quad = Tr_3 V_s(1,3)f^{(1)}(3)\bar{g}(1,2;t) \\
&\quad + Tr_3 V(1,3)\bar{g}(2,3;t)f^{(1)}(1;t)(1 - P_{23}) \\
&\quad - P_{13}\bar{g}(2,3;t)f^{(1)}(1)(1 + P_{13}P_{23}).
\end{aligned} \tag{58}$$

The first term on the right side gives the Hartree–Fock single-particle energy shift:

$$V_{hf}(1;t) = Tr_3 V_s(1,3)f^{(1)}(3),$$
$$V_s(1,3) \equiv V(1,3)\mathscr{S}(1,3).$$

The second term can be transformed by writing the factor $(1 + P_{13}P_{23}) = (1 - P_{23}) + (1 + P_{13})P_{23} = (1 - P_{23}) + P_{23}(1 + P_{12})$. Recall that an overall factor of $\mathscr{S}(1,2)$ has been canceled out in writing (56). Since $(1 + P_{12})\mathscr{S}(1,2) = 0$, the term $P_{23}(1 + P_{12})$ vanishes in this context and Eq. (58) simplifies to

$$\begin{aligned}
&Tr_3 V(1,3)[\bar{g}(2,3;t)f^{(1)}(1;t) \\
&\quad + \bar{g}(1,2;t)f^{(1)}(3)](1 - P_{13} - P_{23}) \\
&\quad = V_{hf}(1,2;t)\bar{g}(1,2;t) \\
&\quad + Tr_3 V_s(1,3)\bar{g}(2,3;t)f^{(1)}(1;t)(1 - P_{23}).
\end{aligned} \tag{59}$$

The second term gives the polarization effects with exchange. The exact equation for $\bar{g}(1,2;t)$ now takes the final form of (19).

References

1. See, e.g., K. El Sayed, S. Schuster, H. Haug, F. Herzel, and K. Henneberger, Phys. Rev. B **49**, 7337 (1994), G. Manzke, K. Henneberger, J. Heeg, K. El Sayed, S. Schuster, and H. Haug, Phys. Stat. Sol. (b) **188**, 395 (1995).

2. R. Binder and S. W. Koch, Progr. Quantum Elect. **19**, 307 (1995).
3. See, e.g., J.-P. Boon and S. Yip, *Molecular Hydrodynamics* (Dover, New York, 1991).
4. P. Danielewicz, Ann. Phys. **152**, 239 (1983).
5. D. B. Boercker and J. W. Dufty, Ann. Phys. (N.Y.) **119**, 43 (1979).
6. N. N. Bogoliubov, *Lectures on Quantum Statistics* (Gordon and Breach, New York, 1967), Vol. 1.
7. A. V. Kuznetsov, Phys. Rev. B. **44**, 8721 (1991); H. Haug, and C. Ell, Phys. Rev. B **46**, 2126 (1992).
8. J. W. Dufty and D. B. Boercker, J. Stat. Phys. **57**, 827 (1989).
9. J. W. Dufty, Contrib. Plasma Phys. **37**, 129 (1997).
10. M. Bonitz, D. Kremp, J. Dufty, and R. Binder, to be published.
11. For a discussion of the non-Markovian Boltzmann equation in this formalism, see D. Kremp, M. Bonitz, W. Kraeft, and M. Schlanges, Ann. Phys., to be published.

Electronic and Structural Properties of Defects in c-BN

R. MOTA,[1] P. PIQUINI,[1] T. M. SCHMIDT,[2] A. FAZZIO[3]

[1]*Departamento de Física, Universidade Federal de Santa Maria, 97119-900, Santa Maria, RS, Brazil*
[2]*Departamento de Ciências Físicas, Universidade Federal de Uberlândia, CxP 593, 38400-902, Uberlândia, MG, Brazil*
[3]*Instituto de Física, Universidade de São Paulo, CxP 66318, 05389-970, São Paulo, SP, Brazil*

Received 3 March 1997; revised 30 April 1997; accepted 8 May 1997

ABSTRACT: Using a molecular cluster with 71 atoms, we studied the electronic and structural properties of nitrogen vacancy, boron antisite, and oxygen in cubic boron nitride through an ab initio Hartree–Fock calculation. We found that all defects introduce a deep state above the middle-energy gap. These defects present a C_{3v} local symmetry. In the case of nitrogen vacancy, the possibility of the F-center formation is discussed. All the calculations were performed using the program code GAMESS. © 1997 John Wiley & Sons, Inc. Int J Quant Chem **65**: 941–946, 1997

Introduction

Boron nitrides exist in both high-density (tetrahedral diamondlike) and low-density (graphitelike) forms or modifications. Of the high-density forms, cubic boron (c-BN) is unique among the group III nitrides in that its zinc-blende structure is the most stable and best characterized form. Then, c-BN, the lightest of III–V semiconductors, is a large band-gap material ($\simeq 6.4$ eV) [1] which has several similarities compared with diamond, such as crystal structure, wide energy band gap, extreme hardness, high thermal conductivity, high melting temperature, and low reactivity [2]. But while diamond can be readily doped only with the *p*-type, c-BN can be doped *p*- and *n*-types when suitable impurities are added [3]. Although it could be an important material for devices of high temperature and high pressure, with many applications in industries in the future, the quality of the samples remains as a major problem. If we compare it with other III–V materials, c-BN has a very high concentration of native defects.

In this article, we report a theoretical calculation of the behavior of native defects in c-BN. The electronic and structural properties of N-vacancy ($Vac_{[N]}$), boron antisite ($B_{[N]}$), and oxygen substitutional ($O_{[N]}$) are calculated. Although several calculations are available for pure materials [4], there are only a few works concerning the theoretical study of the defects in c-BN [5, 6]. Particularly, an interesting work was performed by Gubanov et

Correspondence to: R. Mota.
Contract grant sponsors: CNPq; FAPESP; FAPERGS.

© 1997 John Wiley & Sons, Inc.
CCC 0020-7608 / 97 / 050941-06

al. [6] using LAPW-ASA-TB for vacancies. However, in that calculation, the authors did not include relaxation or asymmetric distortions, basically because they used the muffin-tin approach for the potential. These effects, as we will show, are important to interpret the experimental results. As far as we know, this is the first work to consider distortions induced by the defects in the calculation.

Theoretical Procedure

We simulated the pure crystal through the molecular cluster with 71 atoms

$$(NB_4N_{12}B_{12}N_6H_{36})^{3+}$$

initially in *Td* symmetry, as seen in Figure 1. The hydrogen atoms are introduced to saturate the dangling bonds at the cluster surface, as usual [7, 8]. The net charge of 3+ at the cluster is necessary to get a neutral charge condition as in a crystal. Having defined the molecular cluster, the total energies are calculated using the all-electron Hartree-Fock method in the usual linear combination of atomic orbitals procedure. The atomic basis adopted here is the minimal split-valence 3-21G basis set [9], which consists of $6s3p$ ($3s$) primitive Gaussian functions contracted in $3s2p$ ($2s$) basis functions on each B and N (H) atoms. The size of the set thus ranges from the smallest 242 (for the $Vac_{[N]}$) to 247 (for $O_{[N]}$ and $B_{[N]}$) contracted Gaussian-type functions. The calculations were performed using the program code GAMESS [10]. Before calculating the distortions on the geometric structure, when defects substitute the N central atom in the cluster, we first optimized the defect nearest-neighbor bond distances with respect to the A_1 vibrational mode. This is necessary to avoid spurious forces in the *defect cluster*. As we know from the literature [8], this cluster size is appropriate to study single-impurity distortions.

For the pure c-BN, the calculated eigenvalue separation between the highest occupied molecular orbital (t_2-HOMO) and the lowest unoccupied molecular orbital (a_1-LUMO) obtained is 8.07 eV. A better result for the band gap is obtained using the Mulliken correction [11]: $\Delta E(HOMO - LUMO) = \epsilon_{LUMO} - \epsilon_{HOMO} - J + 2K$, where J and K are the Coulomb and exchange integrals, respectively. Using this correction, the result for the energy gap drops to 6.53 eV, in excellent agreement with the experimental results [1].

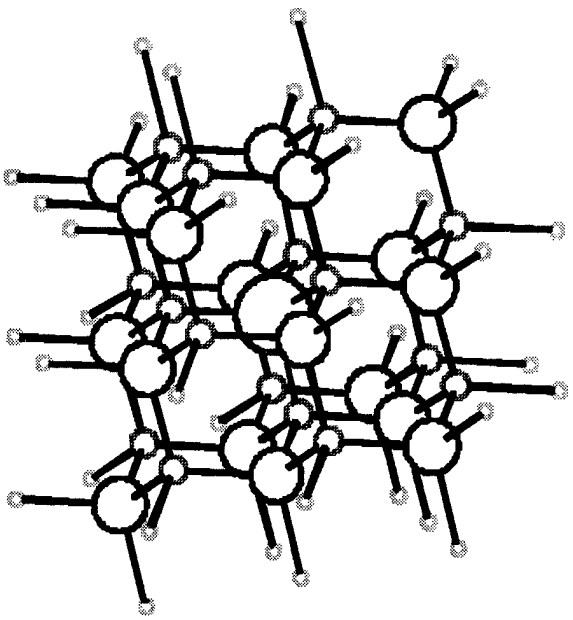


FIGURE 1. Molecular cluster with 71 atoms $(NB_4N_{12}B_{12}N_6H_{36})^{3+}$, initially in *Td* symmetry, with the hydrogen atoms introduced to saturate the dangling bonds at the surface.

Results and Discussion

We show schematically in Figure 2(a), (b), and (c) the electronic energy levels in the gap region for the $B_{[N]}$, $Vac_{[N]}$, and $O_{[N]}$, respectively, using a defect molecule model. On the left side is always the pure system with an $a_1^2t_2^6$ configuration. Our procedure to estimate the energy levels in the gap was to compare the pure cluster and the defect clusters. The electronic energy levels showed in Figure 2 were obtained as differences between the calculated Hartree–Fock eigenvalues. Fortunately, in all defects studied here, the density of states at the top of the valence band practically does not change. In this sense, the top of the valence, used as a reference for the calculated electronic levels, is fairly well defined.

As one can see in the middle of Figure 2(a), the electronic consequence of $B_{[N]}$, before structural minimization, is to introduce a t_2-level occupied with four electrons in the gap region. This configuration presents a degenerated ground state and, consequently, is favorable for a Jahn–Teller distor-

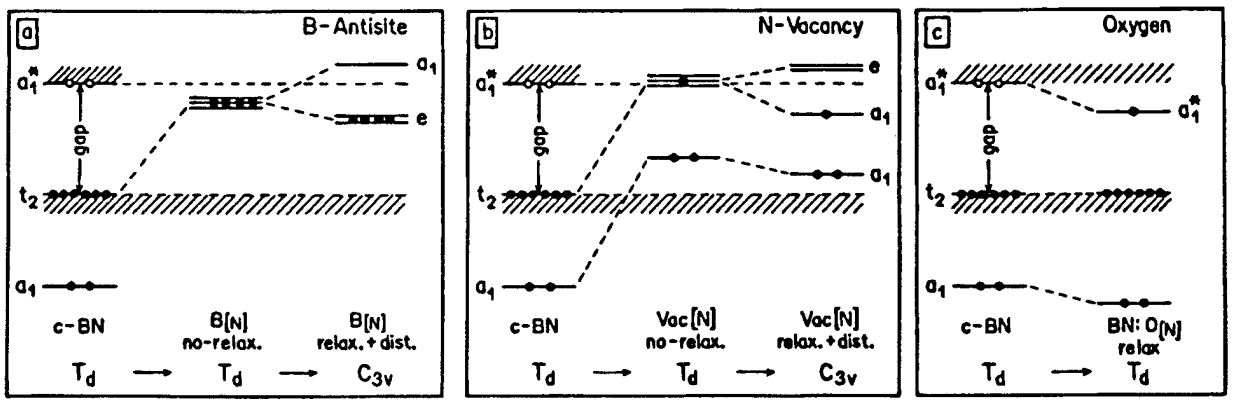


FIGURE 2. Schematic representation of the energy levels in the gap region of c-BN for (a) boron antisite, (b) nitrogen vacancy, and (c) oxygen substitutional.

tion. The optimized geometric structure has a C_{3v} symmetry, where the t_2 orbital is split in a twofold degenerate fully occupied e orbital and an a_1 empty orbital, as shown on the right side of Figure 2(a). The fully occupied e-level, with a ligand character (π-type), is located 4.81 eV above the top of valence band, resulting in a deep donor level. In Figure 3(a) and (b), we show the total charge densities in the (110) plane for the c-BN and c-BN : $B_{[N]}$ systems, respectively. From Figure 3(b), we see that the B antisite atom makes bonds with the B atoms in the σ_v plane of the C_{3v} symmetry.

Concerning the structural properties for the $B_{[N]}$ defect, our results show that the antisite B atom is found in an off-center position. We first performed a breathing mode total energy minimization which leads to a small inward relaxation of 5% in the bond length. Starting from this relaxed configuration, we calculated the total energy changes of the $B_{[N]}$ atom along the $\langle 111 \rangle$ and $\langle 100 \rangle$ directions, as shown in Figure 4. For the distortion in the $\langle 111 \rangle$ direction, toward an intersticial position in a C_{3v} configuration, we find a stable position with an energy gain of 1.34 eV and a displacement of the B

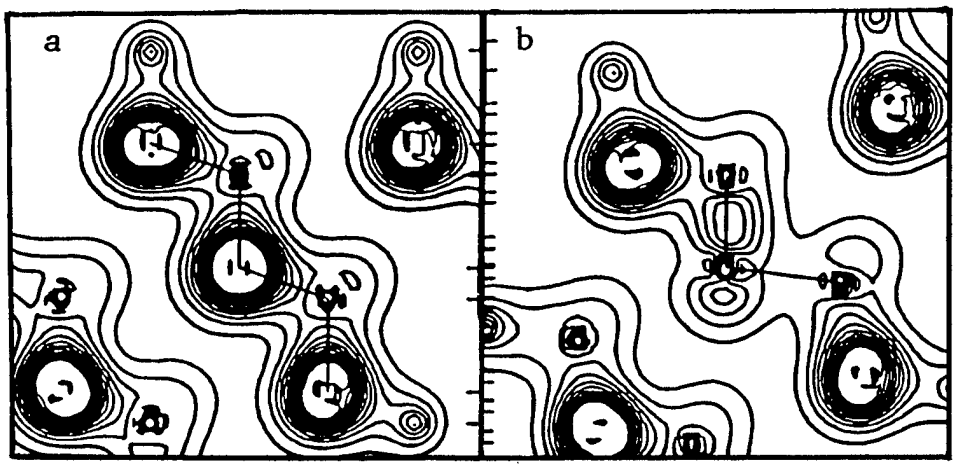


FIGURE 3. Contour plot of the total curves for displacements of B antisite in (110) plane for (a) pure c-BN and (b) B antisite.

atom of 0.28 Å. In addition, the distortion in the ⟨110⟩ direction gives a metastable configuration with C_{2v} symmetry, where the energy gain is 0.65 eV and the displacement of the antisite B atom is 0.16 Å.

With respect to the $Vac_{[N]}$, the calculated breathing mode relaxation of the first neighbor boron atoms gives an outward displacement of 0.31 Å for these atoms. A subsequent C_{3v} mode distortion was observed with one boron atom, B_1, following a ⟨111⟩ direction and the three others, B_2, B_3, and B_4, moving closer to form a triangle, as seen in Figure 5.

As shown in the middle of Figure 2(b), the removal of an N atom, $Vac_{[N]}$, results in a strong perturbation in the electronic configuration of the system with two orbitals, an a_1 fully occupied in the gap region and a t_2 singly occupied resonant in the conduction band, in agreement with Gubanov et al. [6]. After the total energy minimization, a C_{3v} configuration is obtained. The t_2 orbital splits in an a_1 plus an e orbital, as shown on the right side of Figure 2(b). In the gap region, there are two levels with a_1 character ($1a_1^2\,2a_1^1$) located at 1.76 and 4.90 eV above the top of valence band, respectively.

In Figure 6, the wave functions for the two highest occupied orbitals ($1a_1 2a_1$) of the neutral

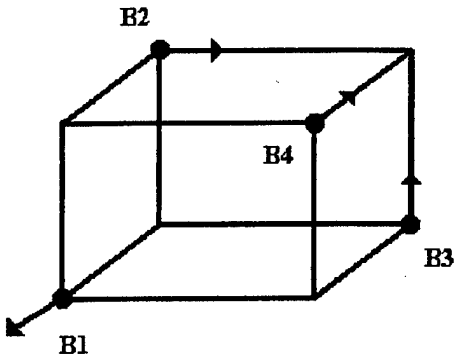


FIGURE 5. $Vac_{[N]}$ the C_{3v} mode distortion, with one boron (B1) following a ⟨111⟩ direction and the three others (B2, B3, and B4) moving closer to form a triangle.

vacancy are presented. In the figure, the (a) and (c) planes contain the B_1-Vac-B_3 centers, while the (b) and (d) planes the B_2-Vac-B_4 ones. The fully occupied $1a_1$ defect orbital in the gap region has a π-character with a charge density shared among the three equivalent (B_2, B_3, and B_4) boron atoms near the vacancy. This trapped charge resembles the F centers that arise in anion vacancies in alkali–halide crystals [12]. Particularly, the formation of F centers in hexagonal BN (h-BN), due to nitrogen vacancy, was proposed by Zunger and Katzir using an extended Huckel method [13]. The

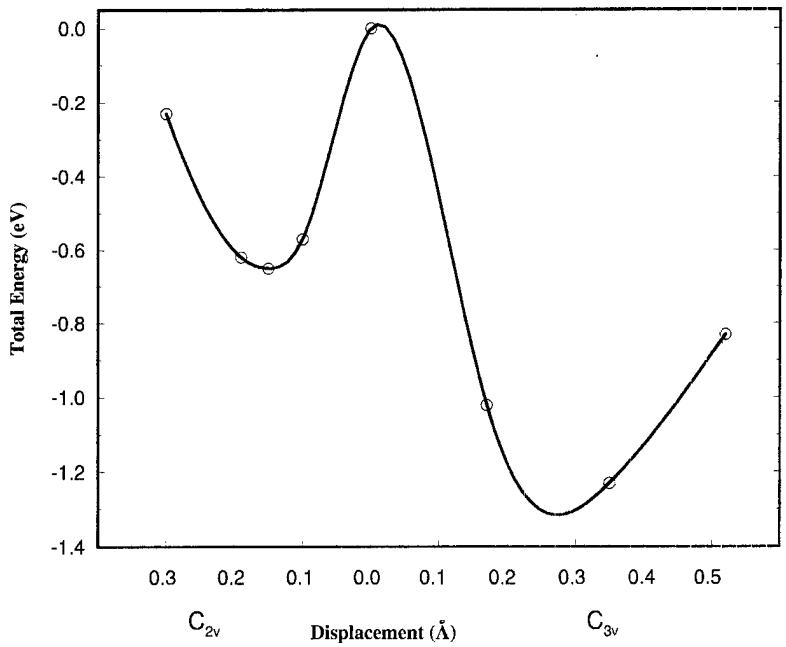


FIGURE 4. Calculated total energy curves for displacement of B antisite in ⟨100⟩ (C_{2v}) and ⟨111⟩ (C_{3v}) directions (see text).

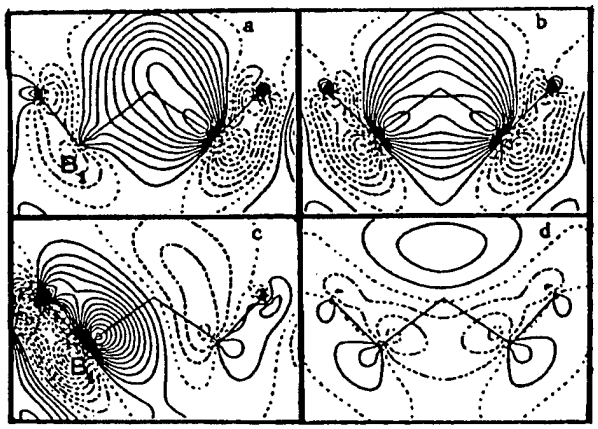


FIGURE 6. Contour plot of the (a,b) $1a_1$ and (c,d) $2a_1$ orbitals. The (a) and (c) planes contain the B_1-Vac-B_3 centers, and the (b) and (d) planes, the B_2-Vac-B_4 centers (see text).

singly occupied $2a_1$ orbital above the middle gap has an electronic distribution strongly localized on the B_1 boron with a π-character. Although there are some similarities between the highest occupied orbitals in c-BN and h-BN, like the π-character and charge-confinement, a very important difference in the energetic ordering of the electronic levels is remarkable. Differently from h-BN, the c-BN could present an F center only for the doubly ionized nitrogen vacancy (Vac^{++}). The essential role played by carbon doping for the formation of F centers in h-BN [14] could also be seen in the case of c-BN, at least for high concentrations of these impurities when a recombination occurs between the electron localized at the $2a_1$ orbital and the hole introduced by the carbon atoms. It is in agreement with experimental EPR results by Fanciulli and Moustakas [15].

The electronic energy levels for the relaxed (right) and unrelaxed (left) configurations at T_d symmetry for the $O_{[N]}$ system are shown schematically in Figure 2(c). We obtained a singly occupied a_1 level with antibonding character that comes from the conduction band 4.70 eV above the top of the valence band. Also, a hyper-deep a_1 state below the top of valence band and a resonant p-type state in the valence band are obtained. By this analysis, we see that the substitutional oxygen impurity introduces an a_1 antibonding state in the gap region.

We obtained the energy minimum when the first neighbors relax $\simeq 0.16$ Å outward (10% in the bond length). But if we look carefully at the total energy surface, we observe that the system distorts from the T_d symmetry toward a C_{3v} configuration, with the oxygen and the boron atoms moving oppositely in the $\langle 111 \rangle$ direction. The oxygen and boron displacements are 0.03 and 0.18 Å, respectively.

Final Remarks

In conclusion, we have discussed the role played by the native defects in c-BN using an ab initio Hartree–Fock method within the cluster approach. For the neutral isolated boron antisite, a Jahn–Teller distortion in the $\langle 111 \rangle$ direction is observed. For the neutral N vacancy, a strong relaxation is found: highly localized a_1 orbital in the vacancy region (F-center precursor) and a t_2 orbital resonant in the conduction band appear before the lattice relaxation. The relaxation (+ distoration) splits the t_2 orbital, leading to a half-occupied a_1 level, close to the conduction band. Our calculations enable us to suggest that the strong EPR signal seen in c-BN [15] could be provided by the trapping of two electrons by acceptor levels introduced by carbon doping. For the neutral $O_{[N]}$, we found that an a_1 orbital, half-occupied, is introduced above the middle of the valence band after lattice relaxation.

ACKNOWLEDGMENTS

The calculations were performed at the CENAPAD/Campinas and LCCA/USP. This work was supported by the Brazilian agencies CNPq, FAPESP, and FAPERGS.

References

1. R. M. Chrenko, Solid State Commun. **14**, 511 (1974); N. Miyata, K. Moriki, O. Mishima, M. Fujisawa, and T. Hattori, Phys. Rev. B **40**, 12028 (1989).
2. A. Meller, *Gmelin Handbuch der Anorganische Chemie, Boron Compounds*, 3rd Supplement (Springer-Verlag, Berlin, 1988), Vol. 3, pp. 1–91; for instance, J. H. Edgar, Ed., *Properties of Group III Nitrides*, (IN-SPEC, London, 1994).
3. R. H. Wentorf, Jr., J. Chem. Phys. **36**, 1990 (1962); O. Mishima, J. Tanaka, S. Yamaoka, and O. Fukunaga, Science **238**, 181 (1987).
4. See, e.g., P. Rodriguez-Hernandez, M. Gonzalez-Diaz, and A. Munos, Phys. Rev. B **51**, 14705 (1995).

5. V. A. Gubanov, L. A. Hemstreet, C. Y. Fong, and B. M. Klein, Appl. Phys. Lett. **69**, 227 (1996); I. Ya. Nikiforov, V. V. Ilyasov, and N. Yu Safontseva, J. Phys.: Condens. Matter **7**, 6035 (1995); Y. Bar-Yam, T. Lei, T. D. Moustakas, D. C. Allan, and M. P. Teter, Mat. Res. Soc. Symp. Proc. **242**, 335 (1992).
6. V. A. Gubanov, Z. W. Lu, B. M. Klein, and C. Y. Fong, Phys. Rev. B **53**, 4377 (1996).
7. L. M. Scolfaro and A. Fazzio, Phys. Rev. B **36**, 7542 (1987).
8. R. Jones and S. Öberg, Phys. Rev. Lett. **69**, 136 (1992).
9. J. S. Binkley, J. A. Pople, and W. J. Hehre, J. Am. Chem. Soc. **102**, 939 (1980).
10. M. W. Schmidt, K. K. Baldridge, J. A. Boatz, S. T. Elbert, M. S. Gordon, J. H. Jensen, S. Kosegi, N. Matsunaga, K. A. Nguyen, S. Su, and T. L. Windus, J. Comput. Chem. **14**, 1347 (1993).
11. C. C. J. Roothaan, Rev. Mod. Phys. **23**, 69 (1951).
12. F. Lüty, Z. Phys. **160**, 1 (1960).
13. A. Zunger and A. Katzir, Phys. Rev. B **11**, 2378 (1975).
14. E. Y. Andrei, A. Katzir, and J. T. Suss, Phys. Rev. B. **13**, 2831 (1975).
15. M. Fanciulli and T. D. Moustakas, Mat. Res. Soc. Symp. Proc. **242**, 605 (1992).

Possibilities of Charge- and/or Spin-Mediated Superconductors and Photo-Induced Superconductors in the Intermediate Region of Metal–Insulator Transitions

HIDEMI NAGAO,[1] MASAKI MITANI,[2] MASAMICHI NISHINO,[2] YASUNORI YOSHIOKA,[2] KIZASHI YAMAGUCHI[2]

[1]*Institute for Molecular Science, Myodaiji, Okazaki 444, Japan*
[2]*Department of Chemistry, Graduate School of Science, Osaka University, Toyonaka, Osaka 560, Japan*

Received 6 March 1997; revised 24 July 1997; accepted 31 July 1997

ABSTRACT: Magnetism, conductivity, and superconductivity of molecular materials are discussed on the basis of extended Hubbard–Peierls Hamiltonians, which involve four parameters; transfer integral (T), electron-lattice interaction (W), and on-site and intersite Coulomb interactions (U, V). The four-component spinor is introduced to define order parameters which characterize four different electronic states (charge density wave, spin density wave, singlet and triplet superconductivities) in a unified fashion. Several intermediate regions in these parameters are interesting and important from current theoretical reasons. Many experimental results clearly show the importance of intermediate correlation regimes for active controls of these states by chemical modifications and by external fields such as high pressure. Several model Hamiltonians such as CT and t–J models are derived for elucidation of potential electronic properties of molecule-based materials. Recent computational results based on the t–J model are utilized to rationalize our J model for spin-mediated superconductivity. Possibilities of magnetic conductors, charge- and/or spin-mediated superconductors, and photoinduced superconductors instead of the charge-mediated Little model are examined in the intermediate region of several metal–insulator transitions. Possible candidates are also proposed on the basis of various circumstantial experimental results. Implications of the calculated results are finally discussed in relation to the recent development of the intersection area among conducting, magnetic, and optical molecular materials. © 1997 John Wiley & Sons, Inc. Int J Quant Chem **65**: 947–964, 1997

Correspondence to: K. Yamaguchi.

International Journal of Quantum Chemistry, Vol. 65, 947–964 (1997)
© 1997 John Wiley & Sons, Inc.
CCC 0020-7608 / 97 / 050947-18

Introduction

In the past decade, magnetism and electron correlation have attracted much interest in relation to high-T_c superconductivity in copper oxides [1]. Many experimental and theoretical efforts have been made for the elucidation of possible interplay between p- and d-electrons of transition-metal oxides in the intermediate or strong electron-correlation regime [2]. In previous articles [3–5], we examined model Hamiltonians for copper oxides to elucidate two key points: (1) How many active orbitals are necessary for modelings of electronic structures of copper oxides? and (2) What kind of model Hamiltonians are derived on the basis of the strength of electron correlations? Concerning the first question, one- to six-band models (N = 1–6) were found to be plausible for copper oxides depending on the purposes and problems under investigation. For the latter question, there were at least four different classes: (1) the t–J model, (2) the spin-fluctuation model, (3) the spin- and charge-fluctuation model, which is referred to as an electron correlation (EC) model [5], and (4) the charge-fluctuation or CT model. Many charge- and/or spin-mediated models are feasible. For example, models (1) and (2) provide a simple equation to estimate the transition temperature (T_c) for spin-mediated superconductivity [3–5]:

$$T_c = -CJ_{ab}, \qquad (1)$$

where C and J_{ab} are, respectively, a phenomenological constant (C = 0.1) and the effective exchange integral for the superexchange-coupled transition-metal ions: M(II)O^{2-}M(II) (**1**) (M = Cu, Ni, etc). Our ab initio computations [4] showed that the J_{ab} value for the Cu(II)O^{2-}Cu(II) unit (**1a**) is over 1000 cm^{-1}, and, therefore, T_c is higher than 100 K in copper oxide superconductors [1, 2]. However, they indicated that copper oxides belong to the intermediate regime (see circle 4 in Fig. 5), and, therefore, charge and phonon degrees of freedom also contribute to the high-T_c superconductivity, although only the spin degrees of freedom is explicitly considered in Eq. (1).

A BRIEF REVIEW OF OUR PREVIOUS WORK

During the past decade, we have been interested in the design and investigation of possible organic, organometallic, and inorganic analogs to copper oxides on the basis of an assumption that these analogs should have low CT excitation energies and large $|J_{ab}|$ values before doping, although many physicists have focused attention on the investigation of possible microscopic mechanisms of the high-T_c superconductivity [2]. Previously [3–5], the possible mechanisms have been examined from the viewpoint of charge and spin degrees of freedom, and several model Hamiltonians such as the Hubbard model [6] have been discussed in relation to magnetism, conductivity, and superconductivity. Since undoped copper oxide was known to be an antiferromagnetic insulator, molecular magnetic compounds thus attracted our special interest [3–5, 7]. Therefore, we may have the first hypothesis for molecular design 1:

*(H1) The first step to molecular design is to find possible isoelectronic units to the Cu(II)O^{2-}Cu(II) (**1a**) system.*

From the above hypothesis, we have first been interested in 1,3-dipolar compounds [8] RYR (R = CH_2, CH, etc; Y = O, S, etc. (**2**) because of their isoelectronic structures with **1** as illustrated in Figure 1. Figure 2 illustrates the orbital energy diagrams for **1** and **2** to clarify their interrelationship. Isoelectronic d–π systems were also designed by replacing the inorganic anion X in metal oxides with an organic π-ligand [9], as illustrated in Figure 2, and isoelectronic π-radical (R) systems were theoretically synthesized by substituting divalent magnetic ions with radical groups (R) under the assumption that the p–d, π–d, and π–R energy gaps should be small so as to reproduce the large antiferromagnetic (negative) exchange integral of **1a**. To confirm the assumption, the complete active space (CAS) three-orbital four-electron {4, 3} configuration interaction (CI) calculations [10] were carried out as illustrated in Figure 3. Since the direct d–d (R–R) interaction is small because of no metal–metal orbital overlap, the p–d, π–d, and π–R orbital interactions play crucial roles in the configuration mixing. The CAS CI calculations, i.e., exact diagonalization of the extended Hubbard model [6], revealed a characteristic feature for the Cu(II)O^{2-}Cu(II) unit (**1a**): low ligand–metal charge-transfer (LMCT) excitation energy (ΔE_{CT}) and strong mixing between the metal biradical (MBR) and ligand–metal charge-transfer (LMCT) configurations because of the large p–d orbital overlap integral and small p–d charge-transfer energy (Δ_{pd}) as illustrated in Figure 4. The strong

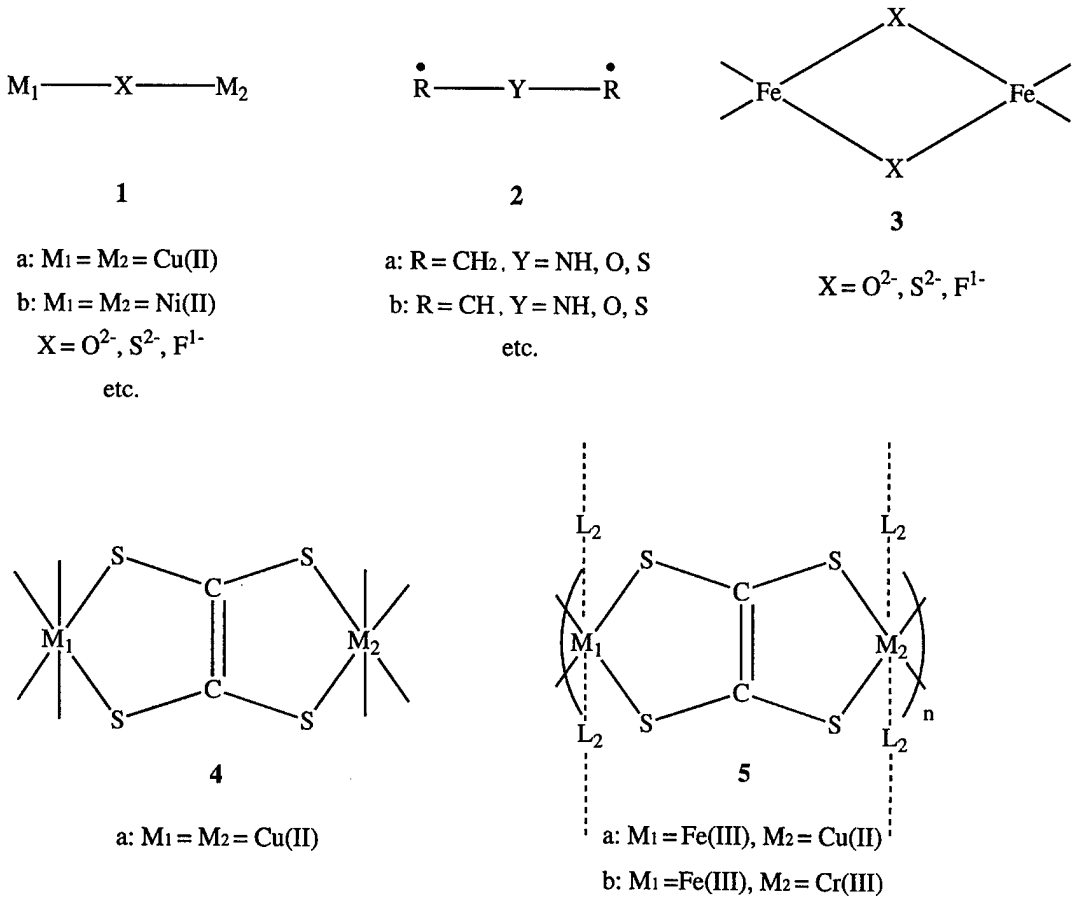


FIGURE 1. The component units for construction of chain, ladder, and sheet with intermediate or strong electron correlations.

mixing between MBR and LMCT also resulted in the cases of several organometallic systems, e.g., the binuclear iron–sulfur system $Fe(II)S_2^{4-}Fe(III)$ (**3**) [11] and the transition-metal tetrathiolate system (**4**) in Figure 1. In fact, the $|J_{ab}|$ value has been estimated from experiment to be over 800 cm^{-1} for the binuclear copper–tetrathiolate complex (**4a**) [12, 13], and this value is comparable to the observed J_{ab} value (-1000 cm^{-1}) for copper oxide. Therefore, we have tried to synthesize one-dimensional (1D) and 2D complexes (**5**) using the tetrathiolate ligand (**4**) as shown in Figure 1. The intrachain J_{ab} values observed by the magnetic measurements were indeed very large; for example, they were 100 and -63 cm^{-1}, respectively, for **5a** {M1 = Fe(III) and M2 = Cu(II)} and **5b** {M1 = Fe(III) and M2 = Cr(III)}. However, the intercolumn interaction for **4** could not be controlled so as to obtain proper crystals since appropriate ligands (L_2) have not been discovered yet [12, 14].

The CAS CI calculations have shown that electronic properties of excited states of the p–d, π–d, and π–R systems in Figure 4 are sensitive to the interaction parameters [10] and that CT excited states such as LMCT are generated by low-energy photoexcitation or even by thermal excitation in special cases. This, in turn, indicates that photoexcitations may induce dramatic changes of electronic, magnetic, and optical properties of these p–d, π–d, and π–R interaction systems under consideration. In the past decades, we have thoroughly investigated dimer and clusters of typical model systems to elucidate the nature of these chemical bonds. The calculated results showed that active controls of charge, spin, and photon properties in the systems are feasible because of strong

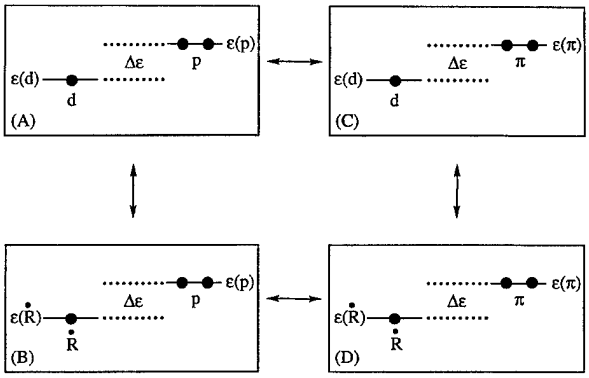


FIGURE 2. Schematic illustrations of the orbital energy levels of isoelectronic p–d, π–d, p–R, and π–R systems, which are schematically explained by A, B, C, and D, respectively.

coupling of three degrees of freedom and nonlinear responses to external fields as has been emphasized in previous articles [15, 16].

PRESENT PURPOSE AND INTEREST

As a continuation of this previous work, we summarize here and extend our basic ideas for molecular design and fully examine theoretical models for conducting, magnetic, and optical phenomena in molecular materials. Our previous J model [4], which was presented before the proposal of the so-called t–J model, is extended on the basis of recent numerical results based on the latter model. Many experimental results are also examined systematically as circumstantial evidence from our theoretical viewpoints presented previously [3, 5]. Several theoretical models or hypotheses will be derived from these investigations for active controls of charge and/or spin-mediated and photoinduced properties of molecular materials. Probably, such a semiempirical approach would be permitted as a chemist's approach at the current stage of both theoretical and experimental studies on molecule-based materials in the intermediate and strong correlation regime. This article contributes to the recent development of the intersection area among conducting, magnetic, and optical molecular materials.

Theoretical Backgrounds

MODEL HAMILTONIANS FOR EXTENDED SYSTEMS

Several microscopic theoretical models [5, 17] are first considered in order to elucidate the nature of itinerant ferromagnetism via electron correlation, spin-mediated high-T_c superconductivity, fractional quantum Hall effect, etc., which are our main concerns in the field of the solid-state quantum chemistry [3, 18]. From the viewpoint of the nature of chemical bonds, conductive, magnetic, optical, and other properties of molecular solids under investigation are governed by three important microscopic variables: (1) the transfer integral

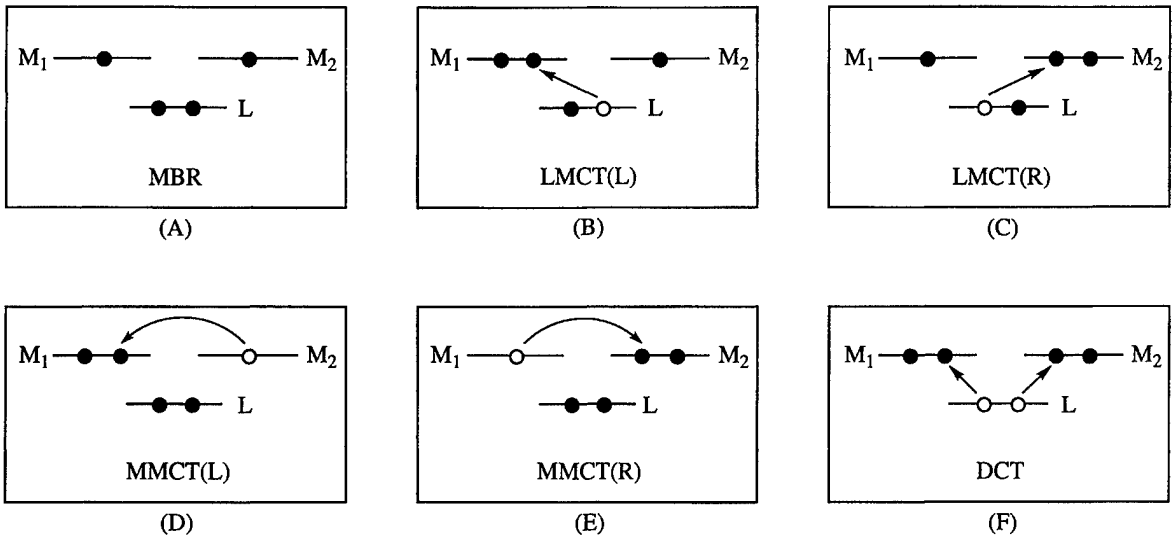


FIGURE 3. Schematic illustrations of six configurations constructed of three active orbitals and four active electrons {4, 3}. Notations are given in the text.

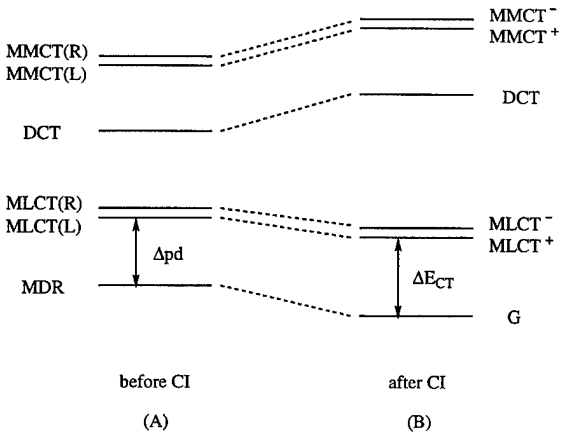


FIGURE 4. The energy levels of the six states (A) before and (B) after full CI calculation of the Hubbard model.

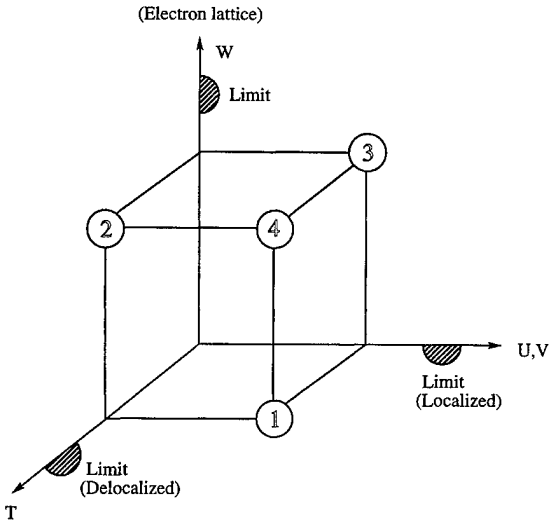


FIGURE 5. Variations of electronic, magnetic, and optical properties with four microscopic molecular parameters: transfer integral (T), electron–phonon coupling (W), and on-site (U) and intersite (V) electron-repulsion integrals. Circles (1–4) denote the intermediate cases (see text).

(T) between d (or radical) and p (or π) orbitals, (2) electron–phonon (lattice) interaction (W), and (3) electron–electron interaction [10], although other factors such as the chemical potential and crystal structure and disorder are also important for molecular materials. T describes the itinerant character of electron or hole, namely, the charge or electron transfer in molecule-based solids. The last term is usually divided into on-site (U) and intersite (V) repulsion integrals. Therefore, the properties (P) of π-radical (R) and π–d interaction systems are, in principle, described by these variables: P = functions (T, W, U, V) as illustrated in Figure 5, and the extended Hubbard–Peierls Hamiltonian involving these parameters (T, W, U, V) should have a general applicability to theoretical treatments of possible new molecule-based materials examined later. This Hamiltonian is often reduced to several simple model Hamiltonians such as the t–J model [5], for which effective variables are derived from the four parameters in Figure 5.

There have been many theoretical studies in the extreme cases illustrated in Figure 5: (i) large T-limit (delocalized limit), large U-limit (localized limit), and large W-limit (Jahn–Teller limit). The behaviors of molecule-based materials in these limits are rather simple, and the nature of them is understood in many cases. On the other hand, several intermediate cases shown in circles 1–4 in Figure 5 are not well known yet because of difficulty of theoretical treatments; it is noteworthy that conventional perturbation approaches break down [5]. However, the characteristics of molecule-based materials are often regarded as the intermediate strengths of four parameters in Figure 5 [3, 4, 18]. This is, in turn, one of the reasons why the molecular materials of our concern are important and interesting from a theoretical viewpoint [5, 18]. Thus, we have the second hypothesis 2:

(H2) New phenomena and science may be expected from thorough and careful investigations of low-dimensional molecular systems in the intermediate regime in Figure 5.

ORDER PARAMETERS FOR MAGNETIC AND SUPERCONDUCTING STATES

The magnetism and superconductivity are typical macroscopic quantum phenomena which can be described by characteristic order parameters. For the purpose, field theoretical formulations are briefly summarized here [17, 19, 20]. The four-component spinor $\Psi(\mathbf{r})$ is introduced to characterize possible electronic phases for molecular materials—(1) charge density wave (CDW), (2) spin density wave (SDW), (3) singlet superconductivity

(SSC), and (4) triplet superconductivity (TSC):

$$\Psi(\mathbf{r}) = \begin{pmatrix} \psi_\uparrow(\mathbf{r}) \\ \psi_\downarrow(\mathbf{r}) \\ \psi_\downarrow^+(\mathbf{r}) \\ -\psi_\uparrow^+(\mathbf{r}) \end{pmatrix}, \tag{2}$$

$$\Psi^+(\mathbf{r}) = \left(\psi_\uparrow^+(\mathbf{r})\psi_\downarrow^+(\mathbf{r})\psi_\downarrow(\mathbf{r}) - \psi_\uparrow(\mathbf{r})\right).$$

$\psi_\alpha^+(\mathbf{r})(\psi_\alpha(\mathbf{r}))$ is the fermion creation (annihilation) field operator with spin α at point r, and it satisfies the anticommutation relations. The subscripts $\uparrow$ and $\downarrow$ mean up and down spins, respectively. The electronic phase is characterized by its order parameter, which is given by the product of spinor fields; $\Psi(\mathbf{r})\Psi^+(\mathbf{r}')$. The product is composed of 16 components and it is factorized into the following forms as

$$\Psi(\mathbf{r})\Psi^+(\mathbf{r}') = \begin{pmatrix} \hat{F}(\mathbf{r},\mathbf{r}') & \hat{D}(\mathbf{r},\mathbf{r}') \\ \hat{D}^+(\mathbf{r},\mathbf{r}') & \hat{F}'(\mathbf{r},\mathbf{r}') \end{pmatrix}, \tag{3}$$

where each block component is given by

$$\hat{F}(\mathbf{r},\mathbf{r}') = \begin{pmatrix} \psi_\uparrow(\mathbf{r})\psi_\uparrow^+(\mathbf{r}') & \psi_\uparrow(\mathbf{r})\psi_\downarrow^+(\mathbf{r}') \\ \psi_\downarrow(\mathbf{r})\psi_\uparrow^+(\mathbf{r}') & \psi_\downarrow(\mathbf{r})\psi_\downarrow^+(\mathbf{r}') \end{pmatrix}$$

$$= \frac{1}{2}\begin{pmatrix} \hat{C}(\mathbf{r},\mathbf{r}') + \hat{S}_z(\mathbf{r},\mathbf{r}') & \hat{S}_x(\mathbf{r},\mathbf{r}') - i\hat{S}_y(\mathbf{r},\mathbf{r}') \\ \hat{S}_x(\mathbf{r},\mathbf{r}') + i\hat{S}_y(\mathbf{r},\mathbf{r}') & \hat{C}(\mathbf{r},\mathbf{r}') - \hat{S}_z(\mathbf{r},\mathbf{r}') \end{pmatrix}, \tag{4}$$

$$\hat{F}'(\mathbf{r},\mathbf{r}') = \begin{pmatrix} \psi_\downarrow^+(\mathbf{r})\psi_\downarrow(\mathbf{r}') - \psi_\downarrow^+(\mathbf{r})\psi_\uparrow(\mathbf{r}') \\ -\psi_\uparrow^+(\mathbf{r})\psi_\downarrow(\mathbf{r}')\psi_\uparrow^+(\mathbf{r})\psi_\uparrow(\mathbf{r}') \end{pmatrix}$$

$$= \frac{1}{2}\begin{pmatrix} \hat{C}'(\mathbf{r},\mathbf{r}') + \hat{S}_z'(\mathbf{r},\mathbf{r}') & \hat{S}_x'(\mathbf{r},\mathbf{r}') - i\hat{S}_y'(\mathbf{r},\mathbf{r}') \\ \hat{S}_x'(\mathbf{r},\mathbf{r}') + i\hat{S}_y'(\mathbf{r},\mathbf{r}') & \hat{C}'(\mathbf{r},\mathbf{r}') - \hat{S}_z'(\mathbf{r},\mathbf{r}') \end{pmatrix} \tag{5}$$

and

$$\hat{D}(\mathbf{r},\mathbf{r}') = \begin{pmatrix} \psi_\uparrow(\mathbf{r})\psi_\downarrow(\mathbf{r}') - \psi_\uparrow(\mathbf{r})\psi_\uparrow(\mathbf{r}') \\ \psi_\downarrow(\mathbf{r})\psi_\downarrow(\mathbf{r}') - \psi_\downarrow(\mathbf{r})\psi_\uparrow(\mathbf{r}') \end{pmatrix}$$

$$= \frac{1}{2}\begin{pmatrix} \hat{\Delta}(\mathbf{r},\mathbf{r}') + \hat{\Delta}_z(\mathbf{r},\mathbf{r}') & \hat{\Delta}_x(\mathbf{r},\mathbf{r}') - i\hat{\Delta}_y(\mathbf{r},\mathbf{r}') \\ \hat{\Delta}_x(\mathbf{r},\mathbf{r}') + i\hat{\Delta}_y(\mathbf{r},\mathbf{r}') & \hat{\Delta}(\mathbf{r},\mathbf{r}') - \hat{\Delta}_z(\mathbf{r},\mathbf{r}') \end{pmatrix}. \tag{6}$$

They can be also rewritten by the field product elements summarized in Table I. The number-density field operator $\hat{C}(\mathbf{r},\mathbf{r}')(\hat{C}'(\mathbf{r},\mathbf{r}'))$ is the antisymmetric spinor and means an order parameter for CDW. The spin-density field operators, $\hat{S}_x(\mathbf{r},\mathbf{r}')$, $\hat{S}_y(\mathbf{r},\mathbf{r}')$, $\hat{S}_z(\mathbf{r},\mathbf{r}')(\hat{S}_x'(\mathbf{r},\mathbf{r}')$, and so on, are the symmetric spinors and correspond to operators for SDW. The order parameters for SSC and TSC are generated from the off-diagonal field operator $\hat{D}(\mathbf{r},\mathbf{r}')$ [19]. Thus, superconductivity is regarded as an off-diagonal long-range order. $\hat{\Delta}(\mathbf{r},\mathbf{r}')$ is the antisymmetric spinor and generates the order parameter for SSC. $\hat{\Delta}_x(\mathbf{r},\mathbf{r}')$, $\hat{\Delta}_y(\mathbf{r},\mathbf{r}')$, and $\hat{\Delta}_z(\mathbf{r},\mathbf{r}')$ are the symmetric spinors and yield order parameters for TSC. The SSC state, whose order parameter does not depend on the Fermi momentum, is isotropic; it is called the *s*-wave. However, the SSC

TABLE I
Order parameters for CDW, SDW, SSC, and TSC.

$\hat{C}(r,r') = \psi_\uparrow(r)\psi_\uparrow^+(r') + \psi_\downarrow(r)\psi_\downarrow^+(r')$	$\hat{S}_y'(r,r') = i\{\psi_\uparrow^+(r)\psi_\downarrow(r') - \psi_\downarrow^+(r)\psi_\uparrow(r')\}$
$\hat{S}_x(r,r') = \psi_\downarrow(r)\psi_\uparrow^+(r') + \psi_\uparrow(r)\psi_\downarrow^+(r')$	$\hat{S}_z'(r,r') = \psi_\downarrow^+(r)\psi_\downarrow(r') - \psi_\uparrow^+(r)\psi_\uparrow(r')$
$\hat{S}_y(r,r') = -i\{\psi_\downarrow(r)\psi_\uparrow^+(r') - \psi_\uparrow(r)\psi_\downarrow^+(r')\}$	$\hat{\Delta}(r,r') = \psi_\uparrow(r)\psi_\downarrow(r') - \psi_\downarrow(r)\psi_\uparrow(r')$
$\hat{S}_z(r,r') = \psi_\uparrow(r)\psi_\uparrow^+(r') - \psi_\downarrow(r)\psi_\downarrow^+(r')$	$\hat{\Delta}_x(r,r') = \psi_\downarrow(r)\psi_\downarrow(r') - \psi_\uparrow(r)\psi_\uparrow(r')$
$\hat{C}(r,r') = \psi_\downarrow^+(r)\psi_\downarrow(r') + \psi_\uparrow^+(r)\psi_\uparrow(r')$	$\hat{\Delta}_y(r,r') = -i\{\psi_\downarrow(r)\psi_\downarrow(r') + \psi_\uparrow(r)\psi_\uparrow(r')\}$
$\hat{S}_x'(r,r') = -\psi_\uparrow^+(r)\psi_\downarrow(r') - \psi_\downarrow^+(r)\psi_\uparrow(r')$	$\hat{\Delta}_z(r,r') = \psi_\uparrow(r)\psi_\downarrow(r') + \psi_\downarrow(r)\psi_\uparrow(r')$

state often depends upon the direction of the momentum whose magnitude equals the Fermi momentum. The SSC state which exhibits dependence on direction is an anisotropic SSC state such as the d-wave. On the other hand, we must consider both orbital and spin degrees of freedom to characterize the TSC state. The order parameters of spin S and angular momentum L are composed of $2S + 1$ spin elements times $2L + 1$ orbital elements. Therefore, TSC have many possibilities such as the p-wave, showing many interesting characteristics. These SSC and TSC states can be characterized by the group-theoretical methods [21].

MODIFIED PHASE DIAGRAMS FOR t–J MODELS

As a typical example for explanation of long-range orders discussed above, let us consider phase diagrams for doped copper oxides. Previous ab initio UHF [4] and CASSCF [22] calculations indicated that extra holes are introduced mainly into the oxygen site for copper oxides [2], being consistent with the so-called t–J model derived from the d–p two- or three-band Hubbard model of the species [23, 24]. Therefore, a reasonable understanding of our J model [4] can be obtained from exact and numerical results obtained by recent exact diagonalizations [25–30] of t–J models for copper oxides. The 1D t–J model was solved exactly in the special case of $J = 2t$ [25], and its numerical solution was also obtained to depict the phase diagram [26]. The t–J models for the 2D lattice were also solved numerically to describe the high-T_c superconductivity for copper oxides [27–30]. All these calculations indicated that the large J value is responsible for the formation of a Cooper pair, supporting the J model in Eq. (1). Here, the phase diagrams obtained by them are utilized for the extension of our model to reproduce experimental results [2].

The t–J model Hamiltonian can be defined as

$$H(t-J) = -t \sum_{i,j,\sigma} (1 - n_{i,-\sigma}) a_{i\sigma}^{+} a_{j\sigma} (1 - n_{j,-\sigma}) + J \sum_{i,j} \mathbf{S}_i \cdot \mathbf{S}_j, \quad (7a)$$

where t denotes the hopping integral for the singlet pair between the Cu- and O-hole spins [23], and the spin operator $\mathbf{S}_i$ and number density are defined by $\mathbf{S}_i = \frac{1}{2} a_{i\alpha}^{+} \sigma_{\alpha\beta} a_{i\beta}$ and $n_i = \sum_\sigma a_{i\sigma}^{+} a_{i\sigma}$, respectively. The phase diagram for the t–J model was obtained using the slave-boson method [25], where $a_{i\sigma}$ is defined by

$$a_{i\sigma} = f_{i\sigma} b_i^{+}. \quad (8)$$

$f_{i\sigma}$ is a fermion operator that carries the spin and b_i^{+} is a boson operator creating a vacancy. The constraint of no double occupancy at the site i is expressed by

$$\sum_\sigma f_{i\sigma}^{+} f_{i\sigma} + b_i^{+} b_i = 1. \quad (9)$$

Then, the t–J model Hamiltonian can be rewritten as

$$H(t-J) = -t \sum_{i,j,\sigma} b_i f_{i\sigma}^{+} f_{j\sigma} b_{j\sigma}^{+} + J \sum_{i,j} \mathbf{S}_i \cdot \mathbf{S}_j - \sum_i \lambda_i \left(\sum_\sigma f_{i\sigma}^{+} f_{i\sigma} + b_i^{+} b_i - 1 \right), \quad (7b)$$

where the Lagrange multiplier λ_i represents the constraint to exclude the double occupancy at each site. The singlet spin-pairing parameter (S_{ij}) is given by

$$S_{ij} = (f_{i\uparrow} f_{j\downarrow} - f_{i\downarrow} f_{j\uparrow}). \quad (10)$$

The 2D t–J model was solved under the mean-field approximation [27–30] and two different transition temperatures, T(SG) and T(BE), were obtained: T(SG) is the transition temperature for the pairing of the spinons below which the fermion response function shows the Meissner effect, while T(BE) is the Bose–Einstein condensation temperature of the boson. T(SG) is a decreasing function of the hole concentration x and becomes zero when $tx_{\max} = J$, where $x_{\max}$ is the maximum concentration for the appearance of superconductivity. On the other hand, T(BE) is an increasing function of x, e.g., $T(\mathrm{BE}) = 4\pi tx = 4\pi Jx$ ($x = \langle b_i^{+} b_i \rangle$). The four different phases were defined by using these two characteristic temperatures, T(SG) and T(BE)—I(FL): the Fermi liquid phase where $\langle b_i \rangle = 0$; II(SG): the spin gap (SG) phase where $\langle S_{ij} \rangle \neq 0$ but $\langle b_i \rangle = 0$; III(SSC): the singlet superconducting phase with the d-wave symmetry where $\langle S_{ij} \rangle \neq 0$ and $\langle b_i \rangle \neq 0$; and IV(EM): the exotic metal phase where $\langle S_{ij} \rangle = 0$ and $\langle b_i \rangle = 0$. The spin gap (SG) appears in the spin excitation spectrum in the phase II(SG). This has been confirmed by an NMR experiment [31]. The superconducting order pa-

rameter [27] in Eq. (6) is given by

$$\Delta_{ij} = (a_{i\uparrow} a_{j\downarrow} - a_{i\downarrow} a_{j\uparrow}) = \langle b_i \rangle^2 \langle S_{ij} \rangle, \quad (11a)$$

where Δ_{ij} is defined by

$$\Delta_{ij} = \int d\mathbf{r}\, d\mathbf{r}' \varphi_i^*(\mathbf{r}) \Delta(\mathbf{r}, \mathbf{r}') \varphi_j(\mathbf{r}'). \quad (11b)$$

φ_i denotes the site wave function. This is not zero in the phase III(SSC), accompanied by the appearance of the mass of the gauge field (the so-called Anderson–Higgs mechanism) [19, 20]; the boson (holon) and fermion (spinon) interact through the gauge field as in the case of QCD theory [17]. Although the slave-boson model explains, indeed, the appearance of a spin gap [31] in the underdoped copper oxide, its behavior near the threshold $x = 0$ is not clear, although the experiment clearly shows the existence of an antiferromagnetic (AF) phase [2].

Therefore, our J model in Eq. (1) is extended so as to reproduce experimental results [2] on the basis of the Ginzburg–Landau (GL) model which has been developed for the RVB state described by the t–J model [32]. From the mean-field results [32], two order parameters, ϕ_{GLF} and ϕ_{GLB}, corresponding to fermion pairing and Bose condensation, respectively, were introduced to define the free energy:

$$F_{GLX}[\phi_{GLX}, \mathbf{a}, \mathbf{A}] = \frac{H_{cX}^2}{8} \int d^2 r \left[2\xi_X^2 \left| \left(\nabla - im\mathbf{a} - i\frac{2e}{c} n\mathbf{A} \right) \phi_{GLX} \right|^2 + 2sgn(T - T(X)) |\phi_{GLX}|^2 + |\phi_{GLX}|^4 \right], \quad (12)$$

where ξ_X and H_{cX} denote the coherence length and critical field, and $m = 2$ and $n = 1$ for the fermion ($X = F$) and $m = 1$ and $n = 0$ for the boson ($X = B$). $\mathbf{a}$ and $\mathbf{A}$ denote the Chern–Simons gauge field [33] and vector potential, respectively. Here, we modify the GL model so as to approximately describe the experimental results [2] in combination with our J model, which was derived from the ab initio molecular orbital results for transition-metal oxides [34]. The three transition temperatures, T(AF), T(SG), and T(BE), are assumed to be proportional to the hole concentration, while the transition temperature T(SSC) for singlet superconductivity is approximately given by the quadratic form of x:

$$T(\mathrm{AF}) = c(\mathrm{AF}) J(x_{\min} - x) \quad (13a)$$

$$T(\mathrm{BE}) = c(\mathrm{BE}) J(x - x_{\min}) \quad (13b)$$

$$T(\mathrm{SG}) = c(\mathrm{SG}) J(x_{\max} - x)(x > x_{\min}) \text{ and } T(\mathrm{SG}) = c(\mathrm{SG}) Jx(x < x_{\min}) \quad (13c)$$

$$T(\mathrm{SSC}) = c(\mathrm{SSC}) J(x - x_{\min})(x_{\max} - x). \quad (13d)$$

$c(X)$ are the constants in Eq. (1), and the existing regions of these phases are defined as follows: antiferromagnetic phase (AF), $0 < x < x_{\min}$; singlet superconductivity phase (SSC), $x_{\min} < x < x_{\max}$; and Fermi liquid phase, $x_{\max} < x$ ($tx_{\max} = J$). Figure 6 illustrates the phase diagram for five different (AF, SG, SSC, FL, EM) phases. The maximum temperature for SSC is suppressed in our model, in conformity with the gauge field fluctuation, etc.

The SSC in the Fermi liquid phase I can be described by the spin fluctuation model [35, 36]. The transition temperature for SSC is expressed by the conventional BCS formula [35–37]

$$T(\mathrm{SSC}) = \Gamma_Q \xi_m (x_{\max} - x) \exp(-1/\lambda), \quad (14)$$

where the cutoff energy is given by the characteristic energy Γ_Q of spin fluctuation (SF) and ξ_m is the magnetic coherence length [37]. The SF model at least works well in the overdoped region I in Figure 6, although its behavior in the underdoped region II is not clear yet. If the true order parameter for the high-T_c superconductivity is discovered in the future, the coherence length, penetration

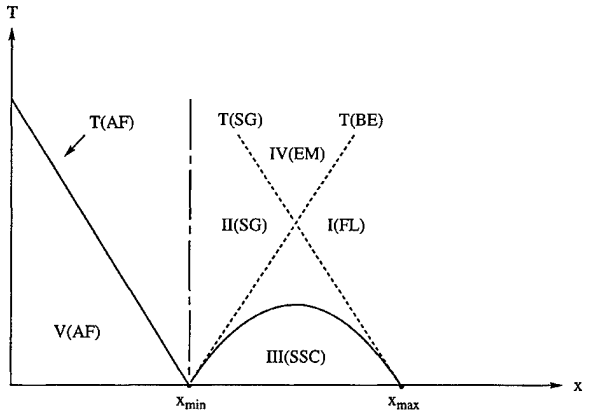


FIGURE 6. Phase diagram for the Fermi liquid I (FL), spin gap II (SG), singlet superconductive III (SSC), exotic metallic IV (EM), and antiferromagnetic V (AF) phases for copper oxide superconductors by the modified slave-boson model.

depth, and transition temperature can be obtained by the same formalism in Eq. (12). The previous J and present modified GL models can be utilized for molecular design of spin-mediated superconductors, although they are phenomenological. In fact, several experimental groups are now conducting synthetic efforts for them as discussed below.

ACTIVE CONTROLS OF PROPERTIES BY EXTERNAL FIELDS

The phase diagram in Figure 6 clearly shows that electronic phases of copper oxides are variable with hole concentration (x). This, in turn, indicates that active control of electronic, conductive, magnetic, and optical properties by chemical modifications and external fields are feasible for potential applications of molecule-based materials to advanced technologies. Concerning these applications, there are several experimental and theoretical reasons why the intermediate regions in Figures 5 and 6 are so interesting:

1. Electronic structures in this regime are often sensitive to external variables (doping of hole or electron, pressure, temperature, external electronic field, photoexcitation, etc.), and the variations with such parameters are nonlinear in many cases.
2. Controls of electronic, magnetic, optical, and other properties with the above variables are feasible in appropriate experimental conditions because of the strong coupling of charge, spin, and phonon degrees of freedom.
3. Mean-field theories often break down because of strong fluctuations, and, therefore, new theories such as gauge field theories in quantum chromodynamics (QCD) [17, 19, 20] would be useful even in the field of solid-state quantum chemistry.

Thus, the switching of conductive, magnetic, and optical properties by the external fields is a key issue for molecule-based materials in the intermediate regime [3, 18]. Figure 7 illustrates the bistability expected in several natural and artificial systems [14, 18]. Although the bistability is indeed one of the guiding principles for the construction of electronic devices, it is equally applicable to the design of new functional materials responsible for active controls [3]. It would be one of the chemist's strategies to obtain molecule-based materials with

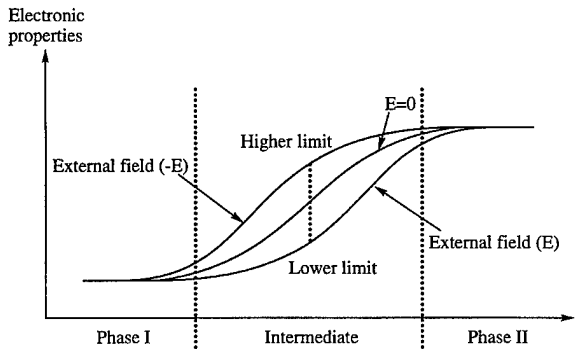


FIGURE 7. Controls of electronic, magnetic, and optical properties of molecule-based materials by external parameters (see text). Switchings by the external fields are feasible in the intermediate regime.

such novel properties, although powerful metal magnets and high-T_c copper oxides have already been discovered. Probably, molecule-based functional systems have common characteristic features with biological systems [18].

Possible Strategies for Charge- and/or Spin-mediated Superconductors

GENERATIONS OF NEW ELECTRONIC PHASES BY CARRIER DOPING

The discovery of high-T_c copper oxide [1] suggested the idea that doping in antiferro- or ferromagnetic systems, more generally molecular charge-transfer (CT) insulators, may provide several exotic electronic phases as illustrated in Figure 8 [3–5]. The antiferromagnetic insulators may be converted upon doping into six different phases: (1) ferromagnetic metal or insulator; (2) spin glass; (3) paramagnetic metal; (4) antiferromagnetic metal; (5) ferrimagnetic metal or insulator; and (6) charge- or spin-mediated superconductor. Recent field theoretical approaches can describe these electronic phases in a systematic manner as shown in Eqs. (2)–(6). Unfortunately, to our knowledge, theoretical determinations of possible phase diagrams for molecular materials [17, 22] are difficult tasks except for a special case such as the Nagaoka theorem [38], because the perturbation theory breaks down for molecular materials under investigation. However, accumulating experimental results suggest that carrier doping into intermediate or strong correlation systems exhibit several interesting phenomena in Figure 8 and other quantum

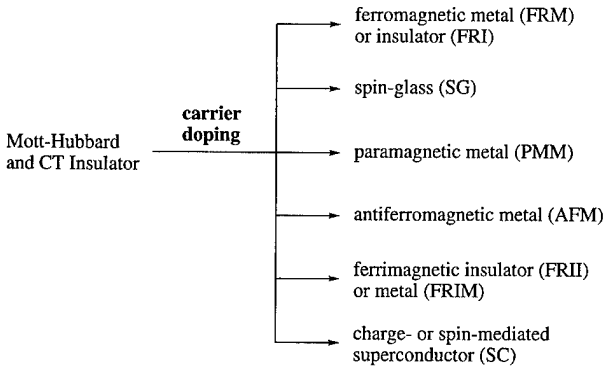


FIGURE 8. Possible phases obtained by carrier doping into Mott–Hubbard and CT insulators.

spin phenomena [17] expected for the low-dimensional systems in Figures 5 and 6. Therefore, a chemist's approach from the theoretical side would search isoelectronic series to copper oxides as employed previously [3], while that of the experimental side is to synthesize new isoelectronic compounds followed by physical observations [14b]. Collaborations from both sides would open the new intersection field in molecular electronic materials. For the theoretical side, the following hypothesis 3 is assumed as [3–5]

(H3) Doping of hole or electron into Mott-Hubbard or CT insulators may provide exotic electronic materials summarized in Figure 8.

CHARGE- AND / OR SPIN-MEDIATED SUPERCONDUCTOR

Although many theoretical studies of doped copper oxides were initiated just after the discovery of the high-T_c superconductivity [1], theoretical attempts to examine possible molecular analogs to them were scarce in 1986 [3–5, 7] although such attempts are now popular in chemistry and material science. As mentioned previously [5], we have therefore started our theoretical attempts to search possible models for charge- and/or spin-mediated superconductors. For the purpose, we assumed a working hypothesis (H4):

(H4) Charge- and / or spin-mediated superconductors may appear in the intermediate region of metal–insulator transitions as illustrated in Figure 9.

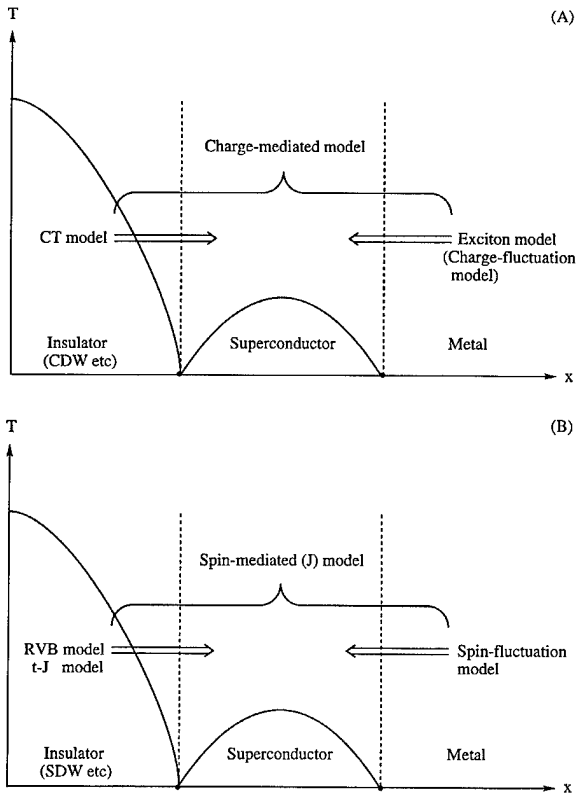


FIGURE 9. Four different approaches to obtain high-T_c superconductors in the intermediate regime of the metal–insulator transitions: (A) charge-mediated superconductor; (B) spin-mediated superconductor.

Figure 9 illustrates possible approaches based on the hypothesis H4. Concerning charge-mediated superconductivity, the introduction of charge fluctuation from the metallic side was already examined by Little [39] in the case of conductive polymers and related species in Figure 9(A). On the other hand, the possible role of CT excitation from the nonmagnetic insulator side in the intermediate region of metal–insulator transitions is not elucidated yet. Therefore, this moot point should be examined later. The spin-fluctuation model is also conceivable from the metallic side in the intermediate regime of antiferro (or ferro) magnetic insulator-to-metal transitions as illustrated in Figure 9(B). On the other hand, the t–J model or RVB model can be used to formulate possible spin-mediated superconductivities from the magnetic insulator side. In the later sections, we therefore examine possible candidates from these theoretical viewpoints.

Models for Exotic Spin-mediated Conductors and Superconductors

ORGANIC AND ORGANOMETALLIC RVB SYSTEMS

First, let us consider the spin-mediated superconductor in relation to copper oxides. The introduction of electron carriers into magnetic insulators is one of the possible ways to obtain spin-mediated superconductors as shown in Figure 9(B). The RVB state with spin frustration is expected to be a possible precursor for the purpose, although it has been interesting from the mechanism of free-radical reactions. For example, the Heisenberg model for organic radicals and radical clusters permit general spin structures such as triangular and cone ones [40, 41]. In fact, these general spin structures as well as spin-frustrated configurations appear even in the three hydrogen D_{3h} system and four hydrogen T_d system which are models of transition structures in exchange-forbidden radical reactions. We have thoroughly investigated these systems to elucidate group-theoretical interrelationships between several theoretical models [40].

After the discovery of the high-T_c superconductivity [1], triangular spin systems have attracted great interest because of the Andersons's resonating valence bond (RVB) theory [42] for magnetism and superconductivity. Many field theoretical models [17] have been presented for the high-T_c superconductivity in conformity with Anderson's proposal. On the other hand, we considered possible organic [10] and organometallic [11] spin-frustration systems such as the triangular ladder (**IV**) and Kagome ladder (**V**) in relation to RVB model for copper oxides as illustrated in Figure 10. Both through-bond and intermolecular approaches are possible to construct such spin networks or topology. The former approach enables us to propose several organic [8] and organometallic [11] candidates composed of the bond units in Figure 4. We also tried to synthesize low-dimensional systems composed of 4Fe—4S clusters with spin frustrations, but amorphous oligomers resulted to prevent further experimental treatments [43]. Instead

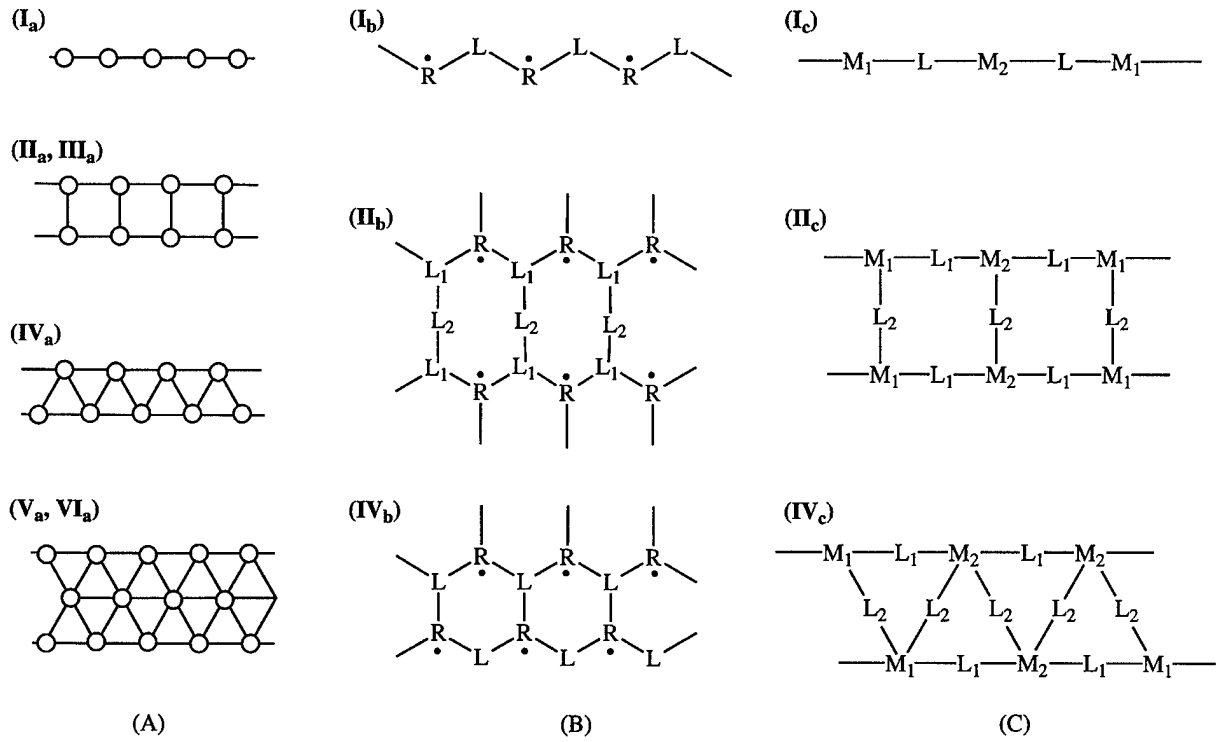


FIGURE 10. 1-D, ladder, and 2-D spin systems with and without holes (or electrons) which are attractive from magnetism and superconductivity.

of the former (through-bond) approach, the latter (through-space) approach is rather simple since many radicals and ion-radicals can be used for component units. For example, three-center units (**2**), nitronyl nitroxide (NN) derivatives, doped TTF and BEDT–TTF molecules, etc., would be building blocks for molecular ladder compounds in Figure 10.

Awaga et al. [44] discovered the organic Kagome system composed of *p*-MPNN, which does not exhibit the magnetic ordering even at low temperature because of strong spin frustration. But introduction of the carrier into this system seems difficult. Enoki [45] also found the triangular lattice composed of the BEDT–TTF plus Br complex. Their preliminary results for the complex showed peculiar magnetic behaviors. Apparently, much more experimental effort is desirable to open a new field in this direction. Then, we have the following hypothesis 5:

(H5) Exotic electronic phenomena may appear upon doping of organic and organometallic resonating valence bond (RVB) systems.

N-BAND MODELS FOR ORGANIC FERROMAGNETS, FERROMAGNETIC CONDUCTORS, AND *p*-WAVE SUPERCONDUCTORS

The ferromagnetism for electron correlated systems with *N*-tuple degenerate orbitals is a classic problem in magnetism because of the potential exchange interaction; the parameters arising from the Coulomb interaction (U, V) in Figure 5 should be considered [46, 47]. If an electron carrier is doped into the systems, the interaction between the conduction electron and the localized spin is realized, showing common features for other systems examined in this article. Recently, revisited interest for degenerated *N*-band systems has arisen from several discoveries. The orbital degeneracy (freedom) such as the three degenerate t_{2g} orbitals of C_{60} (**7**) plays an important role for orbital ferromagnetism [46]. The Hund rule for the orthogonal t_{2g} orbitals favors the high spin state of the dianion and trianion of **7**, but the ground state of the dianion is a singlet, showing the important role of an electron correlation effect as in the case of square planar cyclobutadiene. Thus, the interplay or competition among ferromagnetic exchange from orbital degeneracy, electron correlation (U), and the Jahn–Teller distortion (W) is one of fundamental problems in molecular magnets with *N*-band degeneracy. The TMAE·C_{60} CT complex exhibits complex magnetic behaviors because of these three factors; many spectroscopic experiments are not conclusive and are not settled yet [46].

The backbone and pendant-type polycarbene polymers investigated by the Ito–Takui [48] and Iwamura [49] groups are particularly interesting since the polycarbene species are regarded as the orthogonal two-band (σ and π) systems. Theoretical calculations [7, 50] were carried out to elucidate possible spin states of these species after doping and it was concluded that the doping of carriers into these polymers would become a model for the ferromagnetic conductor and the molecular triplet superconductor. Recently, the Shida and Ito–Takui groups initiated doping experiments into polycarbenes [51].

Recently, Maeno et al. [52] discovered the superconductivity for non-copper oxides: Sr_2RuO_4. A theoretical possibility of triplet superconductivity (TSC) in Table I was pointed out for Sr_2RuO_4 [53]. According to the band calculation [54], the $d\varepsilon(\pi)$–$p\pi$ interaction is essential in this compound in contrast to the $d\gamma(\sigma)$–$p\sigma$ interaction in copper oxide. In our J model in Eq. (1), the T_c for triplet superconductivity should be rather low because the ferromagnetic spin fluctuation is weak in Sr_2RuO_4. If Sr_2RuO_4 is really the triplet superconductor, it supports the isoelectronic analogies in Figure 2. Several recent findings for the inorganic systems may provide the following hypothesis 6 for molecular materials:

(H6) Carrier-doped molecule-based magnets with N-band degeneracy are interesting for ferromagnetism, magnetic conductivity, and triplet superconductivity.

Models for Charge-mediated Superconductors

The transition temperature for spin-mediated superconductors are estimated [5] to be 150 K even at the upper limit, since the largest effective exchange integrals are in the order 1000 cm^{-1}. Therefore, we may change the strategy to obtain the room-temperature superconductor. Several approaches [55] from the metal side in Figure 9(A) were performed. Probably, new approaches differ-

ent from them are necessary for the purpose. Here, let us consider the CT model from the insulator side in Figure 9(A) instead of charge fluctuation (exciton) model by Little [39].

ALKALI-, ALKALI-EARTH-, AND HYDROGEN-TERNARY COMPLEXES

The chemical synthesis of high-T_c superconductors without copper ion is one of a chemist's dreams. According to the working hypothesis H5, let us consider possible model systems in the intermediate region of metal–insulator transitions [56, 57]. Building blocks composed of hydrogen (H) and alkali earth atoms are regarded as the $1s$- and $2s$ orbital pairs having the isoelectronic configurations to those in Figure 2. The alkali (A)- and alkali-earth (B)-atom combinations also provide the same electronic configurations. These simple combinations are interesting because high pressures can be used to obtain solids. The ternary complexes, HBH, HBA, and ABA, are isoelectronic to the three-center four-electron systems depicted in Figures 3 and 4. On the other hand, HHH, HAH, AAH, and AAA components are formally isoelectronic to the one-extra hole-doped three-electron states of the three-center systems in Figure 4. The CT excitations (Δ) can be controlled so as to couple the Cooper ($2e$) pair in the intermediate regime of the metal–insulator transitions. Therefore, three-component solids expressed by $(H)_x(A)_y(B)_z$ would be particularly interesting from the CT mechanism of the high-T_c superconductivity in Figure 9(A). The partial addition of alkali and alkali-earth atoms into metallic hydrogens at high pressure would be one of the charge-fluctuation approach in Figure 9(A). On the other hand, let us consider a model system of the CT mechanism of the partial addition of hydrogen atoms into an insulator, e.g., which is consisted of LiH and BeH_2, at high pressure as shown in Figure 11.

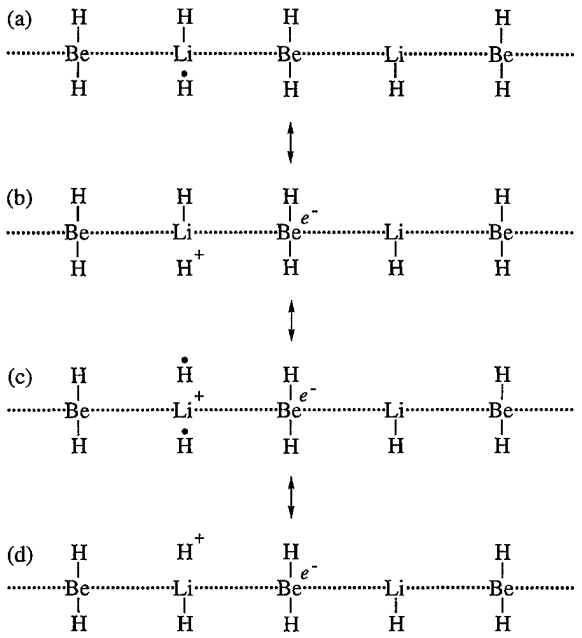


FIGURE 11. A model system of the CT mechanism of the partial addition of hydrogen atom into an insulator which consists of LiH and BeH2 and some possible transition states.

A FORMULATION OF OUR CT MODEL

To clarify the difference between Little [39] and our models, we describe here the model Hamiltonians explicitly. For the underdoped state, a model Hamiltonian is written as

$$H = H_e + H_{e-l} + H_l + H_{e-p} + H_{l-p}, \quad (15)$$

where

$$H_e = \sum_{r,s} \sum_{\sigma} t_{rs}^{\sigma} a_{r\sigma}^{+} a_{s\sigma} + \frac{1}{2} \sum_{r,s,t,u} \sum_{\sigma,\rho} V_{rstu}^{\sigma\rho\rho\sigma} a_{r\sigma}^{+} a_{s\rho}^{+} a_{t\rho} a_{u\sigma}, \quad (15a)$$

$$H_{e-l} = -\sum_{r,s,\sigma} \sum_{i,\rho} U_{rs;i}^{\sigma\rho} a_{r\sigma}^{+} a_{s\sigma} b_{i\rho}^{+} b_{i\rho} - \sum_{r,s,\sigma} \sum_{i,\rho} U_{rs;i}^{\sigma\rho} a_{r\sigma}^{+} a_{s\sigma} \tilde{b}_{i\rho}^{+} \tilde{b}_{i\rho}, \quad (15b)$$

$$H_l = \frac{1}{2} \sum_{i,j,\sigma,\rho} W_{ij}^{\sigma\rho} b_{i\sigma}^{+} b_{j\rho}^{+} b_{j\rho} b_{i\sigma} + \sum_{i,j,\sigma,\rho} W_{ij}^{\sigma\rho} b_{i\sigma}^{+} \tilde{b}_{j\rho}^{+} \tilde{b}_{j\rho} b_{i\sigma} + \frac{1}{2} \sum_{i,j,\sigma,\rho} W_{ij}^{\sigma\rho} \tilde{b}_{i\sigma}^{+} \tilde{b}_{j\rho}^{+} \tilde{b}_{j\rho} \tilde{b}_{i\sigma}, \quad (15c)$$

$$H_{e-p} = \sum_{r,s,\sigma} \sum_{p} g_{rs}^{\sigma}(p) a_{r\sigma}^{+} a_{s\sigma} (c_p - c_p^{+}), \quad (15d)$$

and

$$H_{l-p} = \sum_{i,\sigma} \sum_{p} G_i^{\sigma}(p) \tilde{b}_{i\sigma}^{+} b_{i\sigma} c_p^{+} + H.C. \quad (15e)$$

In Eq. (15a), the first and second terms are kinetic and electron interaction parts, respectively. H_{e-l} means electron–lattice (positive charge) interaction. H_l is the Coulomb interaction between lattices (positive charges). H_{e-p} and H_{l-p} indicate electron–phonon and lattice (positive charge)–phonon interactions, respectively. $a^+_{r\sigma}(a_{r\sigma})$ is the creation (annihilation) operator for an electron at the r-th site with σ spin. $b^+_{i\sigma}$ is the creation operator for a state (positive charge) at the i-th site, which is shown in Figure 11(b) and (d). $\tilde{b}^+_{i\sigma}$ is the creation operator for a state, which is different from the above state, as shown in Figure 11(c). The operators are satisfied with the anticommutation relation. c^+_p, which is a boson, is the phonon creation operator.

In particular, in the underdoped system as shown in Figure 12, the above Hamiltonian is approximated as

$$H = \sum_{r,s}\sum_{\sigma} T^{\sigma}_{rs} a^+_{r\sigma} a_{s\sigma} - V \sum_{r,s,t,u}\sum_{\sigma,\rho} a^+_{r\sigma} a^+_{s\rho} a_{t\rho} a_{u\sigma}, \tag{16}$$

where

$$T^{\sigma}_{rs} = t^{\sigma}_{rs} - \sum_{i,\rho} U^{\sigma\rho}_{rs;i}\left(\langle b^+_{i\rho} b_{i\rho}\rangle + \langle \tilde{b}^+_{i\rho}\tilde{b}_{i\rho}\rangle\right). \tag{17}$$

The second term in Eq. (15a) and H_l of Eq. (15c) are negligible. Therefore, the transition temperature for this approximation may be estimated as the following:

$$T_c = C\Delta, \tag{18}$$

where Δ is the CT excitation energy and C is a constant. We expect that T_C increases above 300 K (see Table II), because the CT excitation energy equals to about 1–3 eV.

On the other hand, for the overdoped state, another model Hamiltonian is considered:

$$H = H_e + H_h + H_{e-h} + H_d, \tag{19}$$

where

$$H_e = \sum_{r,s}\sum_{\sigma} t^{\sigma}_{rs} a^+_{r\sigma} a_{s\sigma} + \frac{1}{2}\sum_{rstu}\sum_{\sigma,\rho} V^{\sigma\rho\rho\sigma}_{rstu} a^+_{r\sigma} a^+_{s\rho} a_{t\rho} a_{u\sigma}, \tag{19a}$$

$$H_h = \sum_{i,j}\sum_{\sigma} h^{\sigma}_{ij} b^+_{i\sigma} b_{j\sigma} + \frac{1}{2}\sum_{i,j,k,l}\sum_{\sigma,\rho} W^{\sigma\rho\rho\sigma}_{ijkl} b^+_{i\sigma} b^+_{j\rho} b_{k\rho} b_{l\sigma}, \tag{19b}$$

$$H_{e-h} = -\sum_{r,s,i,j}\sum_{\sigma,\rho} g^{\sigma\rho\rho\sigma}_{rijs} a^+_{r\sigma} b^+_{i\rho} b_{j\rho} a_{s\sigma}, \tag{19c}$$

and

$$H_d = \sum_{r,i}\sum_{\sigma} D^{\sigma}_{ri}(a^+_{r\sigma} b^+_{i-\sigma} + a_{r\sigma} b_{i-\sigma}), \tag{19d}$$

where $a^+_{r\sigma}(a_{r\sigma})$ is the creation (annihilation) operator for an electron at the r-th site, the beryllium site, with σ spin. $b^+_{i\sigma}$ is the creation operator for a positive charge (hole) at the i-th site with σ spin, where the label i is the lithium site. The operators are satisfied with the anticommutation relation. The first and second terms in Eq. (19a) mean the kinetic and electron interaction parts, respectively. In Eq. (19b), the first and second are the kinetic and Coulomb interactions for the hole. H_{e-h} is the Coulomb interaction between the electron and hole. H_d indicates that an electron (negative charge) and a hole vanish. This means that the charged state becomes neutral as shown in Figure 11(a). This

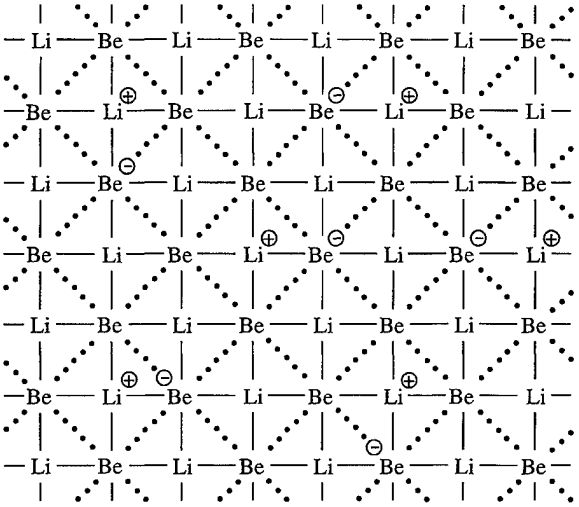


FIGURE 12. Underdoped model system constructed of alkali- and alkali-earth metals.

TABLE II
Three mediums and T_c for superconductors.

Medium	Maximum T_c (K)
Phonon	30
Spin	100
Charge	300

model will reduce to a metal model, which may be a metallic hydrogen model, at the limit of a large amount of a doping hydrogen atom.

DESIGN OF NONMETAL TERNARY SYSTEMS

The magnitude of the CT excitation energy (Δ_{pd}) is one of the possible parameters to elucidate possible organic systems which are isoelectronic to copper oxides. Previously [5], we already examined the CT excitation energies between nonmetal second and third periodic elements. The Δ value for the sulfur (S) and nitrogen (N) pair, namely, transition energy from SN to S^+N^-, is only 0.1 eV, and therefore the $(SN)_x$ polymer corresponds to the overdoped copper oxide [2], which is a normal metal without spin fluctuation. The normal BCS-type superconductivity is expected for the species, in accord with the experiment. On the other hand, the CT energies (Δ_{pp}) for the CS, SiS, PS, and CN pairs are 0.6–1.0 eV, compatible with the undoped copper oxide [58]. Therefore the 1D polymers (**I**), ladders (**II**), and sheet (**III**) consisted of these pairs in Figure 10 could be CT semiconductors/or insulators. The introduction of holes or electrons into these systems by doping may induce the metal–insulator transitions as in the case of copper oxides. For example, the synthesis of ternary solids, $(X)_x(C)_y(N)_z$, $(X)_x(Si)_y(S)_z$, and so on (X = halogen atoms, etc.) would be interesting targets since the solid-state synthesis under the high pressure was developed recently [59]. Then, we may have the following hypothesis H7:

(H7) Charge-transfer models for the high-T_c superconductivity in Figure 9(A) are conceivable in the ternary solids such as $(H)_x(A)_y(B)_z$ and $(X)_x(C)_y(N)_z$.

Models for Photo-induced Molecular Materials

PHOTOINDUCED ORGANIC AND ORGANOMETALLIC CT FERRO- AND FERRIMAGNETS

Photo-induced phase transitions have been considered as an advantage of molecule-based materials. From this viewpoint, the donor–acceptor complexes would be interesting targets for magnetic modification [16]. Possibilities of organic charge-transfer (CT) ferro- and/or ferrimagnets were examined based on the ab initio computations of donor–acceptor (D–A) complexes with radical groups [16]. The intra- and intermolecular effective exchange couplings between ion radicals were examined theoretically as illustrated in Figure 5 in [16]. Possibilities of photo-induced or photo-switched organic magnets were also proposed as illustrated in Figure 13 [16]. To this end, spin sources were introduced into compounds exhibit-

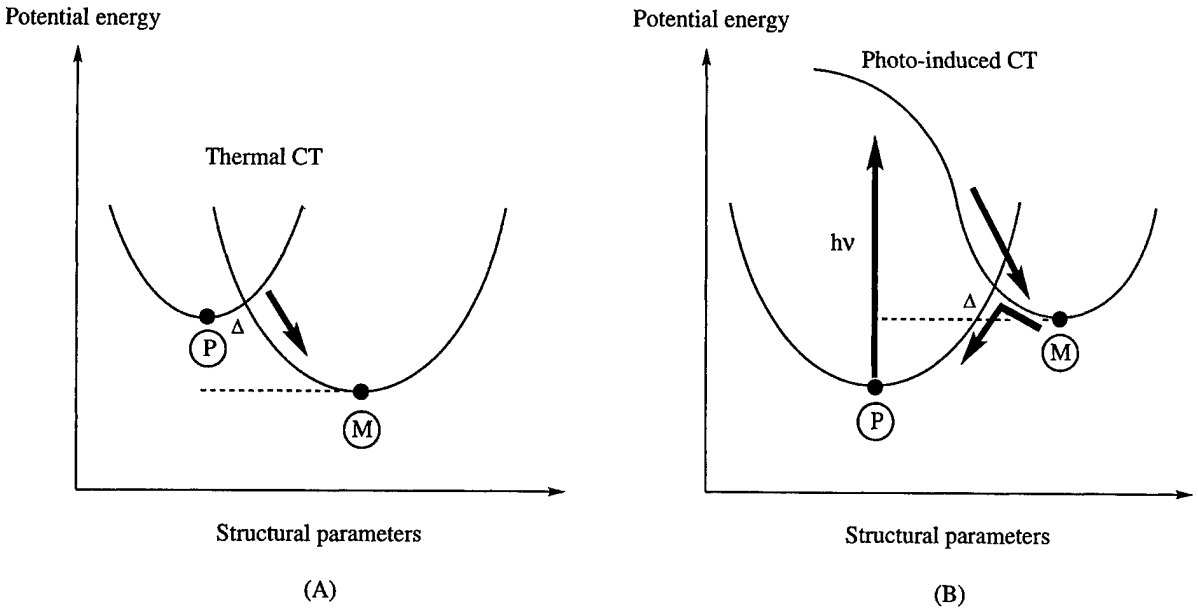


FIGURE 13. Photo-induced or photo-switched organic magnetic materials.

ing the neutral-ionic transitions by photoexcitation: The TTF–chloranil system having a radical substituent is illustrated as an example in [18]. Similarly, magnetic oligomers such as poly(phenylene vinylene) [60], etc., can be used as a donor or acceptor for photo-induced CT magnets [18].

Very recently, Hashimoto et al. [61] demonstrated that the magnetic properties of Prussian blue analogs (MXM', X = CN^{1-}) are controllable by the electrochemical, photochemical, and other techniques, namely, magnetic phase transitions were induced by the external perturbations. Their results lend support our previous attempt, e.g., see [15]. The success of the photo-induced magnetism [61] in the Prussian blue analogs may support possibilities of photo-induced organic magnets as well.

The key issues in these p–d, π–d, and π–R systems are small metal–ligand CT (MLCT) and metal–metal CT (MMCT) excitations in Figure 13. Thus, we may have the following hypothesis 8:

(H8) Photo-induced molecular magnetism and tunable magnets by external fields are expected in p–d, π–d, and π–R systems with small MLCT and MMCT energies in Figure 3.

POSSIBILITIES OF PHOTO-INDUCED SUPERCONDUCTORS

It is significant to consider possibilities of the photo-induced superconductors in an intermediate regime for the metal–insulator transition. Let us consider a model system as shown in Figure 14(a). The phase of the ground state, which is described as region I as shown in Figure 14(b), is an insulator. By irradiating the photon, electrons transit to the excited states which are in region II or III as shown in Figure 14(b). Region III, which is a continuous level region, becomes the metal phase, and, on the other hand, region II, which has a very small energy gap between levels, will be chaotic. We point out that analogously to the above discussions of superconductivity in the intermediate region of metal–insulator transitions the photo-induced superconductive phase may be found in region II but for solving the mechanism of the coupling Cooper pair. Thus, we may have the following hypothesis 9.

(H9) Photo-induced superconductivity by external fields are also expected in a semi-continuous level band in Figure 14.

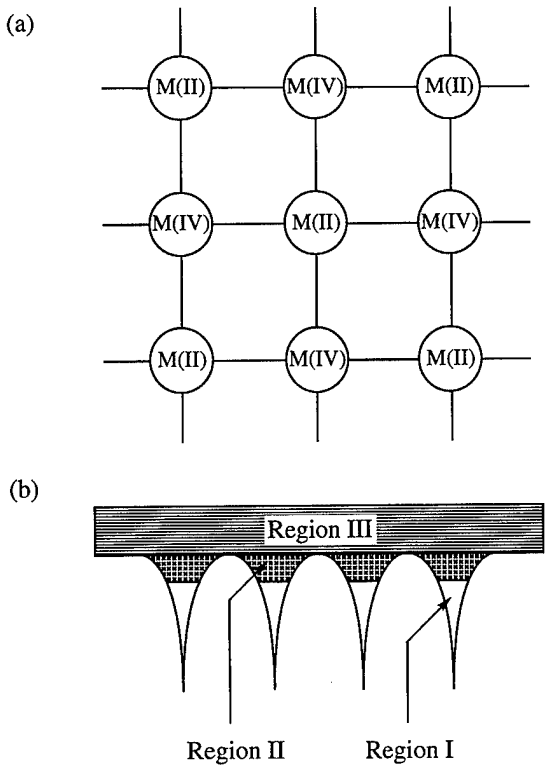


FIGURE 14. A model of photo-induced superconductor and three regions of excited levels: (a) a lattice model of an insulator; (b) energy levels. Discrete energy levels are in region I. Regions II and III describe semicontinuous and continuous levels, respectively.

Discussions and Concluding Remarks

The discovery of high-T_c superconductors [1] enable us to investigate possible organic and organometallic analogs to copper oxides. Previously [3–5], we thoroughly examined some possible model Hamiltonians for copper oxides. N-band (from two to six bands) models for copper oxides were examined by exact diagonalization of the cluster models. From these computational results, CT insulators with strong superexchange interactions were proposed as possible precursors for high-T_c superconductors and exotic molecular magnets. Some typical examples described by the p–d, π–d, and π–R Hamiltonians were also discussed from both charge and spin fluctuation mechanisms for the high-T_c superconductivity. Judging from the cutoff energies, the maximum T_c would be 30, 100, and 300 K for phonon-, spin-, and charge-mediated superconductors as shown in

Table II. During the past 7 years, we have discovered and investigated many experimental conclusions on the basis of the working hypotheses presented previously [3–5]. In this article, we have tried to explain these newly obtained experimental results from theoretical viewpoints. The J model [5] was extended so as to reproduce many experimental results [2]. As cited in many articles in the references, some theoretical computations were carried out to examine guiding principles for constructions of functional materials and active controls of various properties of molecule-based materials. Since theoretical predictions of crystal structures for complex systems discussed here were difficult tasks, numerical calculations of realistic models were performed assuming possible lattices in Figure 10. These computational results and available experiments cited in this article enable us to propose several working hypotheses (H1)–(H9). For the purpose, a theoretical formulation for the CT model was presented. More detailed theoretical formulations for these hypotheses will be given elsewhere.

References

1. J. G. Bednorz and K. A. Muller, Z. Phys. **64**, 189 (1986).
2. (a) A. P. Kampf, Phys. Rep. **249**, 219 (1994); (b) W. Brenig, Phys. Rep. **251**, 153 (1995), and references therein.
3. K. Yamaguchi and T. Fueno, Kagaku **41**, 372 (1986).
4. K. Yamaguchi, T. Takahara, T. Fueno, and K. Nasu, Jpn. J. Appl. Phys. **26**, L1362 (1987); *Ibid.* 26, L2037 (1987); *Ibid.* 27, L509 (1987).
5. K. Yamaguchi, Int. J. Quantum Chem. **37**, 167 (1990).
6. J. Hubbard, Proc. R. Soc. (Lond.) A **276**, 238 (1963).
7. (a) K. Yamaguchi, Y. Toyoda, and T. Fueno, Kagaku **41**, 585 (1986); (b) *Ibid.*, Syn. Met. **19**, 81, 87 (1987); (c) K. Yamaguchi, M. Nakano, and T. Fueno, Kagaku **42**, 583 (1987).
8. K. Yamaguchi, Y. Takahara, T. Fueno, K. Nakasuji, and I. Murata, J. J. Appl. Phys. **27**, L766 (1988).
9. K. Yamaguchi, M. Okumura, T. Fueno, and K. Nakasuji, Syn. Met. **41**, 3631 (1991).
10. K. Yamaguchi, M. Nakano, H. Namimoto, and T. Fueno, Jpn. J. Appl. Phys. **27**, L1835 (1988); *Ibid.*, 27, L479 (1989); *Ibid.*, 28, L672 (1989).
11. K. Yamaguchi, T. Fueno, M.-A. Ozaki, N. Ueyama, and A. Nakamura, Chem. Phys. Lett. **164**, 210 (1989); *Ibid.* **168**, 56 (1990).
12. M. Fujiwara, T. Matsushita, K. Yamaguchi, and T. Fueno, Syn. Met. **41–43**, 3267 (1991).
13. R. Vicente, J. Ribas, S. Alvarez, A. Segui, X. Solans, and M. Verdaguer, Inorg. Chem. **26**, 4004 (1987).
14. (a) K. Yamaguchi, Y. Takahara, T. Fueno, and K. Nasu, Physica C **153–155**, 1213 (1988); (b) M. Fujiwara, S. Takamizawa, W. Mori, and K. Yamaguchi, Mol. Cryst. Liq. Cryst. **279**, 1 (1996).
15. M. Okumura, W. Mori, and K. Yamaguchi, in *Computer Aided Innovation of New Materials II*, M. Doyama, J. Kihara, M. Tanaka, and R. Yamamoto, Eds. (Elsevier, Tokyo, 1993).
16. K. Yamaguchi, H. Namimoto, T. Fueno, T. Nogami, and Y. Shirota, Chem. Phys. Lett. **166**, 408 (1990).
17. (a) E. Fradkin, *Field Theories of Condensed Matter Systems* (Addison Wesley, Reading, MA, 1991); (b) P. A. Lee and N. Nagaosa, Phys. Rev. B **46**, 5621 (1992).
18. (a) K. Yamaguchi, in *Self-Consistent Field: Theory and Applications*, R. Carbo and M. Klobukowski, Eds. (Elsevier, Amsterdam, 1990), p. 727; (b) D. Gatteschi and K. Yamaguchi, in *Molecular Magnetism: From Molecular Assemblies to the Devices*, E. Coronado, Ed. (Kluwer, Dordrecht, The Netherlands, 1996), p. 561.
19. C. N. Yang, Rev. Mod. Phys. **34**, 694 (1962).
20. P. Wiegmann, in *Field Theory, Topology and Condensed Matter Physics*, H. B. Geyer, Ed. (Springer, New York, 1995), p. 177.
21. (a) G. E. Volovik and L. P. Gor'kov, Sov. Phys. JETP **61**, 843 (1985); (b) M. Ozaki, J. Math. Phys. **26**, 1514 (1985); (c) M. Sigrist and K. Ueda, Rev. Mod. Phys. **63**, 239 (1991).
22. S. Yamamoto, K. Yamaguchi, and K. Nasu, Phys. Rev. **42**, 266 (1990).
23. (a) S. C. Zhang and T. M. Rice, Phys. Rev. B **37**, 3759 (1989); (b) M. S. Hybertsen, E. B. Stechel, M. Schluter, and D. R. Jennison, Phys. Rev. B **41**, 11068 (1990).
24. (a) E. Dagotto, J. Riera, and D. Scalapino, Phys. Rev. B **45**, 5744 (1992); (b) T. M. Rice, S. Gopalan, and M. Sigrist, Europhys. Lett. **23**, 445 (1993); (c) E. Dagotto and T. M. Rice, Science **271**, 618 (1996).
25. (a) B. Sutherland, Phys. Rev. B **12**, 3745 (1975); (b) P. Schlottmann, Phys. Rev. **36**, 5177 (1987).
26. M. Ogata, M. U. Luchin, S. Sorella, and F. F. Assaad, Phys. Rev. Lett. **66**, 2388 (1991).
27. (a) L. B. Ioffe and A. I. Larkin, Phys. Rev. B **39**, 8988 (1989); (b) N. Nagaosa and P. A. Lee, Phys. Rev. Lett. **64**, 2450 (1990); (c) M. Grilli and G. Kotlia, Phys. Rev. Lett. **64**, 1170 (1990); (d) P. A. Lee and N. Nagaosa, Phys. Rev. B **46**, 5621 (1992).
28. (a) T. Tanamoto, H. Kohno, and H. Fukuyama, J. Phys. Soc. Jpn. **62**, 717 (1993); *Ibid.* **63**, 2739 (1994); (b) H. Yamagata and H. Fukuyama, J. Phys. Soc. Jpn. **65**, 2204 (1996).
29. (a) Y. Ohta, T. Shimozato, R. Eder, and S. Maekawa, Phys. Rev. Lett. **73**, 324 (1994); (b) T. Tohyama and S. Maekawa, J. Phys. Soc. Jpn. **65**, 1902 (1996).
30. H. Yokoyama and M. Ogata, J. Phys. Soc. Jpn. **65**, 3615 (1966).
31. (a) H. Yasuoka, T. Imai, and T. Shimizu, in *Strong Correlation and Superconductivity*, H. Fukuyama, S. Maekawa, and A. P. Malozeomoff, Eds. (Springer-Verlag, 1989); (b) M. H. Julien, P. Carretta, M. Horvatić, C. Berthier, P. Ségransan, A. Carrington, and D. Colson, Phys. Rev. Lett. **76**, 4238 (1996); (c) Y. Itoh, T. Machi, A. Fukuoka, K. Tanabe, and H. Yasuoka, J. Phys. Soc. Jpn. **65**, 3751 (1996).
32. N. Nagaosa and P. A. Lee, Phys. Rev. B **4**, 966 (1992).
33. S. C. Zhang, Int. J. Mod. Phys. B **6**, 25 (1992).
34. K. Yamaguchi, Y. Takahara, and T. Fueno, in *Applied Quantum Chemistry*, V. H. Smith et al., Eds. (Reidel, Tokyo, 1986), p. 157.

35. (a) H. Monien, D. Pines, and M. Takigawa, Phys. Rev. B **43**, 258 (1991); (b) H. Monien, P. Monthoux, and D. Pines, Phys. Rev. B **43**, 275 (1991).
36. (a) T. Moriya, Y. Takahashi, and K. Ueda, J. Phys. Soc. Jpn. **59**, 2905 (1990); (b) P. Monthoux and D. Pines, Phys. Rev. B **47**, 6069 (1993); (c) T. Moriya and K. Ueda, J. Phys. Soc. Jpn. **63**, 1871 (1994).
37. K. Magishi, Y. Kitaoka, G.-Q. Zheng, K. Asayama, T. Kondo, Y. Shimakawa, T. Manako, and Y. Kubo, Phys. Rev. B **54**, 1 (1996).
38. Y. Nagaoka, Phys. Rev. **147**, 392 (1966).
39. W. A. Little, Phys. Rev. A **134**, 1416 (1964).
40. (a) K. Yamaguchi, Chem. Phys. Lett. **30**, 288 (1975); (b) K. Yamaguchi, Y. Yoshioka, and T. Fueno, Chem. Phys. Lett. **46**, 111 (1976).
41. L. Salem, *Electrons in Chemical Reactions: First Principles* (Wiley, New York, 1982), Chap. 7.
42. P. W. Anderson, Science **235**, 1196 (1987).
43. N. Ueyama, T. Sugawara, A. Nakamura, K. Yamaguchi, and T. Fueno, Chem. Lett. 223 (1988).
44. K. Awaga, A. Yamaguchi, T. Okuno, T. Inabe, T. Nakamura, M. Matsumoto, and Y. Maruyama, J. Mater. Chem. **4**, 1377 (1994).
45. T. Enoki, Private communication.
46. K. Yamaguchi, S. Hayashi, M. Okumura, M. Nakano, and W. Mori, Chem. Phys. Lett. **226**, 372 (1994).
47. (a) L. M. Roth, Phys. Rev. **149**, 306 (1966); (b) S. Inagaki, J. Phys. Soc. Jpn.**39**, 596 (1975); (c) M. Cyrot and C. Lyon-Caen, J. Phys. **36**, 253 (1975).
48. K. Ito, Pure Appl. Chem. **50**, 1251 (1993), and references therein.
49. H. Iwamura, Pure Appl. Chem. **65**, 57 (1993), and references therein.
50. S. Yamanaka, T. Kawakami, M. Okumura, and K. Yamaguchi, Chem. Phys. Lett. **233**, 257 (1995).
51. M. Matsushita, T. Nakamura, T. Momose, T. Shida, Y. Teki, T. Kakui, T. Kinoshita, and K. Itoh, Bull. Chem. Soc. Jpn. **66**, 1333 (1993).
52. Y. Maeno, H. Hashimoto, K. Yoshida, S. Nishizaki, T. Fujita, J. G. Bednorz, and F. Lichtenberg, Nature **372**, 532 (1994).
53. T. M. Rice and M. Sigrist, J. Phys. Condens. Mat. **7**, L643 (1995).
54. T. Oguchi, Phys. Rev. **51**, 1385 (1995).
55. (a) R. E. Peierls, *Quantum Theory of Solids* (Oxford University Press, Oxford, 1955), Chap. 5; (b) L. Salem, Mol. Phys. **11**, 499 (1966); (c) J. Yoshida, K. Nishikawa, S. Aono, Prog. Theor. Phys. **50**, 830 (1973); (d) D. Davis, H. Gutfreund, and W. A. Little, Phys. Rev. B **13**, 4766 (1976); (e) M. Kimura, H. Kawabe, K. Nishikawa, and S. Aono, Bull. Chem. Soc. Jpn. **61**, 4245 (1988).
56. N. F. Mott, *Metal–Insulator Transitions* (Taylor Francis, London, 1990).
57. H. Nagao, H. Kawabe, and K. Yamaguchi, Phys. Rev. B, submitted.
58. D. J. Scalapino, Phys. Rep. **250**, 329 (1995), and references therein.
59. M. Takano, private communication.
60. H. Nishide, T. Kaneko, T. Nii, K. Katoh, E. Tsuchida, and K. Yamaguchi, J. Am. Chem. Soc. **117**, 9229 (1995).
61. (a) O. Sato, T. Iyoda, A. Fujishima, and K. Hashimoto, Science **271**, 49 (1996); (b) *Ibid.* **272**, 704 (1996).

Two Novel Applications of Shepard-Type Interpolation for Polyatomic Systems: Reduced Dimensionality HOCO and Full Dimensionality Ar-HCO

FEDOR N. DZEGILENKO, JIANXIN QI, JOEL M. BOWMAN

Department of Chemistry and Cherry L. Emerson Center for Scientific Computation, Emory University, Atlanta, Georgia 30322

Received 29 March 1997; revised 16 May 1997; accepted 22 May 1997

ABSTRACT: We present potential energy surfaces for two four-atom systems, HOCO and Ar-HCO. In the former system a previous, reduced dimensionality 2 degree-of-freedom model of the OH + CO → H + CO_2 reaction is extended by inclusion of the nonreactive CO stretch. In the latter system, extensive ab initio calculations are done for 19 HCO geometries and 120–150 Ar-HCO planar configurations, for a fixed HCO geometry. In both systems a Shepard-type representation of the global potential is presented in the former system in 3 degrees of freedom, and in the latter system in the full 6 degrees of freedom. © 1997 John Wiley & Sons, Inc. Int J Quant Chem 65: 965–973, 1997

Introduction

It is perhaps too obvious to state the importance of potential energy surfaces for dynamic studies of molecular interactions. Not only are potentials essential, but in many instances they are more important than the choice of dynamical approach, i.e., classical or quantum. During the past 20 years, and especially in the past decade, a number of ab initio potential energy surfaces have been developed for triatomic systems. It is fairly routine now to perform high-quality ab initio calculations at sufficiently many nuclear geometries, of the order of 1000 (corresponding to roughly 10 points per degree of freedom), to determine a global potential for triatomics. The potential is typically obtained by representing the full potential by a functional form with a number of linear and nonlinear parameters which are determined by a least-squares procedure.

This highly successful approach for triatomic systems has obvious and severe limitations for larger systems. For example, for a four-atom sys-

Correspondence to: J. M. Bowman.
Contract grant sponsor: Department of Energy.
Contract grant number: DEFG05-86ER 13568.

© 1997 John Wiley & Sons, Inc.
CCC 0020-7608 / 97 / 050965-09

tem the grid of geometries corresponding to the modest number of 10 points per degree of freedom would result in 10^6 geometries at which electronic energies would be calculated. This is clearly prohibitive for current ab initio methods. Even if one thinks about bypassing a potential function and is willing to attempt electronic structure calculations "on-the-fly," i.e., exactly at grid points where they are needed by the dynamics, the problems are at best very severe for classical dynamics and again prohibitive for quantum dynamics.

Thus, other strategies are needed, and have been developed, for polyatomic systems (where henceforth "polyatomic" refers to systems of four or more atoms). In this study we describe novel applications of a Shepard-type interpolation method to two quite different systems that illustrate different objectives. One is a reduced dimensionality model of the OH + CO → H + CO_2 reaction, and the other is a nonreactive four-atom system, Ar-HCO.

In this type of interpolation a data base of localized and widely distributed (in configuration space) representations of the potential energy surface is used to obtain the surface globally, by means of switching functions. This approach appears to have been used first to obtain a global representation of the HCO potential [1]. In that approach ab initio calculations of the electronic energy were done for 30 widely different geometries. Sufficient calculations were done at each geometry to obtain a local fourth-order force field, and the collection of force fields was then used to interpolate via switching functions to obtain the full potential globally. (That representation was then used to obtain an efficient three-dimensional spline representation of the suface.) More recently, this general approach was adopted for a study of the OHH_2 potential surface [2]. In this case, Hessians were obtained at several hundred geometries and used as a database to obtain a potential centered around the minimum energy path.

A potentially serious problem with a database of force fields in a Shepard-type interpolation is with extrapolation. That is, if one evaluates the potential at points in configuration space that are distant from any of the force fields, the result will be the extrapolated value of a force field, which may contain spurious oscillations or singularities. (By definition, force fields are local representations of the potential, and their behavior beyond their radius of convergence may be quite unphysical.) In the present work we will specifically address this problem and show how it can be overcome.

In the next section we describe the new application of Shepard-type interpolation to a reduced dimensionality model of the reaction OH + CO → H + CO_2. Following that we present a new 6 degree-of-freedom potential surface for Ar-HCO, based on high-quality ab initio electronic energies. A summary and conclusions are given at the end.

Reduced Dimensionality Potential for OH + CO → H + CO_2

The goal here is to construct a reduced dimensionality, 3 degree-of-freedom (3-DOF) potential energy surface for the OH + CO → H + CO_2 reaction suitable for subsequent quantum calculations. The coordinates we consider are the OH internuclear distance, r_{OH}, the CO internuclear distance, r_{CO}, and R, the distance between the centers of mass of the OH and CO fragments. All previous quantum calculations of the reaction dynamics separated the nonreactive CO bond from the dynamics [3–9], and our goal is to insert that mode back into the dynamics, although still within a reduced dimensionality framework. Our motivation for doing this is twofold. First, resonances (due to complex HOCO formation), which dominate the reaction dynamics, in which the nonreactive CO bond is temporarily excited were missing in the previous calculations. Second, in these calculations the description of the vibrational motion of CO_2 is highly approximate because, as is well known, the two CO bonds in CO_2 mix strongly to form normal modes of vibration.

The first quantum studies of this reaction (in which the nonreactive CO mode was uncoupled) were done using a 2-DOF model in which the potential was given in terms of the coordinates r_{OH} and R [3]. In that model the full 6-DOF potential [10] was minimized for fixed values of r_{OH} and R, and with r_{CO} adiabatically separated so that the zero-point motion corresponding to the nonreactive CO bond was added to the minimized 2-DOF potential.

Initially, our idea was to incorporate the CO bond by minimizing the same 6-DOF with respect to the 3 degrees of freedom, R, r_{OH}, and r_{CO}; however, we encountered isolated regions in configuration space where the minimization proce-

dure gave unstable results for extended values of r_{CO}. To overcome this problem, we adopted the following strategy. In regions in R and r_{OH} where the potential behaves smoothly with respect to the variation of the CO distance we minimized the 6-DOF potential for a given R and r_{OH}, and for r_{CO} = 2.2 a.u. (its value at the HOCO minimum). We then varied r_{CO} in the range 1.8–3.2 a.u and fit the resulting potential to a Morse functional form, i.e.,

$$V^i_{\text{morse}}(r_{CO}) = D_i(1. - e^{-\beta_i(r_{CO} - r^i_{CO,eq})})^2, \quad (1)$$

where i refers to a specific point with coordinates (R^i, r^i_{OH}). We did 106 such fits at points shown in Figure 1. These points are centered around the reaction path for OH + CO → H + CO_2, but avoid the regions were the potential did not give satisfactory results. Then we represented the CO-stretch at any value of R and r_{OH} by the following Shepard-like interpolation:

$$V_1(r_{CO}, r_{OH}, R) = \frac{\Sigma_i w_i(r_{OH}, R) V^{(i)}_{\text{morse}}(r_{CO})}{\Sigma_i w_i(r_{OH}, R)}, \quad (2)$$

where w_i is a weight given by

$$w_i = e^{-a_i S_i^2(r_{OH}, R)}, \quad (3)$$

with

$$S_i(R, r_{OH}) = \sqrt{(r_{OH} - r^i_{OH})^2 + (R - R^i)^2}. \quad (4)$$

We varied the range parameter a_i over a wide range [subject to the condition that Eq. (2) reduces to within a few percent of $V^i_{\text{morse}}(r_{CO})$ at the ith point], and found that our fit is insensitive to its exact value. This robustness of the interpolation is due at least in part to the fact that the Morse potentials do not vary greatly over the grid of points in R-r_{OH} space.

We should note that our objective is not to reproduce the potential at selected points. Clearly, by using a Morse to fit the potential and then using the Shepard-like switching among the Morse fits, the final result is in a sense twice removed from the original data. In general, the errors in the Morse fits are much greater than the errors introduced by switching method. With this in mind we examined the precision of Eq. (2) by comparing it to the actual potential in the CO stretch at a value of R and r_{OH} not among the fits. The result is shown in Figure 2 for one example. As seen, the interpolation does provide a realistic representation of the CO stretch potential.

The final 3-DOF potential was then constructed by combining the previous 2-DOF potential [3] with $V_1(r_{CO}, r_{OH}, R)$. However, since that 2-DOF potential contained the local zero-point energy of the CO, we first had to subtract that energy using our $V_1(r_{CO}, r_{OH}, R)$ potential, and then the new 3-DOF potential is given by

$$V(r_{CO}, r_{OH}, R) = V'_{2d}(r_{OH}, R) + V_1(r_{CO}, r_{OH}, R), \quad (5)$$

where V'_{2d} is the previous 2-DOF-dimensional potential of Schatz and Dyck [3] minus the local CO

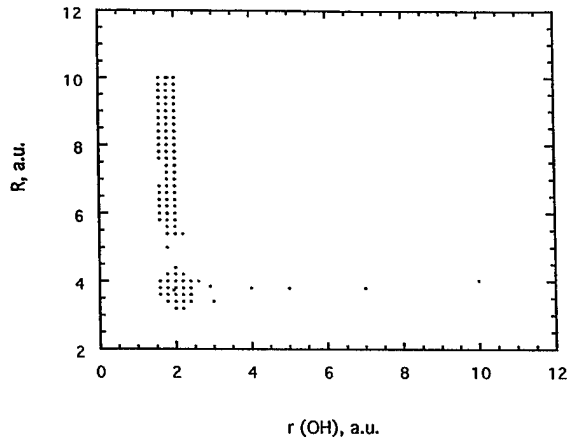


FIGURE 1. Points where the CO stretch potential was fit to a Morse function.

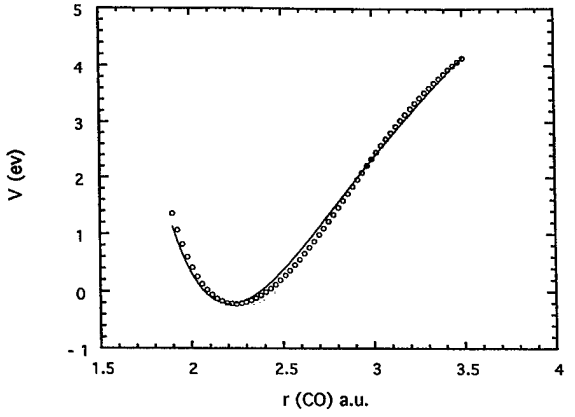


FIGURE 2. Comparison of the actual CO potential (circles) at r_{OH} = 2.0 a.u. and R = 4.8 a.u. and the CO potential from the Shepard interpolation.

zero-point energy. Figure 3 shows a 2-DOF contour plot of the new surface at $r_{CO} = 2.5$ a.u. The potential is smooth and shows a single well corresponding to the cis-HOCO minimum as well as a small barrier in r_{OH} coordinate which is consistent with the 2-DOF surface of Schatz and Dyck. Figure 4 shows a 2-DOF contour plot at fixed $R = 3.73$ a.u (the value of R at the cis-HOCO minimum). The minimum around $r_{CO} = 2.2$ a.u. is very distinct and corresponds to the stable cis-HOCO configuration.

Finally, we note that the zero-point energy of the CO vibration extracted from the 2-DOF effective potential of Schatz and Dyck [3] is significantly lower than the experimental results for the asymptotic OH + CO channel, roughly 900 cm^{-1} compared to 1100 cm^{-1} experimentally. We have calculated the zero-point energy of CO vibration using the new 3-DOF potential of Eq. (5), and it is in within 50 cm^{-1} of the experimental value.

The present application of a Shepard-like interpolation to generate a 3-DOF potential from a 2-DOF one has potentially wide applicability to polyatomic systems in which there are many nonreactive degrees of freedom. If the potential in these degrees of freedom can be represented as sums of functions such as Morse functions, then perhaps a relatively small number of determinations of these functions would suffice to obtain a realistic global representation based on the Shepard-like interpolation in these degrees of freedom.

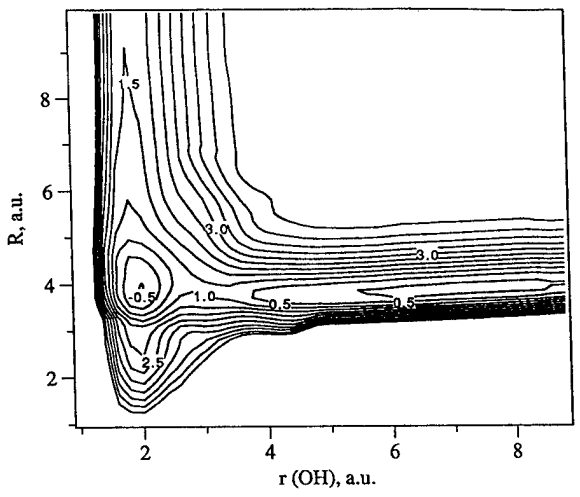


FIGURE 3. Equipotential contour plot in R and r_{OH} for $r_{CO} = 2.5$ a.u. Contour values are in electron volts.

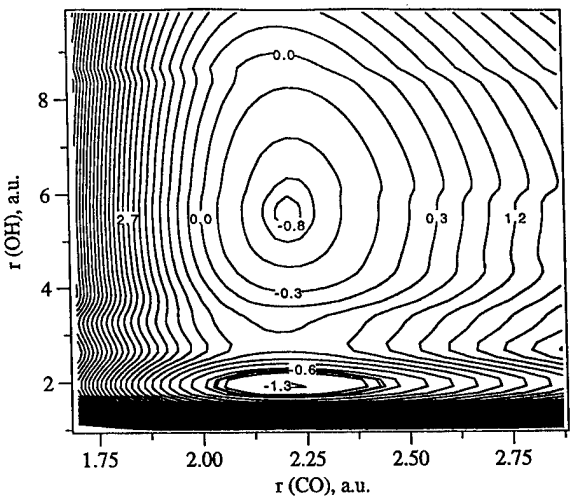


FIGURE 4. Equipotential contour plot of the new potential for $R = 3.73$ a.u. Contour values are in electron volts.

Next we consider another, quite different application of a Shepard-like interpolation to the Ar-HCO system in all 6 degrees of freedom.

Six Degree-of-Freedom Interaction Potential Surface for Ar-HCO

As noted in the Introduction it is impossible to do ab initio calculations in a straightforward six-dimensional scan for a four-atom potential surface, so some other strategy is needed to construct a reasonable potential surface. In the present case, the system of interest is Ar-HCO, and the potential will be used in scattering study of collisional vibration energy transfer and collision-induced dissociation/recombination of HCO. Thus, the potential surface needs to include a fairly wide variation in the HCO geometry. At the very least, it must sample the geometry around the HCO minimum, and the most important energetic pathway to dissociation. In addition, since the interaction potential is of the van der Waals type, many geometries of the Ar atom relative to a given HCO geometry must be considered.

With the above requirements in mind, we adopted the following strategy to construct a reasonable six degree-of-freedom potential. For a given HCO geometry we calculated the electronic interaction energy for 120–150 Ar geometries in the HCO plane. Those energies were then fit to a

functional form, and then the various fits, corresponding to 19 HCO geometries, were used in a Shepard-type interpolation to obtain a representation for the global potential. As above, the objective is not to reproduce the calculated ab initio points. The Shepard-type interpolation is done on the fits to points, and in general the errors in these fits are much greater than the errors introduced by the interpolation of the fits.

Ab initio Calculations

The basis set and the level of correlation and tests of both have been described in detail in Ref. [11]. Briefly, single reference, configuration interaction (CISD) calculations, using double-zeta and triple-zeta basis sets, and counterpoise correction were done using the code MOLPRO [12]. The coordinates we used are body fixed, spherical coordinates with the origin at the center of mass of CO, with the z axis along CO, and H in the xz plane, as shown in Figure 5. The CO distance is denoted by r, the position of H to the center of mass of CO is (R, γ), and in HCO plane the position of Ar is (Q, θ).

For each HCO geometry, θ varied from 0 to 180° in equal intervals of 18° for $\phi = 0$ and also for $\phi = 180°$. For each θ, 6 to 7 Q's were selected according to the shape of the potential cuts. Thus, ab initio calculations were done at between 120 and 150 points per HCO geometry. The 19 HCO geometries considered are given in Table I.

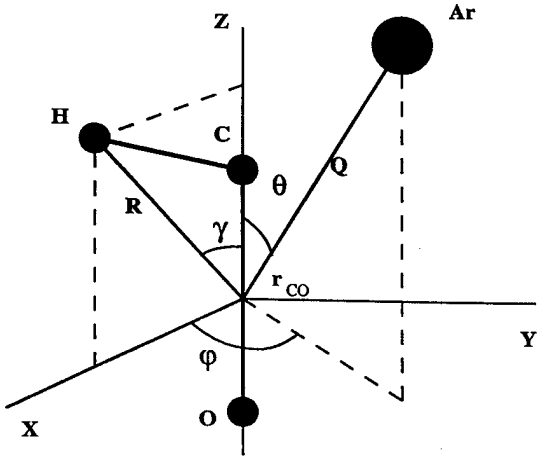


FIGURE 5. Coordinate system for Ar-HCO.

TABLE I
HCO geometries chosen for the ab initio calculation.

Geom. No.	R (bohr)	r (bohr)	γ (degree)
1	3.043	2.288	34.773
2	4.213	2.153	47.261
3	5.669	2.288	34.773
4	3.043	2.288	64.773
5	3.043	2.288	49.773
6	3.043	2.288	19.773
7	3.043	2.488	34.773
8	3.043	2.088	34.773
9	3.043	3.088	34.773
10	7.559	2.143	34.773
11	4.213	2.153	57.261
12	4.213	2.153	37.261
13	4.213	2.303	47.261
14	4.213	2.003	47.261
15	3.590	2.173	40.000
16	3.590	2.173	55.000
17	3.590	2.173	25.000
18	3.590	2.373	40.000
19	3.590	1.973	40.000

In order to make some global comparisons between the ab initio electronic energies and the fits to them, described below, we fit several sets of Ar-HCO energies very precisely by a somewhat complex functional form described earlier [11]. Polar contour plots of the interaction potential (based on these precise fits) are given in Figures 6–8 for the HCO minimum (geometry 1), the H—CO transition state (geometry 2), and nearly dissociated H—CO (geometry 3), respectively. As seen, there is a van der Waals minimum at a cis T-shaped geometry that is nearly independent of the H atom position.

Fits of the Planar Ar-HCO Interaction Potentials

A major factor in considering a functional form to fit the ab initio energies for a fixed HCO geometry is the subsequent use of the fits in a Shepard-type representation of the global surface. As mentioned in the Introduction, a danger in using this type of representation is possible unphysical behavior of the potential in regions away from any of the fits. Thus, it is important to choose a physically

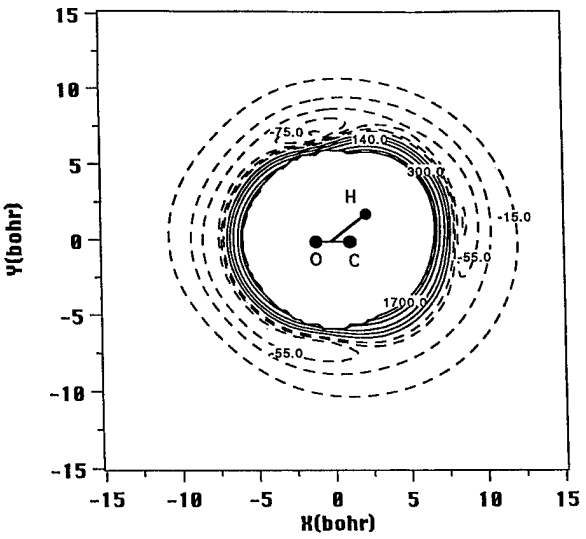


FIGURE 6. Equipotential polar contour plot of ab initio interaction potential of Ar with equilibrium HCO. Contour values are in cm^{-1}.

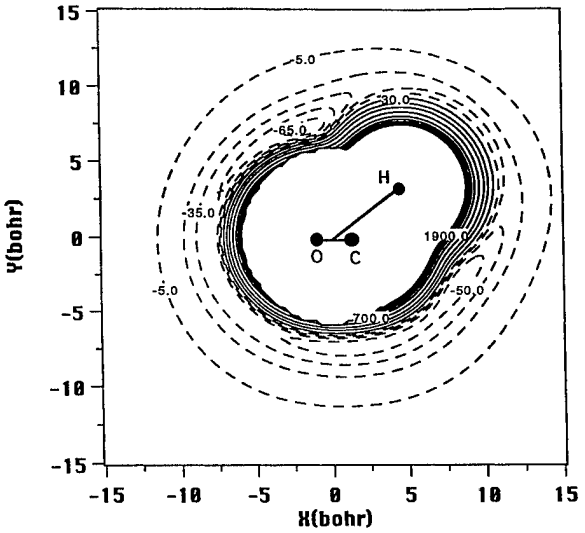


FIGURE 8. Same as Fig. 6, but for Ar with HCO at a nearly dissociated geometry.

reasonable functional form for the fits, even if this entails some sacrifice in the precision of the fit. With this in mind we chose to represent the Ar-HCO interaction potential as the following sum-of-pairs form for a fixed HCO geometry, (R_n, r_n, γ_n) and for planar Ar-HCO configurations:

$$V_n(r_{\text{Ar-H}}, r_{\text{Ar-C}}, r_{\text{Ar-O}}) = \sum_{X=H,C,O} V^{(n)}_{\text{Ar-X}}(R_{\text{Ar-X}}), \quad (6)$$

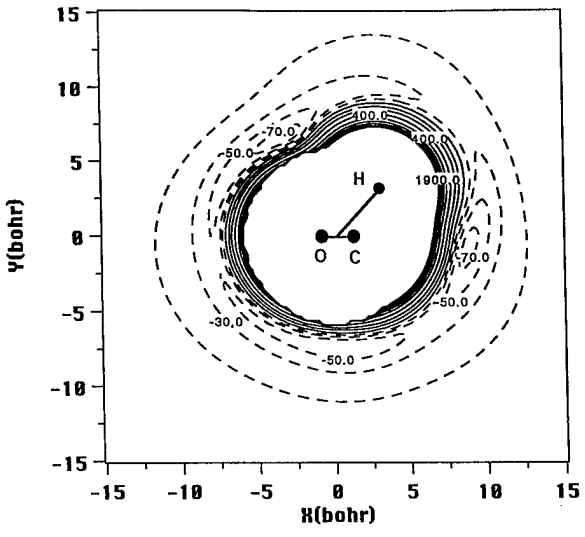


FIGURE 7. Same as Fig. 6, but for with HCO at transition state geometry.

where

$$V^{(n)}_{\text{Ar-X}}(R_{\text{Ar-X}}) = C^{(n)}_{1,X}\exp(-C^{(n)}_{2,X}R_{\text{Ar-X}}) - \frac{C^{(n)}_{3,X}\left[1 - \exp - (R_{\text{Ar-X}}/2)^8\right]}{R^6_{\text{Ar-X}}}. \quad (7)$$

The superscript corresponds to the nth HCO geometry. As seen, there are two linear and one nonlinear parameters $C^{(n)}_{1,X}, C^{(n)}_{2,X}, C^{(n)}_{3,X}$ per two-body potential for a total of nine parameters. They were determined by nonlinear least square fitting to the ab initio energies separately for each HCO geomtery.

The average fit error ranges from 60 to 150 cm^{-1}, depending on the HCO geometry, and over a range of interaction energies that varies from roughly -100 to 7000 cm^{-1}. The fitting error scales roughly with the value of the interaction energy. Polar contour plots of the fitted interaction potentials for three HCO geometries, corresponding to the ab initio ones shown in Figures 6–8, are shown in Figures 9–11. Comparing these, one sees that the fitted potentials are reasonable representations of the ab initio ones. Further examination of the fits are shown in Figure 12 for the cis planar Ar-HCO geometry, and for an out-of-plane configuration, for HCO at its equilibrium geometry. As seen, the fit for the in-plane geometry is quite good, and the one for the out-of-plane one is not as

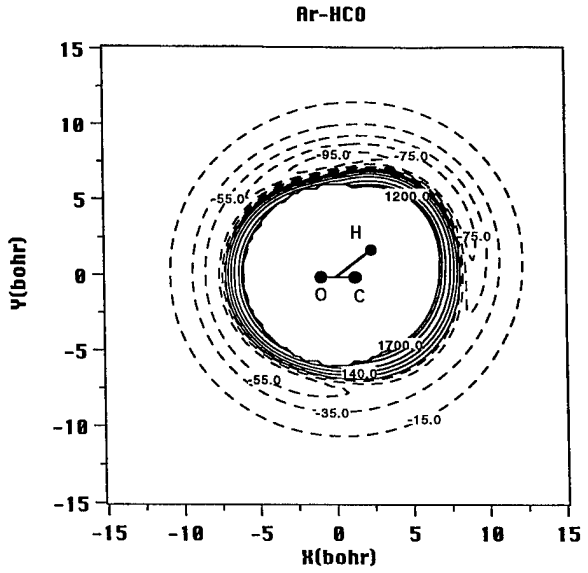


FIGURE 9. Same as Fig. 6 but for the fitted sum-of-pairs potential.

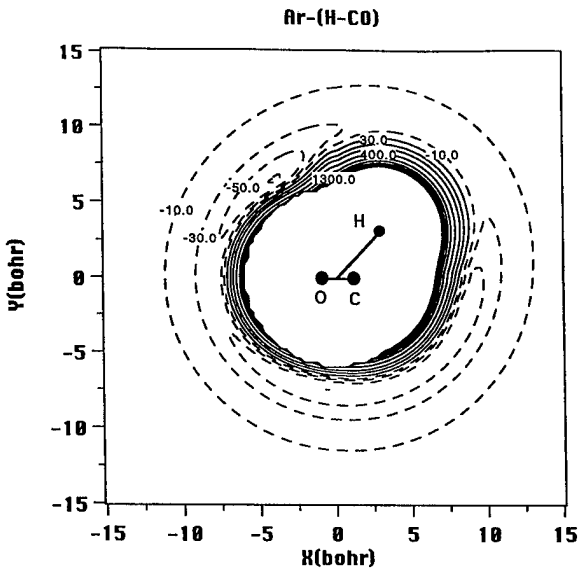


FIGURE 10. Same as Fig. 7 but for the fitted sum-of-pairs potential.

good. This is not surprising given that the fit was made to the ab initio energies only for the in-plane Ar-HCO configuration.

Global Surface

The global 6-DOF potential surface is given by the following Shepard-type representation:

$$V(R_{\text{Ar-H}}, R_{\text{Ar-C}}, R_{\text{Ar-O}}, R, r, \gamma) = \sum_n w_n V_n(R_{\text{Ar-H}}, R_{\text{Ar-C}}, R_{\text{Ar-O}}) \Big/ \sum_n w_n, \quad (8)$$

where the weight function is, as above, a simple Gaussian

$$w_n = \exp\left[-\alpha_1(R - R_n)^2 - \alpha_2(r - r_n)^2 - \alpha_3(\gamma - \gamma_n)^2\right]. \quad (9)$$

The three range parameters were chosen so that the global potential is smooth and close to the fit when the HCO geometry is close to nth geometry. After some trial and error we determined that the values, $\alpha_1 = 2.0$ bohrs^{-2}, $\alpha_2 = 25.0$ bohrs^{-2}, $\alpha_3 = 17.5$ rads^{-2}, satisfied the above criteria well. (These orders of magnitude of the range parameters were mainly determined by the spacing in fits in the corresponding coordinates.)

In order to test the global potential surface, a number of comparisons of the surface were made with additional ab initio calculations. In Figure 13 we compare the global surface with ab initio energies for two planar Ar-HCO configurations, as R is varied over a large range, with r and γ at their values for HCO at equilibrium. As seen, the agreement is reasonable and physically correct, i.e., the

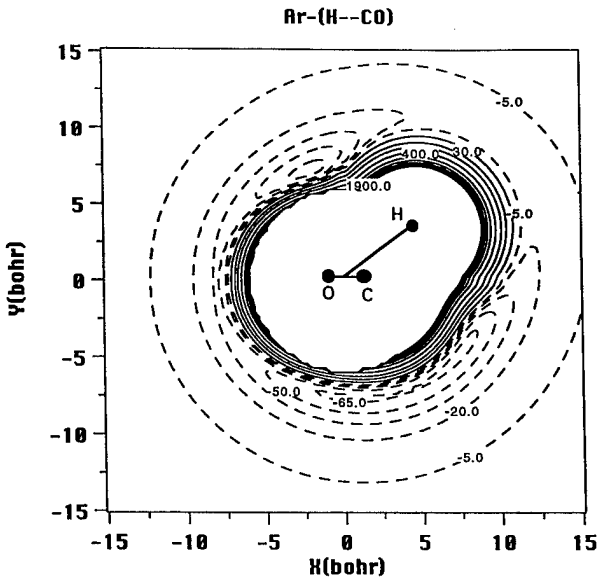


FIGURE 11. Same as Fig. 8 but for the fitted sum-of-pairs potential.

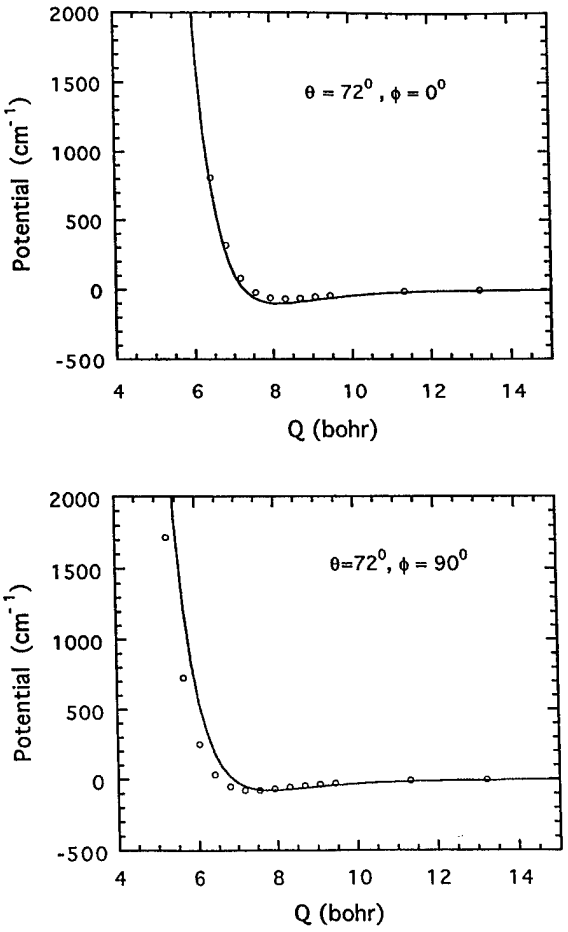


FIGURE 12. Comparison of the interpolated potential (curve) with ab initio (circles) energies as R is varied for $r_{CO} = 2.15$ bohrs and $\gamma = 40°$, for the two indicated Ar geometries.

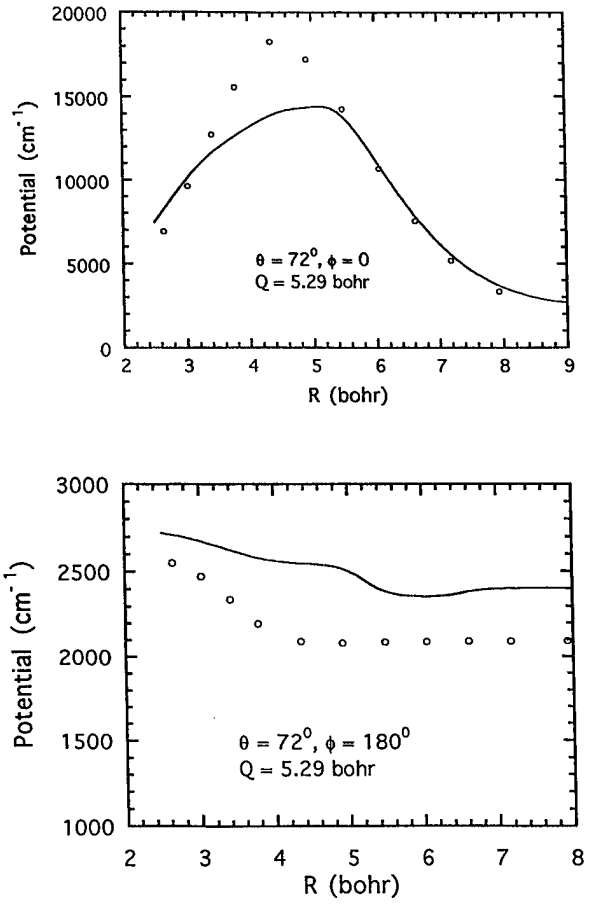


FIGURE 13. Comparison of the interpolated potential (curve) with ab initio (circles) energies for HCO at equilibrium for in-plane and out-of-plane Ar-HCO geometries. The in-plane interpolated potential is the sum-of-two-body fit to the ab initio energies.

interaction is more repulsive in the cis Ar-HCO geometry ($\phi = 0$) than in the trans one ($\phi = 180°$). Another test is for the out-of-plane interaction. This is shown in Figure 14 for HCO at equilibrium, and two values of θ for $Q = 5.67$ a.u. As seen, the behavior of the global surface is quite reasonable.

This potential surface is available upon request to JMB.

Summary and Conclusions

Shepard-type interpolation has been used in two four-atom systems. In the first, a 3 degree-of-freedom reduced dimensionality potential was described for the OH + CO → H + CO_2 reaction. The surface was built up from an existing 2 degree-of-freedom potential by the addition of the nonreactive CO stretch. We minimized the 6 degree-of-freedom potential for fixed values of r_{OH} and R and then fit the CO dependence of the potential to a Morse function. The CO dependence of the potential at an arbitrary value of R and r_{OH} was determined by Shepard interpolation. This surface is currently being used to explore the role of this stretch in HOCO resonances [13].

The second four-atom system considered was Ar-HCO. In this application, high-quality ab initio electronic energies were calculated for 19 HCO geometries and 120–150 planar Ar-HCO geometries for each fixed HCO geometry. The energies were fit using a physically motivated sum of two-body potentials. The global surface was given again by a Shepard interpolation in the HCO coordi-

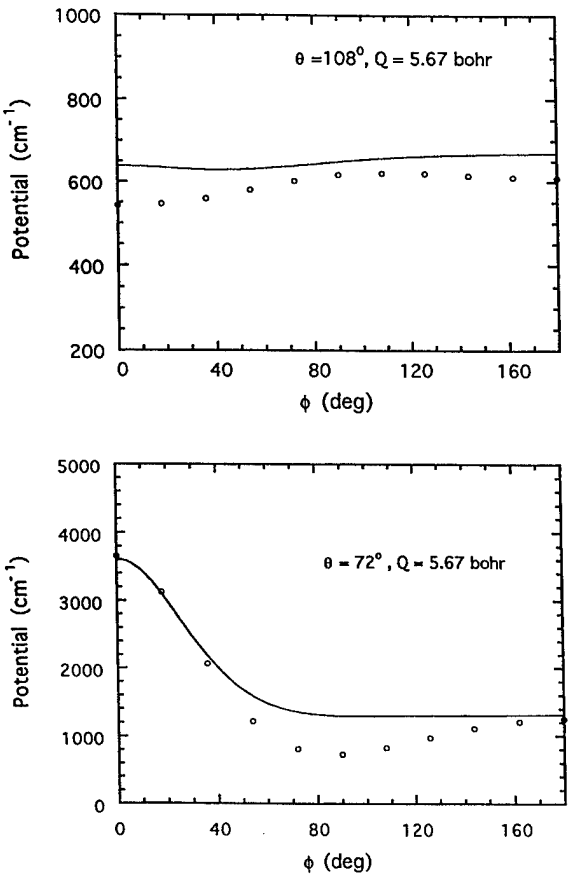


FIGURE 14. Comparison of the interpolated potential (curve) with ab initio (circles) energies for HCO at equilibrium as a function of ϕ, and for the two Ar-HCO geometries indicated.

nates. Several tests of the interpolated surface were presented and demonstrated that the global surface is a good representation of the ab initio energies. This potential is currently being used in quantum calculations of energy transfer, dissociation, and recombination in Ar-HCO collisions [14].

In both examples above, we chose physically motivated representations of fits to the energetics, for HOCO to an existing 6 degree-of-freedom potential, and for Ar-HCO to ab initio calculations. These are in general better behaved than fits that have been used in previous Shepard-type interpolations; however, at the expense of not giving very precise fits to the original potential points.

ACKNOWLEDGMENTS

We thank the Department of Energy (DEFG05-86ER13568) for support of this research.

References

1. J. M. Bowman, J. S. Bittman, and L. B. Harding, J. Chem. Phys. **85**, 911 (1986).
2. (a) J. Ischtwan and M. A. Collins, J. Chem. Phys. **100**, 8080 (1994); (b) M. J. T. Jordan, K. C. Thompson and M. A. Collins, J. Chem. Phys. **102**, 5647 (1995); (c) K. C. Thompson and M. A. Collins, J. Chem. Soc. Farad. Trans. **93**, 871 (1997).
3. G. C. Schatz and J. Dyck, Chem. Phys. Lett. **188**, 11 (1992).
4. D. C. Clary and G. C. Schatz, J. Chem. Phys. **99**, 4578 (1993).
5. M. I. Hernandez and D. C. Clary, J. Chem. Phys. **101**, 2779 (1994).
6. E. M. Goldfield, S. K. Gray, and G. C. Schatz, J. Chem. Phys. **102**, 8807 (1995).
7. D. H. Zhang and J. H. Zhang, J. Chem. Phys. **103**, 6512 (1995).
8. F. N. Dzegilenko and J. M. Bowman, J. Chem. Phys. **105**, 2280 (1996).
9. J. M. Bowman and A. Metropoulos, J. Chem. Soc. Farad. Trans. **93**, 815 (1997).
10. G. C. Schatz, M. S. Fitzcharles, and L. B. Harding, Faraday Discuss. Chem. Soc. **84**, 359 (1987). K. Kudla, G. C. Schatz, and A. F. Wagner, J. Chem. Phys. **95**, 1635 (1991).
11. J. Qi, M. Dyksterhouse, and J. M. Bowman, in *Highly Excited States: Relaxation, Reactions, and Structure*, A. S. Mullin and G. C. Schatz, Eds. (ACS, Washington D.C., 1997).
12. MOLPRO is a package of ab initio programs written by H.-J. Werner and P. J. Knowles, with contributions from J. Almlof, R. D. Amos, M. J. O. Deegan, S. T. Elbert, C. Hampel, W. Meyer, K. Peterson, R. Pitzer, A. J. Stone, and P. R. Taylor.
13. F. Dzegilenko and J. M. Bowman, work in progress.
14. J. Qi and J. M. Bowman, work in progress.

Density Functional Cluster Description of Ionic Materials: Improved Boundary Conditions for MgO Clusters with the Help of Cation Model Potentials

ILYA V. YUDANOV,* VLADIMIR A. NASLUZOV,†
KONSTANTIN M. NEYMAN, NOTKER RÖSCH
Lehrstuhl für Theoretische Chemie, Technische Universität München, 85747 Garching, Germany

Received 29 March 1997; revised 6 June 1997; accepted 19 June 1997

ABSTRACT: Ionic materials can be conveniently described by quantum mechanical cluster models. In these models the electrostatic field of the crystal surrounding is often taken into account by embedding the cluster in an array of point charges (PCs). However, anions at the cluster boundary can be strongly polarized by neighboring positive PCs. These artifacts can be significantly reduced if a model potential description is employed for the nearest-neighbor cations of the surrounding. We have implemented a scheme of total ion model potentials (TIMP) in the density functional code LCGTO-DF. In the present work we compare a number of electronic properties of MgO(001) models, like core-level splittings, electron affinity, and electrostatic potential, computed with the help of TIMP embedding to results obtained for the same clusters surrounded by PCs only. The cluster models range from MgO_5^{8-} to $Mg_{25}O_{25}$. Adsorption of a CO molecule on TIMP embedded cluster models of a regular surface site and the three-coordinated corner Mg^{2+} site is also considered. © 1997 John Wiley & Sons, Inc. Int J Quant Chem **65**: 975–986, 1997

* Permanent address: Boreskov Institute of Catalysis, 630090 Novosibirsk, Russia.
† Permanent address: Institute of Chemistry of Natural Organic Materials, 660049 Krasnoyarsk, Russia.
Correspondence to: N. Rösch.
Contract grant sponsor: Deutsche Forschungsgemeinschaft.
Contract grant sponsor: European Community.
Contract grant number: INTAS Project 93-1876-ext.
Contract grant sponsor: Bayerischer Forschungsverbund Katalyse (FORKAT).
Contract grant sponsor: Fonds der Chemischen Industrie.

© 1997 John Wiley & Sons, Inc.
CCC 0020-7608 / 97 / 050975-12

Introduction

Chemical substances in the solid state can often be efficiently described by quantum mechanical cluster models. Systems with strongly ionic bonds, like alkali halides and alkaline-earth oxides, the properties of which are dominated by long-range Coulomb interaction, are also favorably studied by cluster models. A simple but widely used method to account for electrostatic effects of the crystal surrounding is to embed a model cluster in an array of point charges (PCs). This approach also allows one to reproduce the electrostatic potential outside the cluster in an accurate, yet economic fashion. This is of particular importance for studies of adsorption complexes on strongly ionic substrates which are commonly formed mainly due to electrostatic interactions. However, a disadvantage of the point charge embedding is that PCs on the cluster boundaries can significantly distort the electron density of ions at the cluster edges. Therefore, the accuracy of the calculations depends on the distance between the "chemically interesting" central region of the cluster and its boundaries. In order to shift the boundaries far enough one may be forced to employ extended, i.e., rather expensive cluster models. Clearly, anions with their diffuse and easily polarizable electronic shells will be distorted much stronger by neighboring positive PCs at the cluster boundary than the more compact and less polarizable cations by negative PC neighbors. Thus, evaluation and subsequent rectification of spurious anion-PC effects on calculated observables represent key problems in cluster modeling of ionic metal oxides.

The outlined artifacts can be diminished by substituting model potential (or pseudopotential) cations for positive PCs closest to cluster anions. In this way, it is possible to restore the repulsive contribution of electron shells of the anions and cations which is missed by an embedding in a simple array of PCs. Less efficient from the computational viewpoint is the "brute force" alternative whereby all positive PCs near the cluster borders are replaced by all-electron cations.

The first applications of pseudopotentials in cluster models [1, 2] were devoted to the description of impurities in alkali halide crystals where Hartree–Fock (HF) based model potentials by Huzinaga et al. [3] and complete-cation normconserving pseudopotentials [4] were used. A similar technique was found valuable to describe bulk properties of alkaline-earth oxides [5, 6]. Recently, the general procedure on how to perform calculations on embedded clusters under the assumption of a "frozen" environment and the orthogonality requirements for the wave function of the cluster and the environment have been discussed in detail [7, 8].

CO molecules adsorbed on MgO have frequently been considered as a prototype system for representing metal oxide surface complexes [9]. The properties of CO/MgO cluster models embedded in an array of PCs have been studied extensively, at both the HF and post-HF levels [10, 11] as well as by density functional (DF) methods [12–14]. There is now general agreement that CO binds to the MgO surface mainly due to electrostatic interaction. In the case of PC embedding, the calculated MgO–CO binding energy varies notably with the size of the model cluster [14]. Also, the electrostatic potential above in MgO surface in the region of the adsorbate has been found to depend strongly on shape and size of the model cluster; this effect was traced to the polarization of anions at the cluster borders [15]. Recently published cluster model investigations of MgO based on ab initio model potentials are free of this deficiency [8, 16, 17]. However, no such model potential study has been reported so far within the framework of DF methods.

The present work describes an implementation of the pseudopotential (PP) technique in the LCGTO-DF package (next section). This method has been applied to improve cluster models of MgO by using total ion model potentials (TIMP) to substitute positive PCs at the cluster boundaries. The models and calculational details are outlined in the third section. The present study aims at testing the TIMP technique within a DF implementation rather than at carrying out a comprehensive investigation on a physical or chemical problem of an ionic material. Therefore, MgO has been chosen as a substrate which has been well studied theoretically and experimentally. The calculational results presented demonstrate how significantly features of the cluster models can change due to TIMP improved boundary conditions. One-electron properties of model clusters and the electrostatic potential near an ideal MgO(001) surface have been calculated with the help of TIMP and PC embedded models. Adsorption of CO molecules

on Mg^{2+} cations on the regular MgO(001) surface and on three-coordinated defect sites has also been considered; Results of DF TIMP calculations will be compared to the corresponding ab initio data [17].

OUTLINE OF THE COMPUTATIONAL TECHNIQUE: TOTAL ION MODEL POTENTIALS

TIMP embedding aims at overcoming the limitations of a simple PC embedding scheme for cluster models of ionic substrates by approximately accounting for orthogonality effects of cluster electronic states with respect to states of ions in the environment. PC embedding accounts only for the electrostatic field of ions which, at large distances, can be to good accuracy treated as the field of point charges. However, if one does not take the finite size of the cations into account, the electron density of the cluster will spread to neighboring positive point charges. The "frozen" electron density of these cations is included in the TIMP description, its Pauli repulsion counteracts the attractive potential of the cation charge within the effective ionic radius. For the practical realization of TIMPs used here, the PP approach of replacing the core electrons in calculations involving heavier atoms is modified. All electrons of the model ions are included in the pseudopotential and no basis functions are placed on these centers. In the following, a brief review of angular specified normconserving PPs [4, 18, 19] used in this work is given to introduce their application for constructing TIMPs.

In the all-electron linear combination of Gaussian-type orbitals DF (LCGTO-DF) method [20] the nonrelativistic Kohn–Sham equation can be written as

$$\left\{-\tfrac{1}{2}\nabla^2 + V_{\text{ext}} + V_c[\,\rho] + V_{\text{xc}}[\,\rho, \nabla\rho]\right\}\psi_i = \varepsilon_i\psi_i, \tag{1}$$

where V_{ext} is the nuclear potential, V_c is the Hartree (classical Coulomb) potential of the electron density ρ, and V_{xc} is the exchange–correlation (XC) potential. The one-particle Kohn–Sham (KS) orbitals ψ_i are expanded in a basis of Gaussian-type functions χ_k,

$$\psi_i = \sum_k c_{ki}\chi_k, \tag{2}$$

and these basis functions are set up as symmetrized contractions (linear combinations) of primitive functions

$$\chi_k^l = \bar{C}_m^l(r, \vartheta, \varphi)e^{-\alpha_k r^2}, \tag{3}$$

where $\bar{C}_m^l(r, \vartheta, \varphi)$ is a real solid harmonic (a harmonic polynomial).

In a density functional PP calculation, the interaction of electrons

$$V_{ee} = V_c[\,\rho] + V_{\text{xc}}[\,\rho] \tag{4}$$

is replaced by the interaction of valence electrons and a pseudopotential V_p, which accounts for the core electrons,

$$V_{ee}^p = V_c[\,\rho_v] + V_{\text{xc}}[\,\rho_v] + V_p(\mathbf{r}), \tag{5}$$

where ρ_v denotes the valence electron density. The pseudopotential in a molecular calculation is set up as a superposition of individual atomic contributions V_p^A,

$$V_p(\mathbf{r}) = \sum_A V_p^A(\mathbf{r} - \mathbf{R}_A). \tag{6}$$

According to the angular-momentum-specified normconserving PP approach [14, 18], an atomic pseudopotential can be written as

$$V_p^A = V_L^p + \sum_{l=0}^{L-1}[V_l^p - V_L^p]\sum_{m=-l}^{l}|lm\rangle\langle lm|. \tag{7}$$

Here L is chosen so that $L-1$ equals the maximum angular momentum of the atomic one-electron orbitals which belong to the frozen core. $|lm\rangle$ denotes the spherical harmonic Y_{lm}. In a DF formalism the first term of Eq. (7), V_L^p, is the same for all electrons with $l \geq L$; it originates from the Coulomb and exchange-correlation interaction of the valence electrons with the core shells. We note that this term is a local one in contrast to the angular momentum specified terms which contain the projection operators $|lm\rangle\langle lm|$. These latter terms account for the orthogonality of the valence orbitals with $l < L$ to the core orbitals and contain the proper PPs V_l^p, $l < L$.

The PPs are determined by solving the atomic radial equations

$$\left\{-\frac{1}{2}\frac{d^2}{dr^2} + \frac{l(l+1)}{2r^2} - \frac{Z'}{r} + V_c[\,\rho_v] + V_{\text{xc}}[\,\rho_v + \rho_c^f] + V_l^p\right\}\psi_l^p(r) = \varepsilon_l\psi_l^p(r), \tag{8}$$

where $\psi_l^p(r)$ is the radial part of a nodeless pseudo valence orbitals, constructed from the exact valence orbital following Ref. [18]. ε_l denotes the atomic one-electron eigenvalue of a valence orbital of angular momentum, l, and Z' is the nuclear charge decreased by the charge of the core electrons. Thus, V_l^p is constructed to reproduce the exact valence one-electron energies for electrons in the field of a shielded nuclear charge, but interacting with the valence electron density. The frozen core electron density ρ_c^f is included in the XC potential to account for the nonlinear character of this quantity [18].

To apply the formalism sketched above to TIMPs, all electrons of a model center are included in the PP and $L-1$ is chosen equal to the highest angular momentum of the occupied orbitals. To determine V_l^p, pseudo orbitals of unoccupied levels are employed for each angular momentum l which is present in the occupied orbital manifold.

In the LCGTO-DF implementation, the potentials V_l^p are generated in a numerical atomic DF calculation and are used in tabular form. The core density ρ_c is determined as the difference of the total density from an all-electron atomic calculation and the density due to the pseudo valence orbitals. To describe the Coulomb part of the local term V_L^p, it is represented by a set of s-type Gaussian functions. The coefficients as well as the Gaussian exponents are determined by means of a nonlinear least-squares fit according to the gradient extremum search method [21].

To evaluate matrix elements $\langle \chi_k | V_l^p | \chi_i \rangle$ of the nonlocal terms of V_p^A basis functions χ_k [Eq. (3)] centered on atom B are projected onto spherical harmonics Y_{lm} centered on the PP center A [22]. The projection of a simple Gaussian function is given by

$$[e^{-\alpha(\mathbf{r}-\mathbf{b})^2}]_{lm} = 4\pi Y_{lm}(\Omega) e^{-\alpha(r^2+b^2)} i_l(2\alpha rb), \quad (9)$$

where $\mathbf{r} = (r, \Omega)$; vector $\mathbf{b}$ denotes the position of center B in the coordinate system of a PP center A, and i_l is a modified spherical Bessel function [23]. The real solid harmonic $\bar{C}_m^l$ can be easily represented as a linear combination of complex solid harmonics [24]

$$C_m^l = \left(\frac{4\pi}{2l+1}\right)^{1/2} r^l Y_{lm}. \quad (10)$$

The projection onto complex solid harmonics centered at A is given by [24]

$$\left[C_M^L(\mathbf{r}-\mathbf{b})\right]_{lm} = (-1)^{L-1}\sqrt{\frac{4\pi}{2l+1}\binom{L+M}{l+m}\binom{L-M}{l-m}} \times r^l C_{M-m}^{L-l}(\mathbf{r}), \quad l \le L \quad (11)$$

where $\binom{k}{t}$ is a binomial coefficient. The resulting products of spherical harmonics centered at the same atom [Eqs. (9) and (11) substituted in Eq. (3)] are coupled according to [24]

$$r^{l_1} Y_{l_1 m_1}(\Omega) r^{l_2} Y_{l_2 m_2}(\Omega) = \sum_{LM} r^{l_1+l_2-L} r^L Y_{LM}(\Omega) G_{LM}^{l_1 m_1, l_2 m_2} \quad (12)$$

with $G_{LM}^{l_1 m_1, l_2 m_2}$ being a Gaunt coefficient.

To determine forces in a calculation employing PPs or TIMPs displacement gradients of the matrix elements of V_p with respect to atomic centers are required; they yield contributions which parallel those of the nuclear potential. The differentiation of the projected basis functions with respect to positions of all-electron centers is straightforward and analytical expressions have been derived. Partial derivatives with respect to the coordinates of pseudo centers can be obtained by exploring the translational invariance of the matrix elements.

Although it does not constitute a special problem to construct TIMPs for anions employing the DF representation of the exchange–correlation operator [6], in this work we use only TIMPs for Mg^{2+} cations and represent the oxygen anions by PCs. There are two reasons for this decision: (i) the deficiency of conventional models with embedding of the all-electron (AE) cluster into a PC array has been attributed mainly to the distortion of anions at the cluster borders by positive PCs attracting electron density [16], while the effect of negative PCs on relatively compact AE cation neighbors is of subordinate importance; (ii) since free O^{2-} anions do not exist, additional approximations, like application of a Watson sphere [6] or embedding into a bulk crystal [25], are required for generating such a TIMP. We have generated a PP for the neutral Mg atom ($3s^2 3p^0$ electron configuration). Thus, the frozen density of the Mg^{2+} TIMP corresponds to the shells $1s^2$, $2s^2$, and $2p^6$ of the neutral Mg atom.

Computational Details

In the present study AE cluster models of regular surface sits of MgO(001) range from MgO_5^{8-} to $Mg_{25}O_{25}$; smaller models are all subsystems of the latter cluster. The Mg–O distance in all models was taken from the experimental MgO bulk geometry (2.104 Å). To simulate the Madelung field of the crystal environment, the clusters were embedded in PC arrays of dimension $17 \times 17 \times 2$ which allows us to consider both Mg and O adsorption sites within the same model. If the PC array is extended to a thicker slab ($17 \times 17 \times 6$), only negligible alterations of calculated adsorption properties are observed. For these PCs the charge value for an ideally ionic crystal, ± 2.0 a.u., was assumed. A more strict approach would involve computing the lattice potential through an explicit Ewald summation over the infinite crystal [26–28]. Fortunately, the Madelung field can be very satisfactorily approximated by the field of a finite set of PCs [29]. In case of low-coordinated defect sites (e.g., three-coordinated corner sites of MgO) the PC representation of the crystal field is actually the only reasonable choice.

In the new, more sophisticated model variant all cations that are either nearest or next-nearest neighbors of the outer AE cluster atoms (at the distance of 2.104 and 2.976 Å, respectively) were described by TIMPs. Cations situated at larger distances were still modeled by PCs. Calculations of the Mg_9O_9 cluster with AE Mg^{2+} cations located in the positions previously occupied by TIMPs in the corresponding model (the cluster formula then is $Mg_9O_9Mg_{16}^{32+}$) were also carried out for comparison. To model three-coordinated Mg^{2+} sites of MgO, a cubic array $10 \times 10 \times 10$ point charges was used. The clusters Mg_4O_4 and MgO_3^{4-} at the corner of this cube were treated as AE parts which were surrounded by TIMPs according to the strategy just outlined for models of regular sites.

Orbital basis sets and contraction coefficients, $(15s10p1d) \rightarrow [6s5p1d]$ for Mg (the numbers of primitive Gaussians are given in parenthesis, the numbers of contracted basis functions in brackets) and $(13s8p1d) \rightarrow [6s5p1d]$ for O, have been taken from our previous study of transition-metal atom adsorption on a Mg(100) surface [30]. For the atoms of the CO adsorbate molecule, $(9s5p2d) \rightarrow [5s4p2d]$ basis sets have been employed [14]. The orbital bases were contracted using atomic eigenvectors obtained in the local density approximation (LDA).

To optimize the position of the CO molecule over the MgO(001) surface, calculations for different adsorption heights were carried out, keeping the C–O distance fixed at the value optimized for the free molecule: The equilibrium height was then determined by fitting these energies to a polynomial. Then, to find the harmonic frequency of the C–O vibration and the equilibrium C–O bond length, the position of the CO center of mass was fixed and five points for different C–O distances were calculated ($\Delta q = 0.0$; ± 0.05; ± 0.1 Bohr, where Δq is the displacement from equilibrium bond length of free CO) and fitted by polynomials. To test the implementation of the analytical energy gradients for the pseudopotential technique, the geometry optimization and the frequency calculations were repeated with analytical gradients. Both methods gave the same results within 0.001 Å and 1–2 cm^{-1} for geometrical parameters and harmonic frqeuencies, respectively.

The auxiliary fitting basis sets used in the LCGTO-DF method to represent the electron charge density and the exchange–correlation potential during the self-consistency cycles in single-point calculations were constructed from the orbital exponents in a standard fashion [20]. For the "post-SCF" (self-consistent field) evaluation of the total energy, as well as during the self-consistency cycles of geometry optimiation and frequency calculations employing analytical energy gradients, the exchange–correlation term was calculated using an accurate numerical integration procedure [31].

The local density approximation to the exchange–correlation functional as suggested by Vosko, Wilk, and Nusair (VWN) [32] was used to obtain one-electron energies of the cluster models presented below. To calculate electron affinities and ionization potentials, the total energy was determined evaluating the XC contribution with the help of the generalized gradient approximation (GGA) to the exchange energy as suggested by Becke [33] and to the correlation energy as suggested by Lee, Yang, and Parr (BLYP) [34], employing the self-consistent LDA density. For the automatic geometry optimizations, the total energy and the analytical energy gradients were calculated within the self-consistently employed GGA; two variants were applied, BLYP and the Becke-Perdew form (BP, Becke exchange [33],

Perdew correlation [35]). The standard counterpoise technique [36] was applied to correct binding energies for the basis set superposition error (BSSE).

Results and Discussion

TIMP VERSUS PC EMBEDDING: ONE-ELECTRON PROPERTIES OF CLUSTER MODELS

As mentioned in the introduction, the oxygen anions in cluster models of MgO are strongly polarized by neighboring PCs. In Figure 1 we display charge density plots for TIMP [Fig. 1(a)] and PC embedded [Fig. 1(b)] Mg_9O_9 clusters along with the corresponding charge difference plot [Fig. 1(c)]. A density decrease in the TIMP model with respect to the PC case is marked by dashed lines. One can clearly see that all oxygen anions in the TIMP embedded model exhibit a regular spherical shape, while in the PC embedded model the anions at the cluster border are of ellipsoid-like shape where the charge density extends toward neighboring positive PCs. The charge difference plot [Fig. 1(c)] clearly identifies a nonzero electron density around the nearest-neighbor positive point charges in the PC embedded model. This charge density is transferred from the oxygen anion due to an artificially strong attraction of the naked positive charge which is not balanced by repulsion from core electrons around the cation.

Let us now consider how this distorted electron density affects one-electron properties of the models. In the PC embedded models the one-electron levels lie lower than those in the models with TIMP embedding (Table I) because the attractive potential due to the surrounding positive PCs is overestimated. Both core and valence levels are affected. The band gap of 3.8–4.4 eV as measured by the highest occupied molecular orbital–lowest unoccupied molecular orbital (HOMO–LUMO) splitting calculated for the models with TIMP embedding is in reasonable agreement with the result (3.0 eV at the Γ point) of an Xα band structure calculation on a two-layer MgO slab [37]. However, for well-understood reasons [38], the present LDA value is significantly smaller than the experimental value of 7.8 eV [39]. The energies of the LUMO (−1.2 or −1.5 eV) and HOMO (−5.4 to −5.6 eV; Table I) are also quite close to the corresponding values at the Γ point of a two-layer slab

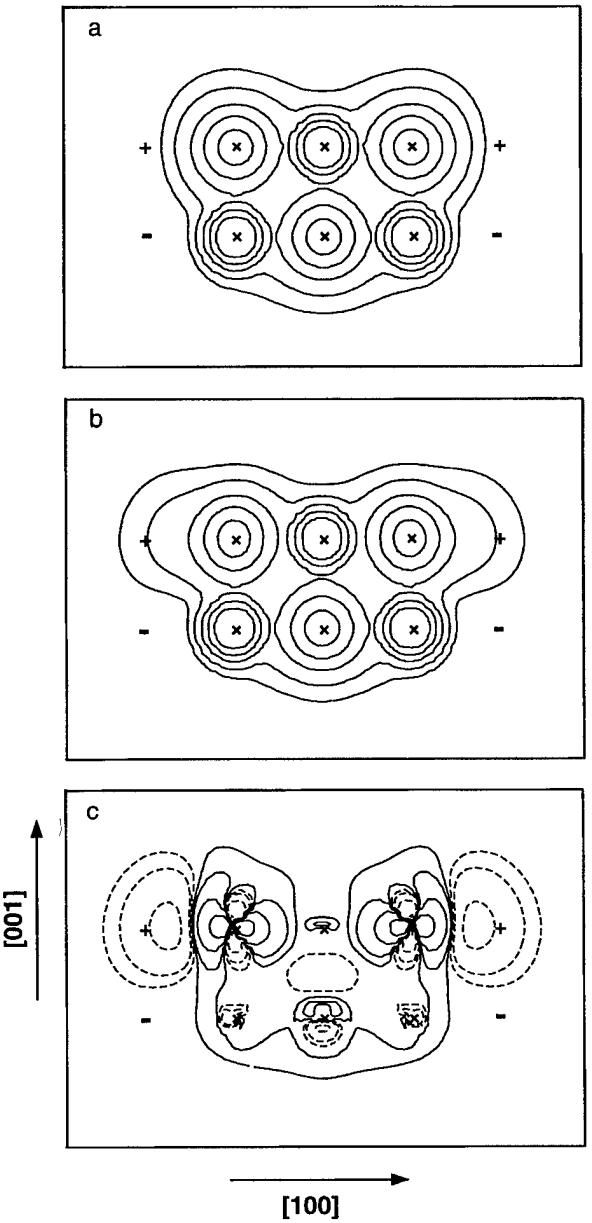


FIGURE 1. Electron density contour maps for the cluster model Mg_9O_9 in the plane containing the fourfold symmetry axis and the O — Mg — O unit: (a) TIMP embedding; (b) PC embedding; (c) density difference $\Delta\rho = \rho(Mg_9O_9, \text{TIMP}) - \rho(Mg_9O_9, \text{PC})$. The contour values in panels (a) and (b) are 0.64, 0.16, 0.045, 0.01, and 0.0025, an additional contour line of 0.0008 a.u. is used in panel (c); dashed lines indicate negative values.

band structure (LUMO −1.5 eV, HOMO −4.5 eV [37]). The shift of the cluster LUMO to low energies in PC embedded models can be rationalized by the finding that this orbital is mainly localized on the most perturbed border atoms. The large

TABLE I
Properties of PC, TIMP, and Mg^{2+} all-electron embedded cluster models of the MgO(001) surface.[a]

	Type of embedding						
	PC			TIMP			Mg^{2+} AE
Property	Mg_5O_5	Mg_9O_9	$Mg_{25}O_{25}$	Mg_5O_5	Mg_9O_9	$Mg_{25}O_{25}$	$Mg_9O_9Mg_{16}^{32+}$
ϵ(LUMO)	−8.78	−6.82	−7.40	−1.17	−1.15	−1.54	−1.46
ϵ(HOMO)	−9.02	−9.69	−9.51	−5.55	−5.43	−5.37	−5.68
$\Delta\epsilon$(HOMO-LUMO)	0.24	2.87	2.11	4.38	4.28	3.83	4.22
EA	6.54	5.05	6.00	−0.47	−0.33	0.18	1.62
IP	11.33	11.42	10.73	7.77	6.93	6.44	7.31
O1s levels							
ϵ(central atom)	−506.86	−507.99	−507.64	−503.42	−503.48	−503.59	−503.70
ϵ(edge atoms)	−508.76	−508.46	−507.76	−503.37	−503.48	−503.58	−503.72
ϵ(corner atoms)	—	−508.75	−507.84	—	−503.44	−503.56	−53.72
$\Delta\epsilon$	1.90	0.76	0.20	0.05	0.04	0.03	0.02
Mg1s levels							
ϵ(central atom)	−1252.12	−1253.12	−1252.35	−1247.96	−1248.11	−1248.18	−1248.34
ϵ(edge atoms)	−1250.04	−1252.06	−1252.54	−1247.92	−1248.04	−1248.16	−1248.27
ϵ(corner atoms)	—	−1250.89	1252.71	—	−1248.02	−1248.16	−1248.22
$\Delta\epsilon$	2.08	2.23	0.36	0.04	0.09	0.02	0.12

[a] HOMO and LUMO one-electron energies (ϵ), electron affinities (EA), ionization potentials (IP), 1s core level energies (ϵ), and their spread $\Delta\epsilon$ (for the largest cluster restricted to the subsystem Mg_9O_9). All energies in eV.

splitting of 1*s* core levels in PC embedded models, especially in the smaller clusters Mg_5O_5 (about 1.9 and 2.1 eV; Table I) and Mg_9O_9 (about 0.8 and 2.2 eV), clearly demonstrates the inequivalence of atoms of the same kind located at different cluster positions. TIMP embedding reduces this level splitting to less than 0.1 eV (Table I). Ideally, ions of one sort belonging to the same layer of a regular MgO(001) surface should have identical core level energies.

As a consequence of the low-lying LUMO, cluster models with simple PC embedding manifest an artificially enhanced electron affinity (EA), e.g., 5.05 eV for Mg_9O_9. Here, EA is determined as the difference of calculated total energies of the neutral embedded cluster and its anion, $EA = E_{(neutral)} - E_{(anion)}$. The EA values for two additional electrons calculated at the BLYP level for the PC embedded clusters Mg_5O_5 and Mg_9O_9 are 8.9 and 7.1 eV, respectively. This implies that the border oxygen anions exhibit a marked oxidative power. We note in passing that no significant electron charge transfer has been found in studies on small adsorbates (e.g., on transition metal atoms [30]) deposited above the central O^{2-} ion of PC embedded clusters. Nevertheless, using PC embedded models for investigations of larger adsorbed species, like metal clusters, can lead to erroneous results if no special care is taken to keep the cluster borders far enough from the adsorption site. The EA overestimation is rectified in TIMP embedded cluster models (Table I).

The calculated ionization potentials (IPs) of PC embedded models of about 11 eV are higher by 2 eV than the experimental value of 9.1 eV [39], while the IPs in TIMP models of about 7 eV are lower than experiment by the same amount (Table I). It is unclear at present to which extent the inaccuracy of the calculated IPs is caused by the DF method itself or by limitations of the cluster models employed. Note that increasing the cluster "thickness" by additional PC layers does not lead to any significant changes.

We conclude this comparison of PC and TIMP embedded cluster models by noting that the TIMP embedding procedure very satisfactorily reproduces all cluster properties discussed here as judged by the results for the AE corresponding cluster models (cf. TIMP Mg_9O_9 and AE $Mg_9O_9Mg_{16}^{32+}$; Table I).

ELECTROSTATIC POTENTIAL ABOVE THE SURFACE

It is generally accepted that the electrostatic potential plays a key role in interactions of adsorbates with ionic substrates. Two recent theoretical investigations are devoted to the study of the

electrostatic potential above the MgO(001) surface in different cluster models. Ferrari and Pacchioni [15] carried out HF calculations on PC embedded models of five-coordinated Mg^{2+} and O^{2-} sites at a regular surface and on three-coordinated O^{2-} corner sites. They found that in PC embedded models the electrostatic potential above regular sites depends significantly on the cluster size and is rather different from that obtained in periodic slab HF calculations. In particular, in PC embedded models the electrostatic potential above a Mg^{2+} site is much stronger and decays slower with the increasing distance from the surface than in the periodic model. At typical adsorbates distances above O^{2-} sites the potential is even of the wrong sign. Nygren et al. [8] studied models of regular surface Mg^{2+} and O^{2-} sites with the help of both PC and TIMP embedding approaches using the HF method. They found that values of the electrostatic potential obtained in TIMP models of various size are rather similar and above Mg^{2+} sites the electrostatic potential is close to that one generated by a single Mg^{2+} cation surrounded by an infinite PC array.

Here we consider the electrostatic potential only above Mg^{2+} sites of regular (001) surface of MgO. Figure 2 shows the dependence of the electrostatic potential felt by a positive unit charge at variable height above the central Mg^{2+} cation of different cluster models. The point charge array of the size used in the cluster embedding, with all ions represented by PCs of charge ± 2.0 a.u., has been taken as a reference. The resulting electrostatic potential (Fig. 2, solid line) is quite similar to that obtained from HF calculations on a slab model [15] or a Mg^{2+} cation surrounded by an infinite array of PCs [8]. Since magnesium oxide is a highly ionic system with a small covalent contribution and nearly complete charge separation, a good quantum chemical model should mimic to a significant extent the electrostatics of the ideal PC representation.

The PC embedded models Mg_5O_5 and Mg_9O_9 (diamonds and squares, respectively) yield an electrostatic potential much larger than that of a PC array. Also the electrostatic potential of these two cluster models extends to significantly larger distances, featuring a rather slow decay which is quite different from that of the reference system.

At variance with the results of PC embedded models, the TIMP strategy yields electrostatic potential curves that are very similar to each other and to the reference curve of the ideal PC system, but are somewhat lower in value than the latter. At distances typical for the location of adsorbed molecules (CO in Fig. 2) the TIMP curves are even

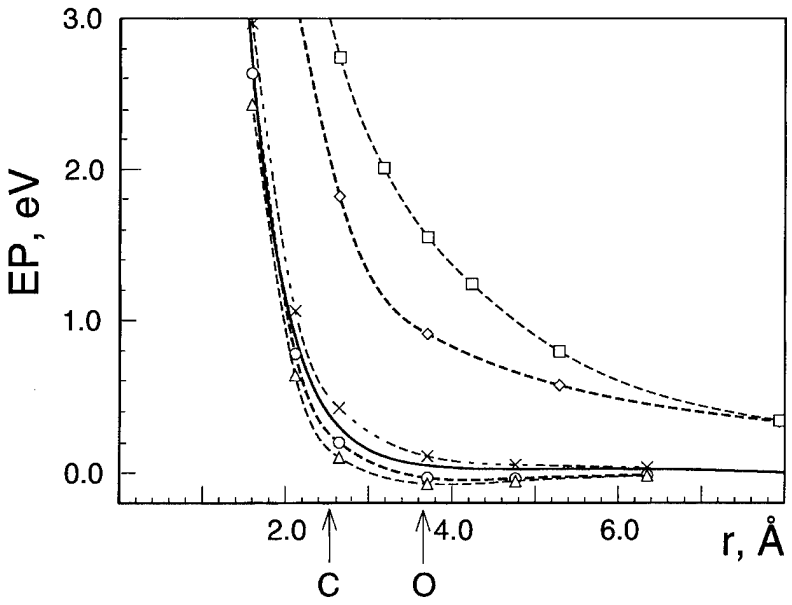


FIGURE 2. Electrostatic potential felt by a positive charge at distance r above the central Mg^{2+} cation in different cluster models of MgO(001). Typical values for the calculated positions of the nuclei of adsorbed CO are indicated by arrows. The results for different models are marked as follows: $17 \times 17 \times 2$ PC array (solid line). MgO_5^{8-} TIMP (△), Mg_9O_9 TIMP (○), $Mg_9O_9Mg_{16}^{32+}$ (×), Mg_5O_5 PC (◇), Mg_9O_9 PC (□).

below zero. This implies that the corresponding model potential for electrons is slightly more repulsive, although the absolute values of the electrostatic potential are very small. The electrostatic potential curves for Mg_5O_5 and Mg_9O_9 TIMP embedded models agree to graphical accuracy; therefore, only the curve for the latter model is shown in Figure 2 (circles). The lower electrostatic potential compared to the reference system can be attributed to a stronger screening of the central Mg^{2+} cation by the electron density of very diffuse shells of neighboring O^{2-} anions. The electrostatic potential produced by the model $Mg_9O_9Mg_{16}^{32+}$ (crosses) where all 16 TIMPs are substituted by AE Mg^{2+} cations is slightly higher than the reference potential due to a small charge transfer from the Mg_9O_9 subsystem into valence orbitals of the 16 cations. Not unexpectedly, all electrostatic potentials calculated at the DF level are in good agreement with the electrostatic potentials obtained for similar models with the help of the HF method [8, 15].

CO ADSORPTION ON REGULAR SURFACE SITES

The interaction of an MgO substrate with an adsorbate like CO provides a good test of the TIMP DF models. The adsorption of CO on the regular MgO(100) surface has been frequently studied theoretically (see, e.g., [9] and references therein). Most of these cluster studies employed the PC embedding approach. The TIMP technique was applied only recently in modified coupled pair functional (MCPF) calculations where the electron correlation was treated with high accuracy [16, 17].

One of the most important characteristics of the MgO–CO interaction derived from quantum chemical calculations is the adsorption energy. In a previous DF study of CO adsorption on MgO(001) [14] based on the BLYP functional we calculated binding energy values of 0.20, 0.21, 0.11, and 0.09 eV for the PC embedded clusters Mg_5O_5, Mg_9O_9, $Mg_{21}O_{21}$, and $Mg_{25}O_{25}$, respectively. (Note that PCs of ± 1.8 a.u. were used.) Based on the analysis of the electrostatic potential in the previous section, one expects a weaker adsorption interaction in TIMP models. Recently, Nygren and Pettersson computed the energy of CO interaction with a TIMP embedded cluster Mg_5O_5 to 0.08 eV at the MCPF level [17]. In our present DF TIMP calculations the interaction of CO with the MgO(001) surface (Fig. 3) turned out to be extremely weak. Although we were able to locate a potential energy minimum at the BLYP level, the binding energy was found to be negative after the BSSE correction was taken into account (Table II). This finding is in line with results of previous DF studies where the BLYP functional was found to underestimate ligand–metal binding energies [31]. The BP exchange–correlation functional yields slightly shorter equilibrium values for the Mg–C distance and

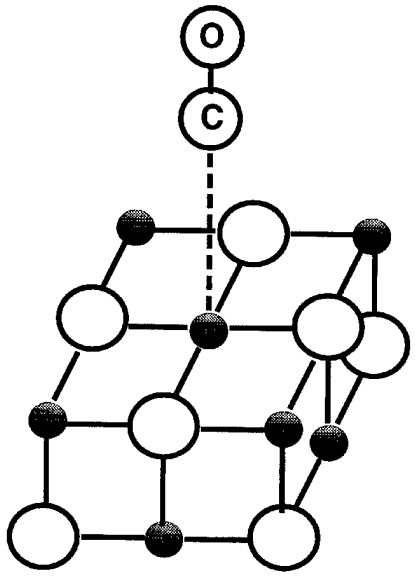


FIGURE 3. Sketch of the cluster model Mg_9O_9–CO.

TABLE II

Observables for CO adsorption on Mg cations of a regular MgO(001) surface calculated for clusters embedded using the TIMP technique or AE Mg^{+2} cations.[a]

	h_e (Mg–C)		D_e	
Cluster model	BLYP	BP	BLYP	BP
TIMP embedding				
MgO_5^{8-}	2.57	2.46	−0.016	0.021
Mg_5O_5	2.53	2.49	−0.011	0.044
Mg_9O_9	2.56	2.49	−0.003	0.054
Mg^{2+} AE embedding				
$Mg_9O_9Mg_{16}^{32+}$	2.56	2.49[b]	0.010	0.066

[a] Surface–CO distance h_e(Mg–C) (in Å) and binding energy D_e (in eV), corrected for the BSSE, both for the BLYP and the BP exchange–correlation energy functionals.

[b] Height as optimized for the TIMP embedded cluster model Mg_9O_9 at BP level.

binding energy values of 0.02–0.05 eV for the various cluster models. These larger values are comparable to the result of the MCPF study, but are still very small, about 1 kcal/mol. Apparently, an accurate description of the CO–MgO interaction at cationic sites of an ideal MgO(001) surface requires the proper evaluation of weak interaction contributions, such as dipole–dipole and van der Waals interactions.

This notable weakening of the interaction of CO with a MgO substrate can be attributed to two features of the TIMP models. First, the electrostatic potential above Mg^{2+} at a distance of about 3 Å where CO molecule is situated is very small; it almost vanishes near the oxygen nucleus (see the previous section). As a consequence, the attraction of the CO molecule to the surface due to the adsorbate polarization is less than in PC embedded models. Second, in the TIMP models the O^{2-} substrate anions are more extended in the direction of the adsorbate. This leads to a stronger repulsion between the CO molecule and the closed shells of the substrate anions. Thus, electrostatic attraction and Pauli repulsion cancel each other, resulting in an almost vanishing adsorption energy. Note that the change of the electrostatic potential is also a consequence of the modified shape of the oxygen anions which in the TIMP models screen the Mg^{2+} cations much better.

It is worth mentioning that the most recent experimental estimations of the adsorption energy of CO on MgO(001) are above 0.4 eV [40, 41] while the most accurate quantum chemical investigations [8] including the present study furnish values lower than 0.1 eV. This clear disagreement has been not resolved although a plausible explanation has been given [8]. Our results allows us to comment on this discrepancy in the next section.

CO ADSORPTION ON THREE-COORDINATED SITES

Finally, we apply the TIMP technique to surface defects where the interaction of a CO molecule is expected to be stronger. Advantages and disadvantages of the various types of embedding models will be more evident. Also, low-coordinated defect sites of MgO are of primary interest for chemical applications such as catalysis. We consider here only models of the three-coordinated Mg site as it is the most characteristic one. Evidently, regular surface sites and three-coordinated corner sites are two limiting cases, and the results for the four-coordinated cationic site are expected to fall between these two limits.

The results for CO adsorption at a three-coordinated corner Mg cationic site are given in Table III. On the unrelaxed site (where the substrate structure is kept frozen at bulk termination), the binding energy for CO adsorption is calculated to 0.47–0.48 eV for the BLYP exchange–correlation functional. The fact that the minimal cluster model MgO_3^{4-} and the stoichiometric cluster Mg_4O_4 yield almost the same results is indicative for the quality of TIMP embedding. The BLYP binding energy value for the unrelaxed corner site is essentially identical to that computed by Nygren and Pettersson with the MCPF method [17]. It is interesting that the CO vibrational frequency shift of 26–27 cm^{-1} is significantly smaller than the value of 56 cm^{-1} obtained by Nygren and Pettersson [17].

For the cluster model MgO_3^{4-} we also considered the relaxation of the top magnesium atom. It moves down toward the O^{2-} anions by 0.32 Å, when the positions of all the other atoms are kept fixed. This is in line with the HF result, 0.26 Å, obtained with PC embedding [42]. At a relaxed corner site, the energy of CO adsorption is calculated to 0.37 eV, about 0.1 eV smaller than at the unrelaxed site. Despite this weaker interaction energy, a larger C–O frequency shift of 39–41 cm^{-1} is obtained. For this model, both BLYP and BP energy functionals yield very similar results (Table III).

TABLE III
Observables for CO adsorption on three-coordinated Mg cations of MgO calculated for clusters embedded using the TIMP techniques.[a]

Cluster model	h_e (Mg–C)	r_e (C–O)	D_e	ω_e	$\Delta\omega_e$
Unrelaxed					
MgO_3^{4-}, BLYP	2.31	1.1290	0.469	2168	26
Mg_4O_4, BLYP	2.31	1.1288	0.482	2169	27
Relaxed					
MgO_3^{4-}, BLYP	2.36	1.1287	0.366	2183	41
MgO_3^{4-}, BP	2.36[b]	1.1284	0.376	2192	39
CO molecule					
BLYP	—	1.1345	—	2142	—
BP	—	1.1340	—	2153	—

[a] Mg–CO distance h_e (Mg–C) and C–O distance r_e (C–O) (in Å), binding energy D_e (in eV, corrected for BSSE), harmonic frequency ω_e of the C–O vibration and the corresponding adsorption-induced frequency shift $\Delta\omega_e$ (in cm^{-1}).

[b] Height as optimized at BLYP level.

Our data for the relaxed three-coordinated site are very similar to experimental data for CO adsorption on MgO films grown over a Mo(100) surface [41]. In this latter work, an infrared (IR) absorption peak at 2178 cm^{-1} (35 cm^{-1} blue-shifted with respect to gas-phase CO) is observed under ultrahigh vacuum conditions at a temperature of 90 K. The adsorption energy has been determined from isothermal adsorption and temperature-programmed desorption to 0.43 and 0.46 eV, respectively [41]. It has been argued [41] that the supported MgO film used in the experimental study exhibits a low concentration of surface defects, but there is no direct information from experiment as to which type of sites are being probed by CO adsorbates. The present DF results support the proposition [17] that only CO adsorption at low-coordinated defect sites of MgO(001), but not at regular five-coordinated Mg sites, yields an adsorption energy exceeding 0.4 eV as measured by He et al. [41].

Summary

We have presented a DF implementation of the TIMP embedding technique which opens opportunities for cluster model studies of ionic materials with improved boundary conditions. Comparative calculations of PC and TIMP embedded cluster models showed that the TIMP approach successfully repairs the main deficiency of PC embedded models, namely the artificial polarization of oxygen anions by positive PCs at the cluster border. TIMP cluster models yield substantially improved one-electron energies. The splitting of core levels of Mg and O atoms in various cluster positions is reduced to less than 0.1 eV. HOMO and LUMO energies come substantially closer to the corresponding values calculated within periodic DF slab models; the HOMO–LUMO gap increases by 1–2 eV. As a consequence of the low-lying LUMO, cluster models with simple PC embedding feature an exaggerated electron affinity; this shortcoming is also rectified in TIMP embedded cluster models. For TIMP cluster models, the electrostatic potential above the central Mg^{2+} cations in the adsorbate region is much weaker than in models with simple PC embedding, resulting in significantly reduced adsorbate–substrate interactions. In these novel TIMP models the adsorption energy of CO on a regular MgO(001) surface is calculated to be only about 0.05 eV at BP level. For the CO adsorption at the partially relaxed three-coordinate corner site the calculated binding energy is 0.38 eV and the CO vibrational frequency shift is 39 cm^{-1}.

ACKNOWLEDGMENTS

The authors are grateful to S. Krüger and U. Birkenheuer for useful discussions. This study has been supported by grants from the Deutsche Forschungsgemeinschaft, the European Community (INTAS Project 93-1876-ext), the Bayerischer Forschungsverbund Katalyse (FORKAT), and the Fonds der Chemischen Industrie.

References

1. Z. Barandiarán and L. Seijo, J. Chem. Phys. **89**, 5739 (1988).
2. N. W. Winter, R. M. Pitzer, and D. K. Temple, J. Chem. Phys. **86**, 3549 (1987).
3. S. Huzinaga, L. Seijo, Z. Barandiaran, and M. Klobukowski, J. Chem. Phys. **86**, 2132 (1987).
4. P. A. Christiansen, Y. S. Lee, and K. S. Pitzer, J. Chem. Phys. **71**, 4445 (1979).
5. J. M. Vail, J. Phys. Chem. Solids **51**, 589 (1990).
6. V. A. Nasluzov, G. L. Gutsev, V. V. Rivanenkov, K. M. Neyman, and A. G. Anshits, Soviet J. Struct. Chem. **33**, 157 (1992).
7. J. A. Mejias and J. F. Sanz, J. Chem. Phys. **102**, 327 (1995).
8. L. G. M. Pettersson, M. Nyberg, J.-L. Pascual, and M. A. Nygren, in *Chemisorption and Reactivity on Supported Clusters and Thin Films: Towards an Understanding of Microscopic Processes in Catalysis*, R. M. Lambert and G. Pacchioni, Eds. (Kluwer, Dordrecht, 1997), p. 425.
9. K. M. Neyman, G. Pacchioni, and N. Rösch, in *Recent Developments and Applications of Modern Density Functional Theory*, J. Seminario, Ed. (Elsevier, Amsterdam, 1996), p. 569.
10. G. Pacchioni, G. Cogliandro, and P. S. Bagus, Surf. Sci. **255**, 344 (1991).
11. G. Pacchioni, G. Cogliandro, and P. S. Bagus, Int. J. Quant. Chem. **42**, 1115 (1992).
12. K. M. Neyman and N. Rösch, Ber. Bunsenges, Phys. Chem. **96**, 1711 (1992).
13. K. M. Neyman and N. Rösch, Chem. Phys. **168**, 267 (1992).
14. K. M. Neyman, S. P. Ruzankin, and N. Rösch, Chem. Phys. Lett. **246**, 546 (1995).
15. A. M. Ferrari and G. Pacchioni, Int. J. Quant. Chem. **58**, 241 (1996).
16. M. A. Nygren, L. G. M. Pettersson, Z. Barandiarán, and L. Seijo, J. Chem. Phys. **100**, 2010 (1994).
17. M. A. Nygren and L. G. M. Pettersson, J. Chem. Phys. **105**, 9339 (1996).
18. G. L. Gutsev, V. K. Gryaznov, and V. A. Nasluzov, Chem. Phys. **154**, 291 (1991).

19. G. L. Gutsev, Adv. Quant. Chem., to appear.
20. B. I. Dunlap and N. Rösch, Adv. Quant. Chem. **21**, 317 (1990).
21. E. F. Brin and B. V. Pavlov, Kinet. Catal. **26**, 193 (1975).
22. I. A. Wilhelmy, Ph.D. Thesis, Technische Universität München, 1994.
23. M. Abramowitz and I. A. Stegun, Eds., *Handbook of Mathematical Functions* (Dover, New York, 1968).
24. D. A. Varshalovich, A. N. Moskalev, and V. K. Khersonskii, *Quantum Theory of Angular Momentum* (World Scientific, Singapore, 1988).
25. J. L. Pascual, L. Seijo, and Z. Barandiarán, J. Chem. Phys. **98**, 9715 (1993).
26. P. P. Ewarld, Ann. Phys. (Leipzig) **64**, 253 (1921).
27. D. E. Parry, Surf. Sci. **49**, 433 (1975); erratum *Ibid.* **49**, 433 (1975).
28. Z. H. Huang and H. Guo, Surf. Sci. **286**, 182 (1993).
29. J. Almlöf and U. Wahlgren, Theor. Chem. Acta **28**, 161 (1973).
30. I. Yudanov, G. Pacchioni, K. Neyman, and N. Rösch, J. Phys. Chem. B **101**, 2786 (1997).
31. V. A. Nasluzov and N. Rösch, Chem. Phys. **210**, 413 (1996).
32. S. H. Vosko, L. Wilk, and M. Nusair, Can. J. Phys. **58**, 1200 (1980).
33. A. D. Becke, Phys. Rev. A **38**, 3098 (1988).
34. C. Lee, W. Yang, and R. G. Parr, Phys. Rev. **B37**, 785 (1988).
35. J. P. Perdew, Phys. Rev. **B33**, 8822 (1986); erratum *Ibid.* **34**, 7406 (1986).
36. S. F. Boys and F. Bernardi, Mol. Phys. **19**, 553 (1970).
37. U. Birkenheuer, Ph.D. Thesis, Technische Universität München, 1994.
38. M. Schlüter and L. J. Sham, Adv. Quant. Chem. **21**, 97 (1990).
39. L. H. Tjeng, A. R. Vos, and G. A. Sawatzky, Surf. Sci. **235**, 269 (1990).
40. C. R. Henry, C. Chapon, and C. Duriez, J. Chem. Phys. **95**, 700 (1991).
41. J.-W. He, C. A. Estarda, J. S. Corneille, M.-C. Wu, and D. W. Goodman, Surf. Sci. **261**, 164 (1992).
42. G. Pacchioni, T. Minerva, and P. S. Bagus, Surf. Sci. **275**, 450 (1992).

Late Transition-Metal Multiple Bonding: Platinum Phosphinidenes and Ruthenium Alkylidenes

MICHAEL T. BENSON, THOMAS R. CUNDARI

Department of Chemistry, University of Memphis, Memphis, Tennessee 38152

Received 29 February 1997; accepted 23 May 1997

ABSTRACT: Transition-metal (TM)–main-group multiply bonded complexes have been heavily studied, due to their usefulness in a variety of applications, e.g., catalysis. The large majority of multiply bonded complexes are early TM systems, but late metal complexes are becoming more common and have been shown to be potent catalysts. An investigation of ligand and substituent effects for representative late TM multiply bonded complexes with heavy (Pt–phosphinidenes) and light (Ru–alkylidenes) elements is presented. Fundamental differences in the response of the metal–ligand multiple bond are observed for light vs. heavy main-group elements for these late TM systems. The results are, in many respects, diametrically opposed to those seen for their early TM congeners. © 1997 John Wiley & Sons, Inc. Int J Quant Chem **65**: 987–996, 1997

Introduction

Transition-metal (TM)–main-group (MG) multiply bonded complexes have been heavily studied since the discovery of metal carbenes in 1964 [1]. Multiply bonded complexes participate in a wide variety of important reactions, such as methane activation by imidos ($L_nM = NR$) [2] and alkane oxidation by oxos ($L_nM = O$) [3]. The majority of TM=MG complexes involve MG elements from the first row and TMs from the early to middle portions of the transition series. Analogs with heavier MG elements are becoming more common [4]. Likewise, multiply bonded complexes of later TMs (TM_{late}=MG) are also being more heavily studied, due in large part to their intermediacy in different catalytic processes [5].

The seeming instability of TM_{late}=MG complexes has been explained to arise from the repulsion between the *d*-orbital electron density on the late TM and MG orbitals that could be used in π-bonding [6]. As described by Mayer for oxos, this leads to the occupation of orbitals with π-antibonding character and, hence, weakening and polarization of the metal–element π-bond [6]. In valence bond terms, such a situation suggests a balance between resonance structures such as **A**

Correspondence to: T. R. Cundari.
Contract grant sponsor: Department of Energy.
Contract grant number: DE-FG05-94ER14460.

© 1997 John Wiley & Sons, Inc.
CCC 0020-7608 / 97 / 050987-10

and **B**. The qualitative model proposed by Mayer should apply:

$$L_nM^+-E^--R \qquad L_nM=E-R$$

A **B**

whether the MG is light or heavy, but the antibonding interaction may exacerbate the already weaker π-bonding power observed in heavier MG elements.

In the majority of cases, the multiple bond is the "active site" which defines the reactivity of a TM=MG complex. The reactivity of TM=MG complexes of early TMs, particularly for light MG elements, is often limited by the thermodynamic and kinetic stability of the multiple bond. While this is advantageous in terms of experimental isolation of such species, it is an obvious limitation in terms of utilizing TM=MG complexes for further reactions. Furthermore, our computations on multiply bonded complexes of early TMs suggest that the strength of the multiple bond engenders a degree of insensitivity to changes in the ligands and substituents, making it difficult to substantially tailor their chemistry through synthetic modification [7]. Conversely, given the instability and metastability of multiple bonds involving later TMs, it may be possible to harness them for synthetic and catalytic benefit if one could assess the sensitivity of TM_{late}=MG complexes to their chemical environment. As it is often difficult to obtain direct, detailed experimental information on TM_{late}=MG complexes, they are ideal candidates for computational research.

In the present research, we chose two TM_{late}=MG systems for study: One involves a lighter MG element (Ru–alkylidenes) and the other a heavier MG element (Pt–phosphinidenes). Our goal is to more fully investigate the bonding in TM_{late}=MG complexes using quantum calculations. An investigation of the electronic and molecular structure of platinum–phosphinidene and ruthenium–alkylidenes complexes is presented. Platinum complexes studied are of the form $(PX_3)_2Pt=PR$, where $(PX_3)_2$ is two monodentate or a single bidentate phosphine and R is an aryl or alkyl group. These systems are models of those recently proposed by Glueck et al. as intermediates in metal-catalyzed olefin hydrophosphination [5a]. The $d^8(X_3P)_2Pt^0$ moiety is isolobal to methylene and other isovalent groups. This suggests some multiple bonding for the PtP bond. On the other hand, the d^8 configuration of $(X_3P)_2Pt^0$ will result in occupation of orbitals which are PtP π-antibonding. It was a goal of this research to determine if electronic effects can stabilize a Pt–phosphinidene. All known phosphinidenes contain very bulky ligands to prevent oligomerization [8]. This research used small models that allow electronic properties to be studied, but kept the models computationally feasible.

In contrast to the instability of platinum phosphinidenes, ruthenium alkylidenes have been synthesized, isolated, and structurally characterized. Alkylidenes of Ru have shown high activity in ring-opening metathesis polymerization (ROMP), ring-closing metathesis (RCM), and acyclic diene metathesis polymerization (ADMET) [9]. Grubbs et al. showed that Ru complexes are very tolerant of functional substrates and catalyze the ROMP of both high- and low-strain cyclic olefins [9a,b]. Ruthenium systems have also been studied as water-soluble catalysts, being stable in protic media [5, 10]. Grubbs et al. increased the metathesis activity of Ru catalysts by replacing the triphenylphosphine ligands with better σ-donating alkylphosphines [9b], so, clearly, the electronics of the metal are an important parameter to be fine-tuned. It has been suggested that the active species in the catalytic process have a ruthenium–carbon multiple bond [9a]. An investigation of ligand and substituent effects on the Ru=C bond is presented. Square pyramidal complexes of the form $Ru(PX_3)_2(Y)_2(=CZ_2)$ have been modeled (where X, Y, Z = H, Cl, F, or Me). As with platinum phosphinidenes, the substituent size has been kept small to keep the computational time reasonable.

Computational Methods

Calculations employed the sequential and parallel versions of the GAMESS quantum chemistry program [11]. The effective core potentials (ECPs) and valence basis sets of Stevens et al. [12] were used for all heavy atoms and the −31G basis set for H. In the Stevens scheme, all ECPs for elements heavier than neon are derived from Dirac–Hartree–Fock calculations and thus implicitly include Darwin and mass–velocity relativistic effects; spin–orbit coupling is averaged out, using a *j*-weighted averaging scheme, in potential generation. ECPs replace the innermost core orbitals for

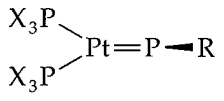
platinum and all core orbitals for MG elements. Thus, the *n*s, *n*p, *n*d, (*n* + 1)s, and (*n* + 1)p shells are treated explicitly for ruthenium and platinum; for the MG elements, *ns* and *np* are treated explicitly. The Pt and Ru valence basis sets are quadruple and triple zeta for the *sp* and *d* shells, respectively, while MG elements have a double-zeta-plus-polarization valence basis.

Geometries were optimized using restricted Hartree–Fock (RHF) and wave functions for closed-shell singlets. Bond lengths and angles for TM complexes are typically predicted to within 1–3% of experiment using this computational scheme, termed RHF/SBK(d), involving complexes in a variety of geometries, oxidation states, and metals from the entire transition series [13].

Results

PLATINUM PHOSPHINIDENES

The geometry of the Pt–phosphinidenes is shown in **1**. All complexes were optimized under C_s symmetry. Substituents are listed in Tables I–IV along with corresponding calculated data. The parent complex, where $PX_3{=}PH_3$ and R = H, is a C_s symmetry minimum with Pt=P = 2.196 Å and Pt=P—H = 102.7°. When Pt=P—H is fixed linear (Pt=P—H = 180°), Pt=P decreases by 0.03–2.166 Å, supporting the idea that forcing phosphorus lone-pair donation to the metal will shorten the bond and strengthen the Pt=P bond. The linear structure is not a minimum, though. Experimental models are rare; Pt—P bonds in the phosphido dimers discussed by Glueck et al. [5a] are roughly 2.335 Å (*trans* to Cl). Calculated Pt=P bond lengths are several percent shorter (~ 2.2 Å), consistent with some multiple bonding character* (Tables I–IV):



1

Alkyl and Silyl Phosphinidenes

The aliphatic and silyl derivatives modeled are listed in Table I. Upon changing the phosphorus substituent from H to Me, Et, ^{i}Pr, and ^{t}Bu, there is very little change in bond length (0.002 Å), although the Pt=P—R angle increases (102.7°, 111.8°, 112.2°, 113.8°, and 114.6°, respectively), due to the larger phosphinidene substituent. The geometries of the two ^{i}Pr conformations studied are shown in **2a** and **2b**; there is no difference in Pt=P bond lengths between **2a** and **2b**, and the Pt=P—R angles differ by only 1.4°. The conformer with methyl groups pointing down, **2b**, is lower in energy by $\approx$ 1 kcal mol^{-1} than that of **2a** at the RHF/SBK(*d*) level of theory. Replacing the phosphinidene substituent in the parent complex with SiH_3 and CH_2SiH_3 has little effect on the

*Throughout the article, the Pt—phosphinidene bond will be indicated as Pt=P to distinguish it from the Pt–phosphine bonds.

TABLE I
Alkyl and silyl phosphinidene derivatives.[a]

X	R	Pt=P (Å)	Pt—P—R (°)	BO(Pt=P)	BO(Pt—R)	*q*(Pt)	*q*(P)[b]
H	H	2.196	102.7	1.810	0.898	−0.645	0.061
H	H (linear)	2.166	180.0	1.759	0.937	−0.442	−0.327
H	Me	2.198	111.8	1.781	0.924	−0.680	0.129
H	Et	2.197	112.2	1.811	0.923	−0.703	0.153
H	^{i}Pr (**2a**)	2.197	113.8	1.778	0.869	−0.718	0.157
H	^{i}Pr (**2b**)	2.197	112.4	1.792	0.875	−0.710	0.148
H	^{t}Bu	2.197	114.6	1.822	0.847	−0.745	0.184
Me	H	2.200	102.9	1.828	0.891	−0.787	−0.040
dpm	H	2.192	102.4	1.734	0.899	−0.443	−0.053
F	H	2.215	101.3	1.614	0.903	−0.665	0.194
H	CH_2SiH_3	2.196	111.9	1.854	0.850	−0.680	0.139
H	SiH_3	2.196	101.9	1.817	0.976	−0.715	−0.003

[a]See structure **1** for definitions of X and R. The bond order (BO) is calculated as described in [14]; atomic charges (q) are determined from a Mulliken population analysis [15].
[b]The atomic charge on the phosphinidene phosphorus is *q*(P).

TABLE II
Halide phosphinidene derivatives.[a]

X	R	Pt=P (Å)	Pt—P—R (°)	BO(Pt=P)	BO(P—R)	q(Pt)	q(P)[b]
H	H	2.196	102.7	1.810	0.898	−0.645	0.061
F	H	2.215	101.3	1.614	0.903	−0.665	0.194
H	Me	2.198	111.8	1.781	0.924	−0.680	0.129
H	CH_2F	2.194	109.2	1.769	0.939	−0.751	0.217
H	CHF_2	2.189	107.8	1.826	0.904	−0.618	0.100
H	CF_3	2.187	106.6	1.820	0.875	−0.645	0.187
H	CH_2Cl	2.193	108.4	1.781	0.891	−0.710	0.233
H	CH_2Br	2.193	107.9	1.790	0.892	−0.703	0.227
H	CH_2I	2.193	107.7	1.793	0.870	−0.700	0.238

[a]See footnote a to Table I.
[b]See footnote b to Table I.

TABLE III
Aromatic phosphinidene derivatives.[a]

X	R	Pt=P (Å)	Pt—P—R (°)	BO(Pt=P)	BO(P—R)	q(Pt)	q(P)[b]
H	H	2.196	102.7	1.810	0.898	−0.645	0.061
H	C_6H_5	2.204	115.1	1.730	1.066	−0.697	−0.012
H	C_6H_5 (**3**)	2.194	108.3	1.750	0.823	−0.647	0.055
H	4-C_6H_4F	2.193	108.3	1.759	0.810	−0.649	0.059
H	2,6-$C_6H_3F_2$	2.188	107.3	1.726	0.718	−0.619	0.183
H	3,5-$C_6H_3F_2$	2.191	108.1	1.756	0.808	−0.640	0.065
H	2,4,6-$C_6H_2F_3$	2.188	107.4	1.735	0.705	−0.619	0.181
H	C_6F_5	2.186	105.9	1.737	0.696	−0.619	0.183
H	Pyridine	2.191	107.9	1.750	0.819	−0.644	0.082

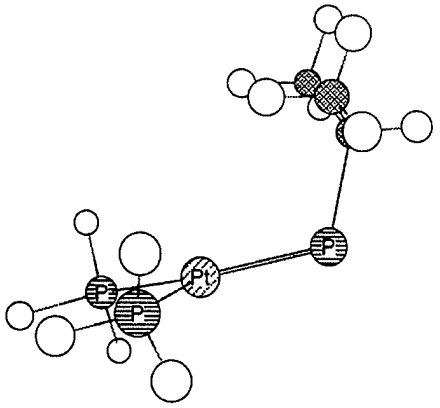
[a]See footnote a to Table I.
[b]See footnote b to Table I.

TABLE IV
Cyano phosphinidene derivatives.

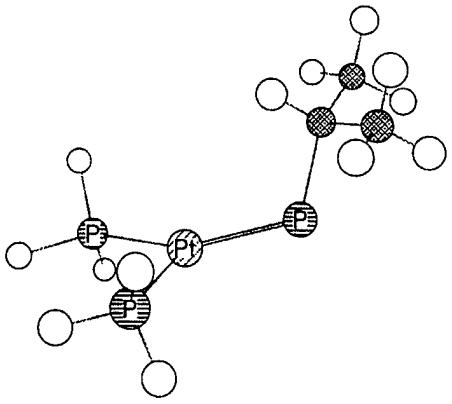
X	R	Pt=P (Å)	Pt—P—R (°)	BO(Pt=P)	BO(P—R)	q(Pt)	q(P)[b]
H	H	2.196	102.7	1.810	0.898	−0.645	0.061
H	CH_2—CN	2.191	109.2	1.821	0.873	−0.687	0.209
H	$C(CN)_3$	2.178	104.5	1.871	0.717	−0.633	0.299
H	$C(CH_3)_2CN$	2.191	111.9	1.829	0.842	−0.728	0.241
dpm	CH_2—CN	2.184	109.3	1.715	0.879	−0.456	0.088

[a]See footnote a to Table I.
[b]See footnote b to Table I.

Pt=P bond length:



2a



2b

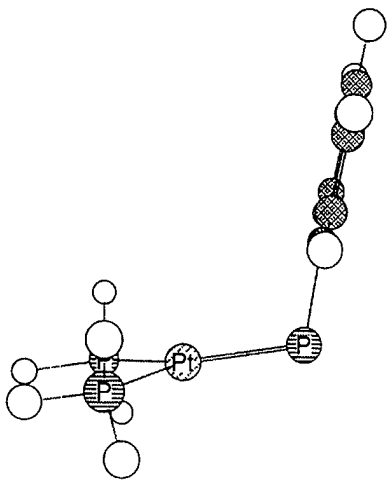
When the phosphine ligands are changed from PH_3 to PMe_3, the Pt=P bond length increases slightly from 2.196 to 2.200 Å. The Pt=P—H angles are near identical: 102.7° in $(PH_3)_2Pt{=}PH$ and 102.9° in $(PMe_3)_2Pt{=}PH$. There is an even larger increase (0.02 Å) in the Pt=P bond length when the parent phosphines are replaced by the very good π-acceptors PF_3. Finally, replacement of the two phosphine ligands with a single bidentate diphosphine (dpm, $H_2PCH_2PH_2$, a model of dppm) shortens the Pt=P bond length from 2.196 to 2.192 Å.

Haloalkyl Phosphinidenes

The haloalkyl-substituted phosphinidenes modeled are listed in Table II. The Pt=P bond length remained constant at 2.193 Å for the halomethyl-substituted derivatives $(H_3P)_2Pt{=}P{-}CH_2X$ (X = Cl, Br, I). The bond angles changed a few degrees over the fluoromethyl series (106.6° [in $(PH_3)_2Pt{=}PCF_3$] – 109.2° [in $(PH_3)_2Pt{=}PCH_2F$]). Upon replacing R = Me with R = CH_2F, the bond length reduces from 2.198 to 2.194 Å and further decreases to 2.189 Å when R = CHF_2 and to 2.187 Å when R = CF_3. This suggests that the Pt=P bond can be affected through the σ framework, assuming the primary influence of the fluorine is by way of inductive (electronegativity) effects.

Aryl Phosphinidenes

Table III lists the aromatic substituents studied. Conformer **3** was assumed for all complexes studied based on experimental models such as $Cp_2Mo{=}PMes^*$ [8a]. A gradual decrease is seen as more fluorines are added, except for the 3,5-difluoro derivative, which increases slightly from the 2,6-difluoro derivative (2.191 vs. 2.188 Å when R = 2,6-$C_6H_3F_2$). The Pt=P bond length decreases from 2.194 to 2.186 Å after completely replacing the phenyl hydrogens with fluorines (R = C_6H_5 vs. R = C_6F_5). Also note that a *para*-F substituent has little effect as can be seen by comparing $(PEt_3)_2Pt{=}P{-}Ph$ with $(PH_3)_2Pt{=}P{-}p\text{-}C_6H_4F$ or $(PH_3)_2Pt{=}P\text{-}2,6\text{-}C_6H_3F_2$ with $(PH_3)_2Pt{=}P\text{-}2,4,6\text{-}C_6H_2F_3$. The shorter Pt=P bond of $(PH_3)_2Pt{=}P{-}2,6\text{-}C_6H_3F_2$ (2.188 Å) vs. that in $(PH_3)_2Pt{=}P{-}3,5\text{-}C_6H_3F_2$ (2.191 Å) can be interpreted as pointing to the greater importance of inductive (σ) over conjugative (π) effects in terms of influencing the Pt–phosphinidene linkage (Table III):



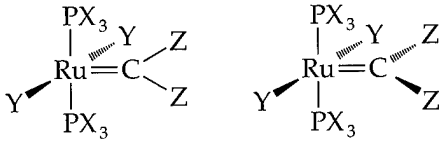
3

Cyanoalkyl Phosphinidenes

An interesting series of complexes are the cyano derivatives listed in Table IV. The bond angles are not correlated with bond length. The shortest bond length has the smallest angle. The largest angle [R = $C(CH_3)_2CN$, Pt=P—R = 111.9°] is likely due to the larger substituent size rather than to any electronic effect. All cyano derivatives have a shorter Pt=P bond length than that of the parent complex (R = H, Pt=P = 2.196 Å). The tricyano complex [R = $C(CN)_3$] has the smallest Pt—P bond length (2.178 Å) of all the complexes modeled, supporting the above statement (Table IV).

RUTHENIUM ALKYLIDENES

The two idealized conformations of the Ru(IV) alkylidenes are shown in **4**. All complexes were optimized under C_{2v} symmetry. Tables V and VI list the substituents along with the corresponding calculated data:



4a 4b

Several five-coordinate ruthenium alkylidenes have been isolated and characterized. The most similar to the model complexes are $RuCl_2$(=CH—*p*-C_6H_4Cl)$(PCy_3)_2$ and $RuCl_2$(=CHCH=CPh_2)$(PCy_3)_2$, both characterized by Grubbs et al. [9f], and cationic [RuCl(=CHCH=CPh_2)(CO)$(P^iPr_3)_2$]$^+$, characterized by Esteruelas et al. [16]. All three complexes correspond to conformer **4b**. $RuCl_2$(=CH—*p*-C_6H_4Cl)$(PCy_3)_2$ has Ru=C = 1.839(3) Å, Ru—Cl = 2.401(1), 2.395(1) Å, and Ru—P = 2.397(1), 2.435(1) Å; $RuCl_2$(=CHCH=CPh_2)$(PCy_3)_2$ has Ru = C = 1.851(21) Å; and [RuCl(=CHCH=CPh_2)(CO)$(PiPr_3)_2$]$^+$ has Ru = C = 1.874(3) Å and Ru—P = 2.4586(8), 2.4307(8) Å. No comparison to Ru—Cl is made in the latter complex since CO is *trans* to chloride. The best model for these systems is X = Me, Y = Cl, Z = H (Me, Cl, H), **4b**. The model has Ru=C = 1.871 Å, Ru—Cl = 2.488 Å, and Ru—P = 2.481 Å (Table V). The Ru–alkylidene bond length is less than 2% different from the X-ray structures, while Ru—P and Ru—Cl are both within 4% of experiment, so that all three metal–ligand bond lengths are in excellent agreement with experiment.

Effect of Phosphine Substituent (X) Modification

The series of phosphine substituents studied (X = H, F, Cl, Me) were modeled for Y = Cl. Phosphine substituent modifications have a relatively

TABLE V
Important bond lengths in ruthenium alkylidenes.[a]

X	Y	Z	Ru—C (**4a***)	Ru—P (**4a**)	Ru—Y (**4a**)	ΔE_{RHF}	Ru—C (**4b**)	Ru—P (**4b**)	Ru—Y (**4b**)
H	H	H	1.853	2.436	1.708	14.3	1.889	2.408	1.743
H	F	H	1.837	2.509	2.000	0.2	1.873	2.481	2.047
H	Cl	H	1.879	2.498	2.440	−2.7	1.886	2.472	2.468
H	Me	H	1.841	2.456	2.169	15.4	1.879	2.431	2.237
H	Cl	H	1.879	2.498	2.440	−2.7	1.886	2.472	2.468
F	Cl	H	1.908	2.443	2.418	−1.0	1.917	2.421	2.438
Cl	Cl	H	1.893	2.502	2.417	0.5	1.914	2.478	2.441
Me	Cl	H	1.869	2.503	2.450	−4.5	1.871	2.481	2.488
H	Cl	H	1.879	2.498	2.440	−2.7	1.886	2.472	2.468
H	Cl	F	1.980	2.500	2.454	1.5	1.990	2.486	2.460
H	Cl	Cl	1.965	2.516	2.447	−0.1	1.984	2.478	2.470
H	Cl	Me	2.007	2.528	2.475	−3.4	1.983	2.474	2.495
H	F	F	1.954	2.513	2.034	0.4	1.976	2.496	2.042
Me	H	H	1.847	2.433	1.711	12.2	1.873	2.415	1.752

[a] See structures **4a** and **4b** for alkylidene conformations. Bond lengths are in Å, and ΔE_{RHF} is the difference between **4a** and **4b**. A negative number indicates conformer **4b** is lower in energy than is conformer **4a**.

small effect on the alkylidene bond length (< 0.04 Å) (Table V). However, from a structural point of view, the sensitivity of the Ru–alkylidenes to phosphine modification is greater than seen for Pt–phosphinidenes.

When replacing phosphine hydrogens in the parent complex (H, H, H) with methyl groups (Me, H, H), the change in Ru = C, Ru—P, and Ru—Cl bond lengths is ≤ 0.01 Å for **4a** and ≤ 0.02 Å for **4b**. The bond lengths in $(H, Cl, H)_a$ are Ru=C = 1.879 Å, Ru—P = 2.498 Å, and Ru—Cl = 2.440 Å. Upon changing X to fluorine $(F, Cl, H)_a$, Ru=C increases by 0.029 to 1.908 Å, Ru—P decreases by 0.055 to 2.443 Å, and Ru—Cl decreases by 0.022 to 2.418 Å. The decrease in Ru—P bond length is consistent with the increased *s*-character on the P lone pair because of the electronegative fluorines [17]. When X is changed from F to Cl $(Cl, Cl, H)_a$, Ru=C and Ru—Cl remain about the same (1.893 and 2.417 Å, respectively). The Ru—P bond length changes by 0.059 to 2.502 Å. When Cl is replaced with Me $(Me, Cl, H)_a$, Ru—P is nearly unchanged (2.503 Å), while Ru=C decreases by 0.024 to 1.869 Å and Ru—Cl increases by 0.033 to 2.450 Å. The geometric changes when the X substituent is modified in conformer **4b** are nearly identical to those just discussed for conformer **4a**.

Analysis of the atomic charge calculated by a Mulliken population analysis (MPA) reveals that (Me, H, H) (both **4a** and **4b**) has the most negative charge on ruthenium. This is in support of Grubbs' finding [9b] that metathesis activity is increased by replacing the triphenylphosphine ligands with better σ-donating alkylphosphines, if the rate-determining step is breaking the C=C double bond. Increased electron density on the metal will increase backbonding into π^* orbitals of the olefin and should facilitate subsequent $[2_\pi + 2_\pi]$ cycloaddition. Further investigation of this point will require a more in-depth computational analysis of the mechanism of olefin metathesis for the Ru–alkylidene catalysts.

In all cases for (X, Cl, H), there is a small (≤ 5 kcal mol^{-1}) energetic difference between conformers **4a** and **4b** regardless of the phosphine substituent. In three cases, conformer **4b** is calculated to be slightly more stable than is **4a**. For the (Cl, Cl, H) complex, the situation is reversed with $(Cl, Cl, H)_a$ more stable than is $(Cl, Cl, H)_b$ by 0.5 kcal mol^{-1}. The experimental catalysts have chloro ligands [9]. Hence, the computations are consistent with experimental observation of two Ru–alkylidene conformers, i.e., the carbene is either orthogonal or parallel to the P—Ru—P axis depending on X [9b]. This point is addressed more below.

For a given set of ligands and substituents, conformer **4b** has a more negative/less positive charge on Ru and a more positive charge on C than have the corresponding atoms in **4a**. In other

TABLE VI
Important charges on ruthenium alkylidenes.[a]

X—P subst.	Y—Ru subst.	Z—C subst.	q(Ru) (**4a***)	q(C) (**4a**)	q(Ru) (**4b**)	q(C) (**4b**)
H	H	H	−0.9262	0.0227	−1.0547	0.0998
H	F	H	0.1691	0.1463	0.0335	0.1831
H	Cl	H	−0.5921	0.1888	−0.7499	0.2285
H	Me	H	−0.9382	0.0194	−1.1218	0.1711
H	Cl	H	−0.5921	0.1888	−0.7499	0.2285
F	Cl	H	−0.6751	0.2063	−0.8217	0.2529
Cl	Cl	H	−0.5380	0.1928	−06856	0.2534
Me	Cl	H	−0.7352	0.1395	−0.9179	0.1916
H	Cl	H	−0.5921	0.1888	−0.7499	0.2285
H	Cl	F	−0.5300	0.6396	−0.4893	0.5369
H	Cl	Cl	−0.3974	0.0496	−1.0020	−0.0680
H	Cl	Me	−0.5856	0.0126	−0.6912	0.0181
H	F	F	0.2791	0.5907	0.2951	0.4937
Me	H	H	−1.0698	−0.0061	−1.2218	0.0743

[a] See structures **4a** and **4b** for alkylidene conformations. The atomic charges (*q*) are determined from a Mulliken population analysis.

words, the rotating about the Ru=C bond leads to increased polarization of the Ru=C bond. As the polarity of a multiple bond is often an important determinant of its reactivity, and solution-phase data suggest that both conformers are accessible for experimental systems, this is an important result.

Effect of Ligand (Y) Modification

Inspection of the data in Table V makes it evident that from a geometric point of view modification of the Ru ligands has a small effect. This is true for both conformers **4a** and **4b**. For example, the parent complex is $(H, H, H)_a$, with Ru=C = 1.853 Å, Ru—P = 2.436 Å, and Ru—H = 1.708 Å. When Ru ligands (Y) in the parent complex are replaced with fluorine $(H, F, H)_a$, Ru=C decreases by only 0.01 to 1.84 Å and Ru—P increases by 0.07 to 2.51 Å. Replacing Y with Cl $(H, Cl, H)_a$ has an opposite effect to F on the Ru=C bond length, i.e., it increases by 0.03 to 1.88 Å. The Ru—P bond length is about the same in $(H, F, H)_a$ and $(H, Cl, H)_a$ at 2.50 Å. Replacing the hydride ligand with a methyl ligand does not result in a large change in geometry. However, as before, changes are more substantial than seen for Pt–phosphinidenes.

Despite the structural similarity of conformers **4a** and **4b** with ligand modification, there are noticeable energetic differences, particularly for non-halide ligands. For halide ligands, conformers **4b** and **4a** are close in energy ($\Delta E_{RHF} < 3$ kcal mol^{-1}, Table VI). As experimental systems have Y = Cl, theoretical results are consistent with experimental observation of two rotamers differing in the orientation of the alkylidene moiety [9b]. On the other hand, there is a distinct preference (> 14 kcal mol^{-1}) for **4a** when strong σ-donors (H, Me) are coordinated to Ru. Halides are π-donors while phosphines are π-acceptors so that they should work to stabilize and destabilize, respectively, the d_π orbitals involved in the multiple bond to the alkylidene C. Thus, it is unexpected that small rotational barriers are seen for Y = halide. The difference may be due, in part, to changes in P—Ru—P and Y—Ru—Y angles which accompany rotation about the Ru=C bond, as compression of these angles away from the alkylidene (increasing Y—Ru=C and P—Ru=C angles) will polarize the d_π orbitals toward the alkylidene C, making for more effective π-bonding. Simple molecular mechanics calculations also suggest that the conformational energy difference about the Ru=C bond between halide and nonhalide ligands is partly steric in origin.

Although the changes in geometry of the Ru–alkylidenes as a function of Y are limited, analysis of calculated properties indicate that interesting changes are taking place in the Ru=C active site. First, it can be seen from the atomic charge calculated by an MPA that replacement of the hydride ligands in $(H, H, H)_a$ with either chlorine or fluorine makes the charge on the Ru more positive/less negative. Likewise, these same modifications make the carbon more positively charged. As the magnitude of the shifts in atomic charge are larger on the Ru than on the C, replacement of electroneutral with electronegative Y decreases the polarization of the RuC double bond. Finally, for both alkylidene conformers, the MPA suggests that the electrophilicity of the Ru center can be substantially enhanced through ligand modification.

Effect of Alkylidene Substituent (Z) Modification

The alkylidene substituents have been modified in the same manner as above, using Z = H, F, Cl, and Me, with X = H and Y = Cl. When the alkylidene substituent in $(H, Cl, H)_a$ is replaced by fluorine, $(H, Cl, F)_a$, the Ru—P and Ru—Cl bond lengths are almost unchanged, but Ru=C is increased from 1.88 to 1.98 Å, a difference of 0.10 Å (5%). When F is replaced with Cl, $(H, Cl, Cl)_a$, again, the Ru—P and Ru—Cl bond lengths are roughly the same. The alkylidene bond length is decreased to 1.97 Å, a difference of 0.02 Å, although the Ru=C bond length is still much longer (0.09 Å) than is $(H, Cl, H)_a$. The longest alkylidene bond length was obtained with methyl substituents on the carbon, $(H, Cl, Me)_a$; the Ru=C bond length is increased to 2.01 Å, a change of 0.13 Å from $(H, Cl, H)_a$. As before, Ru—P and Ru—Cl show relatively small changes with modification of the alkylidene substituents. The Ru=C bond length in (H, Cl, Me) is the only case where conformer **4a** is longer than **4b**. The longer bond length is due to sterics between the phosphine ligands and methyl substituents on the alkylidene carbon. Conformers **4a** and **4b** are very similar in energy for the small phosphines studied here. The bulky phosphines needed to prevent oligomerization (e.g., ^{i}Pr, Cy) in an experimental system will lead to a preference for an alkylidene orientation in which the alkylidene plane is or-

thogonal to P—Ru—P (**4b**), as seen in the solid-state structures of Ru–alkylidenes [9b] and in the lower energy of $(H, Cl, Me)_b$ than of $(H, Cl, Me)_a$ (Table V).

The large change in Ru=C bond length is in contrast to what is seen in early, high-valent alkylidenes [13,18], particularly for second- and third-row TMs that have more covalent bonding than their first-row congeners. In those cases, it is generally observed that metal–carbon double bonds are insensitive to modification of metal ligands and carbon substituents. For example, the Zr = C bond in $H_2Zr{=}CH_2$ is 1.99 Å [18], while that in $H_2Zr{=}CH_2$ is only 0.04 Å (2%) longer. Likewise, for a third-row TM, going from a methylidene $H_3Ta{=}CH_2$ (Ta=C = 1.90 Å) to $H_3Ta{=}Cl_2$ (Ta=C = 1.94 Å) also results in a 2% increase in the metal–ligand multiple bond length [18]. In such cases, substituents such as chlorine generally transmit their influence through the π-system [13,18]. As indicated by atomic charges from an MPA, fluorine yields a substantially more electrophilic alkylidene carbon, suggesting that its influence is transmitted primarily through σ-withdrawing rather than π-donating ability. Interestingly, chlorine substituents led to a larger change in the charge on ruthenium than carbon: $q_{Ru} = -0.59$ and $q_C = 0.19$ $(H, Cl, H)_a$; and $q_{Ru} = -0.40$ and $q_C = 0.05$ $(H, Cl, Cl)_a$. The less positive charge on the alkylidine carbon in $(H, Cl, Cl)_a$ indicates a dominance for the chlorine substituent of π over σ effects.

Discussion

Analyses of computational results for Pt–phosphinidenes and Ru–alkylidenes point to some interesting differences between these late TM, multiply bonded complexes and their more heavily studied, computationally and experimentally, early TM analogs.

For Pt–phosphinidenes, the steric bulk of R has an effect on bond angle, as expected. The substituent size, however, was kept small for computational feasibility, so this was not vigorously pursued. However, the calculation on the $(H_3P)_2$ Pt=PH with a constrained linear Pt=P—H angle suggests that substituents that engender large Pt=P—R angles should serve to strengthen the Pt=P bond. The bidentate phosphine dpm $(H_2PCH_2CH_2)$ also led to a shortening of the Pt=P bond length vs. bis(monodentate–phosphine) analogs.

Halogenated substituents (both aliphatic and aromatic) caused small decreases in the Pt=P bond length. Somewhat surprisingly, the bonding and structure of the Pt–phosphinidene moiety was more sensitive to substituent changes in alkylphosphinidenes than in arylphosphinidenes. Analysis of the molecular orbitals for $(H_3P)_2Pt{=}P{-}CH_3$ and $(H_3P)_2Pt{=}P{-}C_6H_5$ suggests that this may be due to lack of delocalization of phenyl-based MOs to the Pt=P "active site," while in the $(H_3P)_2Pt{=}P{-}CH_3$, there is some mixing of C—H σ orbitals with Pt=P orbitals. These points, taken together, suggest that the Pt=P bond is primarily affected through the σ framework, a conclusion that is consistent with a polarized description of the Pt–phosphinidene bond, **A**.

The largest decreases in Pt=P bond length were caused by cyano substituents. Hence, calculations suggest that bulky phosphinidene substituents (coupled with bulky bidentate phosphine ancillary ligands), combined with cyano phosphinidene substituents, could be a means to obtaining a terminal platinum phosphinidene with sufficient stability for structural characterization.

Strong σ-donor ligands (e.g., hydride) led to large rotational barriers about the Ru=C bond. On the other hand, halide ligands show small differences between Ru–alkylidene conformers (**4a, 4b**). The latter observation is consistent with experiments [9b] that have been interpreted as pointing to two conformers in solution that differ in the orientation of the alkylidene moiety with respect to the other ligands.

The changes in molecular and electronic structure of Ru–alkylidenes as a function of metal ligand and alkylidene substituent are larger than observed for Pt–phosphinidenes studied in this work and also those observed in research on alkylidenes involving high-valent, early TMs [13, 18]. These observations are important in two respects: First, for early TM = MG complexes, there is greater chemical diversity with changes in chemical environment when MG is a heavy element (e.g., phosphorus) [19]. Second, for late TMs, the situation is reversed. Based on observations to date, our current working hypothesis is as follows: For $TM_{early}{=}MG_{light}$ complexes, the strength of the metal–ligand π bond engenders a degree of insensitivity to chemical modification. For $TM_{early}{=}MG_{heavy}$ complexes, the situation is reversed due primarily to weak metal–ligand π

bonding. The $TM_{late}{=}MG_{light}$ complexes must have weaker π bonding than observed for early metal congeners, making them akin, in a conceptual sense, to $TM_{early} = MG_{heavy}$ systems with respect to their response to ligand and substituent modification. Finally, for $TM_{late}{=}MG_{heavy}$ complexes, the inherently weaker π-bonding of the heavier MG elements, coupled with the low-valent nature of the metals, conspire to yield a bonding situation where π-bonding is virtually nonexistent so that any effects on the metal–ligand multiple bond must be transmitted through the σ framework which generally results in small changes.

The foregoing hypotheses suggest that TM=MG complexes involving late TMs, as they are increasingly explored through theory and experiment, will yield new chemistry not observed in the more well-studied early, TM complexes. How these changes can be exploited for catalytic or synthetic benefit will require a more in-depth analysis of the reactivity of these systems. Such studies are now under way in our lab.

ACKNOWLEDGMENTS

Studies of multiply bonded complexes at the University of Memphis are supported by a grant from the Department of Energy (DE-FG05-94ER14460). M. T. B. acknowledges the Van Vleet Foundation (University of Memphis) for fellowship support. Several of the larger calculations were performed at the Cornell Theory Center. Useful discussions with Profs. David S. Glueck (Dartmouth) and Kenneth B. Wagener (University of Florida) are gratefully acknowledged.

References

1. W. A. Nugent and J. M. Mayer, *Metal–Ligand Multiple Bonds* (Wiley, New York, 1988).
2. (a) C. C. Cummins, S. M. Baxter, and P. T. Wolczanski, J. Am. Chem. Soc. **110**, 8731 (1988). (b) C. P. Schaller and P. T. Wolczanski, Inorg. Chem. **32**, 131 (1993). (c) J. de With and A. D. Horton, Angew. Chem., Int. Ed. Engl. **32**, 903 (1993). (d) P. J. Walsh, F. J. Hollander, and R. G. Bergman, J. Am. Chem. Soc. **110**, 8729 (1988). (e) R. D. Profilet, C. H. Zambrano, P. E. Fanwick, J. J. Nash, I. P. Rothwell, Inorg. Chem. **29**, 4364 (1990).
3. (a) P. R. Ortiz de Montellano, Ed., *Cytochrome P-450* (Plenum, New York, 1986). (b) P. C. H. Mitchell and F. Trifiro, J. Chem. Soc., A 3183 (1970).
4. (a) D. C. Bradley, Chem. Rev. **89**, 1317 (1989). (b) K. G. Caulton and L. G. Hubert-Pfaltzgraf, Chem. Rev. **90**, 969 (1990). (c) M. Nandi, D. Rhubright, and A. Sen, Inorg. Chem. **29**, 3066 (1990). (d) M. M. Banaszak Holl, P. T. Wolczanski, and G. D. Van Duyne, J. Am. Chem. Soc. **112**, 7989 (1990). (e) M. H. Chisholm, K. G. Caulton, and Z. Xue, Chem. Mater. **3**, 384 (1991). (f) W. Petz, Chem. Rev. **86**, 1019 (1986). (g) J. F. Harrod, T. Ziegler, and V. Tschinke, Organometallics **9**, 897 (1990). (h) A. H. Cowley and A. R. Barron, Acc. Chem. Res. **21**, 81 (1988). (i) R. Bohra, P. B. Hitchcock, M. F. Lappert, and W. P. Leung, Polyhedron **8**, 1884 (1989).
5. (a) I. V. Kourkine, M. B. Chapman, D. S. Glueck, K. Eichele, R. E. Wasylishen, G. P. A. Yap, L. M. Liable, and A. L. Rheingold, Inorg. Chem. **35**, 1478 (1996). (b) D. M. Lynn, S. Kanaoka, and R. H. Grubbs, J. Am. Chem. Soc. **118**, 784 (1996).
6. J. M. Mayer, Comm. Inorg. Chem. **4**, 125 (1988).
7. T. R. Cundari, J. Am. Chem. Soc. **114**, 7879 (1992).
8. Examples of structurally characterized phosphinidene complexes include: (a) P. B. Hitchcock, M. F. Lappert, and W. P. Leung, J. Chem. Soc. Chem. Commun. 1282 (1987). (b) D. W. Stephan, Z. Hou, and T. C. Breen, Organometallics **12**, 3145, 3158 (1993). (c) C. C. Cummins, R. R. Schrock, and W. M. Davis, Angew. Chem. Int. Ed. Engl. **32**, 756 (1993). (d) A. H. Cowley, B. Pellerin, J. L. Atwood, and S. G. Bott, J. Am. Chem. Soc. **112**, 6734 (1990).
9. (a) S. T. Nguyen, L. K. Johnson, R. H. Grubbs, and J. W. Ziller, J. Am. Chem. Soc. **114**, 3974 (1992). (b) S. T. Nguyen, R. H. Grubbs, and J. W. Ziller, J. Am. Chem. Soc. **115**, 9858 (1993). (c) M. Hillmyer, W. R. Laredo, and R. H. Grubbs, Macromolecules **28**, 6311 (1995). (d) G. C. Fu and R. H. Grubbs, J. Am. Chem. Soc. **115**, 3800 (1993). (e) O. Fujimura, G. C. Fu, and R. H. Grubbs, *J. Org. Chem.* **59**, 4029 (1994). (f) P. Schwab, R. H. Grubbs, and J. W. Ziller, J. Am. Chem. Soc. **118**, 100 (1996). Due to disorder, the bond lengths for $RuCl_2(=CHCH=CPh_2)(PCy_3)_2$ are not listed in the original article [9b].
10. (a) S. T. Nguyen, L. K. Johnson, and R. H. Grubbs, J. Am. Chem. Soc. **114**, 3974 (1992). (b) B. M. Novak and R. H. Grubbs, J. Am. Chem. Soc. **110**, 7542 (1988).
11. M. W. Schmidt, K. K. Baldridge, J. A. Boatz, J. H. Jensen, S. Koseki, N. Matsunaga, M. S. Gordon, K. A. Nguyen, S. Su, T. L. Windus, S. T. Elbert, J. Montgomery, and M. Dupuis, J. Comp. Chem. **14**, 1347 (1993).
12. (a) M. Krauss, W. J. Stevens, H. Basch, and P. G. Jasien, Can. J. Chem. **70**, 612 (1992). (b) W. J. Stevens, H. Basch, and M. Krauss, J. Chem. Phys. **81**, 6026 (1984).
13. T. R. Cundari and M. S. Gordon, Coord. Chem. Rev. **147**, 87 (1996).
14. I. Mayer, Chem. Phys. Lett. **117**, 396 (1985).
15. R. S. Mulliken, J. Chem. Phys. **23**, 1833, 1841, 2338, 2343 (1955).
16. M. A. Esteruelas, F. J. Lahoz, E. Oñate, L. A. Oro, and B. Zeier, Organometallics **13**, 4258 (1994).
17. I. Macleod, L. Manojlovic-Muir, D. Millington, K. W. Muir, D. W. A. Sharp, and R. Walker, J. Organometal. Chem. **97**, C7 (1975).
18. T. R. Cundari and M. S. Gordon, J. Am. Chem. Soc. **114**, 539 (1992).
19. M. T. Benson, T. R. Cundari, Y. Li, and L. A. Strohecker, Int. J. Quantum Chem., Proc. Sanibel Symp. **28**, 181 (1994).

Bethe–Bloch Stopping Power Parameters for Polystyrene, Kapton, and Mylar

L. E. PORTER

Washington State University, Pullman, Washington 99164-1302

Received 2 March 1997; revised 2 May 1997; accepted 14 May 1997

ABSTRACT: Values of several parameters appearing in the modified Bethe–Bloch theory must be known if one is to calculate the stopping power for a given projectile–target combination within the energy interval of applicability of the theory. In the course of the past several years, the author has established values for kapton and mylar target materials through fits of experimental data with the modified Bethe–Bloch theory. During the past year, several sets of measurements of polystyrene stopping powers for light projectiles have been studied so as to extract values of Bethe–Bloch parameters also for this target material. Results of these studies, including uncertainties in the parameter values that reflect the number and accuracy of the measurements analyzed, are summarized in this presentation. © 1997 John Wiley & Sons, Inc. Int J Quant Chem 65: 997–1003, 1997

Introduction

The stopping power of matter for charged particles has been studied for nearly a century now. Not only is this topic one of theoretical importance in several areas of physics, but it holds great significance in numerous areas of experimental physics, i.e., it is often necessary to know with considerable accuracy the energy loss of a charged subatomic projectile during traversal of a known thickness of target material. If one is to avoid energy-loss measurements for every projectile–target combination encountered, a reliable means of calculation must be available. In this connection, the modified Bethe–Bloch theory of stopping power has proved very helpful over a broad range of projectile velocities, provided that values of several parameters of the theory are available [1–4]. In the case of a target that manifests aggregation effects, such as alloys or compounds, other complications arise. In these cases, one must invoke Bragg's rule of (linear) additivity of stopping effects [5]. A technique for calculating energy loss in this sort of target has recently been explained [6–9].

In the past few years, three measurements of the stopping powers of polystyrene for light projectiles have been reported [10–12], two of them

International Journal of Quantum Chemistry, Vol. 65, 997–1003 (1997)
© 1997 John Wiley & Sons, Inc.
CCC 0020-7608 / 97 / 050997-07

[10, 12] covering lower energy intervals than, and one of them [11] overlapping considerably, that explored previously by the author [13, 14]. The current study was undertaken with the goal of analyzing for the first time the recent measurements [10–12] in terms of the modified Bethe–Bloch theory and of comparing extracted values of parameters with those established earlier through experiment [13, 14] and by means of theoretical calculations. In the case of the dominant Bethe–Bloch parameter, the mean excitation energy (I), the previously determined experimental value was 71.1 ± 2.0 eV [14], whereas a very reliable calculated value was 68.7 eV [15]. Nearly a decade ago, the author similarly analyzed several extant sets of stopping power measurements for two other plastics, mylar and kapton, both of which are used widely in numerous areas of physics and the first of which has been extensively utilized in the U.S. space program [6, 7]. The results of these investigations [6, 7] are compared with those of the current study of polystyrene. Moreover, uncertainties in all three sets of extracted parameter values were calculated in the current study for the sake of both clarity and comparison.

Theory

The modified Bethe–Bloch formalism and the method employed in analyzing stopping power measurements for the purpose of extracting values of the various parameters of the formalism were described in previous studies [1–4, 6–9, 13, 14]. The stopping power, S, of an elemental target of atomic weight A and atomic number Z for a projectile of atomic number z and velocity $v = \beta c$ is given by

$$S = \frac{0.30708}{\beta^2} z^2 \frac{Z}{A} L, \tag{1}$$

in units of keV cm^2/mg. Here, L, which represents the (dimensionless) stopping number per target electron, contains three terms:

$$L = L_0 + \xi z L_1 + L_2, \tag{2}$$

where the basic stopping number, L_0, is given by

$$L_0 = \ln\left(\frac{2mc^2\beta^2}{1-\beta^2}\right) - \beta^2 - \ln I - C/Z - \delta/2. \tag{3}$$

The symbol I in this expression signifies the target mean excitation energy, mc^2 represents the rest mass energy of the electron, C is the sum of target shell corrections, and δ stands for the density effect correction needed for highly relativistic projectiles [16]. The mean excitation energy can be determined from a fit to accurate stopping power measurements. Shell corrections can be obtained with the method of Bichsel [17, 18], where Walske K- and L-shell corrections [19, 20] are utilized with appropriate scaling factors employed in the L-shell correction so as to obtain the M- and N-shell corrections:

$$C = C_k(\beta^2) + V_L C_L(H_L \beta^2) + V_M C_L(H_M \beta^2) + V_N C_L(H_N \beta^2). \tag{4}$$

In this expression, C_K and C_L represent the K- and L-shell corrections, respectively, and the V_i and H_i (with $i = L, M, N$) denote the scaling factors.

The L_1 and L_2 terms in Eq. (2) represent two terms of higher order in the projectile atomic number (z). The (zL_1) term is known as the Barkas-effect correction term, where L_1 can be calculated from one of at least three existing formalisms [21–25]. A comparison of the methods [2] has shown that the first [21–23] clearly provides a superior fit to measurements over the broadest projectile energy interval. Thus, this formalism has been used in the stopping number calculated for analyses in the current study. In this case,

$$L_1 = \frac{F(b/x^{1/2})}{Z^{1/2}x^{3/2}}, \tag{5}$$

where F represents a function graphed in [21], $x = (18\,787)\beta^2/Z$, and b denotes the sole free parameter of the formalism. ξ appears in Eq. (2) as an adjustable amplitude of the Barkas-effect term in order to reflect a previous controversy about inclusion of close-collision contributions to the term [1, 9]. The L_2 term, called the Bloch term [26], is given by

$$L_2(y) = \psi(1) - \mathrm{Re}[\psi(1 + iy)], \tag{6}$$

where ψ represents the digamma function [27] and $y = z\alpha/\beta$, with α signifying the fine structure constant.

The several parameters of the three stopping number terms in modified Bethe–Bloch theory, consisting of the mean excitation energy I, the

Barkas-effect parameters b and ξ, and the scaling parameters for the shell corrections V_i and H_i, are all independent of projectile velocity. Whereas the Bloch term clearly depends on the projectile energy and charge, there are no free parameters. Thus, a fit to stopping power measurements to establish values of some subset of the above parameters should yield parameter values that are valid over the projectile energy interval in which the modified Bethe–Bloch formula is valid.

The original Bohr and Bethe theories applied strictly to pure monatomic targets in the gaseous state [28]. A target as simple as an element in the condensed state, or as a homonuclear diatomic molecule in the gaseous state, manifests bonding effects. Extension of Bethe theory to molecules and condensed matter [28] was outlined in a recent report [9]. Both physical-state effects and chemical-bonding effects are often grouped as aggregation effects. A target subject to aggregation effects will henceforth be referred to as a composite target, obvious examples being compounds, alloys, and mixtures. A method of managing aggregation effects, initially advanced by Bragg [5], is to assume linear additivity of stopping effects of constituents in the composite target. This assumption, called "Bragg's rule" or the "additivity rule," is used as a first approximation in the investigation of aggregation effects. In this vein, stopping cross sections, stopping powers, and various parameters in the Bethe–Bloch formula are characterized on the basis of departures from the additivity rule. The current study is based in part on continuing interest in the additivity problem. Calculation of average parameter values has been described previously [22, 29, 30]. The Bloch term [26] contains no target-dependent parameters, but the Barkas-effect correction term [21–23] requires averaging. Moreover, L_0 contains the mean excitation energy, I, and the shell corrections, C—both of which are target-dependent—that must be assigned average values [29, 30]. The general dearth of knowledge of the correct parameter values for target constituents poses an obstacle to implementation of averaging procedures [9]. Consequently, the parameter selected for testing the additivity rule is the mean excitation energy, for which the calculated average (Bragg) value, I_B, can be obtained [28, 29] as

$$\ln I_B = \frac{\Sigma_j n_j Z_j \ln I_j}{\Sigma_j n_j Z_j}, \qquad (7)$$

where n_j, Z_j, and I_j, respectively, represent the atomic concentration, atomic number, and mean excitation energy of the jth component of the composite material. I values extracted from measurements are expected to exceed the respective Bragg values in general, with the largest deviations occurring for strong chemical bonds in low-Z compounds, since in such cases, a large fraction of the total number of electrons participate in the bonding. For a given compound, the chemical binding effect should be greatest at low projectile velocities, since the tightly bound inner-shell electrons contribute less to the stopping than do the outer, valence electrons [31].

Method of Analysis

The basic procedure that is utilized in assigning values to some parameters and searching for values of others through fits to experimental data [1–4, 6–9, 13, 14, 30] is based on the premise that the assigned values, which have been established through prior analyses, are essentially correct. Then, the number and accuracy of the remaining parameter values that can be ascertained are determined by the number and accuracy of the measurements.

In the case of polystyrene, the average atomic number ($\bar{Z}$) is 3.500, the average atomic weight ($\bar{A}$) is 6.509, and the Bragg value [5] of mean excitation energy (I_B) based on current values of constituent mean excitation energies [18] and calculated in the usual manner [1, 6–9] is 69.5 eV. The shell correction scaling parameters for the L shell, calculated according to the Bichsel rubric [17, 18], are $V_L = 0.188$ and $H_L = 1.00$. (The parameter values utilized for polystyrene, mylar, and kapton are displayed in Table I. Constituent mean excitation energies of 19.2 eV for hydrogen, 81 eV for carbon,

TABLE I

Average atomic number ($\bar{Z}$), average atomic weight ($\bar{A}$), logarithmic average mean excitation energy (I_B), and shell correction scaling parameters assigned to polystyrene, mylar, and kapton.

Target	$\bar{Z}$	$\bar{A}$	I_B (eV)	V_L	H_L
Polystyrene	3.50	6.51	69.5	0.188	1.00
Mylar	4.54	8.74	78.7	0.318	1.00
Kapton	5.03	9.80	79.6	0.379	1.00

82 eV for nitrogen, and 106 eV for oxygen were taken from [18].) A typical method of analysis is to fix the values of shell correction scaling parameters and to search for best-fit values of the mean excitation energy (I), the Barkas-effect parameter (b), and the amplitude of the Barkas-effect term (ξ) in a three-parameter fit or to set the value of ξ at unity and proceed to conduct a two-parameter fit. The best fit is established by minimizing the root-mean-square relative deviation of calculated from measured stopping powers, σ. This quantity is defined as

$$\sigma = \left[\frac{1}{N} \sum_{i=1}^{N} \left(\frac{S_m - S_c}{\Delta S_m} \right)_i^2 \right]^{1/2}, \qquad (8)$$

for measurements at N energies, where S_m represents the measured stopping power; S_c the calculated stopping power; and ΔS_m, the statistical uncertainty in the measured value. Thus, a value of σ near unity indicates an acceptable level of agreement between theory and experiment.

Analyses and Results (Protons)

The point of departure in the present study was a reappraisal of the results of a previous analysis [14] by the author of measurements reported by the author and his collaborators [13]. The earlier analysis [14] was conducted prior to introducing an automated fitting routine into the computer code utilized [32,33], i.e., manual searches were carried out to obtain the values ($I = 71.1 \pm 1.8$ eV and $b = 1.90 \pm 0.05$ with $\sigma = 0.70$) in the previous study [14]. The central values were checked with the automated search routine, with the resulting new values, $I = 71.0$ eV, $b = 2.14$, and $\sigma = 0.69$. Thus, it would appear that the lower b value first obtained was a consequence of finding a local minimum close to that located in the automated search. (The above fits were made with V_L at a higher value [0.625] that had been selected for the first analysis [14].) When V_L was reset at 0.188 for the current series of analyses, the results were that $I = 71.0$ eV, $b = 2.26$, and $\sigma = 0.69$. (A three-parameter search for I, b, and ξ proved fruitless, since the value of b became negative [−0.312] and that of ξ very small [0.09], with $\sigma = 0.69$; remaining searches were made in the two-parameter mode.) Clearly, the effect of selecting a smaller value of V_L in the present study had little effect on the derived values of I and b: I remained the same, whereas b rose by 0.12 to 2.26 and σ remained constant.

Analyses of more recent measurements [10,12] followed in an attempt to compare extracted parameter values with those obtained from the measurements by the author and collaborators with 2.2–5.9 MeV protons [13]. The first set of new measurements analyzed was one with 0.02–0.4 MeV protons [10]. A vital question to be answered at the outset was that of the lowest-energy data point that could be included without utilizing a charge-state correction. In other recent studies by the author, it was learned that proton energies extending down to 300 keV could be included without appreciable distortion of extracted parameter values [4,34,35] and that a corresponding lower bound for alpha particles was 1.0 MeV [36,37]. In the present study, proton data points below 300 keV were initially excluded, then only those below 250 keV, and finally only those below 200 keV, in an attempt to stretch the energy interval downward. The test was successful. Thus, the data for 0.2–0.4 MeV were included in the analysis, with resulting values of $I = 71.9$ eV, $b = 1.20$, and $\sigma = 0.04$. Another set of similar measurements [12], from which proton data points from 0.2–0.4 MeV were selected, yielded $I = 69.8$ eV, $b = 1.15$, and $\sigma = 0.28$. The data from [12] are truly composite in nature. Measurements with ^{1}H and ^{2}H projectiles at 40–3000 keV/u were reported. These data were combined with previously reported measurements [10,38] and supplemented by means of analyses with a fitting function [39] in order to extend the covered energy interval upward. The fitting function proposed earlier [39] is an expansion in energy per mass unit for the (reciprocal) stopping power:

$$\varepsilon^{-1} = \sum_{i=0}^{3} a_i E^{\gamma_i}, \qquad (9)$$

where units of keV/u for E will yield units of 10^{-15} eV cm^2/atom for ε. The procedure used was first to establish γ_i values by obtaining the best overall fit to proton stopping powers from 10 to 1000 keV in the Janni tables [40] and then to determine values of the a_i through fits of the experimental data from [10,12,39]. The resulting values of coefficients are purportedly valid for hydrogen projectile energies of 40–400 keV/u [12]. Actual measured stopping powers were obtained from one of the authors [41] in a third set of recent

TABLE II

Extracted values of mean excitation energy (I) and Barkas-effect parameter (b) and associated error function (σ) for each of six measurements of polystyrene stopping power for protons, including the projectile energy interval explored in each case.

Ref.	ΔE_p (MeV)	I (eV)	b	σ
[13]	2.2–5.9	71.0	2.26	0.69
[10]	0.2–0.4	71.9	1.20	0.04
[12]	0.2–0.4	69.8	1.15	0.28
[11]	0.9–3.0	62.2	0.84	0.43
[42]	0.20–0.34	68.3	1.12	0.24
[38]	0.20–0.35	64.8	1.25	0.49

Measurements from [12] with ^{1}H and ^{2}H from 40 to 300 keV/u were supplemented by the authors with results of other measurements [10, 38] and of a fitting function [39] to characterize the data of an extensive compilation [40] so as to extend the energy interval upward.

TABLE III

Extracted values of mean excitation energy (I) and Barkas-effect parameter (b) and associated error function (σ) for each of two measurements of polystyrene stopping power for alpha particles, including the projectile energy interval explored in each case.

Ref.	ΔE_α (MeV)	I (eV)	b	σ
[11]	0.8–2.9	60.7	1.66	1.77
[12]	1.0–3.0	62.5	1.48	0.75

Measurements from [12] with ^{3}He and ^{4}He from 25 to 90 keV/u were supplemented by results of other measurements [11] to extend the energy interval upward.

measurements [11], utilizing 0.9–3.0 MeV protons; analysis yielded $I = 62.2$ eV, $b = 0.84$, and $\sigma = 0.43$. The results of these fits of proton measurements are displayed in Table II, along with results from current fits of two older data sets [38, 42]. These results will be discussed extensively below.

Analyses and Results (Alpha Particles)

Two of the references contained also stopping power measurements for alpha particles [11, 12]. The data for 0.8–2.9 MeV projectiles [11] yielded $I = 60.7$ eV, $b = 1.66$, and $\sigma = 1.77$. (Only one of the nine data points featured a projectile energy below 1.0 MeV.) The measurements for 1.0–3.0 MeV projectiles [12] yielded $I = 62.5$ eV, $b = 1.48$, and $\sigma = 0.75$. Once again, it must be noted that the data from [12] are composite in nature. Measurements with ^{3}He and ^{4}He projectiles at 25–90 keV/u were reported. These data were supplemented by previously reported measurements [11] in order to extend the covered energy interval upward. These data were fit with the function given by Eq. (9) to obtain new (He projectile) values of the coefficients, a_i, purportedly valid for the energy interval from 20 to 750 keV/u [12]. All these results, summarized in Table III, will be discussed further below.

Discussion of Results

In the course of developing the Barkas-effect formalism utilized herein [21–23, 43], it was recommended by two of the authors [43] that, in general, $b = 1.4 \pm 0.1$. Moreover, according to the "13% rule" [18], one might expect that the mean excitation energy for a solid compound of low atomic number will lie some 13% higher than the Bragg value; the Bragg value of I for polystyrene is $I_B = 69.5$ eV, and $1.13 I_B = 78.5$ eV. (Since constituent mean excitation energies have evolved over time, the I_B values given herein may differ from those provided in cited earlier references.) All values of I extracted from experimental data lie well below the "13% rule" prediction, and the proton-based values, instead, provide 68.0 eV as a simple arithmetic average. A reliable calculated value of I is 68.7 eV [15]. Two values of I extracted from stopping power measurements with 70 MeV protons and two different samples of polystyrene, 67.55 and 69.0 eV, were reported recently [44]. Nearly all extracted values of the Barkas-effect parameter (b) are eminently reasonable, the exceptions being those of proton data from [11, 13]. I values obtained from the proton measurements of [11, 13] appear to be somewhat low and high, respectively. Only the alpha particle data of [11] provided a fit characterized by a σ-value greater than unity.

The experiments were conducted with thin-film transmission techniques in [10, 13, 38, 42] and with the Rutherford back-scattering method in [11, 12].

TABLE IV
Recommended values of mean excitation energy (I) and Barkas-effect parameter (b) for polystyrene, mylar, and kapton, with calculated uncertainties (ΔI and Δb).

Target	I (eV)	ΔI (eV)	b	Δb
Polystyrene	71.9	6.5	1.20	0.36
Mylar	80.5	7.0	1.33	0.60
Kapton	78.2	8.1	1.08	0.87

However, the complete data from [12] that were analyzed herein were composite in nature, as noted above. Hence, no systematic trends in extracted parameter values are discernible solely on the basis of the experimental method employed.

Results of searches for parameter values for kapton and mylar were reported previously [6, 7]. However, no uncertainties in the values were provided in those reports. An important feature of the current study is the calculation of uncertainties in recommended values of I and b for polystyrene, mylar, and kapton. These uncertainties, calculated with the method described in detail previously [1, 45], reflect the number and accuracy of the measurements of the stopping power for a given projectile–target combination. Part of the procedure for establishing uncertainties in parameters I and b for mylar and kapton was to calculate best-fit central values with the current version of the fitting program. Hence, the recommended values of these parameters differ slightly from those previously published [6, 7]. The particular measurements chosen for analysis in this portion of the study, were, for each target material, those which reflected the greatest consistency with expectations based on modified Bethe–Bloch theory. All three sets of measurements were made with protons traversing thin-film targets, those utilized being from [10] for polystyrene and from [46] for mylar and kapton. Results of this portion of the analyses are displayed in Table IV. Each uncertainty shown was derived solely from the particular set of measurements analyzed, thus reflecting the number and accuracy of only those measurements.

Summary

Eight experimental studies of the stopping power of polystyrene, six for protons and two for alpha particles, have been reviewed in order to ascertain modified Bethe–Bloch stopping power parameters by consistent data analysis in each case. Four of the six proton studies were conducted with the thin-film transmission method [10, 13, 38, 42], whereas the remaining four measurements were conducted with the Rutherford back-scattering (RBS) technique [11, 12]. The majority of results for mean excitation energy (I) were reasonably consistent with the Bragg value of 69.5 eV or a reliable theoretical value of 68.7 eV [15], although considerable dispersion among derived values was found. All but two extracted values of the Barkas-effect parameter (b) were quite consistent with the expected range of values [43] of 1.4 ± 0.1, one exception occurring in the case of a proton transmission experiment [13] and the other occurring in the case of a proton RBS experiment [11]. Dispersion in extracted parameter values has been encountered in previous reviews of stopping power data [1, 8, 36, 47], but no convincing explanation therefor has yet been advanced. Generally, this dispersion merely reflects obvious dispersion among sets of stopping power measurements—a concern within the stopping power community for several decades. An additional factor contributing to dispersion among reported sets of stopping power measurements is undoubtedly the use of various smoothing functions before listing the actual measurements—a practice openly deplored in a previous study [47]. (An excellent example of this smoothing procedure is the aforementioned report of measurements in [12].) The practice can distort the values of parameters extracted from the data in an analysis based on firm theory.

The situation for kapton targets also required careful assessment [6, 7]. In one study [7], a set of proton measurements was rejected on the basis of quite implausible values of parameters extracted therefrom. Similarly, in the case of mylar targets, another study [7] resulted in doubt being cast on the validity of a set of alpha particle measurements. These selection processes will hopefully be justified by future sets of definitive measurements.

References

1. See, e.g., L. E. Porter, E. Rauhala, and J. Räisänen, Phys. Rev. **B 49**, 11543 (1994).
2. L. E. Porter and H. Lin, J. Appl. Phys. **67**, 6613 (1990).
3. L. E. Porter, Appl. Phys. Lett. **61**(3), 360 (1992).

4. L. E. Porter, Nucl. Instrum. Methods B **88**, 211 (1994).
5. W. H. Bragg and R. Kleeman, Philos. Mag. **10**, 318 (1905).
6. L. E. Porter, Phys. Rev. B **40**, 8530 (1989).
7. L. E. Porter, J. Appl. Phys. **67**, 1639 (1990).
8. L. E. Porter, Rad. Eff. Defects Solids **117**, 197 (1991).
9. L. E. Porter, Phys. Rev. A **50**, 2397 (1994).
10. A. K. M. M. Haque, A. Mohammadi, and H. Nikjoo, J. Phys. D: Appl. Phys. **22**, 1196 (1989).
11. W. E. Wallace, J. B. Rothman, and R. J. Composto, Nucl. Instrum. Methods B **84**, 1 (1994).
12. L. Leblanc, G. G. Ross, and W. E. Wallace, Nucl. Instrum. Methods B **95**, 457 (1995).
13. L. E. Porter, H. Naylor, and J. C. Duder, Nucl. Instrum. Methods **155**, 25 (1978).
14. L. E. Porter, Phys. Rev. B **22**, 2221 (1980).
15. J. C. Ashley, Phys. Rev. B **19**, 5429 (1979).
16. R. M. Sternheimer, M. J. Berger, and S. M. Seltzer, At. Data Nucl. Data Tab. **30**, 261 (1984).
17. H. Bichsel, private communication.
18. *Stopping Power and Ranges for Protons and Alpha Particles*, ICRU Report No. 49 (International Commission on Radiation Units and Measurements, Bethesda, MD, 1993).
19. M. C. Walske, Phys. Rev. **88**, 1283 (1952).
20. M. C. Walske, Phys. Rev. **101**, 940 (1956).
21. J. C. Ashley, R. H. Ritchie, and W. Brandt, Phys. Rev. B **5** 2393 (1972).
22. J. C. Ashley, R. H. Ritchie, and W. Brandt, Phys. Rev. A **8**, 2402 (1973).
23. J. C. Ashley, Phys. Rev. B **9**, 334 (1974).
24. J. D. Jackson and R. L. McCarthy, Phys. Rev. B **6**, 4131 (1972).
25. S. H. Morgan and C. C. Sung, Phys. Rev. A **20**, 818 (1979).
26. F. Bloch, Ann. Phys. (Leipzig) **16**, 285 (1933).
27. M. Abramowitz and I. A. Stegun, Eds., *Handbook of Mathematical Functions* (National Bureau of Standards, Washington, DC, 1964), p. 259.
28. U. Fano, Annu. Rev. Nucl. Sci. **13**, 1 (1963).
29. W. H. Barkas and M. J. Berger, in *Studies in Penetration of Charged Particles in Matter*, National Academy of Sciences–National Research Council Publication No. 1133 (NAS-NRC, Washington, DC, 1967).
30. C. L. Shepard and L. E. Porter, Phys. Rev. B **12**, 1649 (1975).
31. D. Powers and H. G. Olson, J. Chem. Phys. **73**, 2271 (1980).
32. L. E. Porter and R. G. Jeppesen, Nucl. Instrum. Methods **204**, 605 (1983).
33. L. E. Porter and S. R. Bryan, Radiat. Res. **97**, 25 (1984).
34. L. E. Porter, Nucl. Instrum. Methods B **12**, 50 (1985).
35. L. E. Porter, Nucl. Instrum. Methods B **93**, 203 (1994).
36. L. E. Porter, Nucl. Instrum. Methods B **69**, 39 (1992).
37. L. E. Porter, Nucl. Instrum. Methods B **95**, 285 (1995).
38. C. A. Sautter and E. J. Zimmerman, Phys. Rev. A **140**, 490 (1965).
39. C. Eppacher and D. Semrad, Nucl. Instrum. Methods B **35**, 109 (1988).
40. J. F. Janni, At. Data Nucl. Data Tab. **27**, 341 (1982).
41. W. E. Wallace, private communication.
42. D. C. Lorents and E. J. Zimmerman, Phys. Rev. **113**, 1199 (1959).
43. R. H. Ritchie and W. Brandt, Phys. Rev. A **17**, 2102 (1978).
44. T. Hiraoka, K. Kawashima, K. Hoshino, A. Fukumura, and H. Bichsel, Med. Phys. **20**, 135 (1993).
45. L. E. Porter, Radiat. Res. **110**, 1 (1987).
46. E. Rauhala and J. Räisänen. Nucl. Instrum. Methods B **12**, 321 (1985).
47. H. Bichsel and L. E. Porter, Phys. Rev. A **25**, 2499 (1982).

List of Participants

WILLIAM H. ADAMS
Rutgers University
Department of Chemistry
P.O. Box 939
Piscataway, NJ 08855-0939
USA
Phone: 908-445-3758
Fax: 908-445-5312
EMail: adams@rutchem.rutgers.edu

ESTHER AGACINO
Universidad Nacional Autónoma de Mexico
Centro de Investigaciones Teoricas
Avenida 10 de Mayo s/n
Cuautitlan Izcalli, Mexico 54740
Mexico
Phone: 5-623-20-37
Fax: 5-623-20-33
EMail: eav@hp.fciencias.unam.mx

JANOS G. ANGYAN
Universite Henri Poincare
Laboratoire de Chimie Theorique
B.P. 239
Vandoeuvre, Les Nancy Cedex F-54506
France
Phone: 33-3-83-91-25-29
Fax: 33-3-83-91-25-30
EMail: angyan@lctn.u-nancy.fr

JOHAN ÅQVIST
Uppsala University
Department of Molecular Biology
P.O. Box 590
Uppsala S-751 24
Sweden
Phone: 46-18-174109
Fax: 46-18-536971
EMail: aqvist@xray.bmc.uu.se

PETER B. ARMENTROUT
University of Utah
Department of Chemistry
Salt Lake City, UT 84112
USA
Phone: 801-581-7885
Fax: 801-581-8433
EMail: armentrout@chemistry.utah.edu

GUSTAVO A. ARTECA
Laurentian University
Chemistry and Biochemistry
Ramsey Lake Road
Sudbury, Ontario P3E 2C6
Canada
Phone: 705-675-1151
Fax: 705-675-4844
EMail: gustavo@nickel.laurentian.ca

OSMAN ATABEK
CNRS - Universite Paris - Sud
Lab Photophysique Moleculaire
BAT. 213 Campus D'Orsay
Orsay 91405
France
Phone: 33-1-69416132
Fax: 33-1-69156777
EMail: osman@atabek.ppm.u-psud.fr

KYOUNG K. BAECK
University of Florida
Quantum Theory Project
362 Williamson Hall, P.O. Box 118435
Gainesville, FL 32611-8435
USA
Phone: 352-392-1597
Fax: 352-392-8722
EMail: baeck@knusun.kangnung.ac.kr

International Journal of Quantum Chemistry, Vol. 65, 1005–1029 (1997)

© 1997 John Wiley & Sons, Inc.

CCC 0020-7608 / 97 / 051005-25

DIRK BAKOWIES
University of California at San Francisco
Dept. of Pharm. Chem.
Box 0446
San Francisco, CA 94143-0446
USA
Phone: 415-476-4026
Fax: 415-476-0688
EMail: bakowies@clg.ucsf.edu

ANNA BALKOVA
University of Florida
Quantum Theory Project
P.O. Box 118435
Gainesville, FL 32611
USA
Phone: 352-392-1597
Fax: 352-392-8722
EMail: balkova@qtp.ufl.edu

ANDRE D. BANDRAUK
University of Sherbrooke
Chimie-Sciences
2500 Blvd. Universite
Sherbrooke, Quebec J1K 2R1
Canada
Phone: 819-821-7098
Fax: 819-821-8017
EMail: bandrauk@planck.chimie.usherb.ca

GABRIELA BARREIRO
Universidade Federal do Rio de Janeiro
Inst. de Quimica
Rua Maestro Francisco Braga 585, Apto. 202
Rio de Janeiro 22041-070
Brazil

ANDRES BARRIOS
Florida International University
Dept. of Electrical & Computer Eng.
Miami, FL 33199
USA
Phone: 305-348-3017
Fax: 305-348-3707
EMail: hagmann@eng.fiu.edu

RODNEY J. BARTLETT
University of Florida
Quantum Theory Project
381 Williamson Hall, P.O. Box 118435
Gainesville, FL 32611-8435
USA
Phone: 352-392-1597
Fax: 352-392-8722
EMail: bartlett@qtp.ufl.edu

DONALD R. BECK
Michigan Technological University
Dept. of Physics
Houghton, MI 49931
USA
Phone: 906-487-2019
Fax: 906-487-2933
EMail: donald@phy.mtu.edu

SULLIVAN BECK
University of Florida
Quantum Theory Project
345 Williamson Hall, P.O. Box 118435
Gainesville, FL 32611-8435
USA
Phone: 352-392-1597
Fax: 352-392-8722
EMail: beck@qtp.ufl.edu

THOMAS BECK
University of Cincinnati
Dept. of Chemistry
ML172
Cincinnati, OH 45221
USA
Phone: 513-556-4886
Fax: 513-556-9239
EMail: tlb@moe.che.uc.edu

CHRIS BENDER
Albert Einstein College of Medicine
Molecular Pharmacology
1300 Morris Park Ave.
Bronx, NY 10461
USA
Phone: 718-430-2175
Fax: 718-430-8922
EMail: bender@spin.aecom.yu.edu

ATILLA BÉRCES
Steacie Institute for Molecular Science
100 Susses Drive, Room 1150
Ottawa, Ontario K1A 0R6
Canada
Phone: 613-990-0964
Fax: 613-954-5242
EMail: attila@ned1.sims.nrc.ca

JERZY BERNHOLC
North Carolina State University
Dept. of Physics
Box 8202
Raleigh, NC 27695-8202
USA
Phone: 919-515-3126
Fax: 919-515-7331
EMail: bernholc@ncsu.edu

R. STEPHEN BERRY
University of Chicago
Dept. of Chemistry
5735 South Ellis Avenue
Chicago, IL 60637-1403
USA
Phone: 312-702-7021
Fax: 312-702-0805
EMail: berry@rainbow.uchicago.edu

VIRINEYA BERTIN
Universidad Autónoma Metropolitana - Iztapalapa
Dept. de Quimica CIB
AP 55-534
Mexico, DF CP 09340
Mexico
Phone: 52-5-724-4668
Fax: 52-5-724-4666
EMail: neya@xanum.uam.mx

DAVID BEVERIDGE
Wesleyan University
Department of Chemistry
Hall-Atwater Laboratories
Middletown, CT 06457
USA
Phone: 860-685-2575
Fax: 860-685-2211
EMail: dbeveridge@wesleyan.edu

APURBA BHATTACHARJEE
Walter Reed Army Institute of Research
Dept. of Pharmacology
Washington, DC 20307-5100
USA
Phone: 301-295-7085
Fax: 301-295-7755
EMail: apurba_bhattacharjee@wrsmtp-ccmail.army.mil

RICARDO BICCA DE ALENCASTRO
Universidade Federal de Rio de Janeiro
Inst. de Quimica
Bloco A-CT Sala 622, Cidade Univ.
Rio de Janeiro, RJ 21949-900
Brazil
Phone: 55-021-590-3544
Fax: 55-021-290-4746
EMail: bicca@iq.ufrj.br

DAVID M. BISHOP
University of Ottawa
Dept. of Chemistry
P.O. Box 450, STN A
Ottawa, Ontario K1N 6N5
Canada
Phone: 613-562-5181
Fax: 613-562-5170
EMail: dbishop@oreo.uottawa.ca

FRANK E. BLANEY
Computational Chemistry
Smithkline Beecham
New Frontiers Science Park (N) Third Avenue
Harlow, Essex CM19 5AW
UK
Phone: 44-1279-622143
Fax: 44-1279-622348
EMail: frank_e_blaney@sbphrd.com

JONATHAN C. BOETTGER
Los Alamos National Lab.
Group T-1 MS B221
Los Alamos, NM 87545
USA
Phone: 505-667-7483
Fax: 505-665-5757
EMail: jn@lanl.gov

ALEXANDER L. BOLDYREV
University of Utah
Dept. of Chemistry
Salt Lake City, UT 84112-1194
USA
Phone: 801-581-7445
Fax: 801-581-8433
EMail: boldyrev@chemistry.utah.edu

EDWARD A. BOUDREAUX
University of New Orleans
Dept. of Chemistry
Lake Front
New Orleans, LA 70148
USA
Phone: 504-286-6311
Fax: 504-286-6860

AHMED BOUFERGUENE
Florida A & M University
Dept. of Physics
205 Jones Hall
Tallahassee, FL 32307
USA
Phone: 904-599-3470
Fax: 904-599-3577
EMail: boufer@cennas.nhmfl.gov

JOEL M. BOWMAN
Emory University
Dept. of Chemistry
1515 Pierce Drive
Atlanta, GA 30322
USA
Phone: 404-727-6592
Fax: 404-727-6628
EMail: bowman@euch3g.emory.edu

ERKKI BRÄNDAS
Uppsala University
Dept. of Quantum Chemistry
Box 518
Uppsala S-75120
Sweden
Phone: 46-18-183263
Fax: 46-18-502402
EMail: erkki@kvac.uu.se

RIA BROER
University of Groningen
Dept. of Chemical Physics
Nijenborgh 4
Groningen, AG 9747
The Netherlands
Phone: 31-50-634374

ANDERS BROO
University of Florida
Quantum Theory Project
P.O. Box 118435
Gainesville, FL 32611-8435
USA
Phone: 352-392-1597
Fax: 352-392-8722
EMail: broo@qtp.ufl.edu

LUIS BRUNO-BLANCH
Universidad Nacional de La Plata
Depto Ciencias Biological
CC 243
La Plata, Buenos Aires 1900
Argentina
Phone: 54-21-210784 EXT 41
Fax: 54-21-254533
EMail: lbb@nahuel.biol.unlp.edu.ar

JOHNNY BUSTAD
University College of Gavle
Science
S-801 76
Gavle, Sweden
Sweden
Phone: 46-26-648758
EMail: jbd@hgs.se

SYLVIO CANUTO
Universidad de São Paulo
Instituto de Fisica
CPX 66318
São Paulo 05315-970
Brazil
Phone: 55-11-818-6983
Fax: 55-11-818-6831
EMail: canuto@if.usp.br

CRISTIÁN CÁRDENAS-LAILHACAR
University of Florida
Quantum Theory Project
P.O. Box 118435, 345 Williamson Hall
Gainesville, FL 32611-8435
USA
Phone: 352-392-6365
Fax: 352-392-8722
EMail: cardenas@qtp.ufl.edu

RAQUEL CASTILLO
Universitat Jaune I
Dept. de Ciencias Experimentales
Apartat 242
Castellon 12080
Spain
Phone: 34-64-345700
Fax: 34-64-345654
EMail: rcastill@vents.uji.es

SIDONIO CASTILLO
Universidad Autonoma Metropolitana-
Azcapotzalco
Ciencias Basicas
Av. San Pablo #180
Mexico, DF 02200
Mexico
Phone: 52-5-724-4218
Fax: 52-5-723-5940
EMail: sca@hp9000a1.uam.mx

EDUARDO A. CASTRO
Universidad Nacional de La Plata
Dept. of Chemistry
Calle 47 Y 115 C C 962
La Plata, Buenos Aires 1900
Argentina
Phone: 54-21-214037
Fax: 54-21-259485
EMail: castro@biol.unlp.edu.ar

MIGUEL CASTRO
Universidad Nacional Autónoma de Mexico
Dept. de Fisica y Quimica Teorica
Mexico, DF 04510
Mexico
Phone: 52-5-622-3783
Fax: 52-5-616-2010
EMail: castro@papalotl.pquim.unam.mx

CARY F. CHABALOWSKI
U.S. Army Research Lab
AMSRL-WT-PC
Aberdeen Prov. Gr., MD 21005-5066
USA
Phone: 410-278-6095
Fax: 410-278-6150
EMail: cary@arl.mil

BENOIT CHAMPAGNE
Universitaires Notre-Dame de la Paix, à Namur
CTA Lab
Rue de Bruxelles 61
Namur B-5000
Belgium
Phone: 32-81-724557
Fax: 32-81-724530
EMail: benoit.champagne@fundp.ac.be

YAT-PING CHANG
National Taiwan University
Dept. of Chemistry
Room 203
Taipei
Taiwan, ROC
Phone: 886-2-3630231-2326
Fax: 886-2-3636359
EMail: ypchang@rs350.ch.ntu.edu.tw

JOSEPH R. CHAVEZ
Air Force
6221 Cole Lane
Albuquerque, NM 87105
USA
Phone: 505-846-6456
Fax: 505-846-2290
EMail: chavezj@plk.af.mil

JIAN CHEN
University of Florida
Dept. of Physics
215 Williamson Hall
Gainesville, FL 32611
USA
Phone: 352-392-0521
EMail: jchem@physics.ufl.edu

HAI-PING CHENG
University of Florida
Quantum Theory Project
371 Williamson Hall, P.O. Box 118435
Gainesville, FL 32611-8435
USA
Phone: 352-392-1597
Fax: 352-392-8722
EMail: cheng@qtp.ufl.edu

DANIEL M. CHIPMAN
University of Notre Dame
Radiation Laboratory
Notre Dame, IN 46556-0579
USA
Phone: 219-631-5562

SAN-YAN CHU
National Tsing Hua University, Taiwan
Department of Chemistry
Hsinchu
Taiwan
Phone: 866-35-721634
Fax: 886-35-711082
EMail: sychu@chem.nthu.edu.tw

PAUL CHUN
University of Florida
Dept. of Biochem. & Mol. Biol.
Box 100245
Gainesville, FL 32610-0245
USA
Phone: 352-392-3356
Fax: 352-392-2953
EMail: pwchun@pine.circa.ufl.edu

JERZY CIOSLOWSKI
Florida State University
Dept. of Chemistry
Tallahassee, FL 32306-3006
USA
Phone: 904-644-8274
Fax: 904-644-8281
EMail: jerzy@kyoko.chem.fsu.edu

JAMES COFFIN
IBM
1505 LBJ Freeway, 5th Floor
Computational Chemistry
Dallas, TX 75234
USA
Phone: 214-280-3960
Fax: 214-280-2779

ROBERT N. COMPTON
University of Tennessee
Dept. of Chemistry and Physics
401 Buehler Hall
Knoxville, TN 37996
USA
Phone: 423-574-6233
Fax: 423-974-3454
EMail: ahd@ornc.gov

PERE CONSTANS-NIEREA
University of Girona
Inst. of Computational Chemistry
Albereda 3-5
Girona 17921
Spain
Phone: 34-72-418357
Fax: 34-72-418357
EMail: pere@infern.udg.es

DAVID COOPER
University of Liverpool
Dept. of Chemistry
P.O. Box 147
Liverpool L69 3BX
UK
Phone: 44-151-794-3532
Fax: 44-151-794-3588
EMail: dlc@liv.ac.uk

GRANT COOPER
International Physics Health & Energy, Inc.
2260 W. Holcombe Blvd.
Houston, TX 77030
USA
Phone: 713-523-5459
Fax: 713-522-2607

JOAO MANUEL CORDEIRO
Universidad Estadual Paulista
Dept. Fisica e Quimica
Av. Brasil 56, P.O. Box 31
Ilha Solteira, SP 15378-000
Brazil
Phone: 55-18-762-3850
Fax: 55-18-762-4868
EMail: cordeiro@isl000.uesp.ansp.br

MARSHALL CORY
University of Florida
Quantum Theory Project
380 Williamson Hall, P.O. Box 118435
Gainesville, FL 32611-8435
USA
Phone: 352-392-1597
Fax: 352-392-8722
EMail: cory@qtp.ufl.edu

KALINE COUTINHO
Universidad de São Paulo
Instituto de Fisica
CP 66318
São Paulo 05315-970
Brazil
Phone: 55-11-818-6983
Fax: 55-11-818-6831
EMail: kaline@if.usp.br

MAURICIO COUTINHO-NETO
University of Florida
Quantum Theory Project
343 Williamson Hall, P.O. Box 118435
Gainesville, FL 32611-8435
USA
Phone: 352-392-1597
Fax: 352-392-8722
EMail: coutinho@qtp.ufl.edu

T. DANIEL CRAWFORD
University of Georgia
Dept. of Chemistry
1001 Cedar Street
Athens, GA 30602
USA
Phone: 706-542-7738
Fax: 706-542-0406
EMail: crawdad@otanes.ccqc.uga.edu

ARMANDO CRUZ
Instituto Mexicano del Petroleo
AP 14-805
Mexico, DF 07730
Mexico
Phone: 52-5-368-5911 EXT 20270
Fax: 52-5-567-2927
EMail: armando@briseida.sgi.imp.mx

THOMAS CUNDARI
Memphis State University
Dept. of Chemistry
3744 Walker
Memphis, TN 38152
USA
Phone: 901-678-2629
Fax: 901-678-3447
EMail: tcundari@cc.memphis.edu

HERBERT DA COSTA
University of Florida
Quantum Theory Project
P.O. Box 118435, 348 Williamson Hall
Gainesville, FL 32611-8435
USA
Phone: 352-392-7184
Fax: 352-392-8722
EMail: dacosta@qtp.ufl.edu

JOAQUIM DA MOTTA NETO
University of Florida
Quantum Theory Project
348 Williamson Hall, P.O. Box 118435
Gainesville, FL 32611-8435
USA
Phone: 352-392-1597
Fax: 352-392-8722
EMail: quim@qtp.ufl.edu

GURU P. DAS
Wright Laboratory
MLBP
WPAFB, OH 45433
USA
Phone: 937-429-2307
Fax: 937-255-9147
EMail: dasgp@picard.ml.wpafb.af.mil

ROBIN H. DAVIES
University of Wales at Cardiff
Welsh School of Pharmacy
King Edward VII Ave.
Cardiff, Wales CF1 3XF
UK
Phone: 44-1222-874000 EXT 5830
Fax: 44-1222-874149

WAGNER B. DE ALMEIDA
University of Florida
Quantum Theory Project
P.O. Box 118435
Gainesville, FL 32611-8435
USA
Phone: 352-392-1597
Fax: 352-392-8722
EMail: wagner@qtp.ufl.edu

DAN DE KEE
University of Florida
Quantum Theory Project
P.O. Box 118435
Gainesville, FL 32611
USA
Phone: 352-392-9306
Fax: 352-392-8722
EMail: dekee@qtp.ufl.edu

GLENISSON DE OLIVEIRA
Indiana University - Purdue University
Indianapolis
Dept. of Chemistry
402 North Blackford St.
Indianapolis, IN 46202
USA
Phone: 317-274-5342
Fax: 317-274-4701
EMail: glen@chem.iupui.edu

DOMINIQUE DEHARENG
Universite de Liege
Institut de Chimie
B6 Sart Tilman
Liege B-4000
Belgium
Phone: 32-4-3663-499
Fax: 32-4-3663-364
EMail: domi@iris.cip.ulg.ac.be

JANET DEL BENE
Youngstown State University
Dept. of Chemistry
One University Plaza
Youngstown, OH 44555
USA
Phone: 330-742-3466
Fax: 330-742-1579
EMail: fro42008@ysub.ysu.edu

JUAN-CARLOS DEL VALLE
Florida State University
Tallahassee, FL
USA
Phone: 904-644-6452

ERIK DEUMENS
University of Florida
Quantum Theory Project
359 Williamson Hall, P.O. Box 118435
Gainesville, FL 32611-8435
USA
Phone: 352-392-1597
Fax: 352-392-8722
EMail: deumens@qtp.ufl.edu

GEORGES DIVE
University of Liege
Institut de Chimie
B6 Sart Tilman
Liege B-4000
Belgium
Phone: 32-4-366-3499
Fax: 32-4-366-3364
EMail: gd@iris.cir.ul6.ac.be

RUSSELL DRAGO
University of Florida
CLB 408
Gainesville, FL 32611
USA
Phone: 352-392-6043

JAMES DUFTY
University of Florida
Dept. of Physics
215 Williamson Hall, P.O. Box 118440
Gainesville, FL 32611
USA
Phone: 352-392-6693
Fax: 352-392-0524
EMail: dufty@phys.ufl.edu

MICHEL DUPUIS
Pacific Northwest National Laboratory
Mail Stop K1-90
P.O. Box 999, 906 Battelle Boulevard
Richland, WA 99352
USA
Phone: 509-375-6784
Fax: 509-375-6631
EMail: m_dupuis@pnl.gov

MOSTAFA A. EL-SAYED
Georgia Institute of Technology
School of Chemistry
Boggs Building
Atlanta, GA 30332-0400
USA
Phone: 404-894-0294
Fax: 404-894-0294
EMail: mostafa.el-sayed@chemistry.gatech.edu

GÉRHARD G. EMCH
University of Florida
Mathematics Dept.
P.O. Box 118105
Gainesville, FL 32611-8105
USA
Phone: 352-392-0281 EXT 274
Fax: 352-392-8357
EMail: gge@math.ufl.edu

GUILLERMINA L. ESTIU
Universidad Nacional de La Plata
Dept. Quimica
Calle 47 Y 115 CC962
La Plata, Buenos Aires 1900
Argentina
Phone: 54-21-210784 EXT 41
Fax: 54-21-259485
EMail: estiu@nahuel.biol.unlp.edu.ar

TOM EVANS
University of Utah
Dept. of Chemistry
Salt Lake City, UT 84112
USA
Phone: 801-581-5465
Fax: 801-581-8433
EMail: evans@mercury.chem.utah.edu

GREGORY EZRA
Cornell University
Dept. of Chemistry
Baker Laboratory
Ithaca, NY 14853
USA
Phone: 607-255-3949
Fax: 607-255-4137
EMail: gse1@cornell.edu

WILLIAM FARIS
National Science Foundation
Math Science
4201 Wilson Blvd.
Arlington, VA 22230
USA
Phone: 703-306-1997

ANTONIO FERREIRA
University of Memphis
Department of Chemistry
Memphis, TN 38152
USA
Phone: 901-678-4429
Fax: 901-678-3447
EMail: amferreira@cc.memphis.edu

KIM FERRIS
Pacific Northwest Labs.
Materials & Chemical Sci. Ctr.
P.O. Box 999 MS K2-44
Richland, WA 99352
USA
Phone: 509-375-3754

SIGHART FISCHER
Technische Universität München
Theoretische Physik T 38
Boltzmann Str.
Garching B München 85747
Germany
Phone: 49-89-289-12373
Fax: 49-89-289-12444
EMail: jill@jupiter.t30.physik.tu-muenchen.de

EUGENE FLEISCHMANN
Q-Chem Inc.
317 Whipple Street
Pittsburgh, PA 15218
USA
Phone: 609-896-3942
Fax: 609-896-1244
EMail: gene@q-chem.com

GERNOT FRENKING
Phillips Universität Marburg
Dept. of Chemistry
Hans-Meerwein-Strasse
Marburg, Hessen 35032
Germany
Phone: 49-6421-285563
Fax: 49-6421-282189
EMail: frenking@ps1515.chemie.uni-marburg.de

PIOTR FROELICH
Uppsala University
Dept. of Quantum Chemistry
Box 518
Uppsala 751 20
Sweden
Phone: 46-18-183262
Fax: 46-18-502402
EMail: piotr@kvac.uu.se

J. WILLIAM GADZUK
National Institute of Standards and Technology
Gaithersburg, MD 20899
USA
Phone: 301-975-2548
Fax: 301-926-6689
EMail: gadzuk@nist.gov

ANTHONY F. GARITO
University of Pennsylvania
Dept. of Physics and Astronomy
209 South 33 Street
Philadelphia, PA 19104
USA
Phone: 215-898-5810
Fax: 215-898-2010
EMail: garito@afgarito.physics.upenn.edu

JOSE M. GOMEZ LLORENTE
University of La Laguna
Fisica Fundamental
La Laguna 38205
Spain
Phone: 34-22-635448
Fax: 34-22-256973
EMail: jmgomez@ull.es

LIONEL GOODMAN
Rutgers University
Dept. of Chemistry
New Brunswick, NJ 08903
USA
Phone: 908-445-2603
Fax: 908-445-5312
EMail: goodman@rutchem.rutgers.edu

LEONID GORB
National Academy of Sciences of Ukraine
Inst. of Water and Colloid Chemistry
2, Skovorada Str.
Kiev 252680
Ukraine
Phone: 380-44-444-0196
Fax: 380-44-452-0276
EMail: glg@icck.freenet.kiev.ua

ALEX GREEN
University of Florida
ICAAS
P.O. Box 112050
Gainesville, FL 32611-2050
USA
Phone: 352-392-2001
Fax: 352-392-2027

CRISTIANO R. W. GUIMARÃES
Universidade Federal de Rio de Janeiro
Inst. de Quimica
Rua Prof Valadares 193, Apto. 901 - Grajau
Rio de Janeiro, RJ 20561-020
Brazil
Phone: 55-21-268-4837
Fax: 55-21-290-4746
EMail: gis@aix143.iq.ufrj.br

GENNADY L. GUTSEV
University of Florida
Quantum Theory Project
370 Williamson Hall, P.O. Box 118435
Gainesville, FL 32611-8435
USA
Phone: 352-392-1597
Fax: 352-392-8722
EMail: gutsev@qtp.ufl.edu

STEVEN R. GWALTNEY
University of Florida
Quantum Theory Project
345 Williamson Hall, P.O. Box 118435
Gainesville, FL 32611-8435
USA
Phone: 352-392-6365
Fax: 352-392-8722
EMail: gwaltney@qtp.ufl.edu

MASAHIKO HADA
Kyoto University
Dept. of Synthetic Chemistry
Kyoto Sakyo-Ku, Yoshida-Hon-Machi 606
Japan
Phone: 81-75-5663
Fax: 81-75-5910
EMail: hada@synchem.kyoto-u.ac.jp

MARK J. HAGMANN
Florida International University
Dept. of Elect. & Computer Eng.
Miami, FL 33199
USA
Phone: 305-348-3017
Fax: 305-348-3707
EMail: hagmann@eng.fiu.edu

AAGE HANSEN
University of Copenhagen
Dept. of Chemistry
Universitetsparken 5
Copenhagen DK-2100
Denmark
Phone: 45-353-20284
Fax: 45-353-20299
EMail: aage@kl4ibim.ki.ku.dk

FRANK HARRIS
University of Utah
Dept. of Chemistry
Salt Lake City, UT 84112
USA
Phone: 801-581-8445
Fax: 801-585-3207
EMail: harris@dirac.chem.utah.edu

SERGIO ALEJANDRO HASSAN
Universidad Estadual de Campinas (UNICAMP)
Instituto de Fisica Gleb Wataghin
13083-970
Campinas, São Paulo
Brazil
Phone: 55-192-397254 or 392424
Fax: 55-192-393-127
EMail: mago@ifi.unicamp.br

JOHN HEAD
University of Hawaii
Dept. of Chemistry
2545 The Mall
Honolulu, HI 96822
USA
Phone: 808-956-5787
Fax: 808-956-5908
EMail: john@gold.chem.hawaii.edu

ARTHUR HEBARD
University of Florida
Dept. of Physics
215 Williamson Hall, P.O. Box 118440
Gainesville, FL 32611-8440
USA
Phone: 352-392-8842
Fax: 352-392-8586
EMail: afh@phys.ufl.edu

MAGNUS HEDSTRÖM
University of Florida
Quantum Theory Project
362 Williamson Hall, P.O. Box 118435
Gainesville, FL 32611-8435
USA
Phone: 352-392-6973
Fax: 352-392-8722
EMail: hedstrom@qtp.ufl.edu

NIELS ENGHOLM HENRIKSEN
Technical University of Denmark
Dept. of Chemistry
Building 207
Lingby DK-2800
Denmark
Phone: 45-45252029
Fax: 45-45881639
EMail: neh@hcocvx.uni-c.dk

YA-WEN HSIAO
University of Florida
Quantum Theory Project
348 Williamson Hall, P.O. Box 118435
Gainesville, FL 32611-8435
USA
Phone: 352-392-1597
Fax: 352-392-8722
EMail: hsiao@qtp.ufl.edu

ZHENMING HU
Kyoto University
Dept. of Synthetic Chemistry and Biological Chemistry
Sakyo-Ku, Kyoto 606-01
Japan
Phone: 81-75-753-5659
Fax: 81-75-753-5910
EMail: hu@sbchem.kyoto-u.ac.jp

MING-JU HUANG
University of Florida
Center for Drug Discovery
Box 100497
Gainesville, FL 32610
USA
Phone: 904-392-8186
Fax: 904-392-8589
EMail: mjhuang@pine.circa.ufl.edu

YASUYUKI ISHIKAWA
University of Puerto Rico
Chemistry Department
P.O. Box 23346
San Juan, Puerto Rico 00931-3346
USA
Phone: 809-764-0000 EXT 7399
Fax: 809-751-0625
EMail: ishikawa@upracd.upr.clu.edu

ALBERT ISRAEL
Northwestern University
Chemistry
2145 Sheridan Road
Evanston, IL 60208
USA
Phone: 847-491-3423
EMail: albert@chem.nwu.edu

SAUL JACCHIERI
Instituto Adolfo Lutz
Divisao de Biologia
Av. Dr. Arnaldo 351 10 Andar
São Paulo, SP 01246902
Brazil
Phone: 55-11-30610111 EXT 215
Fax: 55-11-2750277

DENIS JACQUEMIN
University of Florida
Quantum Theory Project
P.O. Box 118435
Gainesville, FL 32611-8435
USA
Phone: 352-395-1597
Fax: 352-392-8722
EMail: jacquemin@qtp.ufl.edu

MORTEN O. JENSEN
Copenhagen University
H. C. Orsted Institute
Universitetsparken 5
Kobenhavn O DK-2100
Denmark
Phone: 45-353-20286
EMail: morten@kl4aix.ki.ku.dk

WILLIAM JORGENSEN
Yale University
Chemistry Department
225 Prospect Street
New Haven, CT 06511-8118
USA
Phone: 203-432-3916

ALICIA H. JUBERT
Universidad Nacional de La Plata
Facultad de Ciencias Exactas
CC 962
La Plata 1900
Argentina
Phone: 54-21-259485
Fax: 54-21-259485
EMail: jubert@nahuel.biol.unlp.edu.ar

PETER JURS
Penn State University
Dept. of Chemistry
152 Davey Lab.
University Park, PA 16802
USA
Phone: 814-865-3739
Fax: 814-865-3314
EMail: pcj@psu.edu

SABRE KAIS
Purdue University
Chemistry Department
1393 Brown Building
West Lafayette, IN 47907
USA
Phone: 317-494-5965
Fax: 317-494-0239
EMail: sabre@salam.chem.purdue.edu

JEAN KARLE
Walter Reed Army Institute of Research
Pharmacology
Division of Experimental Therapeutics
Washington, DC 20307-5100
USA
Phone: 301-295-7191
Fax: 301-295-7755
EMail: dr.-jean-karle@wrsmtp-ccmail.army.mil

JEROME KARLE
Naval Research Laboratory
Laboratory for the Structure of Matter
Code 6030 Naval Research Laboratory
Washington, DC 20375-5341
USA
Phone: 202-767-2665
Fax: 202-767-0953
EMail: williams@harker.nrl.navy.mil

SASHI KARNA
U.S. Air Force Phillips Laboratory, VTM
Space Mission Technologies Div.
3550 Aberdeen Ave. SE
Kirtland AFB, NM 87117-5776
USA
Phone: 505-853-3158
Fax: 505-846-2290
EMail: karnas@plk.af.mil

MICHAEL KASHA
Florida State University
Inst. of Molec. Biophys.
452 Molecular Biophysics
Tallahassee, FL 32306
USA
Phone: 904-644-6452

HIROYUKI KAWABE
Kinjo College
Secretarial Department 200
Matto, Ishikawa 924
Japan
Phone: 81-762-76-4411
Fax: 81-762-75-4183
EMail: kawabe@kinjo.ac.jp

MICHAEL E. KELLMAN
University of Oregon
Dept. of Chemistry
Eugene, OR 97403
USA
Phone: 541-346-4196
Fax: 541-346-4643
EMail: kellman@oregon.uoregon.edu

CHARLES BRIAN KELLOGG
University of Georgia
Chemistry
4th Old Chemistry
Athens, GA 30602
USA
Phone: 404-542-2067
Fax: 404-542-0406

ANNE-MARIE KELTERER
Technical University of Graz
Physical and Theoretical Chemistry
Rechbauer Street 12
Graz 8010
Austria
Phone: 43-316-873-8727
EMail: kelterer@ptc.tu-graz.ac.at

JAMES W. KING
Foundation for Chemistry
P.O. Box 116
Balsam, NC 28707-0116
USA
Phone: 704-452-7570
Fax: 704-452-5432
EMail: jwking@sprynet.com

BERNARD KIRTMAN
University of California, Santa Barbara
Dept. of Chemistry
Santa Barbara, CA 93106
USA
Phone: 805-893-2217
Fax: 805-893-4120
EMail: kirtman@sbmm1.ucsb.edu

DOUGLAS J. KLEIN
Texas A & M University
Marine Science Department
P.O. Box 1675
Galveston, TX 77553-1675
USA
Phone: 409-740-4512
Fax: 409-740-4429

MARTIN KLESSINGER
Universität Münster
Organisch-Chemisches Institut
Corrensstr. 40
Muenster D-48149
Germany
Phone: 49-251-8333-241
Fax: 49-251-8339-772
EMail: klessim@uni-muenster.de

GILLES KLOPMAN
University of Florida
Chemistry
P.O. Box 118435
Gainesville, FL 32611
USA
Phone: 352-392-6711

TAKAO KOBAYASHI
Osaka University
Grad. School of Science Chemistry
Toyonaka, Osaka 560
Japan
Phone: 81-6-850-5405
Fax: 81-6-843-7744
EMail: tkoba@chem.sci.osaka-u.ac.jp

PETER KOLLMAN
University of California
Pharmaceutical Chemistry Dept.
School of Pharmacy
San Francisco, CA 94143-0446
USA
Phone: 415-476-4637
Fax: 415-476-0688
EMail: pak@cgl.ucsf.edu

ANATOLI KORKIN
University of Florida
Quantum Theory Project
362 WM Hall, P.O. Box 118435
Gainesville, FL 32611-8435
USA
Phone: 352-392-8113
Fax: 352-392-8722
EMail: korkin@qtp.ufl.edu

SVETLANA KOTOCHIGOVA
National Institute of Standards and Technology
Dept. of Physics
A253 Physics Building, Quince Orchard Road
Gaithersburg, MD 20899
USA
Phone: 301-975-3732
Fax: 301-975-3038
EMail: svetlana@bruce.nist.gov

ATILLA KOVÁCS
Budapest Technical University
Inst. for General & Analytical Chemistry
Srt. Gellert ter 4
Budapest H-1521
Hungary
Phone: 36-1-463-3414
Fax: 36-1-463-4052
EMail: kovacs@ch.bme.hu

JEFFREY L. KRAUSE
University of Florida
Quantum Theory Project
372 Williamson Hall, P.O. Box 118435
Gainesville, FL 32611-8435
USA
Phone: 352-392-1597
Fax: 352-392-8722
EMail: krause@qtp.ufl.edu

CARLOS KUBLI-GARFIAS
National Autonomous University of Mexico
Lab. of Hormonal Chemistry
Apdo Postal 70-469
Mexico, DF 04511
Mexico
Phone: 525-6-223815
Fax: 525-5-500048
EMail: kubli@servidor.unam.mx

HENRY KURTZ
University of Memphis
Dept. of Chemistry
Memphis, TN 38152-6060
USA
Phone: 901-678-4414
Fax: 901-678-3447
EMail: kurtz@cc.memphis.edu

JANOS LADIK
Numberg Universität-Erlangen
Inst. of Theoretical Chemistry
Egerlandstrasse 3
Erlangen D-97058
Germany
Phone: 49-9131-857766
Fax: 49-9131-857736
EMail: ladik@pctc.chemie.uni-erlangen.de

WILLIAM LAIDIG
Procter & Gamble Co.
Miami Valley Laboratories, P.O. Box 538707
Cincinnati, OH 45253-8707
USA
Phone: 513-627-2857

DAVID LANGRETH
Rutgers University
Dept. of Physics & Astronomy
P.O. Box 849
Piscataway, NJ 08855-0849
USA
Phone: 908-445-3882
Fax: 908-445-4400
EMail: langreth@physics.rutgers.edu

PIERRE LEBRETON
University of Illinois at Chicago
Dept. of Chemistry
845 W. Taylor St.
Chicago, IL 60607-7061
USA
Phone: 312-996-5431
Fax: 312-996-0431
EMail: lebreton@uic.edu

ROLAND LEFEBVRE
Univ. de Paris SUD
Laborataire de Photophysique Moleculaire
Lab. Photphys. Molbatiment 213
Orsay F-09405
France
Phone: 33-1-63416533
Fax: 33-1-69416777 or 33-1-69416704
EMail: roland@lefebvre.ppm.u-psud.fr

VOLIA LEMOS
Universidade Estadual de Campinas
Instituto de Fisica 'Glen Wataguin'
CeP 13083-970
Campinas, SP
Brazil
Phone: 55-19-2393137
Fax: 55-19-2393137
EMail: volia@ifi.unicamp.br

JERZY LESZCZYNSKI
Jackson State University
Dept. of Chemistry
1400 Lynch Street
Jackson, MS 39217
USA
Phone: 601-973-3482
Fax: 601-973-3674
EMail: jerzy@tiger.jsums.edu

ANDREW LIASHENKO
Florida State University
SCRI
Box 152
Tallahassee, FL 32306
USA
Phone: 904-644-2782
Fax: 904-644-0068
EMail: andrew@scri.fsu.edu

ANTONIO TADEU LINO
Universidad Federal de Uberlandia
Depto. de Ciencias Fisicas
Campus Santa Monica
Uberlandia, MG 38400-902
Brazil
Phone: 55-34-235-2888
Fax: 55-34-239-4106
EMail: atlino@inga.ufu.br

IGOR LITVINYUK
Florida State University
Chemistry
Institute of Molecular Biophysics
Tallahassee, FL 32306-3015
USA
Phone: 904-644-6452
Fax: 904-644-3257

GUANGHUA LIU
Florida State University
SCRI
495 Dirac Science Library
Tallahassee, FL 32306-4052
USA
Phone: 904-644-7060
Fax: 904-644-0098
EMail: gliu@scri.fsu.edu

GILDA LOEW
Molecular Research Institute
845 Page Mill Road
Palo Alto, CA 94304
USA
Phone: 415-424-9924
Fax: 415-424-9501
EMail: loew@montara.molres.org

PER-OLOV LÖWDIN
University of Florida
Quantum Theory Project
365 Williamson Hall, P.O. Box 118435
Gainesville, FL 32611-8435
USA
Phone: 352-392-1597
Fax: 352-392-8722
EMail: lowdin@qtp.ufl.edu

HECTOR LUNA-GARCÍA
Universidad Autonoma Metropolitana-
Azcapotzalco
Ciencias Basicas
Av. San Pablo 180
Mexico, DF 02200
Mexico
Phone: 915-724-4218
EMail: lghm@hp9000al.uam.mx

GERALD LUSHINGTON
Army Research Laboratory
AMSRL-WM-PC
Aberdeen, MD 21005-5066
USA
Phone: 410-278-6182
Fax: 410-278-6150
EMail: ghl@arl.mil

UKO MARAN
University of Florida
Department of Chemistry
229 Chemistry Research Bldg.
Gainesville, FL 32611-7200
USA
Phone: 352-392-0554
Fax: 352-392-9199
EMail: uko@ufark2.chem.ufl.edu

NORMAN MARCH
Oxford University
6 Northcroft Road
Egham, Surrey TW20 ODU
UK

RUDOLPH A. MARCUS
California Institute of Technology
Division of Chemistry
110 Noyes Lab. Chem. Physics
Pasadena, CA 91125
USA
Phone: 818-395-6566
Fax: 818-792-8485
EMail: ram@caltech;edu

JAN MARKUSSEN
Copenhagen University
Department of Chemistry
Universitetsparken 5
Copenhagen DK-2100
Denmark
Phone: 45-3-532-0286
EMail: jan@kl4aix.ki.ku.dk

JOSE MARTÍNEZ-MAGADÁN
Instituto Mexicano del Petroleo
SIGA, Eje Central Lazaro Cardenas 152, AP 14805
Mexico, DF 07730
Mexico
Phone: 52-3685911

LOU MASSA
City University of New York
Dept. of Chemistry
695 Park Avenue
New York, NY 10021
USA
Phone: 212-772-5330
Fax: 212-772-5332
EMail: massa@mvaxgr.hunter.cuny.edu

RICHARD J. MATHAR
University of Florida
Quantum Theory Project
368 Williamson Hall, P.O. Box 118435
Gainesville, FL 32611-8435
USA
Phone: 352-392-1597
Fax: 352-392-8722
EMail: mathar@qtp.ufl.edu

FRANCISCO JAVIER MELÉNDEZ BUSTAMANTE
Inst. de Estructura de la Materia CSIC
Lab. de Quimica Cuantica
Serrano 123
Madrid E-28006
Spain
Phone: 34-1-585-54-04
Fax: 34-1-585-51-84
EMail: emmelendez@roca.csic.es

CELSO PINTO DE MELO
Universidade Federal de Pernambuco
Departamento de Fisica
50 670-901 Recife PE Brazil
Recife, Pernambuco
Brazil
Phone: 1-55-81-271-8450
Fax: 1-55-81-271-0359
EMail: celso@df.ufpe.br

DAVID A. MICHA
University of Florida
Quantum Theory Project
366 Williamson Hall, P.O. Box 118435
Gainesville, FL 32611-8435
USA
Phone: 352-392-2597
Fax: 352-392-8722
EMail: micha@qtp.ufl.edu

HENDRIK J. MONKHORST
University of Florida
Quantum Theory Project
362 Williamson Hall, P.O. Box 118435
Gainesville, FL 32611-8435
USA
Phone: 352-392-1597
Fax: 352-392-8722
EMail: monkhors@qtp.ufl.edu

MARCO ANTONIO MORA-DELGADO
Universidad Autonoma Metropolitana - Iztapalapa
Dpto. de Quimica
Av. Michoacan y La Purisima, Col Vicentina
Iztapalapa, D F C P 09340
Mexico
Phone: 52-5-724-4675
Fax: 52-5-724-4666
EMail: mam@xanum.uam.mx

JORGE A. MORALES
University of Florida
Quantum Theory Project
348 Williamson Hall, P.O. Box 118435
Gainesville, FL 32611-8435
USA
Phone: 352-392-1597
Fax: 352-392-8722
EMail: morales@qtp.ufl.edu

JOHN D. MORGAN
University of Delaware
Dept. of Physics & Astronomy
Newark, DE 19716
USA
Phone: 302-831-2661
Fax: 302-831-1637
EMail: 32399@udel.edu

AKIHIRO MORITA
Kyoto University
Dept. of Chemistry
Kitashirakawa Sakyo-Ku
Kyoto 606
Japan
Phone: 81-75-753-4006
EMail: morita@kuchem.kyoto-u.ac.jp

RONALDO MOTA
Universidade Federal de Santa Maria
Dept. de Fisica
Santa Maria, RS 97119-900
Brazil
Phone: 55-55-2261616
Fax: 55-55-2262919
EMail: mota@super.ufsm.br

BENGT NAGEL
Royal Institute of Technology
Dept. of Physics
Stockholm S-100 44
Sweden
Phone: 46-8-7907168
Fax: 46-8-104879
EMail: nagel@theophys.kth.se

DENNIS M. NEWNS
IBM
T. J. Watson Laboratory
P.O. Box 218
Yorktown Heights, NY 10598
USA
Phone: 914-945-3551
Fax: 914-945-2141
EMail: dmnewns@watson.ibm.com

MARSHALL NEWTON
Brookhaven National Laboratory
Dept. of Chemistry
P.O. Box 5000
Upton, NY 11973
USA
Phone: 516-344-4366
Fax: 516-344-5815
EMail: newton@bnl.gov

SONJA NIKOLIC
The Rugjer Boskovic Institute
Physical Chemistry Dept.
Bijenicka 54
Zagreb 10001
Croatia
Phone: 385-1-424689
Fax: 385-1-272648
EMail: sonja@olimp.irb.hr

MARCEL NOOIJEN
University of Florida
Quantum Theory Project
343 Williamson Hall, P.O. Box 118435
Gainesville, FL 32611-8435
USA
Phone: 352-392-1597
Fax: 352-392-8722
EMail: nooijen@qtp.ufl.edu

TED O'BRIEN
University of Florida
Quantum Theory Project
201 CRB, P.O. Box 118435
Gainesville, FL 32611
USA
Phone: 352-392-9306
Fax: 352-392-8722
EMail: obrien@qtp.ufl.edu

YNGVE ÖHRN
University of Florida
Quantum Theory Project
363 Williamson Hall, P.O. Box 118435
Gainesville, FL 32611-8435
USA
Phone: 352-392-1597
Fax: 352-392-8722
EMail: ohrn@qtp.ufl.edu

KOJI OHTA
Osaka National Research Institute, AIST, MITI
Dept. of Optical Materials
1-8-31 Midorigaoka
Ikeda, Osaka 563
Japan
Phone: 81-6-727-51-9523
Fax: 81-6-727-51-9628
EMail: ohta@onri.go.jp

JOSEP M. OLIVA
University of Bristol
Dept. of Chemistry
Cantocks Close
Bristol BS8 1TS
UK
Phone: 44-117-928-9000 EXT 4271
Fax: 44-117-925-1295
EMail: j.m.oliva@bristol.ac.uk

MONICA OLIVA
Universitat Jaune I
Dept. de Ciencies Experimentals
Box 242
Castellon 12080
Spain
Phone: 34-64-345741
Fax: 34-64-345654
EMail: oliva@vents.uji.es

JOSE ONUCHIC
University of California, San Diego
Dept. of Physics
9500 Gilman Drive
La Jolla, CA 92093
USA
Phone: 619-534-7067
Fax: 619-534-7697
EMail: jonuchic@ucsd.edu

VINCENT ORTIZ
Kansas State University
Dept. of Chemistry
Manhattan, KS 66506-3701
USA
Phone: 913-532-6665
Fax: 913-532-6666
EMail: ortiz@ksu.edu

ROMAN OSMAN
Mt. Sinai School of Medicine
Dept. Physiology & Biophysics
Box 1218
New York, NY 10029
USA
Phone: 212-241-5609
Fax: 212-860-3369
EMail: osman@msvax.mssm.edu

NEIL OSTLUND
Hypercube, Inc.
419 Phillip St., Unit 7
Waterloo, Ontario N2L 3X2
Canada
Phone: 519-725-4040

GEORGE R. PACK
University of Illinois
College of Medicine
1601 Parkview Ave.
Rockford, IL 61107
USA
Phone: 815-395-5694
Fax: 815-395-5666
EMail: georgep@uic.edu

JOSEPH M. PAIKEDAY
Southeast Missouri State University
Dept. of Physics
One University Plaza MS 6600
Cape Girardeau, MO 63701-4799
USA
Phone: 573-651-2393
Fax: 573-651-2223
EMail: c314scp@semovm.semo.edu

GREG MARTIN PEARL
University of Florida
Quantum Theory Project
P.O. Box 118435
Gainesville, FL 32611
USA
Phone: 352-392-1597
Fax: 352-392-8722
EMail: pearl@qtp.ufl.edu

AJITH S. PERERA
University of Florida
Quantum Theory Project
343 Williamson Hall, P.O. Box 118435
Gainesville, FL 32611-8435
USA
Phone: 352-392-1597
Fax: 352-392-8722
EMail: perera@qtp.ufl.edu

WILLIS PERSON
University of Florida
Department of Chemistry
P.O. Box 117200
Gainesville, FL 32611-7200
USA
Phone: 352-392-0528

PAULO PIQUINI
Universidade Federal de Santa Maria
Dpto. de Fisica
Santa Maria, RS 97119-900
Brazil
Phone: 55-55-2262919
Fax: 55-55-2262919
EMail: ppiquini@oslo.ccne.ufsm.br

PAWEL PISKORZ
Florida State University
SCRI
495 Dirac Science Library
Tallahassee, FL 32306-4052
USA
Phone: 904-644-4060
Fax: 904-644-0098
EMail: pawel@scri.fsu.edu

EMIL POP
Pharmos Corporation
2 Innovation Drive
Alachua, FL 32615
USA
Phone: 352-462-1210
Fax: 352-462-5401
EMail: emilpop@aol.com

JOHN POPLE
Northwestern University
Dept. of Chemistry
2145 Sheridan Road
Evanston, IL 60208-3113
USA
Phone: 847-491-3403
Fax: 847-491-7713
EMail: pople@lithium.chem.nwu.edu

LEONARD E. PORTER
Washington State University
Radiation Safety Office
Pullman, WA 99164-1302
USA
Phone: 509-335-7057
Fax: 509-335-1615
EMail: porterl@mail.wsu.edu

ENRIQUE POULAIN
Instituto Technologico de Tlalnepantla
Division de Estudios de Posgrado
Apdo Postal 750
Tlalnepantla de Baz 54070
Mexico
Phone: 52-5-390-0310
Fax: 52-5-565-3910
EMail: sca@hp9000a1.uam.mx

MICHAEL PROBST
Innsbruck University
Dept. of Inorganic Chemistry
Innrain 520
Innsbruck A-6020
Austria
Phone: 43-512-5075153
Fax: 43-512-5072934
EMail: michael.probst@uibk.ac.at

PETER PULAY
University of Arkansas
Department of Chemistry
Fayetteville, AR 72701-1201
USA
Phone: 501-575-6612
EMail: pp24139@uafsysb.uark.edu

GEORGE PURVIS
Oxford Molecular
P.O. Box 4003
Beaverton, OR 97076
USA
Phone: 503-526-5000
Fax: 503-526-5099
EMail: gpurvis@oxmol.com

CARLOS QUINTANAR
Universidad Nacional Autonoma de México
Facultad de Ciencias
Mexico, DF C.P.04510
Mexico
Phone: 525-622-50-86
Fax: 525-616-15-35
EMail: cqs@moon.iflsicacu.unam.mx

JAMES RABINOWITZ
U.S. Environmental Protection Agency
MD-68, Health Effects Research Laboratory
Research Triangle Park, NC 27711
USA
Phone: 919-541-5714
Fax: 919-541-0694
EMail: sar@linus.herl.epa.gov

MICHAEL RAMEK
Technische Universität Graz
Phys. & Theor. Chemistry
Graz A-8010
Austria
Phone: 43-316-873-8227
Fax: 43-316-873-8720
EMail: ramek@ptc.tu-graz.ac.at

MILAN RANDIC
Drake University
Dept. of Math & Computer Science
Des Moines, IA 50311
USA
Phone: 515-271-2163
Fax: 515-271-2055

VITALY RASSOLOV
Northwestern University
Dept. of Chemistry
2145 Sheridan Road
Evanston, IL 60208
USA
Phone: 847-491-3423
Fax: 847-491-7713
EMail: rassolov@chem.nwu.edu

JOSE RÉCAMIER
Universidad Nacional Autonoma de Mexico
Lab Cuernavaca
Apdo. Postal 48-3
Cuernavaca, Morelos 62251
Mexico
Phone: 52-5-622-7763
Fax: 52-7-317-3077
EMail: pepe@ce.itisicam.unam.mx

WILLIAM RHODES
Florida State University
Dept. of Chemistry
Tallahassee, FL 32306-3006
USA
Phone: 904-644-1227
Fax: 904-644-8281
EMail: rhodes@chem.fsu.edu

RANDY RICH
Silicon Graphics
2011 N. Shoreline Blvd.
Mountainview, CA 94039-7311
USA
Phone: 415-933-1772
Fax: 415-932-1772

NIGEL RICHARDS
University of Florida
Dept. of Chemistry
P.O. Box 117200
Gainesville, FL 32611-7200
USA
Phone: 352-392-3601
Fax: 352-846-2095
EMail: richards@qtp.ufl.edu

UWE RISS
University of Heidelberg
Physikalisch-Chemisches Institut
Heidelberg 69120
Germany
Phone: 49-6221-545209
Fax: 49-6221-545209
EMail: uwer@tc.pci.uni-heidelberg.de

JUVENCIO ROBLES
University of Guanajuato
Facultad de Quimica
Noria Alta A/N
Guanajuato, GTO 36050
Mexico
Phone: 52-473-26885
Fax: 52-473-24250
EMail: roblesj@quijote.ugto.mx

NOTKER RÖSCH
Technische Universität München
Inst. fur Physik. & Theo. Chem.,
Lichtenbergstrasse 4
Garching D-85747
Germany
Phone: 49-89-2891-3616
Fax: 49-89-2891-3622
EMail: rosch@qtp.ufl.edu

RICHARD B. ROSS
PPG Industries Inc.
4325 Rosanna Drive, P.O. Box 9
Allison Park, PA 15101
USA
Phone: 412-492-5359

PIOTR B. ROZYCZKO
University of Florida
Quantum Theory Project
345 Williamson Hall, P.O. Box 118435
Gainesville, FL 32611-8435
USA
Phone: 352-392-1597
Fax: 352-392-8722
EMail: rozyczko@qtp.ufl.edu

KEITH RUNGE
University of Florida
Quantum Theory Project
376 Williamson Hall, P.O. Box 118435
Gainesville, FL 32611-8435
USA
Phone: 352-392-1597
Fax: 352-392-8722
EMail: runge@qtp.ufl.edu

JOHN R. SABIN
University of Florida
Quantum Theory Project
355 Williamson Hall, P.O. Box 118435
Gainesville, FL 32611-8435
USA
Phone: 352-392-1597
Fax: 352-392-8722
EMail: sabin@qtp.ufl.edu

RAYMOND SADEGHI
University of Florida
Quantum Theory Project
379 Williamson Hall, P.O. Box 118435
Gainesville, FL 32611-8435
USA
Phone: 352-392-1597
Fax: 352-392-8722
EMail: rsadeghi@qtp.ufl.edu

VIRAHT SAHNI
Brooklyn College of CUNY
Department of Physics
2900 Bedford Avenue
Brooklyn, NY 11210-2889
USA
Phone: 718-951-5785
Fax: 718-951-4407
EMail: vvvbc@cunyvm.cuny.edu

SHOGO SAKAI
Osaka Sangyo University
Dept. of Information Systems Engineering
Daito 574
Japan
Phone: 81-720-89-2538
Fax: 81-720-89-2539
EMail: sakai@ise.osaka-sandai.ac.jp

JULIO R. SAMBRANO
Universidade Estadual Paulista
Depto de Matematica
CP 473
Bauru, SP 17030 360
Brazil
Phone: 55-16-2721561
EMail: pjrs@power.ufscar.br

RICHARD SAYKALLY
University of California, Berkeley
Dept. of Chemistry
419 Latimer Hall MC 1460
Berkeley, CA 94720-1460
USA
Phone: 510-642-8269
Fax: 510-642-8369
EMail: saykally@cchem.berkeley.edu

HAROLD SCHERAGA
Cornell University
Baker Lab. of Chemistry
Ithaca, NY 14853-1307
USA
Phone: 607-255-4034
Fax: 607-254-4700
EMail: has5@cornell.edu

PETER SCHMIDT
Office of Naval Research
Chemistry Division
Code 1113, 800 North Quincy Street
Arlington, VA 22217-5000
EMail: schmidt@onrhq.onr.navy.mil

WILLIAM F. SCHNEIDER
Ford Motor Co.
Chemistry Dept.
P.O. Box 2053 MD 3083/SLR
Dearborn, MI 48121-2053
USA
Phone: 313-323-2064
Fax: 313-594-2923
EMail: wschnei2@ford.com

DIETER SCHUCH
J.W. Goethe-Universität
Inst. fur Theoretische Physik
Robert-Mayer
D-60054 Frankfurt Am Main
Germany
Phone: 49-69-319523
Fax: 49-69-3088997

KLAUS SCHULTEN
University of Illinois
Beckman Institute
405 N. Mathews Avenue
Urbana, IL 61801
USA
Phone: 217-244-1604
Fax: 217-244-6078
EMail: kschulte@ks.uiuc.edu

SANJA SEKUSAK
Rugjer Boskovic Institute
Dept. of Chemistry
Bijenicka 54, P.O. Box 10
Zagreb
Croatia
Phone: 385-1-4561-089
Fax: 385-1-272-648
EMail: sanja@indigo.irb.hr

JORGE M. SEMINARIO
University of New Orleans
Department of Chemistry
New Orleans, LA 70148
USA
Phone: 504-286-7216
Fax: 504-286-6860
EMail: jsmcm@uno.edu

EUGENE SHAKHNOVICH
Harvard University
Depts. of Chemistry & Chemical Biology
12 Oxford Street
Cambridge, MA 02138
USA
Phone: 617-495-4130
Fax: 617-496-5948
EMail: eugene@diamond.harvard.edu

YASU TERU SHIGETA
Kanazawa University
Dept. of Chemistry
Kakuma Machi
Kanazawa 920-11
Japan
Phone: 81-732-64-5686
EMail: kiyoshi@wriron1.s.kanazawa-u.ac.jp

JEFFREY SKOLNICK
Scripps Research Institute
Dept. of Molecular Biology
10550 North Torrey Pines Road
La Jolla, CA 92037
USA
Phone: 619-784-8821
Fax: 619-784-8895
EMail: skolnick@scripps.edu

YVES G. SMEYERS
Superior Council for Scientific Investigations
Institute of Matter Structure
Calle Serrano No. 123
Madrid E-28006
Spain
Phone: 34-1-5855404
Fax: 34-1-5642431
EMail: emsmeyers@roca.csic.es

JOSE M. SOLER
Universidad Autonoma de Madrid
Dept. Fisica Mat. Cond.
Madrid E-28049
Spain
Phone: 34-1-3975550
Fax: 34-1-3973961
EMail: jose@polar.fmc.uam.es

RAMON SOSA
Universidad de la Republica
Inst. of Physics
Ada Herrera Reissig 565
Montevideo 11300
Uruguay
Phone: 598-2-710905
Fax: 598-2-711630
EMail: rsosa@fing.edu.uy

RICHARD SQUIRE
Marshall University
Chemistry Department
901 W. DuPont Avenue
Belle, WV 25015
USA
Phone: 304-965-3084
Fax: 304-357-1230

VOLKER STAEMMLER
Ruhr-Universität Bochum
Lehrstuhl fur Theoretische Chemie
Universitatsstr 150
Bochum D-44801
Germany
Phone: 49-234-7006752
Fax: 49-234-7094109
EMail: staemm@mokat50.theochem.ruhr-uni-bochum.de

KRASSIMIR K. STAVREV
University of Florida
Quantum Theory Project
380 Williamson Hall, P.O. Box 118435
Gainesville, FL 32611-8435
USA
Phone: 352-392-1597
Fax: 352-392-8722
EMail: stavrev@qtp.ufl.edu

WALTER STEVENS
National Institute of Standards and Technology
Building 221, Room A111
Gaithersburg, MD 20899
USA
Phone: 301-975-5968
Fax: 301-869-4020
EMail: walter.stevens@nist.gov

HEGE STROMSNAS
University of Florida
Quantum Theory Project
P.O. Box 118435
Gainesville, FL 32611-8435
USA
Phone: 352-392-1597
Fax: 352-392-8722

ALEXEI A. STUCHEBRUKHOV
University of California, Davis
Dept. of Chemistry
Davis, CA 95616
USA
Phone: 916-752-7778
Fax: 916-752-8995
EMail: stuchebr@chem.ucdavis.edu

TZU-MIN SU

National Taiwan University
Dept. of Chemistry
Taipei
Taiwan
Phone: 886-2-3630231
Fax: 886-2-3636359
EMail: tmsu@rs350.ch.ntu.edu.tw

JUN-QIANG SUN
University of Florida
Quantum Theory Project
386 Williamson Hall, P.O. Box 118435
Gainesville, FL 32611-8435
USA
Phone: 352-392-1597
Fax: 352-392-8722
EMail: sun@qtp.ufl.edu

KRYSTYNA SZCZEPANIAK-PERSON
University of Florida
Dept. of Chemistry
P.O. Box 117200
Gainesville, FL 32611-7200
USA
Phone: 352-392-4653
Fax: 352-392-0872
EMail: ksperson@pine.circa.ufl.edu

JAMES TALMAN
University of Western Ontario
Dept. of Applied Mathematics
WSC 173
London, Ontario N6A 5B7
Canada
Phone: 519-679-2111, ext. 8800
Fax: 519-661-3523
EMail: jdt@apmaths.uwo.ca

BRIAN THORNDYKE
University of Florida
Computer and Inf. Sciences
301 CSE
Gainesville, FL 32611
USA
Phone: 352-392-1435
EMail: thorndyb@cise.ufl.edu

KATARZYIVA TKACZ-SMIECH
Technical University of Mining and Metallurgy
Faculty of Materials Science & Ceramic
AL MICV IEWICZA 30
Krakow 30-059
Poland
Phone: 48-12-173788
Fax: 48-12-331593
EMail: smiech@uci.agh.edu.pl

SAMUEL B. TRICKEY
University of Florida
Quantum Theory Project
364 Williamson Hall, P.O. Box 118435
Gainesville, FL 32611-8435
USA
Phone: 352-392-1597
Fax: 352-392-8722
EMail: trickey@qtp.ufl.edu

NENAD TRINAJSTIC
Rugjer Boskovic Institute
Dept. of Physics and Chemistry
P.O. Box 1016
Zagreb HR 41001
Croatia
Phone: 385-1-424683
Fax: 385-1-272648
EMail: trina@olimp.irb.hr

JOHN TULLY
Yale University
Dept. of Chemistry
225 Prospect Street
New Haven, CT 06520
USA
Phone: 203-432-3934
Fax: 203-432-6144
EMail: tully@onsager.chem.yale.edu

PIET VAN DUIJNEN
University of Groningen
Dept. of Chemistry
Bldg. 223
Groningen, AG 9747-AG
Netherlands
Phone: 31-50-3634373
Fax: 31-50-3634290
EMail: ptvd@chem.rug.nl

CAROLYNE M. VAN VLIET
Florida International University
Dept. of Elect. & Comp. Engineering
University Park
Miami, FL 33199
USA
Phone: 305-348-3709
Fax: 305-348-3707
EMail: vanvliet@eng.fiu.edu

LASZLO VON SZENTPALY
University of the West Indies
Chemistry Department
Mona Campus
Kingston
Jamaica
Phone: 809-927-1910
Fax: 809-977-1835
EMail: laszlo@uwimona.edu.jm

DAVID WALES
University of Cambridge
University Chemistry Lab.
Lensfield Road
Cambridge CB2 1EW
UK
Phone: 44-01223-336354
Fax: 44-01223-336362
EMail: dw34@clust.ch.cam.uc.uk

JIAN WANG
University of Florida
Quantum Theory Project
P.O. Box 118435
Gainesville, FL 32611
USA
Phone: 352-392-8113
Fax: 352-392-8722
EMail: wang@qtp.ufl.edu

ARIEH WARSHEL
University of Southern California
Chemistry Department
University Park
Los Angeles, CA 90089
USA
Phone: 213-740-4114

JOHN WATTS
University of Florida
Quantum Theory Project
367 Williamson Hall, P.O. Box 118435
Gainesville, FL 32611-8435
USA
Phone: 352-392-6714
Fax: 352-392-8722
EMail: watts@qtp.ufl.edu

CHARLES WEATHERFORD
Florida A & M University
Dept. of Physics
205 Jones Hall
Tallahassee, FL 32307
USA
Phone: 904-599-3470
Fax: 904-599-3577
EMail: weatherf@ccnnas.nhmfl.gov

BRIAN WEINER
Pennsylvania State University
Dept. of Physics
College Place
Dubois, PA 15801
USA
Phone: 814-375-4700
Fax: 814-234-4291
EMail: bqw@psu.edu

HAREL Y. WEINSTEIN
Mt. Sinai School of Medicine
Physiology & Biophysics Dept.
One Gustave L. Levy Place
New York, NY 10029-6574
USA
Phone: 212-241-7018
Fax: 212-860-3369
EMail: hweinstein@msvax.mssm.edu

HORST WEISS
BASF Aktiengesellschaft
Zk/C - Tagungen, Bldg. B1
Ludwigshafen 67056
Germany
Phone: 49-621-60-41949
Fax: 49-621-60-21863
EMail: weiss@steve.zk.basf-ag-de

KENNETH WILSON
University of Florida
Quantum Theory Project
P.O. Box 118435
Gainesville, FL 32611-8435
USA
Phone: 352-392-1597
Fax: 352-392-8722
EMail: wilson@qtp.ufl.edu

PETER WINKLER
University of Nevada
Department of Physics 220
Reno, NV 89557-0058
USA
Phone: 702-784-6792
Fax: 702-784-1398
EMail: winkler@rigel.physics.unr.edu

LINDA WONG
University of Illinois
College of Medicine
1601 Parkview Avenue
Rockford, IL 61107
USA
Phone: 815-395-5691
Fax: 815-395-5666
EMail: lindaw@uic.edu

MARGARET WORKMAN
Purdue University
Department of Chemistry
1393 Brown Building
West Lafayette, IN 47906
USA
Phone: 317-496-2409
Fax: 317-494-0239
EMail: workman@coriolis.atms.purdue.edu

DAVID YARON
Carnegie-Mellon University
Department of Chemistry
4400 5th Avenue
Pittsburgh, PA 15213
USA
Phone: 412-268-1351
Fax: 412-268-1061
EMail: yaron@andrew.cmu.edu

ANTHONY YAU
University of Florida
Quantum Theory Project
P.O. Box 118435
Gainesville, FL 32611-8435
USA
Phone: 352-392-7184
Fax: 352-392-8722
EMail: yau@qtp.ufl.edu

TAI-SHENG YEH
National Taiwan University
Dept. of Chemistry
Taipei 106
Taiwan
Phone: 886-2-3630231 EXT 2326
Fax: 886-2-3636359
EMail: tsyeh@rs350.ch.ntu.edu.tw

ZHIGANG YI
University of Florida
Quantum Theory Project
348 Williamson Hall, P.O. Box 118435
Gainesville, FL 32611-8435
USA
Phone: 352-392-1597
Fax: 352-392-8722
EMail: yi@qtp.ufl.edu

YASUNORI YOSHIOKA
Osaka University
Dept. of Chemistry
Toyonaka, Osaka 560
Japan
Phone: 81-6-850-5807
Fax: 81-6-843-7744
EMail: yyoshi@chem.sci.osaka-u.ac.jp

ANGELICA G. ZACARIAS
Universidad Nacional Automona de Mexico
Dept. de Fisica y Quimica Teorica
Mexico, DF CP 04510
Mexico
Phone: 52-5-622-3783
Fax: 52-5-616-2010
EMail: zacarias@papalotl.pquim.unam.mx

KARL ZACHARY
University of Florida
Dept. of Chemistry
P.O. Box 117200
Gainesville, FL 32611-7200
USA
Phone: 352-392-5876
Fax: 352-392-0872
EMail: karl@physical4.chem.ufl.edu

MICHAEL C. ZERNER
University of Florida
Quantum Theory Project
382 Williamson Hall, P.O. Box 118435
Gainesville, FL 32611-8435
USA
Phone: 352-392-1597
Fax: 352-392-8722
EMail: zerner@qtp.ufl.edu

JOHN ZHANG
New York University
Dept. Chemistry
4 Washington Place, Room 514
New York, NY 10003
USA
Phone: 212-998-8412
Fax: 212-260-7905
EMail: zhang@risc.nyu.edu

XUEHE ZHENG
University of Florida
Quantum Theory Project
201 CRB, P.O. Box 118435
Gainesville, FL 32611
USA
Phone: 352-392-9306
Fax: 352-392-8722
EMail: zheng@qtp.ufl.edu

ALEX ZUNGER
National Renewable Energy Laboratory
1617 Cole Blvd.
Golden, CO 80401
USA
Phone: 303-384-6531
EMail: alex-zunger@nrel.gov

WOJCIECH H. ZUREK
Los Alamos National Laboratory
P.O. Box 1663
Los Alamos, NM 87545
USA
Phone: 505-667-6837
Fax: 505-665-3003
EMail: whz@lanl.gov

Published Symposia of the *International Journal of Quantum Chemistry*

1967 QUANTUM CHEMISTRY SYMPOSIUM NO. 1
(Proceedings of the International Symposium on Atomic, Molecular, and Solid-State Theory)

1968 QUANTUM CHEMISTRY SYMPOSIUM NO. 2
(Proceedings of the International Symposium on Atomic, Molecular, and Solid-State Theory and Quantum Biology)

1969 QUANTUM CHEMISTRY SYMPOSIUM NO. 3 PART 1
(Proceedings of the International Symposium on Atomic, Molecular, and Solid-State Theory and Quantum Biology)

1970 QUANTUM CHEMISTRY SYMPOSIUM NO. 3 PART 2
(Proceedings of the International Symposium on Atomic, Molecular, and Solid-State Theory and Quantum Biology)

1971 QUANTUM CHEMISTRY SYMPOSIUM NO. 4
(Proceedings of the International Symposium on Atomic, Molecular, and Solid-State Theory and Quantum Biology)

1971 QUANTUM CHEMISTRY SYMPOSIUM NO. 5
(Proceedings of the International Symposium on Atomic, Molecular, and Solid-State Theory and Quantum Biology)

1972 QUANTUM CHEMISTRY SYMPOSIUM NO. 6
(Proceedings of the International Symposium on Atomic, Molecular, and Solid-State Theory and Quantum Biology)

1973 QUANTUM CHEMISTRY SYMPOSIUM NO. 7
(Proceedings of the International Symposium on Atomic, Molecular, and Solid-State Theory and Quantum Biology)

1974 QUANTUM CHEMISTRY SYMPOSIUM NO. 8
(Proceedings of the International Symposium on Atomic, Molecular, and Solid-State Theory and Quantum Statistics)
QUANTUM BIOLOGY SYMPOSIUM NO. 1
(Proceedings of the International Symposium on Quantum Biology and Quantum Pharmacology)

1975 QUANTUM CHEMISTRY SYMPOSIUM NO. 9
(Proceedings of the International Symposium on Atomic, Molecular, and Solid-State Theory and Quantum Statistics)
QUANTUM BIOLOGY SYMPOSIUM NO. 2
(Proceedings of the International Symposium on Quantum Biology and Quantum Pharmacology)

1976 QUANTUM CHEMISTRY SYMPOSIUM NO. 10
(Proceedings of the International Symposium on Atomic, Molecular, and Solid-State Theory and Quantum Statistics)
QUANTUM BIOLOGY SYMPOSIUM NO. 3
(Proceedings of the International Symposium on Quantum Biology and Quantum Pharmacology)

1977 QUANTUM CHEMISTRY SYMPOSIUM NO. 11
(Proceedings of the International Symposium on Atomic, Molecular, and Solid-State Theory, Collision Phenomena, and Computational Methods)
QUANTUM BIOLOGY SYMPOSIUM NO. 4
(Proceedings of the International Symposium on Quantum Biology and Quantum Pharmacology)

1978 QUANTUM CHEMISTRY SYMPOSIUM NO. 12
(Proceedings of the International Symposium on Atomic, Molecular, and Solid-State Theory, Collision Phenomena and Computational Methods)
QUANTUM BIOLOGY SYMPOSIUM NO. 5
(Proceedings of the International Symposium on Quantum Biology and Quantum Pharmacology)

1979 QUANTUM CHEMISTRY SYMPOSIUM NO. 13
(Proceedings of the International Symposium on Atomic, Molecular, and Solid-State Theory, Collision Phenomena, Quantum Statistics, and Computational Methods)
QUANTUM BIOLOGY SYMPOSIUM NO. 6
(Proceedings of the International Symposium on Quantum Biology and Quantum Pharmacology)

1980 QUANTUM CHEMISTRY SYMPOSIUM NO. 14
(Proceedings of the International Symposium on Atomic, Molecular, and Solid-State Theory, Collision Phenomena, Quantum Statistics, and Computational Methods)
QUANTUM BIOLOGY SYMPOSIUM NO. 7
(Proceedings of the International Symposium on Quantum Biology and Quantum Pharmacology)

1981 QUANTUM CHEMISTRY SYMPOSIUM NO. 15
(Proceedings of the International Symposium on Atomic, Molecular, and Solid-State Theory, Collision Phenomena, and Computational Quantum Chemistry)
QUANTUM BIOLOGY SYMPOSIUM NO. 8
(Proceedings of the International Symposium on Quantum Biology and Quantum Pharmacology)

1982 QUANTUM CHEMISTRY SYMPOSIUM NO. 16
(Proceedings of the International Symposium on Quantum Chemistry, Theory of Condensed Matter, and Propagator Methods in the Quantum Theory of Matter)
QUANTUM BIOLOGY SYMPOSIUM NO. 9
(Proceedings of the International Symposium on Quantum Biology and Quantum Pharmacology)

1983 QUANTUM CHEMISTRY SYMPOSIUM NO. 17
(Proceedings of the International Symposium on Atomic, Molecular, and Solid-State Theory, Collision Phenomena and Computational Quantum Chemistry)
QUANTUM BIOLOGY SYMPOSIUM NO. 10
(Proceedings of the International Symposium on Quantum Biology and Quantum Pharmacology)

1984 QUANTUM CHEMISTRY SYMPOSIUM NO. 18
(Proceedings of the International Symposium on Atomic, Molecular, and Solid-State Theory, and Computational Quantum Chemistry)
QUANTUM BIOLOGY SYMPOSIUM NO. 11
(Proceedings of the International Symposium on Quantum Biology and Quantum Pharmacology)

1985 QUANTUM CHEMISTRY SYMPOSIUM NO. 19
(Proceedings of the International Symposium on Atomic, Molecular, and Solid-State Theory, Scattering Problems, Many Body Phenomena, and Computational Quantum Chemistry)
QUANTUM BIOLOGY SYMPOSIUM NO. 12
(Proceedings of the International Symposium on Quantum Biology and Quantum Pharmacology)

1986 QUANTUM CHEMISTRY SYMPOSIUM NO. 20
(Proceedings of the International Symposium on Atomic, Molecular, and Solid-State Theory, Scattering Problems, Many Body Phenomena, and Computational Quantum Chemistry)

1986 QUANTUM BIOLOGY SYMPOSIUM NO. 13
(Proceedings of the International Symposium on Quantum Biology and Quantum Pharmacology)

1987 QUANTUM CHEMISTRY SYMPOSIUM NO. 21
(Proceedings of the International Symposium on Quantum Chemistry, Solid-State Theory, and Computational Methods)
QUANTUM BIOLOGY SYMPOSIUM NO. 14
(Proceedings of the International Symposium on Quantum Biology and Quantum Pharmacology)

1988 QUANTUM CHEMISTRY SYMPOSIUM NO. 22
(Proceedings of the International Symposium on Quantum Chemistry, Solid-State Theory, and Computational Methods)
QUANTUM BIOLOGY SYMPOSIUM NO. 15
(Proceedings of the International Symposium on Quantum Biology and Quantum Pharmacology)

1989 QUANTUM CHEMISTRY SYMPOSIUM NO. 23
(Proceedings of the International Symposium on Quantum Chemistry, Solid-State Theory, and Molecular Dynamics)
QUANTUM BIOLOGY SYMPOSIUM NO. 16
(Proceedings of the International Symposium on Quantum Biology and Quantum Pharmacology)

1990 QUANTUM CHEMISTRY SYMPOSIUM NO. 24
(Proceedings of the International Symposium on Quantum Chemistry, Solid State Physics, and Computational Methods)
QUANTUM BIOLOGY SYMPOSIUM NO. 17
(Proceedings of the International Symposium on Quantum Biology and Quantum Pharmacology)

1991 QUANTUM CHEMISTRY SYMPOSIUM NO. 25
(Proceedings of the International Symposium on Quantum Chemistry, Solid State Physics, and Computational Methods)
QUANTUM BIOLOGY SYMPOSIUM NO. 18
(Proceedings of the International Symposium on Quantum Biology and Quantum Pharmacology)

1992 QUANTUM CHEMISTRY SYMPOSIUM NO. 26
(Proceedings of the International Symposium on Atomic, Molecular, and Condensed Matter Theory and Computational Methods)
QUANTUM BIOLOGY SYMPOSIUM NO. 19
(Proceedings of the International Symposium on the Application of Fundamental Theory to Problems of Biology and Pharmacology)

1993 QUANTUM CHEMISTRY SYMPOSIUM NO. 27
(Proceedings of the International Symposium on Atomic, Molecular, and Condensed Matter Theory and Computational Methods)
QUANTUM BIOLOGY SYMPOSIUM NO. 20
(Proceedings of the International Symposium on the Application of Fundamental Theory to Problems of Biology and Pharmacology)

1994 QUANTUM CHEMISTRY SYMPOSIUM NO. 28
(Proceedings of the International Symposium on Atomic, Molecular, and Condensed Matter Theory and Computational Methods)
QUANTUM BIOLOGY SYMPOSIUM NO. 21
(Proceedings of the International Symposium on the Application of Fundamental Theory to Problems of Biology and Pharmacology)

1995 QUANTUM CHEMISTRY SYMPOSIUM NO. 29
(Proceedings of the International Symposium on Atomic, Molecular, and Condensed Matter Theory and Computational Methods)
QUANTUM BIOLOGY SYMPOSIUM NO. 22
(Proceedings of the International Symposium on the Application of Fundamental Theory to Problems of Biology and Pharmacology)

1996 QUANTUM CHEMISTRY SYMPOSIUM NO. 30
(Proceedings of the International Symposium on Atomic, Molecular, and Condensed Matter Theory and Computational Methods)
QUANTUM BIOLOGY SYMPOSIUM NO. 23
(Proceedings of the International Symposium on the Application of Fundamental Theory to Problems of Biology and Pharmacology)

1997 QUANTUM CHEMISTRY SYMPOSIUM NO. 31
(Proceedings of the International Symposium on Atomic, Molecular, and Condensed Matter Theory and Computational Methods)
QUANTUM BIOLOGY SYMPOSIUM NO. 24
(Proceedings of the International Symposium on the Application of Fundamental Theory to Problems of Biology and Pharmacology)

All of the above symposia can be individually purchased from the Subscription Department, John Wiley & Sons.

Guidelines for Electronic Submission

The *International Journal of Quantum Chemistry* strongly encourages authors to deliver the revised version of their manuscripts (text, tables and, if possible, illustrations) on diskette.

Text

- Storage medium: 3½" (preferred) or 5¼" diskette in IBM MS-DOS, Windows, or Macintosh format.
- Software and format: Microsoft Word 6.0 is preferred, although manuscripts prepared using any other microcomputer wordprocessor are acceptable. Refrain from complex formatting; the Publisher will style your manuscript according to the *International Journal of Quantum Chemistry* design specifications. Do not use desktop publishing software such as Aldus Pagemaker or QuarkXPress. If you prepared your manuscript using one of these programs, export the text to a wordprocessing format. Please make sure your wordprocessing program's "fast save" feature is turned off.
- File names: Submit the text and tables of each manuscript as a single file. Name each file with your last name (up to eight letters). Text files should be given the three-letter extension that identifies the file format. Macintosh users should maintain the MS-DOS "eight dot three" file-naming convention.
- Labels: Label all diskettes with your name, the file name, and the wordprocessing program and version used.
- Paper copy: Accompany all files with a printed paper copy.

Illustrations

- Storage medium: Submit as separate files from text files, on separate diskettes or cartridges. 3½" diskettes, Iomega Zip, and 5¼" 44- or 88-MB SyQuest cartridges can be submitted. At authors' request, cartridges and diskettes will be returned after publication.
- Software and format: The preferred formats are TIFF or EPS with pict or tiff preview, although any format that is in general use that is not application-specific is acceptable.
- Resolution: Journal quality reproduction will require greyscale and color files at resolutions yielding approximately 300ppi. Bitmapped line art should be submitted at resolutions yielding 600–1200 ppi. These resolutions refer to the output size of the file; if you anticipate that your images will be enlarged or reduced, resolutions should be adjusted accordingly.
- File names: Illustration files should be given the 2- or 3-letter extension that identifies the file format used (i.e., TIFF, EPS, RGB, etc.).
- Labels: Label all diskettes and cartridges with your name, the file names, formats, sizes, and compression schemes (if any) used. Hard copy output must accompany all files.

Manuscripts and illustrations not conforming to the style of this journal will be returned to the author for reworking, thus delaying their appearance.

??? Questions ???

Sheila Kaminsky
Email: SKaminsk@Wiley.com
Telephone: 212-850-6540
Fax: 212-850-6052



COPYRIGHT TRANSFER AGREEMENT

Date:

To:

Production/Contribution
ID# _____
Publisher/Editorial office use only

Re: Manuscript entitled _____
_____ (the "Contribution")
for publication in _____ (the "Journal")
published by John Wiley & Sons, Inc.

Dear Contributor(s):

Thank you for submitting your Contribution for publication. In order to expedite the publishing process and enable the Publisher to disseminate your work to the fullest extent, we need to have the following copyright transfer agreement signed and returned to us as soon as possible. If the Contribution is not published in any edition of the Journal, the Agreement shall be null and void.

A. The Contributor hereby transfers to John Wiley & Sons. Inc. (the " Publisher"), during the full term of copyright, the full and exclusive rights comprised in the copyright in and to the Contribution, including but not limited to the right to publish, republish, transmit, sell, distribute and otherwise use the Contribution and the material contained therein in electronic and print editions of the Journal and all derivative works, therefrom throughout the world, in all languages and in all media of expression now known or later developed, and to license or permit others to do so.

B. Notwithstanding the above, the Contributor retains all proprietary rights other than copyright, such as patent rights, in any process, procedure or article of manufacture described in the Contribution.

C. The publisher grants back to the Contributor the following:
   1. The right to make and distribute copies of all or part of the Contribution for the Contributor's use in teaching.
   2. The right to use, *after publication* in the Journal, all or part of the material from the Contribution in a book by the Contributor, or in a collection of the Contributor's work.
   3. The royalty-free right to make copies of the Contribution for internal distribution within the institution/company that employs the Contributor subject to the provisions of paragraph E below for a work-made-for hire.
   4. The right to use figures and tables from the Contribution, and up to 250 words of text, for any purpose.
   5. The right to make oral presentations of material from the Contribution.

D. In the case of a Contribution prepared under U.S. Government contract or grant, the U.S. Government may reproduce, royalty-free, all or portions of the Contribution and may authorize others to do so, for official U.S. Government purposes only, *if the U.S. Government contract or grant so requires.*

E. If the Contribution was written by the Contributor as a work-made-for-hire in the course of employment, the Contribution is owned by the company/employer which must sign this Agreement in the space provided below. In such case, the company/employer hereby transfers and assigns to the Publisher the full and exclusive rights in the Contribution specified in paragraph A above. In addition to the rights specified as retained in paragraph B above, the Publisher hereby licenses back to such company/employer, its subsidiaries and divisions, the royalty-free right to use and distribute the Contribution internally or for promotional and non-commercial purposes only. Copies so made shall not be available for re-sale but may be included by the company/employer as part of an information package for licensing purposes.

F. The Contributor and the company/employer agree that any and all copies of the Contribution or any part thereof published under the terms of paragraphs C and E will include a notice of copyright in the Publisher's name and a citation to the Journal.

G. The Contributor represents that the Contribution is the Contributor's original work. If the Contribution was prepared jointly, the Contributor agrees to inform the co-Contributors of the terms of this Agreement and to obtain their signature to this Agreement or their written permission to sign on their behalf. The Contribution is submitted only to this Journal and has not been published before. (If excerpts from copyrighted works are included, the Contributor will obtain written permission from the copyright owners and show credit to the sources in the Contribution.) The Contributor also warrants that the Contribution contains no libelous or unlawful statements, does not infringe on the rights of others, or contain material or instructions that might cause harm or injury.

Check one:

_____ Contributor-owned work

_____ Work-made-for-hire for Employer

_____ U.S. Government work

_____ Contributor's signature _____ Date

_____ Typed or printed name and title

_____ Co-contributor's signature _____ Date

_____ Typed or printed name and title

_____ Institution or company (Employer-for-Hire) _____ Date

_____ Authorized signature of Employer

ATTACH ADDITIONAL SIGNATURE PAGE AS NECESSARY

Note to U.S. Government Employees

A Contribution prepared by a U.S. federal government employee as part of his/her official duties is called a "U.S. Government work." and is in the public domain in the United States. In such case, Paragraph A above applies only outside the United States. If the Contribution was not prepared as part of the employee's duties, it is not a U.S. Government work.

If the Contribution was prepared jointly, and any co-contributor is not a U.S. government employee, *the Contribution is not a U.S. Government work.* In such case, the co-contributor who is not a non-U.S. government employee should be delegated in writing by the other co-contributors to sign this Agreement on their behalf.

International Journal of Quantum Chemistry
Information for Contributors

1. Manuscripts should be submitted in triplicate and accompanied by an executed Copyright Transfer Form to the Editorial Office, International Journal of Quantum Chemistry, Quantum Chemistry Group, University of Uppsala, Box 518, S-75120 Uppsala, Sweden. Authors may also submit manuscripts to the Editorial Office, International Journal of Quantum Chemistry, Quantum Theory Project, 362 Williamson Hall, University of Florida, Gainesville, Florida 32611.

   All other correspondence should be addressed to the Publisher, Professional, Reference, & Trade Group, John Wiley & Sons, Inc., 605 Third Ave., New York, NY 10158.

2. It is the preference of the Editors that papers be published in the English language. However, if the author desires that his paper be published in French or German, it is necessary that a particularly complete and comprehensive synopsis be furnished in English.

3. Manuscripts should be submitted in triplicate (one *original*, two carbon copies) typed *doubled spaced* throughout and on one side of each sheet only, on a *heavy* grade paper with margins of at least 2.5 cm on all sides. Copyright: No article can be published unless accompanied by a signed publication agreement, which serves as a transfer of copyright from author to publisher. A publication agreement may be obtained from the editor or the publisher. A copy of the publication agreement appears in most issues of the journal. Only original papers will be accepted and copyright in published papers will be vested in the publisher. It is the author's responsibility to obtain written permission to reproduce material that has appeared in another publication. A copy of that agreement, executed and signed by the author, is now required with each manuscript submission. (If the article is a "work made for hire," the agreement must be signed by the employer.)

4. A short synopsis (maximum length 200 words) is required. The synopsis should be a summary of the entire paper, not the conclusions alone. If the paper is written in French or German, a synopsis in English should also be prepared. The paper should be reasonably subdivided into sections and, if necessary, subsections.

5. A list of five key words or phrases for indexing must accompany each submission.

6. Authors are cautioned to type—wherever possible—all mathematical and chemical symbols, equations, and formulas. If these must be handwritten, please print clearly and leave ample space above and below for printer's marks; please use only ink. All Greek or unusual symbols should be identified in the margin the first time they are used. Please distinguish in the margins of the manuscript between capital and small letters of the alphabet wherever confusion may arise (e.g., k, K, k). Please underline with a wavy line all vector quantities. Use fractional exponents to avoid root signs.

   The nomenclature sponsored by the International Union of Pure and Applied Chemistry is requested for chemical compounds. Unit abbreviations should follow the practices of the American Institute of Physics. Chemical bonds should be correctly placed, and double bonds clearly indicated. Valence is to be indicated by superscript plus and minus signs.

7. The references should be numbered consecutively in the order of their appearance and should be complete, including authors' initials and—for unpublished lectures or symposia—the title of the paper, the date, and the name of the sponsoring society. Please compile references on a separate sheet at the end of the manuscript. Abbreviations of journal titles should conform to the *Bibliographic Guide for Editors & Authors* published by the American Chemical Society.

   References should be limited to literature citations. Explanatory or supplementary material should be treated either as footnotes to text or appendices. Examples:

   [1] D. N. Zubarev, *Nonequilibrium Statistical Thermodynamics* (Consultants Bureau, Plenum, New York, 1974).

   [2] H. Adachi, M. Tsukada, and C. Satoko, J. Phys. Soc. Jpn. **45**, 875 (1978).

   [3] K. Fukui, T. Yonezawa, C. Nagata, H. Katou, A. Imamura, and K. Morokuma, in *Introduction to Quantum Chemistry* (Kagakudojin, Kyoto, 1963), Vol. 1, p. 197.

8. A limited number of color figures that are of critical importance and that significantly enhance the presentation will be considered for publication at the publisher's expense. Color separations or

transparencies (negatives or positives) are optimal. Color slides are preferable to color prints. Any cropping of the color figure should be clearly indicated. Final decision on publication of color figures will be at the discretion of the Editor.

9. Each table should be supplied on a separate sheet (not interspersed with text). Please supply numbers and titles for all tables. All table columns should have an explanatory heading.

10. Please supply legends for all figures and compile these on a separate sheet.

11. Figures should be professionally prepared and submitted in a form suitable for reproduction (camera-ready copy). Computer-generated graphs are acceptable only if they have been printed with a good quality laser printer. Artwork is generally reduced so that the type in the figures is about 2.5 mm high. The maximum final size of figures for this journal is 16 x 21 cm after reduction. Good glossy photographs are required for halftone reproductions. If in doubt about the preparation of illustrations suitable for reproduction, please consult the publisher at the address given in paragraph 1.

12. Senior authors will receive 50 reprints of their articles without charge. Additional reprints can be ordered and purchased by filling out the form enclosed with the proof.

13. The publisher will do everything possible to ensure prompt publication. It will therefore be appreciated if manuscripts and illustrations conform from the outset to the style of the journal. Contributors should use the *Style Manual* of the American Institute of Physics; papers will otherwise have to be returned to the author for revision.

    Corrected proofs must be sent back to the publisher within two days to avoid the risk of the author's contribution having to be held over to a later issue.

WILEY PHYSICS

ALGEBRAIC METHODS IN MOLECULAR & NUCLEAR STRUCTURE PHYSICS

by Alejandro Frank, Universidad National Autónoma de México and Pieter Van Isacker, University of Surrey, England and Grand Accélérateur National d'Ions Lourds, France

This book provides the basic technical background required in the applications of algebraic models in nuclear physics with an emphasis on group-theoretical techniques. The material is divided into three parts of increasing mathematical complexity. Part I is designed to familiarize the reader with concepts and terminology of group theory as well as with the basic features of boson-fermion systems. Part II is devoted to the study of molecular algebraic models and Part III deals with the interacting boson model of nuclear structure.

Contents:

Part I, Schematic Models: Identical Bosons • Non-identical Bosons • Bosons and Fermions • Supersymmetry and F Spin.

Part II, Molecular Models: Diatomic Molecules • Triatomic Molecules • Bose-Fermi Symmetries and Molecular Electronic Spectra.

Part III, Nuclear Models: The Interacting Boson Model • The Neutron-Proton Interacting Boson Model • The Interacting Boson-Fermion Model • Group Theory and the Algebraic Approach • The Unitary and Orthoganal Algebras • Dragt's Theorem

1994 • 488pp. • 0-471-52640-1 • $64.95

ANGULAR MOMENTUM

An Illustrated Guide to Rotational Symmetries for Physical Systems

by William J. Thompson, University of North Carolina, Chapel Hill

Pedagogically consistent and self-contained, this extensively illustrated guide to rotational symmetries is an excellent learning aid for students of physics, chemistry, and mathematics, as well as a valuable resource for researchers in the physical sciences and applied mathematics. Includes *Mathematica* software that allows you to create vivid images of rotational symmetries.

Contents: The Computer Interface • Symmetry in Physical Systems • Mathematical and Quantal Preliminaries • Rotational Invariance and Angular Momentum • Angular Momentum Eigenstates • Angular Momentum in Quantum Systems • Finite Rotations of Angular Momentum Eigenstates • Combining Two Angular Momentum Eigenstates • Irreducible Spherical Tensors and Spin • Recombining Several Angular Momentum Eigenstates

1994 • 461pp. • 0-471-55264-X • $64.95

PRINCIPLES OF SYMMETRY, DYNAMICS, AND SPECTROSCOPY

by William G. Harter, University of Arkansas, Fayetteville

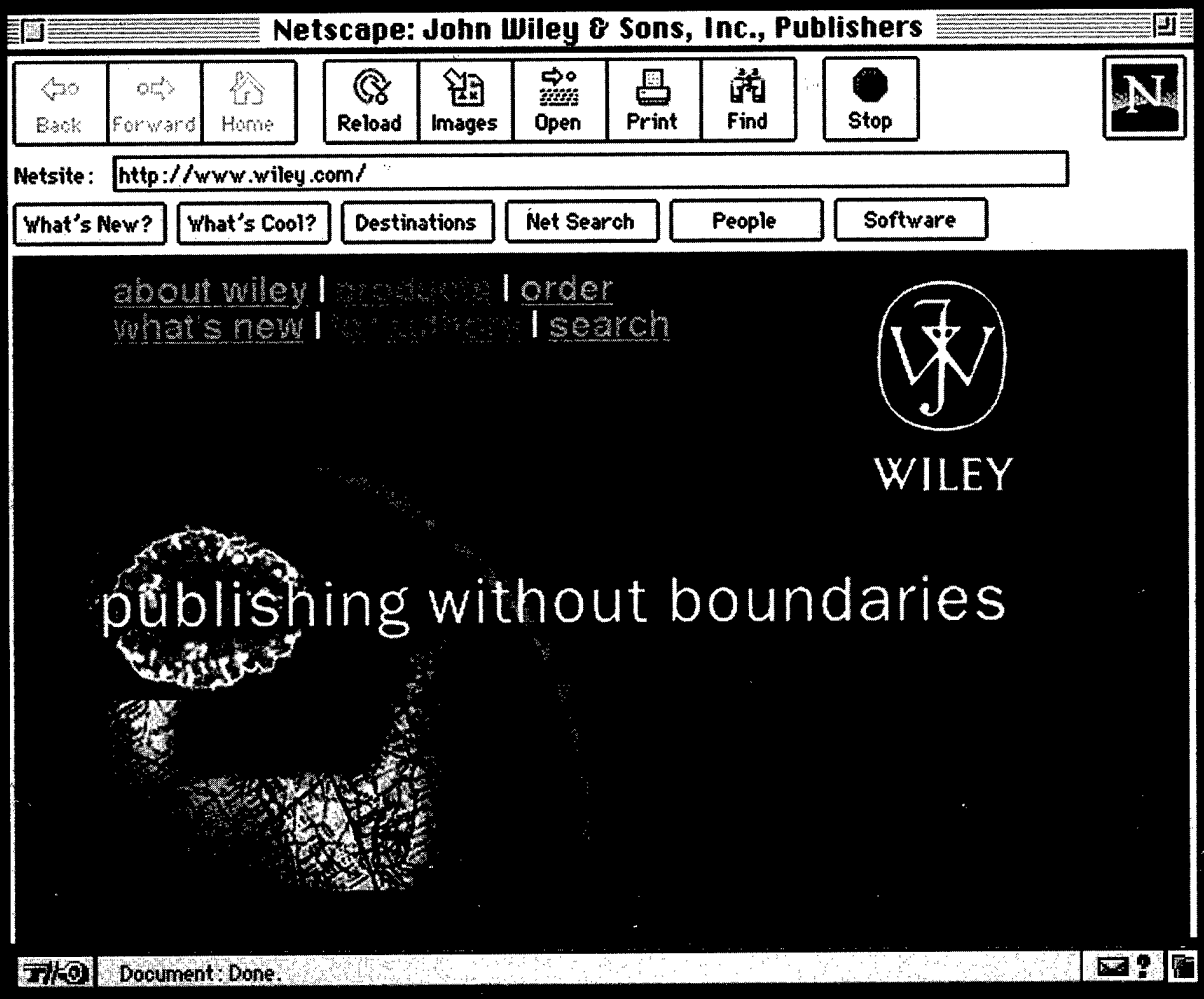
This book is designed to explain the applications of group theory and symmetry analysis to physics by using a novel physical approach. Prof. Harter breaks down the complex mathematics of group theory representation by first introducing the simplest physical problem to show and prove each mathematical concept. These important mathematical quantities are discussed and derived after their need is demonstrated by a physical problem. This approach enables the reader to tackle more complex problems by synthesizing simpler mathematical concepts. This book is a valuable contribution to the rapidly growing field of laser spectroscopy.

Contents: A Review of Matrix Algebra and Quantum Mechanics • Basic Theory and Applications of Symmetry Representations (*Abelian Symmetry Groups*) • Basic Theory and Applications of Symmetry Representations (*Non-Abelian Symmetry Groups*) • Theory and Applications of Higher Finite Symmetry and Induced Representations • Representations of Continuous Rotation Groups and Applications • Theory and Applications of Symmetry Representation Products (*Finite Groups*) • Theory and Application of Symmetry Representation Products (*Continuous Rotation Groups*) • Symmetry Analysis for Semiclassical and Quantum Mechanics: Dynamics with High Quanta

1993 • 846pp. • 0-471-05020-2 • $125.00

JOHN WILEY & SONS, INC.
605 THIRD AVENUE, NEW YORK, NY 10158-0012
To order by phone: (800) 879-4539; To order by fax: (201) 302-2300; Other inquiries (212) 850-6418
Prices subject to change and may be slightly higher outside U.S.A.

JOIN WILEY ONLINE



Drop in and explore. Get the very latest information on new books, journals, and other publications along with special promotions and publicity. Discover a variety of online services, including online journals. Download a sample chapter or software. And much more.

STOP BY TODAY!
www.wiley.com/

WILEY
Publishers Since 1807

0020-7608(1997)65:5;1-1